REPORT DOCUMENTATION PAGE

AFRL-SR-BL-TR-00-

0554

Public reporting burden for this collection of information is estimated to average 1 hour per response, including t
gathering and maintaining the data needed, and completing and reviewing the collection of information. Send cc
collection of information, including suggestions for reducing this burden, to Washington Headquarters Services,
Davis Highway, Suite 1204, Arlington, VA 22202-4302, and to the Office of Management and Budget, Paperwork Reduction ...

ces, this rson

1. AGENCY USE ONLY (*Leave Blank*)	2. REPORT DATE	3. REPORT TYPE AND DATES COVERED
	22 Sep 2000	Final Technical 15 Mar 96 – 30 Sep 99

4. TITLE AND SUBTITLE
Optoelectronics Research Center

5. FUNDING NUMBERS
G
F49620-96-1-0079

6. AUTHORS
S.R.J. Brueck, etal

7. PERFORMING ORGANIZATION NAME(S) AND ADDRESS(ES)
The University of New Mexico
Center for High Technology Materials
1313 Goddard SE
Albuquerque, NM 87106

8. PERFORMING ORGANIZATION REPORT NUMBER
FT34634X

9. SPONSORING / MONITORING AGENCY NAME(S) AND ADDRESS(ES)
Air Force Office of Scientific Research/NE
801 North Randolph Street, Room 732
Arlington, VA 22203-1977

10. SPONSORING / MONITORING AGENCY REPORT NUMBER

11. SUPPLEMENTARY NOTES

12a. DISTRIBUTION / AVAILABILITY STATEMENT
Unlimited

12b. DISTRIBUTION CODE

13. ABSTRACT *(Maximum 200 words)*

The AFOSR Optoelectronics Research Center maintains a broadly based program at the forefront of optoelectronics with efforts in linear and nonlinear materials, device processing, device design, and in device integration. Examples of materials and structures are quantum dots, superlattices, digital alloys, and strained-layer semiconductors, and new nonlinear materials. Processing developments relate to smaller dimensions and improved techniques for the selective deposition, modification and removal of materials. Improved devices, based both on semiconductors and on fibers, also result from increased understanding of the underlying device and material physics and from innovative approaches to device design and synthesis.

14. SUBJECT TERMS	15. NUMBER OF PAGES
optoelectronics	47
	16. PRICE CODE NSP

17. SECURITY CLASSIFICATION OF REPORT	18. SECURITY CLASSIFICATION OF THIS PAGE	19. SECURITY CLASSIFICATION OF ABSTRACT	20. LIMITATION OF ABSTRACT
UNCLASSIFIED	UNCLASSIFIED	UNCLASSIFIED	UNL

NSN 7540-01-280-5500

Standard Form 298 (Rev. 2-89)
Prescribed by ANSI Std. Z39-1
298-102

...TIFIC
...TIAL TO DTIC. THIS
...REVIEWED
...LEASE
...ON IS
...N
...MANAGER

DTIC QUALITY INSPECTED 4

20001030 093

Final Report

Optoelectronics Research Center

Grant #F49620-96-1-0079

For the Period
March 15, 1996 to September 30, 1999

Submitted To:
Air Force Office of Scientific Research

Submitted By:
S.R.J. Brueck, Principal Investigator
Center for High Technology Materials
The University of New Mexico
Albuquerque, NM 87131

Abstract:

The AFOSR Optoelectronics Research Center maintains a broadly based program at the forefront of optoelectronics with efforts in linear and nonlinear materials, device processing, device design, and in device integration. Examples of materials and structures are quantum dots, superlattices, digital alloys, and strained-layer semiconductors, and new nonlinear materials. Processing developments relate to smaller dimensions and improved techniques for the selective deposition, modification and removal of materials. Improved devices, based both on semiconductors and on fibers, also result from increased understanding of the underlying device and material physics and from innovative approaches to device design and synthesis.

I. Introduction

The *Optoelectronics Research Center* (OERC) at the University of New Mexico that was begun in FY87 under the auspices of the Air Force Office of Scientific Research. has functioned in conjunction with the *Center for High Technology Materials* (CHTM), which is being supported by the State and University of New Mexico, and with the *Optoelectronic Materials Center*, which is funded by DARPA. CHTM is an interdisciplinary research organization with faculty and research representation from three departments: Electrical Engineering, Physics, and Chemistry. Since its inception, the AFOSR OERC has become a leading university optoelectronics program with substantial impact on the development of the field.

The goal of the AFOSR OERC is to continue to be at the forefront of advances in optoelectronics. The coupling and increasing merger of optics and electronics has already had important consequences, but the major advances which will occur over the next decade will dwarf those seen to date. These will result from advances in linear and nonlinear materials, device processing, device design, and in device integration. Examples of materials and structures are quantum dots, superlattices, digital alloys, and strained-layer semiconductors, and new nonlinear materials. Processing developments relate to smaller dimensions and improved techniques for the selective deposition, modification and removal of materials. Improved devices also result from increased understanding of the underlying device and material physics and from innovative approaches to device design and synthesis.

Major accomplishments are highlighted in the next section. Section II includes more detailed descriptions. Finally the appendix containing reprints of publications and conference presentations provides much more in-depth reporting of our results.

Major accomplishments include:

A. Quantum Dot and Antimonide Based Diode Lasers

- 2-μm wavelength AlGaAsSb/GaInAsSb multiple quantum well lasers with140K characteristic temperature.
- 1.25-μm quantum dot lasers with ultra-low linewidth enhancement factor (0.1) and threshold current density (16 A/cm^2).
- Studies of the dependence of bandedge emission and electron-hole overlap in type III GaSb/InAs heterojunctions.

B. Vertical Cavity Surface Emitting Lasers (VCSELs) and Subsystem Applications

- Developed a new and reliable technique for achieving quasi-planar oxide-confined microcavity lasers with micron-sized apertures and submilliampere threshold currents.
- Achieved high-performance microcavity VCSELs with different active area geometries and a higher packing density using the etched-trench oxidation technology.
- Achieved high speed oxide-confined VCSELs with low parasitics and a maximum modulation bandwidth of up to 16 GHz.
- Achieved efficient (>32%), low-power dissipation (0.2 mW at threshold) cryogenic VCSELs optimized for low temperature operation (6K to 200 K) using an oxide-confined design with double intracavity contacts, with low operating voltage (<1.5V), submilliampere threshold current (~ 0.15 mA) and high slope efficiency (70 %).

- Achieved long-wavelength semiconductor lasers emitting in the 1.1 μm wavelength region) using multiple InGaAsN/GaAs quantum wells grown on a GaAs substrate by MOCVD. Efficient cw lasing was achieved at temperatures up to 60°C, with high power (>25 mW per facet) and high slope efficiency (25% per facet) at room temperature, and a large characteristic temperature (125 K).
- Efficient, continuous-wave lasing operation of narrow-stripe, oxide-confined, long-wavelength InAs quantum dot lasers in the ground state ($\lambda \approx 1.28$ μm) has been achieved at temperatures up to 100°C, with a very low threshold current density ($J_{th} = 24$ A/cm^2) and high differential quantum efficiency (55%).

C. Mid-IR Fiber Laser and Advanced Fiber Optic Devices

- Demonstrated an efficient and novel depopulation mechanisms for the lower laser level via cross-relaxation (#1) of Er ions at high doping densities and energy transfer to co-doped Pr ions.
- Reported the first observation of passive Q-switching (7 μs pulsewidth, 35 kHz repetition rate) of a mid-IR Er-ZBLAN fiber laser
- Passive Q-switching was achieved by using a liquid gallium mirror as a saturable absorber.
- Demonstrated electro-optic tuning of a FBG fabricated in a thermally-poled fiber. 40 pm of tuning was achieved, corresponding to an electro-optic coefficient of 0.25 pm/V.
- First demonstration of an 2x2 all-fiber electroooptic switch.

D. Nanoheteroepitaxy

- Invented Nanoheteroepitaxy for the elimination of defects in highly mismatched heterostructures
- Developed original theory of Nanoheteroepitaxy
- Demonstrated experimentally many of the predictions of Nanoheteroepitaxy for GaN on Si heterostructures.

II. Detail Description of Technical Results

A. Antimodide Based Diode Lasers

The effect of doping on wave-function overlap and band-edge energy in type III InAs/GaSb structures has been analyzed in this project within the grant. By varying the dopant concentration in type III InAs/GaSb quantum wells, an order of magnitude increase in electron-hole wave function overlap and a significant band edge shift are demonstrated using a self-consistent Schrödinger-Poisson solver. InAs/GaSb type III quantum well structures are of current interest as active regions for mid-IR semiconductor lasers because of their relative simplicity in crystal growth compared to quantum cascade, "W", or type-II interband cascade lasers. InAs/GaSb type III structures, however, rely on spatially-indirect overlap of electron and hole wave functions, which can be weak in non-optimized designs. Unintentionally-doped InAs/GaSb heterojunctions provide little band bending leaving the holes in the GaSb far away from the InAs/GaSb interface. In this case, a modest overlap can only be achieved by growing very thin layers of InAs, providing substantial gain only for near-IR wavelengths. By intentionally doping an InAs/GaSb structure, band-bending can be substantially increased and the holes brought closer to the interface providing a substantial increase in the wave function overlap between the electrons and heavy holes. The large overlap of valence subbands makes intervalence band absorption a concern in

these structures, but these resonances occur mostly in the far-IR. This makes the InAs/GaSb system a good candidate for mid-IR applications.

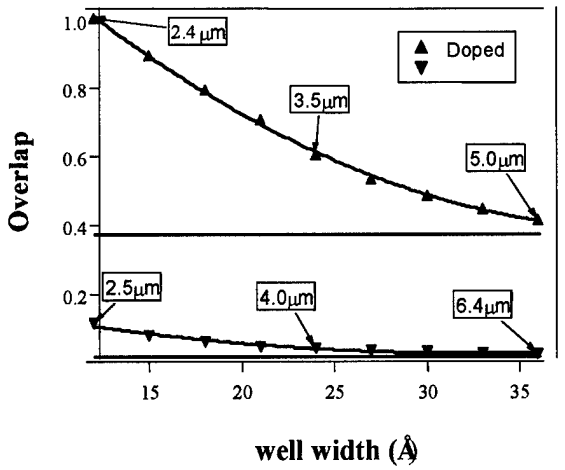


Fig. 1. The calculated wave-function overlap for InAs/GaSb multiple quantum well structures with different InAs well thicknesses for undoped and intentionally doped cases.

The baseline structure to be modeled consists of a narrow InAs well sandwiched between GaSb layers grown on a GaSb substrate. Using a self-consistent Schrödinger-Poisson solver, Fig. 1 shows the inner product (overlap) of the electron state in the InAs well with the first heavy hole subbands in the GaSb layers as a function of InAs well width. The undoped case, for which GaSb is usually unintentionally p-type and the InAs n-type, shows a very small overlap. The unintentional doping concentrations are 10^{17} cm^{-3}. The doped example has an order of magnitude larger overlap even at very long wavelengths. In this instance, both the InAs and GaSb are n-type with a concentration of 10^{17} cm^{-3}. The asymptotic overlap for both cases is shown by the dashed lines, and several emission wavelengths are tagged. With the significant increase in overlap, a substantial decrease in the lasing threshold is expected for all wavelengths.

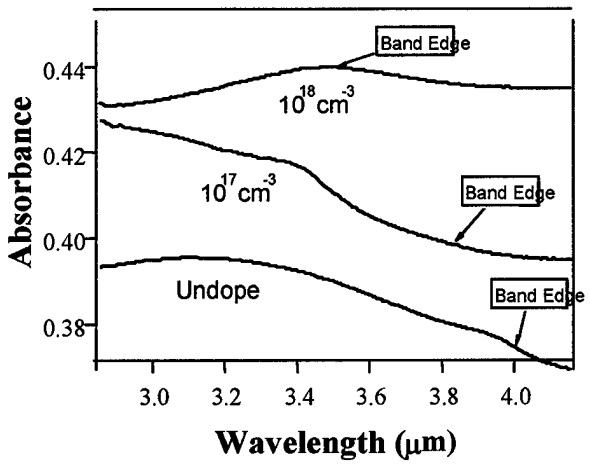


Fig. 2. FTIR absorption spectra measured at 300K for undoped and n-type doped InAs/GaSb superlattices

To monitor the shift in band edge with doping, three test structures were grown by molecular beam epitaxy on GaSb substrates with a 20 period superlattice composed of 24Å of InAs and 400Å of GaSb. Two of the samples were doped n-type with tellurium to a concentration of 10^{17} cm^{-3} and 10^{18} cm^{-3}, and the third wafer was left undoped. Room temperature FTIR data was taken from the samples and is plotted in Fig. 2 along with the calculated band edge. A clear shift in the band edge is evident, and the theoretical and experimental data agree reasonably well. The ability to tailor the wavelength by shifting the heavy hole energies with doping is of particular importance for this system because then the strained InAs well thickness can be optimized to avoid relaxation and doping can be used to tailor the operating wavelength.

In conclusion, it has been shown that doping has a profound effect on the overlap and band edge energy in type III InAs/GaSb quantum wells. Auger recombination should not be substantially increased in these structures because the doping is necessary only in the immediate vicinity of the heterojunction.

B. Extremely Low Room-Temperature Threshold Current Density Diode Lasers Using InAs Dots in an $In_{.15}Ga_{.85}As$ Quantum Well

It has been predicted that the threshold current density of quantum dot lasers should be lower than that of quantum well lasers due to the reduction of density of states.[1] In particular, efforts have been made in the past few years to reduce the threshold current density of quantum dot lasers on GaAs substrates.[2,3] A recently developed approach is to put the InAs dots in a strained $In_{0.2}Ga_{0.8}As$ quantum well.[iii,4] This "dot in a well" (DWELL) design not only improves carrier capture by the dots, but also increases the density of quantum dots (to $7x10^{10}$ cm^{-2}) over growth on GaAs directly. Consequently, ground state lasing from a single layer of dots is possible at reasonable cavity lengths. While competition with radiative quantum well transitions was suggested as a concern,[5] quantum well transitions were not observed in previous work[iii] or in this study. In this letter, further improvements have been made by putting a single layer of InAs quantum dots into a strained $In_{0.15}Ga_{0.85}As$ quantum well. An extremely low threshold current density of 26 A cm^{-2} has been achieved for a 7.8 mm cavity length, cleaved facet laser. Other operating characteristics of these DWELL lasers are described below.

Device Structures and Growth

The laser structure was grown by solid-source molecular beam epitaxy (MBE) on a ⟨100⟩ n^+-GaAs substrate. The laser structure was the same as reported in Ref. [iii] except that $In_{.15}Ga_{.85}As$ was used as the quantum well. The epitaxial structure consists of an n-type (10^{18} cm^{-3}) 300 nm thick GaAs buffer, a 2 μm n-type ($10^{17}cm^{-3}$) lower $Al_{0.7}Ga_{0.3}As$ cladding layer, a 230 nm thick GaAs waveguide surrounding the laser active region, a 2 μm p-type ($10^{17}cm^{-3}$) upper cladding layer, and a p^+–doped ($3x10^{19}$ cm^{-3}) 60 nm thick GaAs cap. This cavity was a low-loss design following Ref. [6]. In the center of the waveguide, an equivalent coverage of 2.4 monolayers of InAs results in quantum dots grown approximately in the middle of the 100 Å $In_{.15}Ga_{.85}As$ quantum well. The quantum dots and quantum well were grown at 510 °C, and all other layers were grown at 610 °C, as measured by an optical pyrometer.

Room temperature photoluminescence (PL) result is shown in Fig.3. The PL linewidth is 37 meV and has been reduced compared with Ref. [iii]. No emission from the quantum well is ob-

served, providing clear proof of minimal competition from quantum well radiative transitions. This implies that the relaxation time from the quantum well to the quantum dots is much faster than the spontaneous lifetime of the quantum well.

Results

Broad area lasers with 100 μm stripe widths were fabricated from this structure. The wafer was then cleaved into 7.8 mm long laser bars. All devices were tested with the epi-side up on a thermoelectric cooler using pulsed excitation. The pulse width was 300 ns with a duty cycle of 0.5%. The temperature of the thermoelectric cooler was set to be 20 °C. The single facet output L-I curve from a typical bar is shown in Fig.4. The lasing threshold current is 200 mA, which corresponds to a threshold current density of 26 A cm^{-2}. The external quantum efficiency is 31%. The lowest previously reported threshold current densities for quantum wells lasers were around 50 A cm^{-2}.[7,8] The near-threshold lasing spectrum at three different injection current levels, 0.90 I_{th} (180mA), 0.95 I_{th} (190mA) and I_{th} (200mA) was measured by an optical spectrum analyzer (OSA) and is shown in Fig. 5. The lasing wavelength is 1.25 μm. Clear spectral narrowing can be observed at 0.95 I_{th} (190mA). A much broader spectrum was also taken at five times the threshold current and is shown in Fig. 6. No emission from the quantum well layer is observed, again suggesting the lack of radiative competition from the quantum well and the rapid capture of carriers by the dots from the well. The dependence of the threshold current on temperature was also measured and is shown in Fig. 7. The characteristic temperature, T_0, is 60 K between 10 °C and 50 °C, and decreases significantly to 34.5 K between 50 °C and 80 °C. Carrier heating out of the quantum well may be one reason the T_0 value of this laser is smaller than predicted T_0 values for quantum dot lasers.[i]

Conclusion

We have demonstrated an extremely low threshold current density DWELL laser with a single layer of InAs quantum dots in an $In_{.15}Ga_{.85}As$ quantum well. This is the first time that the threshold current density performance of quantum dot lasers surpasses that of quantum well lasers. Experimental evidence suggests that the relaxation time from the quantum well to the quantum dots is much shorter than the spontaneous lifetime of the quantum well. The T_0 value for these DWELL lasers is 60 K between 10 °C and 50 °C.

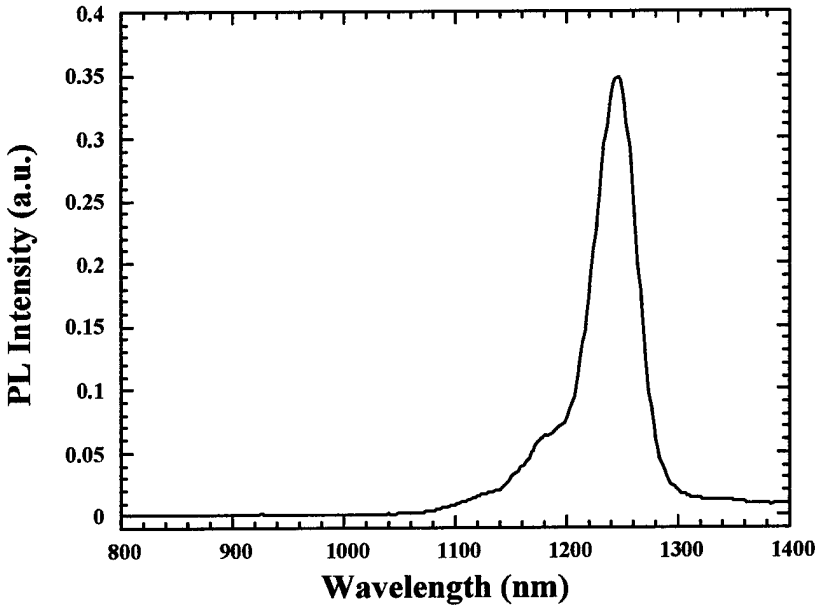


Fig. 3: Photoluminescence spectrum of the laser wafer. No emission from the quantum well is observed. The FWHM is 37 meV.

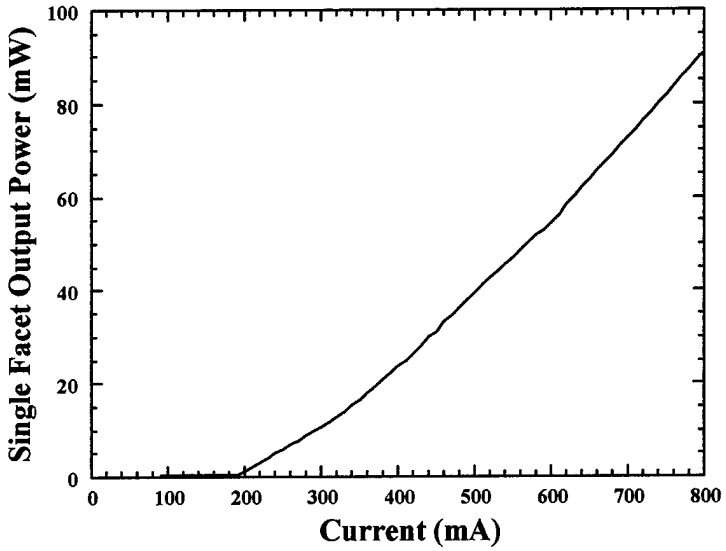


Fig. 4: Single facet output L-I curve of a 7.8 mm cavity length laser. The threshold current density is 26 A cm^{-2}. The external efficiency is 31%.

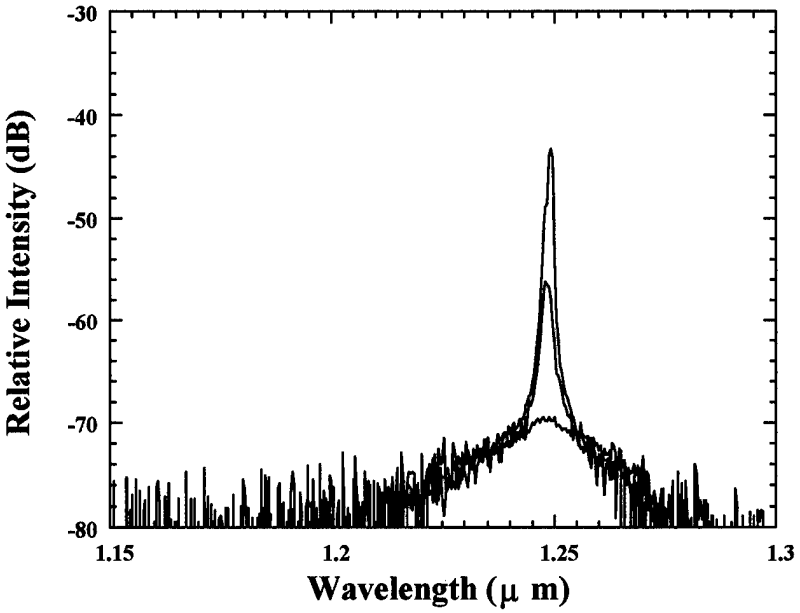


Fig. 5: Lasing spectrum at 0.90 I_{th} (180 mA), 0.95 I_{th} (190 mA), and I_{th} (200 mA).

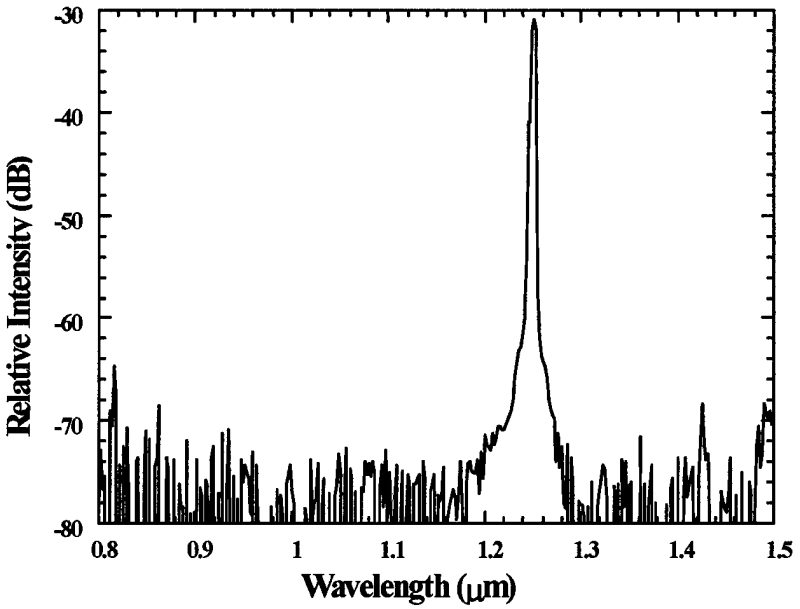


Fig. 6: Lasing spectrum at five times the threshold current density. No emission from the well is observed.

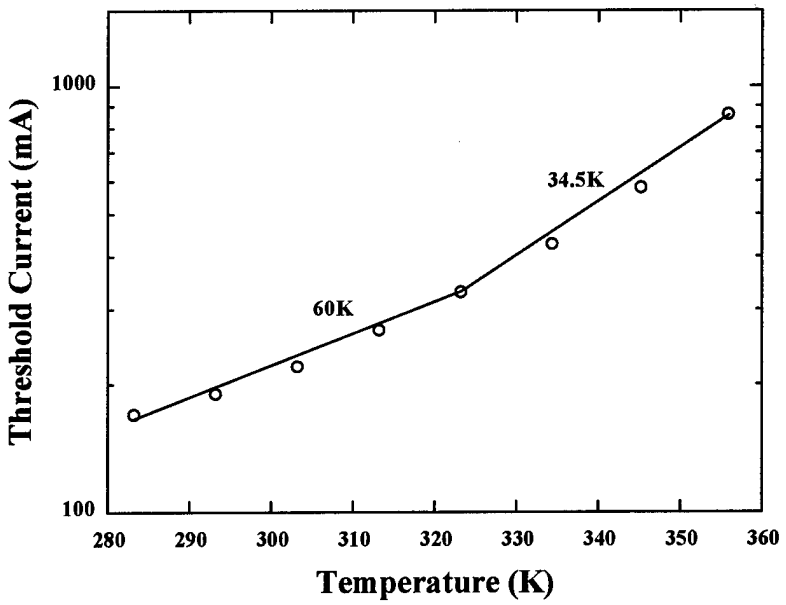


Fig. 7: The threshold current and T_o as a function of temperature for the 7.8 mm cavity length device.

C. High Performance Surface-Emitting Lasers and Integrated VCSEL Arrays

For the monolithic integration of large VCSEL arrays, power dissipation is a critical limiting factor for dense array operation, and individual VCSELs must have a very low current density. In order to reduce the power dissipation, we need to reduce the lasing threshold to a submilliampere, almost threshold-less level. This requires a combination of more effective current confinement, a smaller lasing volume, and better mode control through index guiding. Novel VCSEL structures have been investigated to achieve these objectives. The achievement of VCSEL arrays with low power dissipation is described below.

Efficient, Low-Power-Dissipation VCSELs:

Planarity is desirable for the monolithic integration of VCSELs, and low power dissipation is required for dense arrays. To minimize power dissipation, oxide-confined VCSELs with small active areas and low operating currents have been developed. In conventional (non-planar) oxide-confined VCSELs, the active area is defined by the lateral wet oxidation of the high aluminum content layers from the periphery of an etched mesa, with a typical oxidation length that is ~10-20 μm. Minimizing the thermal and electrical resistances dictate a large mesa size, which requires a longer oxidation time and greater uncertainty in the final aperture size. The oxidation time and uncertainty can be reduced without sacrificing planarity or increasing the mesa size by using a novel technique that uses local oxidation centers from which multiple oxidation fronts can proceed to define an active aperture.

We have developed a quasi-planar technology that facilitates the monolithic integration of oxide-confined VCSELs with very small active area apertures, in which a continuous oxidation front of arbitrary geometry is defined by concatenating the oxidation fronts emanating from a number of crescent-shaped trenches. This approach preserves planarity while providing improved dimensional control and increased accuracy in the production of devices with very small oxide aper-

tures (2-4 μm). The electrical and lasing characteristics of oxide-confined VCSELs fabricated using the quasi-planar etched-trench (ET) technique are in many ways comparable to those of conventional etched mesa (EM) VCSELs. However the dc lasing characteristics of the ET VCSEL arrays show greater uniformity and superior dimension control for devices as small as 2 μm. They also have higher output power and reduced thermal roll-over. Another advantage of the new ET VCSELs is the preservation of planarity without increasing device parasitics. The optical modulation response shows a -3dB bandwidth of more than 12 GHz at $10\times I_{th}$. A maximum modulation bandwidth of up to 16 GHz has been observed.

Efficient VCSEL Arrays with Very Low Threshold and Low Power Dissipation for Cryogenic Applications

VCSELs operating at cryogenic temperatures offer the promise of superior lasing performance as a result of a higher differential gain coefficient, a higher quantum efficiency, lower losses, and lower noise, resulting in a higher modulation bandwidth, lower power dissipation, and a higher power conversion efficiency. High efficiency and low power dissipation make cryo-VCSELs particularly appealing for use as a non-invasive, power-efficient optical means for transferring high-speed image data from infrared sensor arrays housed in a cryogenic environment to external electronic signal processors that may be situated locally or at some distance away. An optical link can provide both electrical and thermal isolation, as well as a larger bandwidth and a longer link span between the imaging array and the external processing electronics.

An efficient cryogenic link requires VCSELs with low operating currents and voltages that are compatible with on-board cryogenic CMOS drive circuits ($\leq$ 2 mA and 3.3 V, respectively). The efficient cw lasing operation of InGaAs/GaAs VCSELs with low threshold voltage and low power dissipation has been achieved over a wide range of cryogenic temperatures (77K to 250K) using an oxide-confinement design that employed double intracavity contacts and undoped DBRs, along with proper alignment of the cavity mode and the gain peak at low temperatures. Low operating voltages were obtained by routing current through two intra-cavity contacts to bypass both distributed Bragg reflector (DBR) mirrors, while lower optical losses were achieved by using undoped DBR mirrors with abrupt heterointerfaces. This resulted in devices with a low operating voltage (<1.5V), submilliampere threshold current (I_{th} ~ 0.15 mA) and low current density (J_{th} = 600 A/cm^2), high slope efficiency (70 %), low power dissipation ((0.2 mW at threshold, 0.81 mW for P_{out} = 0.2 mW) and a high power conversion efficiency (η_{eff} = 31%).

D. Mid-IR Fiber Laser and Advanced Fiber Optic Devices

Mid-IR Fiber Laser

Goal: Research and development of diode-pumped compact, high-power CW and pulsed, tunable mid-IR fiber lasers.

Background: The 2.7 μm transition in Er-ZBLAN is particularly attractive for the design of compact, high-power mid-IR fiber lasers of excellent beam quality as needed for applications ranging from laser surgery to countermeasures and spectroscopic monitoring. The problem with the 2.7 μm laser transition in Er (Fig. 8a) is the fact that the natural lifetime of the lower laser level (9.4 ms) is longer than that of the upper laser level (7.5 ms), leading to a population bottleneck that inhibits efficient steady-state (CW) lasing in Er:ZBLAN fiber lasers.

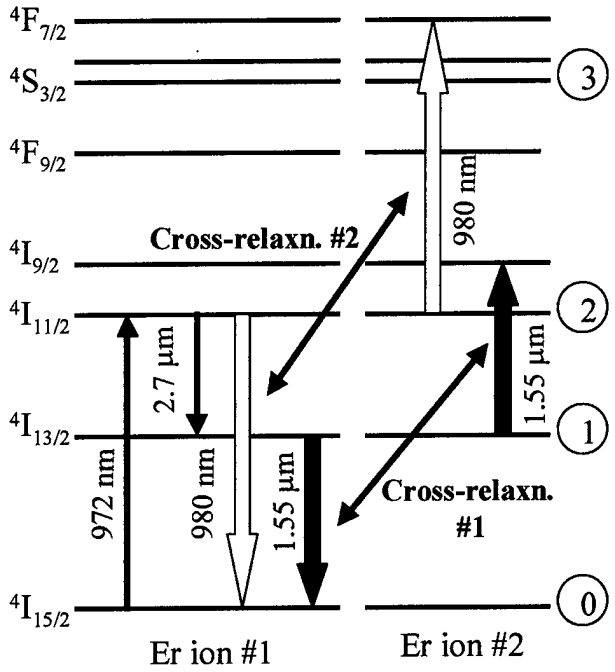


Fig. 8(a): Energy level diagram of Er showing dominant cross-relaxation

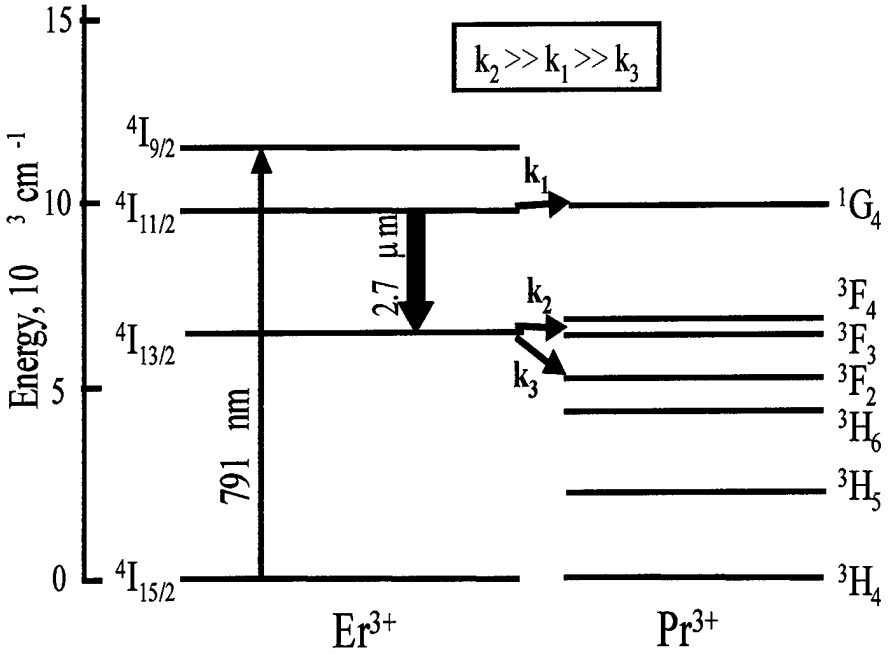


Fig. 8(b): Dominant energy transfer pathways between laser levels in Er and resonantly-matched energy levels in Pr.

Diode-pumped high-power CW mid-IR fiber lasers using cross-relaxation and energy transfer processes:

We have proposed and demonstrated an efficient and novel depopulation mechanisms for the lower laser level via cross-relaxation (#1) of Er ions at high doping densities (Fig. 8a) and energy transfer to co-doped Pr ions (Fig. 8b).

Ion clustering at high doping densities:
The cross-relaxation process in Er shown in Fig. 8a was believed to be significant only at concentrations of >150,000 ppm in bulk glasses. Such concentrations however lead to high intrinsic losses in fibers. On the other hand, our studies show significant percentage of ions in clusters even at concentrations of 10,000 ppm in fibers, thereby facilitating the cross-relaxation process to depopulate the lower laser level of the 2.7 μm transition in Er.

Key Accomplishments:
We performed a precise quantification of the percentage of ion clusters in Er-ZBLAN fibers via measurement of non-saturable optical absorption and fitting of the data to a simple theoretical model for ions in clusters (Fig. 9).

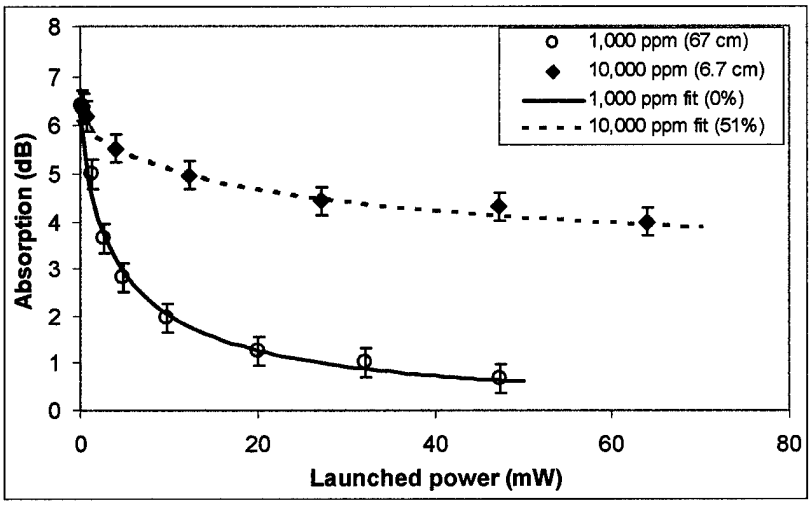


Fig. 9: Plot of the measured and calculated values of the absorption at 972 nm radiation as a function of launched power in two fibers corresponding to significantly dif-

We have demonstrated the presence of 51% ions in clusters for fibers with an average doping density of 10,000 ppm, whereas a similar fiber with an average doping density of 1,000 ppm shows negligible effects of clustering.

Single transverse mode diode pumping at 980 nm :
Key Accomplishments:
We have demonstrated a relatively efficient power-scalable 2.7 μm 10,000 ppm Er-ZBLAN fiber laser pumped by readily available 1W 980 nm laser diodes.

The 12 mW CW power levels and 6.7% slope efficiency reported are significantly higher than those reported previously for any diode-pumped mid-IR fiber laser.

The linearity of the output power even at high pump powers used indicates that this laser can be further optimized to yield much higher output powers.

Diode array pumping at 795 nm:
Key Accomplishments:
We have utilized the enhanced inter-ion cross-relaxation in 20,000 ppm double clad Er-ZBLAN fibers for the realization of high-power (400 mW) diode-pumped 2.7 μm mid-IR lasers.

The fiber laser was demonstrated with a slope efficiency of 12% with respect to the absorbed power and a threshold of 250 mW.

Diode-pumped high-power CW mid-IR fiber lasers using cross-relaxation and energy transfer processes:
Key Accomplishments:
We have utilized energy transfer to Pr ions along with enhanced inter-ion cross-relaxation to de-populate the lower laser level more efficiently.
We have demonstrated a high power (660 mW) CW operation of a diode-pumped 20,000 ppm/5,000 ppm Er/Pr:ZBLAN 2.7 μm fiber laser with a slope efficiency of 13% with respect to the absorbed power (Fig. 10). The linearity of the plot clearly indicates scalability to multi-Watt power levels using high pump powers or more efficient pump coupling and pump absorption techniques.

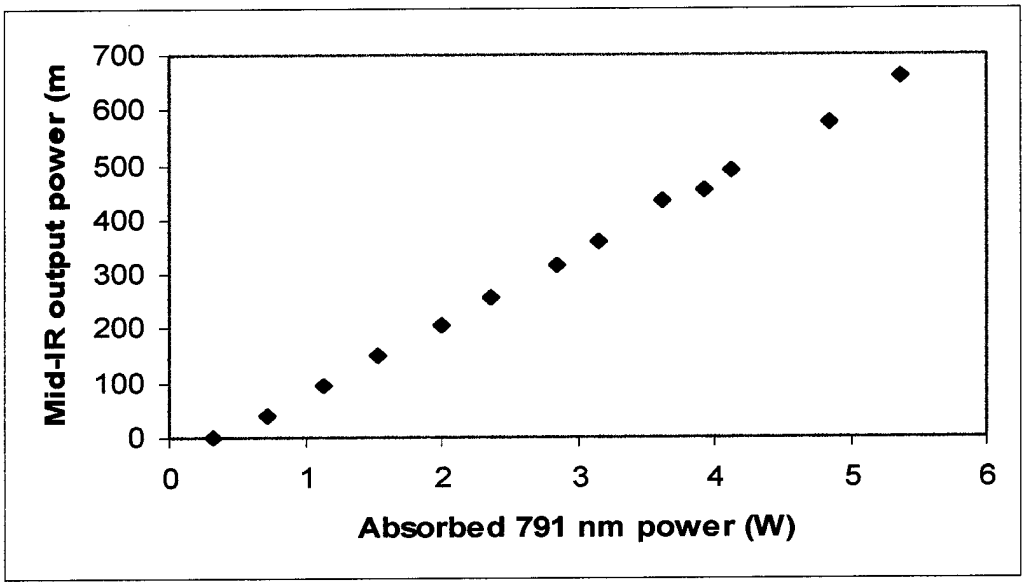


Fig. 10: CW 2.7 μm output power vs. absorbed 791 nm pump power

Passive Q-switching of mid-IR fiber laser:
Compact mid-IR pulsed laser sources with emission wavelengths in the vicinity of 3 μm mid-IR water absorption peak are needed for a number of medical applications.

Key Accomplishments:

We recently reported the first observation of passive Q-switching (7 μs pulsewidth, 35 kHz repetition rate) of a mid-IR Er-ZBLAN fiber laser (Fig. 11).Passive Q-switching was achieved by using a liquid gallium mirror as a saturable absorber[9]

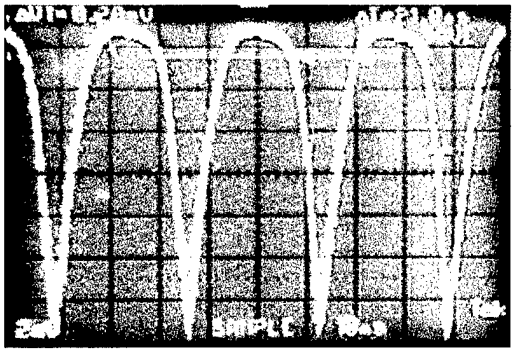


Fig. 11: Pulsed operation of a passively Q-switched Er:ZBLAN 2.8 μm fiber laser

Wavelength tunable mid-IR fiber laser:
Tunable operation of a diode-pumped mid-IR Er-ZBLAN fiber laser in the vicinity of 2.8 μm is needed for high sensitivity spectroscopic detection of important trace gases such as HF, NO, water vapor.

Key Accomplishments:
We recently reported tunable operation of a diode-pumped mid IR Er-doped ZBLAN fiber laser using a bulk grating in the Littrow configuration.

The output wavelengths were tunable from 2.71 μm – 2.83 μm with powers varying from 1 mW – 30 mW (Fig. 12). The tendency of the laser to shift to longer wavelengths at higher pump powers is presumably due to re-absorption effects and saturation of the lower energy levels of the $^4I_{13/2}$ manifold.

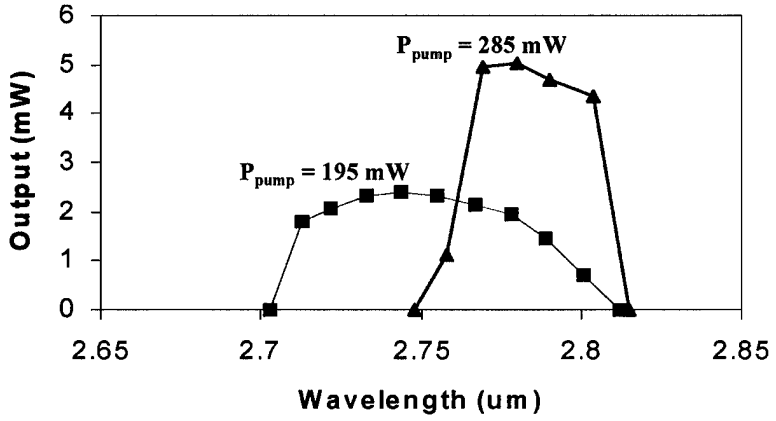


Fig. 12: Tuning curves for diode pumped Er:ZBLAN fiber laser at two different 790 nm

2. Advanced Fiber Optic Devices:
Goal: Research and development of manufacturable, high-performance all-fiber modulators and all-fiber tunable filters for reconfigurable fiber interconnects and "smart" fiber networks.

Thermally stable fiber Bragg gratings (FBGs):
Goal: To improve the thermal stability of FBGs.

Background: The focus of our work is to improve the stability of "fixed FBGs" (to be used subsequently as tunable filters). In particular, we studied several key issues regarding the thermal stability of FBGs, as elaborated below. The thermal stability of FBGs is an important issue for the fabrication of electro-optically tunable FBGs since the as-fabricated FBGs are subjected to temperatures of ~300°C during the thermal poling process (used to make such FBGs electro-optically tunable).

The high-contrast UV interference patterns used to fabricate FBGs are believed to create an index modulation in the fiber via a light-induced distribution of defects. The defects are distributed in shallow trap sites (low activation energy, E_a) and deep trap sites (higher E_a). Upon annealing at elevated temperatures, the lower E_a trap sites and the corresponding index components vanish, leaving behind only <20% of the original index modulation. If the fiber is illuminated by supplementary uniform UV radiation, shallow defects are also formed in the nulls of the interference pattern, reducing the amount of subsequent redistribution from the peaks of the interference pattern, resulting in a more stable "permanent" refractive index modulation. Such a stabilization technique has been demonstrated by Salik et al[10] for weak ($\Delta n \sim 10^{-5}$) Bragg gratings fabricated in non-hydrogen-loaded fibers.

Key Accomplishments:
We have demonstrated a technique (similar to Salik et al) for fabricating thermally-stable strong ($>10^{-3}$) FBGs in hydrogen-loaded fibers by using a phase mask that transmitted ~20% of the zero order. Fig. 13 shows the superior stability of an FBG fabricated by the above-described method when compared to an FBG fabricated in a similar fiber[11] using a holographic method (in which the zero order transmission was suppressed). The higher mean activation energy, E_a=2.9 eV, for trap sites in our work relative to the E_a=1.6 eV inferred for trap sites in Patrick et al. (Fig. 14) is

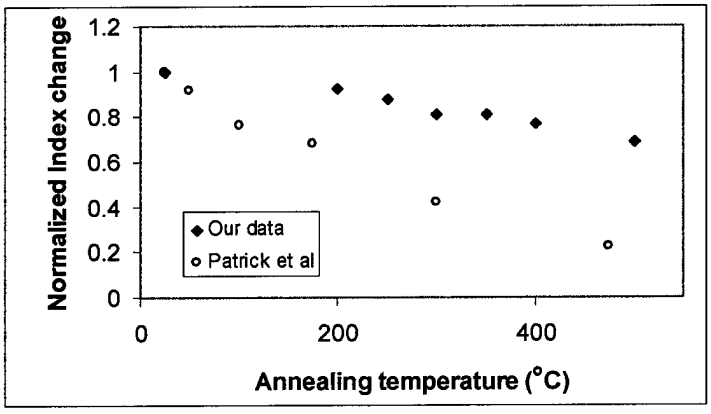


Fig. 13: Results of annealing studies illustrating the superior stability of FBGs fabricated using our technique when compared to the high-

further confirmation of the superiority of our FBG fabrication technique in hydrogen-loaded fibers. We also observe that the defects responsible for the FBG fabricated in 5% GeO_2-doped fiber have higher mean activation energy (Fig. 15, 3.2 eV vs. 2.4 eV for higher GeO_2 conc.). Such

an observation indicates that the FBGs fabricated in fibers with relatively low GeO_2 concentration exhibit superior thermal stability.

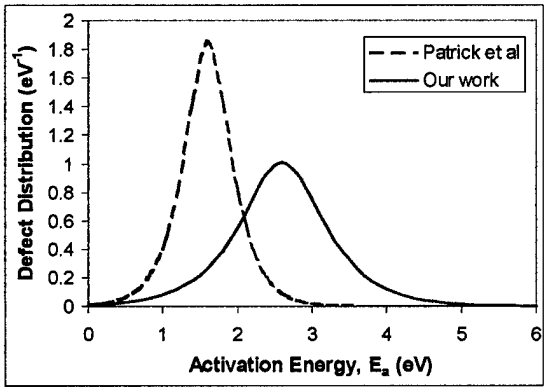


Fig. 14: Plot of the estimated defect distributions (obtained using the model of Erdogan et al. as a function of the activation energy, E_a, for our data as well as that of Patrick et al[11]

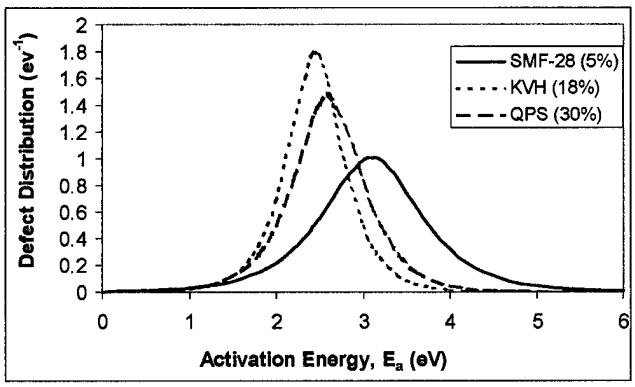


Fig. 15: Distribution of defect activation energies for FBGs fabricated under similar conditions in fibers with three different GeO_2 concentrations.

Electrically –tunable fiber Bragg gratings:

Goal: To fabricate Bragg gratings at 1550 nm in D-shaped fibers, to pole the fiber Bragg grating, and to demonstrate tunability of 10 GHz (80 pm) using voltages of the order of 100 V.

Key Accomplishments:

We have demonstrated electro-optic tuning of a FBG fabricated in a thermally-poled fiber. 40 pm of tuning was achieved, corresponding to an electro-optic coefficient of 0.25 pm/V.

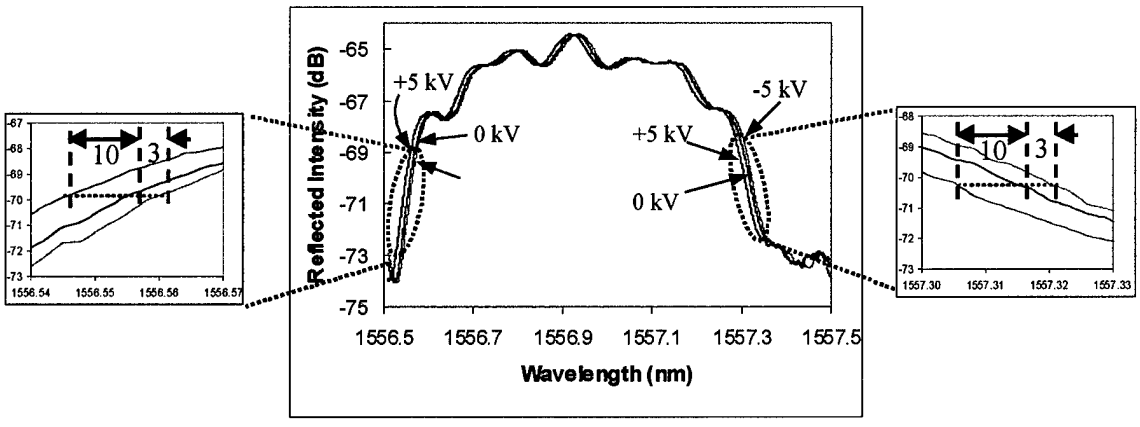


Fig. 16: Reflection spectra of FBG showing asymmetric shifts of 10 pm and 3 pm respectively for 5 kV applied voltage using positive and negative polarities

To eliminate the possibility of the observed tuning due to thermal or piezo-electric effects, we observed the tuning of FBG as a function of reversed polarities (Fig. 16). The tuning in opposite directions corresponding to the reversed polarities confirms the electro-optic tuning mechanism.

2x2 All-Fiber Electrooptic Switch

Recently, we demonstrated an all-fiber switch employing a poled electrooptic fiber segment. A Mach-Zehnder interferometer with a poled electrooptic fiber segment in one arm is formed using commercial 2x2 fiber directional couplers. In the preliminary experiments reported there, the poled segment was fabricated independently, in Andrew Corp. D-fiber, then butt-coupled to pigtails, resulting in an undesirable 5 dB loss that we compensated with a following fiber amplifier. The switch speed was around 2 MHz with 2 kV switching voltage.

Here, we report an improved result with further iterations in the fabrication process. As illustrated in Figure 17, a Mach-Zehnder interferometer is formed using commercial 2x2 fiber directional couplers. Two mechanical controllers, one in the reference arm, one in the input port, were used to adjust the polarization state. A cw YAG laser at 1.06 μm provided the optical source.

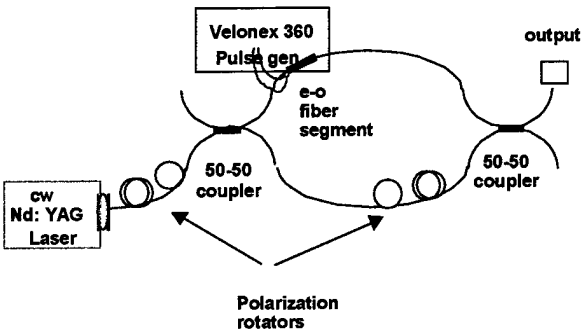


Fig. 17: Experimental arrangement for all-fiber switch.

An RF metal strip line, defined using standard lithography techniques, was deposited atop a 6-cm long D-side of the fiber for high voltage poling and high speed modulation. After the metal line was deposited on the fiber, the fiber was affixed, D-side down, to a silicon wafer using a thin layer of polyimide. Additional layers of polyimide were spun on and cured until the fiber was totally surrounded by polyimide. The total fiber thickness was then polished down to 20 μm. Finally, the fiber was inverted and remounted on a silica glass plate with a blanket deposited metal film and layers of polyimide were spun on and cured. The fiber was poled by applying a high voltage (3 kV) between the top microstrip line electrode and the bottom metal-film ground electrode with the fiber heated to 250°C. After a ten minute poling time, the fiber was allowed to cool with the voltage applied. Additional segments of Andrew e fiber were subsequently butt-coupled to either end. These were spliced to Flexcore 1060 segments, to match the 3dB couplers forming the interferometer. Figure 18 shows the switching voltage to be 1.4 kV. The measured extinction is ~15 dB, this low extinction ratio may be caused from poor balance of light intensity in the two arms. Figure 19 shows an expanded view of the rise time, the optical signal risetime of 30 ns (solid line) is indistinguishable from the rise time of the applied voltage (dotted line). The measured total capacitance C is 16 pF, including the capacitance between the metal RF strip line and ground electrode and the capacitance between connection pads. The electrical resistance R of the RF strip line is 150 Ω, giving an RC rise time of 5.3 ns, consistent with the measurement. The measurement puts a lower bound of 150 MHz on the bandwidth of the poled fiber switch.

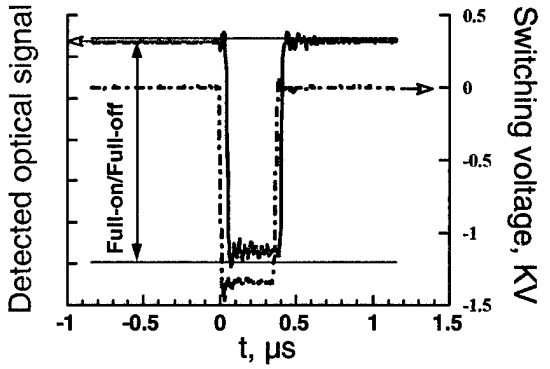


Fig. 18: Detected signal and applied voltage pulse.

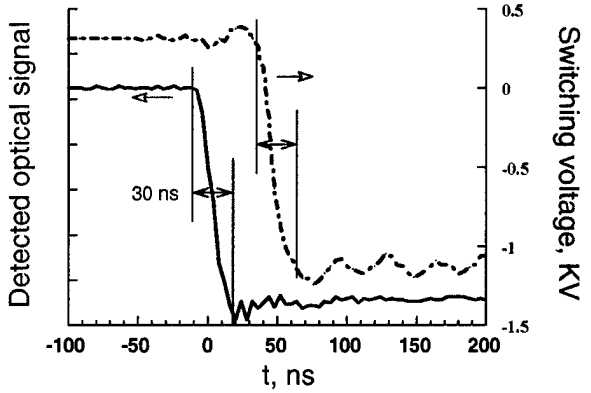


Fig. 19: Expanded view of rise times of both signals. The switch turn on time is limited by the applied voltage pulse.

E. Nanoheteroepitaxy: A Revolutionary Approach to Lattice-Mismatched Heterostructure Growth

During this program we have developed the theory and practice of a new technology for the elimination of mismatch defects in lattice-mismatched heterostructures. We call this approach Nanoheteroepitaxy (NHE).[12] NHE combines three-dimensional stress relief mechanisms, that are uniquely available in nanoscale (< 100 nm) islands, with strain partitioning between the epitaxial layer and the substrate, to achieve a dramatic reduction in the stored strain energy and associated defect density.

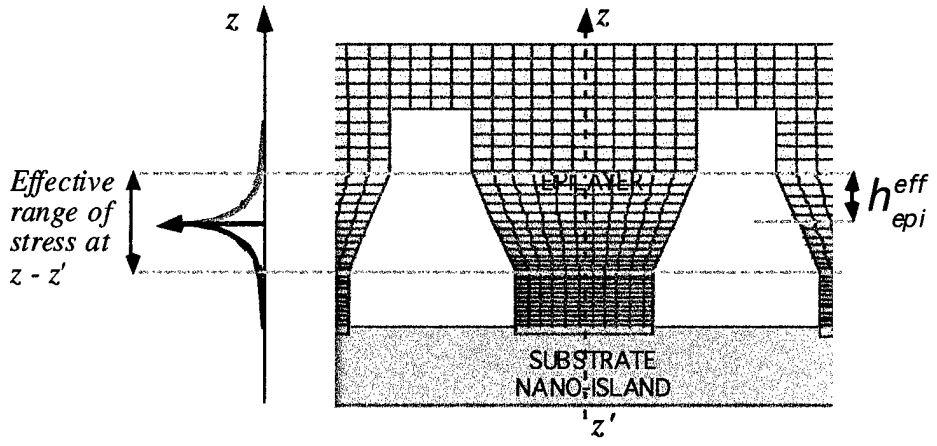


Fig:20: A generic nanoheteroepitaxy sample showing partitioning of mismatch strain between the epilayer and substrate. The exponential decay of strain away from the heterointerface results from 3-D stress relief mechanisms that are unique to NHE.

In the generic NHE approach (Fig. 20), a single crystal substrate is patterned into nanoscale islands separated by a selective growth mask. Selective epitaxy nucleates the epilayer only on top

of the islands. As the layer grows it is able to deform in 3D because it is so small[13], and the mismatch stress decays exponentially on either side of the heterointerface. Once the epilayer thickness exceeds the stress decay length, it is no longer strained and further growth does not increase the stored strain energy. The creation of mismatch defects, e.g., dislocations or stacking faults, requires a minimum strain energy. In the NHE approach this strain energy is dramatically reduced and for many highly mismatched materials it remains too low to form mismatch defects.

Once the epilayer thickness exceeds the effective stress range, the epitaxial growth conditions are modified to promote lateral growth and coalescence as shown at the top of Fig.20. As the effective range of strain is very small in NHE samples (typically < 50 nm) this coalescence can be accomplished when the epilayer is typically ~ 100-nm thick, where it is still compliant. Thus in NHE, we anticipate that coalescence can also be achieved without defect formation. Coalescence in NHE is very different than in the recently developed lateral epitaxial overgrowth techniques.[14,15] In the latter, coalescence occurs for layers that are already several-μm thick and generally results in a highly defected region. XTEM investigation of the coalescence of OMVPE-grown, GaN on SOI, NHE islands (see Fig. 21) supports our expectation and indicates that the coalescence boundary has the potential to be defect free.

NHE is a generic approach applicable to a wide range of important semiconductor materials including: AlGaInAs/Si; AlGaInN/Si; GaInAsSb/Si; and SiGe/Si. In each case the large lattice mismatch between the constituent materials has previously placed severe limits either on the thickness of films or on the minimum achievable defect concentration. Our NHE theory[ix] predicts that these limitations can be relaxed significantly, if not eliminated, using the NHE approach.

Initial Results for NHE GaN/Si

NHE is itself enabled by CHTM's advanced interferometric lithography capability for nanoscale patterning and the availability of this unique capability has allowed us to experimentally test the NHE theory for the extremely mismatched combination of GaN on Si (20 % lattice mismatch.). We have used our established capability in GaN OMVPE growth[16,17] and developed a novel sample structure specifically for GaN on Si (fig 2.)

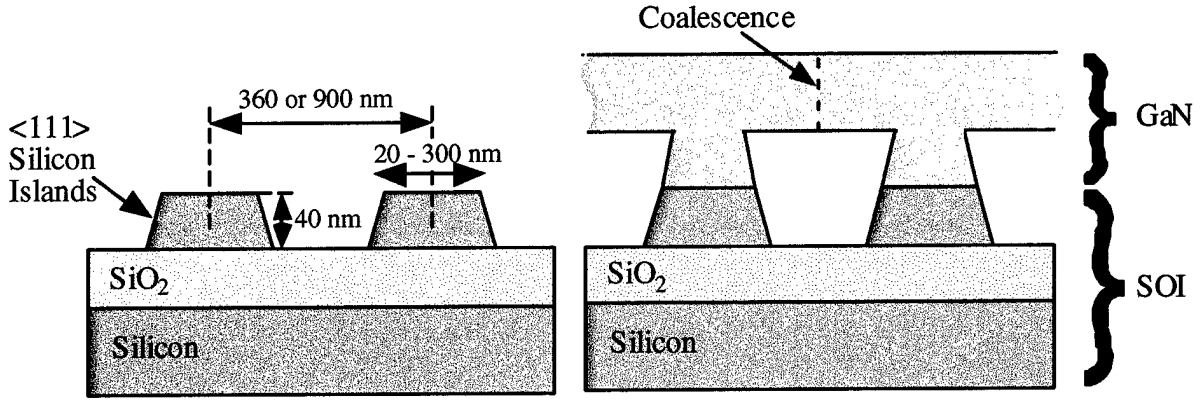
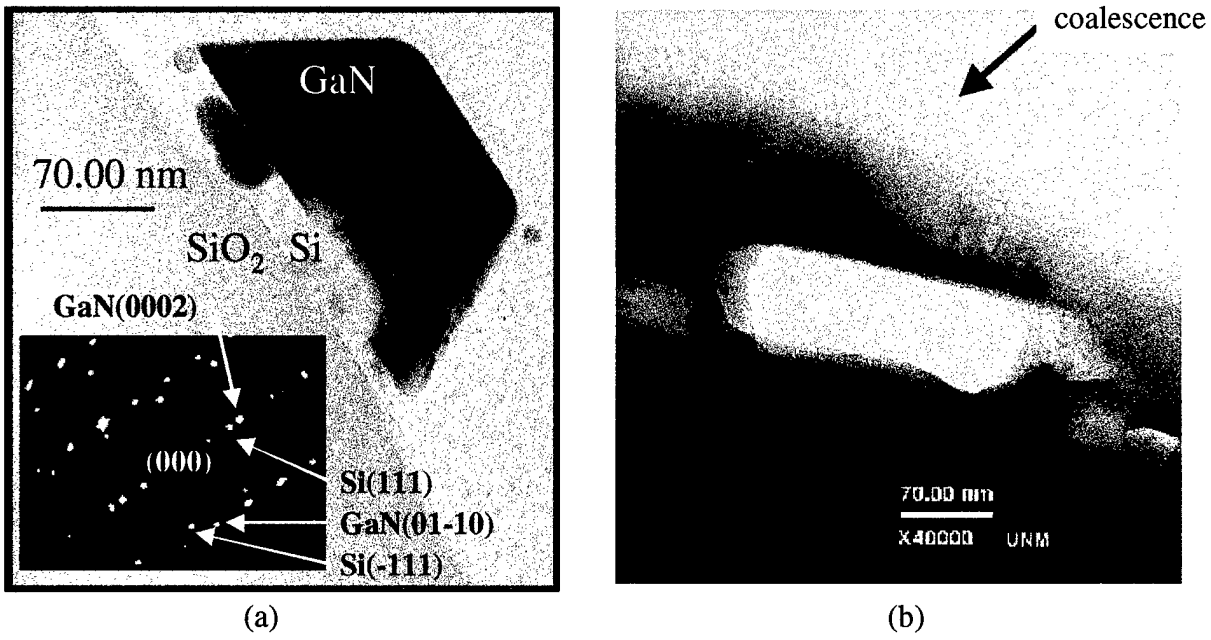


Figure 21: Schematic representation of NHE <111> SOI substrate (left) and GaN film growth stages showing island nucleation and coalescence.

The SIMOX SOI wafers were patterned using interferometric lithography and reactive ion etching to form a 2-dimensional array of <111> silicon islands on top of a field of SiO_2. The height of the islands is 40 nm and diameters in the range 20 to 300-nm are being investigated. The array period of present NHE samples is 360 or 900 nm. GaN is selectively nucleated on the silicon islands using a three step sequence consisting of; an *in-situ* cleaning at a temperature of 878°C for 5 min. in hydrogen, a low temperature (543°C) nucleating layer deposition and, finally, main epilayer growth at high temperature (1031°C). This yields a GaN island thickness of approximately 100 nm prior to coalescence. The exposed SiO_2 layer in the SOI serves as a convenient mask for the selective nucleation of GaN.



(a) (b)

Fig. 22: a) Individual GaN/Si nanoisland. b) Coalescence of two GaN islands

Figure 22a shows GaN growth on a 70-nm diameter Si island. A defected region is observed near the heterointerface. Beyond this region, the decaying strain field (as predicted by NHE theory) is clearly observed. The inset in Fig. 22a is an electron diffraction micrograph taken at the heterointerface and showing the epitaxial alignment of the <111> Si and <0001> GaN directions. Figure 22b shows the coalescence region between two GaN on Si islands. The GaN in this region contains localized defects, possibly nanopipes, but these defects do not propagate in the growth direction. Thus it appears that in the case of a highly mismatched system such as GaN/Si (20% mismatch) the mismatch defects remain localized at the heterointerface.

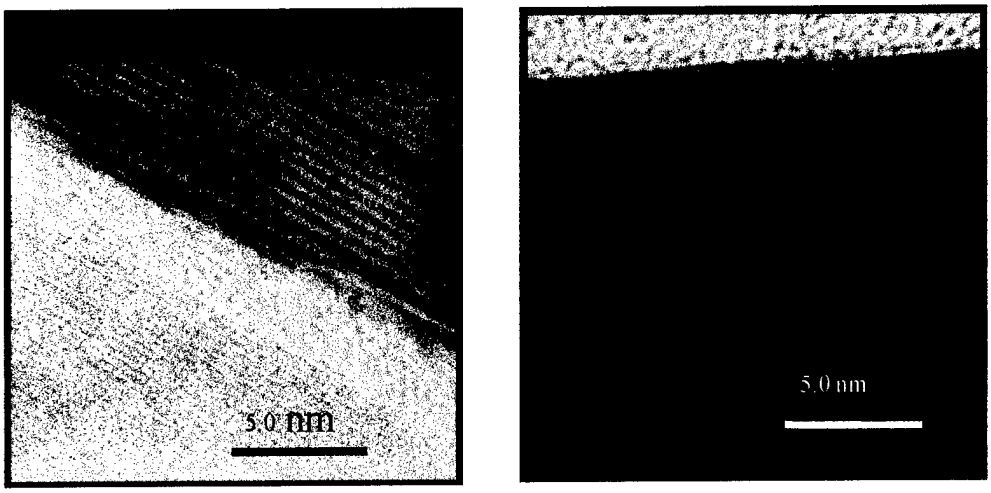


Fig. 23: High resolution TEM reveals defects are located close to the heterointerface (left). The top surface of the GaN (right) is undefected.

Figure 23 shows high-resolution XTEM micrographs of a GaN nanoisland grown on a 300-nm diameter Si island. The defects formed at the interface (left) are in-plane, stacking-fault type defects indicating that defect formation in the NHE sample is also very different to defect formation in the normal planar sample. It is often the case that the closest free surface plays an integral role in the formation of crystalline defects. In the NHE sample the closest surface is generally the edge of the nanoisland (rather than the epilayer surface) and this might well be a cause of the unusual orientation and nature of the defect structures seen in our NHE GaN/Si samples. These defects should be contrasted with those formed during conventional planar growth of GaN on sapphire or on silicon, where the mismatch defects are frequently edge type dislocations that propagate vertically in the <0001> direction.[18] This figure also shows that the majority of the mismatch defects appear to be in the Si side of the heterointerface, verifying the NHE hypothesis that the Si nanoisland will be highly compliant. Away from the interface (Fig. 23, right) the GaN is defect free and unstrained as predicted by NHE theory.

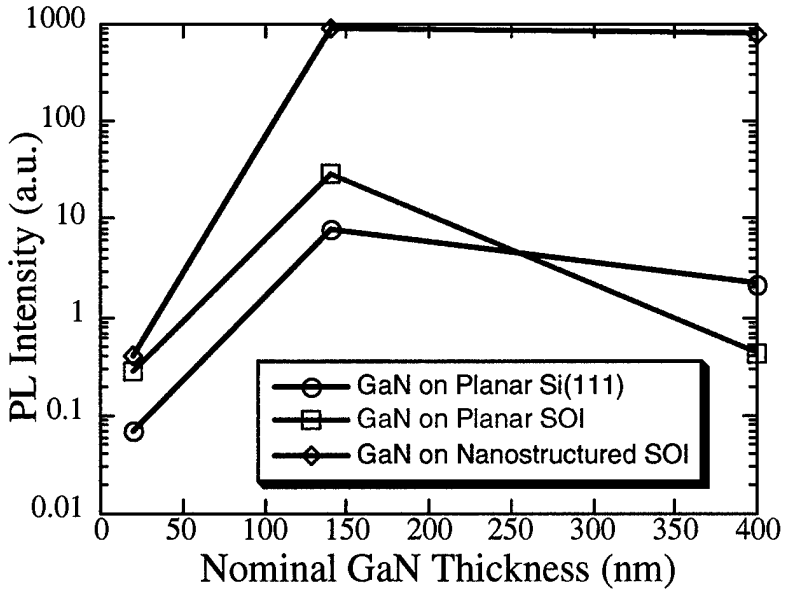


Fig. 24: PL intensity in the NHE sample is much higher and is sustained for thicker layers indicating no new defect formation as layer thickness grows.

Photoluminescence measurements on NHE GaN on Si (Fig 24) show a dramatic increase in intensity compared to PL on GaN grown on planar Si. Figure 24 shows the band-edge (360 nm) PL intensity (300K) for three samples. The highest intensity was measured for the NHE sample and importantly this high intensity is sustained as the GaN layer is grown thicker. For the planar samples (GaN grown on SOI (compliant substrate) and GaN grown on Si) the intensity is lower and falls for epilayer thickness > 150 nm, possibly indicating additional defect formation.

Conclusions

Our experimental results for GaN on Si using the NHE approach are very encouraging. Many of the predictions of the NHE theory have been confirmed (the decaying strain field (Figure 20a), the super compliance of Si-nanoislands (Figure 22a), the unusual defect structure (Figure 13) and the dramatically enhanced PL intensity (Fig. 24). While GaN on Si, with a lattice mismatch of 20%, is an extreme example of mismatched heteroepitaxy; these results give us confidence that less strained materials, such as GaAs on Si, will also follow the predictions of NHE theory. In fact our theory predicts that GaAs on Si can be grown defect free if the nanoisland diameter is reduced to 40 nm. This is within the range of our interferometric nanostructuring capability and will be attempted in future studies.

Our published NHE model[ix] lays out a solid framework for calculating the strain energy at the heteroepitaxial interface for the NHE structure. While our experimental work with the highly mismatched GaN on Si system has confirmed many of the predictions of the NHE theory, it also suggests that the actual strain energy is less than predicted by the model. Furthermore, preliminary studies of coalesced GaN (Fig. 11) indicate that even when defects are formed at the heterointerface, they can be localized at this interface and may not affect the performance of devices grown in the epilayer above them. Part of the overestimate of strain energy by the NHE theory

stems from our conservative approach. For example, we sum the strain energy in the epilayer and the strain energy in the substrate and assume that the total strain energy acts at only at the heterointerface. Furthermore, we calculate the total strain energy at the center of the nano-nucleus, where the strain energy per unit area is a maximum. In practice there will be a decrease of strain energy per unit area towards the edge of the nucleus, which will mean that the average value of this quantity will be lower than the maximum value at the nucleus center. However, a more significant source of disagreement between theory and experiment, that is especially relevant to GaN on Si, is the phenomenon that we have recently identified[19] and we call "active compliance". Clearly, much work remains to be done in improving the accuracy of the NHE model and in the experimental application of NHE to other mismatched heterostructures.

F. Influence of the Microstructure on Transport Properties of p-type GaN:Mg

We have presented an analysis of the hole transport in p-type Mg-doped GaN grown on sapphire substrates by metal-organic-chemical vapor deposition (MOCVD). We found that the experimental Hall mobility cannot be explained solely by traditional extended state scattering mechanisms. Not only are the mobilities not accurately modeled by numerically solving the Boltzmann transport equation (BTE), but the calculated results do not even reflect the trend in experimental mobility values between the investigated samples. We attributed these discrepancies to the microstructure of GaN:Mg grown on sapphire. A microstructure-oriented transport model was presented for an interpretation of the transport of holes in p-type GaN:Mg grown on sapphire. The microstructure-oriented model provides a simplified picture of the microstructure, consisting of two distinct microstructural phases in GaN on sapphire. Using this model for the experimental mobility, the extracted parameters from hole transport measurements were shown to be positively correlated with microstructural parameters determined from x-ray diffraction (XRD) measurements. The experimental mobility of p-type GaN:Mg grown on sapphire can be described as dependent upon the acceptor doping, impurity compensation, and microstructure, including dislocation density, columnar grain size, and grain boundaries.

With improved growth of GaN, the material will approach ideal single crystal quality. In these cases the mobility of p-type GaN:Mg should be well described by traditional extended state scattering mechanisms. The calculated mobility for crystalline p-type GaN:Mg with an activation energy of 150 meV and compensation ratio of K = 0.1 is constant with a value of ~120 cm^2/Vs for substitutional Mg doping less then $1x10^{18}$ cm^{-3} at 300 K. The calculated conductivity shows an upper limit of 10 $(\Omega\ cm)^{-1}$ at 300 K and 30 $(\Omega\ cm)^{-1}$ at 500 K. These results imply that as the growth of p-type GaN:Mg improves, GaN devices that include p-type GaN:Mg will still possess a high spreading resistance.

In addition, we investigated the noise properties of p-type Mg-doped GaN using low frequency noise spectroscopy. The epitaxial GaN:Mg films were grown on a sapphire substrate by metal-organic chemical vapor deposition (MOCVD) in different laboratories. Generation-recombination (g-r) noise and 1/f noise were observed for temperatures above 250 K. The magnitude of the 1/f noise exceeds the g-r noise magnitude for frequencies less than 30 Hz, and the 1/f noise level was characterized by high values of the Hooge parameter, $\alpha \approx 1 - 150$, indicating a high level of structural imperfection. In addition, the integrated noise power spectral density divided by the voltage squared in the frequency range of 1 Hz to 30 Hz, correlated strongly with the structural imperfection of the sample as measured from the asymmetric rocking curve (ω-

scan) FWHM. The generation-recombination noise was related to a high concentration trap level with an activation energy of 120 meV ± 25 meV and a repulsive barrier that is possibly associated with the Mg dopant.

References

[1] Arakawa, Y., and Sakai, H.: 'Multidimensional quantum well laser and temperature dependence of its threshold current', Appl. Phys Lett., **40**(11), 939-941 (1982).

[2] Schäfer, F., Reithmaier, J.P., and Forchel, A.: "High-performance GaInAs/GaAs quantum-dot lasers based on a single active layer", Appl. Phys Lett, **74**(20), 2915-2917 (1999).

[3] Lester, L.F., Stintz, A., Li, H., Newell, T.C., Pease, E.A. , Fuchs, B.A. and MALLOY, K.J.: "Optical characteristics of 1.24μm quantum dot lasers", accepted for publication in IEEE Photonic Technology Letters, August (1999).

[4] Ustinov, V.M., Maleev, N.A., Zhukov, A.E., Kovsh, A.R., Egorov, A. Yu., Lunev, A.V., Volovik, B.V., Krestnikov, I.L., Musikhin, Yu.G., Bert, N.A., Kop'Ev, P.S., Alferov, ZH.I., Ledentsov, N.N., Bimberg, D.: "InAs/InGaAs quantum dot structures on GaAs substrates emitting at 1.3 μm," Appl. Phys. Lett., **74**(19), 2815-2817 (1999).

[5] Sugawara, M., Mukai, K., and Shoji, H.: "Effect of phonon bottleneck on quantum-dot laser performance", Appl. Phys. Lett., **71**(19), 2791-2793 (1997).

[6] Huffaker, D. L., Park G., Zou, Z., Shchekin, O. B., and Deppe, D. G.: "1.3 μm room-temperature GaAs-based quantum-dot Laser," Appl. Phys. Lett., **73**(18), 2564-2566 (1998).

[7] Chand, N., Becker, E.E., Van der Zeil, J.P., Chu, S.N.G., and Dutta, N.K.: "Excellent uniformity and very low (less-than-50A/cm2) threshold current density strained InGaAs quantum-well diode-lasers on GaAs substrate "Appl. Phys. Lett., **58**(20), 1704-1706 (1991).

[8] Turner, G.W., Choi, H.K., and Manfra, M.J.: "Ultralow-threshold (50A/cm2) strained single-quantum-well GaInAsSb/AlGaAsSb lasers emitting at 2.05μm", Appl. Phys. Lett., **72**(8), 876-878 (1998).

[9] P.J. Bennet et al., Appl. Phys. Lett.**73** 1787-1789, 1998.

[10] E. Salik, D.S. Starodubov, V. Grubsky, & J. Feinberg, 'Thermally Stable Gratings in Optical Fibers without Temperature Annealing', *OFC'98 Tech. Digest*, paper ThD3, pp. 56-58, 1998.

[11] T4. H. Patrick, S.L. Gilbert, A. Ligard, and M.D. Gallagher, 'Annealing of Bragg Gratings in Hydrogen-Loaded Optical Fiber', J. Appl. Phys. **78** 2940-2945, 1995.

[12] D. Zubia and S.D. Hersee, "Nanoheteroepitaxy: A New Approach to the Heteroepitaxy of Mismatched Semiconductor Materials", J. Appl. Phys., **85**, 6492 (1999).

[13] S. Luryi and E. Suhir, "New Approach to the High Quality Epitaxial Growth of Lattice-Mismatched Materials," Appl. Phys. Lett. **49**, 140 (1986).

[14] D. Kapolnek, S. Keller, R. Vetury, R. D. Underwood, P. Kozodoy, S. P. Denbaars, U. K. Mishra, "Anisotropic epitaxial lateral growth in GaN selective area epitaxy," Appl. Phys. Lett. **71**, 1204 (1997).

[15] K. Linthicum, T. Gehrke, D. Thomson, E. Carlson, P. Rajagopal, T. Smith, D. Batchelor, and R. Davis, "Pendeoepitaxy of gallium nitride thin films," Appl. Phys. Lett. **75**, 196 (1999).

[16] J. Ramer, A. Hecht, S.D. Hersee, "The Stability and Interface Abruptness of $In_xGa_{1-x}N/In_yGa_{1-y}N$ Multiple Quantum Well Structures Grown by MOVPE on Sapphire", J. Electronic Matls. , **26**, 1109 (1997).

[17] S.D.Hersee, J.C. Ramer* and K.J. Malloy, "The Microstructure of MOCVD GaN on Sapphire", MRS Bulletin, **22**, 45 (1997).

[18] S. Chadda*, M. Pelcynski*, K. Malloy and S. D. Hersee, "Microstructural Study of GaN Grown on Sapphire by MOCVD", Mat. Res. Soc. Symp. Proc., "Growth and Process Characterization of Semiconductor Heterostructures", Vol. **326**, (1994).

[19] D. Zubia, S. H. Zaidi, S. R. J. Brueck and S. D. Hersee, "Nanoheteroexpitaxial Growth of GaN on Si by Organometallic Vapor Phase Epitaxy," Appl. Phys. Lett. **76**, 858 (2000).

APPENDIX

PUBLICATIONS AND PRESENTATIONS

FOR CONTRACT PERIOD MARCH 15, 1996 – SEPTEMBER 30, 1999

S.R.J. Brueck:

X-C. Long, R. A. Myers and S. R. J. Brueck, "A Poled Electrooptic Fiber," Photonics Tech. Lett. **8**, 267-269 (1996).

J. V. Sandusky and S. R. J. Brueck, "A CW External-Cavity Surface-Emitting Laser," Photonics Tech. Lett. **8**, 313-315 (1996).

C. Huang, M. Lang and S. R. J. Brueck "Optical Temperature Measurement by Grating Expansion for Rotating Semiconductor Wafers," Jour. Vac. Sci. Technol. **A14**, 271-277 (1996).

Xiaolan Chen, Saleem H. Zaidi, S. R. J. Brueck and D. J. Devine, "Interferometric Lithography of Sub-Micrometer Sparse Hole Arrays for Field-Emission Display Applications," Jour. Vac. Sci. Technol. **B14**, 3339-3349 (1996).

Saleem H. Zaidi, An-Shiang Chu and S. R. J. Brueck, "Optical Properties of Nanoscale, One-Dimensional Silicon Grating Structures", Jour. Appl. Phys. **80**, 6997-7008 (1996).

J. V. Sandusky and S. R. J. Brueck, "Observation of Spontaneous Emission Microcavity Effects in an External-Cavity Surface-Emitting Laser Structure," Appl. Phys. Lett. **69**, 3993-3995 (1996).

Saleem H. Zaidi and S. R. J. Brueck, "Photoluminescence of Manufactured 1-D Crystalline Si Gratings," Opt. Commun. **135**, 264-268 (1997).

H. S. Gingrich, D. R. Chumney, S-Z. Sun, S. D. Hersee, L. F. Lester and S. R. J. Brueck, "Broadly-Tunable External Cavity Laser Diodes with Staggered Thickness Multiple Quantum Wells," Photonics Tech. Lett. **9**, 155-157 (1997).

X-C. Long and S. R. J. Brueck, "Large-Signal Phase Retardation with a Poled Electrooptic Fiber," Photonics Tech. Lett. **9**, 767-769 (1997).

J. V. Sandusky and S. R. J. Brueck, "Microcavity Effects in an External-Cavity Surface-Emitting Laser," IEEE Jour. Quantum Electron. **QE-33**, 1574-1581 (1997).

T. G. Alley and S. R. J. Brueck, "Visualization of the Nonlinear Optical Space-Charge Region of Bulk, Thermally-Poled Fused-Silica Glass," Opt. Lett. **23**, 1170-1172 (1998).

T. G. Alley, S. R. J. Brueck and R. A. Myers, "Space Charge Dynamics in Thermally Poled Fused Silica," Jour. Noncrystalline Sol. **242**, 165-176 (1998).

V. Metlushko, U. Welp, G. W. Crabtree, Z. Zhang, S. R. J. Brueck, B. Watkins, L. E. DeLong, B. Ilic, K. Chung and P. J. Hesketh, "Nonlinear Flux Line Dynamics in Vanadium Films with Square Lattices of Submicron Holes, "Phys. Rev. **B59**, 603-607 (1999).

P. Vavassori, V. Metlushko, R. M. Osgood III, M. Grimsditch, U. Welp, G. Crabtree, W. Fan, S. R. J. Brueck, B. Ilic and P. J. Hesketh, "Magnetic Information in the Light Diffracted by a Negative Dot Array of Fe, "Phys. Rev. **B59**, 6337-6343 (1999).

X-C. Long and S. R. J. Brueck, "Large Photosensitivity in Lead Silicate Glasses,"Appl. Phys. Lett. **74**, 2110-2112 (1999).

Michael J. O'Brien II, S. R. J. Brueck, V. H. Perez-Luna, L. M. Tender, and G. P. Lopez, "SPR Biosensors: Simultaneously Removing Thermal and Bulk-Composition Effects," Biosensors & Bioelectronics **14**, 145-154 (1999).

X-C. Long and S. R. J. Brueck, "Composition Dependence of the Photoinduced Refractive Index Change in Lead-Silicate Glasses," Opt. Lett. **24**, 1136-1138 (1999).

T. G. Alley, S. R. J. Brueck and Michael Wiedenbeck, SIMS Study of Space Charge Formation in Thermally Poled Fused Silica," Jour. Of Appl. Phys. **86**, 6634-6640 (1999).

V. Metlusko, U. Welp, G. W. Crabtree, R. Osgood, S. D. Bader, L. E. DeLong, Zhao Zhang, S. R. J. Brueck, B. Ilic, K. Chung, and P. J. Hesketh, "Interstitial Flux Phases in a Superconducting Niobium Film with a Square Lattice of Artificial Pinning Centers," Phys. Rev. **B60**, R12 585-588 (1999).

Brueck Invited Presentations and Seminars 96-99

Interferometric Lithography for Field-Emitter Displays
USDC "Open House" for Tool Manufacturers
San Jose, CA 1996

Nonlinearities, SHG and Poling in Silica Fibers
Optical Fiber Conference
San Jose, CA 1996

Perspectives on Glass Poling
First Sino-American Workshop on Microstructured Crystals for Nonlinear Optics
Nanjing, People's Republic of China 1996

Poling of Optical Fiber Materials
Fiber Materials for Electronics, Optoelectronics and Sensors
Materials Research Society
San Francisco, CA 1996

Interferometric Lithography - A Novel Approach to Nanometer Structrures
Symposium on Computational Methods for Simulating IC Manufacturing Processes
Society for Industrial and Applied Mathematics (SIAM) Annual Meeting
Kansas City, MO 1996

Interferometric Lithography - A Novel Approach to Nanometer Structrures
IEEE Lithography Workshop
Maui, HI 1996

Interferometric Lithography for Field-Emitter Devices
AVS Annual Meeting
Philadelphia, PA 1996

Industry-University Interactions in Optoelectronics
OIDA Executive Forum
Washington, DC 1996

Standard Defect Wafers
SEMATECH Analytical Managers Meeting
Austin, TX 1996

Perspectives on Nanoscale Lithography
Sixth NASA Symposium on VLSI Design
Albuquerque, NM 1997

Interferometric Nano-Lithography for Periodic Pinning
Flux, Quantum, and Mesoscopic Effects in Superconducting Materials and Devices
Santa Fe, NM 1997

Interferometric Lithography - A Novel Approach to the nm Regime
2nd International Conference on Future Information Technologies
Kita-Hiroshima, Hokkaido, Japan 1997

Interferometric Lithography for Nanoscale Structures
Gaseous Electronics Conference
Madison, WI 1997

Material and Device Aspects of Poled Fused Silica
American Ceramic Society/Optical Society of America
Bragg Gratings, Photosensitivity, and Poling in Glass Fibers and Waveguides
Williamsburg, VA 1997

Imaging Interferometric Lithography – A Wavelength Division Multiplex Approach to Extending Optics
EIPBN'98
Chicago, IL 1998

Imaging Interferometric Lithography – A Wavelength Division Multiplex Approach to Extending Optics
Gordon Conference on Nanostructure Fabrication
Tilton, NH 1998

Imaging Interferometric Lithography - Optics to the "Max" and Beyond
OpTec Research Conference
Bozeman, MT 1998

Second-Order Nonlinearities in Poled Fibers
European Conference on Optical Communications
Madrid, Spain 1998

Spatial Frequency Analysis of Resolution Enhancement Techniques
Optical Enhancements Workshop, International SEMATECH
Austin, TX 1998

Interferometric Lithography for Nanoscale Fabrication
Laser Applications in Microelectronic and Optoelectronic Manufacturing IV
SPIE Photonics West
San Jose, CA 1999

The Year 2001 Lithography Problem
Optoelectronics'99 (Plenary Presentation)
SPIE Photonics West
San Jose, CA 1999

25-nm Lithography in 2020 (panel discussion)
SPIE Microlithography'99 Emerging Technologies
Santa Clara, CA 1999

Imaging Interferometric Lithography for Sub-Wavelength Resolution
APS Centennial Meeting
Altanta, GA 1999

Poling of Fused Silica - A Never-Ending Process
Novel Optical Materials and Applications (NOMA'99)
Cetraro, Italy 1999

Imaging Interferometric Lithography – Extending Optics to Fundamental Limits and Beyond
Intl. Congress on Optics (ICO'99)
San Francisco, CA 1999

Space Charge in Termally Poled Fused Silica
Bragg Gratings, Photosensitivity and Poling in Glass Waveguides (BGPP'99)
Stuart, FL 1999

Xiaolan Chen*, Saleem H. Zaidi and S. R. J. Brueck
Interferometric Lithography for Field Emitter Displays
Display Works'96
San Jose, CA 1996

S. R. J. Brueck
Nanoscale Si Fabrication and Optical Characterization
Workshop on Compound Semiconductor Materials and Devices
Santa Fe, NM 1996

S. R. J. Brueck
Nonlinearities, SHG and Poling in Silica Fibers
Optical Fiber Conference
San Jose, CA 1996

R. Dixson, J. Schneir, T. H. McWaid, V. W. Tsai, S. H. Zaidi, S. R. J. Brueck and N. T. Sullivan
Accurate Linewidth Metrology using Atomic Force Microscope Tip Characterization
Metrology, Inspection, and Process Control for Microlithography X
SPIE 2725 #60, S. K. Jones, conference chair
San Jose, CA 1996

S. R. J. Brueck
Perspectives on Glass Poling
First Sino-American Workshop on Microstructured Crystals for Nonlinear Optics
Nanjing, People's Republic of China 1996

S. R. J. Brueck
Poling of Optical Fiber Materials
Fiber Materials for Electronics, Optoelectronics and Sensors
Materials Research Society
San Francisco, CA 1996

Saleem H. Zaidi and S. R. J. Brueck
Interferometric Lithography for Nanoscale Fabrication
NanoMES'96
Santa Fe, NM 1996

X-C. Long*, R. A. Myers* and S. R. J. Brueck
Poled Electrooptic Fiber
Conf. on Lasers and Electrooptics'96, paper CWK1
Anaheim, CA 1996

Xiaolan Chen*, Saleem H. Zaidi and S. R. J. Brueck
Multiple Exposure Interferometric Lithography - A Novel Approach to Nanometer Structures
Conf. on Lasers and Electrooptics'96, paper CThJ5
Anaheim, CA 1996

An-Shyang Chu* and S. R. J. Brueck
Modal Analysis of Sub-□m Period nm-Linewidth Gratings
Quant. Electron. and Laser Sci.'96, paper QTuB18
Anaheim, CA 1996

J. V. Sandusky* and S. R. J. Brueck
Microcavity Effects in an External-Cavity Surface-Emitting Laser
Quant. Electron. and Laser Sci.'96, paper QPD11
Anaheim, CA 1996

Xiaolan Chen*, S. H. Zaidi, S. R. J. Brueck, F. M. Schellenberg and R. S. Mackay
Interferometric Lithography - A Novel Approach to Nanometer Structrures
Symposium on Computational Methods for Simulating IC Manufacturing Processes
Society for Industrial and Applied Mathematics (SIAM) Annual Meeting
Kansas City, MO 1996

Xiaolan Chen*, S. H. Zaidi, S. R. J. Brueck, F. M. Schellenberg and R. S. Mackay
Interferometric Lithography - A Novel Approach to Nanometer Structures
IEEE Lithography Workshop
Maui, HI 1996

S. R. J. Brueck
Interferometric Lithography for Field-Emitter Devices
AVS Annual Meeting
Philadelphia, PA 1996

S. R. J. Brueck
Industry-University Interactions in Optoelectronics
OIDA Executive Forum
Washington, DC 1996

X-C. Long*and S. R. J. Brueck
A Fiber Switch using the Electrooptic Effect
PSAA-7: Seventh Annual DARPA Symposium on Photonic Systems
for Antenna Applications
Monterey, CA 1997

S. R. J. Brueck
Perspectives on Nanoscale Lithography
6th NASA Symposium on VLSI Design
Albuquerque, NM 1997

Saleem H. Zaidi, S. R. J. Brueck, R. S. Mackay, F. M. Schellenberg, K. E. Eukert and J. J. Persoff
Interferometric lithography exposure tool for 180-nm structures
SPIE Microlithography'97 Emerging Technologies
Santa Clara, CA 1997

Xiaolan Chen*, Zhao Zheng*, S. R. J. Brueck, R. A. Carpio and J. S. Petersen
Process development for 180-nm structures using interferometric lithography and I-line photoresist
SPIE Microlithography'97 Emerging Technologies
Santa Clara, CA 1997

Jonathan Stohs*, S. R. J. Brueck, D. J. Bossert and D. J. Gallant
Dependence of linewidth enhancement factor on quantum well width and depth in InGaAs/GaAs broad-area lasers
CLEO'97
Baltimore, MD 1997

X-C. Long*, and S. R. J. Brueck
A poled electro-optic fiber switch
CLEO'97
Baltimore, MD 1997

J. V. Sandusky* and S. R. J. Brueck
Microcavity threshold reduction in an external-cavity surface-emitting laser
CLEO'97
Baltimore, MD 1997

S. R. J. Brueck
Interferometric Nano-Lithography for Periodic Pinning
Flux, Quantum, and Mesoscopic Effects in Superconducting Materials and Devices
Santa Fe, NM 1997

S. R. J. Brueck
Interferometric Lithography - A Novel Approach to the nm Regime
2nd International Conference on Future Information Technologies
Kita-Hiroshima, Hokkaido, Japan 1997

S. R. J. Brueck, S. H. Zaidi, X. Chen* and Z. Zhang*
Interferometric Lithography - From Periodic Arrays to Arbitrary Patterns
Micro-and Nano-Engineering'97
Athens, Greece 1997

S. R. J. Brueck
Interferometric Lithography for Nanoscale Structures
Gaseous Electronics Conference
Madison, WI 1997

S. R. J. Brueck, T. Alley*, X.-C. Long*, and R. A. Myers
Material and Fiber Device Aspects of Poled Fused Silica
Amer. Ceramic Soc. Glass Division
Williamsburg, VA 1997

X.-C. Long* and S. R. J. Brueck
A Thermally Poled Electro-optic Fiber
OSA Topical Conf.: Bragg Gratings, Photosensitivity and Poling in Glass Fibers and Waveguides: Applications and Fundamentals
Williamsburg, VA 1997

T. G. Alley*, S. R. J. Brueck and R. A. Myers
An Ion-Exchange Model for Extended-Duration Poling of Bulk Fused Silica
OSA Topical Conf.: Bragg Gratings, Photosensitivity and Poling in Glass Fibers and Waveguides: Applications and Fundamentals
Williamsburg, VA 1997

Xiaolan Chen* and S. R. J. Brueck
Imaging Inteferometric Lithography for Arbitrary Patterns
SPIE Microlithography'98 Emerging Technologies
Santa Clara, CA 1998

Xiaolan Chen*, A. Frauenglass and S. R. J. Brueck
Interferometric Lithography Pattern Delimited by a Mask Image
SPIE Microlithography'98 Emerging Technologies
Santa Clara, CA 1998

Saleem H. Zaidi, S. R. J. Brueck, T. Hill and R. A. Shagam
Mix-and-Match Interferometric and Optical Lithographies for Nanoscale Structures
SPIE Microlithography'98 Emerging Technologies
Santa Clara, CA 1998

Saleem H. Zaidi, Xiaolan Chen* and S. R. J. Brueck
Image Reversal at nm-Scales
SPIE Microlithography'98 Emerging Technologies
Santa Clara, CA 1998

U. Welp, V. Metlushko, G. Crabtree, Z. Zhang*, S. R. J. Brueck,
B. Watkins, L. E. Delong, K. Chung, B. Ilic, and P. J. Hesketh
Vortex Dynamics in Thin Vanadium Films with Periodic Arrays of Pinning Centers
APS March Meeting
Los Angeles, CA 1998

M. J. O'Brien*, V. H. Perez-Luna, L. M. Tender, M. Edmunds,
B. Lascelles, S. R. J. Brueck and G. P. Lopez
Surface-Plasmon-Resonance-Based Array Biosensors for Multianalyte Detection
SPIE Micro- and Nanofabricated Structures and Devices for
Biomedical Environmental Applications
Los Angeles, CA 1998

Xiaolan Chen* and S. R. J. Brueck
Imaging Interferometric Lithography – A Wavelength Division Multiplex Approach to Extending Optics
EIPBN'98
Chicago, IL 1998

V. Metlushko, U. Welp, G. Crabtree, Z. Zhang*, S. R. J. Brueck, B. Watkins, L. E. DeLong, B. Ilic, K. Chung, and P. J. Hesketh
Periodic Arrays of Pinning Centers in thin Vanadium Films
SPIE'98 Annual Meeting
San Diego, CA 1998

V. Metlushko, U. Welp, G. Crabtree, R. M. Osgood, S. D. Bader, D. G. Hinks, Z. Zhang*, S. R. J. Brueck, B. Watkins, L. E. DeLong, B. Ilic, K. Chung, and P. J. Hesketh
Superconducting Nanostructured Materials
Electrochem. Soc. Mtg.
Boston, MA 1998

S. R. J. Brueck
Imaging Interferometric Lithography – A Wavelength Division Multiplex Approach to Extending Optics
Gordon Conference on Nanostructure Fabrication
Tilton, NH 1998

S. R. J. Brueck, T. G. Alley* and X.-C. Long*
Second-Order Nonlinearities in Poled Fibers
European Conference on Optical Communications
Madrid, Spain 1998

S. R. J. Brueck
Spatial Frequency Analysis of Resolution Enhancement Techniques
Optical Enhancements Workshop, International SEMATECH
Austin, TX 1998

T. G. Alley*, S. R. J. Brueck and M. Wiedenback
Space Charge Dynamics in Poled Fused Silica
SPIE Photonics East, *Doped Fiber Devices II*
Boston, MA 1998

Neeraj Magotra, Sriram Divakar*, Chengjie Tu*, S. R. J. Brueck and Xiaolan Chen*
Digital Image Processing Applied to Imaging Interferometric Lithography
IEEE Asilomar Conference on Signals, Systems and Computers
Pacific Grove, CA 1998

S. R. J. Brueck and S. H. Zaidi
Interferometric Lithography for Nanoscale Fabrication
Laser Applications in Microelectronic and Optoelectronic Manufacturing IV
SPIE Photonics West
San Jose, CA 1999

S. R. J. Brueck
The Year 2001 Lithography Problem
Optoelectronics Plenary Presentation
SPIE Photonics West
San Jose, CA 1999

Saleem H. Zaidi and S. R. J. Brueck
Nonlinear Processes to Extend Interferometric Lithography
SPIE Microlithography'99 Emerging Technologies
Santa Clara, CA 1999

S. R. J. Brueck
25-nm Lithography in 2020 (panelist)
SPIE Microlithography'99 Emerging Technologies
Santa Clara, CA 1999

S. R. J. Brueck and Xiaolan Chen*
Spatial Frequency Analysis of Resolution Enhancement Techniques
SPIE Microlithography'99 Optical Lithography
Santa Clara, CA 1999

Xiaolan Chen* and S. R. J. Brueck
Experimental Comparison of Off-Axis Illumination and Imaging Interferometric Lithography
SPIE Microlithography'99 Optical Lithography
Santa Clara, CA 1999

H. Radakrishna*, S. Divakar*, N. Magotra, S. R. J. Brueck and A. Waters
MPI-Based Parallel Implementation of a Lithography Pattern Simulation Algorithm
7th International Conference for High Performance Computing and Networking
Amsterdam, The Netherlands 1999

V. V. Metlusko, U. Welp, G. Crabtree, R. M. Osgood III, D. Hinks, S. D. Bader,
B. Ilic, K. Chung, P. J. Hesketh, P. Neuzil, R. Kumar, L. E. DeLong,
Wenjun Fan* and S. R. J. Brueck
Large-Area Nanostructured Superconducting and Magnetic Materials
APS Centennial Meeting
Atlanta, GA 1999

S. R. J. Brueck
Imaging Interferometric Lithography for Sub-Wavelength Resolution
APS Centennial Meeting
Atlanta, GA 1999

U. Welp, V. V. Metlushko, G. Crabtree, R. M. Osgood III, S. D. Bader,
B. Ilic, K. Chung, P. J. Hesketh, L. E. DeLong, Wenjun Fan* and S. R. J. Brueck
Flux Phases in Superconducting Niobium Films with Square Lattices of Artificial Pinning Centers
APS Centennial Meeting
Atlanta, GA 1999

X.-C. Long, S. R. J. Brueck and M. L. Minden,
A Poled Electrooptic All-Fiber Switch
CLEO'99
Baltimore, MD 1999

P. M. Varganis, A. K. Sharma*, S. H. Zaidi and S. R. J. Brueck
Enhanced Optical Detection in MSM Photodiodes with Nanoscale Gratings
CLEO'99
Baltimore, MD 1999

Xiaolan Chen*and S. R. J. Brueck
Frequency Space Analysis of Resolution Enhancement Techniques - Modeling and Experiment
EIPBN'99
Marco Island, FL 1999

S. R. J. Brueck
Poling of Fused Silica - A Never Ending Process
Novel Optical Materials and Applications,99
Cetraro, Italy 1999

M. J. O'Brien*, R. M. Rabinovich, X-C. Long, J. T. Thompson*, S. R. J. Brueck,
V. H. Perez-Luna and G. P. Lopez
Grating Coupled Cemical and Biological Fiber Optic Sensors
Intl. Conf. On Sensing and Nanostructures (ICOSN'99)
Yokohama, Japan 1999

Saleem Zaidi and S. R. J. Brueck
Interferometric Lithography for Nanostructure Fabrication
Intl. Conf. On Sensing and Nanosctructures (ICOSN'99)
Yokohama, Japan 1999

S. R. J. Brueck
Imaging Interferometric Lithography –
Extending Optics to Fundamental Limits and Beyond
Intl. Congress on Optics (ICO'99)
San Francisco, CA 1999

T. G. Alley*, S. R. J. Brueck and M. Wiedenbeck
Space Charge in Thermally Poled Fused Silica
Bragg Gratings, Photosensitivity and Poling in Glass Waveguides
Stuart, FL 1999

X.-C. Long, S. R. J. Brueck and M. L. Minden
A High Speed Poled-Fiber Switch
Bragg Gratings, Photosensitivity and Poling in Glass Waveguides
Stuart, FL 1999

X.-C. Long and S. R. J. Brueck
Large Photosensitivity in Lead Silicate Glasses
Bragg Gratings, Photosensitivity and Poling in Glass Waveguides
Stuart, FL 1999

V. Metlushko, B. Ilic, H. Koo, R. D. Gomez, U. Welp, G. Crabtree,
Wenjun Fan*, S. R. J. Brueck, P. Neuzil, and R. Kumar
Current Modulation in Superconducting/Magnetic Nanostructured Materials
Intl. Semicon. Device Research Conf.
Charlottesville, VA 1999

Julian Cheng's Publications:

Bo Lu, Y.C. Lu, and Julian Cheng: 'Gigabit-per-sec optical link using optimized low-temperature AlGaAs/GaAs vertical-cavity surface-emitting lasers", IEEE J. of Quantum Electronics, **32**, No. 8, pp. 1347-1359, Aug. (1996).

Julian Cheng, "Surface-Emitting Laser-Based Multiplexing Technologies", SPIE Volume 2690, Wavelength Division Multiplexing Components, pp.70-77, (1996).

G. G. Ortiz, C. P. Hains, Julian Cheng, H. Q. Hou, and J. C. Zolper, "Monolithic integration of $In_{0.2}Ga_{0.8}As$ vertical-cavity surface-emitting lasers with resonance-enhanced quanum-welll photodetectors", Electronics lett., **32**, No. 13, pp. 1205-1207, June (1996).

G.G.Ortiz, C. P. Hains, Julian Cheng, J. C. Zolper, "Efficient cryogenic VCSELs with chirped multi-quantum-wells with a wide operating temperature range", IEEE Photonics Technol. Lett., **8**, No.10, October (1996).

Julian Cheng, Yin-Chen Lu, Bo Lu, and G. G. Ortiz, H. Q. Hou, J. C. Zolper, and M. J. Hafich, "A New Optoelectronic Transceiver and Routing Switch Based on Vertical-Cavity Surface-Emitting Lasers, Photodetectors, and Heterojunction Bipolar Transisitors", Proceeedings of SPIE, Vol. 3500-36, Feb. (1997).

G. G. Ortiz, S. Q. Luong, S. Z. Sun, and Julian Cheng, H. Q. Hou, G. A. Vawter, and E. Hammons: "Monolithic, Multiple Wavelength Vertical-Cavity Surface-Emitting Laser Arrays by Surface-Controlled MOCVD Growth Rate Enhancement and Reduction", IEEE Photonics Technol. Lett., **9**, No. 8, pp. 1069-1071; August (1997).

G. G. Ortiz , C. P. Hains, S. Luong, S. Z. Sun, Julian Cheng, H. Q. Hou, G. A. Vawter and B. E. Hammons: "Multiple Wavelength Vertical-Cavity Surface-Emitting Laser Arrays using Surface-Controlled MOCVD Growth Rate Enhancement and Reduction", OSA Trends in Optics and Photonics (TOPS), Vol. 15: Advances in Vertical-Cavity Surface-Emitting Lasers, edit. C.Chang-Hasnain, pp. 29-35, Sept. (1997).

S. Q. Luong, G. G. Ortiz, Y. Zhou, Jun Lu, C. P. Hains, Julian Cheng, H. Q. Hou, and G. A. Vawter: "Monolithic, Wavelength-Graded VCSEL and Resonance-Enhanced Photodetector Arrays for Parallel Optical Interconnects", IEEE Photonics Technol. Lett., **9**, No. 5, pp. 642-644, May, (1998).

Alduino, Yuxin Zhou, S. Luong, C. P. Hains, and Julian Cheng, "Wavelength Multiplexing and Demultiplexing using Multi-Wavelength VCSEL and Resonance-Enhanced Photodetector Arrays", IEEE Photonics Technol. Lett., **10**, No. 8, pp. 1310-1312, August (1998).

Yuxin Zhou, S. Luong, C.P. Hains, and Julian Cheng: "Oxide-Confined Monolithic, Multiple-Wavelength Vertical-Cavity Surface-Emitting Laser Arrays with a 40 nm Wavelength Span", IEEE Photonics Technol. Lett., **10**, pp. 1527-1529, (1998).

C. Alduino, S. Q. Luong, Yuxin Zhou, C. P. Hains, and Julian Cheng, "Quasi-Planar Monolithic Integration of High-Speed VCSEL and Resonant Enhanced Photodetector Arrays", IEEE Photonics Technology Letters **11**, No. 5, pp. 512-514, May (1999).

(Invited) Julian Cheng, Yuxin Zhou, S. Q. Luong, A. C. Alduino, and C. P. Hains: "Wavelength-Division Multiplexed Optical Interconnects using Monolithic Wavelength-Graded VCSEL and Resonant Photodetector Arrays", Proceedings of SPIE, **3627**, Vertical-Cavity Surface-Emitting Lasers III, (1999).

N. Y. Ki, C. P. Hains, Kai Yang, Jun Lu, P.W. Li, Julian Cheng: "Organometallic vapor phase epitaxy growth and optical characteristics of almost 1.2 μm GaInNAs three-quantum-well laser diodes", Applied Physics Letters, Vol. **75**, No. 8, pp.1051-1053, 23 August, (1999).

Julian Cheng's Conference Papers:

G. Ortiz, Bo Lu, Julian Cheng, C. H. Hains, S.Z. Sun, "VCSELs with non-uniform multiple quantum wells for a very wide temperature range of cw operation", Conference on Lasers and Electrooptics, 1996 Technical Digest Series, 10, pp. 83-84, June 2-7, (1996); Paper JTuH6.

Julian Cheng (Invited Paper): "Reconfigurable Multi-Point Optical Interconnects using Vertical-Cavity Surface-Emitting Laser-Based Optoelectronic Switches Arrays", Electrochemical Society Proceedings, **96-2**, pp. 117-119, (1996).

Julian Cheng (Invited Talk): "Future Optical Data Links and Optical Interconnects", Paper presented at the 1996 Laser and Electro-Optics Society (LEOS) annual meeting, Boston, MA, Nov. (1996).

G.G. Ortiz, Julian Cheng, C. P. Hains, H. Q. Hou, J. C. Zolper, "Monolithic Integration and Individually-Optimized Operation of $In_{0.2}Ga_{0.8}As$ Vertical-Cavity Surface-Emitting Lasers and Resonance Enhanced Quantum-Well Photodetectors", IEEE Laser and Electro-Optics Society Annual Meeting, **2**, pp. 273-274, (1996).

G. G. Ortiz, S. Z. Sun and Julian Cheng, S. Z. Sun, H. Q. Hou,"MOCVD Enhanced and Depleted Growth Rate Regions for Multiple Wavelength Vertical-Cavity Surface-Emitting Laser Arrays", CLEO 1997, May (1997).

G. G. Ortiz, S. Z. Sun and Julian Cheng, S. Z. Sun, H. Q. Hou, "Monolithic Wavelength-Graded VCSEL and Resonance-Enhanced Photodetector Arrays for Parallel Optical Interconnects", LEOS 10th Annual Meeting Conference Proceedings, **2**, Paper WJ-2, pp. 79-80; Nov. (1997).

Alduino, S. Luong, Yuxin Zhou, C. P. Hains, and Julian Cheng: " Wavelength-Division Multiplexing and Demultiplexing using Monolithic Wavelength-Chirped VCSEL and Resonance-Enhanced Photodetector Arrays ", 1998 CLEO Technical Digest , **6**, pp. 367-368, (1998); Paper CThK2.

Julian Cheng: "Optical Multiplexing Technologies Based on VCSELs", Invited paper presented at the La Jolla Advanced-Topics Research School Semiconductor Science and Technology Conference, Sept. 7-11, (1998); La Jolla, CA.

Yuxin Zhou, S. Luong, C.P. Hains, and Julian Cheng, "Oxide-Confined Monolithic, Multiple-Wavelength Vertical-Cavity Surface-Emitting Laser Arrays with a 40 nm Wavelength Span", presented at the LEOS Annual Meeting, Dec. 4, (1998).

Alduino, S. Q. Luong, Yuxin Zhou, C. P. Hains, and Julian Cheng, "A Quasi-Planar Approach to the Monolithic Integration of High-Speed VCSEL and Resonant Photodetector Arrays", and "Conference on Lasers and Electro-Optics, Baltimore, MD; May (1999).

Julian Cheng, N.Y. Li, C. P. Hains, and K. Yang: "Multi-Quantum Well GaInNAs/GaAs Lasers with Low Threshold Current Density Grown by MOCVD", presented at the 57th Device Research Conference; Session VIIB; Santa Barbara, CA; June 28-30, (1999).

N. Y. Ki, C. P. Hains, Jun Lu, Kai Yang, Julian Cheng: "Tellurium Memory Effects on OMVPE-Grown $In_{0.3}Ga_{0.7}As_{0.997}N_{0.003}$/GaAs Laser Diodes", presented at the 41st Electronic Material Conference, Session G; Santa Barbara, CA; June 30-July2, (1999).

Yuxin Zhou, S. Q. Luong, and Julian Cheng: "High-Speed Wavelength Division Multiplexing and Demultiplexing Using Monolithic Quasi-Planar VCSEL and Resonant Photodetector Arrays with Strained InGaAs/GaAs Quantum Wells", 1999 LEOS Annual Meeting; San Francisco, CA: Nov., (1999).

Kai Yang, C. P. Hains, N.Y. Li, and Julian Cheng: "Near Room Temperature CW Lasing Operation of a Narrow-Stripe Oxide-Confined GaInNAs/GaAs Multi-Quantum Well Laser Grown by MOCVD,1999 LEOS Annual Meeting; San Francisco, CA: Nov., (1999).

Kai Yang, C. P. Hains, and Julian Cheng, "Efficient Above-Room-Temperature Continuous-Wave Operation of a GaInNAs/GaAs Multi-Quantum Well Laser Grown by MOCVD", LEOS Summer Topical Meeting on VCSELs; San Diego, CA; July 28-30, (1999); post deadline paper PD-1.

Steve Hersee's Group Publications

X. Wang*, B. Lu and S.D. Hersee, "Direct Imaging of a High Power Diode Laser Cavity using a Transparent ITO Contact", Photonics Technol. Lett., 49-51, (1996).

J. Zolper, M. H. Crawford, A.J. Howard, J. Ramer* and S. D. Hersee, "Morphology and Photoluminescence Improvements from High Temperature Rapid Thermal Annealing of GaN", Applied Phys. Lett., **68,** 200-202, (1996).

X.C. Long, R.A. Myers, S.R.J. Brueck, J.Ramer*, K. Zheng and S.D. Hersee, "GaN Linear Electrooptic Effect", Appl. Phys. Lett., **67** 1349-1351, (1995).

L. Zhang, J. Ramer*, J. Brown, K. Zheng, L.F. Lester and S.D. Hersee, "Electron Cyclotron Resonance Etching Characteristics of GaN in SiCl4/Ar", Applied Phys. Lett., **68,** 367-369, (1996).

G. Goncher, B. Lu, W.L. Luo, J.C. Cheng, S.D. Hersee, S.Z. Sun, R.P. Schneider and J.C. Zolper, "Cryogenic Operation of AlGaAs-GaAs VCSELs at Temperatures from 200 K to 6 K", Photonics Technol. Lett., **8** 316-318 (1996).

H. Li, X. Wang*, S.D. Hersee, "The Measurement of Lateral Index Variations in Unstable Resonator Semiconductor Lasers from Spectrally Resolved Near-Field Images", Photonics Technol. Lett., **9** 31-33, (1997).

H.S. Gingrich, D.R. Chumney, S. -Z. Sun, S.D.Hersee, L.F. Lester and S.R.J. Brueck, "Broadly Tunable External Cavity Laser Diodes with Staggered Thickness Multiple Quantum Wells", Photonics Technol. Lett., **9** 155-157, (1997).

Invited Paper: S.D.Hersee, J.C. Ramer and K.J. Malloy, "The Microstructure of MOCVD GaN on Sapphire", *MRS Bulletin*, **22**(7), 45-51, (1997).

G. Peake*, S.D. Hersee, "GaAs Microlens Arrays Grown by Shadow Masked MOVPE", J. Electronic Matls. , **26**, 1134-1138, (1997).

J. Ramer*, A. Hecht*, S.D. Hersee, "The Stability and Interface Abruptness of InxGa1-xN/InyGa1-yN Multiple Quantum Well Structures Grown by MOVPE on Sapphire", J. Electronic Matls. , **26**, 1109-1113, (1997).

S. Guel-Sandoval*, A.H. Paxton, S.D. Hersee and J. McInerney, "Effective Index Design of a Shaped Conitnous Unstable Resonator for High Power Laser Diodes", Revista Mexicana de Fisica, **43**, 940-951, (1997).

"Nanoheteroepitaxy: A New Approach to the Heteroepitaxy of Mismatched Semiconductor Materials", D. Zubia* and S.D. Hersee, J. Appl. Phys., **85**, 6492-6496, (1999).

"Properties of GaN epilayers grown on misoriented sapphire substrates", Carol Trager-Cowan , S. McArthur, P. G. Middleton, K. P. O'Donnell D. Zubia*, S.D. Hersee, MRS Journal of Internet, accepted Oct 1998: (http://nsr.mij.mrs.org/3/36/)

"Micromachined, Reusable Shadow Mask for Integrated Optical Elements Grown by MOCVD", G.M. Peake* , L. Zhang, N.Y. Li, A.M. Sarangan, C.G. Willison, R.J. Shul and S. D. Hersee, J. Vac. Sci. and Technol., B 17, 2070-2073, (1999).

Steve Hersee's Group Presentations:

H. Li, X, Wang* and S.D. Hersee, "Spectrally Resolved Near-Field Images of Unstable Resonator Diode Lasers and Their Application to the Measurement of Refractive Index", paper WR6, IEEE Laser & Electro-Optics Society Annual Meeting (LEOS '96), Nov. 18 - 21, 1996, Boston, MA

D.J. King, J.C. Ramer*, L. Zhang, S.D. Hersee, L.F. Lester, "Temperature Behavior of Pt/Au Ohmic Contacts to p-GaN", MRS 1997 Spring Meeting, 3/31/96-4/4/96 San Francisco, CA.

Invited Paper: S.D.Hersee, J.Ramer*, K.J. Malloy, "GaN on Sapphire: an Ordered Polycrystal", Fourth WideBandgap and Nitride Workshop, St. Louis, MO, March 11-14, 1997.

S.D.Hersee, J.Ramer*, A. Rice, G. Lui, K.J. Malloy, "The Properties of GaN Grown on Misoriented Sapphire", Fourth WideBandgap and Nitride Workshop, St. Louis, MO, March 11-14, 1997.

G. Peake*, S.D. Hersee, "The Shadow Masked MOVPE Growth and Optical properties of GaAs Microlenses", Eigth Biennial Workshop on Organometallic *VPE*, 13-17th April, 1997, Dana Point, CA.

J. Ramer*, A. Hecht*, S.D. Hersee, "The Stability of InxGa1-xN/InyGa1-yN Structures Grown by MOVPE on Sapphire", Eigth Biennial Workshop on Organometallic VPE, 13-17th April, 1997, Dana Point, CA.

S.D. Hersee, D. Zubia*, A. Rice, G. Liu, J.Ramer* and K.Malloy, "The Microstructure of GaN on Sapphire", presented at 2nd. European GaN Workshop, Valbonne, France, 11-13 June, 1997

Invited Paper: S.D. Hersee, J.C. Ramer* , D. Zubia* and K.M. Hansen*, "MOCVD Growth, Characterization and Stability of High Quality InGaN MQW Structures", 1997 Summer Topical Meeting on "GaN Materials, Processing and Devices", (11-13 August, 1997, Montreal, Canada)

Piotr Perlin, Valentin Iota, Bernie A. Weinstein, Henryk Teisseyre, Tadeusz Suski, Steve Hersee, Christian Kisielowski, Eicke R. Weber, Jinwei Yang, "High-Pressure Investigation of InGaN Quantum Wells", MRS Spring Meeting, San Francisco, CA, April 1998. (published in MRS Symposium Proceedings, Vol 512)

"Auger and Electrical Analysis of Pt/Au and Ni/Au Contacts to p-GaN", D.J. King, L. Zhang, J.C. Ramer, A. Rice, K.J. MALLOY, S.D.HERSEE, L.F. LESTER, paper ThF5 at *LEOS '98* (IEEE Lasers and Electro-Optics Society 1998 Annual Meeting), Orlando, Florida, Dec 1998.

"Integrated Optical Structure Grown by Shadow Masked MOCVD", G.M. Peake, A.M. Sarangan and S.D. HERSEE, paper FQ3 at *LEOS '98* (IEEE Lasers and Electro-Optics Society 1998 Annual Meeting), Orlando, Florida, Dec 1998.

"Shadow Masked OMVPE for Integrated Optical Structures Using a Micromachined Silicon Mask", G.M. Peake*, L. Zhang, N. Li, A.M Sarangan, S.D. Hersee, Ninth Biennial Workshop on Organometallic VPE, 23-27 May, 1999, Ponte Vedra Beach, FL.

"Nanoheteroepitaxy: Selective MOCVD Growth of GaN on Compliant ,Nanostructured Silicon", D. Zubia, S. Zaidi, S.R.J. Brueck, Ninth Biennial Workshop on Organometallic VPE, 23-27 May, 1999, Ponte Vedra Beach, FL.

"Application of Nanoheteroepitaxy (NHE) to the OMVPE Growth of GaN on Silicon", S.D.Hersee, D.Zubia, S.H. Zaidi, S.R.J. Brueck, Lateral Epitaxial Overgrowth Workshop, 2-6 Aug, 1999, Juneau, Alaska.

"Nanostructured SOI Compliant Structures", D.Zubia*, S.H. Zaidi, T. O'Neil*, S. Jaffer, S.R.J. Brueck, S.D.Hersee, First International Conference on Compliant and Alternative Substrate Technology, Buena Vista, FL, Sept. 19-23, (1999).

Ravi Jain's Publications:

E. Poppe, B. Srinivasan and R.K. Jain, 980nm Diode-Pumped Continuous Wave Mid-IR (2.7 mm) Fiber Laser, Electron. Lett., **34**, 2331 (1998).

B. Srinivasan, J. Tafoya, and R.K. Jain, High-Power "Watt-Level" CW Operation of Diode-Pumped 2.7 mm Fiber Lasers Using Efficient Cross-Relaxation and Energy Transfer Mechanisms, Optics Exp. **4**, 490 (1999).

B. Srinivasan, E. Poppe, J. Tafoya, and R.K. Jain, High Power (400 mW) Diode-Pumped 2.7 mm Er:ZBLAN Fiber Lasers Using Enhanced Er-Er Cross-Relaxation Processes, Electron. Lett., **35**, 1338 (1999).

Ravi Jain's Presentations:

"A Compact Blue Upconversion Fiber Laser pumped by a Diode-Pumped Raman Fiber Laser", G.S. Feller, B. Srinivasan, S.G. Grubb, I.J. Booth & R.K. Jain, CLEO, Anaheim, May (1996).

"Self Mode-Locked Operation of a 482nm Tm:ZBLAN Upconversion Fiber Laser", G.S Feller, R.K. Jain, B. Srinivasan, and I.J. Booth, IQEC '96, Sydney, July (1996).

"Fusion Splicing of ZBLAN fibers with the use of Tungsten Filament Heating", B. Srinivasan, M. Erlandsson, G.S. Feller, E.W. Mies, and R.K. Jain, Photonics '96, India, Dec. 1996

"Upconversion Fiber Lasers", B. Srinivasan, G.S. Feller, and R.K. Jain, Invited Paper, Photonics '96, India, December (1996).

"Reproducible Fusion Splicing of Low Melting Point (Fluoride) Optical Fibers With the Use of a Stable Heat Source", B. Srinivasan, M. Erlandsson, G.S. Feller, E.W. Mies, and R.K. Jain, Optical Fiber Communications (OFC '97), Dallas, February (1997).

B. Srinivasan and R.K. Jain, , First Demonstration of Thermally-Poled Electro-Optically Tunable Fiber Bragg Gratings, European Conference on Optical Communications (ECOC), Nice, France, Paper P1.1 (Sep. 1999)

B. Srinivasan and R.K. Jain, First Demonstration of Thermally-Poled Electro-Optically Tunable Fiber Bragg Gratings, OSA Annual Meeting, Paper WI3 (Sep 1999)

B. Srinivasan and R.K. Jain, High-power diode-pumped 2.7 micron fiber lasers using efficient cross-relaxation and energy transfer, OSA Annual Meeting, Paper WA2 (1999)

B. Srinivasan, E. Poppe, R.K. Jain, 40 mW Single Transverse Mode Mid-IR (2.7 mm) CW Output from a Simple Mirror-Free 780 nm Diode-Pumpable Fiber Laser, CLEO '98, Paper CWM2, **6**, 297 (1998).

X. Zhao, B. Srinivasan, P. Pulaski, S. Gupta, and R.K. Jain, Mirror-Free High Power (140 mW) Diode-Pumped 2.7 mm CW Fiber Laser, CLEO-Europe 98, Postdeadline paper (1998).

B. Srinivasan and R.K. Jain, Diode-Pumped High Power Continuous Wave Mid-Infrared Fiber Lasers, Photonics '98, Invited Paper FC-1, New Delhi, India (1998).

B. Srinivasan, G. Monnom, and R.K. Jain, Enhancement of the Efficiency of 2.7 mm Er:ZBLAN Fiber Lasers Via Cluster Formation at High Doping Densities, CLEO '99, Paper CTuK30 (1999).

B. Srinivasan, J. Tafoya, and R.K. Jain, Diode-Pumped High Power CW 2.7 mm Er Fiber Lasers, CLEO '99, Postdeadline paper CPD-23 (1999).

B. Srinivasan and R.K. Jain, First Demonstration of Thermally-Poled Electro-Optically Tunable Fiber Bragg Gratings, Bragg Gratings, Photosensitivity and Poling of Glasses, paper SaB3 (1999).

B. Srinivasan and R.K. Jain, Strong Fiber Bragg Gratings With Significantly Enhanced Thermal Stability, OSA Annual Meeting '99, Postdeadline paper PD22 (1999).

Marek Osinski's Publications:

. P. G. Eliseev, V. A. Smagley, and M. Osiński, "*Threshold current density in optimized UV diode lasers based on gallium nitride*", Technical Digest, CLEO '96 Conference on Lasers and Electro-Optics, **9**, 1996 OSA Technical Digest Series, Anaheim, California, 2-7 June, 1996, Paper CThP4, pp. 457-458.

A. G. Glebov, P. G. Eliseev, and M. Osiński, "*Emission-induced current crowding in diode lasers: Criterion and numerical modeling*", Technical Digest, XX International Quantum Electronics Conference IQEC '96, Sydney, Australia, 14-19 July, 1996, Paper WL89, p. 180.

V. A. Smagley, P. G. Eliseev, and M. Osiński, *"Theory of radiative processes in GaN-based laser structures"*, Technical Digest, XX International Quantum Electronics Conference IQEC '96, Sydney, Australia, 14-19 July, 1996, Paper FL2, pp. 272-273.

P. Perlin, P. G. Eliseev, M. Osiński, M. Banas, and P. Sartori, *"Unusual physical properties of blue light emitting diodes based on InGaN:Zn"*, Conference Proceedings, 23rd International Conference on the Physics of Semiconductors, Berlin, Germany, 21-26 July 1996, **4**, Paper VI.D.6, pp. 2873-2876, World Scientific 1996.

P. Perlin, M. Osiński, P. G. Eliseev, V. A. Smagley, J. Mu, M. Banas, and P. Sartori, *"Low-temperature study of current and electroluminescence in InGaN/AlGaN/GaN double-heterostructure blue light-emitting diodes"*, Applied Physics Letters **69**, No. 12, pp. 1680-1682 (16 September 1996).

V. A. Smagley, P. G. Eliseev, and M. Osiński, *"Comparison of models for calculation of optical gain in gallium nitride"*, Physics and Simulation of Optoelectronic Devices V (M. Osiński and W. W. Chow, Eds.), SPIE International Symposium on Integrated Devices and Applications Optoelectronics '97, San Jose, California, 10-14 February 1997, SPIE Proceedings, **2994**, pp. 129-140.

P. G. Eliseev, A. G. Glebov, and M. Osiński, *"Modeling of current crowding accompanying optical filament formation in semiconductor lasers and amplifiers"*, Physics and Simulation of Optoelectronic Devices V (M. Osiński and W. W. Chow, Eds.), SPIE International Symposium on Integrated Devices and Applications Optoelectronics '97, San Jose, California, 10-14 February 1997, SPIE Proceedings, **2994**, pp. 580-590.

P. G. Eliseev, A. G. Glebov, and M. Osiński, *"Current self-distribution effect in diode lasers: Analytic criterion and numerical* study", Special Issue on Semiconductor Lasers, IEEE Journal of Selected Topics in Quantum Electronics **3**, No. 2, pp. 499-506 (April 1997).

P. G. Eliseev, P. Perlin, J. Furioli, and M. Osiński, *"Characterization and modeling of electroluminescence from single-quantum-well InGaN/AlGaN/GaN green-light-emitting diodes"*, Technical Digest, CLEO '97 Conference on Lasers and Electro-Optics, Baltimore, Maryland, 18-23 May, 1997, **11**, 1997 OSA Technical Digest Series, Paper CTuO3, pp. 110-111.

P. G. Eliseev, A. G. Glebov, and M. Osiński, *"Analysis of current self-distribution induced by self-focusing filamentation in laser diode"*, Technical Digest, CLEO '97 Conference on Lasers and Electro-Optics, Baltimore, Maryland, 18-23 May, 1997, **11**, 1997 OSA Technical Digest Series, Paper CWF21, p. 238.

11. M. Osiński, P. Perlin, H. Schöne, A. H. Paxton, and E. W. Taylor, "*Effects of proton irradiation on AlGaN/InGaN/GaN green light emitting diodes*", Electronics Letters **33**, no. 14, pp. 1252-1254 (3 July 1997).

M. Osiński, P. G. Eliseev, P. Perlin, V. A. Smagley, J. Furioli, and J.-H. Lee, "*Anomalous temperature behavior of optical emission from Nichia AlGaN/InGaN/GaN single-quantum-well LEDs*", Invited Paper, Record of the 16th Electronic Materials Symposium, Minoo, Osaka, Japan, 9-11 July, 1997, Paper SB6, pp. 273-276.

P. G. Eliseev, M. Osiński, and P. Perlin, "*Anomalous spectral shifts and band-tailing in GaN-based quantum-well devices*", Technical Digest, CLEO/Pacific Rim '97, The Pacific Rim Conference on Lasers and Electro-Optics, Chiba, Japan, 14-18 July, 1997, Paper FO4, p. 287.

W. Nakwaski and M. Osiński, "*Available output of two-dimensional surface-emitting laser arrays*", Optical and Quantum Electronics **29**, pp. 639-649 (1997).

M. Osiński, "*Short-wavelength visible light emitters based on group-III nitrides and their potential for space applications*", Critical Review, Advancement of Photonics for Space (E. W. Taylor, Ed.), SPIE International Symposium on Optical Science, Engineering, and Instrumentation SD97, San Diego, California, 28-29 July 1997, SPIE Critical Reviews of Optical Science and Technology, **CR66**, pp. 93-120.

E. W. Taylor, A. H. Paxton, H. Schöne, J. H. Comtois, A. D. Sanchez, M. A. Michalicek, J. E. Winter, S. J. McKinney, M. Osiński, P. Perlin, R. F. Carson, J. P. G. Bristow, J. Lehman, and M. K. Hibbs Brenner, "*Radiation induced effects research in emerging photonic technologies: vertical cavity surface emitting lasers, GaN light emitting diodes and micro electromechanical devices*", Photonics for Space Environments V (E. W. Taylor, Ed.), SPIE International Symposium on Optical Science, Engineering, and Instrumentation SD97, San Diego, California, 30 July 1997, SPIE Proceedings, **3124**, pp. 9-21.

P. G. Eliseev, P. Perlin, J. Lee, and M. Osiński, *"Blue" temperature-induced shift and band-tail emission in InGaN-based light sources*", Applied Physics Letters **71**, No. 5, pp. 569-571 (4 August 1997).

W. Nakwaski and M. Osiński, "*On the thermal resistance of vertical-cavity surface-emitting lasers*", Optical and Quantum Electronics **29**, No. 9, pp. 883-892 (September 1997).

A. A. Leal, M. Osiński, and E. Conforti, "*Effects of a thermal-dependent electric field penetration depth on threshold behavior of surface-emitting lasers*", Microwave and Optical Technology Letters **17**, No. 2, pp. 94-97 (5 Feb. 1998).

P. Perlin, B. A. Weinstein, N. E. Christensen, I. Gorczyca, V. Iota, T. Suski, P. Wiśniewski, M. Osiński, and P. G. Eliseev, "*Cubic InN inclusions as the cause for the unusually weak pressure shift of the luminescence in InGaN*", Nitride Semiconductors (F. A. Ponce, S. P. DenBaars, B. K. Meyer, S. Nakamura, and S. Strite, Eds.), Boston, Massachusetts, 1-4

December 1997, Materials Research Society Symposium Proceedings, **482**, pp. 697-702, Warrendale, Pennsylvania (1998).

H. P. Maruska, M. Lioubtchenko, T. G. Tetreault, M. Osiński, S. J. Pearton, M. Schurman, R. Vaudo, S. Sakai, Q. Chen, and R. J. Shul, "*Introduction of ions into wide band gap semiconductors*", Power Semiconductor Materials and Devices (S. J. Pearton, R. J. Shul, E. Wolfgang, F. Ren, and S. Tenconi, Eds.), Boston, Massachusetts, 1-4 December 1997, Materials Research Society Symposium Proceedings, **483**, pp. 333-344, Warrendale, Pennsylvania (1998).

A. A. Leal, M. Osiński, and E. Conforti, "*Multilayer analysis of anisotropic heat flux in vertical-cavity surface-emitting lasers with quarter-wave semiconducting mirrors*", IEEE Transactions on Microwave Theory and Techniques **46**, No. 3, pp. 208-214 (March 1998).

M. Osiński, P. G. Eliseev, P. Perlin, J. Lee, H. Sato, T. Sugahara, Y. Naoi, and S. Sakai, "*Anomalous temperature behavior and band tailing in InGaN/GaN heterostructures grown on sapphire by MOCVD*", Technical Digest, CLEO '98 Conference on Lasers and Electro-Optics, San Francisco, California, 3-8 May, 1998, Paper CWH5, pp. 276-277.

J. Wang, S. Tottori, M. S. Hao, H. Sato, S. Sakai, and M. Osiński, "*Epitaxial lateral overgrowth of GaN by sublimation method and by MOCVD*", Optoelectronic Materials and Devices (M. Osiński and Y.-K. Su, Eds.), SPIE Photonics Taiwan '98 Symposium, Taipei, Taiwan, 9-11 July, 1998, SPIE Proceedings, **3419**, pp. 7-15.

P. G. Eliseev, G. A. Smolyakov, and M. Osiński, "*Ghost modes and their signature in InGaN diode laser spectra*", Proceedings of the 2nd International Symposium on Blue Laser and Light Emitting Diodes (2nd ISBLLED), Kisarazu, Japan, 29 September - 2 October, 1998, Paper Th-10, pp. 413-416.

M. Osiński and D. L. Barton, "*Accelerated life testing of GaN/InGaN/AlGaN blue light-emitting diodes and high temperature failure mechanism*", Proceedings of the 2nd International Symposium on Blue Laser and Light Emitting Diodes (2nd ISBLLED), Kisarazu, Japan, 29 September - 2 October, 1998, Paper Th-P26, pp. 548-551.

W. Nakwaski and M. Osiński, "*Thermal properties of vertical-cavity surface-emitting semiconductor lasers*", Progress in Optics XXXVIII (E. Wolf, Editor), North-Holland, ISBN 0-444-82907-5, Ch. III, pp. 165-262, 1998.

J. Wang, R. S. Q. Fareed, M. Hao, S. Mahanty, S. Tottori, Y. Ishikawa, T. Sugahara, Y. Morishima, K. Nishino, M. Osinski, and S. Sakai, "*Lateral overgrowth mechanisms and microstructural characteristics of bulk-like GaN layers grown by sublimation method*", Journal of Applied Physics **85**, No. 3, pp. 1895-1899 (1 February 1999).

G. A. Smolyakov, P. G. Eliseev, and M. Osiński, "*Design limitations for InGaN/AlGaN/GaN lasers imposed by resonant mode coupling*", Technical Digest, Nineteenth Annual

Conference on Lasers and Electro-Optics CLEO '99, Baltimore, Maryland, 23-28 May 1999, Paper CtuU5, p. 203.

P. G. Eliseev, G. A. Smolyakov, and M. Osiński, "*'Ghost` modes and resonant effects in AlGaN/InGaN/GaN lasers*", Special Issue on Semiconductor Lasers, IEEE Journal of Selected Topics in Quantum Electronics **5** (3), pp. 771-779, May/June (1999).

M. Osinski, "*Green, blue, and beyond - current status and future prospects for short-wavelength diode laser development*", Invited Paper, Proceedings of 8th International Plastic Optical Fibers (POF) Conference, Makuhari Messe, Chiba, Japan, 14-16 July, 1999, pp. 78-84.

A Poled Electrooptic Fiber

X.-C. Long, R. A. Myers, and S. R. J. Brueck, *Fellow, IEEE*

Abstract— **A simple fabrication technique, readily extensible to volume manufacturing, is presented to produce an electrooptically active fiber segment that can be simply integrated into optoelectronic devices. The fabrication technique offers a dielectric isolation structure surrounding the fiber to allow high field poling, a pair of electrodes used both for poling and for inducing an electrooptic effect that can be lithographically defined for either velocity-matched, high speed RF modulation or quasiphasematched three-wave mixing interactions, and ends of the fiber unaffected by the fabrication and available for splicing with additional fiber sections. An electrooptic coefficient, including overlap between the nonlinearity and the fiber mode, as high as 0.3 pm/V was obtained by combined temperature/electric field poling.**

I. Introduction

PACKAGING COSTS associated with optomechanical coupling of discrete optical components are a major part of the cost for advanced optoelectronic systems. For example, for many high-speed fiber communications systems, the output of a diode laser must be coupled into a single-mode optical fiber, the fiber must in turn be coupled to a $LiNbO_3$ waveguide modulator whose output is again coupled into a fiber. Discrete optical components, e.g., graded-index lenses or micro-lenses, are required at each coupling node to adapt the very different mode profiles and spatial extents of the diode laser and modulator waveguide modes to the fiber mode. Tolerances are fractions of a micrometer to ensure minimal coupling losses and extensive active alignment is typically required. Throughput and yield are limited by the requirement of keeping the system stable while the bonding agents cure. Development of an integral fiber would substantially reduce the manufacturing and packaging costs associated with these systems. This is particularly attractive in view of advances in fiber lasers.

Electric field sensors are another potentially attractive application of electrooptic fibers. The electric power industry has a need for remote sensors to monitor high voltage generation and transmission systems. Integrating electrooptically active fiber sensors with Bragg reflector gratings is a very attractive alternative to currently available sensors.

A third potential application area for electrooptically active fibers is three-wave mixing to enable extension of the wavelength range available with high power diode lasers, which are today confined to the wavelength range from roughly 700 nm to 1 μm. Previous work [1], [2] has shown that the second-order nonlinearity and the electrooptic effect induced in germanosilicate glasses arise from electronic processes and are closely related. The required phase matching is most conveniently achieved by quasiphase matching in which the nonlinearity is either on and off for alternate coherence lengths. More complex poling patterns are readily envisioned to tailor the phase matching bandwidth for specific applications [3].

The discovery of a stable second-order nonlinearity induced in SiO_2 materials [4] has led to a great deal of work aimed at establishing a practical geometry and materials systems for poling both waveguide [5] and fiber electrooptic elements [2], [6].

Recently, a group at the Australian Fiber Optic Research Center has demonstrated [7] a significant improvement in the effective electrooptic coefficient of a fiber with two innovations: a) use of an ultraviolet beam along with an applied electric field to produce the poling in contrast to the use of high temperatures (~100–300 °C) under an applied electric field, and b) provision for wire electrodes internal to the fiber to increase resistance to breakdown during the poling and to provide a better overlap between the nonlinearity and the optical mode volume. They report an electrooptic (r) coefficient of 6 pm/V. This is significantly larger than previously reported [2], [6] (0.05 pm/V) and is sufficiently large for practical application. Their technique, however, still leaves significant packaging and manufacturability issues. Specifically, the fiber is drawn from a preform with two holes for electrode wires that are to be inserted following the fiber drawing. This wire insertion is a difficult manufacturing step. To avoid breakdown, one wire is inserted from each end of the fiber. The modulation frequency is limited to low values since a high-speed traveling wave geometry is not possible. This may be alleviated by inserting the wires through the sides of the fiber, however, splicing to either end of the fiber is difficult because of the electrode voids.

We have developed a simple fabrication technique that provides for ease of manufacturing and packaging. The technique is illustrated in Fig. 1. We start with a commercial "*D*" fiber [8] where one side of the cladding has been removed close to the core. The flat section of the "*D*" fiber is further etched to allow closer approach of the electrode structure to the fiber core. There is an important tradeoff between

Manuscript received October 5, 1995. This work was supported in part by the Air Force Office of Scientific Research.

X.-C. Long is with the Department of Electrical and Computer Engineering, Center for High Technology Materials, University of New Mexico, Albuquerque, NM 87131 USA and the Department of Physics and Astronomy, University of New Mexico, Albuquerque, NM 87131 USA.

R. A. Myers was with the Center for High Technology Materials, University of New Mexico, Albuquerque, NM 87131 USA; he is now with the Department of Physics, University of Auckland, Auckland, New Zealand.

S. R. J. Brueck is with the Center for High Technology Materials, University of New Mexico, Albuquerque, NM 87131 USA and with the Department of Electrical and Computer Engineering, University of New Mexico, Albuquerque, NM 87131 USA.

Publisher Item Identifier S 1041-1135(96)00932-9.

1041–1135/96$05.00 © 1996 IEEE

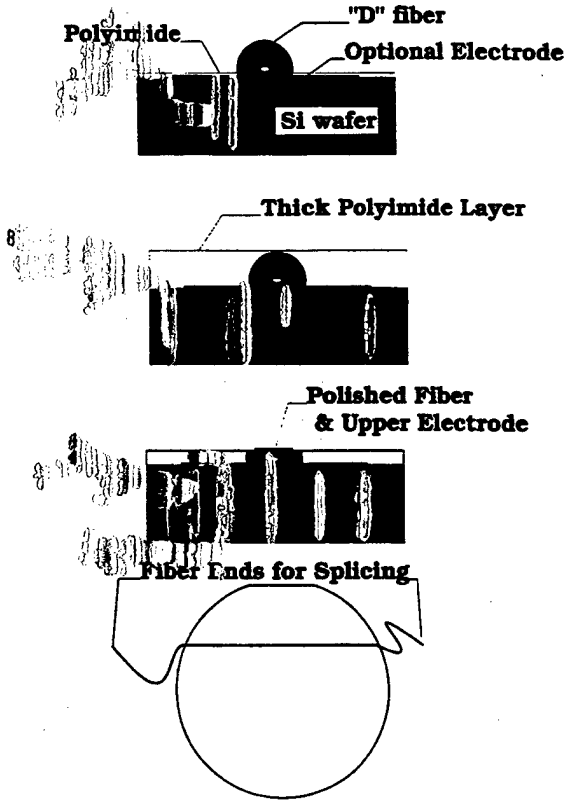


Fig. 1. Schematic representation of the steps involved in the fabrication of an electrooptically active fiber segment.

the proximity of the electrode to the core allowing a larger electrooptic coefficient and at the same time increasing the linear optical loss of the fiber segment. No attempt has yet been made to optimize this distance. The steps in the fabrication process include: 1) etching of the cladding to reduce the core-cladding distance; 2) gluing the fiber, "*D*" side down, to a Si wafer using a thin polyimide layer; 3) surrounding the fiber in polyimide with multiple deposition and curing cycles; 4) polishing the polyimide/fiber to decrease the total thickness; 5) depositing an upper electrode structure (which can be lithographically defined as a high-speed RF circuit or interrupted for quasiphasematching); 6) temperature/electric field poling the fiber; and 7) depositing additional dielectric and electrode layers as required, e.g., for increased RF isolation.

This technology provides: 1) a high-speed RF circuit allowing traveling wave interactions between the RF and optical fields and hence a high speed modulation capability; 2) inexpensive optical packaging by simple splices at both ends of the fiber; and 3) extensibility to simultaneous production of multiple poled fiber sections.

Initial demonstrations were carried out using a single mode, polarization-maintaining, germanosilicate *D*-fiber designed for 633 nm (Andrew Corporation no. 205170-633S-2) [8]. The core is 1.25 × 2.5 μm^2 with 18 wt% Ge doping, and the thickness of the fused silica cladding is only 9 μm on the flat side of the fiber. The total thickness of the core/cladding from the flat to the opposite side of the cladding is 45 μm. Following stripping of the plastic jacket in sulfuric acid at a temperature of 200 °C, the fiber was etched in 48% HF

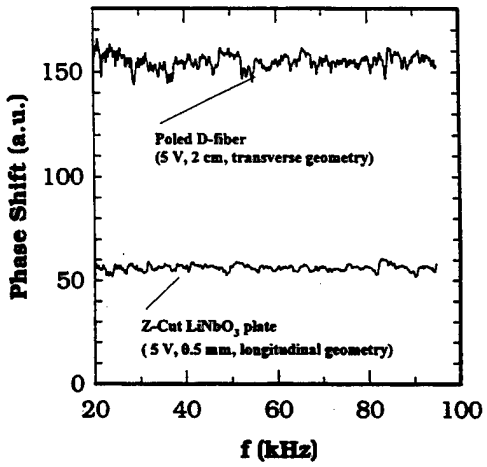


Fig. 2. Phase shift signals from poled fiber and $LiNbO_3$ samples in a Mach-Zehnder interferometer vs. driving electrical frequency.

solution for 3.5 min to further reduce the minimum thickness of the cladding (at the "*D*") to about 5 μm. The linear fiber properties were unchanged by these processing steps. A thin (~1-μm thick) layer of polyimide (UR3 100) was then spun onto a Si wafer and the fiber was affixed to the wafer "*D*" side down using this polyimide layer as an adhesive. The polyimide layer was cured with a dual temperature process at 120 °C and 170 °C for 5 min each. Subsequent to this curing, multiple additional layers of polyimide (UR3 140) were spun onto the wafer until the total thickness reached 40 μm, encapsulating the fiber. Each layer of the polyimide was cured with a dual temperature cycle at 120 °C and 170 °C for 10 min each. The total polyimide stack was then cured at 350 °C for one hour. Then, the fiber/polyimide structure was mechanically polished down to a thickness of ~34 μm, providing a planarized surface for further lithographic steps. A Cr:Au film (30 nm/300 nm) was deposited on top of the polished surface as the second electrode.

The resulting structure was poled by electric field/temperature poling processes over a variety of parameters. The poled interaction length was ~2 cm. To monitor the resulting electrooptic effect, the poled sample was placed in the measurement arm of a Mach–Zehnder interferometer operating at 633 nm. The Mach–Zehnder was a free space geometry with appropriate microscope objectives to couple light into and out of the electrooptically active fiber section.

The Mach–Zehnder signal shows a smooth frequency response as shown in Fig. 2. The absence of narrow acoustic frequency resonances implies that the piezoelectric response has been damped, probably by the polyimide, and demonstrates that the signal is due to the electrooptic effect. The reference signal for calibrating the nonlinearity using the longitudinal electrooptic effect in a $LiNbO_3$ slab is also shown. The $LiNbO_3$ signal is weaker because of the much shorter pathlength and lower applied fields. ITO electrodes are deposited on a 0.5-mm-thick, *Z*-cut $LiNbO_3$ plate. The appropriate electrooptic coefficient for this longitudinal geometry is r_{31} = 9.8 pm/V [9].

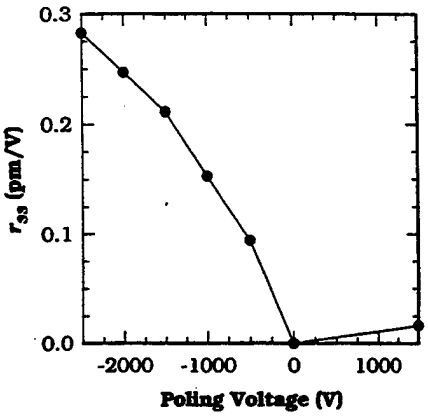


Fig. 3. The relationship between the measured electrooptic coefficient and the poling voltage for a fixed poling temperature (255 °C) and a fixed poling time (10 min).

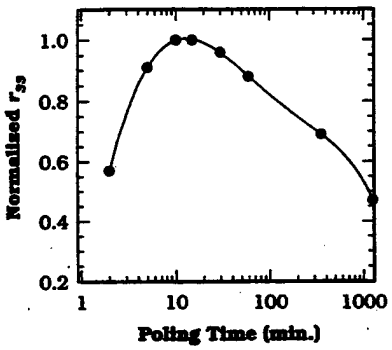


Fig. 4. The relationship between the measured electrooptic coefficient and the poling time for a fixed poling voltage (1.5 kV) and temperature (255 °C).

Fig. 3 shows the relationship between the measured electrooptic coefficient r_{33} and the poling voltage for a fixed poling temperature of 255 °C and a poling time of 10 min. Fig. 4 shows the dependence of r_{33} on the poling time for a fixed poling voltage of 1.5 kV and temperature of 255 °C. The largest coefficient was obtained for a short poling time of only 10 min at the highest applied voltage. Breakdown at the interface between the polyimide and the fiber limited the applied voltage to 2.7 kV. A much smaller signal was observed with a reversed polarity (cathode electrode adjacent to the "*D*"), probably because of a decreased spatial overlap between the nonlinearity and the optical mode.

As expected, the phase shift signal is sensitive to the polarization of input laser light. The ratio of the signal from TE mode to one from TM mode is ~2.4 : 1. This implies that electrooptic coefficient ratio $r_{33} : r_{31}$ is ~2.4 : 1, roughly consistent with the 3 : 1 ratio predicted from a simple symmetry model.

For a unetched *D*-fiber (9 μm core to flat distance) poled under the same conditions, the phase shift signal was reduced by factor of seven. This suggests that further increase of the effective electrooptic coefficient may be possible by etching the cladding layer thickness to less than 5 μm, at the cost of the introduction of some added linear optical loss.

II. Summary

A scaleable, manufacturing technique for producing a large second-order nonlinearity in an optical fiber is reported. A linear electrooptic coefficient as high as 0.3 pm/V is obtained by temperature/electric-field poling a germanosilicate optical fiber using an improved poling geometry. The ability to lithographically define the electrode geometry provides the capability for velocity-matched, high-speed RF circuit definition, and is adaptable to periodic poling for quasiphasematched nonlinear interactions. Integration by simple splicing to additional fiber components is a major advantage. Major areas of application include: high-speed fiber modulators for telecommunications; electric field sensors; and extended wavelength generation by three-wave mixing.

Acknowledgment

The authors thank Chris Kranenberg for useful discussions of polishing techniques.

References

[1] X.-C. Long, R. A. Myers, and S. R. J. Brueck, "Measurement of the linear electrooptic coefficient in poled amorphous silica," *Opt. Lett.*, vol. 19, pp. 1820–1822, 1994.

[2] X.-C. Long, R. A. Myers, and S. R. J. Brueck, "Measurement of linear electrooptic effect in temperature/electric-field poled optical fibers," *Electron. Lett.*, vol. 30, pp. 2162–2163, 1994.

[3] M. L. Bortz, M. Fujimura, and M. M. Fejer, "Increased acceptance bandwidth for quasiphasematched second harmonic generation in $LiNbO_3$ waveguides," *Electron. Lett.*, vol. 30, pp. 34–35, 1994.

[4] R. A. Myers, N. Mukherjee, and S. R. J. Brueck, "Large second-order nonlinearity in poled fused silica," *Opt. Lett.*, vol. 16, pp. 1732–1734, 1991.

[5] R. A. Myers, R. P. Tumminelli, and S. R. J. Brueck, "Stable second-order nonlinearity in SiO_2-based waveguides on Si using temperature/electric-field poling," in *Proc. SPIE*, 1994, vol. 2289, pp. 158–166.

[6] P. G. Kazansky, P. St. J. Russell, L. Dong, and C. N. Pannell, "Pockels effect in thermally poled silica optical fibers," *Electron. Lett.*, vol. 31, pp. 62–63, 1995.

[7] T. Fujiwara, D. Wong, Y. Zhao, S. Fleming, S. Poole, and M. Sceats, "Electrooptic modulation in germanosilicate fiber with UV-excited poling," *Electron. Lett.*, vol. 31, pp. 573–575, 1995.

[8] *Product Selection Guide* Ecore™ Polarization Maintaining Fiber (D-Series), Andrew Co., Orland Park, IL USA, 1992.

[9] W. R. Cook, Jr. and H. Jaffe, in *Electrooptic Coefficients*, K.-H. Hellwege, Ed. Berlin: Springer-Verlag, Londolt-Börnstein New Series, vol. 11, 1979, ch. 5, p. 564.

A CW External-Cavity Surface-Emitting Laser

J. V. Sandusky and S. R. J. Brueck, *Fellow, IEEE*

***Abstract*—Room temperature, continuous wave (CW) operation of an external-cavity, optically-pumped surface-emitting laser is reported. The device is a resonant-periodic gain (RPG) vertical-cavity surface-emitting laser (VCSEL) with the top mirror stack replaced by an epitaxially grown antireflection (AR) coating. An external mirror having a 50-mm radius of curvature completes the resonator in a near hemispherical configuration. Mode spectra, input-output curves, and polarization properties of the device are presented.**

I. Introduction

VERTICAL-CAVITY surface-emitting lasers (VCSEL's) are technologically important because of their low threshold [1], excellent beam quality [2], and potential for chip-to-chip communications [3]. Various authors have investigated VCSEL tuneability [4], mode dynamics [5], spectral linewidths [6], and polarization properties [7]–[9]. In addition to their technological relevance, VCSEL's are also interesting from a fundamental physics perspective because their small size gives rise to microcavity effects such as modified spontaneous emission [10].

While monolithic fabrication of the VCSEL is essential for many device applications, experimental studies of VCSEL characteristics and associated microcavity physics can be aided by external cavity operation allowing a continuous transition from microcavity ($L \sim \lambda$) to macrocavity ($L \gg \lambda$) operation and permitting additional optical components in the cavity such as a Brewster angle plate for polarization control or an intracavity etalon for tuning control. An extended cavity length should also lead to a narrower linewidth laser as a consequence of the higher cavity quality factor Q. Yokouchi *et al.* [4] have reported external cavity operation of a VCSEL at cryogenic temperatures (77 K) with a nearly microscopic cavity that precluded additional cavity optical elements. The work presented here demonstrates room-temperature, optically-pumped external-cavity operation with a macroscopic (50 mm) cavity length.

The epitaxial structure of the external-cavity VCSEL is shown in Fig. 1. The bottom stack is a standard high reflector (HR) composed of alternating quarter wavelength layers of AlAs and $Al_{0.25}Ga_{0.75}As$, with a theoretical reflectance of 99.8% at the 860-nm laser design wavelength. The gain region contains thirty (30) 10-nm-thick GaAs quantum wells with the $Al_{0.2}Ga_{0.8}As$ barrier thickness chosen to satisfy the standing wave criterion while accounting for quantum well—barrier reflections [11].

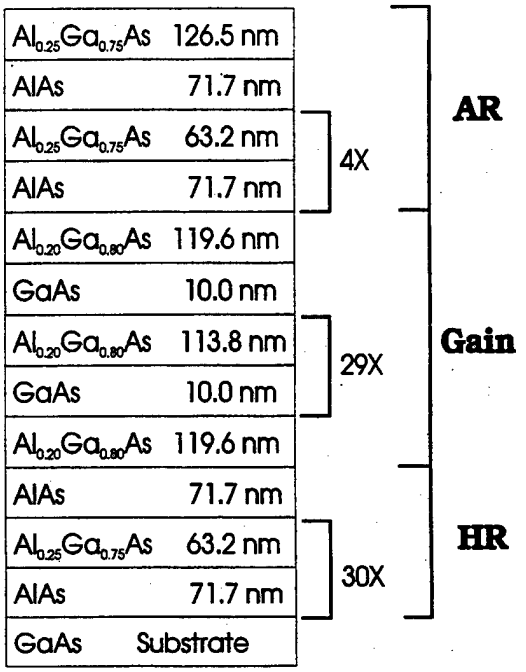


Fig. 1. Epitaxial growth stack for external cavity surface-emitting laser showing the AR coat (top section), gain region (middle section), and high reflector (bottom section).

The final antireflection (AR) stack minimizes reflectance between air and the gain region to avoid coupled cavity oscillations. The higher Al composition in both the HR and AR regions provides a spectral window allowing pumping into the barrier and quantum regions. To test the quality of the AR coating, we grew the AR stack sequence indicated in Fig. 1 over a 1-μm thick $Al_{0.2}Ga_{0.8}As$ layer on a GaAs substrate. The minimum measured reflectance was 0.05% at 858.5 nm.

Fig. 2 shows the predicted (accounting for both dispersion and absorption [12]) and measured reflectance spectra. The spectrum is radically different from a conventional VCSEL in that there is no region of high reflectance, and the resonance reflection dip is very broad. These differences are due to the AR coating that eliminates Fabry-Perot modes and the multiple-quantum-well region absorption that screens out reflections from the HR stack. The predicted reflectance spectra is a poor match to the measured reflectance spectra. We do not expect a good fit in the spectral region 700–860 nm because the model used to predict the reflectance spectra treats the quantum wells

Manuscript received October 10, 1995; revised November 3, 1995. This work was supported in part by the Air Force Office of Scientific Research (AFOSR).

J. V. Sandusky is with the Department of Physics and Astronomy, Center for High Technology Materials, University of New Mexico, Albuquerque, NM 87131 USA.

S. R. J. Brueck is with the Department of Physics and Astronomy and the Department of Electrical and Computer Engineering, Center for High Technology Materials, University of New Mexico, Albuquerque, NM 87131 USA.

Publisher Item Identifier S 1041-1135(96)-01991-X.

1041–1135/96$05.00 © 1996 IEEE

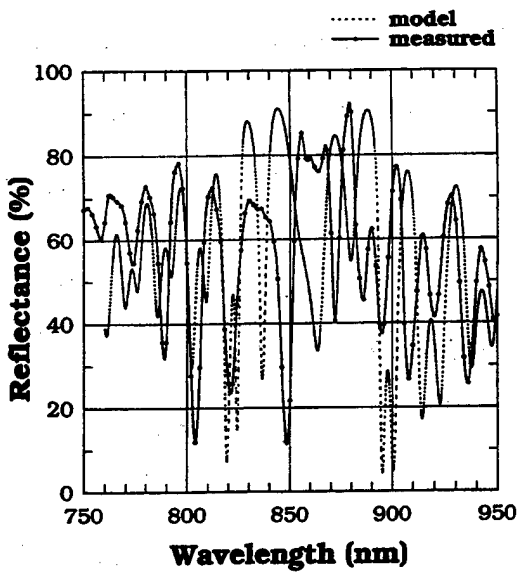


Fig. 2. Theoretical (dotted line) and measured (solid line) reflectance spectra of wafer.

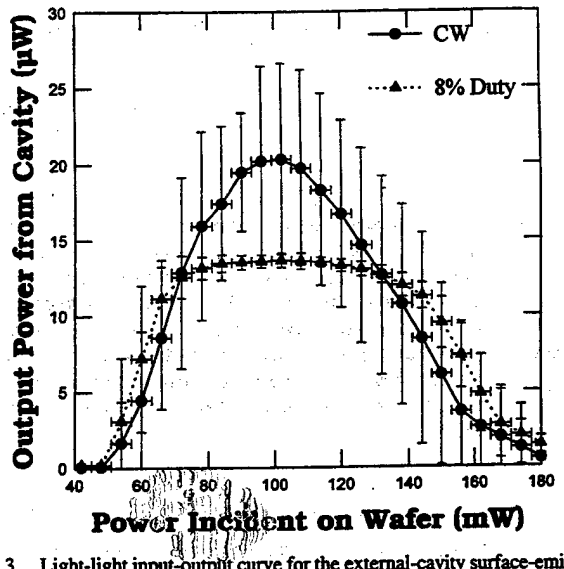


Fig. 3. Light-light input-output curve for the external-cavity surface-emitting laser under CW (circles) and pulsed (triangles; 8% duty cycle, 70 ms pulses) operation.

as having the absorption profile of bulk GaAs, a crude estimate to the true absorption lineshape [13].

The external cavity is a near hemispherical resonator using a 50-mm radius-of-curvature external output coupler dielectrically coated to have ~99.8% reflectance at 860 nm. Excitation is accomplished with the 715-nm output beam from a CW ring-dye laser focused to a beam waist ($1/e^2$ radius in intensity) w of 10–15 μm with 50 mW incident on the wafer at threshold. This yields a pump power density of ~20 kW/cm^2, comparable [14] to monolithic VCSEL's.

Fig. 3 shows an average of five light-light input-output curves under both pulsed (8% duty cycle, 70 ms pulses) and CW conditions. Output power is that observed through the output coupler; input power is that incident on the wafer, uncorrected for reflection. Note the lasing threshold at $P_{\text{th}} \sim$ 50 mW. Heating effects are believed responsible for the decrease in output power beyond ~1.8 $\times P_{\text{th}}$. The device operates at room temperature, and no attempts have been made to heat sink the wafer beyond backside contact mounting to a copper block. The improved repeatability of the input-output curve during pulsed operation compared to CW operation indicates that heating plays a large role. The reason the pulsed input-output curve does not rise as high as the CW curve is probably that the resonator alignment was optimized for low threshold under CW conditions. The low output power (~20 μW) is due to severe undercoupling. Since measurements of the lasing risetime (~150 ns) indicate a gain of ~800 cm^{-1}, we could operate with an output coupling of reflectance 98% instead of the current 99.8%.

The lasing mode spectrum was measured using a 1-m double-pass spectrometer. The typical spectrum shown in Fig. 4(a) was observed for 100 mW of incident pump power. The measured spacing of the modes is 7.4 ± 0.6 pm, which agrees with the $\lambda^2/2L$ resonator longitudinal mode spacing. While it cannot be determined from the mode spectrum whether all of the observed modes are longitudinal, as the

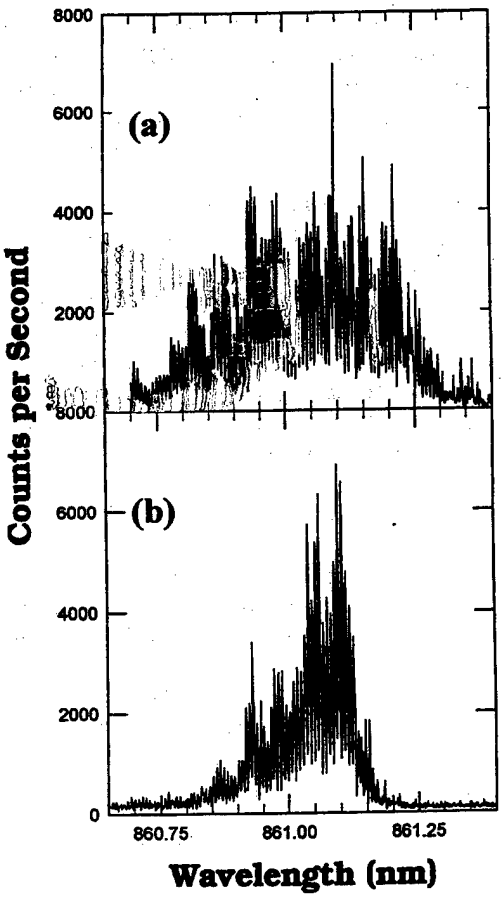


Fig. 4. Lasing mode spectra from the external-cavity surface-emitting laser showing multimode operation under (a) open aperture and (b) 6-mm aperture conditions.

even transverse modes are degenerate with the longitudinal modes in this hemispherical cavity configuration, a Gaussian fit to a linefinder trace of the lasing beam shown in Fig. 5 indicates that operation is primarily TEM$_{00}$ mode. This

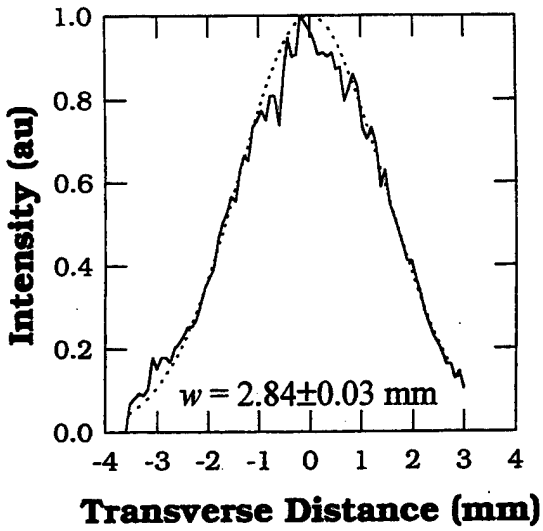


Fig. 5. Linefinder trace of the output lasing beam from the external-cavity surface-emitting laser (solid line) and fit to a Gaussian shape (dotted line), indicating TEM_{00} operation.

mode profile was recorded under conditions of high pump power (~500 mW) in an earlier experimental configuration. Fluctuations in cavity length can initiate lasing on multiple longitudinal modes, and these mode spectra were observed without taking special care to ensure a stable cavity length. However, similar mode spectra have been measured under conditions where the cavity length did not change by more than 20% of the lasing wavelength as measured by an adjacent HeNe Fabry-Perot. Thus, we do not believe fluctuations in cavity length are the source of the multimode operation. In another experiment, we inserted a 6-mm diameter intracavity aperture just before the external mirror. The diameter of the lasing beam on the external mirror depends sensitively on the cavity length, theoretically varying from 1–3 mm as the cavity length changes from 49.9–49.999 mm. The aperture reduced the number of oscillating modes as shown in Fig. 4(b). The two spectra (Fig. 4(a) and (b)) have been realigned because the spectrometer is not reproducible in absolute wavelength on this scale. A similar reduction in the number of modes can be observed by reducing the pump power. The multimode operation and the effects of the aperture are not yet well understood.

Although an unstrained AlGaAs crystal should have no polarization selectivity, most reports are that the lowest order mode from a standard VCSEL is highly linearly polarized along a ⟨110⟩ crystal axis, higher order modes being orthogonally polarized [7]. We also find lasing to be linearly polarized along a ⟨110⟩ crystal axis. Since there are no polarization selective optics in the cavity and no possibility of anisotropic process-induced strain, the polarization must be due to some property of the wafer. Inserting an etalon into the cavity as a Brewster surface at 45° to the ⟨110⟩ direction forces rotation of the lasing polarization. Further experiments will study the variation in threshold as the Brewster surface is rotated.

II. Summary

We have demonstrated the first operation of a room temperature CW external-cavity surface-emitting laser. The operation is highly multilongitudinal mode while maintaining a high degree of linear polarization and a TEM_{00} transverse mode profile over the entire range of pump powers. The capability of inserting polarization and mode control elements in the cavity will allow both study of the physics of the RPG gain structure and applications requiring tunable, single-frequency radiation. Future experiments will also investigate microcavity effects in surface-emitting lasers with the cavity length as a parameter.

Acknowledgment

The authors would like to thank S. Sun and S. D. Hersee for growing the wafer used in these experiments.

References

[1] T. Kawakami, Y. Kadota, Y. Kohama, and T. Tadokoro, "Low-threshold current low-voltage vertical-cavity surface-emitting lasers with low-Al-content *P*-type mirrors grown by MOCVD," *IEEE Photon. Technol. Lett.*, vol. 4, pp. 1325–1327, 1992.

[2] K. Tai, G. Hasnain, J. D. Wynn, R. J. Fischer, Y. H. Wang, B. Weir, J. Gamelin, and A. Y. Cho, "90% coupling of top surface emitting GaAs/AlGaAs quantum well laser output into 8 μm diameter core silica fiber," *Electron. Lett.*, vol. 26, pp. 1628–1629, 1990.

[3] A. E. Willner, C. J. Chang-Hasnain, and J. E. Leight, "2-D WDM optical interconnections using multiple-wavelength VCSEL's for simultaneous and reconfigurable communication among many planes," *IEEE Photon. Technol. Lett.*, vol. 5, pp. 838–841, 1993.

[4] N. Yokouchi, T. Miyamaoto, T. Uchida, Y. Inaba, F. Koyama, and K. Iga, "40 Å continuous tuning of a GaInAsP/InP vertical-cavity surface-emitting laser using an external mirror," *IEEE Photon. Technol. Lett.*, vol. 4, pp. 701–703, 1992.

[5] C. H. Chong and J. Sarma, "Lasing mode selection in vertical-cavity surface-emitting laser diodes," *IEEE Photon. Technol. Lett.*, vol. 5, pp. 761–764, 1993.

[6] H. Tanobe, F. Koyama, and K. Iga, "Spectral linewidth of AlGaAs/GaAs surface-emitting laser," *Electron. Lett.*, vol. 25, pp. 1444–1445, 1989.

[7] F. Koyama, K. Morito, and K. Iga, "Intensity noise and polarization stability of GaAlAs-GaAs surface emitting lasers," *IEEE J. Quantum Electron.*, vol. 27, pp. 1410–1416, 1991.

[8] K. D. Choquette, D. A. Richie, and R. E. Leibenguth, "Temperature dependence of gain-guided vertical-cavity surface emitting laser polarization," *Appl. Phys. Lett.*, vol. 64, pp. 2062–2064, 1994.

[9] T. Mukaihara, G. Koyama, and K. Iga "Engineered polarization control of GaAs/AlGaAs surface-emitting lasers by anisotropic stress from elliptical etched substrate hole," *IEEE Photon. Technol. Lett.*, vol. 5, pp. 133–135, 1993.

[10] D. G. Deppe, "Gain mechanism of the vertical-cavity surface-emitting semiconductor laser," *App. Phys. Lett.*, vol. 57, pp. 1721–1723, 1990.

[11] J. V. Sandusky and S. R. J. Brueck, "Correction to the half-wave spacing for resonant periodic-gain structures," in *SPIE 1995 Annu. Meet. Conf. Proc., Applicat. and Theory of Periodic Structures*, paper 2532-48, to be published.

[12] D. E. Aspnes, S. M. Kelso, R. A. Logan, and R. Bhat, "Optical properties of $Al_xGa_{1-x}As$," *J. Appl. Phys.*, vol. 60, pp. 754–767, 1986.

[13] D. S. Gerber and G. N. Maracas, "A simple method for extraction of multiple quantum well absorption coefficient from reflectance and transmittance measurements," *IEEE J. Quantum Electron.*, vol. 29, pp. 2589–2595, 1991.

[14] D. L. McDaniel Jr., J. G. McInerney, M. Y. A. Raja, C. F. Schaus, and S. R. J. Brueck, "Vertical cavity surface-emitting semiconductor laser with CW injection laser pumping," *IEEE Photon. Tech. Lett.*, vol. 2, pp. 156–158, 1990.

Correction to "A CW External-Cavity Surface-Emitting Laser"

Steven R. J. Brueck and John V. Sandusky

In the above paper,[1] we claimed that this publication reported the first room-temperature, external-cavity operation of a surface-emitting laser. We have since learned of the work of G. C. Wilson *et al.* [1], [2] whose reports of an electrically-pumped room-temperature CW external-cavity surface-emitting laser predate our work. We would like to thank Dr. G. C. Wilson for pointing out this omission.

[1] M. Hadley, G. C. Wilson, K. Y. Lau, and J. S. Smith, "High single-transverse mode output from external cavity surface-emitting laser diodes," *Appl. Phys. Lett.*, vol. 63, p. 1607, 1993.

[2] G. C. Wilson, M. Hadley, J. S. Smith, and K. Y. Lau, "High single-mode output power from compact external-micro-cavity surface-emitting laser diode," *Appl. Phys. Lett.*, vol. 63, p. 3265, 1993.

Manuscript received June 4, 1996.

The authors are with the Center for Technology Materials, EECE Building, Room 125, University of New Mexico, Albuquerque, NM 87131-6081 USA.

Publisher Item Identifier S 1041-1135(96)06533-0.

[1] *IEEE Photon. Technol. Lett.*, vol. 8, pp. 313–315, Mar. 1996.

0041–1135/96$05.00 © 1996 IEEE

Optical temperature measurement by grating expansion for rotating semiconductor wafers

C. Huang,[a] M. Lang, and S. R. J. Brueck[a),b)]
Center for High Technology Materials, University of New Mexico, Albuquerque, New Mexico 87131

(Received 7 August 1995; accepted 22 November 1995)

A noncontact temperature measurement technique, diffraction-order analysis, based on monitoring the change in diffraction angle from a grating as a result of thermal expansion, is described and results for both Si and GaAs are presented. Two incident beams are used to provide a differential measurement, independent of wafer tilt. Image processing techniques are used to calculate the relative temperature in near real time from the optical signals. Good agreement between optical and the thermocouple temperature measurements is obtained, with an accuracy and precision of ±0.3 °C demonstrated over a 20–600 °C temperature range for a GaAs sample. Analysis of the effects of all six rigid-body motions of the wafer on the measurement is presented. The measurement is independent of all translational motions; rotational motions (pitch, roll, and yaw) can all be monitored with the same measurement scheme and the temperature measurement corrected for their effects. In many applications in semiconductor manufacturing, wafers are rotated to ensure uniformity. The diffraction-order analysis technique is demonstrated for a rotating wafer with a 3σ precision of 1.95 °C. © *1996 American Vacuum Society.*

I. INTRODUCTION

Precise and accurate temperature measurements are required in many industrial applications. Specifically in the semiconductor industry, temperature control is needed for a wide range of processes including epitaxy, ion implantation, annealing, oxidation, dielectric deposition, etching, etc. The drive to smaller dimensions is resulting in increased use of highly nonequilibrium rapid thermal processes for which accurate (~1 °C), real-time (milliseconds to seconds) temperature measurement assumes increased importance. Ideally, a temperature measurement should be noncontact, nonintrusive, inexpensive, and broadly applicable throughout a range of manufacturing processes.

Thermistors and thermocouples are direct contact methods of temperature measurement. Because of the requirement for physical contact with the surface, they are best suited for calibration rather than real-time process control. Three classes of noncontact measurements are blackbody radiation, band gap variation, and thermal expansion. The most widely used noncontact temperature probe is pyrometry, which is based on analysis of the optical emission from a hot surface.[1] Pyrometers depend on two main variables: field of view, and material optical properties such as refractive indices and emissivity.[2,3] Problems occur when using transparent objects. Both the refractive index and the emissivity of the object must be known to obtain accurate temperature readings. Additionally in semiconductor processing, patterned layers are grown and deposited on the wafer affecting the emissivity value,[4] even during the process that is being monitored. Monitoring of the reflectivity of opaque materials provides a real-time measure of emissivity which, coupled with pyrometry, is a promising approach to reducing these uncertainties.[4] This remains a critical issue for blackbody radiation methods.

Semiconductor band gaps, and more generally dielectric functions, are highly temperature dependent, providing another optical probe of temperature. Optimally, the measurement is made in transmission,[5] although double pass transmission and reflection from the second surface have also been successful.[6] The patterned structures in Si manufacturing, the rough back surface, and the competition from free carrier absorption at higher temperatures all limit the applicability of these techniques.

Optically monitored thermal expansion techniques share many of the principal advantages of pyrometry: absence of physical contact, simplicity, accuracy, and speed. Of importance, thermal expansion is dependent primarily on the properties of the bulk material and is relatively independent of the mechanical and optical properties of the films used in manufacturing, including any changes in emissivity. The only requirement is that the thermal expansion properties of the material need to be well characterized. In recent years, several temperature sensing schemes based on thermal expansion of semiconductor wafers have been developed. Donnelly[7] developed an infrared (IR) interferometric technique based on transmission through the wafer. This method requires both sides of the wafer to be polished, is limited at high temperatures by free carrier absorption, and is also susceptible to process variations due to either topography or thin film interference effects. Zaidi, Brueck, and McNeil[8] developed a temperature measurement scheme based on projection moiré interferometry requiring a grating on the Si wafer. Lang *et al.*[9] developed signal processing techniques to extend these measurements to real-time applications. Burckel, Zaidi, and Brueck have also reported on a subfeature speckle

[a)]Also at the Dept. of Electrical and Computer Engineering.
[b)]Also at the Dept. of Electrical and Computer Engineering and the Dept. of Physics and Astronomy.

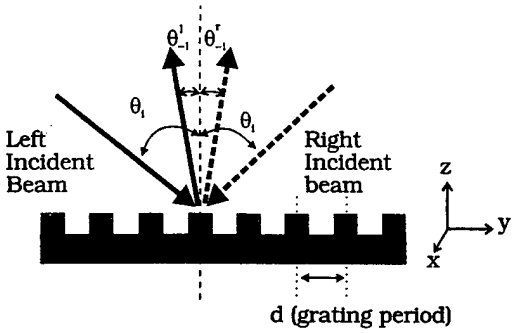


FIG. 1. Experimental configuration for grating temperature measurement.

technique that takes advantage of the rough wafer backside surface.[10]

In many processing steps, the wafer is rotated to ensure uniformity. While this does not affect the pyrometry and band gap measurement temperature probes, clearly it has a large impact on the thermal expansion techniques. In this article, we report an extension of the work of Zaidi *et al.*[8] to rotating wafers for applications such as molecular beam epitaxy and rapid thermal processing where wafer rotation is a standard feature. Additionally, we present analyses of the effects of all six rigid-body mechanical motions of the wafer on the temperature measurement.

II. DIFFRACTION TECHNIQUE

The coefficient of linear expansion α is defined as

$$\alpha(T)=\frac{1}{L}\frac{dL}{dT}, \tag{1}$$

where α is a function of temperature, and L is the length of the sample.

Our temperature measurement method monitors the thermal expansion of a grating. The diffraction of the grating is governed by the grating equation

$$\sin\theta_m=\sin\theta_i+\frac{m\lambda}{d}, \tag{2}$$

where d is the grating period, λ is the incident light wavelength, θ_i is the incident angle, m is the order of the diffraction, and θ_m the diffraction angle for the mth order. The change in angular position of the diffraction order with temperature is given by

$$\Delta\theta_m=-\frac{m\alpha\lambda}{d\cos\theta_m}\Delta T. \tag{3}$$

The diffraction angles are sensitive to both temperature [Eq. (3)] and wafer tilt [Eq. (2)]. As will be shown below, the geometry of Fig. 1, in which two beams are incident on the sample at equal and opposite angles, provides a differential measurement that is independent of tilt to first order. The angle between the two diffracted beams ($\Delta\Phi$) is given by

$$\Delta\Phi=\Delta\theta_m^l+\Delta\theta_n^r=-\left(\frac{m\alpha\lambda}{d\cos\theta_m^l}+\frac{n\alpha\lambda}{d\cos\theta_n^r}\right)\Delta T, \tag{4}$$

where $\Delta\theta_m^l(\Delta\theta_n^r)$ is the angular change of the beam originating from mth order (nth order) diffraction of the left (right) incident beam.

For the experiment reported here, the grating period, optical wavelength, and incident angle are chosen so that the -1 diffraction orders emerge approximately normal to the wafer surface. That is $m=n=-1$, $\cos\theta_m=\cos\theta_n\approx 1$, and

$$\Delta\Phi\approx\frac{2\alpha\lambda}{d}\Delta T$$

and

$$\Delta y\approx D\Delta\Phi\approx\frac{2\lambda\alpha D\Delta T}{d}, \tag{5}$$

where Δy is the change in the separation of the two diffraction spots in the detection plane at a distance D from the grating.

Solving for ΔT

$$T_f\approx T_i+\frac{d}{2\lambda\alpha D}(y_f-y_i), \tag{6}$$

where T_i, T_f are the initial and final temperatures and y_i, y_f are the initial and final spot separations, respectively. If the temperature change is sufficiently large, Eq. (6) must be integrated to allow for the temperature dependence of $\alpha(T)$.

III. EFFECTS OF WAFER RIGID-BODY DEGREES OF FREEDOM

The six rigid-body motions of the sample are (1) translation along the x axis, (2) translation along the y axis, (3) translation along the z axis, (4) rotation around the x axis (pitch), (5) rotation around the y axis (roll), and (6) rotation around the z axis (yaw). The coordinate system relative to the measurement scheme is shown in Fig. 1.

(1), (2) Translation along the x or y axis. This will not have any effect on the angular position of the diffracted beams as long as the incident beam remains on the grating area.

(3) Translation along the z axis. The z translation does not change the incident angle, so the diffraction angles are unaffected by the translation. The only change is in the distance between the sample and the observation plane from D to D' and, as long as this change is very small relative to D, there is no effect on the temperature determination.

(4) Rotation around the x axis (pitch). Figure 2 shows the effect of out-of-plane rotation or tilt of the sample around the x axis, the direction of the grating lines. Before the tilt, the incident angles of the two symmetrically incident beams are both θ_i. If the sample tilts a small angle δ, the incident angles become $\theta_i^l\rightarrow\theta_i+\delta$ and $\theta_i^r\rightarrow\theta_i-\delta$. The grating equations become

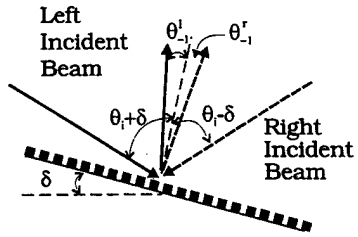


FIG. 2. Effect of sample tilt (pitch).

$$\theta^{\,l}_{-1}=\sin^{-1}[\sin(\theta_i+\delta)-\lambda/d],$$

and

$$\theta^{\,r}_{-1}=\sin^{-1}[\sin(\theta_i-\delta)-\lambda/d]. \tag{7}$$

The angle between the two -1 diffraction-order beams is $\Phi=\theta^{\,l}_{-1}+\theta^{\,r}_{-1}$ and the centroid angle between the two diffracted beams before tilt and after tilt is $\Psi=(\theta^{\,l}_{-1}-\theta^{\,r}_{-1})/2$. Expanding to lowest order in δ gives

$$\Phi\approx\Phi_{\delta=0}+\frac{\lambda\delta^2}{d}$$

and

$$\Psi\approx\delta\sqrt{1-(\lambda/d)^2}. \tag{8}$$

As claimed above, the measurement is differential, that is, the change in the spot separation is second order in the tilt angle, δ. Further, the centroid of the two spots provides a first-order measurement of δ, allowing correction of the temperature measurement.

(5) Rotation around the y axis (roll). Rotation of the sample around the y axis will shift both diffracted beams to the side without affecting the separation between them. The motion of the centroid of the two diffracted beams provides a simple measurement of the y rotation.

(6) Rotation around the z axis (yaw). Figure 3(a) shows how the -1 diffraction-order beams move when the sample is rotated. Figure 3(b) shows the resultant wave vectors for this situation. Here $k=2\pi/\lambda$, $g=2\pi/d$, $l=(2\pi/\lambda)\sin\theta_{-1}$ are the incident beam wave vector, the grating wave vector, and the wave vector of the -1 diffraction order, respectively. Momentum conservation demands

$$\mathbf{l}=\mathbf{k}\sin\theta_i-\mathbf{g}. \tag{9}$$

Before the sample rotation these three vectors are aligned so the vector relationship becomes a simple algebraic relationship. After sample rotation by an angle γ, these three vectors form a triangle and

$$l^2=(k\sin\theta_i)^2+g^2-2gk\sin\theta_i\cos\gamma. \tag{10}$$

Denoting the separation between the diffracted beams by δy, we have

$$\delta y=2\sqrt{\left(\frac{\delta y_{\gamma=0}}{2}\right)^2+\frac{2(1-\cos\gamma)\sin\theta_i D^2 g}{k}}. \tag{11}$$

Note that γ is readily measured by the change in the angle of the vector connecting the two diffracted beam spots in the detection plane. Then, using Eq. (11), $\delta y_{\gamma=0}$ can be evaluated, eliminating the dependence on rotation from the temperature determination. While this correction is second order in the rotation angle γ, the presence of the large factor D^2 makes this a very significant effect that must be monitored and corrected for in the temperature measurement.

In summary, the symmetry of the two beam measurement eliminates much of the dependence on sample rigid-body motion. The measurement is independent of all three translational motions and of rotation around the y axis (roll). The differential measurement is dependent only in second order on rotation around the x axis (pitch) and this dependence can be readily corrected by monitoring the motion of the beam spot centroid. Finally, the dependence of the measurement on rotation of the sample about the z axis (yaw) can be eliminated by monitoring the vector direction between the diffracted spots in the detection plane.

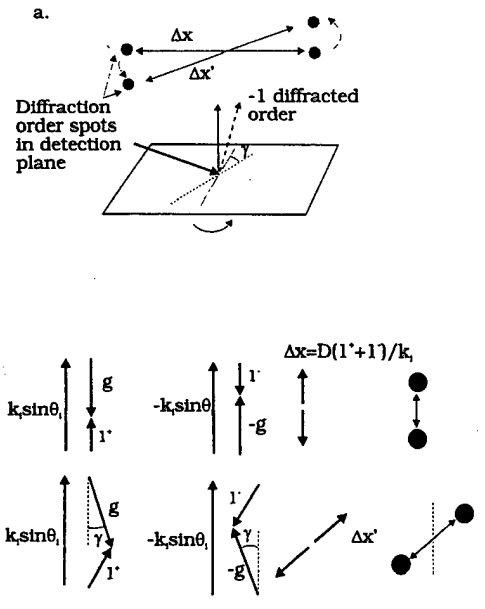


FIG. 3. (a) Demonstration of rotation around the grating axis (yaw). (b) Vector analysis for evaluating the effect of yaw.

IV. EXPERIMENTAL RESULTS

A. Nonrotating sample temperature measurement

The experimental setup is shown in Fig. 4. Samples of either Si or GaAs with interferometrically defined 1.0 μm period gratings (4×4 mm^2 area) etched into the material are placed inside a vacuum chamber on a quartz submount and radiatively heated with a Nichrome wire heater. A He–Ne laser beam ($\lambda=633$ nm) is split into two parts which are incident at angles $\approx\pm39.25°$ to the normal such that -1 orders diffracted from the grating are approximately normal to the sample. For an independent reference with the optical technique, a thermocouple is cemented to the sample. The two diffracted beams are detected by a charge coupled device

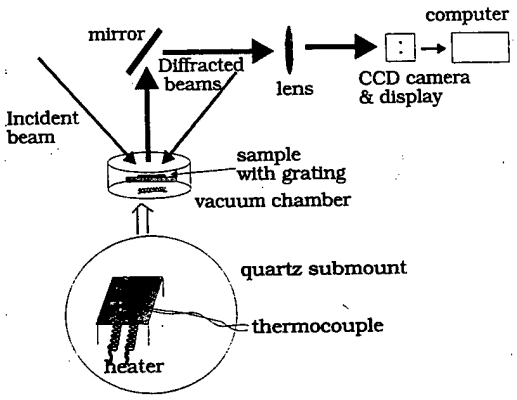


FIG. 4. Experimental setup for temperature measurement.

(CCD) camera and data analysis is performed on a personal computer with a commercial image analysis board.[9]

Recalling Eq. (6), the initial separation y_i, initial temperature T_i, $\alpha(T)$, the grating period d, and distance from sample to camera D are needed to evaluate the final temperature. The initial temperature T_i is obtained from the thermocouple. The initial separation y_i is obtained from the first frame processed. The grating period d can be accurately measured by measuring the Littrow angle for a He–Ne laser source. D is measured by illuminating the entire grating area and fitting the resultant $(\sin x/x)^2$ diffraction intensity pattern. For silicon, $\alpha(T)$ has been well established in the temperature region of interest, 20–1000 °C.[11] The functional form of α used for calculating T_f is given by

$$\alpha_{\mathrm{Si}}(T)=[3.725(1-e^{-5.88\times10^{-3}(T-124)})+5.548\times10^{-4}T]\times10^{-6}(\mathrm{K}^{-1}). \quad (12)$$

For GaAs, Blakemore's results for the thermal expansion coefficient[12] are used, viz.,

$$\alpha_{\mathrm{GaAs}}(T)=(4.24+5.82\times10^{-3}T-2.82\times10^{-6}T^2)\times10^{-6}(\mathrm{K}^{-1}). \quad (13)$$

Figure 5 shows temperature versus time curves for a GaAs sample for three settings of the heater current. The solid curves are from the thermocouple and the experimental points from the optical temperature measurement. The agreement between the thermocouple and optical expansion measurements of the wafer temperature is excellent.

To estimate the precision of the optical technique, repeatability measurements were carried out at room temperature. Figure 6 illustrates the precision of the optical and thermocouple measurements. A repeatability of ±0.3 °C is achieved for the grating expansion technique. Note that the thermocouple values (solid line) are averaged over 1000 readings while the optical measurement is not averaged. Significantly improved precision could be obtained with the simple hardware substitution of an integrating camera system to average the optical image during the signal processing times.

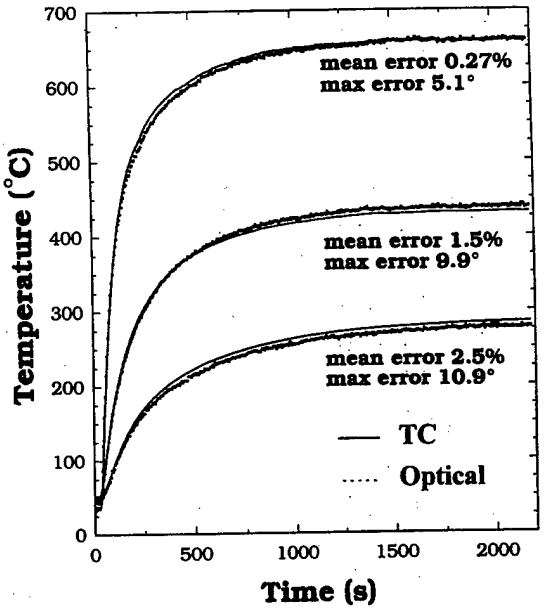


FIG. 5. Comparison of optical and thermocouple measurements of the temperature vs time for several final temperatures using the temperature dependence of GaAs expansion coefficient given in Ref. 11.

B. Rotating sample temperature measurement

In many of the potential applications for this temperature measurement technique in semiconductor manufacturing, including rapid thermal processing (RTP) and molecular beam epitaxy (MBE) growth, the wafers are rotated to enhance process uniformity.[13] Rotation of the substrate introduces an extra complexity into the data acquisition and analysis. Several variations on the optical system were explored. For these experiments, the wafer was mounted off-axis on a rotating platen; glass slides were used to isolate the sample from the metal platen. A radiative heater was positioned radially so that the sample passed under the heater on each revolution.

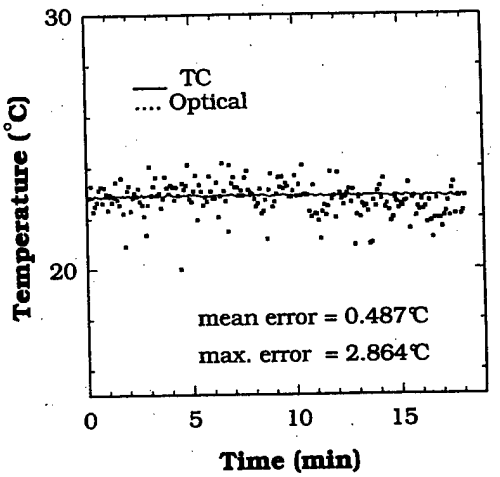


FIG. 6. A measurement precision of ±0.3 °C is achieved around room temperature.

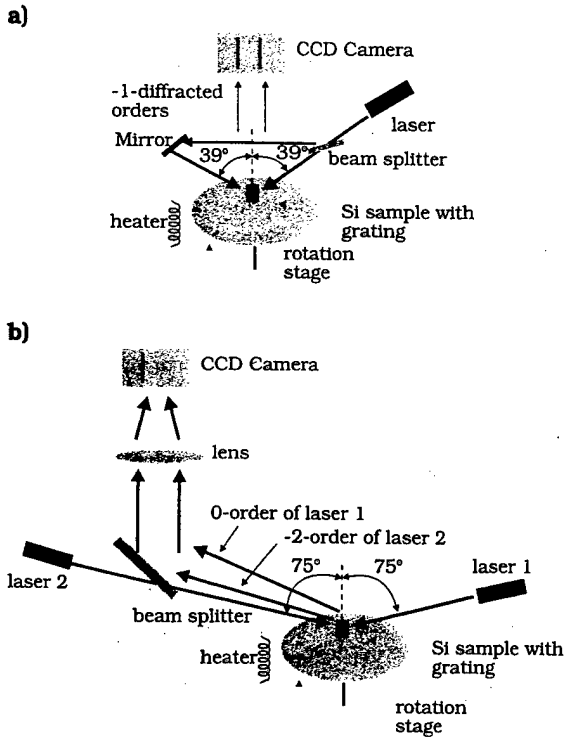


FIG. 7. Two alternate geometries used for temperature measurements on rotating samples. Geometry (a) uses one laser but requires a line of sight between the two beam paths. Geometry (b) uses two separate lasers.

The much lower heating duty cycle meant that the accessible temperature range was much lower than in the nonrotating case where a cw heater was used.

The first setup used for the rotating temperature measurement is shown in Fig. 7(a). As the sample rotated under the laser at a speed of 2 Hz, the diffracted beams move across the CCD array leaving streaks as they pass in opposite directions. The trajectories of the two moving spots in the detection plane obey the parametric relations

$$x^{r,l}=D\ \theta_{-1}^{r,l}\pm\left[D\frac{g}{k}-\sqrt{\left(D\frac{g}{k}\right)^2-(y^{r,l})^2}\right]. \tag{15}$$

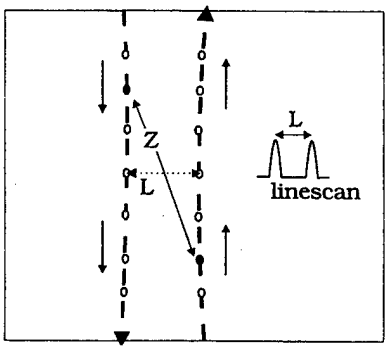


FIG. 8. Diffraction spot trajectories in the detection plane under rotation. The instantaneous distance between the spots is Z; the distance of closest approach, L, is evaluated by a simple 1D line scan across the traces. (The closed circles represent the instantaneous position of the two spots which sweep out the trajectory represented by the open circles.)

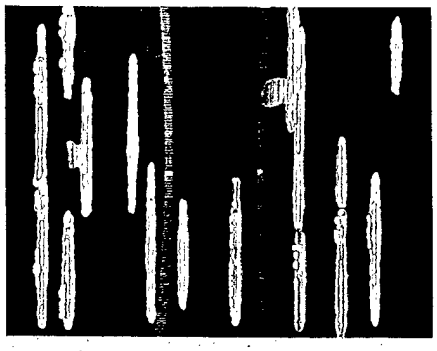


FIG. 9. CCD camera image of the spot trajectories for the geometry of Fig. 7(a).

These trajectories are plotted in Fig. 8 for parameters similar to those of the experiment. In Fig. 8, the dashed lines represent the spot trajectories, Z is the instantaneous distance between the two spots at one point in the scan (denoted by the closed circles), and L is the desired distance between the spots when the grating lines are perpendicular to the detection plane. The data acquisition system continuously monitors the diffraction-order separation. Frames were taken at TV rate (1/30 s) and averaged in real time; note that a triggered system would eliminate the many frames with no diffraction orders and improve the system signal to noise. After 90 frames (3 s) an image (as shown in Fig. 9) was transferred to the computer for calculation of the separation of the diffraction orders. The separation was calculated by taking a horizontal scan line across the center of the monitor. Note that this is much simpler than the nonrotating case since previously a two-dimensional problem had to be solved to account for wafer and mount rotations during heating. In the rotating case, the grating is always in the correct orientation at one point during the revolution and image analysis reduces to a one-dimensional (1D) problem. Signal processing takes about 0.5 s to calculate the distance between the lines, faster than the nonrotating situation. This could be dramatically reduced by using dedicated hardware and software routines.

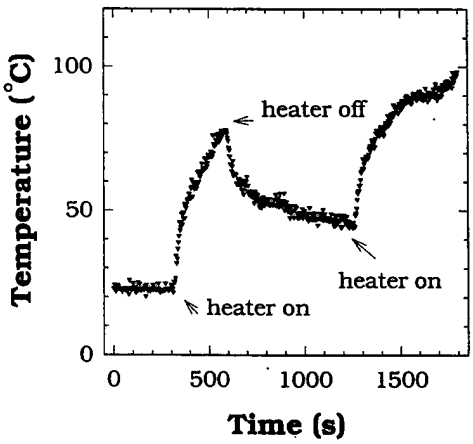


FIG. 10. Optical measurement of temperature for a rotating sample as the heater is cycled on and off; thermocouple measurements were not taken because of the difficulty of making contact with the rotating sample.

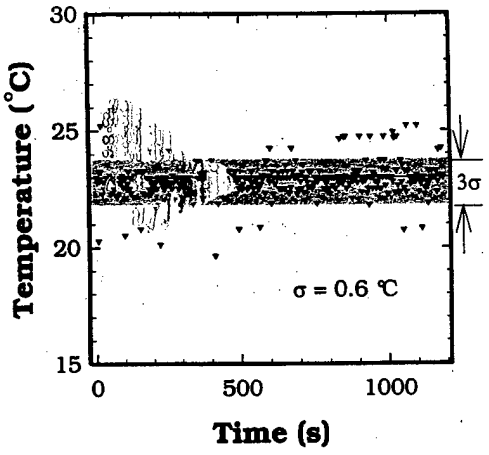


FIG. 11. Precision of the temperature measurement on the rotating sample near room temperature. The shaded bar is a 3σ variation of 1.95 °C.

The limiting factor was rotation speed needed to get two lines on the monitor. Note the good qualitative agreement between the measured traces (see Fig. 9) and the calculated spot trajectories (see Fig. 8).

Figure 10 shows measurements of the temperature versus time with the heater cycled on and off. Clearly, the optical measurement tracks the changes in temperature. No independent thermocouple temperature measurement was made because of the difficulty of a thermocouple making contact with the rotating wafer. The variance of the optical temperature measurement is somewhat larger than that observed without sample rotation. In the static case, the sample was mounted in a vacuum chamber, while in the present experiments only a foil box covered the rotation stage, sample, and heater. Air turbulence affects the current experiment more seriously. In an actual MBE system, the wafer is in ultrahigh vacuum (UHV), so air fluctuation will not be a problem. Thus little effort was expended to improve this aspect of these proof-of-principle measurements. The precision of the measurement around room temperature is illustrated in Fig. 11. The standard deviation σ is 0.6 °C. The shaded bar represents a 3σ variation of 1.95 °C.

In many actual processing systems, both optical access and the capability for mounting optics are severely limited. For example, in MBE growth, the normal access port is typically reserved for pyrometry and optical access is only available at large angles (75°–85° from the normal). An optical path and experimental setup to address these issues is shown by Fig. 7(b). Here two laser sources are used because of the difficulty of adding optical components and the lack of a line of sight between the two opposed ports inside the MBE machine. One beam's diffraction order (−2 in these experiments) and the other beam's zero-order diffraction (specular reflection) are directed to the CCD camera for temperature measurement. When the sample is rotating, the image in the CCD camera of these two diffraction beams is one spot corresponding to the zero-order diffraction and one line that is the diffracted beam moving as a result of the wafer rotation. By calculating the separation of the line and the spot, temperature was measured. The image processing is the same as that of the previous case. The function of the zero-order beam is to eliminate the effects of wobble in the MBE rotation mechanism on the temperature measurement. Recording a camera frame only when the diffracted order is present (once each wafer rotation), the zero-order beam provides instantaneous information on the wafer tilt caused by mechanical wobble and by wafer expansion. Again, the image analysis is one dimensional requiring only analysis of a single line scan that crosses both the zero-order spot and the diffracted-order arc. The results in terms of precision and temperature range are very similar to those obtained in the previous experimental arrangement (Figs. 10 and 11).

V. CONCLUSION

A noncontact temperature measurement method based on optical interrogation of the thermal expansion of a μm scale grating has been investigated. A near real-time system for the diffraction grating method was implemented. Temperature accuracy of ±0.3 °C was demonstrated for a GaAs sample with 4×4 mm^2 grating and over the temperature range from room temperature to the GaAs thermal decomposition limit of approximately 600 °C.

The effects of all possible sample rigid-body motions have been analyzed. The relevant rigid-body rotations can be monitored from the detected diffraction-order spot positions and the temperature measurement corrected for these motions that often unavoidably accompany heating of the wafer and its mechanical support.

For simulated processing equipment such as MBE, temperature was measured while the sample rotated. Several optical arrangements have been investigated with increasing suitability to an actual MBE system. When the sample is rotating, the trajectory of the diffraction orders in the detection plane is lines rather than spots for a static case. Using a 1D line scan perpendicular to the trajectory of the diffraction spots, the distance between the two diffraction orders can be calculated and the temperature measured. The signal processing is simpler and faster in this case than in the nonrotating case. Temperature measurements were demonstrated in several optical configurations from room temperature to ~100 °C with a demonstrated precision of σ=0.6 °C.

The important information concerns the diffraction angle, not the intensity of the diffracted signal. This is important in many potential semiconductor fabrication applications where material is either deposited or removed during the process. The shape of the grating grooves will change as the processing continues affecting the diffracted intensity; the period and diffraction angle, however, will not be affected. Since the area of the grating can be very small, any overall bowing of the wafer due to strained layer growth or thermal expansion mismatch between the layers and the substrate is equivalent to either tilt or pitch of the wafer and can be accounted for by the general formalisms described above.

Additional improvements that would enhance this system performance include use of converging lenses in each beam path before striking the sample to reduce the diffraction spot

sizes at the detector plane, incorporation of a trigger system to gate the camera only when the diffraction spots (lines) are present, use of an integrating CCD camera for increased averaging, improved isolation of air turbulence and platen wobble during rotation, adjustable optical systems to allow both coarse and fine resolution settings, and rigid optical system and precision grating periods to allow initial temperature measurements.

The results presented in this article meet almost all of the requirements of a temperature measurement technique for application in semiconductor growth and processing. Sufficient accuracy and precision for even the most demanding projected applications have been demonstrated. The technique is noncontact, uses inexpensive optical and computer components, is near real time, and has relatively modest optical access requirements. A significant issue is the need for a grating structure on the wafer. Measurements have been carried out with grating areas as small as 50×50 μm^2. As new standards are developed for larger Si wafers, the measurement capabilities offered by the inclusion of a standard grating should be considered. Finally, there is a need for temperature mapping across a wafer as well as for an absolute temperature determination. Perhaps a sensor fusion approach is most useful here; the grating technique can provide the absolute temperature reference while pyrometry or other temperature measurement schemes can provide the required temperature distribution across the wafer. With a stable optical system and precision gratings manufactured at a known wafer temperature, the initial temperature of the wafer can be measured based on the initial diffraction spot measurement. Of importance is the fact that the temperature measurements depend only on the thermal expansion of the substrate and are independent of thin-film emissivity, band gap variation, optical transmission, and expansivity. The universality of this measurement scheme makes it an attractive option for a number of critical temperature measurement tasks in a variety of manufacturing situations.

ACKNOWLEDGMENTS

The authors thanks Dr. Saleem H. Zaidi for many fruitful discussions and for fabricating the GaAs and Si gratings. Andrew Frauenglass provided much useful optomechanical expertise. Support for this work was provided by the Advanced Research Projects Agency as part of the Advanced Materials Science and Processing Consortium.

[1]W. Heimann and U. Mester, Inst. Phys. Conf. Ser. **26**, 219 (1975).
[2]T. J. Quinn, *Temperature*, 2nd ed. (Academic, New York, 1990).
[3]*OS900 Series Infrared Thermometer Operators Manual* (Omega Engineering Inc., Stamford, CT, 1989).
[4]A. T. Fiory, C. S. Schietinger, B. A. Adams, and F. G. Tinsly, Mater. Res. Soc. Sym. Proc. **303**, 139 (1993).
[5]J. C. Sturm, P. V. Schwartz, and P. M. Garone, Appl. Phys. Lett. **56**, 961 (1990).
[6]C. W. Cullen and J. C. Sturm, Mater. Res. Soc. Symp. Proc. **342**, 23 (1994).
[7]V. M. Donnelly, J. Vac. Sci. Technol. A **8**, 84 (1990).
[8]S. H. Zaidi, S. R. J. Brueck, and J. R. McNeil, J. Vac. Sci. Technol. B **10**, 166 (1992).
[9]M. Lang, G. Donohoe, S. Zaidi, and S. Brueck, Opt. Eng. **33**, 3465 (1994).
[10]D. Burckel, S. H. Zaidi, A. Frauenglass, M. Lang, and S. R. J. Brueck, Opt. Lett. **20**, 315 (1995).
[11]Y. Okada and Y. Tokunaru, J. Appl. Phys. **56**, 314 (1984).
[12]J. S. Blakemore, J. Appl. Phys. **53**, R123 (1982).
[13]M. A. Herman and H. Sitter, *Molecular Beam Epitaxy: Fundamentals and Current Status* (Springer, Berlin, 1989).

Interferometric lithography of sub-micrometer sparse hole arrays for field-emission display applications

Xiaolan Chen,[a] Saleem H. Zaidi, and S. R. J. Brueck[a),b),d)]
Center for High Technology Materials, University of New Mexico, Albuquerque, New Mexico 87131

Daniel J. Devine[c)]
Coloray Display Corporation, Fremont, California 94593

(Received 15 March 1996; accepted 26 July 1996)

Interferometric lithography, the use of interactions between coherent laser beams to define sub-wavelength patterns, is well adapted to the periodic nature of field-emitter structures. Techniques to fabricate sparse (hole diameter to pitch ratio of 1:3 or larger) emitter arrays to improve reliability and lifetime are presented. These include: multiple exposures at two different pitches; integration of interferometric and optical imaging lithography; and various multiple beam techniques that both provide a sparse array and result in a two dimensional pattern in a single exposure. Moiré alignment techniques are demonstrated to provide a simple process for aligning multiple levels. Manufacturing related issues such as process latitude and photoresist profiles and their suitability for subsequent processing are also discussed. Exposure-dose process control using latent image monitoring is demonstrated. © *1996 American Vacuum Society.*

I. INTRODUCTION

The flat-panel display market is one of the fastest growing segments of the electronics industry. Field-emission-based displays[1] provide a promising new technology for the production of flat-panel displays. Compared to liquid crystal displays (LCD), field-emission displays (FED) offer a potential of reduced manufacturing complexity and cost, increased brightness, improved viewing angle, and reduced power consumption. Although the lithography demands for FEDs, requiring sub-μm critical dimensions (CD) over very large fields, pose significant manufacturing difficulty in the context of conventional lithography, the periodic nature of field-emitter structures is a natural match to the technique of interferometric (holographic) lithography[2–4] which uses interfering, quasi-monochromatic, coherent laser beams to define patterns without requiring any masking. Interferometric lithography offers the capability for essentially unlimited depth-of-field, large-area,[5] sub-μm patterning with the use of simple and relatively inexpensive optics. Existing laser sources and photoresists are adequate to meet even the most challenging scales ($\sim$0.1 μm diameter) presently being proposed for FEDs. Development of a large-area, high-throughput, sub-μm-scale lithographic technique would be a major step towards realizing the promise of FEDs.

The basic operating principle of field emitters is the creation of a large electric field in the vicinity of the emitter tip by controlling the sharpness of the tip and the tip-gate electrode proximity. The sharpness of the emitter is determined by the process technique used to form the emitter, while the gate-to-emitter distance is determined by the resolution of the lithographic tool. The higher the lithographic resolution, the smaller the gate-to-emitter distance and the lower the turn-on voltage,[6] a critical parameter for FEDs that strongly effects both the overall efficiency and the cost of the driver electronics. Sub-μm resolution lithography also allows a reduction of the area of each pixel for a fixed number of emitters—reducing the gate-to-emitter overlap capacitance and stored energy and further decreasing the cost of the driver electronics. This reduction in stored energy improves reliability by decreasing the energy released in an emitter failure. Additionally, high resolution lithography enables greater emitter redundancy, improving pixel-to-pixel uniformity and requiring less current from individual emitters. Smaller area pixels also enable the FED manufacturer to produce higher resolution displays.

While it is advantageous to increase the number of emitters in a given area, there is a limit to the desirable density. Failure of a single tip is frequently accompanied by ejection of material, the amount of which is directly related to the size of the emitter, into the space above and around the emitter cavity. For display reliability, it is essential that this ejected material not affect the operation of neighboring emitters. Whether this occurs depends on the amount of material ejected, the stored capacitive energy, and the distance to the nearest neighbor emitter. For a given amount of ejected material and stored capacitive energy, there is a radial distance around which the material characteristics will be impacted. If this radius encompasses another emitter and triggers its destruction, the failure will propagate throughout the pixel. Thus, it is essential that the emitter-to-emitter distance be greater than the material deposition distance. The radial distance affected by a single emitter failure was found to be around 2.5 μm for a 1.0 μm gate hole diameter. To provide some margin of safety, a minimum 4 μm pitch is commonly used. As the emitter cavity diameter is reduced, the amount of emitter material is also reduced, and the emitter pitch can likewise be reduced. A rule of thumb is to maintain a diam-

[a)]Also at Department of Electrical and Computer Engineering.
[b)]Also at Department of Physics and Astronomy.
[c)]Present address: Plasmaco, Highland, NY 12528.
[d)]Electronic mail: brueck@chtm.eece.unm.edu

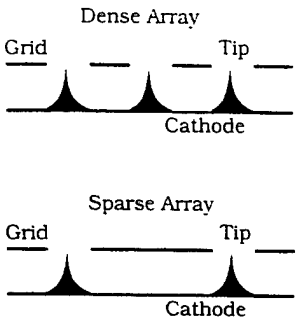


FIG. 1. Comparison of dense (1:1 line:space ratio) and sparse (1:3 line:space ratio) field emitter tip arrays. The sparse arrays allow more significant undercutting of the gate oxide lowering leakage currents and provide sufficient spacing between tips to minimize the chances of a multiple tip failure. The dense arrays provide higher packing and current density.

eter:pitch ratio of 1:4 (This is a line:space ratio of 1:3 in the common lithographic terminology.) Additional advantages to the sparse hole patterning are a reduction in the tip-gate capacitance and in the gate-emitter leakage currents because of the possibility of a more aggressive undercutting of the gate oxide in the fabrication process. This is not possible in dense arrays (as shown in Fig. 1) because of the close proximity of nearest neighbor cavities. As will be shown below, the most common interferometric lithography technique for producing a 2D array of holes, double exposure of a plate with two gratings oriented at 90° to each other,[5,6] optimizes at 1:1 line:space ratios. It is difficult to control the exposure dose for 1:3 line:space ratios, and the resulting photoresist profiles are more sloped and less effective for etch masking than desirable. Because of the importance of sparse hole patterning indicated above, several techniques have been developed in this work to implement the desired 1:3 line:space ratio for FED manufacturing.

II. INTERFEROMETRIC LITHOGRAPHY

Interferometric lithography,[2–4] the use of interfering coherent laser beams to write large areas of sub-micron structures, is naturally suited to the production of large fields of emitter structures. For two plane waves symmetrically incident on a plate at angles of $\pm\theta$, a grating of period $d=\lambda/(2\sin\theta)$ is produced with λ the laser wavelength.[7] For this single exposure, the exposure flux (J/cm^2) as a function of position is given by:

$$F(x)=2F_0[1+\cos(2kx\sin\theta)], \quad (1)$$

where F_0 is the flux (intensity × duration) of the exposure for each individual beam incident on the sample and $k=2\pi/\lambda$. The grating lines are normal to the x-axis, and the phase term has been arbitrarily set to zero. A second exposure with the plate rotated by 90° gives the array of holes. The total exposure flux in this case is given by:

$$F(x,y)=2F_0[2+\cos(2kx\sin\theta)+\cos(2ky\sin\theta)], \quad (2)$$

where we assume the same exposure flux for the second exposure. Figure 2(a) shows a scanning electron microscope

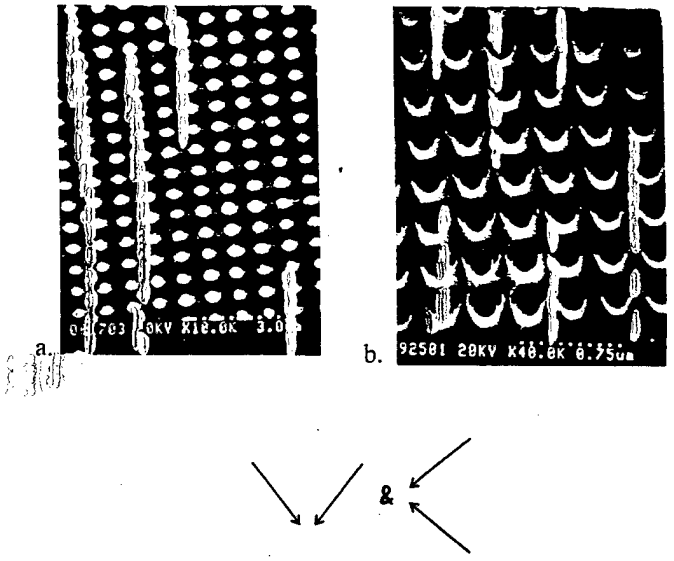


FIG. 2. (a) Dense photoresist array of 0.5-μm holes on 1-μm pitch produced using a 488 nm Ar-ion laser source. (b) Dense photoresist array of 0.18-μm holes on a 0.36-μm pitch produced using a third- harmonic (355 nm) YAG laser source.

(SEM) image of a dense array of 0.5-μm diameter holes in photoresist on a 1-μm pitch produced using a 488-nm Ar-ion laser. A dense array of 0.18-μm holes on a 0.36-μm pitch has also been demonstrated using the third-harmonic radiation (355 nm) from a YAG laser as shown in Fig. 2(b). The image below the figures shows the sequence of exposures, the "&" separates two independent exposures. As will be shown below, the process latitude for this double exposure technique optimizes at a 1:1 line:space ratio and it is difficult to control the exposure to deviate significantly from equal lines and spaces.

III. TECHNIQUES FOR THE DEFINITION OF SPARSE HOLE ARRAYS

Methods of multiple-beam, multiple-exposure interferometric lithography and integration of interferometric lithography with imaging optical lithography to fabricate sparse hole arrays are presented. Moiré patterns arise from multiple-beam interference and the superposition of multiple exposure patterns. Techniques similar to the moiré alignment process we previously developed[8] are applied to the required alignment during sparse hole fabrication.

A. Double exposure pair with two different pitches in each direction

A double exposure pair refers to two exposures in the x-direction and two in the y-direction. The exposure dose for each is adjusted so that holes (cleared photoresist areas) are formed only in the region where the combined flux of all four exposures add to more than the clearing dose. The first exposure is made at a coarse pitch (for example $d_1=2$ μm) and the subsequent second exposure at half this pitch (e.g., $d_2=1$ μm) with the exposure doses adjusted so that only every other exposed region of the double exposure pair can be developed all the way through the photoresist. The exposure flux distribution as a function of position is:

$$F_{\text{double}}(x,y)=\begin{Bmatrix}2F_1[2+\cos(2kx\sin\theta_1)+\cos(2ky\sin\theta_1)]\\ 2F_2[2+\cos(2kx\sin\theta_2+\varphi_x)+\cos(2ky\sin\theta_2+\varphi_y)]\end{Bmatrix}, \quad (3)$$

where the subscripts refer to the respective exposure fluxes and φ_x, φ_y are the phases of the second exposure relative to the first.

Alignment signals for adjusting the second set of exposures so that $\varphi_x=\varphi_y=0$ were derived by diffraction from the latent image gratings formed in the first set of exposures.[8] Figure 3 shows the configuration for this projection moiré alignment. The incident angle θ_2 is chosen so that the $+1$ and -1 diffraction orders of the two incident beams from the latent image grating overlap in the direction normal to the sample surface and form a projected moiré pattern. For our TE polarization incident beams, the intensity of the moiré interference pattern is given by:

$$I_{\text{moiré}}=2\eta^2F_2\{1+\cos[2\pi(1/d_2-2/d_1)x'\phi(\Delta x)]\}, \quad (4)$$

where η is the amplitude diffraction efficiency of the latent image grating, x' is the length coordinate in the detection plane, $\phi(\Delta x)$ is a phase term which contains the position alignment information. $2\phi(\Delta x)$ varies by 2π radians as the wafer moves one period ($d_2\sim d_1/2$) relative to the alignment beams. In the detection plane, the moiré pattern has a periodicity given by:

$$d_{\text{moiré}}=\frac{d_1d_2}{d_1-2d_2}=\frac{\lambda}{2(\sin\theta_2-\lambda/d_1)}. \quad (5)$$

For the degenerate case, $\sin\theta_2=\lambda/d_1$ (i.e., $\sin\theta_2=2\sin\theta_1$, $d_2=d_1/2$), there is only a single moiré fringe. Adjusting the angles so that $\sin\theta_2=2\sin\theta_1$ transverse position of sample so that $2\phi(x)=2m\pi$ (m an integer) gives one bright moiré fringe and the desired position for the second exposure. Figure 4 shows a double exposure pair (two in x, two in y) pattern in a photoresist film on a Si wafer providing sparse holes on a 2-μm pitch. The plateaus apparent in the figure are standing wave patterns in the 0.5-μm thick resist. The standing wave patterns can be eliminated with an antireflection coating (ARC), at the price of an additional processing step. The nonuniformity evident in the figure is due to problems with the photoresist coating. The low NA optical system is simply not capable of carrying the information required to sustain varying hole diameters for adjacent features.

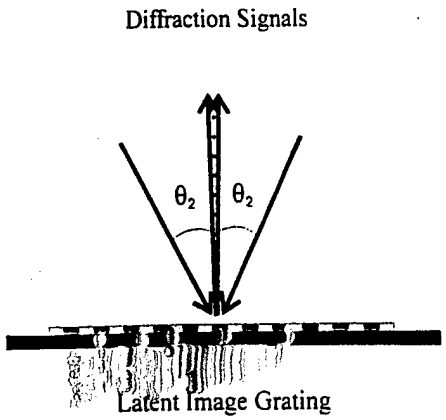


FIG. 3. Experimental configuration for projection moiré alignment. The two beams are incident on the photoresist latent image produced in the first exposure. The angles are adjusted so that there is only a single fringe between the two diffracted beams and the sample position is adjusted so that the fringe is at maximum brightness.

B. Double exposures with a processing step between lithography steps

For the SEM picture shown in Fig. 5, we began with a silicon sample with a 0.1-μm-thick oxide layer. A dense array of holes (0.4-μm diameter, 1-μm-pitch) was printed with a single-period interferometric exposure pair (one in x, one in y) in the resist and reactive-ion etched using a CCl_2F_2 process into the oxide layer using the photoresist pattern as an etch mask. Following the etch process, the first photoresist layer was stripped and a second photoresist layer was spun onto the wafer. In a second single-period interferometric exposure pair, larger holes ($\sim$1-μm diameter) were made. The undeveloped photoresist will protect against printing the unwanted holes in the oxide layer in a subsequent etch step.

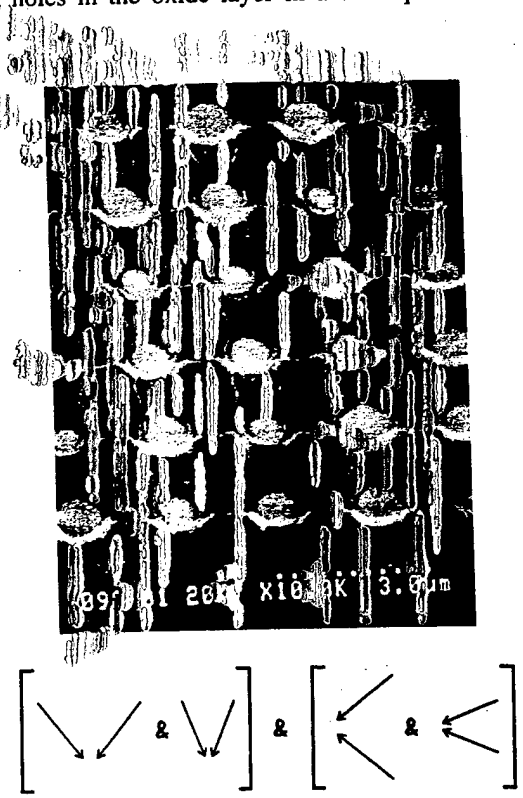


FIG. 4. Sparse array of holes produced by double exposure pairs in the same level of photoresist.

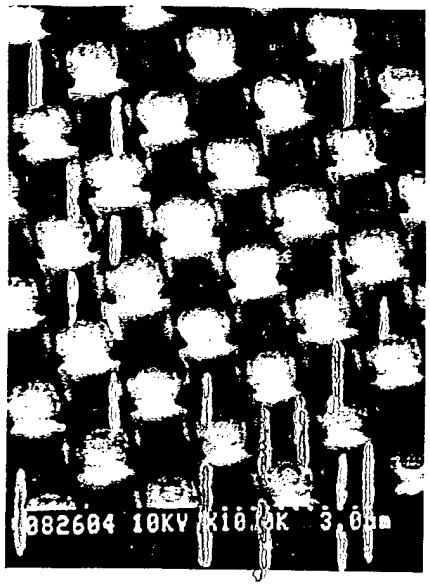


FIG. 5. Sparse array of holes produced by two single exposure pairs in two levels of photoresist. A dense array of holes (0.4-μm diameter, 1-μm pitch) was formed by a single exposure pair and etched into an oxide overlayer. A second photoresist exposure opened up ~1-μm holes on a 2-μm pitch to expose every other row and column of the smaller holes. Alignment between the two levels was effected by the technique described in Fig. 6.

Because the fine pitch array (larger diffraction angle) was printed first, the additional optics shown in Fig. 6 are required to provide the real-time moiré alignment signals. The moiré fringe is circular because the slightly different optical path lengths between the two beams give rise to a Newton's rings interference pattern. The position of the fringe center gives the information on the incident angle which determines the period of the second exposure and the brightness of the center fringe gives the information on the phase (i.e., alignment of large holes over small holes). The order of the exposures could have been reversed with the coarse pitch, large diameter holes defined in the first photoresist step and the fine pitch, smaller diameter holes defined in the second photoresist step. However, we find that it is usually best to print the most critical, smallest features when there is the least topography on the plate to minimize scattering and edge effects. An important point is that it is readily possible to align two interferometric lithography exposures with high accuracy.

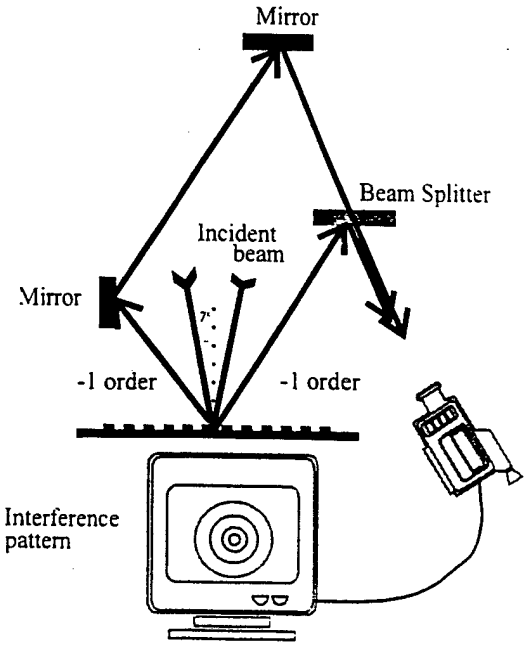


FIG. 6. Experimental configuration for the moiré alignment for the exposure sequence of Fig. 5. The extra optics are required since the small pitch pattern printed first results in a large diffraction angle. As a result of the path length differences, the projected moiré pattern exhibits a Newton's rings cylindrical symmetry.

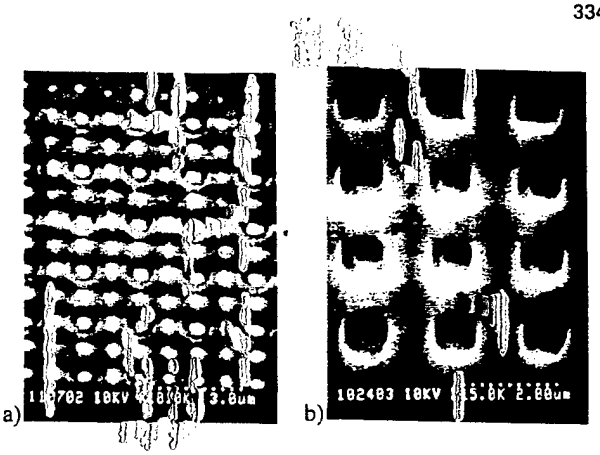


FIG. 7. Sparse array of holes produced by combination of optical and interferometric lithography: (a) optical lithography first, interferometric lithography second; (b) interferometric lithography first, optical lithography second. In both cases, the first pattern was etched into an oxide film and the second pattern was defined in a separate lithography step.

C. Combined optical and interferometric lithography

Similar to the techniques presented in Secs. III A and III B sparse arrays of sub-μm holes can also be produced using multiple step processes where interferometric lithography is used to define the small features (e.g., 0.5-μm) combined with conventional imaging optical lithography for the larger (e.g., 1-μm) features. Both sequences, interferometric lithography followed by conventional lithography and vice versa, have been demonstrated. This technique combines the two processes of defining a sparse hole array and of pixel definition in a single fabrication sequence. Figure 7(a) shows an example of the first approach in which small holes were written into a photoresist film on top of an array of large "wells" produced in an oxide film by conventional lithography and plasma etching. Figure 7(b) shows the inverse process in which a dense array of small holes was written and etched into an oxide film and then conventional lithography was used to place a larger hole array (1-μm holes on 2-μm pitch) over the original holes. To allow alignment between the two lithography techniques, an alignment grating was included on the optical lithography mask. Moiré fringes were formed when the interferometric grating and mask grating were superimposed. The period of the moiré fringes was

used to set the period of the interferometric exposure and the brightness of the fringes was used to set the phase (position) of the exposure. Precision of alignment was limited by the inaccuracy in the period of the *e*-beam defined mask grating. In Fig. 7(b), the alignment varies across even this very small field because of imperfections in the period in the optical mask. Great care in the production of the optical mask, in the temperature uniformity of the mask during exposure, and in the fidelity of the optical system will be necessary to allow matching of these two techniques over large areas. The interferometric system provides an almost perfect grid, defined only by the laser wavelength and by the fidelity of the beam collimation and optical flatness of the flat mirrors. In practice, we had much more success aligning two interferometric exposures over large areas than with mix and match between interferometric and imaging optical exposures.

D. Three-beam exposure for simultaneous exposure of two pitches

Simultaneous multiple exposures at two periods d_1 and $d_2=d_1/2$ are accomplished by changing the optical arrangement to have three coherent beams of equal intensity (F_0) incident at $+\theta$, $-\theta$ and normal to the plate. A calculation of the exposure flux for a single exposure pair (one in x, one in y) gives

$$F_{3\text{-beam}}(x,y,z)=F_0\left\{\begin{array}{l}6+2[\cos(2kx\ \sin\theta)+\cos(2ky\ \sin\theta)]\\+4[\cos(kx\ \sin\theta)+\cos(ky\ \sin\theta)]\cos[kz(1-\cos\theta)]\end{array}\right\}. \tag{6}$$

An intuitive interpretation of this equation is that the interference of the outer two beams gives the double frequency cosines that lead to the smaller structures associated with a dense, small pitch pattern [$d_2=\lambda/(2\sin\theta)$] while the interference of each of these beams with the normally incident beam gives the constant and cosine terms and leads to the larger pitch pattern ($d_1=\lambda/\sin\theta$). The larger pitch pattern is z (distance from the optical system to the plate) dependent. At appropriate z positions, alternate rows and columns of small pitch holes are canceled giving the desired sparse pattern. Benefits of the three-beam configuration are that there is no lateral alignment required as in the previous three cases, and, as will be shown below, the process latitude and photoresist sidewalls are improved over the double exposure technique. A significant trade-off is that the pattern is no longer independent of z (i.e., there is effectively a periodic focus). This is similar to the finite depth-of-field of imaging optical lithography with the exception that the pattern is repetitive in z, as described by the $\cos[kz(1-\cos\theta)]$ term.

The z-positioning is a relatively easy task, accomplished by using a variant of the moiré alignment techniques described above. A premade grating was placed at the sample position and the diffracted orders of the three incident beams form moiré fringes. A bright single fringe indicates the required z-position is achieved. The small numerical aperture associated with the small incident angles still leaves a substantial depth of field ($\sim$5-μm for 0.5-μm holes compared with less than 1-μm for conventional optical lithography at the same CD). Figure 8 shows a pattern created using this concept. The three-beam technique results in a sparse array of holes in a single exposure pair (one in x, one in y) with only a z-position adjustment. Collimated incident beams are required to avoid moiré fringes printed on the sample. The required degree of collimation can be evaluated by a simple calculation akin to Eq. (1). For a single one-dimensional exposure with beams incident at $\theta=0,\theta=\theta_0+\delta$ and $-(\theta_0-\delta)$, exposure intensity pattern is:

$$F(x)=\left[\begin{array}{l}3+2\cos(2kx\ \sin\theta_0\cos\delta)\\+4\cos(kx\ \sin\theta_0\cos\delta)\cos[kz(1-\cos\theta_0)-kx\cos\theta_0\sin\delta]\end{array}\right]. \tag{7}$$

Thus, lack of collimation($\delta\neq 0$) is equivalent to a spatial variation in the wafer height [i.e., $z=z(x)$] and the interferometric cancelation inherent in the sparse array of spots in a three-beam exposure is not uniform across the exposure area. The required collimation is easily found from Eq. (7), viz. $\delta\lesssim\lambda/(4L\cos\theta_0)\sim 10$ μrad for an $L=1$-cm field.

E. Five-beam configuration for simultaneous exposure of complete sparse hole array

The three-beam configuration can be further extended using a five-beam geometry with one beam incident at normal, two additional beams incident as before at angles of $+\theta$ and $-\theta$ with all three beams in a single plane of incidence (de-

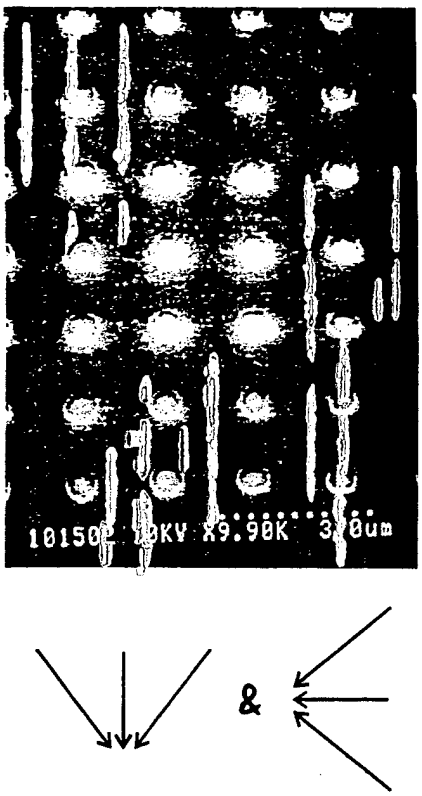


FIG. 8. Sparse array of holes produced by three-beam exposure pair. Note the partial exposure between the holes since each of the three-beam exposures illuminates an array of lines. The holes develop at the intersections of the two orthogonal line sets.

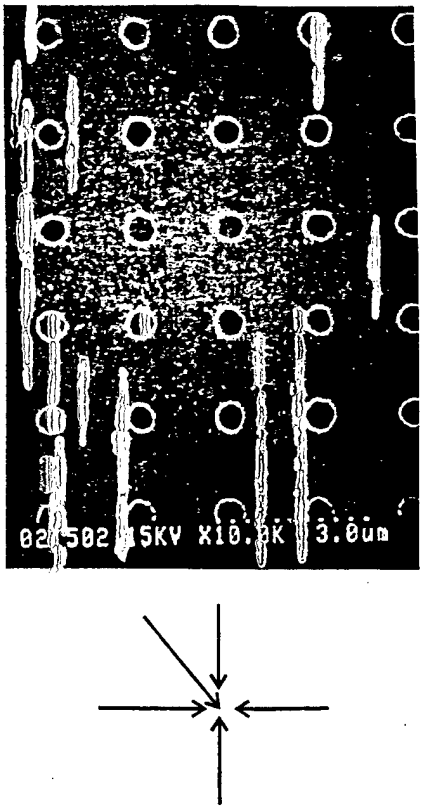


FIG. 9. Sparse array of holes produced by a single five-beam exposure. In contrast to the three beam exposure pair of Fig. 8, the exposure is concentrated at the hole locations resulting in a more efficient use of the available laser energy.

fining the x-plane), and a further two beams incident at $+\theta$ and $-\theta$ in an orthogonal plane of incidence (y-plane). As a result of the vector nature of the electromagnetic field, the equations describing the field and the intensity become slightly more complex. The corresponding exposure flux distribution is:

$$F_{5\text{-beam}}(x,y,z)=F_0\left\{\begin{array}{l}2\{1+\cos(2kx\sin\theta)+\cos^2\theta[1+\cos(2ky\sin\theta)]+\sin^2\theta[1-\cos(2ky\sin\theta)]\}\\+1+8\cos\theta\cos(kx\sin\theta)\cos(ky\sin\theta)\\4[\cos(kx\sin\theta)+\cos\theta\cos(ky\sin\theta)]\cos[kz(1-\cos\theta)]\end{array}\right\}, \quad (8)$$

where we assume all five incident beams have the same incident flux (F_0). This expression is similar to the three beam single exposure pair expression with an additional term arising because of interference between beams in the x-plane and y-plane in this simultaneous exposure. The resulting pattern from the five beams is similar to that of the three-beam exposure pair, but gives the full 2D pattern in a single exposure. An added benefit is that because energy is deposited only on the locations of the holes, the required exposure flux is lower than that of any other technique. Figure 9 shows an example of this exposure. Note that it looks very similar to Fig. 8 with the exception that some residual, incomplete development between the holes in Fig. 8 is eliminated in Fig. 9 because of the more efficient placement of energy only over the hole locations. This technique has similar z-alignment (focus) and collimation requirements to the three-beam exposure pair case.

F. Four-beam configuration for simultaneous exposure of a sparse hole array

Both the three-beam and five-beam configurations have the significant trade-off that the exposure patterns are dependent on z, which must be precisely controlled to achieve the desired pattern. The required z positioning may be a potential problem in flat-panel display applications because of the

inherent lack of flatness of the glass substrates. The z dependence comes from the center beam (normal to the plate) which has a different propagation constant along z than the other beams (e.g., the center beam propagates as e^{-ikz}, the off-axis beams propagate as $e^{-ikz\cos\theta}$). If the central beam is eliminated, a four-beam configuration with the same independence on z (i.e., large depth-of-field) of the two-beam exposures results. The exposure flux distribution is:

$$F_{4\text{-beam}}(x,y)=F_0\left\{\begin{array}{l}2\{1+\cos(2kx\sin\theta)+\cos^2\theta[1+\cos(2ky\sin\theta)]+\sin^2\theta[1-\cos(2ky\sin\theta)]\}\\+8\cos\theta\cos(kx\sin\theta)\cos(ky\sin\theta)\end{array}\right\}. \quad (9)$$

Unlike the single exposure pair case where there is no coherence between the temporally separated x- and y-exposures, all of the optical fields interfere with each other in this geometry. If the polarization of the two beams in the x-plane was rotated by 90° relative to the two beams in y-plane so that there was no interference between the two beam pairs, a simultaneous exposure would result in a dense hole array just as in a single exposure pair. The interference pattern of Eq. (9) is readily evaluated with the result that, rather than the completely eliminated alternating rows and columns of the previous two geometries, extra holes appear at the center of each square of the three-beam exposure pair and five-beam exposure (i.e., a face-centered cubic lattice). This is equivalent to a square array of holes with the centers separated by $\sqrt{2}d_2$ and rotated by 45°. The experimental result is shown in Fig. 10. This technique produces the entire 2D array of holes in a single exposure without requiring either an x- or a z-alignment. The collimation requirement remains the same as in the three beam case. In comparison with a five-beam exposure this geometry requires slightly more energy and produces slightly poorer sidewall angles; however, the major advantage of not requiring a focus adjustment makes this probably the most promising technique for producing sparse hole arrays.

Figure 11 shows an aerial view representation of the various exposures. The two-beam double exposures give rise to a dense array of holes [center-to-center distance $d=\lambda/2\sin(\theta)$], the three-beam double- and five-beam exposures results in a sparser array with alternate rows and columns eliminated ($2d$); finally the four beam geometry gives an intermediate density array where the face-center lattice holes are added to the sparse array ($d\sqrt{2}$). For each of these geometries the exposure and development conditions can be varied to achieve different line:space ratios. There are significant trade-offs in terms of required exposure flux, sidewall profiles, and process latitude that are discussed more fully in the next section.

G. Sparse post array

An alternate technique for the fabrication of field emitters is to start with a sparse post (mesa) array instead of a hole array. Posts are readily generated in the traditional two-beam exposure pair geometry simply by increasing the exposure flux. Figure 12 shows a photoresist sparse post array on a Si substrate. A sparse array is simply made by increasing the exposure flux without any need for alignment in either x or z. The tradeoff is that a significantly higher exposure dose is required since a much larger fraction of the resist has to be exposed. On a area basis, approximately 19 times more area has to be exposed for a 1:4 diameter:pitch post array than for a 1:4 diameter:pitch hole array. As will be shown in the next section, the exposure dose ratio required is even larger (~25 times more fluence required for sparse post arrays as compared with holes) because the aerial image is not uniform up the edge of the posts and significant overexposure of the spaces between the posts is required.

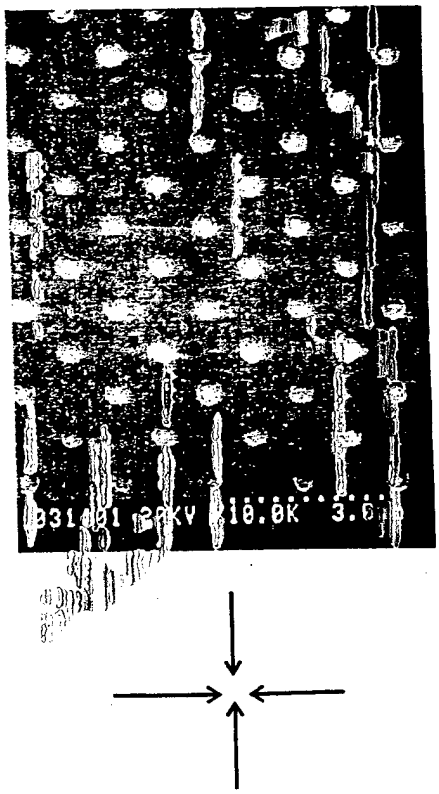


FIG. 10. Sparse array of holes produced by four-beam single exposure that retains the same very large depth of field as the two beam exposures. Again the energy is placed only over the holes resulting in an efficient use of laser energy. The hole pattern corresponds to removing alternate rows and columns from a dense array as in the five-beam case but then replacing an additional hole at the face-centered cubic location.

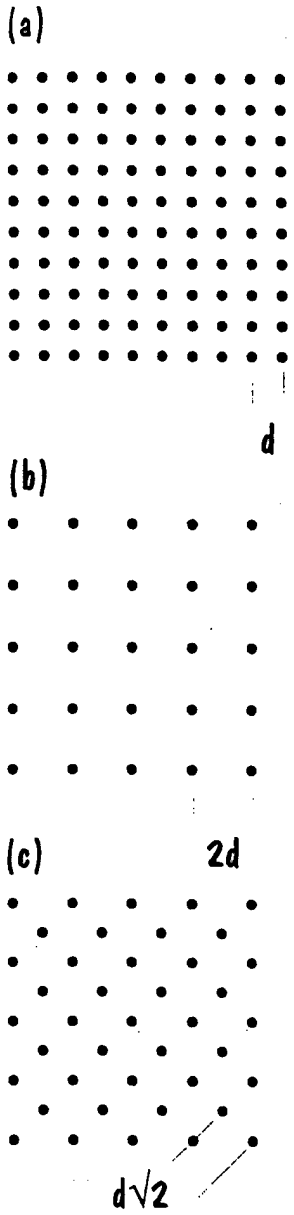


FIG. 11. Aerial view representation of the hole pattern formed by: (a) two-beam double exposure; (b) three-beam double exposure and five-beam exposure; and (c) four beam exposures. For an fixed angle of incidence the respective center-to-center distances are $d=\lambda/2\sin(\theta)$, $2d$, and $d\sqrt{2}$.

IV. EXPOSURE LATITUDE AND PHOTORESIST PROFILE EVALUATION

An investigation of exposure latitude and photoresist profile for sparse hole pattern has been carried out using a very simple, analytic photoresist exposure and developing model initially presented by Ziger and Mack.[9] In this model, the normalized resist thickness after development, τ, is related to the deposited flux in the resist, $F(x)$, by:

$$\tau(x)=1-\left(\frac{1-e^{-F(x)/F_t}}{1-e^{-1}}\right)^n, \tag{10}$$

where F_t is the minimum exposure required to clear the resist, n is an experimentally determined coordination number

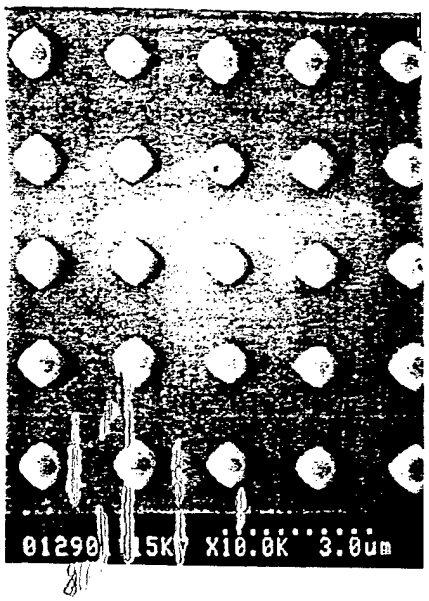


FIG. 12. Sparse array of posts produced by two-beam exposure pair: the exposure fluence has been increased to expose all of the resist in-between the posts. This exposure was carried out in photoresist on a Si substrate.

for the average number of base soluble groups that act in concert to effect the development rate. Although this simple model does not account for substrate reflection, for non-vertical development fronts, and for surface inhibition and other effects that influence the final line shapes, it provides a useful, computationally simple treatment that aids in the development of physical intuition for the interferometric exposure process. We have applied this model to all of the techniques for generating sparse arrays. We find that $n=5$ gives reasonable qualitative agreement with our experiments. This corresponds[10] to a photoresist contrast $\gamma \sim 5$, a reasonable value for the resist systems we have used. The hole diameter can be calculated by evaluating the region for which $F(x)<F_5$. Figure 13 shows the line:period (w:d) ratio as a function of the total flux summed over all of the input beams for different techniques. Note the scale change between the curves for the hole arrays and that for the post array. As noted above, approximately a 25 times larger fluence is required for sparse post as compared with sparse-hole arrays. An advantage of the post array is the relatively greater exposure latitude (i.e., decreased slope of the exposure curve at the desired line:space ratio). Issues that need to be resolved in each experimental situation are the effects of beam intensity mismatch and background scattering (optics flare) on the photoresist features. These effects are relatively unimportant in the case of hole arrays where the total laser fluence is only sufficient to expose small resist areas, but become significant at the much higher fluences required for post arrays. Figure 14 shows the corresponding photoresist line shape for a w:d ratio of 1:4 (a line:space ratio of 1:3) for holes and a w:d ratio of 3:4 (a line:space ratio of 1:3) of posts.

In principle, sparse holes can be generated in the traditional two-beam exposure pair geometry simply by decreasing the exposure flux. The solid curve in Fig. 13 was obtained by substituting the flux distribution for the two-beam

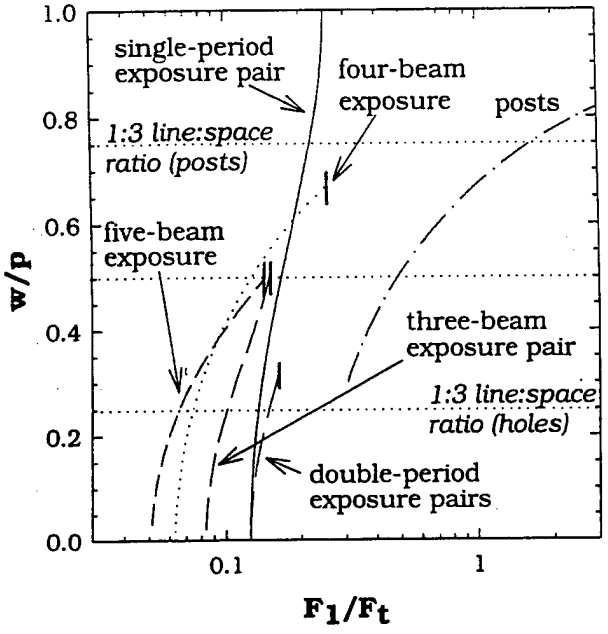


FIG. 13. Calculated process sensitivity (exposure latitude) for the various techniques for sparse hole array fabrication. The positions of dense (1:1) and sparse (1:3) line:space ratios for both holes and posts are indicated by the horizontal dotted lines. Exposure limitations for the multiple beam techniques due to breakthrough of unwanted features are indicated by the heavy vertical bars. Approximately 25× more fluence is required for sparse posts arrays with a single-exposure pair geometry than for sparse hole arrays with a five-beam exposure.

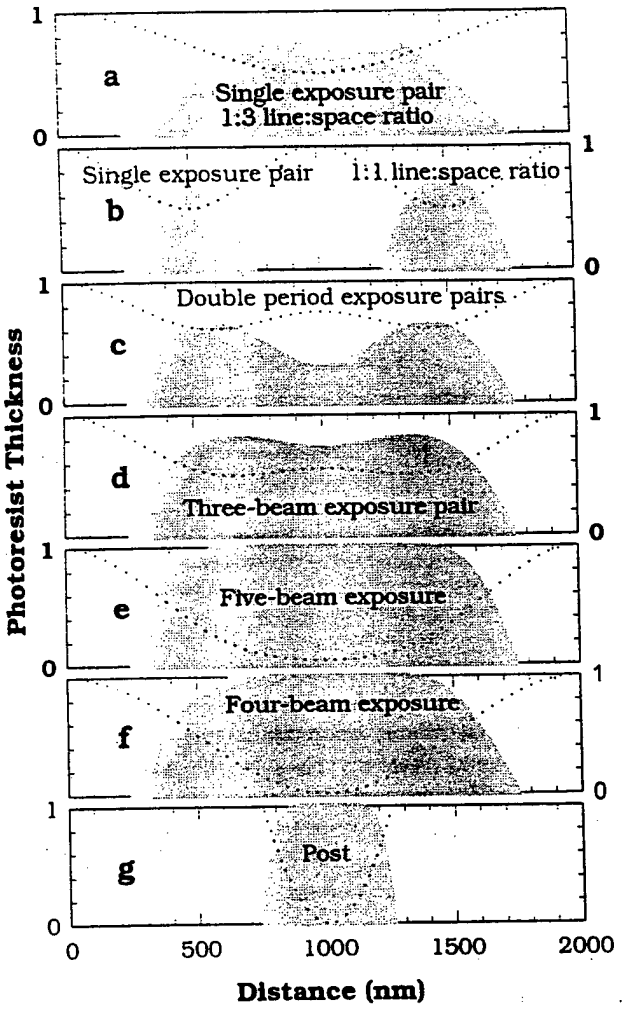


FIG. 14. Calculated photoresist profiles for the various techniques of sparse array fabrication. The shaded areas indicate photoresist left after the develop process; the dotted lines are the aerial image intensity vs position.

exposure [Eq. (2)] into the exposure/develop model [Eq. (10)]. The diameter:period ratio (w:d) can be evaluated with a 1D calculation along the symmetry direction between the holes ($y=0$). The calculation indicates that the 1:4 diameter :period ratio occurs very close to the flux that just clears the resist. at a position of very steep slope where small changes in flux lead to large changes in hole diameter. The corresponding photoresist profile. the shaded region in Fig. 14(a) is very poor with a shallow sidewall angle that will possibly lead to problems in subsequent etch steps. (Note that normalized vertical dimensions. corresponding to the full resist thickness. are shown in Fig. 15; as drawn these correspond to a 0.4-μm thick resist layer. These figures should be scaled for different resist thicknesses.) The resist latitude optimizes (i.e., has the lowest slope) at a 1:1 line:space ratio. The resist profile is also improved at this optimal line:space ratio. Fig. 14(b). The slope steepens again as the holes coalesce to form post arrays.

Calculated from Eq. (3) with the condition that $F_1=F_2$ and $y=0$, the double exposure pairs have a much improved slope at a 1:4 w:d ratio (Fig. 13) and an improved photoresist profile. Fig. 14(c). For the double exposure pair with two different pitches in each direction and double exposures with processing steps between lithography steps [techniques (2) and (3) in last section], the process latitude and sidewall slope for fine pitch are those of the single interferometric exposure pair for a 1:1 line:space ratio. The process latitude for the coarse pitch is much wider as the hole diameter and sidewall are determined by the fine pitch exposure. Three-beam exposure pair and five-beam single exposure curves progressively require a lower photon flux because the energy is deposited only in the desired regions resulting in more efficient use of the available photon flux. The process latitude calculated from Eqs. (6) and (8) at $z=0$ and $y=0$ is better than the double exposure case (lower slope than double exposure pair curve in Fig. 13 at 1:4 w:d ratio) and the photoresist sidewall angle is also improved as can be seen from Figs. 14(d) and 14(e). The four beam technique substantially improves the process latitude and photoresist profiles [Fig. 14(f)] over that of the single exposure pair and double exposure pairs although it is not as good as the three-beam and five-beam cases. It requires slightly more exposure flux than the five beam technique. Each of the multiple beam and multiple exposure techniques provides enhanced process sensitivity and improved photoresist profiles compared to the single exposure pair.

For the sparse post array technique, using the flux distribution of the two-beam exposure pair given by Eq. (2) with the condition $\cos(ky \sin\theta)=0$, the process latitude in Fig. 13

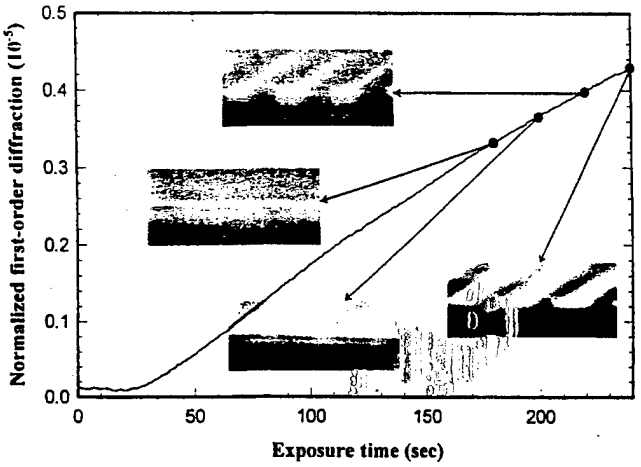


FIG. 15. Real-time diffraction intensity of a 633-nm probe laser beam from the latent grating that forms during exposure and developed photoresist profiles corresponding to the marked exposure fluences. The diffraction signal provides a real-time process monitor to allow correction for variations in actinic laser fluence, in photoresist and underlying film and substrate properties.

indicates a much lower slope (better process latitude) at 3:4 w:d ratio. A more vertical profile is shown in Fig. 14(g) that is well suited to subsequent processing steps. As noted above the disadvantages of the post array are the much greater required exposure fluence and the effects of scattering and beam intensity mismatch on the profiles.

V. REAL-TIME MONITORING

Diffraction-based techniques have been shown to provide convenient, nondestructive, rapid metrology for lithography steps during semiconductor device fabrication.[11] The periodic aerial image pattern of interferometric lithography directly lends itself to real-time exposure monitoring. Modeling techniques can be applied to predict the diffracted power from the latent image based on the optical properties of the substrate. We have monitored the exposure energy with 633-nm He–Ne laser beam diffracted from the latent image. Figure 15 shows the diffracted latent image intensity versus exposure energy and the photoresist profiles at four different exposure fluxes for a 1-μm period 1D grating in 0.2 μm thick resist. The monitored signal is easily used to correct for variations in actinic laser power, photoresist parameters (thickness, sensitivity, moisture content) and substrate properties (complex reflectivity, anti-reflecting coating, scattering, etc.). Similar diffraction monitors have been applied during the development step.[12]

VI. CONCLUSIONS

Interferometric lithography provides an attractive technique for the production of large areas of sub-μm structures. Salient features include: effectively infinite depth of field, periodic patterning without requiring masks, commercially available laser sources, and resist systems to scales well beyond today's projections for either ULSI or display applications. The periodic nature of interferometric lithography is well suited to the use of moiré alignment and overlay techniques and to scatterometry for real-time process control. The wide variety of potential applications includes: ULSI circuits; field-emitter displays; cold-cathode rf sources; high-speed FETs and MSM photodetectors; texturing on physical optics scales for high performance solar cells; and physics investigations including nanostructured materials, novel electronic devices, and nanostructured substrates for epitaxial materials growth.

Specifically for the field-emitter application, there is a requirement for sparse ($\gtrsim$1:3 line:space ratio) arrays of structures including holes and posts. A number of techniques have been demonstrated to provide an improved aerial image for sparse arrays of holes that result in improved process sensitivity and photoresist profile over a traditional two-beam exposure pair. These include both multiple exposure and multiple beam geometries. A five-beam geometry provides the most efficiency in the use of the laser power and at the same time has the best process latitude and most vertical sidewalls for hole arrays. However, a significant disadvantage is the requirement for focus (or z) control. A four-beam geometry provides the same effectively infinite depth of field of the two-beam exposures with only small penalties in terms of exposure fluence and developed photoresist sidewalls. For post arrays, a single-exposure-pair two-beam geometry provides the best process latitude and sidewall angles. The post arrays require significantly more exposure flux because of the much larger area of photoresist that must be exposed. Image reversal or negative resists reverse these considerations for hole and post arrays. Detailed process modeling and experimental confirmation is necessary to sort through the myriad of options and provide insight into the optimal geometries for particular applications. This work is underway both with the simple exposure/develop model presented here and with more sophisticated exposure/develop models that include effects of substrate reflection and of sidewall erosion during development.

A significant issue is the extension to the very large fields required for display applications. While this is not a major emphasis of this work, and has been discussed by others[5] in the context of double-exposure geometries, a few comments are in order. The obvious requirement is for large optics for collimation and manipulation of the multiple beams. Even for very large exposure fields, approaching 1-m diagonal, the coherence of present commercially available lasers is more than sufficient for interferometric exposures over the entire field. In the two beam exposure pair case, if the beams are perfectly collimated, the exposure period is constant across the field. Deviations from collimation will result in slow variations of the period across the field. Whether this is acceptable depends in part on integration of the interferometric exposure with other aspects of the processing and tolerance to alignment variations of subsequent steps, e.g., pixillation,

of the display. For the multiple exposure and multiple beam geometries for producing sparse hole arrays, the required collimation is more demanding since, as discussed in the previous sections, these techniques depend on moiré pattern effects to reduce the hole density.

ACKNOWLEDGMENTS

Partial support for this work was provided by Sandia National Laboratories and the Defense Advanced Research Projects Agency. The authors would like acknowledge helpful discussions with and dedicated experimental assistance of Andrew Frauenglass.

[1]C. A. Spindt, C. E. Holland, A. Rosengreen, and I. Brodie, IEEE Trans. Electron Device **ED-38**, 2355 (1991).
[2]H. Anderson, H. I. Smith, and M. L. Schattenberg, Appl. Phys. Lett. **43**, 874 (1983).
[3]S. H. Zaidi and S. R. J. Brueck, J. Vac. Sci. Technol. B **11**, 658 (1992).
[4]S. H. Zaidi and S. R. J. Brueck, Proc. SPIE **2197**, 869 (1994).
[5]J. P. Spallas, A. M. Hawryluk, and D. R. Kania, J. Vac. Sci. Technol. B **13**, 1973 (1995).
[6]C. O. Bozler, C. T. Harris, S. Rabe, D. D. Rathman, and M. A. Hollis, J. Vac. Sci. Technol. B **12**, 629 (1994).
[7]S. H. Zaidi and S. R. J. Brueck, Appl. Opt. **27**, 2999 (1988).
[8]S. H. Zaidi, A. Frauenglass, and S. R. J. Brueck, Proc. SPIE **2196**, 371 (1994).
[9]D. H. Ziger and C. A. Mack, AIChE J. **37**, 1863 (1991).
[10]C. A. Mack, J. Electrochem. Soc. **134**, 148 (1987).
[11]S. S. H. Naqvi, S. H. Zaidi, S. R. J. Brueck, and J. R. McNeil, J. Vac. Sci. Technol. B **12**, 3600 (1994).
[12]J. A. Britten, R. D. Boyd, and B. W. Shore, Opt. Eng. **34**, 474 (1995).

Optical properties of nanoscale, one-dimensional silicon grating structures

Saleem H. Zaidi,[a] An-Shyang Chu,[b] and S. R. J. Brueck[b),c)]
Center for High Technology Materials, University of New Mexico, Albuquerque, New Mexico 87131

(Received 20 June 1996; accepted for publication 11 September 1996)

We report a detailed study of nanostructure fabrication and optical characterization of sub-μm-period, one-dimensional, Si grating structures. Nanoscale wall width structures were fabricated by combining laser interferometric lithography with anisotropic wet-chemical etching (KOH) and thermal oxidation. Structure wall widths were characterized by Raman scattering (RS) and scanning electron microscopy. Salient features of the RS measurements as a function of wall widths from ~100 to 10 nm were: (a) large cross-section enhancements, ~100×, for linewidths ~50 nm; (b) asymmetric line shapes with tails extending to smaller Raman shifts for linewidths ~20 nm; and (c) splitting of the bulk Raman mode, again to lower Raman shifts, for linewidths ~10 nm. For room temperature photoluminescence (PL) measurements, the grating structures were excited at 257 nm. PL measurements are reported for oxidized and unoxidized grating structures with peaks varying between 380 and 700 nm. PL was only observed for Si structures with dimensions less than about 10 nm. PL intensities and spectral line shapes varied significantly as a result of surface modification treatments such as high temperature anneal in a N_2 atmosphere, immersion in boiling H_2O, and long-term exposure to ambient air. The measurements indicate a strong correlation of the visible PL with crystal size (~5–10 nm); however, it remains unclear if the mechanism responsible is quantum confinement, passivation of the surface by Si:H_x complexes, or optically active surface states. © *1996 American Institute of Physics.* [S0021-8979(96)07024-7]

I. INTRODUCTION

Silicon is a poor luminescent material in comparison with direct band-gap semiconductors such as GaAs. Thus, the observation of efficient, stable room temperature visible photoluminescence (PL) from porous Si (π-Si) (Ref. 1) has generated a great deal of interest in the optical properties of nanoscale Si structures. Although Pickering *et al.*[2,3] had previously reported on PL from π-Si attributing it to a complex mixture of phases, i.e., α-Si:O (and/or α-Si:H), the interpretation by Canham[1] and Lehman and Gosele[4] in terms of quantum confinement effects stimulated intense research efforts towards a comprehensive understanding of the physical mechanisms responsible for the PL. *A clear picture has yet to emerge.*

Research has focused on both the quantum-confinement basis of PL[5–13] and on alternate chemical mechanisms, for example, Si–H_x complexes.[14–17] Recently, a surface state mechanism was proposed in which the PL originates from a spectrum of surface states related to amorphous Si.[18] Interpretation is complicated by the fact that π-Si PL exhibits two bands with widely different response times: orange-red (850–650 nm) PL decaying at time scales ~10 μs, and blue-green (420–540 nm) PL with a much faster (ns) decay rate.[19] This blue emission has been attributed to SiO_x (x~1.4–1.6) complexes.[20–22] In an extensive review of optical properties of π-Si PL by Lockwood,[23] several different sources of PL in anodized Si were analyzed with the tentative conclusion that the red emission appeared to be principally due to confinement in Si nanocrystallites. However, in his summary, Lockwood pointed out that a definitive explanation of the various light-emitting sources in π-Si will only come from a further study of surface chemistry of pores, defects in Si crystallites, and *from studies of uniform Si wires, or dots so as to minimize inhomogeneous broadening effects.*

π-Si formed by anodization has a complex three-dimensional (3D) structure,[2,3] which makes it difficult to isolate chemical effects from crystal-size and electromagnetic effects. A more controlled and uniform fabrication approach would be better suited to investigation of the optical response as a function of the crystal size. Lithographic techniques offer an attractive alternative for fabrication of uniform, nanoscale crystalline structures. Liu *et al.*,[24] and Fischer *et al.*[25] have applied electron and ion-beam lithographic techniques to form 2D columnar structures. These techniques, however, are slow, expensive, and difficult to extend to large areas and to multiple samples with the requisite uniformity. We report a simple fabrication sequence using inexpensive interferometric lithography, anisotropic wet-chemical etching, and oxidation processes that is readily capable of providing samples for fundamental investigation. In addition, all of these technologies are readily, and inexpensively, scaleable to large areas for device applications and are compatible with high volume manufacturing. We present a detailed investigation of the fabrication of nanoscale, sub-μm-period, one-dimensional Si grating structures and their optical response as a function of the crystal size. This article is organized as follows: Sec. II describes nanofabrication techniques for Si nanostructures; Sec. III describes the Raman response as the structure size is reduced from ~100 to less than 10 nm; Sec. IV presents extensive PL measurements of the Si structures with and without thermally grown oxide films, and also includes PL measurements from thermally grown oxide films; and results are summarized and discussed in Sec. V.

[a)]Electronic mail: saleem@chtm.unm.edu
[b)]Also at Department of Physics and Astronomy.
[c)]Also at Department of Electrical and Computer Engineering.

 0021-8979/96/80(12)/6997/12/$10.00 © 1996 American Institute of Physics

II. NANOSTRUCTURE FABRICATION

Interferometric lithography provides an inexpensive method for the fabrication of nanoscale periodic structures over large areas and is ideally suited to a large scale manufacturing environment. Interference effects between two coherent laser beams produce a simple periodic pattern with period, $d=\lambda/2 \sin\theta$, where λ is the wavelength of the exposing beam, and 2θ is the angle between the two intersecting beams.[26,27] In our experiments, grating patterns are first formed in positive photoresist (1350B-SF). After photoresist exposure and development, the grating pattern is transferred to a thermally grown oxide (thickness ~50 nm), or nitride or metal film, using either wet etching, dry etching, or lift-off techniques. The feature widths of the oxide etch mask can be reduced to approximately 1/4 of the grating period by control of the photoresist exposure, development, and pattern transfer processes. An oxide mask is used for anisotropic, wet-chemical etching of Si in 40 wt % KOH solution at room temperature. Although any crystal orientation of Si can be used, for quantum-size fabrication, (110) crystal orientation is advantageous because of the extreme etch rate anisotropy (1:400) between the perpendicular ⟨111⟩ and ⟨110⟩ planes.[28,29] Figures 1(a)–1(c) show examples of scanning electron microscope (SEM) images of Si(110) 1D grating structures with periods 0.8, 0.5, and 0.2 μm, respectively. Grating depths vary from ~1.0 μm [Figs. 1(a) and 1(b)] to ~0.4 μ [Fig. 1(c)]. Note, in particular, the very well-defined grating sidewalls (⟨111⟩ planes); cross-section transmission electron microscope images of these structures show that the sidewalls are nearly perfect; the lines visible in the SEMs correspond to nearly atomic steps. The wall widths (note: we use wall width throughout this article to avoid confusion with spectral linewidths) are approximately 1/4 of the grating period demonstrating the scaling effects of smaller grating periods. Wall widths can be reduced further by pushing the limits of the lithographic processes used for etch masks. This is done primarily by a combination of overexposure and/or overdevelopment of the photoresist, and undercutting the etch mask film during isotropic plasma etching. Using these techniques, we have fabricated grating structures with good yield to wall widths ~1/10 of the period. Figure 2 shows an example of a 0.3-μm-period grating with wall widths of ~0.03 μm.

A convenient method for further reducing grating wall widths is based on oxidation of Si.[30] Figures 3(a)–3(c) show three examples of Si wall widths varying from ~20 to 5 nm, respectively, following oxidation steps. The crystalline Si walls are embedded in thermally grown oxide films. The concave shape of the Si structure is the result of oxidation that proceeds faster on the lower radius of curvature parts of the structure.[31] This provides a partially self-limiting process and improves the uniformity. The SEM in Fig. 3(c) was taken at a magnification of 250 000, the instrumental limit, and shows a Si structure of wall width ~5 nm. Wet-chemical etching of (110) Si, combined with interferometric lithography and oxidation, provides an extremely convenient and robust technique for producing nanometer-scale Si structures.

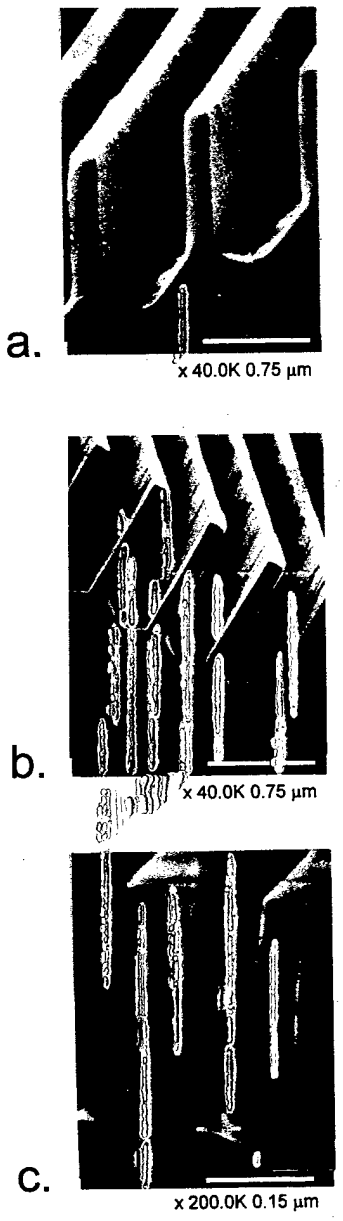


FIG. 1. Scanning electron microscope (SEM) pictures of Si ⟨110⟩ gratings: (a) 0.8 μm period, (b) 0.5 μm period, and (c) 0.2 μm period.

These techniques can easily be extended to (100) Si wafers using well-known dry etching processes. Figure 4 shows three examples of 1D and 2D structures fabricated in (100) Si using reactive ion etching (RIE) techniques. The structures in Figs. 4(a) and 4(c) were fabricated using a Cr lift-off mask, while the 1D structure in Fig. 4(b) was fabricated by first making an intermediate metal mask using reactive ion-beam milling of a blanket Al film followed by RIE using a CCl_2F_2-based chemistry. These structures, although not as sharply defined as the KOH-etched structures, nevertheless maintain their crystalline nature, and can be subsequently thinned by oxidation. These results demonstrate that simple and inexpensive interferometric lithography techniques can be applied for fabrication of large area, uniform, nanoscale feature width Si structures, providing a powerful approach

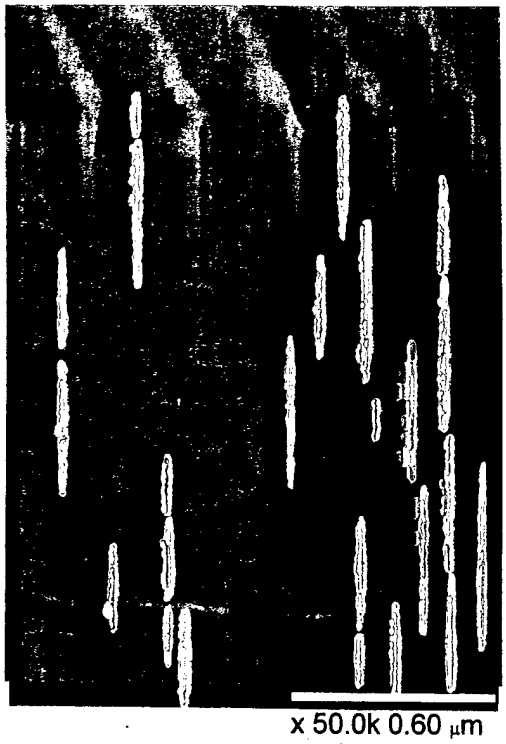


FIG. 2. SEM image of one-dimensional Si ⟨110⟩ grating with period 0.3 μm, wall width of ~30 nm and depth of 1.3 μm.

for optical and electrical characterization of nanoscale Si structures.

III. RAMAN SCATTERING MEASUREMENTS

The optical response of these sub-μm-period, nanoscale wall width Si grating structures has been investigated by reflectance, Raman scattering (RS) and photoluminescence measurements. Our emphasis here is to report on experimental results with reference to nanoscale wall width Si structures. In future publications, we plan to offer a theoretical framework describing the experimental results on reflectance, RS, and PL; our preliminary findings are that electromagnetic resonance effects play a large role in these periodic structures. Figure 5 shows an example of angular and spectral reflectance measurements from 0.36-μm-period gratings with wall widths ~70 nm and depth ~1.0 μm, for comparison, reflectance measurements from bulk Si under identical conditions are also plotted. There is very low reflectance from the surface of the grating sample over broad angular and spectral variations, suggesting an application for concentrator solar cells.[32]

RS measurements show a strong dependence on the Si wall widths. Variations of RS line shapes with decreasing crystal size have been reported for studies of π-Si,[7,33] of spherical Si particles embedded in oxide matrix,[34–36] and of laser-annealed amorphous Si films.[37,38] Goodes *et al.*[33] carried out extensive Raman scattering measurements of π-Si films and observed a single peak at 520 cm^{-1} (corresponding to bulk Si) plus a broad tail extending to low frequencies that was attributed to crystal sizes <10 nm. Splitting of the Raman mode for small structures has also been observed.[7] Similar size-dependent line shapes have been observed by others.[34–38]

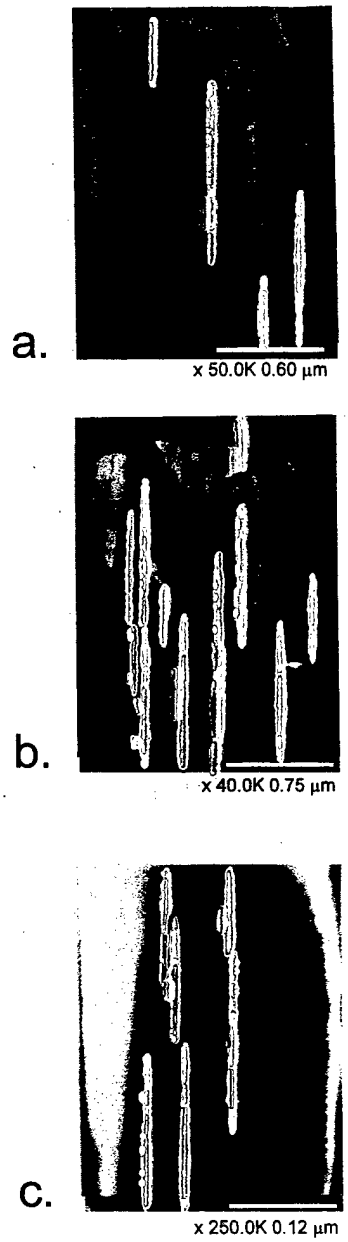


FIG. 3. SEM images of oxidized Si ⟨110⟩ gratings, wall widths are (a) ~25 nm, (b) ~10 nm, and (c) ~5 nm.

Micro-RS measurements were taken in a backscattering geometry using a 40× microscope objective to focus the 488 nm laser beam onto the sample (~10-μm-diam spot size). Spectra were analyzed with a 3/4 m double spectrometer and a cooled GaAs photomultiplier with photon-counting electronics. Three distinct regimes were identified: (a) for grating wall widths >200 nm, the Raman line shape and cross section is identical to that for bulk Si; (b) for grating wall widths ~50–100 nm, large (100× greater than bulk Si) signal enhancements are observed with line shapes unchanged from bulk Si except for slight shifts and broadening; and (c) for wall widths <30 nm, line shapes show a number of dramatic

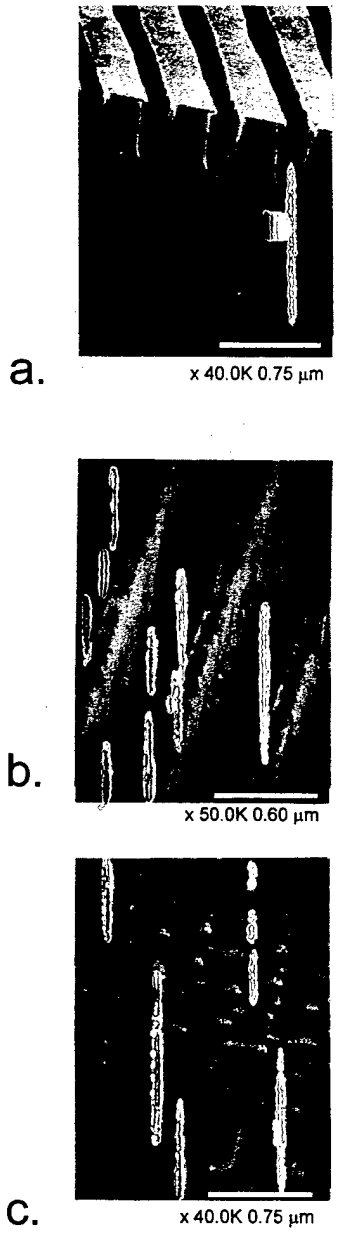


FIG. 4. SEM images of 1D (a) and (b) and 2D (c) Si ⟨100⟩ gratings fabricated with reactive-ion etching.

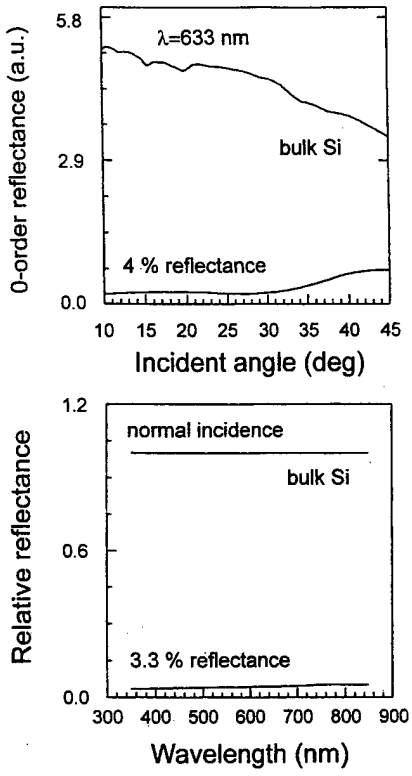


FIG. 5. Angular (a) and wavelength (b) dependencies of the reflectivity of a 0.36 μm period, 70 nm wall width, ~1 μm deep Si grating structure. Also plotted are the respective variations for a bulk Si sample.

changes including asymmetry and splitting of the threefold degenerate bulk mode while the cross section is still significantly enhanced over the bulk value when corrected for the volume.

Figure 6(a) shows an example of an enhanced Raman signal from ~50 nm wall-width grating structures (period 0.36 μm, depth ~1.0 μm); for comparison, the Raman signal from bulk Si measured under identical conditions is plotted on the same scale. Figure 6(b) shows the same data with the peak heights normalized, the peak at ~530 cm^{-1} shift is due to a pump laser plasma line deliberately leaked through to provide an absolute wavelength calibration. Figure 6(a) shows that the maximum intensity of the signal from the grating is ~15 times larger than that from bulk. The reflected plasma line intensity from the grating samples is much weaker because of the reduced reflectivity compared with bulk. Taking into account the reduced volume of material in the grating samples (wall width-to-period ratio of ~7) and the increase in the Raman linewidth from ~3.5 cm^{-1} for the bulk to 5 cm^{-1} for the gratings (integrated signal ratio enhancement ~1.4), a cross-section enhancement of ~140 is observed. This Raman enhancement can be explained qualitatively by electromagnetic cavity (wall width $\sim\lambda/2n$) resonances.[39] Because of the relatively low Q of these resonances above the Si band gap, both the pump and Raman-shifted wavelengths are within the resonance peak. This resonance effect was previously observed by Murphy and Brueck for randomly organized Si structures,[40] and Chew and Wang[41] for spherical particles.

The normalized data in Fig. 6(b) show that in addition to the signal enhancement, the peak shift is decreased by ~1.2 cm^{-1}, and the linewidth is broadened to ~5 cm^{-1} in comparison with ~3.5 cm^{-1} width of the signal from bulk Si. The frequency shifts of the Raman peak might be attributed to stress effects. Anastassakis *et al.*[42] demonstrated that in the presence of uniaxial stress, the $q\approx 0$ degeneracy of the optical phonons is removed resulting in splitting and shifts of the Raman mode. A strain of $\sim 5\times 10^9$ dyne would result in a frequency shift of ~1.2 cm^{-1}. A broadening of the Raman mode has also been attributed to crystal-size effects.[43] In this model, the additional broadening, $\Delta\nu_s$, is related to the crystal size d, which produces an uncertainty in the q vector $\approx 2\pi/d$, and is given by $\sim -A(\Delta q)^2$, where, for Si, A is ~2 cm^{-1} nm^2 and Δq is a rough measure of the extent of the breakdown of the $\Delta k=0$ Raman selection rule for a finite

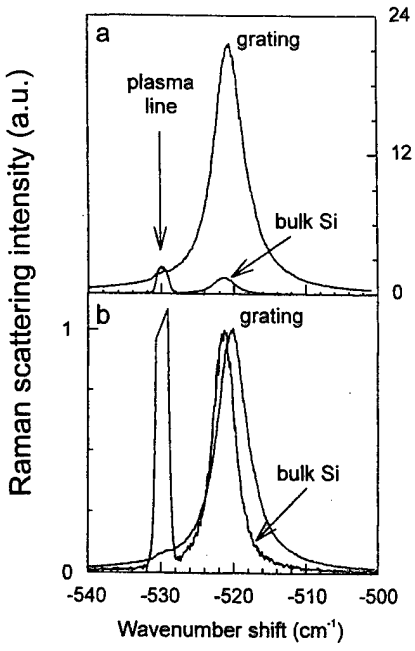


FIG. 6. Enhanced Raman scattering signal from a ~50 nm wall width Si grating structure (period 0.36 μm, depth ~1 μm: (a) signals from bulk and grating samples under identical conditions showing the strong ~140× integrated cross-section enhancement; (b) signals normalized to same peak height to illustrate shift and broadening of the grating Raman signal.

crystal dimension d. From the measured values of $\Delta\nu_s$, it is possible to estimate the crystal-size $d \sim 2\pi/\Delta q$. Therefore, for a broadening of ~5 cm^{-1}, $\Delta q \sim 1.6$ nm^{-1}, which corresponds to a grain size of ~4 nm. This broadening is asymmetric with a broader wing towards lower qs. From SEM measurements, our structures are at least ~50 nm wide and the linewidths are symmetric, which suggests that size effects cannot account for the broadening and shifts.

Figure 7 shows examples of Raman spectra from grating wall widths ~20 nm, as evaluated by SEM; again, for comparison, the Raman signal from bulk Si, normalized to the same maximum signal, is also plotted. Figures 7(a)–7(c) and 7(e) show a similar behavior: a central peak shifted only slightly if at all from the bulk mode and a strong asymmetry to smaller Raman shifts. The relative strength of the asymmetric tail varies significantly between spectra. The asymmetric profile in Fig. 7(a) is from a 0.2-μm-period grating that has not been subjected to oxidation treatment, similarly the line shape in Fig. 7(e) is also from a 0.36-μm-period grating without oxidation demonstrating the capability of lithographic techniques for forming ~20 nm wall width structures without the need for additional oxidation thinning. The data in Figs. 7(b)–7(d) are from 0.94-μm-period oxidized gratings [see Fig. 3(a)]. In this size regime, the Raman spectra are very sensitive to wall width, whereas the presence of oxide films has negligible effect on the line shape. The spectral variations in Figs. 7(b)–7(d) are due to slight variations of wall width from sample to sample, and even within the same sample. For all Raman measurements, a 40× objective was used to focus the laser beam onto the sample with the spot diameter ~10 μm, so that the measurements are sampling a very small area of the sample, and it was impossible to precisely correlate the area measured by SEM with the sample region probed by the Raman measurement. The measured Raman signal from structures in this regime showed an enhancement ~3.5 in comparison with bulk Si.

The increasing asymmetry and broadening of the Raman mode is believed to be the result of the contributions of nonzone-center phonons as described above and the effects of phonon confinement. Using a simple theoretical model first developed by Richter *et al.*,[44] asymmetric line shapes resulting from crystal-size related relaxation of the $\Delta k \sim 0$ Raman momentum selection rule can be evaluated.[29] For the highly asymmetric line shapes in Fig. 7, this model predicts crystal sizes of ~3–4 nm, much smaller than the SEM estimates of 20 nm. The asymmetric spectral line shapes in Fig. 7 appear to be a convolution of two peaks, one centered at 520 cm^{-1} and a second ranging from 518 to 515 cm^{-1} in the various spectra; this is consistent with a splitting of threefold degenerate optical phonons predicted by Kanellis *et al.*[45] for thin slabs of Si.

This splitting of the bulk mode becomes more pronounced as wall widths are further reduced. Figure 8 shows three examples of Raman spectra measured from Si grating structures with Si wall widths ~5–10 nm. The data in Fig. 8(a) are from a 0.94-μm-period oxidized grating [Figs. 3(b) and 3(c)], while the data in Fig. 8(b) is from an oxidized grating structure from which oxide film has been removed by HF treatment. Finally, the data in Fig. 8(c) are from a grating

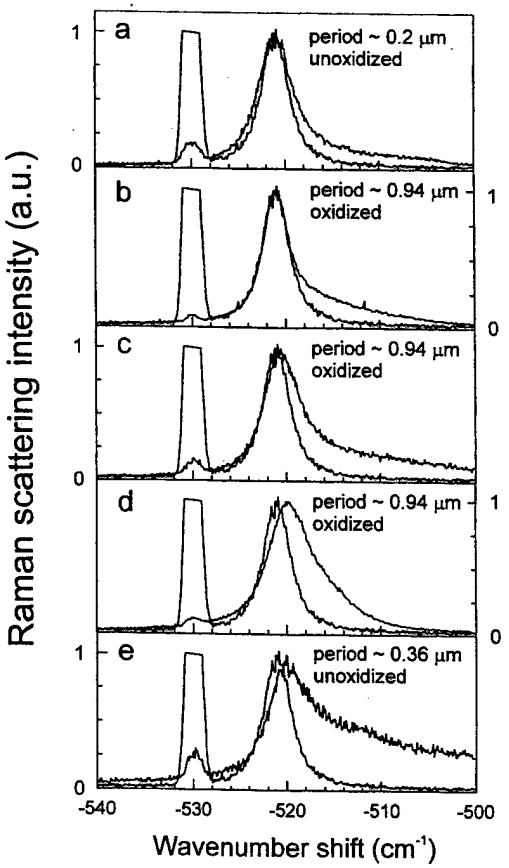


FIG. 7. Asymmetric Raman line shapes from grating structures with ~20 nm wall widths.

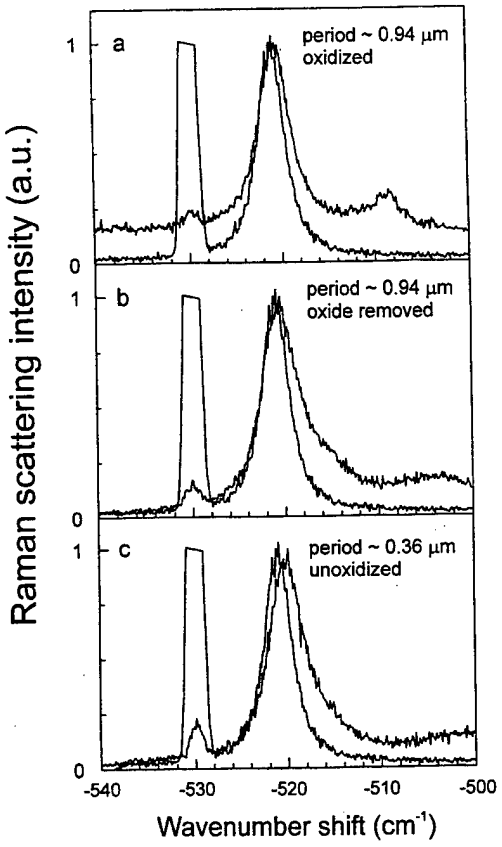


FIG. 8. Splitting of the Raman line shape for gratings with wall widths of ~5–10 nm.

structure formed without oxidation, demonstrating again the possibility of forming ~5–10 nm structures directly by interferometric lithography techniques. Notice that, in addition to the main peak at ~520 cm^{-1} shift, there are relatively weaker secondary peaks centered at ~510 cm^{-1} [Fig. 8(a)], ~505 cm^{-1} [Fig. 8(b)], and ~500 cm^{-1} [Fig. 8(c)]. These line shapes are very different from the highly asymmetric ones that result from the simplest modeling of the breakdown of the momentum selection rule and demonstrate that more significant physical effects are occurring at this nanoscale-size range. Also notice the increased base line of the signal in Fig. 8(a), this is the short wavelength tail of the PL signal that will be discussed in detail below. In our Raman scattering work with nanoscale wall width Si gratings, we have always associated splitting of the Raman mode with an onset of visible PL. Also, the maximum signal enhancement from these nanoscale, wall width structures was ~1.5 in comparison with bulk Si.

All of the Raman data presented above was measured for incident and scattered electric fields parallel to the grating walls (along a ⟨112⟩ crystal direction). The well-defined geometric nature of grating structures allows an investigation of polarization selection rules. We have investigated the four possible backscattering configurations: (a) incident electric field E parallel to the grating walls and analyzer (placed between the sample and the entrance slit of the spectrometer) parallel to $E(V/V)$, (b) E parallel to grating walls and analyzer perpendicular to $E(V/H)$, (c) E perpendicular to grating walls and analyzer parallel to $E(H/H)$, and (d) E perpendicular to grating walls and analyzer perpendicular to $E(H/V)$. Polarization measurements were carried out by keeping the incident beam polarization fixed and rotating the gratings by 90° for electric field to be parallel and perpendicular to grating walls, the analyzer was rotated for each orientation of the grating. After grating rotation, a somewhat different spot was sampled; however, under repeated measurements, similar behavior is observed suggesting accuracy of the trends illustrated by these measurements. Figure 9 shows a set of measurements for grating wall widths ~10 nm, the grating structure was fabricated without oxidation. For the V/V configuration in Fig. 9(a), two peaks centered at 520 and 502 cm^{-1} are observed; for the V/H configuration in Fig. 9(b), an identical line shape is observed except that the signal intensity is reduced by a factor of 10. However, taking into account the spectrometer selection ratio of ~10 with respect to vertically and horizontally polarized light, the horizontal and vertical polarizations are excited with equal strength by the incident electric field parallel to grating walls. The H/H configuration in Fig. 9(c) shows two peaks at 520 and 510 cm^{-1}, while the H/V configuration in Fig. 9(d) is highly asymmetric without distinguishing the second peak. The signal strength in Fig. 9(d) after correcting for spectrometer selectivity is almost twice that of the H/H configuration. Finally, it is significant that the second peak (at 510 cm^{-1}) shows a smaller shift in comparison with Figs.

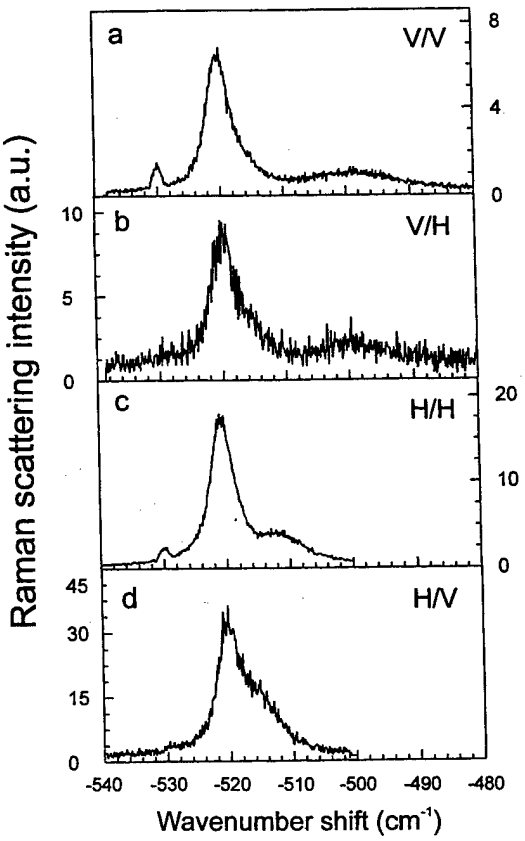


FIG. 9. Polarization resolved Raman line shapes for a ~10 nm wall width grating structure.

9(a) and 9(b) where the incident electric field is parallel to the grating walls.

In summary, Raman scattering provides an extremely sensitive probe of crystalline Si wall widths. The measured line shapes show similar behavior for π-Si, spherical particles, and laser-annealed amorphous Si films. Finally, the polarization behavior provides additional information on lattice dynamics of nanoscale structures.

IV. PHOTOLUMINESCENCE MEASUREMENTS

Room temperature PL measurements were carried out for cw 257-nm excitation (intracavity doubled Ar–ion laser) in a backscattering geometry using a real-time optical multichannel analyzer, system equipped with a 1/4 m spectrometer and an IR enhanced, thermoelectrically cooled CCD camera. For system calibration, we evaluated the PL from the quartz beam splitter used in our optical collection setup. The PL from the beam splitter was very weak and broadband in comparison with the grating signal. In all measurements, this background signal was recorded under identical conditions and subtracted from the grating signal to eliminate background effects.

Measurements were carried out over a wide range of Si grating wall widths, profiles, and depths. Significant PL was only measured from samples with estimated 5–10 nm wall widths irrespective of their periods. As mentioned above, a useful indicator of the onset of PL was splitting of the bulk Raman mode.

In our initial PL measurements on gratings formed by KOH etching without any additional oxidation, we found very bright, but highly localized, areas that emitted in the yellow when pumped at 488 nm. These were invariably near areas of the grating damaged during processing raising the possibility that this PL was from some undetermined particulate contamination or from residual metallic or photoresist particles remaining from the processing. Data presented here for Si and Si/SiO_2 structures are only reported for regions of the samples where constant PL intensity was maintained for sample translations of a few millimeters, insuring that the signals are not due to particulate contamination. As demonstrated earlier, the grating linewidths can be reduced either through process control, or by oxidation. Oxidation provided better wall width uniformity over larger areas. We present PL measurements from oxidized and unoxidized gratings separately. For oxidized gratings, background (base line) PL measurements were carried out from nongrating parts of the same sample. For comparison with oxidized grating PL, wet (H_2O ambient) and dry (O_2 ambient) thermally grown oxide films were also investigated. Finally, for comparison with π-Si PL, grating structures were partially anodized such that there was a transition from completely porous structure to a nonporous grating structure on the same sample. The PL peaks varied across the entire visible spectrum from 700 to 400 nm in these samples. The following three sections present detailed PL measurements from oxide films, oxidized Si gratings, and Si gratings without oxide films.

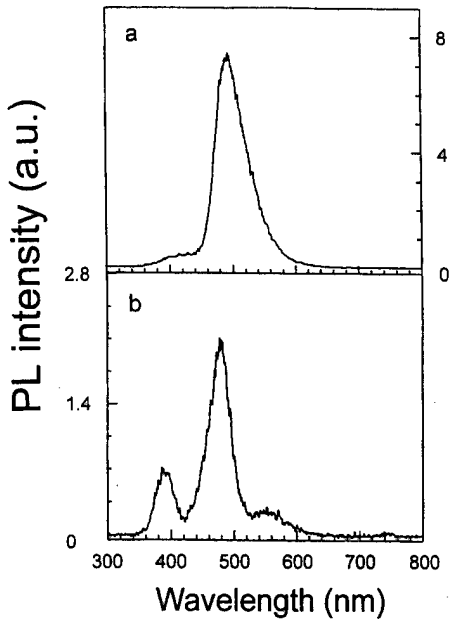


FIG. 10. PL measurements at an excitation wavelength of 257 nm for a thermal oxide film grown on a ⟨100⟩ Si surface: (a) 100 nm thick, (b) 700 nm thick.

A. PL measurements from thermally grown oxide films on ⟨100⟩ and ⟨110⟩ Si

Figure 10 shows PL measurements from two oxide films grown on ⟨100⟩ Si in H_2O ambient atmosphere. The PL intensity from the 100-nm-thick film [Fig. 10(a)] is stronger than that from the 700-nm-thick film [Fig. 10(b)]. For the 100-nm-thick film, the PL line shape shows a dominant peak at ~500 nm, and a much weaker feature at ~400 nm. For the 700-nm-thick film, three peaks can be distinguished: a strong peak at ~480 nm and two weaker peaks at ~400 and 550 nm.

These films had been exposed to ambient air for long periods before the PL spectra were taken. We investigated the effects of surface conditions on the PL by subjecting them to both high temperature annealing and boiling water treatments. For high temperature annealing, oxide films were placed in a furnace in a N_2 atmosphere and heated to ~1000 °C for 30 min. For boiling water treatment, oxide films were placed in boiling deionized water for 15 min. High temperature annealing completely quenched the oxide PL that was not restored by a subsequent boiling water treatment. The PL partially recovered following a two-week exposure to air without any noticeable difference in line shape from the first measurements. Boiling water treatment of luminescent (unannealed) oxide films promoted the growth of the 400 nm peak while suppressing the 500 nm peak. Figure 11 shows PL measurements from a 200-nm-thick SiO_2 film grown in an ambient H_2O atmosphere on a ⟨110⟩ Si wafer. Comparison of PL before [Fig. 11(a)] and after [Fig. 11(b)] boiling treatment shows that the PL efficiency of the 400 nm peak is improved by a factor of 4 while the 500 nm peak is almost quenched. We also investigated PL from oxide films grown in an O_2 ambient atmosphere with qualitatively similar results. Qualitatively similar, but significantly weaker, PL

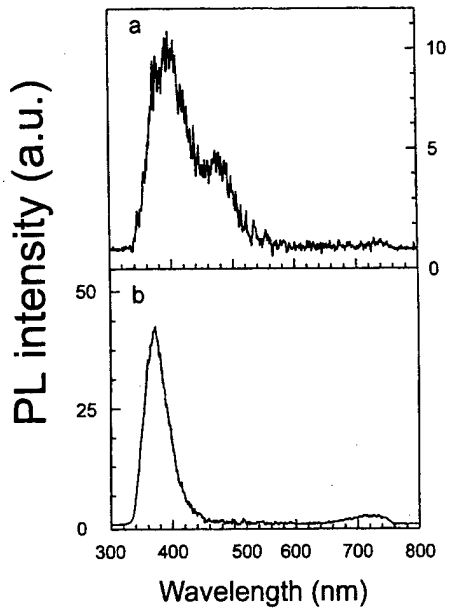


FIG. 11. Variation in PL for a 200 nm thick oxide film on ⟨110⟩ Si: (a) as-grown film, (b) after boiling water treatment for 15 min.

line shapes were observed from as-grown oxide films on ⟨111⟩ Si faces.

B. PL measurements from oxidized Si gratings

Figure 12 shows a PL measurement from a wet oxidized Si grating [cf. Fig. 3(b)]; for comparison, PL from a nongrating region of the same sample is also shown (both measurements after long term exposure to ambient air). The enhancement of the grating signal over the oxide signal is ~400 and the grating signal shows spectral features including symmetric shoulders at 420 and 540 nm with a peak nominally at ~470 nm. The cutoff at 760 nm is instrumental. Comparison of grating PL with oxide PL (Figs. 10 and 11) shows that (a) the grating PL is significantly broader, and (b) the grating PL peak ~470 nm is close to the spectral peak of the 700-nm-thick thermal oxide PL. The PL signal in both cases showed a fast degradation under UV excitation with an irreversible lifetime of only milliseconds.

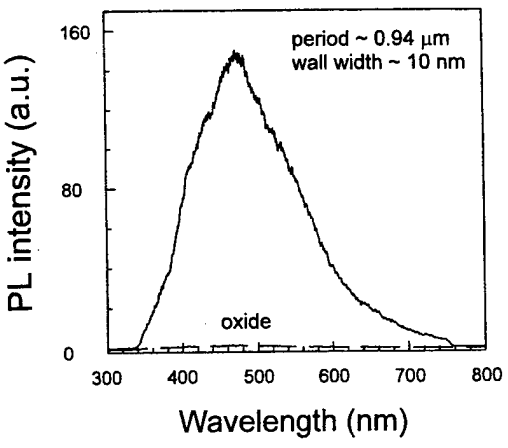


FIG. 12. Photoluminescence from thermally oxidized gratings, for comparison the PL from nongrating part of the same sample is also shown.

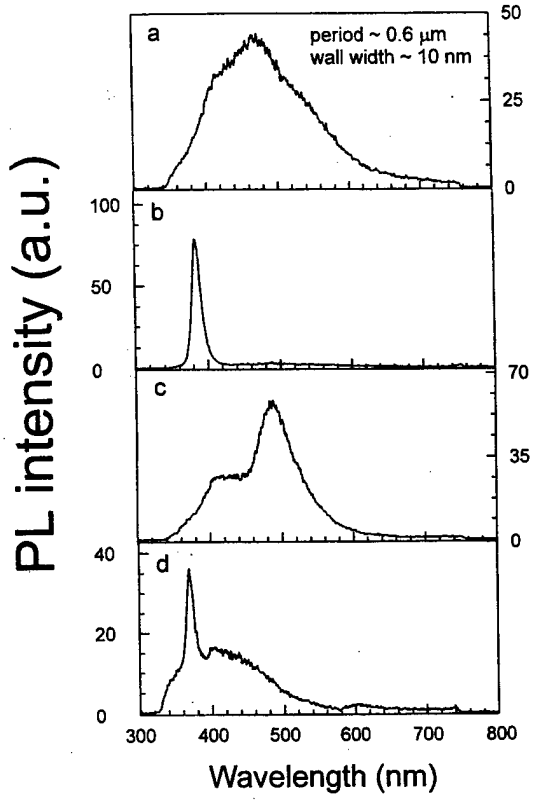


FIG. 13. Measurements of photoluminescence from different thermally oxidized grating structures: (a) and (b) are from different parts of the same sample, (c) and (d) are from a different sample.

Figure 13 shows a series of PL measurements from different wet oxidized Si grating samples. The grating periods were ~0.6 μm, depth ~1.0 μm, and wall widths ~10 nm. Figures 13(a) and 13(b) are from different regions of the same sample and Figs. 13(c) and 13(d) are from a second sample. Perhaps the most interesting feature of these spectra is the emergence of a very narrow peak around 370–380 nm in regions of both samples. This same feature has been observed in a number of different samples and is possibly associated with regions of extremely thin Si structures where one-dimensional effects become important.[46,47]

As with the oxide films, we investigated the variation of oxide grating PL with high temperature annealing and boiling water treatments. Figure 14 shows the results of these treatments on the grating PL shown in Fig. 12. Annealing almost quenches the PL (dotted line; the vertical scales in Figs. 12 and 14 are comparable); however, there is still a weak, broad PL. Following boiling water treatment of the same sample, PL is somewhat recovered (solid line) in distinct contrast to the behavior of the blanket oxide PL where the boiling water treatment did not restore the luminescence that had been quenched with a N_2 anneal. The PL peak is shifted to ~430 nm, and no longer has shoulders in comparison with Fig. 12. Figure 15 shows the results of similar treatments on the sample giving the PL shown in Fig. 13(b).

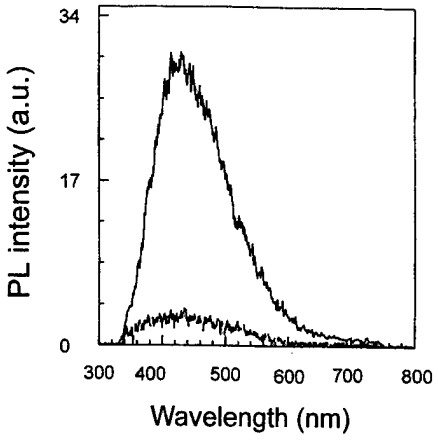


FIG. 14. Oxidized grating PL (shown in Fig. 12) variation following high temperature annealing (dotted line) and subsequent boiling water treatment (solid line).

Figure 15(a) shows that high temperature N_2 annealing quenches the 380 nm peak, while promoting growth of a broad PL peaking ~500 nm with almost comparable intensity. Figure 15(b) shows that boiling water treatment of the same sample, subsequent to the N_2 anneal, does not produce any further changes in the PL.

C. PL measurements from nonoxidized gratings

We have also carried out detailed PL measurements of Si gratings that were fabricated with KOH etching and were not deliberately oxidized. For these nonoxidized gratings, the processing steps are all low temperature, therefore, some residual photoresist particles may be trapped on the surface even though the photoresist is stripped before KOH etching and is also attacked by the KOH solution. For an understanding of photoresist PL response, we carried out detailed PL

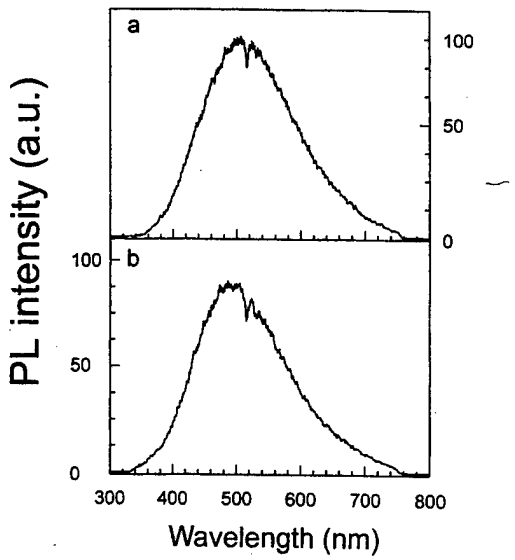


FIG. 15. Another example of PL variation of thermally oxidized gratings [shown in Fig. 13(b)] following high temperature annealing (dotted line) and subsequent boiling water treatment (solid line).

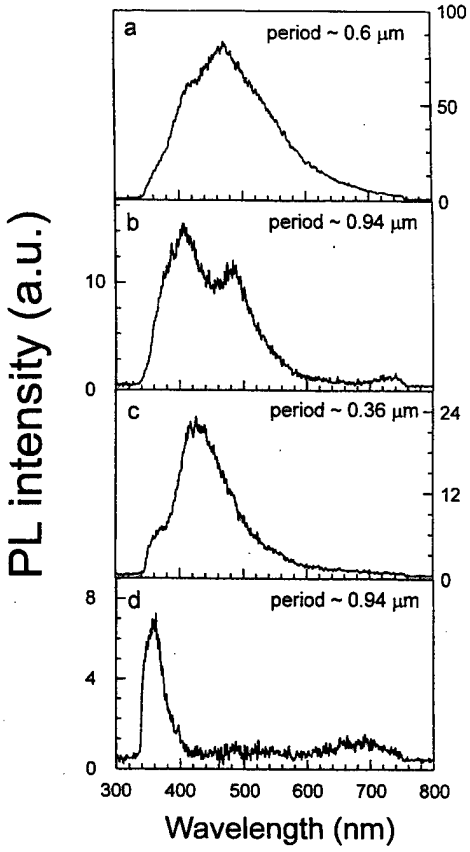


FIG. 16. Measurements of photoluminescence from KOH-etched grating structures with nominal wall widths ~10 nm: (a) period 0.6 μm, (b) period 0.9 μm, (c) period 0.36 μm, and (d) period 0.9 μm.

measurements of developed photoresist films. At 257 nm excitation, photoresist PL response was broad with features at 660, 580, 520, and 480 nm. The overall photoresist PL response did not show any similarity to the PL from Si grating structures.

Figure 16 shows PL measurements from various KOH-etched grating structures, the grating periods varied from 0.2 to 0.9 μm, with nominal wall widths of ~10 nm. Our objective in presenting these measurements is to illustrate the variety of different spectral line shapes that have been observed from these nanoscale wall width gratings. The PL line shape in Fig. 16(a) is almost identical to oxidized grating PL shown earlier in Fig. 12. The PL line shapes in Fig. 16(b) and 16(c) are different from oxidized-Si grating PL, although the 400 nm peak in Fig. 16(c) is similar to the boiling water treated oxidized-Si grating PL shown in Fig. 14. The sharp line feature in Fig. 16(d) is similar to the narrow lines in Figs. 13(b) and 13(d), although significantly weaker.

We have also investigated variation of nonoxidized grating PL with annealing and boiling water treatments. The dotted line in Fig. 17 shows that high temperature annealing quenches the PL shown in Fig. 16(a) leaving a weak peak at ~400 nm. The solid line in Fig. 17 shows that the PL from the same sample following a subsequent boiling water treatment is greatly enhanced with a peak ~350 nm. Another interesting feature is the emergence of a weaker peak ~700 nm. Comparison of the PL spectra in Figs. 16(d) and 17

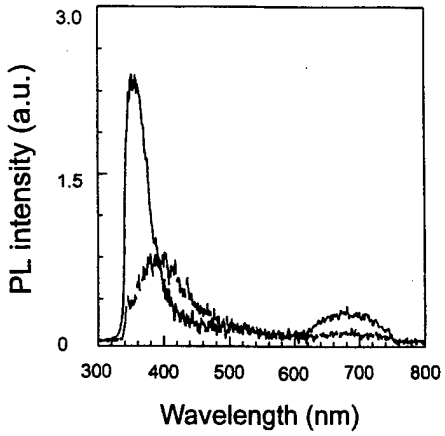


FIG. 17. Variation in PL of KOH-etched grating structures [shown in Fig. 16(a)] following high temperature annealing (dotted line) and subsequent boiling water treatment (solid line).

show that the line shapes are almost identical even though they were obtained from two different samples subjected to different processing histories. The common point being the nanoscale wall widths.

Finally, we have also investigated π-Si films including some grating structures that had been made partially porous. Figure 18 shows PL measurements from ~10 nm wall width Si gratings that had been subjected to a limited, nonuniform electrochemical treatment (ethanol-HF solution at 45 mA/cm^2 for several seconds, cf. Ref. 2) such that one end of the grating structure became completely porous, while the other end remained nonporous. SEM studies of the sample showed that the grating was largely washed out on the porous end of the sample while it remained intact at the nonporous end. The PL measurements in Figs. 18(b)–18(d) are from this sample as the excitation is translated from the completely porous to the nonporous end. For reference, PL from a π-Si sample is shown in Fig. 18(a). Notice that for this combined grating/π-Si sample, PL peaks vary from ~660 to 460 nm [Figs. 18(b) and 18(c)]. The PL peak in Fig. 18(d) is similar to the PL from other grating structures such as shown in Fig. 16(c).

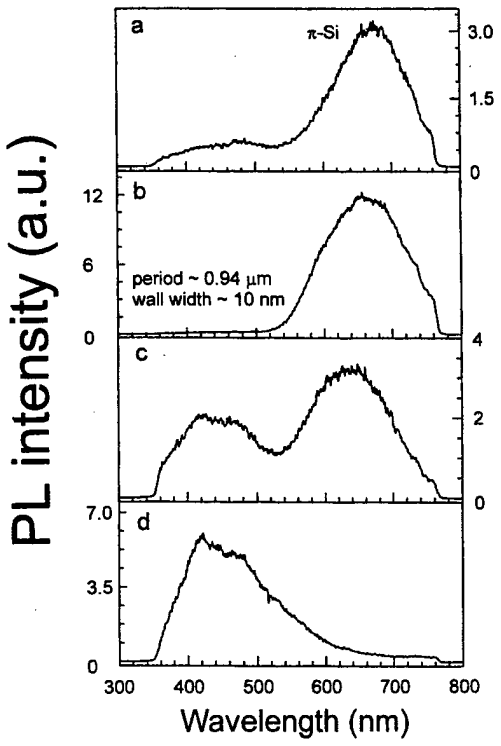


FIG. 18. PL measurements from gratings with varying degree of porosity: (a) π-Si for reference, (b) and (c) 0.9 μm period (110) Si grating structures made partially porous, and (d) same grating structure with no porosity. All measurements are from the same sample, but different locations.

In summary, we have demonstrated similar PL line shapes from oxidized and nonoxidized grating structures. The PL in all cases degrades to background levels under UV photoexcitation on millisecond time scales.

V. DISCUSSION

We report interferometric lithography, etching, and oxidation techniques that together provide a versatile manufacturing sequence for the formation of nanoscale crystalline Si structures as verified by Raman scattering and SEM measurements. Raman scattering measurements show distinct size effects including large enhancements, asymmetric line shapes, and splitting of the threefold degenerate bulk mode. Measurable PL signals are generally associated with structures showing this splitting of the Raman spectrum. A number of interesting PL features are demonstrated including a range of line shapes with peak wavelengths varying from ~700 to 380 nm and very different linewidths. Two notable results are the presence of narrow sharp line features at 370–380 nm, and the absence of the red emission peaks usually associated with π-Si, the lone exceptions being the weak 700 nm peaks in Figs. 16(d) and 17. We have explored the impact of surface treatments such as high temperature annealing in a N_2 atmosphere and immersion in boiling water on the PL. Under most conditions, the grating PL is significantly more intense and shows a richer variety of spectral features than that from blanket oxide films as well as a different response to the various surface treatments.

This blanket-oxide film PL clearly is not related to any Si crystal-size effects. In an extensive investigation of time-resolved PL from bulk vitreous SiO_2 (suprasil-W) and amorphous thermal oxide films, Stathis and Kastner[48] reported bulk SiO_2 PL peaks at 650, 560, 460, and 290 nm. For thermal oxide films grown by dry oxidation on Si, the 560 and 460 nm bands were not observed. In addition, even in the bulk material, the 460 nm band was only observed at low temperatures. McKnight and Palik[49] reported observation of the 460 nm band following e-beam irradiation of thermally grown oxide films. Similar results were reported by Skuja *et al.*[50] following neutron irradiation of α-SiO_2 films. These results suggest that the origin of the 460 nm band is related to oxide defects. DiMaria *et al.*[51] reported strong electroluminescence peaks at 650 and 470 nm from Si-rich chemical vapor deposition SiO_2 films and proposed quantum-size effects in nanoscale α-Si islands as possibly responsible for the PL. Pliskin[52] investigated the infrared properties of SiO_2 films deposited under a variety of conditions and quantified

the SiOH and H_2O concentrations. Hartstein *et al.*[53] investigated Si-rich SiO_2 films using attenuated total reflection techniques and showed significant (10^{21} cm^{-3}) amounts of SiOH, H_2O, and SiH in as-deposited films, but no detectable H groups following 1000 °C anneal. We can, therefore, hypothesize that the thermally grown oxide films form SiOH complexes, either in the bulk or at the Si/SiO_2 interface, under exposure to air that result in the room temperature PL. High temperature annealing results in hydrogen desorption and quenching of the PL, and the process is reversed again on exposure to air. In view of the nanostructure Si results, it is significant that immersion in boiling water does not restore the PL.

Before discussing the grating PL results, it is important to note that passivation of the surface can play an equally large role in determining the photoluminescence signal strength as does the radiative matrix element associated with size effects and/or radiative centers. This is illustrated by a very simple rate equation analysis that includes both radiative (τ_r) and nonradiative (τ_{nr}) decay mechanisms for excited carriers. The result is

$$PL \propto \frac{P}{1+\tau_r/\tau_{nr}}, \tag{1}$$

where P is the excitation rate. An effect that modifies the PL spectrum or efficiency cannot be uniquely ascribed to changing either the radiative or nonradiative lifetimes.

It is instructive to review briefly some relevant features of π-Si PL. Tischler *et al.*[54] showed that simultaneous exposure to O_2 and laser illumination quenched the red emission from π-Si. Also, Robinson *et al.*[5] showed that thermal annealing of π-Si in ultrahigh vacuum (UHV) resulted in quenching of the red emission. Considering the temperature-related desorption of SiOH, H_2O and SiH_x reported by Hartstein *et al.*,[53] we can hypothesize that π-Si emission is related to $Si{:}H_x$ complexes associated with crystalline Si nanostructures. This is similar to the models of Koch *et al.*[18] and of Qin and Jia[55] in which the quantum size effect is responsible for the absorption with surface states being implicated in the emission process. This is supported by visible, wideband (up to 520 nm) optical emission from Si:H particles reported by Furukawa and Miyasato[10] from 2–5 nm diam crystalline Si particles surrounded by $=SiH_2$ groups. Dinh *et al.*[56] have reported 500–600 nm emission from 3–5 nm Si clusters exposed to ambient air for extended periods; as-grown cluster samples, formed in UHV by laser ablation of a Si target, did not show any luminescence.

Thermal annealing of the both oxide and nonoxide Si gratings results in significant reduction of the PL efficiency except for the case shown in Fig. 15. Almost complete recovery of the grating PL is found following immersion in boiling deionized water; in distinct contrast to the case of blanket-oxide films where the luminescence is not restored by immersion in boiling water following a high temperature anneal. These observations suggest that surface passivation plays a key role in efficient luminescence from Si nanostructures. For the KOH etched gratings, our surfaces are almost perfect ⟨111⟩ planes; for the oxidized gratings, there is a variation in the surface planes, which are buried under ~500–1000-nm-thick oxide layers. Using Fourier transform infrared spectroscopy, Watanabe *et al.*[57] reported that boiling water treatment of freshly HF-etched ⟨111⟩ Si produces an automically smooth surface homogeneously covered with silicon monohydride (-SiH) normal to the surface and free of oxidation. The water treatment seems to react with Si di- and trihydrides to replace them from the surface leaving SiH bonds.

The blue emission reported from oxidized π-Si structures is similar to the PL measured from the Si gratings. Our results again suggest that both nanostructured Si and Si–H bonds play a role in the PL. The sharp spectral feature at ~370–380 nm [Figs. 13(b) and 13(d)] shows significant similarities to the 340 nm σ–σ^* excitonic emission of linear Si polymer chains.[46]

In summary, we report a number of optical characteristics of nanoscale, one-dimensional Si grating structures as wall widths are reduced from ~100 to ~10 nm. The techniques used to form these structures are simple, inexpensive, and adaptable to large-scale microelectronics manufacturing. These structures with enhanced surface areas may play an important role in future development of high efficiency solar cells, field-emission devices, and Si light emitters. A more detailed understanding of PL mechanisms will emerge by continuation of this work in fabrication and electrical excitation of 1D and 2D structures. PL lifetime measurements will provide additional information about the nature of the recombination processes. The important role of Si–H bonds can be investigated by controlled hydrogen (H, H_2) diffusion processes. Finally, it is important to develop a theoretical framework, both for the microscopic mechanisms giving rise to the photoluminescence and for their interactions with electromagnetic fields in this periodic, nanoscale regime.

[1] L. T. Canham, Appl. Phys. Lett. **57**, 1046 (1990).
[2] C. Pickering, M. I. J. Beale, D. J. Robbins, P. J. Pearson, and R. Greef, J. Phys. C **17**, 6535 (1984).
[3] C. Pickering, M. I. J. Beale, D. J. Robbins, P. J. Pearson, and R. Greef, Thin Solid Films **125**, 157 (1985).
[4] V. Lehman and U. Gosele, Appl. Phys. Lett. **58**, 856 (1991).
[5] M. B. Robinson, A. C. Dillon, D. R. Haynes, and S. M. George, Appl. Phys. Lett. **61**, 1414 (1992).
[6] T. Van Buren, Y. Gao, T. Tiedje, J. R. Dahn, and B. M. Way, Appl. Phys. Lett. **60**, 3013 (1992).
[7] R. Tsu, H. Shen, and M. Dutta, Appl. Phys. Lett. **60**, 112 (1992).
[8] Z. Sui, P. P. Leong, I. P. Herman, G. S. Higashi, and H. Temkin, Appl. Phys. Lett. **60**, 2086 (1992).
[9] V. Petrova-Koch, T. Muschik, A. Kux, B. K. Meyer, F. Koch, and V. Lehman, Appl. Phys. Lett. **61**, 943 (1992).
[10] S. Furukawa and T. Miyasato, Jpn. J. Appl. Phys. 1 **27**, L2207 (1988).
[11] H. Takagi, H. Ogawa, Y. Y. Yamazaki, A. Ishizaki, and T. Nakagiri, Appl. Phys. Lett. **56**, 2379 (1990).
[12] S. Furukawa and T. Miyasato, Phys. Rev. B **38**, 5726 (1988).
[13] Y. Kanemitsu, T. Ogawa, K. Shiraishi, and K. Takeda, Phys. Rev. B **48**, 4883 (1993).
[14] Z. Y. Xu, M. Gal, and M. Gross, Appl. Phys. Lett. **60**, 1375 (1992).
[15] M. S. Brandt, H. D. Fuchs, M. Stutzmann, J. Weber, and M. Cardona, Solid State Commun. **81**, 307 (1992).
[16] A. Roy, A. Chaimani, D. D. Sarma, and A. K. Sood, Appl. Phys. Lett. **61**, 1655 (1992).
[17] T. George, M. S. Anderson, W. T. Pike, T. L. Lin, R. W. Fathuer, K. H. Jung, and D. L. Kwong, Appl. Phys. Lett. **60**, 2359 (1992).
[18] F. Koch, V. Petrova-Koch, and T. Muschik, J. Lumin. **57**, 271 (1993).
[19] D. I. Kovalev, I. D. Yaroshetzki, T. Muschik, V. Petrova-Koch, and F. Koch, Appl. Phys. Lett. **64**, 214 (1994).

[20] S. M. Prokes, Appl. Phys. Lett. **62**, 3244 (1994).
[21] L. Tysbeskov, Ju. V. Vandyshev, and P. M. Fauchet, Phys. Rev. B **49**, 7821 (1994).
[22] A. Kux, D. Kovalev, and F. Koch, Appl. Phys. Lett. **66**, 49 (1995).
[23] D. J. Lockwood, Solid State Commun. **92**, 101 (1994).
[24] H. Liu, D. K. Biegelsen, N. M. Johnson, F. A. Ponce, and R. F. W. Pease, J. Vac. Sci. Technol. B **11**, 2352 (1993).
[25] P. B. Fischer, K. Dai, E. Chen, and S. Y. Chou, J. Vac. Sci. Technol. B **11**, 2524 (1993).
[26] Saleem H. Zaidi and S. R. J. Brueck, Appl. Opt. **27**, 2999 (1988).
[27] Saleem H. Zaidi and S. R. J. Brueck, J. Vac. Sci. Technol. B **11**, 658 (1993).
[28] D. L. Kendall, J. Vac. Sci. Technol. A **8**, 3598 (1990).
[29] An-Shyang Chu, Saleem H. Zaidi, and S. R. J. Brueck, Appl. Phys. Lett. **63**, 905 (1993).
[30] Dah-Bin Kao, J. P. McVittie, W. P. Nix, and K. C. Saraswat IEEE Trans. Electron Devices **ED-34**, 1008 (1987); *ibid.* **ED-35**, 25 (1988).
[31] H. I. Liu, D. K. Biegelsen, F. A. Ponce, N. M. Johnson, and R. F. W. Pease, Appl. Phys. Lett. **64**, 1383 (1994).
[32] Saleem H. Zaidi, An-Shyang Chu, and S. R. J. Brueck, Proc. ASES **93**, 1 (1993).
[33] S. R. Goodes, T. E. Jenkins, M. I. J. Beale, J. D. Benjamin, and C. Pickering, Semicond. Sci. Technol. **3**, 483 (1987).
[34] T. Kanata, H. Murai, and K. K. Kubota, J. Appl. Phys. **61**, 969 (1987).
[35] T. Okada, T. Iwaki, Y. Yamamoto, H. Kasahara, and K. Abe, Solid State Commun. **49**, 809 (1984).
[36] N. Ohtani and K. Kanamura, Solid State Commun. **75**, 711 (1990).
[37] Z. Iqbal and S. Veprek, J. Phys. C **15**, 377 (1982).
[38] J. F. Morhange, G. Kanellis, and M. Balkanski, Solid State Commun. **31**, 805 (1979).
[39] M. Moskovits, Rev. Mod. Phys. **57**, 783 (1985).
[40] D. L. Murphy and S. R. J. Brueck, Opt. Lett. **8**, 494 (1983).
[41] H. Chew and D.-S. Wang, Phys. Rev. Lett. **49**, 490 (1982).
[42] E. Anastassakis, A. Pinczuk, E. Burstein, F. H. Pollak, and M. Cardona, Solid State Commun. **8**, 133 (1970).
[43] M. Cardona and G. Guntherodt, in *Light Scattering in Solids* (Springer, Berlin, 1980), Vol. II, p. 80.
[44] H. Richter, Z. P. Wang, and L. Ley, Solid State Commun. **39**, 625 (1981).
[45] G. Kanellis, J. F. Morhange, and M. Balkanski, Phys. Rev. B **21**, 1543 (1980).
[46] W. L. Wilson and T. W. Weidman, J. Phys. Chem. **95**, 4568 (1991).
[47] Y. Kanemitsu, K. Suzuki, Y. Nakayoshi, and Y. Masumoto, Phys. Rev. B **46**, 3916 (1992).
[48] J. H. Stathis and M. A. Kastner, Phys. Rev. B **35**, 2972 (1987).
[49] S. W. McKnight and E. D. Palik, J. Non-Cryst. Solids **40**, 595 (1980).
[50] L. N. Skuja, A. N. Streletsky, and A. B. Pakovich, Solid State Commun. **50**, 1069 (1984).
[51] D. J. DiMaria, J. R. Kirtley, E. J. Pakulis, D. W. Dong, T. S. Kuan, F. L. Pesavento, T. N. Theis, J. A. Cutro, and S. D. Brorson, J. Appl. Phys. **56**, 401 (1984).
[52] W. A. Pliskin, J. Vac. Sci. Technol. **14**, 1064 (1977).
[53] A. Hartstein, D. J. DiMaria, D. W. Dong, and J. A. Kucza, J. Appl. Phys. **51**, 3860 (1980).
[54] M. A. Tischler, R. T. Collins, J. H. Stathis, and J. C. Tsang, Appl. Phys. Lett. **60**, 639 (1992).
[55] G. G. Qin and Y. Q. Jia, Solid State Commun. **86**, 559 (1993).
[56] L. N. Dinh, L. L. Chase, M. Balooch, L. J. Terminello, and F. Wooten, Appl. Phys. Lett. **65**, 3111 (1994).
[57] S. Watanabe, N. Nakayama, and T. Ito, Appl. Phys. Lett. **59**, 1458 (1991).

Observation of spontaneous emission microcavity effects in an external-cavity surface-emitting laser structure

J. V. Sandusky[a),c)] and S. R. J. Brueck[a),b)]
Center for High Technology Materials, University of New Mexico, Albuquerque, New Mexico 87131

(Received 13 September 1996; accepted for publication 21 October 1996)

We report both enhancement and inhibition of spectrally integrated, cavity-normal room temperature spontaneous emission (SpE) in an external-microcavity surface-emitting laser as the cavity length is varied. The use of an external cavity permits changes in resonator length without altering the semiconductor properties. Measurements of the SpE radiation pattern and spectrum under conditions of enhancement and inhibition are compared to the macrocavity continuum limit. A transition of continuum behavior occurs as the cavity length is increased beyond the spontaneous emission coherence length. © *1996 American Institute of Physics.* [S0003-6951(96)03052-5]

The vertical-cavity surface-emitting laser (VCSEL) is both a natural tool for the investigation of microcavity physics and a technologically important device.[1,2] Recent experiments and modeling have shown that microcavity physics plays an important role in establishing the VCSEL lasing threshold[3,4] and linewidth.[5] A microcavity resonator can considerably increase the efficiency of light emitting diodes (LEDs).[6] Most recently, the microcavity has been used to produce Fock number states of the electromagnetic field.[7] The reduction of VCSEL lasing threshold and the increase in LED efficiency are primarily driven by the reduced photon density of states inherent in short cavities, which directs more of the spontaneous emission (SpE) onto the optical axis.[8] Most experiments[9,10] investigating VCSEL microcavity SpE have relied on differing growth conditions to affect changes in cavity length. This technique is inevitably subject to potential sample-to-sample material variations. In this work, we overcome that limitation by introducing an external mirror which allows the resonator length to be changed without any impact on material properties. Further, much larger changes in cavity length can be achieved in an external-cavity configuration, allowing us to observe the microcavity to macrocavity transition.

The typical VCSEL high reflectivity (HR) top mirror is replaced in these experiments by an epitaxially grown anti-reflection (AR) coating which minimizes coupled-cavity effects. The active region consists of a 30-QW resonant-periodic-gain (RPG)[11] section with the spacing between quantum wells ($\sim\lambda/2n$) chosen to account for QW-barrier reflections.[12] The back mirror is a 30 pair $Al_{0.30}Ga_{0.70}As$/AlAs high reflector ($R\sim99.8\%$) and the external cavity is completed by a planar dielectric mirror ($R\sim99.8\%$). The HR and AR coatings have a center wavelength of ~835 nm and a bandwidth of ~50 nm. The epitaxial structure of the device is shown in Fig. 1. The average thickness of the layers was determined by high resolution x-ray diffraction. Photoluminescence from the HR and AR regions was used to determine the Al composition.[13] None of the layers were intentionally doped.

The microcavity is a plano–plano Fabry–Perot resonator whose end mirrors are the epitaxial HR and the external mirror. The first experimental step is to remove the GaAs substrate so that the quantum wells can be excited from the HR side of the cavity. This avoids possible artifacts from variations in the amount of pump absorbed with cavity length due to Fabry–Perot resonances, since the AR coating is not designed for the pump wavelength. Since ~99% of the pump beam is absorbed in a single pass, reflection of the pump beam by the external mirror after a first pass does not appreciably change the amount of absorbed pump power. Removal of the GaAs substrate was accomplished using a 6.6:1 volume ratio citric acid:hydrogen peroxide etchant.[14] The epitaxy was then bonded to a high thermal conductivity sapphire submount using UV-curing optical adhesive.

Excitation of both the QW and spacer regions is provided by the beam from a cw ring-dye laser operating at 716 nm with 10 mW focused by a 27-cm focal length lens. The resulting pump power density is at least 30 dB below the

$Al_{0.30}Ga_{0.70}As$	123.8 nm		AR
AlAs	65.7 nm		
$Al_{0.30}Ga_{0.70}As$	61.9 nm	4X	
AlAs	65.7 nm		
$Al_{0.23}Ga_{0.77}As$	121.7 nm		Gain
GaAs	10.0 nm		
$Al_{0.23}Ga_{0.77}As$	115.9 nm	29X	
GaAs	10.0 nm		
$Al_{0.23}Ga_{0.77}As$	121.7 nm		
AlAs	65.7 nm		HR
$Al_{0.30}Ga_{0.70}As$	61.9 nm	30X	
AlAs	65.7 nm		
GaAs	Substrate		

FIG. 1. Epitaxial growth stack for the external cavity surface-emitting laser showing the antireflection coat (top section), gain region (middle section), and high reflector (bottom section).

[a)]Also Department of Physics and Astronomy.
[b)]Also Department of Electrical and Computer Engineering.
[c)]Electronic mail: sandusky@unm.edu

 0003-6951/96/69(26)/3993/3/$10.00 © 1996 American Institute of Physics

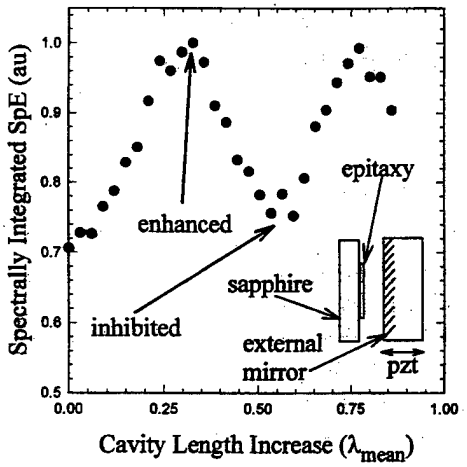


FIG. 2. The variation of the on-axis, spectrally integrated SpE as a function of increasing cavity length. Points of enhanced and inhibited SpE are marked. The total cavity length is ~22 μm with about 16 μm (optical length) within the epitaxial layers.

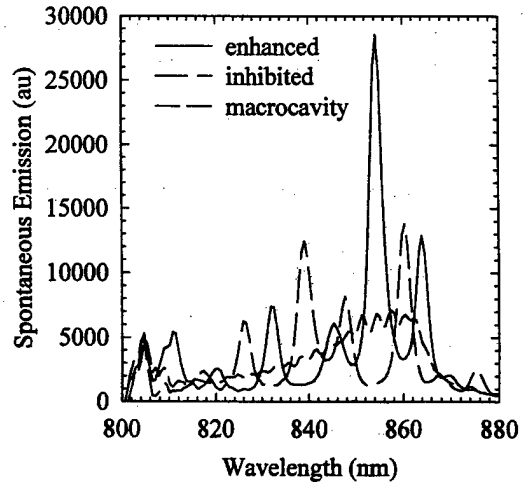


FIG. 3. On-axis SpE spectra for the points of enhanced (solid) and inhibited (dashed) SpE marked in Fig. 4. Dotted line is the spectrum in the macrocavity limit.

lasing threshold of 120 mW focused to a 15 μm $1/e^2$ beam waist radius. We thus neglect the role of stimulated emission.

An optical multichannel analyzer (OMA) is used to measure the SpE spectrum along the optical axis. The OMA has a resolution of 2.5-nm full width at half-maximum (FWHM) and its spectral response has been normalized against a blackbody radiator. A PIN photodiode rotating on the arc of a circle centered on the optical axis measures the spectrally integrated SpE radiation pattern with a resolution of ~2°. Both color-glass and dielectric filters are used to prevent any leakage of pump radiation into the detection system. We estimate at most a 5% error in the angular measurements from the spectral dependence of these filters.

Figure 2 shows successive enhancement and suppression of the cavity-normal spectrally integrated SpE as the cavity length is varied through ~0.75 λ_{mean}, where $\lambda_{mean} \approx 844$ nm is the mean SpE wavelength. The variation of the on-axis spectrally integrated SpE with cavity length is 25%. The total cavity length for this configuration, calculated from the longitudinal mode spacing, is ~22 μm, with ~16 μm internal to the epitaxy. All lengths are given in terms of optical (rather than physical) path.

Figure 3 compares the SpE spectrum under the conditions of enhancement and inhibition indicated in Fig. 2. Note that under the enhancement condition, the peaks to the left of the central peak alternate in relative intensity, probably resulting from the RPG longitudinal mode selectivity which couples strongly only to even or only to odd numbered modes.

Azimuthal SpE radiation patterns are shown in Fig. 4. The circles are from a cavity longer than 100 μm and represent the macrocavity limit. The squares are from a short cavity (~20 μm) under enhancement conditions. Note that the angular spread is much narrower than for the macrocavity. The triangles are from a short cavity under inhibition conditions. The inverse phase relationship between the enhanced and inhibited curves evident at 18° is maintained at least to 40°.

To observe the transition to continuum behavior, we use the photodiode to measure the enhanced and inhibited, spectrally integrated, wafer-normal SpE intensity for total cavity lengths up to ~55 μm as shown in Fig. 5. A total cavity length ~21 μm is the shortest which could be achieved within experimental constraints. Note that, as expected,[3] relatively little modulation is observed for cavity lengths exceeding the 37-μm SpE coherence length defined by λ_{mean}^2/σ, where σ is the rms spectral width of the SpE in the macrocavity limit.

Björk recently reported a method for estimating the change in total (spectrally and angularly integrated) SpE with cavity length.[15] The method involves finding the SpE rate for each angular mode of the cavity and then summing the contribution from each mode. The quantum wells are approximated by perfect dipoles and the angular integration is performed in the limit of unit reflectivity mirrors. Extending Björk's model to include asymmetric and RPG resonator designs, we find that for the relatively long cavity lengths (compared to λ_{mean}) used in these experiments there should be less than a 1% variation in total cavity SpE with cavity

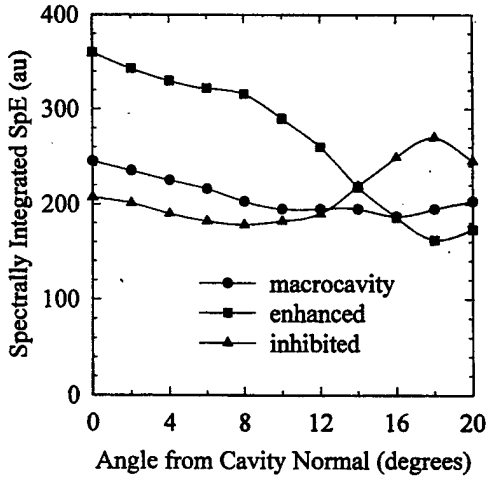


FIG. 4. SpE azimuthal radiation patterns under conditions of enhancement (squares), inhibition (triangles), and in the macrocavity limit (circles). The lines are fits to the data to provide a guide to the eye.

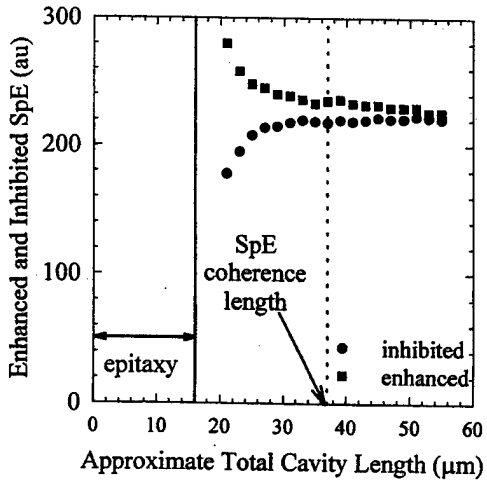


FIG. 5. Magnitude of the enhanced (squares) and inhibited (circles) on-axis, spectrally integrated SpE as a function of cavity length. The SpE coherence length is ~37 μm and the optical thickness within the epitaxy is ~16 μm.

length. Thus, the observed narrowing of the radiation pattern is primarily responsible for changes in the wafer-normal SpE intensity.

In summary, we have measured microcavity induced narrowing of the SpE radiation pattern leading to modulation of the spectrally integrated wafer-normal SpE in an external-cavity surface-emitting laser. We have observed the transition to continuum behavior as the cavity length is increased beyond the SpE coherence length. Future experiments will attempt to measure the reduction in the lasing threshold due to the increased on-axis SpE intensity.

The authors would like to thank S. Sun and S. D. Hersee for growing the wafer used in these experiments, and Jeff Ramer for measuring the x-ray diffraction spectra. Partial support for this work was provided by the Air Force Office of Scientific Research.

[1] K. Tai, G. Hasnain, J. D. Wynn, R. J. Fischer, Y. H. Wang, B. Weir, J. Gamelin, and A. Y. Cho, Electron. Lett. **26**, 1628 (1990).
[2] A. E. Willner, C. J. Chang-Hasnain, and J. E. Leight, IEEE Photonics Technol. Lett. **5**, 838 (1993).
[3] D. G. Deppe, Appl. Phys. Lett. **57**, 1721 (1990).
[4] C. Lei and D. G. Deppe, J. Appl. Phys. **71**, 2530 (1992).
[5] G. P. Agrawal and G. R. Gray, Appl. Phys. Lett. **59**, 399 (1991).
[6] H. De Neve, J. Blondelle, R. Baets, P. Demeester, P. Van Daele, and G. Borgs, IEEE Photonics Technol. Lett. **7**, 287 (1995).
[7] F. De Martini, G. Di Giuseppe, and M. Marrocco, Phys. Rev. Lett. **76**, 900 (1996).
[8] H. Yokoyama, K. Nishi, T. Anan, Y. Nambu, S. D. Brorson, E. P. Ippen, and M. Suzuki, Opt. Quantum Electron. **24**, S245 (1992).
[9] T. J. Rogers, D. G. Deppe, and B. G. Streetman, Appl. Phys. Lett. **57**, 1858 (1990).
[10] T. Yamauchi, Y. Arakawa, and M. Nishioka, Appl. Phys. Lett. **58**, 2339 (1991).
[11] M. Y. A. Raja, S. R. J. Brueck, M. Osinski, C. F. Schaus, J. G. McInerney, T. M. Brennan, and B. E. Hammons, IEEE J. Quantum Electron. **QE-25**, 1500 (1989).
[12] J. V. Sandusky and S. R. J. Brueck, Proc. SPIE **2532**, 48 (1995).
[13] S. Adachi, J. Appl. Phys. **58**, R1 (1985).
[14] M. Otsubo, T. Oda, H. Kumabe, and H. Miki, J. Electrochem. Soc. **123**, 676 (1976).
[15] G. Björk, IEEE J. Quantum Electron. **QE-30**, 2314 (1994).

Reprinted from

OPTICS COMMUNICATIONS

Optics Communications 135 (1997) 264–268

Photoluminescence of manufactured 1-D crystalline Si gratings

Saleem H. Zaidi [1], S.R.J. Brueck [2]

Center for High Technology Materials, University of New Mexico, Albuquerque, NM 87131, USA

Received 20 August 1996; accepted 16 October 1996



ELSEVIER

FOUNDING EDITOR

F. Abelès

EDITORS

J.C. Dainty
Blackett Laboratory, Imperial College
London SW7 2BZ, UK

Phone: +44-171-594-7748
FAX: +44-171-594-7714
Email: OPTCOMM@IC.AC.UK

L.M. Narducci
Physics Department, Drexel University,
Philadelphia, PA 19104, USA

Phone: +1-215-895-2711
FAX: +1-215-895-6757
+1-215-895-4999
Email: LORENZO@WOTAN.PHYSICS.
DREXEL.EDU

W.P. Schleich
Abteilung für Quantenphysik, Universität Ulm
D-89069 Ulm, Germany

Phone: +49-731-502-2510
FAX: +49-731-502-2511
Email: OPTCOM@PHYSIK.UNI-ULM.DE

ADVISORY EDITORIAL BOARD

Australia
R.C. McPhedran, Sydney
C.J.R. Sheppard, Sydney
A.W. Snyder, Canberra
W.H. Steel, Seaforth, NSW

Brazil
L. Davidovich, Rio de Janeiro

Canada
J. Chrostowski, Ottawa
R. Vallee, Sainte-Foy

China
Jin Yue Gao, Changchun

Finland
A.T. Friberg, Espoo
S. Stenholm, Helsinki

France
J.L. Bobin, Paris
P. Chavel, Orsay
C. Flytzanis, Palaiseau
G. Grynberg, Paris
J.P. Huignard, Orsay
T. Lopez-Rios, Grenoble
J. Margerie, Caen
M. May, Paris
D.B. Ostrowsky, Nice

Germany
O. Bryngdahl, Essen
T.W. Hänsch, Munich
G. Huber, Hamburg
J. Jahns, Hagen
A. Laubereau, Munich
R. Ulrich, Hamburg
H. Walther, Garching
B. Wilhelmi, Jena

Hong Kong
Shi Yao Zhu, Kowloon

India
G.S. Agarwal, Hyderabad

Israel
E. Marom, Tel-Aviv

Italy
M. Allegrini, Messina
F.T. Arecchi, Florence
M. Inguscio, Florence
A. Renieri, Rome

Japan
T. Asakura, Sapporo
S. Kawakami, Sendai

Lithuania
A.P. Piskarskas

New Zealand
D.F. Walls, Auckland

Poland
A. Kujawski, Warsaw

The Netherlands
Q.H.F. Vrehen, Leiden
J.P. Woerdman, Leiden

United Kingdom
W.J. Firth, Glasgow
R. Loudon, Colchester
G.H.C. New, London
W. Sibbett, St. Andrews
B. Wherrett, Edinburgh

Russia
Y.I. Khanin, Nizhny-Novgorod
N.I. Koroteev, Moscow
V.S. Letokhov, Moscow
B.Ya. Zel'dovich, Chelyabinsk

Spain
M. Nieto-Vesperinas, Madrid

Switzerland
R. Thalmann, Wabern
H.P. Weber, Bern

USA
N.B. Abraham, Bryn Mawr, PA
D.Z. Anderson, Boulder, CO
H.J. Carmichael, Eugene, OR
M. Cronin-Golomb, Medford, MA
J.C. de Paula, Haverford, PA
J.W. Goodman, Stanford, CA
R.M. Hochstrasser, Philadelphia, PA
E.P. Ippen, Cambridge, MA
J.S. Krasinski, Stillwater, OK
N. Lawandy, Providence, RI
D. Marcuse, Holmdel, NJ
D. Psaltis, Pasadena, CA
G.I. Stegeman, Orlando, FL
E. Wolf, Rochester, NY

Aims and Scope
Optics Communications ensures the rapid publication of contributions in the field of optics and interaction of light with matter.

Abstracted/indexed in:
Chemical Abstracts; Current Contents: Engineering, Computing and Technology; Current Contents: Physical, Chemical & Earth Sciences; EI Compendex Plus; Engineering Index; INSPEC.

Subscription Information 1997
Volumes 133–144 (72 issues) of Optics Communications (ISSN 0030-4018) are scheduled for publication.
Prices are available from the publisher upon request. Subscriptions are accepted on a prepaid basis only. Issues are sent by SAL (Surface Air Lifted) mail wherever this service is available. Please address all enquiries regarding orders and subscriptions to:

Elsevier Science B.V.
Order Fulfilment Department
P.O. Box 211, 1000 AE Amsterdam
The Netherlands
Tel. +31 20 4853642, Fax: +31 20 4853598

Claims for issues not received should be made within six months of publication (mailing) date.

Advertising Offices
International: Elsevier Science, Advertising Department, The Boulevard, Langford Lane, Kidlington, Oxford, OX5 1GB, UK; Tel: +44 (0) 1865 843565; Fax: +44 (0)1865 843976
USA and Canada: Weston Media Associates, Dan Lipner, P.O. Box 1110, Greens Farms, CT 06436-1110, USA; Tel: +1 (203) 261 2500; Fax: (203) 261 0101
Japan: Elsevier Science Japan, Marketing Services, 1-9-15 Higashi-Azabu, Minato-ku, Tokyo 106, Japan; Tel: +81 3 5561 5033; Fax: +81 3 5561

US mailing notice – Optics Communications (ISSN 0030-4018) is published semi-monthly by Elsevier Science NL (P.O. Box 211, 1000 AE Amsterdam, Netherlands). Annual subscription price in the USA is US$ 3704 (valid in North, Central and South America only), including air speed delivery. Periodicals postage paid at Jamaica, NY 11431.
USA Postmasters: Send changes to Optics Communications, Publications Expediting, Inc., 200 Meacham Avenue, Elmont, NY 11003. Airfreight and mailing in the USA by Publications Expediting Inc., 200 Meacham Avenue, Elmont, NY 11003.

The paper used in this publication meets the requirements of ANSI/NISO Z39.48-1992 (Permanence of Paper). Printed in the Netherlands

North-Holland, an imprint of Elsevier Science

ELSEVIER

15 February 1997

ELSEVIER

Optics Communications 135 (1997) 264–268

OPTICS COMMUNICATIONS

Photoluminescence of manufactured 1-D crystalline Si gratings

Saleem H. Zaidi [1], S.R.J. Brueck [2]

Center for High Technology Materials, University of New Mexico, Albuquerque, NM 87131, USA

Received 20 August 1996; accepted 16 October 1996

Abstract

An innovative fabrication process for forming 1-D, nanoscale linewidth grating and wire structures in (100) Si is reported. Scanning electron microscope and Raman scattering measurements demonstrate crystalline structures with widths as small as ~ 1.5 nm. For structures $\lesssim$ 10 nm, room temperature photoluminescence measurements (257 nm excitation) show spectral peaks ~ 380–500 nm. In contrast to the Raman scattering results, which show a definite correlation with structure widths, the PL spectra are relatively invariant as structure widths are reduced below 10 nm.

Keywords: Raman scattering; Si quantum size effects; Room temperature Si photoluminescence

Nanoscale crystalline semiconductors with physical sizes $\lesssim$ 10 nm show distinct changes in physical properties [1] arising from quantum-size effects. As a result of the inherently large surface-volume ratios, the observed electronic properties are also driven in part by surface physics and local bonding chemistry. Since Canham [2] first attributed visible room temperature photoluminescence (PL) from porous Si (π-Si) to quantum confinement, a number of first-principles calculations predicting an increase in the bandgap for Si crystal sizes $\lesssim$ 5 nm have been reported [3–8]. Extensive experimental work [9–11] has been carried out with the aim of understanding the physical mechanisms responsible for the visible PL from π-Si. Modeling efforts have focused on quantum-confinement, Si:H_x complexes, and surface-state mechanisms. A fully satisfactory picture has yet to emerge. Part of the problem lies in the complexity [12] of the 3-D structure of π-Si formed by conventional anodization that makes it difficult to controllably isolate surface from crystal-size effects. A fabrication approach based on lithography combined with standard semiconductor processing techniques is better suited to establish the size dependence of the optical response. This fabrication approach must be able to consistently reproduce patterns at $\lesssim$ 10 nm scale, which is well beyond the limits of conventional imaging optical lithography. Serial electron-beam lithography has better resolution, down to about 100 nm; however, it is slow and difficult to control to produce large areas of uniform structures. Liu et al. [13] and Fischer et al. [14] have applied e-beam lithography to fabricate 2-D Si post structures for characterization of band gap variations. Fischer et al. reported [14] weak luminescence ~ 750 nm that they attributed to ~ 20-nm diameter posts. Very recently, Nassiopoulos et al. have reported [15] on the fabrication and photoluminescence properties of Si nanostructures fabricated by deep-UV lithography coupled with reactive-ion etching. We present a novel fabrication sequence combining interferometric lithography, anisotropic wet-chemical etching, and three-dimensional oxidation which provides, for the first time, a capability of forming < 10 nm Si structures over large areas with low damage and well-controlled physical structures and surface chemistries. Optical characterization of these structures shows a continuous evolution of the phonon Raman lineshapes as the structure dimensions are reduced as well as the onset of visible photoluminescence (~ 500 nm) for structure dimensions below ~ 10 nm.

Interferometric lithography provides a simple and inexpensive alternative for the fabrication of large areas of

[1] E-mail: saleem@chtm.eece.unm.edu.

[2] Also at Department of Electrical and Computer Engineering and Physics and Astronomy.

0030-4018/97/$17.00 Copyright © 1997 Elsevier Science B.V. All rights reserved.
PII S0030-4018(96)00644-X

nanoscale linewidth structures [16]. The scale of these structures can be reduced, while at the same time improving the dimensional uniformity, by combinations of Si anisotropic etching [17] and thermal oxidation [18]. One-dimensional grating structures are first formed in positive photoresist and a lift-off process is used to form a Cr pattern that serves as an etch mask for subsequent reactive ion etching (RIE) in a CCl_2F_2 plasma (rf power ~ 150 W, pressure ~ 70 mTorr). Fig. 1a shows a scanning electron microscope (SEM) image of a 2.0-μm period (linewidth ~ 0.9 μm, depth ~ 0.9 μm) grating etched into Si. The Cr etch mask in Fig. 1a was aligned along a [100] direction to expose ⟨011⟩ planes in the approximately vertical sidewalls. Fig. 1b shows a SEM image of the grating (Fig. 1a) following ~ 20-minutes of room temperature etching in a 40% KOH solution. For (100) Si, with the etch mask aligned along a [110] direction, wet-chemical etching produces [17] V-shaped grooves formed by intersecting ⟨111⟩ planes. In the present geometry, a more complex three-dimensional profile is formed. Three significant features are: (a) ~ 100-nm linewidths in the middle of each grating line, (b) limiting higher order, low etching rate planes at the top and bottom of grating lines, and (c) inhomogeneous steps on the sidewalls due to other low etch directions revealed by the imperfections in the RIE process. To reduce the linewidths in the narrow necking regions in the middle of these structures to quantum dimensions, controlled thermal oxidation processes [18] were carried out

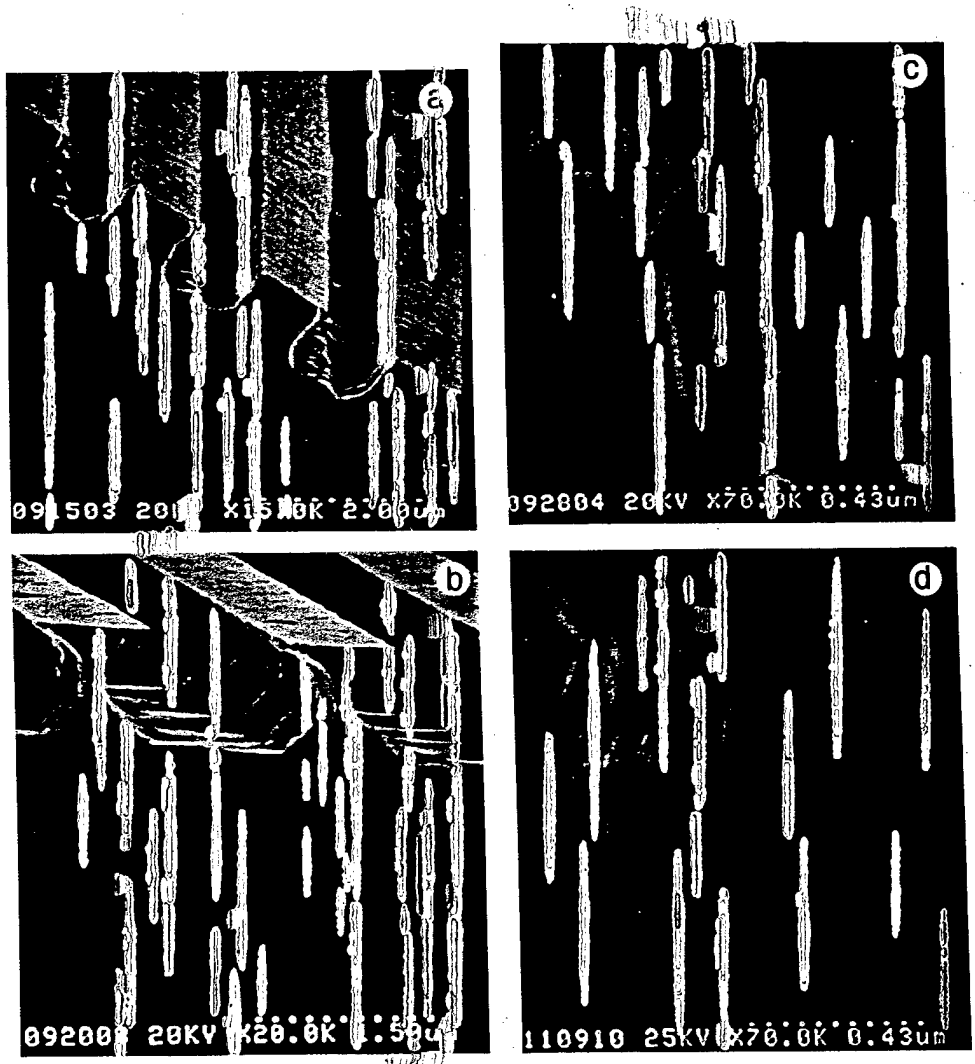


Fig. 1. Sequence of SEMs illustrating nanostructure fabrication. (a) Rectangular grating (period 2 μm, linewidth 0.9 μm, depth 0.9 μm formed in (100) Si by combination of interferometric lithography, Cr lift off to form a hard etch mask, and anisotropic RIE (CCl_2F_2 @ mTorr); (b) undercut profiles following ~ 20 min wet etch in 40% KOH; (c) ~ 50 nm minimum linewidth Si structure following oxida (1000°C in O_2 atmosphere at ~ 3 sccm); and (d) ~ 5 nm minimum linewidth structure (smallest resolvable by the SEM because of e-b induced oxidation).

The Si dry oxidation was carried out in an O_2 atmosphere (rate ~ 3 sccm) at a temperature of $\sim 1050°C$. Figs. 1c and 1d show SEM micrographs where the narrowest portions of the lines have been reduced to 20 and to ~ 5 nm. Notice that the sidewall step-size variations have been smoothed by the oxidation. Also, Fig. 1d demonstrates that this fabrication process can also be used to form free-standing isolated Si wires on Si substrates by continuing the oxidation past the point where the neck is completely pinched off. SEM inspection of these structures reveals significant linewidth variations arising primarily from the inhomogeneous step-size variations on the sidewalls. For structures $\lesssim 10$ nm, SEM characterization is difficult because of a rapid, e-beam-induced oxidation of the remaining Si material. A realistic picture of these structures is one of isolated crystalline wire, or slab-like structures (thickness of ~ 1–10 nm, lengths and heights ~ 0.2–0.5 μm) embedded in thermally grown oxide films.

The optical response of these nanoscale structures has been investigated by Raman scattering (RS) and PL measurements. RS has been extensively used for the characterization of π-Si [19], spherical Si nanoscale particles in an oxide matrix [20], and laser annealed amorphous Si films [21]. These measurements all show a sharp peak at ~ 521 cm^{-1} corresponding to the bulk Si plus a broad peak extending to low frequencies attributed to crystal sizes $\lesssim 10$ nm. Backscattering RS measurements were carried out using a $40\times$ objective to focus the 488-nm laser beam onto the sample (~ 10 μm diameter spot size). Spectra were analyzed with a 3/4-m double spectrometer and a cooled GaAs photomultiplier with photo-counting electronics. Figs. 2a–d show as-measured spectra from varying samples and positions, while Figs. 2e–h show the same measurements after subtracting the RS signal measured from a non-grating region of the same sample (this bulk Raman signature is plotted in Fig. 2h). This signal subtraction is appropriate since the nanoscale structures represent only a small fraction of the sample area. The ordering of the figures is in increasing shift from the bulk Si line. Because of the nonuniformities, this does not correspond to any systematic variation of position on the sample. The sharp line feature at ~ 530 cm^{-1} is a laser plasma line that serves as an absolute frequency marker (and an indicator of the spectrometer resolution). Comparison of Figs. 2a and 2e shows that the Raman lineshape from the nanostructures is down-shifted by ~ 2 cm^{-1} from the bulk Si peak and is highly asymmetric, with an apparent low frequency shoulder. Fig. 2b shows the emergence of a second peak from this shoulder at ~ 515 cm^{-1}, the subtracted signal in Fig. 2f shows a broad (FWHM ~ 8 cm^{-1}) lineshape down-shifted by about 5 cm^{-1}. Fig. 2c shows a pronounced peak at ~ 507 cm^{-1}, and a shoulder at ~ 517 cm^{-1}. The subtracted signal in Fig. 2g reveals the presence of two peaks approximately centered at ~ 507 and 516 cm^{-1} respectively. Finally, Fig. 2d shows a broad peak at ~ 495 cm^{-1}, and a shoulder at ~ 518 cm^{-1}. The

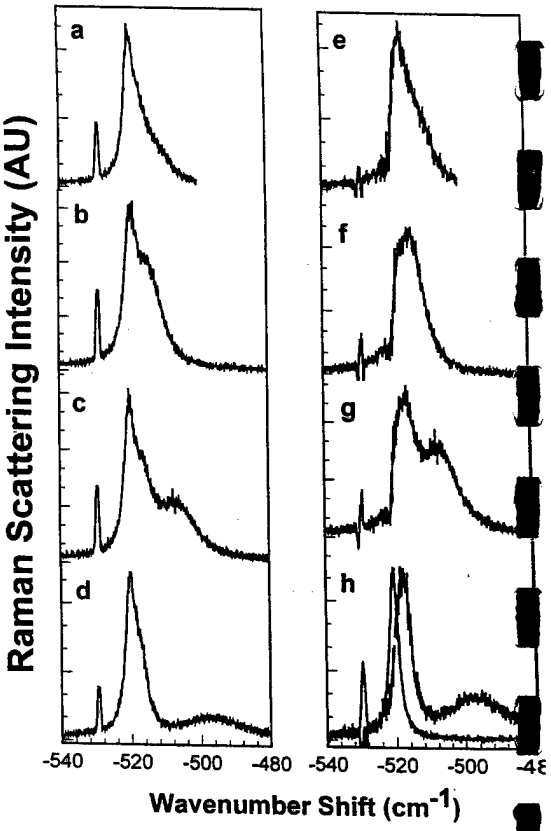


Fig. 2. LO phonon Raman lineshapes from Si nanostr (excitation wavelength 488 nm). The left column are as-meas spectra, the right column are nanostructure spectra after sub tion of the bulk Si spectrum from a non-grating region sample. Features are softening, asymmetry and splitting co with calculations of the phonon frequencies of Si slabs.

subtracted signal in Fig. 2h shows two well-defined pe a stronger peak at ~ 518 cm^{-1} with FWHM ~ 5.4 cn and weaker peak significantly broadened to ~ 13 centered at ~ 495 cm^{-1}. For comparison, the b Raman peak also shown in Fig. 2h has a FWHM $\sim$ cm^{-1}. In summary, the RS measurements in Fig. 2 der strate a continuous evolution of the bulk Raman r crystal dimensions are reduced below 10 nm. Th shape broadening can be attributed to a breakdown o momentum selection rule [22].

Room temperature PL measurements of these structures were carried out in a backscattering co tion using a $10\times$ reflective microscope objective to a 257-nm laser beam (intracavity doubled Ar-io onto the sample. Spectra were analyzed using a r optical multiple-channel analyzer system equipped v thermoelectrically-cooled, IR enhanced CCD camer measurements were carried out for two spectra 340–740 and 580–980 nm. In the visible-near I the PL signal was weak with some structure at ~ 64

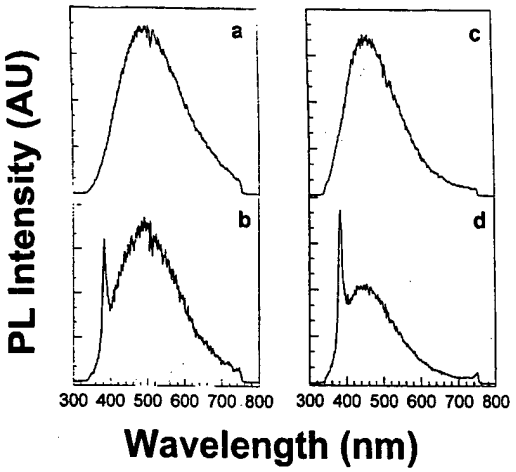


Fig. 3. Photoluminescence from Si nanostructures (257-nm excitation). Two columns are different spots of the same sample. Top spectra are immediately following fabrication (or equivalently after 1000°C N_2 anneal); bottom spectra are after long term (~ weeks) exposure to laboratory ambient. The sharp spectral feature at 380 nm is quenched by the high temperature anneal.

800 nm. The PL intensity at these spectral positions was not consistent, and exhibited a rapid degradation under the laser excitation. In the 340–740 nm spectral range, relatively strong, stable, reproducible PL was measured. Fig. 3 shows the primary features of the PL measurements from these oxidized grating structures. Figs. 3a and 3c show that the characteristic PL lineshape is broad (FWHM ~ 170–200 nm), slightly asymmetric to longer wavelengths, with peaks varying from ~ 500 nm (Fig. 3a) to ~ 460 nm (Fig. 3c) blue-shifted in comparison with π-Si PL (650–850 nm). An interesting feature of the PL is the emergence of a sharp line at ~ 380 nm (Figs. 3b and 3d) following prolonged exposure to air. These peaks are quenched following ~ 1000°C annealing in a N_2 atmosphere while the broad PL observed in Figs. 3a and 3c is unaffected by this annealing. The spectral lineshape of the 380-nm peak strongly resembles the 340-nm σ–σ^* excitonic emission observed from linear Si back-bone polymers [23]. As opposed to the RS measurements, although it is only enabled by forming $\lesssim$ 10 nm structures, the PL response does not show a strong dependence on crystal size.

The RS measurements shown in Fig. 2 are consistent with first-principles calculations reported by Kanellis et al. [24]. They calculated frequencies of the long wavelength optical modes of thin slabs of Si parallel to ⟨111⟩ planes, and predicted a splitting of the in-plane and out-of-plane modes for slab thicknesses below ~ 10 nm. Fig. 4a shows results of their calculations; both modes decrease in frequency exponentially with decreasing slab thickness. The out-of-plane mode frequencies are lower than the in-plane mode leading to a splitting of the three-fold degenerate bulk Raman mode. The broad, asymmetric Raman peaks observed in Figs. 2a–b and 2e–f appear to be a combination of two peaks that are too close to be resolved. From Fig. 4a, it is suggested that for crystal sizes ~ 8–10 nm the frequencies of both modes are split, but are too close to be resolved. Thus, the RS measurements of Figs. 2a, 2 represent crystalline dimensions of ~ 10 nm. For th frequency shifts measured in Figs. 2c and 2g, the calcu lated frequencies from Fig. 4a are in good agreement fo estimated crystal dimensions of ~ 2 nm. For a broad mod at 495 cm^{-1} (Figs. 2d and 2h), the calculated crystallin dimension is ~ 1.5 nm, and the in-plane mode would hav a frequency of ~ 512 cm^{-1} which is not in good agree ment with the observed mode at ~ 518 cm^{-1}. This dis crepancy can be attributed to nonuniform crystal sizes, an the fact that the Kanellis model was formulated for a fre surface with perfect ⟨111⟩ planes. The nanoscale crys talline structures under observation are embedded in the mally grown oxide and, in addition, have imperfect side walls. Therefore, the RS data in Fig. 2 suggest crystallin sizes in the ~ 1.5- to 10-nm range.

Most first-principles calculations of Si band gap vari tions with crystal sizes (assuming wires, dots etc.) predi an exponential increase in the bandgap as crystal sizes a reduced from 10 nm to 1 nm. Fig. 4b shows results three of these calculations. Read et al. [3] calculated th bandgap shift for wires as a function of the diameter, H et al. [7] and Wang et al. [8] reported calculations f spherical dots. All assumed hydrogen passivated surface

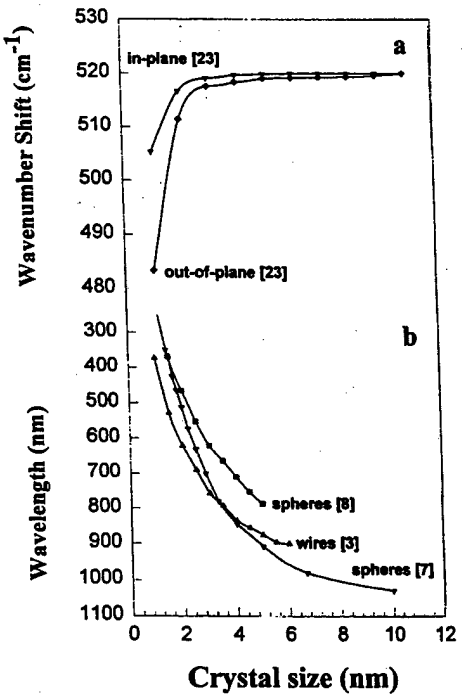


Fig. 4. First-principles calculations of the Raman and photoluminescence response of Si as a function of crystal size in 1–10 range. The Raman calculation was done for a slab, and calculations were for wires and spheres.

Wang et al. also investigated the dependence of the bandgap on shape and orientation of the quantum dots, and concluded that a unified curve exists for quantum dot spheres, cubes, and rectangular boxes. An interesting feature of these calculations is the similar variation in both Raman and PL response for crystal sizes below 10 nm. However, comparison of our RS and PL measurements shows that the systematic crystal-size related Raman response is not matched by the almost size-independent photoluminescence.

A comparison of grating PL with that from π-Si and from uniform SiO_2–Si interfaces is also pertinent. π-Si exhibits two spectral bands [25]: orange-red (850–650 nm) emission from as-prepared material, and blue-green (420–540 nm) emission from oxidized π-Si. The blue-emission has been attributed to SiO_x ($x \sim 1.4$–1.6) complexes [26]. The oxidized grating PL is similar to the blue-emission from oxidized π-Si. We have also investigated PL from thermally-grown oxide films. For some films, the measured intensity was similar to the grating PL with a peak $\sim$ 490 nm, and a significantly sharper FWHM at $\sim$ 56 nm than observed for the nanostructured material. As opposed to the grating PL where only the narrow 380-nm line was quenched, the oxide PL was completely quenched by a high temperature, N_2-atmosphere, annealing process. This suggests that grating PL origin is different than the oxide PL.

In summary, we have demonstrated a simple, innovative nanofabrication processing sequence using (100) oriented Si wafers. The fabrication techniques can be adapted to form either gratings, or free standing isolated Si wires embedded in thermally grown oxide films. Scanning electron microscope and Raman scattering measurements demonstrate crystal sizes from $\sim$ 1 to 10 nm. The Raman results show a splitting and softening of the degenerate LO phonon spectra with smaller dimensions. Room temperature PL measurements show peaks in the spectral range from 460–500 nm that are associated with dimensions of $\lesssim$ 10 nm, but, in contrast to the Raman results, are not strongly dependent on crystal size. A sharp spectral feature appearing at 380 nm is associated with long term exposure to air and associated changes in the interface chemistry. This feature is quenched by a high temperature annealing cycle, while the broader nanostructure-related features at 460–500 nm are unaffected by the same annealing cycles. These results demonstrate that both nanostructure effects and surface/interface chemical bonding have strong impacts on the Si photoluminescence behavior.

Partial support for this work was provided by the Ballistic Missile Defense Organization/AST and the Air Force Office of Scientific Research and the Adva Projects Research Agency.

References

[1] M.G. Bawendi, M.L. Steigerwald and M.L. Brus, Annu. Phys. Chem. 41 (1990) 477.
[2] L.T. Canham, Appl. Phys. Lett. 57 (1990) 1046.
[3] A.J. Read, R.J. Needs, K.J. Nash, L.T. Canham, Calcott and A. Qteish, Phys. Rev. Lett. 69 (1992) 123
[4] F. Buda, J. Kohanoff and M. Perrinello, Phys. Rev. Lett. (1992) 1272.
[5] T. Ohno, K. Shiraishi and T. Ogawa, Phys. Rev. L (1992) 2400.
[6] C.G. Van de Walle and J.E. Northrup, Phys. Rev. Lett. (1993) 1116.
[7] N.A. Hill and K.B. Whaley, Mater. Res. Soc. Symp 358 (1995) 25.
[8] L-W Wang and A. Zunger, J. Phys. Chem. 98 (1994) 2
[9] See, for example, the review by D.J. Lockwood, Soli Commun. 92 (1994) 101.
[10] K.A. Littau, P.J. Szajowski, A.J. Muller, A.R. Kort L.E. Brus, J. Phys. Chem. 97 (1993) 1224.
[11] T. Suemoto, K. Tanaka, A. Nakajima and T. Itakura Rev. Lett. 70 (1993) 3659.
[12] C. Pickering, M.I.J. Beale, D.J. Robbins, P.J. Pearson Greef, J. Phys. C 17 (1984) 6535.
[13] H. Liu, D.K. Biegelsen, N.M. Johnson, F.A. Pon R.F.W. Pease, J. Vac. Sci. Technol. B 11 (1993) 23
[14] P.B. Fischer, K. Dai, E. Chen and S.Y. Chou, J. V Technol. B 11 (1993) 2524.
[15] A.G. Nassiopoulos, S. Grigoropoulos and P. Papadimi in: Advanced Luminescent Materials, Vol. 95-25, e Lockwood, P.M. Fauchett, N. Koshida and S.R.J. (The Electrochemical Society, Pennington, NJ, 1996 296–306.
[16] S.H. Zaidi and S.R.J. Brueck, J. Vac. Sci. Tech (1993) 658.
[17] E. Bassous, IEEE Trans. Elect. Dev. ED-25 (1978) 11
[18] D-B Kao, J.P. McVittie, W.D. Nix and K.C. Saraswat, Trans. Elect. Dev. ED-34 (1987) 1008.
[19] S.R. Goodes, T.E. Jenkins, M.I.J. Beale, J.D. Benja C. Pickering, Semicond. Sci. Technol. 3 (1988) 483.
[20] N. Ohtani and K. Kawamura, Solid State Commu (1990) 711.
[21] Z. Iqbal and S. Veprek, J. Phys. C 15 (1982) 377.
[22] H. Tanino, S. Amano, H. Kawanami and H. Matsu Appl. Phys. 70 (1991) 7068.
[23] W.L. Wilson and T.W. Weidman, J. Phys. Chem. 4568.
[24] G. Kanellis, J.F. Morhange and M. Balkanski, Phys. 21 (1980) 1543.
[25] D.I. Kovalev, I.D. Yaroshetzki, T. Muschik, V. Pet and R. Koch, Appl. Phys. Lett. 64 (1994) 214.
[26] S.M. Prokes, Appl. Phys. Lett. 62 (1994) 3244.

Instructions to Authors (short version)

(A more detailed version of the instructions is published in the preliminary pages of each volume)

Submission of papers

Manuscripts (one original and two copies), should be sent to one of the Editors, whose addresses are given on the inside of the journal cover.

Original material. Submission of a manuscript implies that the paper is not being simultaneously considered for publication elsewhere and that the authors have obtained the necessary authority for publication.

Refereeing. Submitted papers will be refereed and, if necessary, authors may be invited to revise their manuscript. Authors are encouraged to list the names (addresses and telephone numbers) of up to five individuals outside their institution who are qualified to serve as referees for their paper. The referees selected will not necessarily be from the list suggested by the author.

Types of contributions

The journal Optics Communications publishes short communications and full length articles in the field of optics and quantum electronics.

Short communications are brief reports of significant, original and timely research results that warrant rapid publication. The length of short communications is limited to six journal pages. Proofs will not be mailed to authors prior to publication unless specifically requested.

Full length articles are subject to the same criteria of significance and originality but give a more complete and detailed account of the research results. Proofs of all full length articles will be mailed to the corresponding author, who is requested to return the corrected version to the publisher within two days of receipt.

Manuscript preparation

All manuscripts should be written in good English. The paper copies of the text should be prepared with double line spacing and wide margins, on numbered sheets. See notes opposite on electronic version of manuscripts.

Structure. Please adhere to the following order of presentation: Article title, Author(s), Affiliation(s), Abstract, classification codes (PACS and/or MSC) and keywords, Main text, Acknowledgements, Appendices, References, Figure captions, Tables.

Corresponding author. The name, complete postal address, telephone and Fax numbers and the E-mail address of the corresponding author should be given on the first page of the manuscript.

PACS codes/keywords. Please supply one to four classification codes (PACS and/or MSC) and 1–6 keywords of your own choice for indexing purposes.

References. References to other work should be consecutively numbered in the text using square brackets and listed by number in the Reference list. Please refer to a recent issue of the journal or to the more detailed instructions for examples.

Illustrations

Illustrations should also be submitted in triplicate: master set and two sets of copies. The *line drawings* in master set should be original laser printer or plotter out or drawn in black india ink, with careful lettering, la enough (3–5 mm) to remain legible after reduction printing. The *photographs* should be originals, with so what more contrast than is required in the printed vers They should be unmounted unless part of a composite ure. Any scale markers should be inserted on the ph graph itself, not drawn below it.

Colour plates. Figures may be published in colour, if thi judged essential by the editor. The publisher and the au will each bear part of the extra costs involved. Fur information is available from the publisher.

After acceptance

Important. When page proofs are made and sent ou authors, this is in order to check that no undetected er have arisen in the typesetting (or file conversion) proc No changes in, or additions to, the edited manuscript be accepted.

Copyright transfer. You will be asked to transfer copyr of the article to the publisher. This transfer will ensure widest possible dissemination of information.

Electronic manuscripts

The publisher welcomes the receipt of an electronic ver of your accepted manuscript (preferably encoded LaTex). If you have not already supplied the final, revi version of your article (on diskette) to the Journal Edi you are requested to send a file with the text of accepted manuscript directly to the Publisher by e-mai on diskette (allowed formats 3.5" or 5.25" MS-DOS 3.5" Macintosh) to the address given below. Please n that no deviations from the version accepted by the Ed of the journal are permissible without the prior and exp approval by the Editor. Such changes should be cle indicated on an accompanying printout of the file.

Author benefits

No page charges. Publishing in Optics Communicatior free.

Free offprints. The corresponding author will receive offprints free of charge. An offprint order form will be plied by the publisher for ordering any additional paid prints.

Discount. Contributors to Elsevier Science journals entitled to a 30% discount on all Elsevier Science book

Further information (after acceptance)

Elsevier Science B.V., Optics Communications
Issue Management Physics and Materials Science
P.O. Box 2759, 1000 CT Amsterdam, The Netherlan
Fax: +31 20 4852319
E-mail: PHYSDESK@ELSEVIER.NL

Broadly Tunable External Cavity Laser Diodes with Staggered Thickness Multiple Quantum Wells

H. S. Gingrich, D. R. Chumney, S.-Z. Sun, S. D. Hersee, L. F. Lester, *Member, IEEE,* and S. R. J. Brueck, *Fellow, IEEE*

Abstract— **Widely tunable low-threshold current laser diodes fabricated from an engineered multiple-quantum-well (MQW) gain structure consisting of three compressively strained $In_{0.2}Ga_{0.8}As$ wells of different thicknesses are reported. Using a grating in an external cavity, a continuous-wave tuning range of 70 nm (911–981 nm) is measured for a 155-μm semiconductor cavity length device at a current of 32 mA. This is the lowest reported bias current for a semiconductor laser with this broad a tuning range. A maximum continuous wave tuning of 80 nm (901–981 nm) has been measured at a bias current of 95 mA. At long wavelengths, a suppression of amplified spontaneous emission and preferential population of the lowest energy well were observed.**

Index Terms— **Laser tuning, quantum-well devices, quantum-well lasers, semiconductor lasers, tunable circuits/devices, tunable semiconductor lasers.**

I. Introduction

MUCH effort has been devoted to the development of broadly tunable semiconductor lasers for use in systems such as wavelength division multiplexing (WDM) which require discrete wavelength channels, or in applications that need continuous, mode-hop-free tuning, such as absorption spectroscopy. Wide, continuous tuning of laser diode sources is best accomplished either thermally [1] or with a grating in an external cavity [2]. If the need for continuous tuning is relaxed, then a broad array of semiconductor laser structures incorporating monolithic tuning elements is available, including: Y-branch lasers [3], vertical coupler filter lasers [4], sampled (super structure) grating DBR lasers [5], [6], vertical grating assisted codirectional coupler lasers with rear sampled grating reflectors [7], and distributed forward-coupled lasers [8]. The purpose of this letter is to present the characteristics of external cavity tuned laser diodes fabricated from a novel multiple-quantum-well (MQW) gain medium.

Ideally, a tunable semiconductor laser should have minimal threshold current and output power variation across a broad wavelength range of operation. Quantum-well (QW) materials offer low threshold currents coupled with a broad tuning range, as well as the ability to tailor the gain medium to a specific wavelength range. Past work on broadly tunable QW laser diodes has focused on materials which contain either multiple identical wells [9] or stepped QW's [10].

This letter presents initial investigations of an alternative MQW approach, wherein the transition energies from the first conduction to the first heavy hole subband (CB1-HH1) are staggered in each of three wells to broaden the gain spectrum. This MQW design is similar in concept to that reported for broad-band LED's [11]. Gain calculations show a wider and flatter profile than that of a material which consists of three identical QW's. The use of nonidentical QW's allows tailoring of the wavelength range and emphasis on particular bands of the gain spectrum through preferential population of the wells. Our tuning experiments show that this is possible using the feedback of an external cavity grating which induces carrier redistribution to a specific well through mode competition and spectral variations in carrier lifetime in the staggered thickness QW structure.

II. Experiment

The strained triple QW laser material was grown using metal-organic chemical vapor deposition, with 1.5-μm $Al_{0.70}Ga_{0.30}As$ cladding layers and 0.15-μm graded AlGaAs separate confinement layers. The gain region consisted of three $In_{0.2}Ga_{0.8}As$ QW's of 80-, 60-, and 45-Å thicknesses, separated by 150-Å $Al_{0.25}Ga_{0.75}As$ barriers. Ridge waveguide lasers (9-μm wide) were fabricated by standard contact photolithography. After cleaving into 150–300-μm-long bars, a two layer anti-reflection (AR) coating of HfO_2–MgF_2 was electron-beam evaporated onto one facet (witness piece reflectivity was <1.3% with a center wavelength of 950 nm). Lasers were soldered onto copper heat sinks and mounted onto a thermoelectric cooler.

The external cavity consisted of an objective lens (Newport F-L20) that collimated the light from the AR-coated side of the laser and directed it onto a 1200 line/mm ruled diffraction grating mounted in a Littrow configuration. Output from the diode was collected with another identical objective lens, coupled into a multimode fiber, and fed into an optical

Manuscript received September 16, 1996; revised October 21, 1996. This work was supported in part by DARPA. The work of H. S. Gingrich was supported by the U.S. Air Force PALACE Knight Program.

H. S. Gingrich is with the Center For High Technology Materials and the Department of Physics and Astronomy, University of New Mexico, Albuquerque, NM 87131-6081 USA.

D. R. Chumney was with the Center For High Technology Materials and the Department of Electrical and Computer Engineering, University of New Mexico, Albuquerque, NM 87131-6081 USA. He is now with Intel Corporation, Rio Rancho, NM, 87124 USA.

S.-Z. Sun is with the Center For High Technology Materials, University of New Mexico, Albuquerque, NM 87131-6081 USA.

S. D. Hersee and L. F. Lester are with the Center For High Technology Materials and the Department of Electrical and Computer Engineering, University of New Mexico, Albuquerque, NM 87131-6081 USA.

S. R. J. Brueck is with the Center For High Technology Materials, the Department of Physics and Astronomy, and the Department of Electrical and Computer Engineering, University of New Mexico, Albuquerque, NM 87131-6081.

Publisher Item Identifier S 1041-1135(97)01209-3.

1041–1135/97$10.00 © 1997 IEEE

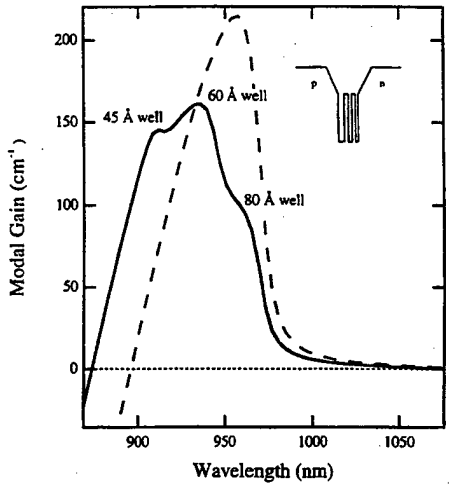


Fig. 1. Calculated modal gain profile for staggered thickness QW material (solid line) and for three identical 80-Å $In_{0.2}Ga_{0.8}As/Al_{0.25}Ga_{0.75}As$ QW's (dotted line). A constant quasi-Germi level is assumed. Sheet density is 1.75 $\times$ $10^{12}/cm^2$.

spectrum analyzer. The AR coating and the short cavity length were necessary to suppress the Fabry–Perot (FP) modes of the cavity to allow the feedback from the grating to determine the lasing wavelength. We obtained optimum tuning results when the wavelength of minimum reflectivity of the AR coating was aligned to the peak in the spontaneous emission. For a 150-μm cavity length laser, good external cavity tuning was achieved with an AR coating of 2% or less at the spontaneous emission peak.

Fig. 1 compares the calculated modal gain profile of the staggered thickness well structure with that of a MQW with three identical 80-Å $In_{0.2}Ga_{0.8}As$ wells. Only the $n = 1$ levels were included in the calculation. For the same total sheet charge density, the gain of the MQW with staggered QW thicknesses is noticeably wider and less peaked. The material parameters for the InGaAs–GaAs–AlGaAs QW systems were taken from [12], and spectral broadening was taken into account using a Lorentzian lineshape function. Quasi-Fermi levels are assumed constant across the three wells [13]. The well thicknesses of 80, 60, and 45 Å have calculated CB1-HH1 transitions of 970, 944, and 912 nm, respectively. The central wavelength was chosen to allow for easy spectroscopic coverage of the 942-nm absorption line of H_2O. The photoluminescence spectrum of the material shows three distinct peaks, centered at 975, 950, and 930 nm. Therefore, the actual gain spectrum will be shifted and roughly 13 nm narrower than the calculated one.

III. Results

For a 155-μm semiconductor gain length device which had an AR coating on one mirror and a slightly angled facet on the other, a maximum CW tuning range of 80 nm (from 901–981 nm) was obtained. The threshold current, I_{th}, was 95 mA at the extreme edges of the tuning range and optical powers were typically several mW. The tuning of the laser to short wavelengths was limited by the onset of parasitic lasing in the internal FP cavity [see Fig. 4(a)]. A 70-nm tuning range was achieved with a lower I_{th} of 32.0 mA at the extreme edges

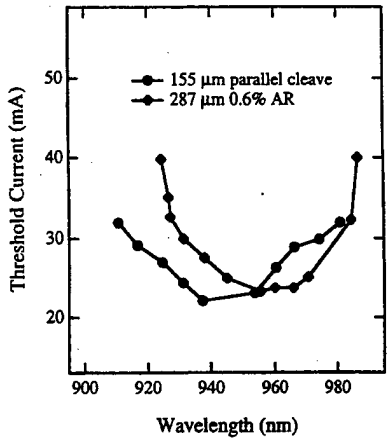


Fig. 2. Threshold current as a function of wavelength for two devices with different cavity lengths.

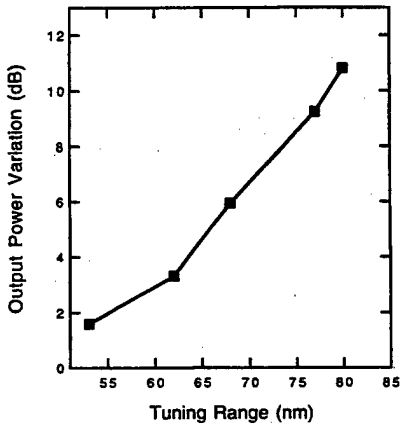


Fig. 3. Variation in output optical power as a function of tuning range, with the current kept just above I_{th}. The variation is defined as the highest output power less the lowest output power measured across the tuning range.

of the tuning range in a second 155-μm device with parallel facets; this is less than half of the I_{th} reported by Hall *et al.* [10] using a stepped-QW laser with a similar cavity length. These results are attributed to the use of an MQW, which yields a lower I_{th} in short cavity lasers, and the staggered thickness wells, which broaden the gain compared to the case of identical wells. A third laser with a 287-μm gain length tuned to longer wavelengths than the first two, bringing the combined tuning range to 86 nm (901–987 nm) for all devices. Fig. 2 shows the threshold current as a function of wavelength, and Fig. 3 details the variation in output power. The minimum threshold current for the 155-μm laser was 22.1 mA at 938 nm; with the current kept near I_{th} while adjusting the grating, the laser tuned over 60 nm with only a 3-dB change in optical power. The 32-mA maximum I_{th} for the 70-nm tuning is the smallest of which we are aware for this tuning range.

When operating near 980 nm, it was observed that the amplified spontaneous emission (ASE) bulge in the spectrum near 940 nm was less pronounced than when lasing near 910 nm, as shown Fig. 4. For lasing at sufficiently long wavelengths, only the lowest energy well can provide gain, and any carriers in the higher energy QW's only contribute to spontaneous emission. Thus, the suppression of ASE near 940

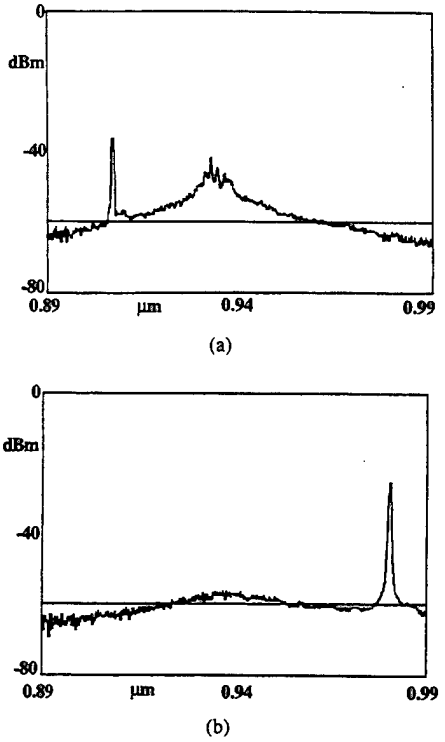


Fig. 4. Spectral characteristics of a 155-μm external cavity tuned laser diode. Lasing wavelength for (a) is 911 nm, lasing wavelength for (b) is 981 nm. The current is 32 mA. Note drop in ASE at long wavelengths. The −60-dB line has been added to aid the eye. The lines near 940 nm in (a) are due to residual cavity effects and limit the tuning range at the shorter wavelength; they are not present except when near the short wavelength extreme of the tuning range.

nm while lasing at 980 nm indicates a preferential population of the lowest energy well. When lasing at shorter wavelengths, all three wells contribute to the gain; therefore, all three wells are populated. Without preferential population of one well, there is no mechanism for suppressing the ASE. The preferential population of the lower energy well suggests that the external cavity feedback reduces the carrier lifetime in the lowest well relative to the others, allowing lasing mode competition to cause a redistribution of the carriers among the wells, draining carriers from the higher energy wells and populating the lowest energy well. This redistribution of carriers would modify the gain profile, increasing the gain of the long wavelength modes. As noted above, at 300 K the MQW system seeks quasi-Fermi levels which are essentially flat across the QW's; yet the present work shows that the flatness of the quasi-Fermi levels can be affected through the carrier redistribution caused by strong feedback.

IV. Conclusion

A tuning range of 70 nm was obtained from a device at a current of only 32.0 mA. While the CW tuning range was not as large as some previously reported results [10] for the 0.9–1.0-μm range, the threshold current was lower than any of which we are aware. A second device of the same material provided 80 nm of tuning; a total tuning range of 86 nm was observed for the staggered-thickness QW structure. The redistribution of carriers from the spontaneous modes to the lasing mode is currently under investigation. We speculate that this effect is due to a redistribution of carriers between wells resulting from an interaction between the cavity modes and the gain media, an effect which would not be possible in a material composed of three identical wells. The staggered thickness QW material also shows a broader, flatter gain profile than that of a material which consists of three identical QW's; in addition, it allows for the suppression of ASE while lasing at long wavelengths. Future material designs will incorporate wells spaced out further in wavelength to give additional broadening of the modal gain profile.

References

[1] M. Öberg, S. Nilsson, T. Klinga, and P. Ojala, "A three electrode distributed bragg reflector laser with 22 nm wavelength tuning range," *IEEE Photon. Technol. Lett.*, vol. 3, pp. 299–301, 1991.

[2] C. P. Seltzer, M. Bagley, D. J. Elton, S. Perrin, and D. M. Cooper, "160 nm continuous tuning of an MQW laser in an external cavity across the entire 1.3 μm communications window," *Electron. Lett.*, vol. 27, pp. 95–96, 1991.

[3] M. Kuznetsov, P. Verlangieri, A. G. Dentai, C. H. Joyner, and C. A. Burrus, "Widely tunable (45 nm, 5.6 THz) multi-quantum-well three-branch Y3-lasers for WDM networks," *IEEE Photon. Technol. Lett.*, vol. 5, pp. 879–882, 1993.

[4] R. C. Alferness, U. Koren, L. L. Buhl, B. I. Miller, M. G. Young, T. L. Koch, G. Raybon, and C. A. Burrus, "Broadly tunable InGaAsP/InP laser based on a vertical coupler filter with 57-nm tuning range," *Appl. Phys. Lett.*, vol. 60, pp. 3209–3211, 1992.

[5] V. Jayaraman, A. Mathur, L. A. Coldren, and P. D. Dapkus, "Extended tuning range in sampled grating DBR lasers," *IEEE Photon. Technol. Lett.*, vol. 5, pp. 489–491, 1993.

[6] H. Ishii, H. Tanobe, F. Kano, Y. Tohmori, Y. Kondo, and Y. Yoshikuni, "Quasicontinuous wavelength tuning in super-structure-grating (SSG) DBR lasers," *IEEE J. Quantum Electron.*, vol. 32, pp. 433–441, 1996.

[7] M. Öberg, S. Nilsson, K. Streubel, J. Wallin, L. Bäckbom, and T. Klinga, "74 nm wavelength tuning range of an InGaAsP/InP vertical grating assisted codirectional coupler laser with rear sampled grating reflector," *IEEE Photon. Technol. Lett.*, vol. 5, pp. 735–738, 1993.

[8] M.-C. Amann, B. Borchert, S. Illek, and T. Wolf, "Widely tunable distributed forward coupled (DFC) laser," *Electron. Lett.*, vol. 29, pp. 793–794, 1993.

[9] H. Tabuchi and H. Ishikawa, "External grating tunable MQW laser with wide tuning range of 240 nm," *Electron. Lett.*, vol. 26, pp. 742–743, 1990.

[10] D. C. Hall, J. S. Major, Jr., N. Holonyak, Jr., P. Gavrilovic, K. Meehan, W. Stutius, and J. E. Williams, "Broadband long-wavelength operation (9700 Å $\gtrapprox \lambda \lessapprox$ 8700 Å) of $Al_yGa_{1-y}As$–GaAs–$Ga_{1-x}As$ quantum well heterostructure lasers in an external grating cavity," *Appl. Phys. Lett.*, vol. 55, pp. 752–754, 1989.

[11] I. J. Fritz, J. F. Klem, M. J. Hafich, A. J. Howard, and H. P. Hjalmarson, "Broad-band light-emitting diode for 1.4–2.0 μm using variable-composition InGaAs quantum wells," *IEEE Photon. Technol. Lett.*, vol. 7, pp. 1270–1272, 1995.

[12] P. S. Zory, Jr., Ed., *Quantum Well Lasers.* Boston, MA: Academic, 1993, p. 79.

[13] P. A. Evans, P. Blood, and J. S. Roberts, "Carrier distribution in quantum well lasers," *Semiconduct. Sci. Technol.*, vol. 9, pp. 1740–1743, 1994.

Large-Signal Phase Retardation with a Poled Electrooptic Fiber

X.-C. Long and S. R. J. Brueck, *Fellow, IEEE*

***Abstract*— A linear electrooptic coefficient of 0.3 pm/V is induced in a germanosilicate fiber by thermal/electric-field poling. Reducing the fiber thickness by simple mechanical polishing following the poling, leads to a half-wave drive voltage of only 75 V for a 12-cm active length with no measurable linear optical loss in the fiber. The induced linear electrooptic coefficient shows no decay at room temperature for over four months, and only a 10% decay after heating to 90 °C for 1000 h.**

***Index Terms*—Electrooptic effect, fiber, glass poling.**

I. Introduction

LINEAR electrooptic coefficients ranging from 0.002 to 6 pm/V induced by electric field poling, thermal/electric-field poling and UV-excited poling have been reported for silica-based bulk glasses [1], waveguides [2]–[4], and fibers [5]–[9]. Significant research efforts are aimed at understanding the microscopic origins of the nonlinearity and at further improving the processing to enhance its magnitude. Another important direction is to develop device configurations and geometries based on the currently available electrooptic coefficients for applications such as switches, modulators, optical frequency mixers, electric field sensors, and tunable filters. As we show, these coefficients are already large enough for practical implementations; further, there is an important cross-coupling between materials and device efforts.

We have reported [9] previously on a planarized fiber-poling structure which allows us to apply a high field across a polished fiber and results in a linear electrooptic coefficient as high as 0.3 pm/V using a commercially available D-fiber. This fabrication technique has several advantages including: low cost volume manufacturing capability; planar structure to allow lithographic definition of high-speed circuits; and unaffected fiber ends to provide low-cost pigtailing. Here, we report the first observation of a half-wave phase shift in these poled fibers with a driving voltage as low as 75 V applied over a 12-cm active length ($V_\pi L$ = 900 V·cm). A major factor leading to this low drive voltage is polishing of the fiber after poling to reduce the total thickness to ~13 μm, thereby, increasing the field for a given voltage. Excellent thermal stability is observed.

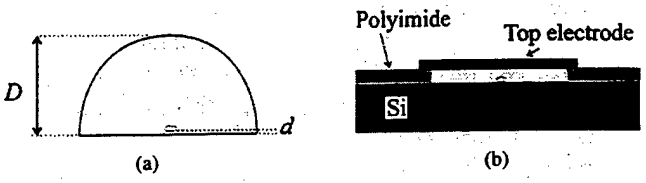


Fig. 1. Fiber cross sections: (a) as received; (b) following reduction in d (the distance from the surface to the core-cladding interface) by polishing, mounting onto Si bottom electrode, poling, polishing to reduce D (the overall fiber thickness), and application of a top electrode.

A single-mode polarization-maintaining germanosilicate "D"-fiber designed [10] for 1.3-μm applications was used. The core is 1.25 × 2.5 μm^2 with 18 wt% Ge doping, and the thickness, d, of the fused silica cladding is 14.25 μm on the flat ("D") side of the fiber (cf. Fig. 1). The total diameter of the fiber, D, from the flat to the opposite side of the cladding is 70 μm. During poling it is important to have d as small as possible. We have previously shown [9] that the electrooptic coefficient is very sensitive to this distance as a result of charge transport processes across the cladding and charge trapping at the core–cladding interface. For a 633-nm single-mode fiber, the electrooptic coefficient r_{33} increased by almost an order of magnitude as d was decreased from the as-fabricated value of ~9 to ~5 μm by HF etching. Since the high voltage that can be applied across the fiber during poling scales as D, it is important to initially keep D as large as possible. Bulk studies have shown [11] that the resulting nonlinearity is insensitive to D since charge transport processes result in a space charge region localized near the anode. Moreover, once the nonlinearity is formed, D should be reduced as much as possible to enhance the response to an applied voltage. Reduction in both d and D is limited by added optical loss as the evanescent optical fields come into contact with the lossy electrodes. For these experiments, D was reduced to ~13 μm, comfortably above the region where the added optical loss is significant. In our first experiments, HF etching was used to reduce d; this resulted in significant roughening of the cladding surface and unacceptable scattering loss. For these experiments, as detailed below, we used mechanical polishing to reduce both d and D. Polishing produced a much improved surface quality and did not result in any measurable scattering loss for these short lengths(~10 cm) of fiber.

A thin (~1-μm thick) layer of polyimide (UR3100) was spun onto a Si wafer and the fiber, after stripping away the plastic encapsulation, was affixed to the wafer "D" side up

Manuscript received January 27, 1997; revised February 20, 1997. This work was supported in part by the Air Force Office of Scientific Research.

X.-C. Long is with the Department of Physics and Astronomy, Center for High Technology Materials, University of New Mexico, Albuquerque, NM 87131 USA.

S. R. J. Brueck is with the Department of Physics and Astronomy and the Department of Electrical and Computer Engineering, Center for High Technology Materials, University of New Mexico, Albuquerque, NM 87131 USA.

Publisher Item Identifier S 1041-1135(97)04069-X.

1041–1135/97$10.00 © 1997 IEEE

using this polyimide layer as an adhesive. The polyimide layer was then cured with a dual temperature process at 120 °C and 170 °C for 5 min each. Subsequent to this curing, additional layers of polyimide (UR3140) ~10-μm thick were spun onto the wafer. Each layer of the polyimide was cured with a dual temperature cycle at 120 °C and 170 °C for 10 min. After the fiber was totally encapsulated, the total polyimide stack was cured at 350 °C for 1 h. Then, the fiber/polyimide structure was mechanically polished down to less than ~5 μm between the core and flat surface of the cladding. Since we do not have an accurate measurement technique to monitor d, polishing was halted well before there was any measurable change in the linear optical properties of the fiber. This step needs to be optimized in future work.

In order to get a better measurement of the optical loss versus d for the planar fiber structure, measurements were made on a set of D-fibers provided by BT laboratories with d values of 0.5, 0.75, and 2 μm that were determined at the preform stage. These telecommunication fibers are single mode at a 1.55-μm wavelength with 8-μm diameter circular cores. The refractive index difference between core and cladding layers is $n_{\text{core}} - n_{\text{cladding}} = 0.005$. The measured optical losses, with the fibers mounted onto the Si wafers in the same geometry as the poled fiber devices, were 2.3, 1.25, and 0.08 dB/cm, respectively. The optical loss will be even lower for the D-fibers used for poling since these fibers have a larger refractive index difference ($n_{\text{core}} - n_{\text{cladding}} = 0.036$) and smaller elliptic core size(1.25×2.5 μm^2) resulting in a more tightly confined mode.

The fiber was removed and reattached to another Si wafer "D" side down with a similar polyimide process. The high-field electrical breakdown resistance of the polyimide was enhanced with an additional curing at 275 °C for 12 h. Following curing, the fiber/polyimide structure was mechanically polished to provide a planar surface. A Cr:Au film (30/300 nm) was deposited to form the top electrode.

The resulting structure was heated to 255 °C and a −5-kV dc voltage was applied between the top electrode and the Si bottom anode. Breakdown was typically observed for dc voltages above 6 kV for this geometry. After 10 min at this temperature, the sample was cooled to room temperature with the voltage applied. The poled interaction length was ~12 cm. The resulting electrooptic effect was monitored by placing the poled sample in the measurement arm of a free-space Mach–Zehnder interferometer [1] operating at 633 nm. Appropriate microscope objectives coupled light into and out of the electrooptically active fiber segment. The induced r_{33} of 0.3 pm/V was determined by comparison with the phase shift obtained in a longitudinal geometry Z-cut $LiNbO_3$ sample (ITO electrodes; 500-μm active length; $r_{31} = 9.8$ pm/V, [12]) in the reference arm of the interferometer.

After poling, mechanical polishing of the fiber structure was continued to reduce D to 13 μm. Deposition of metal top electrodes resulted in heating of the samples and degradation of the poling; therefore, a liquid $CuSO_4$ salt solution was used as the top electrode for our initial measurements.

The polished poled fiber structure was again placed in the measurement arm of the Mach–Zehnder interferometer. The

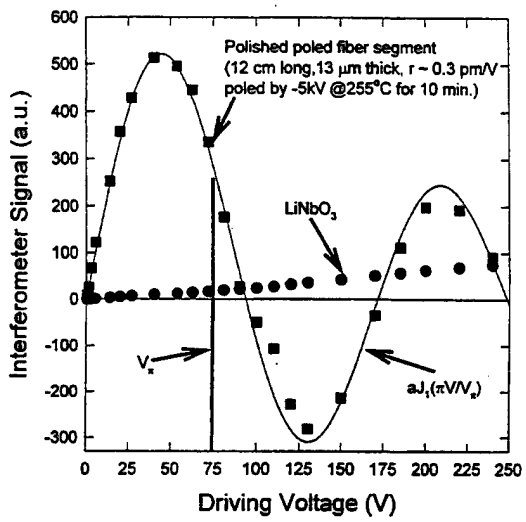


Fig. 2. Interferometer response for voltage applied to poled fiber and to a $LiNbO_3$ reference sample in a Mach–Zehnder interferometer. The solid curve is a fit to a first order-Bessel function giving a half-wave driving voltage $V_\pi = 75$ V for the poled fiber structure. The longitudinal geometry, $LiNbO_3$ reference sample is 0.5-mm thick with ITO electrodes.

interferometer signal was sensed with a balanced homodyne receiver consisting of two identical p-i-n detectors fabricated on the same substrate. The detector signal S is given by [13]

$$S = \alpha(1-2\varepsilon)(I_1 - I_2) + 4\alpha\sqrt{I_1 I_2 \varepsilon(1-\varepsilon)} \cdot \cos\left(\pi \frac{V}{V_\pi} \sin \omega t + \phi_0\right) \quad (1)$$

where α is a constant describing the photodetector responsivity and amplifier gain, ε is the power transmission coefficient of the final interferometer beam splitter, I_1 and I_2 are light intensities in the two interferometer arms before the final beamsplitter. The applied voltage V is at angular frequency ω. The dc phase difference ϕ_0 due to the path length difference in the two arms of the interferometer is set to $\pi/2$ by adjusting a compensator in the reference arm of the interferometer. The half-wave voltage $V_\pi = \lambda D/n^3 r_{33} l$ is related to the electrooptic coefficient of the poled fiber r_{33}, the active device length l, and the total thickness of the polished fiber structure D. Then (1) can be written as

$$\begin{aligned} S &= \alpha(1-2\varepsilon)(I_1 - I_2) + 4\alpha\sqrt{I_1 I_2 \varepsilon(1-\varepsilon)} \cdot \sin\left[\frac{\pi \sin(\omega t) V}{V_\pi}\right] \\ &= \alpha(1-2\varepsilon)(I_1 - I_2) + 4\alpha\sqrt{I_1 I_2 \varepsilon(1-\varepsilon)} \cdot \sum_{n=0}^{\infty} J_{2n+1}\left(\frac{\pi V}{V_\pi}\right) \sin[(2n+1)\omega t] \end{aligned} \quad (2)$$

where J_{2n+1} is the integer Bessel function of order $2n+1$. A lock-in amplifier, referenced to the applied electric field, responds to the first harmonic component of the signal, i.e., to $J_1(\pi V/V_\pi)$.

The Mach–Zehnder lock-in amplifier signal is shown in Fig. 2. The signal is insensitive to driving frequency over the 1–100-kHz range, demonstrating that the signal is due to the electrooptic effect. Piezoelectric responses are damped by the polyimide overcladding. The fit to a first-order Bessel function

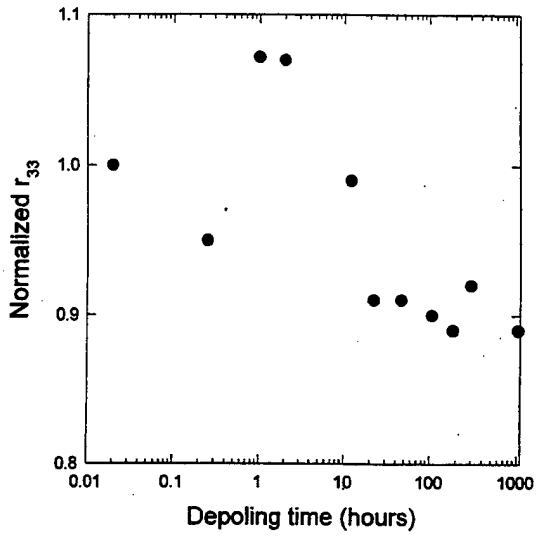


Fig. 3. Induced electrooptic coefficient in a poled fiber versus depoling time at 90 °C. The fluctuations are due to alignment variations. Degradation is less than ~10% over 1050 h.

is also shown in Fig. 2. The half-wave voltage V_π was 75 V for a $V_\pi l$ product of 900 V·cm. The reference signal for calibrating the nonlinearity using the longitudinal electrooptic effect in a $LiNbO_3$ sample is also shown. The $LiNbO_3$ signal is weaker because of the much shorter active pathlength (500-μm longitudinal geometry) and lower applied fields.

Since this fiber is not single-mode at the measurement wavelength of 633 nm, several modes could be observed at the fiber output depending on the coupling conditions into the fiber. To ensure that the observed signal was not due to mode conversion, a spatial filter that only transmitted a single spatial mode was placed after the output microscope objective. No signal was observed when the driving voltage was applied to the poled fiber indicating that the intensity distribution among the modes was unaffected by the applied voltage.

Stability of the thermal poling is a major issue for practical applications. No decay of the electrooptic coefficient was observed for a fiber poled (255 °C, −3 kV) and stored in laboratory ambient without any special precautions for over four months. The poled fiber was put in a oven at 90 °C to investigate the thermal stability. The sample was periodically removed from the oven and the electrooptic effect remeasured. The results are shown in Fig. 3. Much of the observed fluctuation is due to variations in the alignment from measurement to measurement; the electrooptic coefficient shows no more than ~10% decay after 1050 h at 90 °C.

There are several immediate directions for further optimization of the device structure. The fiber-loss measurements presented above suggest that D can be further reduced to ~4 μm while keeping the insertion loss to <1 dB for a 12-cm-long active device. Without any improvement in the effective r_{33}, this gives a half-wave voltage of only ±11.5 V at 633 nm and ±23.6 V at 1.3 μm for a push–pull configuration. There is experimental evidence from bulk silica measurements that the distribution of the nonlinearity extends over a distance of ~5–10 μm from the surface, and from fiber measurements [9] that d is a critical parameter. The wide variations observed by different workers in different fibers using different poling geometries [5]–[9] suggest that there are both material and geometric variations to be further exploited.

II. Conclusion

A linear electrooptic coefficient of 0.3 pm/V was obtained by temperature/electric-field poling a germanosilicate optical fiber using an improved poling geometry. By reducing the fiber thickness by polishing after poling, the half-wave driving voltage V_π was reduced to as low as 75 V. No measurable linear optical loss is associated with the processing to obtain this electrooptic response. Thermal stability was at least 4 months at room temperature, and 1050 h at 90 °C. Prospects are excellent for improvements in both the nonlinear coefficient and the device geometry leading to reductions in $V_\pi l$. A 2 × 2 integrated poled electrooptic fiber switch with low fiber-to-fiber loss can be formed by splicing polarization maintaining fiber couplers to the poled fibers. Since the device geometry is planar, a microwave stripe line can be integrated as the top electrode, using standard lithographic techniques, resulting in megahertz or higher switching rates.

Acknowledgment

The authors thank J. Mcalarney from Andrew Corp. and Dr. G. D. Maxwell and R. Cecil of BT laboratory for providing of D-fibers for these experiments, and A. Frauenglass for developing the fiber polishing machine.

References

[1] X.-C. Long, R. A. Myers, and S. R. J. Brueck, "Measurement of the linear electrooptic coefficient in poled amorphous silica," *Opt. Lett.*, vol. 19, pp. 1820–1822, 1994.

[2] A. C. Liu, M. J. F. Digonnet, and G. S. Kino, "Electro-optic phase modulation in silica channel waveguide," *Opt. Lett.*, vol. 19, pp. 466–468, 1994.

[3] R. A. Myers, R. P. Tumminelli, and S. R. J. Brueck, "Stable second-order nonlinearity in SiO_2-based waveguides on Si using temperature/electric-field poling," in *Proc. SPIE*, 1994, vol. 2289, pp. 158–166.

[4] M. Abe, T. Kitagawa, K. Hattori, A. Himeno, and Y. Ohmori, "Electro-optic switch constructed with a poled silica-based waveguide on Si substrate," *Electron. Lett.*, vol. 30, pp. 893–894, 1996.

[5] L. Li and D. N. Payne, "Permanently-induced linear electro-optic effect in silica optical fibers," in *Dig. Conf. Integrated and Guided Wave Opt.*, Opt. Soc. Amer., 1989, paper TuAA2-1.

[6] X.-C. Long, R. A. Myers, and S. R. J. Brueck, "Measurement of linear electrooptic effect in temperature/electric-field poled optical fibers," *Electron. Lett.*, vol. 32, pp. 2162–2163, 1994.

[7] P. G. Kazasky, P. St. J. Russell, L. Dong, and C. N. Pannell, "Pockels effect in thermally poled silica optical fibers," *Electron. Lett.*, vol. 31, pp. 62–63, 1995.

[8] T. Fujiwara, D. Wong, Y. Zhao, S. Fleming, S. Poole, and M. Sceats, "Electrooptic modulation in germanosilicate fiber with UV-excited poling," *Electron. Lett.*, vol. 31, pp. 573–575, 1995.

[9] X.-C. Long, R. A. Myers, and S. R. J. Brueck, "A poled electrooptic fiber," *IEEE Photon. Technol. Lett.*, vol. 8, pp. 227–229, 1996.

[10] *Product Selection Guide [Ecore™ Polarization Maintaining Fiber (D-Series)]*., Andrew Corp., Orland Park, IL, 1992, no. 205 170-1300S-2.

[11] R. A. Myers, N. Mukherjee, and S. R. J. Brueck, "Large second-order nonlinearity in poled fused silica," *Opt. Lett.*, vol. 16, pp. 1732–1734, 1991.

[12] W. R. Cook, Jr. and H. Jaffe, *Electrooptic Coefficients*, K.-H. Hellwege, Ed. Berlin: Springer-Verlag, 1979, Londolt-Börnstein New Series, vol. 11, ch. 5, p. 564.

[13] G. L. Abbas, V. W. S. Chan, and T. K. Yee, "A dual-detector heterodyne receiver for local oscillator noise suppression," *J. Lightwave Technol.*, vol. LT-3, pp. 1110–1122, 1985.

Microcavity Effects in an External-Cavity Surface-Emitting Laser

J. V. Sandusky and S. R. J. Brueck, *Fellow, IEEE*

Abstract— **Microcavity-induced lasing threshold reduction and modulation of the spontaneous emission coherence length with cavity length in an external-cavity resonant-periodic-gain, surface-emitting laser is reported. In contrast to comparing different epitaxial growths, external-cavity operation allows changing the cavity length without affecting material properties as well as arbitrarily long resonator lengths. The transition to the macrocavity domain is observed by extending the cavity length beyond the spontaneous emission coherence length. The maximum change in the spontaneous emission rate induced by the cavity QED effect in the presence of resonant periodic gain is calculated. As expected, for cavities longer than several wavelengths, microcavity Fabry–Perot resonance effects dominate over cavity QED in determining the cavity-normal spontaneous emission power and coherence length. A simple model of the cavity-normal spontaneous emission coherence length and spontaneous emission power emitted from a Gaussian source placed in an ideal Fabry–Perot cavity is consistent with our observations.**

Index Terms— **CW lasers, Fabry–Perot resonators, laser resonators, laser tuning, optical resonators, optics, quantum-well lasers, semiconductor lasers, spontaneous emission, surface-emitting lasers.**

I. Introduction

THE VERTICAL-CAVITY surface-emitting laser (VCSEL) is both a natural tool for the investigation of microcavity physics and a technologically important device [1], [2]. Recent experiments and modeling have shown that microcavity physics impacts the VCSEL lasing threshold [3], [4] and linewidth [5]. A microcavity resonator can considerably increase the efficiency of light-emitting diodes (LED's) [6]. Most recently, the microcavity has been applied to the production of Fock number states of the electromagnetic field [7]. The reduction of VCSEL lasing threshold and the increase in LED efficiency are primarily driven by the reduced photon density of states inherent in short cavities, which directs more of the spontaneous emission (SpE) onto the optical axis. Most experiments [8], [9] investigating VCSEL microcavity SpE have relied on multiple epitaxial growths or lateral growth-rate variations to effect changes in cavity length. This technique is inevitably subject to potential sample-to-sample material variations. In this paper, an external cavity mirror [10] is used to vary the resonator length without any impact on material properties. Further, much larger changes in cavity length can be achieved in an external-cavity configuration, allowing observation of the microcavity-to-macrocavity transition.

The effects of resonators on SpE can be divided into three broad regimes, depending on the resonator length L. If L is of order $\lambda(L \sim \lambda)$, cavity quantum electrodynamic (C-QED) effects such as Rabi flopping (in the strong-coupling limit) or radiative lifetime modification (in the weak-coupling limit) are present. If the resonator length is long compared to λ but comparable to the free-space SpE coherence length $l_c(L \sim l_c \gg \lambda)$ where l_c is proportional to the inverse of the SpE spectral width, C-QED effects are negligible. Nonetheless, since the cavity longitudinal mode spacing $\Delta\lambda = \lambda^2/2L$ is of the same order as the emission bandwidth $\lambda^2/2l_c$, the spectrally integrated SpE and the SpE coherence length depend on L. This is the microcavity regime that we explore herein. If the resonator is long compared to both l_c and $\lambda(L \gg l_c \gg \lambda)$, microcavity effects are negligible and the only impact of the resonator is to set the resonant wavelengths; the SpE power and the SpE coherence length are independent of L.

Previously [11] we reported the experimental observation of the microcavity effects of enhancement and inhibition of the spectrally integrated wafer-normal SpE and changes in the SpE radiation pattern as the cavity length was varied. Here, we quantify the measured microcavity-induced SpE coherence length modulation and demonstrate, for the first time in VCSEL's, a linear relationship between the lasing threshold and the cavity length in the microcavity regime. A simple model is presented that evaluates the impact of cavity resonances on the emission from a Gaussian source placed in an ideal Fabry–Perot cavity of length $L \sim l_c \gg \lambda$ and captures many of the observed effects.

We extend Björk's model [12] of single-quantum-well C-QED monochromatic spontaneous emission-rate modification to include multiple quantum wells (QW's) arranged in a resonant periodic-gain [13] (RPG) configuration, and calculate the maximum spontaneous emission rate increase induced for an RPG cavity of length L. The result indicates that RPG produces a slightly increased C-QED effect compared to an equivalent single-quantum-well resonator. The C-QED effect on cavity-normal emission, however, is negligible compared to the purely classical Fabry–Perot resonance effects for the relatively long cavity length experimentally employed ($L \sim l_c \gg \lambda$).

II. Background

A simple model of the filtering effects of a high-finesse Fabry–Perot etalon on a broad-band source serves to illustrate

Manuscript received February 28, 1997; revised May 19, 1997. This work was supported in part by the Air Force Office of Scientific Research.

J. V. Sandusky was with the Center for High Technology Materials, University of New Mexico, Albuquerque, NM 87131-6081 USA. He is now with Jet Propulsion Laboratory, California Institute of Technology, Pasadena, CA 91109–8099 USA.

S. R. J. Brueck is with the Center for High Technology Materials, University of New Mexico, Albuquerque, NM 87131-6081 USA.

Publisher Item Identifier S 0018-9197(97)06213-1.

0018–9197/97$10.00 © 1997 IEEE

the impact of cavity resonances. In a given direction, the transmitted spectrum for a high-finesse etalon is a series of sharp peaks whose envelope is the spectral distribution of the source. The transmitted wavelengths λ satisfy the resonance condition that an integer multiple of half-wavelengths fit within the effective cavity length $L\cos(\theta)$, *viz.*

$$m\frac{\lambda}{2} = L\cos(\theta), \qquad m = 1, 2, 3, \cdots \tag{1}$$

where θ is the angle the incident light makes with the etalon of thickness L. For given L and θ, there are an infinite number of resonant wavelengths λ_m which satisfy (1). The spacing between resonant wavelengths $\Delta\lambda = \lambda_m - \lambda_{m+1}$ is $2L\cos(\theta)/[m(m+1)]$. If the cavity length is macroscopic, say $\sim$1 mm, the number of half-wavelengths m at $\lambda = 1\,\mu$m is $\sim$2000 and the spacing is nearly constant $\Delta\lambda \approx 2L/m^2 \approx \lambda^2/2L \approx 0.5$ nm. If the light source has a nominal width $\sim$100 nm, the filtered spectrum will contain $\sim$200 equally spaced peaks. Slightly varying the cavity length will alter the exact resonant wavelengths λ_m but, because the spectral distribution of the source is so densely sampled, the spectrally integrated signal is invariant with cavity length.

At the opposite extreme, consider an extremely short etalon with $L = 1\,\mu$m. The resonant wavelengths are $\lambda_1 = 2\,\mu$m, $\lambda_2 = 1\,\mu$m, $\lambda_3 = 0.667\,\mu$m, and so on. Although an infinite number of resonant wavelengths remain, only one is within the 100-nm spectral bandwidth. The transmitted spectrum then contains a single peak. As the cavity length is varied, the magnitude of this peak and therefore the spectrally integrated signal traces out the spectral distribution of the source. In this case, the integrated intensity depends on the cavity length.

III. Fabry–Perot Resonance Effect on SpE from a Gaussian Source

Now instead of filtering the light source with the etalon, consider placing the source inside of the etalon (i.e., a cavity). We concentrate on the regime ($L \sim l_c \gg \lambda$) so that the only influence of the cavity on the emitter is to determine which wavelengths λ are emitted at which angles θ, and the angularly integrated SpE is independent of cavity length. Calculations justifying the approximation of fixed angularly integrated SpE are presented in Appendix A.

In most experiments, the SpE power emitted onto the optical axis is measured rather than the angularly integrated SpE. Using Björk's model (Appendix A), which treats the QW's as infinite planes of randomly oriented in-plane dipoles and SpE as emission stimulated by incident vacuum fluctuations, we find that the fraction f_m of the angularly integrated spontaneous emission launched onto the optical axis at the wavelength $\lambda_m = 2L/m$ is

$$f_m = \frac{3}{2}\frac{1}{m}\left[1 - \cos\left(2m\pi\frac{d_1}{L}\right)\right] \tag{2}$$

where d_l is the distance between the QW and mirror (Fig. 1). The mirrors are infinite in extent and emission into guided-wave modes in the plane of the mirrors is neglected. The $1/m$ behavior of f_m arises from the m angular modes of the wavelength λ_m, and the constant 3/2 arises from the directionality of the dipole radiation pattern. The distance d_l from the QW to a mirror affects f_m strongly as it describes the location of the QW relative to the standing wave antinodes. Note that if the QW is located on either mirror ($d_l = 0$ or L), then there is no emission from the cavity because the mirrors are locations of vacuum-fluctuation field nodes.

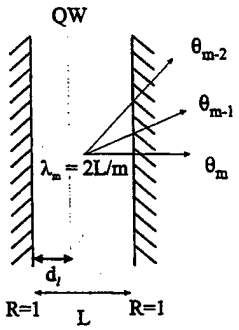


Fig. 1. Fabry–Perot cavity of length L with a QW spaced a distance d_l from the left mirror. Plane-wave vacuum fluctuations are incident from the right.

The SpE power is readily defined as the photon energy E times the spontaneous emission rate at photon energy E. Heuristically, the SpE coherence length is the optical path difference over which significant interference effects occur. A formal definition [14] of the coherence length is the rms width of the first-order correlation function $g^{(1)}$ or its spectral Fourier transform. We adopt the spectral rms definition (9) because it can be readily computed from the experimentally determined spectrum.

A specific lineshape must be assumed in order to calculate the SpE power and coherence length. Gaussian and Lorentzian lineshape functions are commonly used to describe spectra. The emission from a semiconductor QW is not accurately described by either of these functions because of the effects of the detailed semiconductor band structure and carrier dynamics. The Lorentzian lineshape has a much slower roll-off for large energies; its $1/E^2$ behavior prohibits any evaluation of rms spectral width. For this reason, we concentrate on emission from a Gaussian source. We expect that the essential physical dependence of the SpE coherence length and SpE power on cavity length should not depend on the exact details of the source spectral shape. The Gaussian lineshape is described by

$$\mathrm{SpE}(E) = \frac{\zeta}{\sqrt{2\pi}}\frac{1}{\Delta E}\exp\left[-\frac{1}{2}\left(\frac{E - E_0}{\Delta E}\right)^2\right] \tag{3}$$

where E_0 is the center energy and $2.36 \times \Delta E$ is the FWHM. We interpret this lineshape as the rate at which the source emits photons of energy E. The parameter ζ is the constant spectrally integrated power which accounts for the possibility of nonradiative recombination and loss to guided wave modes.

We take our cavity mirrors to have near-unity reflectance, i.e., the spectral width of a longitudinal mode is much smaller than the source spectral width ΔE. This is a good approximation for the $\sim$99% reflectance dielectric reflectors used experimentally [10], [11]. We also take the mirror bandwidth to be much broader than ΔE. Typical mirror bandwidths ($\sim$100

nm) are much larger than QW emission bandwidths of ~10 nm.

The first observable we evaluate is the total spontaneous emission power P emitted onto the optical axis, obtained by multiplying the spontaneous emission rate $\mathrm{SpE}(E_m)$ by the fraction f_m of the SpE launched onto the optical axis and the photon energy E_m, then summing over m

$$P(L) = \sum_{m=1}^{\infty} P_m \tag{4}$$

$$P_m = E_m \cdot f_m \cdot \mathrm{SpE}(E_m) \tag{5}$$

$$E_m = \frac{hc}{2L} m \tag{6}$$

where h is Planck's constant and c is the speed of light.

The mean emitted photon energy $\overline{E}(L)$ and the mean squared photon energy $\overline{E^2}(L)$ are

$$\overline{E}(L) = \sum_{m=1}^{\infty} E_m \frac{P_m(L)}{P(L)} \tag{7}$$

$$\overline{E^2}(L) = \sum_{m=1}^{\infty} E_m^2 \frac{P_m(L)}{P(L)} \tag{8}$$

$$l_c(L) = \frac{hc}{\sqrt{\overline{E^2}(L) - [\overline{E}(L)]^2}}. \tag{9}$$

In the limit that one mirror is removed ($L \to \infty$), the series tend to integrals which are most easily analyzed if we extend the integration over photon energy to include negative energies. The error introduced by extending the integration limits is exceedingly small so long as the Gaussian has a narrow bandwidth ΔE compared to its central energy $E_0 (\Delta E \ll E_0)$. The integrals yield [15]

$$P(L \to \infty) = \frac{3}{2}\zeta \left\{ 1 - \cos\left(4\pi \frac{d_l}{\lambda_0}\right) \cdot \exp\left[-\left(2\sqrt{2}\pi \frac{d_l}{l_{c0}} \right)^2 \right] \right\} \tag{10}$$

and (11) and (12), shown at the bottom of the page, where l_{c0} is the macrocavity (free-space) spontaneous emission coherence length

$$l_{c0} = \frac{hc}{\Delta E}. \tag{13}$$

The output power and spectral properties depend on the location of the QW relative to the remaining mirror. This one-mirror microcavity effect is similar in principle to the work of Drexhage [16] which involved changes in the radiation pattern of molecules in close proximity to a mirror. We note from the form of the exponential in (10)–(12) that microcavity effects will be important for QW to mirror distances comparable to the free-space coherence length ($d_l \sim l_{c0}$), in agreement with the physical arguments of Deppe [17].

In the narrow-linewidth limit ($\Delta E \to 0$), the output power varies sinusoidally with the distance of the QW from the mirror. The mean photon energy approaches E_0 and the mean squared photon energy approaches E_0^2. The coherence length approaches infinity as expected for a source of zero spectral width.

We can remove the remaining mirror and approach the macrocavity limit by taking $d_l \to \infty$. The formulas reduce to

$$P(L \to \infty, d_l \to \infty) = \frac{3}{2}\zeta \tag{14}$$

$$\overline{E}(L \to \infty, d_l \to \infty) = E_0 \tag{15}$$

$$\overline{E^2}(L \to \infty, d_l \to \infty) = E_0^2 + \Delta E^2 \tag{16}$$

$$l_c(L \to \infty, d_l \to \infty) = l_{c0} = \frac{hc}{\Delta E}. \tag{17}$$

The output power approaches $(3\zeta/2)$, the mean photon energy approaches E_0, and the coherence length approaches the macrocavity coherence length $l_{c0} = hc/\Delta E$.

The series in (4), (7), and (8) are difficult to evaluate analytically for arbitrary L, but lend themselves readily to numerical summation. In Fig. 2, we present the normalized SpE power $P(L)/[(3\zeta/2)]$ as a function of the normalized cavity length L/l_{c0} for the symmetric case of a QW at the cavity center and for the asymmetric case of a QW placed $\lambda_0/4$ from one mirror. We take $\Delta E/E_0 = 1/100$ which is typical of semiconductor QW SpE. In the asymmetric case, the SpE power oscillates about the macrocavity limit $P(L \to \infty)/[(3\zeta/2)] = 1$ with period $\lambda_0/2$. The cavity-normal output power is doubled for $L = 10 \times \lambda_0$ and is nearly zero for $L = 10.25 \times \lambda_0$. In the symmetric case, the SpE power

$$\overline{E}(L \to \infty) = E_0 \left\{ 1 - \frac{4\pi \frac{d_l}{l_{c0}} \frac{\Delta E}{E_0} \sin\left(4\pi \frac{d_l}{\lambda_0}\right) \exp\left[-\left(2\sqrt{2}\pi \frac{d_l}{l_{c0}} \right)^2 \right]}{1 - \cos\left(4\pi \frac{d_l}{\lambda_0}\right) \exp\left[-\left(2\sqrt{2}\pi \frac{d_l}{l_{c0}} \right)^2 \right]} \right\}. \tag{11}$$

$$\overline{E}^2(L \to \infty) = E_0^2 + \Delta E^2 + \Delta E^2 \frac{\left[\left(4\pi \frac{d_l}{l_{c0}}\right)^2 \cos\left(4\pi \frac{d_l}{\lambda_0}\right) - 8\pi \frac{d_l}{l_{c0}} \frac{E_0}{\Delta E} \sin\left(4\pi \frac{d_l}{\lambda_0}\right) \right] \exp\left[-\left(2\sqrt{2}\pi \frac{d_l}{l_{c0}} \right)^2 \right]}{1 - \cos\left(4\pi \frac{d_l}{\lambda_0}\right) \exp\left[-\left(2\sqrt{2}\pi \frac{d_l}{l_{c0}} \right)^2 \right]} \tag{12}$$

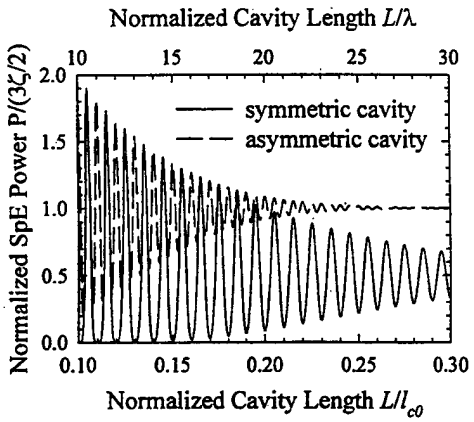


Fig. 2. The theoretical variation of the on-axis spectrally integrated spontaneous emission power as a function of increasing cavity length for $\Delta E/E_0 = 1/100$. In the symmetric case, the QW is in the center of the cavity whereas for the asymmetric case it is a distance $\lambda_0/4$ from one mirror.

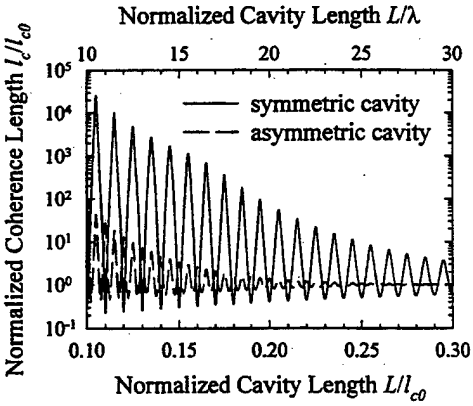


Fig. 3. The theoretical variation of the on-axis spontaneous emission coherence length as a function of increasing cavity length for $\Delta E/E_0 = 1/100$. In the symmetric case, the QW is in the center of the cavity whereas for the asymmetric case it is a distance $\lambda_0/4$ from one mirror.

approaches the macrocavity limit $P(L)/[(3\zeta/2)] = \frac{1}{2}$ with an oscillation period λ_0. The period is doubled compared to the asymmetric case because the center of the cavity changes from node to antinode for the wavelength λ_0 when the cavity length is increased by $\lambda_0/2$. The normalized output power approaches 1/2 because half of the longitudinal modes always have a node at the cavity center so that the QW couples to only half of the available modes.

Fig. 3 shows the SpE coherence length for the symmetric and asymmetric cases. The coherence length for the asymmetric case can be as much as an order of magnitude larger than for the macrocavity. The coherence length enhancement is much larger (~40 dB) for the symmetric case because of the complete longitudinal mode discrimination at the center of the cavity. By comparing Figs. 2 and 3, we see that the SpE power and SpE coherence length oscillate in phase. These predicted increases in coherence length and power have important implications for communications applications employing LED transmitters because they imply increased signal-to-noise ratio and therefore decreased bit error rate. In the limit of extremely short cavities, the LED microcavity spectral properties approach those of a laser.

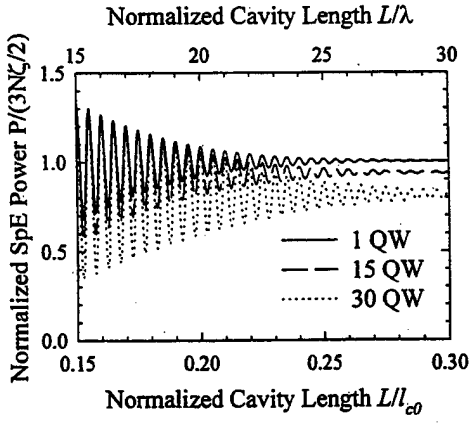


Fig. 4. The theoretical variation of the on-axis spectrally integrated spontaneous emission power per QW in a RPG design as a function of increasing cavity length for $\Delta E/E_0 = 1/100$. The number of QW's is indicated. The first QW is placed a distance $\lambda_0/4$ from one mirror.

So far we have discussed only the simple case of a single QW. To describe resonant periodic-gain (RPG) structures, we need to account for the emission from N QW's spaced $\lambda_0/2$ apart, with the first QW $\lambda_0/4$ from one mirror. We accomplish this by setting $d_l = \lambda_0/4 + (M-1)\lambda_0/2$ and summing (2) from $M = 1$ to $M = N$, then normalizing to N. Fig. 4 shows the normalized SpE power per QW $P(L)/[(3N\zeta/2)]$ as a function of cavity length for RPG designs incorporating 1, 15, and 30 QW's. The depth of modulation becomes larger as the number of QW's increases; RPG increases the visibility of microcavity effects compared to a SQW resonator.

Note that, in the long-cavity limit, an increased number of QW's results in a decrease in the cavity-normal output power per QW. This is due to the increase in longitudinal mode discrimination with increasing numbers of QW's which prevents the QW's from coupling to all of the available emission modes. This longitudinal mode discrimination also increases the SpE coherence length modulation depth and increases its long-cavity value, as shown in Fig. 5. These calculations indicate that a 30-QW RPG design should exhibit a factor ~2 of modulation in SpE power and coherence length with cavity length.

IV. Experimental

The usual VCSEL high-reflectivity (HR) top mirror is replaced in these experiments by an epitaxially grown antireflection (AR) coating which minimizes coupled-cavity effects. The active region consists of a 30-QW RPG section with the spacing between QW's ($\sim\lambda/2n$) chosen to account for QW-barrier reflections [18]. The back mirror is a 30-pair $Al_{0.3}Ga_{0.7}As$–AlAs high reflector ($R \sim 99.8\%$) and the external cavity is completed by a planar dielectric mirror ($R \sim 99.8\%$). The HR and AR coatings have a center wavelength of ~835 nm and a bandwidth of ~50 nm. The external mirror has a center wavelength ~860 nm and a bandwidth of ~300 nm. The epitaxial structure of the device is shown in Fig. 6 and discussed in detail in [11].

The QW's are optically excited through the external dielectric mirror by focusing the beam from a CW ring dye

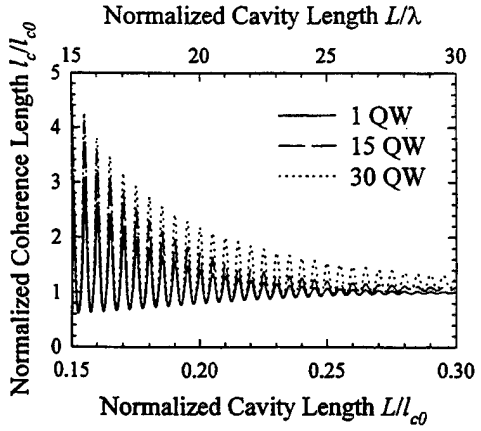


Fig. 5. The theoretical variation of the on-axis spontaneous emission coherence length in a RPG design as a function of increasing cavity length for $\Delta E/E_0 = 1/100$. The number of QW's is indicated. The first QW is placed a distance $\lambda_0/4$ from one mirror.

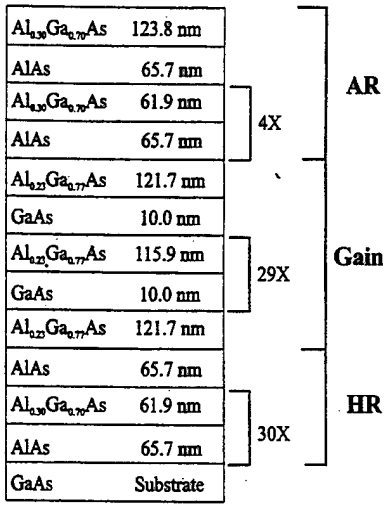


Fig. 6. The epitaxial device structure showing the AR coating, the RPG region, and the HR end mirror.

laser to a $1/e^2$ beam waist power radius $w \approx 15\,\mu$m. The experimental setup is shown in Fig. 7. The acceptance angle of the collection system is sufficiently small that only the forward angular mode is observed. We make measurements only at cavity lengths for which the pump beam ($\lambda_p \approx 716.66$ nm) resonates in the external cavity so that the absorbed pump power is independent of cavity length. We report the external cavity length L_{ext} in terms of the parameter n such that $n \times \lambda_p/2 = L_{\text{ext}}$ which we estimate from the external-cavity free-spectral range. Since the internal-cavity optical path length is more than $30 \times \lambda/2$, we are clearly in the regime $L \gg \lambda$.

Fig. 8 shows the spectrally integrated wafer-normal SpE power and coherence length as a function of n. Variations of up to 50% in the spectrally integrated SpE power and 30% in coherence length are measured. The coherence length is calculated from the spectrum via $l_c = \lambda^2/\sigma$ where λ is the mean wavelength and σ is the rms spectral width. This is the wavelength equivalent of the definition (9) used in the model. The instrumentally limited linewidth does not

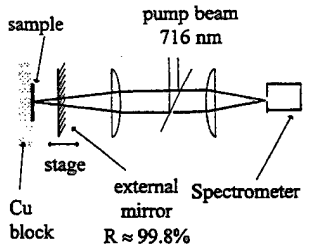


Fig. 7. Experimental setup for spontaneous emission and lasing experiments. A spectrometer monitors the cavity-normal spontaneous emission and lasing wavelength. Observations are made only at cavity lengths for which the pump beam resonates in the external cavity.

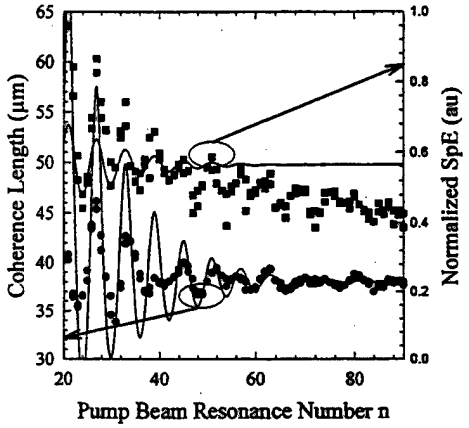


Fig. 8. Comparison of the measured (symbols) and theoretical (lines) on-axis spontaneous emission coherence length and output power as a function of pump resonance number n such that $n \times \lambda_p/2 = L_{\text{ext}}$. For $n = 20$, $L_{\text{ext}} \sim 7\,\mu$m.

impact the measured l_c which is dominated by the longitudinal mode spacing. Although other experimenters [8]–[10] have previously demonstrated that cavity resonances affect the SpE spectrum, the changes have not usually been represented in terms of the SpE coherence length. This natural parameter concisely describes the overall change in spectral shape.

Also shown in Fig. 8 are the SpE power and coherence length predicted by the model for $\Delta E/E_0 = 0.008$ which corresponds to the measured 16-nm FWHM of the QW photoluminescence from a reference sample without any cavity. The model correctly describes the period and phase relationship between the SpE power and coherence length and is in qualitative agreement with the magnitude of the observed oscillations. However, the SpE power is predicted to have symmetric modulation about the long-cavity limit whereas experimentally an asymmetric modulation is observed. Nonetheless, the agreement is satisfying in light of the large number of differences between our approximations and the experiment, including: describing the emission lineshape as a Gaussian, assuming infinite mirror bandwidth and transverse extent, ignoring total internal reflection and emission into guided wave modes, and neglecting the wavelength-dependence of phase change on reflection and the complicated dependence of reflectivity on incident angle inherent in the Bragg mirrors experimentally employed.

The impact of these approximations on the model's predictions can be expected to be small for the following reasons.

First, any smooth singly peaked lineshape should produce modulation depth similar to the Gaussian lineshape when the cavity length is near the spontaneous emission coherence length; the exact lineshape is not critical. Second, the mirror bandwidths are at least three times larger than the spontaneous emission bandwidth and they have such large transverse dimensions (millimeters) relative to the cavity length (micrometers) that they are essentially infinite in lateral extent. Spontaneous emission at wavelengths outside the mirror bandwidth does not depend strongly on cavity length and merely decreases the depth of modulation observed. Third, although much of the light emitted from the QW's is trapped by total internal reflection at the semiconductor–air interface or is emitted into guided wave modes in the plane of the sample, the strength of this coupling does not change with cavity length because the external cavity does not support guided wave modes (the refractive index of air is smaller than the refractive index of both the external mirror and the semiconductor). The main consequence, then, of these loss mechanisms is to effectively reduce the external quantum efficiency of the device. Fourth, the dependence of effective cavity length on wavelength arising from the wavelength-dependent phase change on reflection inherent in Bragg mirrors can be neglected for $L \gg \lambda$. Finally, the complicated dependence of Bragg mirror reflectivity on incident angle means that we are not assured that a resonator of length $L = m\lambda/2$ formed using Bragg mirrors has either m angular resonances or that each resonance receives an equal fraction of the SpE. However, as long as the number of angular modes is reduced by one for each $\lambda/2$ reduction in cavity length, the model can be expected to be essentially valid.

Fig. 9 shows the light input–light output (I/O) curve for the device under the conditions of enhancement and inhibition. The solid curves are linear fits showing the linear rise in SpE with pump power below the enhancement-condition threshold $P_{\text{th}} \approx 200$ mW. The lasing wavelength is ≈861 nm and the external cavity length is ~10 μm. We partially correct for the influence of heating by piezoelectrically tuning the external cavity length to maintain the conditions for pump beam resonance. The roll-over of the I/O curve is typical for VCSEL's. Note that under inhibition conditions the device does not reach threshold. We performed our SpE experiments at pump powers ~2 mW so that stimulated emission is negligible.

Perhaps the most technologically important microcavity effect is the reduction in lasing threshold. Although microcavity effects have been partially credited with the very low thresholds recently achieved in oxide-confined VCSEL's [19], it is difficult to establish how much of the threshold reduction is due to the vastly improved current confinement and how much is due to the Fabry–Perot resonance effect. In our configuration, it is possible to make a measure of the lasing threshold where the only variable is the cavity length. The results clearly illustrate the importance of the microcavity effects.

The threshold pump power P_{th} is shown as a function of pump beam resonance number n in Fig. 10 for three lasing wavelengths. The spacing between sampled wavelengths (~1

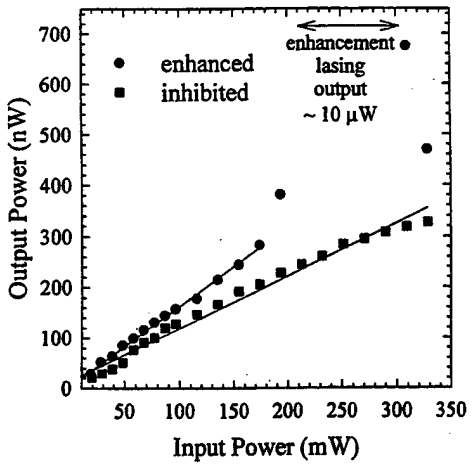


Fig. 9. The measured I/O curve under conditions of enhancement (circles) and inhibition (squares) showing a linear rise in output power with pump power below the enhancement lasing threshold $P_{\text{th}} \sim 200$ mW. No lasing is observed under inhibition conditions.

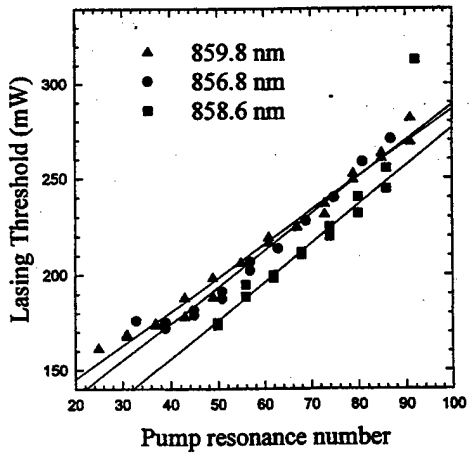


Fig. 10. The measured threshold pump power for three lasing wavelengths as a function of pump resonance number n such that $n \times \lambda_p/2 = L_{\text{ext}}$. For $n = 20$, $L_{\text{ext}} \sim 7$ μm. The linear reduction in the number of angular Fabry–Perot modes with decreasing cavity length increases the fraction of spontaneous emission coupled into the optical axis, reducing threshold. The last point for $\lambda = 858.6$ nm was excluded from the linear fit.

nm) is approximately the usual longitudinal mode spacing $\lambda^2/2L$ times (1–5/6). The factor (1–5/6) comes from sampling the cavity length at spacing $\Delta L = \lambda_p/2 \approx 5/6 \times \lambda_l/2$, where λ_l is the primary lasing wavelength ≈860 nm. The wavelength accuracy is instrument-limited to ~0.6 nm. There is a linear reduction in threshold with decreasing cavity length at each of the three wavelengths. As previously pointed out, a Fabry–Perot resonator $m \times \lambda/2$ long permits m angular modes. As the cavity length is reduced by $\lambda/2$, the number of angular modes is reduced by one. Correspondingly, a larger fraction of the total SpE is emitted into each mode, decreasing the lasing threshold.

We have investigated other probable causes of the linear dependence of lasing threshold on cavity length. Cavity loss due to diffraction of the beam around the edges of the mirrors is known to depend on cavity length [20]. The magnitude of the effect, however, is exceedingly small (fractional power loss $\sim 10^{-7}$) because of the large dimensions of the mirrors compared to the cavity length, and depends nonlinearly on

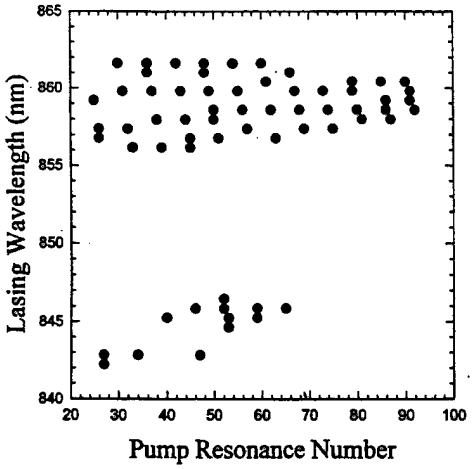


Fig. 11. The lasing wavelength as a function of pump resonance number n such that $n \times \lambda_p/2 = L_{\text{ext}}$. For $n = 20$, $L_{\text{ext}} \sim 7\ \mu$m. The device tunes continuously from 855 to 862 nm and permits a mode jump to 845 nm.

cavity length. For the high-reflectivity mirrors used, we expect that intracavity diffraction is the primary loss mechanism for the cavity. This mechanism, however, increases as $1 + (L/L_R)^2$ where $L_R \approx 350\,\mu$m is the Rayleigh diffraction range and is approximately constant over the range of cavity lengths investigated. The transverse mode structure was found to be multimodal, giving rise to a lasing linewidth of 0.05 nm as measured by a scanning Fabry–Perot spectrometer. The transverse mode structure dependence on cavity length was not investigated. However, because changes in diffraction loss which might impact the transverse mode structure and therefore the lasing threshold can be expected, based on the above arguments, to be small and depend nonlinearly on cavity length, we have concluded that the Fabry–Perot resonance effect is primarily responsible for the linear dependence of lasing threshold on cavity length.

Fig. 11 shows the lasing wavelength versus pump beam resonance number n. The device tunes continuously from 855 to 862 nm with a mode jump to 845 nm.

V. Summary

We have compared measured modulation of the cavity-normal spontaneous emission power and coherence length as a function of cavity length to the prediction of a simple model based on the impact of Fabry–Perot resonance on the emission from a Gaussian source. The model smoothly describes the transition from microcavity to macrocavity and correctly predicts that the power and coherence length oscillate in phase. It is also in agreement with the magnitude of the observed oscillations. Further, the model indicates that RPG longitudinal mode selectivity increases the modulation depth and therefore the visibility of microcavity-induced power and coherence modulation with cavity length. We have also experimentally shown a linear reduction of lasing threshold with decreasing cavity length due to the linear decrease in the number of angular Fabry–Perot modes at the lasing wavelength for an RPG design incorporating 30 QW's. These experiments directly demonstrate the importance of microcavity effects in VCSEL's.

Appendix A

The essential physics of the C-QED effect is that if an emitting atom is close enough to a mirror it may interact with the reflection of its photon before the emission is complete (also works in a cavity if close to both mirrors). If the reflected photon is in phase with the emitting atom's dipole moment, then the emission becomes self-stimulating and the spontaneous emission rate increases. If this enhancement occurs for all angles of emission, such as for a cavity of length $L = \lambda/2$, the angularly integrated and therefore the total SpE rate will be increased over the free-space rate. If the reflected photon is out of phase, the spontaneous emission rate will be decreased.

Björk's model [12] of C-QED SpE rate modification in the weak-coupling regime treats the VCSEL as a symmetric Fabry–Perot cavity containing a single QW. The cavity end mirrors extend to infinity and have fixed reflectivity R and phase change π. The QW's are infinite planes of point dipoles with random in-plane orientation. Björk calculates the SpE as stimulated emission driven by plane-wave vacuum fluctuations incident on the cavity. The SpE rate is determined via Fermi's Golden Rule, using the overlap between the QW's and the standing-wave electric field formed by the incident vacuum fluctuations as the driving term. By integrating over all incident angles, we arrive at the total SpE rate which we normalize to the free-space value by taking the limit of zero mirror reflectivity. The model ignores emission into guided wave modes in the sample plane and thus represents a "best case" scenario not likely to be achieved experimentally.

In order to describe the asymmetric multiple-quantum-well (MQW) resonator used in these experiments, it is necessary to generalize Björk's model. Our generalization allows a QW to be placed anywhere within the cavity of length L by varying the its distance d_l from the left mirror (Fig. 1). Since Björk gives an excellent description of the procedure for obtaining the overlap as a function of angle and the consequent total SpE rate, we merely state the results for our generalization

$$F_{\text{FP}}(\theta) = \frac{1-R}{1 - 2R\cos\left[\frac{2\pi}{\lambda}2L\cos(\theta)\right] + R^2} \tag{A1}$$

$$F_{\text{QW}}(\theta) = 1 - 2\sqrt{R}\cos\left[\frac{2\pi}{\lambda}2d_l\cos(\theta)\right] + R \tag{A2}$$

$$F_{\text{POL}}(\theta) = 1 + \cos^2(\theta) \tag{A3}$$

$$F_{\text{RAD}}(\theta) = F_{\text{FP}}(\theta) \cdot F_{\text{QW}}(\theta) \cdot F_{\text{POL}}(\theta). \tag{A4}$$

Separating the radiation pattern $F_{\text{RAD}}(\theta)$ into three terms allows identification of the roles which the whole cavity, the QW, and the polarization dependence play. The Fabry–Perot function F_{FP} contains the usual resonance behavior associated with the Fabry–Perot modes for a cavity of length L; $(1 - R) \times F_{\text{FP}}$ is the etalon transmission. The QW function F_{QW} describes the location of the QW relative to the standing wave antinodes at the wavelength λ. The function F_{POL} describes the angular dependence of unpolarized vacuum fluctuation coupling to the dipole plane.

To find the total emission rate Γ, we integrate F_{RAD} over θ. The integral, as in Björk's work, is taken in the limit of unity mirror reflectance, so that the FP function can be treated as

a delta function and the integral becomes a summation. The result is

$$\Gamma = \frac{3}{8}\frac{\lambda}{L}\sum_{m=1}^{\mathrm{int}(L/(\lambda/2))}\left[1-\cos\left(\frac{2d_l}{L}m\pi\right)\right]\cdot\left[1+\left(\frac{\lambda/2}{L}m\right)^2\right]. \quad \text{(A5)}$$

Selecting $d_l = 0$ or L locates the QW at a mirror, quenching emission from the cavity. Symmetric structures are described by $d_l = L/2$ for which case the cosine function becomes $(-1)^m$ and (A5) matches Björk's (11). This describes the selective coupling of the QW to the m = odd modes. For asymmetric structures $d_l \neq L/2$, the selectivity is not absolute.

We have implicitly calculated Γ for the case of vacuum fluctuations incident from the right. However, because Γ is invariant under the interchange of right and left $(d_l \rightarrow L - d_l)$, the result does not depend on direction. This symmetry is a result of the limit of unity mirror reflectivity which restricts emission entirely to the Fabry–Perot resonant angles.

The RPG structure is described by N QW's spaced $\lambda/2$ apart, with the first QW $\lambda/4$ from either mirror. To find the total spontaneous emission rate, we set $d_l = \lambda/4 + (M-1)\lambda/2$ and sum (A5) from $M = 1$ to $M = N$. We then normalize the result to the number N of QW's. This summation neglects the possible stimulation of SpE from one QW by another and may therefore be expected to underestimate the maximum C-QED effect in RPG VCSEL's.

For clear comparison with the case of a symmetric single-quantum-well (SQW) cavity, we also take $L = N\lambda/2$. The variation in the SpE rate per QW Γ_{RPG} with N is

$$\Gamma_{\mathrm{RPG}} = \frac{3}{4}\left(\frac{4}{3}+\frac{5}{2N}+\frac{1}{6N^2}\right). \quad \text{(A6)}$$

For $N = 1$, this merely replicates Björk's result $\Gamma_{\mathrm{RPG}} = 3$, a tripling of the SpE rate. For $N = 30$, $\Gamma_{\mathrm{RPG}} = 1.06$. As $N \rightarrow \infty$, we return to the free-space rate $\Gamma_{\mathrm{RPG}} = 1$. If we compare Γ_{RPG} to the SpE rate Γ_1 for a SQW at the center of a cavity of the same length $L = N\lambda/2$

$$\Gamma_1 = \frac{3}{4}\frac{N+1}{N}\left(1+\frac{N+2}{3N}\right), \qquad N = 1,3,5,\cdots \quad \text{(A7)}$$

we find that Γ_{RPG} exceeds Γ_1 by 5% for $N = 3$ and by 1.1% for $N = 31$. Thus we conclude that RPG increases the microcavity SpE rate per QW compared to a SQW in a cavity of the same length. To make a fair comparison, we have restricted our analysis to N = odd so that both the cavity of length $N\lambda/2$ containing N QW's and the cavity of length $N\lambda/2$ containing a SQW have strong overlap with normally incident vacuum fluctuations.

In real devices, the maximum increase of 1.06 in the SpE rate for $N = 30$ will be substantially reduced by emission into guided wave modes which contain the bulk [21] of the SpE power from VCSEL's. The total SpE rate is thus effectively fixed for cavities containing many QW's.

REFERENCES

[1] K. Tai, G. Hasnain, J. D. Wynn, R. J. Fischer, Y. H. Wang, B. Weir, J. Gamelin, and A. Y. Cho, "90% coupling of top surface emitting GaAs/AlGaAs quantum well laser output into 8 μm diameter core silica fiber," *Electron. Lett.*, vol. 26, pp. 1628–1629, 1990.

[2] A. E. Willner, C. J. Chang-Hasnain, and J. E. Leight, "2-D WDM optical interconnections using multiple-wavelength VCSEL's for simultaneous and reconfigurable communication among many planes," *IEEE Photon. Technol. Lett.*, vol. 5, pp. 838–841, 1993.

[3] D. G. Deppe, "Gain mechanism of the vertical-cavity surface-emitting semiconductor laser," *App. Phys. Lett.*, vol. 57, pp. 1721–1723, 1990.

[4] C. Lei and D. G. Deppe, "Optical gain enhancement in Fabry-Perot microcavity lasers," *J. Appl. Phys.*, vol 71, pp. 2530–2535, 1992.

[5] G. P. Agrawal and G. R. Gray, "Intensity and phase noise in microcavity surface-emitting semiconductor lasers," *Appl. Phys. Lett.*, vol. 59, pp. 399–401, 1991.

[6] H. De Neve, J. Blondelle, R. Baets, P. Demeester, P. Van Daele, and G. Borgs, "High efficiency planar microcavity LED's: Comparison of design and experiment," *IEEE Photon. Technol. Lett.*, vol. 7, pp. 287–289, 1995.

[7] F. De Martini, G. Di Giuseppe, and M. Marrocco, "Single-mode generation of quantum photon states by excited single molecules in a microcavity trap," *Phys. Rev. Lett.*, vol. 76, pp. 900–903, 1996.

[8] T. J. Rogers, D. G. Deppe, and B. G. Streetman, "Effect of an AlAs/GaAs mirror on the spontaneous emission of an InGaAs-GaAs quantum well," *Appl. Phys. Lett.*, vol. 57, pp. 1858–1860, 1990.

[9] T. Yamauchi, Y. Arakawa, and M. Nishioka, "Enhanced and inhibited spontaneous emission in GaAs/AlGaAs vertical microcavity lasers with two kinds of quantum wells," *Appl. Phys. Lett.*, vol. 58, pp. 2339–2341, 1991.

[10] H. Yokoyama, K. Nishi, T. Anan, Y. Nambu, S. D. Brorson, E. P. Ippen, and M. Suzuki, "Controlling spontaneous emission and threshold-less laser oscillation with optical microcavities," *Opt. Quantum Electron.*, vol. 24, pp. S245–S272, 1992.

[11] J. V. Sandusky and S. R. J. Brueck, "Observation of spontaneous emission microcavity effects in an external-cavity surface-emitting laser structure" *Appl. Phys. Lett.*, vol. 69, pp. 3993–3995, 1996.

[12] Gunnar Björk, "On the spontaneous emission lifetime change in an ideal planar microcavity—transition from a mode continuum to quantized modes," *IEEE J. Quantum Electron.*, vol. 30, pp. 2314–2318, 1994.

[13] M. Y. A. Raja, S. R. J. Brueck, M. Osinski, C. F. Schaus, J. G. McInerney, T. M. Brennan, and B. E. Hammons, "Resonant periodic gain surface-emitting semiconductor lasers," *IEEE J. Quantum Electron.*, vol. 25, pp. 1500–1511, 1989.

[14] L. Mandel and E. Wolf, *Optical Coherence and Quantum Optics*. New York: Cambridge Univ. Press, 1995, sec. 4.3.3.

[15] I. S. Gradshteyn and I. M. Ryzhik, *Table of Integrals, Series, and Products*, 5th ed. New York: Academic, 1994, sec. 3.958.

[16] K. H. Drexhage, "Interaction of light with monomolecular dye layers," in *Progress in Optics*, E. Wolf, Ed. Amsterdam, The Netherlands: North-Holland, 1974, vol. 12.

[17] D. G. Deppe, "Gain mechanism of the vertical-cavity surface-emitting semiconductor laser," *Appl. Phys. Lett.*, vol. 57, pp. 1721–1723, 1990.

[18] J. V. Sandusky and S. R. J. Brueck, "Correction to the half-wave spacing for resonant periodic-gain structures," in *SPIE, Application and Theory of Periodic Structures*, San Diego, CA, 1995, vol. 2532–2548, pp. 182–191.

[19] D. L. Huffaker, J. Shin, and D. G. Deppe, "Lasing characteristics of low threshold microcavity lasers using half-wave spacer layers and lateral index confinement," *Appl. Phys. Lett.*, vol. 66, pp. 1723–1725, 1995.

[20] A. E. Siegman, *Lasers*. Mill Valley, CA: University Science Books, 1986.

[21] T. Zhang, J. G. Wohlbier, K. D. Choquette, and N. Tabatabaie, "Microcavity vacuum-field configuration and the spontaneous emission power," *IEEE J. Select. Topics Quantum Electron.*, vol. 1, pp. 606–615, 1995.

J. V. Sandusky, photograph and biography not available at the time of publication.

S. R. J. Brueck (S'71–M'71–SM'89–F'93), photograph and biography not available at the time of publication.

Visualization of the nonlinear optical space-charge region of bulk thermally poled fused-silica glass

Thomas G. Alley

Center for High Technology Materials and Department of Physics and Astronomy, University of New Mexico, Albuquerque, New Mexico 87106

S. R. J. Brueck

Center for High Technology Materials and Departments of Physics and Astronomy and Electrical and Computer Engineering, University of New Mexico, Albuquerque, New Mexico 87106

Received March 31, 1998

We etched thermally poled fused-silica coverslips in 49% HF for 30 s transverse to the poling direction to reveal structural details of the nonlinear region. A peaked ridge below the anode surface, corresponding to a slower etch rate than that of the bulk SiO_2, was located ~5 μm below the anode surface for a poling time of 30 s. The ridge moved deeper into the glass logarithmically with poling time. This trend is qualitatively consistent with a recent model for the formation of the space-charge region that includes injection of hydrogen ions at the anode surface. © 1998 Optical Society of America

OCIS codes: 160.2750, 190.0190, 190.4160, 190.4400, 190.4370.

When fused-silica bulk glasses,[1] waveguides,[2] or optical fibers[3,4] are electrically poled at an elevated temperature, a large second-order nonlinearity with a $\chi^{(2)} \sim 1$ pm/V can be established in a thin (~10-μm-wide) region near the anodic surface. This phenomenon is of great interest for applications such as electro-optic modulation and nonlinear frequency conversion. The extent and distribution of this nonlinear region have been subjects of several investigations. Myers and co-workers,[1,2] using repeated etching and second-harmonic (SH) measurements, reported that the region was ~4 μm wide and peaked at the surface for 15-min poling and extended to ~8 μm for 2-h poling. Kazansky *et al.*[5] probed the nonlinearity with a laser beam focused across the side of a poled sample and found the peak of the SH signal at 12 μm below the surface. Kazansky *et al.*[6] measured charge distributions in thermally poled silica glass with a laser-induced pressure-pulse probe and found regions of alternating charge at the anode. Pureur *et al.* recently found, using a prism-assisted Maker-fringe technique, that the peak of the nonlinearity is located below the anode surface at a depth that is dependent on poling temperature and voltage.[7]

Margulis and Laurell[8] measured the regions of bulk glass that are affected by the poling process by using an interferometer to monitor HF etch rates continuously. Poled regions were etched more slowly than unpoled regions. After they poled for 225 min, Margulis *et al.* found a negatively charged region that was 5.5 μm deep along with a positively charged region that was 34 μm deep.

The correlation among the etch rates and the local fields, charges, and structural changes in the glass has not been elucidated completely. Agarwal and Tomozawa[9] found that an increase in etch rate was correlated with an increase in the glass's fictive temperature, applied hydrostatic pressure, and compressive stress. They postulated that the increased etch rate corresponds to a decrease in the average Si–O–Si bond angle that leads to higher reactivity. Carlson *et al.*[10] showed that an ionic depletion region in glass was more resistant to HF than untreated glass. Lesche *et al.*[11] attributed an observed field dependence of the etch rate to partial orientation of the HF molecules.

We report a study of HF etching transverse to the poling direction to reveal a cross section of the nonlinear region of thermally poled glass. Coverslips of flamed-fused Heraeus T08 fused silica [~1 part in 10^6 (ppm) Na, 100 ppm OH] were thermally poled at 275 °C and 4.3 kV in an ambient atmosphere. The 170–180-μm-thick coverslips were placed atop soda-lime glass (microscope slide) current limiters, which were in turn placed atop Al foil cathodes. Al foil anodes were placed in contact with the top surfaces of the coverslips. The field was turned on once the sample reached a steady temperature of 275 °C. At the end of the designated poling period, the oven door was opened and the sample was allowed to cool while the voltage was applied. The samples cooled from 275 to 200 °C in 1 min, by which time the current level typically decreased by at least an order of magnitude. We checked the SH nonlinearity by placing the samples into a Q-switched Nd:YAG laser beam (1.06 μm) and measuring the SH signal at 532 nm. All samples reported here, regardless of poling time, yielded similar levels of SH generation within a standard deviation of ~14%.

After poling, we broke the samples to expose a cross section of the nonlinear region. This usually resulted in a relatively smooth surface, although the side under compression during breaking (the cathode) was often marred by compression fractures. The samples were then immersed in 49% HF acid for 30 s. After they were rinsed, the samples were viewed with an optical microscope or profiled with an atomic force microscope (AFM).

The etching profile varies somewhat along the sample as seen in Fig. 1 (for a sample poled for 30 s). The ridges are indicative of a slower HF etch rate than that of the rest of the sample and are typically

0146-9592/98/151170-03$15.00/0 © 1998 Optical Society of America

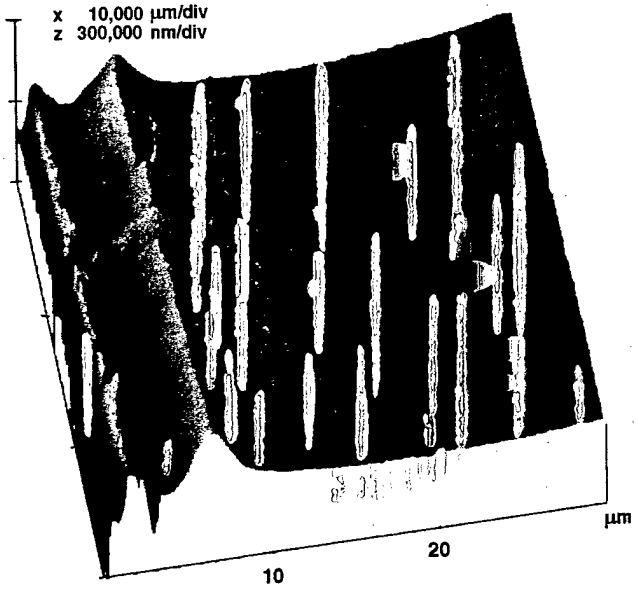


Fig. 1. AFM image of a poled fused-silica coverslip (T = 275 °C, V = 4.3 kV, $t \sim 30$ s) etched transversely to the poling direction. The anode was at the left edge. Two ridges (regions of slower etch rates) are evident, one within approximately 1 μm of the anode edge and a second, higher ridge ~5 μm deep. The vertical scale is 400 nm/division.

200–300 nm high. The typical bulk etch rate is 300–400 nm per 30 s in 49% HF. The depth into the sample of the first ridge varies significantly from position to position along the cross section. The position of the second ridge shows a quite-consistent trend with poling time, as seen in Fig. 2. The data points shown in the inset are taken from a single sample on which three ITO electrodes were deposited with a 3-mm interelectrode spacing. The 4.3-kV poling voltage was applied to each electrode for a different time period. There was a slight current leakage to the other electrodes, but the resultant voltages were small (~100 V) compared with the 4.3-kV poling voltage. The second peak moves deeper into the sample roughly logarithmically with poling time. Other samples from a different glass supplier showed significantly increased inhomogeneity and much less well-defined behavior, even though the SH signals were comparable for both types of glass. An unpoled coverslip was also etched; the result was featureless, with no observed deviations from the bulk etch rate.

Figure 2 also shows the same trend for several different samples with different poling periods. Each data point represents an individual sample. Again, the logarithmic trend of ridge depth with poling time is clear. A straight-line fit to the logarithm of the poling time is shown, as well as a model calculation of the space-charge-depletion edge depth. This model, described more fully in Ref. 12, is based on injection of slow hydrogenated ions[13] (e.g., H_3O^+) into a high-field negatively charged region at the anode that was depleted of more-mobile Na^+ ions. The model allows the two ionic carriers to have drastically different mobilities. Based on current measurements, shown in Fig. 3, and observations of multiple poling effects, the mobilities used in the model calculation were $\mu_{Na} = 7.5 \times 10^{-11}$ cm^2 V^{-2} s^{-1} and $\mu_H = 5 \times 10^{-4}\ \mu_{Na}$. For these parameters a depletion regions forms quickly (~1 to 2 min), followed after a much longer time by formation of a positively charged region of excess H^+ ions under the surface. As can be seen in Fig. 3, the model provides a rough qualitative fit to the data. The flattening in the middle of the model curve corresponds to the establishment of the depletion region. We took current measurements to monitor the space-charge relaxation; Fig. 3 shows one result. The increase

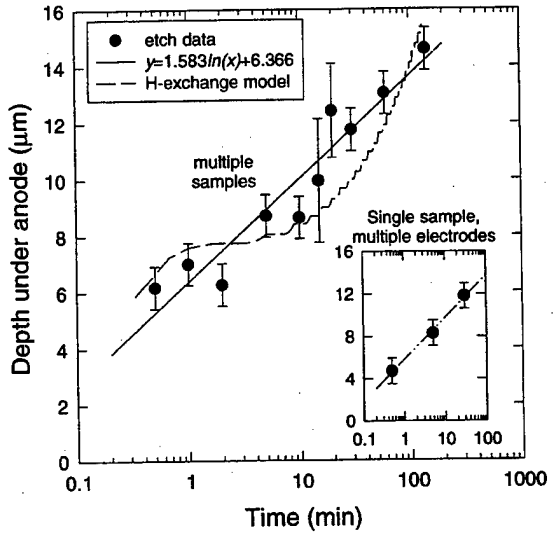


Fig. 2. Depth of the second ridge below the anode as a function of poling time. The three points in the inset correspond to a single sample with varying poling times on isolated electrodes. The main set of points corresponds to separate samples poled for varying times. The fit to a simple logarithmic time dependence is shown for both data sets, as is the result of a model that invokes motion of a fast ionic species (Na^+) at short times, which corresponds to the current variation shown in Fig. 3 and to charge exchange with a much less mobile ionic species (possibly H_3O^+) at longer times.

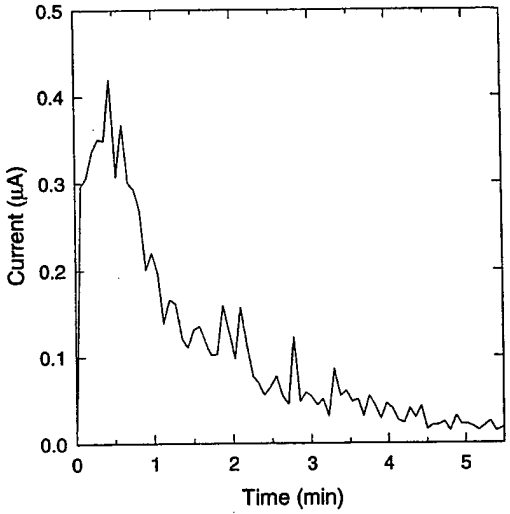


Fig. 3. Current versus time, showing depletion-region formation. The spikes result from surface arcing.

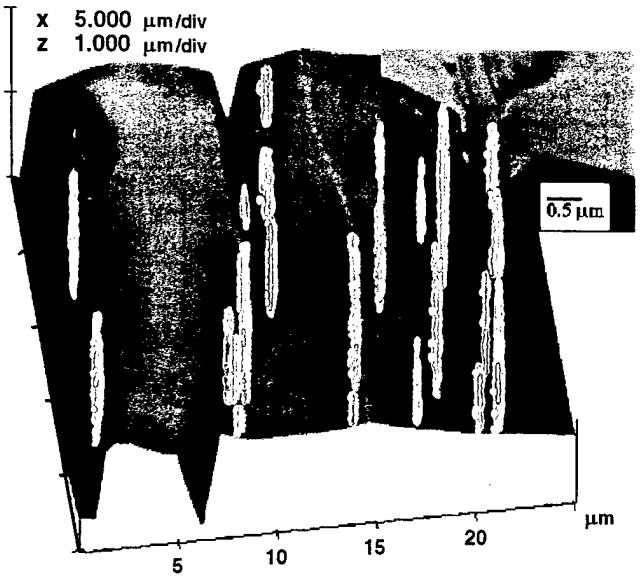


Fig. 4. AFM image of a poled fused-silica coverslip (T = 275 °C, V = 4.3 kV, $t \sim 140$ min). The second ridge has moved relatively uniformly to a depth of ~14 μm. The depth of the first ridge is much less uniform, varying from ~3 to 7 μm. A narrow, deep groove has formed between the two ridges. The cross section of the ridge is shown in the inset scanning electron microscope image.

in current in the first half-minute most likely is due to initial impurity distributions at the surface. The ~2-min decay of the current corresponds to the formation of a space-charge region. The observation that the second ridge continues to move deeper into the sample for times beyond that required for space-charge formation is strong evidence that positive charge injection continues at the anode. Since the SH signals are not changing substantially during this evolution, the nonlinear susceptibility is clearly varying dramatically.

The ridges represent a decreased etch rate compared with that of the bulk glass. It is possible that the typical etch profile reflects the high-electric-field profile that is present in the space-charge region. We should caution that in the case described in Ref. 11, the electric field was normal to the etched surface, whereas in the present case the electric field is parallel to the etched surface. If the etch profile is indicative of the internal field, the presence of two ridges is evidence for two negatively charged depletion regions separated by a positively charged or neutral region. It is also possible that the local field or the sign of the local charge causes structural stress, changing the bond angles and reactivity.

Other significant subfeatures were observed on all samples poled for ~60 min or longer. As can be seen in Fig. 4, for a sample poled for 140 min, an ~0.75-μm-deep narrow channel forms, reflecting a substantially increased etch rate. The channel is always located between the two ridges, yet its position varies along the sample, making a quantitative analysis difficult. The inset shows a cross-section scanning electron microscope image of the channel. The channel seems too narrow to reflect an electric-field variation and is more likely indicative of compressive stress[9] or a localized defect accumulation.

This experiment provides, for what is believed to be the first time, a spatially resolved visualization of the nonlinear region in thermally poled fused silica through cross-sectional HF etching. A ridge corresponding to a decreased etch rate moves deeper into the sample logarithmically with poling time, which is qualitatively consistent with the predictions of a recent hydrogen-ion-exchange model for the development of the depletion region. The ridges may reflect the electric-field profile in the glass, but the observation of a channel with an increased etching rate for extended poling times suggests that more-complicated effects are also occurring. Notably, this measurement demonstrates that the extent and hence the strength of the second-order nonlinear susceptibility [$\chi^{(2)}$] is varying significantly with poling time even though the SH signals are not. This result is consistent with the electric-field-induced nonlinearity models that predict that $\chi^{(2)}$ is proportional to E, and thus the SH signal is proportional to $(\int E\mathrm{d}x)^2 \sim V^2$.

Partial support for this work was provided by the U.S. Air Force Office of Scientific Research. T. G. Alley acknowledges the sponsorship of the U.S. Air Force Research Laboratory. The authors thank D. Keller for his assistance with the AFM measurements.

References

1. R. A. Myers, N. Mukherjee, and S. R. J. Brueck, Opt. Lett. **15,** 1733 (1991).
2. R. A. Myers, X. C. Long, S. R. J. Brueck, and R. P. Tumminelli, Electron. Lett. **31,** 1604 (1995).
3. X. C. Long and S. R. J. Brueck, IEEE Photon. Technol. Lett. **9,** 767 (1997).
4. P. G. Kazansky, P. St. J. Russell, and H. Takebe, J. Lightwave Technol. **15,** 1484 (1997).
5. P. G. Kazansky, A. Kamal, and P. St. J. Russell, Opt. Lett. **18,** 1141 (1993).
6. P. G. Kazansky, A. R. Smith, P. St. J. Russell, G. M. Yang, and G. M. Sessler, Appl. Phys. Lett. **68,** 269 (1996).
7. D. Pureur, A. C. Liu, M. J. F. Digonnet, and G. S. Kino, in *Bragg Gratings, Photosensitivity, and Poling in Glass Fibers and Waveguides: Applications and Fundamentals,* Vol. 17 of 1997 OSA Technical Digest Series (Optical Society of America, Washington, D.C., 1997), p. 302.
8. W. Margulis and F. Laurell, Opt. Lett. **21,** 1786 (1996).
9. A. Agarwal and M. Tomozawa, J. Non-Cryst. Solids **209,** 166 (1997).
10. D. E. Carlson, K. W. Hang, and G. F. Stockdale, J. Am. Ceram. Soc. **57,** 295 (1974).
11. B. Lesche, F. C. Garcia, E. N. Hering, W. Margulis, I. C. S. Carvalho, and F. Laurell, Phys. Rev. Lett. **78,** 2172 (1997).
12. T. G. Alley, R. A. Myers, and S. R. J. Brueck, in *Bragg Gratings, Photosensitivity, and Poling in Glass Fibers and Waveguides: Applications and Fundamentals,* Vol. 17 of 1997 OSA Technical Digest Series (Optical Society of America, Washington, D.C., 1997), p. 293.
13. G. Hetherington, K. H. Jack, and M. W. Ramsay, Phys. Chem. Glasses **6,** 6 (1965).

ELSEVIER

Journal of Non-Crystalline Solids 242 (1998) 165–176

JOURNAL OF NON-CRYSTALLINE SOLIDS

Space charge dynamics in thermally poled fused silica

Thomas G. Alley [a,1], S.R.J. Brueck [a,b,*], Richard A. Myers [a,2]

[a] *Center for High Technology Materials and Department of Physics, University of New Mexico, Albuquerque, NM 87106, USA*
[b] *Department of Electrical and Computer Engineering, University of New Mexico, Albuquerque, NM 87131, USA*

Received 9 February 1998; received in revised form 27 July 1998

Abstract

Measurements of the transient behavior of both the second-harmonic generation signal and the poling current for type-II fused silica samples under a variety of poling histories are reported. The applied voltage was switched between +5 kV, 0 V, and −5 kV with the sample maintained at 275°C. Observations include: multiple time scales (seconds to minutes) for development of the non-linearity depending on the poling history; a transient second-harmonic signal on the new cathode side of the sample following voltage reversal; and hysteretic incubation intervals before growth of the non-linearity. These observations are incompatible with the usual single mobile ion (e.g. Na^+) model for establishing the strong local electric field that leads to the non-linearity. An expanded model including ion-exchange between a high mobility ion (as Na^+) and a much lower mobility ion (related to H^+) provides a good qualitative fit to the experiments. © 1998 Elsevier Science B.V. All rights reserved.

PACS: 42.70.Ce; 42.65.Ky; 77.22.Jp; 72.80.Ng

1. Introduction

Silica-based glass optical fibers dominate optical communications. Passive devices such as Bragg grating filters are finding increasing application in telecommunications systems and are particularly important for evolving wavelength-division-multiplexed (WDM) architectures. Active, electrically tunable waveguide and fiber devices based on a second order non-linearity ($\chi^{(2)}$) in SiO_2 would find important systems applications.

Amorphous SiO_2 normally has a macroscopic inversion symmetry that, in the electric dipole approximation, forces $\chi^{(2)}$ to zero. Myers et al. found that a large, permanent $\chi^{(2)}$ (~1 pm/V) can be created by high-voltage (~5 kV) poling of a bulk fused silica sample at ~250°C (thermal poling) [1]. While observation of this non-linearity has since been extended to thin-films and fibers [2–4] a complete understanding of the mechanisms underlying the formation of the non-linearity has yet to be achieved. In an earlier paper, we proposed the following mechanism: (i) charge transport of mobile cations (e.g. Na^+) through the glass toward the cathode; (ii) formation of an anodic space-charge region of width $w_0 = \sqrt{2\varepsilon V/eN}$ (with ε the dielectric constant, V the applied voltage, e the magnitude of the electronic charge and N the Na density); (iii) resulting in a large, static electric field

* Corresponding author. Tel.: +1-505 272 7800; fax: +1-505 272 7801; e-mail: brueck@chtm.unm.edu.
[1] Present address: Laser Division, Air Force Research Laboratory, Albuquerque, NM 87117, USA.
[2] Present address: Radiation Monitoring Devices, Inc., Waterton, MA 02172, USA.

0022-3093/98/$ – see front matter © 1998 Elsevier Science B.V. All rights reserved.
PII: S0022-3093(98)00788-1

$[E_{dc} = qN(w_0 - x)/\varepsilon; x \leqslant w_0]$) peaked at the anode surface; and (iv) fixing of these charge and field distributions on cooling with the field applied [1]. In bulk fused silica the primary charge transport is via sodium ions (Na^+). In high-purity deposited glass thin films and in fibers, other cations may play a similar role. The strong electric field breaks the centrosymmetry and an effective $\chi^{(2)}$ is established via the third order susceptibility:

$$\chi^{(2)} = 3\chi^{(3)}E_{dc} \tag{1}$$

and/or the orientation of dipoles [5]

$$\chi^{(2)} \propto \frac{\beta pME_{dc}}{5kT}, \tag{2}$$

where β is the hyperpolarizability, p is the dipole moment, M is the density of dipoles, k is Boltzmann's constant, and T is the temperature. In either case, $\chi^{(2)}$ is proportional to E_{dc}. Most experiments have used the second-harmonic (SH) signal to measure the non-linearity. As has been confirmed in a number of experiments [6,7], the SH power is proportional to the square of the integrated electric field as long as the scale length is less than the glass SH coherence length, l_{coh}:

$$P_{SHG} \propto \left| \int E_{dc} e^{2\pi i x/l_{coh}} dx \right|^2 \approx \left| \int E_{dc} dx \right|^2 \propto V^2. \tag{3}$$

While this single carrier model explains many of the experimental observations, there are also a number of incompatible experimental observations. Included are the detailed spatial distribution of the non-linearity, the observation of multiple time scales for the poling, and the dependence of the non-linearity on the sample thermal poling history. Below we report additional observations including a transient cathodic non-linearity that are also inconsistent with the single carrier species model. To resolve these discrepancies we propose an additional charge transport associated with the establishment of the large E_{dc}, namely, ion exchange associated with water or another mobile cation. The time scale for hydrogen transport ($\sim$ hours) is much longer than that for Na (<1 min), leading to the observed multiple time scales and the dependence on the sample history. These observations and the resulting charge exchange model are detailed below along with a discussion of the considerable literature concerning H^+ charge transport in silica-based glasses.

1.1. The depletion layer/space charge region

There is a great deal of evidence supporting the establishment of a negatively charged, depletion region in poled silicate glasses. Early measurements of a space charge region in fused silica and other glasses used imbedded foil voltage probes [8,9]. A majority of the applied potential appeared across a thin anodic region. A space-charge layer depleted of alkali ions with a corresponding high electric field is observed in field-assisted glass-to-metal sealing in borosilicate glasses [10–12]. A sodium and calcium depleted region was measured in soda–lime glass after dc poling [13,14]. He et al. [15] modeled the development of the space charge region in glasses under room temperature and low applied potential conditions (1–10 V), finding results consistent with our initial single carrier model.

1.2. Spatial extent and structure of the non-linear region

Generally, the thermal poling non-linearity has been found in a 5–20 μm thick region underneath the anode. Several experiments have provided additional information on the location of the space charge region and the non-linearity showing that there is more than just a simple, uniformly negatively charged region. Kazansky and Russell used a focused laser to probe the non-linear layer and observed that the non-linearity peaked 12 μm below the anode surface with a 7 μm spatial extent [16]. Kazansky et al. [17] measured charge distributions in thermally poled silica glass via a laser induced pressure pulse probe (LIPP) technique and found regions of alternating charge below the anode. They postulated the formation of real space charge layers and dipole polarization. Using an HF etching technique, Margulis et al. measured the regions of glass effected by the poling process [18]. For a long poling time of 225 min, they found a 5.5 μm deep region which they associated with negative charge, as well as a region out to 34 μm associated with a weak excess of positive charge.

Myers et al. found that long poling times extended the space charge region further into the glass [1,6]. By repeated etching of 1.6 mm thick poled samples, followed by SH measurement, they found that the depth of the non-linearity was greater for a sample poled for 2 h. (SH reduced to 10% at 8 μm etch depth) compared to one poled for 15 min (SH reduced to 10% at 3.5 μm etch depth). Pureur et al. have recently shown, using a prism-assisted Maker-fringe technique, that the peak of the non-linearity is located below the anode surface with a depth dependent on poling temperature and voltage [19]. Takebe et al. compared samples poled in laboratory air versus samples poled in vacuum. Because of differences in measured SH levels, they concluded that an atmospheric molecular species was affecting the formation of the non-linearity [7].

1.3. Field-assisted ion exchange

Ion exchange is a standard method of making optical waveguides in glasses [20,21]. Application of an external field can enhance this exchange as analyzed theoretically by Abou el Leil and Cooper [22]. Their charge exchange model was developed for borosilicate and soda–lime silicate glasses, which typically have much higher concentrations of ionic species (e.g. 10^{21} cm^{-3}) than does fused silica ($\sim 10^{16}$ cm^{-3}). The model is based on a quasi-neutral approximation which assumes that the sum of the densities of the two ionic species is a constant, independent of position, during the exchange process and hence that the applied electric field is uniform across the sample. Oven et al. [23] showed that this quasi-neutrality model was a good approximation and evaluated an example for $M = 1/3$ (As we show below, this quasi-neutrality assumption is inappropriate if the mobilities of the exchanged ions are very different as in the case of Na^+ and H^+ in fused silica ($M \sim 10^{-4}$) when the model must be modified to include the non-negligible voltage drops across the boundary region between the charge carrier concentration fronts and the slow carrier drift region.)

When fused silica is thermally poled, interaction with the atmosphere or with a hydrated surface can result in a field-assisted ion-exchange process. If an ionic species is present at the fused silica surface, the space charge region does not form as simply as in the single carrier model. A space charge develops under poling [24], but it is dynamic [6,25] and evolves on the time scale of the slow carrier. A possible cause of the observed dynamic behavior is that moisture is injected into the sample in the form of a hydrogenated species such as H^+ or H_3O^+. The hydrogenated ions are produced by high field ionization at the anode surface, or from field-assisted evolution of OH bonds into H_3O^+ [26,27].

1.4. Sodium mobilities

Reported values for Na^+ mobility in different glasses, including fused silica, vary greatly. Stagg measured a sodium mobility of 5×10^{-7} cm^2 V^{-1} s^{-1} in SiO_2 films at 250°C [28]. Page et al. gave a mobility of 2×10^{-9} cm^2 V^{-1} s^{-1} in soda–lime glass [29]. Schaeffer et al. found that the mobility of sodium ions was lowest for high OH-containing SiO_2 [30]. Interpolating data gathered from Drury and Roberts [31] leads to a value at 400°C of approximately 3×10^{-11} cm^2 V^{-1} s^{-1} for fused silica with 150 ppm OH (e.g. Herasil) and 3×10^{-9} cm^2 V^{-1} s^{-1} for fused silica with 10 ppm OH (e.g. Infrasil). By examining the rise time of the SH signal, Myers calculated an effective Na mobility in fused silica (Optosil) of $\sim 10^{-10}$ cm^2 V^{-1} s^{-1} at 250°C, assuming a space charge density of 10^{16} cm^{-3} [6]. Shin and Tomozawa have recently reported extensive measurements of conductivities in fused silica [34]. Interpolating to 270°C from their data for type II fused silica, and assuming a 1 ppm carrier concentration, gives a mobility of $\sim 5 \times 10^{-10}$ cm^2 V^{-1} s^{-1}. Our recent measurements, again for a 1 ppm concentration, have shown a sample-dependent range of mobilities from 10^{-11} to 5×10^{-9} cm^2 V^{-1} s^{-1}. This range could be due to variations in either ionic or total impurity concentrations and distributions.

1.5. Hydrogen in many forms in fused silica

Fused silica is classified into four types depending on the method of formation and the water content. Two of these classifications, type II and III, are 'wet' silicas, with a large content of OH,

usually present on the order of 100–1000 ppm. The reported ionic mobility of hydrogen also varies, depending on the bonding configuration and the presence of aluminum impurities. Hydrogen can exist in at least four bonding configurations: as interstitial molecular water, as ions bound at SiOH sites, as loosely bound ions at reduced SiOAlOH sites, and as tightly bound ions at aluminosilicate sites (SiOH–Al) [26,32–38].

1.6. Hydrated glass surfaces

It is known that silica surfaces and films become hydrated when exposed to water. Many authors have reported measurements of water diffusion in silica glass as a function of temperature and time [35,37]. The diffusion process is explained by molecular water diffusing into the glass and then reacting with the SiO_2 network to make OH groups followed by structural relaxation.

Yamamoto and Namikawa [26,27] showed that glass surfaces are much more hydrated than the bulk. They attributed reversible changes in conductivity of both synthetic (type III) and flame fused (type II) silicas on heat treatment to changes in the OH content of hydrated surface layers. They postulated that these effects resulted from shifts in the chemical equilibrium between the water and the glass silicon–oxygen bonds.

1.7. Hydrogen injection and transport

Krieger and Lanford [13] as well as Lepienski et al. [14] submitted soda–lime glass to a dc potential and used nuclear reaction analysis to determine hydrogen profiles after treatment. Soda–lime glass is much more conducting than fused silica due to its large concentration of ionic species such as sodium (~16 wt%), however a depletion region still forms. Both groups found the type of electrodes used were important in determining hydrogen ion exchange. Krieger and Lanford found hydrogen pile-up at the edge of the sodium depletion region. For non-hydrogen-blocking electrodes, there was an ion exchange with substitution of hydrogen for sodium near the anode region. Lepienski et al. found that etching the surface of the glass prior to poling made a significant difference in the hydrogen profile concentration, implying that the surface already contained excess hydrogen. They also found differences in the profiles for samples with deposited versus 'contact/pressed-on' electrodes. Contact electrodes allowed a continual hydrogen ion exchange, presumably from external surface moisture, whereas the deposited electrodes only allowed movement of hydrogen already present near the surface.

Hetherington et al. observed high temperature (800°–1300°C) electrolysis in fused silica and concluded that protons were injected through atmospheric moisture present at Pt electrodes [38]. The movement of hydrogen was much slower than sodium. Hetherington et al. extrapolated available literature data and gave a mobility ratio $M \sim 10^{-4}$ between hydrogen and sodium in fused silica. Lanford et al. [39] found that the best fit to data taken on diffusion (without field-assistance) of hydrogen and sodium in soda–lime glass at 90°C was $M \sim 10^{-3}$. This large difference in mobilities makes this ion exchange process quite different from a traditional field-assisted ion exchange. Qualitatively this is simple to understand, a space charge region will form increasing the local electric field to equalize the velocities (μE) of the two species. Because the field required is large for $M \ll 1$, a substantial portion of the applied voltage is dropped across the depletion region and/or the low mobility drift region, decreasing the field applied to the fast ions. In conventional ion-exchange experiments, the ionic mobilities are comparable and the exchange region is much thinner than the sample so that the field in the bulk region is unaffected.

Carlson studied proton injection and presented electrical-conduction and IR absorption data in soda–lime silicate glass [40] showing field-assisted ion exchange of protons and an ion-depletion region. Abou el Leil and Snitzer investigated field-assisted ion exchange in type III fused silica using alkali-containing electrodes and concluded that the exchange was protons or a hydrogenated species exchanged for alkali ions [41]. Ernsberger emphasized that hydrogen is diffused and transported into glass only as an oxygenated species such as molecular water or hydronium (H_3O^+),

and not as a bare proton ion [42,43]. Lanford et al. showed a three for one replacement of hydrogen atoms for Na atoms in soda–lime glass, implying that hydronium was the mobile species [39]. Nogami and Abe found that proton conduction in a 'wet' silica (sol–gel) glass is 'water-cooperative' with the conduction process described by protons hopping between hydroxyl and water molecules, and the activated state again being H_3O^+ [44]. Several other observations on proton transport and diffusion in vitreous silica have been reported [45–47].

2. Experimental procedures

Dynamic measurements were carried out in situ with an electric field applied to the heated sample as shown in Fig. 1 [5,25]. To control the poling atmosphere, the sample was placed in a chamber with a quartz window. The sample was heated and laser light (a CW mode-locked Nd:YAG laser with $\lambda = 1.06$ μm, ~200 ps pulses, repetition rate 82 MHz, chopped at a 50% duty cycle) was focused onto the top surface. The focal spot diameter was ~50 μm with an average power density of ~10 kW/cm^2. Observations were through a deposited, transparent indium-tin-oxide (ITO) electrode. The sample thickness (5–10 mm) was much greater than the optical depth-of-focus (~300 μm) so that only a single surface region of the sample was probed. The optical path includes transmission through the sample, reflection from a polished Si wafer used as the bottom electrode, and retransmission through the sample. After appropriate filtration, a photomultiplier was used to detect the SH light. The voltage applied to the electrodes (ITO and Si wafer) could be switched in polarity or shorted, on a time scale of ms, using vacuum relay switches. Applied voltages were limited to ±5 kV to avoid electrical breakdown in the atmospheric pressure ambient. An electrometer was connected between the Si electrode and ground to monitor the current through the sample. Current due to surface conduction was minimized by using large samples compared with the ITO electrode dimensions and by careful cleaning of the samples; a guard electrode was not used. The currents observed on switching polarities were much larger than in the steady-state, suggesting that surface conduction effects were minimal.

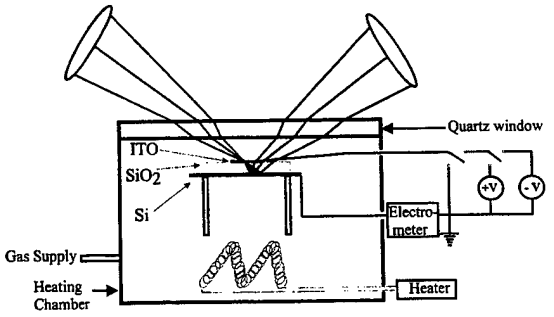


Fig. 1. In situ arrangement for measuring SH signal and electrical current during formation of the second-order nonlinearity in fused silica.

3. Results

3.1. Dynamic behavior and shortfalls in the single charge carrier model

The dynamic behavior of the electrical current and SH signal is shown in Fig. 2 for a fixed temperature of 275°C. At least two time scales are apparent. When the sample is poled for the first time (+5 kV; SH from the anode side), there is first an incubation period of ~4 min during which the current is relatively large and unchanging and there is no observed SH signal. As the current decreases over a period of several tens of minutes (as a result of the formation of a blocking space-charge region), the SH signal grows for this 6 mm thick sample (commercial grade type II silica). (The step in the current at about 22 min is an artifact and should be ignored.) On shorting the sample (not shown), both the current and the nonlinearity fall rapidly on a time scale of 10s of seconds rather than minutes. Fig. 2 also shows the current and SH signals upon reapplying a voltage of the same polarity to the sample. Both the current and the SH respond on the ~10 s time scale, comparable to the fall times and much faster than the original poling. After the rapid response there is a continuing slow rise in the SH signal accom-

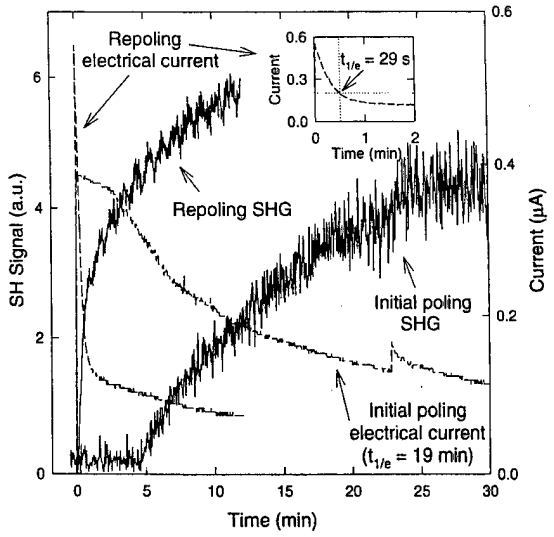


Fig. 2. Multiple time scales are observed for repeated poling/depoling cycles. The initial poling shows an incubation period preceding a slow SH growth, while the current decays over 10's of minutes. On repoling (following a short circuit to ground) the SH signal rises rapidly and the current falls sharply over 10s of seconds before reverting to the slow time scale. The discontinuity in the initial poling current at about 22 min is an experimental artifact and should be ignored.

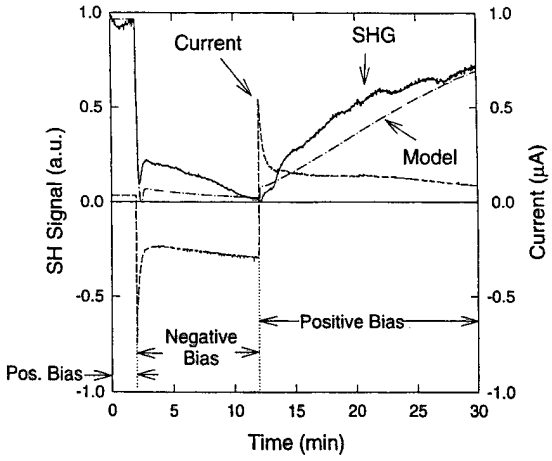


Fig. 3. Effect of field reversal on SH signal and electrical current in 6 mm thick type II fused silica. Voltages applied were ±5 kV at ~275°C. The curve labeled model is a simulation result as discussed in the text.

panied by a fall in the current on the original time scale of 10s of min.

A transient SH signal under the new cathode following voltage reversal, as seen in Fig. 3, is another effect that cannot be explained by the single carrier model. Here, the sample has been prepared for a long poling time at a positive bias establishing a steady-state SH signal and the current has dropped to low levels. The bias is then directly switched from +5 to −5 kV. The SH signal at the new cathode drops towards zero and then rises again on the fast time scale (10s of s) while a rapid current transient is observed. The SH signal then decays towards zero on the 10 min time scale while the current rises. This SH signal is evidence of a significant voltage drop occurring under the new cathode that is inconsistent with the single carrier model. Finally, the polarity of the applied voltage is again switched. There is a rapid (10 s time scale) current transient followed by a slow steady decay. The SH signal does not show any structure on the fast time scale but grows during the current decay at the long (10 min time scale) of the original poling (cf. Fig. 2). Note that this observation may explain some of the puzzling reports [48,49] of surface and bulk poling regimes. If the sample charge distribution is frozen while a SH region is present on both sides of the sample, a Maker-fringe experiment will show fringes with a period consistent with volume (bulk) poling.

Another interesting feature is observed with field reversal. Often, but not always, when the field is reversed, there is a delay before SH signal growth, similar to the incubation period observed in connection with the original poling. A level of current substantially higher than after space-charge formation accompanies this incubation period. An example of this is seen in Fig. 4. Prior to this poling with positive bias, the sample had undergone poling with an applied voltage of −5 kV on the ITO electrode for ~90 min. After the poling with negative bias, the sample was cooled to room temperature and reheated after several hours without any applied voltage. As the figure shows, on applying a +5 kV bias, there was a period of about 20 min when the current was high. Only after this charge movement is complete does the space charge region form and the SH signal appear. We have observed a correlation between the duration poling is maintained at the reverse bias

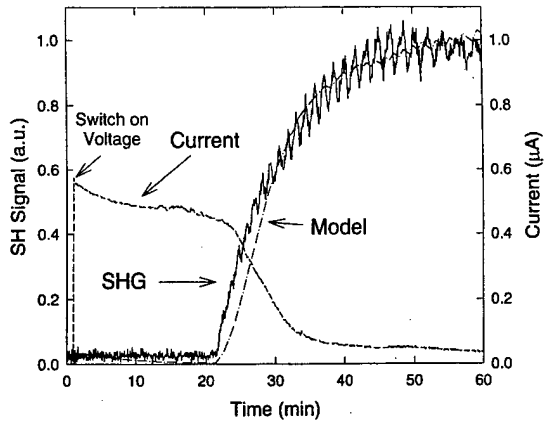


Fig. 4. Delay of growth (incubation period) of SH for a 6 mm type-II fused silica sample poled at +5 kV. The sample had been previously poled for ~90 min at −5 kV. The model is shown for qualitative comparison, see text for details. The ripples in the SH signal are frequently, but not always, observed.

and the length of this incubation period, with saturation of the incubation time for long reverse polings. A similar conductivity plateau before space charge formation has been observed in experiments done at much lower voltages and is called the dc conductivity level [24].

Significant experimental observations include: (1) a SH signal under a new cathode following field reversal, implying a space charge region; and (2) the multiple time scales for signal formation. These observations have led us to extend the transport model for fused silica poling.

4. Model

4.1. Brief review of the single carrier model

When fused silica is thermally poled, the field in the space charge region can be quite large. For a first estimate, the field strength (E_{dc}) and space charge width (w_0) can be calculated following Von Hippel et al. [5], assuming a single ionic carrier. The electric field is given by

$$E_{dc} = \frac{eN}{\varepsilon}(w_0 - x)\ 0 < x < w_0 = 0 \quad x > w_0, \qquad (4)$$

where

$$w_0 = \sqrt{2\varepsilon V/eN}.$$

The fixed charge density N, associated with immobile non-bridging oxygen hole centers (NBO^-), is equal to the mobile Na^+ density of $\sim 2 \times 10^{16}$ cm^{-3} for type II silica [51]. This gives $w_0 \sim 10$ μm and a peak electric field of $E_{dc} \sim 1 \times 10^7$ V cm^{-1} at the surface for $\varepsilon = 3.8\varepsilon_0$. This peak electric field approaches the nominal fused silica breakdown field strength, $\sim 3 \times 10^7$ V cm^{-1} [51]. This depletion width is in qualitative agreement with typical results for the extent of the non-linearity [1,5]. The dynamics of the formation of the depletion region for the single mobile carrier model are described by [50]

$$w(t) = w_0 \tanh\left(\frac{t}{2\tau}\right), \qquad (5)$$

where $\tau = w_0 L/2\mu V$ and L is the sample width.

4.2. Assumptions and approximations for the multiple-carrier model

In order to describe the observed dynamic behavior of the second-order non-linearity, we postulate that the space charge region and associated high electric field are affected by injection of a second ionic species. Most likely, based on the work discussed above, this second species is associated with hydrogen (H^+ or H_3O^+) and will be denoted as H^+ below. Other species such as Ca^{++} or K^+ may also play a role.

Several assumptions are necessary to fit the experimental data:

1. We require a fast carrier (Na^+) to explain processes that occur on fast (~10 s) time scales.
2. A second, slower positive carrier (H_3O^+) is needed to explain slow (~10 min) processes.
3. The SH signal under the new cathode implies a voltage drop associated with a buildup of positive charge. A voltage drop will occur on field reversal *only* if the buildup leads to a positive charge accumulation in excess of the background charge density.
4. After field reversal, as the excess positive charge is pushed back out, the sodium ion movement is effectively blocked by the presence of the slow H^+ ions (channel stuffing);

i.e., the Na^+ motion is dependent on the H^+ concentration.

5. Interdiffusion during this blocking phase results in a mixture of hydrogen and sodium ion concentrations; the resulting mobility is between that of sodium and hydrogen ions.

4.3. Simplifications to the numerical computation

In general the current equation contains two terms, a field conduction term and a diffusion term

$$j = e\mu En + eD\left(\frac{\partial n}{\partial x}\right)$$

where e is the electronic charge, n is the ionic carrier concentration, and D is the diffusion coefficient, related to the mobility by the Nernst–Einstein relation $\mu = (eD/kT)$. The scale length L for which these two terms are approximately of equal importance can be estimated by combining this expression with Poisson's equation, viz.

$$\frac{kT}{e}\left(\frac{n}{L}\right) \approx nE \approx enNL/\varepsilon \Rightarrow L \approx L_D \approx \sqrt{\frac{\varepsilon kT}{e^2N}}. \quad (6)$$

L_D is the Debye length for screening an external field from a free carrier plasma. At a temperature of 275°C and a background charge density of 1 ppm, L_D is approximately 30 nm $\ll w_0 \sim 10$ μm, justifying the approximation $j = e\mu En$ which dramatically simplifies the numerical computations.

However, this approximation breaks down when the fields are reversed and the fast ions are blocked by the slow ions. In this situation, there is no net charge density and no variation in the local electric field and diffusion is the only active process. By neglecting diffusion we are forced to assume point #5 above. A more complete model would include diffusion and this intermixing and the intermediate mobility would arise naturally from the calculation.

4.4. Development of the model

The injection of hydrogen at the surface is described by the continuity equation,

$$\frac{\partial j}{\partial x} = -e\frac{\partial n_H}{\partial t} \quad (7)$$

along with the initial and boundary conditions,

$$n_{tot}(0 < x < d, t = 0) = 0 \qquad n_{tot}(x = 0, t) = +\eta_H, \quad (8)$$

where η_H, the charge density at the anode surface normalized to the initial Na^+ density, is an adjustable parameter that describes the injection of hydrogen ions. The hydrogen charge distribution, n_H, can be evaluated by using a simple backward differencing method provided E is known. The electric field is found from Poisson's equation:

$$E(x) = E_0 + \frac{e}{\varepsilon}\int_0^x n_{tot}(x')\,dx', \quad (9)$$

where the field at the surface, E_0, is determined by the circuit condition that the total voltage drop across the sample equals the applied voltage. If only the Na^+ ions are mobile, a further condition in the steady-state is that the field must go to zero at the edge of the depletion region, $E(x \geqslant w) = 0$, otherwise the Na^+ ions would continue to move to screen the field.

When a field is first applied the high mobility carriers respond initially and drift towards the cathode leaving behind a space-charge region that results in a high field region adjacent to the anode (as in the single carrier model). In response to this field, positive hydrogen ions are drawn into the depletion region with a charge distribution $n_H(x)$. The total charge density is given by $n_{tot}(x) = n_{Na}(x) + n_H(x) - N$.

4.5. Model results: unlimited supply of hydrogen

Fig. 5 shows the evolution of the total charge density distribution for an applied voltage of +5 kV assuming that there is a negligible space charge region at the cathode. Several poling times up to 10 min are shown for a 6 mm thick sample. For this example several parameters are fit to the experimental observations: μ_{Na} of 5×10^{-9} cm^2 V^{-1} s^{-1} (to fit the fast rise/fall times of 30 s, assumption 1); μ_H of 2×10^{-13} cm^2 V^{-1} s^{-1} (to fit the slow 20 min rise times, Assumption 2).

In order to be consistent with the experimental observation of a non-linearity under the cathode after field reversal, it is necessary to have a positive

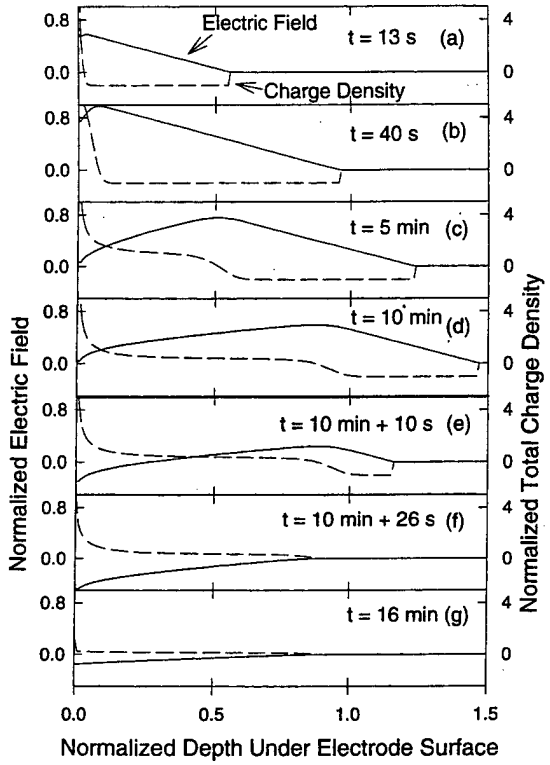


Fig. 5. Evolution under field reversal of the electric field and total charge density as Na^+ and H^+ redistribute. The depth and electric field are normalized to the steady-state values of the single carrier model. The total charge density is normalized to the background negative charge density. (a) to (d) show the evolution of the poling at +5 kV. At 10 min between (d) and (e), the voltage is reversed. (e) and (f) show the electric field drop as sodium ions neutralize the depletion layer. (g) shows the decrease in the electric field as excess positive charge is pushed out at the surface.

charge accumulation above the background charge density near the surface (Assumption 3). Within our model, this is controlled by adjusting $\eta_H \sim 10$. If $\eta_H < 1$, the positive charge accumulation never rises above the background level; the distribution saturates for $\eta_H \gtrsim 5$ and is quite insensitive to the assumed value. For this case, η_H is constant with time, i.e. there is an unlimited supply of hydrogen ions.

At 13 s from the application of the voltage (Fig. 5(a)), the Na^+ ions have moved towards the cathode to partially form the depletion region and a strong anodic field has been established. The x-axis is normalized to the single-carrier depletion width Eq. (6). After 40 s (Fig. 5(b)) there has been some H^+ injection at the anode and the Na^+-depletion width has adjusted to maintain the overall voltage drop across the sample. The peak electric field has moved in from the surface. These trends are continued for longer times of 5 and 10 min (Fig. 5(c) and (d)): H^+ continues to be pulled in by the field forming a double layer of positive and negative charge, but at a decreasing rate because the field is decreasing; the edge of the Na^+ depletion region moves further into the sample, and the width of the depletion region decreases as more of the voltage is dropped across the H^+ accumulation region; the peak of the electric field moves into the sample and decreases. The H^+ density decreases to the background charge density (i.e. one-for-one charge exchange) within a scale comparable to the depletion width. As long as this depth is small compared to the SH coherence length, the SH signal (proportional to V^2) is constant once the depletion region has formed.

In the simulation, the applied voltage is reversed to −5 kV at $t = 10^+$ min. After a capacitive charging time (ms), a field of $-2V/d$ is added to the field shown in Fig. 5(d). Fig. 5(e) shows the charge and field distributions 10 s later. The depletion width has decreased as the Na ions move in response to the reversed field, but the H^+ ions have not yet responded. The SH signal is proportional to the square of the voltage drop at the new cathode which is almost zero for this charge distribution. A depletion region (not shown) is also formed at the other end of the sample, the new anode. After an additional 16 s (Fig. 5(f)), the depletion region has been completely eliminated and the remaining field is due to the H^+ accumulation. Because there is still a voltage drop, there is a SH signal. At longer times, the excess H^+ concentration is pushed out of the sample and the SH signal decays.

The calculated evolution of the SH signal corresponding to the charge distributions of Fig. 5 is shown as the curve labeled model in Fig. 3. A steady-state level of the SH is established after some time at a positive bias (as in Fig. 5(a)–(d)). Note that the charges are still redistributing during this time but that there is no effect on the SH

signal. On voltage reversal, the SH signal decreases rapidly to zero and then recovers on the time scale of the Na^+ motion. The signal then decreases to zero on the time scale of the H^+ motion. If the sample had been shorted rather than biased at the opposite polarity, the SH signal would have smoothly decreased to zero on the short time scale even though an inhomogeneous charge distribution remains. Although the relative level of the SH after field reversal is less than observed, the model qualitatively explains the observation of a SH signal at the new cathode after field reversal. The evolution of the signal following a second field reversal is discussed below.

We must also extend the modeling to the opposite electrode to get a complete analysis of the charge distributions. Experimentally we observe either a slow (approximately 20 min) growth in the SH starting immediately after the voltage reversal (Fig. 3) or, under other poling histories, an incubation period followed by the slow growth (Figs. 2 and 4). These observations force the final two assumptions: that the Na^+ ions are blocked once they have moved up to the H^+ front and the depletion region is eliminated (Fig. 5(f)); and that the Na^+ and H^+ intermix in the vicinity of the front between them to form a region with an intermediate mobility μ_M. This assumption is forced by fitting to the observed incubation period before formation of the non-linearity under certain poling sequences (Fig. 4). Abou el Leil and Cooper showed that this intermixing occurs upon field reversal [22]. Because our computation neglects diffusion, we can only approximate this mixing as a region with an effective mixed mobility. The mixed mobility falls in-between the mobilities for sodium and hydrogenated ions alone. Fitting the rise in SH signal shown in Fig. 4, gives a mixed mobility of approximately 2×10^{-10} cm^2 V^{-1} s^{-1}, 25 times less than the sodium mobility.

After several field reversal cycles, these assumptions lead to an inhomogeneous starting distribution with H^+ ions at both sides of the sample, a mixed ionic zone at both ends and finally a Na^+ zone extending over the bulk of the sample. If the prior poling left an excess region of H^+ ions on the initial anode (new cathode after field reversal) there is an incubation period with a time scale set by $\mu_H V/w$ (the depletion width) while the excess H^+ ion density is pushed out of the sample. Following removal of the excess H^+, a depletion region forms under the opposite electrode at a time scale of $\mu_M V/L$ where μ_M is the mixed mobility and the applied voltage is dropped across the bulk of the sample of thickness L. If there is no excess H^+ ion density (as in Fig. 3 where the excess density was pushed out of the sample during the negative bias cycle and has not yet accumulated on the opposite side) the non-linearity begins to grow immediately on applying the reverse voltage.

4.6. Model results: limited supply of hydrogen ions

If hydrogen blocking electrodes are used, prior surface hydration, will act as a limited supply of H^+. To illustrate this condition, Fig. 6 shows the time evolution of the electric field and space charge

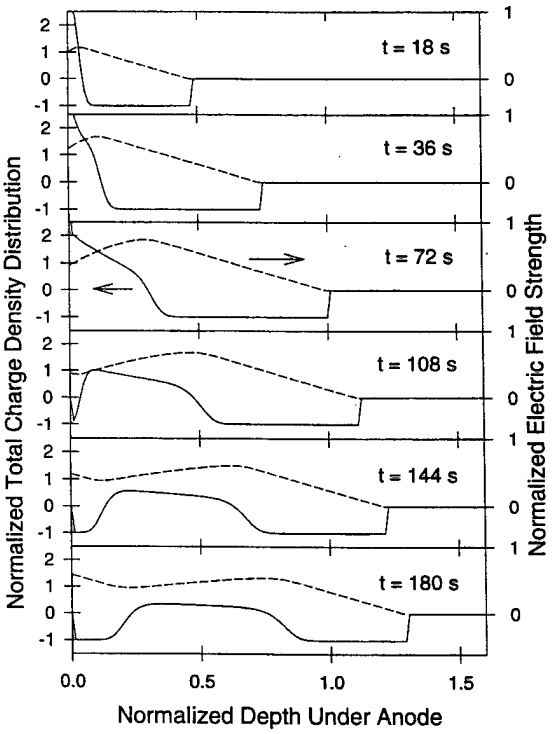


Fig. 6. Evolution of electric field and total charge density under a limited supply of H^+ ions for a sample width of 180 μm and $\mu_{Na} = 10^{-11}$ cm^2 V^{-1} s^{-1} and $\mu_H = 10^{-2}$ μ_{Na}. At $t = 90$ s, the supply of hydrogenated ions at the anode surface was set to zero.

for a 180 μm thick sample. In this case a sodium mobility of 10^{-11} cm^2 V^{-1} s^{-1} was used in order to simulate experimental observations. A H^+ mobility of 10^{-2} μ_{Na} was also used, a smaller mobility would be equally valid to illustrate the physics. As the depletion region forms, H^+ is pulled into the sample. In this case we see the positive charge buildup as before, but on a shorter time scale due to the thin sample and resultant larger initial electric field (V/d). At 90 s, the supply of H^+ runs out ($\eta_H \rightarrow 0$) leaving a pulse of slow positive charge moving into the sample. A negatively charged depletion region once again forms at the anodic surface resulting in a triple (negative–positive–negative) charge layer, with an electric field peak at the anodic surface and another deeper into the sample. This might explain the alternating polarity regions of charge measured with the LIPP technique [17].

4.7. Microscopic mechanism

There remains uncertainty as to the mechanism for the non-linearity (cf. Eqs. (1) and (2)). Our model does not address the microscopic mechanisms other than to assume a linear dependence of $\chi^{(2)}$ on the local electric field. We briefly investigated setting the non-linearity proportional to the product of the hydrogen density and the local field $n_H E_{dc}$ where n_H is the hydrogen ion density. This might be the case if the non-linearity required hydrogen ions for dipole orientation. This leads to a higher relative SH signal level under the new cathode on field reversal (Fig. 3) closer to the experimental observation than was found with the simple $\chi^{(2)} \propto \chi^{(3)} E_{dc}$ model. However, the result is insufficient to draw any firm conclusions. Qualitatively, $\chi^{(2)} \propto \chi^{(3)} E_{dc}$ suffices to understand the dynamic behavior of thermal poling.

5. Conclusion

Dynamic second-harmonic generation experiments show features that are incompatible with the simple single ionic species model often used to explain poled fused silica second-harmonic signal. Other measurements have shown a complex spatial distribution of non-linearity under the anode that is incompatible with the single mobile species model. These features are qualitatively explained with a model incorporating two mobile ionic species with drastically different mobilities ($\sim 10^4$:1). The very high fields in the anodic depletion region break the macroscopic centrosymmetry (enabling the non-linearity) and lead to ion exchange between the fast and slow species which results in continuing changes in the charge, field and non-linearity distributions.

Acknowledgements

Partial support for this work was provided by the Air Force Office of Scientific Research. T.G.A. acknowledges the sponsorship of the Air Force Research Laboratory.

References

[1] R.A. Myers, N. Mukherjee, S.R.J. Brueck, Opt. Lett. 15 (1991) 1733.
[2] P.G. Kazansky, L. Dong, P.St.J. Russell, Opt. Lett. 19 (1994) 701.
[3] R.A. Myers, S.R.J. Brueck, R.P. Tumminelli, in: M.J.F. Digonnet (Ed.), SPIE Proc. 2289 (1994) 98.
[4] X.C. Long, R.A. Myers, S.R.J. Brueck, Electron Lett. 30 (1994) 2162.
[5] N. Mukherjee, R.A. Myers, S.R.J. Brueck, J. Opt. Soc. Am. B 11 (1994) 665.
[6] R.A. Myers, PhD dissertation, University of New Mexico, 1995.
[7] H. Takebe, P.G. Kazansky, P.St.J. Russell, K. Morinaga, Opt. Lett. 21 (1996) 468.
[8] J. Cohen, J. Appl. Phys. 28 (1957) 795.
[9] T.M. Proctor, P.M. Sutton, J. Am. Ceram. Soc. 43 (1960) 173.
[10] G. Wallis, D. Pomerantz, J. Appl. Phys. 40 (1969) 3946.
[11] R.G. Gossink, J. Am. Ceram. Soc. 61 (1978) 539.
[12] G. Wallis, J. Am. Ceram. Soc. 53 (1970) 563.
[13] U.K. Krieger, W.A. Lanford, J. Non-Cryst. Solids 102 (1988) 50.
[14] C.M. Lepienski, J.A. Giacometti, G.F. Leal Rerreira, F.L. Freire, Jr., C.A. Achete, J. Non-Cryst. Solids 159 (1993) 204.
[15] Z. He, G. Borchardt, W. Wegner, Fresenius' J. Anal. Chem. 348 (1994) 264.
[16] P.G. Kazansky, A. Kamal, P.St.J. Russell, Opt. Lett. 18 (1993) 1141.

[17] P.G. Kazansky, A.R. Smith, P.St.J. Russell, G.M. Yang, G.M. Sessler, Appl. Phys. Lett. 68 (1996) 269.
[18] W. Margulis, F. Laurell, Opt. Lett. 21 (1996) 1786.
[19] D. Pureur, A.C. Liu, M.J.F. Digonnet, G.S. Kino, in: Bragg Gratings, Photosensitivity, and Poling in Glass Fibers and Waveguides: Applications and Fundamentals, OSA Technical Digest Series 17 (1997) 302.
[20] R.V. Ramaswamy, R. Srivastava, J. Lightwave Tech. 6 (1988) 984.
[21] M. Abou el Leil, Annu. Rev. Mater. Sci. 23 (1993) 255.
[22] M. Abou el Leil, A.R. Cooper, J. Am. Ceram. Soc. 62 (1979) 390.
[23] R. Oven, D.G. Ashworth, M.C. Page, J. Phys.: Condens. Matter 4 (1992) 4089.
[24] D.W. Shin, M. Tomozawa, J. Non-Cryst. Solids 211 (1997) 237.
[25] T.G. Alley, R.A. Myers, S.R.J. Brueck, in: M.J.F. Digonnet, F. Ouellette (Eds.), Doped Fiber Devices, SPIE Proc. 2841 (1996) 202.
[26] K. Yamamoto, H. Namikawa, J. Ceram. Soc. Jpn. (Int. Ed.) 102 (1994) 656.
[27] K. Yamamoto, H. Namikawa, J. Ceram. Soc. Jpn. (Int. Ed.) 103 (1995) 897.
[28] J.P. Stagg, Appl. Phys. Lett. 31 (1977) 532.
[29] M.C. Page, R. Oven, D.G. Ashworth, Electon. Lett. 27 (1991) 2073.
[30] H.A. Schaeffer, J. Mecha, J. Steinmann, J. Am. Ceram. Soc. 62 (1979) 343.
[31] T. Drury, J.P. Roberts, Phys. Chem. Glasses 4 (1963) 79.
[32] R.H. Doremus, J. Electrochem. Soc.: Solid State Science (1968) 181.
[33] S.R. Hofstein, IEEE Trans. Elec. Dev. ED–14 (1967) 749.
[34] D.W. Shin, M. Tomozawa, J. Non-Cryst. Solids 203 (1996) 262.
[35] K.M. Davis, M. Tomozawa, J. Non-Cryst. Solids 201 (1996) 177.
[36] H. Wakabayashi, M. Tomozawa, J. Am. Ceram. Soc. 72 (1989) 1850.
[37] R.H. Doremus, J. Mater. Res. 10 (1995) 2379.
[38] G. Hetherington, K.H. Jack, M.W. Ramsay, Phys. Chem. Glasses 6 (1965) 6.
[39] W.A. Lanford, K. Davis, P. Lamarche, T. Laursen, R. Groleau, R.H. Doremus, J. Non-Cryst. Solids 33 (1979) 249.
[40] D.E. Carlson, J. Am. Ceram. Soc. 57 (1974) 461.
[41] M. Abou el Leil, E. Snitzer, Commun. Am. Ceram. Soc. (1984) C-250.
[42] F.M. Ernsberger, Phys. Chem. Glasses 21 (1980) 146.
[43] F.M. Ernsberger, J. Am. Ceram. Soc. 66 (1983) 747.
[44] M. Nogami, Y. Abe, Phys. Rev. B 55 (1997) 12108.
[45] V. Garino Canina, M. Priqueler, Phys. Chem. Glasses 3 (1962) 43.
[46] P.J. Jorgenson, F.J. Norton, Phys. Chem. Glasses 10 (1969) 23.
[47] Y. Abe, H. Hasono, W.H. Lee, T. Kasuga, Phys. Rev. 48 (1993) 15621.
[48] H. Nasu, H. Okamoto, A. Mito, J. Matsuoka, K. Kamiya, Jpn. J. Appl. Phys. 32 (1993) L406.
[49] L.J. Henry, A.D. DeVilbiss, T.E. Tsai, J. Opt. Soc. Am. B 12 (1995) 2037.
[50] A. Von Hippel, E.P. Gross, J.G. Jelates, M. Geller, Phys. Rev. 91 (1953) 568.
[51] Quartz glass for optical data and properties, Hereaus Amersil Inc, 3473 Satellite Boulevard, Duluth, GA, 30136-5821.

Large photosensitivity in lead–silicate glasses

X.-C. Long and S. R. J. Brueck[a)]
Center for High Technology Materials, University of New Mexico, Albuquerque, NM 87106

(Received 4 January 1999; accepted for publication 17 February 1999)

Strong, permanent surface-relief and refractive index gratings are written in lead–silicate glasses by irradiation with the output of a pulsed KrF excimer laser (248 nm) through a phase mask. Diffraction efficiencies as high as 10% are obtained. The diffraction efficiency of the refractive index grating after removal of the surface-relief grating shows that a very large photoinduced refractive index change ($\Delta n_0 = 0.09 \pm 0.02$) is obtained. © *1999 American Institute of Physics.* [S0003-6951(99)03815-2]

Photosensitivity, the long-term change of a glass refractive index following optical irradiation, has found application in telecommunications[1] and data storage.[2] The preponderance of the investigations in optical fiber have been devoted to germanosilicate glasses with Δn, the index difference between irradiated and nonirradiated material, saturating at about 0.01 for hydrogen-loaded fibers with limited stability at elevated temperatures.[1] For data storage, crystalline phase change materials have been explored because of the large index changes available. However, these materials are not useful for fiber applications. Glasses with higher photosensitivity are desirable for improved performance in both fiber and volume storage applications.

Lead–silicate glass has a very large third-order optical nonlinearity. The third-order nonlinear refractive index for Schott lead silicate glass SF59 is $n_2 = 5 \times 10^{-19}\ \mathrm{m^2/W}$, ($\chi^{(3)} = 6.2 \times 10^{-21}\ \mathrm{m^2/V^2}$) which is about 30 times that of pure silica glass ($\chi^{(3)} = 2.0 \times 10^{-22}\ \mathrm{m^2/V^2}$).[3] Recently a large second-order optical nonlinearity ($\chi^{(2)} \approx 7$ pm/V) induced by thermal poling and electron beam scanning was reported[4,5] in these materials. These large nonlinearities led us to speculate on the photosensitivity of lead–silicate glasses.

We report here the observation of a large photosensitivity for lead–silicate glass. Permanent gratings were formed in lead–silicate glass with ultraviolet (UV) exposure at 248 nm using a KrF excimer laser beam. A large index change ($\Delta n_0 = 0.09 \pm 0.02$) was obtained which, to our knowledge, is the highest value reported for any glass. This induced refractive index change appears permanent and showed no decay upon heating to 360 °C for a 1 h duration.

Various lead-content silicate glasses were investigated with lead compositions varying from 40% to 71%. ZF7 lead–silicate glass (PbO–70.93 wt %, SiO_2–27.27 wt %, Na_2O–0.6 wt %, K_2O–1.0 wt %, As_2O_3–0.3 wt %) has the highest lead composition we investigated. The optical transmission is similar to the SF glass series from Schott Glass Co. with a UV cutoff around 350 nm. All of the lead glasses investigated: F2, SF11, SF6, and ZF7 are photosensitive at 248 nm. Detailed studies are presented only for ZF7 glass. This glass is photosensitive across a wide spectral region range including 193 nm (ArF laser), 248 nm (KrF laser), 266 nm (fourth harmonic of *Q*-switched YAG laser). No photosensitivity was observed for irradiation at 355 nm (third harmonic of *Q*-switched YAG laser), very close to the optical absorption edge.

The same silica phase mask (period of 738 nm) was used for grating formation at all wavelengths, resulting in varying contrast between the fundamental and second spatial harmonic grating exposures. For normal incidence KrF laser illumination, the measured phase mask power transmission was 12.5% for the zero order, 37.5% for the ±1 orders and 6.25% for ±2 orders. The glass sample was placed in physical contact with the surface of the silica phase mask. The incident pulse energy density was 132 mJ/cm^2 per pulse with a repetition rate of 10 Hz.

After a few minutes of UV laser irradiation, a strong grating was observed in the glass sample. The strength of the grating, monitored by first-order diffraction of a HeNe laser beam, initially increased with exposure time and saturated for exposure times of ~10 min. Figure 1 is a scanning electron micrograph (SEM) showing the induced surface relief grating on the lead silica glass after 10 min. irradiation. In Fig. 1(a), a grating with a period $d = 738$ nm is clearly seen. In Fig. 1(b), corresponding to a different location on the same grating, the frequency-doubled period $d/2$ is evident. This differs from observations of grating formation in As_2S_3 glass where the grating is mainly due to photoexpansion and the response drops off dramatically for short period gratings.[6] Atomic force microscope (AFM) images of the ZF7 surface show similar results. The height of the surface relief grating is approximately 70 nm. The inhomogeneity of the grating is most likely due to optical effects related to the finite spatial and temporal coherence of the KrF laser source[7] coupled with the multiple scattered orders from our phase mask and the varying contact distances.

A HeNe laser beam was used to measure the diffraction efficiency of the grating. Diffraction is observed at angles corresponding to the fundamental grating (probing only the variation at period d) and at the second-order angle (involving interference between the second-order diffraction from the period d grating and the first-order diffraction from the period $d/2$ grating). The diffraction efficiencies were 10.8% (first-order angle) and 4.1% (second-order angle) for a

a)Also with: Departments of Physics and Astronomy and Electrical and Computer Engineering; electronic mail: brueck@chtm.unm.edu

 © 1999 American Institute of Physics

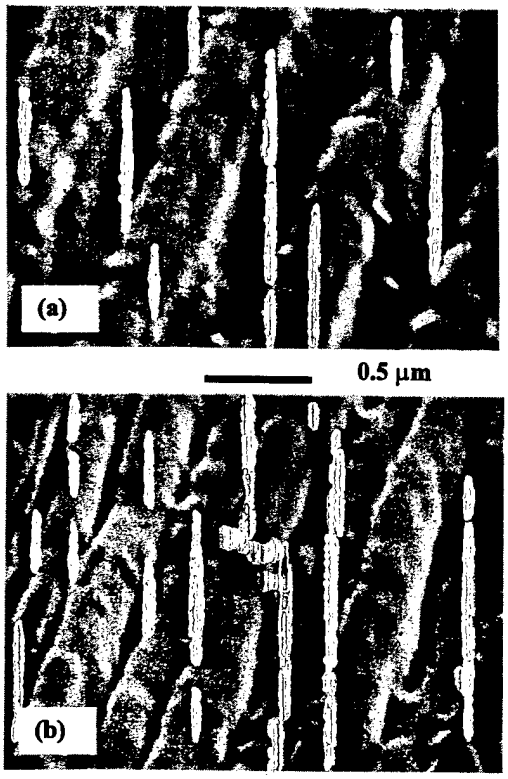


FIG. 1. Scanning electron micrograph of surface relief gratings in two portions of a ZF7 sample after 248 nm irradiation through a 738 nm phase mask: (a) with period of 738 nm; (b) with double period of 369 nm.

s-polarized HeNe beam at an incident angle (external) of $\theta_{ext}=60°$. For the measured 70 nm height h of the surface relief grating and the refractive index difference between the glass and air $\Delta n=0.8$, we calculate a diffraction efficiency of $\eta=10.03\%$ using the formula $\eta=(\pi h\Delta n/\lambda\cos\theta)^2$, very close to the measured value of 10.8%, suggesting that the surface relief grating is responsible for the majority of the diffracted signal. To confirm this hypothesis, we placed a drop of index matching fluid ($n\sim1.8$) atop the grating and pressed another ZF7 glass plate to the grating surface; the diffraction efficiency was reduced to ~0.8%.

We then polished the grating surface in steps to remove the surface relief grating and observe the diffracted light from the induced index grating. An additional surface-relief grating with a large 100 μm period and 1900 nm depth was made in the neighborhood of photoinduced grating by standard lithography and etching. The depth of the physical grating was measured with a stylus profilometer before any polishing and after the final polishing step. A linear dependence of the polish depth versus polish time was assumed, giving a polish depth of ~25 nm for each step. The diffraction efficiencies of the grating are monitored after each polish step as shown in Fig. 2 for the same grating shown in Fig. 1. The diffraction efficiency drops sharply from 10.8% down to 0.4% as the top 75 nm surface layer is polished away, corresponding to removal of the surface-relief grating. The efficiency of both first-order and second-order diffraction signals are comparable over the depth range from 75 to 300 nm, suggesting that gratings with periods of both d and $d/2$ were induced in the glass with comparable intensities.

We assume that the modulation of the refractive index decreases exponentially with depth (attenuation coefficient

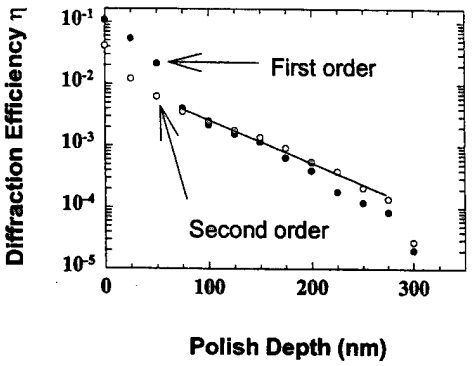


FIG. 2. Depth profile of the diffraction efficiency for UV laser induced grating on lead–silicate glass. The diffraction efficiency drops sharply as the surface relief grating when ~70 nm height is removed. The measured (solid circles for first order and open circles for second order) and modeled [Eq. (1)] diffraction efficiency indicate a peak refractive index modulation $\Delta n_0=0.09\pm0.02$ with an exponential decay length of 125 nm resulting from the strong absorption at the 248 nm writing wavelength.

α_{UV}) because of the UV absorption of the glass, that is $\Delta n(z)=\Delta n_0 e^{-\alpha_{UV}z}$, where Δn_0 is the index modulation at the surface of the sample. Following a previously developed theory,[8] the refractive index change Δn_0 can be evaluated using the diffraction efficiency formula for an unslanted grating with s-polarized incident light:

$$\eta=\left(\frac{\pi\Delta n_0}{\lambda\alpha_{UV}\cos\theta}\right)^2 e^{2\alpha_{UV}h}, \quad (1)$$

where η is the diffraction efficiency, h is the cumulative polish depth, λ is the wavelength of the diffracted light, and θ is the incident angle in the medium.

Using Eq. (1) to fit the data in Fig. 2, we obtain $\Delta n_0=0.09\pm0.02$ and $\alpha_{UV}=1/125\ \text{nm}^{-1}$. The shallowness of the induced grating is mainly caused by the large ZF7 absorption coefficient at the 248 nm KrF excimer laser wavelength. If we use a source with wavelength between 300 and 350 nm to write a grating in the lead silicate glass, a much larger penetration length should be obtained since a lower absorption coefficient is expected for these wavelengths. Diffraction efficiency as high as 90% might be obtained if the thickness of a uniform index grating could be extended to 4.2 μm assuming the same refractive index change of $\Delta n_0=0.09$.

Finally the thermal stability of the photoinduced index change was examined. The photoinduced diffraction grating, after polishing away the surface relief structures, was heated to temperatures of 100, 200, 250, and 360 °C for 1 h durations. After each heat treatment the grating diffraction efficiency was measured at room temperature. No decay of the diffraction efficiency was observed over this temperature range.

This large photoinduced index change may be due to glass structure changes or to color center formation. It has been reported[9] that color centers were formed in a lead–silica glass through two-photon absorption of a pulsed doubled YAG laser (532 nm). No photosensitivity was observed in these bulk glasses for irradiation at 532 nm at intensities up to the threshold for surface damage. More work is need to understand the microscopic physics and investi-

gate the relationships between photoinduced refractive index changes and the composition of lead glasses.

In summary, a high diffraction efficiency grating (10%) was induced in lead–silica glass by irradiation with a pulsed, 248 nm KrF excimer laser through a silica phase mask. The primary scattering mechanism was surface relief. By monitoring the diffraction efficiency as the surface was polished down, a photoinduced refractive index change Δn as high as 0.09 extending ~ 125 nm into the glass was deduced.

The authors thank Monica L. Minden of HRL Laboratories for loan of the phase mask, Mingxin Qiu of Kyushu Institute of Technology of Japan for a useful discussion, B. Srinivasan for assistance with the excimer laser and for discussions of photosensitivity, and Carlos Ozuna, Andrew Frauenglass, and Karen DeZetter for help with the SEM and AFM studies. Support for this work was provided by AFOSR and DARPA.

[1] A. Othonos, Rev. Sci. Instrum. **68**, 4309 (1997).
[2] A. Partovi, T. Erdogan, V. Mizrahi, P. J. Lemaire, A. M. Glass, and J. W. Fleming, Appl. Phys. Lett. **64**, 821 (1994).
[3] E. M. Vogel, M. J. Weber, and D. M. Krol, Phys. Chem. Glasses **32**, 231 (1991).
[4] M. Qiu, F. Pi, and G. Orriols, Appl. Phys. Lett. **73**, 3040 (1998).
[5] M. Qiu, T. Mizunami, H. Koya, F. Pi, and G. Orriols, in *Proceedings of Nonlinear Optics: Materials, Fundamentals, and Applications* (IEEE, Piscataway, NJ, 1998), p. 370.
[6] S. Ramachandran, S. G. Bishop, G. P. Guo, and D. J. Brady, IEEE Photonics Technol. Lett. **8**, 1041 (1996).
[7] P. E. Dyer, R. J. Farley, and R. Giedl, Opt. Commun. **115**, 327 (1995).
[8] N. Uchida, J. Opt. Soc. Am. **63**, 280 (1973).
[9] K. W. Delong, V. Mizrahi, G. I. Stegeman, M. A. Saifi, and M. J. Andrejco, J. Opt. Soc. Am. B **7**, 2210 (1990).

Composition dependence of the photoinduced refractive-index change in lead silicate glasses

X.-C. Long

Center for High Technology Materials, University of New Mexico, Albuquerque, New Mexico 87106

S. R. J. Brueck

Center for High Technology Materials and Departments of Electrical and Computer Engineering and Physics and Astronomy, University of New Mexico, Albuquerque, New Mexico 87106

Received February 24, 1999

A large photoinduced refractive-index change (as great as $\Delta n = 0.21 \pm 0.04$) is obtained in lead silicate glasses by irradiation with the frequency-quadrupled output of a Q-switched YAG laser (266 nm). An approximately exponential relationship is found between the photoinduced refractive-index change and the lead cation mole fraction over the composition range from 18.7% to 57%. The induced refractive-index change is permanent and shows no decay after heating to 360 °C during 1 h. Dispersion of the refractive-index change suggests that the photosensitivity is associated with changes in the intrinsic glass absorption edge. © 1999 Optical Society of America

OCIS codes: 050.1950, 160.2750, 350.2770, 060.2400, 090.7330, 130.3130.

Recently we reported the observation of large photosensitivity for lead silicate glass.[1] Permanent gratings were formed with UV exposure at 248 nm with a KrF excimer laser beam. A large index change ($\Delta n = 0.09 \pm 0.02$) was obtained in ZF7 lead silicate glass (40-mol.% PbO). This large photosensitivity may find application in telecommunications[2] and data storage.[3] For fiber grating application, a few mole percent of PbO can be doped into glasses to enhance the photosensitivity of silica glass fibers. Currently, a hydrogen-loading technology is used to enhance the photosensitivity in germanosilicate fibers. The index difference Δn between irradiated and nonirradiated material saturates at ~0.01 for hydrogen-loaded fibers with limited stability at elevated temperatures.[2] For some fiber applications, such as fiber filters and fiber dispersion compensators,[4] stronger photosensitivity would be desirable. For volume optical holographic data storage, inexpensive materials with high optical quality, high photosensitivity, large refractive-index change, and long shelf life are still necessary. Also, large photosensitivity in silica-based glass would make it possible to fabricate planar light-wave circuit devices by direct UV writing.

We report here a detailed investigation of the dependence of the photoinduced refractive-index change on the composition of lead silicate glasses. The heavy-metal cation lead contributes to the large photosensitivity. An exponential relationship is found between the photoinduced refractive-index change and the lead concentration over the range from 19 to 57 mol.%. The largest index change ($\Delta n = 0.21 \pm 0.04$ at 633 nm) was obtained in SF59 glass by irradiation with a 266-nm laser source at a fluence of 25 mJ/cm^2 per pulse (10 ns, 10 Hz, 10 min) and a total dose of 150 J/cm^2. The induced refractive-index change is permanent and does not exhibit any decay after heating to 360 °C for more than 1 h. The dispersion of the photoinduced index is consistent with a change in the absorption near the fundamental absorption edge of the glass. Extrapolating to telecommunications wavelengths, the index change is $\Delta n \sim 0.16$.

We chose to use lead silicate glasses ZF7 and the Schott glass series F2, SF2, SF11, SF6, and SF59 with which to study the dependence of the photoinduced refractive-index change on the lead composition. The lead oxide content varies from 18.7 to 57 mol.%. The detailed materials compositions of the glasses are listed in Table 1. The optical absorption edge varies with the lead content of the glass. The optical bandgap is 2.71 eV for 80-mol.% PbO glass, increasing to 3.38 eV for 50-mol.% PbO silicate glass.[5]

The irradiation source was the frequency-quadrupled output of a Q-switched YAG laser (~10 ns, 10-Hz repetition rate) at 266 nm. A silica phase mask (738-nm period) optimized for a 248-nm excimer laser was used. A strong zero-order beam was observed for 266-nm illumination. The zero-order light was eliminated with a 45° silica prism (Fig. 1), which also changed the incident angles to 5.7°, yielding an ~1.3-μm-period grating. Another advantage of using this arrangement was that the glass samples were kept far from any optical surfaces, eliminating any potential contamination from glass photoablation. The high spatial and temporal coherence of the YAG laser is essential in this configuration. The laser energy was ~6-mJ/pulse over an area of 0.4 cm × 0.6 cm, yielding an incident energy density of 25 mJ/cm^2 per pulse.

All the polished glass samples were irritated under the same conditions for this composition comparison study, i.e., 25 mJ/cm^2 per pulse fluence for 10 min with a 10-Hz repetition rate. We used a He–Ne laser beam to measure the diffraction efficiency of the grating following irradiation. Both surface-relief and refractive-index gratings were observed for all the glasses studied. The highest diffraction efficiency (20%) was obtained for the highest lead content (SF59,

0146-9592/99/161136-03$15.00/0 © 1999 Optical Society of America

Table 1. Composition of Lead Silicate Glasses in mol.% and (wt.%)

Glass	PbO	SiO_2	Na_2O	K_2O	Al_2O_3	TiO_2	As_2O_3
F2	18.7(45.1)	70.7(45.7)	5.4(3.6)	4.9(5.0)	–	–	0.3
SF2	22.9(50.8)	68.5(40.9)	0.8(0.5)	7.3(6.8)	–	–	0.5(1)
SF11	33.2(63.3)	56.9(29.2)	0.9(0.5)	–	2.9(2.5)	5.8(4.0)	0.3(0.5)
ZF7	40 (70.9)	57.2(27.3)	1.2(0.6)	1.3(1.0)	–	–	0.2(0.3)
SF6	40.4(71.3)	56.7(26.9)	2.0(1.0)	–	0.6(0.5)	–	0.2(0.3)
SF59	57 (83)	40 (17)	–	–	–	–	–

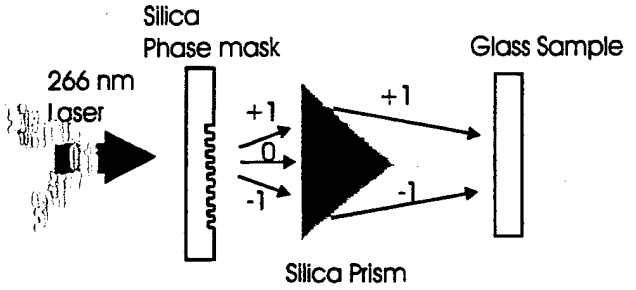


Fig. 1. Experimental arrangement for writing gratings in lead silicate glasses. The source is a 266-nm, fourth-harmonic Q-switched YAG laser. The silica phase mask with period of 738 nm is designed for 248 nm. The silica prism is used to completely reject the zero-order transmitted light as well as to separate the glass samples from the phase mask.

57 mol.%) glass. This high diffraction efficiency arises primarily from the ~100-nm-deep surface relief grating. In contrast, only a weak diffraction signal was observed for F2 glass, which has the lowest lead content (18.7 mol.%). To extract the photoinduced refractive-index change we incrementally polished away both the surface-relief grating and the underlying index grating and monitored the diffraction efficiency η after each polish step. The details of the technique are described in our previous Letter.[1] As an example, the diffraction efficiency η versus the polish depth for SF59 and F2 glasses is shown in Fig. 2. For SF59 the photoinduced grating provided a relatively high diffraction efficiency ($\eta \sim 1\%$) once the ~100-nm surface-relief grating was removed. For F2 a shallow surface-relief grating with height of 20 nm diffracted only ~0.2% of the incident light. We assume that the modulation of the refractive index decreases exponentially with depth (attenuation coefficient α_{UV}) because of the UV absorption of the glass, that is, $\Delta n(z) = \Delta n \exp(-\alpha_{UV} z)$, where Δn is the index modulation at the surface of sample. Following a previously developed theory,[6] the refractive-index change Δn can be evaluated by use of the diffraction efficiency formula for a vertical, unslanted grating with s-polarized incident light:

$$\eta = \left(\frac{\pi \Delta n}{\lambda \alpha_{UV} \cos\theta}\right)^2 \exp(-2\alpha_{UV} h), \qquad (1)$$

where η is the diffraction efficiency, h is the cumulative polish depth, λ is the wavelength of the diffracted light, and θ is the incident angle in the medium. Using Eq. (1) to fit our measured data, we found photoinduced index changes Δn of 0.21 and 0.007 for glasses SF59 and F2, respectively. The photoinduced index changes Δn and absorption α_{UV} obtained for all the measured glasses are listed in Table 2.

The photoinduced refractive-index change Δn and the UV absorption length α_{UV} are plotted in Fig. 3 against the lead cation mole percent. The photoinduced index change refers to the left-hand (logarithmic) scale; the absorption length is on the right-hand (linear) scale. Both parameters are well correlated to the PbO mole percent. The index change is exponential in Pb content; the absorption length is

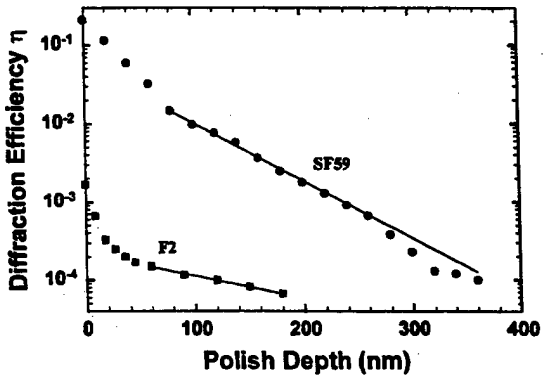


Fig. 2. Depth profile of the diffraction efficiency for a UV-laser-induced grating on lead silicate glass SF59 (F2). The diffraction efficiency drops sharply as the surface-relief grating with ~100-nm (~20-nm) depth is removed. The measured and modeled [by Eq. (1)] diffraction efficiencies, indicated by filled circles and solid curves, respectively, indicate peak refractive-index modulation of $\Delta n = 0.21 \pm 0.04$ ($\Delta n = 0.007 \pm 0.002$) with an exponential decay length of 118 nm (303 nm) that results from the strong absorption at the 266-nm writing wavelength.

Table 2. Fitting Parameters for the Photosensitive Index Grating Parameters Δn and α_{UV} for Various Lead Silicate Glasses

Parameter	SF59	ZF7	SF6	SF11	SF2	F2
Δn	0.21	0.056	0.053	0.033	0.019	0.007
$1/\alpha_{UV}$ (nm)	118	140	157	200	277	303

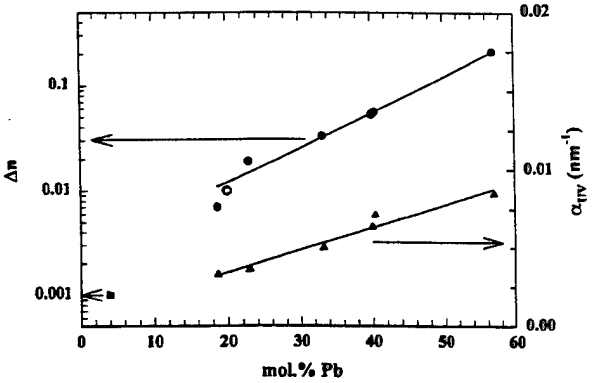


Fig. 3. Photoinduced refractive-index changes versus heavy-metal lead cation in mole percent (filled circles) and exponential fit (solid lines). Open circle, from Ref. 7 for glass $55GeO_2-20PbO-10BaO-10ZnO-5K_2O$ (mol.%); filled square, from Ref. 8 for glass $47SnF_2-47PO_{2.5}-4PbO-2SnCl_2$ (mol.%).

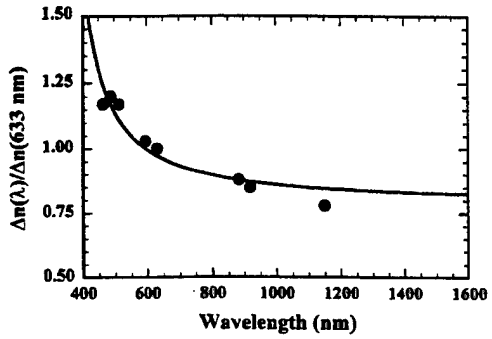


Fig. 4. Dispersion of Δn for the lead silicate glass SF59. The index change values were normalized to the value at 633 nm. Solid curve, a fit to a simple Sellmeier dependence with a characteristic wavelength of 353 nm.

linear in Pb content. Two recent reports of photosensitivity in PbO related glasses are also plotted in Fig. 3. In one report, a photoinduced refractive-index change Δn as great as 0.01 was obtained for the $55GeO_2-20PbO-10BaO-10ZnO-5K_2O$ (mol.%) glass film system deposited by excimer laser ablation.[7] This photoinduced refractive-index change Δn versus lead mole percent fits well with our data, as shown in Fig. 3 by the open circle. The other reported saturated photoinduced refractive-index change $\Delta n \sim 0.001$ is obtained after irradiation with a pulsed XeCl excimer laser (309 nm) in $47SnF_2-47PO_{2.5}-4PbO-2SnCl_2$ (mol.%).[8] The sample was capped by SiO_2 plates during exposure to eliminate formation of a surface-relief grating. This data point is lower than would be obtained by extrapolation of the Pb concentration dependence that we observe (filled square in Fig. 3). For high Pb mole percent compositions, the photoinduced refractive-index change must saturate. An exponential dependence of the third-order nonlinear susceptibility $\chi^{(3)}$ on Pb mole fraction was reported previously.[9]

We used several lasers with various wavelengths to measure the dispersion of the photoinduced refractive-index change Δn in SF59 glass. The laser wavelengths were 488 and 514 nm from an Ar^+ laser; 596.3, 632.8, and 1150 nm from He–Ne lasers; and 883.5 and 918.3 nm from a tunable Ti:sapphire laser. The refractive-index changes at various wavelengths normalized to that at 633 nm are shown in Fig. 4. The solid curve is a fit to a simple Sellmeier curve, $\Delta n \sim \lambda/\sqrt{\lambda^2 - \lambda_0^2}$, with $\lambda_0 \sim 353$ nm close to the band-edge value of ~370 nm, suggesting that the photosensitivity is associated with local modifications to the glass structure rather than with impurity levels. At telecommunications wavelengths of 1.3 and 1.55 μm, the Δn is ~0.8 of that at 633 nm with little dispersion, because these wavelengths are far removed from the absorption band edge of the glass.

Finally, the thermal stability of the photoinduced index change was examined. The photoinduced diffraction gratings, after the surface-relief structures were polished away, were heated to temperatures of 100, 200, 250, and 360 °C for 1-h intervals. After each heat treatment the grating diffraction efficiency was measured at room temperature. No decay of the diffraction efficiency was observed, even at 360 °C.

In summary, the photoinduced refractive-index change in lead silicate glass is strongly correlated with the PbO composition, of the glass. There is an exponential relationship between the photoinduced refractive-index change and the lead concentration, in mole percent of PbO, over the range from 18.7 to 57 mol.%. A large index change, as great as 0.21 at 633 nm extrapolated to 0.17 at 1550 nm, is observed in SF59 glass. The dispersion is consistent with a modification of the glass structure. The index change is permanent and shows no decay when the glass is heated to temperatures as high as 360 °C for 1 h. These large, thermally stable photosensitivities are attractive for applications in telecommunications, integrated optics, and data storage.

Support for this research was provided by the U.S. Air Force Office of Scientific Research and by the Defense Advanced Research Projects Agency. Useful discussions with Mingxin Qiu of Kyushu Institute of Technology (Japan) are gratefully acknowledged. S. R. J. Brueck's e-mail address is brueck@chtm.unm.edu.

References

1. X.-C. Long and S. R. J. Brueck, Appl. Phys. Lett. **74,** 2110 (1999).
2. A. Othonos, Rev. Sci. Instrum. **68,** 4309 (1997).
3. A. Partovi, T. Erdogan, V. Mizrahi, P. J. Lemaire, A. M. Glass, and J. W. Fleming, Appl. Phys. Lett. **64,** 821 (1994).
4. N. M. Litchinitser, B. J. Eggleton, and D. B. Patterson, J. Lightwave Technol. **15,** 1303 (1997).
5. A. Barbulescu and L. Sincan, Phys. Status Solidi A **85,** K129 (1984).
6. N. Uchida, J. Opt. Soc. Am. **63,** 280 (1973).
7. S. Mailis, A. A. Anderson, S. J. Barrington, W. S. Brocklesby, R. Greef, H. N. Rutt, R. W. Eason, N. A. Vainos, and C. Grivas, Opt. Lett. **23,** 1751 (1998).
8. S. Radic, R. J. Essiambre, R. Boyd, P. A. Tick, and N. Borrelli, Opt. Lett. **23,** 1730 (1998).
9. E. M. Vogel, M. J. Weber, and D. M. Krol, Phys. Chem. Glasses **32,** 231 (1991).

Secondary ion mass spectrometry study of space-charge formation in thermally poled fused silica

Thomas G. Alley[a] and S. R. J. Brueck[b]
Center for High Technology Materials, University of New Mexico, Albuquerque, New Mexico 87106

Michael Wiedenbeck[c]
Institute of Meteoritics and Advanced Materials Laboratory, University of New Mexico, Albuquerque, New Mexico 87106-4342

(Received 15 March 1999; accepted for publication 10 September 1999)

Applying a dc electric field across a fused silica sample at elevated temperatures followed by cooling the sample with the field applied (thermal poling) leads to a second-order nonlinearity that has been linked to the formation of a space-charge region in bulk glass. The first microscopic information on the extent of the space-charge region and its behavior with poling time is reported using secondary ion mass spectrometry to monitor the distribution of charged impurities. Lithium and sodium ions are observed to form depletion regions. Potassium and sodium ions as well as a hydrogenated species appear to be injected from the surface. The extent of the space-charge region evolves approximately logarithmically with poling time well after the nonlinearity as measured by second-harmonic generation has been established. The evolution of the space charge region can be qualitatively understood by an ion-exchange model that allows interaction of two ionic carriers with vastly different mobilities. © *1999 American Institute of Physics.* [S0021-8979(99)02524-4]

I. INTRODUCTION

Thermal poling to create a second-order nonlinearity ($\chi^{(2)} \sim 1$ pm/V) has been reported in bulk fused silica,[1] in silica waveguides,[2] and germanosilicate optical fibers.[3] This poling technique has been used to produce electro-optically active fibers,[3] as well as quasi-phase-matched frequency-doubling fibers.[4] Various groups have investigated the extent and distribution of this nonlinear region using second-harmonic Maker fringe techniques,[1,5] laser scanning/second-harmonic generation (SHG) transverse to the sample's poling direction,[6] laser induced pressure pulse probe,[7] and etching techniques.[8,9] These investigations indicate that the nonlinear region extends to 5–15 μm with a peak buried below the anode surface. Recently, we reported results of an etching technique which allowed the spatially resolved visualization of the space charge region by etching samples transverse to the poling direction, revealing structural details.[10] HF acid was used to etch perpendicular to the sample cross section cleaved after poling, revealing different etch rate regions. One feature, a ridge reflecting a slower etch rate than the rest of the sample, moved deeper into the sample logarithmically with poling time. As will be shown below, this ridge is associated with the edge of an ionic depletion layer in the space-charge region.

In this study, we present microscopic information on the nonlinear region, obtained by a detailed secondary ion mass spectrometry (SIMS) investigation of the thermal poling-induced nonlinear region in fused silica glass. As-received fused silica coverslip samples (Heraus-Amersil, TO8, type-II fused silica with nominal 1–10 ppm alkali metal impurities) were thermally poled, checked for second-harmonic generation, and then examined via SIMS. The results agree qualitatively with a recently proposed[11] multicarrier model which assumes a large relative difference (10^3–10^4) in mobilities between a fast ionic species (e.g., Na^+) and a slow carrier (e.g., H_3O^+). The dynamic properties of the charge transport and of the nonlinearity, which is proportional to the local electric field, are closely linked. The results demonstrate the importance of understanding and controlling the charge transport properties of these glass materials to optimize the nonlinear response.

A. Background on ion probes and space-charge profiling in glasses

While several methods have been identified and used to study space-charge regions in sodium-rich glasses, none to date have been applied to low-alkali fused silica. Carlson[12] used ion scattering spectrometry (ISS) in combination with ion milling to study a sodium silicate glass. He found a cation-depleted region, but could not distinguish ion types. Lepienski *et al.*[13] used nuclear techniques to study the space-charge region in soda-lime glass. They used nuclear reaction analysis from a proton beam for detection of Na, Rutherford backscattering spectrometry (RBS) from an ionized He beam for detection of Ca, and elastic recoil detection (ERD) from an ionized He beam for detection of hydrogen. Samples were poled at 17 kV/cm and 150 °C for varying times. Depletion layers of Na and Ca were found 0.1–0.3 μm deep. Hydrogen accumulation regions were found at the inside edge of the Na

[a]Present address: Laser Div., Air Force Research Laboratory (AFRL/DELO), Kirtland AFB, NM 87117.
[b]Also at Departments of Physics and Astronomy and of Electrical and Computer Engineering, UNM, Albuquerque, NM 87106.
[c]Present address: ProjektBereich 4.2, GeoForschungsZentrum Potsdam, D 14473 - Potsdam, Germany.

 © 1999 American Institute of Physics

depletion for samples with deposited electrodes, while a hydrated layer was found in the Na depletion region for a "press-on" electrode.

Gossink[14] used SIMS to analyze a field-assisted glass-to-metal seal, and demonstrated the formation of a depletion region in a sodium silicate glass after applying 400 V at 500 °C in a vacuum. He identified a layer 0.3–0.5 μm deep depleted of Na^+, Ca^+, and K^+. He also observed a region 0.1–0.2 μm wide depleted of Mn^+ and Mg^+. Gossink[15] pointed out that depth profiling in glass using SIMS can be problematic due to surface charging and migration of mobile ions induced by this charging. He concluded that satisfactory charge compensation could be obtained through the use of a metal diaphragm when negative ion bombardment is used. Gossink also noted that conversion of ion count rates into absolute concentrations is difficult due to the variability of secondary ion yields with the element, the glass matrix, and the local environment.

B. Relative alkali ion mobilities in fused silica

The various alkali ions have different mobilities in fused silica, with the sodium ion having the largest mobility by approximately one order of magnitude over Li, the next most mobile ion. In fused silica glass, the relative mobility relationship was observed by Doremus[16] as Na>Li>K in a type II and type III glass at 380 °C. For the type II (GE204) glass, he found $\mu_{Li}=0.15\mu_{Na}$ and $\mu_K<0.002\mu_{Na}$, while in the type III (Spectrosil) glass, $\mu_{Li}=0.03\mu_{Na}$ and $\mu_K=0.0007\mu_{Na}$. Jain and Varshneya[17] also found a similar relationship (Na>Li>K) in a type I (GE214) glass for temperatures below 600 °C. The initial alkali impurity content was 4 ppm and the Al_2O_3 impurity content was 61 ppm. At approximately 350 °C, resistivity measurements were $\rho_{Li}\sim 13\rho_{Na}(\mu_{Li}\sim 0.075\mu_{Na})$ and $\rho_K\sim 2700\rho_{Na}(\mu_K\sim 0.0004\mu_{Na})$.

II. EXPERIMENT

We report a study of the formation of the space-charge region in thermally poled fused silica using SIMS. As-received coverslips of flame-fused silica [170–180 μm thick, ~1 part in 10^6 (ppm) Na, 100 ppm OH] were thermally poled at 275 °C and 4.3 kV in a laboratory ambient atmosphere. The coverslips were placed atop soda-lime glass (microscope slide) current limiters, which were in turn placed atop Al foil cathodes. Al foil anodes were also placed in contact with the top surfaces of the coverslips. The field was turned on once the sample reached a temperature of 275 °C. At the end of the designated poling period, the oven door was opened and the sample was allowed to cool with the voltage applied. The samples cooled from 275 to 200 °C in ~1 min, at which point the current level had typically decreased by an order of magnitude. We checked the second-order nonlinearity by placing the samples into a Q-switched Nd:YAG laser beam (1.06 μm) and measuring the second-harmonic (SH) signal at 532 nm. All samples reported here, with exception of the "depoled" sample, regardless of poling time, yielded similar levels of SH generation within a standard deviation of 14%.

In SIMS analyses, an ion beam is used to sputter away surface layers of the sample. A mass spectrometer separates the ionized atoms sputtered from the surface by their mass-to-charge ratio. As the sputtering process proceeds, a crater is formed into the sample. By measuring the depth of the sputter crater produced during an analysis, and assuming a constant sputtering rate (nm per second), the variations in ion intensity as a function of time can be converted into relative changes in elemental concentration as a function of depth below the sample surface. SIMS provides detailed information about an element's distribution versus depth, but because of the species and sample dependent ionization probabilities noted above, SIMS does not provide information on absolute concentration unless compared against an independently calibrated reference sample. Without an absolute calibration, we have not corrected for isotopic abundances. For the species presented here, all correction factors are less than 9% and are neglected.

A Cameca ims 4F ion microprobe was used to study poled fused silica. A focused $^{16}O^-$ primary ion beam sputtered material from sample surfaces. The primary beam was nominally 12.5 kV and 200 nA, focused to ~100 μm diameter on the sample surface. The beam was rastered over a 50×50 μm^2 area. Secondary ions were accelerated through a nominal 4.5 kV potential to which a 50 V energy offset had been applied. Samples were coated with a ~50 nm gold film to prevent electrical charging during analysis. A field aperture was used to restrict ion collection to an ~33-μm-diam region in the center of the sputter crater.

The cover slip samples used in the SIMS analyses above were type II fused silica from Heraeus Amersil commercially available as TO8. Ten species were analyzed during this study: ^{1}H(100), ^{7}Li(1), ^{23}Na(1), ^{24}Mg(0.1), ^{27}Al(20), ^{30}Si, ^{39}K(0.8), ^{40}Ca(1), ^{48}Ti(1), and ^{56}Fe(0.8). Figures in parenthesis are typical bulk concentrations (elemental weight ppm) given in the glass manufacturer's catalog.[18] Mass separation was achieved using a sector magnet that was stepped through the above mass sequence; each mass station was integrated for 2 s during each of the magnet cycles. The first few cycles (0.1–0.5 μm depth depending on sputter rate) are not reliable because SIMS has not reached equilibrium. Ion detection used a 16 dynode electron multiplier operated in pulse counting mode. The limit of detection of this technique is estimated at <5 ppm. The milling depth is determined by scanning the sputter crater with a stylus profilometer; depth resolution of the final sputtered crater is limited by a conical shape. At shallow depths the resolution is better than 0.5 μm; at final depths the resolution degrades to ~2 μm. Despite the nonoptimal resolution imposed by the need to perform lengthy profiles, we are clearly able to discern important features in the distributions of the various elements.

III. RESULTS

The ion count rates are presented as a ratio of counts of an individual element to the counts of ^{30}Si. This normalization eliminates some of the sharp changes in counts observed at the surface. Figure 1 shows SIMS analyses for a typical unpoled type II (Heraeus TO8) fused silica cover slip (se-

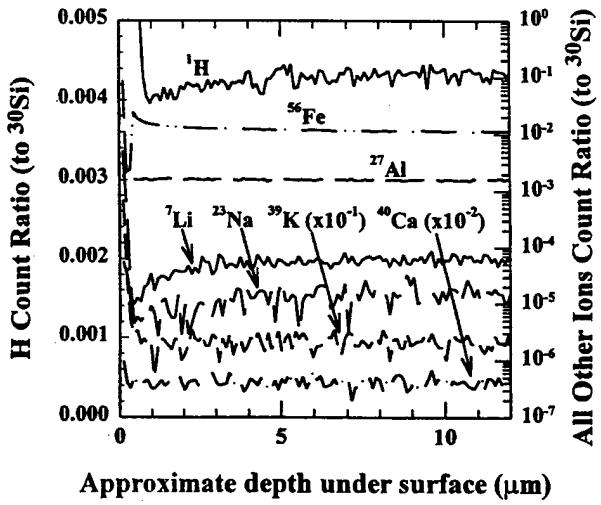


FIG. 1. Secondary ion mass spectrometry (SIMS) analysis of a typical unpoled, as-received TO8 fused silica sample. Note the slight depletion of Li and Na within 2–3 μm of the surface.

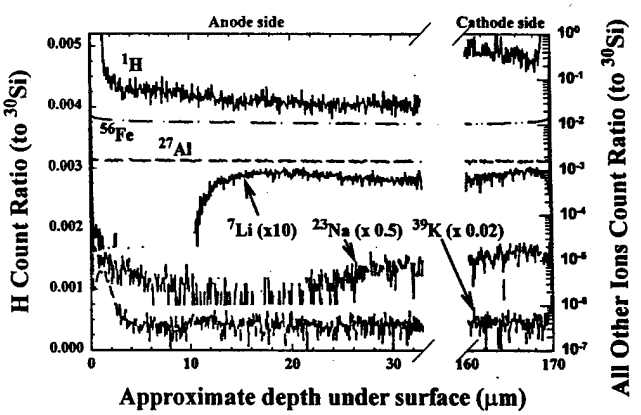


FIG. 2. SIMS analysis of both the anodic and cathodic regions of a TO8 fused silica sample poled for 20 min at 275 °C. The two regions of the profile are from separate measurements on opposite sides of the sample. On the anode side, the Na concentration is reduced to about 25 μm below the surface and there is an injection of ions from the surface. The Li concentration shows an abrupt edge (resolution limited consistent with a Debye screening length at the edge of the electrical depletion region) and an excess concentration in the region of the Na concentration reduction. There is a peak in the K concentration just below the surface. There is much less structure on the cathodic side.

lected from three baseline samples) as a function of depth into material. The count rates were scaled as noted to separate the curves for presentation. The distribution of each element should only be compared with itself, due to the differences in ionization rates. The H, Al, and Fe counts are much greater than others. The H concentration is on a linear scale (left vertical axis), all of the other curves are on logarithmic scales (right vertical axis). Note the large H concentration in the topmost 0.5 μm. H is present in many forms in fused silica, as interstitial H_2O, as OH and as H_2. SIMS does not provide any information on the local state before the sputtering. Note that in the unpoled glass there was a slight depletion in Li and Na in the first few μm's under the surface. This is possibly due to ion exchange, perhaps with H ions resulting from surface polishing and storage in air. One might also question if this depletion might result from charge migration under the ion bombardment during the SIMS measurement. We expect that the charge migration effect from the SIMS measurement is very small compared to the charge migration caused by thermal poling because (1) the negative ion bombardment was accomplished in combination with a gold film coated on the sample to prevent charging,[15] and (2) the ionic mobilities of the sample were low during SIMS measurement (room temperature and low induced voltage) compared to the mobilities found at elevated temperatures and high applied voltages during thermal poling. He *et al.*[19] have theoretically shows that ion depletion in glass from typical SIMS analytical conditions (room temperature, several volt potential drop) is only expected to reach 10's of nm's into the sample. Thus, SIMS induced charge migration is a more significant issue for ultrathin-film measurements than for the very deep (~10 μm) profiles found in these poling experiments.

Figure 2 shows both the anodic and cathodic near-surface regions for a Heraeus TO8 cover slip poled for 20 min at 4.3 kV and 275 °C. For the sake of clarity, only H, Li, Na, and K are plotted. On the anode side a dip (approximately tenfold reduction in density) in the distribution of Na is evident, indicating depletion extending from ~5 to ~26 μm. Also, a more abrupt depletion in Li is evident to a depth of ~11 μm. The only other ion with apparent mobility was K, where an excess is detected within the first 3 μm as K^+ is pulled in from the surface (presumably from surface contamination). The accumulation of Na within the first 10 μm may also be due to surface injection of Na^+ from surface contamination. There is also an accumulation of Li above the bulk level between its depletion edge and the depletion edge of Na. This accumulation suggests that extra Li ions are maintaining the charge density constant up to the vicinity of the Li concentration edge. The sharp fall-off of the Li concentration is consistent with a charge depletion region with a width related to the Debye screening length[11] $L_D = \sqrt{\epsilon \kappa T / e^2 N} \sim 30$ nm at $T = 275$ °C and $N \sim 1$ppm, where $\epsilon = 3.8\epsilon_0$ is the glass dielectric constant and e the electronic charge. (The experimental resolution is set by the inhomogeneous depth of the crater at ~0.5 μm.) In contrast, the Na edge is much broader, suggesting interdiffusion of Na and Li ions without any variation in charge density.

On the cathode side (Fig. 2) no depletion regions are observed. There is, however, a slight accumulation in Li, peaking about 2–3 μm under the cathode surface, and of Na, peaking at 3–4 μm under the cathode surface. The very different SIMS profiles for the anode and cathode surfaces further demonstrate that measurement-induced ionic movement is small compared to the effects of the high-temperature, high-voltage poling.

We investigated the evolution of these depletion regions with poling time; four samples were analyzed. The samples were poled at 4.3 kV, ~275 °C for 0.5, 2, 20, and 140 min, respectively. Pieces from these samples were also used in the etching experiment previously reported.[10] Figure 3 shows the result of SIMS analyses of the near-surface anodic regions. For the sake of clarity, only H, Li, Na, K and, in Fig. 3(d), Ca are plotted. Li, Na, K, and Ca are plotted on a logarithmic scale, while H is plotted on a linear scale to highlight its

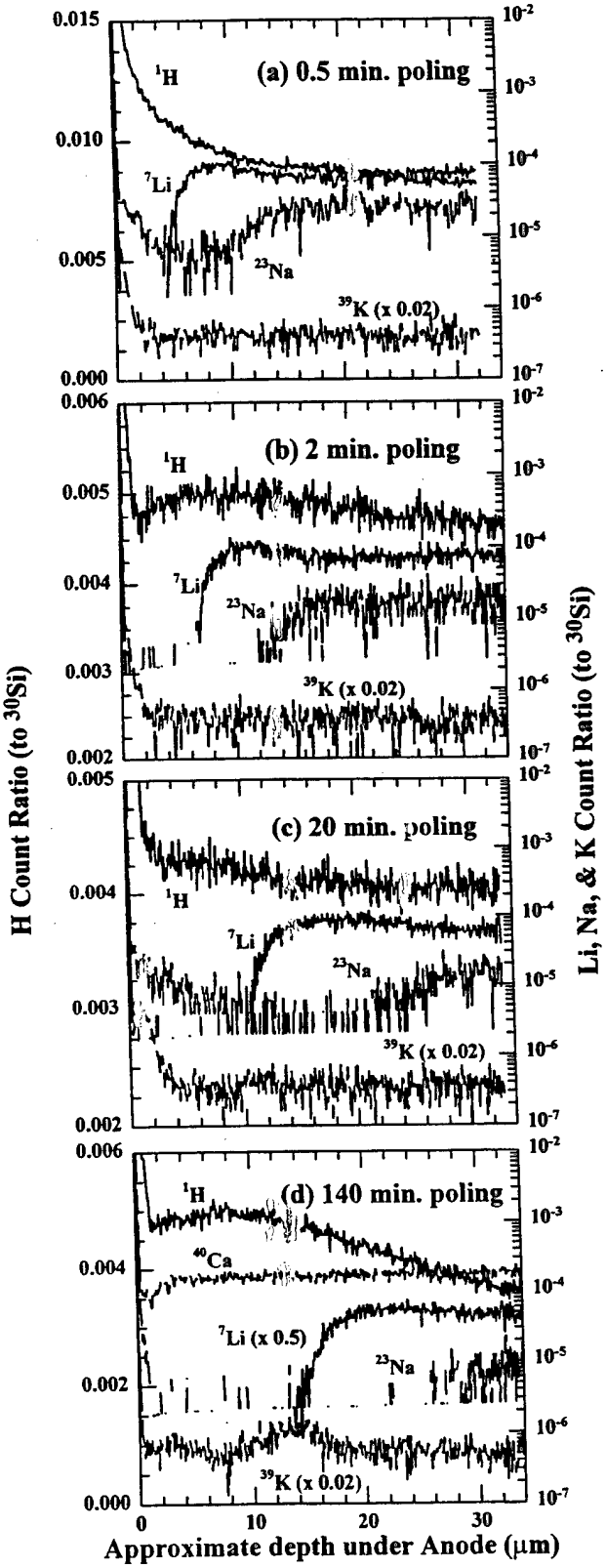


FIG. 3. Dependence of the anodic concentration profiles on poling time at 275 °C. The depletion regions continue to move deeper under the surface even for 140 min. poling times.

distribution. Figure 3(c) is a repeat of a portion of Fig. 2.

The Li and Na depletion layers move deeper into the sample with poling time. Taking a rough measurement of the depletion edges (3 dB down from the bulk levels), this trend

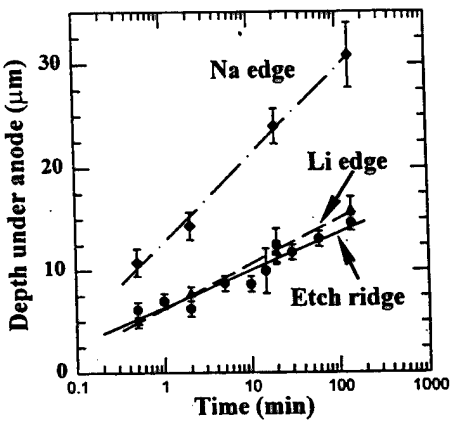


FIG. 4. Poling time dependence of the Na and Li depletion edges. The position of a ridge observed in etching experiments is in good agreement with the Li depletion edge.

is plotted in Fig. 4 along with the etching data previously presented in Ref. 10. The movement with poling time of the Li depletion edge correlates extremely well with the movement of the second etching ridge. Thus, the ridge from the etching experiment corresponds to the edge of the depletion region.

Noteworthy trends in Fig. 3 include the accumulation of Li between its depletion edge and the depletion edge of Na for all poling times and the consistently abrupt Li depletion edge. For longer poling times, K is pulled into the glass from the surface. In Fig. 3(c), there is a well-developed peak of K moving into the sample from the surface. In Fig. 3(d), there is also a peak, although not as well defined, that has moved all the way up to the Li depletion edge. In Fig. 3(a), a surface accumulation of Na, presumably from surface injection, is again observed, similar to that in Fig. 3(c). We have observed a similar near-anode accumulation for a purer type-III fused silica (suprasil) sample with much lower Na impurity levels, implying it was introduced at the surface.[20] The lack of surface introduced Na in Figs. 3(b) and 3(d) could be due to the different handling histories of the glass, leading to a lower level of surface contamination. In Fig. 3(d), the distribution of Ca is plotted to show that for a sample poled for a long period, a small Ca depletion region forms at the anode. All of these samples show an excess H concentration (on a linear scale) extending throughout the regions where the Na concentration is reduced. However, these excess concentrations were not consistently observed for all of the samples investigated. Hydrogen can exist in many different forms inside the glass (H, H_2, OH, H_3O, . . .) with many different electronic configurations, potentially obscuring any mobile ionic forms. The H distribution as detected by SIMS does not provide clear evidence of hydrogenated ions such as H_3O^+ contributing to the total space-charge distribution.

We have previously shown that both repoling ($V \rightarrow -V$) and depoling ($V \rightarrow 0$) lead to interesting dynamic SHG behavior that is inconsistent with a simple, single-mobile carrier model and led us develop the two carrier dynamic model.[11] An important feature of this model is the large dif-

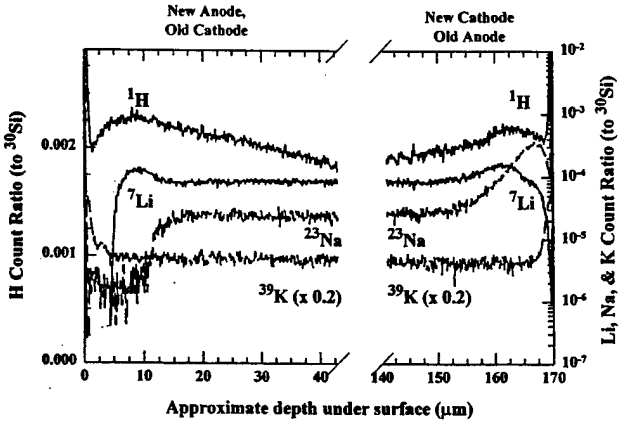


FIG. 5. Anodic and cathodic regions for a repoled sample. Original poling for 2 min at 275 °C followed by a reversed poling for 0.5 min. The new anode side shows similar results to a single poling. The new cathode shows excess concentrations of Na and Li over the depletion region of the original poling.

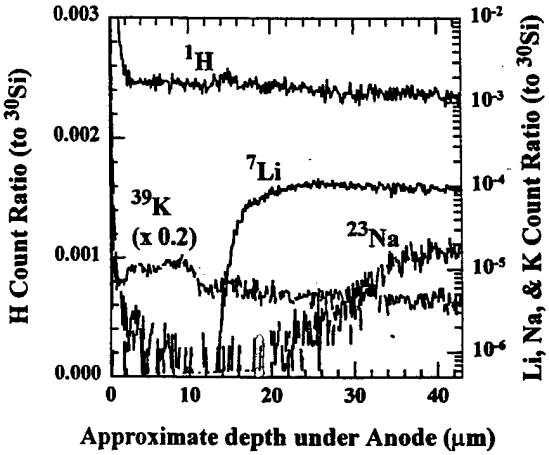


FIG. 6. Anodic region of a depoled sample. Original poling for ~155 min, depoling ($V=0$) for 1 min followed by cooling. No second-harmonic signal was observed after depoling, but depletion regions are still clearly evident.

ference in mobilities $\sim 10^3 - 10^4$ between the two charge carriers.

We investigated these regimes with SIMS. A cover slip sample was poled and then repoled with the field reversed. Initially, the sample was poled for 5 min at 4.3 kV, ~275 °C. After cooling with voltage applied, the sample was manually turned over and reheated with no voltage applied. Once heated to ~275 °C, 4.3 kV was applied for 1.5 min before allowing the sample to cool with voltage still applied. Both sides of the sample were examined with SIMS (Fig. 5). The behavior of the new anode side was similar to that of the sample poled for 2 min [Fig. 3(b)], except the depletion edges were not quite as deep below the anode surface. On the new cathode side, we see some very interesting effects. Before field reversal, the new-cathode side was the anode, so a depletion layer existed in the near-surface region. When the field is reversed, both the Na and Li ions respond to the new field distribution by drifting towards the new-cathode surface. The Na peak has moved through the Li peak, consistent with the higher mobility of Na. If no other effects came into play, these excess charges should collapse to a very narrow distribution ($\sim L_D$) just at the surface. Instead we observe a broad excess distribution, roughly comparable in depth to the initial-poling depletion width for both Li and Na implying that there is another effect in the near surface region that lowers the alkali-ion mobilities. Based on the experimental evidence of a transient cathodic nonlinearity on field reversal and of an incubation period before observation of SHG, we have previously postulated[11] that excess H_3O^+ or other low-mobility ionic species competed with the $Na^+$for defect sites and effectively blocked the charge transport towards the new cathode, resulting in a net positive charge distribution extending in from the new cathode that clears on the time scale of the low mobility blocking species.

The voltage drop associated with this charge distribution explain the observations[11] of a transient nonlinearity at the new cathode and an incubation period before establishing the nonlinearity on the new anode for long initial poling periods. There have been literature reports of Maker-fringe experiments consistent with nonlinear thicknesses corresponding to the entire glass thickness.[21–23] These have been associated with a fundamentally different poling mechanism than the surface poling due to a large electric field in the anodic depletion region. If a sample with a positive cathodic charge layer from Na pile-up is cooled while a SH region is present on both sides of the sample, a Maker-fringe experiment will show a fringe period consistent with volume (bulk) poling, even though the nonlinear regions are confined to both surfaces.

A "depoled" sample was analyzed with SIMS. This sample had been poled multiple times for a total of 155 min and was finally depoled by shorting the heated sample to ground (~1 min) and cooling. No second-harmonic signal was observable after depoling. Figure 6 shows the result of SIMS analysis of the anode side. The depths of the Na and Li depletion edges are similar to the sample poled for 140 min. There is also a wide peak of K, which was also observed in the 140 min sample [Fig. 3(d)]. Clearly, the Li and Na distributions did not move very far in the short depoling time. This is again consistent with our two-carrier model in which a positive charge layer (from H_3O^+ transport from the surface) followed by a negative (Li^+ and Na^+ depletion) charge layer forms below the anode. When a sample is depoled, the fast alkali ions need only move back towards the anode surface enough that the integrated electric field (i.e., the voltage drop) at the anode is zero to satisfy the circuit condition. Under these conditions, there is still a space-charge region but with alternating charges and electric field directions. As long as the widths are less than a coherence length, there is no SHG signal because the SHG in the positive and negatively poled regions interfere destructively. Electric fields remain in the surface regions, and if the sample were maintained at an elevated temperature the charge distribution would continue to evolve back towards the initial conditions.

The accumulation peaks of K on the anode side of a poled sample observed in Fig. 2, Fig. 3(d), and Fig. 6 appear to correlate with the deep, narrow groove that sometimes is observed in the etching experiments,[10] reflecting a localized region with a faster etch rate than that of the bulk glass. This

association is not conclusive, however, because in the etching experiment the location of the groove relative to the anode surface varied substantially, with a maximum depth under the anode always less than the etching ridge (associated with the edge of the depletion region). As was shown in a previous preliminary report,[20] this is also consistent with observations in a synthetic fused silica sample (type III SiO_2) which exhibited an accumulation of K near the anode upon being poled, and when etched, resulted in a groove in the same approximate location. This appears to be a concentration- rather than a field-dependent effect since there is always a strong electric field in the region where the groove appears.

IV. DISCUSSION

The SIMS data combined with the etching data demonstrate:

(1) The alkali depletion region in type II glasses continues to move deeper into the sample with increased poling time at an approximately logarithmic rate, while the SH signal level stays at comparable levels for all measured poling times. This indicates that the electric field strength (and consequently the $\chi^{(2)}$) must vary dramatically. SH measurements are only sensitive to the integrated field (i.e., the voltage drop across the depletion/accumulation region).

(2) In an ion-exchange process, Na, K, and possibly a hydrogenated species are injected into the sample from surface contamination during poling.

(3) The ridge associated with a decreased etching rate in the etching experiments correlates well with the edge of the depletion region, marked by the abrupt Li concentration gradient. The groove associated with an increased etching rate in the etching experiments is likely correlated with an accumulation of K injected into the glass from the anode surface.

(4) Migration of Na towards the cathode for repoling is hindered near the cathode surface edge by other impurity accumulations (e.g., K and/or H), causing the Na to "pile up" in the previous depletion region. This variation of the mobility with local conditions is related to many of the effects observed in SH field reversal experiments and appears to be a new phenomenon not previously discussed in the literature.

The $\ln(t)$ behavior (Fig. 4) for the depth of the space-charge region is inconsistent with the single-carrier description of the formation of the space-charge region that was initially proposed[1] to describe the poling phenomenon. In type II fused silica (flame fused natural quartz) which has alkali impurity levels of several ppm, the sodium ion is thought to be the major carrier. Even in SiO_2 glasses with fewer impurities (type III and IV synthetic fused silica), sodium ions are believed to be the predominant source of conductivity.

A single-carrier model predicts that a depletion region will reach a steady state width w in a time τ given by

$$\tau = \sqrt{\frac{\epsilon L^2}{2eN\mu^2 V}}, \tag{1}$$

where ϵ is the dielectric constant, L is the sample width, N is carrier density, μ is the mobility of the carrier, and V is the applied voltage. For a thin sample ($L=180$ μm) and assuming 1 ppm impurity levels ($N\sim 2\times 10^{16}$ cm^{-3}), $\epsilon = 3.8\epsilon_0$, $V=4.3$ kV, and $\mu = 5\times 10^{-9}-10^{-11}$ cm^2 V^- s^{-1} (our observed mobility range), the depletion region steady state formation time is calculated to be $\tau\sim 0.4$–200 s. The cross-sectional etching experiment[11] and the present SIMS experiment show that the space-charge region does not achieve a short term steady state, but instead exhibits an approximate $\ln(t)$ dynamic behavior. This behavior, along with *in situ* second-harmonic/conductivity observations, led us to postulate an expanded two-carrier model that includes carriers with vastly different mobilities (ratio $\sim 10^3$–10^4). As a depletion layer forms due to the migration of the fast carrier (e.g., Na^+), the second, slow carrier is injected into the high-field depletion region. The surface injection results in a continuing evolution of the space-charge region, thus a steady state is not reached on the time scale of even 2 h experiments. In the long time limit, the two-carrier model predicts that the edge of the depletion region evolves as $\sqrt{t}$, rather than the observed $\sim\ln(t)$ behavior, probably because there is actually a continuum of mobilities involved in the dynamic behavior.

From the SIMS experiments, Na, Li, K, and even Ca are mobile within the poling times examined. Na and Li form well-defined depletion regions within $\sim$0.5 min. Conductivity measurements on coverslip samples showed a large drop in conductivity, indicating that the majority of charge migration is over in 1–2 min.[10] The initial migration is likely to be that of Na and Li ions. After the large conductivity drop, a lower conductivity level persisted decreasing slowly with time. The lower conductivity level is likely to be that of slower ions, mostly injected from the surface, such as K and possible H_3O^+. The lower conductivity after the initial drop corresponds to continued evolution of the space-charge region. The approximate $\ln(t)$ behavior of the depletion edge implies that there is a range of mobilities among the ionic carriers, and possibly a continuum of mobilities. Given that each mobile ion will have a range of activation energies dependent its local environment, it is not unreasonable to postulate that there is a range of mobilities for a single ionic carrier.

V. SUMMARY

The use of SIMS and cross-sectional etching techniques have allowed the first direct microscopic observations of the frequency-doubling space-charge region in poled fused silica. The SIMS experiments presented here have allowed interpretation of topographical features produced in the etching experiments. Ridges observed in cross-sectional etching experiments correlate with depletion-region edges. The SIMS analysis of thermally poled fused silica samples has shown that multiple positive ions are mobile. Li and Na ions both form depletion regions near the anode. K and Na ions are observed to be injected into the depletion region from the anode surface. Na ion migration towards the cathode surface after field reversal can be hindered before Na ions reach the

surface, presumably as a result of hydrogenated or impurity-containing surface layers. An inescapable conclusion is that the mobilities of ionic species in silica glasses are correlated under some conditions. The depletion region on the anode side evolves with poling time and the depletion edge moves deeper into the glass with an approximate $\ln(t)$ behavior. The movement of the depletion edge to greater depths is caused by injection of impurities at the anode surface, and the logarithmic behavior implies a range of mobilities among the multiple carriers.

ACKNOWLEDGMENTS

Support for this work was provided by the Air Force Office of Scientific Research and the Defense Research Projects Agency. TGA acknowledges the sponsorship of the Air Force Research Laboratory.

[1] R. A. Myers, N. Mukherjee, and S. R. J. Brueck, Opt. Lett. **16**, 1732 (1991).
[2] R. A. Myers, X. C. Long, S. R. J. Brueck, and R. P. Tumminelli, Electron. Lett. **31**, 1604 (1995).
[3] X. C. Long and S. R. J. Brueck, IEEE Photonics Technol. Lett. **9**, 767 (1997).
[4] P. G. Kazansky, P. St. J. Russell, and H. Takebe, J. Lightwave Technol. **15**, 1484 (1997).
[5] D. Pureur, A. C. Liu, M. J. F. Digonnet, and G. S. Kino, in *Bragg Gratings, Photosensitivity, and Poling in Glass Fibers and Waveguides: Applications and Fundamentals*, OSA Technical Digest Series **17**, 302 (1997).
[6] P. G. Kazansky, A Kamal, and P. St. J. Russell, Opt. Lett. **18**, 1141 (1993).
[7] P. G. Kazansky, A. R. Smith, P. St. J. Russell, G. M. Yang, and G. M. Sessler, Appl. Phys. Lett. **68**, 269 (1996).
[8] W. Margulis and F. Laurell, Opt. Lett. **21**, 1786 (1996).
[9] B. Lesche, F. C. Garcia, E. N. Hering, W. Margulis, I. C. S. Carvalho, and F. Laurell, Phys. Rev. Lett. **78**, 2172 (1997).
[10] T. G. Alley and S. R. J. Brueck, Opt. Lett. **23**, 1170 (1998).
[11] T. G. Alley, S. R. J. Brueck, and R. A. Myers, J. Non-Cryst. Solids **242**, 165 (1998).
[12] D. E. Carlson, J. Am. Ceram. Soc. **57**, 291 (1974).
[13] C. M. Lepienski, J. A. Giacometti, G. F. Leal Ferreira, F. L. Freire, Jr., and C. A. Achete, J. Non-Cryst. Solids **159**, 204 (1993).
[14] R. G. Gossink, J. Am. Ceram. Soc. **61**, 539 (1978).
[15] R. G. Gossink, Glass Technol. **21**, 125 (1980).
[16] R. H. Doremus, Phys. Chem. Glasses **10**, 28 (1969).
[17] V. Jain and A. K. Varshneya, J. Am. Ceram. Soc. **73**, 409 (1990).
[18] Quartz glass for optical data and properties, Heraeus Amersil Inc., 3473 Satellite Boulevard, Duluth, GA 30136.
[19] Z. He, G. Borchardt, and W. Wegener, Fresenius J. Anal. Chem. **348**, 264 (1994).
[20] T. G. Alley, S. R. J. Brueck, and M. Wiedenbeck, in *Doped Fiber Devices II*, edited by M. J. F. Digonnet and F. Oullette (SPIE, Bellingham, 1999), Vol. 3542.
[21] H. Nasu, H. Okamoto, A. Mito, J. Matsuoka, and K. Kamiya, Jpn. J. Appl. Phys., Part 2 **32**, L406 (1993).
[22] L. J. Henry, A. D. DeVilbiss, and T. E. Tsai, J. Opt. Soc. Am. B **12**, 2037 (1995).
[23] H. Imai, S. Horinouchi, N. Asakuma, K. Fukao, D. Matsuki, H. Hirashima, and K. Sasaki, J. Appl. Phys. **84**, 5415 (1998).

Perspectives on Nanoscale Lithography

S. R. J. Brueck
Center for High Technology Materials, University of New Mexico, Albuquerque, NM 87131

I. Introduction

Progress in very large scale integration (VLSI) has been characterized by an ever decreasing feature size. Transverse dimensions of transistor features have decreased from ~ 5 μm in 1970 (4K DRAM) to 0.35 μm today (64M DRAM). This continuous improvement in feature size has been codified as an integral part of "Moore's Law" which projects an exponential feature size decrease characterized by a reduction of 50% in linear dimensions every three years. This "law" underlies the semiconductor industry planning as exemplified in the National Technology Roadmap for Semiconductors[1].

Throughout this progress, optical lithography has remained the dominant lithographic technique for manufacturing applications. Many advances have been made in optical lithography to allow this dramatic scale reduction. The optical wavelength used in state-of-the-art lithographic tools has decreased from mercury G-line (436 nm) to mercury I-line (365 nm) to 248 DUV (KrF laser). There is presently a major push towards development of 193-nm ArF laser-based steppers continuing this historical trend. At the same time optical systems have been improved from numerical apertures (*NA*) of 0.2 to ~0.6-0.7.

There are several factors that together suggest that continued improvements along these directions are likely to slow and that the industry will have to undergo a significant change in lithographic technique if it is to maintain its historical rate of reduction in feature size. Chief among these is the reduction of the feature size to below the available optical wavelengths. Additionally, there is an increasing premium on linewidth control for high-speed circuit operation, even as the scale reduction below the wavelength is making linewidth control more difficult. A further major issue is the complexity of the masks required for future ULSI generations. This complexity is, by definition, increasing by a factor of four each generation (i. e. four times as many transistors on a chip). In addition, many of the potential solutions to the optical lithography problem, collectively know as resolution-enhancement techniques, lead to increased mask complexity (serifs, helper bars, and other sub-resolution features) or require a three dimensional mask in place of the traditional chrome-on-glass two-dimensional masks (phase-shift techniques). These trends are increasing the difficulty and cost, and reducing the yield of masks.

Notwithstanding these difficulties it is also important to appreciate the difficulties of a rapid changeover from traditional optical lithography techniques. The industry has an accumulated investment and experience base of literally billions of dollars and hundreds of thousands of man-years in optical lithography. Clearly, it is important to leverage this investment to the greatest extent possible. Optical lithography techniques will be used for as long as possible and innovative new concepts will continue to be generated to meet the resolution requirements and allow continued growth of the industry.

6th NASA Symposium on VLSI Design, to be published

II. Nanoscale Lithography Alternatives

The current industry perspective is that 193-nm excimer-laser-based lithography will be adequate for the 180-nm critical dimension (CD) generation (i. e. 1-Gb DRAMs planned for initial manufacturing in 2001). Major efforts are underway in the United States (SVG Lithography, ISI), in Japan (Nikon, Cannon), and in Europe (ASM Lithography) to meet the challenges of turning this experimental program into a manufacturing worthy tool.

The situation is far less defined for the following generation (130 nm CDs for the 2003/2004 time frame). There are active research programs underway in a number of technologies, each of these has advantages and critical issues. No consensus has yet emerged as to which, if any, of these technologies is going to take the place of optics as the industry mainstay. Some of the alternatives along with the major issues (a personal view) are summarized in Table I.

TABLE I: Alternative nanoscale lithographic techniques.

TECHNIQUE	FEATURES	ISSUES
X-ray	1 nm synchrotron source; 1×-proximity mask	1×-mask; cost/granularity; mask-wafer gap; proximity effects.
X-ray	plasma point source of X-rays	above & collimator
Extreme ultraviolet (EUV)	13-nm laser-produced plasma; 4× all-reflective, aspheric reduction optics	source; optics figure and reflectivity; mask issues
e-beam direct write	shaped e-beam	throughput; proximity effects; data handling; grid accuracy
projection e-beam (SCALPEL)	scatter mask; 4× reduction electron optics	mask durability, proximity corrections; throughput
advanced optical lithography	193- ⇒ 157- ⇒126-nm; resolution enhancements: proximity correction, phase shift, off-axis illumination.	optics, resolution vs. depth-of-field vs. process latitude; masks; data handling requirements
interferometric lithography	coherent interference effects to extend optics; mix-and-match between interferometric and optical tools.	extension to realistic patterns; requirement for multiple exposures and alignment.

Proximity X-ray lithography is the most developed alternative. A difficult 1× mask silicon nitride membrane patterned with a heavy metal absorber is required. The precision and stability of this mask must be consistent with 130-nm CD groundrules. The synchrotron is itself a major issue. Granularity refers to the need to add an additional synchrotron once the available number of exposure stations have been added around the ring. Almost all of these techniques suffer from some degree of proximity correction requirement. This refers to the fact that the printed pattern is influenced by adjacent features; requiring modifications to the mask that depend on the local topology. This dramatically increases the computational power and time needed to make the mask as well as posing enormous metrology and inspection demands.

Point X-ray sources are an alternative to large expensive X-ray synchrotron sources. Here the major issues are brightness and durability, since these are high energy pulsed-power discharges. A major difficulty is that there are virtually no optical materials at these X-ray wavelengths so that traditional optical elements are unavailable. One specific need is a collimator to both collect more of the solid-angle of emission and reduce vignetting over the mask-wafer gap.

Extreme ultraviolet (EUV) lithography is a promising technique based on a laser-produced plasma source at ~ 13-nm. This is a reduction optical approach requiring a reflective mask and aspheric reflective optics. Multilayer reflectors are required to achieve sufficient reflectivity at this wavelength.

Electron-beam lithography has more than adequate resolution for this generation. The major issue here is writing speed and throughput. Again, there are proximity effects which require intensive, on the fly, calculations of dose and beam shape. Since the beam is directed by electric and magnetic fields, grid accuracy and precision are also major issues. SCALPEL is a projection e-beam technique that uses a mask to locally scatter electrons out of the beam.

For wavelengths below the 193-nm ArF wavelength, transmitting optical materials are no longer available (except perhaps CaF_2 at 157 nm) and a transition to an all-reflective system is required. Most likely, the transition to reflective optics will result in a significant reduction in the possible NAs, reducing the benefit of shorter wavelengths. Optical sources with sufficient average power for high throughput manufacturing are another major problem for wavelengths shorter than 193 nm. Since these systems will be working closer to theoretical diffraction limits than current lithography, the trade-offs between resolution, depth-of-field and process latitude will become more problematical.

Interferometric lithography uses coherent optical sources to push optics to theoretical limits. The period of the interference between two coherent beams incident on a wafer at equal and opposite angles, θ, is just $p = \lambda/[2\sin\theta]$. Since is easy to adjust q so that $\sin\theta \sim 1$, the limiting period is $\lambda/2$ and the CD for equal lines and spaces is $\lambda/2$. With available lasers, it is straightforward to make patterns out to ~ 50-nm, well beyond the current industry needs. The difficulty here is going beyond simple line:space or via hole arrays to real circuit patterns. Industry is currently exploring the use of interferometric lithography to produce test structures for advanced generation process development well ahead of the timelines imposed by the availability of lithographic tools for these generations.

III. Interferometric Lithography

Multiple-exposure interferometric lithography[2-4] provides an possible solution to this need for complex circuit patterns. Interferometric lithography has already demonstrated the necessary resolution for 180-nm and even 90-nm structures, using commercially available near-UV laser sources (355 nm, 3ω YAG/ 364 nm, Ar-ion) and well developed I-line resists, and can be readily extended to future lithography generations (130-nm, 90-nm, 70-nm, 50-nm) with existing laser sources at much lower cost than other approaches. Major features of interferometric lithography include a maskless, large-field capability for sub-wavelength structures (CD ~ $\lambda/4$ for dense

structures) with an essentially infinite depth-of-field (literally 1 m) produced with very simple, low-NA optical components (primarily flat mirrors). The fabrication of dense (1:1 line:space ratio) arrays of lines and via holes and sparse (1:10 line:space ratio) arrays of lines has been demonstrated. These periodic structures are ideal for the process development needs outlined above.

Figure 1 shows the basic idea of interferometric lithography. For two coherent, plane wave laser beams at a wavelength λ incident on a photoresist layer on a wafer at angles of $\pm\theta$, a grating of period $p = \lambda/(2\sin\theta)$ is formed. For this single exposure, the exposure flux (J/cm^2) as a function of position is given by:

$$F(x) = 2F_0\left[1 + \cos(2kx\sin\theta)\right] \tag{1}$$

where F_0 is the flux (intensity × duration) of each beam (assumed equal) and $k = 2\pi/\lambda$. This expression has no explicit z-dependence, consistent with the large depth of field. The grating lines are parallel to the y-axis, and the phase term has been arbitrarily set to zero. Since the intensity at the minima goes to zero, the modulation $M = [(F_{max}-F_{min})/(F_{max}+F_{min})] = 1$.

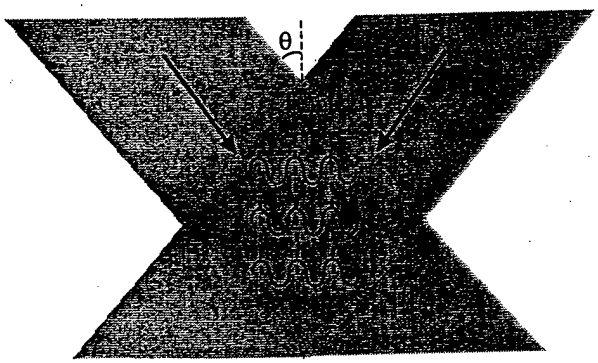


Figure 1: Interferometric lithography results from the interference of two coherent, plane-wave laser sources incident on a photoresist coated wafer at symmetric angles $\pm\theta$.

As is the case with any lithographic technique, the nonlinear response of the photoresist results in a sharpened profile for the developed photoresist as contrasted with the aerial image of Eq. 1. The periodicity of the pattern is specified by the exposure geometry; the developed resist CD depends on the flux as well as the develop parameters and can be varied over a wide range[5]. In particular, because the flux does go to zero at the minima, it is possible to achieve very small line:space ratios by extending the exposure to high flux levels. Figure 2 shows two examples of 1-D 0.18 μm CD structures, the figure on the left shows a dense 1:1 line:space pattern with a pitch of 0.3 μm; on the right a sparse 1:10 line:space pattern with a pitch of 2 μm. The differences between the two exposures are in the periods (θ) and the exposure flux.

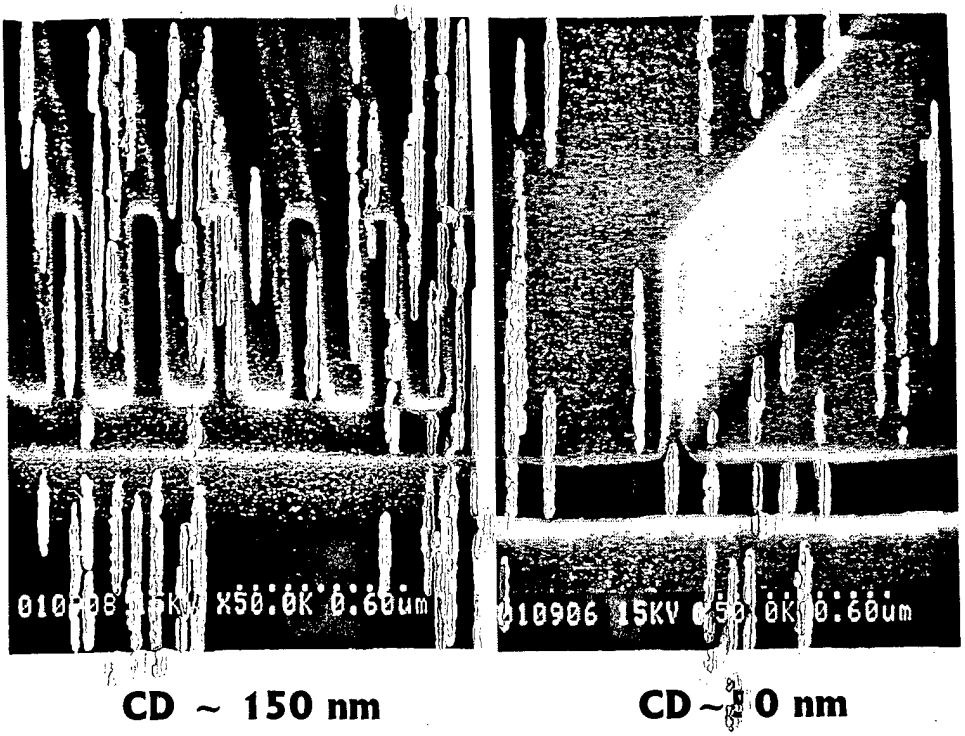


Figure 2: Dense (left) and sparse (right) structures at I-line. Both structures are in Shipley 505 resist (0.6-μm thick) using both a bottom ARC and a post-exposure bake.

The major issue with interferometric lithography is not the scale, but extensions from simple line:space patterns to complex, nonrepetitive circuit patterns. The most straightforward approach is to mix-and-match between interferometric and imaging optical lithography. Interferometric lithography could be used to write the fine features, e. g. gates or interconnect via holes, and a lower resolution optical lithography, either in the same photoresist level or with additional intermediate processing steps, used to delimit the extent of the interferometric exposure. The resolution limit on the optical lithography is, at worst for 1:1 line:space structures, only ½ of that required to define the structure. Multiple exposure and multiple-beam interferometric techniques extend the range of structures available from interferometric lithography.

However, the traditional flexibility of independently specifying each resolution element in an optical image is not available to interferometric lithography. Thus, application of this technology will require a dialog with the circuit design community as well as the manufacturing community. For example, many memory products have both highly periodic core areas and aperiodic control circuitry. The application of interferometric lithography would be highly simplified, if there could be a common grid at the circuit CD underlying both regions. Then, for example, an interconnect via hole level could be printed by interferometric lithography, a dense set of holes selected by optical lithography in the core regions, and a sparser set of holes selected for the control regions. At present, there is no correlation between positions in these two regions. This is just a simple example of the dialog that has to be in place if interferometric lithography is to progress from test structures to ULSI manufacturing.

IV. Summary

Lithography is a potential showstopper for the industry at the 130-nm CD node and beyond. At present there is no clear path from the numerous experimental development technologies to a high volume manufacturing tool. Time is short; the industry need is for a operational and verified tool set by 2000 to allow for initial manufacturing in 2003. Interferometric lithography provides an alternative, optics-based lithographic capability that has demonstrated sufficient resolution for the next several ULSI generations. This capability is already being exploited for test structures to allow development of next generation process capabilities concurrently with general purpose lithographic techniques. Application of interferometric lithography to manufacturing will depend both on the development of multiple exposure and multiple beam techniques to write more complex cells, and on an interaction with the design process to allow manufacturing by interferometric lithography.

Acknowledgments:

Support for this work was provided by the Defense Advanced Projects Agency and by Sandia National Laboratories. Many people have contributed to the developments in interferometric lithography reported here and to my understanding of the challenges facing all lithographic techniques. At UNM I am indebted to Xiaolan Chen, Dr. Saleem Zaidi, and Zhao Zheng. Many people at SEMATECH have contributed to process development efforts and to the application to test structures including Ron Carpio, Scott Mackay, John Petersen and Frank Schellenberg.

---

[1] National Technology Roadmap for Semiconductors, (Semiconductor Industry Assoc., 1994).

[2] S. H. Zaidi and S. R. J. Brueck, Multiple Exposure Interferometric Lithography, Jour. Vac. Sci. Tech. **B11**, 658 (1993).

[3] S. H. Zaidi and S. R. J. Brueck, Multiple Exposure Interferometric Lithography, in Optical/Laser Microlithography VII, T. Brunner, ed., SPIE **2197**, 869 (1994).

[4] X. Chen, S. H. Zaidi, S. R. J. Brueck and D. J. Devine, "Interferometric lithography of sub-micrometer sparse hole arrays for field-emission applications," Jour. Vac. Sci. Tech. **B14**, 3339-3349 (1996).

[5] X. Chen, Z. Zhang, S. R. J. Brueck, R. A. Carpio, and J. S. Petersen, "Process Development for 180-nm Structures using Interferometric Lithography and I-Line Resist," SPIE, to be published.

Imaging interferometric lithography: A wavelength division multiplex approach to extending optical lithography

Xiaolan Chen[a] and S. R. J. Brueck[a),b),c)]
Center for High Technology Materials, University of New Mexico, Albuquerque, New Mexico 87106

(Received 29 May 1998; accepted 16 September 1998)

The critical dimension (CD) limits of conventional optical lithography follow directly from the low-pass filter characteristics of the imaging optical system ($|k| \lesssim 2\pi \mathrm{NA}/\lambda$ where λ is the optical wavelength and NA the numerical aperture). In contrast, the linear systems limits of optics extend to spatial frequencies of $4\pi/\lambda$ (interference between counterpropagating beams at grazing incidence). Imaging interferometric lithography is introduced as a technique to approach this linear systems limit while retaining the arbitrary pattern capability of an imaging optical system. Multiple, wavelength-division-multiplexed exposures are used, each exposure recording a different portion of frequency space. A conventional, coherent illumination exposure provides the low frequency information, within the lens passband. Offset exposures provide the high spatial frequency information. Off-axis illumination shifts a portion of the high spatial frequency diffraction from the mask into the lens passband and interference with a reference beam resets the frequencies once they are transmitted through the optical system. For a typical x-y geometry pattern, offset exposures in the x and y directions provide a sufficient coverage of frequency space. Model calculations illustrate that the imaging capabilities of imaging interferometric lithography (IIL) for dense features extend to $\sim\lambda/3$ (130 nm at I line; 65 nm at an ArF exposure wavelength). Initial experiments are reported at I line with a modest (NA=0.04) optical system. The results are in good agreement with the model calculations. A resolution enhancement of $\sim 3\times$ from dense 6 μm CDs for a conventional, coherent illumination exposure to ~dense 2 μm CDs for an IIL exposure sequence is demonstrated. © *1998 American Vacuum Society.* [S0734-211X(98)12806-8]

I. INTRODUCTION

The resolution limit of diffraction-limited optical lithography (OL) is often described by the simple Rayleigh formula

$$R = \kappa_1 \lambda/\mathrm{NA}, \tag{1}$$

where κ_1 is related to process latitude, λ is the wavelength, and NA the optical system numerical aperture. Practical constraints limit κ_1 to ~0.6 so that the maximum resolution for an I line wavelength (365 nm) and a 0.6 NA lens is $R \sim \lambda \sim 365$ nm. Several approaches to improving this resolution are being explored. The most straightforward approach is to reduce the wavelength. Advanced commercial lithography tools are now using a 248 nm KrF laser illumination source and intensive development is underway on 193 nm ArF-laser based systems. Resolution enhancement techniques (RET) such as phase-shift masks (PSMs),[1] optical proximity correction (OPC),[2] and off-axis illumination (OAI)[3] are alternate approaches to improving the resolution at a given wavelength. In effect, these techniques allow a reduction in κ_1. Each of these has inherent trade-offs in terms of manufacturability versus resolution.

The Rayleigh resolution limit can be understood simply as the inverse of the bandwidth for the range of spatial frequencies passed by the lens ($|k| \lesssim k_o \mathrm{NA}$ where $k_o = 2\pi/\lambda$). The available frequency space supported by optics extends much further to $|k| = 2k_o$, e.g., to counterpropagating waves at grazing incidence to the wafer. Thus the linear system response of an OL system is dominated by the low-pass filter characteristics of the lens, not by any fundamental limitations of optical wave propagation. The RET techniques all improve the resolution by enhancing the spatial frequencies between NA/λ and 2NA/λ, resulting in a more nearly uniform transfer function out the highest frequencies support by the optical system. However, again they are limited by the spatial frequency bandwidth imposed by the lens NA, not by the ultimate linear systems constraints of optics.

Interferometric lithography[4,5] (IL) is based on the coherent interference of a small number of nominally plane-wave optical beams incident on a photoresist layer. Because there is no lens involved, it is very easy to achieve spatial scales approaching the fundamental linear systems limit of optics and much smaller than those available from imaging systems at the same wavelength. For an exposure with two coherent laser beams incident on a wafer at angles $\pm\theta$ with respect to the wafer normal, the normalized aerial exposure dose is $D(x) = 1 + \cos[2k_o x \sin(\theta)]$. It is easy to access angles such that $\sin\theta \sim 1$ so that the limiting pitch is $\lambda/2$ and for dense, 1:1 line:space patterns the limiting critical dimension is $\lambda/4$ or ~90 nm at I line (365 nm). We have previously demonstrated[5,6] line/space and hole/post arrays approaching this limit. These patterns have utility as test structures for the semiconductor industry as well as other applications such as field-emitter arrays[7] where periodic patterns are desired. Us-

a)Also at the Department of Electrical and Computer Engineering.
b)Also at the Department of Physics and Astronomy.
c)Electronic mail: brueck@chtm.unm.edu

ing additional beams in a single exposure and overlaying multiple exposures allows these results to be extended to more complex, but still repetitive, two-dimensional (2D) patterns.[8] Moiré alignment techniques have been developed and demonstrated[9] to allow mix-and-mismatch patterns between multiple IL levels and between IL and OL levels.

However, the pattern flexibility of IL still falls far short of that required for actual ultralarge scale integration (ULSI) levels which contain very large numbers of spatial frequencies ($\sim 10^{10}$ for a 2×2 cm^2 die and a 200 nm dense pitch). Imaging interferometric lithography[10,11] (IIL) is a newly developed approach that integrates the best features of OL and IL to provide the arbitrary pattern capability of OL with resolution approaching that of IL. The key innovation in IIL is to replace one of the individual plane waves of IL with a large number of spatial frequencies collected with an optical system. Off-axis illumination is used to downshift the high spatial frequency components generated with a mask to low frequencies where they are collected within the lens bandpass, and interference with the remaining plane wave of IL along with the square law intensity response of the photoresist resets the frequencies at the wafer. Multiple exposures provide coverage of a sufficient region of frequency space to achieve a faithful image. IIL can provide the highest spatial frequencies available to optics while still retaining the capability of OL to parallel process large numbers of spatial frequencies and hence provide arbitrary pattern flexibility.

IIL is a wavelength division multiplex (WDM) approach to lithography. The finite lens bandpass is overcome by multiple frequency offsets, recording different portions of frequency space in each exposure. The nonlinear relationships between electric field and intensity, both in the scattering from the mask and the exposure of the photoresist enable the frequency shifts that make IIL possible. These are directly analogous to the heterodyne frequency shifts, enabled by material nonlinearities, familiar from communications. The individual exposures are (partially) coherent; the summation of intensities from multiple exposures in the resist is incoherent. Most likely in an engineered manufacturing system, the multiple exposures necessary for IIL would be accomplished within a single pass of the wafer through the exposure tool by using appropriate combinations of time gating and multiple, incoherent optical sources.

IIL is related to the concept of optical system superresolution first discussed by Lukosz.[12] The initial concept used multiple gratings to diffract different portions of the image frequency content simultaneously into the lens passband and to rest the frequencies after the lens. Because of the simultaneous interference of multiple orders, the image field was limited [striped for one-dimensional (1D) gratings, checkerboard for 2D gratings]. Fukuda *et al.*[13] recently evaluated a variant of this idea and found it to be impractical because of the limited spatial field resulting from the multiple grating diffraction orders and of the unacceptable aberrations introduced by the gratings and substrates.

Von Bunau *et al.* have analyzed[14] and demonstrated[15] a multiple exposure technique to improve the process latitude and depth-of-focus for isolated features within the spatial frequency constraints of OL systems. We demonstrate that IIL not only improves the process latitude but also extends the spatial frequency coverage of an optical system. For the present experiments, with a very limited optical system, an improvement of $\sim3\times$ in the resolution for dense features is demonstrated. Based on the modeling results, a resolution extending out to the linear systems limits of optics, $\sim\lambda/3$ for arbitrary structures is anticipated.

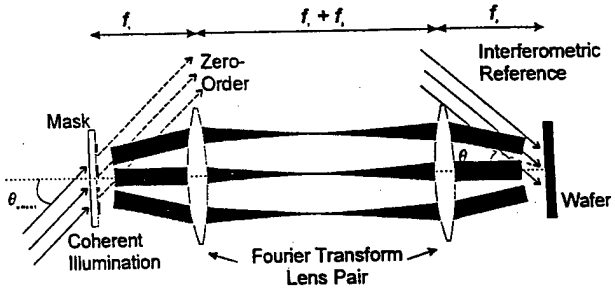


FIG. 1. Imaging interferometric lithography optical system. The high spatial frequency components (large diffraction angle) of the mask diffraction are shifted into the optical system passband by off-axis illumination. After passing through the optical system these frequency components are reset by interference with a plane-wave reference beam at the wafer plane.

The next section provides a brief introduction to the theory of IIL for the special case of coherent illumination. The experimental arrangement and results are then described. The discussion briefly compares IIL to other RET techniques. Only IIL can extend the frequency coverage out to $2/\lambda$ and achieve the limiting resolution of optics.

II. IMAGING INTERFEROMETRIC LITHOGRAPHY

In spatial frequency space, a two-beam IL exposure dose $\{D(x)=2D_o[1+\cos(2k_o x \sin\theta)]\}$ corresponds to three delta functions at spatial frequencies of 0 and $\pm 2k_o \sin\theta$. In contrast, a conventional, normal-illumination, coherent OL exposure records all of the spatial frequency components within a circle of radius k_oNA centered about the origin with a unity modulation transfer function (MTF). While the square-law intensity response of the photoresist results in spectral intensity components between k_oNA and $2k_o$NA, any high frequency information corresponding to a dense nanoscale pattern with a fundamental frequency above k_oNA is entirely lost. Incoherent or partially coherent illumination change the details, but not the essence, of this conclusion.

Figure 1 shows a prototypical IIL optical arrangement. Off-axis illumination with a coherent plane wave is used to shift the high spatial frequency content of the image diffraction into the lens passband. At the wafer, a plane-wave reference beam is reintroduced at the same off-axis angle (adjusted for any demagnification). By virtue of the square-law intensity response of the photoresist, interference between the image spatial frequency components transmitted through the lens and the reference beam resets the image spatial frequencies at the wafer. In principle, the wafer and the mask can be tilted relative to the optical axis. This has some advantages in terms of the available frequency coverage, but

the disadvantage of using the lens in a nontelecentric fashion likely overweighs this benefit. For simplicity, only a configuration with the wafer and the mask normal to the optical axis is presented here.

The intensity at the wafer is described as

$$
\begin{aligned}
I_{x\,\mathrm{offset}}(x,y) &= \Bigg| e^{-ik_{\mathrm{off}}x} + \beta \sum_{k_x} \sum_{k_y} F_{k_x,k_y} \\
&\quad \times M_c(k_x - k_{\mathrm{off}}; k_y) e^{i[(k_x - k_{\mathrm{off}})x + k_y y]} \Bigg|^2 \\
&= 1 + \beta^2 \sum_{k_x} \sum_{k_y} \sum_{k_x'} \sum_{k_y'} F_{k_x,k_y} F^*_{k_x',k_y'} M_c(k_x \\
&\quad - k_{\mathrm{off}}; k_y) M_c(k_x' - k_{\mathrm{off}}; k_y') \\
&\quad \times e^{i[(k_x - k_x')x + (k_y - k_y')y]} + \beta \sum_{k_x} \sum_{k_y} F_{k_x,k_y} \\
&\quad \times M_c(k_x - k_{\mathrm{off}}; k_y) e^{+i[k_x x + k_y y]} \\
&\quad + \beta \sum_{k_x} \sum_{k_y} F^*_{k_x,k_y} M_c(k_x - k_{\mathrm{off}}; k_y) e^{-i[k_x x + k_y y]},
\end{aligned}
\tag{2}
$$

where F_{k_x,k_y} is the electric-field Fourier component of the mask diffraction at the spatial frequencies k_x and k_y; M_c is the electric-field MTF of the optical system ($=1$ for $\sqrt{(k_x - k_{\mathrm{off}})^2 + k_y^2} \leq k_o \mathrm{NA}$; $=0$ otherwise); k_{off} is the x directed offset in the spatial frequencies introduced by the off-axis illumination. The β term represents the possibility of adjusting the relative intensities of the diffracted components passing through the lens to the reference beam. Initially, we take $\beta = 1$; the added flexibility this term provides is discussed more fully below. The final two terms in Eq. (1) are the desired result. The image Fourier components arising from diffraction of the illuminating beam at the mask are downshifted by k_{off}. All of those within a circle of radius NA/λ pass through the lens (the M_c function) and are upshifted back to the original spatial frequency (k_x and k_y) by interference with the reference beam. Because an image is positive definite, the coverage extends to two conjugate circles in intensity frequency space [in analogy with the $\pm 2k_o \sin(\theta)$ terms in IL] even though only a single sideband region is passed by the lens. Because of the asymmetry of the single sideband, this exposure is not telecentric. Telecentricity could be recovered, at the expense of additional complexity, by incorporating symmetrically disposed reference beams. By changing the offset angle, different regions of frequency space can be recorded at the wafer using multiple exposures. As always, the square-law photoresist response also results in additional spectral intensity (the constant and the low frequency intensity convolution term); these unwanted low frequency terms effectively decrease the contrast over that of an ideal image. This is very similar to the contrast reduction in conventional imaging as the Rayleigh limit is approached. The important question is "is the contrast sufficient to achieve the necessary CD control." A full answer is beyond the scope of this article. The modeling results suggest that ±5% dose control will be adequate for a 130 nm CD at I line; however, much more detailed investigation, both experimental and theoretical, is necessary to address this question.

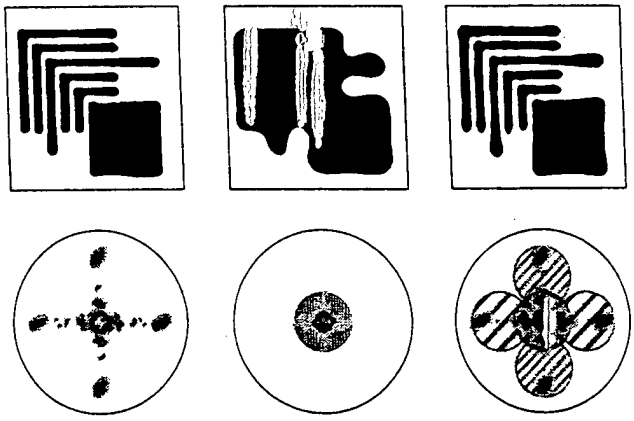


FIG. 2. Modeling for a complex pattern with a CD of 130 nm and an optical system NA of 0.65. The left column shows the results of coherently adding all of the possible frequency components within the linear systems limit of optics ($|k| < 2k_0$). The top panel shows the real-space image which, aside from some corner rounding, is a faithful rendition of the desired pattern. The bottom panel shows the corresponding frequency-space intensity distribution. The middle column shows the effect of a conventional, coherent illumination exposure. The low-pass filter characteristic of the lens eliminates the high-spatial frequencies corresponding to the dense line-space pattern. Finally, the right column shows the results of a three-exposure IIL sequence. The offset exposures restore the high frequencies and a good image is achieved. The regions of frequency space covered by the various exposures are shown.

Finally a full IIL exposure sequence consists of the incoherent addition of as many as three exposures, one offset in the x direction, one offset in the y direction, and a third conventional coherent exposure to provide the low frequency information, viz.,

$$
I_{\mathrm{total}}(x,y) = I_{x\,\mathrm{offset}}(x,y) + I_{y\,\mathrm{offset}}(x,y) + \alpha L_{\mathrm{coh}}(x,y). \tag{3}
$$

The α parameter allows adjustment of the relative spectral content at high versus low frequencies. This will be discussed more fully below.

A simple modeling effort adds important physical insight. A test structure containing dense and sparse lines at the CD as well as a large feature, 10×CD on a side, is shown on the top left of Fig. 2. All of these figures are for a 130 nm CD and an I line exposure wavelength with a lens NA of 0.65 corresponding to an effective κ_1 (=CD×NA/λ) of 0.23. This unit cell is repeated with an overall size of 40×40 CD^2. As will be discussed below, these results scale directly to the much lower NA and larger CD used in the first experiments. Larger, more complex patterns at the same CD and half-pitch contain a much denser array of spatial frequencies within the same regions of spatial frequency space. To first order, the photoresist is modeled as a simple threshold filter, only areas exposed to fluences above a threshold are developed. While this is a vastly oversimplified description of a lithographic response, it gives a good first approximation of the capabilities of IIL without requiring detailed photoresist modeling.

For reference, the left column of the figure shows two views of the linear systems limits of optics—a single coherent exposure including all spatial frequencies extending out to $2/\lambda$ with a unity MTF. This cannot be realized by any optical system, but serves as a goal for super-resolution techniques. The top left shows the real-space image; the bottom left shows the corresponding spatial-frequency-space intensity pattern. Aside from some edge corner rounding, the real space pattern replicates the mask pattern very well (note that this is for a dense CD of 130 nm at a 365 nm exposure wavelength or $\sim\lambda/3$). The radius $2k_o$ circle bounding the frequency-space plot represents the spatial frequency limit of optics, corresponding to sin $\theta=1$ for an interferometric exposure. Because of the x-y arrangement of the features (Manhattan geometry), the majority of the intensity lies along the k_x and k_y axes. The peaks at high frequency along both axes correspond to the spatial frequency of the dense line:space features at the CD (the nested "ells"). Most of the spectral intensity for the large box is at low frequencies but the edge definition extends out to high spatial frequencies.

The middle column of Fig. 2 shows the result of a single, coherent OL exposure (normal incidence illumination). The high spatial frequency information in the test pattern, corresponding to the dense lines, is cutoff by the lens restrictions as is born out by the spatial frequency plot. The result is a single, nondescript feature. No refinement of the process (i.e., lower κ_1) can give the desired result; the necessary high spatial frequency information is simply not present in the OL image.

In contrast, the right column of Fig. 2 shows the same views of the result of a three-exposure IIL process. Two offset exposures [horizontal and vertical each centered near the maximum spatial frequency offset possible (k_0) for the optical configuration of Fig. 1] provide the high spatial frequencies that were missing from the conventional optical exposure. The spectral regions covered in each exposure are indicated in the Fourier space view. The undulations along the (real space) feature edges are due to the extra low frequency components that accompany the offset exposures [the first two terms in Eq. (1)] and to the still incomplete coverage of frequency space. The x-y distribution of spatial frequencies is typical of Manhattan geometries; it is not necessary to completely cover Fourier space to get a good image. The analysis also shows that there is a substantial process window (>10%); more detailed modeling and experimentation are necessary to verify this preliminary conclusion.

III. EXPERIMENTAL ARRANGEMENT

Our first demonstration of IIL was carried out at I-line wavelengths using a single longitudinal mode, TEM_{00} Ar-ion laser source at 364 nm. The illumination system consisted of a 20× microscope objective and a 20 μm pinhole followed by a 50 cm focal length collimating lens overfilling the 6×6 cm^2 reticle. The binary chrome-on-glass reticle consisted of repetitive patterns as in Fig. 2 in four quadrants at CDs of 2, 3, 4, and 5 μm. The 1×-imaging system consisted of two simple achromatic doublet lenses (geometrical NA of 0.125)

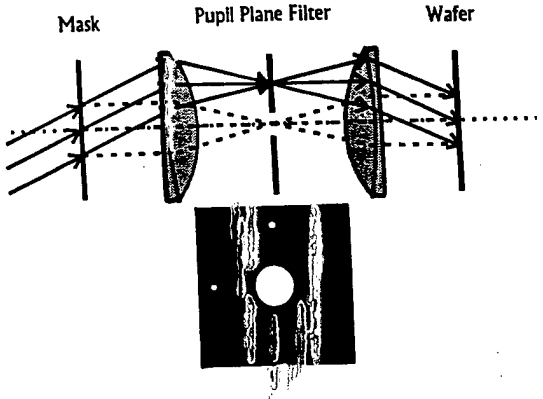


FIG. 3. Optical system used for the experiments. The lenses were simple achromatic doublets with a geometrical NA of 0.125. A pupil-plane filter was used to restrict the NA to 0.04 to provide a more nearly diffraction limited image. The two small holes cut into the pupil plane filter to pass the offset reference beams for the IIL exposures are also indicated.

stopped down, with an aperture in the Fourier plane, to a NA of 0.04 to assure nearly diffraction-limited operation (Fig. 3). Because the geometric NA of the optical system extended well beyond the usable, nearly diffraction-limited NA, it was possible, in these first demonstration experiments, to use the higher NA portions of the lens to transmit the off-axis reference beams. The offset illumination angle was chosen such that the fundamental spatial frequency of the dense 2 μm CD pattern (1/4 μm^{-1}) passed through the center of the lens aperture. For a 1× optical system the required reference beam angle at the wafer is the same as the offset illumination angle and corresponds to an NA of 0.09. Because of the lens aberrations at this high NA, the reference wave front was distorted in the wafer plane, as monitored with a shearing interferometer, corresponding to a spatially varying alignment error. The interferometric reference beams for the offset exposures were passed through small (~300 μm diameter) holes in the pupil plane aperture stop. In practice, the illumination angle was adjusted until the zero-order beam was transmitted through the small hole in the aperture plane. Multiple exposures were accomplished simply by blocking and unblocking portions of the illumination beam. Since the mask and wafer were not moved between exposures and a single optical system imaged both the signal and reference portions of the image, no additional alignment was necessary. Exposures were on 0.25-μm-thick photoresist-coated (Shipley 510L diluted 1:1 with thinner) Si wafers.

IV. EXPERIMENT

Figure 4 shows the results of a conventional (normal incidence) coherent exposure for the 3, 4, and 5 μm CD structures. The high frequency components of the 3 μm structure are eliminated by the lens leaving only an outline of the total structure. While some structure is evident for the 4 μm CD structure, there is insufficient resolution to define the pattern. The 5 μm CD structure is almost resolved. This pattern is characteristic of a coherent optical system just at cutoff. The fundamental frequency defining the line:space patterns is transmitted by the optical system but the slightly higher fre-

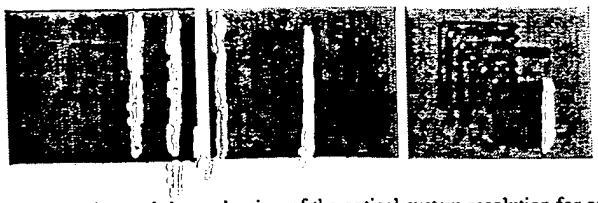


FIG. 4. Experimental determination of the optical system resolution for conventional, coherent illumination. Patterns are the same as Fig. 2 with CDs of 3, 4, and 5 μm. The pattern for the 5 μm CD is characteristic of a coherently illuminated optical system just at cutoff. The resolution is estimated at a dense 6 μm CD corresponding to a κ_1 of 0.66.

quencies necessary to define the edges and corners of the structures are blocked by the low-pass characteristic of the optical system. Thus, for a conventional coherent illumination exposure, we estimate that this optical system has a resolution of ~6 μm; this corresponds to a $\kappa_1 \sim 0.66$ in good agreement with the standard resolution formula [Eq. (1)].

The exposure results for the 2 μm CD pattern are shown in Fig. 5. The top left panel shows the result of a conventional, coherent OL exposure. The pattern is in good qualitative agreement with the model calculation shown on the bottom left panel of the figure. Also note the similarity between the model calculation of Fig. 2 ($\kappa_1 = 0.23$) and that of Fig. 5 ($\kappa_1 = 0.22$). The middle column shows the result of the two offset exposures without the low frequency exposure. Now the dense patterns are evident, but the large lower right box is absent. Note that this image is reversed, in the top image the photoresist has been removed everywhere except in the pattern, in this image, because the low frequency spatial components are not present, the photoresist is unexposed everywhere except for the spaces in-between the narrow lines. Again, there is good qualitative agreement with the model calculations. To speed up the model calculation a pixel size of CD/12 was used which results in the jagged edges which would be smooth curves with a finer grid. Finally, the right column shows the result of all three exposures. There is a good image of the entire pattern as expected from the model calculations. The resolution of the optical system has been increased by ~3× from 6 μm for a single exposure to 2 μm for an IIL exposure sequence, corresponding to an effective κ_1 of 0.22.

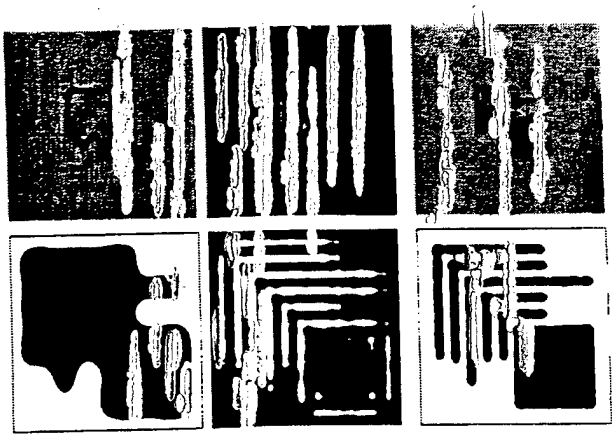


FIG. 5. Exposure results (top) and model calculations (bottom) for a 2 μm CD pattern and an optical system NA of 0.04. The left column is the result of a conventional, coherent illumination exposure. The middle column shows the result of the two offset exposures without the low frequency exposure; and the right column shows the result of a three-exposure IIL sequence. The resolution has been improved by 3× over conventional illumination with an effective κ_1 of 0.22.

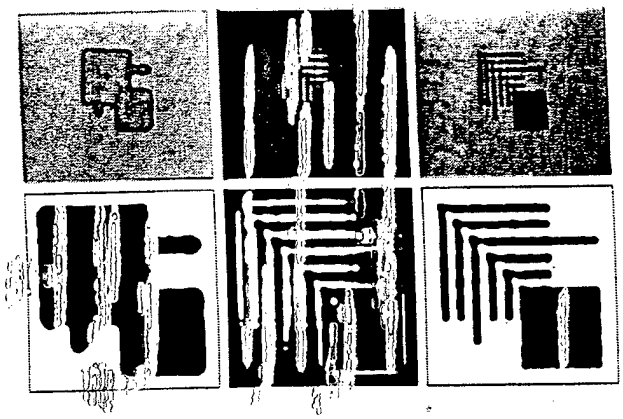


FIG. 6. Similar results for a 3 μm CD structure from a different portion of the reticle imaged in the same exposure as the 2 μm CD structure shown in Fig. 2 demonstrating that a large region of frequency space is covered in the IIL exposures.

Comparable results were obtained for the 3 μm CD patterns in a different portion of the field in the same exposure sequence as shown in Fig. 6 illustrating that a wide range of spatial frequencies are simultaneously transferred from the mask to the image. Note that for the particular exposure levels used, the outline of the large box is beginning to be visible in the middle column (two offset exposures only). This is directly analogous to the time domain response of a simple high-pass RC filter which transmits spikes only at the leading and trailing edges of a long pulse.

V. SUMMARY AND CONCLUSIONS

Imaging interferometric lithography eases many of the constraints that are putting pressure on conventional optical lithography and offers a path to ultimate linear systems limits of optics that extend to dense CDs of $\lambda/3$ for arbitrary patterns. Additionally, IIL eases rather than compounds the mask problem. For the exposure scheme outlined here, the mask requirement is simply a faithful binary chrome-on-glass rendition of the desired pattern, reduction optics are applicable and there is no requirement for either the optical proximity correction or the phase-shift control that are making current mask requirements so difficult.

Because the image is printed in multiple exposures, there are additional degrees of freedom that are not available in traditional optical lithography. The parameters that characterize the various exposures include the offset spatial frequency [k_{off}, Eq. (2)], the relative exposure dose for the high and low frequency components [α, Eq. (3)], and the relative field strength of the offset reference beams [β^{-1}, Eq. (2)]. Each of these parameters impacts aspects of the final image including the fine pattern details and the process latitude (CD control). A full discussion of these effects is beyond the scope of this article and will be presented elsewhere. For example, the contours of Fig. 2 were calculated for a β of 3

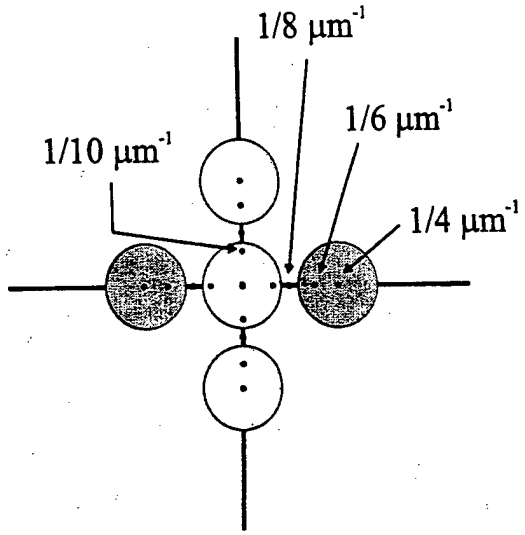


FIG. 7. Spatial frequency space plot corresponding to the experiment. Note that the fundamental frequency of the dense 4 μm CD features is in the gap between the low and high frequency exposures. Consequently, the 4 μm pattern did not print in these experiments.

to increase the high spatial frequency components relative to the low frequencies. The experimental results of Figs. 5 and 6 were obtained with $\beta=1$ and $\alpha=0.8$.

Perhaps the largest variation can be obtained by varying the offset. In Fig. 2, the offset circles in frequency space overlap slightly with the low frequency exposure. In the calculation, a pupil plane filter was assumed to avoid double counting of the spatial frequency components in the overlap regions. As an aside, this overlap is what limits the resolution of off-axis illumination approaches by giving more weight (higher MTF) to the low frequency components. For the experiment, the offset angle (corresponding to an NA of 0.09) was over twice the optical system NA of 0.04, so that there was a gap between the circles as shown in Fig. 7. This offset was chosen to place the fundamental spatial frequency of the dense 2 μm CD structures in the center of the lens for the offset exposure. The 4 μm CD patterns did not print in this exposure because the fundamental spatial frequency of the dense 4 μm CD pattern, corresponding to a NA of 0.045, fell within the gap. In this case, a small change in the offset angle to provide overlap between the spatial frequency space covered in each exposure would ensure that all features were printed. Finally, only those Fourier components printed in each exposure need be provided by a specific mask; a set of simplified masks (larger features) can be substituted for a complete mask.

As discussed in the introduction, all of the current RET techniques enhance the spatial frequency content between NA/λ and 2NA/λ. OPC uses subresolution features to increase these spectral intensities, and then suffers a differential attenuation in the optical system resulting in a closer match to the desired spectral intensities in the final image. PSMs introduce subharmonic features in the mask (e.g., alternating phase shifts) arranged so as to reduce the zero-order intensity and enhance the frequency components at $\pm f/2$ which then interfere using the resist square-law response to produce a pattern at f which can extend to 2NA/λ. OAI is most closely related to IIL. The limitation of passing the off-axis beams through the imaging lens constrains the maximum spatial frequency to 2NA/λ. The effective MTF is decreased at higher spatial frequencies because of the multiple counting of the lower frequencies. Only IIL offers the possibility of extending the frequency response beyond 2NA/λ to the linear systems limit of 4/λ thereby allowing smaller feature definition while still retaining the arbitrary pattern capabilities of imaging.

It is important to recognize that the multiple incoherently summed exposures do not imply multiple passes through multiple steppers. All of the exposures could be accomplished simultaneously simply by using multiple, mutually incoherent, laser sources. The optical system will necessarily be more complex than existing imaging systems, but once engineered and aligned the complexity of IIL is transparent to the operator and the system throughput is unaffected. Indeed, today's quadrupole off-axis illumination schemes in effect provide an incoherent summation of four simultaneous partially coherent exposures, closely related to the requirements of IIL.

The access to different parts of spatial frequency space allows application of much of the apparatus of linear systems theory that has been so successful in communications and image processing applications. These will be discussed in a future publication along with a more detailed analysis of the effects of the various parameters on the lithographic results.

ACKNOWLEDGMENTS

The authors thank Dr. Saleem Zaidi and Andrew Frauenglass for numerous helpful discussions and expert technical assistance. Dr. Wiliam Swantner and Dr. Janusz Wilczinski provided much useful insight into optical systems and lithography requirements. Partial support for this work was provided by DARPA.

[1]M. D. Levenson, N. S. Viswanathan, and R. A. Simpson, IEEE Trans. Electron Devices ED-29, 1828 (1982).
[2]A. Nakae, K. Kamon, T. Hanawa, K. Moriizumi, and H. Tanabe, Jpn. J. Appl. Phys., Part 1 35, 6396 (1996).
[3]K. Kamon, T. Miyamoto, Y. Myoi, H. Nagata, M. Tanaka, and K. Horie, Jpn. J. Appl. Phys., Part 1 30, 3021 (1991).
[4]E. H. Anderson, C. M. Horowitz, and H. I. Smith, Appl. Phys. Lett. 43, 874 (1983).
[5]S. H. Zaidi, S. R. J. Brueck, F. M. Schellenberg, R. S. Mackay, K. Uekert, and J. J. Persoff, Proc. SPIE 3048, 248 (1997).
[6]X. Chen, Z. Zhang, S. R. J. Brueck, R. A. Carpio, and J. S. Petersen, Proc. SPIE 3048, 309 (1997).
[7]X. Chen, S. H. Zaidi, S. R. J. Brueck, and D. J. Devine, J. Vac. Sci. Technol. B 14, 3339 (1996).
[8]S. H. Zaidi and S. R. J. Brueck, J. Vac. Sci. Technol. B 11, 658 (1993).
[9]S. H. Zaidi, S. R. J. Brueck, T. Hill, and R. N. Shagam, Proc. SPIE 3331, 406 (1998).
[10]S. R. J. Brueck, Microlithography World 7, 2 (1998).
[11]X. Chen and S. R. J. Brueck, Proc. SPIE 3331, 214 (1998).
[12]W. Lukosz, J. Opt. Soc. Am. 56, 1463 (1966).
[13]H. Fukuda and R. M. von Bunau, J. Vac. Sci. Technol. B 14, 4162 (1996).
[14]R. M. von Bunau, H. Fukuda, and T. Terasawa, Proc. SPIE 2726, 375 (1996).
[15]R. M. von Bunau and H. Fukuda, Jpn. J. Appl. Phys., Part 1 35, 6400 (1996).

Marek Osiński

TECHNICAL DIGEST

Summaries of papers presented at the
Conference on Lasers and Electro-Optics

Conference Edition

The Moscone Center
San Francisco, California
May 3-8, 1998

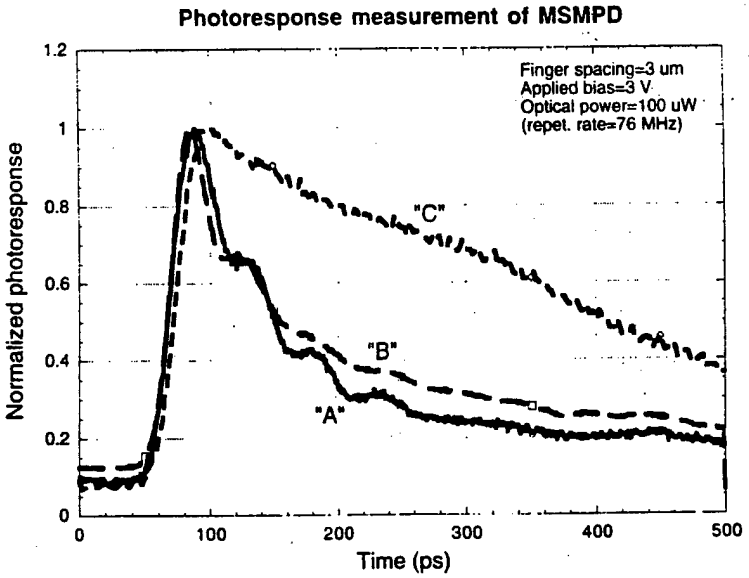
1998 OSA Technical Digest Series
Volume 6

CLEO '98 SPONSORED BY
IEEE/Lasers and Electro-Optics Society
OSA-Optical Society of America

In Cooperation with:
Quantum Electronics Division of the European Physical and Optical Society
Japanese Quantum Electronics Joint Group

Optical Society of America
2010 Massachusetts Avenue, NW
Washington, DC 20036-1023

OSA.



CWH3 Fig. 2. Photoresponse of MSM photodetectors for three different epi-structures.

CWH4 **3:15 pm**

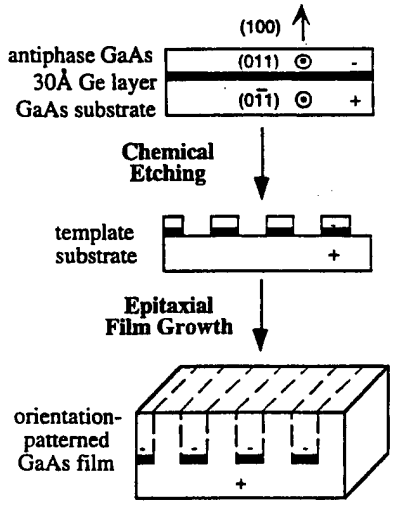
MBE growth of laterally antiphase-patterned GaAs films using thin Ge layers for waveguide mixing

Loren A. Eyres, Christopher B. Ebert, Martin M. Fejer, James S. Harris, Jr., *Solid State and Photonics Laboratory, Stanford University, Stanford, California 94305-4090*

QPM frequency conversion in waveguides has proven useful for both mid-IR generation and wavelength division multiplexing (WDM) wavelength shifting using both semiconductor and ferroelectric materials.[1–3] Semiconductor devices are attractive for these applications because of their large nonlinear susceptibilities (120 pm/V), wide transparency range, and potential integration with pump lasers, but to date semiconductor waveguide device performance has been limited by waveguide losses in the near-IR, attributed to optical scattering from fabrication-induced waveguide corrugations. Where previous technology has employed semiconductor wafer fusion to fabricate an orientation template that then serves as a substrate for epitaxial regrowth of an orientation-patterned waveguide, we have developed a technique for all-epitaxial fabrication of orientation-patterned GaAs templates that has the potential to reduce surface corrugations and associated waveguide losses in nonlinear devices grown on these substrates.

This technique takes advantage of polar-on-nonpolar epitaxy by introducing a thin lattice-matched Ge layer between the substrate and a top GaAs film. The lower crystal symmetry of the GaAs relative to the Ge makes possible the nucleation on a Ge surface of two different GaAs orientations, which differ by a crystal inversion. By controlling the orientation of the top GaAs layer using a combination of substrate misorientation, growth temperature, and arsenic species, we force the top GaAs layer to grow antiphase relative to the underlying GaAs substrate, as illustrated in the top diagram of Fig. 1. We have observed the highest quality antiphase GaAs films using (100) GaAs substrates misoriented 4° off toward (111)B and a tetrameric As flux. We used 30-Å-thick Ge layers, though this can be reduced below 20 Å. Reflection high-energy electron diffraction (RHEED) patterns from the GaAs films and anisotropic etching confirm that the top GaAs layers are antiphase to the substrate with the exception of small antiphase domains (APDs), which nucleate at the Ge surface layer and annihilate during GaAs growth.

Using this structure, we have performed lithography and wet chemical etching to etch through the top GaAs and Ge layers and expose the substrate in selected regions, leaving a template with modulated orientation across the surface, following the outline of Fig. 1. Performing molecular beam epitaxy (MBE) regrowth on this template, we have grown laterally rotation-patterned 1.5-μm-thick GaAs films. Smooth surfaces are observed for both GaAs orientations, though some disorder is visible at the antiphase boundary (APB) between the two different orientations, which is traceable to roughness on the template edge after wet chemical etching. Improved etching uniformity should minimize this limitation.



CWH4 Fig. 1. Outline of orientation-patterned GaAs fabrication process using thin Ge layers.

In summary, we have developed an all-epitaxial technique to fabricate orientation-patterned GaAs films. This technique could make possible orientation-patterned waveguide devices with extremely small (<100 Å) corrugations and thereby reduce associated waveguide losses in these devices, as scattering losses scale nonlinearily with corrugation amplitude.

1. S.J.B. Yoo, C. Caneau, R. Bhat, M.A. Koza, A. Rajhel, N. Antoniades, Appl. Phys. Lett. **68**, 2609 (1996).
2. C.Q. Xu, H. Okayama, M. Kawahara, Electron. Lett. **30**, 2168 (1994).
3. K.P. Petrov, S. Waltman, E.J. Dlugokencky, M. Arbore, M.M. Fejer, F.K. Tittle, L.W. Hollberg, Appl. Phys. B **54**, 567 (1997).

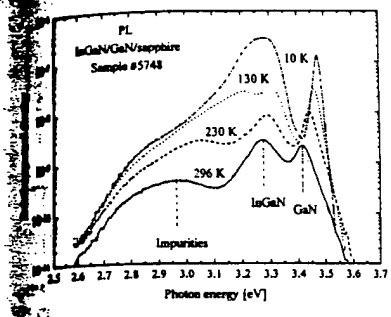
CWH5 **3:30 pm**

Anomalous temperature behavior and band tailing in InGaN/GaN heterostructures grown on sapphire by MOCVD

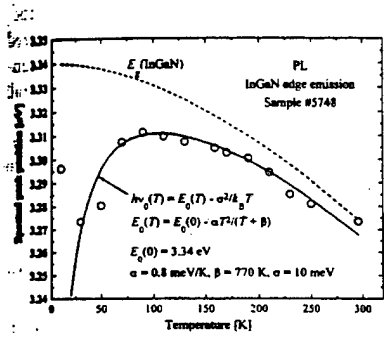
Marek Osiński, Petr G. Eliseev, Piotr Perlin, Jinhyun Lee, Hisao Sato,* Tomoya Sugahara,* Yoshiki Naoi,* Shiro Sakai,* *Center for High Technology Materials, University of New Mexico, 1313 Goddard SE, Albuquerque, New Mexico 87106; E-mail: osinski@chtm.unm.edu*

InGaN is very attractive as the active region material for optoelectronic devices emitting near-UV and blue/green light.[1] However, in spite of tremendous progress in realization of GaN/InGaN/AlGaN light-emitting diodes and diode lasers, the underlying fundamental processes of carrier recombination in InGaN are still poorly understood. For example, controversies surround the role of localized excitons in optical gain, or self-formation of quantum dots in InGaN. Light emission from single-quantum-well (SQW) blue and green light-emitting diodes (LEDs) was studied extensively, and it was shown that their unusual temperature, current, and hydrostatic pressure behavior was consistent with involvement of density-of-states (DOS) band tails in the optical emission process.[2] In this paper, we demonstrate that thicker InGaN/GaN heterostructures exhibit behavior similar to that observed in SQW LEDs.

Samples under study were grown on (0001) sapphire substrates by atmospheric-pressure metal-organic chemical-vapor deposition (MOCVD). A low-temperature AlGaN buffer layer was grown at 500°C, followed by a ~0.4-μm-thick GaN layer grown at 1050°C, and a InGaN layer grown at 800°C. Thickness and composition of $In_xGa_{1-x}N$ layers varied from 20 to 110 nm and from $x = 0.06$ to $x = 0.09$, respectively. Growth of single-heterostructure samples was stopped at that point, while an additional 0.1-μm-thick cap layer of GaN was grown at 1050°C for double-heterostructure (DH) samples. All layers were nominally undoped.



CWH5 Fig. 1. Temperature evolution of PL spectra from a GaN/InGaN/GaN DH sample with 40-nm-thick InGaN layer; 325-nm line of He-Cd laser was used to excite the luminescence. Incident power was 4.5 mW, focused to a 50-μm-diameter spot.



CWH5 Fig. 2. Experimental (circles) and calculated (solid line) variation of the peak photon energy of InGaN emission with temperature. Note that the blueshift in the 30–100 K interval is opposite to InGaN bandgap variation with temperature.

PL spectra (cf. Fig. 1) display a characteristic anomaly observed previously[3] in SQW LEDs: the InGaN edge emission shifts towards the blue with increasing temperature, while the GaN edge emission undergoes a redshift, consistent with thermal variation of the bandgap energy.

The blueshift of InGaN emission under nondegenerate conditions can be explained assuming the radiative transitions occur between states located below the bandgap. In the simplest case, these states can be represented as Gaussian band tails, leading to temperature-dependent peak photon energy as shown in Fig. 2, with $\sigma^2 = \sigma_e^2 + \sigma_h^2$, where σ_e^2 and σ_h^2 are the dispersions of electron and hole tails of the DOS, respectively. The term $-\sigma^2/k_BT$ produces a Stokes-type shift of the peak relative to its nominal position at the bandgap energy.[4] Note that the fitting parameters $E_0(0)$, α, and β shown in Fig. 2 agree very well with expected values of InGaN bandgap at 0 K and Varshni parameters describing the temperature variation of the bandgap.

At temperatures lower than 30 K, PL peak position is affected by degeneracy of the level occupation and is sensitive to the pumping intensity even at low excitation rates. The blueshift evolves into a redshift above ~100 K, as predicted by the model.

The parameter σ describes inhomogeneous edge broadening caused by the band tails. The nature of this broadening may relate to the high density of structural defects (dislocations) and/or to fluctuations of local alloy composition. Also, dislocations may be pinned by In segregation in their vicinity, thus providing local variations in the bandgap. Edge-type dislocations can themselves produce bandgap variations due to hydrostatic pressure effects in the elastic-stress field that surrounds them. Previous estimates[5] indicate that dislocation density of $\sim 10^9$ cm^{-2}, quite typical for nitride materials, should be sufficient to explain the value of 10 meV for σ.

*Department of Electrical and Electronic Engineering, University of Tokushima, 2-1 Minami-Josanjima, Tokushima 770, Japan

1. S. Nakamura, G. Fasol, *The Blue Laser Diode: GaN Based Light Emitters and Lasers* (Springer-Verlag, Berlin, 1997).
2. M. Osiński, P. Perlin, P.G. Eliseev, J. Lee, V.A. Smagley, Proc. 2nd International Conf. Nitride Semiconductors ICNS'97, Tokushima, Japan, 27–31 Oct., 1997, Paper F3–4, pp. 508–509.
3. P. Perlin, M. Osiński, P.G. Eliseev, in III-V Nitrides, F.A. Ponce, T.D. Moustakas, I. Akasaki, B.A. Monemar, eds., Proceedings MRS Symposium Boston, MA, 2–6 Dec., 1996, **449**, pp. 1173–1178.
4. P.G. Eliseev, P. Perlin, J. Lee, M. Osiński, Appl. Phys. Lett. **71**, 569 (1997).
5. V.A. Smagley, P.G. Eliseev, M. Osiński, in Physics and Simulation of Optoelectronic Devices V, M. Osiński, W.W. Chow, eds., Proc. SPIE **2994**, 129–140 (1997).

CWH6 **3:45 pm**

Low-temperature scanning tunneling microscope-induced luminescence of GaN

S. Evoy, C.K. Harnett, H.G. Craighead, T.J. Eustis,* W.A. Davis,** M.J. Murphy,† W.J. Schaff,† L.F. Eastman,† *School of Applied and Engineering Physics, Cornell University, Ithaca, New York 14853*

The GaN system is of great interest for optoelectronic applications in the blue spectral region. Blue light-emitting diodes and GaN-based lasers have been developed in spite of high dislocation densities and luminescence from deep states. Such issues prompted an ongoing interest in spatially resolved cathodoluminescence (SRCL) studies of the system. For example, SRCL results suggest that yellow luminescence is associated with the presence of extended defects and specifically with the existence of low angle grain boundaries.[1]

Such studies are traditionally performed by fitting a scanning electron microscope (SEM) with collection optics. Scanning tunneling microscope-induced luminescence (STL) offers an increased spatial resolution and an accurate control of the injection bias. These additional advantages show great potential for nanoscale studies of GaN luminescence.

The STL of metal-organic chemical-vapor deposition (MOCVD) and molecular beam epitaxy (MBE)-grown GaN was first reported in Garni *et al.*[2] and Envoy *et al.*,[3] respectively. Furthermore, recent STL results support the increase of defect luminescence at grain boundaries.[4] These studies were performed at room temperature and did not include maps of the photon emission. We will present the STL of MBE-grown material using a liquid helium (LHe) cooled UHV scanning tunnel microscope (STM) and will discuss luminescence images at various wavelengths. To our knowledge, this is the first report of low-temperature STL of GaN. We also complement our STL study using low-temperature SEM-induced cathodoluminescence (SEM-CL).

Experiments were performed on Si-doped (n-type) α-GaN films grown on sapphire by MBE. Doping concentrations in the range of $n = 10^{18}$ to 10^{19} cm^{-3} were used. SEM-CL reveals submicrometer features and evidence of small quantities of cubic crystallites in some samples. At T=14°K, the near-band edge (D°X) transition dominates the spectra, with yellow luminescence below the detection limit.

A low-temperature STM was also used for the injection of carriers. As reported in Garni *et al.*,[2] luminescence intensity follows a parabolic increase with positive tip bias. No luminescence is observed at negative tip polarity, as expected from n-doped material.

Preliminary spectroscopic analysis involving band-pass filters suggest near band-edge emission, as well as emission covering the visible range. Nanocrystallites similar to those observed in SEM-CL are apparent in both topographic and luminescence images. We will present luminescence images of various wavelengths and correlate these findings with the issues described above.

This work was funded by NSF through the Cornell Materials Science Center and the DoD Tri-Services Center for Atmoic Scale Spectroscopy.

*Department of Materials Science and Engineering, Cornell University, Ithaca, New York 14853
**Rome Laboratory Photonics Center, 25 Electronic Parkway, Rome, New York 13441-4115
†School of Electrical Engineering, Cornell University, Ithaca, New York 14853

1. F.A. Ponce, D.P. Bour, W. Gotz, P.J. Wright, Appl. Phys. Lett. **68**, 57 (1996).
2. B. Garni, Jian Ma, N. Perkins, Jutong Liu, T.F. Kuech, M.G. Lagally, Appl. Phys. Lett. **68**, 1380 (1996).
3. S. Evoy, H.G. Craighead, W.A. Davis, T.J. Eustis, M.J. Murphy, W.J. Schaff, L.F. Eastman, in *Conference on Lasers and Electro-Optics*, Vol. 11 of OSA 1997 Technical Digest Series (Optical Society of America, Washington DC, 1997), paper CTu02.
4. A. Liebheit, M. Schwartzkopff, P. Radojkovic, E. Hartmann, E. Hechtl, V. Petrova-Koch, F. Koch, J. Lumine. **72–74**, 994 (1997).

EPITAXIAL LATERAL OVERGROWTH OF GaN BY SUBLIMATION METHOD AND BY MOCVD

Jie Wang, S. Tottori, M. S. Hao, Hisao Sato, Shiro Sakai, and Marek Osiński*

Satellite Venture Business Laboratory, University of Tokushima, 2-1 Minami-Josanjima, Tokushima 770, Japan

**Permanent address: Center for High Technology Materials, University of New Mexico, 1313 Goddard SE, Albuquerque, New Mexico 87106, USA*

ABSTRACT

Selective overgrowth method has been used to grow GaN epitaxial layers by metalorganic chemical vapor deposition (MOCVD) and sublimation technology. MgO, Si and SiO_2, which have different thermal conductivities and thermal expansion coefficients, have been chosen as mask materials. The microstructure of selectively grown GaN and the lateral growth mechanisms of sublimation and MOCVD have also been investigated by transmission electron microscopy (TEM) and scanning electron microscopy. The effect of different mask materials on reduction of dislocation density is discussed. The experimental results indicate that Si is the best mask material for GaN lateral overgrowth. The dislocation density is about 10^9 cm^{-2} above the window areas, and it is reduced to 10^6 cm^{-2} in the lateral overgrowth region above the Si mask.

Key words: GaN, MOCVD, Sublimation, Lateral overgrowth

1. INTRODUCTION

Lateral overgrowth has been vigorously studied recently as a method of reducing the dislocation density in GaN grown on sapphire or 6H-SiC(0001) substrates [1]-[8]. The most commonly chosen mask material is SiO_2. However, the very low thermal conductivity of SiO_2 and large mismatch in thermal expansion coefficients with GaN are serious problems when lateral growth temperature of GaN is about 1050 °C. For this reason, we have considered alternative mask materials. According to the data listed in Table I, both Si and MgO have large thermal conductivities, about 107 and 44 times larger than that of SiO_2, respectively, and comparable to that of GaN. In addition, the thermal expansion coefficient mismatch of Si/GaN and MgO/GaN is smaller than that of SiO_2/GaN. Thus, it is of interest to investigate Si and MgO as alternative mask materials for lateral overgrowth of GaN.

Table I: Key parameters of GaN and relevant mask materials

Material	Lattice parameters [Å]	Thermal conductivity [W/cmK]	Thermal expansion coefficients [$10^{-6}K^{-1}$]
GaN	$a = 3.189$, $c = 5.185$	1.3	along a: 5.59; along c: 3.17
SiO_2	amorphous	0.014	0.5
MgO	$a = 4.216$	0.6	10.5
Si	$a = 5.4301$	1.5	3.59

For the lateral overgrowth of GaN, the coalescence of the layer is dependent on the width and direction of stripe window opening in the mask material. Nakamura *et al.* [2] have reported that in order to achieve an overgrown GaN layer with flat surface over the entire substrate, as much as 20-μm thick GaN layer had to be grown by metalorganic chemical vapor deposition (MOCVD). In that case, 4-μm-wide stripe windows with 5 μm spacers oriented along the <1$\bar{1}$00> direction of GaN were opened in a 1-μm-thick SiO_2 mask. Even thicker GaN layer (up to 100 μm) grown on a partly covered GaN with SiO_2 mask was reported very recently [5]. The device structure was then fabricated on top of that layer. In view of the high cost of growing thick epitaxial layers by MOCVD due to their low growth rate, this approach might result in prohibitively expensive wafers not suitable for commercial production. It is therefore important to explore other possible approaches to growing thick epitaxial layers that would not carry a high-cost overhead.

Sublimation method is a promising technique for growth of bulk GaN crystals or thick GaN films on crystalline substrates. In our previous research work, we have grown bulk crystals of the maximum size of about 3 mm in length and 0.8 mm in diameter [9], [10]. Compared to MOCVD, the sublimation technique is very attractive for lateral overgrowth due to very fast growth rate [9]-[11]. Sublimation growth apparatus is relatively simple and, since it is an atmospheric process, the scale up is easier. It is also an inexpensive process, because the sources are only metallic gallium and a small amount of NH_3 gas, while the growth rate is very large. In general, these features of the sublimation method make it a good candidate for growth of thick films on large area substrates. In particular, it can become a method of choice for lateral overgrowth on a partly covered GaN on sapphire substrate.

In this paper, we report for the first time very encouraging results for lateral overgrowth of GaN obtained by the sublimation growth method. The microstructure of selectively grown GaN layer and the lateral growth mechanism of sublimation and MOCVD have been investigated by scanning electron microscopy (SEM) and transmission electron microscopy (TEM).

2. EXPERIMENTAL

GaN overgrowth on partly covered sapphire substrates has been carried out by sublimation method and by two-flow MOCVD at atmospheric pressure. The substrates used for lateral growth were 2~3-μm thick GaN layers grown on sapphire substrates by MOCVD. Following the MOCVD growth, the MOCVD-GaN surface was patterned with Si, MgO, and SiO_2 masks by electron beam evaporation at room temperature. The mask thickness was 0.1~0.2-μm. Various patterns were opened by conventional photolithography, including star-like shapes and stripe windows with different widths and spacings [11].

The sublimation system used in the growth has been described in our previous paper [9]. The source powder was synthesized by heating liquid Ga in NH_3 atmosphere at 1000 °C. During the growth, the source powder and substrate were placed in a graphite crucible, and 50 sccm of NH_3 was introduced into the crucible. The growth temperature was varied from 970 °C to 1000 °C. After 1 hour of growth at 995 °C, the vertical and lateral dimensions of the overgrown GaN material were about 20 μm and 60 μm, respectively, with the Si or SiO_2 mask stripe oriented parallel to the $<1\bar{1}00>$ crystallographic direction of GaN [11]. In contrast, the typical growth rate using MOCVD is only about 1 μm/h. After the sublimation growth, the color of source powder becomes black instead of the original gray color, indicating that the active species in the source powder were exhausted [12]. Therefore, the grown layer thickness was not proportional to the growth time in the sublimation technique.

3. RESULTS AND DISCUSSION

Initially, three different materials listed above (Si, SiO_2, and MgO) as well as bare sapphire were used as substrates for GaN deposition by sublimation, without any patterning. The densities of GaN nuclei on the MgO and sapphire were about 100 times larger than those on Si and SiO_2. Similarly, MOCVD growth on MgO and sapphire substrates produced GaN films, while no growth occurred with Si and SiO_2 substrates. These results indicate that there would be a serious problem with using MgO as patterned mask material for lateral growth, due to the fact that GaN can grow directly on MgO surface. Consequently, most of our investigations were carried out using Si and SiO_2 masks.

Fig. 1 shows a diffraction pattern of cross-sectional TEM sample of sublimation-GaN/MgO/MOCVD-GaN sandwich structure. The diffraction dots arranged periodically are from MOCVD-GaN buffer, while the diffraction dots formed cyclically are from MgO. As deposited on MOCVD-GaN at room temperature, MgO is amorphous. However, during 1050 °C GaN lateral overgrowth by the sublimation technique, the amorphous MgO underwent annealing and became polycrystalline, as shown in Fig.1.

The presence of mask material is very effective in terminating the threading dislocations originating at the MOCVD-GaN buffer layer, which otherwise would

penetrate all the epitaxial layers in the wafer. We have observed this to be the case independently of the mask material, and in each case the dislocations would end at the GaN-mask interface. However, as shown in Fig. 2, new dislocations have been generated at the interface of MgO and GaN. There are many stacking faults in GaN layer, especially, near GaN/MgO interface. This is the consequence of nucleation of GaN directly on the MgO mask material, as opposed to lateral overgrowth.

Fig. 3 is a low magnification cross-sectional TEM micrograph of laterally overgrown GaN, in which 10-μm-wide stripe windows with 25-μm-wide spacers, oriented along the <11$\bar{2}$0> direction of GaN, were opened in a 0.1-μm-thick Si mask. In the window region, almost all the dislocations from the MOCVD layer propagated across the interface between MOCVD-GaN and sublimation-GaN. The density of dislocations in these areas is comparable with that of the underlying GaN buffer. However, in the region above Si mask, the dislocations extending from GaN buffer layer are terminated by the Si layer. It is important to note that in contrast to MgO mask, no new dislocations were generated at the Si/sublimation-GaN interface. As a result, large dislocation density of about 10^9 cm^{-2} above the window areas has been reduced to ~10^6 cm^{-2} in the lateral overgrowth areas.

The lateral growth rates under sublimation and MOCVD growth conditions depend on the direction of the stripe window, similarly to the behavior reported earlier in other MOCVD and vapor-phase-epitaxy (VPE) experiments [3], [8]. The overgrowth rate in the sublimation method is about 6 times larger for stripe windows oriented along the <1$\bar{1}$00> direction of GaN than for stripes parallel to the <11$\bar{2}$0> direction. The lateral overgrowth rate is also 3 times faster than the vertical growth rate. For stripes parallel to GaN<1$\bar{1}$00>, the width of the laterally overgrown region is as large as 60 μm after only 1 hour of sublimation growth at 995 °C. Thus, it becomes very easy to achieve planar or flat GaN layers over the entire surface. This is illustrated in Fig. 4, showing the cross-sectional SEM micrograph from a GaN/Si/GaN structure grown selectively by sublimation at 990 °C. Label A indicates the position of the sublimation-GaN layer, the thin bright region labeled B is the 0.1-μm-thick Si layer, C is the MOCVD-GaN buffer layer and D is the sapphire substrate. The width of Si mask in this case was 25 μm. After only 1 hour of growth on this mask pattern, the coalescence of the laterally overgrown GaN made it possible to achieve a flat GaN surface over the entire substrate.

The lateral and vertical growth rates also depend on the growth temperature, growth time and the amount of GaN source powder (in the sublimation method) or the flow of TMG and NH_3 (in the MOCVD), but the ratio of lateral to vertical thickness depends only on the stripe orientation. The lateral growth rate in MOCVD with the window stripe along the <1$\bar{1}$00> direction is also about 3 times larger than that of vertical growth. However, the absolute rate of lateral growth is only 3 μm/h, which is about 20 times slower than in the sublimation method. Fig. 5 shows a cross-sectional SEM micrograph of the sample in which the width of Si mask was only 10 μm and the

orientation of stripe was parallel to the <1$\bar{1}$00> direction of GaN. In spite of a very long (7 hours) process of MOCVD growth at 1050 °C with 5 sccm of TMG, the sample has not coalesced yet.

Substantial reduction in the dislocation density in regions located above the Si mask can be observed using TEM, as shown Fig. 3 and Fig. 6. Fig. 6 is a low magnification cross-sectional TEM micrograph of GaN grown by the sublimation method on patterned Si mask. All dislocations extending from the GaN buffer layer underneath the Si mask are terminated at the GaN-Si interface. Another interesting observation is that the threading dislocations that penetrate into the sublimation-GaN region above the window in Si mask tend to change their direction by 90°, from nearly perpendicular to the interface of MOCVD-GaN and sublimation-GaN, to nearly parallel with the interface. Thus, even the density of dislocation located above the window is reduced. This property is very beneficial for growing device structures in region above the overgrown material.

4. CONCLUSIONS

A systematic comparative study of lateral overgrowth of GaN using various mask materials has been performed using the MOCVD and sublimation growth techniques. Si, MgO, and SiO_2 have been investigated as mask materials deposited above the MOCVD-GaN buffer, with the goal of determining the best approach towards fabrication of low-defect-density GaN for high-performance devices. Our experimental results show that Si is the best material for fabricating the mask due to the largest thermal conductivity and smallest mismatch of thermal expansion with GaN. MgO turned out to be unsuitable for this purpose, as GaN nucleation occurs on MgO surface. Compared to MOCVD, sublimation method is much more suitable for lateral overgrowth, due to very fast growth rate. Using this method, it is very easy to achieve planar or flat GaN layers over the entire wafer surface within a short time of growth (only 1 hour) and with quite large distance (as big as 25 μm) between adjacent windows. In addition, threading dislocations entering the sublimation-overgrown GaN turn their direction from the nearly perpendicular to the interface to parallel with the interface. In principle this should allow to obtain very low dislocation density material suitable for high-power and high reliability devices.

5. ACKNOWLEDGMENT

One of the authors (M.O.) wishes to express his gratitude to Prof. Shiro Sakai for the hospitality extended during the one-year-long visit at the Satellite Venture Business Laboratory of the University of Tokushima in 1997.

6. REFERENCES

1. Y. Kato, S. Kitamura, K. Hiramatsu, and N. Sawaki, "Selective growth of wurtzite GaN and $Al_xGa_{1-x}N$ on GaN/sapphire substrates by metalorganic vapor phase epitaxy", *J. Cryst. Growth* **144**, pp. 133-140, 1994.

2. S. Nakamura, M. Senoh, S.-I. Nagahama, N. Iwasa, T. Yamada, T. Matsushita, H. Kiyoku, Y. Sugimoto, T. Kozaki, H. Umemoto, M. Sano, and K. Chocho, "InGaN/GaN/AlGaN-based laser diodes with modulation-doped strained-layer superlattices", *Jpn. J. Appl. Phys., Pt. 2 (Lett.)* **36**, pp. L1568-L1571 (1997).

3. D. Kapolnek, S. Keller, R. Vetury, R. D. Underwood, P. Kozodoy, S. P. Den Baars, and U. K. Mishra, "Anisotropic epitaxial lateral growth in GaN selective area epitaxy", *Appl. Phys. Lett.* **71**, pp. 1204-1206 (1997).

4. X. Li, A. M. Jones, S. D. Roh, D. A. Turnbull, S. G. Bishop, and J. J. Coleman, "Characteristics of GaN stripes grown by selective-area metalorganic chemical vapor deposition", *J. Electronic Materials* **26**, 306 (1997).

5. S. Nakamura, M. Senoh, S. I. Nagahama, N. Iwasa, T. Yamada, T. Matsushita, H. Kiyoku, Y. Sugimoto, T. Kozaki, H. Umemoto, M. Sano, and K. Chocho, "High-power, long-lifetime InGaN/GaN/AlGaN-based laser diodes grown on pure GaN substrate", *Jpn. J. Appl. Phys.* **37**, L309 (1998).

6. T. S. Zheleva, O. H. Nam, M. D. Bremser, and R. F. Davis, "Dislocation density reduction via lateral epitaxy in selectively grown GaN structures", *Appl. Phys. Lett.* **71**, 2472 (1997).

7. A. Sakai, H. Sunakawa, and A. Usui, "Defect structure in selectively grown GaN films with low threading dislocation density", *Appl. Phys. Lett.* **71**, pp. 2259-2261 (1997).

8. A. Usui, H. Sunakawa, A. Sakai, and A. A. Yamaguchi, "Thick GaN epitaxial growth with low dislocation density by hydride vapor phase epitaxy", *Jpn. J. Appl. Phys.* **36**, L899 (1997).

9. S. Kurai, K. Nishino, and S. Sakai, "Nucleation control in the growth of bulk GaN by sublimation method." *Jpn. J. Appl. Phys., Pt. 2 (Lett.)* **36**, pp. L184-L186 (1997).

10. Y. Naoi, K. Kobatake, S. Kurai, K. Nishino, H. Sato, M. Nozaki, S. Sakai, and Y. Shintani, "Characterization of bulk GaN grown by sublimation technique", *Proc. 2nd International Conf. on Nitride Semiconductors ICNS'97*, Tokushima, Japan, 27-31 Oct. 1997, pp. 264-265.

11. J. Wang, S. Tottori, H. Sato, M. S. Hao, Y. Ishikawa, T. Sugahara, K. Yamashita, and S. Sakai. "Lateral overgrowth on patterned GaN on sapphire by sublimation technique", submitted to *Jpn. J. Appl. Phys.*

12. S. Sakai, S. Kurai, K. Nishino, K. Wada, H. Sato, and Y. Naoi, "Growth of GaN by sublimation technique and homoepitaxial growth by MOCVD", in *III-V Nitrides* (F. A. Ponce, T. D. Moustakas, I. Akasaki, and B. A. Monemar, Eds.), Boston, MA, 2-6 Dec., 1996, *Mat. Res. Soc. Symp. Proc.* **449**, 15 (1997).

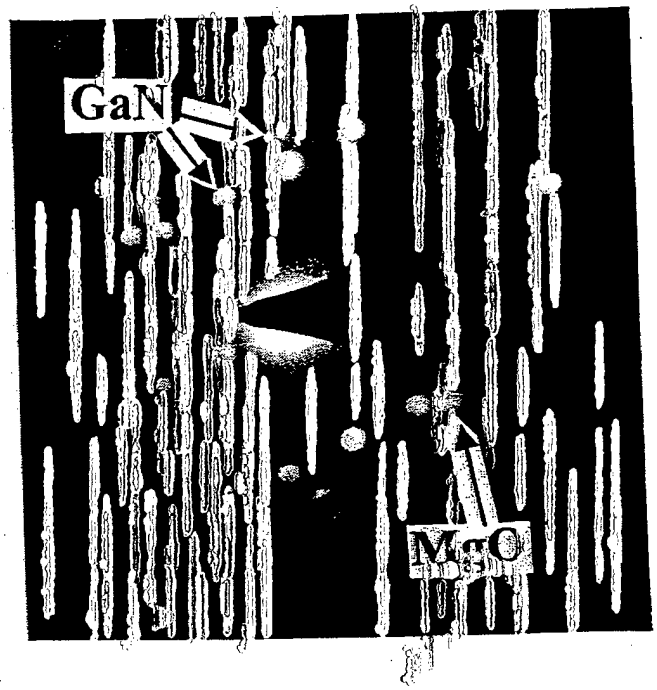


Fig. 1. A diffraction pattern of cross-sectional TEM sample of Sublimation-GaN/MgO/MOCVD-GaN sandwich structure.

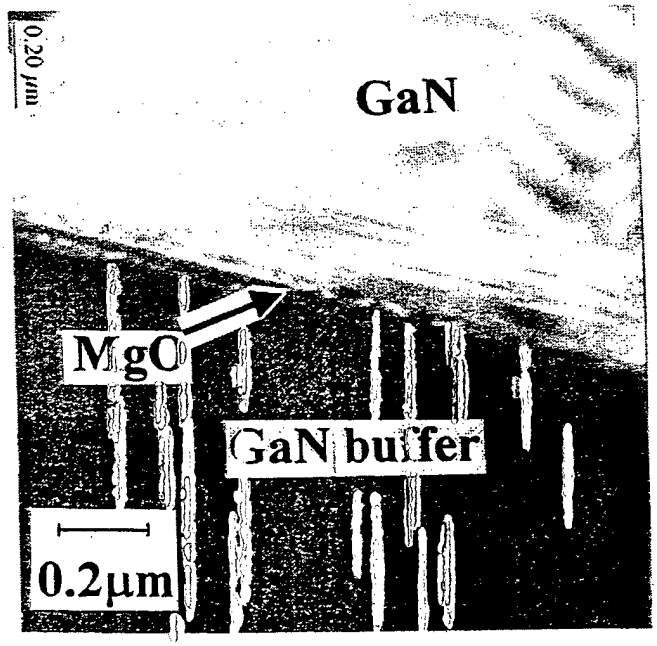


Fig. 2. Cross-sectional TEM micrograph of a selectively grown GaN on MgO mask.

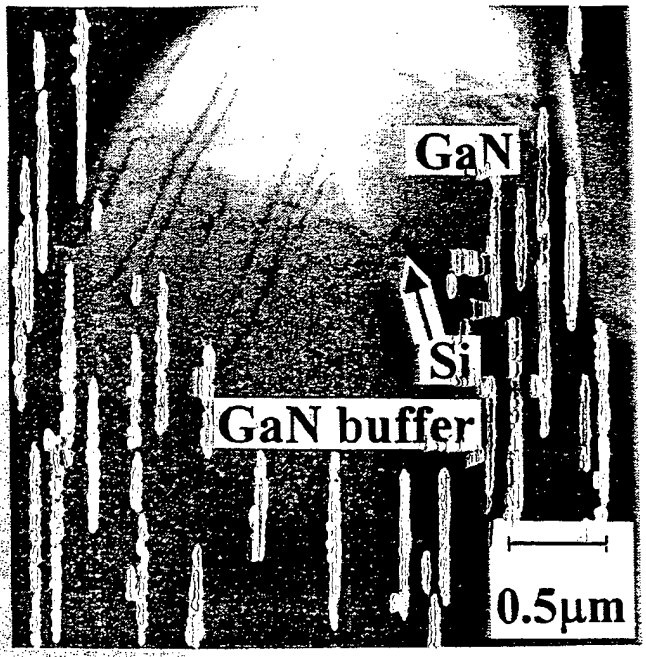


Fig. 3. Cross-sectional TEM micrograph of a selectively grown GaN on Si mask.

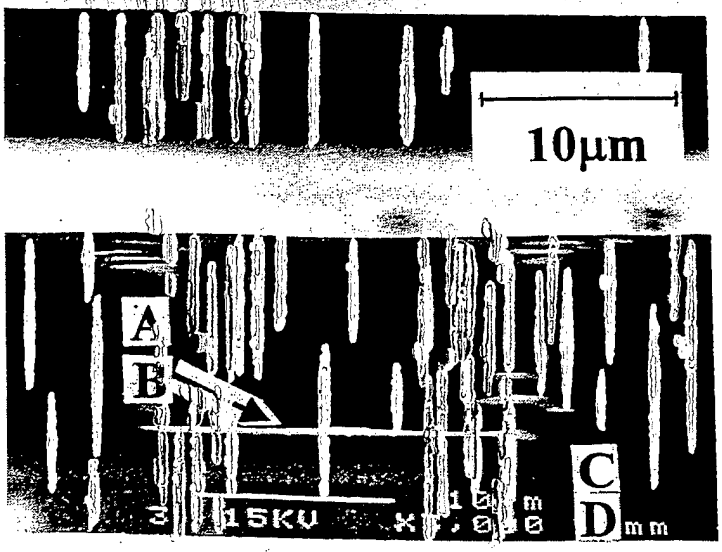


Fig. 4. Cross-sectional SEM micrograph of GaN grown selectively by sublimation at 990 °C. The width of Si mask is 25 μm and the direction of stripe is $<1\bar{1}00>$.

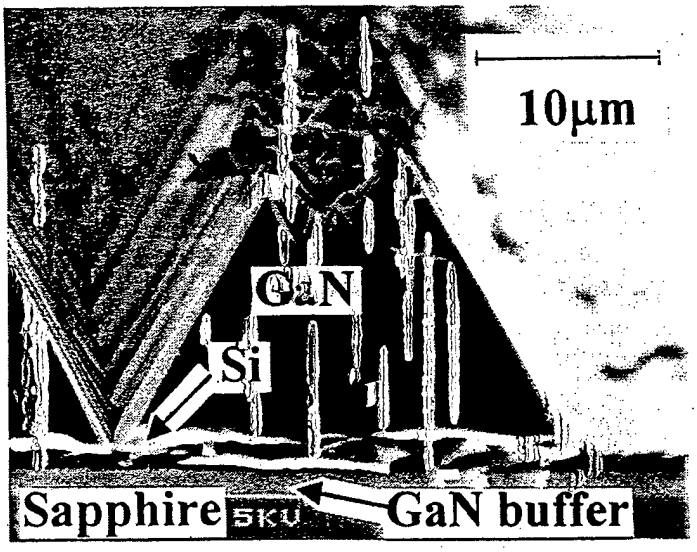


Fig. 5. Cross-sectional SEM micrograph of GaN grown selectively by MOCVD. The width of Si mask is 10 μm and the direction of stripe is $<1\bar{1}00>$.

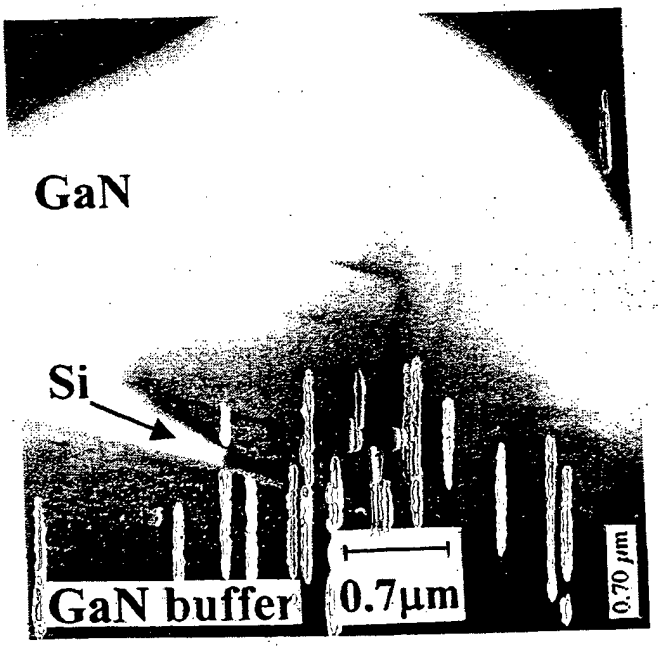


Fig. 6. A low magnification cross-sectional TEM micrograph of GaN grown by sublimation method.

Lateral overgrowth mechanisms and microstructural characteristics of bulk-like GaN layers grown by sublimation method

Jie Wang,[a] R. S. Qhalid Fareed, M. Hao, and S. Mahanty
Satellite Venture Business Laboratory, University of Tokushima, 2-1 Minami josanjima, Tokushima, Japan

S. Tottori, Y. Ishikawa, T. Sugahara, Y. Morishima, and K. Nishino
Department of Electrical and Electronic Engineering, University of Tokushima, 2-1 Minami josanjima, Tokushima, Japan

M. Osinski
Centre for High Technology Materials, The University of New Mexico, Albuquerque, New Mexico 87106

S. Sakai
Department of Electrical and Electronic Engineering, University of Tokushima, 2-1 Minami josanjima, Tokushima, Japan

(Received 24 July 1998; accepted for publication 26 October 1998)

The selective overgrowth method has been used to grow bulk-like GaN layers by sublimation method. Si and SiO_2, which have a different evaporation rate, thermal conductivity, and thermal expansion coefficient, have been chosen as mask materials. The effect due to the reduction of dislocation density with different mask materials has been discussed. The lateral growth rates strongly depend on the direction of the mask stripe. For the stripe windows aligned in GaN$\langle 1\bar{1}00\rangle$ direction, the lateral growth rate is approximately four times higher than with stripe direction in GaN$\langle 11\bar{2}0\rangle$. The microstructure of selectively regrown GaN has been investigated by transmission electron microscopy, scanning electron microscopy, and cathodoluminescence to understand the lateral growth mechanisms in sublimation. The threading dislocations in the region of laterally regrown GaN are extended in two different ways. First, the threading dislocations are perpendicularly propagated into the top surface in the window region. In this case, the density of the threading dislocation is about 10^9 cm^{-2} within the window regions of the mask and is reduced to 10^6 cm^{-2} in the lateral overgrowth region of the mask due to termination of further propagation of dislocation by the mask. Second, the direction of propagation of dislocations is changed parallel to the *c* plane in laterally overgrown GaN, and finally, it changes in the direction perpendicular to the *c* plane in the middle region of the mask. © *1999 American Institute of Physics.* [S0021-8979(99)06603-7]

I. INTRODUCTION

Since no suitable substrate is presently available for GaN growth, most device structures have been fabricated on sapphire or 6H–SiC substrates.[1–3] Due to the large lattice mismatch, nitride epitaxial layers contain a high density of extended defects, which affect the device performance. One of the methods to reduce dislocation density in an active region of a device is to use the lateral overgrowth method.[4–11] In this method, the threading dislocations present in the GaN layers, originating at the GaN/sapphire interface, are blocked by the mask. The density of threading dislocation is dramatically reduced in the laterally regrown regions.

Most of the researchers have used SiO_2 as the mask material for the lateral growth. However, its low thermal conductivity and large mismatch of thermal expansion with GaN are serious problems when the lateral growth temperature of GaN is about 1050 °C. Compared to SiO_2, Si has a larger thermal conductivity and the thermal expansion coefficient mismatch of Si/GaN is smaller than that of SiO_2/GaN, as listed in Table I. Thus, it is reasonable to choose Si as the mask material for the lateral overgrowth of GaN.

Compared to metalorganic chemical vapor deposition (MOCVD), the sublimation technique is the most suitable and simple method for lateral overgrowth.[12–14] The sublimation method is a promising technique to grow bulk GaN crystals or thick GaN films on crystalline substrates. Since the system of this sublimation technique is very simple and is only an atmospheric process, scaling up is easier. It is also a cost effective process since only metallic gallium and NH_3 are used as sources. It should be emphasized that the growth rate in sublimation is very high. Over 50-μm-thick GaN films can be deposited by sublimation in 1 h of growth at 1050 °C. These features of the sublimation method are important to grow thick GaN films on the large area substrates and make this technique very attractive for the lateral overgrowth of GaN on a partly covered GaN on sapphire substrate. In our previous research work, we have grown bulk crystals of GaN with a maximum size of about 3 mm in length and 0.8 mm in diameter.[12,13]

[a]Electronic mail: jiewang@svbl.tokushima-u.ac.jp

 © 1999 American Institute of Physics

TABLE I. Parameters of GaN and relevant mask materials.

Materials	Lattice parameters (Å)	Thermal conductivity (W/cm K)	Coefficients of thermal expansion (10^{-6} K^{-1})
GaN	$A=3.189$, $C=5.185$	1.3	$A=5.59$, $C=3.17$
SiO_2	Amorphous	0.014	0.5
Si	$A=5.4301$	1.5	3.59

II. EXPERIMENT

The lateral overgrowth of GaN has been carried out by the sublimation technique. During the growth, the source powder and substrate were placed in a graphite crucible and 50 sccm of NH_3 were introduced into the crucible. The growth temperature varied from 970 to 1100 °C. After 1 h of growth at 995 °C, the source powder becomes black from the original color of gray, indicating that the active species in the source powder were exhausted. Therefore, the grown layer thickness was not proportional to the growth time. Under these growth conditions, the growth rate is very high in the initial stages, but as the experiment progresses, growth rate decreases with time and finally stops due to the exhaustion of effective Ga source.

Each of the initial 1.5–3.0-μm-thick GaN films was grown by MOCVD. These films were subsequently deposited with the 0.1–0.2 μm Si and SiO_2 films by electron beam evaporation at room temperature. Stripe windows with different direction, width and, space were patterned by the conventional photolithography.[14] Prior to the lateral overgrowth of sublimation, the patterned GaN substrates were first cleaned by acetone, methanol, and deionized water. Then they were dipped in KOH solution for 10 min using the photoassisted wet-etching method to remove the surface oxide of the underlying GaN layer.

The microstructure of selectively regrown GaN bulk-like layers and the lateral growth mechanisms have been investigated by transmission electron microscopy (TEM), scanning electron microscopy (SEM), and cathodoluminescence (CL).

III. RESULTS AND DISCUSSION

The strong dependence of growth conditions on the stripe orientation during the lateral overgrowth of GaN using MOCVD has been reported by many researchers. The optimized lateral overgrowth conditions of MOCVD have been presented by Kapolnek[6] and Nam *et al.*[15] However, the growth mechanisms of sublimation and MOCVD are very different. Hence, it is essential to know the best lateral overgrowth conditions in the sublimation method. In order to investigate orientational dependence of the lateral growth rate in sublimation, a star-like mask pattern was used. The mask pattern consists of a star feature with lines at 30° angular span, parallel to the $\langle 1\bar{1}00\rangle$ and $\langle 11\bar{2}0\rangle$ directions surrounded by the large masked regions. The star consists of 12 consecutive lines of 10 μm opening width. Figure 1(a) is a top-view SEM image of a selectively regrown GaN sample with a star-like mask pattern grown at 995 °C for 1 h. The lateral growth rate varies between its maximum and minimum values at 60° intervals. The growth rate is the maximum when the stripe window is aligned along the $\langle 1\bar{1}00\rangle$ direction of GaN, as in the case of MOCVD.[15] After growth for 1 h with the stripe direction of GaN$\langle 1\bar{1}00\rangle$, the lateral and vertical growth lengths are about 60 and 20 μm, respectively. It is important to note that the rate of lateral growth is about three times larger than the rate of vertical growth. However, the lateral growth length is only 15 μm at the same growth condition when the stripe direction is parallel to the GaN$\langle 11\bar{2}0\rangle$. These results are almost the same with that of MOCVD overgrowth.[15]

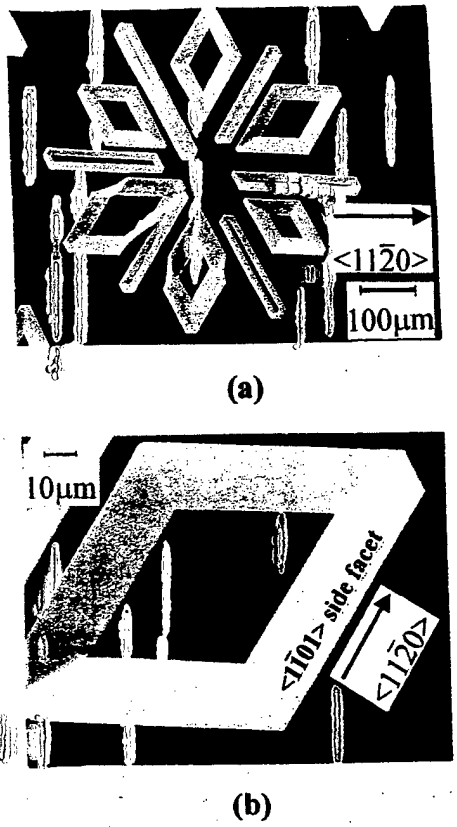


FIG. 1. (a) Top-view SEM image of a GaN sample with star-like mask pattern grown at 995 °C for 1 h. (b) Top-view SEM image of a lateral regrown GaN with an opening stripe window along the direction of GaN$\langle 1\bar{1}00\rangle$.

Figure 1(b) is a top-view SEM image of laterally regrown GaN sample with one opening stripe at the same growth condition shown in Fig. 1(a), the stripe direction being oriented along GaN$\langle 1\bar{1}00\rangle$. As usual, the stripe subsequently developed into a rhombus with $\{1\bar{1}01\}$ side facets with the edge of the rhombus along $\langle 11\bar{2}0\rangle$. In only a few cases, vertical $\{11\bar{2}0\}$ side facets were developed in the middle region of the rhombus. These results are different from that of MOCVD overgrowth. It usually forms rectangular stripes with vertical $\{11\bar{2}0\}$ side facets for MOCVD overgrowth.[15] However, for the stripe direction along $\langle 1\bar{1}00\rangle$, the result of sublimation overgrowth similar to that of MOCVD overgrowth, and a stripe with $\{1\bar{1}01\}$ side facets have always been developed as shown in Fig. 1(a). Due to the very high growth rate in sublimation, it was assumed that

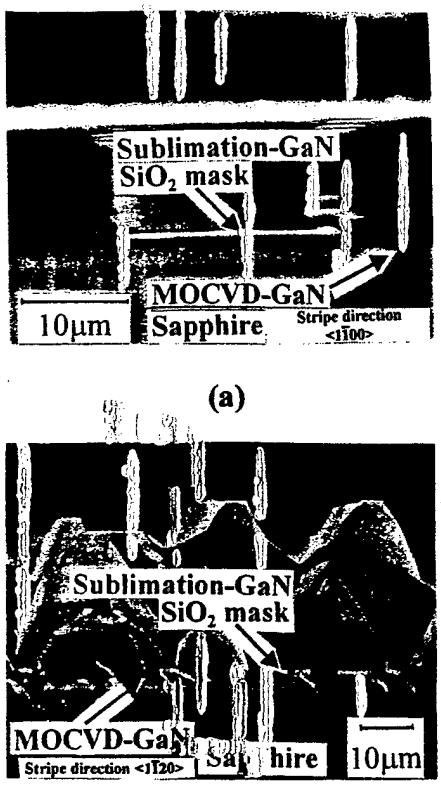


FIG. 2. (a) Cross-section SEM micrograph from selective grown GaN within 10 μm wide stripe windows spaced 20 μm apart and stripe direction in GaN$\langle 1\bar{1}00\rangle$. (b) Cross-section SEM micrograph of sample within 10-μm-wide stripe windows spaced only 8 μm apart and stripe direction in GaN$\langle 11\bar{2}0\rangle$.

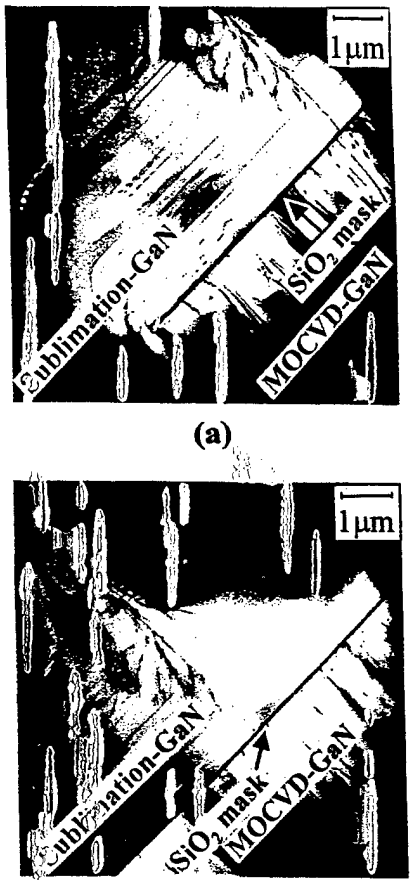


FIG. 3. (a) Cross-section TEM micrograph from a selectively grown GaN on the SiO_2 mask with stripe direction in $\langle 1\bar{1}00\rangle$ and having $\{1\bar{1}01\}$ side facets. (b) Cross-section TEM micrograph from a selectively grown GaN in the middle region of the SiO_2 mask with stripe direction in $\langle 1\bar{1}00\rangle$ and having $\{1\bar{1}01\}$ side facets.

it would be difficult to control the roughness of (0001) top surface. However, the top surface is found to be atomically flat, as shown in Fig. 1(b). Hence, it is possible to have a continuous thick layer and can be directly used as substrates for homoepitaxial growth of GaN.

Figure 2(a) is the cross-section SEM micrograph from a selectively regrown GaN sample within 10-μm-wide stripe windows spaced 20 μm apart with the stripe direction in GaN$\langle 1\bar{1}00\rangle$. Since the lateral growth rate is about three times larger than that of vertical growth, it is very easy for coalescence and to form a continuous film with a very flat surface. However, for the stripe direction of GaN$\langle 11\bar{2}0\rangle$, the situation of lateral overgrowth becomes very different. Due to low lateral growth rate, it is very difficult for the coalescence and to form a continuous film. Fig. 2(b) is the cross-section SEM micrograph of a sample within 10-μm-wide stripe windows spaced only 8 μm apart and stripe direction in GaN$\langle 11\bar{2}0\rangle$. After vertical growth length reaches 40 μm, coalescence takes place, but the surface is still very rough.

The distribution of threading dislocations in the region of laterally regrown GaN strongly depends on the formation of $\{1\bar{1}01\}$ and $\{11\bar{2}0\}$ side facets. Figure 3(a) is a cross-section TEM micrograph from a selectively regrown GaN on the SiO_2 mask with stripe direction in $\langle 1\bar{1}00\rangle$ and having $\{1\bar{1}01\}$ side facets. In the region of regrown GaN, the perpendicular propagation of threading dislocations in an underlying MOCVD-GaN layer was intersected by $\{1\bar{1}01\}$ side facets in the window region, and threading dislocations changes its direction parallel to the c plane. Then parallel propagation of threading dislocations extends into the mask region till the middle of the mask and they are intersected again by $\{1\bar{1}01\}$ side facets formed in the middle region of the mask. Thus, the extension of parallel threading dislocations changed direction again perpendicular to the c plane in the middle region of the mask, as shown in Fig. 3(a). Finally, all the dislocations were focused on the middle region of the mask to form a high-density threading dislocation band with a width of 2–3 μm, and they perpendicularly propagated to the top surface, as shown in Fig. 3(b). In this case, the $\{1\bar{1}01\}$ side facet acts as a mirror to refraction of dislocations.

Figure 4 shows a cross-section TEM micrograph from a selectively regrown GaN on the Si mask with stripe direction in $\langle 1\bar{1}00\rangle$ and having vertical $\{11\bar{2}0\}$ side facets. In this case, the perpendicular extension of threading dislocations has been terminated by the Si mask in the mask region. However, in the stripe window region, almost all disloca-

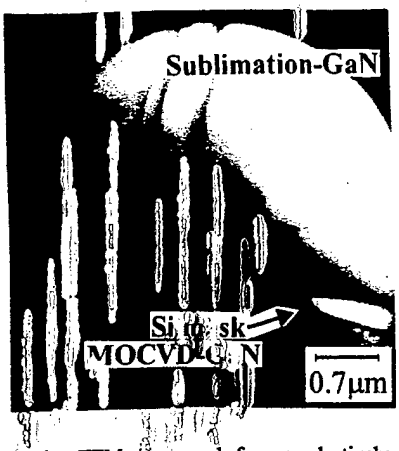


FIG. 4. Cross-section TEM micrograph from a selectively grown GaN on the Si mask with stripe direction in $\langle 1\bar{1}00\rangle$ and having $\{11\bar{2}0\}$ side facets.

tions in initial MOCVD-GaN layer propagate into sublimation-GaN layers. Since there is no $\{1\bar{1}01\}$ side facet to intersect vertical threading dislocations, the dislocations subsequently propagate to the top surface of the regrown GaN. If the surface of initial MOCVD-GaN substrate was thoroughly clear prior to the select growth of GaN by sublimation, no threading dislocations were newly generated at the interface. In this case, the density of threading dislocations is about 10^9 cm^{-2} above the window areas, and is reduced to 10^6 cm^{-2} in the lateral overgrowth region on the Si mask. From Fig. 4, we did not find the voids in the central region of the sublimation-GaN on the masks. These voids were mostly observed in MOCVD grown layers under the lateral growth conditions, wherein rectangular stripe with vertical $\{11\bar{2}0\}$ side facets developed.

To investigate the distribution of radiative defects across the sublimation-GaN layer, room temperature CL experiments have been performed. The sample used for CL measurement contains the SiO_2 mask of 8-μm-wide windows spaced 8 μm apart with stripe direction in $\langle 1\bar{1}00\rangle$ and having $\{1\bar{1}01\}$ side facets. Prior to the CL measurement, the top and cross-section surfaces of the sample were polished. Figure 5(a) shows the sample structure and the thin lines show $\{1\bar{1}01\}$ side facets. Figure 5(b) shows the room temperature cross-section CL images taken at 362 nm corresponding to the band-edge emission of GaN. It clearly shows a strong emission in region II. However, in regions I and III, it is difficult to observe the luminescence at 362 nm. Zheleva *et al.* have reported the inferior quality of regrown GaN in region I and the density of threading dislocations is about 10^9 cm^{-2} in region I.[9] The change in the direction of the threading dislocations is focused in region III, as shown in Fig. 3. Thus, the weak band-edge emission of GaN is acceptable in these two regions. The edges between white and black regions are near $\{1\bar{1}01\}$ side facets.

According to TEM measurement, the density of the threading dislocation in region I is almost the same with the underlying MOCVD-GaN layer. However, the emission at 362 nm can be observed in the region of underlying MOCVD-GaN layer, and there is no emission from region I. Thus, the impurities and point defects originating from the

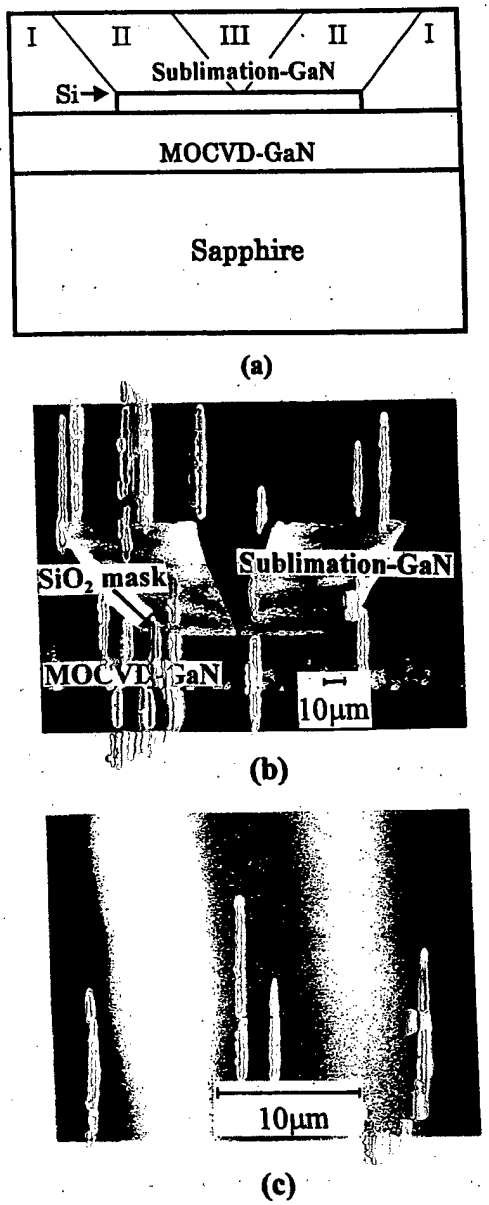


FIG. 5. (a) Structure of lateral overgrowth GaN sample used for CL measurement. (b) Room temperature cross-section CL images taken at 362 nm corresponding to the band-edge emission of GaN. (c) Top-view CL images of the sample taken at 362 nm at room temperature.

sublimation growth are other causes for the reduction of band-edge emission. Figure 5(c) is a top-view CL image of the sample taken at 362 nm at room temperature. The results correspond to that shown in Figs. 3 and 5(b). It is worth noting, the stronger emission is in region II than that in the underlying MOCVD-GaN layer.

For the sample with vertical $\{11\bar{2}0\}$ side facets, the threading dislocations are focussed on the window regions of the regrown GaN layer, and no new dislocations are generated on the mask regions in spite of Si and SiO_2 used as mask materials. For the sample with $\{1\bar{1}01\}$ side facets and in the window region, all threading dislocations turn the direction into the mask region, and no threading dislocations were observed in the top region of window. In this case, there is no difference in using Si and SiO_2 as mask materials.

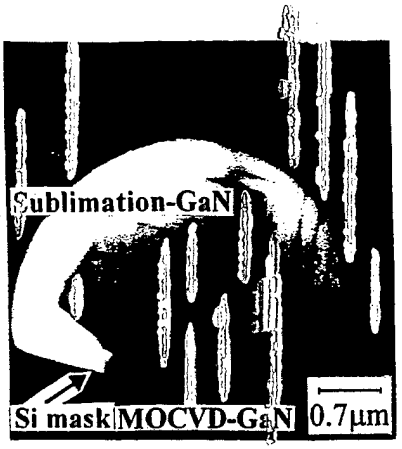


FIG. 6. Cross-section TEM micrograph of the lateral overgrowth GaN sample by sublimation with the Si mask and stripe direction in $\langle 11\bar{2}0 \rangle$.

In spite of the directional change of threading dislocations in the window region of the SiO_2 mask region for the sample with $\{1\bar{1}01\}$ side facets, many new stacking faults are found to be generated due to the very low thermal conductivity and large mismatch of thermal expansion with GaN, as observed in Fig. 3. In this case, the threading dislocations turning from the window region act as "seed" to cause the stacking faults in the region of the mask. Detailed studies of the phenomenon will be presented elsewhere. This different situation happens when the Si mask material is used. The threading dislocation density of perpendicular propagation is almost the same as that of parallel propagation, as shown in Fig. 6. It is difficult to observe the newly generated dislocation in the Si mask region.

IV. CONCLUSION

Lateral overgrowth of GaN has been carried out using the sublimation method. Compared to MOCVD, the sublimation technique is very suitable for lateral overgrowth due to a higher growth rate. The lateral growth rate of a stripe window along $\langle 1\bar{1}00 \rangle$ direction is about three times larger than that of vertical growth, and it is easy to form a continuous film with a mirror-like surface. However, in the stripe direction of $\langle 11\bar{2}0 \rangle$, the rate of lateral overgrowth is even less than that of vertical growth and is difficult to grow continuously with a flat surface. For the sample with formation of vertical $\{11\bar{2}0\}$ side facets, the threading dislocations in the regrown GaN layers are mainly distributed in the window regions and only a small number of dislocations turn a 90° bend into the mask region. However, for the sample grown with $\{1101\}$ side facets, almost all threading dislocations in the window region turn the direction from the nearly perpendicular to the *c* plane to parallel to the *c* plane. The formation of the 2–3 μm threading dislocation band in the middle region of the mask is very beneficial for growing device structure in top region. Si and SiO_2 materials have been chosen to make the mask on the MOCVD-GaN layers. Experimental results also show that Si is a better material for fabricating the mask due to the larger thermal conductivity and smaller thermal mismatch with GaN. For the sample with $\{1101\}$ side facets, many stacking faults near the SiO_2 mask in selectively regrown GaN are observed. However, it is difficult to find newly generated stacking faults or threading dislocations in the regrown GaN layer with the Si mask.

[1] S. Nakamura and G. Fasol, *The Blue Laser Diode* (Springer, Heidelberg, 1997).
[2] H. Morkoç, S. Strite, G. B. Gao, M. E. Lin, B. Sverdlov, and M. Burns, J. Appl. Phys. **76**, 1363 (1994).
[3] S. N. Mohammad, A. A. Salvador, and H. Morkoç, Proc. IEEE **83**, 1306 (1995).
[4] Y. Kato, S. Kitamura, K. Hiramatsu, and N. Sawaki, J. Cryst. Growth **144**, 133 (1994).
[5] S. Nakamura *et al.*, Jpn. J. Appl. Phys., Part 2 **36**, L1568 (1997).
[6] D. Kapolnek, S. Keller, R. Vetury, R. D. Underwood, P. Kozodoy, S. P. Den Baars, and U. K. Mishra, Appl. Phys. Lett. **71**, 1204 (1997).
[7] X. Li, A. M. Jones, S. D. Roh, D. A. Turnbull, S. G. Bishop, and J. J. Coleman, J. Electron. Mater. **26**, 306 (1997).
[8] S. Nakamura *et al.*, Jpn. J. Appl. Phys., Part 2 **37**, L309 (1998).
[9] T. S. Zheleva, O. H. Nam, M. D. Bremser, and R. F. Davis, Appl. Phys. Lett. **71**, 2472 (1997).
[10] A. Sakai, H. Sunakawa, and A. Usui, Appl. Phys. Lett. **71**, 2259 (1997).
[11] A. Usui, H. Sunakawa, A. Sakai, and A. A. Yamaguchi, Jpn. J. Appl. Phys., Part 2 **36**, L899 (1997).
[12] S. Kurai, K. Nishino, and S. Sakai, Jpn. J. Appl. Phys., Part 2 **36**, L184 (1997).
[13] Y. Naoi, K. Kobatake, S. Kurai, K. Nishino, H. Sato, M. Nozaki, S. Sakai, and Y. Shintani, J. Cryst. Growth **190**, 163 (1997).
[14] J. Wang, S. Tottori, H. Sato, M. S. Hao, Y. Ishikawa, T. Sugahara, K. Yamashita, and S. Sakai, Jpn. J. Appl. Phys., Part 1 **37**, 4475 (1998).
[15] O. H. Nam, M. D. Bremser, T. S. Zheleva, and R. F. Davis, Appl. Phys. Lett. **71**, 2638 (1997).

CLEO®'99

Conference on Lasers and Electro-Optics

1999 Technical Digest Series

May 23–28, 1999

CLEO '99 Sponsored by
IEEE/Lasers and Electro-Optics Society

Optical Society of America

In Cooperation with:
Quantum Electronics Division of the European Physical Optical Society

Japanese Quantum Electronics Joint Group

OSA
Optical Society of America

TECHNICAL DIGEST

SUMMARY OF PAPERS PRESENTED AT THE CONFERENCE ON LASERS AND ELECTRO-OPTICS

3. T.J. Schmidt, Y.H. Cho, G.H. Gainer, J.J. Song, S. Keller, U.K. Mishra, and S.P. DenBaars, Appl. Phys. Lett. 73, 560 (1998).
4. T.J. Schmidt, S. Bidnyk, Y.H. Cho, A.J. Fischer, J.J. Song, S. Keller, U.K. Mishra, and S.P. DenBaars, MRS Internet J. Nitride Semicond. Res. 4S1, G6.54 (1999).

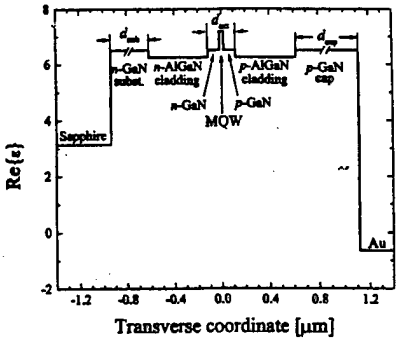
CTuU5 **5:30 pm**

Design limitations for InGaN/AlGaN/GaN lasers imposed by resonant mode coupling

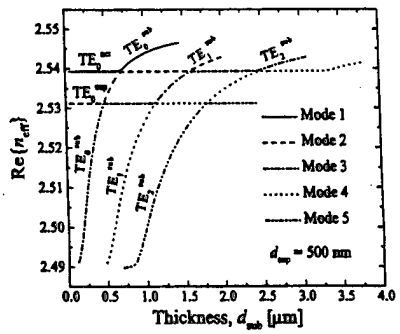
Gennady A. Smolyakov, Petr G. Eliseev,* Marek Osiński, *Center for High Technology Materials, University of New Mexico, 1313 Goddard SE, Albuquerque, New Mexico 87106 USA; E-mail: osinski@chtm.unm.edu*

Present-day InGaN/AlGaN/GaN semiconductor lasers typically contain a multiple optical waveguide structure, with refractive indices of several layers (GaN buffer-substrate, active region, cap layer) higher than those of cladding layers. This leads to complex behavior of optical modes that has recently been subject of several investigations.[1–5] In particular, resonant effects have been obtained in simulations of modes localized in the active region, with modulation of modal gain when thicknesses of active waveguide core or cladding layers were changed.[1,2] Those numerical solutions traced only the modes localized in the active layer, which is not sufficient to understand the nature of these resonances. Here, we show that resonant effects in nitride lasers result from coupling between nearly-degenerate normal modes of the entire laser structure, similarly to the case of InGaAs-based lasers analyzed previously.[6,7] We also demonstrate the strong role of the parasitic waveguide thicknesses, in addition to previously investigated parameters.

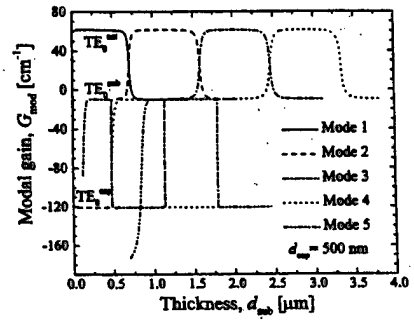
The analysis is performed in terms of TE normal modes of a multiple waveguide system, found as solutions of the scalar wave equation for a realistic profile of complex permittivity in a nitride laser structure (see Fig. 1). To demonstrate the resonant effects, we vary the thicknesses of various passive layers (GaN cap d_{cap}, GaN substrate layer d_{sub}, or claddings d_{clad}) and follow the solutions for several transverse modes. Calculated results are plotted in terms of the effective index and modal gain.



CTuU5 Fig. 1. Permittivity profile of a typical InGaN/AlGaN/GaN diode laser. The active region is assumed to consist of four $In_{0.15}Ga_{0.85}N$ quantum-well layers separated by three $In_{0.02}Ga_{0.98}N$ barriers. The material gain in the quantum wells is taken as 1000 cm^{-1} at the fixed wavelength of 400 nm. The absorption coefficient α is taken as 10 cm^{-1} in all remaining layers except for the Au contact layer, where the extinction coefficient $\kappa = 1.7$ corresponds to $\alpha = 5.34 \times 10^5$ cm^{-1}.



CTuU5 Fig. 2. Calculated effective index n_{eff} for the first 5 lowest-order normal modes of TE polarization in the three-waveguide system of the p-GaN cap layer, active waveguide, and n-GaN substrate layer as a function of the GaN substrate layer thickness d_{sub}. Normal modes 1, 2, 3, . . . are identified by careful tracing of the solution for n_{eff} near the resonance. The notation TE_N^{act}, TE_N^{cap}, and TE_N^{sub}, (N = 0, 1, 2 . . .) identifies the TE_N modes of the corresponding individual uncoupled waveguides (active layer, cap layer, and substrate layer) to which the normal modes of the structure are very close for a particular range of values of d_{sub}.



CTuU5 Fig. 3. Modal gain G_{mod} calculated for the same first 5 lowest-order normal modes of TE polarization and the same InGaN/AlGaN/GaN laser structure as in Fig. 2.

The effective index and modal gain for the first five normal modes in the three-waveguide system of GaN substrate layer—active waveguide—GaN cap layer are shown in Figs. 2–3 as a function of d_{sub}. The cap layer thickness is in this case fixed at d_{cap} = 500 nm. Multiple resonances both in the active waveguide—GaN substrate system and in the GaN cap layer—GaN substrate system can be clearly seen. Dramatic drop in the modal gain occurs at every point of resonance, i.e. when the complex propagation constants of the modes localized in the active region and in the substrate become very close to each other. Note that the mode TE_0^{act} localized in the active layer actually corresponds to a sequence of normal modes emerging at subsequent resonances. We have found similar resonant effects and resonant values for d_{cap} in the active waveguide—GaN cap layer system. Obviously, a device with an unfortunate design of d_{cap} or d_{sub} close to the resonant values would either have a much higher threshold, or would not lase at all.

We have found that the resonances become broader for thinner optical barriers, which means that AlGaN claddings should be kept reasonably thick. This result agrees with observations of Nakamura *et al.*,[8] who noticed that spectral modulation of superluminescence spectra, one of the signatures of resonant mode coupling,[6,7] became much smaller when optical barriers were made thicker. However, we should emphasize that even with thin claddings it is still possible to avoid the resonances when laser design is combined with careful analysis of mode coupling.

In conclusion, we have analyzed numerically the optical modes of a system of coupled waveguides characteristic of InGaN/AlGaN/GaN laser diodes and explained the nature of resonant effects in those devices. The results demonstrate that in order to obtain low-threshold operation, special care must be taken when deciding on what particular values should be chosen for d_{cap}, d_{sub}, d_{act}, and d_{clad}. Optimization of laser design should include conscious avoidance of resonant values for any combination of these parameters.

*Also with P.N. Lebedev Physics Institute, Russian Academy of Sciences, Moscow, Russia

1. V.E. Bougrov and A.S. Zubrilov, J. Appl. Phys. 81, 2952 (1997).
2. M.J. Bergmann and H.C. Casey, J. Appl. Phys. 84, 1196 (1998).
3. M. Onomura, S. Saito, K. Sasanuma, G. Hatakoshi, M. Nakasuji, J. Rennie, L. Sugiura, S. Nunoue, M. Suzuki, J. Nishio, and K. Itaya, Conf. Digest, 1998 IEEE 16th Int. Semicond. Laser Conf., Nara, Japan, 4–8 Oct. 1998, p. 7.
4. M.P. Mack, D.K. Young, A.C. Abare, M. Hansen, L.A. Coldren, J.S. Speck, E.L. Hu, D.D. Awschalom, and S.P. DenBaars, Conf. Digest, 1998 IEEE 16th Int. Semicond. Laser Conf., Nara, Japan, 4–8 Oct. 1998, p. 9.
5. S. Heppel, J. Off, F. Scholz, and A. Hangleiter, Conf. Digest, 1998 IEEE 16th Int. Semicond. Laser Conf., Nara, Japan, 4–8 Oct. 1998, p. 11.
6. P.G. Eliseev and A.E. Drakin, Laser Phys. 4, 485 (1994).
7. I.A. Avrutsky, R. Gordon, R. Clayton, and J.M. Xu, IEEE J. Quantum Electron. 33, 1801 (1997).
8. S. Nakamura, M. Senoh, S. Nagahama, N. Iwasa, T. Yamada, T. Matsushita, H. Kiyoku, Y. Sugimoto, T. Kozaki, H. Umemoto, M. Sano, and K. Chocho, Appl. Phys. Lett. 72, 2014 (1998).

Ghost Modes and Resonant Effects in AlGaN–InGaN–GaN Lasers

Petr G. Eliseev, *Senior Member, IEEE*, Gennady A. Smolyakov, and Marek Osiński, *Senior Member, IEEE*

***Abstract*—Many diode laser structures, including those based on group-III nitride system, contain passive waveguide layers of higher refractive index than in the adjacent layers. Modes of such passive waveguides ("passive" modes) can interact with an active layer mode ("active" mode), giving rise to two kinds of normal modes or "supermodes" of a laser structure. Away from resonance, one of them is localized predominantly in the active region ("lasing" mode), while the other ones are located mostly in passive waveguides ("ghost" modes). The *lasing* mode is the mode at which laser generation occurs. The lossy *ghost* modes are parasitic modes of a laser structure that can consume energy from the active region. Resonant coupling occurs when the lasing mode and a ghost mode are in phase synchronism. In this paper, the concept of ghost modes is applied to InGaN-based diode lasers. The values for critical thickness are calculated for p-GaN cap layer and for n-GaN buffer/substrate layer for a particular multilayer laser structure. The typical thickness of 0.5 μm of AlGaN-cladding layer is found to be insufficient to prevent rather strong coupling between the modes. Under the resonant coupling conditions, the modal gain is shown to be strongly suppressed, allowing no lasing at all.**

***Index Terms*—Coupled-mode analysis, ghost modes, group-III nitrides, optical waveguide theory, resonant coupling, semiconductor lasers, short-wavelength lasers.**

I. Introduction

THE CONCEPT of *ghost* modes was originally introduced to explain some spectral features (periodic modulation in the envelopes of laser emission spectra) observed in InGaAs–GaAs–AlGaAs diode lasers on GaAs substrates [1]. Essentially, the issue was that passive waveguides existed within the diode chip, supporting their own systems of guided passive modes that could interact with an active layer mode (this effect was called *the internal mode coupling* [1]). The chip of those laser diodes was mostly transparent to the emission generated in the InGaAs active region. A very similar situation exists in InGaN–GaN–AlGaN laser diodes on sapphire [2]–[9] and GaN [10]–[12] substrates, where the laser emission easily penetrates into all the layers of the chip due to diffraction and scattering and can be accumulated within the layers with guiding properties. In an early study on spectral properties of InGaN–GaN–AlGaN diode lasers [13], a "subband" modulation effect was found, closely resembling that observed in InGaAs lasers. All this indicates that the concept of ghost modes could be of practical importance for InGaN-based lasers.

A typical design of a nitride-based laser incorporates a multiple optical waveguide structure (albeit unintentional), with refractive indices of several layers (GaN buffer/substrate, active region, etch-stop layers, GaN cap layer, and some auxiliary layers introduced to stabilize the epitaxial structure) being higher than those of adjacent layers. When any of the AlGaN cladding layers is thin (500 nm or less), the laser light may penetrate into passive waveguides. This could lead to additional optical losses, higher threshold current, and lower efficiency of the device. A particularly strong effect is expected in the case of *phase synchronism*, when the phase velocities of eigenmodes of individual waveguides, treated as uncoupled, would be the same. Under those conditions, resonant mode coupling would occur, with significant reduction of the optical confinement factor and suppression of the modal gain. It is worthy to mention that low Al-content and thin cladding layers of AlGaN are of technological advantage (lower misfit stresses, shorter and simpler growth process). Therefore, a thin-cladding structure should be carefully optimized when designing an InGaN-based diode laser. In experimental studies of InGaN–GaN–AlGaN lasers, a complicated spectral and spatial effects have been reported [14]–[16]. In waveguide calculations, the resonant-like modal behavior has been observed [17]–[19]. Thus, the internal mode coupling described in [1] seems indeed to be very important in new InGaN-based laser structures.

Complex behavior of modes in multilayer systems can be understood using the approach of normal modes of coupled waveguides (see, e.g., [20]). In this paper, we apply this approach to InGaN-based laser structures. In Section II, the concept of ghost modes is discussed in more detail. The InGaN–GaN–AlGaN laser structure is described in Section III. The numerical technique adopted for solving the wave equation is briefly discussed in Section IV. The effective index and the modal gain of normal modes are calculated as a function of the thickness of either the passive waveguides (p-GaN cap layer and n-GaN buffer/substrate) or the optical barriers (AlGaN cladding layers). The results of calculations are gathered in Section V. We consider separately the resonances in the active waveguide—cap layer system and in the active waveguide—GaN buffer/substrate system. We find that interaction between the lasing mode and the ghost modes can suppress the modal gain substantially, or even stop the

Manuscript received December 1, 1998; revised May 28, 1999. This work was supported by the Defense Advanced Research Projects Agency under the Optoelectronic Materials Center program and by the Air Force Office of Scientific Research.

P. G. Eliseev is with the Center for High Technology Materials, University of New Mexico, Albuquerque, NM 87106 USA. He is also with the Physics Institute, Russian Academy of Sciences, Moscow, 117924 Russia.

G. A. Smolyakov and M. Osiński are with the Center for High Technology Materials, University of New Mexico, Albuquerque, NM 87106 USA.

Publisher Item Identifier S 1077-260X(99)06947-6.

1077–260X/99$10.00 © 1999 IEEE

TABLE I
OPTICAL PARAMETERS OF THE MATERIALS COMPRISING THE InGaN–GaN–AlGaN MQW LASER STRUCTURE

Material	n	k	Thickness [nm]	Comments
Au	1.5	1.7	∞	Electrode material; data at 400 nm
Cr	2.75	3.0	∞	Electrode material; data at 488 nm
p-GaN	2.55	0.000032	100-2000	p-cap layer
p-$Al_{0.14}Ga_{0.86}N$	2.50	0.000032	300-800	p-cladding (optical barrier) layer
p-GaN	2.55	0.000032	100	p-waveguide layer
$In_{0.15}Ga_{0.85}N$(4)	2.75	-0.0032	4×3.5	QWs (gain coefficient 1000 cm^{-1})
+ $In_{0.02}Ga_{0.98}N$(3)	2.63	0.000032	3×7	barriers (absorption ~10 cm^{-1})
n-GaN	2.55	0.000032	100	n-waveguide layer
n-$Al_{0.14}Ga_{0.86}N$	2.50	0.000032	300-800	n-cladding (optical barrier) layer
n-GaN	2.55	0.000032	100-4000	n-buffer/substrate
α-Al_2O_3	1.77	0.000032	∞	sapphire substrate

lasing action entirely. Finally, Section VI contains discussion of the results presented in Section V and conclusions. The results shown in this paper should be useful in group-III nitride laser design as they provide guidelines for waveguide structure optimization and the rules how to avoid the undesirable resonances with ghost modes.

II. CONCEPT OF GHOST MODES

An accurate analysis of a coupled waveguide system gives field configurations (normal modes) that are often approximated by *supermodes* (see, e.g., [20]). These are in-phase or in-antiphase superpositions of the modes of individual uncoupled waveguides. This approximation is valid only *far away from resonance*, when the modes have different phase velocities.

Consider first the off-resonance situation. In this case, it is easy to identify the modes of individual uncoupled waveguides as the components of which a supermode is built up. For simplicity, consider a system of two waveguides and assume that one of the interacting modes is that of the active layer (*active* mode, for example, a mode of the active InGaN–GaN–AlGaN waveguide), while the other one is a mode of a passive waveguide (*passive* mode, for example, of p-GaN cap layer). The in-phase and out-of-phase superpositions of these modes give us the supermodes or normal modes that actually exist in this two-waveguide system. One of these modes is localized predominantly in the active region (*lasing supermode*, at which lasing action can occur), while the other one is located mostly in the passive waveguide (*ghost supermode*). In the case of the lasing supermode, the passive mode component can be observed as a local maximum of near-field intensity profile at the cap layer position. The highly doped cap-layer waveguide has a high internal loss, due to both free-carrier absorption and absorption in the contact metal. Therefore, coupling of the active mode to the cap-layer passive modes introduces some additional modal losses, thus reducing the modal gain of the lasing supermode [1]. The modal gain suppression is proportional to the coupling coefficient, with the latter decreasing exponentially as the thickness of the optical barrier (AlGaN cladding layer) increases. The lossy ghost supermode is a parasitic mode of the laser structure that can consume energy from the active region. In this case, the active mode can be viewed as a local maximum of the near-field intensity profile that the ghost supermode acquires at the active layer position.

Consider now the case when the phase velocities of the modes of individual uncoupled waveguides are very close to each other. In this case the language of supermodes may not be appropriate and we will instead consider only the exact solutions (normal modes) of the wave equation for a multilayer waveguide system. The two normal modes still resemble the in-phase and out-of-phase combinations of uncoupled modes of individual waveguides. However, contributions of the active mode and the passive mode into each of the two normal modes are now comparable. This implies a much weaker optical confinement for the lasing mode, which now experiences much greater optical losses in the passive waveguide. Consequently, the modal gain of the lasing mode decreases, and this may result in no lasing action at all. On the contrary, the ghost mode "benefits" under such close-to-resonance conditions, since it receives more optical power from the active region. Its modal gain increases, but not necessarily sufficiently to reach the lasing threshold. Obviously, it is possible to have an unlucky laser design (i.e., with resonant mode coupling) when the laser would not operate even though its active region is of perfect quality and properly supplied with high material gain. As shown in Section V, the accurate analysis demonstrates that normal modes change their character in passing through the resonance, that is the lasing mode turns into the ghost mode and vice versa. In other words, the lasing mode does not correspond to a single normal mode, but to a sequence of normal modes with the mode order increasing by one at each subsequent resonance. Generalizing this consideration for systems of more than two (active and passive) coupled waveguides in multilayer laser structures, we define ghost modes as the normal modes that have near-field distribution concentrated mostly in the passive waveguides.

III. DEVICE STRUCTURE UNDER CONSIDERATION

A typical InGaN–GaN–AlGaN laser structure (see, e.g., [2], [21]) consists of multiple layers (19 or more, including metal electrodes) with different optical parameters. The layers with

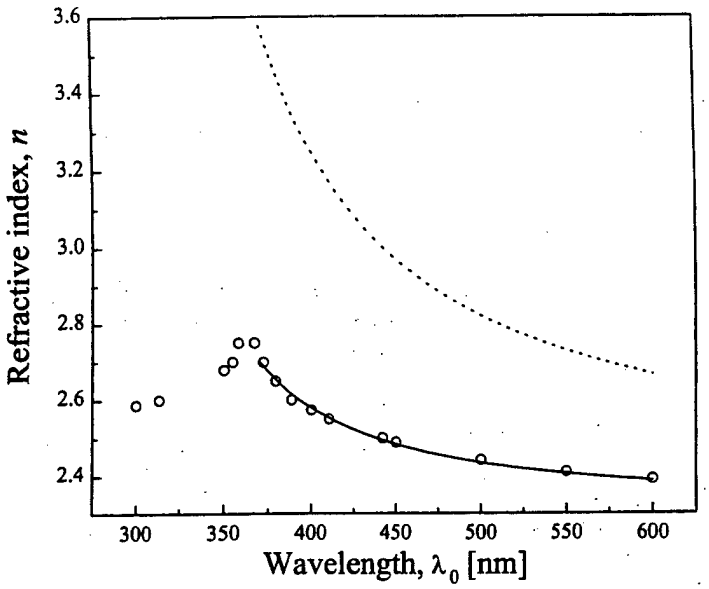


Fig. 1. Refractive index of GaN. Circles: Experimental data from [22]. Solid curve: Sellmeier fit to these data. Dotted curve: Group index calculated from the Sellmeier fit.

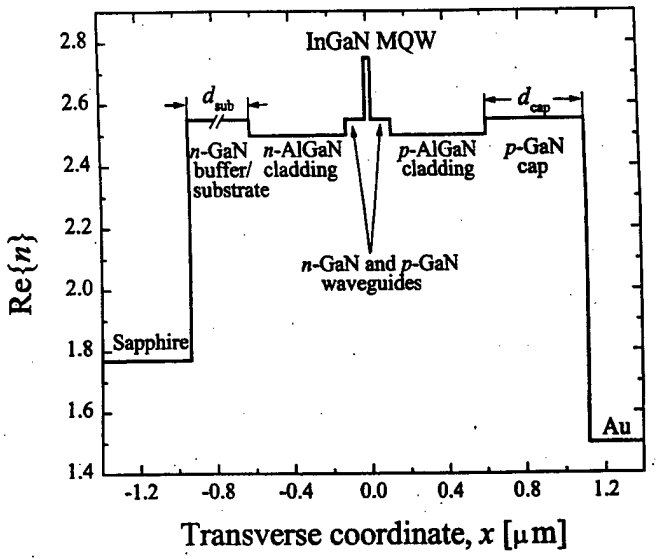


Fig. 2. Refractive index profile in a typical InGaN–AlGaN–GaN diode laser.

low values of the refractive index include sapphire substrate, AlGaN claddings, and metallic contacts, whereas p-GaN cap layer, the system of active layers and n-GaN buffer/substrate layer all form separate waveguides. Note that all the layers are quite transparent to the laser emission, with the obvious exception of contact layers. Penetration of the optical field from the cap layer into metal is limited to a very short distance. For example, at the wavelength of 400 nm the penetration depth into the gold electrode is ~120 nm. The ghost mode, then, is sensitive to the optical parameters of a very thin intermediate layer formed at the nitride–metal interface. Since those parameters are not known, instead, we use the parameters of pure metals like Au, Cr, or Ti often employed as contact and adhesive materials. The values of optical parameters used in our calculations are listed in Table I for metal electrodes and for other layers in the laser structure. Note that the extinction coefficient of 3.2×10^{-5} corresponds at the wavelength of 400 nm to the absorption coefficient of 10 cm^{-1}.

The refractive index of GaN is calculated using the Sellmeier approximation of the experimental data given in [22]:

$$n^2(\lambda) = A + B/[1 - (C/\lambda)^2]$$

with fitting parameters $A = 4.37$; $B = 1.0$; $C = 0.3$ μm (the part of the dispersion curve corresponding to the normal dispersion below the absorption edge was fitted in the range from 370 to 600 nm). We also calculate the group index of GaN, important for interpretation of longitudinal mode emission spectra from GaN-based lasers:

$$n_g(\lambda) = n + B/nS^2$$

where $S = (\lambda/C) - (C/\lambda)$. The results are shown in Fig. 1. Correction for AlGaN was made using the data for $Al_{0.1}Ga_{0.9}N$ from [22] by linear interpolation of Sellmeier parameters. Since no refractive index measurements have been reported for InGaN, we assume that the InGaN alloy at the lasing wavelength of 400 nm is characterized by the same index as GaN at its lasing wavelength of ~370 nm.

We consider an active region composed of four $In_{0.15}Ga_{0.85}N$ active quantum-well layers separated by three $In_{0.02}Ga_{0.98}N$ barrier layers. These seven layers are treated as one active layer with averaged optical parameters. The active layer as well as the n-GaN and p-GaN waveguide layers form together a 235-nm-thick active waveguide. The material gain inside the quantum wells is assumed to be 1000 cm^{-1} for a fixed wavelength of 400 nm. The refractive index profile of the laser structure assumed in our calculations is shown in Fig. 2.

IV. Calculation Technique

We consider a unidirectional propagation of modes in a planar multiwaveguide system, with one active waveguide having material gain in the core, and the remaining waveguides being passive. Taking into account that laser emission from InGaN quantum wells is predominantly of linear TE polarization, we restrict our consideration to TE modes. Note, however, that in the case of metal-clad waveguide (the p-GaN cap layer), the lowest order TM ghost mode exists in the case of a very thin cap layer, whereas the TE ghost mode appears at rather large cap thickness (~200 nm for the structure described in Table I).

Assuming only transverse (vertical) spatial dependence of the electrical field amplitude $E_y(x)$, we solve the scalar wave equation for TE modes:

$$\partial^2 E_y/\partial x^2 + [k_0^2\epsilon(x) - \beta^2]E_y = 0$$

where k_0 is the free-space wave vector, $\epsilon(x)$ is the complex dielectric constant profile of the multilayer structure of Fig. 2, and β is the longitudinal propagation constant. Using a combination of the complex Newton method and the Runge–Kutta method of integration of the fourth order, we find well-behaved guided wave solutions of the wave equation. The calculated results for normal modes are presented in terms of the modal effective index $n_{\text{eff}} = \text{Re}\beta/k_0$ and modal gain $G = -2\text{Im}\beta$. Note that although the concept of supermodes (understood

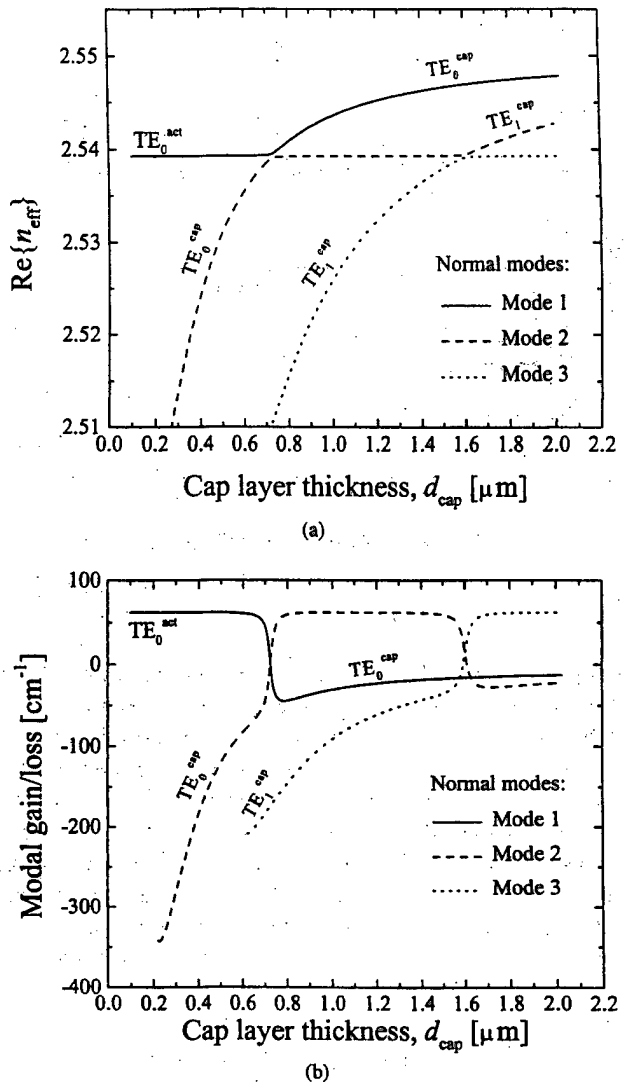


Fig. 3. Calculated effective index (a) and modal gain (b) for the first three lowest order normal modes in the two-waveguide system of the active waveguide and p-GaN cap layer. The notation TE_N^{act}, TE_N^{cap} $(N = 0, 1, 2\cdots)$ identifies the TE_N modes of the corresponding individual uncoupled waveguides (active layer, cap layer) to which the normal modes of the structure are very close for a particular range of values of d_{cap}.

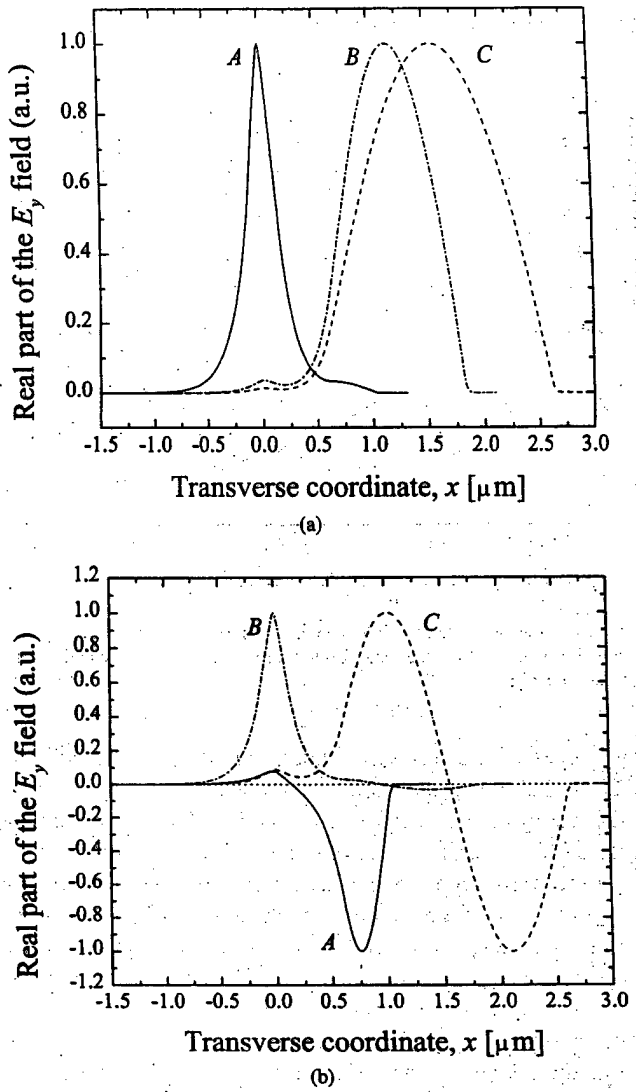


Fig. 4. Distribution of electrical field $E_y(x)$ for the two lowest order normal modes of the two-waveguide system of the active waveguide and p-GaN cap layer, corresponding to conditions below the first resonance ($d_{cap} = 400$ nm, curves A), between the first two resonances ($d_{cap} = 1.2$ μm, curves B), and between the second and third resonance ($d_{cap} = 2$ μm, curves C). (a) Normal mode 1. (b) Normal mode 2.

as superpositions of individual waveguide modes) is useful in understanding the nature of solutions, the normal modes of the laser structure are found here without invoking the coupled-mode theory.

V. Results of Calculations

A. Resonance in the "Active Waveguide–Cap Layer" System

The effective index and modal gain for the first three normal modes versus the thickness d_{cap} of the p-GaN cap layer are shown in Fig. 3 for p-AlGaN cladding layer thickness of 500 nm and Au taken as the p-side contact material. The calculated effective index of the lasing mode is ~2.539, whereas that of the ghost modes varies from ~2.5 to ~2.549. However, the effective index curves for normal modes of coupled waveguides do not cross. Rather, we can specify the points of *anti-crossing* (resonance) when two curves come very close to each other.

Evolution of the electrical field distribution $E_y(x)$ with increasing cap layer thickness d_{cap} is illustrated in Fig. 4 for the first two normal modes. The normal mode 1 resembles the TE_0 mode of the isolated active region waveguide (TE_0^{act}) up to the point when the first anti-crossing occurs. Up to that point, the normal mode 1 is the lasing mode of the structure or, in the language of coupled-mode theory, an in-phase supermode with the main maximum of intensity in the active region and a small intensity peak in the cap layer [cf. Fig. 4(a), curve A]. After the first anti-crossing point, the normal mode 1 changes its character to become a ghost mode that can be viewed as an in-phase supermode with the main maximum of intensity in the cap layer and a small intensity peak in the active region. Except for this insignificant side peak, it resembles closely the TE_0 mode of the isolated cap layer (TE_0^{cap}) [cf. Fig. 4(a), curves B and C].

The normal mode 2 appears first as a ghost mode and resembles the TE_0^{cap} mode up to the point when the first anti-

crossing occurs. It corresponds to an in-antiphase supermode with the main maximum of intensity in the cap layer and a small intensity peak in the active region [cf. Fig. 4(b), curve A]. After the first anti-crossing point, it changes its character to become the lasing mode of the structure. It can be thought of then as an in-anti-phase supermode with the main maximum of intensity in the active region and a small intensity peak in the cap layer [cf. Fig. 4(b), curve B]. It resembles closely the TE_0^{act} mode and has almost constant effective index all the way up to the point of the second anti-crossing, where the normal mode 2 changes its character once again to become a ghost mode. This time, however, it has two main intensity peaks in the cap layer and a small one in the active region. The latter being insignificant, the mode is close to the TE_1 mode of the isolated cap layer (TE_1^{cap}) [cf. Fig. 4(b), curve C].

The behavior of the normal mode 3 is very similar to that of the normal mode 2 with the only exception that the number of intensity peaks in the cap layer (whether primary or secondary) in each of the three regimes of behavior increases by one compared to mode 2. The same pattern of behavior applies also to all the subsequent normal modes. As the thickness d_{cap} gradually increases, all normal modes, except for the first one, experience resonance two times, first starting as a ghost mode of a certain order (i.e., with a certain number of nodes in the cap layer), then turning into the lasing mode, and ending up as a ghost mode once again but of a higher order (i.e., with the number of nodes in the cap layer increased by one). Note that the number of undesirable small intensity peaks acquired by the lasing mode in the cap layer increases by one after each successive resonance, which accounts for a slow reduction in its modal gain with increasing d_{cap}. Note also that the number of parasitic ghost modes in the structure increases with an increase in d_{cap}, which may have a negative effect on the overall efficiency of the device.

The calculated value of d_{cap} for the first resonance in the two-waveguide Au-clad structure is about 724 nm. In the case of the Cr-clad structure, the first resonance occurs at $d_{cap} = 733$ nm. The second resonant values of d_{cap} are 1605 nm and 1615 nm, respectively, with periodicity of resonances being the same in both cases (~880 nm).

Fig. 5 shows in more detail how the modal gain of the first two normal modes depends on d_{cap} for three different values of the optical barrier thickness d_{clad}. It is evident from this figure that a dip in the modal gain is characteristic of the lasing mode under resonant conditions. Increasing the optical barrier thickness makes the resonance narrower. It is still present even when the optical barrier is very thick, but cannot be fully resolved numerically because of limited computational accuracy. In Fig. 5, this is the case of $d_{clad} = 600$ nm, where the narrow resonance region is marked with a dotted line. The maximum value of ~62 cm^{-1} for the modal gain of the lasing mode is reached only when the corresponding normal modes have a dominant maximum of intensity within the active waveguide. This occurs only away from resonance, and the modal gain in this case is almost the same as it would be for the uncoupled TE_0^{act} mode. Close to resonance, the modal gain falls down dramatically, in spite of the same high

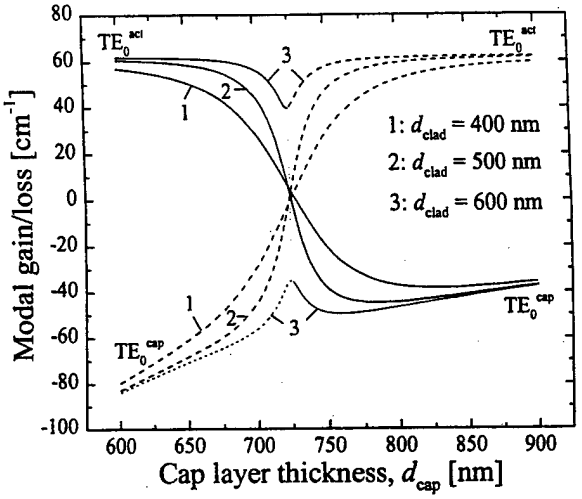


Fig. 5. Modal gain for the first two normal modes of TE polarization in the two-waveguide system of the active waveguide and Au-clad p-GaN cap layer as a function of the GaN cap layer thickness d_{cap}, calculated for three different values of the optical barrier thickness d_{clad}.

value of material gain (1000 cm^{-1}) in the quantum wells. The minimum of the modal gain (the point of intersection of modal gain curves at resonance) is almost independent of the thickness of the optical barrier. In the particular case of the 500-nm thick AlGaN optical barrier, the calculated minimum modal gain is ~2 cm^{-1} for Au contact and ~1.55 cm^{-1} for Cr contact. Obviously, these levels of modal gain are not sufficient to reach lasing threshold. Therefore, a laser with a resonant value of d_{cap} would not be able to operate. The fact that the resonance becomes broader as the optical barrier gets thinner implies that in order to avoid an inadvertent resonance, it is important to keep the optical barriers reasonably thick.

B. Resonance in the "Active Waveguide–GaN Buffer/Substrate" System

In this section, we consider possible effects that another passive waveguide in the InGaN-based diode laser chip, namely n-GaN buffer/substrate, can have on laser performance. To be closer to the real situation in InGaN-based diode lasers, we now treat the full system of three waveguides: p-GaN cap layer, active waveguide and n-GaN buffer/substrate. The thickness of the cap layer is fixed at $d_{cap} = 500$ nm (chosen to stay away from resonance with the active waveguide), while the n-GaN buffer/substrate thickness d_{sub} is varied from 0.05 μm to 4 μm.

In the system of three coupled waveguides, it is convenient to distinguish between the ghost modes of the cap layer (located primarily in the cap layer) and the ghost modes of the GaN buffer/substrate (located primarily in the GaN buffer/substrate layer).

The effective index and modal gain for the first five normal modes in this three-waveguide system are shown in Fig. 6 as a function of the GaN buffer/substrate thickness d_{sub}. Multiple resonances occur both in the "active waveguide–GaN buffer/substrate" system and in the "GaN cap layer–GaN buffer/substrate" system. Qualitatively, in the case of the

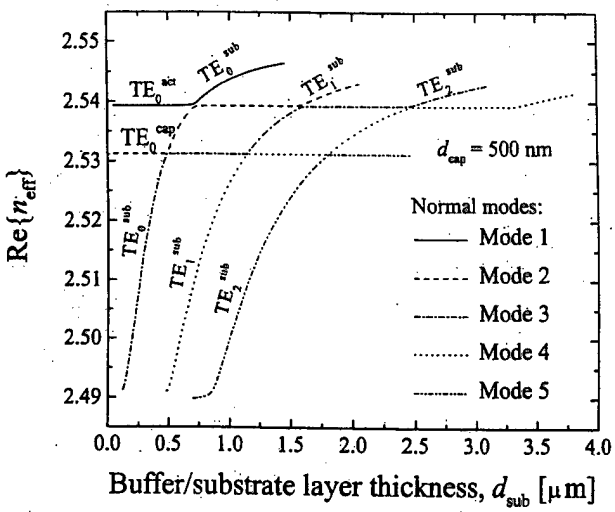


Fig. 6. Calculated effective index (a) and modal gain (b) for the first five lowest order normal modes of TE polarization in the three-waveguide system of the p-GaN cap layer, active waveguide, and n-GaN buffer/substrate layer as a function of the GaN buffer/substrate layer thickness d_{sub}. The notation TE_N^{act}, TE_N^{cap}, and TE_N^{sub}, $(N = 0, 1, 2 \cdots)$ identifies the TE_N modes of the corresponding individual uncoupled waveguides (active layer, cap layer, and buffer/substrate layer) to which the normal modes of the structure are very close for a particular range of values of d_{sub}.

"active waveguide–GaN buffer/substrate" interaction, the behavior of the normal modes is quite similar to that of the "active waveguide–cap layer" interaction described in the precedent section, and the periodicity of the resonances is also ~880 nm. The dips in the modal gain at the points of resonance are not, however, as deep as in the previous case, since the buffer/substrate waveguide is not nearly as lossy as the metal-clad cap layer (cf. Table I). The minimum modal gain is now about 25 cm^{-1}, while the maximum value reached away from resonance remains to be ~62 cm^{-1}. Nevertheless, diode lasers with resonant values of d_{sub} will have much higher threshold than well-designed devices.

Evolution of normal modes in a system of three coupled waveguides can be much more complicated than in a system of two coupled waveguides. In the particular case illustrated in Fig. 6, this increased complexity is manifested by a sequence of additional resonances in the "cap layer—GaN buffer/substrate" system, occurring with periodicity of ~650 nm in d_{sub}. It is interesting to note here that as the thickness d_{sub} gradually increases, all the normal modes of the order higher than 2 can experience resonance four times, starting first as the buffer/substrate ghost modes, then turning into cap-layer ghost modes, after that turning again into buffer/substrate ghost modes, then becoming the lasing mode, and eventually ending up once again as buffer/substrate ghost modes. Note also that for each value of d_{sub} this particular system of three coupled waveguides supports only one lasing mode, and only one ghost mode of the p-GaN cap layer, whereas the number of ghost modes of the n-GaN buffer/substrate increases with an increase in d_{sub}. The system of normal modes could easily be of even greater complexity should the individual cap layer waveguide or the active waveguide support more than one transverse mode.

C. Comments on Spectral Effects of Ghost Modes

We considered above how the modal gain of the normal modes depends on the thickness of the passive waveguides and optical barriers. Qualitatively, a similar behavior can be expected for the normal modes when the geometry of the device is fixed but the wavelength is varied. The only difference will be due to refractive index dispersion that should be properly included into consideration.

The main spectral effect of internal mode coupling is a periodic modulation of the superluminescent spectrum, similar to that reported in [2], [23]. The periodicity of spectral modulation observed in [2], [23] was 0.25 nm, and it could not be explained by an unintentional longitudinal Fabry–Perot cavity formed inside the laser structure. A similar effect is known in InGaAs-based lasers [1], where it can be understood within the framework of waveguide treatment by taking into account the ghost modes of a thick GaAs substrate. It should therefore be expected that a similar effect in InGaN-based lasers can arise from the presence of substrate ghost modes. However, the ghost modes of GaN buffer/substrate can produce only a much larger spectral periodicity, due to relatively small thickness of the n-GaN buffer/substrate and, correspondingly, to the relatively low order of the ghost modes. To account for the observed spectral periodicity of 0.25 nm, we then have to consider a composite sapphire/n-GaN substrate. Obviously, the resonant effects on the modal gain would be much weaker in that case, since the photon exchange with sapphire substrate is significantly reduced at GaN/sapphire interface. The periodicity of spectral modulation, though, can be reasonably well predicted.

When parasitic waveguides are thick, the number of transverse ghost modes is large, with a small spectral separation between two adjacent modes. In very thick waveguides (such as composite waveguide of n-GaN and sapphire substrate), this spectral distance is sufficiently small compared to the spectral bandwidth of the emission spectra. The distant mirror at the bottom of the sapphire substrate assists in forming ghost modes. Coupling to these modes can cause some periodic modulation in the superluminescent spectrum. In a typical

InGaN–GaN–AlGaN diode laser structure [23], the claddings are 500 nm thick, and the substrate is composite. It includes four layers of the total thickness ~203 μm. The spectral periodicity of ghost modes is

$$\Delta\lambda \sim \lambda/m$$

where m is the order of the ghost mode of the composite substrate. The value of m depends on the boundary conditions at the bottom of the substrate. They are not well known when the substrate is in contact with a heat-sinking material. If, however, there is no optical contact (the interface is sapphire–air), the dielectric constant step is $\Delta\varepsilon = 2.133$, using 1.77 for the refractive index of sapphire. Estimation of the order of the mode that can be resonantly coupled to the active mode gives

$$m = (2d/\lambda)(\Delta\varepsilon)^{1/2}$$

where d is the waveguide thickness. At $\lambda = 400$ nm, we obtain $m = 1460$, and the periodicity of resonances will be $\Delta\lambda = 0.2697$ nm. This is sufficiently close to the observed subband periodicity of 0.25 nm [2], [23] to consider internal mode coupling as a plausible explanation of the "subband modulation" effect.

We present no accurate calculation for the effect of coupling to ghost modes of the sapphire substrate as the waveguide theory predicts a very low penetration of the laser light into sapphire substrate for the structure shown in Fig. 2. However, the waveguide theory does not take into account the effect of light scattering that may also be responsible for the mode coupling. It is reasonable to expect an enhanced level of scattering at the interface of sapphire and the highly defective low-temperature GaN buffer layer.

VI. Discussion and Conclusions

Numerical analysis of a system of multiple coupled waveguides clearly shows a strong effect that ghost modes located primarily at passive waveguides can have on the modal gain of the lasing mode. The typical thickness for optical barrier (AlGaN cladding layer) between the active waveguide and the p-GaN cap layer and between the active waveguide and the n-GaN buffer/substrate is about 500 nm, which is not sufficient for strong optical isolation. Consequently, internal mode coupling may occur, and at some specific values of the passive waveguide thickness it can become resonantly enhanced.

The modal gain suppression at resonance is the result of a strong decrease in the optical confinement factor Γ. Close to resonance, the volume of the lasing mode is increased due to substantial optical flux within the passive waveguide. Correspondingly, the lasing mode experiences additional optical losses in the passive waveguide. If the passive waveguide is the cap layer, the losses in the metal cladding are of importance.

In the case of resonant coupling with Au-clad cap layer, we found the critical thickness d^* of ~724 nm for the first resonance to occur. The resonance with the cap-layer ghost mode can be easily avoided if the cap layer thickness less than d^* is used. However, it is also important to note that

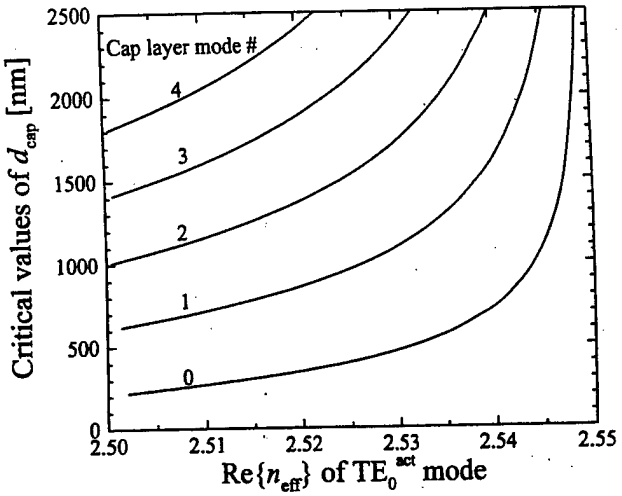


Fig. 7. Calculated dependence for the resonant thickness of the cap layer on the effective index of the uncoupled fundamental mode of the active waveguide. The numbers labeling the curves indicate the order of the corresponding uncoupled cap-layer mode.

the first resonant thickness d^* depends on the effective index of the lasing mode. The calculated dependence is shown in Fig. 7. Thus, proper design of the active waveguide is critical, as it determines the effective index of the lasing mode. For example, a greater number of QW's in the MQW structure will increase the effective index, making the resonant thickness of the cap layer larger. Also, an increase in the GaN-waveguide-layer thickness would produce an increase in the effective index.

In the case of internal mode coupling with GaN buffer/substrate, the resonance occurs with periodicity of 880 nm as the buffer/substrate thickness d_{sub} is increased. The critical values for the buffer/substrate thickness are 710, 1590, 2470, 3350, 4230 nm, and so on. Note that these values are also sensitive to the effective index of the lasing mode, with the dependence being quite identical to that of Fig. 7. At resonance with the buffer/substrate ghost modes, the calculated minimum modal gain is not as low as it is at resonance with cap-layer ghost modes. This is due to substantial contribution of the absorption in metal cladding in the latter case. Since the waveguide approach does not take into account the light scattering effects, our analysis neglects possible additional optical losses due to light scattering in the highly defective low-temperature GaN buffer layer adjacent to sapphire substrate. In a real laser structure, such scattering loss can lead to even lower modal gain at the points of resonance in the "active waveguide–GaN buffer/substrate" system.

The typical thickness of n-GaN buffer/substrate is 2–4 μm, therefore it can coincide occasionally with some of the critical values for resonant mode coupling. When such coincidence does occur, the modal gain of the lasing mode can be dramatically suppressed even though the active layers are supplied with high material gain. In diode laser manufacturing, the quality of a wafer with such critical thickness of the GaN buffer/substrate could be questioned, while the true origin of no-lasing (or high lasing threshold) would be the internal mode coupling. Therefore, considerations of resonant mode coupling

should be part of the laser design process to select the optimal thickness for the GaN buffer/substrate layer. In order to avoid the effect of resonant suppression of the modal gain by ghost modes, all parasitic waveguide thicknesses should be away from their expected resonant values. It is also possible to reduce the possibility of an unintentional resonance by making the optical barriers stronger, by increasing the thickness and/or Al content of cladding layers.

The important rules applied to the normal modes in a multiple-waveguide system when the thickness d of one of parasitic waveguides changes are as follows:

1) The calculated effective index of normal modes $n_{\text{eff}}(d)$ closely follows the corresponding curves for the modes of individual uncoupled waveguides everywhere except for the regions where *anti-crossing* (*resonance*) occurs. Since no crossing really occurs, there is no spatial mode degeneracy even if the modes of individual uncoupled waveguides might have the same phase velocity.
2) According to this anti-crossing behavior, the lasing mode (located primarily in the active waveguide) does not correspond to a single normal mode, but instead is represented by a series of different normal modes with gradually increasing mode order. The normal modes change their character (in terms of the location of the dominant peak in their intensity profile) at each anti-crossing point.
3) Away from anti-crossing points, the modal profile for each normal mode is close to that of the corresponding mode of an individual uncoupled waveguide, but contains additional contributions from the allowed modes of other waveguides.
4) When phase velocities of the modes of individual uncoupled waveguides coincide, the resonant coupling takes place. In such case, the interacting modes share optical flux almost equally, and the modal gain in both normal modes can be substantially suppressed.

In conclusion, we considered numerically the optical modes of a system of coupled waveguides characteristic of InGaN–AlGaN–GaN laser diodes. The diode chip contains parasitic waveguides (p-GaN cap layer, n-GaN buffer/substrate layer), and the normal modes located primarily in these waveguides (ghost modes) can interact resonantly with the lasing mode, causing a strong modal gain suppression. The means to prevent the undesirable suppression of modal gain include the use of stronger optical barriers and avoidance of the resonant values for the thickness of parasitic waveguides. The results of our analysis are important in laser design as well as in interpretation of some unusual patterns of behavior in InGaN-based diode lasers.

REFERENCES

[1] P. G. Eliseev and A. E. Drakin, "Analysis of the mode internal coupling in InGaAs/GaAs laser diodes," *Laser Phys.*, vol. 4, no. 3, pp. 485–492, 1994.

[2] S. Nakamura and G. Fasol, *The Blue Laser Diode—GaN Based Light Emitters and Lasers*. Berlin, Germany: Springer-Verlag, 1997.

[3] S. Nakamura, "GaN-based blue/green semiconductor laser," *IEEE J. Select. Topics Quantum Electron.*, vol. 3, pp. 435–442, Apr. 1997.

[4] M. P. Mack, A. Abare, M. Aizcorbe, P. Kozodoy, S. Keller, U. K. Mishra, L. Coldren, and S. DenBaars, "Characteristics of indium-gallium-nitride multiple-quantum-well blue laser diodes grown by MOCVD," *MRS Internet J. Nitride Semiconduct. Res.*, vol. 2, Sept. 1997, Art. 41.

[5] S. Nakamura, "InGaN-based laser-diodes," *Annu. Rev. Mater. Sci.*, vol. 28, pp. 125–152, 1998.

[6] S. Nunoue, M. Yamamoto, M. Suzuki, C. Nozaki, J. Nishio, L. Sugiura, M. Onomura, K. Itaya, and M. Ishikawa, "Reactive ion-beam etching and overgrowth process in the fabrication of InGaN inner stripe laser diodes," *Jpn. J. Appl. Phys., Pt. 1*, vol. 37, no. 3B, pp. 1470–1473, Mar. 1998.

[7] D. P. Bour, M. Kneissl, L. T. Romano, M. D. McCluskey, C. G. Van de-Walle, B. S. Krusor, R. M. Donaldson, J. Walker, C. J. Dunnrowicz, and N. M. Johnson, "Characteristics of InGaN-AlGaN multiple-quantum-well laser diodes," *IEEE J. Select. Topics Quantum Electron.*, vol. 4, pp. 498–504, June 1998.

[8] S. Nakamura, "High-power InGaN-based blue laser diodes with a long lifetime," *J. Cryst. Growth*, vol. 195, nos. 1–4, pp. 242–247, Dec. 1998.

[9] Y. Park, B. J. Kim, J. W. Lee, O. H. Nam, C. Sone, H. Park, E. Oh, H. Shin, S. Chae, J. Cho, I. H. Kim, J. S. Khim, S. Cho, and T. I. Kim, "Characteristic of InGaN/GaN laser diode grown by a multi-wafer MOCVD system," *MRS Internet J. Nitride Semiconduct. Res.*, vol. 4, no. 1, pp. 1–6, Jan. 19, 1999.

[10] S. Nakamura, M. Senoh, S. Nagahama, N. Iwasa, T. Yamada, T. Matsushita, H. Kiyoku, Y. Sugimoto, T. Kozaki, H. Umemoto, M. Sano, and K. Chocho, "High-power, long-lifetime InGaN/GaN/AlGaN-based laser-diodes grown on pure GaN substrates," *Jpn. J. Appl. Phys., Pt. 2 (Lett.)*, vol. 37, no. 3B, pp. L309–L312, Mar. 15, 1998.

[11] S. Nakamura, M. Senoh, S. Nagahama, N. Iwasa, T. Yamada, T. Matsushita, H. Kiyoku, Y. Sugimoto, T. Kozaki, H. Umemoto, and M. Sano, "InGaN/GaN/AlGaN-based laser-diodes grown on GaN substrates with a fundamental transverse mode," *Jpn. J. Appl. Phys., Pt. 2 (Lett.)*, vol. 37, no. 9AB, pp. L1020–L1022, Sept. 15, 1998.

[12] M. Kuramoto, C. Sasaoka, Y. Hisanaga, A. Kimura, A. A. Yamaguchi, H. Sunakawa, N. Kuroda, M. Nido, A. Usui, and M. Mizuta, "Room-temperature continuous-wave operation of InGaN multi-quantum-well laser diodes grown on an n-GaN substrate with a backside n-contact," *Jpn. J. Appl. Phys., Pt. 2 (Lett.)*, vol. 38, no. 2B, pp. L184–L186, Feb. 15, 1999.

[13] S. Nakamura, M. Senoh, S. Nagahama, N. Iwasa, T. Yamada, T. Matsushita Y. Sugimoto, and H. Kiyoku, "Subband emissions of InGaN multi-quantum-well laser diodes under room-temperature continuous wave operation," *Appl. Phys. Lett.*, vol. 70, no. 20, pp. 2753–2755, May 19, 1997.

[14] M. Onomura, S. Saito, K. Sasanuma, G. Hatakoshi, M. Nakasuji, J. Rennie, L. Sugiura, S. Nunoue, M. Suzuki, J, Nishio, and K. Itaya, "Analysis of transverse modes of nitride-based laser diodes," in *Conf. Dig., 16th IEEE Int. Semicond. Lasers*, Nara, Japan, Oct. 1998, pp. 7–8, paper MB1.

[15] S. Heppel, J. Off, F. Scholz, and A. Hangleiter, "Complex spectral behavior of the waveguide modes in GaInN/GaN laser structures," in *Conf. Dig., 16th IEEE Int. Semiconduct. Lasers*, Nara, Japan, Oct. 1998, pp. 11–12, paper MB3.

[16] D. K. Young, M. P. Mack, A. C. Abare, M. Hansen, L. A. Coldren, S. P. DenBaars, E. L. Hu, and D. D. Awschalom, "Near-field scanning optical microscopy of indium gallium nitride multiple-quantum-well laser diodes," *Appl. Phys. Lett.*, vol. 74, no. 16, pp. 2349–2351, Apr. 19, 1999.

[17] V. E. Bougrov and A. S. Zubrilov, "Optical confinement and threshold currents in III–V nitride heterostructures: Simulation," *J. Appl. Phys.*, vol. 81, no. 7, pp. 2952–2956, Apr. 1, 1997.

[18] M. J. Bergmann and H. C. Casey Jr., "Optical-field calculations for lossy multiple-layer $Al_xGa_{1-x}N/In_xGa_{1-x}N$ laser diodes," *J. Appl. Phys.*, vol. 84, no. 3, pp. 1196–1203, Aug. 1, 1998.

[19] P. G. Eliseev, G. A. Smolyakov, and M. Osiński, "Ghost modes and their signature in InGaN diode laser spectra," in *Proc. 2nd Int. Symp. Blue Laser and Light Emitting Diodes, 2nd ISBLLED*, Kisarazu, Japan, Paper Th-10, Sept. 29–Oct. 2, 1998, pp. 413–416.

[20] H. Haus, *Waves and Fields in Optoelectronics*. Englewood Cliffs, NJ: Prentice-Hall, 1984, section 7.6, pp. 217–220.

[21] S. Nakamura, M. Senoh, S. Nagahama, N. Iwasa, T. Yamada, T. Matsushita, Y. Sugimoto, and H. Kiyoku, "First room-temperature continuous-wave operation of InGaN multi-quantum-well-structure laser diodes," presented at the IEEE LEOS 9th Annu. Meeting, Boston, MA, Nov. 18–21, 1996, paper PD1.1.

[22] H. Amano, N. Watanabe, N. Koide, and I. Akasaki, "Room-temperature low-threshold surface-stimulated emission by optical pumping from

Green, blue, and beyond - current status and future prospects for short-wavelength diode laser development

(Invited Paper)

Marek Osiński

Center for High Technology Materials, University of New Mexico,
1313 Goddard SE, Albuquerque, New Mexico 87106, USA
Tel. (505) 272-7812, Fax (505) 272-7801, Email: osinski@chtm.unm.edu

1. Introduction

Diode lasers emitting at short wavelengths are very attractive for many commercial applications, such as high-density optical storage systems, high-resolution and color printing and scanning, projection displays, UV lithography, and spectroscopy/biohazard sensing. The diffraction-limited spot size of focused laser light is proportional to the emission wavelength, which improves the surface density of optical memories or resolution of printers as square of the inverse wavelength. Digital versatile disks (DVDs), which came onto the market in 1996, rely on red AlInGaP diode lasers and have a data capacity of about 4.7 Gbytes, compared to 0.65 Gbytes for standard compact disks. By moving to violet wavelengths, the capacity could be increased to 15 Gbytes, sufficient to store a full-length (2h) color movie on a single disk. Short-wavelength diode lasers could also improve the performance of laser printers and undersea optical communications.

The family of group-III nitrides (InN, GaN, AlN and their ternary and quaternary alloys) represents an important trio of semiconductors because of their direct bandgaps which span the range of 1.95-6.2 eV, including the entire visible region from 650 nm and extending well out into the UV at 200 nm. They form a complete series of ternary alloys which, in principle, makes available any bandgap within this range. This, together with the fact that they also generate efficient luminescence, has been the main driving force behind their recent technological expansion. In a remarkably short time, the nitrides have caught up with and, at least in the blue-violet range, surpassed the wide-bandgap II-VI compounds (ZnCdSSe or ZnMgSSe) as primary materials for short-wavelength optoelectronic devices. So far, however, green light emission has

only been demonstrated in II-VI diode lasers, although their serious problems with reliability (the longest room-temperature cw lifetime is still only ~400 h [1]) may preclude them from ever being commercialized.

2. Present leaders in the nitride diode laser race

In spite of many concurrent efforts worldwide at research laboratories in industry, government institutions, and universities, only a handful of groups have so far been able to demonstrate electrically pumped III-N lasers. As was the case earlier with nitride-based LEDs, Nichia Chemical Industries in Japan holds an unquestionable lead over everybody else, with estimated device lifetimes exceeding 10,000 h under room-temperature cw operation conditions [2], and with first steps towards commercialization taken in January 1999. The next best result, reported by Fujitsu, is 57 h of room-temperature cw operation [3]. Other companies that reported cw operation but with much shorter device lifetimes (ranging from 1 hour to less than a minute) are, in chronological order: CREE Research (USA), Sony, Xerox, NEC, and Matsushita. Other members of the exclusive nitride laser club, although at this point enjoying only a pulsed operation status, are Toshiba, University of California at Santa Barbara, Hewlett Packard – Japan in collaboration with Meijo University, SDL (USA), Pioneer, and Samsung.

3. Common workhorse – group-III nitrides on sapphire or SiC substrates

The most common substrate materials for growing GaN and other group-III nitrides are electrically insulating sapphire and conductive hexagonal (4H or 6H) SiC. However, growth on those highly mismatched produces a columnar material, consisting of many hexagonal grains. Individual grains are slightly tilted and rotated with respect to each other, which gives rise to *very large dislocation densities*, typically 10^9-10^{10} cm^{-2}. Any other semiconductor system with such high extended-defect densities would be completely useless for optoelectronic applications. Yet, both high-brightness light-emitting diodes and low-threshold-current-density diode lasers have been demonstrated in the III-N system. In fact, all commercial blue and green InGaN/AlGaN/GaN LEDs have very high threading dislocation densities that do not seem to affect their performance or reliability. Our early experiments with high-pulsed-current pumping of blue LEDs [4] did, however, indicate that presence of defects may have detrimental effect on

the diode laser lifetime by providing a path for *p*-contact metal to migrate down towards the *p-n* junction under high forward voltage conditions required to reach the lasing threshold. This results in shorting of the *p-n* junction. This prediction has been subsequently confirmed by many groups trying to achieve III-N diode lasers, who observed that failed lasers would typically exhibit a short in their electrical characteristics.

4. Present favorite – ELOG

The longest diode laser lifetime that was achieved in ridge-waveguide InGaN/AlGaN/GaN multiple-quantum-well lasers grown on sapphire is 300 h [5]. At that point, however, it became clear that diode lasers do require a much better material quality and a different approach was necessary. One technique to reduce the density of threading dislocations is to mask out a large part of the defective material, leaving just small opening for seeding the continued growth that would then largely proceed in lateral direction, creating virtually dislocation-free regions over the masked areas. This procedure, known as *epitaxial lateral overgrowth* (ELOG), is at present the main tactic towards long-lifetime nitride-based diode lasers.

By continuing the ELOG growth beyond the point of coalescence of adjacent masked regions, it is possible to produce layers of *n*-GaN thick enough (100-200 μm) to be used as *free-standing conductive substrates* by removing the original sapphire substrates. Using this approach, high-quality diode lasers with projected lifetimes exceeding 10,000 h have been demonstrated by Nichia [2]. In addition to improving the crystalline quality and making it easy to cleave Fabry-Perot structures, the use of ELOG-GaN substrates offers an option of adopting the usual vertical design of diode lasers, with the *n*-type contact underneath the GaN substrate. Thus, the need to etch the top mesa for making the *n*-side contact is eliminated, although we note that this option has not yet been used in Nichia lasers. Finally, for devices mounted *n*-side down, lasers with removed sapphire substrates should benefit from improved thermal flow, as thermal conductivity of GaN (1.3 W/cm-K) is significantly higher than that of sapphire (0.35 W/cm-K).

Composite best results for InGaN/AlGaN/GaN lasers on ELOG substrates, as reported by Nichia, are:

- Threshold current I_{th} = 16 mA (typical 30-60 mA)

- Threshold current density J_{th} = 1.2 kA/cm^2 (typical 3 - 4 kA/cm^2)
- Threshold voltage V_{th} = 4.3 V (typical 4.5 - 5.0 V)
- Maximum operation temperature T = 100°C
- Emission wavelength λ = 380 - 450 nm (best 400 nm)
- Lifetime > 10,000 hours at 20 °C and 5 mW; > 1,000 hours at 50 °C and 5 mW
- Maximum output power P = 420 mW
- Quantum efficiency η = 39% (1.2 W/A)

In spite of these very encouraging data, ELOG substrates may not, after all, offer the ultimate solution for III-N lasers. Present offering of diode laser "samples", introduced by Nichia in January 1999, illustrates the difficulties that still exist with commercialization of nitride-based diode lasers using ELOG substrates. Rather than introducing the laser as a commercial product at a price consistent with mass consumer market applications, Nichia only offers single samples at a very high cost (about $2,000 per laser) for "evaluation purposes". This indicates that while ELOG approach is capable of producing champion devices with lifetimes exceeding 10,000h, it may be very difficult to achieve sufficiently high yield, necessary for low-cost high-volume manufacturing.

5. Alternative approaches – homoepitaxy, pendeo-epitaxy, compliant substrates, and nanoheteroepitaxy

The most straightforward, and ultimately probably the most successive approach for reliable and inexpensive III-N lasers, is to use high-quality GaN or InGaN substrates. Unfortunately, in spite of enormous surge of interest in nitrides for over 5 years now, such substrates are not yet available. It is impossible to employ well-known methods of bulk semiconductor growth such as Bridgman or Czochralski for III-N crystal growth because of the extremely high melting temperatures and nitrogen vapor pressures required.

Three main routes pursued in parallel towards the goal of developing bulk GaN are: high-pressure (HP) growth, sublimation growth (SG), and hydride or halide vapor-phase epitaxy (VPE). VPE-grown GaN, while relatively easy and inexpensive [6], has failed so far to produce

epitaxial structures of higher optical quality than those grown on sapphire. The *high-pressure growth* is the most advanced technique in terms of producing high-quality GaN (dislocation density less than 10^4 cm^{-2}) [7] and demonstrating superior optical quality of MOCVD-grown homoepitaxial structures on HP-GaN [8], but the crystals are still very small and very expensive in fabrication (it takes 200 h to grow a 100 mm^2 crystal!). Successful growth of HP-GaN has been so far limited to only one research group at the High Pressure Research Center in Warsaw, Poland, which in itself indicates the inherent difficulty of the process. MOCVD homoepitaxy on SG-GaN has been shown to produce improved-quality material [9], but the size of SG-GaN crystals is still considerably smaller than that of HP-GaN, and it is very difficult to use them in practice until they become significantly larger. Compared to the large number researchers working now in the filed of group-III nitrides, the effort towards achieving high-quality bulk substrates seems to be disproportionately small.

Pendeo-epitaxy is a variation of ELOG introduced recently at North Carolina State University [10], in which the lateral overgrowth proceeds from side walls of GaN trenches etched down in conventional epitaxial layers grown on SiC substrates. Mot likely this approach will suffer from problems similar to usual ELOG structures, namely the difficulties with obtaining high yield from the wafer that contains alternating regions of high-quality and low-quality material, and possible propagation of defects into originally defect-free regions under lasing conditions.

Another interesting approach that so far has not yet been fully exploited is utilization of the so-called *compliant substrates*, in which a thin overlayer of a compliant material absorbs most of the strain in lattice-mismatched growth, resulting in a high-quality epitaxial structure. Initial results of GaN growth on SOI (silicon-on-insulator) [11] and LGO (lithium gallate, $LiGaO_2$) [12] look indeed promising, although reported characterization of GaN layers is rather incomplete (for example, no data are available on threading dislocation density).

Nanoheteroepitaxy is a technique somewhat related to compliant substrate approach, pursued at the University of New Mexico, in which the substrate material is prepared by lithographic etching of very deep trenches, leaving tall and narrow (10–100 nm) ridges or columns that can easily accommodate the strain of mismatched growth [13]. Theoretical estimates indicate that lattice mismatch as high as 4.2% (well within the mismatch between GaN and 6H-SiC, for

example) can be totally absorbed by the nanopatterned substrate. With careful control of the size and pitch of the patterned ridges/columns, it may well be possible to achieve defect-free single-crystal GaN that would not suffer from the usual problems of highly defective windows and coalescence regions that are present in ELOG layers.

6. Remaining challenges

III-N diode lasers are still in the very early stages of their development. Some of the remaining challenges that will likely be overcome in the near future are: improved performance of edge-emitting lasers (higher output power, lower voltage, lower threshold current), improved thermal management, stable single-mode operation (development of distributed-feedback lasers), extension of the emission wavelength into the blue and green spectral regions, and demonstration of electrically pumped VCSELs. Theoretical understanding of III-N lasers is still rather immature (some controversial or unresolved issues include, for example, the role of piezoelectric fields, localized states, many-body effects, and extended defects, degree of strain relaxation, InGaN compositional nonuniformities and formation of quantum-dot-like regions, *etc.*) and the expected further progress in this area will certainly assist in meeting the goals set for nitride-based diode lasers.

7. References

1. E. Kato, H. Noguchi, M. Nagai, H. Okuyama, S. Kijima, and A. Ishibashi, Electron. Lett. **34**, pp. 282-284 (1998).
2. S. Nakamura, M. Senoh, S. Nagahama, N. Iwasa, T. Yamada, T. Matsushita, H. Kiyoku, Y. Sugimoto, T. Kozaki, H. Umemoto, M. Sano, and K. Chocho, Jpn. J. Appl. Phys., Pt. 2 (Lett.) **37**, pp. L309-L312 (1998).
3. A. Kuramata, S. Kubota, R. Soejima, K. Domen, K. Horino, P. Hacke, and T. Tanahashi, Jpn. J. Appl. Phys., Pt. 2 (Lett.) **38**, pp. L481-L483 (1999).
4. D. L. Barton, J. Zeller, B. S. Phillips, P.-C. Chiu, S. Askar, D.-S. Lee, M. Osiński, and K. J. Malloy, Proc. 33rd Annual IEEE International Reliability Physics Symp., Las Vegas, NV, 4-6 April 1995, Paper 3B.3, pp. 191-199.

5. S. Nakamura, M. Senoh, S.-I. Nagahama, N. Iwasa, T. Yamada, T. Matsushita, Y. Sugimoto, and H. Kiyoku, Jpn. J. Appl. Phys., Pt. 2 (Lett.) **36**, pp. L1059-L1061 (1997).

6. M. K. Kelly, R. P. Vaudo, V. M. Phanse, L. Görgens, O. Ambacher, and M. Stutzmann, Jpn. J. Appl. Phys., Pt. 2 (Lett.) **38**, pp. L217-L219 (1999).

7. S. Porowski, MRS Internet J. Nitride Semicond. Res. **4S1**, Article G1.3 (1999).

8. M. Kamp, C. Kirchner, V. Schwegler, A. Pelzmann, K. J. Ebeling, M. Leszczyl lski, I. Grzegory, T. Suski, and S. Porowski, MRS Internet J. Nitride Semicond. Res. **4S1**, Article G10.2 (1999).

9. H. Sato, T. Sugahara, Y. Naoi, and S. Sakai, Jpn. J. Appl. Phys., Pt. 1, **37**, pp. 2013-2015 (1998).

10. T. S. Zheleva, S. A. Smith, D. B. Thomson, K. J. Linthicum, P. Rajagopal, and R. F. Davis, J. Electron. Materials **28**, pp. L5-L8 (1999).

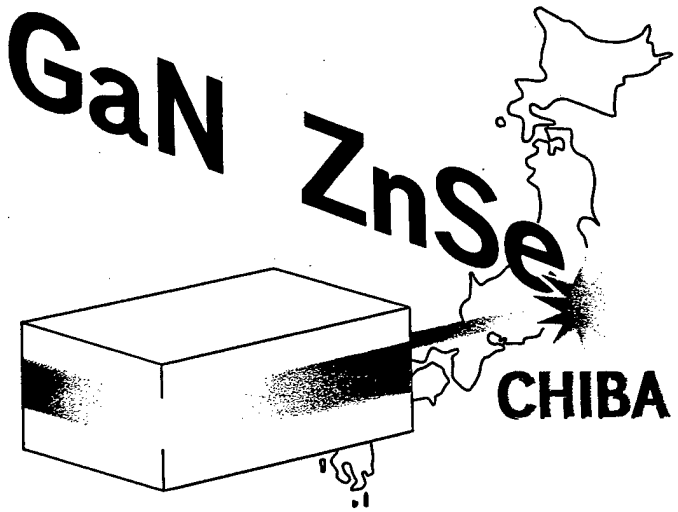
11. J. Cao, D. Pavlidis, A. Eisenbach, A. Philippe, C. Bru-Chevallier, and G. Guillot, Appl. Phys. Lett. **71**, pp. 3880-3882 (1997).

12. W. A. Doolittle, T. Kropewnicki, C. Carter-Coman, S. Stock, P. Kohl, N. M. Jokerst, R. A. Metzger, S. Kang, K. K. Lee, G. May, and A. S. Brown, J. Vac. Sci. Technol. B: Microelectron. & Nanometer Structures **16**, pp. 1300-1304 (1998).

13. D. Zubia and S. D. Hersee, J. Appl. Phys. **85**, pp. 6492-6496 (1999).

Proceedings of the 2nd International Symposium on

Blue Laser and Light Emitting Diodes



September 29 - October 2, 1998

Kazusa Akademia Center,
Kisarazu, Chiba, Japan

Ghost Modes and their Signature in InGaN Diode Laser Spectra

Petr G. ELISEEV[1], Gennady A. SMOLYAKOV, and Marek OSIŃSKI
Center for High Technology Materials, University of New Mexico, 1313 Goddard SE
Albuquerque, NM, 87106
Phone (505) 272-7812, Fax (505) 272-7801, E-mail: osinski@chtm.unm.edu
[1]On leave from P. N. Lebedev Physics Institute, Moscow, Russia

We define "ghost modes" as those that exist in a diode laser chip and can interact resonantly with the lasing mode. Ghost modes are associated with passive layers that have the property of dielectric waveguide (cap layer, as an example). The condition for strong internal coupling is 1) penetration of the laser emission into passive waveguide volume; and 2) phase synchronism between the lasing mode and the ghost. The concept of ghost modes is applied to InGaN-based diode laser. In particular, it can be used to explain the "subband" emission effect - spectral modulation of the envelope of superluminescent modes.

1. Introduction

InGaN-based multi-quantum-well laser structures are new active materials for laser diodes in visible and UV wavelength ranges [1-4]. The nitride materials are grown as multi-layer films on sapphire or on other heterogeneous substrates. Optical isolation between separate structure layers and between the nitride film and the substrate is usually not perfect, particularly due to small thickness of confining layers. As a result, laser emission penetrates into the layers outside of the active region and into the substrate. It can be accumulated by guiding layers of the diode chip and reflected by remote surfaces, in particular, by the bottom surface of the substrate. The important property of the chip structure is transparency of all the layers to laser emission. This property is the same as in the case of InGaAs QW lasers grown on GaAs substrate. In [5], a model of coupled active and passive waveguides was developed and applied to InGaAs lasers. It considers various "parasitic" waveguides existing in the laser chip (cap layer, stop-etch layers, substrate). Each waveguide supports a system of modes ("ghost" modes) which generally are quite different from the excited mode (or modes) of the active region ("lasing mode"). However, ghost modes can interact with the lasing mode and can consume energy from the lasing mode. Such an interaction was called "internal mode coupling" [5]. It modifies spatial configuration of the output emission as compared to the unperturbed active mode.

2. Mode Interaction in a Two-Waveguide System

Consider two separate waveguides and with their own individual modes: one is the *lasing* mode of the active waveguide and the other is the *ghost* mode of the parasitic waveguide. When emission of the lasing mode penetrates into the parasitic waveguide, the modal profile is regularly perturbed by some subsidiary maximum of intensity located in the parasitic waveguide. Such a perturbation can be small and not important. However, the interaction of modes can be resonantly strong if their oscillation frequencies coincide and their phase velocities along the longitudinal axis coincide (synchronism). Mode resonance and synchronism are the rules selecting one of the variety of ghost modes, if any, to be coupled with the active mode. When these conditions are satisfied, the interacting modes form a "supermode" which looks like a superposition (in-phase or out-of-phase) of the individual modes. The supermode profile corresponds to sharing the optical flux between two waveguides. This means that the modal gain (and optical confinement factor Γ) is resonantly reduced and additional losses are introduced due to absorption in passive material and in metal (when parasitic waveguide is the cap layer). If we scan gradually the lasing wavelength, resonances can occur between the active mode and ghost modes. A resonance with the very

lossy ghost mode of the cap layer, where absorption in the contact metal produces strong internal loss, can stop lasing action altogether [5]. This illustrates how serious the issue of modal interactions can be.

3. Application to InGaN Diode Lasers

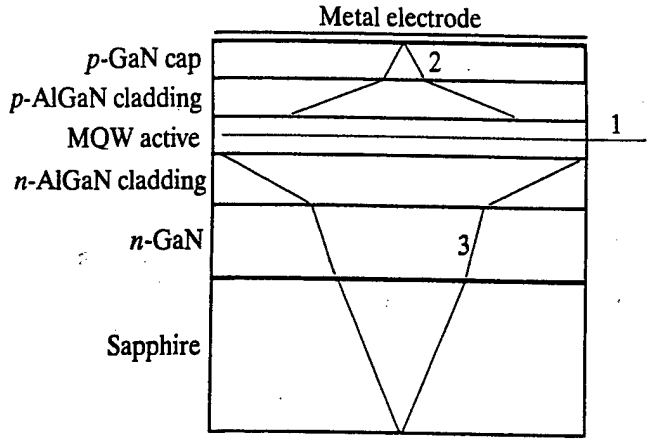


Fig. 1. Schematic representation of the laser chip (guiding regions are shadowed) and of mode ray trajectories: 1) active mode, 2) cap-layer mode, 3) substrate mode.

The real InGaN/GaN laser structure (see, for example, Ref. [2]) contains a number of layers (19 or more, including metal electrodes) with different optical parameters. There are layers with relatively lower or higher refractive index. Materials with low index are cladding layers, sapphire and metals, whereas *p*-GaN cap layer, the system of active layers and *n*-GaN layer all form separate waveguides. Note that all layers are transparent to the laser emission. Parasitic waveguides at both sides of the active one can extract some optical power to themselves providing additional optical losses and reducing the modal gain. In the cap layer due to dielectric asymmetry the ghost mode is forbidden if the thickness is smaller than the critical value. This allows one to exclude the influence of the cap layer by taking its thickness to be sufficiently smaller than the critical value. This value generally depends on the sort of metallic material. Radiation penetrates into metal for a short distance. For example, for gold electrode, the penetration depth for 400 nm radiation is ~120 nm. Therefore, the mode profile is sensitive to the material parameters in the close vicinity of the interface. Since optical parameters of the thin intermediate layer between nitride and metal are not known we decided to use the parameters of pure metals like Au, Cr, Ti which are used often as contact and adhesive materials. For the waveguide Au/GaN/$Al_{0.07}Ga_{0.93}N$, we assume parameters as follows: Au, n = 1.5, k = 1.7 [8]; GaN, n = 2.55, k = 0.000032; $Al_{0.07}Ga_{0.93}N$, n = 2.5, k = 0.000032; in InGaN active material the gain was taken to be equal to 1000 cm^{-1}. The scheme of the laser structure is shown in Fig. 1. The first resonant value of GaN layer thickness for TE mode in the Au-clad structure is near 724 nm, the second resonance occurs at 1605 nm.

Figs. 2 and 3 illustrate the phenomenon of internal mode coupling between the lasing TE mode and the ghost mode of the cap layer. The optical barrier between two waveguides is assumed to be provided by 500-nm thick cladding layer of $Al_{0.07}Ga_{0.93}N$. The plots in Fig. 2 show the dependence of the modal effective index on the thickness of the cap layer. At small values of d_{cap} there is no TE modes in the cap. The laser oscillation can be achieved in the TE mode of the active waveguide, and the real part of the effective index does not depend on d_{cap} from very beginning to ~700 nm. It is the horizontal part of curve *1* (stable value is 2.538). The ghost mode in the cap appears when d_{cap} exceeds 220 nm. Its effective index is rather lower than that of the lasing mode as represented by the tilted part of curve *2*. However, the index grows up and approaches the value of 2.538 near the point where d_{cap} is 724 nm. Above the resonant point d_{cap} = 724 nm the laser oscillation jumps to the mode represented by curve *2* which remains stable in the range from ~750 nm to ~1605 nm where the second resonance

occurs (not shown in Fig. 2). Modes *1* and *2* are generally supermodes of the twin waveguide. Mode *1* is in-phase combination of TE modes of both waveguides whereas mode *2* is their out-of-phase combination. Outside of resonance each mode has a small perturbation (maximum) in the tail which affects their properties very weakly. But at resonance there are comparable maximums in both modes in each waveguide. Modal exchange at the resonant point is accompanied by a dip in the modal gain as it is seen in Fig. 3. The modal value of ~62 cm^{-1} is reached in each modes *1* and *2* only when they have predominating maximum in the active waveguide which is the case out of resonance. At the resonant point the modal gain drops down even though the material gain in the active waveguide does not change. The minimal modal gain was calculated to be ~ 2 cm^{-1} for Au-clad case and ~1.55 cm^{-1} for Cr-clad case. Obviously, such a gain is not sufficient to maintain the laser oscillation. Therefore, lasing would be stopped near the resonant point. The width of the gain dip is ~30 nm, and periodicity of the dips is ~880 nm, therefore it seems to be easy to avoid an occasional drop of the modal gain due to such mode coupling. This analysis manifests the importance of this phenomenon when the coupling happens to be strong. Weak interaction should be seen by its effect on mode selectivity, because the small dips of the modal gain can be overcome by laser oscillation jumping into another spectral mode with higher quality factor.

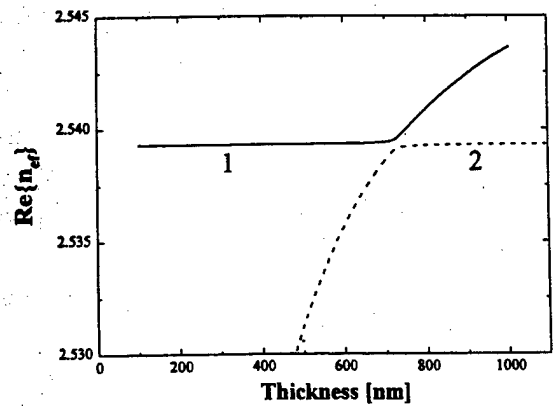


Fig. 2. The real part of the effective index of TE modes in the two-waveguide system of the MQW active waveguide and the cap-layer waveguide versus the cap-layer thickness. Curve 1 corresponds to the in-phase supermode whereas curve 2 corresponds to the out-of-phase supermode.

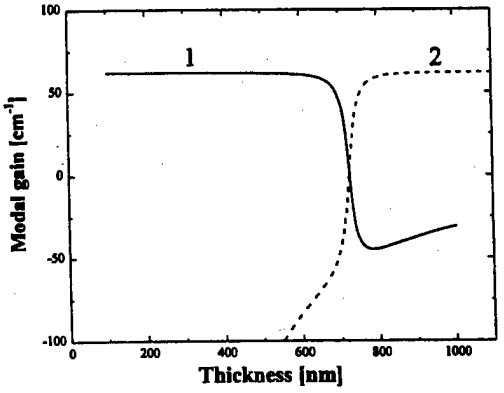


Fig. 3. The modal gain of TE modes in the same two-waveguide system as in Fig. 2, as function of the cap-layer thickness. At the point of the modal exchange (~710 nm), a deep suppression of the modal gain occurs. It produces a gap of ~30 nm on the cap-layer thickness scale where laser action is canceled by strong optical losses within electrode material and by reduction of the optical confinement factor.

A thick waveguide is formed by nitride and sapphire substrate materials at the other side of the active region. The spectrum of modes is more dense than in the thin cap layer. Therefore, they have more chances to fall into resonance with the active mode. In principle, most of modes of large volume can be far from resonance as they have the effective index close to that of the waveguide material but not the same as in the lasing mode. However, there are some ghost modes near their cut-off points. They have somewhat reduced effective index due to weak confinement. This provides an opportunity for their phase synchronism with the active mode and leads to the periodic spectral variation of the quality factor of active longitudinal modes. Its minimums correspond to the internal coupling with some ghost mode. Thus, the coupling to ghost modes occurs rather easily in the vertical direction. Emission spectra of ridge-waveguide

lasers operating in CW mode at wavelength near 400 nm are described in Ref. [2]. A feature of the spectr was found, namely, periodic *subband* emission with an energy separation of 2 meV (0.25 nm wavelength scale). This was observed as a modulation of the regular standing-wave superluminesc spectrum below the oscillation threshold, and as laser mode hopping with an increase of the operati current. The hopping occurs to another longitudinal mode over several intermodal spacings into the n subband. We have to emphasize that spectral modulation is a common effect when two or more me systems interact. It was observed earlier in a composite-cavity [6] as a result of interference in coupl Fabry-Perot cavities; also it was found in solitary cavity units as a result of uncontrollable intra-cav reflection [7]. Such a reflection can occur due to structural defects of the active waveguide (microcr inclusion, growth terrace). Effects of this type (longitudinal and lateral coupling) as unintentio phenomenon are of quite occasional character. In order to explain the systematic modulation in spectra suggest to consider the vertical coupling to ghost modes which is a characteristic of a wafer rather than individual diodes. Therefore, it occurs more systematically than occasional longitudinal and late coupling. In typical InGaN laser diode structure [2] the claddings are 500-nm thick, so the optical barrier not quite strong. The substrate is composite and consists of four layers of total thickness ~203 μm. main guiding part is GaN layer (~3 μm) provi ling the periodicity of about 27 nm, which is out of ran shown by plots in Ref. [2]. Due to high transparency of the sapphire substrate the reflection from bottom will affect periodically the mode properties of non-resonant mode in a composite substra waveguide. Spectral periodicity of such modes is $\Delta\lambda \sim \lambda/m$, where m is the order of the ghost mode of t composite substrate. Value m depends on the boundary conditions of this waveguide. They are not we known at the bottom side where the substrate is in contact with a heat-sinking metal. If there is no optic contact (the interface is sapphire-air) the dielectric constant step is $\Delta\varepsilon = 2.133$, using 1.77 for the refracti index of sapphire. Estimation of the order of the mode that can be coupled to the active one gives m $(2d/\lambda)(\Delta\varepsilon)^{1/2}$, where d is the waveguide thickness. At $\lambda = 400$ nm we obtain $m = 1460$, and the periodicity of resonances will be $\Delta\lambda = 0.2697$ nm. This is close to the subband periodicity observed in Ref. [2] namely, 0.25 nm. Although our estimate may not be very accurate due to the uncertainty of boundary conditions, the resonance coupling can give spectral periodicity in the range observed experimentally.

4. Conclusions

We have considered the model of internal mode coupling in InGaN diode lasers grown on sapphire Specific configurations of the laser structure have been found which should be avoided in laser design to prevent strong optical losses caused by coupling with the cap layer. The ways to exclude the resonance with the cap layer are 1) provide sufficient optical barrier between the active region and the cap layer, 2) select the cap layer thickness below the critical value at which the resonant internal mode coupling can occur. Spectral modulation of the laser output has been considered in terms of internal coupling to the ghost modes of the substrate.

References

[1] S. Nakamura and G. Fasol, *The Blue Laser Diode*, Springer-Verlag, Berlin, 1997.

[2] S. Nakamura et al., Appl. Phys. Lett., **70** (20), 2753 (1997).

[3] I. Akasaki, S. Sota, H. Sakai, T. Tanaka, M. Koike, and H. Amano, *Electron. Lett.*, **32** (12), 1105 (1996).

[4] S. Nakamura, M. Senoh, S. Nagahama, N. Iwasa, T. Yamada, T. Matsushita, Y. Sugimoto, and H. Kyoku, *Appl. Phys. Lett.*, **68**, 2105 (1996).

[5] P. G. Eliseev and A. E. Drakin, *Laser Physics*, **4** (3), 485 (1994).

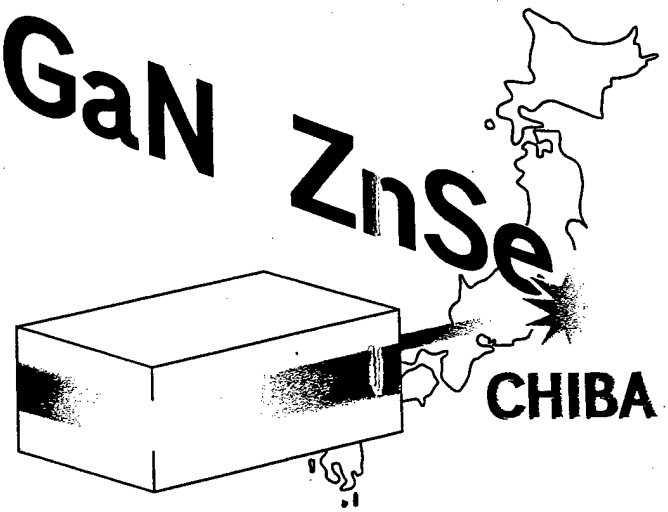
[6] P. G. Eliseev, I. Ismailov, M. A. Manko, V. P. Strakhov, *Pis'ma ZhETF*, **9**, 594 (1969); also: D. Ackerman, P. G. Eliseev, A. Keiper, M. A. Manko, S. Raab, *Kvant. Elektronika*, **1** (1), 85 (1971).

[7] D. Hofstetter, L. T. Romano, R. L. Thornton, D. P. Bour, N. M. Johnson, *Appl. Phys. Lett.*, **71** (22), 3200 (1997, Dec. 01).

[8] A. J. Mo es, *Optical Materials Properties*, Plenum, NY etc., 1971.

Proceedings of the 2nd International Symposium on

Blue Laser and Light Emitting Diodes



September 29 - October 2, 1998

Kazusa Akademia Center,
Kisarazu, Chiba, Japan

Accelerated Life Testing of GaN/InGaN/AlGaN Blue Light-Emitting Diodes and High Temperature Failure Mechanism

Marek OSIŃSKI and Daniel L. BARTON[1]
Center for High Technology Materials, University of New Mexico, 1313 Goddard SE
Albuquerque, New Mexico 87106, USA
Phone (505) 272-7812, Fax (505) 272-7801, E-mail: osinski@chtm.unm.edu
[1]Also with Sandia National Laboratories, Albuquerque, New Mexico 87185-1081, USA

Results of high-temperature life testing of blue double-heterostructure LEDs are reported. Observed reduction in light output is attributed to degradation of the encapsulating plastic.

1. Introduction

Our studies of device lifetime and the main degradation mechanisms in Nichia blue LEDs date back to Spring 1994. Following the initial studies of rapid failures under high-current electrical pulses where metal migration was identified as the cause of degradation, we have placed a number of Nichia NLPB-500 double-heterostructure LEDs on a series of life tests. The first test ran for 1000 hours under normal operating conditions (20 mA at 23 °C). As no noticeable degradation was observed, the second room-temperature test was performed with the same devices but with a range of currents between 20 and 70 mA. Table I specifies the driving currents for all 20 devices placed under test. After 1600 hours, some degradation in output intensity was observed in devices driven at 60 and 70 mA, but it was still less than 20%. The subsequent tests included stepping up the temperature by 10 °C in 500 h intervals up to a final temperature of 95 °C in test 11, using the same currents as those applied in the second test [1]. In this paper, we summarize the main results of the accelerated life testing at elevated temperatures.

Table I. Driving Conditions for Various Tested LEDs. Devices #19 and 20 are "older" generation devices

Current [mA]	Device numbers
20	1,2,3,20
30	4,5,6
40	7,8,9
50	10,11,12
60	13,14,15
70	16,17,18,19

2. High-Temperature Life Test Results

Fig. 1 shows the data from the last 510-hour test, during which the ambient temperature was maintained at 95 °C. The observed degradation rates are significantly higher than those recorded in the previous test, conducted at 85 °C. In particular, the LEDs driven at currents exceeding 50 mA suffer from a rapid degradation process. In spite of a significant reduction in the LED output, corresponding *I-V* curves show little variation, strongly suggesting that the degradation may be package-related.

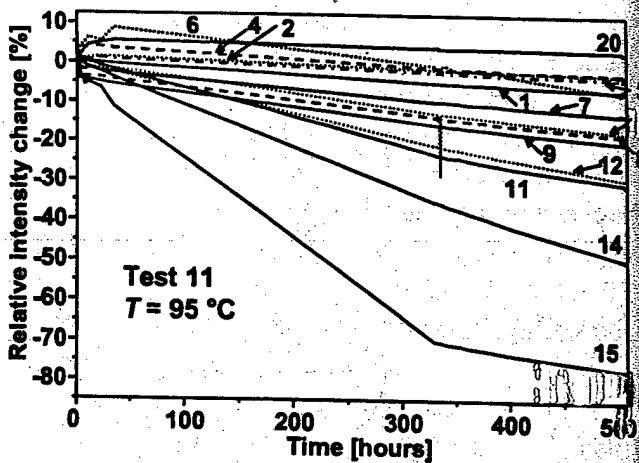


Fig. 1. Relative change in intensity of remaining Nichia blue LEDs at 95 °C for the final 510 hours of testing.

3. LED Temperature Measurements

In order to understand the cause of the observed degradation, we have examined the effects of forward current on the temperature of the LED. First, we measured the change in the LED temperature with forward current for an LED kept in a room temperature environment. For this analysis, a thermocouple was attached to the heat sink of the LED. The results are shown in Fig. 2 where the LED temperature and the applied power are plotted against the forward current. Fig. 2 indicates that the temperature of the LED (as measured external to the package) could increase by over 40 °C at the current levels used in the life test. The use of an external point on the package to measure these temperatures means that the temperature of the diode could have been significantly higher than what was measured.

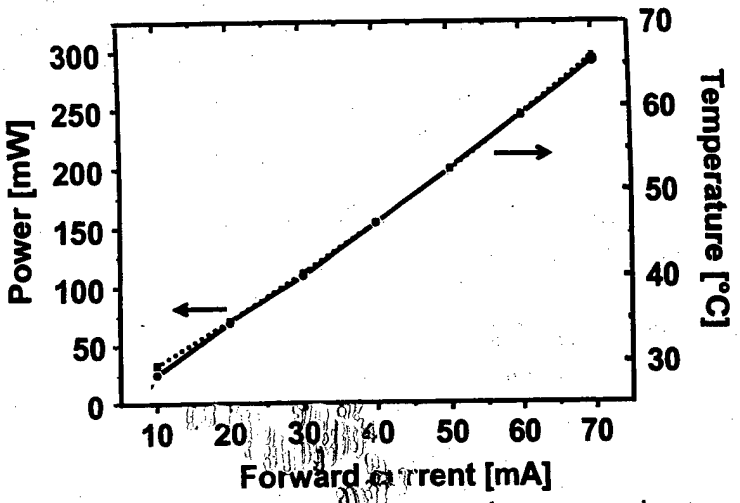


Fig. 2. LED power dissipation and measured temperature rise at various currents at room temperature.

A more accurate way to determine the temperature of the diode is to measure the junction voltage. To make this measurement, a control LED was placed in a burn-in oven and allowed to come to thermal equilibrium with the oven temperature. To minimize changes in the voltage across the junction due to self-heating, the junction voltage was measured when the LED was first turned on. An HP 4145 semiconductor parameter analyzer was used for the measurement, allowing the voltage to be accurately measured within 10 ms after the current was applied. This process was repeated at currents from 10 mA to 70 mA (coinciding with the range of currents used in the life tests) and at temperatures from 30 °C to 150 °C. The resulting data, plotted in Fig. 3, show that there is a linear relationship between the voltage measured across the junction and the temperature of the junction. From these data, a better estimate of the encapsulant temperature near the interface with the LED can be made.

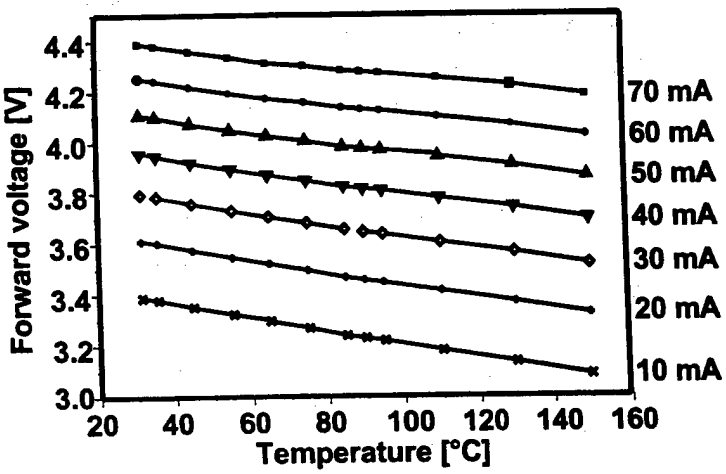


Fig. 3. Forward junction voltage measured at turn-on for various currents and temperatures.

To calculate the diode temperatures experienced by the LEDs in test 11, a similar LED was placed in an oven at 95 °C and allowed to come to thermal equilibrium. The same forward currents that were used in the life tests were then applied and allowed to stabilize, meaning that the final temperature resulting from the ambient temperature and self-heating had been reached. This point was determined by observing the junction voltage and waiting for it to stop decreasing. The results along with the temperature measured on the external thermocouple are summarized in Table II.

Table II. LED forward voltage at various currents in a 95 °C ambient

Forward current [mA]	Voltage [V]	Thermocouple temperature [°C]
10	3.1689	96.5
20	3.3669	97.5
30	3.538	98.4
40	3.7019	99.6
50	3.8679	100.9
60	4.0378	102.2

Using the linear fit parameters from the data in Fig. 3 along with the data in Table II, the junction temperatures were calculated for each forward current. The results are shown in Fig. 4. The calculations show that for forward currents of 50 mA and higher, the junction temperature was in excess of 145 °C. For currents smaller than 30 mA, where, according to the data in Fig. 1, the degradation rate is significantly lower, the temperature is less than 135 °C. While the exact temperature at which the plastic begins to darken has not been determined, the temperature where the degradation begins to affect this material in a time frame important to LED lifetimes is shown in Section 4 to be between 135 and 145 °C.

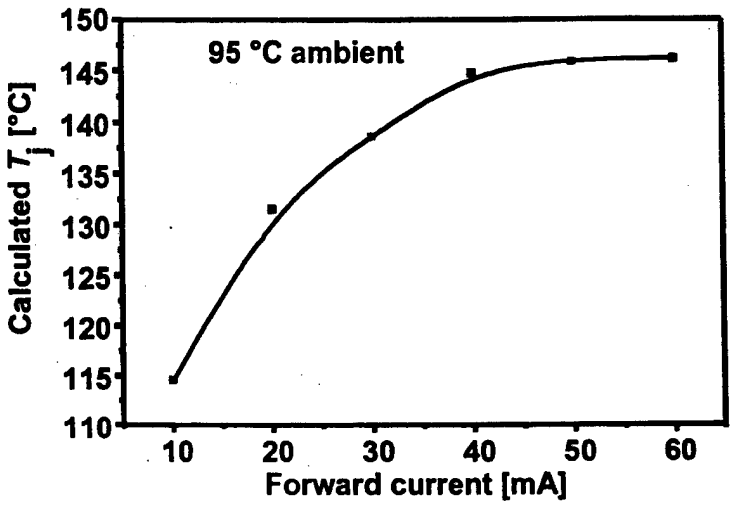


Fig. 4. Calculated junction temperature (T_j) at various forward currents (ambient temperature 95 °C).

4. Plastic Degradation Study

Analysis of the junction temperature described in Section 3 suggests that for currents above 40 mA in a 95 °C ambient the temperature of the diode can exceed 140 °C. This means that the LED output degradation shown in Fig. 1 may be related to a combination of ambient temperature and the LED self-heating. We have therefore investigated sensitivity of the encapsulating plastic material to elevated ambient temperatures. Fig. 5 shows three sections of plastic removed from a Nichia LED control sample. The piece on the left has not been exposed to more than normal room temperature and has a clear appearance. The sample in the middle was placed in a burn-in oven at 150 °C in air for 133 h. This sample has turned to a deep brown color. The sample in the right was placed in the same oven at 200 °C for 130 minutes and shows a similar change to the sample exposed to 150 °C, only to a lesser degree. This test indicated that at temperatures of around 150 °C (or slightly lower) the plastic can change by a purely thermal effect in such a manner that the light output of the LED could be attenuated. While no visible browning of the plastic was observed on the outside of the package in the LEDs used in the life test, local darkening of the plastic could be noticed near the interface with the LED. It should be emphasized that the plastic temperature of 150 °C is very close to the estimated junction temperature during Test 11.

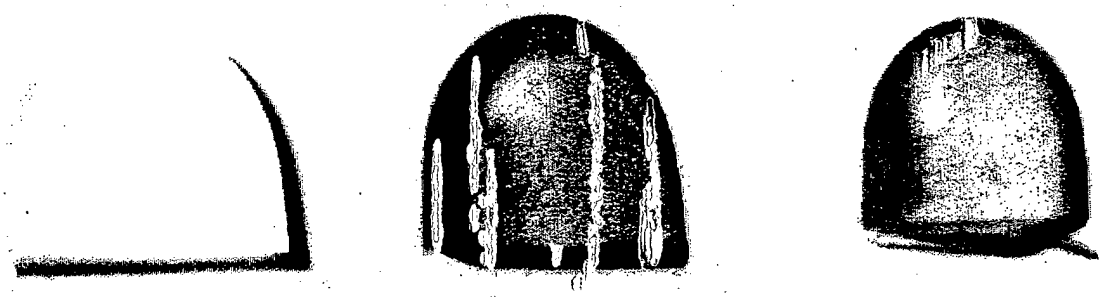


Fig. 5. Sections of Nichia LED package material: (left) unstressed, (middle) after 133 h thermal stress at 150 °C, (right) after 130 min thermal stress at 200 °C.

5. Summary and Conclusions

None of our life tests of Nichia NLPB-500 blue LEDs, totaling more than 7,300 h (most of which was under harsher than normal conditions) for each of the devices shown in Fig. 1, produced significant degradation on any of the devices in a manner consistent with a degradation mechanism attributable to the device itself. These results indicate that Nichia devices enjoy a remarkable longevity in spite of their high density of defects[3]. Earlier analysis of the degradation characteristics of the plastic packaging material demonstrated that a degradation in light output at high currents (greater than 50 mA) could be caused by the ultraviolet light emitted by the LED at close-to-room temperatures [2]. At higher ambient temperatures, however, the degradation mechanism changes from a light-intensity related mechanism to a pure thermal mechanism. By calculating the junction temperature of the diode at the life test temperatures, excellent correlation was made between the observed degradation rate and the temperatures achieved through the combination of ambient temperature and diode self-heating. This analysis was supported by the observation of darkening in plastic encapsulant samples exposed to temperatures consistent with those calculated from the junction temperature measurements.

Acknowledgments

The support of the Defense Advanced Research Projects Agency (DARPA) and the New Energy and Industrial Technology Development Organization (NEDO) of Japan is gratefully acknowledged. Part of this work performed at Sandia National Laboratories was supported by the U.S. Department of Energy under contract DE-AC04-94AL85000. Sandia is a multiprogram laboratory operated by Sandia Corporation, a Lockheed Martin Company, for the United States Department of Energy.

References

[1] C. J. Helms, N. H. Berg, D. L. Barton, B. S. Phillips, and M. Osiński, in *Fabrication, Testing, and Reliability of Semiconductor Lasers*, edited by M. Fallahi and S. C. Wang, SPIE Proc. **2683**, San Jose, CA, 31 Jan. - 1 Feb. 1996, pp. 74-80.

[2] D. L. Barton, M. Osiński, P. Perlin, C. J. Helms, and N. H. Berg, *Proc. 35th Annual IEEE International Reliability Physics Symp.*, Denver, CO, 8-10 Apr. 1997, pp. 276-281.

[3] D. Barton, J. Zeller, B. Phillips, P. Chiu, S. Askar, D. Lee, M. Osinski, and K. Malloy, *Proc. 33rd Annual IEEE International Reliability Physics Symp.*, Las Vegas, NV, 4-6 Apr. 1995, pp. 191-199.

Weber, J., 1969, Evidence for discovery of gravitational radiation, Phys. Rev. Lett. 22, 1320.
Weiss, R., 1972, Electronically coupled broadband gravitational antenna, Q. Progr. Rep. Lab. Electron. MIT 105, 54.
Winkler, W., K. Danzmann, A. Rüdiger and R. Schilling, 1991, Heating by optical absorption and the performance of interferometric gravitational-wave detectors, Phys. Rev. A 44, 7022.
Winkler, W., A. Rüdiger, R. Schilling, K.A. Strain and K. Danzmann, 1994, Birefringence-induced losses in interferometers, Opt. Commun. 112, 245.
Winkler, W., R. Schilling, K. Danzmann, J. Mizuno, A. Rüdiger and K.A. Strain, 1994, Light scattering described in the mode picture, Appl. Opt. 33, 7547.

E. WOLF, PROGRESS IN OPTICS XXXVIII
© 1998 ELSEVIER SCIENCE B.V.
ALL RIGHTS RESERVED

III

THERMAL PROPERTIES OF VERTICAL-CAVITY SURFACE-EMITTING SEMICONDUCTOR LASERS

BY

WŁODZIMIERZ NAKWASKI*

Institute of Physics, Technical University of Łódź, ul. Wólczańska 219, 93005 Łódź, Poland

MAREK OSIŃSKI**

Center for High Technology Materials, University of New Mexico, 1313 Goddard SE, Albuquerque, NM 87131, USA

* Also with the Department of Electrical and Computer Engineering, University of New Mexico, Albuquerque, NM 87131, USA.
** Also with the Department of Electrical and Computer Engineering, and the Department of Physics and Astronomy, University of New Mexico, Albuquerque, NM 87131-6081, USA.

CONTENTS

	PAGE
§ 1. INTRODUCTION	167
§ 2. COMPARISON OF VERTICAL-CAVITY SURFACE-EMITTING AND EDGE-EMITTING DIODE LASERS	168
§ 3. EFFECTS OF TEMPERATURE ON VCSEL OPERATION	182
§ 4. FUNDAMENTALS OF THERMAL MODELING OF VCSELs	205
§ 5. COMPREHENSIVE THERMAL MODELS OF VCSELs	218
§ 6. CONCLUSIONS	254
ACKNOWLEDGMENTS	255
REFERENCES	256

§ 1. Introduction

Vertical-cavity surface-emitting lasers (VCSELs) generate considerable interest due to their unique features which distinguish them from conventional edge-emitting lasers (EELs): narrow low-divergence circular non-astigmatic output beam, inherent dynamic single-longitudinal-mode operation, geometry suitable for integration into two-dimensional (2D) arrays or for monolithic integration with electronic devices, compatibility with vertical-stacking architectures, and so on. Rarely, the paramount role of thermal effects in VCSELs is listed among those features, perhaps because it usually represents an obstacle rather than an advantage. Ever since the inception of VCSELs, thermal problems have plagued their development (Iga, Koyama and Kinoshita [1988], Geels and Coldren [1991], Hasnain, Tai, Dutta, Wang, Wynn, Weir and Cho [1991]), and to this date they represent a major hurdle that must be overcome if massive integration into 2D arrays is ever to be realized (Osiński and Nakwaski [1995a]).

Compared to EELs, VCSELs have a number of unique features which make them potentially more immune to damage caused or accelerated by external ambient. These include complete isolation of the active region from the external medium, a very small active-region volume, the potential for temperature-insensitive operation, and high internal optical power density (low radiative carrier lifetime). These properties make VCSELs attractive for applications in harsh environments.

In spite of the remarkable progress achieved over the last several years (e.g., Iga [1992a,b], Coldren, Geels, Corzine and Scott [1992], Iga and Koyama [1993], Huffaker, Deppe, Kumar and Rogers [1994], Morgan [1994], Chang-Hasnain [1994], Morgan, Lehman, Liu, Hibbs-Brenner and Bristow [1997], Coldren, Hegblom, Strzelecka, Ko, Akulova and Thibeault [1997], Morgan [1997], the continuous wave (CW) performance and integration scale of VCSELs are still seriously limited by their thermal behavior. To this day, closely packed VCSEL arrays can be operated only if the array elements are excited sequentially, one at a time. Average heat-flux densities generated inside the active regions of VCSELs are often extremely high (~300 W/mm^2 in 10-μm diameter etched-well VCSELs (Nakwaski and Osiński [1991a]), compared to ~30 W/mm^2 in 15-μm wide stripe-geometry edge-emitting lasers (Nakwaski [1984]), both

evaluated at CW currents 2 times higher than the pulsed threshold). This leads to a substantial increase in temperature, accompanied by a corresponding increase in the threshold current density, a shift in the emission wavelength, and a reduction of the optical output power. Efficient heat dissipation, along with an ultra-low threshold, is therefore critical for large-scale integration into 2D arrays. In addition, since the operating lifetime of semiconductor lasers usually decreases exponentially with temperature, it is essential to design lasers with consistently low self-heating.

In this chapter, we give a comprehensive review of temperature-dependent phenomena in VCSELs, followed by a discussion of various comprehensive approaches used so far to model thermal properties of VCSELs. The chapter is organized as follows. In § 2, the main differences between properties of VCSELs and EELs are highlighted. In § 3, we discuss in more detail the experimental data on various device characteristics affected by temperature. The basics of thermal VCSEL modeling are formulated in § 4. In § 5, we describe comprehensive analytical and numerical thermal models of VCSELs. Such models are especially important if device design needs to be optimized.

§ 2. Comparison of Vertical-Cavity Surface-Emitting and Edge-Emitting Diode Lasers

The main structure difference between edge-emitting diode lasers (EELs) and vertical-cavity surface-emitting diode lasers (VCSELs), reflected in their very names, is illustrated in fig. 1. In EELs, stimulated radiation traveling between resonator mirrors propagates in the plane parallel to the p–n junction, remaining all the time within the active region. In VCSELs, the lasing radiation travels in the direction perpendicular to the p–n junction plane and is amplified inside the active region only during a small fraction of each round trip.

Several important consequences follow from the vertical-cavity configuration. First of all, the coupling between the optical field and the gain medium is much weaker in VCSELs than in EELs, therefore a much higher gain would normally be required in VCSELs to achieve a lasing threshold comparable to that of EELs. The high gain requirement can be mitigated to some extent by reducing the radiation losses, which is accomplished mainly by utilizing VCSEL resonator mirrors of much higher reflectivity (very close to unity) than in standard EELs. This, however, causes an increase in densities of both internal stimulated and spontaneous radiation within the VCSEL resonator and a decrease in the differential quantum efficiency. Consequently, the design of high performance

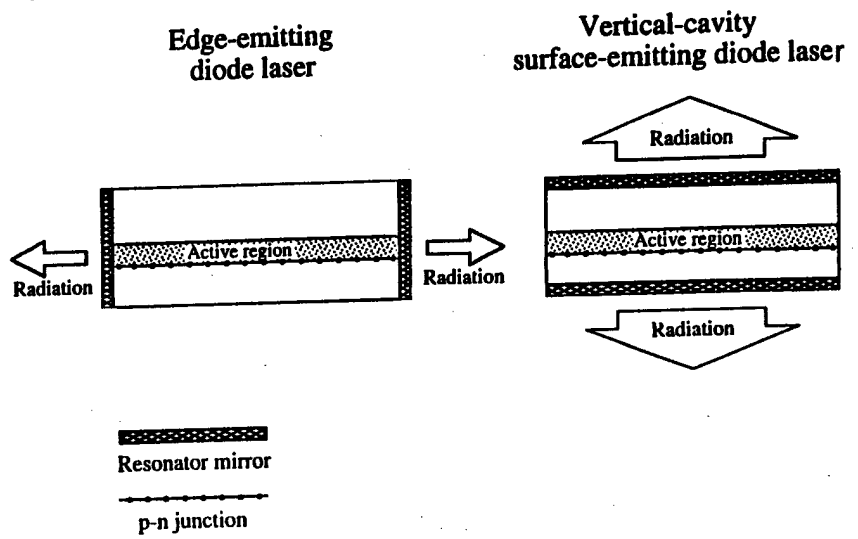


Fig. 1. Schematic configuration of edge-emitting diode lasers (EELs) and vertical-cavity surface-emitting diode lasers (VCSELs).

VCSELs involves a compromise between low-threshold and high-efficiency requirements. Low-threshold VCSELs should have smaller active regions, fewer quantum wells, and mirrors of reflectivities as high as possible, whereas highly efficient VCSELs should have larger emitting areas, more quantum wells, and lower-reflectivity mirrors (cf. Scott, Geels, Corzine and Coldren [1993]).

Another important consequence of vertical-cavity configuration is the very small magnitude of the cavity length L. While in EELs L is typically between 100 μm and 500 μm, the effective length of VCSEL resonators (cf. eq. 7, below) is usually in the range of as little as about 1 μm (Hasnain, Tai, Yang, Wang, Fischer, Wynn, Weir, Dutta and Cho [1991], Taylor and Evaldson [1994]) to several micrometers (Iga, Koyama and Kinoshita [1988]). The *longitudinal-mode spacing* $\Delta\lambda_{FP}$ for the Fabry–Perot (FP) resonator can be approximately written as (Young [1993]):

$$\Delta\lambda_{FP} = \frac{\lambda^2}{2n_G L}, \tag{1}$$

where n_G is the group refractive index (eq. 4) and λ is the radiation wavelength. Taking $\lambda = 0.85$ μm and $n_G = 4.3$ for GaAs (see table 3, p. 183) gives $\Delta\lambda_{FP} = 4.2$ Å for EELs with cavity length $L = 200$ μm, compared to $\Delta\lambda_{FP}$ as large as 840 Å for VCSELs with effective cavity length $L_{eff} = 1$ μm. For that reason, usually several longitudinal modes are close to the gain peak in EELs, resulting in multimode

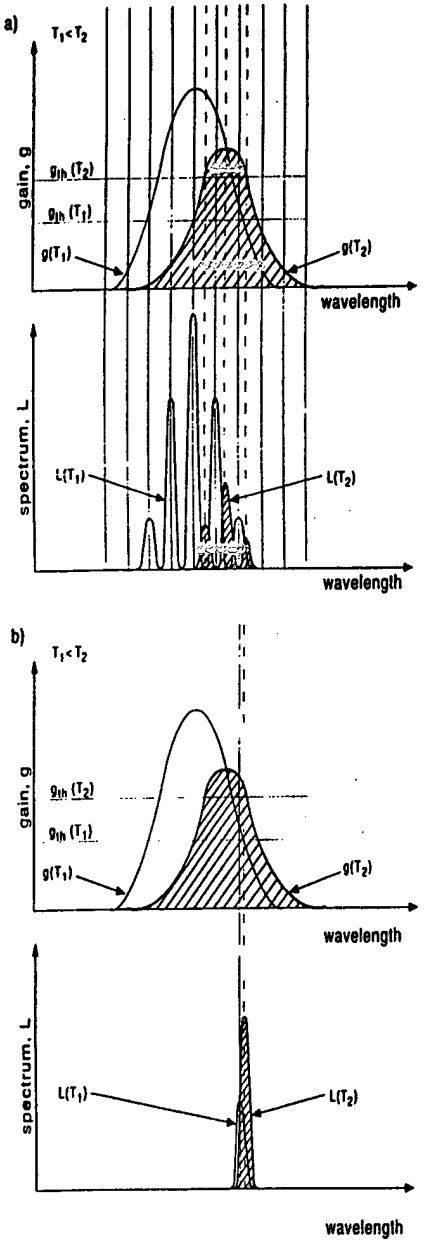


Fig. 2. Illustration of different reactions of output spectra from (a) EELs and (b) VCSELs to an increase in their active-region temperature.

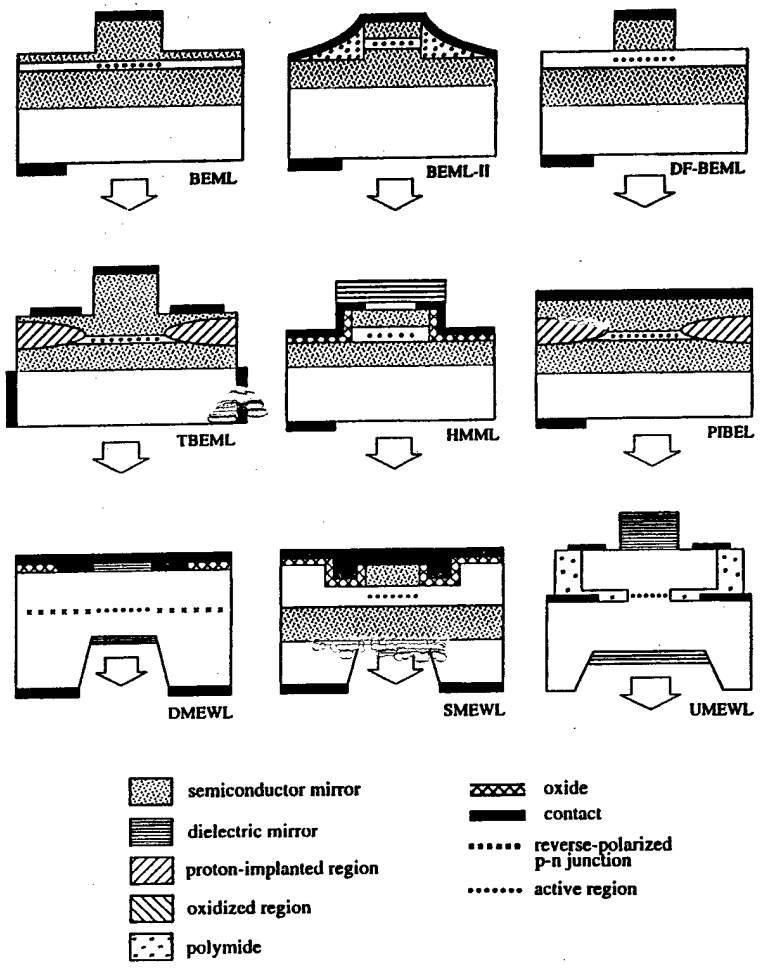


Fig. 3a. Schematic illustration of bottom-emitting VCSELs. See table 1 for abbreviations.

spectral characteristics (see fig. 2a). In contrast, only one (if any) longitudinal mode is within the spectral gain bandwidth in VCSELs (fig. 2b); therefore, they always lase a single longitudinal mode. Inherently, VCSELs operate in a single longitudinal mode even under modulation conditions, which is one of their most important advantages.

Over the last few years, numerous VCSEL structures of different designs were studied. Figure 3 presents schematic structures of some of these devices

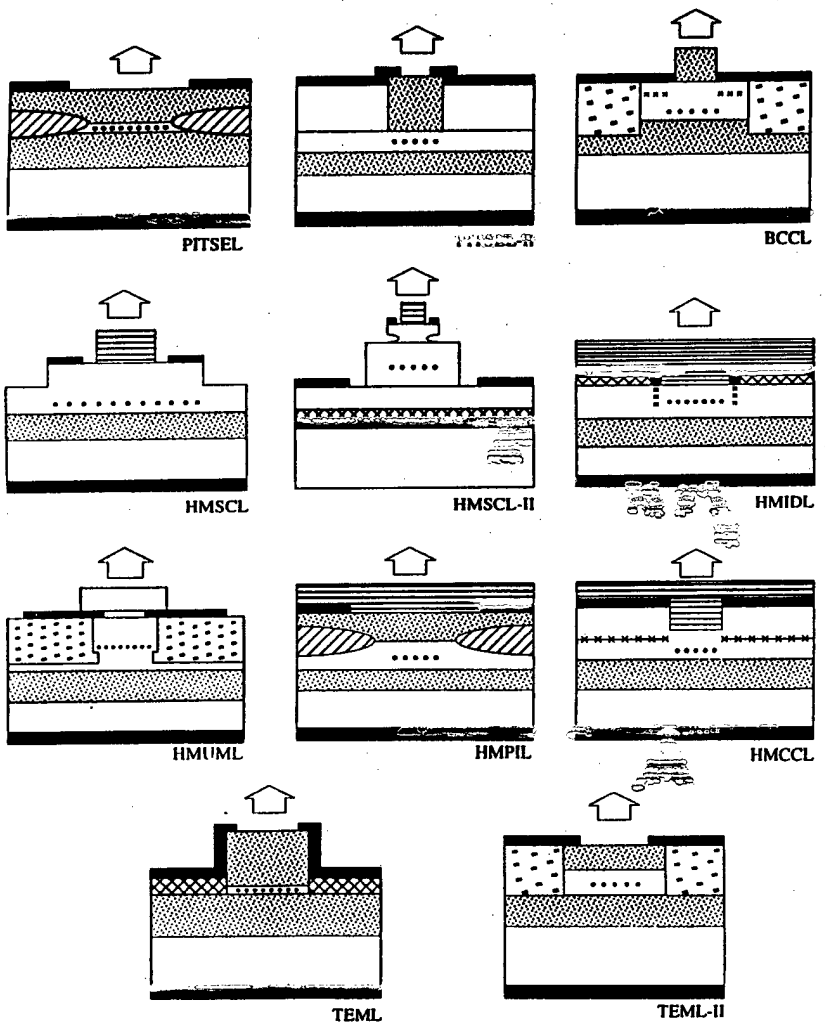


Fig. 3b. Schematic illustration of top-emitting VCSELs.

referred to in this chapter, together with designated abbreviations by which they are identified. Table 1 contains a summary of key features of these devices.

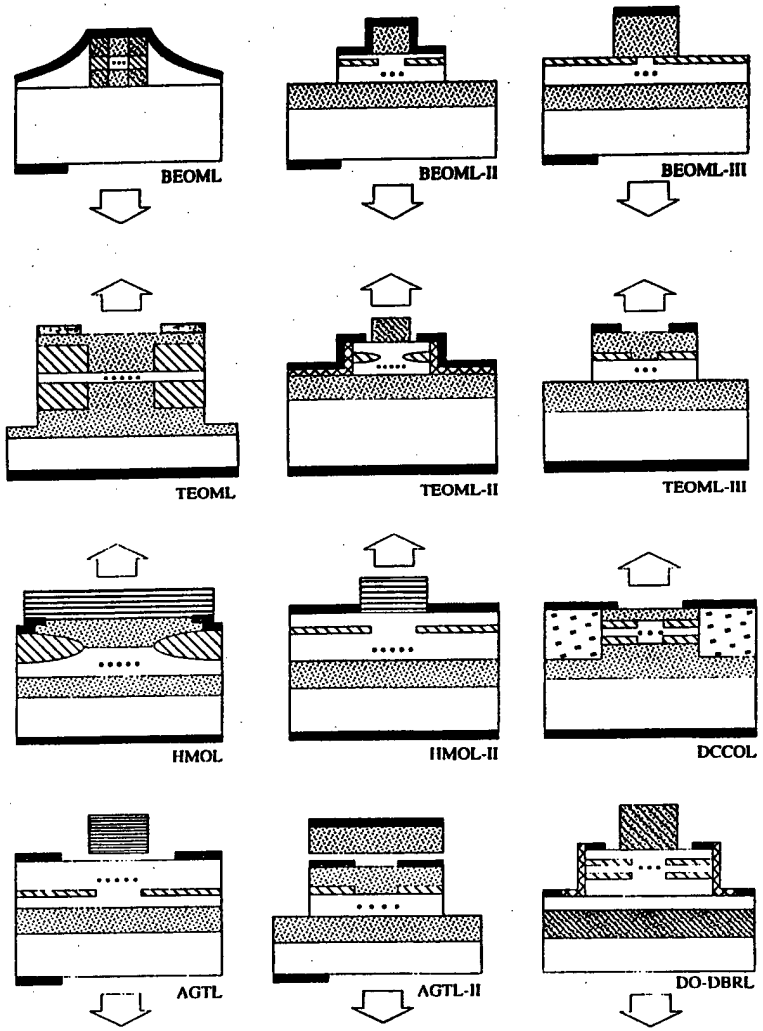


Fig. 3c. Schematic illustration of oxidized VCSELs.

Table 1
Vertical-cavity surface-emitting laser structures

Abbreviation	Active region	Spacer cavity	Bottom reflector	Top reflector	Reference
PITSEL-ATT-A	4×10 nm $GaAs/Al_{0.2}Ga_{0.8}As$ MQW	GRIN $Al_xGa_{1-x}As$ $0.3 \leqslant x \leqslant 0.6$ 2 waves	30.5 periods $AlAs/Al_{0.15}Ga_{0.85}As$ stair-case barriers	20 periods $AlAs/Al_{0.15}Ga_{0.85}As$ stair-case barriers	Hasnain, Tai, Dutta, Wang, Wynn, Weir and Cho [1991]; Hasnain, Tai, Yang, Wang, Fischer, Wynn, Weir, Dutta and Cho [1991]
PITSEL-ATT-B	4×10 nm $GaAs/Al_{0.3}Ga_{0.7}As$ MQW	GRIN $Al_xGa_{1-x}As$ $0.3 \leqslant x \leqslant 0.6$ 2 waves	29.5 periods $AlAs/Al_{0.14}Ga_{0.86}As$ stair-case barriers	20 periods $AlAs/Al_{0.14}Ga_{0.86}As$ stair-case barriers	Tu, Wang, Schubert, Weir, Zydzik and Cho [1991]
PITSEL-UNM	4×8 nm $GaAs/Al_{0.15}Ga_{0.85}As$ MQW	GRIN $Al_xGa_{1-x}As$ $0.15 \leqslant x \leqslant 1.0$ 1 wave	43.5 periods $AlAs/Al_{0.15}Ga_{0.85}As$ graded barriers	24 periods $AlAs/Al_{0.15}Ga_{0.85}As$ graded barriers	Zhou, Cheng, Schaus, Sun, Zheng, Armour, Hains, Hsin, Myers and Vawter [1991]
PITSEL-SNL	3×8 nm $Ga_{0.46}In_{0.54}P/(Al_{0.5}Ga_{0.5})_{0.5}In_{0.5}P$ MQW	$Al_{0.5}In_{0.5}P$ 2×3 waves	55.5 periods $AlAs/Al_{0.5}Ga_{0.5}As$ parabolic-graded barriers	36 periods $AlAs/Al_{0.5}Ga_{0.5}As$ parabolic-graded barriers	Schneider, Choquette, Lott, Lear, Figiel and Malloy [1994]
PITSEL-II-UU	3 InGaAs/GaAs MQW	$Al_{0.3}Ga_{0.7}As$ 1 wave	30.5 periods $Al_{0.7}Ga_{0.3}As/GaAs$	28 periods $Al_{0.7}Ga_{0.3}As/GaAs$ graded and δ-doped barriers	Zeeb, Reiner, Ries, Möller and Ebeling [1995]
HMIDL-SFIT	1 μm GaAs DH	$Al_{0.15}Ga_{0.85}As$ >1 μm	20.5 periods $AlAs/Al_{0.15}Ga_{0.85}As$	7 periods SiO_2/TiO_2	Wüthrich, James, Ganière and Reinhart [1990]

continued on next page

Table 1, *continued*

Abbreviation	Active region	Spacer cavity	Bottom reflector	Top reflector	Reference
HMUML-UCSB	0.3 μm InGaAsP DH ($\lambda_g = 1.3$ μm)	InP/InGaAsP 1.4 μm	27 periods AlAs/GaAs digital alloy grading + λ GaAs	4 periods Si/SiO_2	Dudley, Babic, Mirin, Yang, Miller, Ram, Reynolds, Hu and Bowers [1994]
HMSCL-RIT	9×7 nm InGaAsP/InGaAsP MQW	InP/InGaAsP 5 waves	50 periods InGaAsP/InP	5 periods Si/SiO_2	Streubel, Rapp, André and Wallin [1996]
HMSCL-II-CU	30×6 nm InGaAsP/InGaAs strain-compensated MQW	1.42 μm InP + 0.44 μm InGaAsP	SiO_2/Al	4 periods Si/SiO_2	Chua, Zhu, Lo, Bhat and Hong [1995]
HMPIL-HTC	3×7 nm GaAs MQW	$Al_{0.6}Ga_{0.4}As$ 1 wave	30.5 periods $AlAs/Al_{0.16}Ga_{0.84}As$ graded barriers	8 periods $AlAs/Al_{0.16}Ga_{0.84}As$ graded barriers + 5.5 periods SiO_2/TiO_2	Morgan, Hibbs-Brenner, Lehman, Kalweit, Walterson, Marta and Akinwande [1995]
HMCCL-BTL	1.55 μm InGaAsP ($\lambda_g = 1.4$ μm)	InP 1 wave	45 periods InP/InGaAsP ($\lambda_g = 1.4$ μm)	4 periods Si/Al_2O_3	Fisher, Huang, Dann, Elton, Harlow, Perrin, Reed, Reid and Adams [1995]
BCCL-TUM	3×8 nm $In_{0.18}Ga_{0.82}As/GaAs$ MQW	$In_{0.35}Ga_{0.65}As$ 860 nm	27 periods AlAs/GaAs	18 periods AlAs/GaAs	Rochus, Hauser, Röhr, Kratzer, Boehm, Klein, Traenke and Weimann [1995]

continued on next page

Table 1, *continued*

Abbreviation	Active region	Spacer cavity	Bottom reflector	Top reflector	Reference
TEML-UCB	3×8 nm $In_{0.2}Ga_{0.8}As/GaAs$ MQW	$Al_{0.33}Ga_{0.67}As$ 2×1500 Å	33.5 periods $Al_{0.9}Ga_{0.1}As/GaAs$ superlattice barriers	7 periods $Al_{0.9}Ga_{0.1}As/GaAs$ superlattice barriers + external cavity	Hadley, Wilson, Lau and Smith [1993]
TEML-II-NTT	6 $GaAs/Al_{0.2}Ga_{0.8}As$ MQW	$Al_{0.3}Ga_{0.7}As$ 1 wave	34.5 periods $Al_{0.15}Ga_{0.85}As/AlAs$	20 periods $Al_{0.15}Ga_{0.85}As/Al_{0.5}Ga_{0.5}As/AlAs$	Ohiso, Kohama and Kurokawa [1995]
BEML-UCSB	3×8 nm $In_{0.2}Ga_{0.8}As/GaAs$ MQW	$Al_{0.2}Ga_{0.8}As$ 1 wave	18.5 periods AlAs/GaAs graded barriers + Au contact	16 periods AlAs/GaAs graded barriers	Geels, Thibeault, Corzine, Scott and Coldren [1993]
BEML-II-TIT	3×8 nm $In_{0.2}Ga_{0.8}As/GaAs$ MQW	$Al_{0.4}Ga_{0.6}As$ 1 wave	22 periods AlAs/GaAs graded barriers	25 periods AlAs/GaAs graded barriers + metalization	Mukaihara, Hayashi, Hatori, Ohnoki, Matsutani, Koyama and Iga [1995]
DF-BEML-UCSB	7×7 nm InGaAsP MQW	InGaAsP 5.2 waves	25.5 periods AlAs/GaAs graded barriers	24 periods AlAs/GaAs graded barriers	Babic, Dudley, Streubel, Mirin, Bowers and Hu [1995]; Babic, Streubel, Mirin, Margalit, Bowers and Hu [1995]
TBEML-UU	3×8 nm $In_{0.2}Ga_{0.8}As/GaAs$ MQW	$Al_{0.4}Ga_{0.6}As$ 1 wave	24.5 periods AlAs/GaAs stair-case barriers	20 periods AlAs/GaAs stair-case barriers + metalization	Wipiejewski, Panzlaff, Zeeb and Ebeling [1994]

continued on next page

Table 1, *continued*

Abbreviation	Active region	Spacer cavity	Bottom reflector	Top reflector	Reference
AGTL-SU	2×6 nm $In_{0.21}Ga_{0.79}As/GaAs$ MQW	$AlAs/Al_{0.31}Ga_{0.69}As/GaAs$ 2 waves	22.5 periods GaAs/AlAs	$2\times SiO_x/SiN_x\{\}/SiO_x$ + λ/4 GaAs + metalization + air gap + 7 periods InP/InGaAsP + 5 periods SiO_2/TiO_2	Sugihwo, Larson and Harris [1997]
AGTL-II-UCB	3 GaAs MQW	AlAs 1 wave	24 periods	4.5 periods + air gap + 22.5 periods + Au metalization	Vail, Li, Yuen and Chang-Hasnain [1996]
DMEWL-TIT-A	2 μm InGaAsP DH ($\lambda_g = 1.3$ μm)	InP 5.8 μm	SiO_2/Au/Zn/Au	λ/4-SiO_2/Au	Uchiyama and Iga [1984]
DMEWL-TIT-B	2.5 μm GaAs DH	$Al_{0.3}Ga_{0.7}As$ (2.7 μm) $Al_{0.1}Ga_{0.9}As$ (0.3 μm)	5 periods SiO_2/TiO_2	$Au/SiO_2/TiO_2/SiO_2$	Koyama, Kinoshita and Iga [1989]
DMEWL-OFL	12×4 nm InGaAsP/InGaAsP ($\lambda_g = 1.1$ μm) MQW	InP 5 μm	8.5 periods Si/Al_2O_3 + Au metalization	6 periods Si/SiO_2	Uchiyama and Kashiwa [1995]; Uchiyama, Yokouchi and Ninomiya [1997]
SMEWL-ATT	0.5 μm GaAs DH	$Al_{0.3}Ga_{0.7}As$ 300 nm	5 periods $Al_{0.1}Ga_{0.9}As/Al_{0.7}Ga_{0.3}As$	22 periods $AlAs/Al_{0.1}Ga_{0.9}As$	Tai, Fischer, Seabury, Olsson, Huo, Ota and Cho [1989]

continued on next page

Table 1. *continued*

Abbreviation	Active region	Spacer cavity	Bottom reflector	Top reflector	Reference
UMEWL-UCSB	0.5 μm InGaAsP DH ($\lambda_g = 1.3$ μm)	InP 4 μm	5 periods Si_3N_4/Si	5 periods Si_3N_4/Si	Wada, Babic, Crawford, Reynolds, Dudley, Bowers, Hu, Merz, Miller, Koren and Young [1991]
HMML-NTT	9×1%-compressibly strained InGaAsP/InGaAsP MQW	InGaAsP ($\lambda_g = 1.2$ μm)	25 periods GaAs/AlAs + 10.5 periods InP/InGaAsP	7 periods InP/InGaAsP + 5 periods SiO_2/TiO_2	Ohiso, Amano, Itoh, Tateno, Tadokoro, Takenouchi and Kurokawa [1996]
PIBEL-ATT	3×8 nm $In_{0.2}Ga_{0.8}As/GaAs$ MQW	GaAs 1 wave	20 periods AlAs/GaAs	14 periods AlAs/GaAs	Jewell, Scherer, McCall, Lee, Walker, Harbison and Florez [1989]
BEOML-TIT	3×8 nm $In_{0.2}Ga_{0.8}As/GaAs$ MQW		22.5 periods AlAs/GaAs	20 periods AlAs/GaAs graded barriers + metalization	Hayashi, Mukaihara, Hatori, Ohnoki, Matsutani, Koyama and Iga [1995]
BEOML-II-UCSB	3×8 nm $In_{0.17}Ga_{0.83}As/GaAs$ MQW	$Al_{0.3}Ga_{0.7}As$ 1 wave	18.5 periods AlAs/GaAs digital alloy grading	21 periods $Al_{0.9}Ga_{0.1}As/GaAs$ Au metalization	Thibeault, Bertilsson, Hegblom, Strzelecka, Floyd, Naone and Coldren [1997]
BEOML-III-UCSB	3×8 nm $In_{0.174}Ga_{0.826}As/GaAs$ MQW	$Al_{0.5}Ga_{0.5}As$ 0.24 μm	18.5 periods AlAs/GaAs graded barriers	26 periods $Al_{0.75}Ga_{0.25}As/GaAs$ + 1 period GaAs/AlAs graded and δ-doped barriers	Floyd, Thibeault, Coldren and Merz [1996]

continued on next page

Table 1, *continued*

Abbreviation	Active region	Spacer cavity	Bottom reflector	Top reflector	Reference
TEOML-SNL-A	4×6 nm $In_{0.56}Ga_{0.44}P/(Al_{0.5}Ga_{0.5})_{0.5}In_{0.5}P$ MQW	AlGaInP 1 wave	55.5 periods AlAs/$Al_{0.5}Ga_{0.5}As$ parabolically graded barriers	34 periods AlAs/$Al_{0.5}Ga_{0.5}As$ parabolically graded barriers	Crawford and Schneider [1995]; Choquette, Schneider, Crawford, Geib and Figiel [1995]
TEOML-SNL-B	3×InGaAs MQW	AlGaAs 1 wave	38 periods $Al_{0.96}Ga_{0.04}As/GaAs$ uniparabolically graded barriers	25 periods $Al_{0.96}Ga_{0.04}As/GaAs$ uniparabolically graded barriers	Lear, Schneider, Choquette, Kilcoyne, Figiel and Zolper [1994]; Choquette, Schneider, Lear and Geib [1994]; Lear, Choquette, Schneider and Kilcoyne [1995]
TEOML-II-USC	3×6 nm $In_{0.15}Ga_{0.85}As/GaAs$ MQW	$Al_{0.5}Ga_{0.5}As$ 1 wave	30 periods AlAs/GaAs	4 periods AlAs oxide/GaAs	MacDougal, Dapkus, Pudikov, Zhao and Yang [1995]; Yang, MacDougal and Dapkus [1995]
TEOML-III-KAIST	4×8 nm $Al_{0.11}Ga_{0.89}As/Al_{0.3}Ga_{0.7}As$ MQW	AlGaAs 1 wave	40 periods $Al_{0.3}Ga_{0.7}As/Al_{0.9}Ga_{0.1}As$ linearly graded barriers	26 periods $Al_{0.3}Ga_{0.7}As/Al_{0.9}Ga_{0.1}As$ linearly graded barriers	Shin, Ju, Shin, Ser, Kim, Lee, Kim and Lee [1996]
TEOML-III-UU	3×8 nm $GaAs/Al_{0.2}Ga_{0.8}As$ MQW	$Al_{0.5}Ga_{0.5}As$ 1 wave	30.5 periods AlAs/$Al_{0.2}Ga_{0.8}As$	26 periods $Al_{0.9}Ga_{0.1}As/Al_{0.2}Ga_{0.8}As$ step-graded and δ-doped barriers	Schnitzer, Fiedler, Grabherr, Jung, Reiner, Zick and Ebeling [1996]; Jäger, Grabherr, Jung, Michalzik, Reiner, Weigl and Ebeling [1997]

continued on next page

Table 1. *continued*

Abbreviation	Active region	Spacer cavity	Bottom reflector	Top reflector	Reference
HMOL-UTA	3×6 nm $In_{0.2}Ga_{0.8}As$/GaAs MQW	GaAs 1 wave	26 periods AlAs/GaAs	1 period AlAs/GaAs +4–6 periods $ZnSe/CaF_2$	Huffaker, Deppe and Rogers [1994]; Huffaker, Shin, Deng, Lin, Deppe and Streetman [1994]
HMOL-II-UTA	8 nm $In_{0.2}Ga_{0.8}As$/GaAs SQW	$Al_{0.96}Ga_{0.04}As$ + $Al_{0.75}Ga_{0.25}As$/GaAs superlattice + 1/2 wave GRIN AlGaAs	26 periods AlAs/GaAs	5–7 periods MgF/ZnSe	Huffaker, Graham, Deng and Deppe [1996]
DCCOL-SNL	3×8 nm $In_{0.2}Ga_{0.8}As$ MQW	GRIN AlGaAs 1 wave	38 periods $GaAs/Al_{0.92}Ga_{0.08}As$ uniparabolically graded barriers	18 periods $GaAs/Al_{0.92}Ga_{0.08}As$ uniparabolically graded barriers	Lear, Mar, Choquette, Kilcoyne, Schneider and Geib [1996]; Choquette, Chow, Crawford, Geib and Schneider [1996]
DO-DBRL-USC	2×6.5 nm $In_{0.2}Ga_{0.8}As$ ($\lambda_g = 0.99\,\mu m$) GaAs MQW	AlGaAs–GaAs–InGaAs 1 wave	7 periods AlAs oxide/GaAs	5 periods AlAs oxide/GaAs	MacDougal, Yang, Bond, Lin, Tishinin and Dapkus [1996]

continued on next page

Table 1, notes

Abbreviations

PITSEL, proton-implanted top-surface-emitting laser
HMIDL, hybrid-mirrors in-diffused laser
HMUML, hybrid-mirrors undercut-mesa laser
HMSCL, hybrid-mirrors strain-compensated laser
HMPIL, hybrid-mirrors proton-implanted laser
HMCCL, hybrid-mirrors current-confinement laser
BCCL, buried current-confinement laser
TEML, top-emitting mesa laser
BEML, bottom-emitting mesa laser
DF, double-fused
TBEML, tunable bottom-emitting mesa laser
AGTL, air-gap tunable laser
DMEWL, dielectric-mirrors etched-well laser
SMEWL, semiconducting-mirrors etched-well laser
UMEWL, undercut-mesa etched-well laser
HMML, hybrid-mirrors mesa laser
PIBEL, proton-implanted bottom-emitting laser
BEOML, bottom-emitting oxidized mesa laser
TEOML, top-emitting oxidized mesa laser
HMOL, hybrid-mirrors oxidized laser
DCCOL, double-current-confinement oxidized laser
DO-DBRL, double-oxide DBR laser

ATT, AT&T Bell Laboratories
UNM, University of New Mexico
SNL, Sandia National Laboratories
UU, University of Ulm
CU, Cornell University
SFIT, Swiss Federal Institute of Technology
UCSB, University of California at Santa Barbara
RIT, Royal Institute of Technology
HTC, Honeywell Technology Center
BTL, BT Laboratories
TUM, Technische Universität, München
UCB, University of California at Berkeley
NTT, NTT Opto-electronics Laboratories
TIT, Tokyo Institute of Technology
SU, Stanford University
OFL, Optoelectronics Furukawa Laboratory
USC, University of Southern California
UTA, University of Texas at Austin
KAIST, Korean Advanced Institute of Science and Technology

MQW, multiple quantum well
SQW, single quantum well
DH, double heterostructure
GRIN, graded index
λ_g, bandgap wavelength

§ 3. Effects of Temperature on VCSEL Operation

In this section, temperature-related effects on VCSEL performance are presented, including the temperature dependence of the longitudinal mode spectra, the transverse-mode structure, the threshold current, and the output power.

3.1. TEMPERATURE DEPENDENCE OF THE LONGITUDINAL MODE SPECTRA

In a resonant cavity of length L, filled with a homogeneous material of refractive index n_R, *the wavelength* λ_M *of a longitudinal mode* M is given approximately by (neglecting phase shifts at the cavity boundaries):

$$\lambda_M = \frac{2n_R L}{M}. \tag{2}$$

The rate of longitudinal mode wavelength change with temperature is determined by the temperature sensitivity of the refractive index and by the thermal expansion of the cavity length (Mroziewicz, Bugajski and Nakwaski [1991], p. 151):

$$\frac{d\lambda_M}{dT} = \frac{\lambda_M}{n_G}\left[\left(\frac{\partial n_R}{\partial T}\right)\Big|_\lambda + n_R \alpha_T\right], \tag{3}$$

where α_T is the linear thermal expansion coefficient, and n_G is the group index,

$$n_G = n_R - \lambda_M \left(\frac{\partial n_R}{\partial \lambda}\right)\Big|_T. \tag{4}$$

The partial derivatives $(\partial n_R/\partial T)|_\lambda$ and $(\partial n_R/\partial \lambda)|_T$ in eqs. (3) and (4) are to be evaluated at constant wavelength and temperature, respectively. The refractive index in semiconducting materials changes approximately linearly with temperature. Near the lasing wavelength of 0.85 μm, a value of $(\partial n_R/\partial T)|_\lambda = 4 \times 10^{-4}\,K^{-1}$ can be extracted from the data of Marple [1964] for GaAs, and $1 \times 10^{-4}\,K^{-1}$ can be extracted from the data of Grimmeiss and Monemar [1971] for AlAs. For InP, a similar value of $3 \times 10^{-4}\,K^{-1}$ near the bandgap can be obtained from the data of Pettit and Turner [1965]. The latter value has been also assumed by Bissessur, Ettinger, Fernandez and Davies [1993] for the quaternary InGaAsP materials. These values are about an order of magnitude higher than the product of the group index and the linear expansion coefficient, listed in tables 2 and 3. Hence, the longitudinal mode wavelength shift is determined primarily by the temperature dependence of the refractive index.

Table 2
Thermal expansion coefficient α_T near 300 K

Material	α_T [10^{-6}/°C]	Reference(s)
GaAs	6.4–6.9	Swaminathan and Macrander [1991]; Adachi [1985]
AlAs	4.9–5.2	Swaminathan and Macrander [1991]; Adachi [1985]
$Al_xGa_{1-x}As$	$6.4 - 1.2x$	Adachi [1985]
InP	4.56	Adachi [1992]
$In_{1-x}Ga_xAs_yP_{1-y}$ [a]	$4.56 + 1.18y$	Adachi [1992]

[a] Lattice-matched to InP, with $x = 0.4527y/(1-0.0311y)$.

Table 3
Group index n_G near 300 K

Material	Wavelength	n_G	Reference
GaAs	0.85 μm	4.3	Buus [1983]
$Al_{0.2}Ga_{0.8}As$	0.85 μm	4.2	Determined from data given by Casey and Panish [1978]
$In_{0.73}Ga_{0.27}As_{0.6}P_{0.4}$ [a]	1.30 μm	4.3	Buus and Adams [1979]
$In_{0.6}Ga_{0.4}As_{0.85}P_{0.15}$ [b]	1.55 μm	4.6	Buus and Adams [1979]

[a] Bandgap wavelength $\lambda_g = 1.3$ μm. [b] Bandgap wavelength $\lambda_g = 1.55$ μm.

The diode laser cavity is not homogeneous; hence, except for devices where the optical field is very well confined within the active region, eqs. (2) and (3) only approximately describe the actual situation. For EELs, the refractive index n_R should be replaced with the effective index n_{eff}, which averages the refractive indices of the active region and the claddings with proper weights determined by field penetration into the claddings (Thompson [1980], p. 118).

Rather than employing discrete mirrors, most VCSEL designs incorporate distributed Bragg reflectors (DBRs). For a DBR consisting of alternating quarter-wave layers of thicknesses and refractive indices d_L, n_L, and d_H, n_H, respectively, *the center wavelength of its reflectivity spectrum* is determined by the optical thickness of the DBR period:

$$\lambda_{DBR} = 2(n_L d_L + n_H d_H). \tag{5}$$

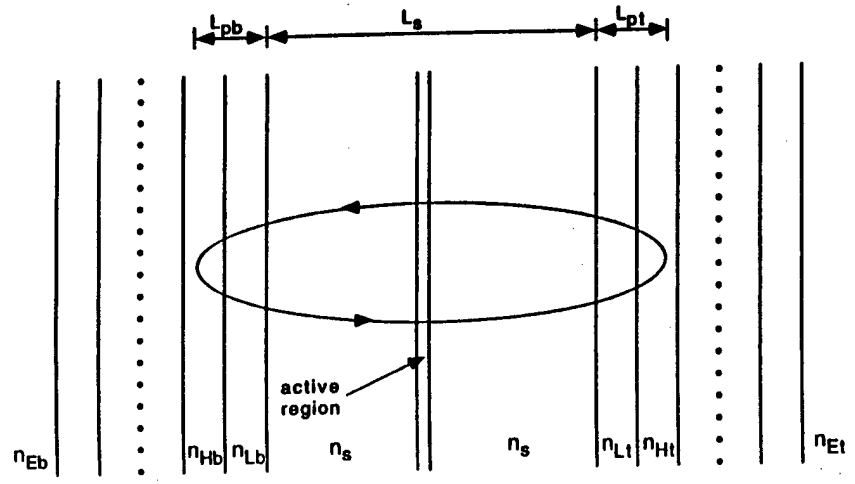


Fig. 4. Schematic structure of a typical VCSEL cavity, showing the refractive indices of the bottom exit medium (n_{Eb}), high- and low-index layers of the bottom DBR (n_{Hb}, n_{Lb}), spacer medium (n_s), low- and high-index layers of the top DBR (n_{Ht}, n_{Lt}), and the top exit medium (n_{Et}), as well as bottom and top phase penetration depths (L_{pb}, L_{pt}) and the spacer thickness L_s.

The temperature variation of the Bragg wavelength, λ_{DBR}, is then described by a formula analogous to eq. (3) (Dudley, Crawford and Bowers [1992]):

$$\frac{d\lambda_{DBR}}{dT} = \frac{n_L d_L \alpha_{T,L} + n_H d_H \alpha_{T,H} + d_L \left(\frac{\partial n_L}{\partial T}\right)\Big|_\lambda + d_H \left(\frac{\partial n_H}{\partial T}\right)\Big|_\lambda}{\frac{1}{2} - d_L \left(\frac{\partial n_L}{\partial \lambda}\right)\Big|_T - d_H \left(\frac{\partial n_H}{\partial \lambda}\right)\Big|_T}, \tag{6}$$

where $\alpha_{T,L}$ and $\alpha_{T,H}$ are thermal expansion coefficients of the low- and high-index material, respectively. Again, the terms containing $\alpha_{T,L}$ and $\alpha_{T,H}$ are much smaller than those containing the variation of the refractive index with temperature, and the dispersion terms are much smaller than $\frac{1}{2}$. Experimentally, $d\lambda_{DBR}/dT$ was determined to be 0.87 Å/°C for a GaAs/AlAs mirror centered at 0.98 μm, and 1.1 Å/°C for an InP/InGaAsP (bandgap wavelength $\lambda_g = 1.15$ μm) mirror centered at 1.32 μm (Dudley, Crawford and Bowers [1992]).

A typical VCSEL cavity, shown schematically in fig. 4, consists of two DBRs separated by a spacer region which incorporates the active region. The spacer thickness L_s (including the optically equivalent active-region thickness) and the phase penetration depths of the top and bottom DBRs L_{pt}, L_{pb}, respectively, combine into an *effective VCSEL cavity length* L_{eff}:

$$L_{eff} = L_s + L_{pt} + L_{pb}, \tag{7}$$

where (Babic and Corzine [1992])

$$L_{p\alpha} = \frac{\lambda_{DBR,\alpha}}{4n_s}\left[\frac{q_\alpha}{1-p_\alpha}\frac{(1-s_\alpha^2 p_\alpha^{N_\alpha-1})(1-p_\alpha^{N_\alpha})}{1-q_\alpha^2 s_\alpha^2 p_\alpha^{2N_\alpha-2}}\right] \qquad \alpha = \text{t, b}, \tag{8}$$

with

$$q_\alpha = \frac{n_{IL\alpha}}{n_{IH\alpha}}, \tag{9}$$

$$p_\alpha = \frac{n_{L\alpha}}{n_{H\alpha}}, \tag{10}$$

$$s_\alpha = \frac{n_{EL\alpha}}{n_{EH\alpha}}. \tag{11}$$

Here, $\lambda_{DBR,\alpha}$ (α = t, b) is the center wavelength of the top (t) or bottom (b) DBR, N_α is the total number of quarter-wave layers, n_s is the refractive index of the spacer region (assumed to be homogeneous), and q_α, p_α, and s_α are, respectively, the ratios of the lower to higher refractive indices at the interfaces of the incident (I) medium and the DBR, the Bragg mirror layers, and the DBR/exit (E) medium. For a top-emitting VCSEL, the exit medium for the top reflector is normally the air, and for the bottom reflector it is the substrate. For a bottom-emitting VCSEL, the top exit medium is usually the metallic contact, and the bottom exit medium is the air.

The longitudinal modes in a VCSEL cavity can be found by considering the round-trip phase condition that takes into account propagation in the cavity of the effective length L_{eff} given by eqs. (7)–(11) and the detuning between the mode wavelength, λ_M, and the center wavelengths of the two DBRs, $\lambda_{DBR,t}$ and $\lambda_{DBR,b}$. Assuming a homogeneous spacer medium, we obtain the following *longitudinal mode resonant condition*:

$$\lambda_M = \frac{2n_s L_{eff}}{M + 2n_s\left[\left(\frac{L_{pt}}{\lambda_{DBR,t}}\right) + \left(\frac{L_{pb}}{\lambda_{DBR,b}}\right)\right]}. \tag{12}$$

In an ideal VCSEL cavity with a thin (quantum well) active layer and two Bragg mirrors of identical center wavelength, λ_{DBR}, the thickness of the spacer region should be chosen such as to select $\lambda_M = \lambda_{DBR}$. In this case, eq. (12) simplifies to an expression fully analogous to eq. (2):

$$\lambda_M = \frac{2n_s L_s}{M}. \tag{13}$$

Note that because of the $\lambda_M = \lambda_{DBR}$ condition, only one longitudinal mode can be supported by an ideal VCSEL cavity. In addition, the effective cavity length,

L_{eff}, no longer appears in the resonance condition (13). We see that the optical thickness of the spacer must be an integer multiple of the half-wave $\lambda_{DBR}/2$. In VCSELs with quantum-well active regions, the additional requirement for the maximum of the standing wave intensity pattern to occur at the center of the spacer limits M to even numbers; i.e., $n_s L_s$ must be equal to an integer multiple of λ_{DBR}. The control of the spacer thickness is less critical in VCSELs with bulk active regions (over 400 Å thick), since the standing-wave intensity maximum will always be located somewhere within the active layer.

The mode wavelength shift with temperature in an ideal VCSEL cavity is still given by eq. (3) with the spacer index n_s, provided that the spacer material satisfies the following *thermal dispersion matching condition*:

$$\frac{(\partial n_s/\partial T)|_\lambda}{n_s} = d_L \frac{(\partial n_L/\partial T)|_\lambda + d_H\,(\partial n_H/\partial T)|_\lambda}{n_L d_L + n_H d_H} \tag{14}$$

Equation (14) was derived by neglecting the thermal expansion and wavelength dispersion terms in eqs. (3) and (6).

Measurements of the temperature variation of the lasing wavelength in GaAs/AlGaAs-based VCSELs give the *mode shifts* near room temperature in the range of 0.56–0.90 Å/°C (e.g., Van der Ziel, Deppe, Chand, Zydzik and Chu [1990], Hasnain, Tai, Yang, Wang, Fischer, Wynn, Weir, Dutta and Cho [1991], Tell, Leibenguth, Brown-Goebeler and Livescu [1992], Wipiejewski, Panzlaff, Zeeb and Ebeling [1993], Catchmark, Morgan, Kojima, Leibenguth, Asom, Guth, Focht, Luther, Przybylek, Mullay and Christodoulides [1993], Geels, Thibeault, Corzine, Scott and Coldren [1993], Norris, Chen and Tien [1994]) for both pulsed and CW operation. Most of the reported values are very close to the measured center wavelength shift of 0.87 Å/°C in the GaAs/AlAs DBR mirrors (Dudley, Crawford and Bowers [1992]), indicating that condition (14) seems to be satisfied in GaAs/AlGaAs devices. They are also comparable to mode shift rates in GaAs/AlGaAs Fabry–Pérot EELs, which are typically about 0.50 Å/°C (Mroziewicz, Bugajski and Nakwaski [1991], p. 151). Because of the higher thermal resistance of VCSELs (see table 4), the VCSEL active region heats up with the ambient temperature at a faster rate than in edge emitting lasers. Hence, the observed wavelength shift should be somewhat larger than in edge-emitters. This is indeed the case, which confirms that eq. (3) describes well the mode wavelength shift in VCSELs.

Figure 5 illustrates the lasing wavelength shift with temperature under both pulsed and CW conditions for two PITSELs with the active-region diameter of 16 μm and with different room-temperature values of λ_M. It is clear that under pulsed conditions, $\lambda_M(T)$ dependence can remain linear over a wide temperature

Table 4
Thermal resistance R_{TH}

R_{TH} (K/W)	Size (μm)	Structure[a]	Reference
300[b]	6×6	HMIDL-SFIT	Wüthrich, James, Ganière and Reinhart [1990]
1788	15Ø	PITSEL-ATT-A	Hasnain, Tai, Yang, Wang, Fischer, Wynn, Weir, Dutta and Cho [1991]
1250	10×10	deep-etched BEML-UCSB	Coldren, Geels, Corzine and Scott [1992]
1000	10×10	shallow-etched BEML-UCSB	Geels, Thibeault, Corzine, Scott and Coldren [1993]
800	15Ø	PITSEL-ATT-A	Wu, Tai and Huang [1993]
920	16Ø	PITSEL-UNM	Lu, Zhou, Cheng and Malloy [1994]
2100	16Ø	PITSEL-UNM	Lu, Zhou, Cheng, Malloy and Zolper [1994]
3000[b]	11Ø	wafer-fused HMUML-UCSB	Dudley, Babic, Mirin, Yang, Miller, Ram, Reynolds, Hu and Bowers [1994]
233–345[c]	60Ø	TEML-UCB	Norris, Chen and Tien [1994]
274–384[c]	60Ø	TEML-UCB	Chen, Hadley and Smith [1994]
2500	7×7	TEOML-SNL	Choquette, Schneider, Lear and Geib [1994]
613	21Ø	Au-plated BEML-UCSB	Wipiejewski, Young, Peters, Thibeault and Coldren [1995]
4221	4.5Ø	Au-plated BEML-UCSB	Wipiejewski, Young, Peters, Thibeault and Coldren [1995]
800	20Ø	BEML-II-TIT	Mukaihara, Hayashi, Hatori, Ohnoki, Matsutani, Koyama and Iga [1995]
1300	10Ø	BEML-II-TIT	Mukaihara, Hayashi, Hatori, Ohnoki, Matsutani, Koyama and Iga [1995]
3000	6Ø	BEML-II-TIT	Mukaihara, Hayashi, Hatori, Ohnoki, Matsutani, Koyama and Iga [1995]
800	20Ø	PITSEL-ATT-A	Morgan, Hibbs-Brenner, Marta, Walterson, Bounnak, Kalweit and Lehman [1995]
1210	16Ø	TEML-II-NTT	Ohiso, Tateno, Kohama, Wakatsuki, Tsunetsugu and Kurokawa [1996]
660	26Ø	TEML-II-NTT	Ohiso, Tateno, Kohama, Wakatsuki, Tsunetsugu and Kurokawa [1996]
2550	2×2	HMOL-UTA with SQW	Huffaker and Deppe [1996]
2280	3.5×3.5	HMOL-UTA with SQW	Huffaker and Deppe [1996]

continued on next page

Table 4, *continued*

R_{TH} (K/W)	Size (μm)	Structure[a]	Reference
1615	5.4 Ø	BEOML-II-UCSB with SQW	Akulova, Thibeault, Ko and Coldren [1997]

[a] For an explanation of the abbreviations see table 1.
[b] Pulsed operation.
[c] For current range from $I_{th,cw}$ to $3I_{th,cw}$, where $I_{th,cw}$ is the threshold current for CW operation.

range, although different regimes characterized by different values of $d\lambda_M/dT$ may exist. For example, the slope of $\lambda_M(T)$ changes at 300 K for the "865 nm mode" device. Under the CW conditions, $\lambda_M(T)$ deviates significantly from a linear behavior, mostly because of varying degree of heating occurring at the CW threshold current, at which the data were taken (cf. § 3.2).

Knowledge of the wavelength shift rate with temperature can be used

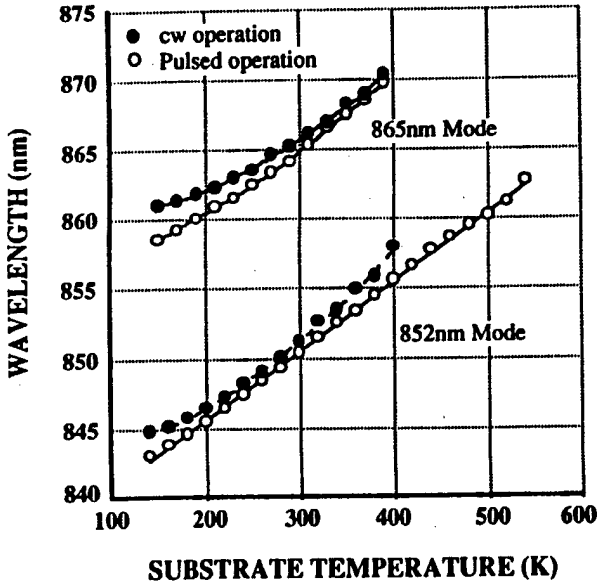


Fig. 5. Wavelength shift with temperature for two 16 μm PITSELs with different lasing mode positions relative to a common gain peak (847 nm at 300 K), measured under pulsed (100 ns, 0.1% duty cycle) and CW conditions (after Lu, Zhou, Cheng, Malloy and Zolper [1994]). The devices were placed on a temperature-controlled stage and the substrate temperature is assumed to be equal to the stage temperature.

conveniently to estimate the average active-region temperature, necessary to evaluate the thermal resistance of the device (defined by eq. 49, below). This approach has been employed widely, giving the estimates of thermal resistance in various VCSELs between 233 and 4221 K/W (see table 4). These values are much higher than typical thermal resistances of EELs, ranging between 20 and 50 K/W (e.g., Joyce and Dixon [1975], Manning [1981], Hughes, Gilbert and Hawrylo [1985]).

3.2. TEMPERATURE DEPENDENCE OF THE THRESHOLD CURRENT

The lasing threshold in all diode lasers is determined by the balance between optical gain and losses. With increasing temperature, two main effects take place: the energy gap in III–V semiconductors shrinks (see table 5), and the carrier density distribution within each band broadens, with its peak shifting further into the band. The bandgap shrinkage is dominant, and the net result of these two opposing effects is that the gain-peak shifts towards the longer wavelengths. In addition, the gain peak is lowered at a given carrier concentration. Thus, even if the optical losses were to remain unchanged, the threshold current would have increased with temperature, since higher current density is required to maintain the same gain level. In addition, optical losses do increase with temperature, since the higher density of carriers necessary to maintain the required gain level results in increased free-carrier absorption in the active region. Somewhat less important, at least at room temperature and above, is an increase in free-carrier absorption that can occur in passive layers, caused by temperature-dependent impurity ionization.

These considerations assume implicitly that all current flowing through the diode laser results in radiative transitions. However, only a fraction of electron–hole pairs recombines radiatively. Nonradiative processes can also be temperature dependent, either directly, or indirectly via increased carrier density necessary to balance the optical loss. An example of such a process is Auger recombination that increases rapidly with carrier density. Another mechanism of carrier loss is leakage along a shunt path away from the active region or straight over the quantum-well active region. The current density associated with the latter process can be described using a simple expression, analogous to the standard current–voltage equation for a p–n junction (Scott, Corzine, Young and Coldren [1993]):

$$j_{leak} = j_0 \exp\left[-\frac{E_{gB} - \Delta F_{cv}}{k_B T_A}\right], \tag{15}$$

Table 5
Temperature dependence of bandgap E_g and peak gain g_{max}

Material	$-\partial E_g/\partial T$ [10^{-4} eV/°C]	$-(\partial g_{max}/\partial T)_N$ (cm^{-1}/°C)
GaAs[a]	3.9–4.6[e,f,g]	1.4[k]
AlAs	5.1–5.2[e,f]	
$Al_xGa_{1-x}As$	$3.95 + 1.15x$[f]	
InP	3.3–4.0[h,i]	
$In_{0.73}Ga_{0.27}As_{0.6}P_{0.4}$[b]	3.25–3.82[i,j]	1.48[l]
$In_{0.6}Ga_{0.4}As_{0.85}P_{0.15}$[c]	3.75[i]	1.22[l]
$In_{1-x}Ga_xAs_yP_{1-y}$[d]	$4.0-0.3y$[i]	

[a] The values of $\partial E_g/\partial T$ are not independent of temperature. Using the results of Thurmond [1975] for GaAs, we obtain $\partial E_g/\partial T = -5.405\times10^{-4}\,T(T+408)/(T+204)^2$ eV/°C.
[b] Bandgap wavelength $\lambda_g = 1.3$ μm.
[c] Bandgap wavelength $\lambda_g = 1.55$ μm.
[d] Lattice-matched to InP, with $x = 0.4527/(1-0.0311y)$.
[e] Swaminathan and Macrander [1991], p. 16.
[f] Adachi [1985].
[g] Yan and Coldren [1990].
[h] Lautenschlager, Garriga and Cardona [1987].
[i] Adachi [1992].
[j] Dutta and Nelson [1982].
[k] Extracted from theoretical curves reported by Stern [1973].
[l] Extracted from theoretical curves reported by Dutta and Nelson [1982].

where E_{gB} is the local bandgap energy in the cladding (barrier) region (dependent on temperature), ΔF_{cv} is the local separation of quasi-Fermi levels in the active region (dependent on both carrier concentration and temperature), k_B is the Boltzmann constant, and T_A is the local active-region temperature. For index-guided bottom-emitting mesa lasers, deeply etched just through the active region, the parameter j_0 was fitted to 8×10^3 kA/cm^2 (Scott, Corzine, Young and Coldren [1993]).

Another implicit assumption is that the laser operates at the gain-peak wavelength, and that the lasing wavelength follows the gain-peak shifts with temperature. This is true only when the spacing between the longitudinal modes in the lasing cavity is small, as in conventional Fabry–Pérot lasers. If the spacing is large or if some additional frequency-selective elements are used, the gain-peak wavelength will not coincide with the lasing wavelength. This situation occurs in distributed-feedback (DFB) and distributed-Bragg-reflector (DBR) EELs, and is characteristic of all VCSELs. Depending then on the sign of the

initial detuning from the gain peak at room temperature, the lasing wavelength can approach the gain peak or depart from it. In the former case, which takes place when the room-temperature lasing wavelength is offset from the gain peak towards the longer wavelengths, the increase in threshold current described in the first paragraph is partially compensated by the simultaneous shift of the lasing wavelength towards the gain peak. Conversely, if the room-temperature lasing wavelength is on the short-wavelength side of the gain peak, temperature variation of the threshold current will be accelerated.

According to Chow, Corzine, Young and Coldren [1995], many-body Coulomb interactions between carriers are not canceled completely by plasma screening. This leads to a decrease in the wavelength dependence of the threshold carrier concentration and consequently, a greater tolerance to the changes in the resonance/gain overlap with temperature on the low-temperature side of the threshold minimum.

It is clear that the complex interplay between all these mechanisms can result in a variety of different patterns of threshold current evolution with temperature. Yet, it is a common practice to describe the temperature dependence of the threshold current using the *Arrhenius-type relation,*

$$I_{th}(T) = I_{th}(300\,\mathrm{K})\exp\left(\frac{T-300\,\mathrm{K}}{T_0}\right), \tag{16}$$

with T in Kelvin and the *characteristic temperature* T_0 used as a measure of temperature sensitivity of the threshold current. With T_0 constant, eq. (16) usually approximates the actual threshold variation within a certain temperature interval. More generally, T_0 is itself a function of temperature, and for an arbitrary $I_{th}(T)$ dependence it can be defined simply as

$$T_0(T) = \frac{\mathrm{d}\left\{\ln\left[\dfrac{I_{th}(T)}{I_{th}(300\,\mathrm{K})}\right]\right\}}{\mathrm{d}T}. \tag{17}$$

In spite of its limited applicability to VCSELs, eq. (16) is the only analytical form in which the temperature dependence of the VCSEL threshold current was reported. Not surprisingly, measured values of T_0 for VCSELs are scattered widely and sensitive to device structure (see tables 6a,b). They range from very high (practically infinite) values in devices where the threshold current remains practically constant within a certain temperature range (cf. Geels, Thibeault, Corzine, Scott and Coldren [1993]), through moderate values of 130–150 K, (see, e.g., Uchiyama, Ohmae, Shimizu and Iga [1986] and Iga, Koyama and

Table 6a
Characteristic temperature T_0 for pulsed operation

T_0 (K)	Range (K)	Size (μm)	Structure	Reference
200	100–220	20–30 Ø	DMEWL-TIT-A	Uchiyama, Ohmae, Shimizu and Iga [1986]
70	220–263	20–30 Ø	DMEWL-TIT-A	Uchiyama, Ohmae, Shimizu and Iga [1986]
210	283–363	15 Ø	PITSEL-ATT-A	Hasnain, Tai, Yang, Wang, Fischer, Wynn, Weir, Dutta and Cho [1991]
47.5	223–253	8×8	UMEWL-UCSB	Wada, Babic, Crawford, Reynolds, Dudley, Bowers, Hu, Merz, Miller, Koren and Young [1991]
26.8	253–339	8×8	UMEWL-UCSB	Wada, Babic, Crawford, Reynolds, Dudley, Bowers, Hu, Merz, Miller, Koren and Young [1991]
24	203–253	20×20	wafer-fused HMUML-UCSB	Wada, Babic, Ishikawa and Bowers [1992]
47	203–298	8×8	wafer-fused HMUML-UCSB	Wada, Babic, Ishikawa and Bowers [1992]
67	200–300	11 Ø	wafer-fused HMUML-UCSB	Dudley, Babic, Mirin, Yang, Miller, Ram, Reynolds, Hu and Bowers [1994]

Kinoshita [1988]), to negative values in devices that are detuned towards the longer wavelengths (cf. fig. 8).

Thus, in stark contrast to Fabry–Perot-type EELs, the T_0 parameter in VCSELs becomes more of a design parameter (Tell, Brown-Goebeler, Leibenguth, Baez and Lee [1992]), than a material- or structure-related characteristic. Since the arbitrary temperature sensitivity of a VCSEL threshold current can be obtained in principle, this opens up a possibility of designing *temperature-insensitive VCSELs*, with infinitely large T_0. Some interesting examples of such constructions were demonstrated not only for ambient room temperatures (Young, Scott, F.H. Peters, Thibeault, Corzine, M.G. Peters, Lee and Coldren [1993], Kajita, Kawakami, Nido, Kimura, Yoshikawa, Kurihara, Sugimoto and Kasahara [1995]), but also for cryogenic conditions (Lu, Luo, Hains, Cheng, Schneider, Choquette, Lear, Kilcoyne and Zolper [1995], Ortiz, Hains, Lu, Sun, Cheng and Zolper [1996], Goncher, Lu, Luo, Cheng, Hersee, Sun, Schneider and Zolper [1996]), and elevated temperatures (Dudley, Ishikawa, Babic, Miller, Mirin, Jiang, Bowers and Hu [1993], Catchmark, Morgan, Kojima, Leibenguth,

Table 6b
Characteristic temperature T_0 for CW operation

T_0 (K)	Range (K)	Size (μm)	Structure	Reference
115	288–323	15 Ø	SMEWL-ATT	Tai, Fischer, Seabury, Olsson, Huo, Ota and Cho [1989]
120	250–300	10 Ø	DMEWL-TIT-B	Extracted from data reported by Koyama, Kinoshita and Iga [1989]
210	293–363	15 Ø	PITSEL-ATT-A	Hasnain, Tai, Dutta, Wang, Wynn, Weir and Cho [1991]
130	283–323	15 Ø	PITSEL-ATT-A	Hasnain, Tai, Yang, Wang, Fischer, Wynn, Weir, Dutta and Cho [1991]
330	273–298	10 Ø	PITSEL-ATT-B	Tu, Wang, Schubert, Weir, Zydzik and Cho [1991]
80	328–348	10 Ø	PITSEL-ATT-B	Tu, Wang, Schubert, Weir, Zydzik and Cho [1991]
40	283–353	20×20	PIBEL-ATT	Von Lehmen, Banwell, Carrion, Stoffel, Florez and Harbison [1992]
60[a]	328–393	10×10	shallow-etched BEML-UCSB	Geels, Thibeault, Corzine, Scott and Coldren [1993]
156	293–318	10 Ø	PITSEL-SNL	Schneider, Choquette, Lott, Lear, Figiel and Malloy [1994]

[a] Determined using the active-region temperature.

Asom, Guth, Focht, Luther, Przybylek, Mullay and Christodoulides [1993], Shoji, Otsubo, Matsuda and Ishikawa [1994], Lu, Zhou, Cheng, Malloy and Zolper [1994], Morgan, Hibbs-Brenner, Marta, Walterson, Bounnak, Kalweit and Lehman [1995], Ohiso, Tateno, Kohama, Wakatsuki, Tsunetsugu and Kurokawa [1996]).

It should be emphasized that the temperature T usually used in eq. (17) in experimental determination of T_0, is the ambient (stage or heat sink) temperature (cf. § 4.2). Under low-duty-cycle pulsed conditions, it coincides with the active-region temperature. The pulsed and CW values of T_0 should be very similar if the active-region temperature is used instead of the ambient temperature, except for weakly guiding or weakly antiguiding VCSEL structures (cf. § 3.3) in which lateral nonuniformity of CW temperature profiles plays an important role.

It should be noted that the temperature sensitivity of the threshold current depends on the size of the active region. Larger devices usually exhibit lower values of the characteristic temperature T_0, which results from poorer overlap

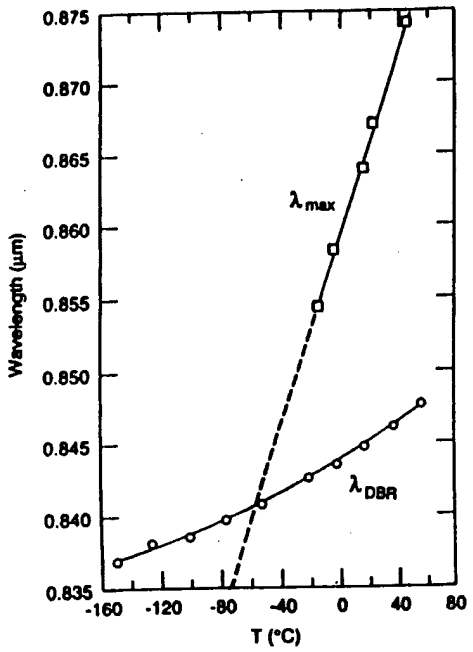


Fig. 6. Temperature effects on the gain-peak wavelength λ_{max} and the vertical-cavity mode wavelength λ_{DBR} in a PITSEL. The $\lambda_{max} = \lambda_{DBR}$ point corresponds to the minimum threshold current. T_0 is negative in the region when λ_{DBR} is offset towards longer wavelengths relative to λ_{max}. After Tell, Brown-Goebeler, Leibenguth, Baez and Lee [1992].

between the gain and photon density profiles (Wada, Babic, Ishikawa and Bowers [1992]) as well as from worsening thermal properties, with increasingly one-dimensional heat flow.

The shift of the gain spectrum in VCSEL structures can be determined experimentally by fabricating Fabry–Pérot EELs from VCSEL wafers and measuring the lasing wavelength shift with temperature. Typical measured values of $d\lambda_{max}/dT$ for GaAs/AlGaAs VCSELs are (3.2–3.4) Å/°C (e.g., Geels, Thibeault, Corzine, Scott and Coldren [1993], Tell, Brown-Goebeler, Leibenguth, Baez and Lee [1992], Scott, Corzine, Young and Coldren [1993]), which is greater than the analogous value of ~2.5 Å/°C in conventional EELs. The accelerated shift of gain-peak wavelength is probably caused by heating associated with higher series resistance of multilayer EELs incorporating horizontal Bragg reflectors and by reabsorption of amplified spontaneous emission in the vertical direction, enhanced by high-reflectivity horizontal Bragg

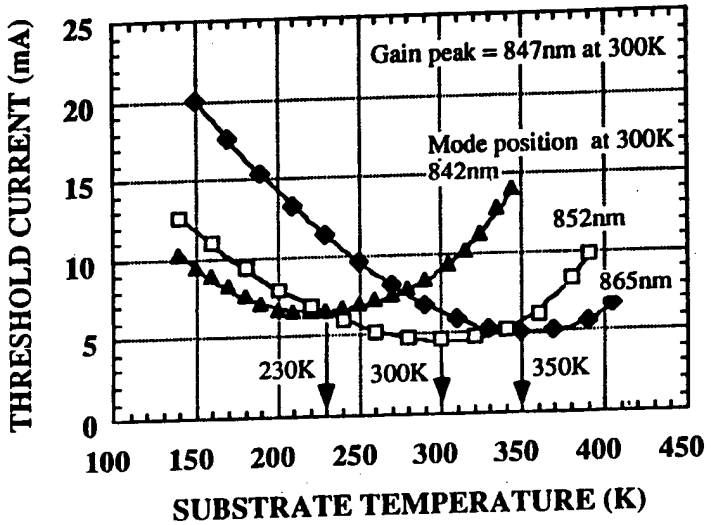


Fig. 7. Temperature dependence of the CW lasing threshold currents for three 16 μm PITSELs with different lasing mode positions relative to a common gain peak (847 nm at 300 K). The minimum threshold current occurs close to the temperature where the gain peak and lasing mode wavelengths coincide (after Lu, Zhou, Cheng, Malloy and Zolper [1994]).

mirrors. On the other hand, as illustrated in fig. 6, the observed mode wavelength shift (cf. § 3.1) is 4–5 times slower than the gain-peak wavelength shift.

For each VCSEL design there exists an optimal temperature, for which an ideal alignment between the gain spectrum and the vertical-cavity resonant mode takes place. This usually coincides with the condition for minimum $I_{th}(T)$, provided optical and electrical losses are not changing drastically around this temperature. Figure 7 presents typical $I_{th}(T)$ curves for three PITSELs with different lasing mode positions at 300 K (Lu, Zhou, Cheng, Malloy and Zolper [1994]). The larger the room-temperature detuning of λ_{DBR} towards the longer wavelengths, the higher the temperature at which the threshold current reaches minimum.

Figure 8 shows the temperature dependence of T_0 extracted from the data of fig. 7 using eq. (17). It is clear that T_0 can be considered constant only over a very limited range of temperatures, away from the vertical asymptote. The asymptotes in fig. 8 correspond to the minima of $I_{th}(T)$ curves in fig. 7.

The temperature dependence of the threshold current in VCSELs, with a minimum occurring near the temperature at which λ_{DBR} and λ_{max} are aligned, resembles that of frequency-selective EELs, such as DFB or DBR lasers. In edge-emitting DFB lasers, however, $I_{th}(T)$ characteristics may be more complicated,

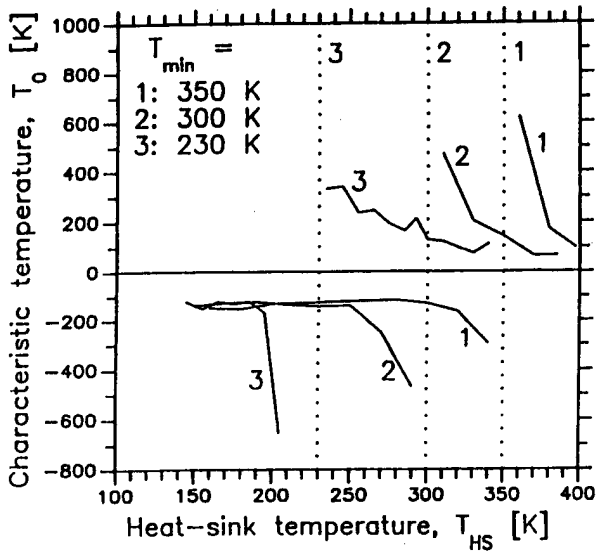


Fig. 8. Temperature dependence of the characteristic temperature T_0 extracted from the data of fig. 7.

with multiple minima corresponding to various transverse modes (cf. Aiki, Nakamura and Umeda [1976]).

3.3. TEMPERATURE DEPENDENCE OF TRANSVERSE-MODE PROPERTIES

Compared to EELs, transverse-mode properties of VCSELs are considerably more complex. Transverse modes in VCSELs are determined by an intricate interplay of gain profile, absorption, diffraction, reflection, spatial filtering, built-in index waveguiding, and temperature distribution (Scott, Young, Thibeault, Peters and Coldren [1995], Michalzik and Ebeling [1995]). Depending on the particular VCSEL structure, some of these effects can be more important than others, but rarely can a single mechanism be identified as the dominant one. In addition, VCSEL cavities can usually support many transverse modes (Valle, Sarma and Shore [1995a]), especially in large-diameter ($\gtrsim 20\,\mu$m) devices or in strongly index-guided structures. Hence, mode competition and single-transverse-mode control are important problems, even though the device operates in a single longitudinal mode.

The difficulties with transverse mode control are best illustrated by the small value (4.4 mW) of the fundamental-mode CW output power achieved so far (Lear, Schneider, Choquette, Kilcoyne, Figiel and Zolper [1994]). Coupling to an external cavity, which is a proven technique for increasing the single-mode output power in EELs, has until now resulted in single-mode CW powers of only 2–2.4 mW (Hadley, Wilson, Lau and Smith [1993], Wilson, Hadley, Smith and Lau [1993]). Spatial filtering with the aid of a graded-index lens has recently extended this value to only 4.5 mW (Koch, Leger, Gopinath, Wang and Morgan [1997]). This contrasts with significantly larger single-mode powers of 36–100 mW in the same external-cavity VCSELs injected with 100 ns pulses at 0.1% duty cycle (Hadley, Wilson, Lau and Smith [1993], Wilson, Hadley, Smith and Lau [1993]). The large difference between the pulsed and CW results clearly illustrates the strong effect of heating on the transverse mode structure.

One of distinct features of VCSELs is that their threshold currents for pulsed and CW operations are often very similar to each other and that the CW threshold can sometimes be even lower than the pulsed one (e.g., Hasnain, Tai, Yang, Wang, Fischer, Wynn, Weir, Dutta and Cho [1991]). This is caused by the so-called *thermal lensing effect*, which focuses the radiation in regions of higher temperature because of temperature-dependent refractive index.

Thermal lensing can strongly influence the transverse mode structure in so-called gain-guided (or carrier-guided) diode lasers without a built-in waveguide in the p–n junction plane, where lateral confinement of the optical field occurs via a combination of gain guiding and index antiguiding (e.g., Nash [1973], Cook and Nash [1975], Thompson [1980] (chapter 6.4.1.), Hadley, Hohimer and Owyoung [1987], Cherng and Osiński [1991]). A similar situation takes place in VCSELs with no built-in lateral waveguide, for example in PITSELs (e.g., Hasnain, Tai, Yang, Wang, Fischer, Wynn, Weir, Dutta and Cho [1991], Chang-Hasnain, Harbison, Hasnain, Von Lehmen, Florez and Stoffel [1991], Zeeb, Möller, Reiner, Ries, Hackbarth and Ebeling [1995]), and, partially, in TBEMLs (Michalzik and Ebeling [1993]). In low-duty-cycle short-pulse operation, when thermal effects are negligible, the confinement of the optical field in the radial direction occurs via a combination of gain guiding, carrier antiguiding, absorption, diffraction (Babic, Chung, Dagli and Bowers [1993], Jansen van Doorn, van Exter and Woerdman [1995]), and spatial filtering at the top contact. Carrier antiguiding tends to defocus the optical field, which leads to large diffraction losses (Hasnain, Tai, Yang, Wang, Fischer, Wynn, Weir, Dutta and Cho [1991], Dutta, Tu, Hasnain, Zydzik, Wang and Cho [1991]). Under CW conditions, the active-region heating results in a non-uniform, bell-shaped temperature distribution which peaks in the active region and falls off in the radial direction (cf. fig. 16 in § 5.1.1). Since $(\partial n_R/\partial T)|_\lambda$ is positive (see § 3.1), the thermal contribution to the refractive index also peaks in the active region, causing the thermal lensing effect. Nonuniformity of the temperature distribution

becomes more pronounced with increasing pumping current, to the point where real-index guiding associated with temperature profile may become dominant, resulting in tighter focusing of the optical field. Experimental observations of narrowing near-field patterns of the bell-shaped fundamental transverse mode with increasing current in PITSELs (Chang-Hasnain, Harbison, Florez and Stoffel [1991], Chang-Hasnain, Harbison, Hasnain, Von Lehmen, Florez and Stoffel [1991]) have been confirmed by the calculations of Michalzik and Ebeling [1993]. Thermally-induced waveguiding improves the overlap between the optical field and the gain region and reduces the diffraction loss.

In the intermediate regime of relatively long pulses (over 100 ns long), the build-up of thermal waveguide leads sometimes to anomalously long time delays in lasing. When the pulse amplitude is only slightly larger than the CW threshold current, the time delay before the onset of lasing can be as long as several μs (Hasnain, Tai, Yang, Wang, Fischer, Wynn, Weir, Dutta and Cho [1991]). The time delay rapidly decreases with increasing current and reaches the "normal" level of 25 ns when the pumping current amplitude exceeds the pulsed threshold value.

A quantitative analysis of the thermal lensing and its effects on the time delay in PITSELs is given by Dutta, Tu, Hasnain, Zydzik, Wang and Cho [1991]. At the beginning of a low-amplitude pulse, threshold losses are higher than the modal gain, and therefore lasing action cannot start. As the device starts to heat up, thermal lensing begins to play a more and more important role, steadily reducing diffraction losses. The observed time delay is simply equal to the time necessary to create a sufficiently strong thermally-induced waveguide. A similar phenomenon has been observed by Prince, Patel, Kasemset and Hong [1983] in carrier-guided stripe-geometry EELs and was explained in terms of thermally-controlled dynamic evolution of waveguide properties.

While a thermally-induced waveguide is beneficial from the point of view of lowering the CW threshold current, it can at the same time facilitate excitation of higher-order transverse modes. At higher currents, a stronger real-index thermal waveguide supports a larger number of high-order modes which can then compete with the fundamental mode. Therefore, the dynamic switch-on response of VCSELs initially contains sometimes a single-lobe profile (the fundamental transverse mode), and after the time (dependent on pumping conditions) necessary for the thermal waveguide to build up transforms into a double-lobe profile (the first-order transverse mode) (Yu and Lo [1996], Buccafusca, Chilla, Rocca, Feld, Wilmsen, Morozov and Leibenguth [1996]). Once the thermal waveguide is established, the main mode competition mechanism switches to *spatial hole burning* (e.g., Vakhshoori, Wynn, Zydzik, Leibenguth, Asom, Kojima and Morgan [1993], Scott, Geels, Corzine and Coldren [1993], Scott, Young, Thibeault, Peters and Coldren [1995], Valle, Sarma and Shore [1995b], Law and Agrawal [1997]). The fundamental transverse mode is localized in the central part of the active region, therefore the stimulated recombination associated with this mode takes place primarily in this area. This depresses the local carrier density and the gain in the central part of the laser cavity, reducing the modal gain for the fundamental mode, while allowing the carriers to build-up near the edges of the active region and increasing the modal gain of higher-order doughnut-shaped transverse modes. Eventually, the laser ends up operating in multiple transverse modes.

In VCSELs with no built-in lateral waveguide or with weak index-guiding, spatial hole burning can cause a positive-feedback phenomenon known as *self focusing*, which further reinforces the real-index thermal waveguide (see Wilson, Kuchta, Walker and Smith [1994]). A depression in the carrier concentration produces a local increase in the refractive index which can further intensify the stimulated emission, locally reducing the carrier concentration, and so on. A similar effect can also arise from thermal lensing via absorption of the emitted light within the core of thermal waveguide.

A depression in carrier density, similar to that caused by the spatial hole burning, can also be caused by *nonuniformity of current injection* in devices with annular contacts (see Osiński, Nakwaski and Varangis [1994]). The two effects can be distinguished by observing the spontaneous emission profile, which is proportional to carrier density distribution. Nonuniformity due to current spreading should also manifest itself below the lasing threshold, while spatial hole burning can occur only above threshold. The only experiments reported so far by Vakhshoori, Wynn, Zydzik, Leibenguth, Asom, Kojima and Morgan [1993] and by Wilson, Kuchta, Walker and Smith [1994], involving measurements of the spontaneous emission profile above threshold, indicate that at moderate currents the spontaneous emission profile has a doughnut shape. Further above threshold, when higher-order transverse modes become excited, the carrier density profile is sensitive to details of the laser structure. For example, smooth profiles were observed by Wilson, Kuchta, Walker and Smith [1994] in their bottom-emitting VCSELs with circular top contacts, indicating that spatial hole burning was the dominant effect. In contrast, Vakhshoori, Wynn, Zydzik, Leibenguth, Asom, Kojima and Morgan [1993] observed dark spot near the center of the spontaneous emission profile even high above threshold, which suggests that nonuniform injection was the main effect in their top-emitting devices with annular contacts.

Nonuniform current injection, with current crowding near the edges of the

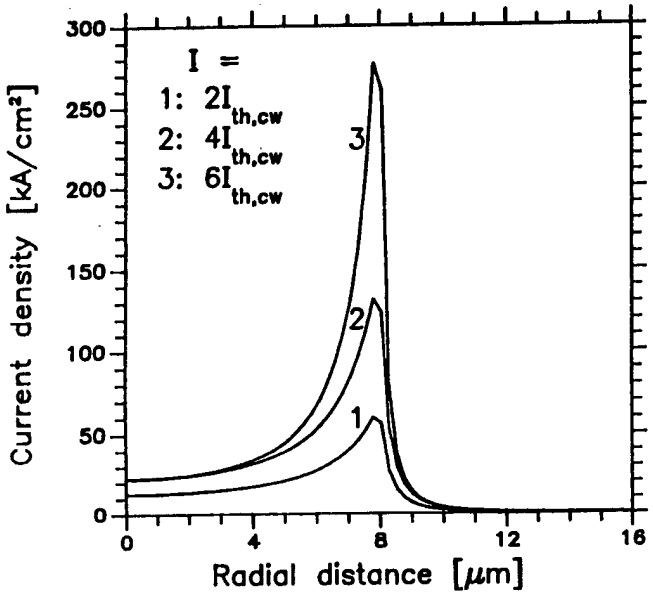


Fig. 9. Current density profiles in the p–n junction plane for a 16 μm etched-well GaAs/AlGaAs VCSEL (structure DMEWL-TIT-B) with parameters given by Nakwaski and Osiński [1993].

active region in VCSELs with annular contacts (e.g., Nakwaski and Osiński [1991b], Nakwaski, Osiński and Cheng [1992], Wada, Babic, Ishikawa and Bowers [1992], Scott, Geels, Corzine and Coldren [1993]), also favors excitation of higher-order transverse modes. To some extent, the nonuniform injection is counterbalanced by the ambipolar radial diffusion of carriers prior to their recombination (Sarzała and Nakwaski [1997]), which makes the local gain distribution more uniform than the current-density distribution (e.g., Wada, Babic, Ishikawa and Bowers [1992], Chong and Sarma [1993], Sarzała, Nakwaski and Osiński [1995]). Nevertheless, the gain profile still has an on-axis minimum and is better matched to the higher-order transverse modes than to the fundamental one. This effect is usually not strong enough to suppress the fundamental mode near threshold, but gains in importance with increasing pumping level, as the current crowding becomes more and more intense (see fig. 9). The better overlap of the gain profile with the optical field of the higher-order modes may then become sufficient to overcome the higher diffraction loss suffered by these modes.

Nonuniformity of the current density in devices with annular contacts can be largely leveled out if the heterointerfaces between the alternating layers of

Bragg mirrors are not graded (Michalzik and Ebeling [1993]). This, however, increases the series resistance (the specific heteroresistance between p-GaAs and p-AlAs layers can be as high as $2.5\times10^{-4}\,\Omega\mathrm{cm}^2$) and results in more intense Joule heating.

Built-in index antiguiding can be used as a mechanism for extending the single-transverse mode operation range, since the higher-order modes suffer a higher diffraction loss penalty than the fundamental mode (e.g., Chang-Hasnain, Wu, Li, Hasnain, Choquette, Caneau and Florez [1993], Wu, Chang-Hasnain and Nabiev [1994], Wu, Li, Nabiev, Choquette, Caneau and Chang-Hasnain [1995], Yoo, Chu, Park, Park and Lee [1996]). The negative index step between an equivalent index of the DBR reflector and the surrounding high-index medium can be made as large as 0.18 (Wu, Chang-Hasnain and Nabiev [1993]), hence the antiguide cannot be affected significantly by the much smaller (one-two orders of magnitude) positive index step due to radial temperature profile. So far, however, this approach has had only limited success. While the near-field intensity profiles in bottom-emitting passive-antiguide-region InGaAs/AlGaAs VCSELs show no symptoms of thermal lensing, spatial hole burning or self-focusing, the maximum single-transverse-mode power is still limited to only 1.2 mW (Wu, Chang-Hasnain and Nabiev [1993], Wu, Li, Nabiev, Choquette, Caneau and Chang-Hasnain [1995]). Introducing higher doping at the active region perimeter to increase free-carrier losses and using low-reflectivity ring contacts on the top VCSEL reflector were other mode selection methods postulated by Morgan, Guth, Focht, Asom, Kojima, Rogers and Callis [1993].

Another class of temperature-insensitive waveguide involves *strong index guiding* (Jewell, Scherer, McCall, Lee, Walker, Harbison and Florez [1989], Geels, Corzine, Scott, Young and Coldren [1990], Geels and Coldren [1990,1991], Shimizu, Babic, Dudley, Jiang and Bowers [1993], Dudley, Babic, Mirin, Yang, Miller, Ram, Reynolds, Hu and Bowers [1994], Young, Kapila, Scott, Malhotra and Coldren [1994], Yoffe, van der Vleuten, Leys, Karouta and Wolter [1994], Yoo, Park and Lee [1994]). Compared to strongly antiguiding VCSELs, index-guiding structures have a serious disadvantage of lowering the threshold of higher-order-mode excitation (Chang-Hasnain, Orenstein, Von Lehmen, Florez, Harbison and Stoffel [1990], Schröder, Grothe and Harth [1996]). Consequently, fundamental-transverse-mode operation can be maintained only over a very limited current range near threshold.

3.4. TEMPERATURE DEPENDENCE OF THE OUTPUT POWER

Because of the thermal lensing effect (see § 3.3), the threshold current for

the CW operation in PITSELs is often distinctly lower than for the pulsed one. The external differential quantum efficiency, which is the laser parameter proportional to the slope of the light–current characteristic above the threshold current, is, however, much higher for the pulsed operation (Hasnain, Tai, Yang, Wang, Fischer, Wynn, Weir, Dutta and Cho [1991]). Similarly, maximum available output power and the operating current range are enhanced under pulsed conditions.

From fig. 7, we may conclude that in order to obtain efficient CW high-power operation of VCSELs at room temperature, their cavity-mode positions at this temperature should be on the long-wavelength side of the gain spectrum. Although such lasers may have higher threshold currents for pulsed operation than those with aligned cavity-mode and gain-peak positions, nevertheless their CW threshold currents will be lower because of the *active-region heating* provided the cavity-mode and gain-peak wavelengths are matched at the active-region temperature). However, since the active-region temperature depends on the driving current, the conditions for minimum threshold current would in general be different from the conditions for maximum output power. This is illustrated in fig. 10, showing the temperature dependence of light–current (L–I) characteristics of a PITSEL device with a room-temperature detuning of the cavity mode by 18 nm towards the longer wavelengths. The CW lasing threshold for this device, shown also in fig. 7, has a minimum at 350 K. All L–I characteristics display a typical thermal roll-off behavior, indicating that over the wide temperature range of 90 K–400 K, the output power P_{out} is thermally limited. The maximum output power is determined primarily by the temperature variation of the peak gain (see table 5) and by changes in the external *differential quantum efficiency* η_d. The latter can be extracted from fig. 10 using the following formula (Agrawal and Dutta [1993]):

$$\eta_d(T) = \frac{e\lambda(T)}{hc}\frac{dP_{out}}{dI}, \tag{18}$$

where e is the electron charge, h is Planck's constant, and c is the speed of light. Equation (18) implies that all output power from a top-emitting VCSEL is collected through the top mirror.

Figure 11 shows the temperature dependence of η_d, calculated by applying Eq. (18) for the device of fig. 10. The raising part of L–I curves, not too far above threshold, is used to determine η_d. $\lambda(T)$ is obtained from the data of fig. 5, taking the CW lasing wavelength for the "865 nm mode" and extrapolating down to 90 K. In any case, the wavelength variation represents only a very small correction to η_d determined from the slope efficiency dP_{out}/dI with a constant

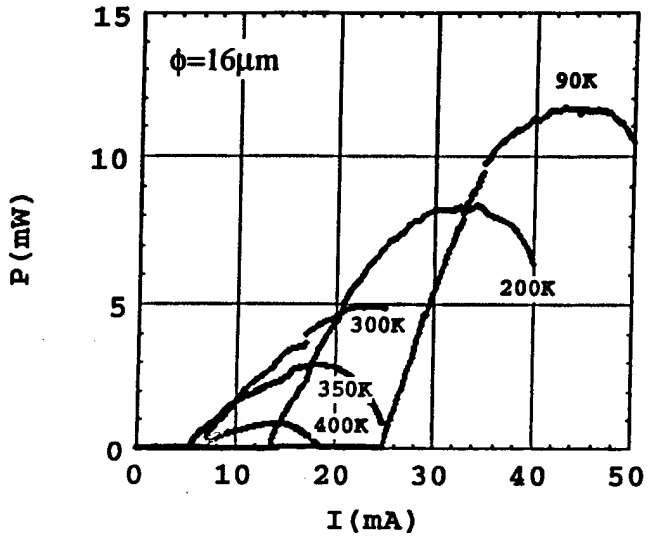


Fig. 10. Temperature evolution of the light–current characteristics for a 16 μm PITSEL shown in fig. 7 as having minimum CW threshold at 350 K (mode wavelength 865 nm at 300 K) (after Lu, Zhou, Cheng and Malloy [1994]).

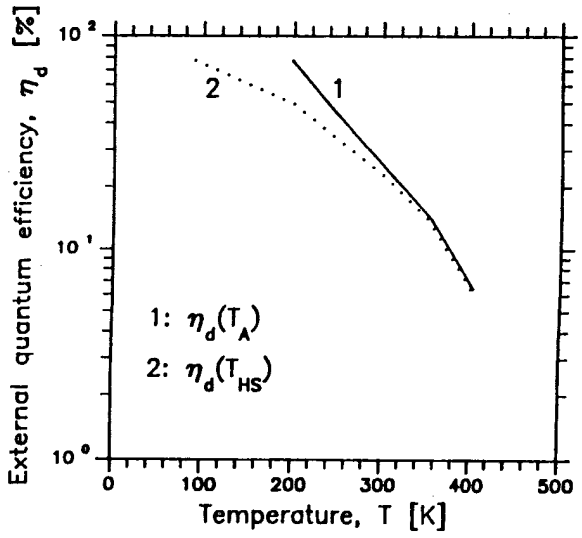


Fig. 11. Temperature dependence of the differential quantum efficiency η_d for the device in fig. 10, using either the stage temperature T_{HS} (dotted line) or the active-region temperature T_A (solid line) as the argument in $\eta_d(T)$.

wavelength. The logarithmic scale in fig. 11 is chosen to verify whether an exponential formula analogous to eq. (16),

$$\eta_d(T) = \eta_d(300\ \mathrm{K})\exp\left(\frac{T - 300\ \mathrm{K}}{T_\eta}\right), \tag{19}$$

with a constant characteristic temperature T_η, would hold for VCSELs, as it does for EELs (e.g., Papannareddy, Ferguson and Butler [1987]). Note that sometimes a simpler approximation is used (Wipiejewski, Peters, Thibeault, Young and Coldren [1996]): $\eta_d(T) = \eta_{max}(1 - \Delta T/T_{max})$, where T_{max} is the characteristic roll-over temperature of the laser. The two curves in fig. 11 correspond to results obtained using either the stage temperature T_{HS} (dotted line) or the active-region temperature T_A (solid line) as the argument in $\eta_d(T)$. T_A is estimated using the wavelength shift between the CW and pulsed operation shown in fig. 5, again extrapolating down to 90 K. Under pulsed conditions, the "865 nm mode" device has two clear regimes of linear wavelength shift, characterized by $\partial\lambda_M/\partial T = 0.41$ Å/°C for $90 \leqslant T_{HS} < 300$ K, and $\partial\lambda_M/\partial T = 0.59$ Å/°C for $300 \leqslant T_{HS} < 400$ K. The deviation of the CW wavelength from the pulsed one gives then the following estimates of the active-region temperature at CW threshold: $T_A = 198$ K at $T_{HS} = 90$ K, $T_A = 239$ K at $T_{HS} = 200$ K, $T_A = 310$ K at $T_{HS} = 300$ K, $T_A = 354$ K at $T_{HS} = 350$ K, and $T_A = 403$ K at $T_{HS} = 400$ K.

If the stage temperature T_{HS} is used (dotted curve in fig. 11), T_η decreases steadily with T_{HS} ($T_\eta = 241$ K for $90 \leqslant T_{HS} < 200$ K, $T_\eta = 129$ K for $200 \leqslant T_{HS} < 300$ K, $T_\eta = 104$ K for $300 \leqslant T_{HS} < 350$ K, and $T_\eta = 63$ K for $350 \leqslant T_{HS} < 400$ K). Hence, it is clear that if T_{HS} is used as an argument in $\eta_d(T)$, eq. (19) can be used only over a very small temperature range. Conversely, using the active-region temperature T_A (solid curve in fig. 11), produces two regimes of behavior ($T_\eta = 91$ K for $198 \leqslant T_A < 310$ K, and $T_\eta = 62$ K for $310 \leqslant T_A < 403$ K) that coincide with the two regions of constant pulsed-wavelength shift rate (cf. fig. 5).

It is interesting to note that the value of $T_\eta = 91$ K agrees very well with $T_{sp} = 93$ K (valid for $300\ \mathrm{K} \leqslant T_A \leqslant 440$ K) determined experimentally by Chen, Hadley and Smith [1994], where T_{sp} is the characteristic temperature for the spontaneous emission efficiency variation with temperature. This indicates that reduction of internal quantum efficiency, rather than changes in optical losses, is the main effect responsible for the temperature variation of the external quantum efficiency η_d.

The increase in slope of $\partial\lambda_M/\partial T$ and the reduction in T_η from 91 K to 62 K around $T_A = 310$ K is most likely caused by the onset of carrier leakage over the heterobarriers (cf. eq. 15). In EELs, opening of an additional current leakage path would have unavoidably reduced the value of T_0. In VCSELs, this process is obscured by strong variations of $I_{th}(T)$ caused by the detuning between the gain peak and the cavity mode (cf. § 3.2). Nevertheless, fig. 7 does display an asymmetry between the low- and high-temperature branches of $I_{th}(T)$, indicating a faster growth at high temperatures. Additional corroborating evidence is provided by fig. 8, where, compared with low-temperature behavior, T_0 reaches lower values on the high-temperature side of the asymptotes. While T_0 for the "865 nm mode" device (curve 3 in fig. 8) continues to fall at 400 K, the "852 nm mode" device (curve 2 in fig. 8) reaches a floor of $T_0 = 62$–65 K. Although more studies of this subject are needed to eliminate the possibility of a serendipitous coincidence, the close matching of the high-temperature values of T_0 and T_η for the same device is remarkable. Moreover, a T_η of 62 K is very close to the high-temperature value of $T_0 = 60$ K reported by Geels, Thibeault, Corzine, Scott and Coldren [1993] for a BEML, indicating that the phenomenon responsible for the low T_0 values at high temperatures may be the same in different VCSEL structures. Carrier leakage over heterobarriers could indeed represent such common mechanism, since both PITSELs and BEMLs incorporate quantum-well active-regions.

§ 4. Fundamentals of Thermal Modeling of VCSELs

Thermal modeling of VCSELs is a very involved task because of:

(i) a multilayer structure (sometimes containing over a hundred layers), often of nonplanar or buried-type designs, with many heterojunctions, graded layers, strained layers, single or multiple quantum wells, superlattices, oxide and oxidized layers, barriers, etched wells or mesas, etc. (cf. fig. 3); and

(ii) the necessity of taking into account many mutual nonlinear interactions between particular physical phenomena; i.e., thermal, electrical, optical and sometimes also mechanical and photochemical processes, taking place during laser operation (cf. fig. 15, below).

In analytical modeling of VCSELs, their complex structure imposes the necessity of solving the equations describing their operation separately for each homogeneous region. Mutual correlation of those partial solutions, with the aid of proper boundary conditions (see, e.g., Nakwaski and Osiński [1994]), should then be carried out. This method is very time-consuming, and therefore simplified approaches are sometimes adopted, transforming the inhomogeneous laser structure made of isotropic materials into an equivalent homogeneous, but anisotropic medium (see, e.g., Osiński and Nakwaski [1993a], Osiński, Nakwaski

and Varangis [1994], Osiński, Nakwaski and Leal [1994], Sarzała, Nakwaski and Osiński [1995]).

The second of the above mentioned factors, i.e., mutual interactions between individual physical processes occurring during a diode laser operation, whose incomplete review will be presented in fig. 15, obliges us to use a self-consistent approach. A flow chart of a typical self-consistent diode laser simulation will be presented in fig. 14.

4.1. HEAT CONDUCTION EQUATION

For the transient-state condition, *the heat conduction equation* in a medium of cylindrical symmetry is of the following form (Oezisik [1980]):

$$\nabla \{k [r, z, T(r,z)] \nabla T(r,z)\} = \frac{k}{\kappa} \frac{\partial T}{\partial t} - g(r,z), \tag{20}$$

which for a uniform medium with temperature-independent k, κ, and g may be reduced to

$$\frac{\partial^2 T}{\partial r^2} + \frac{1}{r} \frac{\partial T}{\partial r} + \frac{\partial^2 T}{\partial z^2} = \frac{1}{\kappa} \frac{\partial T}{\partial t} - \frac{1}{k} g(r,z). \tag{21}$$

In the above equations, k and κ stand for the thermal conductivity and the thermal diffusivity, respectively, and $g(r,z)$ is the distribution of the volume density of heat generation (in W/cm^3). In the steady-state case, the first term of the right-hand-side of eqs. (20) and (21) vanishes. Examples of room-temperature values of thermal conductivities for several semiconductor materials commonly used in VCSEL structures are listed in table 7.

To solve the thermal conduction equation (20) (or 21), it is necessary to formulate an appropriate set of *boundary conditions*. VCSEL structures are usually axially symmetric, so the first boundary condition is written as follows (cf. fig. 12):

$$\left.\frac{\partial T}{\partial r}\right|_{r=0} = 0. \tag{22}$$

In a typical packaging scheme, the outer surfaces of VCSELs are exposed to interaction with an external ambient medium (usually air). In principle, this may result in heat transfer to the external ambient medium via the direct contact of air particles with the laser walls and subsequent diffusion and convection processes. In natural convection, the flux of heat from the surface

Table 7
Thermal conductivity k

Material	k (W/mK)	Reference
GaAs	44	Adachi [1985]
AlAs	91	Adachi [1985]
$Al_xGa_{1-x}As$	$100/(2.27+28.83x-30.0x^2)$	Adachi [1985]
InP	68	Kudman and Steigmeier [1964]
$In_{0.73}Ga_{0.27}As_{0.6}P_{0.4}$ [a]	5.5	Nakwaski [1988]
$In_{0.63}Ga_{0.37}As_{0.79}P_{0.21}$ [b]	5.15	Nakwaski [1988]
$In_{0.6}Ga_{0.4}As_{0.85}P_{0.15}$ [c]	5.1	Nakwaski [1988]

[a] Bandgap wavelength $\lambda_g = 1.3\,\mu m$.
[b] Bandgap wavelength $\lambda_g = 1.45\,\mu m$.
[c] Bandgap wavelength $\lambda_g = 1.55\,\mu m$.

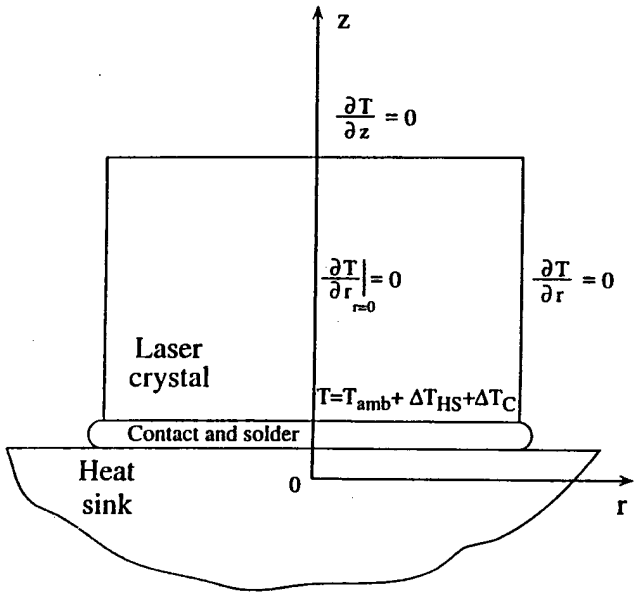


Fig. 12. Boundary conditions of the thermal conduction equation for VCSELs.

is approximately proportional to the 5/4 power of the difference between the surface temperature and the ambient temperature (Carslaw and Jaeger [1988], p. 21). In VCSELs, however, considerable temperature increase occurs only in

the vicinity of the active region, buried deep inside the device. The temperature at the outer surfaces is usually only slightly higher than that of the surrounding medium. Thus, heat transfer through the surfaces is very small compared to a very efficient heat conduction through the laser heat sink and can be neglected completely. Consequently, the outer surfaces of the VCSEL chip can be assumed to be adiabatic (cf. fig. 12):

$$\left.\frac{\partial T}{\partial r}\right|_{\text{side walls}} = 0, \tag{23}$$

$$\left.\frac{\partial T}{\partial z}\right|_{\text{upper walls}} = 0. \tag{24}$$

Heat flux conduction through the VCSEL base (see fig. 12) produces a temperature increase inside the contact and solder layers (ΔT_C) as well as inside the heat sink (ΔT_{HS}). The corresponding boundary condition can be written as follows:

$$T|_{\text{bottom walls}} = T_{\text{amb}} + \Delta T_{HS} + \Delta T_C, \tag{25}$$

where T_{amb} stands for the temperature of the ambient and ΔT_{HS} and ΔT_C are to be determined and will be analyzed in the next section.

4.2. HEAT-SINK AND CONTACT/SOLDER-LAYER TEMPERATURE INCREASE

Exact determination of the temperature increase ΔT_{HS} in the heat sink usually requires an involved three-dimensional thermal analysis. An estimate of ΔT_{HS} can, however, be made using the concept of the *effective diameter*, D_E, for the heat flux entering the heat sink from the device, as proposed by Nakwaski and Kontkiewicz [1985] for cylindrically symmetric devices. This approach is based on an assumption that a uniform heat flux entering the heat sink through an effective circular thermal contact of diameter D_E will cause exactly the same average temperature increase ΔT_{HS} in the heat sink as the actual nonuniform heat flow. D_E can be determined using the following expression:

$$D_E = 2 \lim_{\Delta d_a \to 0} \left(\pi k_a \frac{\Delta R_{TH}}{\Delta d_a} \right)^{-1/2}, \tag{26}$$

where R_{TH} is the laser thermal resistance (defined by eq. 49) and Δd_a is the thickness of a hypothetical additional layer (of a thermal conductivity k_a) between the heat sink and the device.

Once D_E is determined, the average temperature increase ΔT_{HS} inside the heat sink can be found using the following formula (Carslaw and Jaeger [1988], p. 216):

$$\Delta T_{HS} = \frac{16 Q_T}{3\pi^2 D_E k_{HS}}, \tag{27}$$

where Q_T stands for the total power of the heat flux entering the heat sink, and k_{HS} is the thermal conductivity of its material. In the derivation of eq. (27), the heat sink is assumed to be much larger than the laser chip.

To determine ΔT_C, the thicknesses of all the intermediate layers between the laser chip and the heat sink (i.e., contact and solder layers, and for some VCSEL structures also oxide layers) should be averaged over the effective diameter D_E. The average temperature increase within these layers ΔT_C can then be expressed as

$$\Delta T_C = \frac{4 Q_T}{\pi D_E^2} \sum_i \frac{d_{i,\text{av}}}{k_i}, \tag{28}$$

where the summation should be carried out over the intermediate layers, $d_{i,\text{av}}$ are their averaged thicknesses and k_i are their thermal conductivities.

4.3. HEAT SOURCES

Diode lasers are supplied with the electric power which, in processes of current spreading, carrier recombination as well as emission and absorption of radiation, is transformed into output power and heat in a way illustrated in fig. 13.

In VCSELs, the following heat generation mechanisms should be taken into consideration: volume and barrier Joule heating, nonradiative recombination of carriers, absorption of spontaneous radiation, and absorption of laser radiation. Distributions of these heat sources are directly associated with distributions of carrier concentration, current density, and spontaneous and stimulated radiation intensities, hence they are influenced by current spreading, carrier diffusion and waveguiding mechanisms. Their magnitudes are influenced in turn by such device and material parameters as internal quantum efficiency, threshold current density, threshold carrier concentration, absorption coefficients, electrical resistivities – all nonlinearly dependent on temperature.

The *power balance in a semiconductor laser* may be presented in the following form:

$$P = UI = (U_{pn} + IR_S)I$$

=	I^2R_S	Joule heating
	$+U_{pn}I_{th}(1-\eta_{sp})$	nonradiative recombination at threshold
	$+U_{pn}I_{th}\eta_{sp}(1-f_T)$	absorption of spontaneous radiation inside the active region at threshold
	$+U_{pn}I_{th}\eta_{sp}f_T$	escape spontaneous radiation at threshold
	$+U_{pn}(I-I_{th})(1-\eta_i)(1-\eta_{sp})$	nonradiative recombination for $I > I_{th}$ (29)
	$+U_{pn}(I-I_{th})(1-\eta_i)\eta_{sp}(1-f_T)$	absorption of spontaneous radiation inside the active region for $I > I_{th}$
	$+U_{pn}(I-I_{th})(1-\eta_i)\eta_{sp}f_T$	escape spontaneous radiation for $I > I_{th}$
	$+U_{pn}(I-I_{th})(\eta_i-\eta_d)$	absorption of stimulated radiation outside the active region
	$+U_{pn}(I-I_{th})\eta_d$	laser output power.

In the above equations, P is the electric power supplied to the laser, U is the total voltage drop inside the device, U_{pn} is the voltage drop at the p–n junction, I and I_{th} are the operation current and the threshold current, respectively, η_{sp}, η_i, and η_d are the quantum efficiencies: internal for spontaneous emission and for lasing radiation as well as differential external for lasing, respectively, and f_T is the radiative transfer coefficient for spontaneous emission (cf. § 4.3.1).

All heat sources in semiconductor lasers are associated with current densities, carrier concentrations or radiation intensities, which are nonuniform. Therefore these heat generation processes are nonuniform not only along the z axis (because of different structure layers of different heat yields) but also along the r axis inside all homogeneous layers.

With the exception of the Joule barrier heating, all heat generation processes represent volume heat sources. They are, however, often treated as flat (planar) heat sources located in the middle of their generation regions. Such approximation can deteriorate the accuracy of the calculated temperature profiles, especially in the close vicinity of the heat source, so it may be used only when the heat sources are relatively thin.

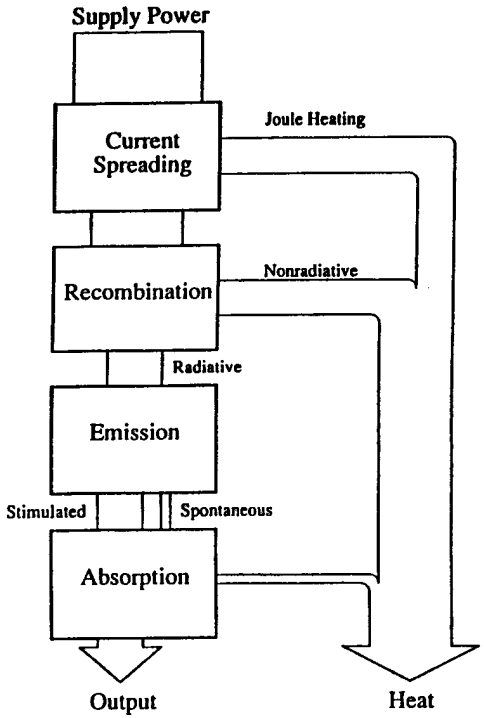


Fig. 13. Power balance in diode lasers.

4.3.1. *Active-region heating*

Nonradiative recombination of carriers takes place within the active region, where carriers of both kinds (electrons and holes) can meet each other. This process is associated with the *efficiency of radiative recombination*, which for an ideal injection is simply equal to the *internal quantum efficiency*.

Below the threshold, i.e., for $j < j_{th}$, where j and j_{th} stand for the operation current density and the threshold current density, respectively, most of the electric power supplied to the active region is transformed into heat because the internal quantum efficiency for the spontaneous emission η_{sp} is much less than unity. Then the volume density g_A (in W/cm^3) of active-region heat generation may be expressed as

$$g_A = \frac{U_{pn}j(1-\eta_{sp})}{d_A} \qquad j \leqslant j_{th}, \tag{30}$$

where d_A stands for the active region thickness (cumulative thickness in the case of multi-quantum-well active regions). This expression should be modified slightly if we take into account absorption of some part of spontaneous radiation in the active region and radiative transfer of the remaining part out of this region:

$$g_A = \frac{U_{pn} j (1 - \eta_{sp} f_T)}{d_A} \qquad j \leq j_{th}, \tag{31}$$

where f_T stands for the radiative transfer coefficient (Kobayashi and Furukawa 1975], Nakwaski [1979]):

$$f_T = 2\sin^2\left(\frac{\alpha_{cr}}{2}\right), \tag{32}$$

with

$$\alpha_{cr} = \arctan\left(\frac{n_{R1}}{\sqrt{n_{R2}^2 - n_{R1}^2}}\right). \tag{33}$$

and where n_{R1} and n_{R2} are the refractive indices of the cladding and the active-region materials, respectively.

Above the laser threshold, an analogous equation reads as follows (Kobayashi and Furukawa [1975], Nakwaski [1979]):

$$g_A = \frac{U_{pn}(1 - \eta_{sp} f_T)[j_{th} + (j - j_{th})(1 - \eta_i)]}{d_A} \qquad j > j_{th}, \tag{34}$$

where η_i is the internal quantum efficiency of the stimulated emission.

Whenever intense heating takes place, it is important to remember that the threshold current density j_{th} is not a constant device parameter, but is itself temperature dependent. As the pumping current density j increases, so does the active-region temperature, and therefore j_{th} is also current dependent. To emphasize this, Scott, Geels, Corzine and Coldren [1993] have introduced the concept of a current-dependent *effective threshold current density* $j_{th,e} \equiv j_{th}(j)$. Alternatively, we could write $j_{th} \equiv j_{th}(T_A)$, where T_A is the average active-region temperature.

For high reliability, the quality of semiconductor laser materials must be very good. Consequently, in most cases the internal quantum efficiency for stimulated emission η_i is very close to unity (Petermann [1991]). Thus, eq. (34) reduces to:

$$g_A = \frac{U_{pn} j_{th,e}(j)(1 - \eta_{sp} f_T)}{d_A} \qquad j > j_{th,e}. \tag{35}$$

In the case of proton-bombarded VCSELs, e.g., in PITSELs, this part of the spontaneous radiation, which is leaving the active region, is mainly absorbed in the closest vicinity of the active region; i.e., in surrounding it highly absorbing (of high absorption coefficient α) areas exposed during their fabrication to a stream of protons. Thicknesses ($=\alpha^{-1}$) of these new heat sources are very low. Therefore, it is quite a good approximation to assume that these absorption events take place also inside the active region. Then, the radiative transfer coefficient f_T should be put equal to zero in all the above expressions.

Saturation of the voltage drop $U_{pn}(r)$ at the p–n junction above the lasing threshold (e.g., Sommers [1971], Paoli [1973]) should also be taken into account. It does not simply mean that $U_{pn}(r)$ is taken as a constant distribution for all currents above the threshold, because an increase in the pumping is followed by an increase in the active-region temperature, which results in an increase in the threshold current. Therefore, for a given value of the pumping current, the saturated profile of the voltage drop at the p–n junction should correspond to an actual active-region temperature increase.

In laser structures, where diffusion of minority carriers within the active region before their recombination (radiative or nonradiative) plays an important role, i.e., in lasers without radial carrier confinement mechanisms, it is more justified to associate the above heat generation with carrier concentration distribution rather than with a current density profile. Each act of nonradiative recombination is followed by heat generation of energy equal to about $h\nu$, where h is the Planck constant, and ν is the laser radiation frequency. Generally, especially in lasers with quantum-well active regions, this energy may be different than the energy eU_{pn}, where e is the unit charge. Then this heat generation consists of two processes – carrier thermalization and carrier recombination, whose sum must give the supply energy eU_{pn}. Even if they are separated in space, they both occur inside or very close to the active region. Therefore we may neglect their separation. Equation (35) will be then modified to the following form:

$$g_A = \frac{P_A}{N_{A,e}} n_{th,e}(j)(1 - \eta_{sp} f_T) \qquad j > j_{th,e}, \tag{36}$$

where P_A stands for the total effective threshold power generated (mainly nonradiatively) inside the active region, defined as

$$P_A = 2\pi \int_0^{r_s} U_{pn}(r) j_{th,e}(r)\, r\, dr \qquad [\mathrm{W}], \tag{37}$$

and $N_{A,e}$ is the total carrier number composing the effective threshold within the active region:

$$N_{A,e} = 2\pi d_A \int_0^{r_S} n_{th,e}(r)\, r\, dr, \tag{38}$$

with r_S the structure radius and $n_{th,e}$ the threshold effective carrier concentration (associated with $j_{th,e}$). In the above, we assume that all the heat generation inside the active region is distributed uniformly over $N_{A,e}$ recombining carriers.

4.3.2. *Absorption of laser radiation*

Absorption of laser radiation is associated with generation of heat of a volume density g_{abs}:

$$g_{abs} = p_{int}\alpha \qquad [W/cm^3], \tag{39}$$

where α is the absorption coefficient (different in various layers) for the laser radiation and p_{int} is its internal density inside the resonator:

$$p_{int}(r) = U_{pn}(r)\,[j(r) - j_{th,e}(r)] \qquad [W/cm^2]. \tag{40}$$

Note that according to the suggestions of Petermann [1991], the internal quantum efficiency for stimulated emission is taken equal to unity in the above equations.

4.3.3. *Absorption of spontaneous radiation*

In contrast to a stimulated radiation, spontaneous radiation is always emitted isotropically in all directions. Some part of its vertical component is reflected at boundaries between the active region and the cladding layers as well as from the resonator mirrors and is effectively absorbed within the active region, which was already taken into account in § 4.3.1. The in-plane emission, on the other hand, can be amplified significantly by stimulated processes within the active region Onischenko and Sarma [1997]).

Spontaneous radiation reaches sometimes distant regions of the laser. Its absorption may, therefore, occur in many different places. For that reason, a distribution of heat generation associated with this absorption is usually difficult to determine, unless the active region is surrounded by highly absorptive areas, as in PITSELs (§ 4.3.1).

4.3.4. *Joule heating*

In all layers, a current flow is followed by generation of the volume Joule heating g_J:

$$g_J = j^2\rho \qquad [W/cm^3], \tag{41}$$

where ρ stands for the electrical resistivity (in Ωcm).

A current flow through a potential barrier as contacts and heterobarriers is in turn followed by a generation of the Joule heat of a surface density q_B:

$$q_B = j^2 R_B \qquad [W/cm^2], \tag{42}$$

where R_B is the specific contact resistance (in Ωcm^2) of the barrier.

4.4. SELF-CONSISTENT APPROACHES

The thermal conductivity, k, of a semiconductor material is a temperature-dependent parameter. This dependence is especially important for relatively high temperature increases because of its strong nonlinear behavior. It may be easily taken into account with the aid of the Kirchhoff transformation (Carslaw and Jaeger [1988], p. 11):

$$\Theta = \frac{1}{k(T_R)} \int_{T_R}^{T} k(T)\, dT. \tag{43}$$

Then all of the calculations are carried out for the transformed temperature Θ; i.e., as if the thermal conductivity were constant. These temperature profiles should afterwards be recalculated for the temperature-dependent thermal conductivity case, using the inverse transformation. In eq. (43), T_R stands for the reference temperature. Usually we assume it to be equal to the lowest temperature inside a semiconductor medium; i.e.,

$$T_R = T_{amb} + \Delta T_{HS} + \Delta T_C. \tag{44}$$

The detailed form of the reverse transformation depends on a functional dependence $k(T)$ in a temperature range of interest. At temperatures around and

over room temperature, for example, the thermal conductivity of GaAs may be expressed as (Amith, Kudman and Steigmeier [1965]):

$$k_{\mathrm{GaAs}}(T) = 0.44 \cdot (300/T)^{1.25} \quad [\mathrm{W/cm\,K}], \tag{45}$$

and that of InP as

$$k_{\mathrm{InP}}(T) = \left[\frac{1.47 + (T - 300)}{117}\right]^{-1} \quad [\mathrm{W/cm\,K}]. \tag{46}$$

Equation (46) was obtained on the basis of fig. 1, published by Kudman and Steigmeier [1964]. Introducing successively eqs. (45) and (46) to eq. (43), we get the inverse transformation formula for GaAs in the following form:

$$T = T_{\mathrm{R}}\left[1 - \frac{k_{\mathrm{GaAs}}(T_{\mathrm{R}})\Theta}{528}\left(\frac{T_{\mathrm{R}}}{300}\right)^{4}\right]^{1/4} = T_{\mathrm{R}}\left[1 - \frac{\Theta}{1200}\left(\frac{T_{\mathrm{R}}}{300}\right)^{11/4}\right]^{-1/4}, \tag{47}$$

and that of InP as

$$T = 128 + (T_{\mathrm{R}} - 128)\exp\left[\frac{k_{\mathrm{InP}}(T_{\mathrm{R}})\Theta}{11\,700}\right]. \tag{48}$$

In all the above equations, temperature should be put in Kelvin.

Thermal diffusivities κ of semiconductor materials are also dependent on temperature. It is not, however, possible to take into consideration at the same time the temperature dependencies of both these thermal material parameters; i.e., $k(T)$ and $\kappa(T)$, using a transformation analogous to that presented above. Therefore, in detailed analytical transient thermal analyses, i.e., when both the above parameters should be included, another method of calculation, namely the so-called staircase approach, is recommended. For each time step, Δt, temperature profiles are determined using values of k and κ found in a previous calculation step, starting from an initial temperature of the entire structure equal to that of the ambient (T_{amb}).

There is still another temperature-dependent term in the thermal conduction equation (20) – including the volume power density of a heat generation; i.e., g. This is because many material parameters (such as electrical resistivities, refractive indices, absorption coefficients) and device parameters (such as threshold current and quantum efficiencies), which influence the heat generation, are strongly dependent on temperature. The above may be included in the model using the self-consistent approach, when in successive iteration loops of the

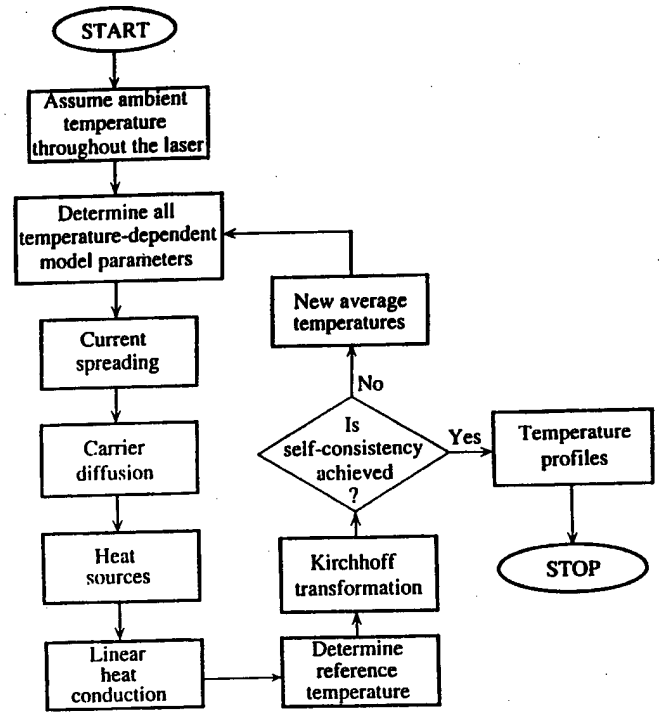


Fig. 14. Flow chart of the thermal–electrical self-consistent calculations in VCSELs.

calculation values of the above parameters determined in the previous loop are used. Self-consistency is assumed to be reached when differences between results of calculations obtained in two consecutive loops are below given limits.

Strictly speaking, not only material and device parameters but also distributions of current densities and carrier concentrations within the whole laser structure are dependent on current temperature profiles. This is because the current spreading and the carrier diffusion phenomena are temperature-dependent processes. Therefore in more exact thermal analyses of VCSELs, the thermal–electrical self-consistent procedure is recommended (fig. 14), in which mutual interactions between thermal and electrical processes in the laser are included.

Even more exact is the thermal–electrical–optical self-consistent approach in which optical processes, with their mutual interactions with both the thermal and electrical processes, are also taken into consideration. The full picture of mutual

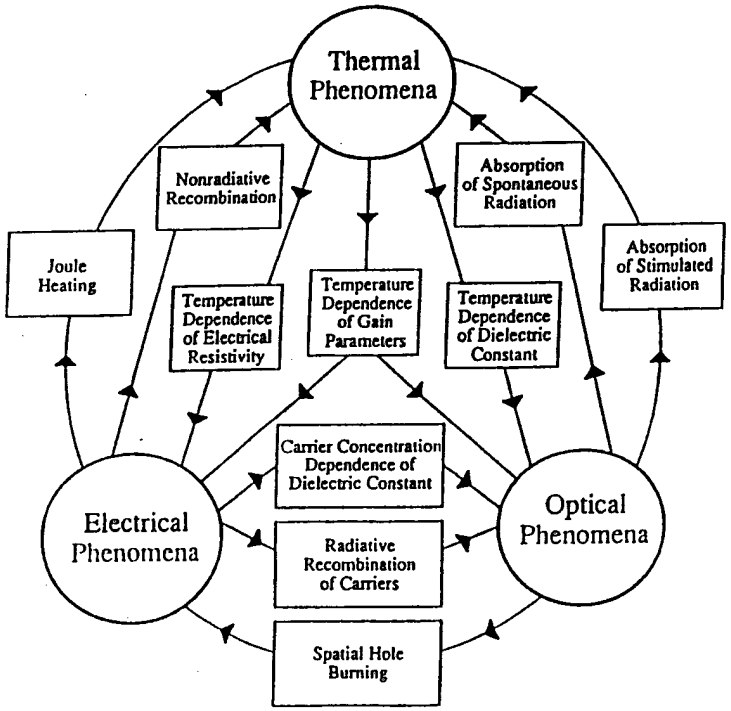


Fig. 15. Mutual interactions between thermal, electrical, and optical processes in semiconductor lasers.

interactions between all these processes is shown in fig. 15. In VCSELs with strained active regions, additionally mechanical processes should be included.

§ 5. Comprehensive Thermal Models of VCSELs

The key parameter used in all simplified treatments of steady-state thermal problems in diode lasers is the thermal resistance R_{TH} (in K/W), defined as the ratio of the average active-region temperature increase $\Delta T_{A,av}$ to the total dissipated thermal power Q_T (Joyce and Dixon [1975], Manning [1981]):

$$R_{TH} = \frac{\Delta T_{A,av}}{Q_T}. \tag{49}$$

It should be noted that although the thermal resistance is a very useful parameter to compare the thermal properties of various devices, it may sometimes give misleading information. Consider, for example, a device with a very poor electrical contact between the device chip and the heat sink. The resultant heat, generated at the laser/heat sink interface, would be very efficiently extracted by the heat sink (assuming it is made of a high thermal conductivity material), so its influence on the active-region heating would be relatively small. However, the heat generated near the heat sink would still contribute to the total heat power Q_T. Therefore, when eq. (49) is used to determine R_{TH}, such a device would have lower thermal resistance than a well mounted laser with low-electrical resistance contact.

Thermal–electrical behavior of VCSELs is described by a coupled system of partial differential equations with complicated boundary conditions. The approaches towards solving these equations can be classified into two major types: analytical and numerical models. In analytical models, the solution is written in the form of an analytical expression, usually at the expense of some approximations imposed by the postulated form of the solution. In numerical models, no functional form of the solution is sought, hence details of the device structure can be rendered more faithfully. However, in contrast to analytical models where the accuracy of the solution can be easily controlled, it is more difficult to verify that the purely numerical solution does not contain significant errors. Details of hitherto known analytical and numerical comprehensive thermal VCSEL models are compared in table 8a and table 8b, respectively.

5.1. COMPREHENSIVE ANALYTICAL MODELS

5.1.1. Multilayer radially uniform structures

The first comprehensive approach to the thermal properties of VCSELs was developed by Kinoshita, Koyama and Iga [1987], Iga, Koyama and Kinoshita [1988], and Iga and Koyama [1990], who assumed only a single flat-disk heat source located in the center of the active region, but considered the influence of multilayer device structure on the 2D heat-flux spreading. The heat exchange with the exterior is assumed to take place only through the heat sink, with adiabatic boundary conditions for all remaining surfaces defining the device. For each layer, assumed to be radially uniform, 2D azimuthally symmetric temperature profiles are expressed in terms of infinite series containing the Bessel and hyperbolic functions. The expansion coefficients are found by imposing the boundary conditions of continuity of the temperature and heat flux profiles across the interfaces between the layers. The method is analogous to that proposed originally by Joyce and Dixon [1975] for edge-emitting lasers. The main

Table 8a
Analytical comprehensive thermal VCSEL models

Ref.	Year	Structure	Method	Current spreading	Carrier diffusion	Structure modeling	Heat sources[a]						Self-consistency[b]			
							NR	SP	ST	VJ	BJ	CJ	$k(T)$	Th-El	Th-Op	El-Op
1	1987	DMEWL	Fourier	–	–	crude	+	–	–	–	–	–	–	–	–	–
2	1991	DMEWL	Green	+	–	good	+	+	–	+	–	+	+	+	+[c]	–
3	1992	PITSEL	Fourier	+	–	exact	+	+	+	+	+	–	+	+	+[c]	–
4	1995	DMEWL	Green	+	–	good	+	+	+	+	–	+	+	+	+[c]	–
5	1995	PITSEL	Green	+	–	fair	+	+	–	+	–	–	–	–	–	–

[a] Abbreviations: NR, nonradiative recombination; SP, absorption of spontaneous radiation; ST, absorption of stimulated radiation; VJ, volume Joule heating; BJ, barrier Joule heating at heterojunctions; CJ, barrier Joule heating at the p-side contact.
[b] Abbreviations: $k(T)$, temperature-dependent thermal conductivity; Th-El, thermal–electrical; Th-Op, thermal–optical; El-Op, electrical–optical.
[c] Partly.

References

(1) Kinoshita, Koyama and Iga [1987]
(2) Nakwaski and Osiński [1991a,b, 1993]
(3) Nakwaski and Osiński [1992c, 1994]
(4) Osiński and Nakwaski [1995b]
(5) Zhao and McInerney [1995]

Table 8b
Numerical comprehensive thermal VCSEL models

Ref.	Year	Structure	Method[a]	Current spreading	Carrier diffusion	Structure modeling	Heat sources[b]						Self-consistency[b]			
							NR	SP	ST	VJ	BJ	CJ	$k(T)$	Th-El	Th-Op	El-Op
1	1993	UMEWL	FDM	–	–	fair	+	?	–	–	–	–	–	–	–	–
2	1993	TBEML	FEM	+	–	exact	+	+	+	+	+	–	+	–	–	–
3	1994	HMML	FEM	+	–	fair	+	+	–	–	–	–	–	–	–	–
4	1994	TEML	CVM	+	–	fair	+	+	+	+	+	–	–	–	–	–
5	1994	PITSEL	FEM	+	–	fair	+	+	+	+	+	+	–	+	+	–
6	1995	DMEWL	FEM	+	–	exact	+	+	–	+	–	+	+	+	–	–
7	1995	DMEWL	FEM	–	–	fair	+	+	–	–	–	–	–	–	–	–
8	1995	PITSEL	FEM	+	+	exact	+	+	+	+	+	+	+	+	+	–
9	1996	PITSEL	FEM	+	+	fair	+	+	+	+	–	–	–	–	+	+

[a] Abbreviations: FDM, finite-difference method; FEM, finite-element method; CVM, control-volume method.
[b] See table 8a.

References

(1) Shimizu, Babic, Dudley, Jiang and Bowers [1993]
(2) Michalzik and Ebeling [1993]
(3) Piprek and Yoo [1994]
(4) Norris, Chen and Tien [1994], Chen, Hadley and Smith [1994], and Chen [1995]
(5) Piprek, Wenzel and Sztefka [1994], Piprek, Wenzel, Wünsche, Braun and Henneberger [1995]
(6) Rahman, Lepkowski and Grattan [1995]
(7) Baba, Kondoh, Koyama and Iga [1995a]
(8) Sarzała, Nakwaski and Osiński [1995]
(9) Hadley, Lear, Warren, Choquette, Scott and Corzine [1996]

limitation of this approach is that it neglects any structural nonuniformity in the radial direction. Consequently, in the case of buried-heterostructure DMEWLs (e.g., Koyama, Kinoshita and Iga [1989], see also fig. 3 and table 1), to which it was applied, neither the lateral confining layers nor the dielectric mirrors on the heat-sink side could be accounted for.

The model of Kinoshita, Koyama and Iga [1987], Iga, Koyama and Kinoshita [1988], and Iga and Koyama [1990] is not self-consistent; i.e., the effect of calculated temperature profiles on material parameters and heat source efficiencies was not considered. In VCSELs, where heating is much more intense than in EELs, non-self-consistent models can underestimate the severity of the thermal problems. The first self-consistent treatment of thermal problems in VCSELs (Nakwaski and Osiński [1991a,b]) was applied to buried-heterostructure DMEWL devices and is discussed in § 5.1.2. As a matter of fact, this was the very first self-consistent thermal–electrical model applied to any semiconductor laser, including the edge emitters and high-power laser arrays.

While the radially nonuniform DMEWL structure is too complex for the model of Kinoshita, Koyama and Iga [1987], Iga, Koyama and Kinoshita [1988], and Iga and Koyama [1990] to give accurate results, the same model can be applied to radially uniform structures, such as PITSELs. The thermal conductivity of highly electrically-resistive regions which funnel the injected current into the active region is practically unaffected by the implantation process (Vook [1964]), which combined with the planarity of the PITSEL structure, makes it particularly suitable to be modeled analytically.

We have incorporated an analytical approach similar to that of Kinoshita, Koyama and Iga [1987] in the analysis of PITSELs, as a portion of our comprehensive, thermal–electrical self-consistent model (Nakwaski and Osiński [1992a,c, 1994]), featuring the temperature-dependent distribution of multiple heat sources, and the temperature dependence of material and device parameters. In the analysis, all important heat-generation mechanisms are taken into account, including nonradiative recombination, reabsorption of spontaneous radiation in the active region, free-carrier absorption of laser radiation, volume Joule heating and absorption of stimulated radiation in all the layers, and barrier Joule heating at heterojunctions. These distributed heat-generation processes are lumped into three uniform flat-disk heat sources, each of the active-region diameter $D_A = 2r_A$, located in the centers of the active region and two Bragg mirrors. An analytical solution is obtained for the entire structure separately for each heat source. Using the superposition principle, a cumulative temperature distribution in the whole volume of the device is determined by adding together contributions from all heat sources. Subsequently, a self-consistent solution is found with the

aid of an iteration procedure, taking into account the temperature dependencies of material and device parameters, including thermal conductivities, threshold current, electrical resistivities, voltage drop at the p–n junction, free-carrier absorption as well as internal and external differential quantum efficiencies. The flow chart of numerical calculations of this type is shown in fig. 14, where, however, carrier diffusion is included additionally. Note that large temperature variations in VCSELs affects substantially their lasing characteristics, because of strongly nonlinear thermal–electrical interactions, eventually leading to thermal runaway.

For each flat heat source situated between the jth and the $(j+1)$th layers and for each ith layer, we are looking for the transformed temperature distribution in the following form:

$$\Theta_{j,i}(r,z) = T_{amb} + \Delta T_{HS} + \Delta T_C + \alpha_{j,i,0} + \beta_{j,i,0}(z - z_{i-1}) + \sum_{n=1}^{\infty} \{\alpha_{j,i,n}\cosh[\kappa_n(z - z_{i-1})] + \beta_{j,i,n}\sinh[\kappa_n(z - z_{i-1})]\} \frac{J_0(\kappa_n r)}{J_0^2(\kappa_n r_S)}, \tag{50}$$

where r_S is the structure radius, z_i is the coordinate of the top boundary of the ith layer, $z_{i-1} \leqslant z_i$ and κ_n are successive roots of the equation:

$$J_1(\kappa_n r_S) = 0. \tag{51}$$

J_0 and J_1 are the zeroth-order and the first-order Bessel functions of the first kind, while $\alpha_{j,i,n}$ and $\beta_{j,i,n}$ are the expansion coefficients to be determined below. Cumulative profiles of the transformed temperature $\Theta(r,z)$ should be recalculated using the reverse transformation (cf. § 4.4).

The $\alpha_{j,i,n}$ and $\beta_{j,i,n}$ coefficients are determined from the boundary conditions of temperature profiles and heat fluxes at all the boundaries between various layers. For temperature profiles, we obtain from eq. (50):

$$\alpha_{j,i,0} + \beta_{j,i,0} d_i = \alpha_{j,i+1,0}, \tag{52}$$

$$\alpha_{j,i,n}\cosh(\kappa_n d_i) + \beta_{j,i,n}\sinh(\kappa_n d_i) = \alpha_{j,i+1,n} \qquad \text{for } n \geqslant 1, \tag{53}$$

where d_i is the thickness of the ith layer, whereas for heat fluxes we have:

$$k_i\beta_{j,i,0} = \begin{cases} k_{i+1}\beta_{j,i+1,0} & \text{for } i \neq j, \\ k_{i+1}\beta_{j,i+1,0} + q_j(r_A/r_S)^2 & \text{for } i = j, \end{cases} \tag{54}$$

$$k_i[\alpha_{j,i,n}\sinh(\kappa_n d_i)+\beta_{j,i,n}\cosh(\kappa_n d_i)] = \begin{cases} k_{i+1}\beta_{j,i+1,n} & \text{for } i\neq j \wedge n\geqslant 1, \\ k_{i+1}\beta_{j,i+1,n}+\dfrac{2q_j r_A J_1(\kappa_n r_A)}{(\kappa_n r_S)^2} & \text{for } i=j\wedge n\geqslant 1. \end{cases} \tag{55}$$

where k_i is the ith layer thermal conductivity and q_j stands for the density of a given heat flux generated at the boundary between the jth and the $(j+1)$th layers.

From the boundary conditions (24) and (25), we have:

$$\alpha_{j,1,n}=0 \quad \text{for } n\geqslant 0, \tag{56}$$

and

$$\beta_{j,N,0}=0, \tag{57}$$

$$\alpha_{j,N,n}\sinh(\kappa_n d_N)+\beta_{j,N,n}\cosh(\kappa_n d_N)=0 \quad \text{for } n\geqslant 1. \tag{58}$$

Using eq. (54), we can write

$$\beta_{j,i,0}=\begin{cases}\left(\dfrac{q_j}{k_i}\right)\left(\dfrac{r_A}{r_S}\right)^2 & \text{for } 1\leqslant i\leqslant j, \\ 0 & \text{for } j<i\leqslant N,\end{cases} \tag{59}$$

where N is the total number of structure layers and hence, from eq. (52), we get

$$\alpha_{j,i,0}=q_j\left(\frac{r_A}{r_S}\right)^2\sum_{i'=1}^{\min(i-1,j)}\left(\frac{d_{i'}}{k_{i'}}\right). \tag{60}$$

We now introduce the $r_{j,i,n}$ coefficients, defined as

$$r_{j,i,n}=\frac{\beta_{j,i,n}}{\alpha_{j,i,n}} \quad \text{for } i\neq 1. \tag{61}$$

Then, taking eqs. (53) and (55) for $i\neq j$, we obtain

$$r_{j,i+1,n}=\frac{k_i}{k_{i+1}}\frac{\tanh(\kappa_n d_i)+r_{j,i,n}}{1+r_{j,i,n}\tanh(\kappa_n d_i)} \quad \text{for } i\neq j, \tag{62}$$

and from eq. (58) we have:

$$r_{j,N,n}=-\tanh(\kappa_n d_N) \quad \text{for } n\geqslant 1. \tag{63}$$

Again using eqs. (53) and (55) for $i\neq j$, but now for $i=1$, and taking advantage of eq. (56), we get:

$$\beta_{j,1,n}=\alpha_{j,2,n}\,\mathrm{cosech}(\kappa_n d_1) \quad \text{for } n\geqslant 1, \tag{64}$$

and

$$r_{j,2,n}=\left(\frac{k_1}{k_2}\right)\coth(\kappa_n d_1) \quad \text{for } n\geqslant 1. \tag{65}$$

Now we can determine for $2\leqslant i\leqslant N$ all $r_{j,i,n}$ working inward from $r_{j,2,n}$ and $r_{j,N,n}$. To determine all $\alpha_{j,i,n}$, we once more return to eqs. (53) and (55), but this time for $i=j$. After some mathematical manipulation, we find:

$$\alpha_{j,j,n}=\frac{2q_j r_A J_1(\kappa_n r_A)}{\kappa_n^2 r_S^2\left[A_{j,j,n}\sinh(\kappa_n d_j)+B_{j,j,n}\cosh(\kappa_n d_j)\right]} \quad \text{for } n\geqslant 1, \tag{66}$$

with

$$A_{j,j,n}=k_j-k_{j+1}r_{j,j,n}r_{j,j+1,n}, \tag{67}$$

$$B_{j,j,n}=k_j r_{j,j,n}-k_{j+1}r_{j,j+1,n}. \tag{68}$$

The remaining $\alpha_{j,i,n}$ coefficients can be determined from eq. (53), which after using the $r_{j,i,n}$ coefficients can be rewritten in the following form:

$$\alpha_{j,i+1,n}=\alpha_{j,i,n}\left[\cosh(\kappa_n d_i)+r_{j,i,n}\sinh(\kappa_n d_i)\right] \quad \text{for } n\geqslant 1. \tag{69}$$

All the $\beta_{j,i,n}$ coefficients can then be found from eq. (61).

Figure 16 shows the pumping current dependence of radial temperature profiles in the midplane of the active region calculated for a 35-μm PITSEL (Zhou, Cheng, Schaus, Sun, Zheng, Armour, Hains, Hsin, Myers and Vawter [1991]). The total number of layers in the simulation, from the highly doped cap layer on the p-type DBR side to the solder contact below the substrate, including the linearly graded interfaces, is 284. Note that the CW threshold current for this device is 10.2 mA, hence the lowest profile in fig. 16 shows the temperature profile just above threshold. Superlinear increase in the temperature at the center of the active region ($r=0$) in response to increased pumping

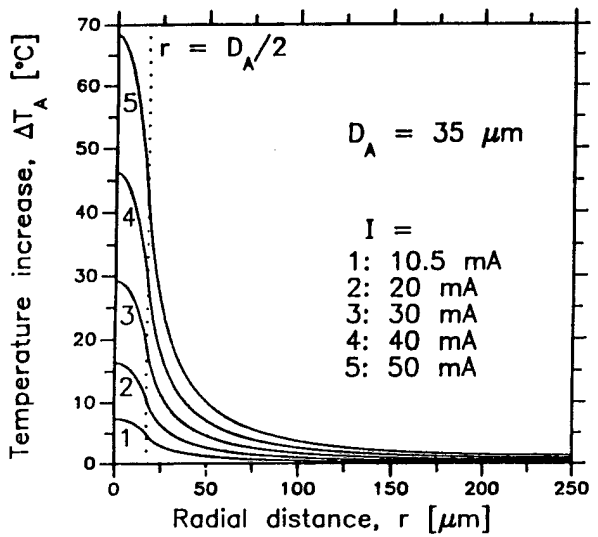


Fig. 16. Radial temperature profiles in the plane containing the active region of a 35 μm GaAs/AlGaAs/AlAs PITSEL for various CW pumping currents, calculated using self-consistent thermal–electrical model. Chip diameter D_S is 500 μm.

current can be seen clearly. Consequently, the temperature profile becomes increasingly inhomogeneous, with a large temperature step between the center and the edge ($r = r_A$) of the active region. This results in the creation of a strong thermal waveguide (cf. § 3.3), with the refractive index step as large as 1.4×10^{-2} at $I = 50$ mA, which corresponds to an index step that would have been obtained if the active region were surrounded by $Al_{0.02}Ga_{0.98}As$ rather than GaAs. On the other hand, since the slope dT/dr is a measure of the lateral heat flow, it is evident that the importance of 2D heat flow increases with the pumping current.

Pumping-current evolution of the relative share of three major heat sources in the same PITSEL device is illustrated in fig. 17. The active-region heating is a dominant heat source near threshold, but gradually the p-type mirror heating takes over, due to its roughly quadratic dependence on the pumping current. The situation reverses again near the thermal runaway limit, where we observe an accelerated increase in relative importance of the active-region heating, caused primarily by nonlinear processes intensifying the nonradiative recombination.

Figure 18 illustrates the current dependence of the thermal resistance, R_{TH}, as defined in eq. (49), for PITSELs of the same vertical structure as in figs. 16 and

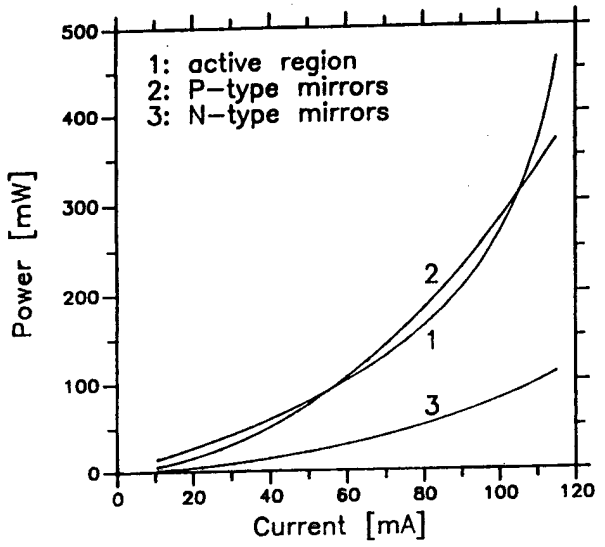


Fig. 17. Yields of three major heat sources in the 35 μm-diameter PITSEL of fig. 16 shown as a function of the pumping current.

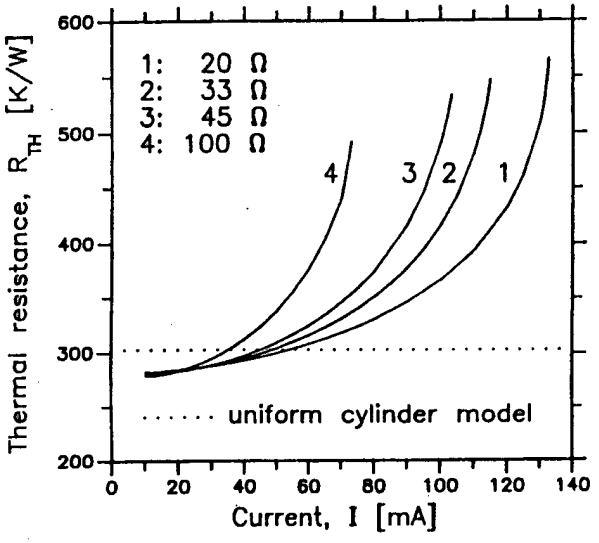


Fig. 18. Pumping-current dependence of thermal resistance R_{TH} for 35 μm-diameter PITSELs with various electrical series resistances. Curve 2 corresponds to the device simulated in figs. 16 and 17 and reported by Zhou, Cheng, Schaus, Sun, Zheng, Armour, Hains, Hsin, Myers and Vawter [1991].

17. In addition to the experimentally realized device with the series resistance $R_{s,0} = 33\,\Omega$ (curve 2), we also consider hypothetical devices with lower (curve 1) or larger (curves 3 and 4) series resistances. Corresponding threshold voltages are readjusted using the following equation:

$$U_{th}(R_s) = U_{pn} + [U_{th}(R_{s,0}) - U_{pn}] \left(\frac{R_s}{R_{s,0}} \right), \tag{70}$$

where U_{pn} is the contribution of the p–n junction to the threshold voltage, assumed to be independent of the series resistance R_s, and determined from the I–V characteristic of the 33 Ω device. No variation of pulsed threshold current with R_s is assumed to take place. The CW threshold, however, does depend on R_s due to changing temperature of the active region, although for the devices considered here these changes are very small, primarily due to the high value of $T_0 = 210\,K$ (Hasnain, Tai, Dutta, Wang, Wynn, Weir and Cho [1991]) (cf. table 6b, p. 193) assumed in the calculations.

Although R_{TH} is usually treated as a constant parameter with a value characteristic of any particular device, (cf. table 4, p. 187), it is clear that due to nonlinear processes it varies substantially with the pumping current (see Nakwaski and Osiński [1992b]). The relatively high values of R_{TH} displayed in fig. 18 are caused primarily by the "junction-up" configuration of PITSELs. The horizontal dotted line represents the thermal resistance calculated using the simplified uniform cylinder model (Nakwaski and Osiński [1992d]). It is clear that this model represents a reasonable approximation only in the linear regime, near the lasing threshold.

The effect of the series electrical resistance on the average temperature increase of the active region $\Delta T_{A,av}$, used in calculation of the thermal resistance R_{TH}, is illustrated in fig. 19. Due to nonlinear processes, the penalty for a too high series resistance of the device increases rapidly with the pumping current. The operating current range of the 100 Ω device is nearly half that of the low-series-resistance (20 Ω) device.

Zhao and McInerney [1995] have recently reported an analytical solution of the thermal conduction equation for a GaAs/AlGaAs PITSEL volume using the Green's function approach proposed for surface-emitting LEDs by Nakwaski and Kontkiewicz [1985]. In the model, the complex multilayer VCSEL structure seems to be replaced with an equivalent uniform structure, although the authors did not mention anything about it: in the solution, average (?) values of thermal conductivity and diffusivity are used for the entire VCSEL volume. The model would be exact if Green's function solutions (with unknown expansion coefficients) were assumed separately for each uniform structure layer. Then

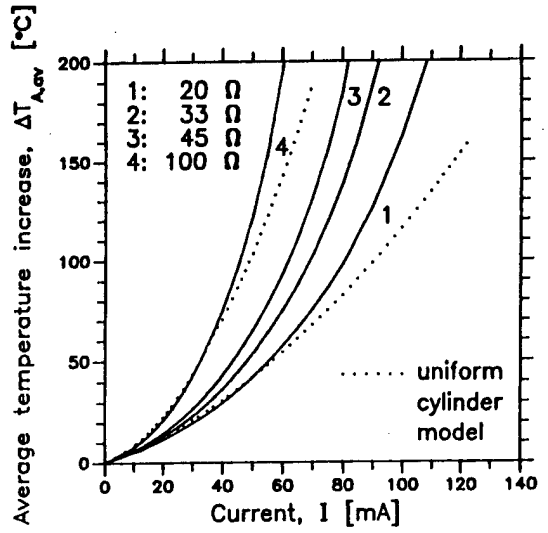


Fig. 19. Pumping-current dependence of the average active-region temperature increase $\Delta T_{A,av}$ in a 35 μm-diameter PITSEL. Curve 2 corresponds to the device reported by Zhou, Cheng, Schaus, Sun, Zheng, Armour, Hains, Hsin, Myers and Vawter [1991] and simulated in figs. 16 and 17.

the coefficients would be found from continuity conditions at all layer edges for profiles of both temperature and heat flux, similarly as in the approaches proposed for VCSELs by Nakwaski and Osiński [1992c] and earlier for EELs by Joyce and Dixon [1975]. As heat sources, Zhao and McInerney considered nonradiative recombination and absorption of spontaneous emission in the active region and volume Joule heating in layers of current spreading. Unfortunately, they did not solve exactly the current-flow process, using a simplified approach with two adjusting parameters of values difficult to estimate. The temperature dependence of all model parameters was neglected. Because of all the above facts, the exactness of the model seems to be very limited. Nevertheless, the model was used later in an interesting analysis of transverse modes in VCSELs (Zhao and McInerney [1996]).

5.1.2. Multilayer radially nonuniform structures

5.1.2.1. GaAs/AlGaAs lasers. Most VCSEL structures are either nonplanar, or contain laterally nonuniform layers confining the carriers, defining the waveguide/antiguide, or acting as reflectors. The analytical approach of § 5.1.1

may only be used for such structures for which the radially nonuniform layers can be replaced with thermally equivalent uniform layers.

An alternative analytical approach that takes into consideration lateral nonuniformity without requiring thermal equivalencies in the radial direction has been developed by Nakwaski and Osiński [1991a,b, 1993] and applied to buried-heterostructure DMEWLs (Koyama, Kinoshita and Iga [1989]) (see fig. 3 and table 1). First, current spreading between the etched-well substrate and the heat sink is found using approximate analytical formulae (Bugajski and Kontkiewicz [1982], Nakwaski and Osiński [1993]). Realistic, radially nonuniform, multiple heat sources associated with different layers of the device are considered, each with axially uniform distribution across the layer thickness. The following heat sources are included: the active region, the N-type and the P-type cladding layers and the p-side contact resistance. The device is then divided into two concentric cylinders (internal with $0 \leqslant r \leqslant D_A/2$ and external with $D_A/2 < r \leqslant D_S/2$) such that within each cylinder all layers are radially uniform. While the dividing wall at $r = D_A/2$ is considered to be thermally insulating, prior to finding the solution of the heat spreading problem the heat generated by each source is redistributed between the two cylinders using an electrical analog model (Nakwaski and Osiński [1991a]). Due to the smaller size of the inner cylinder, the redistribution of heat within that cylinder, containing the active region, is considered to be more accurate. For each cylinder, the multilayer structure is replaced with a thermally equivalent medium and an analytical solution for the temperature profiles is found for each ith heat source using the Green's function method in the following form:

Region I :

$$\Theta_{i,\mathrm{I}}(r, z_{\mathrm{eq,I}}) = T_R + \sum_{m=1}^{\infty} \sum_{n=1}^{\infty} A_{nm,i,\mathrm{I}} \, \mathrm{J}_0\left(\frac{j_{1,n} r}{r_A}\right) \sin\left(\frac{c_m z_{\mathrm{eq,I}}}{d_{\mathrm{eq,I}}}\right), \tag{71}$$

Region II :

$$\Theta_{i,\mathrm{II}}(r, z_{\mathrm{eq,II}}) = T_R + \sum_{m=1}^{\infty} \sum_{n=1}^{\infty} A_{nm,i,\mathrm{II}} \, \mathrm{J}_0\left(\frac{j_{1,n}(r - r_A)}{r_S - r_A}\right) \sin\left(\frac{c_m z_{\mathrm{eq,II}}}{d_{\mathrm{eq,II}}}\right). \tag{72}$$

In the above equations, T_R stands for the reference temperature equal to the temperature at the bottom edge of the laser crystal, r_A and r_S are the radii of the active region and of the laser structure, respectively, $j_{1,n}$ ($n = 1, 2, 3, \ldots$) is the nth zero of the first-order Bessel function of the first kind, $c_m = \pi(m - \frac{1}{2})$ ($m = 1, 2, 3, \ldots$) is the $(m+1)$-st zero of the cosine function, $z_{\mathrm{eq},\alpha}$ denotes the z coordinate after the space transformation, and $d_{\mathrm{eq},\alpha}$ is its value for the bottom of

the etched well (the n-GaAs/N-AlGaAs interface), both for Region α ($\alpha = \mathrm{I}, \mathrm{II}$). The coefficients $A_{nm,i,\mathrm{I}}$ and $A_{nm,i,\mathrm{II}}$ are calculated using the following formulae:

$$A_{nm,i,\mathrm{I}} = \frac{4\left[\cos\left(\frac{c_m z_{\mathrm{eq},i-1,\mathrm{I}}}{d_{\mathrm{eq,I}}}\right) - \cos\left(\frac{c_m z_{\mathrm{eq},i,\mathrm{I}}}{d_{\mathrm{eq,I}}}\right)\right]}{r_A^2 k_{\mathrm{eq,I}} \mathrm{J}_0^2(j_{1,n}) c_m \left[\left(\frac{j_{1,n}}{r_A}\right)^2 + \left(\frac{c_m}{d_{\mathrm{eq,I}}}\right)^2\right]} \times \int_0^{r_A} g_{i,\mathrm{eq},is}(r) \, \mathrm{J}_0\left(\frac{j_{1,n} r}{r_A}\right) r \, \mathrm{d}r, \tag{73}$$

$$A_{nm,i,\mathrm{II}} = \frac{4\left[\cos\left(\frac{c_m z_{\mathrm{eq},i-1,\mathrm{II}}}{d_{\mathrm{eq,II}}}\right) - \cos\left(\frac{c_m z_{\mathrm{eq},i,\mathrm{II}}}{d_{\mathrm{eq,II}}}\right)\right]}{(r_S^2 - r_A^2) \, k_{\mathrm{eq,II}} \, \mathrm{J}_0^2(j_{1,n}) \, c_m \left[\left(\frac{j_{1,n}}{r_S - r_A}\right)^2 + \left(\frac{c_m}{d_{\mathrm{eq,II}}}\right)^2\right]} \times \int_{r_A}^{r_S} g_{i,\mathrm{eq},is}(r) \, \mathrm{J}_0\left(\frac{j_{1,n}(r - r_A)}{r_S - r_A}\right) r \, \mathrm{d}r, \tag{74}$$

where $k_{\mathrm{eq},\alpha}$ stands for the equivalent thermal conductivity of Region α, $z_{\mathrm{eq},i,\alpha}$ is the transformed coordinate of the top of the ith layer in Region α, and $g_{i,\mathrm{eq},is}$ is the equivalent distribution of the ith heat source after its redistribution.

In each loop of the self-consistent calculations, the cumulative profiles of transformed temperature are found using the superposition principle by adding together contributions from all heat sources. Then, the actual temperature profiles are determined by performing the inverse Kirchhoff transformation (cf. § 4.4). At the boundary between the two cylinders, the temperature profiles are matched by adjusting the profile of the outer cylinder to the level of the inner cylinder. The adjustment only affects the near vicinity of the boundary, on the side of $r > D_A/2$.

A very important feature of the model is its self-consistency (cf. § 4.4), which accounts for mutual interactions between thermal and electrical phenomena. In an iterative loop, temperature dependencies of many material and device parameters are considered, including thermal conductivity, electrical resistivity, threshold current, quantum efficiencies, and voltage drop at the p–n junction. Also, the temperature dependence of all important heat generation mechanisms is taken into account, including nonradiative recombination, absorption of spontaneous emission, as well as the Joule heating in all layers. The model described here represents the first application of a self-consistent approach to thermal problems in any semiconductor laser, including the edge emitters. We

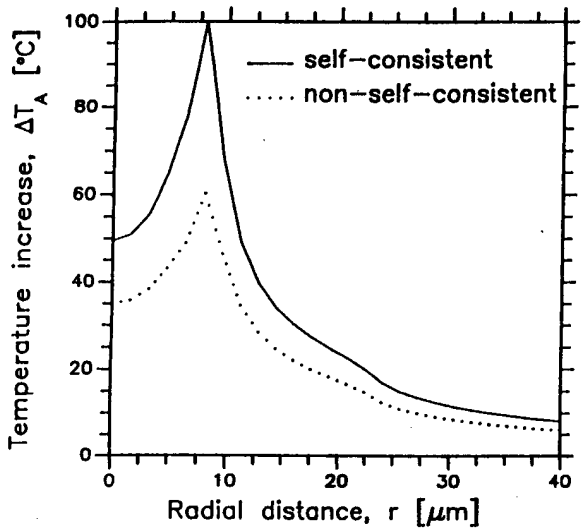


Fig. 20. Radial temperature profiles in the plane containing the active region of a 16 μm buried-heterostructure GaAs/AlGaAs DMEWL for the pumping current $I = 5I_{th,P}$ ($I_{th,P} = 38.4$ mA), where $I_{th,P}$ stands for the room-temperature pulsed threshold current, calculated using self-consistent thermal–electrical model (solid line) or taking the output of the first loop of the iterative process as a non-self-consistent solution (dotted line). Chip diameter D_S is 500 μm. The kink near $r = 23$ μm corresponds to the edge of the outer oxide layer.

have subsequently used the self-consistent approach in all of our comprehensive thermal modeling, including the model described in § 5.1.1.

The importance of self-consistency is illustrated in fig. 20, comparing radial temperature profiles in the active-region of a 16 μm GaAs/AlGaAs DMEWL, obtained using the self-consistent solution (solid line) and taking the output of the first loop of the iterative process as a non-self-consistent solution (dotted line). The device structure is similar to that of Koyama, Kinoshita and Iga [1989], except for an enhanced P-AlGaAs-cladding doping level of 2×10^{18} cm^{-3} which significantly improves device thermal properties (see Nakwaski and Osiński [1991a,c]). A pumping current of 192 mA was assumed, corresponding to 5 times the room-temperature pulsed threshold current. Clearly, at currents significantly above the threshold, the non-self-consistent solution grossly underestimates the active-region temperature increase.

Another interesting feature displayed in fig. 20 is the on-axis dip in the temperature profile, which is a direct consequence of nonuniform current injection. Associated with the dip is a thermally induced antiguide. Self-consistent analysis reported by Nakwaski and Osiński [1991a,c,d] and Osiński

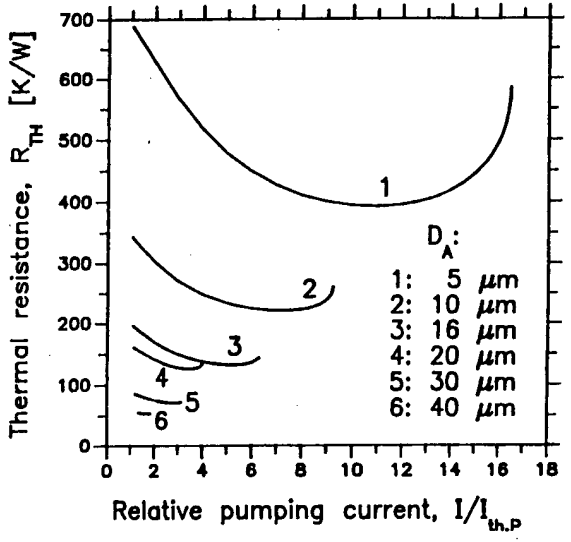


Fig. 21. Current-dependence of thermal resistance for buried-heterostructure GaAs/AlGaAs DMEWLs of various active-region diameters D_A.

and Nakwaski [1992] reveals that the sign of thermal waveguiding in the active region can be controlled by the N-AlGaAs doping level. Increasing the N-AlGaAs doping level beyond the value of $N = 7\times10^{17}$ cm^{-3} used in fig. 20, results in improved uniformity of the injected current density. This is manifested initially by flattening of the active-region temperature profile, and eventually by occurrence of a maximum at $r = 0$ for $N = 7\times10^{18}$ cm^{-3}. Freedom to engineer thermal waveguide in the active region is a characteristic feature of all etched-well VCSELs. Depending on the application, it might be more beneficial to focus the output light into a narrower spot or to spread it over a wider area without changing the active-region diameter. A thermal antiguide can also enhance single-transverse-mode operation (cf. § 3.3).

Figure 21 displays the current dependence of thermal resistance R_{TH} for DMEWL devices with various active-region diameters. Except for their lateral dimensions, the devices have the same structure as the device of fig. 20. Comparison with fig. 18 reveals a device-type-dependent variation of R_{TH} with current. While the $R_{TH}(I)$ curves increase monotonically in PITSELs, they have distinct minima in DMEWL, particularly for small-size emitters that can operate in CW mode far above threshold (curves 1 and 2 in fig. 21). These seemingly contradictory results can be understood by considering various factors that can influence the evolution of R_{TH} with current.

Figures 18 and 21 indicate that the thermal resistance in VCSELs is governed by a number of mechanisms that may affect the $R_{TH}(I)$ dependence in opposite ways. Variation of VCSEL thermal resistances with a pumping current is caused by a temperature dependence of thermal conductivities of constituent materials and by a change of intensities of various heat generation processes located in different places of a laser. The former mechanism always increases the value of R_{TH}, whereas the latter one may increase or decrease R_{TH} depending on the laser structure. This is a reason for a different $R_{TH}(I)$ shown in figs. 18 and 21.

An increase in the pumping current invariably heats up the device, which in turn reduces the thermal conductivity and increases the thermal resistance $R_{TH}^{(\alpha)}$ associated with every heat source α. This effect is nearly negligible at low currents, but steadily becomes more and more significant at higher currents, as evidenced in fig. 21 by a sudden increase in R_{TH} near the thermal runaway conditions. A more subtle effect is that of the heat source distribution. The thermal resistance of the device is obtained by summing together fractional resistances $R_{TH}^{(\alpha)}$ with weights Q_α/Q_T determined by the relative shares of corresponding heat sources. If the relative share of heat sources with high fractional resistances $R_{TH}^{(\alpha)}$ increases, the total thermal resistance will have a tendency to increase. As shown in fig. 18, this is obviously the case of PITSELs. However, if the relative share of heat sources with high fractional resistances $R_{TH}^{(\alpha)}$ decreases, the variation of total R_{TH} will depend on which of the two opposite mechanisms prevails: the increase in thermal conductivity or the lower average fractional resistance. It follows from fig. 21 that this more complex behavior is the case for DMEWLs.

In a typical VCSEL configuration, where all heat flux is directed towards the heat sink located on the side opposite to the output mirror, the fractional resistances of all heat sources of the same diameter are determined primarily by their distance from the heat sink. Hence, in a junction-up configuration of PITSELs, the P-type Bragg mirror has the largest fractional resistance, while in DMEWLs mounted junction-down the P-AlGaAs cladding layer has the lowest fractional resistance. The Joule heating associated with DBRs or cladding layers is roughly proportional to I^2 (this dependence would have been exact if current spreading mechanisms and electrical resistivities were independent of temperature) and, at least well below the thermal runaway, tends to grow faster than the active-region heating. Due to relatively high electrical resistivity of p-type semiconductors, the p-type Joule heat sources are the most important ones to consider since they end up having higher weights Q_α/Q_T. From the above considerations it follows that the p-type Joule heat sources in PITSELs, being on the high end of fractional thermal resistances, cause a further increase in R_{TH}

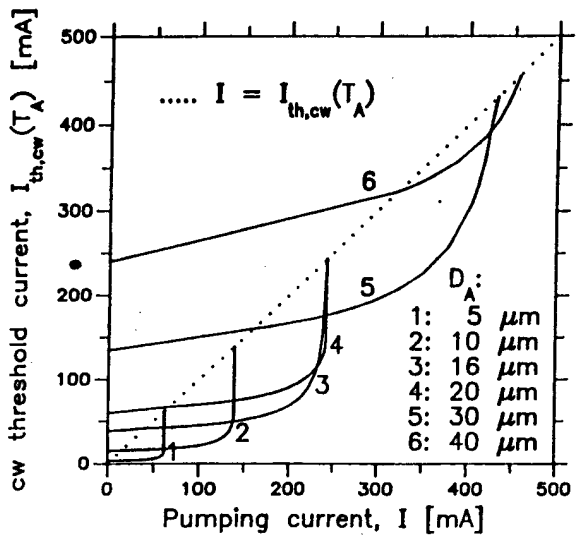


Fig. 22. Graph of effective CW threshold current $I_{th,cw}(T_A)$ variation with pumping current for buried-heterostructure GaAs/AlGaAs DMEWLs of various active-region diameters D_A. The ambient temperature is 300 K. Device parameters are the same as in fig. 21.

with current. In contrast, the increasing share of low-thermal-resistance P-type Joule heat sources in DMEWLs tends to reduce the total R_{TH} with current. That is why fig. 21 shows a reduction of R_{TH}, as long as the device is well below the thermal runaway regime where nonlinear effects cause a fast increase in the share of the active-region heating.

When no direct current flows through the laser (and, consequently, the active-region temperature is equal to ambient temperature), the CW threshold can be considered to coincide with the pulsed threshold. With increasing CW pumping current, the active-region temperature rises, hence *the CW threshold*, $I_{th,cw}(T_A)$, also increases. In order to avoid confusion with the CW threshold current, $I_{th,cw}$, corresponding to the onset of CW lasing action, the current-dependent CW threshold has been termed *the effective CW threshold*, after Scott, Geels, Corzine and Coldren [1993]. Figure 22 shows the evolution of the effective CW threshold current with pumping current for DMEWLs of various active-region diameters. If the thermally-induced increase in the effective CW threshold $I_{th,cw}(T_A)$ is slower than the increase in the pumping current I, at some pumping level the condition $I = I_{th,cw}(T_A) = I_{th,cw}$ will be met and the laser will start CW operation. The onset of CW lasing corresponds to the lower intersection of the $I_{th,cw}(T_A)$ curve (solid lines in fig. 22) with the $I = I_{th,cw}(T_A)$ line (dotted line).

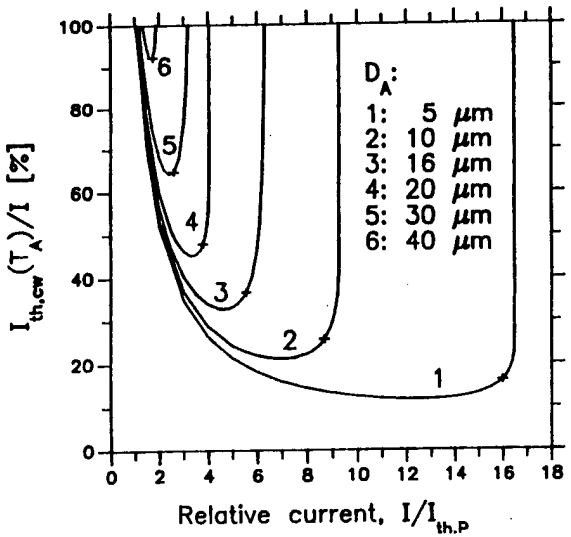


Fig. 23. Fraction of the total pumping current taken by the effective CW lasing threshold $I_{th,cw}(T_A)$ as a function of the total pumping current expressed in pulsed-threshold units, calculated for various values of the active-region diameter D_A. Crosses represent pumping conditions at which $[I - I_{th,cw}(T_A)]$ reaches a maximum. The ambient temperature is 300 K. Device parameters are the same as in fig. 21.

However, as the pumping current is increased further, $I_{th,cw}(T_A)$ starts increasing superlinearly, and eventually thermal runaway takes place. The CW lasing action is no longer possible when the second intersection of the $I_{th,cw}(T_A)$ curve with the $I = I_{th,cw}(T_A)$ line is reached. Thus, fig. 22 shows the entire CW operating range for each device. Within this range, the optical output power is roughly proportional to the excess pumping current $[I - I_{th,cw}(T_A)]$. For any particular device size, there exists an optimal pumping level such that $[I - I_{th,cw}(T_A)]$ reaches a maximum.

Another representation of the operating range (between the onset of CW lasing and the thermal runaway) for room-temperature CW excitation of etched-well VCSELs is illustrated in fig. 23. The value of $I_{th,cw}(T_A)/I$ can be interpreted as a measure of the efficiency of converting the supplied electrical energy into the energy dissipated into heat. It can be seen that from the point of view of their efficiency, the lowest-diameter devices display the best behavior. For 5 μm devices, only 10–20% of the pumping power is used to reach the threshold in the pumping current range of $4I_{th,P}$ through $16I_{th,P}$. Also, both the operating range, expressed in terms of the pulsed threshold current $I_{th,P}$, and the relative surplus

current available over and above the effective CW threshold, are the largest for small-diameter devices. With an increasing active-region diameter, the operating range shrinks systematically, while an ever increasing portion of the pumping current must be consumed to support the CW lasing action. When $D_A = 40$ μm, at least 90% of the pumping power is used up just to attain the threshold. As illustrated by fig. 23, the reduced operating range with increasing active-region diameter is directly associated with intense heating. However, even though the efficiency characteristics are superior for devices with the smallest D_A, their total output power remains small.

The points marked by crosses in fig. 23 indicate the pumping conditions such that $[I - I_{th,cw}(T_A)]$ (and, approximately, the optical power) reaches a maximum. It is worthwhile noting that optimal conditions for optical power and overall efficiency do not coincide, and the maximum output power is always reached at a pumping level higher than that yielding a maximum overall efficiency.

The self-consistent analytical model described in this section has also been used to optimize the DMEWL device design for high-power low-thermal-resistance operation (Osiński and Nakwaski [1992]). The tradeoff between an increasing pumping power, increasing $I_{th,cw}(T_A)$, and a shrinking operating range as the active region becomes wider, leads to an optimal value of $D_A = 16$ μm. The devices of this size offer the largest surplus current $[I - I_{th,cw}(T_A)]$ and, consequently, the largest total output power. Further optimization of the inner structure of 16 μm devices results in the thermal resistance R_{TH} of only 188 K/W at the pumping level of $I = 3I_{th,P}$. The average active-region temperature increase at that pumping level is less than 49 °C. Note that this value of R_{TH} is significantly lower than the lowest limit in table 4 for TEML devices with 60 μm diameters (cf. Norris, Chen and Tien [1994], Chen, Hadley and Smith [1994]), especially if one recognizes that the rough scaling of R_{TH} with the active-region area indicates that the thermal resistance of 16 μm devices should be ~14 times higher than that of 60 μm devices.

5.1.2.2. InGaAsP/InP lasers. Compared with short-wavelength devices, thermal problems in all-semiconductor long-wavelength InGaAsP/InP VCSELs are exacerbated by a smaller refractive index step between InP and InGaAsP (0.2–0.3 vs. ~0.5 for AlGaAs/AlAs), which requires about a twice larger number of quarter-wave layers in distributed Bragg reflectors (DBRs) to achieve high reflectivities indispensable for low threshold current density. In addition, due to longer wavelength, all layers in the DBRs must be thicker. Thus, it can be expected that thermal behavior of long-wavelength VCSELs may be even more critical for device operation than is the case for GaAs-based VCSELs.

In view of these difficulties, dielectric mirrors are often used in long-wavelength VCSELs, in place of semiconducting Bragg reflectors (e.g., Wada, Babic, Crawford, Reynolds, Dudley, Bowers, Hu, Merz, Miller, Koren and Young [1991], Uchida, Miyamoto, Yokouchi, Inaba, Koyama and Iga [1992], Tadokoro, Okamoto, Kohama, Kawakami and Kurokawa [1992], Miyamoto, Uchida, Yokouchi, Inaba, Mori, Koyama and Iga [1993], Baba, Suzuki, Yogo, Iga and Koyama [1993a,b], Baba, Yogo, Suzuki, Koyama and Iga [1993, 1994]). This, however, imposes further limitations on the current path, and consequently on the electrical series resistance of the device. While room-temperature pulsed operation of electrically pumped VCSELs with dielectric mirrors was obtained both at 1.3 μm (Wada, Babic, Crawford, Reynolds, Dudley, Bowers, Hu, Merz, Miller, Koren and Young [1991]) and 1.5 μm (Uchida, Miyamoto, Yokouchi, Inaba, Koyama and Iga [1992]), so far room-temperature (up to 36 °C) CW operation has been very recently achieved only at 1.3 μm (Uchiyama, Yokouchi and Ninomiya [1997]).

An alternative approach was proposed by Dudley, Ishikawa, Babic, Miller, Mirin, Jiang, Bowers and Hu [1993]. They used wafer fusion to integrate GaAs/AlAs mirrors with InP/InGaAsP double heterostructures. These lasers did not show any symptoms of device degradation despite a 3.7% lattice mismatch between the wafers. VCSELs fabricated using wafer fusion have demonstrated room-temperature pulse operation at 1.3 μm (Dudley, Babic, Mirin, Yang, Miller, Ram, Reynolds, Hu and Bowers [1994]) and at 1.5 μm (Babic, Dudley, Streubel, Mirin, Bowers and Hu [1995]), and recently also room-temperature CW operation at 1.5 μm (Babic, Streubel, Mirin, Margalit, Bowers, Hu, Mars, Yang and Carey [1995]).

The first comprehensive, self-consistent thermal–electrical analytical model of dielectric-mirror etched-well laser operation at long-wavelengths has been reported by Osiński and Nakwaski [1995b]. The model features a realistic, current-dependent distribution of heat sources and incorporates calculation of lasing threshold.

The circular planar buried heterostructure VCSELs modeled in this section (see the DMEWL structure in fig. 3a) are similar to those developed by Baba, Suzuki, Yogo, Iga and Koyama [1993a,b] and Baba, Yogo, Suzuki, Koyama and Iga [1993, 1994]. The reported external differential efficiency is very low ($\eta_d = 0.16\%$), and consequently the output power is very small. It is therefore worthwhile to examine the design of these lasers with the goal of identifying the main factors which determine their performance.

Nearly all semiconductor layers of the laser are made of InP (cf. fig. 24). Only the active region is manufactured from InGaAsP ($\lambda_g = 1.37$ μm, where λ_g stands for the bandgap wavelength) and the cap layer is produced from InGaAs. (The thin n-type InGaAsP layer reduces heat flux penetration of the substrate layer, which is negligible and is neglected in the model). Both the above layers are relatively thin. Their thermal conductivities, however, are many times lower than that of InP, so they greatly influence the heat-spreading process.

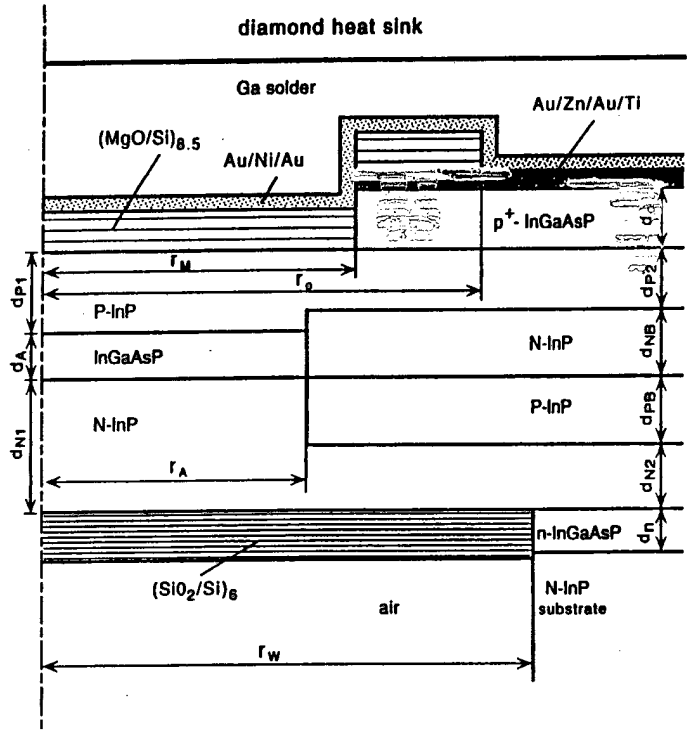


Fig. 24. Schematic structure of an InGaAsP/InP circular planar buried-heterostructure dielectric-mirrors etched-well laser (after Baba, Yogo, Suzuki, Koyama and Iga [1993, 1994]).

Heat fluxes penetrate poorly low-thermal-conductivity areas, and when they do penetrate them, they go across these layers along the shortest possible path inside them. Therefore we may assume approximately a one-dimensional (1D) heat flow through both these layers, perpendicular to their long edges.

The space transformation was proposed by Nakwaski [1983] to solve similar problems. The transformation is fully justified for 1D heat flow. Therefore we may apply it to the InGaAsP active region, to the InGaAs cap layer, and also to the dielectric layers of the output mirror (of even lower thermal conductivity), replacing them by appropriate thermally equivalent layers of InP (see fig. 25).

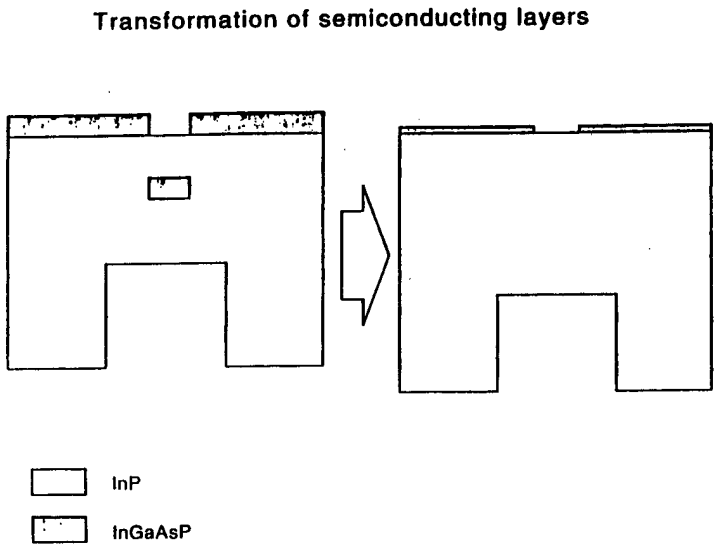


Fig. 25. Thermal equivalent of the central part of the circular buried heterostructure VCSEL under consideration.

After the transformation, the entire bulk of the device can be treated as a homogeneous InP cylinder.

The following heat generation mechanisms are included in the model:
- nonradiative recombination and absorption of the spontaneous radiation within the active region,
- absorption of the laser radiation in all layers of the resonator,
- volume Joule heating in all layers of the current path, and
- barrier Joule heating at the p-side contact.

For each of the heat generation areas, the transformed temperature profile (after the Kirchhoff transformation, cf. § 4.4) is calculated for the entire laser structure, and next the cumulative transformed temperature profile is found with the aid of the superposition principle, using the approach similar to that reported for GaAs/AlGaAs lasers by Nakwaski and Osiński [1991a, 1993].

The threshold carrier concentration is determined by considering the balance of gain and losses, with the gain coefficient changing linearly with the carrier density. The following loss mechanisms are included: free-carrier absorption in n-InP, intervalence band absorption in p-InP, active-region loss, diffraction loss, as well as absorption and scattering losses in dielectric mirrors. Threshold current is then found, taking account of Auger recombination, carrier loss due

to trap and interface recombination, and carrier leakage over the heterobarrier. Analytical approximations are used in the model to describe the current spreading in the device.

The main goal of the analysis was to determine which parameters have significant influence on device characteristics and to identify means of improving the device performance. In the following, we present a systematic discussion of the role of the most crucial device parameters.

Large differences between theoretical and experimental values of front and back mirror reflectivities indicate that the mirrors suffer from scattering loss, absorption, or poor control of layer thicknesses. While improvement of mirror quality may not be easy in practice, it is interesting to see what advantage could be expected from increased mirror reflectivity. From our calculations, we see that improvement in mirror quality leads to a dramatic reduction of the threshold current. This in turn reduces considerably the Joule heating and the Auger recombination, resulting in a reduction of the total generated heat power, the active region temperature increase, and the thermal resistance. At a fixed pumping current, the output power increases substantially.

Contrary to experimental results reported by Baba, Suzuki, Yogo, Iga and Koyama [1993b], our analysis indicates that the laser would operate in CW mode at an ambient temperature of 5°C, but not at 14°C. This may indicate that the particular device for which near-room-temperature CW operation was achieved may have had superior properties, such as very low scattering loss in the dielectric mirrors. In order for a 12 μm device to lase at 14°C, the mirror reflectivities must be increased to at least 99.8% and 99.9% for the front and the rear mirrors, respectively. The device with only a slightly lower front-mirror reflectivity of 99.7% would not lase in CW mode at that temperature. Mirror quality in the device reported by Baba, Suzuki, Yogo, Iga and Koyama [1993b] was therefore most probably higher than that measured typically for otherwise identical devices or Bragg mirrors.

In the above VCSELs, dielectric SiO_2/Si DBR structures were used as the front mirrors. It is worthwhile to consider how much improvement can be expected by replacing thermally insulating SiO_2 layers with highly conducting MgO layers, which are almost as good thermal conductors as InP. In order to account for a lower refractive index contrast between Si and MgO, compared to SiO_2/Si system, the number of periods in the front reflector is increased from 6 to 7. It is seen from our results that the above improvement is sufficient, for example, to make the difference between lasing and non-lasing at 14°C in 14 μm devices.

Let us now investigate the influence of the active-region diameter on device characteristics. Figure 26 shows that the original 12 μm diameter (Baba, Yogo,

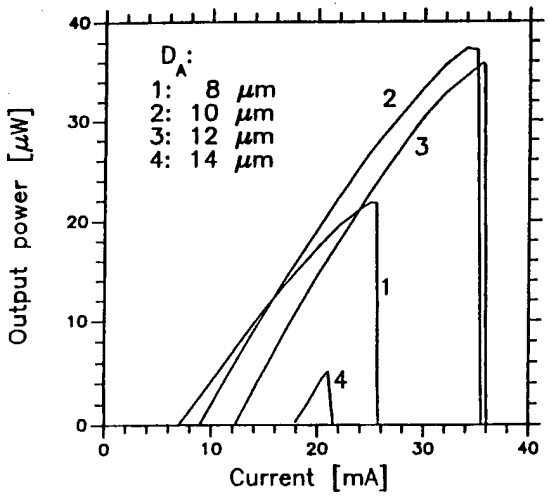


Fig. 26. Light–current characteristics calculated for etched-well 1.3 μm InGaAsP/InP lasers of various active-region diameters D_A of 7 periods of MgO/Si quarter-wave dielectric layers.

Suzuki, Koyama and Iga [1993]) is close to optimal. A slight improvement in maximum output power is expected for devices with 10 μm diameter. Altogether, however, the range of the active-region diameter for which the device would lase CW at 14°C is remarkably narrow. Figure 26 also illustrates the importance of nonlinear thermal effects in long-wavelength VCSELs. Thermally reduced roll-off of the light–current characteristics is much rapid than that calculated for GaAs/AlGaAs etched-well VCSELs by Osiński and Nakwaski [1995a].

In the range of the active-region diameters D_A between 8 μm and 14 μm, the thermal resistance, R_{TH}, reduces with decreasing D_A (e.g., at $I = 20$ mA, $R_{TH} \simeq 520$ K/W for $D_A = 14$ μm, and $R_{TH} \simeq 350$ K/W for $D_A = 8$ μm). This variation is, however, much smaller than the dynamic range of R_{TH} for each device, caused by an increasing share (with increasing current) of the P-InP Joule heat source with low fractional thermal resistance. For example, for $D_A = 10$ μm, $R_{TH} \simeq 1030$ K/W near threshold ($I = 9$ mA), and drops down to ~180 K/W near thermal runaway ($I = 35$ mA).

Known comprehensive analytical thermal VCSEL models are compared in table 8a (p. 220) taking into account the method used, accuracy of the structure modeling achieved, heat sources included and self-consistencies taken into consideration.

5.2. COMPREHENSIVE NUMERICAL MODELS

The comprehensive analytical approaches discussed in § 5.1 require extensive computations in order to determine the series expansion coefficients in temperature profiles. In addition, they can only be applied to those VCSELs whose structures are consistent with the formulation of the method. A purely numerical approach to heat conduction problems offers more flexibility in terms of defining the device structure, and is often easier to implement since existing general-purpose software packages can be utilized. In the following, we discuss the reported numerical models of VCSELs, focusing on essential features defining the model and addressing various assumptions and approximations made by their authors.

One potential problem with the application of multi-purpose finite-element packages is a difficulty in obtaining self-consistent solutions of nonlinear thermal problems. Accurate treatment would normally require an iterative approach. This can easily become a very complex task, since for each element, local values of device and material parameters would have to be determined using the average local temperatures. Besides, most authors choose to accept a linear solution of the problem, neglecting the temperature dependence of thermal conductivity, which can easily lead to significant errors. Therefore, it is usually recommended to prepare one's own numerical code for a strictly specified VCSEL structure, enabling an iterative self-consistent approach.

The finite difference method (FDM) was used to model thermal behavior of UMEWLs (cf. table 1 and fig. 3) by Shimizu, Babic, Dudley, Jiang and Bowers [1993]. The authors lumped all heat generation processes into the active region and neglected the temperature dependence of both heat generation mechanisms and thermal conductivities, which confines applicability of the model to relatively low operation currents. They also considered the heat sink contribution to the thermal resistance, assuming the heat flux at the laser/heat-sink interface to be uniform. A dramatic reduction in heat-sink thermal resistance was obtained for diamond heat sinks compared to the standard copper ones. A similar conclusion was reached by Osiński and Nakwaski [1993b], using the analytical model of PITSELs described in § 5.1.1.

Thode, Csanak, Hotchkiss, Snell and Campbell [1995] have reported on the FDM, time-dependent VCSEL model, which requires extensive mainframe computer resources to implement. To shorten the CPU time, the simulation region is limited to a cylinder of 12 μm radius and 6.75 μm height. A uniform mesh is used, therefore 80 uniform regions of average (?) material parameters are defined. The PISCES code was applied to approximate temperature

profiles. No details about heat sources and modeling thermal structure are given.

Piprek and Yoo [1994] used the finite-element method (FEM) to model operation characteristics of the 1.55 μm HMMLs. A single, uniform heat source located at the active region was assumed. For simplicity, each DBR mirror was replaced with an equivalent, uniform but thermally anisotropic medium, whose radial and axial thermal resistivities are calculated using formulae given by Osiński and Nakwaski [1993a]. This approximation, appropriate when simple analytical formulae are applied, is questionable when a fully numerical FEM solution is sought, as it inevitably deteriorates the accuracy of the numerical solution. This is especially important when layers of very different thermal conductivities are located close to small heat sources, as in the case of VCSELs. Since the FEM modeling can easily handle multilayer structures, it is better to avoid such approximations. More advanced was the model of Piprek, Wenzel and Sztefka [1994], prepared for the 0.98 μm InGaAs/AlGaAs PITSELs, where additionally the current spreading effect was considered and all important heat sources were taken into account, including active-region heating, laser light absorption as well as volume, contact and barrier Joule heating and some thermal–electrical–optical interactions. The model was generalized succesfully by Piprek, Wenzel, Wünsche, Braun and Henneberger [1995] for long-wavelength VCSELs. Surprisingly, the very important temperature dependence of the thermal conductivity seems not to have been taken into consideration in these otherwise quite sophisticated models. Nevertheless, this simulation was used to model long-wavelength VCSEL performance characteristics (Piprek, Babic and Bowers [1996]).

FEM was also used by Michalzik and Ebeling [1993] in their comprehensive self-consistent thermal model of TBEMLs (cf. table 1 and fig. 3a), which includes the temperature dependence of thermal conductivity. The main emphasis is laid on realistic modeling of current spreading in a rather complicated TBEML structure, achieved with the aid of a 2D resistance network model. The electrical conductivity profile in the proton-implanted region is assumed to have Gaussian tails with different decay constants in the radial and axial directions. Multiple heat sources are considered, including distributed Joule heating (with an exception of the p-type contact Joule heating), heterobarrier heating, absorption of stimulated radiation within the laser cavity, and absorption of spontaneous radiation within the active region. The calculated temperature distribution is then used to define a thermally induced, axially nonuniform waveguide. VCSEL cavity modes are found by applying a one-dimensional transfer matrix method, similar to that developed for graded-index optical fibers

by Morishita [1991]. Carrier diffusion and spatial hole burning effects are neglected. Transverse profiles of cavity modes are found to be sensitive to driving current via the thermal lensing effect (cf. § 3.3). Calculated modal gains are then used to determine threshold gain, threshold carrier density, and threshold current density, including the effects of detuning between the mode and the gain peak wavelengths (cf. § 3.2.). The model does not include any feedback between the temperature distribution in the device and the electrical properties (including redistribution of the heat sources), nor between the calculated optical fields and the thermal–electrical phenomena. It was used later by Michalzik and Ebeling [1995] to determine CW performance characteristics of PITSELs.

Baba, Kondoh, Koyama and Iga [1995a] reported the FEM thermal model of InGaAsP/InP DMEWLs. The model is rather approximate, without any self-consistency. Its boundary conditions are artificial: without any justification, constant temperature is simply assumed to be maintained for all walls of the cylinder of 50 μm radius and 50 μm height. Only one heat source within the active region (nonradiative recombination and absorption of spontaneous emission) is considered. With the aid of the model, it was found that thermal resistances R_{TH} of 1.3 μm DMEWLs using MgO/Si mirrors are nearly half of those using SiO_2/Si ones. Similar simulation of BEMLs (Baba, Kondoh, Koyama and Iga [1995b]) revealed that R_{TH} of devices with GaAs/AlAs DBRs fused epitaxially to InGaAsP/InP emitting layers is 1/3 of that with InGaAsP/InP DBRs.

Another comprehensive thermal model of VCSELs was proposed by Norris, Chen and Tien [1994] and Chen, Hadley and Smith [1994] for p-substrate GaAs/AlGaAs TEMLs (cf. table 1 and fig. 3) with short-period-superlattice DBRs. It should be emphasized that these devices will in general have much poorer electrical and thermal properties than other AlGaAs-based VCSELs, since thermal and electrical conductivities in very thin layers are much higher than in their bulk counterparts, especially along the axial direction. In the model, a very careful evaluation of heat generation mechanisms is carried out including radiative transfer of spontaneous emission from the active region, nonradiative recombination, absorption of spontaneous and stimulated radiation, and all barrier and volume Joule heating processes except for the contact heating. Detailed analysis of the current flow is performed, including the thermionic and tunneling currents through heteroboundaries, the effect of band-gap discontinuity on the heterointerface resistance, and the anisotropy in the electrical conductivities caused by quantum effects in layered structures. However, carrier diffusion effects are neglected. Somewhat surprisingly, the temperature dependencies of material parameters and heat generation processes

are not included in this otherwise quite sophisticated model, which compromises its accuracy and limits its applicability to the linear regime well below thermal runaway. In addition, the entire VCSEL cavity, comprising the active region and the short-period-superlattice GaAs/AlGaAs DBR mirrors, is replaced with a uniform thermally equivalent medium, characterized by the anisotropic thermal conductivity ($k_r = 12$ W/mK and $k_z = 10$ W/mK), which is a rather crude approach for purely numerical modeling.

The same control volume method was used by Chen [1995] to compare thermal characteristics of various VCSEL structures. In the analysis, the microscale electrical and thermal conduction within VCSELs multi-layered volumes were taken into account, including anisotropy of both electrical resistivity and thermal conductivity. The study reveals the interesting fact that the p-type substrate VCSELs (e.g., Hadley, Wilson, Lau and Smith [1993]) are characterized by lower thermal resistances than the n-type substrate VCSELs (e.g., Young, Scott, F.H. Peters, M.G. Peters, Majewski, Thibeault, Corzine and Coldren [1993], Hasnain, Tai, Yang, Wang, Fischer, Wynn, Weir, Dutta and Cho [1991]). For all the VCSEL structures under consideration, the calculated maximum temperature rise occurs along the optical axis. This is in contrast to the results reported by Nakwaski and Osiński [1991a, 1993] for the etched-well VCSEL, where the temperature profiles peak usually (but not always, depending on the VCSEL structure) close to the edge of the active region. It is, however, very difficult to compare the results of the very sophisticated, self-consistent model given by Nakwaski and Osiński [1991a, 1993], which is very sensitive to modeling details (compare discussion of fig. 20), with those presented by Chen [1995]. The heat generation profiles assumed by Chen [1995] are, for example, essentially different from those determined by Nakwaski and Osiński (cf. Nakwaski and Osiński [1991e]).

Rahman, Lepkowski and Grattan [1995] have used FEM to model the thermal properties of GaAs/AlGaAs DMEWLs. With the exception of the numerical calculation procedure, the model is almost identical to the analytical one reported earlier by Nakwaski and Osiński [1991a]. All important heat sources are included in this simulation. Details of the complex multilayered buried-heterostructure are taken into account. Full thermal–electrical self-consistency is achieved. Surprisingly, the algorithm of this ambitious simulation is convergent very quickly. The solution is given in the form of temperature and heat-flux profiles as well as isotherm contour maps.

Sarzała, Nakwaski and Osiński [1995] developed a comprehensive, fully self-consistent thermal–electrical finite-element model to investigate the thermal properties of GaAs/AlGaAs PITSELs (cf. table 1 and fig. 3). In the model,

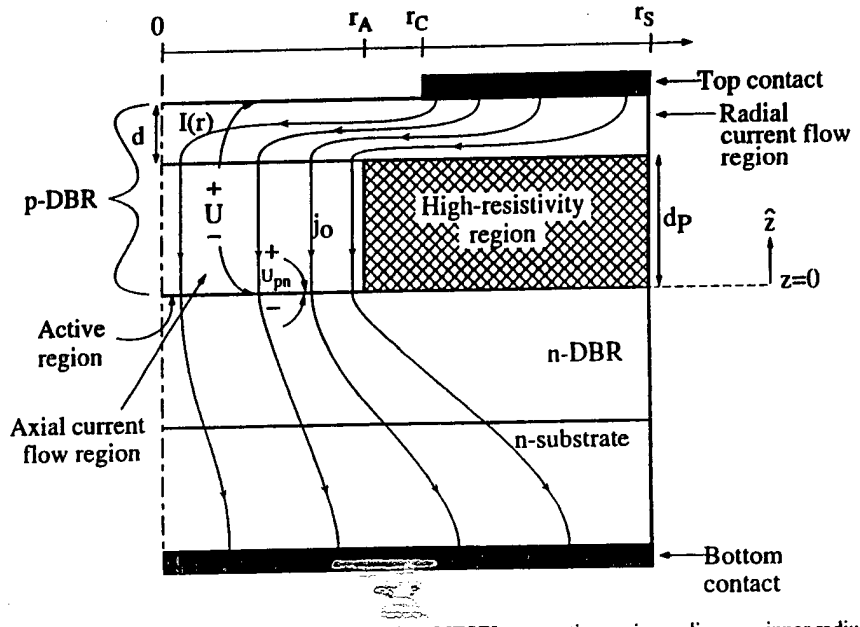


Fig. 27. Schematic illustration of current flow in a PITSEL. r_A, active region radius; r_C, inner radius of the annular contact; r_S, structure (chip) radius; d, thickness of the current spreading (radial current flow) region; d_p, thickness of the high-resistance proton-implanted region; U, voltage drop between the top contact and the active region; U_{pn}, voltage drop across the p–n junction; $I(r)$, radial current in the current spreading region; $j_0(r)$, axial current density in the current confinement region.

special attention is paid to radial carrier diffusion (Sarzała and Nakwaski [1997]) within the layer containing the active region and to its influence on temperature profiles. The radial diffusion is enhanced in structures of cylindrical geometry, so this effect is expected to play a significant role in the heat generation as well as in the heat spreading processes in PITSELs.

Knowledge of the local current density in the entire volume of the device is essential for proper treatment of the Joule heating source. The main factors affecting the current density distribution are: the cylindrical symmetry of the device, the annular shape of the top contact, and a very high electrical resistivity of the region exposed to the proton bombardment. Figure 27 shows schematically the current flow in a PITSEL structure. The top section, labeled as the radial-current-flow region, plays the dominant role in determining the radial distribution of the current injected into the active region. Inside the p-GaAs contact layer and an upper part of the P-type DBR mirror, not affected by the proton bombardment, an approximately two-dimensional (2D) radial flow of current $I(r)$ takes place. After that, in an inner part of the P-type DBR mirror, which was not exposed to

Layer #	Thickness	Conductivity
1	d_1	ρ_1
2	d_2	ρ_2
3	d_3	ρ_3
4	d_4	ρ_4
•	•	•
•	•	•
•	•	•
N	d_N	ρ_N

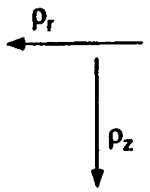


Fig. 28. Electrically equivalent anisotropic medium concept for a multilayer medium.

proton bombardment (axial current flow region), an approximately 1D current flow of a density $j_0(r)$ occurs, directed downwards along the main laser axis. Afterwards, a three-dimensional (3D) current spreading towards the bottom contact takes place below the p–n junction in the N-type DBR mirror and the n-type GaAs substrate. Note that due to the azimuthal symmetry, 2D and 3D current flows actually reduce to 1D (radius-dependent) and 2D problems, respectively.

In order to account for the multilayer composition of the DBR regions, we introduce an equivalent anisotropic medium illustrated in fig. 28, with radial and axial electrical resistivities ρ_r and ρ_z, calculated according to the following expressions (Osiński, Nakwaski and Cheng [1992]):

$$\rho_r = \frac{d_{tot}}{\sum_{i=1}^{N}(d_i/\rho_i)}, \tag{75}$$

$$\rho_z = \frac{\sum_{i=1}^{N} d_i\rho_i}{d_{tot}}, \tag{76}$$

where d_i and ρ_i stand for the thickness and the resistivity of the ith layer, N is the total number of layers contained in the region, and d_{tot} is their cumulative thickness.

The basic equations describing the current and voltage distributions in the top section of the device, comprising the radial and axial current flow regions, were given by Osiński, Nakwaski and Varangis [1994] (refer to fig. 27 for explanation of some of the symbols used):

$$\frac{dU(r)}{dr} = \left(\frac{\rho_r}{2\pi r d}\right) I(r), \tag{77}$$

$$\frac{dI(r)}{dr} = 2\pi r j_0(r), \tag{78}$$

$$U(r) = U_{pn}(r) + j_0(r)\rho_{zP}d_P, \tag{79}$$

$$j_0(r) = j_s \exp[\beta U_{pn}(r)], \tag{80}$$

where j_s is the reverse saturation current density at the p–n junction, β is the diode parameter, ρ_r is the effective resistivity in the lateral direction in the radial current flow region, and ρ_{zP} is the effective resistivity in the vertical direction in the axial current flow region. Approximate analytical solution to the above set of equations is given by Nakwaski [1995].

Before the carriers injected into the active region recombine radiatively or nonradiatively, they diffuse in the radial direction. Note that since the injected current density peaks near the edges of the active region, diffusion can occur in two directions: towards the center and away from the active region. In a cylindrically symmetric structure, the carrier diffusion is governed by the following equation:

$$D_a\left[\frac{\partial^2 n(r)}{\partial r^2} + \frac{1}{r}\frac{\partial n(r)}{\partial r}\right] - Bn^2(r) - \frac{n(r)}{\tau_{nr}} + \frac{j_0(r)}{ed_A} = 0, \tag{81}$$

where $n(r)$ is the carrier concentration, d_A is the active region thickness, D_a is the ambipolar diffusion constant, B is the radiative bimolecular recombination constant, τ_{nr} is the carrier lifetime with respect to the nonradiative recombination, $j_0(r)$ is the pumping current density, and e is the electron charge. In our calculations, we adopt the following values of the above parameters, reported by Lengyel, Meissner, Patzak and Zschauer [1982]: $D_a = 40\,\mathrm{cm^2/s}$, $B = 9.7\times10^{-11}\,\mathrm{cm^3/s}$, and $\tau_{nr} = 1.8\times10^{-8}\,\mathrm{s}$.

For an ideal laser structure, i.e., with perfect grading of all heterobarriers, its total series electrical resistance, R_{id}, is determined theoretically from known values of electrical resistivities and thicknesses of all the layers. For any particular device, the residual heterobarrier electrical resistance, R_{HB}, is then found from the measured value of resistance R and the calculated value of R_{id}:

$$R_{HB} = R - R_{id}. \tag{82}$$

In the model, the R_{HB} resistance is assumed to be distributed equally among all gradient layers in the p-type DBR mirror.

Operation-current dependence of the external quantum efficiency η_d was deduced from an experimental light–current characteristic reported by Zhou,

Cheng, Schaus, Sun, Zheng, Armour, Hains, Hsin, Myers and Vawter [1991]. A self-consistent solution is found numerically in the entire volume of the laser with the aid of an iteration procedure, taking into account the local-temperature dependencies of material and device parameters, including thermal conductivities, electrical resistivities, reverse saturation current density, free-carrier concentrations, absorption coefficients, threshold current, as well as internal and external differential quantum efficiencies. The flow chart of numerical calculations is illustrated in fig. 14, without, however, determination of a threshold current. Note that strongly nonlinear thermal–electrical interactions, enhanced by large temperature variations in VCSELs, affect substantially their lasing characteristics, eventually leading to thermal runaway.

Multiple nonhomogeneous heat sources are considered, including the carrier-concentration-dependent active-region heating (nonradiative recombination and absorption of spontaneous radiation), current-density-dependent volume and barrier (p-side contact and heterobarriers) Joule heat generations as well as internal-radiation-density-dependent absorption of laser radiation. More details may be found in the paper of Sarzała, Nakwaski and Osiński [1995].

In terms of thermal properties, the main effect of carrier diffusion is a reduction of the active-region temperature, compared with the temperature obtained at the same pumping current without diffusion. According to eq. (36), the local density of heat generated in the active-region plane is proportional to the local carrier density. Without diffusion, the active-region heat source would be contained within the circle $r \leqslant r_A$, and its spatial profile would be similar to that of current density. Consequently, intense heat generation would take place mostly around the edges of the active region. As a result of diffusion, the local carrier density decreases, especially at the edges of the active region, while the area occupied by the heat source becomes larger. The heat generated outside the circle $r \geqslant r_A$ is conducted away much more easily than the heat generated inside the active region. This leads to a significant reduction in the active-region temperature increase, as illustrated in fig. 29.

Figure 29 can be regarded as representing the key result of a paper presented by Sarzała, Nakwaski and Osiński [1995]. In addition to a remarkable lowering of the active-region temperature, dramatic changes take place in the radial temperature profiles. Without diffusion, the temperature profiles essentially reflect the nonuniform current injection, with large maxima at the edges of the active region. Inclusion of the diffusion results in nearly complete disappearance of these maxima. Only at very high pumping levels one can discern a slight positive slope of the $T_A(r)$ curve. The uniformity of temperature profiles within the active region is truly astonishing, bearing in mind that it was obtained with

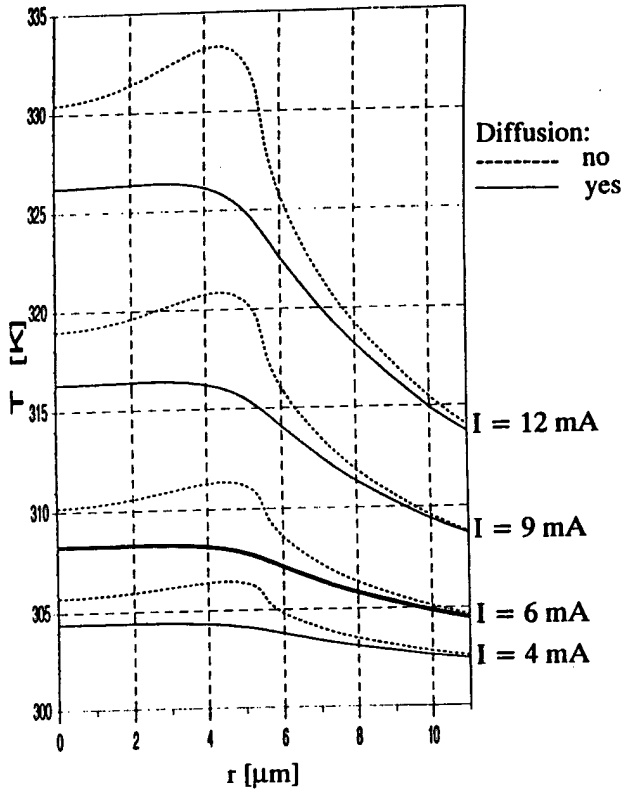


Fig. 29. Comparison of radial temperature profiles in the active-region plane, calculated with diffusion (solid lines) and without diffusion (broken lines) for indicated pumping currents.

highly inhomogeneous current injection. In fact, if a uniform active-region heat source is assumed in PITSELs, as by Nakwaski and Osiński [1994], the radial temperature profile has a bell shape. Hence, a slightly raised carrier density near the active-region edges turns out to be optimal for getting a uniform temperature distribution inside the entire active region. It should be emphasized, however, that the radial temperature profiles may well depend on the active-region diameter D_A. For devices with larger values of D_A, we expect a greater nonuniformity of injected current profiles, carrier density profiles, and active-region temperature profiles.

The analysis demonstrates that the carrier diffusion influences strongly the distribution of the main heat source located in the active region. As a result, both current- and heat-flux distributions are modified and a temperature spike,

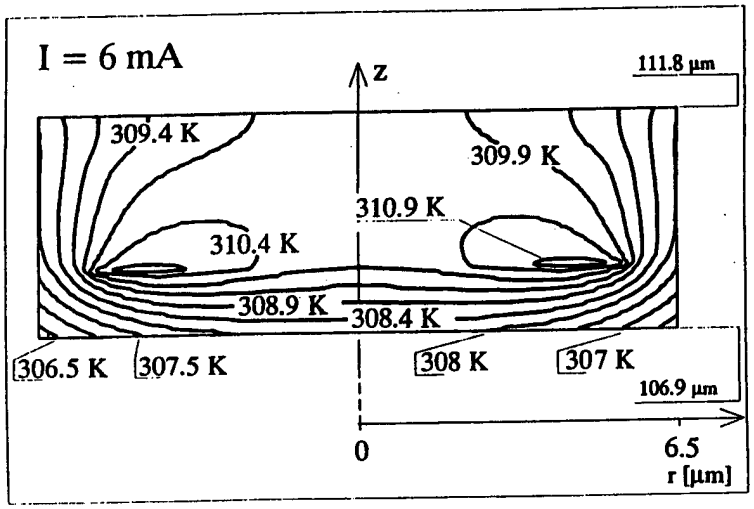


Fig. 30. Isotherm profiles in the vicinity of the active region in an 11 μm PITSEL driven at 6 mA, calculated by neglecting diffusion effects. The isotherms are drawn at intervals of ~0.5°C. Note characteristic refraction effects at the interfaces between high- and low-thermal conductivity layers.

which appears at the edge of the active region when carrier diffusion is neglected, smooths out and practically disappears. This redistribution of carrier density results in a smaller number of carriers near the edges of the active region, which reduces considerably the modal gain for high-order modes and favors the excitation of the fundamental transverse mode.

Figures 30 and 31 display the isotherm profiles in a section of the device comprising the active region, obtained without and with diffusion, respectively. The two flat maxima in fig. 30, with the temperature of 310.9 K, are located in the active-region plane and correspond to the maximum of the 6 mA dashed line in fig. 29. They disappear entirely in fig. 31, and the active region has a remarkably flat temperature profile, again in accordance with the 6 mA solid line in fig. 29. Instead a lower-temperature maximum, just above 308.3 K, emerges in the central part of the P-type mirror.

Recently, Hadley, Lear, Warren, Choquette, Scott and Corzine [1996] have presented the results of their comprehensive (and very sophisticated in its optical part) full thermal–electrical–optical numerical modeling of PITSELs using a finite-difference technique. The model considers the following major physical processes (i) the ohmic transport of carriers through the cladding layers to an active region, (ii) the heat transport from multiple heat sources toward a heat

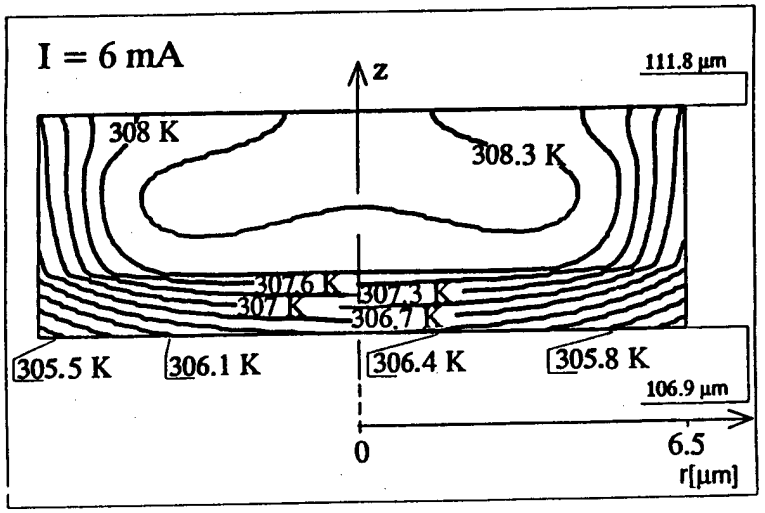


Fig. 31. Isotherm profiles in the vicinity of the active region in an 11 μm PITSEL driven at 6 mA, with diffusion effects taken into account. The isotherms are drawn at intervals of ~0.3°C.

sink, (iii) the radial diffusion of carriers inside the active region, and (iv) the multimode optical field. In the model, many important features are taken into consideration, including carrier leakage effects, interaction of transverse modes with carriers, effects arising from the strained band structure usually present in the quantum wells, and so on. The model also contains some thermal–optical (*thermal lensing effect*) and electrical–optical (*spatial holeburning effect*) self-consistency procedures. Three main heat generation mechanisms are taken into account, namely nonradiative recombination, reabsorption of radiation, and ohmic dissipation. A temperature increase inside the contact layers and the heat sink does not seem to be taken into account. The authors claimed to successfully predict the threshold current, output powers, and transverse-mode behavior of gain-guided VCSELs, including thermal rollover effects at high injection currents. At least the last prediction is a real surprise: the validity of the above approach seems to be confined to only relatively low operation currents because both the heat and the carrier transports are assumed to be linear and the model does not contain the thermal–electrical self-consistent procedure. As in the model of Piprek and Yoo [1994], multi-layered DBR mirrors are replaced with an equivalent uniform and anisotropic medium whose composite thermal conductivities (and also some other model parameters) are additionally modified to reproduce the measured device temperature rise. Thus, the agreement between theory and experiment can hardly be regarded as a confirmation of the models

validity. Nevertheless, the above model seems to be now the most advanced thermal–electrical–optical simulation of a VCSEL operation.

An intricate thermal VCSEL analysis has been recently reported by Ning, Indik and Moloney [1995], Ning, Indik, Moloney and Koch [1995], and Ning and Moloney [1995]. They have introduced plasma and lattice temperatures as two independent variables described by kinetic equations coupled to the conventional laser equations for carrier density and field amplitude. According to this approach, lattice and plasma each absorb heat from their respective heat sources and dissipate heat to their heat sinks. In the CW region, lattice and plasma can each hold their individual temperatures and maintain a constant temperature difference because of the sustained pumping as well as the heat exchange and dissipation. New achievements of this approach seem, however, to be too subtle to have practical meaning now. Besides, there are also some essential drawbacks of this analysis. First of all, it considers important laser variables (e.g., temperature, carrier concentration and current density) as position independent, average quantities whereas their three-dimensional profiles are very important to model correctly VCSEL operation. Furthermore, most of decay rates in the kinetic equations are used as adjustable parameters. All construction and material details are hidden in these parameters. Their values, as used in example numerical calculations, are not justified or evaluated by any means. Finally, the above parameters depend, for example, on VCSEL thermal and electrical resistances, whose exact determination now seems to be more essential for modeling of VCSEL operation, than a subtle distinction between the temperatures of lattice and plasma. Thus, the approach based on this distinction seems to be premature at this moment, but it should not be neglected. It should serve as an important direction in which present VCSEL 3-D models can be extended and should be included into self-consistent comprehensive VCSEL analysis in future.

Numerical comprehensive thermal VCSEL models are compared in table 8b (p. 221). In the course of time, they become more and more involved, but also more and more exact.

§ 6. Conclusions

Although vertical-cavity surface-emitting lasers (VCSELs) are generally considered to be very promising, their relatively poor thermal properties still represent the main obstacle on the way towards their wide application, and are especially pressing when integration into densely-packed two-dimensional arrays is contemplated. To overcome these difficulties, a good understanding of the thermal problems must be reached. In particular, detailed modeling of heat generation processes, heat-flux spreading, and mutual interactions between thermal, electrical, and optical phenomena is desirable to design thermally optimized devices. As long as the optical output power in VCSELs remains small, the coupling between optical and thermal effects can be ignored in determining the temperature distribution inside the device. On the other hand, thermal–electrical interactions are very important, and thermal–electrical self-consistency is essential for realistic modeling of thermal effects. It is also important to include a realistic distribution of heat sources in the model. The current-induced variation of thermal resistance is very sensitive to VCSEL structure, and in particular to the relative distribution of heat sources and their location with respect to the heat sink.

This chapter summarizes the present understanding of thermal effects in VCSELs. It is clear that these effects are preponderant and affect almost all device characteristics. As a rule, elevated temperature has a detrimental effect on these characteristics and should be minimized. There are, however, exceptions to this rule. Some aspects of thermal behavior of VCSELs may actually be beneficial. For example, thermally-induced optical waveguide in devices with no built-in lateral guiding helps to reduce losses and lower the threshold current. Unique opportunities for thermal-waveguide engineering exist in etched-well VCSELs. Elevated temperature may be also beneficial in VCSELs with transparent electrodes [Chua, Thornton, Treat, Yang and Dunnrowicz [1997]). Finally, non-monotonous variation of threshold current with temperature has been exploited to design temperature-insensitive devices.

Acknowledgments

Much of our work reported here would not have been possible without the active contribution and support of many of our colleagues. In particular, we would like to acknowledge numerous fruitful discussions and advice from Julian Cheng of the University of New Mexico, Albuquerque, USA, and G. Ronald Hadley of the Sandia National Laboratories, Albuquerque, USA, as well as from Maciej Bugajski and Bohdan Mroziewicz of the Institute of Electron Technology, Warsaw, Poland. We are grateful to Bo Lu and Ping Zhou of the University of New Mexico, USA, for technical discussions and for providing their data on the temperature dependence of the threshold current. We acknowledge valuable contributions from our students, Robert P. Sarzała, Jacek Wilk, Georgi K.

Yanakiev, Petros M. Varangis, Antonio Leal, Jonathan Stohs, Gilles du Crest, and Joachim Kastner. We are also thankful to Mrs. Katarzyna A. Steele (Jezierska) and Mr. Bill Johnson for their apt technical assistance. This work was supported by the Polish State Committee for Scientific Research (KBN) (Grant # 8-T11B-018-12), the National Science Foundation (NSF), the Advanced Research Projects Agency (AREA), the Air Force Office for Scientific Research, and the New Energy and Industrial Technology Development Organization (NEDO) of Japan.

References

Adachi, S., 1985, J. Appl. Phys. **58**, R1.
Adachi, S., 1992, Physical Properties of III–V Semiconductor Compounds: InP, InAs, GaAs, GaP, InGaAs, and InGaAsP (Wiley, New York).
Agrawal, G.P., and N.K. Dutta, 1993, Semiconductor Lasers, 2nd Ed. (Van Nostrand Reinhold, New York) p. 59.
Aiki, K., M. Nakamura and J.-I. Umeda, 1976, IEEE J. Quantum Electron. **QE-12**, 597.
Akulova, Y.A., B.J. Thibeault, J. Ko and L.A. Coldren, 1997, IEEE Photon. Technol. Lett. **9**, 277.
Amith, A., I. Kudman and E.F. Steigmeier, 1965, Phys. Rev. **138**, A1270.
Baba, T., T. Kondoh, F. Koyama and K. Iga, 1995a, Opt. Rev. **2**, 123.
Baba, T., T. Kondoh, F. Koyama and K. Iga, 1995b, Opt. Rev. **2**, 323.
Baba, T., K. Suzuki, Y. Yogo, K. Iga and F. Koyama, 1993a, Electron. Lett. **29**, 331.
Baba, T., K. Suzuki, Y. Yogo, K. Iga and F. Koyama, 1993b, IEEE Photon. Tech. Lett. **5**, 744.
Baba, T., Y. Yogo, K. Suzuki, F. Koyama and K. Iga, 1993, Electron. Lett. **29**, 913.
Baba, T., Y. Yogo, K. Suzuki, F. Koyama and K. Iga, 1994, Jpn. J. Appl. Phys. Pt. I **33**, 1905.
Babic, D.I., Y. Chung, N. Dagli and J.E. Bowers, 1993, IEEE J. Quantum Electron. **QE-29**, 1950.
Babic, D.I., and S.W. Corzine, 1992, IEEE J. Quantum Electron. **QE-28**, 514.
Babic, D.I., J.J. Dudley, K. Streubel, R.P. Mirin, J.E. Bowers and E.L. Hu, 1995, Appl. Phys. Lett. **66**, 1030.
Babic, D.I., K. Streubel, R.P. Mirin, N.M. Margalit, J.E. Bowers and E.L. Hu, 1995, Electron. Lett. **31**, 653.
Babic, D.I., K. Streubel, R.P. Mirin, N.M. Margalit, J.E. Bowers, E.L. Hu, D.E. Mars, L. Yang and K. Carey, 1995, IEEE Photon. Technol. Lett. **7**, 1225.
Bissessur, H., R.D. Ettinger, F.A. Fernandez and J.B. Davies, 1993, IEEE Photon. Technol. Lett. **5**, 764.
Buccafusca, O., J.L.A. Chilla, J.J. Rocca, S. Feld, C. Wilmsen, V. Morozov and R. Leibenguth, 1996, Appl. Phys. Lett. **68**, 590.
Bugajski, M., and A.M. Kontkiewicz, 1982, Electron Technol. **13**(4), 63.
Buus, J., 1983, IEEE J. Quantum Electron. **QE-19**, 953.
Buus, J., and M.J. Adams, 1979, IEE J. Solid State Electron Dev. **3**, 189.
Carslaw, H.S., and J.C. Jaeger, 1988, Conduction of Heat in Solids (Clarendon Press, Oxford).
Casey Jr, H.C., and M.B. Panish, 1978, Heterostructure Lasers, Part A: Fundamental Principles (Academic Press, New York) p. 44.
Catchmark, J.M., R.A. Morgan, K. Kojima, R.E. Leibenguth, M.T. Asom, G.D. Guth, M.W. Focht, L.C. Luther, G.P. Przybylek, T. Mullay and D.N. Christodoulides, 1993, Appl. Phys. Lett. **63**, 3122.

Chang-Hasnain, C.J., 1994, Vertical cavity surface-emitting laser arrays, in: Diode Laser Arrays, eds D. Botez and D.R. Scifres (Cambridge University Press, Cambridge), ch. 9, p. 368.
Chang-Hasnain, C.J., J.P. Harbison, L.T. Florez and N.G. Stoffel, 1991, Electron. Lett. **27**, 163.
Chang-Hasnain, C.J., J.P. Harbison, G. Hasnain, A.C. Von Lehmen, L.T. Florez and N.G. Stoffel, 1991, IEEE J. Quantum Electron. **QE-27**, 1402.
Chang-Hasnain, C.J., M. Orenstein, A. Von Lehmen, L.T. Florez, J.P. Harbison and N.G. Stoffel, 1990, Appl. Phys. Lett. **57**, 218.
Chang-Hasnain, C.J., Y.A. Wu, G.S. Li, G. Hasnain, K.D. Choquette, C. Caneau and L.T. Florez, 1993, Appl. Phys. Lett. **63**, 1307.
Chen, G., 1995, J. Appl. Phys. **77**, 4251.
Chen, G., M.A. Hadley and J.S. Smith, 1994, J. Appl. Phys. **76**, 3261.
Cherng, C.-P., and M. Osiński, 1991, J. Appl. Phys. **70**, 4617.
Chong, C.H., and J. Sarma, 1993, IEEE Photon. Technol. Lett. **5**, 761.
Choquette, K.D., W.W. Chow, M.H. Crawford, K.M. Geib and R.P. Schneider Jr, 1996, Appl. Phys. Lett. **68**, 3689.
Choquette, K.D., R.P. Schneider Jr, M.H. Crawford, K.M. Geib and J.J. Figiel, 1995, Conference on Lasers and Electro-Optics, CLEO'95, Baltimore, MD, May 22–26, Paper CPD5-1.
Choquette, K.D., R.P. Schneider Jr, K.L. Lear and K.M. Geib, 1994, Electron. Lett. **30**, 2043.
Chow, W.W., S.W. Corzine, D.B. Young and L.A. Coldren, 1995, Appl. Phys. Lett. **66**, 2460.
Chua, C.L., R.L. Thornton, D.W. Treat, V.K. Yang and C.C. Dunnrowicz, 1997, IEEE Photon. Technol. Lett. **9**, 551.
Chua, C.L., Z.H. Zhu, Y.H. Lo, R. Bhat and M. Hong, 1995, IEEE Photon. Techn. Lett. **7**, 444.
Coldren, L.A., R.S. Geels, S.W. Corzine and J.W. Scott, 1992, Opt. Quantum Electron. **24**, S105.
Coldren, L.A.C., E.R.H. Hegblom, E.M.S. Strzelecka, J.K. Ko, Y.A.A. Akulova and B.J.T. Thibeault, 1997, Proc. SPIE **3003**, 2.
Cook, D.D., and F.R. Nash, 1975, J. Appl. Phys. **46**, 1660.
Crawford, M.H., and R.P. Schneider Jr, 1995, Conference on Lasers and Electro-Optics, CLEO'95, Baltimore, MD, May 22–26, Paper CWB1.
Dudley, J.J., D.I. Babic, R.P. Mirin, L. Yang, B.I. Miller, R.J. Ram, T.E. Reynolds, E.L. Hu and J.E. Bowers, 1994, Appl. Phys. Lett. **64**, 1463.
Dudley, J.J., D.L. Crawford and J.E. Bowers, 1992, IEEE Photon. Technol. Lett. **4**, 311.
Dudley, J.J., M. Ishikawa, D.I. Babic, B.I. Miller, R.P. Mirin, W.B. Jiang, J.E. Bowers and E.L. Hu, 1993, Appl. Phys. Lett. **61**, 3095.
Dutta, N.K., and R.J. Nelson, 1982, J. Appl. Phys. **53**, 74.
Dutta, N.K., L.W. Tu, G. Hasnain, G.J. Zydzik, Y.H. Wang and A.Y. Cho, 1991, Electron. Lett. **27**, 208.
Fisher, M.A., Y.-Z. Huang, A.J. Dann, D.J. Elton, M.J. Harlow, S.D. Perrin, J. Reed, I. Reid and M.J. Adams, 1995, IEEE Photon. Technol. Lett. **7**, 608.
Floyd, F.D., B.J. Thibeault, L.A. Coldren and J.L. Merz, 1996, Electron. Lett. 1996, **32**, 114.
Geels, R.S., and L.A. Coldren, 1990, Appl. Phys. Lett. **57**, 1605.
Geels, R.S., and L.A. Coldren, 1991, Electron. Lett. **27**, 1984.
Geels, R.S., S.W. Corzine, J.W. Scott, D.B. Young and L.A. Coldren, 1990, IEEE Photon. Technol. Lett. **2**, 234.
Geels, R.S., B.J. Thibeault, S.W. Corzine, J.W. Scott and L.A. Coldren, 1993, IEEE J. Quantum Electron. **QE-29**, 2977.
Goncher, G., B. Lu, W.-L. Luo, J. Cheng, S. Hersee, S.Z. Sun, R.P. Schneider and J.C. Zolper, 1996, IEEE Photon. Technol. Lett. **8**, 316.
Grimmeiss, H.G., and B. Monemar, 1971, Phys. Status Solidi A **5**, 109.
Hadley, G.R., J.P. Hohimer and A. Owyoung, 1987, IEEE J. Quantum Electron. **QE-23**, 765.

Hadley, G.R., K.L. Lear, M.E. Warren, K.D. Choquette, J.W. Scott and S.W. Corzine, 1996, IEEE J. Quantum Electron. **QE-32**, 607.
Hadley, M.A., G.C. Wilson, K.Y. Lau and J.S. Smith, 1993, Appl. Phys. Lett. **63**, 1607.
Hasnain, G., K. Tai, N.K. Dutta, Y.H. Wang, J.D. Wynn, B.E. Weir and A.Y. Cho, 1991, Electron. Lett. **27**, 915.
Hasnain, G., K. Tai, L. Yang, Y.H. Wang, R.J. Fischer, J.D. Wynn, B. Weir, N.K. Dutta and A.Y. Cho, 1991, IEEE J. Quantum Electron. **QE-27**, 1377.
Hayashi, Y., T. Mukaihara, N. Hatori, N. Ohnoki, A. Matsutani, F. Koyama and K. Iga, 1995, Electron. Lett. **31**, 560.
Huffaker, D.L., and D.G. Deppe, 1996, IEEE Photon. Technol. Lett. **8**, 858.
Huffaker, D.L., D.G. Deppe, K. Kumar and T.J. Rogers, 1994, Appl. Phys. Lett. **64**, 97.
Huffaker, D.L., D.G. Deppe and T.J. Rogers, 1994, Appl. Phys. Lett. **65**, 1611.
Huffaker, D.L., L.A. Graham, H. Deng and D.G. Deppe, 1996, IEEE Photon. Technol. Lett. **8**, 974.
Huffaker, D.L., J. Shin, H. Deng, C.C. Lin, D.G. Deppe and B.G. Streetman, 1994, Appl. Phys. Lett. **65**, 2642.
Hughes, J.J., D.B. Gilbert and F.Z. Hawrylo, 1985, RCA Rev. **46**, 200.
Iga, K., 1992a, Opt. Quantum Electron. **24**, S97.
Iga, K., 1992b, Int. J. High Speed Electron. Systems **3**, 263.
Iga, K., and F. Koyama, 1990, Surface Emitting Laser, Ohm-sha, Chapter 2.2, pp. 22–27.
Iga, K., and F. Koyama, 1993, Vertical-Cavity Surface Emitting Lasers and Arrays, in: Surface Emitting Semiconductor Lasers and Arrays, eds G.A. Evans and J.M. Hammer (Academic Press, Boston), p. 71.
Iga, K., F. Koyama and S. Kinoshita, 1988, IEEE J. Quantum Electron. **QE-24**, 1845.
Jäger, R., M. Grabherr, C. Jung, R. Michalzik, G. Reiner, B. Weigl and K.J. Ebeling, 1997, Electron. Lett. **33**, 330.
Jansen van Doorn, A.K., M.P. van Exter and J.P. Woerdman, 1995, Appl. Phys. Lett. **66**, 3561.
Jewell, J.L., A.L. Scherer, S.L. McCall, Y.H. Lee, S. Walker, J.P. Harbison and L.T. Florez, 1989, Electron. Lett. **25**, 1123.
Joyce, W.B., and R.W. Dixon, 1975, J. Appl. Phys. **46**, 855.
Kajita, M., T. Kawakami, M. Nido, A. Kimura, T. Yoshikawa, K. Kurihara, Y. Sugimoto and K. Kasahara, 1995, IEEE J. Select. Topics Quantum Electron. **1**, 654.
Kinoshita, S., F. Koyama and K. Iga, 1987, Proc. Tech. Group Meet., IECE Jpn., paper OQE86-188, p. 23.
Kobayashi, T., and Y. Furukawa, 1975, Jpn. J. Appl. Phys. **14**, 1981.
Koch, B.J., J.R. Leger, A. Gopinath, Z. Wang and R.A. Morgan, 1997, Appl. Phys. Lett. **70**, 2359.
Koyama, F., S. Kinoshita and K. Iga, 1989, Appl. Phys. Lett. **55**, 221.
Kudman, I., and E.F. Steigmeier, 1964, Phys. Rev. **133**, A1665.
Lautenschlager, P., M. Garriga and M. Cardona, 1987, Phys. Rev. B **36**, 4813.
Law, J.Y., and G.P. Agrawal, 1997, IEEE J. Quantum Electron. **QE-33**, 462.
Lear, K.L., K.D. Choquette, R.P. Schneider Jr and S.P. Kilcoyne, 1995, Appl. Phys. Lett. **66**, 2616.
Lear, K.L., A. Mar, K.D. Choquette, S.P. Kilcoyne, R.P. Schneider Jr and K.M. Geib, 1996, Electron. Lett. **32**, 457.
Lear, K.L., R.P. Schneider Jr, K.D. Choquette, S.P. Kilcoyne, J.J. Figiel and J.C. Zolper, 1994, IEEE Photon. Techn. Lett. **6**, 1053.
Lengyel, G., P. Meissner, E. Patzak and K.-H. Zschauer, 1982, IEEE J. Quantum Electron. **QE-18**, 618.
Lu, B., W.-L. Luo, C. Hains, J. Cheng, R.P. Schneider Jr, R.P. Choquette, K.L. Lear, S.P. Kilcoyne and J.C. Zolper, 1995, IEEE Photon. Technol. Lett. **7**, 447.
Lu, B., P. Zhou, J. Cheng and K.J. Malloy, 1994, Proc. SPIE **2147**, 12.

Lu, B., P. Zhou, J. Cheng, K.J. Malloy and J.C. Zolper, 1994, Appl. Phys. Lett. **65**, 1337.
MacDougal, M.H., P.D. Dapkus, V. Pudikov, H. Zhao and G.M. Yang, 1995, IEEE Photon. Techn. Lett. **7**, 229.
MacDougal, M.H., G.M. Yang, A.E. Bond, C.-K. Lin, D. Tishinin and P.D. Dapkus, 1996, IEEE Photon. Technol. Lett. **8**, 310.
Manning, J.S., 1981, J. Appl. Phys. **52**, 3179.
Marple, D.T.F., 1964, J. Appl. Phys. **35**, 1241.
Michalzik, R., and K.J. Ebeling, 1993, IEEE J. Quantum Electron. **QE-29**, 1963.
Michalzik, R., and K.J. Ebeling, 1995, IEEE J. Quantum Electron. **QE-31**, 1371.
Miyamoto, T., T. Uchida, N. Yokouchi, Y. Inaba, K. Mori, F. Koyama and K. Iga, 1993, Conference on Lasers and Electro-Optics, CLEO'93, Baltimore, MD, May 2–7, 1993, p. 316.
Morgan, R.A., 1994, Proc. SPIE **2147**, 97.
Morgan, R.A., 1997, Proc. SPIE **3003**, 14.
Morgan, R.A., G.D. Guth, M.W. Focht, M.T. Asom, K. Kojima, L.E. Rogers and S.E. Callis, 1993, IEEE Photon. Technol. Lett. **5**, 374.
Morgan, R.A., M.K. Hibbs-Brenner, J.A. Lehman, E.L. Kalweit, R.A. Walterson, T.M. Marta and T. Akinwande, 1995, Appl. Phys. Lett. **66**, 1157.
Morgan, R.A., M.K. Hibbs-Brenner, T.M. Marta, R.A. Walterson, S. Bounnak, E.L. Kalweit and J.A. Lehman, 1995, IEEE Photon. Technol. Lett. **7**, 441.
Morgan, R.A., J.A. Lehman, Y. Liu, M.K. Hibbs-Brenner and J.P. Bristow, 1997, Proc. SPIE 3004, Paper 3004-13.
Morishita, K., 1991, IEEE Trans. Microwave Theory Tech. **MTT-29**, 348.
Mroziewicz, B., M. Bugajski and W. Nakwaski, 1991, Physics of Semiconductor Lasers (North-Holland, Amsterdam).
Mukaihara, T., Y. Hayashi, N. Hatori, N. Ohnoki, A. Matsutani, F. Koyama and K. Iga, 1995, Electron. Lett. **31**, 647.
Nakwaski, W., 1979, Sov. J. Quantum Electron. **9**, 1544.
Nakwaski, W., 1983, Opt. Quantum Electron. **15**, 513.
Nakwaski, W., 1984, IEE Proc. Pt. I (Solid-State Electron Dev.) **131**, 94.
Nakwaski, W., 1988, J. Appl. Phys. **64**, 159.
Nakwaski, W., 1995, Appl. Phys. A **61**, 123.
Nakwaski, W., and A.M. Kontkiewicz, 1985, IEEE Trans. Electron. Devices **32**, 2282.
Nakwaski, W., and M. Osiński, 1991a, IEEE J. Quantum Electron. **QE-27**, 1391.
Nakwaski, W., and M. Osiński, 1991b, Jpn. J. Appl. Phys. Pt. 2 (Lett.) **30**, L596.
Nakwaski, W., and M. Osiński, 1991c, Proc. SPIE **1582**, 277.
Nakwaski, W., and M. Osiński, 1991d, Conference on Lasers and Electro-Optics, CLEO'91, Baltimore, MD, 12–17 May, 1991, Paper CWF26, pp. 262–263.
Nakwaski, W., and M. Osiński, 1991e, IEEE Photon. Technol. Lett. **3**, 979.
Nakwaski, W., and M. Osiński, 1992a, Conference on Lasers and Electro-Optics, CLEO'92, Anaheim, CA, 10–15 May, 1992, Paper JThA6, pp. 386–387.
Nakwaski, W., and M. Osiński, 1992b, LEOS 1992 Summer Topical Meeting Digest on Smart Pixels, Santa Barbara, CA, 10–12 Aug., 1992, Paper TuA4, pp. 47–48.
Nakwaski, W., and M. Osiński, 1992c, Proc. SPIE **1788**, 108.
Nakwaski, W., and M. Osiński, 1992d, Electron. Lett. **28**, 1283.
Nakwaski, W., and M. Osiński, 1993, IEEE J. Quantum Electron. **QE-29**, 1981.
Nakwaski, W., and M. Osiński, 1994, Proc. SPIE **2146**, 365.
Nakwaski, W., M. Osiński and J. Cheng, 1992, Appl. Phys. Lett. **61**, 3101.
Nash, F.R., 1973, J. Appl. Phys. **44**, 4696.
Ning, C.Z., R.A. Indik and J.V. Moloney, 1995, J. Opt. Soc. Am. B **12**, 1993.

Ning, C.Z., R.A. Indik, J.V. Moloney and S.W. Koch, 1995, Proc. SPIE 2399, 617.
Ning, C.Z., and J.V. Moloney, 1995, Opt. Lett. 20, 1151.
Norris, P.M., G. Chen and C.-L. Tien, 1994, Int. J. Heat Mass Transfer 37 (Suppl. 1) 9.
Oezisik, M.N., 1980, Heat Conduction (Wiley, New York), pp. 6, 8.
Ohiso, Y., C. Amano, Y. Itoh, K. Tateno, T. Tadokoro, H. Takenouchi and T. Kurokawa, 1996, Electron. Lett. 32, 1483.
Ohiso, Y., Y. Kohama and T. Kurokawa, 1995, Jpn. J. Appl. Phys. Pt. 1, 34, 6073.
Ohiso, Y., K. Tateno, Y. Kohama, A. Wakatsuki, H. Tsunetsugu and T. Kurokawa, 1996, IEEE Photon. Technol. Lett. 8, 1115.
Onischenko, A., and J. Sarma, 1997, IEE Proc. Optoelectron. 144, 39.
Ortiz, G.G., C.P. Hains, B. Lu, S.Z. Sun, J. Cheng and J.C. Zolper, 1996, IEEE Photon. Technol. Lett. 8, 1423.
Osiński, M., and W. Nakwaski, 1992, Proc. SPIE 1634, 61.
Osiński, M., and W. Nakwaski, 1993a, Electron Lett. 29, 1015.
Osiński, M., and W. Nakwaski, 1993b, Conference on Lasers and Electro-Optics, CLEO'93, Baltimore, MD, 2–7 May, 1993, Paper CTuN5, pp. 150–152.
Osiński, M., and W. Nakwaski, 1995a, IEEE J. Selected Topics Quantum Electron. 1, 681.
Osiński, M., and W. Nakwaski, 1995b, Proc. SPIE 2399, 372.
Osiński, M., W. Nakwaski and J. Cheng, 1992, Proc. SPIE 1788, 121.
Osiński, M., W. Nakwaski and A. Leal, 1994, Proc. SPIE 2147, 85.
Osiński, M., W. Nakwaski and P.M. Varangis, 1994, Proc. SPIE 2146, 388.
Paoli, T.L., 1973, IEEE J. Quantum Electron. QE-9, 267.
Papannareddy, R., W. Ferguson and J.K. Butler, 1987, J. Appl. Phys. 62, 3565.
Petermann, K., 1991, Laser Diode Modulation and Noise (Kluwer Academic Publishers/KTK Scientific Publishers, Dordrecht/Tokyo), p. 34.
Pettit, G.D., and W.J. Turner, 1965, J. Appl. Phys. 136, 2081.
Piprek, J., D.I. Babic and J.E. Bowers, 1996, Appl. Phys. Lett. 68, 2630.
Piprek, J., H. Wenzel and G. Sztefka, 1994, IEEE Photon. Technol. Lett. 6, 139.
Piprek, J., H. Wenzel, H.-J. Wünsche, D. Braun and F. Henneberger, 1995, Proc. SPIE 2399, 605.
Piprek, J., and S.J.B. Yoo, 1994, Electron. Lett. 30, 866.
Prince, F.C., N.B. Patel, D. Kasemset and C.S. Hong, 1983, Electron. Lett. 19, 435.
Rahman, B.M.A., S.P. Lepkowski and K.T.V. Grattan, 1995, IEE Proc. Optoelectron. 142, 82.
Rochus, S., M. Hauser, T. Röhr, H. Kratzer, G. Boehm, W. Klein, G. Traenke and G. Weimann, 1995, IEEE Photon. Technol. Lett. 7, 968.
Sarzala, R.P., and W. Nakwaski, 1997, IEE Proc. Optoelectron. 144, in press.
Sarzala, R.P., W. Nakwaski and M. Osiński, 1995, Int. J. Optoelectron. 10, 357.
Schneider Jr. R.P., K.D. Choquette, J.A. Lott, K.L. Lear, J.J. Figiel and K.J. Malloy, 1994, IEEE Photon. Technol. Lett. 62, 313.
Schnitzer, P., U. Fiedler, M. Grabherr, C. Jung, G. Reiner, W. Zick and K.J. Ebeling, 1996, Electron. Lett. 32, 2145.
Schröder, S., H. Grothe and W. Harth, 1996, Electron. Lett. 32, 348.
Scott, J.W., S.W. Corzine, D.B. Young and L.A. Coldren, 1993, Appl. Phys. Lett. 62, 1050.
Scott, J.W., R.S. Geels, S.W. Corzine and L.A. Coldren, 1993, IEEE J. Quantum Electron. QE-29, 1295.
Scott, J.W., D.B. Young, B.J. Thibeault, M.G. Peters and L.A. Coldren, 1995, IEEE J. Selected Topics Quantum Electron. 1, 638.
Shimizu, M., D.I. Babic, J.J. Dudley, W.B. Jiang and J.E. Bowers, 1993, Microw. Opt. Technol. Lett. 6, 455.

Shin, H.-E., Y.-G. Ju, J.-H. Shin, J.-H. Ser, T. Kim, E.-K. Lee, I. Kim and Y.-H. Lee, 1996, Electron. Lett. 32, 1287.
Shoji, H., K. Otsubo, M. Matsuda and H. Ishikawa, 1994, Electron. Lett. 30, 409.
Sommers, H.S., 1971, Appl. Phys. Lett. 19, 424.
Stern, F., 1973, IEEE J. Quantum Electron. QE-9, 290.
Streubel, K., S. Rapp, J. André and J. Wallin, 1996, IEEE Photon. Technol. Lett. 8, 1121.
Sugihwo, F., M.C. Larson and J.S. Harris Jr, 1997, Appl. Phys. Lett. 70, 547.
Swaminathan, V., and A.T. Macrander, 1991, Material Aspects of GaAs and InP Based Structures (Prentice Hall, Englewood Cliffs), p. 15.
Tadokoro, T., H. Okamoto, Y. Kohama, T. Kawakami and T. Kurokawa, 1992, IEEE Photon. Technol. Lett. 4, 409.
Tai, K., R.J. Fischer, C.W. Seabury, N.A. Olsson, T.-C.D. Huo, Y. Ota and A.Y. Cho, 1989, Appl. Phys. Lett. 55, 2473.
Taylor, G.W., and P.A. Evaldson, 1994, IEEE J. Quantum Electron. QE-30, 2262.
Tell, B., K.F. Brown-Goebeler, R.E. Leibenguth, F.M. Baez and Y.H. Lee, 1992, Appl. Phys. Lett. 60, 683.
Tell, B., R.E. Leibenguth, K.F. Brown-Goebeler and G. Livescu, 1992, IEEE Photon. Technol. Lett. 4, 1195.
Thibeault, B.J., K. Bertilsson, E.R. Hegblom, E. Strzelecka, P.D. Floyd, R. Naone and L.A. Coldren, 1997, IEEE Photon. Technol. Lett. 9, 11.
Thode, L., G. Csanak, R. Hotchkiss, C. Snell and M. Campbell, 1995, Proc. SPIE 2399, 348.
Thompson, G.H.B., 1980, Physics of Semiconductor Laser Devices (Wiley, Chichester).
Thurmond, C.D., 1975, J. Electrochem. Soc. 122, 1133.
Tu, L.W., Y.H. Wang, E.F. Schubert, B.E. Weir, G.J. Zydzik and A.Y. Cho, 1991, Electron. Lett. 27, 457.
Uchida, T., T. Miyamoto, N. Yokouchi, Y. Inaba, F. Koyama and K. Iga, 1992, 12th International Semiconductor Laser Conference, Takamatsu, Japan, Sept. 21–25, 1992, p. 212.
Uchiyama, S., and K. Iga, 1984, IEEE J. Quantum Electron. QE-20, 1117.
Uchiyama, S., and S. Kashiwa, 1995, Electron. Lett. 31, 1449.
Uchiyama, S., Y. Ohmae, S. Shimizu and K. Iga, 1986, J. Lightwave Technol. 4, 846.
Uchiyama, S., N. Yokouchi and T. Ninomiya, 1997, IEEE Photon. Technol. Lett. 9, 141.
Vail, E.C., G.S. Li, W. Yuen and C.J. Chang-Hasnain, 1996, Electron. Lett. 32, 1888.
Vakhshoori, D., J.D. Wynn, G.J. Zydzik, R.E. Leibenguth, M.T. Asom, K. Kojima and R.A. Morgan, 1993, Appl. Phys. Lett. 62, 1448.
Valle, A., J. Sarma and K.A. Shore, 1995a, Opt. Commun. 115, 297.
Valle, A., J. Sarma and K.A. Shore, 1995b, IEEE J. Quantum Electron. QE-31, 1423.
Van der Ziel, J.P., D.G. Deppe, N. Chand, G.J. Zydzik and S.N.G. Chu, 1990, IEEE J. Quantum Electron. QE-26, 1873.
Von Lehmen, A., T. Banwell, L. Carrion, N. Stoffel, L. Florez and J. Harbison, 1992, Electron. Lett. 28, 21.
Vook, F.L., 1964, Phys. Rev. 135, A1742.
Wada, H., D.I. Babic, D.L. Crawford, T.E. Reynolds, J.J. Dudley, J.E. Bowers, E.L. Hu, J.L. Merz, B.I. Miller, U. Koren and M.G. Young, 1991, IEEE Photon. Technol. Lett. 3, 977.
Wada, H., D.I. Babic, M. Ishikawa and J.E. Bowers, 1992, Appl. Phys. Lett. 60, 2974.
Wilson, G.C., M.A. Hadley, J.S. Smith and K.Y. Lau, 1993, Appl. Phys. Lett. 63, 3265.
Wilson, G.C., D.M. Kuchta, J.D. Walker and J.S. Smith, 1994, Appl. Phys. Lett. 64, 542.
Wipiejewski, T., K. Panzlaff, E. Zeeb and K.J. Ebeling, 1993, IEEE Photon. Technol. Lett. 5, 889.
Wipiejewski, T., K. Panzlaff, E. Zeeb and K.J. Ebeling, 1994, Proc. SPIE 2147, 48.

Wipiejewski, T., M.G. Peters, B.J. Thibeault, D.B. Young and L.A. Coldren, 1996, IEEE Photon. Technol. Lett. **8**, 10.
Wipiejewski, T., D.B. Young, M.G. Peters, B.J. Thibeault and L.A. Coldren, 1995, Electron. Lett. **31**, 279.
Wu, C.C., K. Tai and K.F. Huang, 1993, Electron. Lett. **29**, 1953.
Wu, Y.A., C.J. Chang-Hasnain and R. Nabiev, 1993, Electron. Lett. **29**, 1861.
Wu, Y.A., C.J. Chang-Hasnain and R. Nabiev, 1994, IEEE Photon. Technol. Lett. **6**, 924.
Wu, Y.A., G.S. Li, R.F. Nabiev, K.D. Choquette, C. Caneau and C.J. Chang-Hasnain, 1995, IEEE J. Selected Topics Quantum Electron. **1**, 629.
Wüthrich, C., J.H. James, J.D. Ganière and F.K. Reinhart, 1990, Electron. Lett. **26**, 1600.
Yan, R.H., and L.A. Coldren, 1990, Appl. Phys. Lett. **57**, 267.
Yang, G.M., M.H. MacDougal and P.D. Dapkus, 1995, Conference on Lasers and Electro-Optics, CLEO'95, Baltimore, MD, May 22–26, Paper CPD4-1.
Yoffe, G.W., W.C. van der Vleuten, M.R. Leys, F. Karouta and J.H. Wolter, 1994, Electron. Lett. **30**, 794.
Yoo, B.-S., H.Y. Chu, M.S. Park, H.-H. Park and E.-H. Lee, 1996, Electron. Lett. **32**, 116.
Yoo, B.-S., H.-H. Park and E.-H. Lee, 1994, Electron. Lett. **30**, 1060.
Young, D.B., A. Kapila, J.W. Scott, V. Malhotra and L.A. Coldren, 1994, Electron. Lett. **30**, 233.
Young, D.B., J.W. Scott, F.H. Peters, M.G. Peters, M.L. Majewski, B.J. Thibeault, S.W. Corzine and L.A. Coldren, 1993, IEEE J. Quantum Electron. **QE-29**, 2013.
Young, D.B., J.W. Scott, F.H. Peters, B.J. Thibeault, S.W. Corzine, M.G. Peters, S.-L. Lee and L.A. Coldren, 1993, IEEE Photon. Technol. Lett. **5**, 129.
Young, M., 1993, Optics and Lasers Including Fibers and Optical Waveguides (Springer, Berlin) p. 138.
Yu, S.F., and C.W. Lo, 1996, IEE Proc. Optoelectron. **143**, 189.
Zeeb, E., B. Möller, G. Reiner, M. Ries, T. Hackbarth and K.J. Ebeling, 1995, IEEE J. Select. Topics Quantum Electron. **1**, 616.
Zeeb, E., G. Reiner, M. Ries, B. Möller and K.J. Ebeling, 1995, Conference on Lasers and Electro-Optics, CLEO'95, Baltimore, MD, May 22–26, Paper CWB4.
Zhao, Y.-G., and J.G. McInerney, 1995, IEEE J. Quantum Electron. **QE-31**, 1668.
Zhao, Y.-G., and J.G. McInerney, 1996, IEEE J. Quantum Electron. **QE-32**, 1950.
Zhou, P., J. Cheng, C.F. Schaus, S.Z. Sun, K. Zheng, E. Armour, C. Hains, W. Hsin, D.R. Myers and G.A. Vawter, 1991, IEEE Photon. Technol. Lett. **3**, 591.

AFOSR Grant
Final Report (March 15, 1996 to September 30, 1999)

Influence of the Microstructure on Transport Properties of p-type GaN:Mg

A. K. Rice, K. J. Malloy

We have presented an analysis of the hole transport in p-type Mg-doped GaN grown on sapphire substrates by metal-organic-chemical vapor deposition (MOCVD). We found that the experimental Hall mobility cannot be explained solely by traditional extended state scattering mechanisms. Not only are the mobilities not accurately modeled by numerically solving the Boltzmann transport equation (BTE), but the calculated results do not even reflect the trend in experimental mobility values between the investigated samples. We attributed these discrepancies to the microstructure of GaN:Mg grown on sapphire. A microstructure-oriented transport model was presented for an interpretation of the transport of holes in p-type GaN:Mg grown on sapphire. The microstructure-oriented model provides a simplified picture of the microstructure, consisting of two distinct microstructural phases in GaN on sapphire. Using this model for the experimental mobility, the extracted parameters from hole transport measurements were shown to be positively correlated with microstructural parameters determined from x-ray diffraction (XRD) measurements. The experimental mobility of p-type GaN:Mg grown on sapphire can be described as dependent upon the acceptor doping, impurity compensation, and microstructure, including dislocation density, columnar grain size, and grain boundaries.

With improved growth of GaN, the material will approach ideal single crystal quality. In these cases the mobility of p-type GaN:Mg should be well described by traditional extended state scattering mechanisms. The calculated mobility for crystalline p-type GaN:Mg with an activation energy of 150 meV and compensation ratio of K = 0.1 is constant with a value of ~120 cm^2/Vs for substitutional Mg doping less then $1x10^{18}$ cm^{-3} at 300 K. The calculated conductivity shows an upper limit of 10 $(\Omega\ cm)^{-1}$ at 300 K and 30 $(\Omega\ cm)^{-1}$ at 500 K. These results imply that as the growth of p-type GaN:Mg improves, GaN devices that include p-type GaN:Mg will still possess a high spreading resistance.

In addition, we investigated the noise properties of p-type Mg-doped GaN using low frequency noise spectroscopy. The epitaxial GaN:Mg films were grown on a sapphire substrate by metal-organic chemical vapor deposition (MOCVD) in different laboratories. Generation-recombination (g-r) noise and 1/f noise were observed for temperatures above 250 K. The magnitude of the 1/f noise exceeds the g-r noise magnitude for frequencies less than 30 Hz, and the 1/f noise level was characterized by high values of the Hooge parameter, $\alpha \approx 1-150$, indicating a high level of structural imperfection. In addition, the integrated noise power spectral density divided by the voltage squared in the frequency range of 1 Hz to 30 Hz, correlated strongly with the structural imperfection of the sample as measured from the asymmetric rocking curve (ω-scan) FWHM. The generation-recombination noise was related to a high concentration trap level with an activation energy of 120 meV ± 25 meV and a repulsive barrier that is possibly associated with the Mg dopant.

List of Publications:

1. A. K. Rice and K. J. Malloy, Bulk Noise Processes in Magnesium-doped GaN Grown on Sapphire, Conference Proceedings, Noise in Physical Systems and 1/f Fluctuations: Editors P. H. Handel and A. L. Chung (AIP Press 1998).

2. A. K. Rice and K. J. Malloy, Microstructural Contributions to Transport in P-type Magnesium-doped GaN, J. Appl. Phys. (Submitted November 1999).

3. A. K. Rice and K. J. Malloy, Bulk Noise processes and their Correlation to Structural Imperfections in Magnesium-doped P-type GaN Grown on Sapphire, J. Appl. Phys. (Submitted November 1999).

List of Presentations:

1. A. K. Rice and K. J. Malloy, Temperature dependent Hall measurements and Bulk noise processes in GaN:Mg, Fifth Wide Bandgap Nitride Semiconductor Workshop, Aug. 1998.

2. A. K. Rice and K. J. Malloy, Bulk Noise Processes in GaN:Mg grown on Sapphire, VII. Van der Ziel Symposium on Quantum 1/f noise and other Low Frequency Fluctuations in Electronic Devices, Aug. 1998.

PUBLISHED
Quantum 1/f noise and other Low Frequency Fluctuations in Electronic Devices, P.H. Handel Editor AIP Conference Proceedings 466 Woodbury, NY 1999.

BULK NOISE PROCESSES IN MAGNESIUM-DOPED GaN GROWN ON SAPPHIRE

A. K. Rice, K. J. Malloy

Center for High Technology Materials, University of New Mexico
Albuquerque, NM 87106

Abstract. We report low frequency noise measurements on Mg-doped GaN. The bulk sample studied was grown by MOCVD on a sapphire substrate. Ohmic contacts were made by annealing a Pt/Au metallization to a sample with volume 1 cm x 0.3 cm x 2 μm. The noise properties were studied at 300K to 400K for a wide range of frequencies (1 Hz-100 kHz). A constant current was applied to the sample and the noise voltage between two other contacts was measured using a lock-in amplifier. Generation recombination (g-r) noise and 1/f noise are observed for temperatures above 300 K. The generation-recombination noise is related to a trap level with activation energy of 183 meV, coinciding with the Mg level in the bulk region. The spectral density of the noise fluctuations typically varied from 10^{-11} V^2/Hz at 1 Hz to 10^{-16} V^2/Hz for 100 kHz.

INTRODUCTION

GaN has drawn attention recently due to its large bandgap with emission in the UV and blue wavelengths. Today, there are many challenges that are hindering the development of GaN devices. One such challenge is the p-type GaN material. GaN has proven to be difficult to dope p-type due to a high n-type background concentration and the lack of a shallow p-type acceptor. Successful p-type doping has been achieved with magnesium although the material is compensated and typically possesses high resistivity, low mobility, and an activation energy in the range of 150 – 200 meV. Devices based on this material have been shown to posses higher noise power densities and hooge[1,2,3] parameters than equivalent GaAs and Si devices, possibly due to the large number of dislocations, 10^8 – 10^{10} cm^{-2}, and resulting structural inhomogeneity. An understanding of the noise processes in bulk GaN:Mg is essential to assessing the reliability and quality of GaN-based.

EXPERIMENTAL DESCRIPTION

The samples investigated were grown on sapphire substrates by metal-organic chemical vapor deposition (MOCVD). A 2 μm thick p-type layer of GaN doped with magnesium was grown on a GaN buffer layer. The GaN:Mg was activated at 700°C for 20 minutes prior to metallization. Ohmic contacts were made by annealing a Pt/Au metallization at 750 °C for 10 minutes. A carrier concentration at room temperature of 7×10^{16} cm^{-3} was measured using a Hall bar geometry with dimensions 1 cm x 0.3 cm x 2 μm, and an activation energy of 177 meV was determined from temperature dependent resistivity measurements. Noise measurements were performed using the same Hall bar. The noise characteristics were measured in the frequency range of 1 Hz to 100 kHz using a Stanford Research Systems SR830 digital lock-in amplifier. The noise density power spectrum for each sample was examined for a temperature range of 300K to 400K. A constant current was placed across two contacts and the fluctuation in voltage was measured at two other contacts. At each measurement frequency the sample was allowed to stabilize for 45 seconds and 100 data points were averaged.

RESULTS AND DISCUSSIONS

The dominant transport mechanism in these samples is the electric field-induced drift of holes in the valence band. These holes originate from the Mg-acceptor level, located approximately 177 meV above the valence band edge as determined from Hall measurements. Under near-equilibrium, steady-state conditions there is no net accumulation of charge and the generation rate must equal the recombination rate. But, there will be a microscopic variation the generation-recombination rates. It is this microscopic fluctuation that is observed as noise. The noise power density, $S_v(\omega)$, for a generation-recombination (g-r) noise process possesses a Lorentzian spectrum of the form

$$S_v(\omega) = A\frac{\tau}{1+(\omega\tau)^2}, \qquad (1)$$

where $A = \frac{V^2 N_T}{v p_o^2}$ is a measure of the individual processes, τ is the characteristic time of the g-r process, V is the voltage across the sample, N_T is the concentration of bulk traps, v is the sample volume, and p_o^2 is the density of free carriers at $E_f = E_T$[4]. The characteristic time τ is expected to follow an Arrhenius equation

$$\tau = \tau_o \exp\left(\frac{E_T}{kT}\right), \qquad (2)$$

where τ_o is a constant and E_T is the activation energy of the level involved in the g-r process. Figure 1 displays the noise power density divided by the voltage squared, $\frac{S_v}{V^2}$, versus frequency. The magnitude of the 1/f noise exceeds the g-r noise magnitude for frequencies less than 30 Hz. Above 30 Hz g-r noise for one trap level is predominant. As shown in Fig. 1 the experimental data can be fit to one g-r level and 1/f noise. In order to determine τ accurately it is convenient to multiply the measured noise power density by $\omega = 2\pi f$ and divide by the voltage squared. A plot of $\frac{S_v \omega}{V^2}$ versus frequency on a log linear scale will exhibit a peak at $f = 1/2\pi\tau$, the characteristic frequency of the g-r process[5]. The activation energy, E_T, of the g-r process can be obtained from a plot of $\log(\tau T^2)$ verse the inverse temperature. Figure 2 displays the normalized noise density, $\frac{S_v \omega}{V^2}$, versus frequency at 300 K, 350K, and 400K. At 300 K a clear g-r noise component is observed while two g-r noise components are observed at 350 K and 400 K.

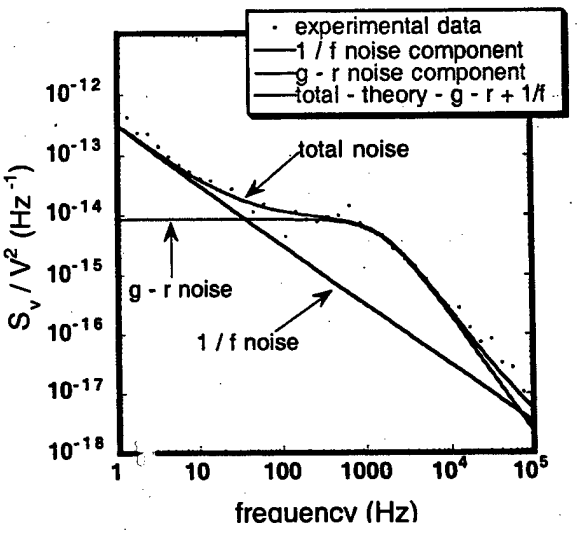


FIGURE 1. Excess noise in GaN:Mg at 300K

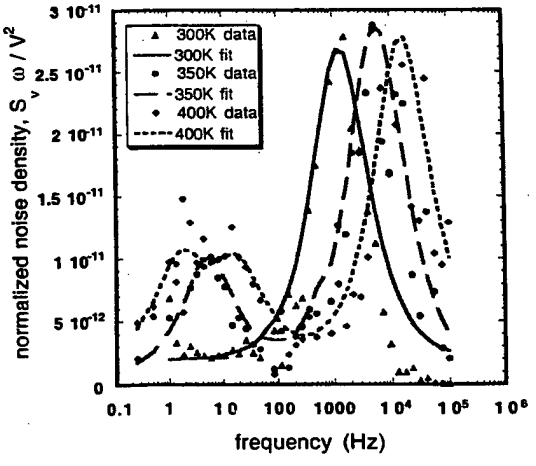


FIGURE 2. Normalized noise spectra for bulk GaN:Mg at T = 300 K, T = 350 K, and T = 400 K.

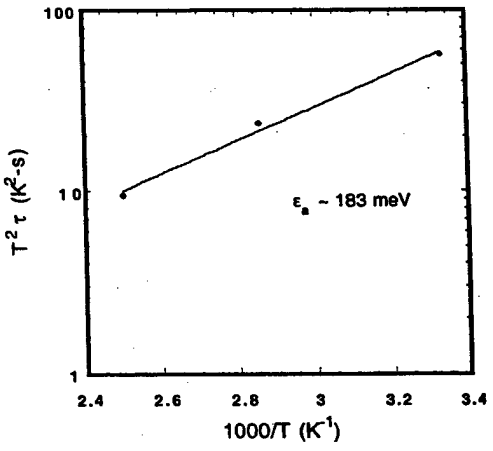


FIGURE 3. Arrhenius plot of the inverse time constant $f=1/2\pi\tau$. A level can be identified at 183 meV above the valance band.

The Arrhenius plot for the GaN:Mg sample studied is shown in Fig. 3. We find a trap located at 183 meV above the valance band with a concentration of $N_T = 5 \times 10^{18}$ cm^{-3} and capture cross section of 1.4×10^{-22} cm^2. The activation energy and trap concentration are close to the magnesium activation energy of 177 meV and concentration of ~1.5×10^{18} cm^{-3} obtained from temperature dependent Hall and resistivity measurements. The measured capture and emission rates were unusually slow for a level located at 183 meV and the capture cross section is less than expected for an attractive coulombic center. We attribute this g-r level to the bulk GaN neutral regions and not to any depletion regions that may exist in the bulk owing to the structural defects. Such depletion region contributions are excluded since studies on metal contacts to p-GaN have indicated that the Fermi level is pinned between 0.39 eV to 0.43 eV of the valence band edge[6]. Since g-r noise processes originate from levels near the Fermi level and an activation energy of 183 meV was measured, any g-r process in the depletion region should possess an activation energy greater than the observed activation energy of 183 meV. Furthermore, traps in the depletion regions do not remain a constant energy away from the Fermi level and thus give rise to broad, poorly defined noise peaks.

CONCLUSION

We have used noise spectroscopy to observe a trap level with activation energy of 183 meV and concentration of $N_T = 1.5 \times 10^{18}$ cm^{-3} in bulk, neutral GaN:Mg. This level seems to be associated with the Mg acceptor level. The trap activation energy and concentration are in agreement with those values obtained for temperature dependent Hall and resistivity measurements although the cross section is unusually low.

REFERENCES

1. D. V. Kuksenkov, H. Temkin, A. Osinsky, R. Gaska, and M. A. Khan, J. *Appl. Phys.* **83** (4), 2142 (1998).
2. N. V. D'yakonova, M. E. Levinshtein, S. Contreras, and W. Knap, *Semiconductors* **32** (3), 257 (1998).
3. D. V. Kuksenkov, H. Temkin, R. Gaska, and J. W. Yang, *IEEE Electron Device Letters* **19** (7), 222 (1998).
4. A. J. Madenach and H. Stoll, 'Noise Spectrosopy of Traps in Ion Implanted Polysilicon Thin Films," presented at the 9th International Conference on Noise in Physical Systems, Monreal, May 1987.
5. B. K. Jones, *Advances in Electronics and Electron Physics*, San Deigo: Acedemic Press, Inc. 1994, pp. 201-257.
6. D. J. King, Masters Thesis, University of New Mexico, July 1998.

SUBMITTED J. Appl. Phys.
Nov. 1999

Bulk Noise Processes and their Correlation to Structural Imperfections in Magnesium-doped P-type GaN Grown on Sapphire

A. K. Rice, K. J. Malloy

Center for High Technology Materials, University of New Mexico
Albuquerque, NM 87106

Abstract

We investigate the noise properties of p-type Mg-doped GaN using low frequency noise spectroscopy. The epitaxial GaN:Mg films were grown on a sapphire substrate by metal-organic chemical vapor deposition (MOCVD) in different laboratories. Generation-recombination (g-r) noise and 1/f noise are observed for temperatures above 250 K. The magnitude of the 1/f noise exceeds the g-r noise magnitude for frequencies less than 30 Hz, and the 1/f noise level is characterized by high values of the Hooge parameter, $\alpha \approx 1-150$, indicating a high level of structural imperfection. In addition, the integrated noise power spectral density divided by the voltage squared in the frequency range of 1 Hz to 30 Hz, correlates strongly with the structural imperfection of the sample as measured from the asymmetric rocking curve (ω-scan) FWHM. The generation-recombination noise is related to a high concentration trap level with an activation energy of 120 meV ± 25 meV and a repulsive barrier that is possibly associated with the Mg dopant.

I. Introduction

GaN has been the subject of extensive study recently due to its large bandgap and emission in the UV and blue wavelengths. Currently, many challenges hinder the further development of GaN devices. One such challenge is the p-type GaN material. GaN has proven to be difficult to dope p-type due to a high n-type background concentration and the lack of a shallow p-type acceptor. Successful p-type doping has been achieved with magnesium although the material is compensated and typically possesses high resistivity, low mobility, and a conductivity activation energy in the range of 150 – 200 meV[1-4]. Typically, the GaN film structure is investigated with transmission electron microscopy,[5,6] atomic-force microscopy,[7,8] and x-ray diffraction[9,10]. However, low frequency noise analysis can be a powerful tool for examining compound semiconductors,[11] yielding information about crystal defects and interfaces. This paper will discuss two types of noise processes both used as a diagnostic tool: generation-recombination noise (g-r) and one-over-f (1/f) noise. Devices based on this material have been shown to posses higher noise power densities and Hooge[12-14] parameters than equivalent GaAs and Si devices, possibly due to the large number of dislocations, $10^8 - 10^{10}$ cm^{-2}, and the resulting structural inhomogeneity. An understanding of the microstructure and its effects on the low frequency noise processes in bulk GaN:Mg is essential to assessing the reliability and quality of GaN based devices.

A. Generation-Recombination noise

Generation-recombination noise is a fluctuation in conductivity due to a number fluctuation of charge carries. Under near-equilibrium, steady-state conditions there is no net accumulation of charge and the generation rate must equal the recombination rate. But there will be a microscopic variation the generation-recombination rates. It is this microscopic fluctuation that is observed as noise.

The spectrum for g-r noise between states in the band and a trap at one energy level is given by

$$S_v = \frac{\tau V^2 A}{1+(\omega\tau)^2}, \qquad (1)$$

where S_v is the noise spectral power density having units of V^2/Hz, and the unitless quantity $A \approx N_T v^{-1} p_o^{-2}$ represents the relative magnitude of the individual g-r process[15,16] and is an approximation at energy $E_f = E_T$. N_T is the density of traps, τ is the characteristic time of the g-r process, V is the voltage across the sample, v is the volume, and p_o is the density of free carriers when $E_f = E_T$.

The characteristic time τ is expected to follow an Arrhenius equation

$$\tau = \tau_o \exp\left(\frac{E_T}{kT}\right), \qquad (2)$$

where τ_o is a constant and E_T is the activation energy of the level involved in the g-r process.

B. One-over-f (1/f) Noise

The next important noise characteristic is 1/f noise. 1/f noise is a conductance fluctuation in which the noise spectrum is inversely proportional to the frequency. The origin of 1/f noise is still unknown. However an empirical formula describing the 1/f noise spectrum is frequently employed. For a homogeneous material, the noise power spectral density for a 1/f noise process is given by the form[17]

$$S_v = \frac{V^2 B}{f}, \qquad (3)$$

where $B = \alpha/N$ is a measure of the 1/f noise, α is a unitless constant referred to as the Hooge parameter, and N is the total number of free carriers. The Hooge parameter is a means for assessing the relative noise in different materials. Furthermore, under these conditions Eq.

(3) is interpreted as a noise mechanism due to conduction fluctuations in the volume, particularly mobility fluctuations.

Although the causes of 1/f noise are not completely understood, the 1/f noise magnitude is affected by non-ohmic contacts and defect-state traps, located in the bulk material or at the surface, that cause current flow to become disrupted by variations in the trapping rate.

II. Experimental Procedure

The noise properties of four samples are investigated. The samples examined were grown on sapphire substrates by metal-organic chemical vapor deposition (MOCVD) in two different laboratories. Samples I, III, and IV were grown in the same laboratory and sample II was grown in a different laboratory. The samples examined are p-type and possess temperature dependent resistivity activation energies between 150 meV and 180 meV. Hall measurements were performed using a Hall bar geometry with dimensions 1 cm x 0.3 cm x t μm, where t is the thickness of the sample. Ohmic contacts were fabricated and the GaN:Mg was activated by annealing a Pt/Au metallization at 750°C for 10 minutes[18]. The room temperature hole concentration and mobility were between 7×10^{16} cm^{-3} and 2.5×10^{17} cm^{-3}, and 7 $cm^2V^{-1}s^{-1}$ and 15 $cm^2V^{-1}s^{-1}$, respectively. Charge neutrality places the Fermi level at between 150 meV and 180 meV above the valence band.

The GaN:Mg film structure was studied by low frequency noise spectroscopy and by X-ray diffraction (XRD). The noise characteristics were measured using the Hall bar samples, from 1 Hz to 100 kHz with a Stanford Research Systems SR830 digital lock-in amplifier. The noise power spectral density was examined for a temperature range of 250 K to 400 K for each sample. The voltage noise was measured under constant current conditions with a four terminal configuration. Each sample was allowed to stabilize for 45 seconds and 100 data points were averaged at each measurement frequency. In addition, the GaN:Mg film

microstructure was studied by examining the high resolution x-ray diffraction rocking curve (ω scan). High-resolution x-ray diffraction was performed using a triple axis diffractometer with an analyzer crystal. In this configuration, the resolution limit of the instrument is 13 arcseconds.

III. Results and Discussion

Figure 1 displays the noise power spectral density divided by V^2, S_V/V^2, for sample I at 300 K. As shown the experimental data are well fit with one g-r level noise source and 1/f noise, with the magnitude of the 1/f noise exceeding the g-r noise magnitude for frequencies less than 30 Hz. This general combination of 1/f and g-r noise is observed in the S_V/V^2 spectrum for each sample as shown in Fig. 2.

A. Microstructural contributions to the measured 1/f noise

As increased structural inhomogeneity implies an increase in crystal defects, current constrictions, and interfaces, it is reasonable to expect an increase in the magnitude of 1/f noise. The S_V/V^2 spectrum, for frequencies in the range of 1 Hz to 30 Hz and temperatures between 250 and 400 K, is strongly correlated to the microstructure as characterized by asymmetric x-ray diffraction.

The symmetric, (00*l*), rocking curve FWHM were investigated and a weak correlation between the FWHM and 1/f noise magnitude was observed. Symmetric rocking curves are sensitive to pure screw or mixed dislocations that lie parallel the c axis with burgers vectors of **b** = ±[00.1] (pure screw) or ±[10.1], ±[01.1], ±[11.1], (mixed) and insensitive to pure edge threading dislocations that lie in the [00.1] direction, since they possess burgers vectors of either ±[10.0], ±[11.0], or ±[01.0][9,10]. Thus the symmetric rocking curve does not reflect all of the crystal defects or dislocations in the film. However, the broadening of the asymmetric rocking curve contains contributions from pure screw, mixed, and pure edge

dislocations. We find a strong correlation between the 1/f noise magnitude and the asymmetric, (*hkl*), rocking curve (ω-scan) FWHM as shown in Fig. 3. Thus, we may hypothesize that 1/f noise is particularly dependent on pure edge threading dislocations and that 1/f noise analysis is a possible transport-based method for determining crystal quality.

In addition, the Hooge parameter was calculated using the volume between the voltage contacts and values of $\alpha \approx 1-150$ were obtained for the samples studied. Recently, 1/f noise was observed in n-type GaN and a Hooge parameter of $\approx 5-7$ was found[13]. Generally, a value of $\alpha \leq 10^{-3}$ is obtained for homogeneous materials[19]. Hence, the high value of α is consistent with the poor crystalline quality and a large level of structural imperfections found in MOCVD GaN grown on sapphire. Figure 3 summarize this strong correlation between the integrated noise power spectral density divided by V^2, the Hooge parameter, and the (11.2) rocking curve FWHM. As displayed, the logarithms of the integrated S_v/V^2 and the Hooge parameter are directly proportional to the asymmetric rocking curve FWHM. In the limit of smaller (11.2) rocking curve FWHM's, the 1-30 Hz integrated S_v/V^2 is less than 10^{-13} Hz^{-1} and the Hooge parameter appears to become less than 1.

B. Origin of the g-r noise

Above 30 Hz, g-r noise associated with one trap level predominates. The g-r noise level is best examined by multiplying the S_v/V^2 by the angular frequency, ω, yielding the normalized noise power spectral density, $S_v\omega V^{-2}$. Subsequently, Fig. 4 displays the normalized noise power spectral density, $S_v\omega V^{-2}$ for sample I at 300 K, 335 K, 350 K, and 400 K. At 300 K, one definitive g-r noise level is observed while two g-r noise components are observed at 335 K, 350 K and 400 K. A plot of the normalized noise power spectral density on a log linear scale will exhibit a peak at $f = (2\pi\tau)^{-1}$, the characteristic frequency of

the g-r level[20]. The characteristic time was determined by applying a least square fit of Eq. (1) to the measured $S_v\omega V^{-2}$ spectrum. The activation energy, E_T, of the g-r process can then be obtained from a plot of $\log(\tau T^2)$ versus the inverse temperature. Only data in the frequency range of 100 Hz to 100 kHz was analyzed by an Arrhenius plot since there was not a sufficient amount of reliable low frequency data, f < 100 Hz.

The Arrhenius plot for the GaN:Mg samples studied is shown in Fig. 5. We find a trap located at 120 meV ± 25 meV and 106 meV ± 25 meV above the valance band with concentrations of $1.5\text{x}10^{20}$ cm^{-3} and $3\text{x}10^{20}$ cm^{-3} and capture cross sections of $1.6\text{x}10^{-21}$ cm^2 and $7.5\text{x}10^{-21}$ cm^2 for sample I and II, respectively. The associated g-r noise is significant only when the location of the trap or the center in the forbidden gap is within a few k_bT of the Fermi level. Consequentially, trap levels in the region 50 meV – 75 meV around the Fermi level will be the primary contributors to g-r noise.

The measured characteristic rates were unusually slow for a level located at 120 meV and the capture cross section is suggestive of a neutral or repulsive center, and the high concentration (slightly greater than the total Mg concentration of $1\text{x}10^{20}$ cm^{-3} as measured by SIMS in these samples) is suggestive of a Mg complex or other structural defect. Furthermore, this g-r level originates in the bulk GaN neutral regions and not in any depletion regions that may exist in the bulk owing to the structural defects. Since g-r noise processes originate from levels near the Fermi level and an activation energy of 120 meV was measured, any g-r process in the depletion region should possess an activation energy greater than the observed activation energy. Furthermore, traps in the depletion regions do not remain a constant energy away from the Fermi level and therefore give rise to broad, poorly defined, g-r noise peaks.

IV. Summary

We have used low-frequency noise analysis to examine MOCVD-grown p-type GaN:Mg. We observed a strong correlation between the integrated 1/f noise power and the structural imperfection of the sample as measured from the (ω-scan) FWHM of (11.2) x-ray diffraction peaks. The derived Hooge parameters are considerably larger than those of homogeneous semiconductors. Hence noise measurements imply MOCVD-grown GaN:Mg is a low quality material probably due to structural imperfections such as dislocations and grain boundaries. In addition, we have used noise spectroscopy to observe two trap levels giving rise to g-r noise in MOCVD-grown GaN:Mg. The most prominent g-r noise source has an activation energy of ~120 meV ± 25 meV and a concentration of ~$1x10^{20}$ cm^{-3} in the bulk neutral regions of two GaN:Mg samples grown in different laboratories. This level is possibly associated with the Mg dopant or a structural defect and its cross section suggests a repulsive center.

Figure Captions

Figure 1:

Noise power spectral density, S_V/V^2, for p-GaN:Mg at 300 K. Solid circles represent experimental data for sample I. The total noise is well fit by 1/f noise and g-r noise. The curve labeled total noise is a result from a least-squares fit of the sum of equation (1) and (3). The individual 1/f and g-r noise contributions to the total noise are also shown.

Figure 2:

Noise power spectral density divided by the applied voltage squared, S_V/V^2, for p-GaN:Mg at 300 K. Open circles, solid circles, solid squares, and open triangles represent experimental data for samples I to IV, respectively.

Figure 3:

The integrated noise power spectral density divided by V^2 and the Hooge parameter as a function of (11.2) rocking curve FWHM. Solid triangles and solid circles represent the integrated S_V/V^2 from 1 to 10 Hz and the Hooge parameter, respectively.

Figure 4:

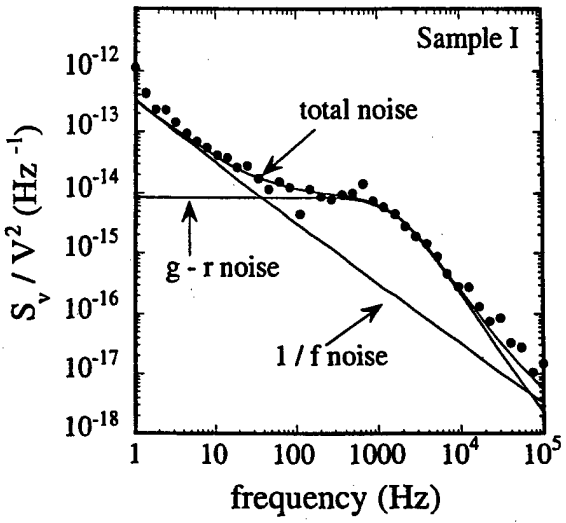
Normalized noise power spectral density, $S_V\omega/V^2$, for p-GaN:Mg. Solid circles, crosses, open squares, and open circles with dots are experimental data from sample I at 300 K, 335 K, 350 K, and 400 K, respectively. 1/f noise appears as a constant horizontal line and g-r noise is represented by a Lorentzian curve.

Figure 5:

Arrhenius plot of τT^2 versus inverse temperature. An activation energy of 120 meV ± 25 meV and 106 meV ± 25 meV, trap concentrations of 1.5×10^{20} cm^{-3} and 3×10^{20} cm^{-3}, and apparent capture cross sections of 1.6×10^{-21} cm^2 and 7.5×10^{-21} cm^2 were calculated for sample I and II, respectively.

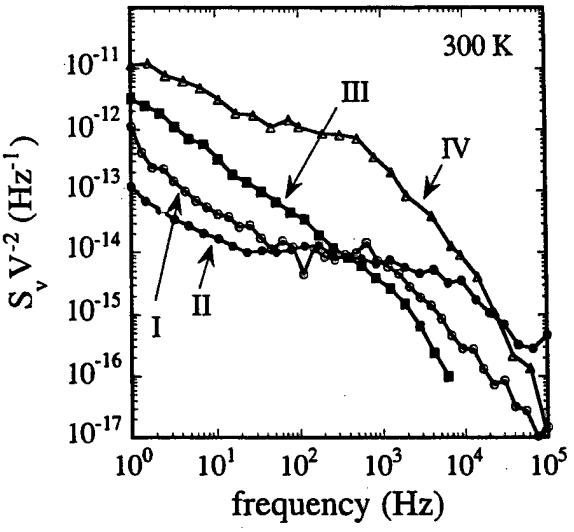
A. K. Rice

Figure 1



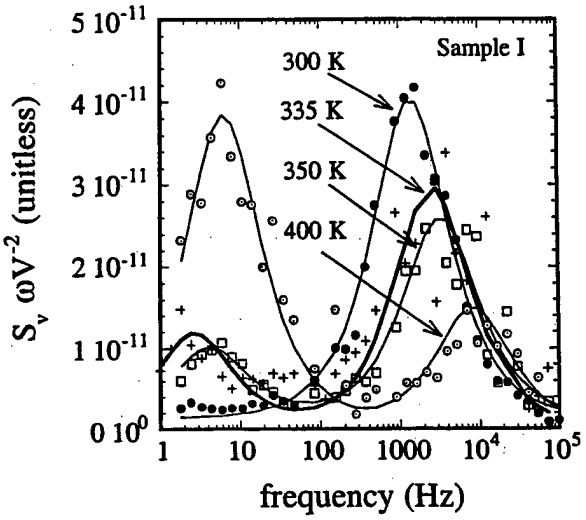
A. K. Rice

Figure 2



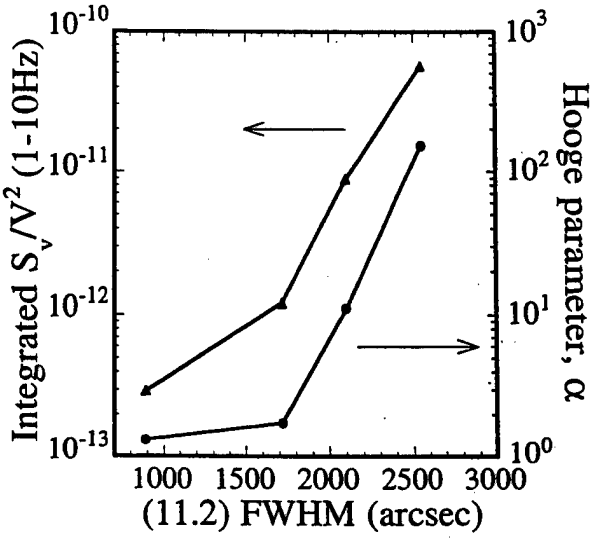
A. K. Rice

Figure 3



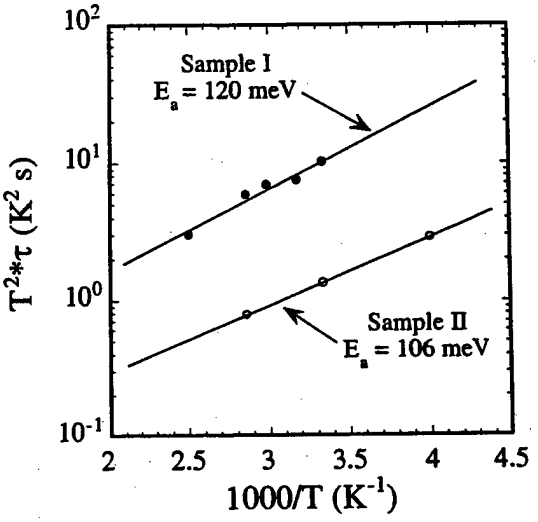
A. K. Rice

Figure 4



A. K. Rice

Figure 5



References

[1]T. Tanaka, A. Watanabe, H. Amano, Y. Kobayashi, I. Akasaki, S. Yamazaki, and M. Koike, Appl. Phys. Lett. **65,** 593 - 594 (1994).

[2]W. Götz, N. M. Johnson, J. Walker, D. P. Bour, H. Amano, and I. Akasaki, Appl. Phys. Lett. **67,** 2666 - 2668 (1995).

[3]W. Götz, N. M. Johnson, J. Walker, D. P. Bour, and R. A. Street, Appl. Phys. Lett. **68,** 667 - 669 (1996).

[4]H. Nakayama, P. Hacke, M. R. H. Kahn , T. Detchprohm, K. Hiramatsu, and N. Sawaki, Jpn. J. Appl. Phys. **35,** L282 - L284 (1996).

[5]F. A. Ponce, D. Cherns, W. T. Young, and J. W. Steeds, Appl. Phys. Lett. **69,** 770-772 (1996).

[6]K. Hiramatsu, S. Itoh, H. Amano, I. Akasaki, N. Kuwano, T. Shiraishi, and K. Oki, J. of Crystal Growth **115,** 628-633 (1991).

[7]S. D. Hersee, J. C. Ramer, and K. J. Malloy, MRS Bulletin **22,** 45 - 51 (1997).

[8]P. J. Hansen, Y. E. Strausser, A. N. Erickson, E. J. Tarsa, P. Kozodoy, E. G. Brazel, J. P. Ibbetson, U. Mishra, V. Narayanamurti, S. P. DenBaars, and J. S. Speck, Appl. Phys. Lett. **72,** 2247-2249 (1998).

[9]B. Heying, X. H. Wu, S. Keller, Y. Li, D. Kapolnek, B. P. Keller, S. P. DenBaars, and J. S. Speck, Appl. Phys. Lett. **68,** 643-645 (1996).

[10]T. Metzger, R. Höpler, E. Born, O. Ambacher, M. Stutzmann, R. Stömmer, M. Schuster, H. Göbel, S. Christiansen, M. Albrecht, and H. P. Strunk, Philosophical Magazine A **77,** 1013-1025 (1998).

[11]L. K. J. Vandamme, IEEE Trans. Electon Devices **41,** 2176-2187 (1994).

[12]D. V. Kuksenkov, H. Temkin, A. Osinsky, R. Gaska, and M. A. Khan, J. Appl. Phys. **83,** 2142-2146 (1998).

[13]N. V. D'yankonova, M. E. Levinshtein, S. Contreras, W. Knap, B. Beaumont, and P. Gilbart, Semiconductors **32,** 257-260 (1998).

[14]D. V. Kuksenkov, H. Temkin, R. Gaska, and J. W. Yang, IEEE Electron Device Lett. **19,** 222-224 (1998).

[15]The expression for A follows from the Copeland[16] formula for g-r noise in a n-type semiconductor. Using the deep level capture and emission processes, an expression of the noise current for a generation-recombination process, Fermi-Dirac statistics, and nondegenerate Boltzmann statistics the g-r noise spectrum is given as $S_I = \frac{A'}{1+(\omega\tau)^2}$, and $A' = \frac{2I^2\tau N_T}{n^2\nu}\frac{(BN_c/n)\exp(E_T/k_bT)}{\left[1+(BN_c/n)\exp(E_T/k_bT)\right]^2}$, where τ is the characteristic time, B is the spin degeneracy for the deep level, N_c and n are the density of states in the conduction band and free carrier concentration, respectively. Assuming non degenerate Boltzmann statistics $n = N_c\exp(E_F/k_bT)$ and approximating the magnitude of A' at $E_F = E_T$, yields $A' \approx N_T\nu^{-1}n_o^{-2}$, where n_o is the electron concentration for $E_T = E_F$. The same process holds for a p-type semiconductor, giving an analogous expression for A stated in the section below Eq. (1).

[16]J. A. Copeland, IEEE Trans. on Electron Devices **ED-18,** 50 - 53 (1971).

[17]F. N. Hooge, Phys. Lett. **29A,** 139-140 (1969).

[18]D. J. King, L. Zhang, J. C. Ramer, S. D. Hersee, and L. F. Lester, in *Material Research Society Symposium Proceedings*, San Francisco, Ca, 1997, p. 421 - 426.

[19]F. N. Hooge, IEEE Trans. on Electron Devices **41,** 1926 (1994).

[20]B. K. Jones, IEEE Trans. Electron Devices **41,** 2188-2197 (1994).

SUBMITTED J. Appl. Phys.
Nov. 1999

Microstructural Contributions to Hole Transport in p-type GaN:Mg

A. K. Rice, K. J. Malloy

Center For High Technology Materials, University of New Mexico, Albuquerque, 87106

Abstract

We present an analysis of hole transport in p-type Mg-doped GaN grown on sapphire substrates by metal-organic-chemical vapor deposition (MOCVD). We find that the experimental Hall mobility cannot be explained solely by traditional extended state scattering mechanisms. Not only are the mobilities not accurately modeled by numerically solving the Boltzmann transport equation (BTE), but the calculated results do not even reflect the trend in experimental mobility values between the investigated samples. We attribute these discrepancies to the microstructure of GaN:Mg grown on sapphire. A microstructure-oriented transport model is presented for an interpretation of the transport of holes in p-type GaN:Mg grown on sapphire. The microstructure-oriented model provides a simplified picture of the microstructure, consisting of two distinct microstructural phases in GaN on sapphire. Using this model for the experimental mobility, the extracted parameters from hole transport measurements are shown to be positively correlated with microstructural parameters determined from x-ray diffraction (XRD) measurements. The experimental mobility of p-type GaN:Mg grown on sapphire can be described as dependent upon the acceptor doping, impurity compensation, and microstructure, including dislocation density, columnar grain size, and grain boundaries.

I. Introduction

The transport characteristics of p-type Mg-doped GaN have generated much interest in recent years since the achievement of p-type GaN [1]. Initial concerns followed with the realization that p-type GaN:Mg possesses a high resistivity due to compensation, a hole activation energy of 150 – 200 meV and a low hole mobility [2-5] [6,7]. Furthermore, the microstructure of GaN:Mg grown on sapphire is inhomogeneous, and can be characterized as an ordered polycrystal [8,9] in which individual grains are of high crystalline quality but they are tilted and twisted with respect to one another. The role of this GaN:Mg microstructure on hole transport will be addressed.

This paper presents an analysis of the Hall mobility for GaN:Mg as thus far, a complete understanding of transport in p-type GaN:Mg is lacking. Such an analysis can be a powerful means of characterizing semiconductor transport, yielding information about the impurity concentration, impurity compensation, carrier scattering mechanisms, material parameters, and in this case, film microstructure. This analysis includes calculation of the mobility of crystalline GaN:Mg by numerically solving the Boltzmann transport equation (BTE). A numerical calculation of the BTE is necessary because it accurately accounts for the inelastic scattering mechanisms dominant at high temperature. All major scattering processes, screening, and overlapping of wave-functions have been incorporated.

It is found that unlike the hole mobility in other III-V compound semiconductors, the hole mobility of GaN:Mg cannot be explained solely by traditional extended state scattering mechanisms. Differences between the calculated and experimental Hall mobilities are observed throughout the entire temperature range investigated. However, this study will focus on the discrepancies observed at high temperature where optical phonon scattering is dominant. The

final interpretation of the behavior of the Hall mobility in GaN:Mg includes the effects of an inhomogeneous microstructure. The influence of the microstructure on the electrical properties of GaN:Mg qualitatively explains the discrepancies between the experimental Hall mobility and the calculated crystalline mobility of GaN:Mg.

In support of the Hall analysis, the GaN:Mg microstructure is examined by high resolution x-ray diffraction (XRD), scanning electron microscopy (SEM), and atomic force microscopy (AFM), and a correlation required by our model between the film structure and the mobility is observed. Finally, with the improvement in the growth of GaN:Mg, hole transport will approach single crystalline GaN:Mg. Hence, calculated limits of pure crystalline p-type GaN:Mg conductivity and mobility will be presented.

II. Transport Calculation

Transport theory in compound semiconductors assumes the validity of the effective mass approximation, Bloch wave functions, perturbation theory, and the Boltzmann transport equation. In this study the hole mobility for crystalline GaN:Mg was calculated by iteratively solving the BTE following Nag's book [10], providing an accurate calculation for both low and high temperatures. The mobility calculation explicitly takes into account carrier screening and overlapping wave-functions and includes ionized impurity, non-polar acoustic phonon (deformation potential), piezoelectric, non-polar optical phonon (deformation potential), and polar optical phonon scattering mechanisms. Each scattering mechanism exhibits a characteristic temperature dependence, and by analyzing the temperature dependence of the carrier mobility, the relative importance of each mechanism is obtained. Furthermore, by comparing calculated and experimental mobilities, the contributions of each scattering mechanism to the mobility are determined. However, in order to calculate the mobility due to various scattering mechanisms it

is necessary to use reasonable physical parameters for GaN:Mg. Hence, the following section addresses the material parameters used in the transport study.

A. Material Parameters

The material parameters used in this calculation are summarized in Table I. There are many uncertainties about the electronic band structure of wurtzite GaN, particularly the valence band. However, theoretical calculations in conjunction with experiments have provided estimates for various properties of the valence band. The parameters necessary for performing the transport calculations include hole effective masses, Γ point valence band energies, dielectric constants, optical phonon energy, scattering potentials, piezoelectric constants, the mass density, and the acoustical velocity.

Transverse and longitudinal effective masses for the heavy hole band (HH), light hole band (LH), and split off band (SO) of GaN have been estimated in theoretical band calculations [11]. Subsequently, the effective mass, for the HH, LH, and SO bands, is obtained from $m^* = \left(m_\perp^2 m_\parallel\right)^{1/3}$, giving $m_{HH}^* = 1.89 m_o$, $m_{LH}^* = 0.337 m_o$, and $m_{SO}^* = 0.813 m_o$, where m_o is the electronic mass. In addition, theoretical band calculation [11] along with experimental data [12-15] have predicted that the valence band for p-type GaN consists of three non-degenerate bands. The Γ point energies employed were an average of the following E_{LH} = 5.84 meV [11], 6 meV [12-15] and E_{SO} = 26.1 meV [11], 22 meV [14], 28 meV [13], 18 meV [12], 24 meV [15] yielding, E_{LH} = 6 meV and E_{SO} = 24 meV. Moreover, the density of states effective mass for the valence band is defined as $m_h^{*\frac{3}{2}} = m_{HH}^{*\frac{3}{2}} + m_{LH}^{*\frac{3}{2}} \exp\left(\frac{-E_{LH}}{k_b T}\right) + m_{SO}^{*\frac{3}{2}} \exp\left(\frac{-E_{SO}}{k_b T}\right)$, giving, at 300 K $m_h^* \approx 2m_o$. The low and high frequency dielectric constants were taken as 9.5 and 5.35 [16], respectively. Since, the longitudinal optical phonon energy has been reported as 90 meV [17], 91.2 meV [18], and 92 meV [16],

an average value of 91 meV was employed, yielding a longitudinal polar optical temperature of $\hbar\omega/k_b = \theta = 1055$ K. However, current uncertainties in the valence band structure are such that the scattering potentials in p-type GaN are not accurately known. Kim et. al. [19] have calculated the acoustic deformation potential to be 0.8 eV with an uncertainty of at least 2 eV. Hence, a value of 1 eV has been adopted for the acoustic deformation potential, E_{npa}. Furthermore, the optical deformation potential, E_{npo}, for most III-V compound semiconductors is approximately a factor of two larger than the acoustic deformation potential [20]. Thus, 2 eV has been used for the optical deformation potential. The piezoelectric constant, h_{pz} or e_{14}, has been estimated from data on n-type GaN mobility [21] as 0.375 C m^{-2} and from electromechanical coupling coefficients of n-type GaN [21] as 0.6 Cm^{-2}. Hence, a value of $h_{pz} = 0.5$ Cm^{-2} has been adopted. The lattice mass density was taken as $\rho = 6.1 \times 10^3$ kgm^{-3} [22]. Finally, the acoustic velocity, s, was calculated from the estimated longitudinal elastic constant [17], c_ℓ, where $c_\ell = \rho s^2$. The estimated longitudinal constant is $c_\ell = 26.53 \times 10^{10}$ Nm^{-2}, yielding $s = 6.59 \times 10^3$ ms^{-1}.

Given the valence band structure for wurtzite GaN is only spin-degenerate [11] at k = 0, transport only in the heavy hole, HH, band has been considered. The concentration in the light hole, LH, or split-off, SO, band is less than 5% to 15% of the free hole concentration in the temperature range studied An improvement of this initial transport calculation is the inclusion of parallel band conduction in the HH, LH, and SO bands. Comparing the HH, LH, and SO effective mass and assuming the scattering rate is the same as for the heavy hole band, the mobility for the light hole band and split off band are estimated at $6\mu_{HH}$ and $2\mu_{HH}$, respectively, where μ_{HH} is the mobility in the heavy hole band. If parallel band conduction were considered, the Hall mobility would be given by

$$\mu_H = \frac{p_{LH}\mu_{LH}^2 + p_{HH}\mu_{HH}^2 + p_{SO}\mu_{SO}^2}{p_{LH}\mu_{LH} + p_{HH}\mu_{HH} + p_{SO}\mu_{SO}}, \quad (1)$$

where μ_{LH} and μ_{SO} represent the light hole and split off hole mobility and p_{HH}, p_{LH}, and p_{SO} denote the heavy hole, light hole, and split off hole carrier concentration, respectively. At high temperature where $p_{HH} \sim 0.8\ p$, $p_{LH} \sim 0.05\ p$, and $p_{SO} \sim 0.15\ p$, the net effect of Eq. (2.1) is to increase the modeled mobility by approximately twice the heavy hole band mobility. Thus, including parallel band effects will increase the calculated mobility as compared to transport only in the heavy hole band. Also, the affect of scattering between the HH, LH, and SO band may also be accounted for. Realizing the e improvements can be incorporated in the future, only transport in the heavy hole band is considered.

II. Temperature Dependent Hall Measurements

A. Experimental Details

The samples investigated were grown on sapphire substrates by metal-organic chemical vapor deposition (MOCVD). Samples I, III, and IV were grown in the same laboratory, while sample II was grown in a different laboratory. The samples studied consist of a p-type layer of GaN doped with magnesium grown on an undoped GaN layer. The total thickness of each sample determined from an ellipsometry measurement is 2.8 μm, 2.8 μm, 2.9 μm, and 3.5 μm for samples I, II, III, and IV, respectively. The GaN:Mg was activated and ohmic contacts were formed by annealing a Pt/Au metallization at 750°C in flowing N_2 for 10 minutes [23]. Hall effect measurements were performed using a Hall bar to obtain the sheet resistivity, sheet carrier concentration, and mobility as a function of temperature between 120 K to 500 K. Repeatable Hall measurements were obtained only after allowing the temperature to stabilize for 5 minutes

and averaging 100 data points. The minimum temperature at which Hall measurements could be performed was determined by the voltage compliance of the Hall current source.

B. Carrier Concentration Analysis of Experimental Hall Data

The temperature dependence of the hole concentration for sample I and II is shown in Fig. 1. For each sample the value of the acceptor concentration, N_A, compensation ratio, $K = N_D/N_A$, and the activation energy E_a, were determined by performing a least-squares fit to the experimental Hall hole concentration, p, as a function of temperature. An equation giving the free hole concentration was found by applying Boltzmann statistics and charge neutrality yielding

$$p + N_D^+ = \frac{N_A}{\frac{g_o}{g_1}\exp\left(\frac{E_A - E_F}{k_b T}\right) + 1}, \qquad (2)$$

where $g_o = 2$ and $g_1 = 1$ are the degeneracies of the unoccupied and occupied acceptor states, respectively.

The values of N_A, K, and E_a, obtained by fitting the charge balance equation to the hole concentration data as a function of temperature for the samples are given in Table II. Also included in Table II are the room temperature mobility and carrier concentration. In addition, samples I, II, and III were investigated by secondary-ion-mass spectroscopy (SIMS). The results reveal a physical acceptor concentration of approximately 10^{20} cm^{-3} for each sample. The difference between the physical magnesium concentration, 10^{20} cm^{-3}, and the acceptor concentration determined from Hall measurements, given in Table II, implies that not all magnesium is electrically active.

For reasons that will be discussed in Section V, regarding the effect of the microstructure on transport properties, it was not possible to derive a consistent fit for ionized impurity concentrations from both the carrier concentration and the mobility data.

C. Mobility Analysis of Experimental Hall Data

The calculated mobility for single crystal GaN:Mg, as a function of temperature is shown in Fig. 2. Polar optical phonon, non-polar optical phonon, piezoelectric, and non-polar acoustical phonon scattering mechanisms have been included. Due to the polar nature of GaN [24], piezoelectric and polar optic scattering mechanisms are dominant at low and high temperatures, respectively. Furthermore, this lattice limited mobility curve sets a upper mobility limit for single crystal GaN:Mg.

Figures 3 (a) and (b) display the hole mobility of GaN:Mg as a function of temperature for sample III and II, respectively. Shown are the calculated mobility curve, the combined lattice scattering curve, the ionized impurity scattering curve, and the experimental data. The two dominant scattering mechanisms for impure crystalline GaN:Mg are ionized impurity scattering at low temperatures and polar optical scattering at high temperatures. Two observations can be made from Fig. 3. The calculated mobility is at least a factor of 4 greater than the experimental data for all samples and temperatures, and the experimental data shows different high temperature, lattice-limited mobilities in each sample. Figure 4 (a) and (b) correspondingly displays the experimental hole mobility and the calculated mobility as a function of temperature for each sample studied. Examining Fig 4, we see not only are the mobilities not accurately modeled by solving the BTE, but that the calculated results do not even reflect the trend in experimental mobility values between samples. For example, sample II has a higher ionized

impurity concentration than sample III, a fact reflected in the BTE calculation giving a lower mobility. However, the experimental results are exactly reversed - the sample with more impurities, sample II, has a higher mobility.

Clearly more factors control transport than have been included in the BTE solution. For example, neutral impurity scattering has been neglected. The inclusion of neutral impurity scattering, for sample II, reduces the total mobility by at most 15%, using the material parameters, N_A, N_D, and E_a, as determined from the Hall measurement. In this case the density of neutral impurities is given by $N_N = N_A - N_D - p$. Assuming the density of neutral impurities, N_N, to be the physical magnesium concentration of approximately 10^{20} cm^{-3} the mobility is further reduced. However, this modeled mobility curve possesses a weaker temperature dependence than the experimental mobility at low and high temperature and a maximum value of 19 cm^2/Vs. This modeled mobility is too low, probably because the neutral impurity scattering model assumes isolated and non-interacting neutral impurities, highly unlikely with such a large value of N_N. Hence, two limits of neutral impurity scattering have been provided. The largest mobility assumes the number of neutral impurities is determined by the acceptor concentration, while the lower limit depends upon the total magnesium concentration. The actual contribution of neutral impurity scattering probably lies within these two limits.

Although some of the material parameters for GaN:Mg are uncertain, the uncertainties are not large enough to account for the discrepancy between the calculated and experimental curves. Piezoelectric and optical polar phonon are the two major lattice scattering mechanisms in p-type GaN:Mg. The uncertainties in these two scattering mechanisms are now addressed.

At 100 K, the piezoelectric mobility must be reduced so that the total mobility, including ionized impurity mobility and piezoelectric mobility, fit the experimental mobility. For example,

in Fig. 5 (b), a 30 percent increase in the piezoelectric constant to a value of 0.67 Cm^{-2}, or, a decrease in the acoustic velocity of 25 percent to a value of $4.93x10^3$ ms^{-1} is required to fit the experimental mobility. This value of h_{pz} = 0.67 Cm^{-2} is possible correction for the low temperature discrepancies, however, the discrepancies at high temperature are still unaccounted for.

For high temperature, optical polar phonon scattering is dominant. Polar optical phonon scattering is dependent upon the low and high frequency dielectric constant. At 450 K, a reduction of 360 percent is required to fit the calculated mobility to the experimental mobility. This requires that $(k_o^{-1} - k_s^{-1})$ increase by 500 percent to a value of approximately 0.5, from the utilized value of 0.0816. The previous discussion suggests that the deviation in the calculated mobility cannot be explained by solely the uncertainty in the material parameters employed. Furthermore, since material parameters are constant between samples, only such factors as ionized impurities and crystalline qualities (dislocation density, grain boundary area, and grain size) are varying between samples. We attribute the mobility discrepancies to the role of these microstructure variations in GaN on sapphire.

IV. Discussion of Film Structure

Figures 5 (a), (b), and (c) display a secondary electron microscopy (SEM) image of a cleaved edge of sample I, II, and III, respectively. Qualitatively, sample II is the most homogeneous, while more uniform inhomogeneous microstructures appear in the other samples.

Atomic-force-microscopy (AFM) is a powerful method of characterizing film surfaces. Upon examining the film surface, some information about the bulk material can be obtained. Figures 6 (a) and (b) display AFM images of the sample II and III, respectively. The white and black regions in the AFM image denote a peak and a valley, respectively. The AFM image

shown in Fig. 6 (a) reveals 'wall-like' growth regions where it appears two columnar grains have coalesced. Furthermore, upon investigating Fig. 6 (b) the circled region contains 'black dots' that are lined up. They are thought to be dislocations clustered in the grain boundary region mapping out a grain region.

TEM studies of the microstructure of n-type GaN grown on sapphire have shown grain sizes ranging from 50 to 500 nm [25] with dislocations mainly clustered at the low angle grain boundaries. Scanning capacitance microscopy has also revealed possible grain sizes of 1 μm [26]. In regions surrounding both pure edge and mixed/screw dislocations, they observed a reduced change in capacitance with applied voltage as compared to 'dislocation free' regions. These regions tended to lie along the boundaries formed during the coalescence of island GaN in the early stages of growth. In addition, cathodoluminescence microscopy has revealed a correlation between grain size and yellow luminescence [9]. They proposed defect states inside grains at the low-angle grain boundaries are the origin of the yellow luminescence. Although these studies have investigated n-type GaN, it is reasonable to assume the microstructure of GaN:Mg also consists of an ordered polycrystal containing grain and grain boundary regions. This statement is supported, in part, by the investigation of the GaN:Mg film structure by SEM and AFM, as shown in Fig. 5 and 6, respectively.

Transport studies in n-type GaN [27-30] have alluded to the role of the microstructure on the transport properties. Tang et al. [27] observed discrepancies in their high temperature n-GaN mobility data and corrected their calculated fit with a 'crystal defect' scattering mechanism that possessed a $CT^{-1.5}$ temperature dependence, where C is a fitting constant. Furthermore, D. C. Look et al. [31] used N_A and $(k_o^{-1} - k_s^{-1})$ as fitting parameters and noticed a 30% discrepancy from the $(k_o^{-1} - k_s^{-1})$ literature value, implying at higher temperatures the calculated fit needed to be

reduced by 30%. However, GaN on sapphire typically possesses dislocation densities on the order of $10^8 - 10^{10}$ cm^{-2} [25,32]. Therefore dislocation scattering may contribute to the reduction in the experimental mobility, and has been recently examined in n-type GaN [28-30]. Dislocation scattering is usually treated as based either on an electrostatic interaction with carriers [33] or on the strain field interaction with carriers [34]. Both scattering mechanisms assume non-interacting dislocations, unlikely in heavily dislocated GaN and contrary to TEM studies of GaN on sapphire [25]. More importantly, the temperature coefficients for the electrostatic and strain field scattering mechanisms are both positive (meaning the scattering rate decreases with increasing temperature) and fail to explain the discrepancies observed at high temperature. Thus while it is possible dislocation scattering describes the discrepancies at low temperature [28-30], it cannot explain the high temperature differences. Instead, we choose to model the discrepancies between the experimental and calculated Hall mobility as the result of hole transport in two distinct microstructural phases in GaN on sapphire.

V. Microstructural Based Discussion of Electrical Properties

To interpret the discrepancies between the experimental and the calculated mobility a microstructure-oriented transport model, similar to one first proposed by Bube [35], has been invoked. This model is attractive because it provides a simplified picture of the microstructure and takes into account that carriers must traverse through two electrically distinct regions. The model consists of an inhomogeneous semiconductor possessing single crystal grain regions of dimension l_g, and resistivity ρ_g, separated by disordered grain boundary regions of dimension l_{gb} and resistivity ρ_{gb}, as illustrated in Fig. 7 (a).

The apparent resistivity and the apparent Hall voltage are calculated and the Hall constant, free carrier density, and the Hall mobility are subsequently derived. The conductivity

of an inhomogeneous material as shown in Fig. 7 (a) supports two parallel current paths. One path traverses the grain boundary region while the second path travels through the grain and the grain boundary region in series. Based on the theory just described the general equation for the measured resistivity is given by

$$\rho = \frac{(1+\beta)(\rho_g + \rho_{gb}\beta)}{1+\beta+\alpha\beta+\beta^2}, \tag{3}$$

where $\beta = l_{gb}/l_g$ and $\alpha = \rho_g/\rho_{gb}$.

The inhomogeneous transport model, as shown in Fig. 7 (a), simply reduces to transport in one element, as shown in Fig. 7 (b). Subsequently, the Hall voltage was treated as a series-parallel assemblage of the basic unit as indicated in Fig. 7 (b). Using the equivalent circuit, shown in Fig. 7 (c), an expression for the Hall voltage, ΔV_H, is ascertained. The measured Hall constant R is related to ΔV_H by $R = \frac{\Delta V_H}{JB(l_g + l_{gb})}$, where J is the total current density and B is the applied magnetic field. The apparent carrier density, p_{app}, and the Hall mobility, μ_{app}, are calculated from the Hall constant, R, via $p = (R\,q)^{-1}$ and $\mu = R/\rho$. For $\alpha, \beta << 1$, it can be shown that the measured free carrier concentration can be expressed as

$$p_{app} = \frac{p_g}{1+\beta(1+\beta/\alpha)}, \tag{4}$$

and the apparent Hall mobility as

$$\mu_{app} = \mu_g \frac{\alpha}{\alpha+\beta} + \beta\mu_{gb}. \tag{5}$$

Figures 8 (a) and (b) display the apparent free carrier concentration and the apparent Hall mobility as a function of β for various α values. As will be shown later in the section, typical values of β and α are approximately 10^{-3} and 10^{-4}, respectively. Hence, from Eq. (4) and Fig. 8 (a), the apparent carrier density is principally determined by the grain carrier density. Thus, the

experimentally measured values for N_A, K, and E_a change little upon including the effects of inhomogeneity. However, from Eq. (5) and Fig. 8 (b) the apparent Hall mobility is greatly influenced by the sample inhomogeneity, for example, $\mu_{app} \sim 0.1\ \mu_g$ for $\alpha = 10^{-4}$ and $\beta = 10^{-3}$. Hence, the sample inhomogeneity prevents a consistent fit of the ionized impurity concentration from both the carrier concentration and the mobility data.

Recall $\beta = l_{gb}/l_g$ is a constant but $\alpha = \rho_g/\rho_{gb} = \dfrac{\mu_{gb}p_{gb}}{\mu_g p_g}$ will vary with temperature. Thus, the apparent Hall mobility will depend upon β, p_{gb}/p_g and μ_{gb}/μ_g. The grain region is assumed single crystal GaN, thus, the grain region material parameters p_g and μ_g are known from our previous mobility calculations given in Section III part C. The inhomogeneous material has been modeled as crystalline particles separated by disordered interparticle regions. This simple ohmic conduction model essentially consists of an assemblage of series and parallel temperature dependent resistors.

Instead of fitting the p_g/p_{gb} ratio directly, the grain boundary material is assumed to posses a potential barrier or step (positive or negative), V_B. Hence, the equation used to model the hole concentration in the grain boundary region is $p_{gb} = p_g \exp(-qV_B/k_bT)$, where q, k_b, and T represent the electronic charge, boltzmann constant, and temperature, respectively. Regardless of the functional relationship describing p_g/p_{gb}, our model simply fits the ratio, p_g/p_{gb}.

Other models of transport between the grain and grain boundary exist and a nice review is given by Lahiri et. al. [36]. For example, the earliest concept focused on dopant-segregation [37], assuming the dopant atoms mostly segregate into the grain boundary layers and hence cannot contribute to the electrical conduction. A non-ohmic conduction model based on the assumption that a potential barrier is created by trapped carriers in the grain boundaries has also been

investigated [38,39]. For this case the transport was modeled by field emission and thermionic emission of carriers over the barrier. Another approach proposed drift-diffusion transport in crystalline-amorphous-crystalline semiconductor system [40,41]. Using these other possible methods only changes what parameter you are indirectly fitting. Furthermore, very little is known about the grain boundary region for p-type GaN:Mg, in particular if carrier trapping is present and the amount of disorder in the grain boundary region, hence, a simple ohmic conduction model was used. Once more information about the p-type grain boundary is known a more accurate model can be evoked.

A least squares fit of Eq. (5) to the temperature dependent experimental Hall mobility for each sample was performed. The fitting parameters were β, V_B, A, and B, where A and B are related to the apparent grain boundary mobility by $\mu_{gb} = (A\,T^{1.5} + B\,T^{-1.5})^{-1}$. This equation used to model the grain boundary mobility is a traditional mobility equation using Matthiessen's rule to add the mobility assuming two scattering mechanisms, ionized impurity scattering and polar optical phonon lattice scattering. This initial assumption was again used due to the lack of information known about the grain boundary region. Once more information is available; a more accurate representation of transport in the grain boundary region can be employed. Figure 9 displays the results of the least squares fit for sample I. Shown are mobility curves for crystalline GaN:Mg (in the grain region), the experimental data, the grain boundary region, and the microstructure-oriented model. The extracted parameters, β^{-1}, V_B, A, and B are displayed in Table III.

The best fit to the experimental mobility data requires that the apparent grain boundary mobility be on the order of 0.01 cm^2/Vs and possess a slight temperature dependence. The apparent grain boundary mobility is not the actual mobility in the grain boundary region.

Instead, it is the result of the energy dependence of the mobility of a disordered material combined with the energy dependence of the carriers injected from the grain region. Developing this argument, at low temperature the majority of the carriers injected from the grain region into the grain boundary posses a low energy; hence, they enter the low mobility states in the grain boundary region. As the temperature increases the number of injected carriers possessing higher energy will increase and they will begin to enter the extended states of the grain boundary region and the apparent mobility increases. As the temperature increases further, the grain boundary mobility eventually begins to decrease due to lattice scattering. As stated previously, dislocation scattering may influence the mobility at low temperature, as shown n-type GaN [30]. Our model accounts for dislocation scattering indirectly in the temperature dependence of the grain boundary mobility at low temperature.

The voltage barrier, V_B, located between the grain and grain boundary region was fitted to both positive and negative values. This implies there are many possible mechanisms influencing the barrier height, for example, band gap narrowing, due to heavy doping in the grain boundary region or a mobility edge arising from disorder in the grain boundary region. The barrier height, V_B, will be positive or negative if disorder effects or heavy doping effects dominate, respectively. For the samples investigated it appears heavy doping effects in the grain boundary region are dominant, and the values of V_B correspond to room temperature p_g/p_{gb} ratios of 0.5 to 1.

The discrepancies between experimental mobility and the calculated mobility are probably due to a combination of parameters, however, the average grain size to grain boundary size ratio of the material, as determined from transport, is one parameter that can be

independently verified. Subsequently, in support of this inhomogeneous transport model, the GaN:Mg film microstructure was characterized by x-ray diffraction.

VI. X-Ray Diffraction Analysis

High-resolution x-ray rocking curves were performed using a triple axis diffractometer with an analyzer crystal. In this configuration, the resolution limit of the instrument is 13 arcseconds. The lateral coherence length, the heterogeneous strain normal to the surface, the amount of tilt and the rotation each columnar grain possesses is determined from the investigation of (00*l*) symmetric (ω-scan) rocking curve, radial (ω/2θ) scan, and asymmetric (105) ϕ scan FWHM.

A. Analysis of the Symmetric Rocking Curve

For the resolution limits stated above, the symmetric, (00*l*), rocking curve (ω-scan) breadth is controlled only by the out-of plane mi orientation or tilt, α_{tilt}, and by the lateral correlation length, $L_{\parallel}$, parallel to the sample surface. The contributions from each of these broadening mechanism can be determined by following a procedure similar to the Williamson-Hall plot [42]. Here, $\beta_{\Omega}(\sin\theta)/\lambda$ is plotted against $(\sin\theta)/\lambda$, where β_{Ω} is the integral width of the ω-scan, λ is the X-ray wavelength, and 2θ is the scattering angle.

The Williamson-Hall plot separates the tilt and lateral coherence contribution of the reciprocal space breadth due to tilt and lateral coherence. The broadening in reciprocal space due to tilt will increase with scattering order, while the breadth due to the presence of a lateral correlation length is independent of the distance from the k-space origin. Thus, if a linear superposition of the coherence length and tilt FWHM line profiles is assumed, then the breadth in reciprocal space is $\Delta K = \Delta K_{L_{\parallel}} + \Delta K_T$, where $\Delta K_{L_{\parallel}}$ and ΔK_T represent the breadth due to the

lateral coherence length and the out-of plane misorientation, respectively. Subsequently, from the y-intersection, y_o, and slope, m, of a linear fit to the $\beta_\Omega(\sin\theta)/\lambda$ versus $(\sin\theta)/\lambda$ plot, the correlation length, $L_{\|} = 0.9/(2y_o)$, and the tilt angle, $\alpha_{tilt} = m$, are estimated. Figure 10 displays the Williamson-Hall plot for the (00*l*) rocking curve FWHM for each sample investigated. The lateral correlation lengths and the tilt angles are provided in Table IV. As shown, sample II sample possesses columnar grains with larger in-plane coherence lengths and a tilt smaller by half, with respect to the c axis, than the three other samples.

The density of screw dislocations, $N_{|000l|}$, can be estimated [43,44] from the assumption that the affect of screw dislocations is to provide an over all tilt to the columnar grain. This is a reasonable assumption since the burgers vector is along the dislocation line for a screw dislocation. The following equation estimates the density of screw dislocations,

$$N_s = \frac{\alpha_\Omega^2}{4.35|b_c|^2}, \qquad (6)$$

where $|b_c| = 0.5185$ nm, is the burgers vector of the c-type threading dislocation. The estimated density of screw dislocations is provided in Table IV. As shown, sample II is estimated to possess almost and order of magnitude less density of screw dislocations than the other three GaN samples investigated.

B. Analysis of the Symmetric Radial Scan

Information on the heterogeneous strain perpendicular to the surface, the coherence length perpendicular to the surface, and the density of edge dislocations can be obtained from an investigation of the symmetric (00*l*) radial scan ($\omega/2\theta$) FWHM and the asymmetric (105) ϕ scans. Under the assumptions that broadening of the (00*l*) symmetric radial scan is only due to a coherence length normal to the surface, $L_\perp$, and heterogeneous strain, $\varepsilon_\perp$, $L_\perp$ and $\varepsilon_\perp$ can be

estimated following a similar procedure outlined in Section VI Part A. The broadening in reciprocal space due to strain is proportional to the scattering order while the broadening due to a small coherence length is independent of the scattering order. Hence, the y-intercept, y_o, and slope, m, of a linear fit to $\beta_{\omega/2\theta}\cos\theta/\lambda$ plotted against $\sin\theta/\lambda$ (Williamson-Hall plot) [42] provide an estimation of $L_\perp = 0.9/(2y_o)$ and $\varepsilon_\perp = m/4$. From a best linear fit, the heterogeneous strain and coherence normal to the surface are estimated, and the results are provided in Table V.

The y-intercept of the best linear fit was close to zero or negative, yielding unbelievably large perpendicular coherence lengths, possibly implying the broadening may be thickness limited. However, the heterogeneous strain was determined and sample II possesses a strain roughly an order of magnitude less than that in the other samples studied.

C. Analysis of Asymmetrical (105) Φ scan FWHM

The amount of twist or rotation with respect to the c axis is estimated from an asymmetrical ϕ scan, as shown in Fig. 11. The breadth of the ϕ scan is assumed to be the amount of rotation, α_ϕ, each sample experiences, and the results for a (105) ϕ scan are displayed in Table VI. Furthermore, if the rotation is assumed to be due to a-Type threading dislocations then an estimation of the density of edge dislocation can be made following the equation given by Gay et. al. [43] and modified by Dunn and Koch [44]

$$N_E = \frac{\alpha_\phi^2}{4.35 b_E^2}, \qquad (7)$$

where the burgers vector, $|\mathbf{b}_E| = 0.3189$ nm, is for a pure edge dislocation. This equation applies for isolated dislocations. However, in GaN the dislocations are also clustered at the low angle grain boundaries. Thus, Eq. (7) is modified to account for the clustered dislocations between the

grains, as characterized by $L_{\|}$, from Section VI Part A. The density of edge dislocations for this case is given as

$$N_E = \frac{\alpha_\phi}{2.1|b_E|L_{\|}}. \qquad (8)$$

The two extreme cases just addressed provide a range for the estimation of pure edge dislocations in the investigated samples, since both cases presumably apply. Table VI provides the density of edge dislocations, calculated from Eqs. (7) and (8) for each sample.

VII. Correlation between XRD and Microstructure-Oriented Model Coherence Length

An apparent correlation between the lateral correlation length, $L_{\|}$, as determined from x-ray diffraction, and the extracted ratio $\beta^{-1} = l_g/l_{gb}$, as determined from the inhomogeneous transport model, has been observed. The correlation between $L_{\|}$ and β^{-1} is shown in Fig. 12. The less than perfect correlation is due in part to the following reasons. Clearly more factors control transport than have been included. For example, the transport may depend upon the different degrees of twist or tilt between adjoining grains, and each sample realistically possesses a different range of grain sizes but only an average size was estimated. Furthermore, the effects of many factors giving rise to the discrepancies between the experimental and modeled mobility have been reduced to one parameter, β^{-1}, the grain to grain boundary length ratio. In addition, β^{-1}, a ratio, was compared to a physical length, $L_{\|}$. Ideally, one would like to correlate the grain size l_g, as determined from transport, and the lateral coherence length, $L_{\|}$, as determined from XRD. However, no independent information about the grain boundary exists. Thus, the less then ideal correlation between $L_{\|}$ and β^{-1} can manifest itself in the difference in l_{gb} for each sample.

The microstructure of sample IV probably accounts for the one inconsistent point

observed in Fig. 12 between the grain length to grain boundary length ratio, β^{-1}, and the lateral grain size, $L_{\|}$, as determined by XRD. The material of sample IV possesses room temperature mobility comparable to the sample II, yet its' film structure, as characterized by XRD was among the worst of the samples investigated. XRD examines the entire layer thickness and may appear poor due to the quality of the film near the buffer layer. Yet, the transport of holes will occur in the higher crystalline quality material, typically located in the top half of GaN samples. If parallel conduction is occurring, the measured Hall mobility is a non-linear combination of the mobility and carrier concentration in each layer given by

$$\mu_H = \frac{W_1 p_1 \mu_1^2 + W_2 p_2 \mu_2^2}{W_1 p_1 \mu_1 + W_2 p_2 \mu_2}, \qquad (7)$$

where W_1 and W_2 represent the thickness of the two layer material, p_1 and p_2 denote the carrier concentration for the two layers, and μ_1 and μ_2 are the mobility in each layer. It is expected that the extended state mobility of the layer adjacent to the GaN/air interface is greater than the mobility of the more disordered region near the GaN/buffer interface. Hence, transport will depend on the more homogeneous layer near the GaN/air interface.

In addition, experimental mobility is not correlated with the lateral coherence length, $L_{\|}$. This is understandable since the experimental mobility is dependent upon the acceptor concentration, impurity compensation, and the microstructure. For example, just as the mobility of p-type GaN:Mg grown on sapphire cannot be modeled by only considering the traditional extended state scattering mechanisms, the mobility cannot be modeled by only considering the material quality.

In summary, it has been shown that the experimental mobility of GaN:Mg is influenced by the microstructure. A model has been provided to explain the high temperature discrepancies between the mobility numerically calculated to accurately account for the inelastic scattering of

polar optic phonons and the experimental mobility. Furthermore, a correlation required by the inhomogeneous model between the lateral correlation length, as determined by x-ray diffraction, and the extracted ratio, $\beta^{-1} = l_g/l_{gb}$ was observed.

Eventually, with improved growth of GaN, the material will approach ideal single crystal quality. Such an improved quality might be expected for the "lateral epitaxial overgrowth (LEO)" material now being investigated in several laboratories [45-49] or other novel growth technique [50]. In these cases the mobility of p-type GaN:Mg should be well described by traditional extended state scattering mechanisms. Hence, the next section will address the limits in GaN:Mg conductivity and mobility for ideal single crystal GaN:Mg.

VI. Conductivity and Mobility Limits in Single Crystal GaN:Mg

Figures 13 (a) and (b) display the calculated mobility and conductivity for crystalline p-type GaN:Mg with an activation energy of 150 meV and compensation ratio of K = 0.1 as a function of Mg doping concentration. As shown, the conductivity has an upper limit of 10 $(\Omega\ cm)^{-1}$ at 300 K and 30 $(\Omega\ cm)^{-1}$ at 500 K. Hence, as the growth of p-type GaN:Mg improves, GaN devices that include p-type GaN:Mg will still possess a high spreading resistance.

VII. Summary

From the analysis of the p-type GaN:Mg Hall mobility, it has been shown that the experimental Hall mobility cannot be explained solely by traditional extended state scattering mechanisms. We see not only are the mobilities not accurately modeled by solving the BTE, but that the calculated results do not even reflect the trend in experimental mobility values between samples. While dislocation scattering may control the low temperature mobility it does not explain the discrepancies observed for high temperature. A microstructure-oriented model is

presented for an interpretation of the transport of holes in p-type GaN:Mg grown on sapphire. The microstructure-oriented model provides a simplified picture of the microstructure, consisting of two distinct microstructural phases in GaN on sapphire. Using this model for the experimental mobility, the extracted parameters from hole transport measurements were shown to be positively correlated with microstructural parameters determined from XRD measurements. The experimental mobility of p-type GaN:Mg grown on sapphire can be described as dependent upon the acceptor doping, impurity compensation, and microstructure, including dislocation density, columnar grain size, and grain boundaries.

Table Captions

Table I:

Material parameters used for calculating the mobility of p-type GaN:Mg.

Table II:

Impurity concentrations, compensation ratio, activation energy, 300 K free hole concentration, and 300 K mobility each sample investigated.

Table III:

Parameters extracted from the microstructure-oriented model. They include β^{-1}, the ratio of grain length to grain boundary length, A and B, coefficients of the apparent grain boundary mobility, and V_B, the extracted barrier height.

Table IV:

Parameters extracted from the rocking curve Williamson-Hall plot. They include $L_{\parallel}$, α_{tilt}, and N_s, which respectively denote the lateral coherence length, angle of tilt, and density of screw dislocations.

Table V:

Parameters extracted from the radial scan Williamson-Hall plot. They include $L_{\perp}$ and $\varepsilon_{\perp}$ which respectively denote the average coherence length and the amount of strain normal to the surface.

Table VI:

Parameters extracted from the asymmetrical ϕ scan. They include α_ϕ, N_E, and $N_E^{'}$, which respectively denote the average twist each columnar grain possesses, the number of edge dislocation assuming they are isolated, and the number of edge dislocations assuming they are clustered at a low angle grain boundary.

Figure Captions:

Figure 1:

Hall hole concentration as a function of inverse temperature for p-GaN. Solid triangles and open squares represent experimental data for the sample I and II, respectively. Solid lines result from least–squares fits of the charge balance equation to the experimental data.

Figure 2:

Individual hole lattice scattering mechanisms for GaN:Mg. (a) PO = polar optical phonon, (b) NPO = non-polar optical phonon, (c) NPA = non-polar acoustical phonon, (d) PZ = piezoelectric, (e) lattice limited = combined lattice scattering.

Figure 3:

Calculated and experimental hole mobility as a function of temperature. II = ionized impurity, total = total calculated mobility, solid dots are experimental data, (a) Sample I: $N_A = 14 \times 10^{18}$ cm^{-3}, K = 0.58, $E_a = 153$ meV, (b) Sample II: $N_A = 9.6 \times 10^{18}$ cm^{-3}, K = 0.15, $E_a = 173$ meV.

Figure 4:

Hall mobility as a function of temperature for p-type GaN:Mg. (a) Experimental data: Solid squares, solid diamonds, solid circles, and open circles represent experimental mobility for sample I, II, III, and IV, respectively, (b) mobility calculation for each sample investigated using material parameters given in Table I and II.

Figure 5:

SEM images taken of a cleaved edge for three samples: (a) sample II, (b) sample I, and (c) sample III.

Figure 6:

Atomic force microscopy (AFM) topographs for samples in this study, (a) sample II, (b) sample III.

Figure 7:

Schematic representation of Bube's model with grains of dimensions, l_g, separated by grain boundaries of dimensions, l_{gb}. (b) Basic unit of a grain showing bulk (g) and boundary (gb) regions. (c) Equivalent circuit to describe the Hall voltage. V_H and ΔV_H are the Hall voltage, j_1 and j_2 are the current density for the two current pathways in the basic unit, and r_g, r_{gb1}, r_{gb2}, V_g, V_{gb1}, and V_{gb2} are the resistance and voltage drop across the grain (g) and grain boundary (gb) regions used to calculate the Hall voltage.

Figure 8:

(a) The apparent carrier concentration divided by the grain carrier concentration ratio plotted as a function of $\beta = l_{gb}/l_g$ for various values of $\alpha = \rho_g/\rho_{gb}$. (b) The apparent mobility divided by the grain mobility ratio plotted as a function of $\beta = l_{gb}/l_g$ for various values of $\alpha = \rho_g/\rho_{gb}$. For typical values of β and α the inhomogeneity influences the carrier concentration Hall measurement less than the mobility measurement.

Figure 9:

Mobility as a function of temperature. Shown are the grain (crystalline) mobility, grain boundary mobility, experimental mobility for the sample I, and least squares fit of the experimental data to the apparent mobility, given in Eq. (2.5), from the microstructure-oriented model.

Figure 10:

Williamson-Hall plot of the rocking curve FWHM of symmetric XRD peaks.

Figure 11:

Asymmetrical (105) ϕ-scan for sample II.

Figure 12:

Shown is the extracted ratio of grain to grain boundary length, $\beta^{-1} = l_g/l_{gb}$, as determined from the microstructure-oriented model, as a function of $L_{\parallel}$, as determined from XRD. The straight line represents a best linear fit to the data.

Figure 13:

(a) Calculated low-field hole mobility for p-type GaN:Mg as function of the Mg concentration for ambient temperatures of 100 K, 300 K, and 500 K. (b) Calculated conductivity for p-type GaN:Mg as a function of Mg doping compensation for ambient temperatures of 100 K (solid), 300 K (dashed), and 500 K (solid). For compensation, $K = 0.1$ and $E_a = 150$ meV.

Table I:

Heavy hole effective mass	m_h^*	$1.89m_o$ [i]
Light hole effective mass	m_l^*	$0.337\ m_o$ [i]
Split-off effective mass	m_{so}^*	$0.813\ m_o$ [i]
Light hole energy	E_{lh} (meV)	6 [i-v]
Split-off hole energy	E_{so} (meV)	24 [i-v]
Low frequency dielectric constant	k_s	9.5 [vi]
High frequency dielectric constant	k_o	5.35 [vi]
Longitudinal polar optical temperature	Θ (K)	1055 [vi-viii]
Non-polar acoustical deformation potential	E_{NPA} (eV)	1 [ix]
Non-polar optical deformation potential	E_{NPO} (eV)	2 [x]
Piezoelectric constant	h_{14} (C m^{-2})	0.5 [xi]
Mass density	ρ (10^3 kg m^{-3})	6.10 [xii]
Acoustical velocity	s (10^3 m s^{-1})	6.59 [vii]

i. Ref. [11], ii. Ref. [12], iii. Ref. [13], iv. Ref. [14], v. Ref. [15], vi. Ref. [16], vii. Ref. [17], viii. Ref. [18], ix. Ref. [19], x. The optical deformation potential is assumed to be approximately twice the value of the acoustic deformation potential following Wiley [20]. Most III-V p-type semiconductors have E_{npo}/E_{npa} ~2. xi. Ref. [21], xii. Ref. [22].

i. A. K. Rice

Table II:

Sample	N_A (10^{18} cm^{-3})	N_D (10^{18} cm^{-3})	K	E_a (meV)	p (10^{17} cm^{-3})	μ (cm^2/Vs)
I	14	8.2	0.58	153	0.7	6.2
II	9.6	1.5	0.15	173	2.03	15.2
III	2.4	0.7	0.3	183	0.8	7.7
IV	7.0	3.3	0.48	148	1	15.9

A.K. Rice

Table III

Sample	$\beta^{-1} = l_g/l_{gb}$	A (V s cm^{-2} K$^{-3/2}$)	B(V s cm^{-2} K$^{3/2}$)	V_B (mV)
I	207	3.4×10^{-3}	2.4×10^{4}	0.6
II	351	3.4×10^{-3}	1.3×10^{4}	-8.7
III	223	4.4×10^{-3}	1.7×10^{4}	-5.4
IV	311	3.8×10^{-3}	2.3×10^{4}	-19.8

Table IV

Sample	$L_{\|}$ (nm)	α_{tilt} (deg)	N_s (10^7 cm^{-2})
I	594	0.15	59
II	835	0.06	9.4
III	219	0.11	32
IV	331	0.13	44

Table V

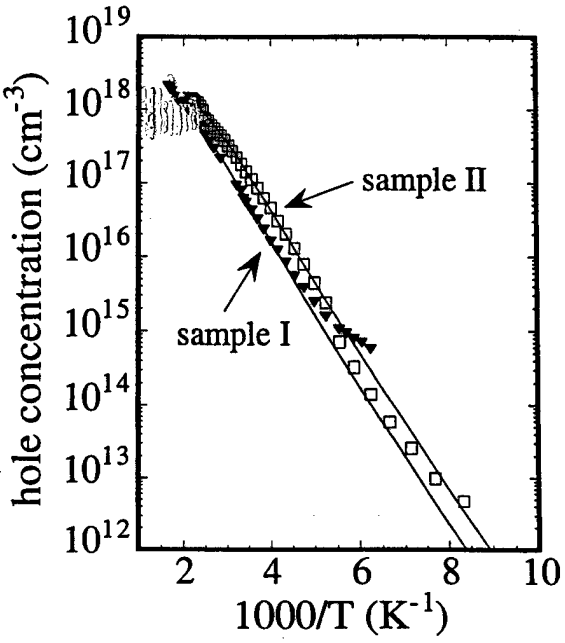
Sample	$L_\perp$ (nm)	$\varepsilon_\perp$, strain
I	15946	1.0×10^{-4}
II	3665	3.2×10^{-5}
III	-	2.2×10^{-4}
IV	-	1.8×10^{-4}

Table VI

Sample	α_ϕ (105) (deg)	N_E (cm^{-2}) (105)	N_E' (cm^{-2}) (105)
I	0.7795	4.2×10^{10}	3.4×10^{9}
II	0.3749	9.7×10^{9}	1.2×10^{9}
III	0.86	5.1×10^{10}	1.0×10^{10}
IV	0.8946	5.5×10^{10}	7.0×10^{9}

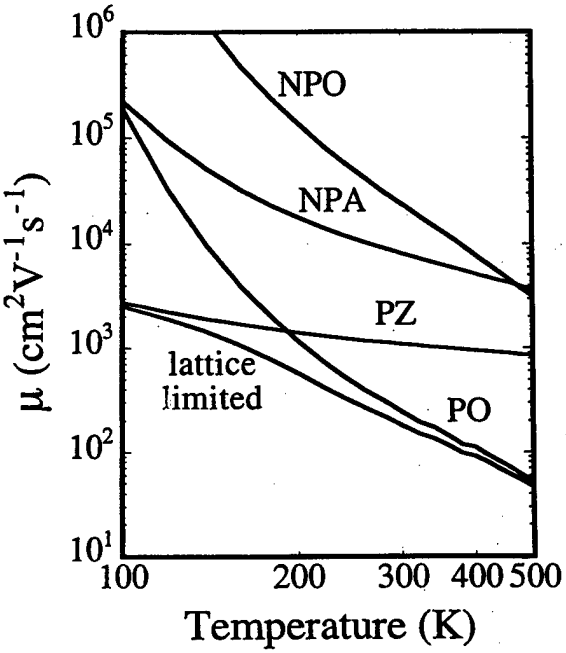
A. K. Rice

Figure 1:



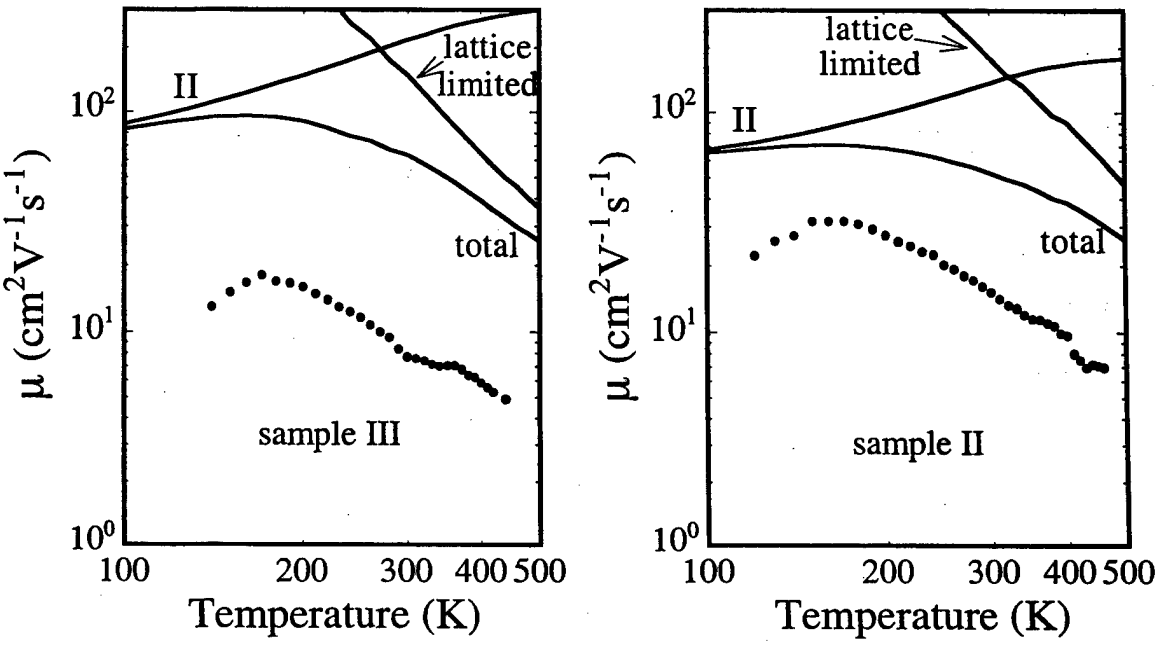
A. K. Rice

Figure 2:



A. K. Rice

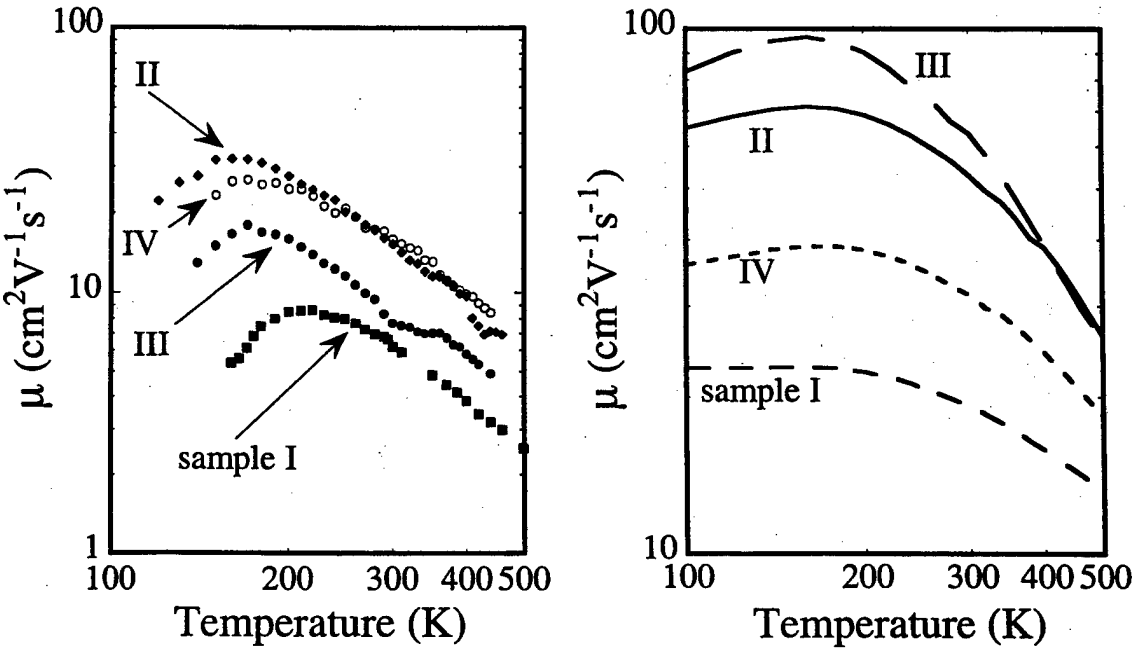
Figure 3:



(a) (b)

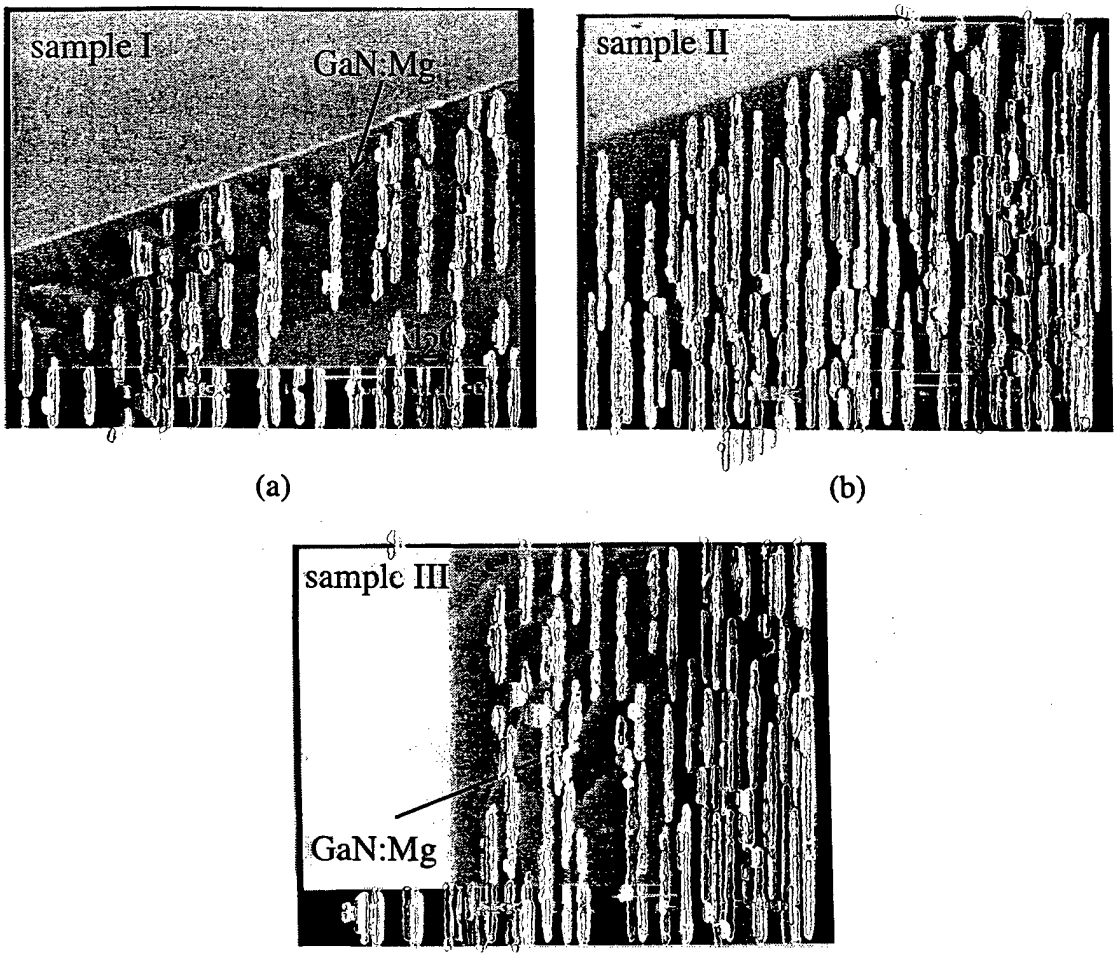
A. K. Rice

Figure 4:



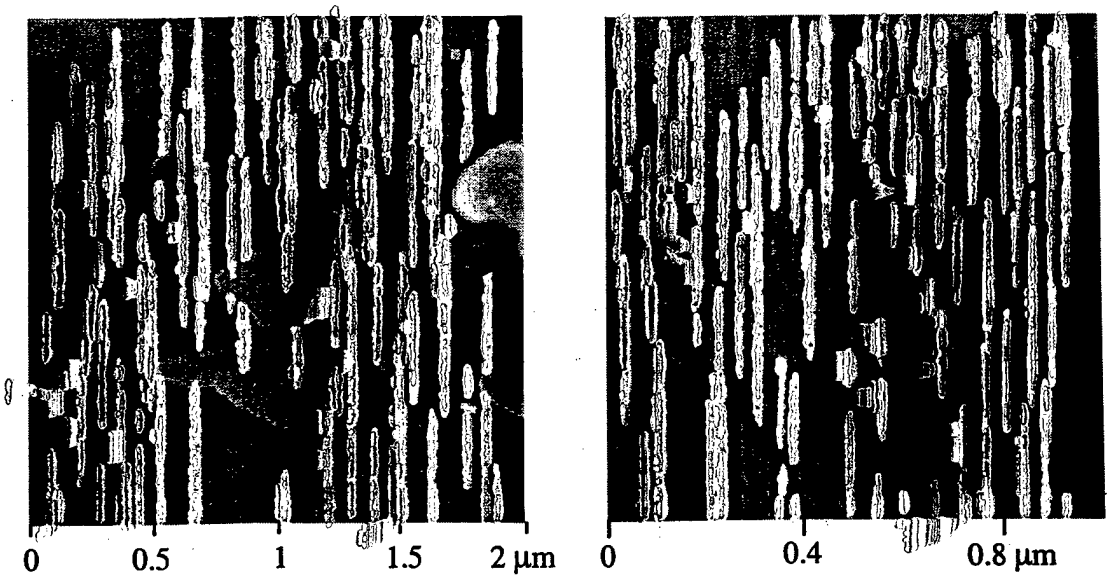
A. K. Rice

Figure 5



A.K. Rice

Figure 6



(a) (b)

A.K. Rice

Figure 7

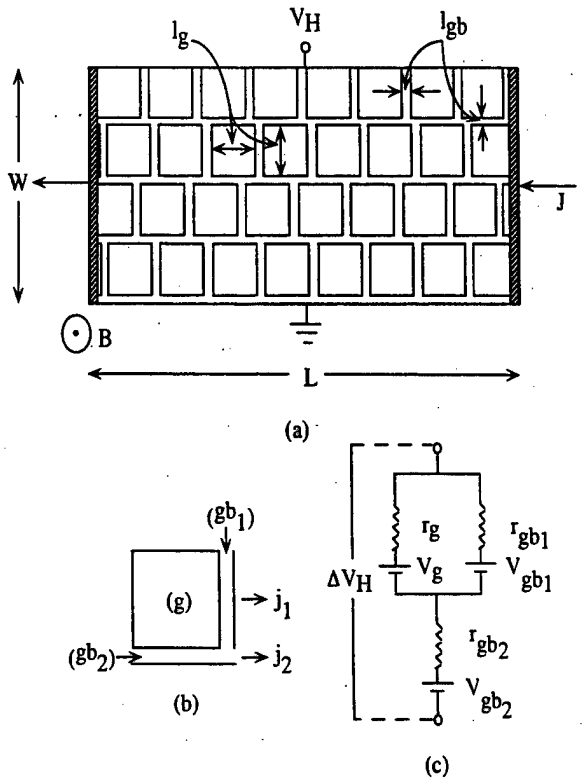
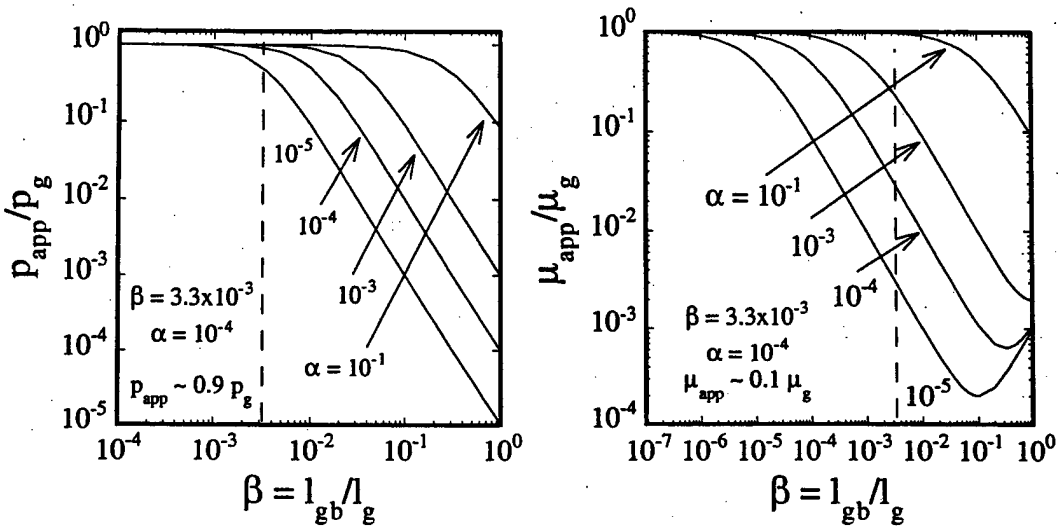
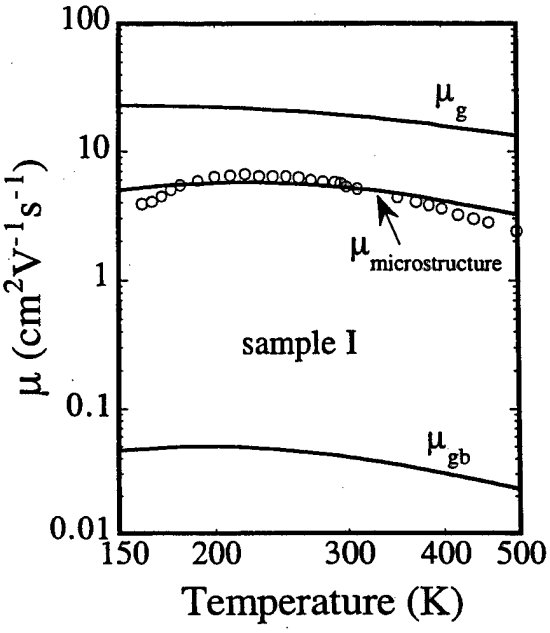


Figure 8


p_{app}/p_g
10^0
10^{-1}
10^{-2}
10^{-3}
10^{-4}
10^{-5}
$\beta = 3.3x10^{-3}$
$\alpha = 10^{-4}$
$p_{app} \sim 0.9\ p_g$
10^{-5}
10^{-4}
10^{-3}
$\alpha = 10^{-1}$
10^{-4} 10^{-3} 10^{-2} 10^{-1} 10^0
$\beta = l_{gb}/l_g$
(a)
μ_{app}/μ_g
10^0
10^{-1}
10^{-2}
10^{-3}
10^{-4}
$\alpha = 10^{-1}$
10^{-3}
10^{-4}
$\beta = 3.3x10^{-3}$
$\alpha = 10^{-4}$
$\mu_{app} \sim 0.1\ \mu_g$
10^{-5}
10^{-7} 10^{-6} 10^{-5} 10^{-4} 10^{-3} 10^{-2} 10^{-1} 10^0
$\beta = l_{gb}/l_g$
(b)

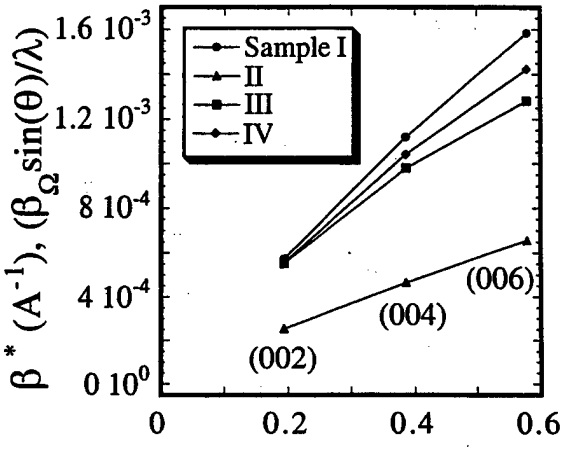
A.K. Rice

Figure 9



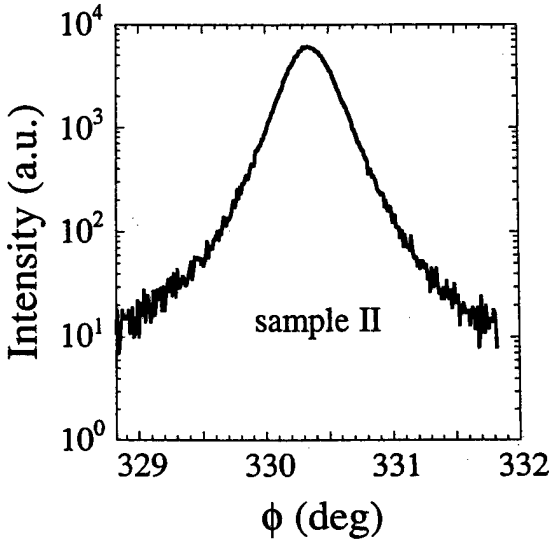
A.K. Rice

Figure 10



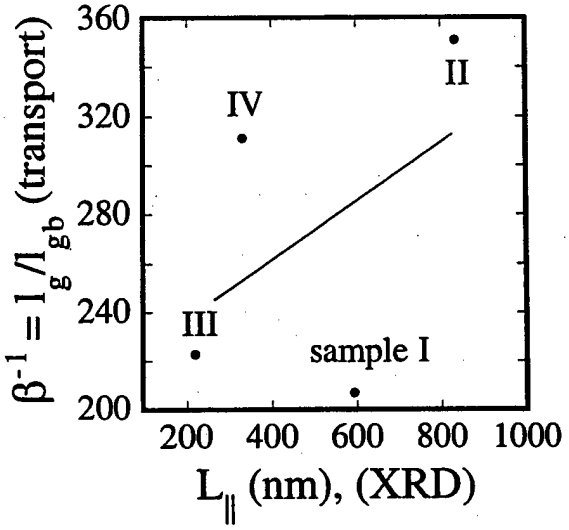
A.K. Rice

Figure 11



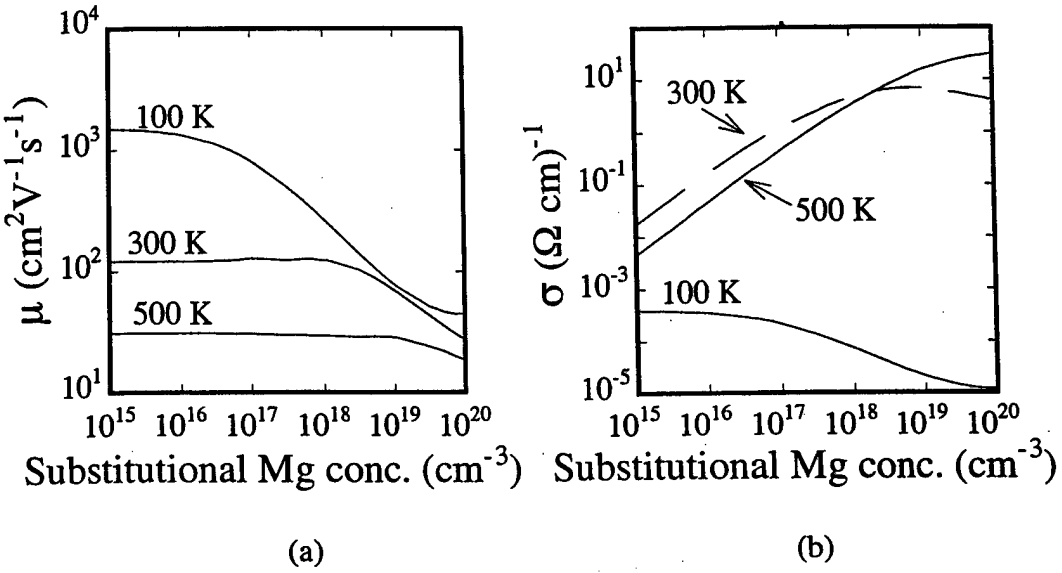
A.K. Rice

Figure 11



A.K. Rice

Figure 12



References

1 H. Amano, M. Kito, K. Hiramatsu, and I. Akasaki, Jpn. J. Appl. Phys. **28,** L2112 - L2114 (1989).

2 W. Götz, N. M. Johnson, J. Walker, D. P. Bour, and R. A. Street, Appl. Phys. Lett. **68,** 667 - 669 (1996).

3 W. Götz, N. M. Johnson, J. Walker, D. P. Bour, H. Amano, and I. Akasaki, Appl. Phys. Lett. **67,** 2666 - 2668 (1995).

4 T. Tanaka, A. Watanabe, H. Amano, Y. Kobayashi, I. Akasaki, S. Yamazaki, and M. Koike, Appl. Phys. Lett. **65,** 593 - 594 (1994).

5 H. Nakayama, P. Hacke, M. R. H. Kahn , T. Detchprohm, K. Hiramatsu, and N. Sawaki, Jpn. J. Appl. Phys. **35,** L282 - L284 (1996).

6 L. Sugiura, M. Suzuki, and J. Nishio, Appl. Phys. Lett. **72,** 1748-1750 (1998).

7 S. Fujita, M. Funato, D.-C. Park, Y. Ikenaga, and S. Fujita, MRS Internet J. Nitride Semicond. Res. **4S1,** G6.31 (1999).

8 S. D. Hersee, J. C. Ramer, and K. J. Malloy, MRS Bulletin **22,** 45 - 51 (1997).

9 F. A. Ponce, D. P. Bour, and W. Götz, Appl. Phys. Lett. **68,** 57-59 (1996).

10 B. R. Nag, *Electron Transport in Compound Semiconductors*, Vol. 11, 1st ed. (Springer-Verlag, New York, 1980).

11 Y. C. Yeo, T. C. Chong, and M. F. Li, J. Appl. Phys. **83,** 1429-1436 (1997).

12 R. Dingle, D. D. Sell, S. E. Stokowski, and M. Ilegems, Phys. Rev. B **4,** 1211-1218 (1971).

13 B. Monemar, Phys. Rev. B **10,** 676-681 (1974).

14 D. Volm, K. Oettinger, T. Streibl, D. Kovalev, M. Ben-Chorin, J. Diener, B. K. Meyer, J. Majewski, L Eckey, A. Hoffmann, H. Amano, I. Akasaki, K. Hiramatsu, and T. Dechprohm, Phys. Rev. B **53,** 16 543-16 550 (1996).

15 K. Pakula, A. Wysmolek, K. P. Korona, J. M. Baranowski, R. Stepniewski, I. Grzegory, M. Bockowski, J. Jun, S. Krukowski, M. Wroblewski, and S. Porowski, Solid State Commun. **97,** 919-922 (1996).

16 A. S. Barker and M. Ilegems, Phys. Rev. B **7,** 743-750 (1973).

17 D. L. Rode, in *Semiconductors and Semimetals Transport Phenomena*; *Vol. 10*, edited by A. C. B. R. K. Willardson (Academic Press, inc., New York, 1975), p. 1-89.

18 V. W. Chin, T. L. Tansley, and T. Osotchan, J. Appl. Phys. **75,** 7365 - 7372 (1994).

19 K. Kim, W. R. L. Lambrecht, and B. Segall, Phys. Rev. B **53,** 16 310 - 16 327 (1996).

20 J. D. Wiley, in *Semiconductors and Semimetals*; *Vol. 10*, edited by R. K. W. a. A. C. Beer (Academic Press, New York, 1975), p. 91 -174.

21 A. D. Bykhovski, V. V. Kaminski, M. S. Shur, Q. C. Chen, and M. A. Kahn, Appl. Phys. Lett. **68,** 818 - 819 (1996).

22 Landolt-Börstein, *Semiconductors, Group IV Elements and III-V Compounds*, Vol. III/17a (Springer-Verlag, New York, 1980).

23 D. J. King, L. Zhang, J. C. Ramer, S. D. Hersee, and L. F. Lester, in *Temperature Behavior of Pt/Au Ohmic Contacts to p-GaN*, San Francisco, Ca, 1997.

24 W. A. Harrison, *Electronic Structure and the Properties of Solids - The Physics of the Chemical Bond* (Dover, New York, 1989).

25 W. Qian, M. Skowronski, M. De Graef, K. Doverspike, L. B. Rowland, and D. K. Gaskill, Appl. Phys. Lett. **66,** 1252-1254 (1995).

26 P. J. Hansen, Y. E. Strausser, A. N. Erickson, E. J. Tarsa, P. Kozodoy, E. G. Brazel, J. P. Ibbetson, U. Mishra, V. Narayanamurti, S. P. DenBaars, and J. S. Speck, Appl. Phys. Lett. **72,** 2247-2249 (1998).

27 H. Tang, W. Kim, A. Botchkarev, G. Popovici, F. Hamdani, and H. Morkoç, Solid State Electron. **42,** 839-847 (1998).

28 N. G. Weimann, L. F. Eastman, D. Doppalapudi, H. M. Ng, and T. D. Moustakas, J. Appl. Phys. **83,** 3656 - 3659 (1998).

29 H. M. Hg, D. Doppalapudi, T. D. Moustakas, N. G. Weimann, and L. F. Eastman, Appl. Phys. Lett. **73,** 821 - 823 (1998).

30 D. C. Look and J. R. Sizelove, Phys. Rev. Lett. **82,** 1237 - 1240 (1999).

31 D. C. Look, J. R. Sizelove, S. Keller, Y. F. Wu, U. K. Mishra, and S. P. DenBaars, Solid State Commun. **102,** 297-300 (1997).

32 R. C. Powell, N. -E. Lee, Y. -W. Kim, and J. E. Green, J. Appl. Phys. **73,** 189-204 (1993).

33 B. Pödör, Phys. Stat. Sol. **16,** K167 (1966).

34 D. L. Dexter and F. Seitz, Phys. Rev. **96,** 964-965 (1952).

35 R. H. Bube, Appl. Phys. Lett. **13,** 136-139 (1968).

36 S. K. Lahiri, S. Das, B. Umapathi, and S. Kal, IETE J. of Research **43,** 193-205 (1997).

37 M. M. Mandurah, K. C. Saraswat, C. R. Helms, and T. I. Kamins, J. Appl. Phys. **51,** 5755-5763 (1980).

38 J. Y. W. Seto, J. Appl. Phys. **46,** 5247-5254 (1975).

39 M.M. Mandurah, K. C. Saraswat, and T. I. Kamins, IEEE Trans. on Electron Devices **ED-28,** 1163-1171 (1981).

40 D. M. Kim, A. N. Khondker, S. S. Ahmed, and R. R. Shah, IEEE Trans. Electron Devices **ED-31,** 480-493 (1984).

41 A. N. Khondker, D. M. Kim, S. S. Ahmed, and R. R. Shah, IEEE Trans. Electron Devices **ED-31,** 493-500 (1984).

42 G. K. Williamson and W. H. Hall, Acta Metall. **1,** 22-31 (1953).

43 P. Gay, P. B. Hirsch, and A. Kelly, Acta Metall. **1,** 315-319 (1953).

44 C. G. Dunn and E. F. Koch, Acta Metall. **5,** 548-554 (1957).

45 T. S. Zheleva, O.-H. Nam, M. Bremser, and R. F. Davis, Appl. Phys. Lett. **71,** 2472 - 2474 (1997).

46 O.-H. Nam, M. D. Bremser, T. S. Zheleva, and R. F. Davis, Appl. Phys. Lett. **71,** 2638 - 2640 (1997).

47 H. Marchand, J. P. Ibbetson, P. T. Fini, P. Kozodoy, S. Keller, S. DenBaars, J. S. Speck, and U. K. Mishra, MRS Internet Journal Nitride Semiconductor Research **3** (1998).

48 H. Marchand, X. H. Wu, J. P. Ibbetson, P. T. Fini, S. Keller, J. S. Speck, S. P. DenBaars, and U. K. Mishra, Appl. Phys. Lett. **73,** 747-749 (1998).

49 T. S. Zheleva, W. M. Ashmawi, O.-H. Nam, and R. F. Davis, App. Phys. Lett. **74,** 2492-2494 (1999).

50 D. Zubia and S. D. Hersee, J. Appl. Phys. **85,** 6492-6496 (1999).

Oxide-Confined Monolithic, Multiple-Wavelength Vertical-Cavity Surface-Emitting Laser Arrays with a 40-nm Wavelength Span

Yuxin Zhou, S. Luong, C. P. Hains, and Julian Cheng, *Senior Member, IEEE*

Abstract— **Monolithic, multiple-wavelength, vertical-cavity surface-emitting laser arrays grown by controlling the metal–organic chemical vapor deposition epitaxial growth rate on a patterned substrate, and using selective oxidation for current confinement, have been demonstrated with a periodic, graded wavelength span of 40 nm. Near room-temperature, electrically pumped continuous-wave lasing is achieved over the entire 40-nm range, with uniform threshold currents of 4.5 mA ± 1.0 mA, and with output powers ranging from 0.4–1.3 mW.**

Index Terms— **Monolithic VCSEL arrays, multiwavelength lasers, patterned MOCVD growth, wavelength-division multiplexing.**

WAVELENGTH-DIVISION multiplexing (WDM) increases the data throughput in a fiber-based optical interconnect, while amortizing the cost of the interconnect over multiple wavelength channels. WDM also provides a means for mapping two-dimensional (2-D) optical signals into a one-dimensional (1-D) array, or mapping a 1-D array into a single fiber, to facilitate the transmission of parallel optical data channels across larger distances using a fiber ribbon cable. To implement WDM at a local interconnect level using vertical-cavity surface-emitting lasers (VCSEL's) requires an inexpensive means for achieving wavelength-graded arrays in a controllable and reproducible manner, while preserving uniform device characteristics within each array. One method for accomplishing both objectives is by locally controlling (scaling) the metal–organic chemical vapor deposition (MOCVD) growth rate of VCSEL's on a topographically patterned growth surface [1]. By perturbing the flow and concentration gradients of the reactant species, the growth rate can be locally enhanced or reduced [2], [3], resulting in a resonance structure whose layer thicknesses and resonance wavelength are scalable. Using this technique, we have previously achieved periodic wavelength-graded VCSEL [2] and resonant photodetector [3] arrays with a wavelength span of ~30-nm using proton-implantation for VCSEL current confinement, and the repeatability of the wavelength grading for different arrays has been demonstrated [3]. The use of selective oxidation for current confinement can potentially achieve VCSEL arrays with smaller active areas and lower operating currents, but the applicability of this wavelength grading technique to nonplanar oxide-confined VCSEL arrays has not been tested. In this work, we demonstrate that oxide-confined VCSEL arrays can be grown on a patterned, nonplanar substrate, and show that near room-temperature, continuous-wave (CW) lasing can be achieved over a wavelength-grading range of 40 nm.

For this work, a GaAs substrate was patterned into periodic arrays of ridges and channels with varying widths (w) but a constant spatial period ($p = 250$ μm) using standard contact photolithography and chemical etching. The pattern was oriented along the $\langle 01\bar{1} \rangle$ direction and the etch depth is ~5 μm. We define the spatial duty factor of the pattern as $DF = \pm(1 - w/p)$, where w is the width of the ridge (+) and channel (−), respectively. Following surface preparation steps to remove any oxide, a standard GaAs–AlGaAs VCSEL structure (with $\lambda = 843$ nm) is grown by low pressure MOCVD on a rotating substrate (~100 r/m). The growth is carried out at 725 °C, with a pressure of 60 torr, a V/III ratio ~100, and a growth rate of ~8 Å/s. The active region consists of a graded-index separate-confinement-heterostructure (GRINSCH) containing four 120-Å-thick GaAs quantum wells separated by 100-Å-thick $Al_{0.15}Ga_{0.85}As$ barrier layers, which is sandwiched between a 25-pair, p-doped distributed Bragg reflector (DBR) mirror on top and a 38.5-pair, n-doped DBR mirror on the bottom. Each DBR mirror consists of $Al_{0.15}Ga_{0.85}As$–$Al_{0.92}Ga_{0.08}As$ quarter-wave layers with linearly composition-graded heterointerfaces, except for the three DBR pairs that are adjacent to the active region, which contain 591-Å-thick $Al_{0.98}Ga_{0.02}As$ layers for selective wet oxidation. The doping concentrations of the DBR's are graded from $5.0 \times 10^{17}/cm^3$ near the active region to $2.0 \times 10^{18}/cm^3$ away from the active region. The VCSEL's were processed by standard techniques using dry etched mesas, and were oxidized in a furnace at 440 °C using a steam source consisting of 3 l/m of N_2 bubbled through H_2O at 82 °C. The VCSEL arrays consist of 20 wavelength elements with a center-to-center spacing of 250 μm yielding an array length of 5 mm. The background growth variation yields a lasing wavelength shift of <2.5 nm over this distance.

Fig. 1 shows the lasing wavelength as a function of duty factor for a linear array of 9-μm VCSEL's under CW operation at room temperature (RT = 297 K), and at 268 K, as well as pulsed operation (6-ns pulses, 0.001 duty cycle) at 297 K.

Manuscript received May 28, 1998; revised July 17, 1998. This work was supported by Air Force Office of Scientific Research and by the Defense Advanced Research Projects Agency.

The authors are with the University of New Mexico, Center for High Technology Materials, Albuquerque NM 87106 USA.

Publisher Item Identifier S 1041-1135(98)07932-4.

1041–1135/98$10.00 © 1998 IEEE

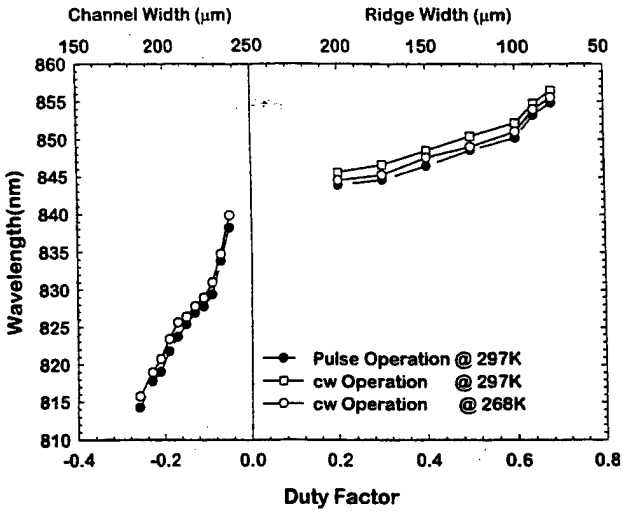


Fig. 1. Wavelength of the lasing mode as a function of spatial duty factor for elements of a monolithic, oxide-confined VCSEL array (9-μm active area) under CW and pulsed lasing operation at 297 K, and under CW lasing operation at 268 K, with the last two showing a 40-nm wavelength grading range by including both the enhanced and reduced growth rate regimes (ridges and channels).

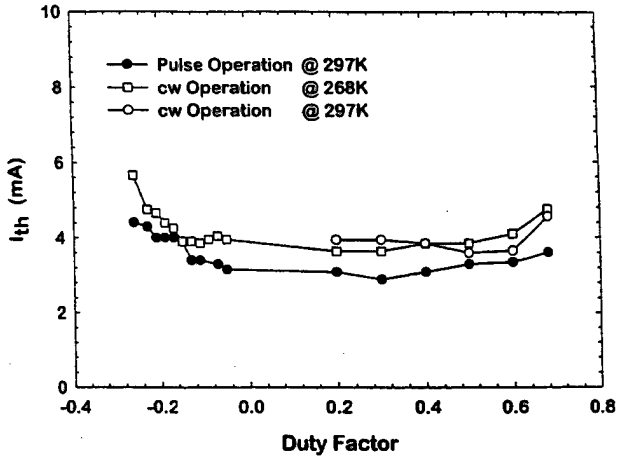


Fig. 2. Threshold current as a function of spatial duty factor for a multiwavelength VCSEL array under CW and pulsed lasing operation at 297 K, and under CW lasing operation at 268 K, showing the achievement of uniform threshold currents.

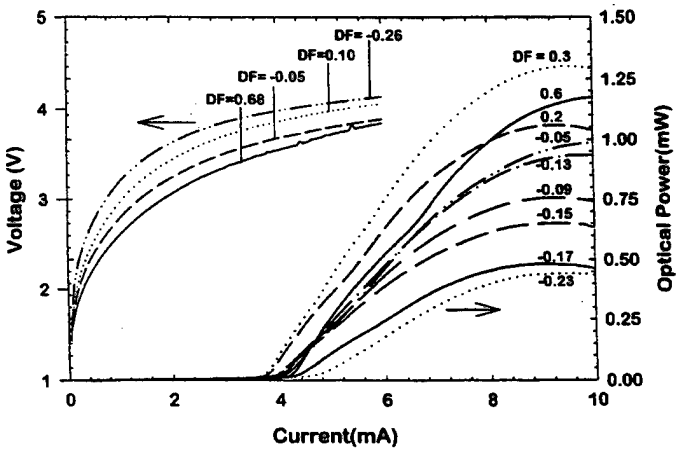


Fig. 3. Light versus current (L–I), and voltage versus current (V–I) characteristics of VCSEL's from a wavelength-graded array under CW operation at 268 K, with different spatial duty factors spanning the wavelength grading range.

The emission wavelengths of all devices were measured at 1.1 $\times I_{th}$, where I_{th} is the lasing threshold current. At RT, all elements of the array lased under pulsed operation with a wavelength grading span of 40 nm, while CW lasing only occurred at the longer wavelengths with a 10-nm span. The curtailment of the CW lasing range is due to an unintended red-shift of the quantum-well gain spectrum, which resulted in a reduced modal gain for devices (in the channels) whose lasing modes occur at shorter wavelengths. The higher I_{th}, lower efficiency and increased self-heating in these devices prevented them from achieving CW lasing at RT. To off-set the gain misalignment, the VCSEL array was thermoelectrically cooled to blue-shift the gain spectrum of the quantum wells to shorter wavelengths lying in the middle of the wavelength grading range. At 268 K, CW lasing was achieved by all elements of the VCSEL array with a total wavelength grading range of 40 nm, as shown in Fig. 1. For each device, the CW lasing wavelength at 268 K is ~0.5–1.0 nm longer than its pulsed lasing wavelength at RT, reflecting the effect of self-heating under CW operation. Although cooling the array from RT to 268 K blue-shifts the lasing mode by ~1.5 nm, the presence of self-heating produces a net red-shift of ~0.5 nm *vis a vis* pulsed operation at RT, suggesting a ~40 K rise in junction temperature during CW operation. At RT, the CW lasing wavelength is also increased by ~1.5–2.0 nm (~40 K) over the pulsed lasing wavelength as a result of self-heating.

As shown in Fig. 2, the VCSEL array showed uniform threshold currents (and voltages), which range from 3.0 to 4.5 mA (3.6 to 3.9 V) for pulsed operation at 297 K, and from 3.5 to mA (3.7 to 4.1 V) for CW operation at 268 K. These variations reflect the wavelength dependence and the finite width of the optical gain spectrum. The higher threshold voltages were due to the unexpectedly low doping of the p-DBR, which increased the heterojunction barrier resistance and caused significant heating of the devices under CW operation.

Evidence of the blue-shifting of the gain peak by cooling can be seen by comparing the minimum values of I_{th} for CW operation at 268 K and at RT, which shows a shift from 850.5 nm (DF = 0.5) at RT to 844.5 nm (DF = 0.3) at 268 K. The broader wavelength grading span for CW lasing at 268 K results from both the improved mode-gain alignment and the improved efficiency (higher gain, lower loss) at lower temperatures. The small shift in Ith between RT and 268 K operation shows that parasitic effects such a carrier leakage and nonradiative recombination do not play a significant role.

Fig. 3 shows the electrical and lasing characteristics of devices from a multiwavelength array under CW operation at 268 K with maximum optical output powers between 0.4 and 1.3 mW. The electrical characteristics are only weakly dependent on DF, but the lasing characteristics show that even with the improved mode-gain alignment at 268 K, the gain spectrum still favors the longer wavelength (ridge) devices over the shorter wavelength (valley) devices, with the former having higher peak powers than the latter. This shows that although scaling the growth rate has reduced the wavelength

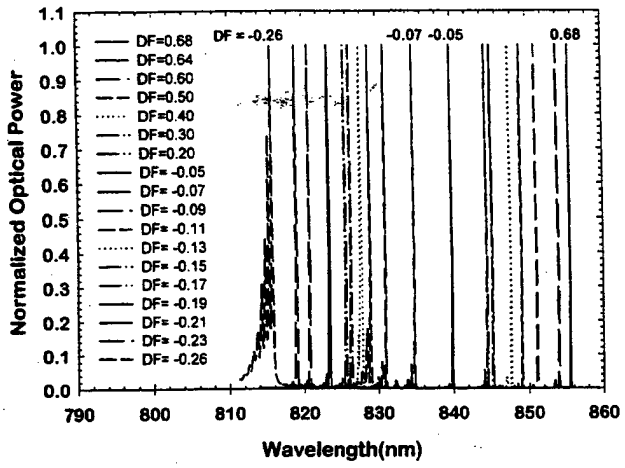


Fig. 4. The normalized CW lasing spectra of 9-μm VCSEL's from a single, monolithic, wavelength-graded array operating at 1.1 × I_{th} and 268 K.

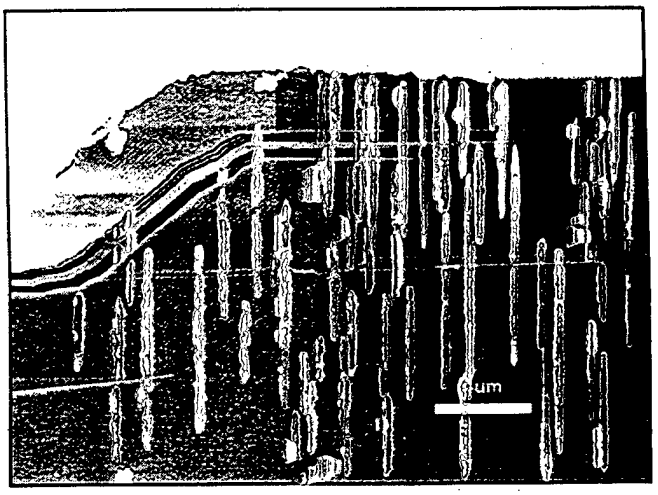


Fig. 5. Electron micrograph showing a cross section of the VCSEL epilayer structure grown on a nonplanar substrate, which clearly delineates all the epilayers and demonstrates continuous oxidation (dark lines) over an etched mesa structure.

dependence of the optical loss [4], the finite width of the optical gain spectrum can still produce nonuniform (albeit more uniform) lasing characteristics for arrays with a wide wavelength grading range. Arrays with more uniform threshold currents and output powers can be achieved in the future by broadening the gain spectrum and centering it in the middle of the wavelength grading range.

The CW lasing spectra (268 K) of VCSEL's from a single array with a 40-nm wavelength grading range are shown in Fig. 4. The spectra are single-mode with a more than 20-dB sidemode suppression ratio up to ~1.4 × I_{th}, except at the lower extreme of the grading range. The uneven wavelength separations are due to the values of DF provided by the current mask set, which can be chosen later to produce the desired wavelength spacing and grading span. Finally, Fig. 5 shows a cross-sectional view of the epilayer structure, illustrating the quality of the epimaterial as well as the uniform propagation of the oxidation fronts (the three dark lines above and below the active region) across a nonplanar surface.

In conclusion, we have demonstrated for the first time a monolithic array of multiple-wavelength, oxide-confined VCSEL's that have achieved near-RT CW lasing with uniform device characteristics and a wavelength span of 40 nm. This was done using a simple patterned growth technique that provides much design flexibility in wavelength selection and spacing. This technique is well-suited for realizing 2-D VCSEL arrays with uniform characteristics whose emission wavelengths are graded in only on dimension. It is less well-suited for achieving 2-D wavelength grading due to the greater directional variations of the spatial duty factor.

REFERENCES

[1] F. Koyama, T. Mukaihara, Y. Hayashi, N. Ohnoki, N. Hatori, and K. Iga, "Wavelength control of vertical cavity surface-emitting lasers by using nonplanar MOCVD," *IEEE Photon. Technol. Lett.*, vol. 7, pp. 10–12, Jan. 1995.

[2] G. G. Ortiz, S. Q. Luong, S. Z. Sun, J. Cheng, H. Q. Hou, G. A. Vawter, and E. Hammons, "Monolithic, multiple wavelength vertical-cavity surface-emitting laser arrays by surface-controlled MOCVD growth rate enhancement and reduction," *IEEE Photon. Technol. Lett.*, vol. 9, pp. 1069–1071, Aug. 1997.

[3] S. Q. Luong, G. G. Ortiz, Y. Zhou, J. Lu, C. P. Hains, J. Cheng, H. Q. Hou, and G. A. Vawter, "Monolithic wavelength-graded VCSEL and resonance-enhanced photodetector arrays for parallel optical interconnects," *IEEE Photon. Technol. Lett.*, vol. 10, pp. 642–644, May 1998.

[4] G. G. Ortiz, C. P. Hains, S. Luong, S. Z. Sun, J. Cheng, H. Q. Hou, G. A. Vawter, and B. E. Hammons, "Multiple wavelength vertical-cavity surface-emitting laser arrays using surface-controlled MOCVD growth rate enhancement and reduction," in *Trends in Optics and Photonics (TOPS), Vol. XV: Advances in Vertical-Cavity Surface-Emitting Lasers*, C. J. Chang-Hasnain, Ed., Washington, DC: Opt. Soc. Amer., 1997, pp. 29–35.

Monolithic integration of $In_{0.2}Ga_{0.8}As$ vertical-cavity surface-emitting lasers with resonance-enhanced quantum well photodetectors

G.G. Ortiz, C.P. Hains, J. Cheng, H.Q. Hou and J.C. Zolper

Indexing terms: Integrated optoelectronics, Vertical cavity surface emitting lasers, Photodetectors

Vertical-cavity surface-emitting lasers (VCSELs) have been monolithically integrated with resonance-enhanced photodetectors (REPDs) using a single epilayer design, to produce a simple array of sources and detectors for optical interconnect applications. The detectors, which contain a three quantum well InGaAs absorption region, achieve quantum efficiencies as high as 85%, and the VCSELs achieved threshold current densities as low as 850A/cm² and differential quantum efficiencies as high as 50%.

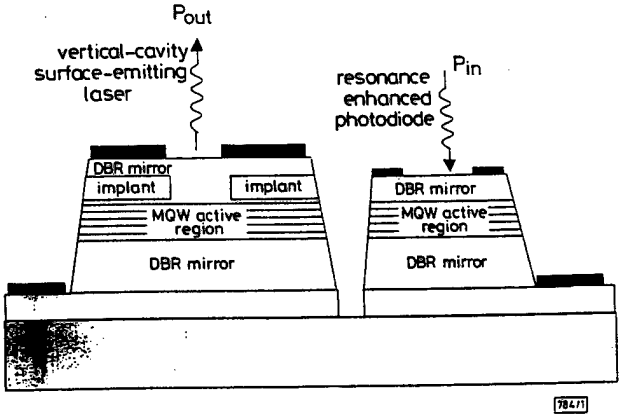


Fig. 1 *Epitaxial structure of the integrated VCSEL and REPD. The active region is composed of three 80Å InGaAs quantum wells. It is placed between two distributed Bragg reflector (DBR) mirrors. The VCSEL uses all 24 mirror pairs of the top DBR, whereas the REPD uses only 11*

In high density parallel optical interconnect applications, it is often advantageous to integrate monolithically the optical source, photodetector and switching functions on the same substrate. This allows the functional integration of all the optical interconnection and optoelectronic interface functions in a very compact format. It also simplifies the optical interconnect package by facilitating the integration of the optoelectronic components with the optical routing and beam focusing functions, e.g. by the use of diffractive optics and holographic optical elements. As an example, compact, reconfigurable optical routing networks have been previously demonstrated [1, 2]. These networks interconnect many electronic processing modules by routing their data simultaneously through parallel optical channels, using monolithic arrays of optoelectronic routing switches that integrate VCSELs with *pin* photodetectors (PIN) and heterojunction bipolar transistors (HBTS). One drawback of this monolithic approach is that the epi layers of the p-i-n photodetector also serve as the base-collector junction of the HBT, which leads to a non-optimum design that compromises the performance of both the PIN and the HBT. In particular, this limits both the modulation bandwidth and the responsivity of the photodetectors. It is therefore desirable to increase the responsivity of the detector without compromising the speed of the HBTs. To address these issues a resonant cavity is used to enhance the quantum efficiency of the detector. To keep transit times short the absorption length is reduced to a few quantum wells and the carrier transit time is dominated by the thin active region of the VCSEL. This has the added advantage of allowing us to use the same epitaxial growth for both detectors and sources in our optoelectronic switch arrays.

An improvement of the quantum efficiencies of thin absorptive semiconductor layers was proposed and demonstrated [3] by placing the thin absorbing layers in a resonant cavity formed by highly reflective mirrors. Enhanced absorption has been demonstrated by the use of semiconductor quarter wave stacks [3], metallic layers [4] and dielectric quarter wave stacks [5] as the mirrors of the cavity. By modifying the reflectivities of the distributed Bragg mirrors that are used in the VCSEL structure, the Q of the resonance cavity can be reduced, to obtain a detector that has very high absorption efficiency.

In this Letter, a novel approach to the integration of the optical source and photodetection functions is demonstrated by the use of a single epitaxial design that provides optimum performance for a VCSEL and a resonance-enhanced photodetector (REPD). In this design (Fig. 1), the VCSEL and REPD share a common multi-quantum-well active region, but are embedded within different resonance cavities to achieve the optimum performance for both the VCSEL and the detector. Since the optimum VCSEL performance requires a resonance cavity with very high mirror reflectivities [6], whereas the optimum performance for a REPD requires a cavity with a lower reflectivity [3], the use of a single design compromises both. In this new design the cavity of the REPD is embedded realised by chemically removing some of the AlAs/AlGaAs quarter-wave layers from the top DBR mirror. The number of quarter-wave layers in the bottom DBR mirror is then chosen to provide the optimum performance for the VCSEL and the REPD. Here the epilayer design is optimised for a top-surface-emitting and top-surface-absorbing topology. However, by using strained $In_{0.2}Ga_{0.8}As$ quantum wells, it is also possible to design a structure in which light can be emitted or absorbed through either the top or bottom surface, thus providing, in principle, the possibility of a bi-directional optical switch.

The epilayer design contains a one-wavelength-thick active region that consists of three 80Å thick $In_{0.2}Ga_{0.8}As$ quantum wells separated by 100Å thick GaAs barrier layers, which are bound by two compositionally graded $Al_xGa_{1-x}As$ cladding layers, with x graded from 0 to 0.47. The DBR mirrors are composed of $Al_{0.15}Ga_{0.85}As/Al_{0.93}Ga_{0.07}As$ quarter-wave pairs with biparabolic graded hetero-interfaces, with 38.5 pairs for the bottom DBR mirror and 24 pairs for the top DBR mirror. All the layers have a doping level of $2 \times 10^{18}cm^{-3}$, except for a GaAs layer in the top DBR mirror that is doped at $1 \times 10^{19}cm^{-3}$. This provides the contact layer for the REPD after the 13 uppermost mirror pairs are removed from the top DBR thereby leaving 11 quarter-wave pairs for the top DBR mirror of the detector. A half-wavelength GaAs layer, doped to $1 \times 10^{19}cm^{-3}$, provides the top contact layer for the VCSEL.

The VCSEL is proton-implanted at 370keV with a dose of $3 \times 10^{14}cm^{-2}$ to define the active area aperture. After implantation thirteen of the top quarter-wave mirror pairs are selectively removed from the detector regions using chemical etchants to remove alternately the $Al_{0.15}Ga_{0.85}As$ and $Al_{0.93}Ga_{0.07}As$ layers. Numerical simulations were used to design a cavity with a Q that would have a full-width at half-maximum (FWHM) of 2nm. This design yields an absorption efficiency $A(\lambda)$ of 93% (at $\lambda = 943nm$), with a cavity of 11 DBR pairs in the top mirror and 38.5 DBR pairs on the bottom mirror. Higher absorption efficiencies can be obtained, but at the cost of reducing the FWHM. The responsivity $R(\lambda)$ of the detector, is given by $A(\lambda)\eta_i e/h\nu$, where $A(\lambda)$ is the absorption efficiency, $h\nu$ is the photon energy, and η_i is the internal quantum efficiency or photoelectric conversion efficiency.

The reponsivity of the detectors is measured using a wavelength tunable titanium-sapphire laser operating in the CW mode, which produces a narrow spectrum with a FWHM of less than 1Å, see Fig. 2. The spectrum of the source is verified to be singlemode with a high resolution monochromator, before the responsivity is measured at each wavelength. The photodetectors exhibit excellent performance across the sample, with peak responsivities as high as 0.65A/W at 943.5nm, under a reverse bias of 3V, and with a corresponding external quantum efficiency $\eta_e = \eta_i A(\lambda)$, of ~85%. The dark current is 0.3μA at −3V and the reverse breakdown voltage is 12V. From the measured responsivity the external quantum effi-

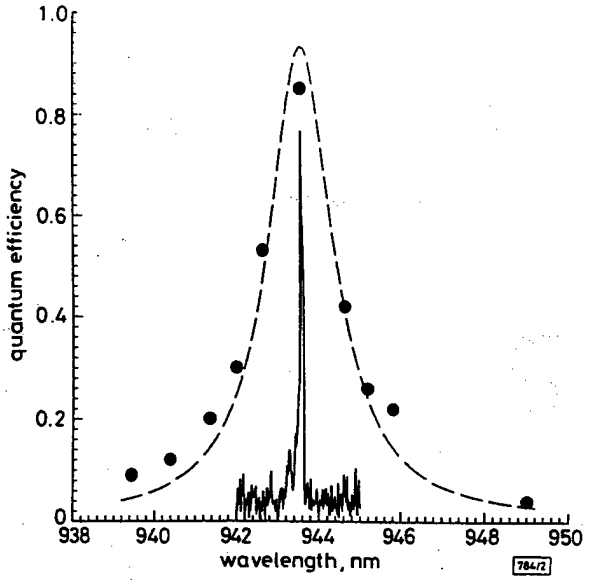


Fig. 2 *External quantum efficiency of the resonance-enhanced photodetector (REPD) against wavelength. The measured response (solid circles) shows good agreement with the calculated absorption efficiency (broken curve). Also shown is the spectrum of the singlemode tunable Ti:sapphire source with a FWHM of 1 Å (solid curve)*

this value against the various measured wavelengths, as in Fig. 2, yields the detector's measured spectral response. The FWHM of the resonance-enhanced photo-detector is found to be ≃ 20Å, which is in very good agreement with the designed value. The VCSELs demonstrate very good DC operating characteristics. Devices with active area diameters varying from 8μm to 16μm (see Fig. 3) exhibit threshold currents in the 1.5 – 2.5mA range, differential quantum efficiencies of 20 – 50%, maximum output powers of 1.2 – 3.5mW, and threshold current densities as low as 850A/cm². Although these VCSELs were designed for low threshold rather than high output power, their output levels are comparable to those of conventional VCSELs. The devices exhibited higher operating voltages (≃3.5V) than expected as a result of the unintended low doping level in a few of the p-side DBR layers.

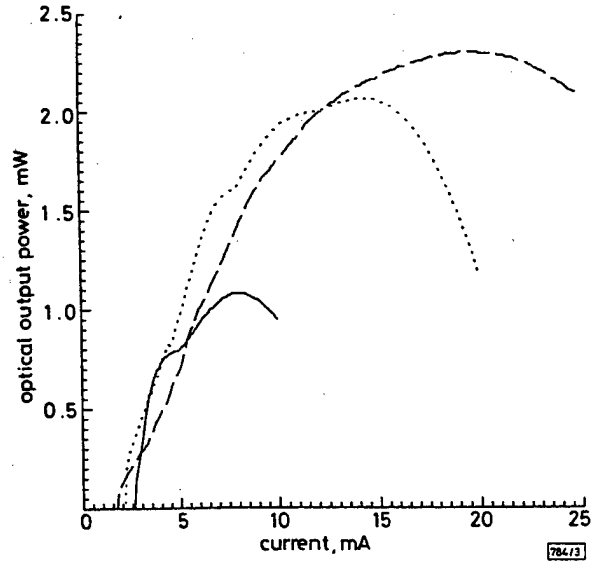


Fig. 3 *Typical light-current characteristics of the $In_{0.2}Ga_{0.8}As$ VCSELs with different active area diameters*

——— 8μm
····· 12μm
– – – – 16μm

In conclusion, we have demonstrated successful monolithic integration of a resonance-enhanced photodetector with a vertical-cavity surface-emitting laser on the same substrate and using the same epilayer design. Photodetectors with external quantum efficiencies of 85% have been achieved without sacrificing the performance of the VCSELs. This simple two-dimensional array of sources and photodetectors can thus be easily integrated into high-density, parallel, optoelectronic interconnect applications.

Acknowledgments: The work at UNM was supported by AFOSR and the DARPA/ETO Optoelectronics program. The work performed at Sandia was supported by DOE contract DE-AC04-76DP00789. The authors would like to thank S. Luong for his assistance in device fabrication. G.G. Ortiz acknowledges the support of the NASA/JPL MSEIO doctoral fellowship programme.

© IEE 1996
21 March 1996
Electronics Letters Online No: 19960782

G.G. Ortiz, C.P. Hains and J. Cheng (*University of New Mexico, Center for High Technology Materials, EECE Building, Room 125, Albuquerque, NM 87131, USA*)

H.Q. Hou and J.C. Zolper (*Sandia National Laboratory, Albuquerque, NM 87185, USA*)

References

1 ALDUINO, A.C., ORTIZ, G.G., HAINS, C., LU, B., SCHNEIDER, R.P., KLEM, J., and ZOLPER, J.C.: '500 multifunctional binary optical switching fabric', *Electron. Lett.*, 1995, **31**, (18), pp. 1570–1571

2 LU, B., LU, Y.C., ALDUINO, A.C., ORTIZ, G.G., and CHENG, J.: 'Optically-cascaded, multi-stage switching operation of a multifunctional binary optical/optoelectronic switch', *IEEE Photonics Technol. Lett.*, 1995, **7**, (12), pp. 1427–1429

3 CHIN, A., and CHANG, T.Y.: 'Multilayer reflectors by molecular-beam epitaxy for resonance enhanced absorption in thin high-speed detectors', *J. Vac. Sci. Technol. B*, 1990, **8**, (2), pp. 339–342

4 DODABALAPUR, A., and CHANG, T.Y.: 'Resonant-cavity InGaAlAs/InGaAs/InAlAs phototransistors with high gain for 1.3-1.6 μm', *Appl. Phys. Lett.*, 1992, **60**, (8), pp. 929–931

5 HUNT, N.E.J., SCHUBERT, E.F., and ZYDZIK, G.J.: 'Resonant-cavity p-i-n photodetector utilizing an electron-beam evaporated Si/SiO_2 microcavity', *Appl. Phys. Lett.*, 1993, **63**, (3), pp. 391–393

6 ZHOU, P., CHENG, J., SCHAUS, C.F., SUN, S.Z., ZHENG, K., ARMORE, E., HAINS, C., HSIN, W., MYERS, D.R., and VAWTER, G.A.: 'Low series resistance high efficiency GaAs/AlGaAs vertical-cavity surface-emitting lasers with continuously-graded mirrors grown by MOCVD', *IEEE Photonics Technol. Lett.*, 1991, **3**, (7), pp. 591–593

Monolithic Wavelength-Graded VCSEL and Resonance-Enhanced Photodetector Arrays for Parallel Optical Interconnects

S. Q. Luong, G. G. Ortiz, Y. Zhou, Jun Lu, C. P. Hains, Julian Cheng, *Senior Member, IEEE*, H. Q. Hou, *Member, IEEE*, and G. A. Vawter, *Member, IEEE*

***Abstract*— Monolithic arrays of wavelength-graded vertical-cavity surface-emitting lasers (VCSEL's) and resonance-enhanced photodetectors (PD's) have been realized with the same epilayer structure using the topography-controlled enhancement and reduction of the metal–organic chemical vapor deposition (MOCVD) growth rate on a patterned substrate. The repeatability of this technique was demonstrated by using different VCSEL and resonance-enhanced photodetector (REPD) arrays from the same wafer.**

***Index Terms*—Integrated optoelectronics, semiconductor laser arrays, optical array, optical communication, optical interconnections, optoelectronic devices, photodetectors, wavelength-division multiplexing.**

MONOLITHIC arrays of graded multiple-wavelength optical sources and wavelength-selective photodetectors are useful for wavelength-division-multiplexed (WDM) optical interconnect applications. Used together, these arrays can minimize optical crosstalk between neighboring channels in a parallel free-space optical interconnect by rejecting the light from neighboring wavelength-differentiated channels. Alternatively, different channels can be wavelength-multiplexed on a single fiber to enhance the data throughput, while the transmitted data is fanned out to different receivers and demultiplexed using wavelength-selective photodetectors. To achieve these ends, a method is needed to achieve wavelength-graded arrays of optical sources and wavelength-selective photodetectors in a controllable and reproducible manner.

Although multiwavelength vertical-cavity surface-emitting laser (VCSEL) arrays can be achieved by varying the thickness of only the active layer [1]–[3], these resulted in varying mirror losses and nonuniform device characteristics. We have previously shown [4] that lower loss dispersion and greater device uniformity can be obtained by using a wavelength-grading scheme that scales the thickness of all the epilayers within the resonance structure. This was achieved by controlling the epitaxial growth rate of all the epilayers on a topographically patterned substrate, which resulted in the repeatable, periodic grading of the resonance wavelength over a span of ~30 nm [4]. The appeal of this approach also lies in the fact that it is a single-growth process that requires little additional processing. In this letter, we show that wavelength-graded arrays of wavelength-selective resonance-enhanced photodetectors (REPD's) can also be achieved in a similar manner. The repeatability of this technique is demonstrated by using different arrays of VCSEL's and REPD's from the same wafer. Using an embedded resonance-cavity structure as described in [5], the multiwavelength VCSEL and REPD arrays can be monolithically integrated on the same epilayer structure to achieve closer wavelength matching between individual source and detector elements.

As described in [4], controlled wavelength-grading is achieved by using the surface topography on a patterned substrate to modify the local flow and transport of the reactant species during epitaxial growth by metal–organic chemical vapor deposition (MOCVD). By taking advantage of the concentration gradients produced by the local accumulation and reduction of the reactant species over ridges and within channels, respectively, we can alternately enhance or reduce the growth rate of all the epilayers in a controllable manner [6], [7]. The growth rate, and thus the resonance wavelength of the resulting VCSEL, have been found to depend on the width, depth, spacing, duty factor (DF) and aspect ratio of the surface features. By controlling these parameters, and using both the growth rate enhancement and reduction regimes, the emission spectra of a VCSEL array can be varied over a wider range of wavelengths [4].

Wavelength-graded REPD arrays can be achieved using the same growth techniques and the same epilayer structure as the VCSEL. In this integrated epilayer design [5], the VCSEL and the REPD share a common active region, which is embedded within different resonance cavities that are designed to achieve optimum performance for the VCSEL and the photodetector, respectively. The weaker resonance cavity of the REPD is embedded within the stronger resonance cavity of the VCSEL, both of which share the same active region and the same high-reflectivity lower distributed Bragg reflector (DBR) mirror, but

Manuscript received November 10, 1997; revised January 15, 1998. The work of S. Q. Luong, G. G. Ortiz, Y. Zhou, J. Lu, C. P. Hains, and J. Cheng was supported by the Air Force Office of Scientific Research and the DARPA/ETO Opto-electronics program. The work of H. Q. Hou and G. A. Vawter was supported by the DOE under Contract DE-C04-76DP00789.

S. Q. Luong, Y. Zhou, J. Lu, C. P. Hains, and J. Cheng are with the University of New Mexico, Center for High Technology Materials, Albuquerque, NM 87106 USA.

G. G. Ortiz was the University of New Mexico, Center for High Technology Materials, Albuquerque, NM 87106 USA. He is now with the Jet Propulsion Laboratory, Pasadena, CA 91109 USA.

H. Q. Hou and G. A. Vawter are with Sandia National Laboratory, Albuquerque, NM 87185 USA.

Publisher Item Identifier S 1041-1135(98)03024-9.

1041–1135/98$10.00 © 1998 IEEE

differ in the number (N) of DBR pairs in their upper mirrors. The REPD's are realized by chemically removing some of the DBR pairs from the upper mirror in selected areas of the wafer [5], thus decreasing the Q of the cavity and increasing the width of its resonance and its photoresponse. The optimum number ($N = 10$) is chosen to achieve optimum absorption efficiency for the REPD in a top-surface-emitting (absorbing) geometry [5].

To achieve wavelength-grading of the REPD's and VCSEL's, a patterned GaAs substrate containing arrays of photolithographically defined ridges and channels was chemically etched to a depth of ~ 5 μm along the $\langle 01\bar{1} \rangle$ direction. Each array contains a pattern of ridges and channels with varying widths (w and $p-w$, respectively), but with a constant spatial period ($p = 250$ μm). The spatial duty factor, defined as DF $= 1 - w/p$ for the ridges, and DF $= -[1 - (p-w)/p](<0)$ for the channels, is therefore variable within each array. Following surface preparation steps to remove any oxide, a standard (nominally 843 nm) AlGaAs–GaAs VCSEL structure is grown by low-pressure MOCVD on a rotating substrate ($\sim$100 rpm). The growth is carried out at 725 °C, with a pressure of 60 torr, a V/III ratio of $\sim$100, and a growth rate of $\sim$8 Å/s. The active region consists of a graded-index, separate-confinement-heterostructure (GRINSCH) containing four 80-Å-thick GaAs quantum wells separated by 100-Å-thick $Al_{0.16}Ga_{0.84}As$ barrier layers, which is sandwiched between a 25-pair, p-doped DBR on the top and a 38.5-pair, n-doped DBR on the bottom. The DBR's consist of $Al_{0.15}Ga_{0.85}As$–$Al_{0.93}Ga_{0.07}As$ layers that are doped to a level of $1 \times 10^{18}/cm^3$, except for a single pair of $Al_{0.10}Ga_{0.90}As$–$Al_{0.93}Ga_{0.07}As$ layers in the upper DBR that is doped to $1 \times 10^{19}/cm^3$, which serves as the contact layer for the REPD. The VCSEL array is fabricated using standard proton–implant–isolation techniques, while the REPD array is obtained by selectively removing 15 upper DBR mirror pairs from the VCSEL epi-structure in selected areas of the wafer.

Fig. 1 shows the responsivity of four REPD's with a wavelength span of $\sim$20 nm, corresponding to different values of DF. The degree of growth rate enhancement (+) or reduction (−) that is needed to achieve these spectral shifts (relative to the 843-nm planar reference), i.e., the growth rate scaling factors S (in %), are also shown. Numerical simulations have shown that a wavelength span of 30 nm can be achieved by $S = \pm$ 1.5% relative to the planar growth rate for a 843-nm VCSEL. The duty factor for these devices ranges from -0.26 ($S = -1.0\%$) to 0.68 ($S = +2.0\%$). The peaks are spaced $\sim$8 nm apart and show good spectral isolation between the four wavelength channels (>12–15 dB when wavelength-matched VCSEL's are used for sources). All the responsivity spectra exhibit a full-width at half-maximum (FWHM) of 4 nm, while the peak responsivity varies from 0.32 A/W to 0.49 A/W between devices (absorption efficiency between 47% and 73%). A photograph of the monolithic REPD arrays is shown in the inset of Fig. 1.

The reduced responsivity and its device-to-device variations are due to the dependence of the absorption efficiency $\eta_\alpha(\lambda)$ on the absorption coefficient $\alpha(\lambda)$, which varies with the resonance wavelength λ of each device. For $N = 10$, the

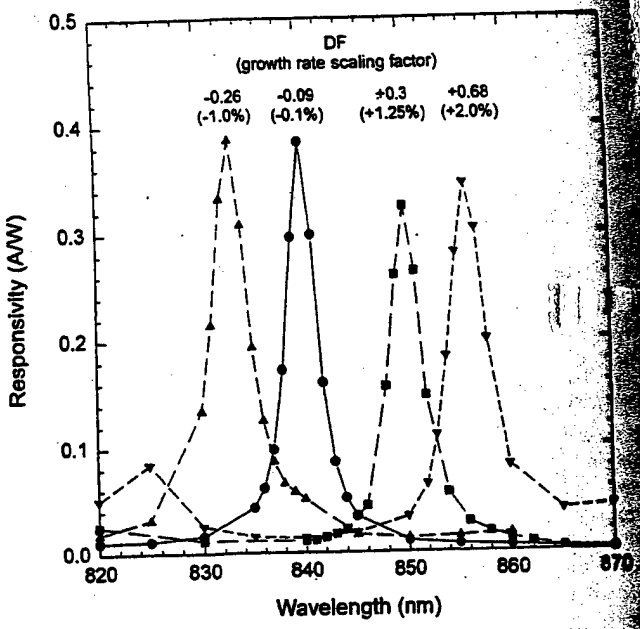


Fig. 1. Responsivity spectra of four devices from a monolithic multiwavelength REPD array corresponding to different values of the spatial duty factor DF. The scaling factor (in parenthesis) denotes the amount of growth rate enhancement (+%) or reduction (−%) needed to achieve the desired spectral shift from 843 nm (reference wavelength) for each device.

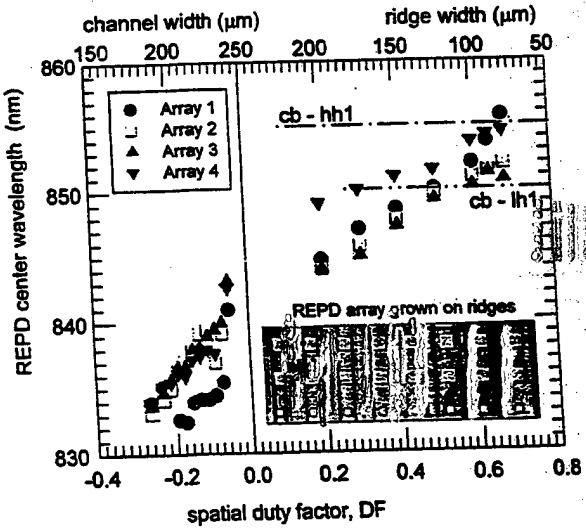


Fig. 2. Center wavelengths of the absorption spectra of resonance-enhanced photodetectors from several different multiwavelength arrays (photograph in inset) grown on *different areas* of a single wafer, as a function of the spatial duty factor.

calculated efficiency η_α decreases with $\alpha(\lambda)$ across the wavelength span of the REPD array, within which α varies from 1.0×10^4 cm^{-1} to 2.5×10^4 cm^{-1} (the latter at the excitonic absorption peaks, 850 and 855 nm). The calculated efficiency ($\sim$60%–75%) changes slowly with wavelength except near the exciton peaks, where it drops to 40%–45%. The measurements are in good accord with the calculated efficiency.

Fig. 2 shows the resonance wavelengths of five different wavelength-graded REPD arrays from different areas of the same wafer as a function of DF, including devices from both the ridge (growth enhancement) and channel (growth

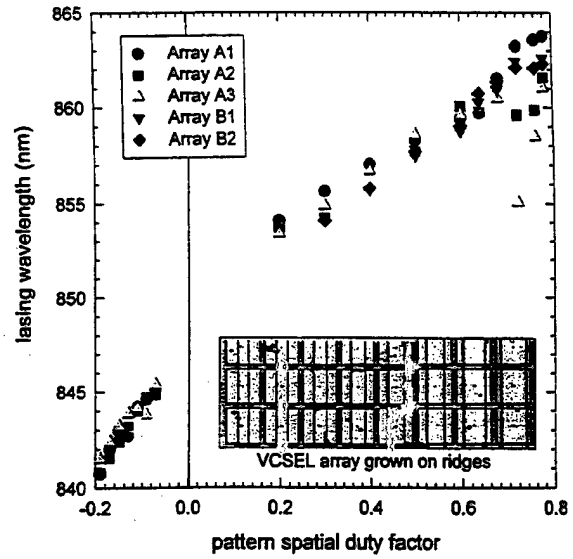


Fig. 3. The lasing wavelength for VCSEL's from five monolithic, multi-wavelength arrays (photograph in inset) grown on *different areas* of a single wafer as a function of spatial duty factor, demonstrating the repeatability of the controlled wavelength variations. Notice the greater regularity of the VCSEL arrays (12-μm active area), except on very narrow ridges (large DF).

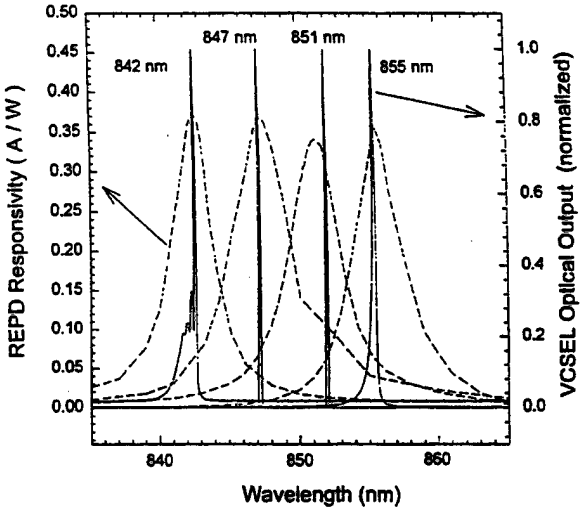


Fig. 4. The measured responsivity (in A/W) and CW lasing spectra of four elements from two REPD and VCSEL arrays that are in close proximity to each other.

reduction) regions in each array. The results demonstrate the repeatability of the wavelength variation from array to array, each spanning a spectral range of ~20–25 nm. For each value of DF, some interarray wavelength variations can be observed. These are partly caused by the difficulty of positioning the large-area REPD's within the (narrower) ridges and channels, and by residual nonuniformities in the growth rate.

Monolithic arrays of wavelength-graded, proton-implant-confined VCSEL's corresponding to different values of DF have also been realized on the same wafer by utilizing the full resonance structure. The room-temperature pulsed lasing spectra of these devices show a wavelength span of ~25 nm, a sidemode-suppression ratio (SMSR) of >20 dB and a FWHM of ~2 Å. These VCSEL arrays also demonstrated good continuous-wave (CW) lasing characteristics over a wavelength span of ≈20 nm, with uniform threshold currents of 5.5 ± 0.5 mA and output powers of ~0.5 mW for all devices [4]. Fig. 3 plots the lasing wavelengths of five different arrays from the same wafer as a function of spatial DF, again demonstrating the repeatability of this wavelength-grading technique. The VCSEL arrays achieved greater uniformity than the REPD arrays due to the smaller dimensions of the VCSEL's active area. The data suggests that a wavelength variation of <2 nm can be achieved for DF <0.7. The linear dependence of wavelength on DF allows design flexibility in choosing sources for both dense or coarse WDM systems. The inset in Fig. 3 shows a photograph of multiwavelength VCSEL arrays that are grown on ridges with varying width.

These VCSEL and REPD arrays were taken from different areas of the wafer (wavelength variations ≤2%), which accounts for the (~8 nm) shift in their respective wavelength grading range. Closer wavelength matching can be achieved by placing the VCSEL's in closer proximity to the REPD's. Fig. 4 plots the measured responsivity spectra of four REPD's and the emission spectra of four corresponding VCSEL's in two neighboring wavelength-graded arrays, which shows that their wavelengths track each other over a spectral range of ~13 nm.

In conclusion, a simple single-growth technique for obtaining both wavelength-graded VCSEL and wavelength-selective REPD arrays have been demonstrated. The arrays produced by the use of this technique can achieve improved wavelength-matching, which is useful for WDM and demultiplexing in a WDM optical interconnect system.

References

[1] W. Yuen, G. S. Li, and C. J. Chang-Hasnain, "Multiple-wavelength vertical-cavity surface-emitting laser arrays with a record wavelength span," *IEEE Photon. Technol. Lett.*, vol. 8, pp. 4–6, Jan. 1996.

[2] H. Saito, I. Ogura, and Y. Sugimoto, "Uniform CW operation of multiple-wavelength vertical-cavity surface-emitting lasers fabricated by mask molecular beam epitaxy," *IEEE Photon. Technol. Lett.*, vol. 8, pp. 1118–1120, Sept. 1996.

[3] T. Wipiejewski, M. G. Peters, E. R. Hegblom, and L. A. Coldren, "Vertical-cavity surface-emitting laser diodes with post-growth wavelength adjustment," *IEEE Photon. Technol. Lett.*, vol. 7, pp. 727–729, July 1995.

[4] G. G. Ortiz, S. Q. Luong, J. Cheng, H. Q. Hou, G. A. Vawter, and B. E. Hammons, "Monolithic, multi-wavelength VCSEL arrays by surface-controlled MOCVD growth rate enhancement and reduction," *IEEE Photon. Technol. Lett.*, vol. 9, pp. 1069–1071, Aug. 1997.

[5] G. G. Ortiz, C. P. Hains, J. Cheng, H. Q. Hou, and J. C. Zolper, "Monolithic integration of InGaAs VCSEL's with resonance-enhanced quantum-well photo-detectors," *Electron. Lett.*, vol. 32, no. 13, pp. 1205–1207, June 1996.

[6] P. Demeester, P. Van Daele, and R. Baets, "Growth behavior during nonplanar metalorganic vapor phase epitaxy," *J. Appl. Phys.*, vol. 63, no. 7, pp. 2284–2290, 1988.

[7] L. Buydens, P. Demeester, M. Van Ackere, A. Ackaert, and P. Van Daele, "Thickness variations during MOVPE growth on patterned substrates," *J. Electron. Mater.*, vol. 19, no. 4, pp. 317–321, 1990.

Monolithic, Multiple-Wavelength Vertical-Cavity Surface-Emitting Laser Arrays by Surface-Controlled MOCVD Growth Rate Enhancement and Reduction

G. G. Ortiz, *Member, IEEE*, S. Q. Luong, S. Z. Sun, Julian Cheng, *Member, IEEE*, H. Q. Hou, *Member, IEEE*, G. A. Vawter, *Member, IEEE*, and B. E. Hammons

***Abstract*— Monolithic, multiple-wavelength vertical-cavity surface-emitting laser (VCSEL) arrays have been obtained by the surface-controlled enhancement and reduction of the MOCVD epitaxial growth rate, achieving a periodic, graded wavelength span greater than 30 nm. Room-temperature (RT), electrically pumped continuous-wave (CW) lasing is demonstrated, with uniform threshold currents of 5.5 ± 0.5 mA with typical output powers of 0.5 mW. We show here for the first time both the enhancement and the reduction of the growth rate of the entire VCSEL structure and demonstrate the controlled variation of the VCSEL lasing wavelength over a widened spectral range by exploiting both effects.**

***Index Terms*— Monolithic, multiple-wavelength lasers, patterned MOCVD growth, surface-emitting lasers, wavelength division multiplexing.**

MULTIPLE-WAVELENGTH vertical-cavity surface-emitting laser (VCSEL) and photodetector arrays are useful for wavelength-multiplexed fiber-optic networks and for optical crosstalk isolation in parallel free-space interconnects. Multiple-wavelength VCSEL arrays have been obtained by varying the thickness of the Fabry–Perot cavity [1]–[3] or by controlling the wavelength through nonplanar growth [4]. Significant effort has been demonstrated in employing techniques that vary the cavity thickness such as using thermal gradients during growth of a spacer layer [1], by *in situ* masking during molecular beam epitaxy (MBE) growth [2], and through anodic oxidation and selective etching [3].

In this letter, we have investigated a technique that varies both the thickness of the cavity as well as the thickness of the epilayers of the VCSEL's distributed Bragg reflectors (DBR's). The cavity loss of the VCSEL varies as a function of wavelength due to the wavelength dependence of the DBR's reflectivity. A variation in cavity loss of 13% across a 30-nm range (centered at 850 nm) has been estimated for VCSEL's where the thickness of each layer of the DBR's is scaled by the same percentage as the cavity thickness is changed. This compares to a 35% variation in cavity loss for the case where only the cavity thickness is changed and the VCSEL DBR's are common to all devices. Because this variation in cavity loss translates into a nonuniform threshold gain [2] across the wavelength range, we have the potential of realizing arrays with very uniform device characteristics, by scaling the thickness of all the epilayers in the VCSEL structure. We show here for the first time both the enhancement and the reduction of the growth rate of the entire VCSEL epilayer structure on a topographically patterned substrate. And, by exploiting these effects, we demonstrate the controlled variation of the lasing wavelengths of a VCSEL array over an extended spectral range with uniform device characteristics.

The principle behind this technique is based on the fact that in metal organic chemical vapor deposition (MOCVD), the growth rate on an etched surface differs from that on a planar substrate [5]. The flow and transport of the reactant species are modified by the surface topography, thus producing local variations in the reactant concentrations and the growth rate. The rate is enhanced above a ridge, and is reduced within a channel relative to the nominal growth rate on a large planar area. In each case the growth rate has been found to be dependent on the width of the features, the etch depth and the spacing between features [5], [6]. By taking advantage of the concentration gradients produced by the local accumulation and reduction of the reactant species over ridges and within channels, respectively, we are able to vary the growth rate of the VCSEL epilayer structure in a controllable manner, and have fabricated multiple-wavelength VCSEL arrays with a wide range of lasing wavelengths.

These concepts are schematically illustrated in Fig. 1. The enhanced growth rate above the ridges produces a thicker VCSEL structure with a longer resonance cavity and therefore a longer lasing wavelength. Within the etched channels the opposite effect occurs, with a reduced growth rate producing a thinner resonance structure and a shorter lasing wavelength. For this work, patterned GaAs substrates containing arrays of ridges and channels were prepared using standard contact

Manuscript received March 24, 1997; revised April 9, 1997. The work of G. G. Ortiz was supported by the Air Force Office of Scientific Research and the Defence Advanced Research Projects Agency/Electronic Technology Organization Optoelectronics program and by the NASA/JPL MSEIO doctoral fellowship program. The work of S. Q. Luong, S. Z. Sun, and J. Cheng was supported by the Air Force Office of Scientific Research and the Defence Advanced Research Projects Agency/ETO Optoelectronics program. The work of H. Q. Hou, G. A. Vawter, and B. E. Hammons was supported by the U.S. Department of Energy under Contract DE-AC04-76DP00789.

G. G. Ortiz is with the University of New Mexico, Center for High Technology Materials, Albuquerque, NM 87131 USA on leave from the Jet Propulsion Laboratory, Pasadena, CA USA.

S. Q. Luong, S. Z. Sun, and J. Cheng are with the University of New Mexico, Center for High Technology Materials, Albuquerque, NM 87131 USA.

H. Q. Hou, G. A. Vawter, and B. E. Hammons are with Sandia National Laboratories, Albuquerque, NM 87185 USA.

Publisher Item Identifier S 1041-1135(97)05689-9.

1041–1135/97$10.00 © 1997 IEEE

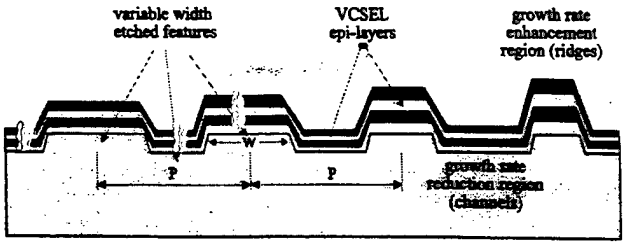


Fig. 1. Schematic showing the effect of growth rate enhancement and reduction on a patterned substrate. The thickness of all the epilayers of the VCSEL structure scale with the growth rate, which depends on the feature width, etch depth and spacing between features.

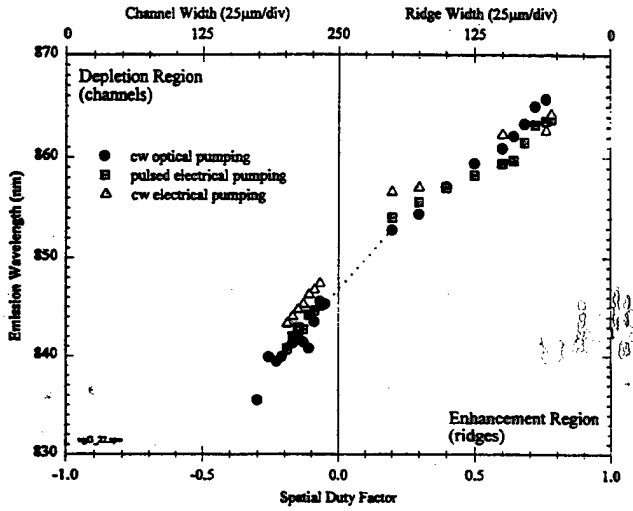


Fig. 2. Emission wavelength versus spatial duty factor demonstrating wavelength grading in both the enhanced and reduced growth rate regimes (ridges and channels).

lithography and chemical etching. Each array contains ridges and channels with varying widths (w and $p-w$, respectively), but with a constant spatial period ($p = 250$ μm). We define a spatial duty factor for the patterns of the two regions as DF $= 1 - w/p$ for the ridges and DF $= -(1 - (p - w)/p)$ (<0) for the channels. The pattern defined by lithography therefore contains ridges and channels with varying spatial duty-factor. Following standard surface preparation steps to reduce surface oxidation and to improve the quality of growth, an AlGaAs–GaAs VCSEL structure is grown by low-pressure MOCVD on a rotating substrate. This structure contains a graded-index separate-confinement-heterostructure multiple-quantum-well (GRIN-SCH-MQW) active region with four 12-nm quantum wells (QW's) and 10-nm spacers, which is sandwiched between a 25-pair, p-doped DBR on the top and a 38.5-pair, n-doped DBR on the bottom. All the heterointerfaces in each DBR have linearly graded AlGaAs compositions, and the doping concentrations of the DBR layers are also graded, from 5×10^{17} cm^{-3} near the active region to 2×10^{18} cm^{-3} away from the active region.

The dependence of the Fabry–Perot cavity resonance on spatial duty factor was investigated by optically pumping both the ridges (growth rate enhancement region) and the channels (growth rate reduction region) using a spatially resolved beam from a Ti:Sapphire laser operating below the VCSEL

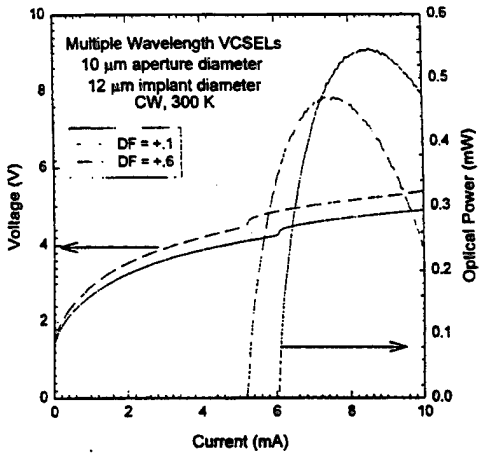


Fig. 3. Typical light versus current (L–I) and current versus voltage (I–V) characteristics under room temperature CW operation for implant-confined VCSEL's in a monolithic multiple-wavelength array.

reflectance stopband. The open symbols in Fig. 2 indicate the emission wavelength of the optically pumped devices, showing that the cavity mode can be controllably varied over a wavelength range greater than 30 nm. These results show an almost linear relationship between the wavelength and the spatial duty factor. The uneven spacing of wavelengths with respect to the duty factor is caused by our particular mask design. However, we can exercise design control over the spacing between wavelengths by taking advantage of the linear dependence of the wavelength on spatial duty factor (DF). For example, a mask design containing the appropriate values of DF can be chosen to achieve an evenly spaced wavelength distribution. Also, by designing our mask to have a tight spread in duty factor, we can obtain very small wavelength spacing between our devices (dense WDM), as seen in the depletion region of Fig. 2. Alternatively, we may design our mask to have a larger spread in DF to achieve larger wavelength spacing (coarse WDM), as seen in the enhancement region of Fig. 2.

The epilayer quality and device performance of the epitaxial material regrown on the topographically patterned substrate are comparable to those obtained from a control sample that was grown sequentially on a planar epiready wafer. Top surface-emitting, proton implant-confined VCSEL's with 12-μm diameter active regions and 10-μm diameter optical apertures were fabricated in both the ridge and channel regions simultaneously. The typical room-temperature (RT) continuous-wave (CW) characteristics of the devices are shown in Fig. 3. All devices have uniform threshold currents (5.5 ± 0.5 mA) and threshold voltages (4 V). The high voltage was caused by the unexpected low p-doping in the top DBR layers, which was also observed in the planar control wafer. The peak output powers were typically 0.5 mW and decreased to 0.2 mW at the short-wavelength edge of the lasing range due to the misalignment between the cavity mode and the gain peak. The uniformity of the device characteristics can be further improved by broadening the optical gain spectrum through the use of nonuniform quantum wells with different thickness or compositions [2], [7].

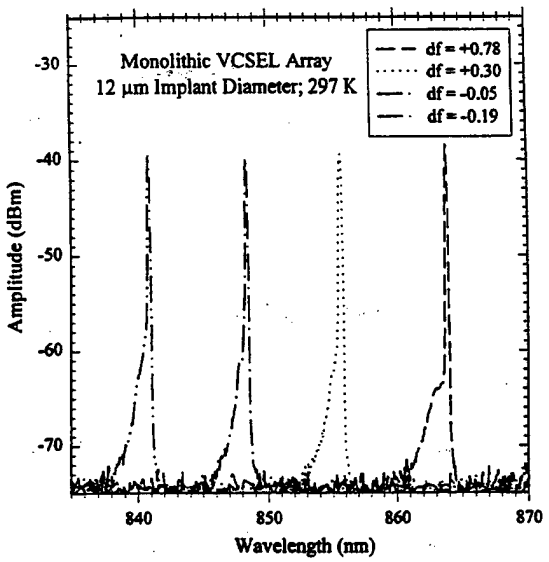


Fig. 4. The CW lasing spectra of electrically pumped VCSEL's from a monolithic wavelength graded array containing devices from both the enhanced and reduced growth rate regimes.

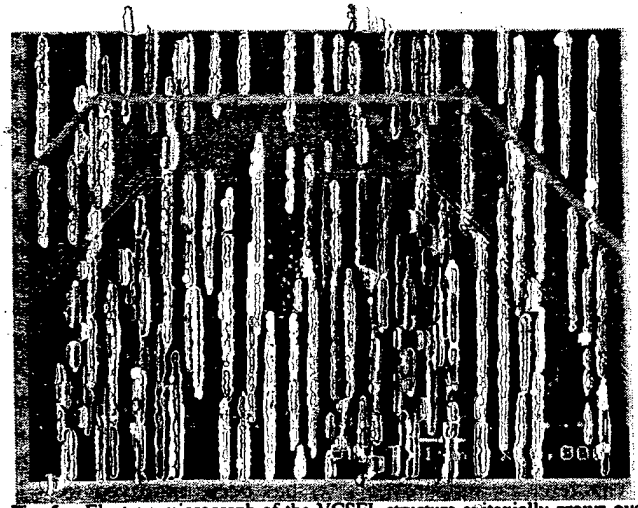


Fig. 5. Electron micrograph of the VCSEL structure epitaxially grown over a very narrow etched ridge on a GaAs surface, showing clear definition of all the epilayers and good quality of growth.

The CW lasing spectra of several electrically pumped devices corresponding to different spatial duty factors are shown in Fig. 4, and the lasing wavelengths for all devices are plotted in Fig. 2 for comparison with the optically pumped results. The lasing wavelength of each VCSEL was measured by keeping the operating bias power, and therefore the internal self-heating, constant at approximately 33.5 mW. An RT CW lasing span of over 20 nm is demonstrated with a side mode suppression ratio greater than 30 dB for all VCSEL's. Due to limitations in the device processing mask design, we were unable to fabricate devices over the entire range of wavelengths, and therefore only a reduced lasing span is demonstrated by the electrically pumped VCSEL's (Fig. 2). However, all devices are expected to lase, as shown by the optical pumping experiments and by the quality of the epilayer structure that is grown on ridges that are even less than 1 μm in width (Fig. 5). Although wavelength grading was previously demonstrated using only the growth rate enhancement regime [4], our data indicates that a greater wavelength range can be achieved by also utilizing regrowth within the channels (growth rate reduction regime).

In conclusion, we have demonstrated a novel technique for obtaining a monolithic multiple-wavelength VCSEL array that is simple to produce and allows much flexibility in wavelength control. The arrays from this work achieved RT CW lasing with a wavelength span greater than 20 nm by electrical-injection and greater than 30 nm by optical pumping, with uniform device characteristics.

REFERENCES

[1] W. Yuen, G. S. Li, and C. J. Chang-Hasnain, "Multiple-wavelength vertical-cavity surface-emitting laser arrays with a record wavelength span," *IEEE Photon. Technol. Lett.*, vol. 8, pp. 4–6, Jan. 1996.

[2] H. Saito, I. Ogura, and Y. Sugimoto, "Uniform CW operation of multiple-wavelength vertical-cavity surface-emitting lasers fabricated by mask molecular beam epitaxy," *IEEE Photon. Technol. Lett.*, vol. 8, pp. 1118–1120, Sept. 1996.

[3] T. Wipiejewski, M. G. Peters, E. R. Hegblom, and L. A. Coldren, "Vertical-cavity surface-emitting laser diodes with post-growth wavelength adjustment," *IEEE Photon. Technol. Lett.*, vol. 7, pp. 727–729, July 1995.

[4] F. Koyama, T. Mukaihara, Y. Hayashi, N. Ohnoki, N. Hatori, and K. Iga, "Wavelength control of vertical cavity surface-emitting lasers by using nonplanar MOCVD," *IEEE Photon. Technol. Lett.*, vol. 7, pp. 10–12, Jan. 1995.

[5] P. Demeester, P. Van Daele, and R. Baets, "Growth behavior during nonplanar metalorganic vapor phase epitaxy," *J. Appl. Phys.*, vol. 63, no. 7, pp. 2284–2290, 1988.

[6] L. Buydens, P. Demeester, M. Van Ackere, A. Ackaert and P. Van Daele, "Thickness variations during MOVPE growth on patterned substrates," *J. Electron. Mater.*, vol. 19, no. 4, pp. 317–321, 1990.

[7] G. G. Ortiz, C. P. Hains, B. Lu, S. Z. Sun, J. Cheng and J. C. Zolper, "Cryogenic VCSEL's with chirped multiple quantum wells for a very wide temperature range of CW operation," *IEEE Photon. Technol. Lett.*, vol. 8, pp. 1423–1425, Nov. 1996.

Wavelength Multiplexing and Demultiplexing Using Multiwavelength VCSEL and Resonance-Enhanced Photodetector Arrays

A. Alduino, *Student Member, IEEE,* Yuxin Zhou, S. Luong, C. P. Hains, and Julian Cheng, *Senior Member, IEEE*

***Abstract*— A novel wavelength-division-multiplexed optical interconnect is demonstrated in which optical data from a monolithic wavelength-chirped VCSEL array is multiplexed onto a single fiber, and then demultiplexed using an array of wavelength-selective resonance-enhanced photodetectors with closely matched resonance wavelengths. This is demonstrated under both dc and 125-Mb/s data modulation, achieving an optical crosstalk rejection ratio of ~ -10 dB (-7.5 dB) for channels that are spaced 6 nm (4 nm) apart.**

***Index Terms*— Monolithic VCSEL arrays, multiwavelength sources, optical interconnects, resonant enhanced photodetectors, wavelength-division multiplexing.**

MONOLITHIC arrays of wavelength-graded vertical-cavity surface-emitting lasers (VCSEL's) and wavelength-selective resonance-enhanced photodetectors (REPD's) are useful for a variety of wavelength division multiplexing (WDM) applications in local area optical interconnects. Multiple channels of wavelength-encoded data can be multiplexed together and transmitted in parallel through a single optical fiber to enhance the data throughput. Demultiplexing can be achieved by using a passive wavelength demultiplexer, such as a grating, or by fanning out the optical signal to different nodes, each containing a wavelength-selective photodetector with a different wavelength passband, as shown in Fig. 1(a). Multiple wavelength VCSEL and REPD arrays can also be used to minimize optical crosstalk between neighboring channels in a parallel free-space optical interconnect. In both cases, a highly selective wavelength response is needed to minimize the optical crosstalk between neighboring channels.

We describe below an experimental demonstration of a fiber-based "broadcast and select" WDM interconnect technology using an array of wavelength-graded VCSEL's [1] and an array of wavelength-selective REPD's [2] with matching wavelengths. The REPD's are multiquantum well absorbers that are embedded within a resonant cavity, which selectively absorbs light that lies within its narrow wavelength passband. The wavelength selectivity of an REPD, or equivalently the optical crosstalk between adjacent WDM channels, depends upon the spectral width of the resonant absorption. The narrower its spectral response, the larger the number of closely spaced wavelength channels that may be multiplexed.

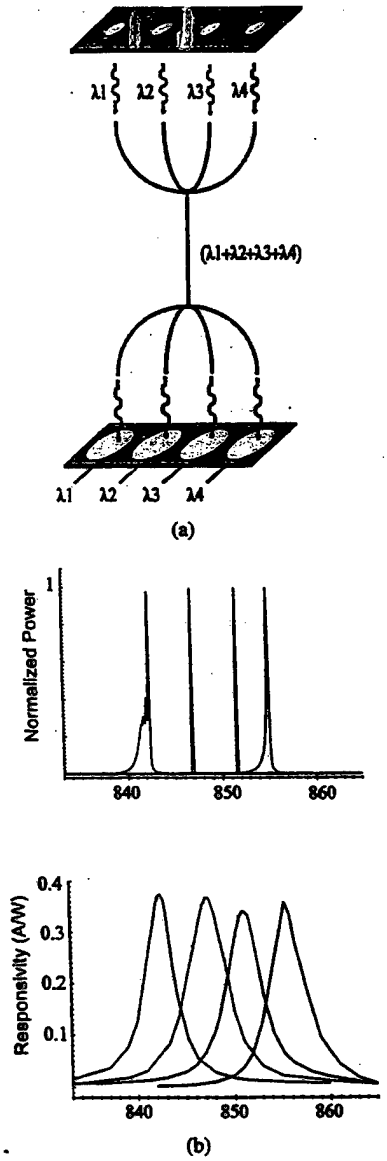


Fig. 1. (a) Schematic of the WDM interconnect architecture and experimental configuration. (b) Responsivity spectra of four wavelength-selective REPD's, and the normalized lasing spectra of four VCSEL's with closely matching resonance wavelengths, from two monolithic, multiwavelength source, and photodetector arrays.

Manuscript received May 4, 1998; revised June 1, 1998. This work was supported by Air Force Office of Scientific Research and by the Defense Advanced Research Projects Agency/ETO under the Ultra Photonics program.

The authors are with the Center for High Technology Materials, University of New Mexico, Albuquerque NM 87106 USA.

Publisher Item Identifier S 1041-1135(98)06289-2.

1041–1135/98$10.00 © 1998 IEEE

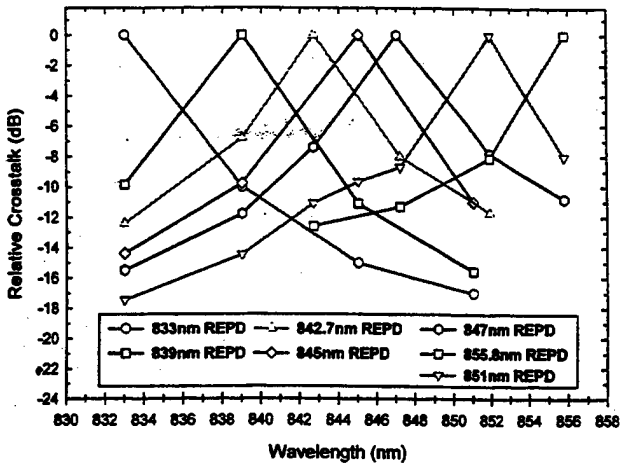


Fig. 2. Normalized dc photoresponse of seven REPD's to the optical inputs from seven wavelength-matching VCSEL's, showing the optical crosstalk levels for wavelength channels with different spacing.

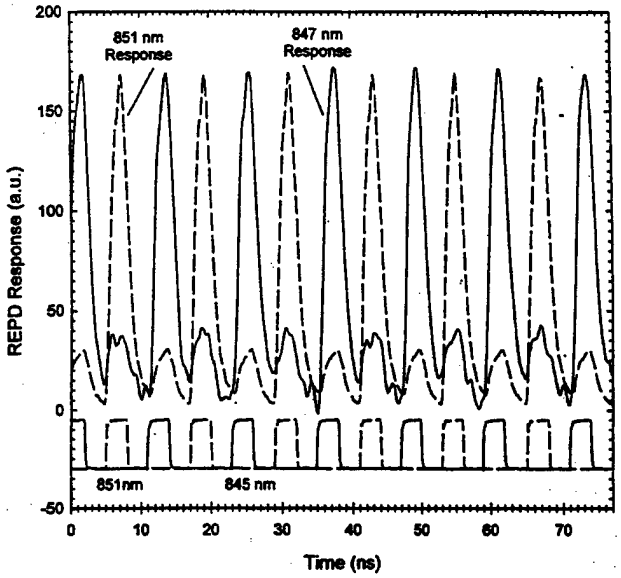


Fig. 3. Wavelength demultiplexing of high-speed modulated data channels (125 Mb/s, 4-ns pulses) using REPD's with a resonance wavelength separation of $\Delta\lambda \cong 4$ nm, showing optical crosstalk rejection ratios of -7.8 and -6.7 dB for the 851 and 847 nm REPD's, respectively.

We have previously demonstrated a technique for realizing wavelength-graded VCSEL and REPD arrays on the same epilayer structure, [3] which allows a close wavelength correlation between the source and detector elements. This technique relies upon the local modification of the growth rate due to surface morphology during metal–organic chemical vapor deposition (MOCVD) [4]–[6]. The growth rate is enhanced on ridges, and is reduced in valleys, in direct proportion to the spatial duty factor, which is defined as $(1-w/p)$ for the ridges and $-(1-w/p)$ for the valleys, where p is the pitch and w is the width of the ridge or valley. By patterning the substrate prior to growth with ridges and valleys with a varying spatial duty factor, the local growth rates of all the epilayers can be uniformly scaled in a reproducible and controllable manner. This allows the resonance wavelength of the VCSEL or REPD structure to be controllably varied across the wafer. Fig. 1(b) shows the CW lasing spectrum and the optical responsivity for several elements of a VCSEL array and a REPD array with closely matching wavelengths.

The optical crosstalk, or equivalently the channel selectivity, between different wavelength channels has been characterized under both dc and large signal modulation. To demonstrate wavelength multiplexing, the optical outputs of several VCSEL's from this multiwavelength array are combined by a fiber coupler and transmitted through a multimode fiber. At the receiver end, the signal is fanned out by a coupler, and the individual wavelength channels are demultiplexed (selected) by different elements of the REPD array.

For the dc measurement, seven VCSEL sources with wavelength spacing between 2 and 6 nm were used to probe the responsivity of seven REPD's spanning a wavelength range of 23 nm. The reproducibility of the wavelength grading from array to array is <2 nm. Within each array the lasing wavelengths are currently not evenly spaced, but can be redesigned to be so by choosing appropriate values of DF [1]. The photocurrent of each wavelength-selective REPD was measured individually in response to each of the transmitting wavelength channels. The optical crosstalk level was then calculated and the results plotted in Fig. 2. The optical crosstalk between neighboring channels depends on their spacing $\Delta\lambda$, and has an average value of -7.5 dB for $\Delta\lambda = 4$ nm, and -10.2 dB for $\Delta\lambda = 6$ nm. The crosstalk between the next nearest neighbor channels drops to ~ -11 dB for $\Delta\lambda = 8$ nm, and ~ -15 dB for $\Delta\lambda = 12$ nm. The signal rejection efficiency of each REPD is controlled by the spectral width of its responsivity, which has a full-width at half-maximum (FWHM) of ~ 4 nm. The upper mirror of these 850-nm devices has 10 DBR pairs, with a reflectivity of $R_{\text{top}} = 94.39\%$ that varies by only $\pm 0.23\%$ over the entire 40-nm wavelength grading range. This reduced wavelength dispersion in the mirror loss results from the ability to scale the growth rate of all the epilayers of individual devices to match the variation in the lasing mode. A narrower spectral width may be achieved by increasing the upper mirror reflectivity, which also results in an array with lower responsivity. For a given material absorption coefficient, the optimum design is a tradeoff between absorption efficiency and wavelength selectivity. Reducing the material absorption coefficient, e.g., using the 980-nm REPD's of [3], will decrease the spectral width without sacrificing responsivity, thus reducing the optical crosstalk and allowing a larger number of wavelength channels to be multiplexed.

The optical crosstalk was also measured under large-signal data modulation using a similar experimental configuration. Two VCSEL's from the multiwavelength array were simultaneously modulated using temporally displaced (nonoverlapping) data patterns. Each REPD was mounted in a high-speed package containing a transimpedance (TZ) amplifier with a bandwidth of 1.2 GHz. Fig. 3 shows the experimental demultiplexing results at a data rate of 125-Mb/s return-to-zero (RZ) [250-Mb/s nonreturn-to-zero (NRZ), 4-ns pulses], for a channel spacing of $\Delta\lambda = 4$ nm. The launched power for all the wavelength channels was intentionally equalized with a typical value of 100 μW/channel launched into a multimode fiber, the

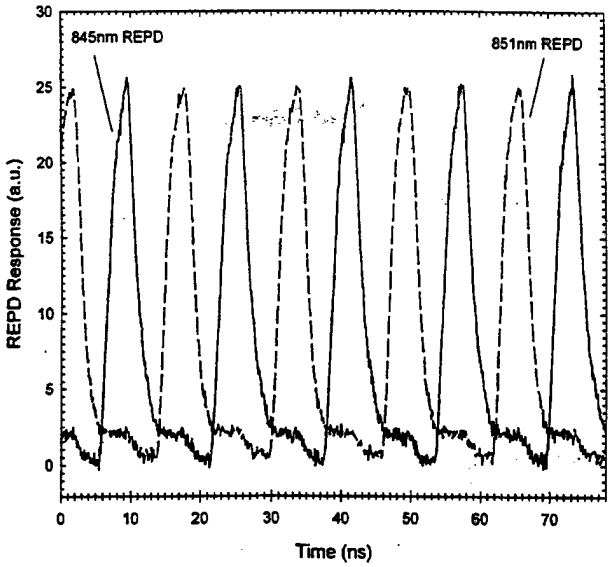


Fig. 4. Wavelength demultiplexing of high-speed modulated data channels (125 Mb/s 4-ns pulses) using REPD's with a resonance wavelength separation of $\Delta\lambda \cong 6$ nm, showing optical crosstalk rejection ratios of -10.5 dB and -10.0 dB for the 845 and 851 nm REPD's, respectively.

optical power incident on each REPD was 35 μW/channel. In each time trace, the higher and lower pulses represent the amplitudes of the photoresponse of each REPD to the optical data channels at resonant and nonresonant wavelengths. The response of the 851-nm REPD and the 847-nm REPD show a crosstalk level of -7.8 dB and -6.7 dB, respectively, which are in good agreement with the average dc crosstalk level of ~ -7.5 dB for $\Delta\lambda = 4$ nm. Fig. 4 shows the results of the same modulation experiment when the two channels are separated by $\Delta\lambda = 6$ nm. For this case, the equalized launched power was 160 μW/channel, and the power incident on each REPD was 60 μW/channel. The photoresponse of the 851 nm REPD and the 845-nm REPD show a crosstalk level of -10.0 dB and -10.5 dB, respectively, which are within 0.5 dB of the average measured dc crosstalk level of -10.2 dB for $\Delta\lambda = 6$ nm. The large signal modulation response was limited by the capacitance of the REPD's (200 μm area), which resulted in a fall-time of >4 ns (Fig. 4).

In conclusion, we have demonstrated a novel WDM optical interconnect scheme in which the outputs of a monolithic multiwavelength VCSEL array are wavelength-multiplexed and transmitted on a single fiber, and then demultiplexed by individual wavelength-selective REPD's with matching wavelength passbands. The MUX/DEMUX operations have been demonstrated at a data rate of 125 Mb/s, with a crosstalk level of -10 dB. The modulation response can be significantly improved by reducing the size of the REPD's, while lower crosstalk (greater spectral selectivity) and a closer channel spacing can be realized by reducing the width of the REPD's spectral response. Bit-error-rate measurements will be carried out on a future generation of higher speed REPD's to determine the power penalty due to interchannel crosstalk.

REFERENCES

[1] G. G. Ortiz, S. Q. Luong, S. Z. Sun, J. Cheng, H. Q. Hou, G. A. Vawter, and E. Hammons, "Monolithic, multiple wavelength vertical-cavity surface-emitting laser arrays by surface-controlled MOCVD growth rate enhancement and reduction," *IEEE Photon. Technol. Lett.*, vol. 9, pp. 1069–1071, Aug. 1997.

[2] S. Q. Luong, G. G. Ortiz, Y. Zhou, J. Lu, C. P. Hains, J. Cheng, H. Q. Hou, and G. A. Vawter, "Monolithic wavelength-graded VCSEL and resonance-enhanced photodetector arrays for parallel optical interconnects," *IEEE Photon. Technol. Lett.*, vol. 10, pp. 642–644, May 1998.

[3] G. G. Ortiz, C. P. Hains, J. Cheng, H. Q. Hou, and J. C. Zolper, "Monolithic integration of InGaAs VCSEL's with resonance-enhanced quantum-well photo-detectors," *Electron. Lett.*, vol. 32, no. 13, pp. 1205–1207, June 1996.

[4] P. Demeester, P. Van Daele, and R. Baets, "Growth behavior during nonplanar metalorganic vapor phase epitaxy," *J. Appl. Phys.*, vol. 63, no. 7, pp. 2284–2290, 1988.

[5] L. Buydens, P. Demeester, M. Van Ackere, A. Ackaert, and P. Van Dael, "Thickness variations during MOVPE growth on patterned substrates," *J. Electron. Mater.*, vol. 19, no. 4, pp. 317–321, 1990.

[6] F. Koyama, T. Mukaihara, Y. Hayashi, N. Ohnoki, N. Hatori, and K. Iga, "Wavelength control of vertical cavity surface-emitting lasers by using nonplanar MOCVD," *IEEE Photon. Technol. Lett.*, vol. 7, pp. 10–12, 1995.

IEEE PHOTONICS TECHNOLOGY LETTERS, VOL. 11, NO. 5, MAY 1999

Quasi-Planar Monolithic Integration of High-Speed VCSEL and Resonant Enhanced Photodetector Arrays

A. C. Alduino, *Student Member, IEEE*, S. Q. Luong, Yuxin Zhou, *Student Member, IEEE*, C. P. Hains, and Julian Cheng, *Senior Member, IEEE*

Abstract—**We describe the quasi-planar monolithic integration of oxide-confined vertical-cavity surface-emitting laser (VCSEL) and resonant enhanced photodetector (REPD) arrays. These high speed devices are fabricated using an approach in which current apertures with a range of different sizes are formed by concatenating a number of discrete crescent shaped oxidation fronts. This approach preserves planarity while improving dimensional control for devices with very small oxide apertures (<4 μm). It resulted in VCSEL's with electrical and optical characteristics that are comparable to those of etched-mesa devices, while producing high-speed REPD's with a rise time of ~65 ps.**

Index Terms—**Monolithic integration, monolithic VCSEL arrays, resonant-enhanced photodetection.**

MONOLITHIC arrays of vertical-cavity surface-emitting lasers (VCSEL's) and resonance-enhanced photodetectors (REPD's) can be monolithically integrated into optoelectronic arrays that perform useful functions in optical switching and wavelength-division-multiplexing (WDM) applications. Multiwavelength VCSEL and REPD arrays have previously been realized using both proton implantation [1] and selective oxidation [2] for current confinement. However, the selective oxidation presents a problem for monolithic integration due to the disparate size requirements of the current apertures for the VCSEL (<10 μm) and the REPD (>30 μm), which share a common epilayer structure [3]. The VCSEL's and REPD's are typically isolated mesa structures from whose periphery selective lateral oxidation proceeds. For VCSEL's the oxidation length is chosen as a tradeoff between the accuracy of the final oxide aperture and the need for a low contact resistance, it typically exceeds 10 μm. As a result of this oxidation length, the concomitant lateral oxidation of the larger REPD mesas produces a large parasitic capacitance that reduces the bandwidth of the photoresponse. It is thus desirable to develop a new oxidation technique for monolithic integration that can accommodate a range of different oxide apertures with arbitrary geometries while improving dimensional control, preserving planarity, and minimizing device parasitics (capacitance as well as resistance). This has been achieved using a variant of the etched-trench oxidation technology described in references [4]–[6], which resulted in quasi-planar high-speed VCSEL and REPD arrays with dimensions as small as 2 μm.

In monolithic integration, arrays are patterned into etched mesas to facilitate selective lateral oxidation and to electrically isolate neighboring devices. The size of the mesa is determined not only by the desired electrical and thermal characteristics, but also by the requirements of dense integration. Smaller mesa sizes result in denser arrays, but cause higher electrical and thermal resistance, resulting in less efficient device performance. To minimize power dissipation in dense arrays, devices with a small oxide aperture are needed. However, due to limits in the accuracy of the oxidation rate, very small microcavities cannot be accurately and reliably achieved without reducing the mesa size and oxidation length, which increases the electrical and thermal resistances. For a given process control accuracy, the percentage error in the dimension of the oxide aperture can become unacceptably high when the final dimension is small compared to the total oxidation length. The oxidation length (and time) can be reduced without reducing mesa size or sacrificing planarity by the introduction of local oxidation centers such as etched holes [4], [5], from which multiple lateral oxidation fronts can proceed to define an enclosed oxide aperture. Arbitrary oxide aperture geometries can be defined using discrete etched holes [6], or alternatively by using linear or crescent-shaped segments of etched trenches, from which oxide fronts as narrow as 2 μm can be concatenated to form a single continuous aperture. By not removing all of the surrounding semiconductor material, not only has quasi-planarity been maintained, but the thermal resistance is also decreased to alleviate thermal rollover.

This technique has been applied to the quasi-planar monolithic integration of VCSEL and REPD arrays. The device fabrication begins with the deposition of the circular upper p-metal pattern containing the open crescent-shaped segments that allow a circular oxidation front to be formed by selective wet oxidation to define the active areas of the VCSEL's and REPD's. The number of segments is increased with larger oxide aperture size (four for VCSEL's and eight for REPD's) in order to provide uniform current spreading from regions lying outside the circular trenches. This is followed by dry etching through these open segments to a depth below the active region to expose the $Al_{0.98}Ga_{0.02}As$ layers

Manuscript received December 18, 1998; revised February 5, 1999. This work was supported by the Defense Advanced Research Projects Agency and the Air Force Office of Scientific Research.

The authors are with the Center for High Technology Materials, University of New Mexico, Albuquerque, NM 87106 USA.

Publisher Item Identifier S 1041-1135(99)03603-4.

1041–1135/99$10.00 © 1999 IEEE

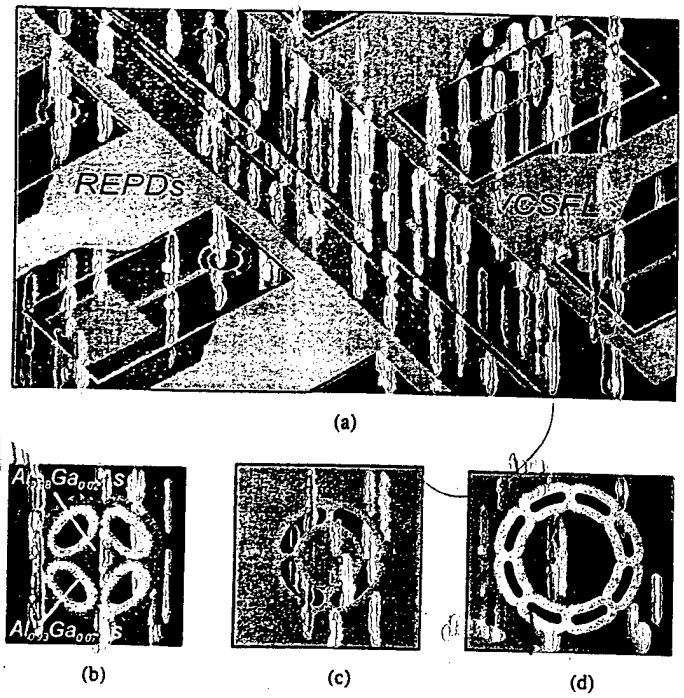


Fig. 1. (a) Demonstrates the quasi-planar monolithic integration of VCSEL's with resonance-enhanced photodetectors (REPD's). (b)–(d) shows the concatenation of ~3 μm oxidation fronts from crescent-shaped apertures to form continuous current apertures for both VCSEL's (a) and (b) and REPD's (c).

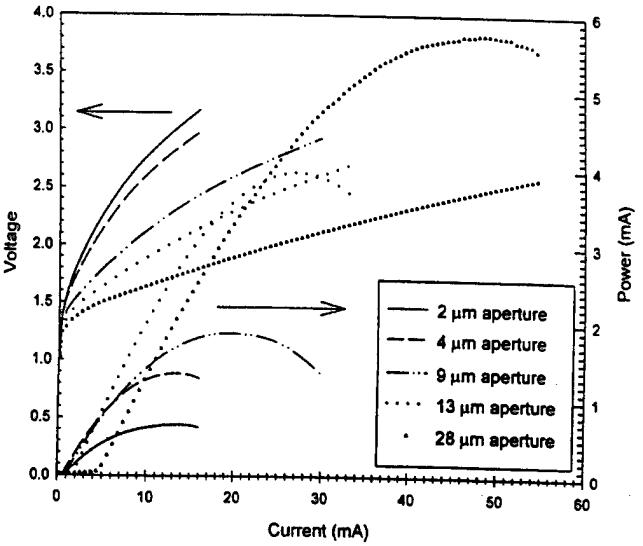


Fig. 2. The dc electrical and optical characteristics of a range of etched trench (ET) fabricated VCSEL's.

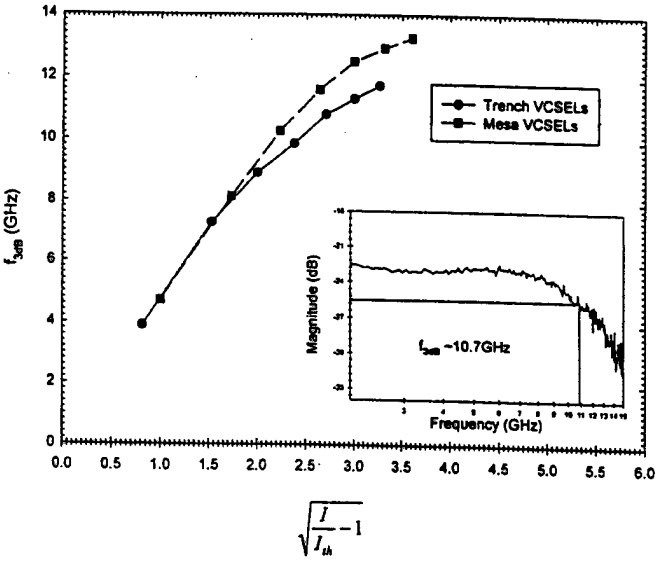


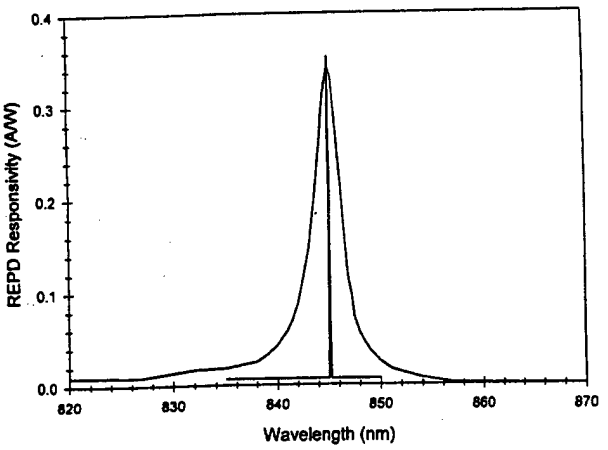
Fig. 3. Comparison of $f_{3\text{ dB}}$ (−3-dB frequency of $|S_{21}|$) for etched trench and etched mesa VCSEL's demonstrating comparable performance. Inset: $|S_{21}|$ curve of an etched trench fabricated VCSEL at $I = 9 * *I_{th}$.

for wet oxidation. After oxidation, all the surrounding areas are bombarded with a multilevel proton implant for device isolation. Finally, the bottom n-contact is deposited. All of the devices were designed to have coplanar strip lines in order to evaluate their high speed response. This necessitated a postimplant mesa etch (hence quasi-planar) to allow metal contact to the substrate to be made from the upper surface for the coplanar strip line geometry. Fig. 1(a) shows the monolithic integration of both VCSEL and REPD arrays using the ET approach. Fig. 1(b)–(d) shows the formation of continuous oxidation fronts from discrete etched trench segments (3 μm wide) with oxide apertures of 2, 6, and 20 μm, respectively. With a total device area whose diameter is only ~14 μm larger than that of the active area, the ET technique potentially allows higher density monolithic integration of both VCSEL and REPD arrays.

An important advantage of this ET technique is that the oxidation length is decreased to 2–3 μm. This allows more precise control of the final aperture to be achieved, especially for devices with small active areas (<4 μm). For an etched mesa (EM) device with a 2-μm active region and a 10-μm oxidation length, an uncertainty in the oxidation rate of ±5% would lead to an uncertainty of ±0.5 μm (25%) in the active area diameter. For an ET VCSEL with a 2-μm active region and an oxidation length of 2 μm, the same uncertainty in oxidation rate would result in an uncertainty of only ±0.1 μm (5%), a fivefold improvement.

The dc electrical and lasing characteristics of the ET VCSEL's are shown in Fig. 2 for devices with diameters ranging from 2 to 28 μm. All devices have low threshold voltages (1.45–1.60 V) and exhibited no evidence of leakage currents. The CW lasing characteristics of the VCSEL's have threshold currents ranging from 0.9 mA for the 2-μm devices to 4.3 mA for the 28-μm devices, with slope and wall-plug efficiencies of 16%–20% and 8%–11%, respectively. These values are comparable to those values for the EM devices that were also fabricated using the same wafer. One notable difference between the ET VCSEL's and EM VCSEL's is that although both have comparable peak optical output powers (0.7 mW for 2-μm devices to 5.8 mW for the 28-μm devices), thermal rollover occurs at a much higher current for the former, suggesting a lower thermal resistance. The EM VCSEL's show a slightly lower threshold current than the ET VCSEL's for devices with very small active areas.

An important advantage of the ET approach is the reduction of parasitic areas caused by oxidation. The high speed modulation characteristics of ET and EM VCSEL's have been investigated, and the results are shown in Fig. 3, which



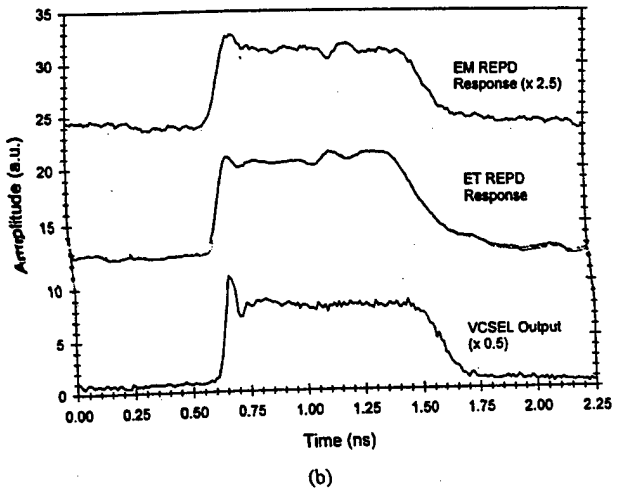


Fig. 4. (a) The dc photoresponsivity spectrum of a 30-μm aperture ET-REPD, showing ~3.5 nm FWHM and a peak responsivity of 0.34 A/W, along with the lasing spectrum of a typical VCSEL. (b) The large signal modulation response of an ET-REPD and an EM-REPD (upper traces) to the modulated optical output of an ET-VCSEL (lower trace) showing a rise time of ~65 ps.

TABLE I
COMPARISON OF THE CONTRIBUTIONS TO THE CAPACITANCE OF 30-μm ET AND EM REPD'S

	Etched Mesa	Etched Trench
C_{junc}	0.42 pF	0.33 pF
C_{ox}	0.32 pF	0.12 pF
C_{pad}	0.19 pF	0.40 pF
C_{tot} (calculated)	0.93 pF	0.85 pF
C_{tot} (measured)	0.99 pF	0.95 pF

compares $f_{3\,dB}$ (the −3-dB modulation bandwidth) versus $\sqrt{(I/I_{th})-1}$ (where I and I_{th} are the bias and threshold currents, respectively) for two ~6 μm active area VCSEL's fabricated using the different approaches. The figure inset shows a typical $|S_{21}|$ versus frequency curve for an ~6-μm trench VCSEL biased at $I = 9^*I_{th}$. At low bias current levels the $f_{3\,dB}$ frequencies are identical, but as the bias current increases the EM devices show a slightly higher speed, with a maximum frequency of 13.5 GHz versus 11.8 GHz. The increase in modulation bandwidth expected from the decrease in oxide parasitic capacitance is partly annulled by the larger parasitic capacitance of the contact pads due to the higher dielectric constant of the semiconductor ($\varepsilon_r \sim 13.13$), compared to that of the polyimide ($\varepsilon_r \sim 3.3$).

The typical photoresponse of the ET REPD's, measured at a reverse bias of 5 V, is presented in Fig. 4. Fig. 4(a) shows the dc responsivity of a typical REPD, demonstrating a spectral bandwidth [full-width at half-maximum (FWHM)] of ~3.5 nm and a peak responsivity of ~0.34 A/W (50%) at the resonant wavelength, along with the lasing spectra of a typical ET VCSEL. Fig. 4(b) shows the large signal modulation response of an REPD with a 30-μm optical aperture in response to the optical modulation from a 6-μm VCSEL source. The response shows a 10%–90% rise time of ~65 ps, which represents a significant improvement over the bandwidth of earlier etched mesa devices [7], which had a much larger mesa. Also shown is the response of a 30-μm EM REPD showing almost identical rise and fall times. This can be understood by comparing the different contributions to the capacitance for the 30-μm EM and the 30-μm ET devices, as shown in Table I. While the ET device has a lower contribution from the oxide and junction areas (C_{junc} and C_{OX}), this is offset by the larger capacitance of the contact pad (C_{pad}) as described above.

In conclusion, we have demonstrated a novel quasi-planar fabrication technique for integrating VCSEL's and REPD's in high-density arrays for applications in high-speed WDM networks. This technique can accommodate a range of different oxide apertures with arbitrary geometries (circular or square) while improving dimensional control for small active areas.

REFERENCES

[1] G. G. Ortiz, S. Q. Luong, S. Z. Sun, Julian Cheng, H. Q. Hou, G. A. Vawter, and B. E. Hammons, "Monolithic, multiple wavelength vertical-cavity surface-emitting laser arrays by surface-controlled MOCVD growth rate enhancement and reduction," *IEEE Photon. Tech. Lett.*, vol. 9, pp. 1069–1071, Aug. 1997.

[2] Y. Zhou, S. Luong, C. P. Hains, and J. Cheng, "Oxide-confined monolithic, multiple-wavelength vertical-cavity surface-emitting laser arrays with a 40-nm wavelength span," *IEEE Photon. Technol. Lett.*, vol. 10, pp. 1527–1529, Nov. 1998.

[3] G. G. Ortiz, C. P. Hains, Julian Cheng, H. Q. Hou, and J. C. Zolper, "Monolithic integration of $In_{0.2}Ga_{0.8}As$ vertical-cavity surface-emitting lasers with resonance-enhanced quantum-well photodetectors," *Electron. Lett.*, vol. 32, no. 13, pp. 1205–1207, June 1996.

[4] R. P. Schneider, Jr., "A new planar Laser," *IEEE Spectrum*, vol. 35, pp. 52–53, Feb. 1998.

[5] C. L. Chua, R. L. Thornton, and D. W. Treat, "Planar laterally oxidized vertical-cavity lasers for low-threshold high-density top-surface-emitting arrays," *IEEE Photon. Technol. Lett.*, vol. 9, pp. 1060–1062, Aug. 1997.

[6] C. L. Chua, R. L. Thornton, D. W. Treat, and R. M. Donaldson, "Anisotropic apertures for polarization-stable laterally oxidized vertical-cavity lasers," *Appl. Phys. Lett.*, vol. 73, no. 12, pp. 1631–1633, Sept. 12.

[7] A. C. Alduino, S. Luong, Y. Zhou, C. P. Hains, and J. Cheng, "Wavelength multiplexing and demultiplexing using multi-wavelength VCSEL and resonance-enhanced photodetector arrays," *IEEE Photon. Technol. Lett.*, vol. 10, pp. 1310–1312, Sept. 1998.

Proceedings of the 1999 Conference of Lasers and Electro-Optics, May, 1999.

A Quasi-Planar Approach to the Monolithic Integration of High Speed VCSEL and Resonant Photodetector Arrays

A. C. Alduino, S. Q. Luong, Yuxin Zhou, C. P. Hains, and Julian Cheng

University of New Mexico

Center for High technology Materials

1313 Goddard SE

Albuquerque, NM 87106

We describe the monolithic integration of oxide-confined VCSELs and resonant photodetectors with small active area apertures using a quasi-planar approach in which the continuous oxidation front is locally defined by a discrete pattern of crescent-shaped trenches.

Monolithic arrays of VCSELs and resonant enhanced photodetectors (REPDs) can be integrated into optoelectronic circuits that perform useful functions in optical switching and wavelength division multiplexing (WDM) applications [1]. For these and other optoelectronic interconnect applications, planarity is desirable for monolithic integration, and low power dissipation is required for dense arrays. To minimize power dissipation, oxide-confined VCSELs with small active areas and low operating currents are needed. In the standard (non-planar) technique for fabricating oxide-confined VCSELs, the active area is defined by the lateral wet oxidation of the high aluminum content layers from the periphery of an etched mesa, with a typical oxidation length of >10 μm. Minimizing the thermal and electrical resistances dictate a large mesa size, at the cost of a longer oxidation time and hence greater uncertainty in the final aperture size. The oxidation time and uncertainty can be reduced without sacrificing planarity or increasing the mesa size by introducing local oxidation centers (*e.g.,* etched holes [2,3]) from which multiple oxidation fronts can proceed to define an active aperture. Figure 1 shows a set of discrete crescent-shaped trenches (~3μm wide) that can be used to form a continuous oxide aperture with an oxidation length as small as 2μm. Figure 1(a) shows the proximate integration of both VCSELs and REPDs on a single wafer, while figs. 1(c) and 1(d) show their respective oxidation fronts. A low electrical resistance is provided by a contact area that extends beyond the outer boundary of the etched trenches.

The electrical and lasing characteristics of oxide-confined VCSELs fabricated using the quasi-planar etched-trench (ET) technique have been compared with those of etched mesa VCSELs (EM) fabricated from the same wafer. Their dc lasing characteristics (fig. 2) show comparable performance over a range of aperture sizes, with the smaller EM VCSELs (<4μm) having a slight advantage in threshold current, and the larger ET VCSELs (>12μm) having higher power. The electrical characteristics show a slight advantage in threshold voltage for the ET devices. One advantage of the ET VCSEL is the preservation of planarity without increasing device parasitics. This is demonstrated by comparing the high frequency modulation response of VCSELs and REPDs made using these two techniques. The ET and EM VCSELs show a similar optical modulation response as a function of current (fig. 3a), each with a -3dB bandwidth of ~4 GHz at $2\times I_{th}$, increasing to more than 12 GHz at $10\times I_{th}$.

REPDs with a small active area (~30μm) have also been fabricated using this technique, with a peak absorption efficiency of ~70% at a wavelength of ~850nm, which is closely matched to the wavelength of the VCSELs. The large-signal modulation esponse of the REPD/VCSEL transceiver pair is shown in fig. 3b, which exhibits a 10%-90% rise time of ~70ps.

We have demonstrated a planar technique that uses a pattern of etched trenches to define the active area of VCSELs and REPDs to facilitate their planar integration. This technique produced devices with dc and high frequency characteristics that are comparable to the etched mesa VCSELs, while providing increased accuracy in the production of devices with small (<4μm) apertures.

Multi-Quantum Well GaInNAs/GaAs Lasers with Low Threshold Current Density Grown by MOCVD

Julian Cheng, N.Y. Li, C. P. Hains, and K. Yang
University of New Mexico, Center for High Technology Materials
1313 Goddard SE, Albuquerque, NM 87106, (505)272-7846

The $Ga_{1-x}In_xN_yAs_{1-y}$/GaAs material system represents a promising approach for achieving long wavelength semiconductor lasers with a large characteristics temperature (T_o) as well as VCSELs on a high-quality GaAs substrate. For VCSELs, this epitaxial approach takes advantage of the large index difference of GaAs/AlAs DBR mirrors (thus smaller growth thickness), as well as the established processing technology of AlGaAs/GaAs VCSELs. Pulsed lasing of edge-emitting $Ga_{1-x}In_xN_yAs_{1-y}$/GaAs quantum well (QW) lasers has previously been achieved at 1.18 μm and at 1.31 μm at room temperature using material grown by gas source MBE [1], with a threshold current as low as 1.4 kA/cm^2. However, the progress in MOCVD-grown GaInNAs/GaAs material has lagged behind, and the best result to date was achieved by a 2-QW laser under pulsed lasing conditions [2], with a lasing wavelength of ~1.18 μm and a threshold current density of 3.37 kA/cm^2. This paper reports a signficant improvement in the performance of MOCVD-grown $Ga_{1-x}In_xN_yAs_{1-y}$/GaAs lasers. Using a new MOCVD regrowth technique [3], 3-QW $Ga_{1-x}In_xN_yAs_{1-y}$/GaAs edge-emitting lasers with x=0.3 and y ~ 0.3-0.4 % have been achieved, with lasing wavelengths in the 1.15-1.19 μm regime and threshold current density as low as ~600-700 A/cm^2, which is the lowest for any MOCVD-grown devices. Ridge-waveguide lasers as well as planar broad stripe lasers defined by the selective lateral wet oxidation of an $Al_{0.98}Ga_{0.02}As$ layer have been fabricated.

The GaInNAs lasers were grown in an IR-heated, horizontal flow OMVPE reactor on N$^+$ GaAs substrates oriented at 6° off (100) towards <111>A. The $In_{0.3}Ga_{0.7}As_{0.997}N_{0.003}$/GaAs QWs were grown at 535°C using trimethylindium, trimethylgallium, 100% arsine, and dimethylhydrazine (DMHy). Diethyltellurium and carbon tetrachloride were used as Te-doping and C-doping precursors, respectively. The growth rate of the $In_{0.3}Ga_{0.7}As_{0.995}N_{0.005}$ and GaAs layers were 5.4, and 8 Å/sec, respectively, and the ratio of [DMHy]/([DMHy]+[AsH_3]) was fixed at 0.6. To eliminate the Te memory effect [3] that reduced the radiative efficiency of the GaInNAs/GaAs MQWs, in-situ cleaning the quartz reactor and graphite susceptor with hydrogen chloride at 830°C were employed prior to the regrowth of the MQW active region and the p-cladding layer.

Pulsed lasing has been achieved at room temperature by edge-emitting GaInNAs/GaAs lasers with 3 QWs (7 nm wells separated by 10 nm barriers), $Al_{0.3}Ga_{0.7}As$ cladding layers, a cavity length of 1000 μm and a stripe width W that varyies from 2 μm to 60 μm. The light-vs-current characteristic and lasing spectrum of a device with W= 60 μm are shown in fig. 1, with a threshold current of 350 mA and a current density of ~635 A/cm^2, and a lasing wavelength of ~1.165 μm at 1.0 A. The temperature dependence of the threshold current for these devices show a characteristic temperature of T_o= 125 K - 133 K. The longest lasing wavelength achieved was ~1200 nm. The dependence of the lasing characteristics on W has been obtained. Figure 2 shows the characteristics of a laser with W=25 μm, which was defined by the selective wet oxidation of an $Al_{0.98}Ga_{0.02}As$ layer. The device has a threshold current of 245 mA and a threshold current density of 950 A/cm^2, with a lasing wavelength of ~1.16 μm.

[1] M. Kondow, et al., IEEE J. Quantum electronics, Vol. 3, pp.719-730, 1997.
[2] S. Sato, S. Satoh, Electron. Lett., Vol. 34, no. 15, pp. 1495-1497, 1998.
[3] N. Y. Li, C. P. Hains, K. Yang, and J. Cheng, submitted to Appl. Phys. Lett., 1999.

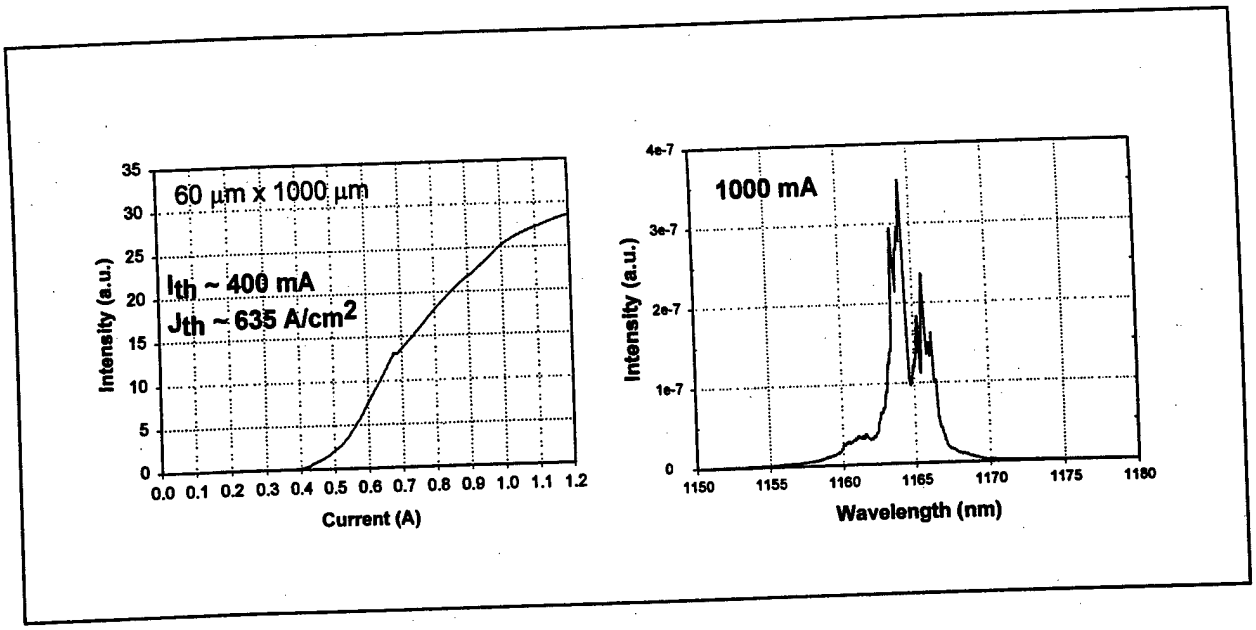


Figure 1. The pulsed lasing characteristic and lasing spectrum of a 3-QW GaInNAs/GaAs laser with W=60 μm at 300 K.

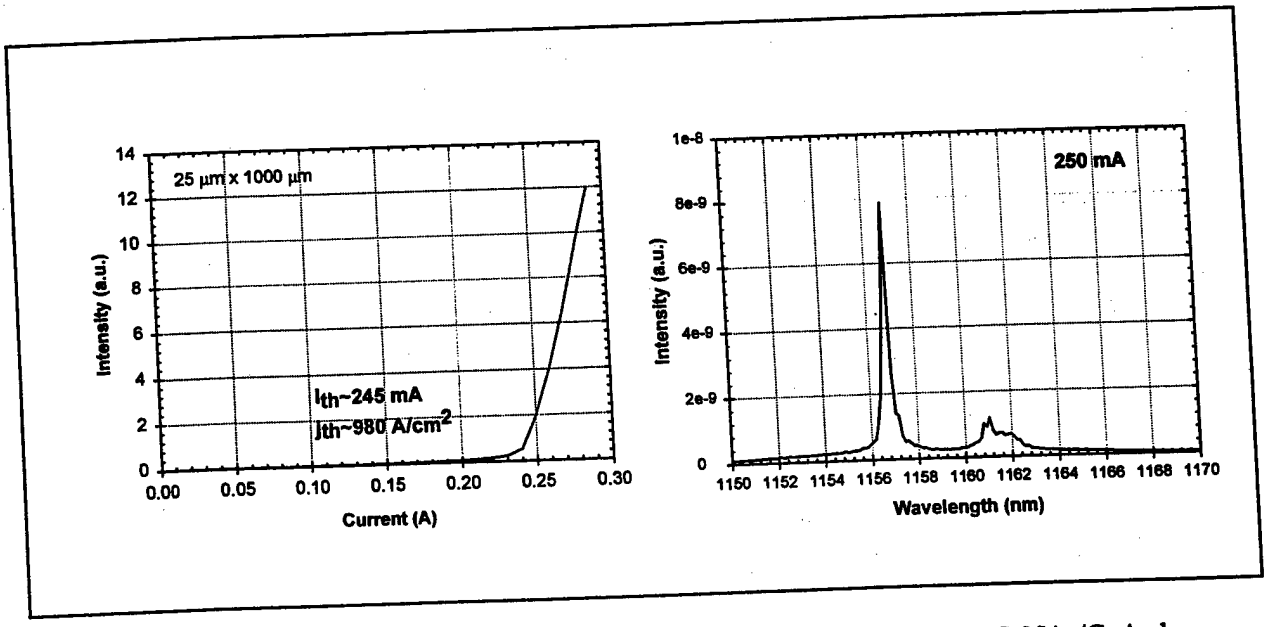


Figure 2. The pulsed light-vs-current characteristic and lasing spectrum of a 3-QW GaInNAs/GaAs laser at 300 K, with W = 25 μm defined by the selective lateral oxidation of an $Al_{0.98}Ga_{0.02}As$ layer.

Proceedings of the 1999 LEOS Annual Meeting, San Francisco, CA. November 9, 1999.

High-Speed Wavelength Division Multiplexing and Demultiplexing Using Monolithic Quasi-Planar VCSEL and Resonant Photodetector Arrays with Strained InGaAs/GaAs Quantum Wells

Yuxin Zhou, S. Q. Luong, and Julian Cheng
University of New Mexico, Center for High Technology Materials
Albuquerque, NM 87106

Monolithic arrays of multiple wavelength vertical-cavity surface-emitting lasers (VCSEL's) and resonance-enhanced photodetectors (REPD's) with matching wavelengths are useful for fiber-based *wavelength-division multiplexed* (WDM) optical interconnects, which achieve optical parallelism using a single fiber instead of a multiple fiber array. Multiple wavelength channels can be optically multiplexed together and transmitted through a single fiber, and then fanned out (broadcast) to different nodes, where they are demultiplexed (selected) using REPDs with different wavelength selectivity. Wavelength multiplexing and demultiplexing were previously demonstrated by the use of 850 nm VCSELs and REPDs [1], whose performance was limited in both modulation bandwidth (<125 Mb/s) and in the interchannel wavelength separation (~6 nm) that is needed to achieve a crosstalk rejection of greater than 10 dB. Greater modulation speed has been achieved by the use of monolithic, quasi-planar VCSEL and REPD arrays [2] operating at data rates approaching 1 Gb/s, while improved optical crosstalk isolation has been achieved using 920 nm VCSELs and REPDs containing strained InGaAs/GaAs quantum wells.

The REPDs are achieved by removing an appropriate number of DBR pairs from the upper mirror of the VCSEL to achieve an optimum trade-off between the spectral selectivity (spectral FWHM of the absorption band) and the peak absorption efficiency of the photodetector. The lower material absorption coefficient of the InGaAs quantum wells (~6000 cm^{-1}, vs 13,000 cm^{-1} for GaAs QWs) allows REPDs to be designed with a narrower wavelength selectivity (2.5 nm FWHM, vs 4.0 nm for GaAs) while retaining a high peak absorption efficiency (> 90%) as well as an optimal laser design. The narrower wavelength selectivity leads to a reduction of the optical crosstalk between channels, thus allowing more wavelength channels to be used within a given spectral band. The optical crosstalk between different wavelength channels, or equivalently the channel selectivity, has been characterized under large signal modulation conditions. Figure 1 shows the cw asing spectra of two VCSELs (upper trace) and the photoresponse spectra of two REPDs (lower trace) from a monolithic array whose center wavelengths (917.89 nm and 921.77 nm) are separated by 3.9 nm. The optical outputs of the VCSELs are modulated and multiplexed together by a fiber coupler, and then transmitted through a multi-mode fiber. The photocurrent response of the 28 μm diameter REPD used in the receiver shows an asymmetric spectrum with a FWHM of 2.5 nm, which reflects the asymmetry of the absorption spectrum of the quantum well photodetector. The dc optical crosstalk of the 917.89 nm and 921.77 nm REPDs were at -12.2dB and -8.4dB respectively.

In order to achieve a higher modulation speed, quasi-planar VCSEL and REPD arrays with co-planar contacts (fig. 2) were used to minimize the device parasitics by reducing the oxidation length [2]. Figure 3 shows the large signal optical modulation response of the 921.77 nm VCSEL and the corresponding REPD under zero dc bias. The VCSEL drive signal consists of 1 ns pulses with a 50 MHz repetition rate. The REPD shows a (10%-90%) rise time of ~100 ps, closely tracking that of the VCSEL. On the other hand, the fall time of the REPD is characterized by a long (850 ps) tail due to lateral carrier diffusion in the detector, which limits its large-signal modulation performance.

A WDM link was experimentally tested by combining the optical outputs of two VSCELs that are modulated by 500 Mbs RZ (return-to-zero) data into a multimode fiber and measuring the response of each REPD to the multiplexed signal. The modulated optical output of the VCSELs and the demultiplexed photoresponse of the corresponding REPDs are shown in Figure 3, which shows an optical crosstalk level of -10.4 dB and -8.2 dB for the 917.89 nm REPD and the 921.77 nm REPD, respectively. These values are slightly lower than those achieved under dc conditions due to the diffusion tail of the REPDs. Wavelength multiplexing and demultiplexing have thus been demonstrated at a data rate of >500 Mb/s using channels that are 4 nm apart.

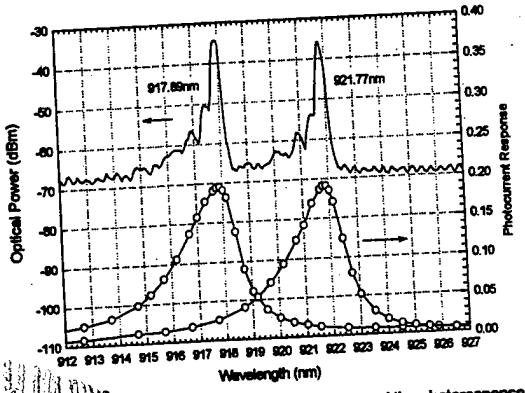


Figure 1. The optical spectra of two VCSELs (upper trace) and the photoresponse spectra of two corresponding REPD's (lower trace) with a ~4.0 nm wavelength separation.

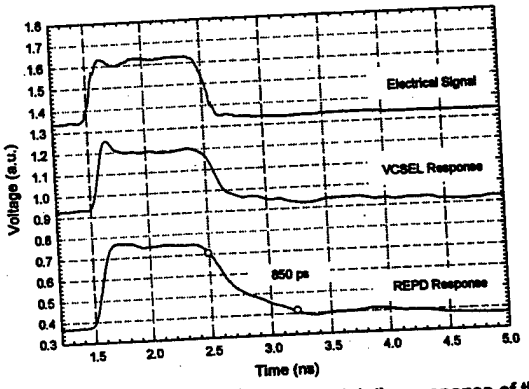


Fig. 3. The large-signal optical modulation response of the VCSEL and photocurrent response of an REPD with matched wavelength

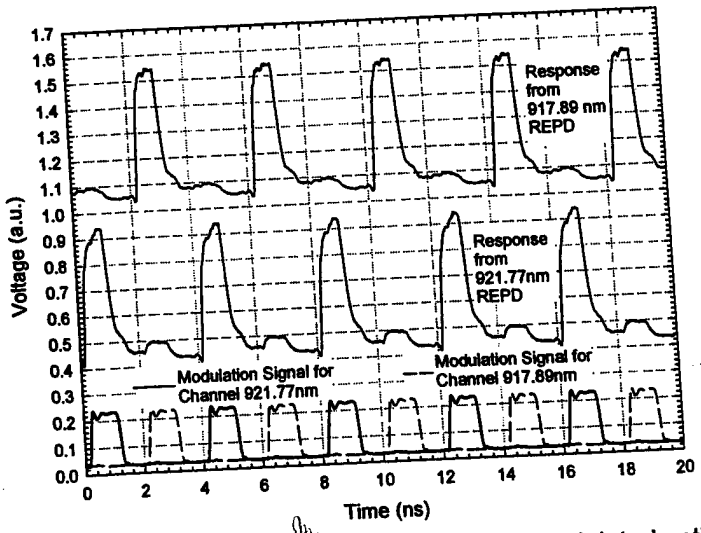


Fig. 4. Wavelength demultiplexing of high-speed modulated optical data channels (500 Mb/s RZ, 1 ns pulses) using REPD's with a resonance wavelength separation of $\Delta\lambda \sim 4$ nm.

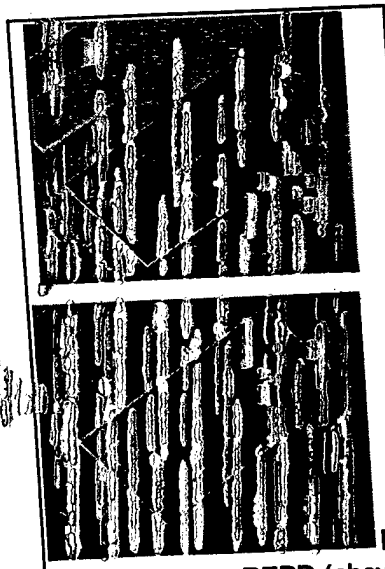


Fig. 2. Quasi-planar REPD (above) and VCSEL (below) device structure.

To be published in IEEE Photonics Technology Letters, Vol. 12, no. 2, Feb., 2000.

High-Speed Wavelength Division Multiplexing and Demultiplexing Using Monolithic Quasi-Planar VCSEL and Resonant Photodetector Arrays with Strained InGaAs Quantum Wells

Yuxin Zhou, and Julian Cheng, *Senior Member IEEE*

Abstract – **We demonstrate the high-speed (gigabit-per-sec) operation of a wavelength-division-multiplexed optical interconnect, which is implemented by multiplexing the optical data from a multiple wavelength vertical-cavity surface-emitting laser (VCSEL) array into a single optical fiber, and demultiplexing the composite data stream using an array of resonance-enhanced photodetectors (REPD) with matching resonance wavelengths. By using VCSELs and REPDs with a new quasi-planar oxide-confinement design for improved high speed performance, and using strained InGaAs/GaAs quantum wells to achieve a better trade-off between optical responsivity and wavelength selectivity, WDM operation has been demonstrated under 1 Gb/s data modulation, with an optical crosstalk rejection ratio of better than -10 dB for wavelength channels that are spaced ~4 nm apart.**

Wavelength-division multiplexing (WDM) can greatly increase the data throughput in a fiber-based optical interconnect by facilitating the transmission of parallel optical data channels across larger distance through a single optical fiber instead of a multi-fiber ribbon cable. Monolithic arrays of wavelength-graded vertical-cavity surface-emitting lasers (VCSEL's) and wavelength selective photodetectors are potentially useful for WDM applications in the local optical interconnect environment [1,2], where low cost is a critical determinant for their deployment. Many different wavelength channels from the VCSEL array can be multiplexed together on a single fiber and transmitted to different destination nodes, where individual data channels can be selected by using either a passive wavelength demultiplexer or a wavelength-selective resonance-enhanced photodectector (REPD).

We have previously demonstrated a fiber-based "broadcast and select" WDM interconnect technology using monolithic arrays of wavelength-graded VCSEL's and REPD's with matching wavelengths, which were fabricated using a common epilayer structure containing four GaAs quantum wells (QW) with lasing wavelengths in the 850 nm regime and using proton implantation for current confinement [3]. The wavelengths of each array were graded by using an MOCVD epitaxial growth technique that controllably varied the local growth rate of all the epilayers on a topographically patterned substrate in a non-material-selective manner [1], resulting in resonance structures whose wavelengths can be graded over a ~40 nm range. This first generation of wavelength-graded VCSEL and REPD arrays were used to demonstrate wavelength multiplexing and demultiplexing at a data rate of up to 125 Mb/s [3], which was limited by an inefficient non-planar design for monolithically integrating VCSELs with REPDs. An improved quasi-planar technology for integrating oxide-confined devices on the same susbtrate has been developed, which resulted in higher speed VCSELs (~12 GHz bandwidth) and REPDs (75 ps rise time) [4]. These improved devices can be used to achieve a high-speed optical WDM interconnect that can operate at a data rate of >1 Gb/s.

In addition to the smaller bandwidth, the use of GaAs QWs (with an absorption coefficient of $\alpha=1.3\times10^4$ cm^{-1}) in the earlier WDM link also led to a non-optimum trade-off between the optical responsivity (absorption efficiency) of the REPD and its wavelength discrimination ability (the spectral width of the photoresponse, ~4 nm), which led to significant variations in the responsivity across the wavelength grading range. The use of strained InGaAs/GaAs QWs with a lower material absorption coefficient ($\alpha\sim6.0\times10^3$ cm^{-1}) produces better optimized REPD arrays with an improved wavelength selectivity (~2 nm), higher absorption efficiency (>90%), as well as a more uniform responsivity over the wavelength grading range. A narrower spectral width results in greater wavelength selectivity and lower optical crosstalk between channels, while allowing more wavelength channels to be used within a given spectral band. Figure 1(a) shows the calculated absorption efficiency spectra for two REPDs centered at 850 nm and 980 nm, respectively, referenced to the normalized lasing spectrum of the VCSEL to which each REPD is wavelength matched. The 850 nm REPD structure contains four 10 nm thick GaAs/$Al_{0.2}Ga_{0.8}As$ quantum wells sandwiched between two distributed Bragg reflector (DBR) mirrors containing 9 and 38.5 pairs of $Al_{0.15}Ga_{0.85}As$-$Al_{0.92}Ga_{0.08}As$ quarter-wave layers, respectively. Assuming $\alpha=1.3\times10^4$ cm^{-1} for the GaAs

Manuscript received September xx, 1999. This work was supported by DARPA and AFOSR.
The authors are with the University of New, Mexico Center for High Technology Materials, 1313 Goddard SE, Albuquerque NM 87106.

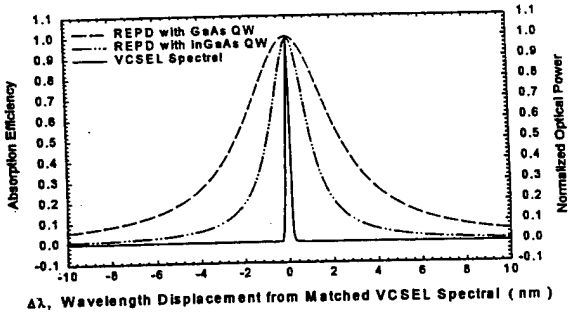


Fig. 1 (a)

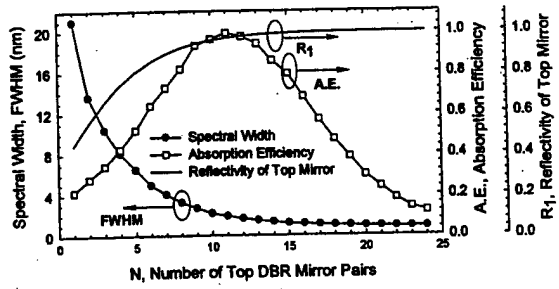


Fig. 1 (b)

Figure 1. (a) A comparison of the wavelength selectivity of REPD's containing GaAs quantum wells and strained InGaAs quantum wells using their calculated absorption efficiency spectra, each centered with respect to the lasing spectrum of a wavelength-matched VCSEL. (b) The dependence of the peak absorption efficiency and the spectral width (FWHM) of the photoresponse of a REPD on the number of DBR pairs and on the reflectivity of the upper mirror. The REPD contains 4 InGaAs quantum wells and was designed for operation at 920 nm.

QW's, the responsivity spectrum has a peak efficiency of ~100% and a full width at half maximum (FWHM) of ~4.7 nm. The 980 nm REPD contains four $In_{0.1}Ga_{0.8}As/Al_{0.1}Ga_{0.9}As$ QW's (8 nm thick) sandwiched between two DBR mirrors containing 11 and 38.5 pairs of $Al_{0.92}Ga_{0.08}As/Al_{0.1}Ga_{0.9}As$ quarter-wave layers, respectively. Assuming $\alpha=6.0\times10^3$ cm^{-1} for the InGaAs QW's, the responsivity spectrum has a peak efficiency of ~100% and a FWHM of ~2 nm. Thus, for two neighboring WDM channels with a fixed 4 nm wavelength spacing, the 980 nm REPD has a higher optical discrimination ratio (16.5:1) than the 850 nm REPD (3.8:1). Moreover, the 980 nm REPD permits a more optimum trade-off between peak absorption efficiency and wavelength selectivity as a result of its smaller material absorption coefficient. Figure 1(b) shows the dependence of the spectral width and the peak absorption efficiency of the 980 nm REPD photoresponse on the reflectivity R_1 of the upper DBR mirror (or equivalently, on the number N of upper DBR pairs), assuming that R_2=1 for the bottom mirror. A maximum absorption efficiency of ~1 is achieved with N=11, giving rise to a reflectivity of R_1 = 96.37% and a spectral FWHM of ~ 2 nm (compared to N=10 and FWHM=4 nm for the 850 nm REPD). A narrower spectral width can be achieved by increasing N and R_1, but only at the expense of a lower responsivity.

The VCSEL's and REPD's used in the WDM experiment both have oxide-confined active area apertures, and were monolithically integrated into quasi-planar arrays (figure 2 inset) using the etched trench (ET) approach to define the oxide apertures [4]. This approach reduces the total device area and minimizes the parasitic oxide capacitance to achieve an improved modulation response, while preserving the coplanar contact geometry without polyimide planarization. Another advantage of the etched trench technique is that more precise dimensional control of the oxide apertures can be obtained by reducing the oxidation length, which also minimizes the device parasitics. Individual ET VCSELs with a 6 μm active area have a small-signal modulation bandwidth of >10 GHz, while the large signal photoresponse of the REPD has a rise time of 65 ps.

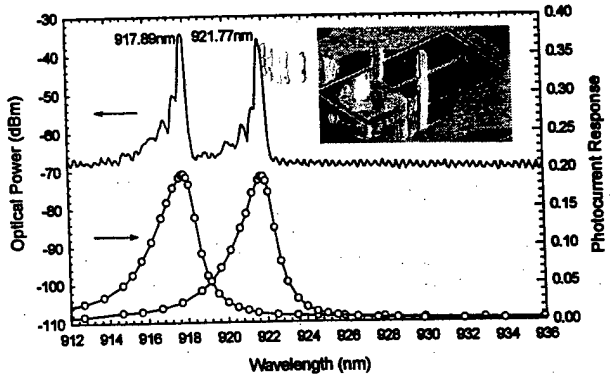


Figure 2. The composite lasing spectrum of two wavelength-multiplexed VCSEL channels with a 3.9 nm wavelength separation (upper trace), and the photoresponse spectra of two REPDs with matched resonance wavelengths (lower trace). Inset: shows SEM photomicrographs of a quasi-planar VCSEL (above) and REPD (below) fabricated using the etched-trench approach for oxide confinement.

To demonstrate wavelength multiplexing, the optical outputs of two VCSEL's from an array with a 3.9 nm wavelength separation were combined using a 3 dB fiber coupler and transmitted through a multimode fiber. In the dc measurement, two channels with center wavelengths at 917.9 nm and 921.8 nm were used. In fig. 2, the upper trace shows the cw lasing spectra of two VCSELs from an array with a 6 □m oxide aperture, while the lower trace shows the photoresponse spectra of two wavelength-matched REPD's from a neighboring array with a 28 □m diameter optical window. The dc response of each REPD shows an asymmetric photocurrent spectrum with a FWHM of 2.5 nm. The dc optical crosstalk from neighboring channels has been determined to be –12.2 dB and –8.4 dB for the 917.9 nm REPD and the 921.8 nm REPD, respectively. The difference is attributable to the asymmetry of their photoresponse spectra.

The optical crosstalk was also tested under large-signal data modulation conditions. The two VCSELs were biased slightly below threshold, and were simultaneously modulated using two temporally displaced and non-

overlapping 500 Mb/s RZ (return-to-zero) data patterns consisting of 1 ns wide pulses with a 1V peak-to-peak amplitude (which is equivalent to a 1 Gb/s NRZ data stream). The launched power for both channels were intentionally equalized to ~100 □W per channel. Their optical outputs were combined (wavelength multiplexed) and transmitted through a single optical fiber, and the response of each REPD to the multiplexed optical data stream is individually measured to demonstrate demultiplexing using a wavelength-selective photodetector. The photoresponse of each REPD was measured using a high-speed coplanar probe, which was followed by two cascaded dc-coupled amplifiers each with 18 dB gain and a bandwidth of 7 GHz. The lower time trace in fig. 3 shows the two temporally-displaced modulation signals of the VCSELs, while the two upper traces show the demultiplexed photoresponse of the two REPD's. The stronger and weaker pulses in each trace represent the amplitudes of the photoresponse of each REPD to the optical data at the resonant and nonresonant wavelengths, respectively. The latter represents the optical crosstalk level, which is –10.4 dB for the 917.9 nm REPD, and is –8.2 dB for 921.8 nm REPD. These values are slightly lower than those measured under dc conditions, which is due to the slower carrier diffusion tail in the temporal response of the REPD. The photoresponse of the REPD to optical modulation from a VCSEL with a matching wavelength shows a (10%-90%) rise time of ~100 ps, while the fall time of the REPD is characterized by a slower decay (850 ps) caused by lateral carrier diffusion in the photodetector, which can be improved by modifying the electrode's geometry.

A good eye diagram was also observed under large-signal data modulation. Each VCSEL was individually modulated by a NRZ pseudo-random data stream with a length of $(2^{23}-1)$ bits, and their optical outputs were multiplexed in a single fiber and transmitted to two REPDs. Each REPD was mounted in a high-speed package containing a transimpedance amplifier with a bandwidth of 1.25 GHz, followed by a limiting amplifier with a bandwidth of 1GHz. The inset of figure 3 shows a 1.25 Gb/s eye-diagram for the demultiplexed signal of the matched wavelength channel obtained under conditions for a bit error rate (BER) of $<10^{-11}$. High-speed wavelength demultiplexing has thus been achieved by this simple WDM link at a data rate of 1.25 Gb/s, which is limited by the speed of the receiver (including the REPD).

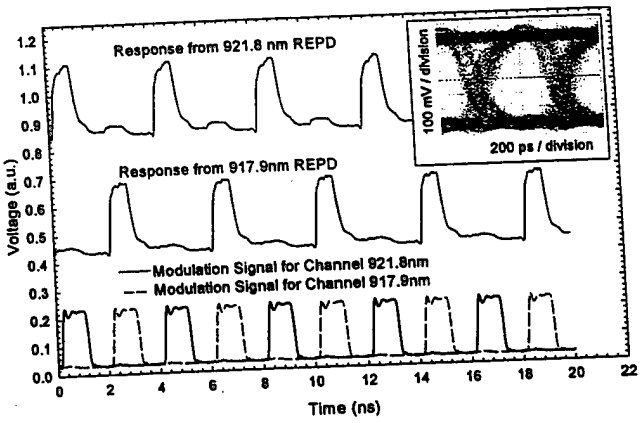


Figure 3. Demultiplexed signals (upper traces) from two wavelength-matched REPDs in response to high-speed modulation (500 Mb/s RZ, 1 ns pulses) from two wavelength-multiplexed data channels with a wavelength separation of □□ ~ 3.9 nm. Inset: The 1.25 Gb/s eye diagram measured by a REPD-based optical receiver in response to illumination by a multiplexed optical signal at a BER of $< 10^{-11}$.

In conclusion, we have demonstrated a simple WDM-based optical interconnect that uses wavelength-graded VCSEL and REPD arrays with matching wavelengths. Wavelength multiplexing and demultiplexing have been demonstrated at a data rate of 1.25Gb/s, with a crosstalk level of –10 dB between channels for a 4 nm wavelength spacing, and a BER performance of $<10^{-11}$. The data rate can be further improved to the OC-48 level by modifying the geometry of the REPD to reduce its diffusion-limited response and the RC parasitics.

REFERENCES:

[1]. G. G. Ortiz, S. Luong, Julian Cheng, H. Q. Hou, G. A. Vawter, and B. E. Hammons, "*Monolithic, multi-wavelength VCSEL arrays by surface-controlled MOCVD growth rate enhancement and reduction,*" IEEE Photon. Technol. Lett., Vol.9, pp.1069-1071, Aug. 1998.

[2]. S. Q. Luong, G. G. Ortiz, Y. Zhou, J. Lu, C. P. Hains, J. Cheng, H. Q. Hou, and G. A. Vawter, "*Monolithic wavelength-graded VCSEL and resonance-enhanced photodetectorfor parallel optical interconnects,*" IEEE Photon. Technol. Lett., Vol.9, pp.1069-1071, Aug. 1998.

[3]. J. J. Yoo, J. E. Leight, C. Kim, G. Giaretta, W. Yuen, A. E. Willner and C. J. Chang-Hasnain: "*Experimental Demonstration of a Multihop Shuffle Network Using WDM Multiple-Plane Optical Interconnection with VCSEL and MQW/DBR Detector Arrays*", IEEE Photon. Technol. Lett., Vol.10, No.10, pp.1507-1509, October 1998.

[4]. A. Alduino, Yuxin Zhou, S. Luong, C. P. Hains, and Julian Cheng, "*Wavelength multiplexing and demultiplexing using multiwavelength VCSEL and resonance-enhanced photodetector arrays,*" IEEE Photon. Technol. Lett., Vol.10, No.9, pp.1310-1312, September 1998.

[5]. A. C. Alduino, S. Luong, Yuxin. Zhou, C. P. Hains, and Julian Cheng, "*Quasi-planar monolithic integration of high-speed VCSEL and resonance enhanced photodetector arrays,*" IEEE Photon. Technol. Lett., Vol.11, No.5, pp.512-514, May 1999.

Room-Temperature Pulsed Operation of Triple-Quantum-Well GaInNAs Lasers Grown on Misoriented GaAs Substrates by MOCVD

C. P. Hains, *Member, IEEE,* N. Y. Li, *Member, IEEE,* K. Yang, *Student Member, IEEE,* X. D. Huang, *Student Member, IEEE,* and Julian Cheng, *Senior Member, IEEE*

***Abstract*— The lasing operation of three-quantum-well GaInNAs stripe geometry lasers grown by MOCVD on 0° and 6° misoriented (100) GaAs substrates, respectively, have been demonstrated and their performance is compared for the first time. Both devices achieved room temperature, pulsed lasing operation at an emission wavelength of 1.17 μm, with a threshold current density of 667 A/cm^2 for lasers grown on 6° misoriented substrates, and 1 kA/cm^2 for lasers grown on 0° misoriented substrates. The threshold for the lasers grown on 6° misoriented substrates compares favorably with the best results for GaInNAs lasers. Lasers with narrower stripe width and a planar geometry have also been demonstrated by the use of lateral selective wet oxidation for current confinement, with a threshold current density of 800 A/cm^2 for 25-μm-wide devices.**

***Index Terms*— GaInNAs, MOCVD, quantum-well laser, semiconductor laser.**

LONG-WAVELENGTH laser diodes emitting at 1.3 and 1.55 μm are key photonic components for optical fiber communication systems. Currently, these lasers are predominantly based on GaInAsP alloys grown on InP substrates, which have a higher temperature sensitivity (and a smaller characteristic temperature T_o) compared to shorter wavelength lasers that are grown on GaAs substrates. The high temperature sensitivity is primarily due to Auger recombination and the weak electron confinement resulting from the small conduction band offset in the GaInAsP–InP material system. GaInNAs alloys grown on GaAs substrates have been proposed as a possible alternative to the GaInAsP–InP system for achieving lasers with a higher characteristic temperature [1], [2]. Using a $Ga_{0.9}In_{0.1}N_{0.02}As_{0.98}$ active layer and $Al_{0.1}Ga_{0.9}As$ cladding layers that are grown on a GaAs substrate, a conduction band energy discontinuity as high as 570 meV can be achieved [3], leading to better electron confinement and better temperature characteristics. GaInNAs–GaAs lasers with a characteristic temperature of $T_o \sim 125$ K have been reported [1], [4].

Pulsed lasing of edge-emitting GaInNAs–GaAs quantum-well (QW) lasers has previously been achieved at 1.2 μm and at 1.31 μm at room temperature using material grown by gas source molecular beam epitaxy (MBE), with threshold currents as low as 888 A/cm^2 [5] and 6.74 kA/cm^2 [6], respectively. However, the progress in MOCVD-grown GaInNAs–GaAs material has lagged behind that of MBE until recently, and the best results to date have been achieved by a two-quantum-well laser (50-μm stripe width) that lased at a wavelength of 1.24 μm with a threshold current density of 660 A/cm^2 [7] and a single-quantum-well laser operating at 1.28 μm with a threshold current density of 800 A/cm^2 [8]. Room-temperature continuous-wave (CW) lasing operation in MOCVD grown material has not been achieved until recently, due to either a low optical gain or high internal loss. In order to improve upon the former, the effect of (a) increasing the number of quantum wells, and (b) epitaxial growth on misoriented substrates have been investigated in this work. Using MOCVD growth [9], the lasing operation of a three-quantum-well $Ga_{0.7}In_{0.3}N_{0.003}As_{0.997}$–GaAs edge-emitting laser has been achieved for the first time on (100) GaAs substrates that are misoriented by 0° or 6° toward [111]A. Pulsed lasing has been achieved at room temperature, with a wavelength of 1.17 μm and a threshold current density of 667 A/cm^2, which compares favorably against the benchmark (660 A/cm^2) set by MOCVD-grown GaInNAs lasers [7].

Test structures containing one, two, and three 7-nm-thick $Ga_{0.7}In_{0.3}N_{0.003}As_{0.997}$ quantum wells separated by 10-nm-thick GaAs barrier layers and capped with GaAs were grown on 0° substrates for comparison purposes. All samples exhibited good surface morphology, and photoluminescence measurements performed on these samples showed that the photoluminescence intensity varied linearly with the number of quantum wells. Based on these results, all laser structures were grown using a three-quantum-well active region.

Fig. 1 shows schematically the epilayer structure of the GaInNAs–GaAs MQW laser, which uses either a broad-area contact geometry consisting of 60-μm-wide p-contact stripes [Fig. 1(a)], or an oxide-confined planar geometry [Fig. 1(b)] that limits lateral current spreading and is potentially scaleable to very narrow stripe widths. The active region consists of three 7-nm-thick $Ga_{0.7}In_{0.3}N_{0.003}As_{0.997}$ quantum wells separated by 10-nm-thick GaAs barrier layers. The active region is bounded on either side by a 140-nm-thick undoped GaAs waveguide layer. These are in-turn bounded by p-doped and n-doped $Al_{0.3}Ga_{0.7}As$ cladding layers with thicknesses of 1.2 and 1.5 μm, respectively. The epilayer structure was grown on standard (100) n-type GaAs substrates as well as on (100) n-type GaAs substrates that are misoriented by 6°

Manuscript received April 19, 1999; revised July 9, 1999.

The authors are with the University of New Mexico, Center for High Technology Materials, Albuquerque, NM 87106 USA.

Publisher Item Identifier S 1041-1135(99)07754-X.

1041–1135/99$10.00 © 1999 IEEE

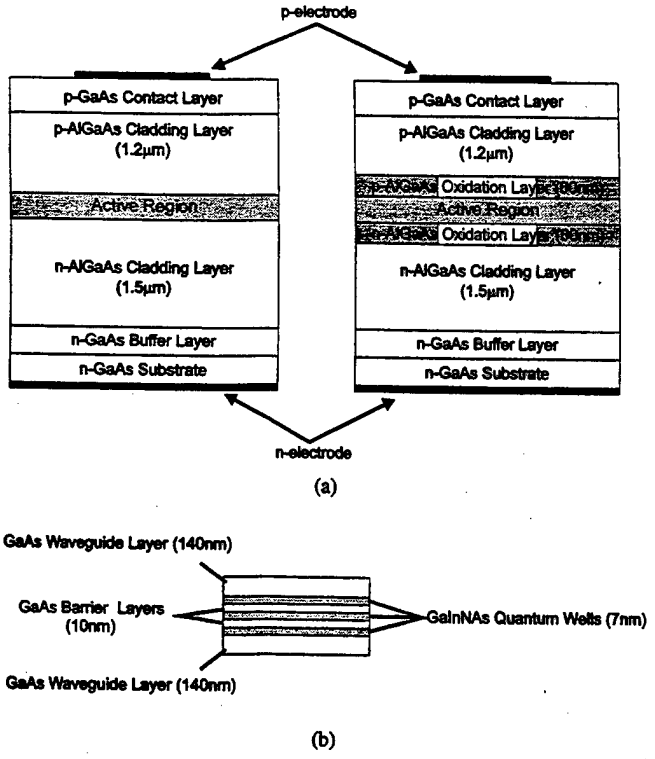


Fig. 1. Schematic diagram of GaInNAs laser diode (a) standard structure and (b) oxide-confined structure.

toward [111]A. The growth was performed by low pressure MOCVD using dimethylhydrazine (DMHy) as the nitrogen source, and diethyltellurium and carbon tetrachloride for the n-type and p-type doping, respectively. The n-doped GaAs buffer and AlGaAs cladding layers of this structure were grown at 725 °C, while the active and p-doped regions were grown at a reduced temperature of 535 °C to improve the nitrogen incorporation. The In and N compositions were determined using secondary ion mass spectroscopy and double-crystal X-ray diffraction measurements. The growth rate of the GaInNAs active layer and the GaAs cladding layers were 5.4 and 8 Å/s, respectively, and the ratio of [DMHy]/([DMHy]+[AsH_3]) was fixed at 0.6. To eliminate the deleterious Te memory effect [9] on the radiative efficiency of the GaInNAs–GaAs quantum wells, *in situ* cleaning the quartz reactor and graphite susceptor was carried out in a hydrogen chloride ambient at 830 °C prior to the regrowth of the GaAs waveguide, MQW active region, and the p-cladding layers.

The room-temperature photoluminescence (PL) spectra of the laser structures grown on the 0° and 6° substrates are shown in Fig. 2. The samples were pumped by a Ti:Sapphire laser emitting at 808 nm with a power varying from 100 to 550 mW. In each case, the peak PL intensity varies linearly with optical pump power within this range. Throughout the entire range of pump power, the laser structure grown on the 6°-off substrate shows a peak PL intensity that is between 1.4 and 2.0 times higher than that of the sample grown on the 0°-off substrate, indicating a substantial improvement in the optical properties of the material grown on the misoriented substrate. The ratio of their slope efficiencies is 1.28, which reflects the difference in their radiative efficiencies. A comparison of the 0°-off and 6°-off PL spectra for a pump power of 440 mW is shown in the inset of Fig. 2.

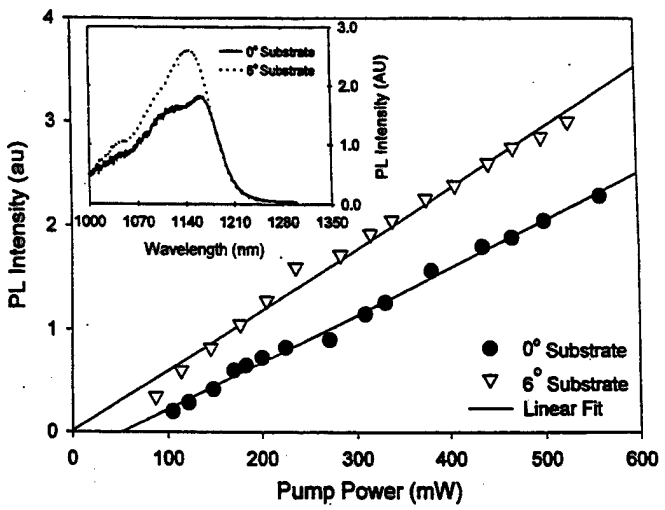


Fig. 2. Peak photoluminescence of GaInNAs laser structures grown on 0°-off and 6°-off GaAs substrates as a function of pump intensity. Inset shows photoluminescence spectra of both wafers at 440-mW pump power.

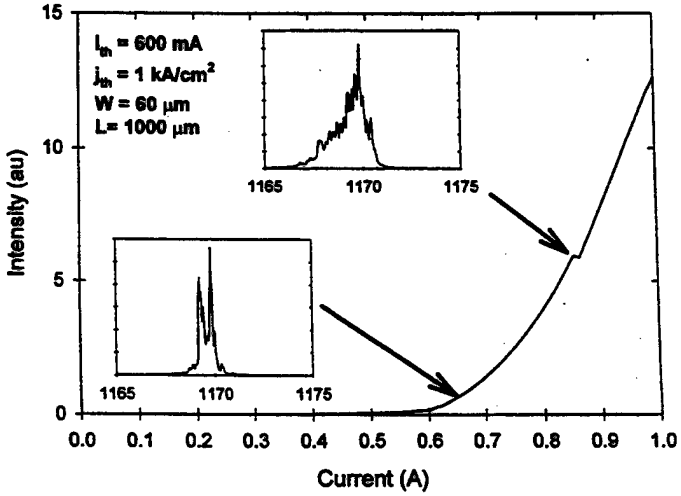


Fig. 3. *L–I* for lasers grown on a standard GaAs substrate, measured under pulsed operation (100 MHz, 3% duty cycle) at room temperature. Insets show lasing spectra at $I = 1.1 \times I_{th}$ and $I = 1.4I_{th}$.

The lasers of Fig. 1(a) were fabricated by patterning the Ti–Pt–Au metal stripes for the p-contact (~60 μm wide), followed by thinning the substrate to a thickness of ~100 μm and the deposition of the Au–Ge–Ni–Au n-contact on the substrate surface. The samples were then cleaved into 1000-μm-long bars and bonded onto copper heat sinks prior to device characterization.

The light output versus injected current (*L–I*) characteristics for the lasers that are grown on the 0° and 6° misoriented substrates are shown in Figs. 3 and 4, respectively. The devices were measured at room temperature using 300-ns pulses with a 10-μs period (3% duty cycle). The lasers grown on the 0°-off substrate show a lasing threshold current of I_{th} = 600 mA, corresponding to a nominal threshold current density of 1 kA/cm^2. Lasers grown on the 6°-off substrate show a threshold current of I_{th} = 420 mA, corresponding to a

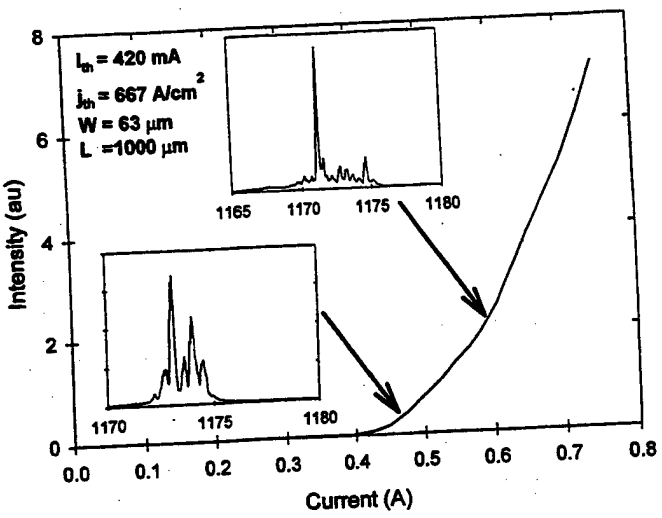


Fig. 4. L–I for lasers grown on a 6° misoriented substrate, measured under pulsed operation (100 MHz, 3% duty cycle) at room temperature. Insets show lasing spectra at $I = 1.1 \times I_{\text{th}}$ and $I = 1.4 I_{\text{th}}$.

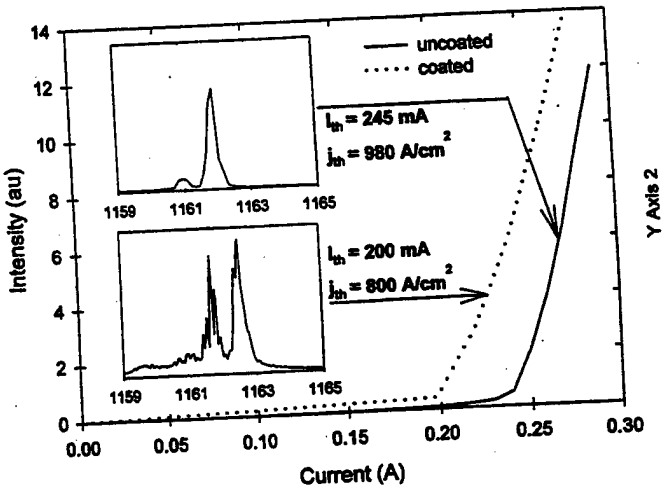


Fig. 5. L–I for oxide confined lasers grown on a 6° misoriented substrate with coated and uncoated facets, measured under pulsed operation (100 MHz, 3% duty cycle) at room temperature. Insets show lasing spectra at $I = 1.1 \times I_{\text{th}}$.

nominal threshold current density of 667 A/cm^2, which is 33% lower than that of lasers grown on the 0°-off substrate. The difference (33%) in their threshold current density is mainly attributed to the difference in their differential optical gain as manifested by the ratio of their radiative efficiencies (28%).

The lasing spectra for devices that are grown on a 0°-off substrate are shown in the insets of Fig. 3. The spectrum at a bias current of $1.1 \times I_{\text{th}}$ (inset 1) shows two narrow lasing modes, while the spectrum at a higher bias of $1.4 \times I_{\text{th}}$ (inset 2) shows that many lasing modes are excited. The lasing spectra for lasers that are grown on a 6°-off GaAs substrate, Fig. 4 (insets), show similar behavior as a function of drive current, and a slightly shorter emission wavelength.

In order to reduce the stripe width to much smaller dimensions while maintaining planarity and minimizing the effects of lateral current spreading, GaInNAs lasers have also been fabricated using the structure depicted in Fig. 1(b), which uses the selective lateral wet oxidation of two added $Al_{0.98}Ga_{0.02}As$ layers adjacent to the active layer [10] to confine the current to a smaller active area aperture. This technique is familiar to oxide-confined VCSEL technology and is readily scaleable to active area dimensions as small as 2 μm, while also providing weak index guiding. In Fig. 5, we illustrate this approach using a moderate aperture (stripe) width of 25 μm and a cavity length of 1 mm. A threshold current density of 980 A/cm^2 was achieved on devices grown on 6°-off GaAs substrates, compared to 667 A/cm^2 for the 60-μm-wide stripe geometry devices (Fig. 4). The threshold was reduced to 800 A/cm^2 by coating the facets with high reflectance dielectric mirrors with reflectivities of 1.0 and 0.9, respectively. The lasing spectra of the coated and uncoated devices at a bias current of $\sim 1.1 \times I_{\text{th}}$ are shown in the insets of Fig. 5 and show lasing at a nominal wavelength of 1162 nm.

In summary, lower threshold current and higher optical gain have been achieved by the growth of high-quality triple-quantum-well GaInNAs–GaAs lasers on misoriented GaAs substrates using MOCVD, with an emission wavelength of 1.17 μm and a threshold current density as low as 667 A/cm^2, which is comparable to the performance of the best documented devices. A significant improvement in the lasing characteristics of GaInNAs lasers has been achieved by the use of 6°-misoriented (100) GaAs substrates instead of the standard 0°-off (100) substrates. A planar oxide-confined laser structure with low threshold current (800 A/cm^2 for 25-μm stripes) was also demonstrated, which can be potentially scaleable to very small active stripe dimensions.

REFERENCES

[1] M. Kondow, T. Kitatani, S. Nakatsuka, M. C. Larson, K. Nakahara, Y. Yazawa, and M. Okai, "GaInNAs: A novel material for long-wavelength semiconductor lasers," *IEEE J. Select. Topics Quantum Electron.*, vol. 3, pp. 719–730, June 1997.

[2] S. Sato and S. Satoh, "Room-temperature pulsed operation of strained GaInNAs/GaAs double quantum well laser diode grown by metal organic chemical vapor deposition," *Electron. Lett.*, vol. 34, no. 15, pp. 1495–1497, 1998.

[3] M. Kondow, K. Uomi, A. Niwa, T. Kitatani, S. Watahiki, and Y. Yazawa, "GaInNAs: A novel material for long-wavelength-range laser diodes with excellent high-temperature performance," *Jpn. J. Appl. Phys.*, vol. 35, no. 2B, pp. 1273–1275, 1996.

[4] M. Kondow, S. Nakatsuka, T. Kitatani, Y. Yazawa, and M. Okai, "Room-temperature continuous wave operation of GaInNAs/GaAs laser diode," *Electron. Lett.*, vol. 32, no. 24, pp. 2244–2245, 1996.

[5] M. Kondow, S. Nakatsuka, T. Kitatani, Y. Yazawa, and M. Okai, "Room-temperature pulsed operation of GaInNAs laser diodes with excellent, high-temperature performance," *Jpn. J. Appl. Phys.*, vol. 35, no. 11, pp. 5711–5713, 1996.

[6] K. Nakahara, M. Kondow, T. Kitatani. M. C. Larson, and K. Uomi, "1.3-μm continuous-wave operation in GaInNAs quantum-well lasers," *IEEE Photon. Technol. Lett.*, vol. 10, pp. 487–488, Apr. 1998.

[7] S. Sato and S. Satoh, "Room temperature continuous wave operation of 1.24 μm GaInNAs lasers grown by metal organic chemical vapor deposition," *IEEE 16th Int. Semiconductor Laser Conf.*, Nara, Japan, 1998, postdeadline paper PD-5.

[8] F. Hohnsdorf, J. Koch, S. Leu, W. Stoltz, B. Borchert, and M. Druminski, "(GaN)(InAs)/GaAs single quantum well lasers for emission wavelengths in the range 1.28–1.38 μm," *Electron. Lett.*, vol. 35, no. 7, pp. 571–572, 1999.

[9] N. Y. Li, C. P. Hains, K. Yang, and J. Cheng, "Tellurium memory effects on OMVPE-grown $In_{0.3}Ga_{0.7}As_{0.997}N_{0.003}$/GaAs laser diodes," *Electronic Materials Conf.*, Santa Barbara, CA, 1999.

[10] J. Cheng, N. Y. Li, C. P. Hains, and K. Yang, "Multi-quantum well GaInNAs/GaAs lasers with low threshold current density grown by MOCVD," *IEEE Device Research Conf.*, Santa Barbara, CA, 1999.

Organometallic vapor phase epitaxy growth and optical characteristics of almost 1.2 μm GaInNAs three-quantum-well laser diodes

N. Y. Li,[a] C. P. Hains, K. Yang, J. Lu, and J. Cheng
Center for High Technology Materials, University of New Mexico, Albuquerque, New Mexico 87106

P. W. Li
Department of Electronic Engineering, I-Shou University, Kaohusing, Taiwan, Republic of China

(Received 29 March 1999; accepted for publication 28 June 1999)

We report organometallic vapor-phase epitaxy (OMVPE) growth and optical characteristics of 1.17–1.20 μm double-heterostructure laser diodes with three $Ga_{0.7}In_{0.3}N_{0.003}As_{0.997}$ (7 nm)/GaAs(10 nm) quantum wells (GaInNAs/GaAs QWs). Three GaInNAs/GaAs QWs were successfully grown by OMVPE using dimethylhydrazine as the N precursor. Strong room-temperature photoluminescence at the 1.17–1.19 μm regime with a full width at half maximum of 33 meV has been routinely achieved. By using three GaInNAs/GaAs QWs as the gain medium of the GaInNAs laser, room temperature operation with a threshold current density of 1.2 kA/cm^2 has been successfully demonstrated. © *1999 American Institute of Physics.* [S0003-6951(99)02834-X]

Recently, a semiconductor alloy, $Ga_{1-x}In_xN_yAs_{1-y}$, which can be lattice matched or strained to a GaAs substrate, has been extensively studied by molecular beam epitaxy (MBE)[1,2] and organometallic vapor phase epitaxy (OMVPE),[3–5] since a great potential has been shown to realize long-wavelength edge-emitting laser diodes and vertical-cavity surface-emitting laser diodes in the 1.1–1.3 μm regime with high-temperature performance for future low-cost and high-capacity optical data links. So far, there are many papers reported about epitaxial growth and material properties of GaNAs,[6,7] GaNP,[8,9] and GaInNAs.[10–12] However, reports on OMVPE growth of almost 1.2 μm GaInNAs laser diodes are very few. Sato and Satoh reported the room-temperature (RT) pulsed operation of 1.160 and 1.185 μm OMVPE-grown laser diodes by using a lattice-matched GaInNAs bulk active layer[4] and two strained GaInNAs/GaAs quantum wells (QWs),[5] respectively. However, the threshold current densities (J_{th}) of these two structures were relatively high and they were 9.9 and 3.4 kA/cm^2, respectively. Compared to GaInAs laser diodes, many studies reported that the J_{th} of GaInNAs laser diodes exhibited an increased tendency with increasing N concentration and lasing wavelength, ascribed to the inferior crystalline quality of GaInNAs.[10,11] To reduce the J_{th} of long-wavelength (>1.1 μm) GaInNAs laser diodes, a higher optical gain from QWs is highly desirable. In this letter, therefore, we present an attempt at improving the J_{th} of an OMVPE-grown GaInNAs laser diode by introducing three $Ga_{0.7}In_{0.3}N_{0.003}As_{0.997}$ (7 nm)/GaAs(10 nm) (GaInNAs/GaAs) QWs.

We investigate the OMVPE growth and characterizations of three GaInNAs/GaAs QWs, and apply them to the laser diode structure similar to that of Sato and Satoh.[4,5] Te memory effects on the optical properties of OMVPE-grown GaInNAs/GaAs QWs is briefly described. Optical characteristics of GaInNAs laser diodes using *in situ* hydrogen chloride (HCl) cleaning and OMVPE regrowth techniques are analyzed with a focus toward improving the J_{th}. We successfully demonstrate the RT pulsed operation of as-cleaved GaInNAs laser diodes with a J_{th} of 1.2 kA/cm^2, and it is the lowest value among the GaInNAs (Refs. 1–4) laser diodes reported to date.

GaInNAs three-quantum-well (TQW) laser diodes were grown in an IR-heated, horizontal flow, Thomas Swan OMVPE reactor, equipped with a gas foil rotation system for substrate rotation. The typical rotation speed of a 2 in. substrate was 60 rpm. Pd-diffused ultra-high purity H_2 was used as the ambient and carrier gas. Three undoped GaInNAs/GaAs QWs were grown at 535 °C and 60 Torr using trimethylindium, trimethylgallium, 100% arsine (AsH_3), and dimethylhydrazine (DMHy). For the GaInNAs TQW laser diode structures, diethyltellurium (75 ppm diluted in H_2) and carbontetrachloride (508 ppm diluted in H_2), were used as Te- and C-doping precursors, respectively. The total gas flow rate was 12 l/min, and the typical growth rates of GaInNAs and GaAs were 5.4 and 8.0 Å/s, respectively. The ratio of DMHy/(DMHy+AsH_3) was typically fixed at 0.6. The In and N composition were determined by secondary ion mass spectroscopy (SIMS) and high-resolution x-ray diffraction measurements. Photoluminescence (PL), ellipsometry, SIMS, and light–current (L–I) characteristics were analyzed to evaluate the optical qualities of GaInNAs laser diodes.

With the optimum growth condition of GaInNAs, a series of samples with different periods ($n=1-3$) of GaInNAs/GaAs QWs was investigated. The GaInNAs/GaAs QWs was grown on an N^+ (100) GaAs substrate. Initially, a 200-nm-thick GaAs buffer layer was grown at 725 °C, and then the growth temperature was decreased to 535 °C for GaInNAs/GaAs QWs and a GaAs cap layer (50 nm). A typical RT PL result of three GaInNAs/GaAs QWs is shown in Fig. 1. The PL wavelength for the three GaInNAs/GaAs QWs is observed at 1.186 μm with a full width at half maximum (FWHM) of 33 meV, indicating the quality of these QWs is excellent. The PL intensity as a function of the pe-

[a]Corresponding author. Current address: Emcore Corporation, Emcore PhotoVoltaics, 10420 Research Road, SE. Albuquerque, NM 87123. Electronic mail: nelson_li@emcore.com

 © 1999 American Institute of Physics

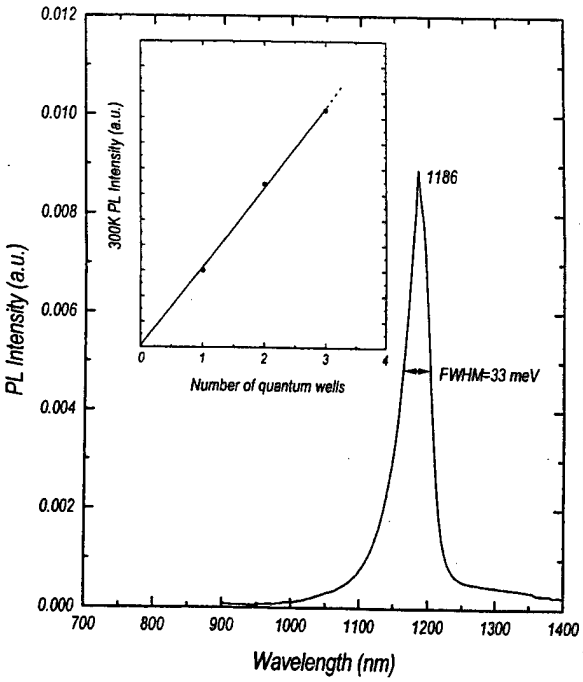


FIG. 1. Room-temperature PL spectrum of three $Ga_{0.7}In_{0.3}N_{0.003}As_{0.997}$/GaAs QWs. The inset shows PL intensity as a function of the number of $Ga_{0.7}In_{0.3}N_{0.003}As_{0.997}$/GaAs QWs.

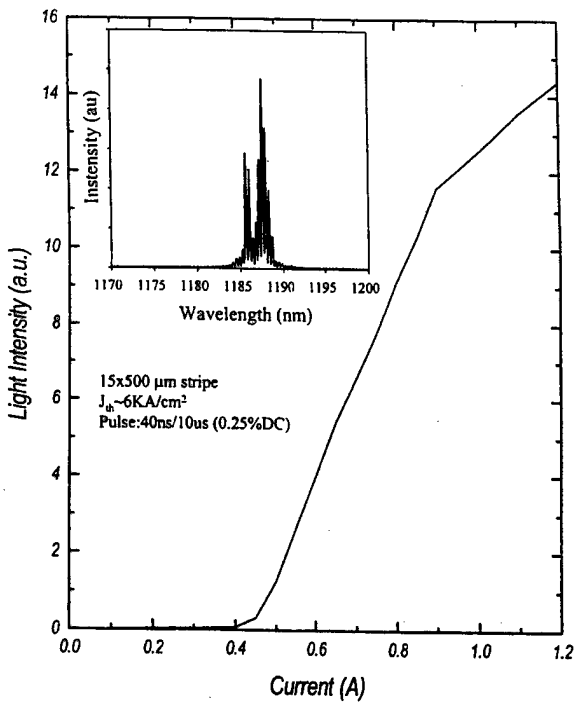


FIG. 3. Light output vs current characteristics and lasing spectrum of a GaInNAs TQW laser. The cavity length and stripe width are 500 and 15 μm, respectively.

riods of GaInNAs/GaAs QWs is shown in the inset of Fig. 1. It is apparently shown that the RT PL intensity increases linearly with increasing the periods of GaInNAs/GaAs QWs. This experimental result demonstrates that the J_{th} of GaInNAs laser diodes can be effectively reduced by introducing the three GaInNAs/GaAs QWs. The refractive index of strained $Ga_{0.7}In_{0.3}N_{0.003}As_{0.997}$ was measured to be 4.22 by ellipsometry and simulations.[13] The ellipsometric analysis of the three GaInNAs/GaAs QWs is based on the double-layer model developed by So.[14] The derived refractive index of strained GaInNAs is much larger than that of GaAs, AlGaAs, and InGaP, which enables GaInNAs to be favorable as the active region for long-wavelength (>1.1 μm) lasers.

Figure 2 illustrates the layer structure of a GaInNAs TQW laser diode grown on an N^+ GaAs substrate oriented 6° off (100) towards $\langle 111\rangle A$ in the following sequence: n-GaAs:Te buffer layer (200 nm, $n=2\times10^{18}\,cm^{-3}$), n-$Al_{0.3}Ga_{0.7}As$:Te lower cladding layer (1400 nm, $n=2\times10^{18}$ graded to $7\times10^{17}\,cm^{-3}$), undoped active region (350

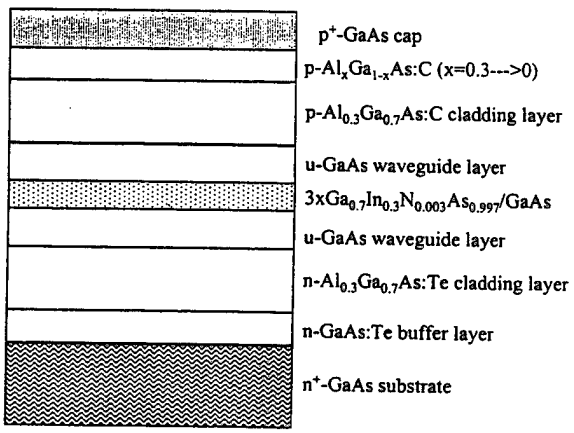


FIG. 2. Schematic structure of the GaInNAs TQW laser diode.

nm), p-$Al_{0.3}Ga_{0.7}As$:C upper cladding layer (1400 nm, $p=7\times10^{17}$ graded to $2\times10^{18}\,cm^{-3}$), p-$Al_xGa_{1-x}As$:C grading layer (100 nm, $x=0.3$–0, $p=2\times10^{18}$ graded to $1\times10^{19}\,cm^{-3}$), and p^+-GaAs:C contact layer (100 nm, $p=2\times10^{19}\,cm^{-3}$). The active region consists of three strained $Ga_{0.7}In_{0.3}N_{0.003}As_{0.997}$ (7 nm)/GaAs(10 nm) QWs sandwiched between two 140-nm-thick undoped GaAs waveguide layers.

The epitaxial layers described above were then processed into a ridge-waveguide structure with a cavity length of 500 μm and a stripe width varying from 2 to 15 μm. We found that the J_{th} decreased rapidly with increasing the stripe width, mainly due to reduced scattering loss around the ridge. The J_{th} was found to be saturated around 6 kA/cm^2 when the stripe width is approaching 15 μm. Figure 3 shows the light output power versus injected current characteristics of a GaInNAs TQW laser diode, labeled sample A, with a stripe width of 15 μm at RT under pulsed operation with 0.04 μs pulse, 0.25% duty cycle. The J_{th} is ~6 kA/cm^2. The lasing spectrum of the GaInNAs TQW laser is shown in the inset of Fig. 3. The threshold current is 450 mA corresponding to the J_{th} of ~6 kA/cm^2. The peak lasing wavelength is about 1.187 μm. So far, the longest lasing wavelength achieved in this study is 1.195 μm. Although significant scattering loss presents in the ridge-waveguide structure, the J_{th} of this GaInNAs TQW laser diode, however, is not as good as expected and can be elucidated from the following PL results.

A systematic PL study was investigated to explore the cause of high J_{th} in sample A. Figure 4 shows RT PL of GaInNAs/GaAs TQW laser diodes, samples A, B, and C, grown under different growth conditions. During the growth of sample A, a 5 min growth interruption was introduced after the growth of 1.4 μm n-$Al_{0.3}Ga_{0.7}As$:Te cladding layer to minimize the Te memory effects on the subsequent growth

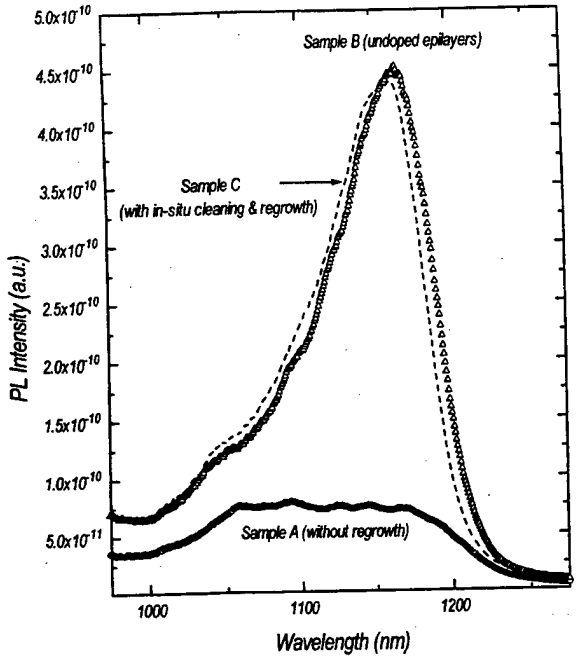


FIG. 4. Room-temperature PL spectra of GaInNAs TQWs, samples A, B, and C, grown under different growth conditions.

of waveguide layers and QWs. Sample B was nominally the same as sample A except all epilayers were intentionally undoped. As shown in Fig. 4, the PL intensity of sample A is very weak compared to sample B. SIMS results[15] show that $\sim 0.3-2\times10^{20}\,\mathrm{cm}^{-3}$ Te atoms exist in the QWs of sample A, possibly attributed to the desorption of DETe from the stainless tube walls, the quartz reactor walls, or the graphite susceptor during the low-temperature growth of QWs, since Te has a tendency to incorporate at lower growth temperatures.

To circumvent the Te memory effect, sample C was grown by using *in situ* cleaning and regrowth techniques. The growth was stopped after the deposition of a 20-nm-thick lower GaAs waveguide layer. The sample was then transferred into the N_2 ambient glovebox with a dew point lower than $-65\,^{\circ}\mathrm{C}$, corresponding to approximately 2.5 ppm H_2O in N_2. Finally, *in situ* cleaning quartz reactor and susceptor under HCl was carried out at 830 °C for 20 min, followed by the regrowth of undoped lower GaAs waveguide (120 nm), three GaInNAs/GaAs QWs, undoped upper GaAs waveguide (140 nm), upper p-AlGaAs cladding (1.4 μm), and p^+-GaAs cap (100 nm) layers. The PL intensity of sample C shows almost an order of magnitude higher than that of sample A, and is comparable to that of sample B, indicating the unintentional Te incorporation in the QWs was effectively eliminated.

Figure 5 shows the measured RT $L-I$ characteristics of a regrown GaInNAs TQW laser diode, sample C, under pulsed operations with a 0.3 μs pulse, 3% duty cycle. The stripe width and the cavity length were 63 and 1000 μm, respectively. The threshold current of sample C was about 750 mA, corresponding to a J_{th} of $1.2\,\mathrm{kA/cm}^2$. This is a low reported RT J_{th} for an as-cleaved OMVPE-grown

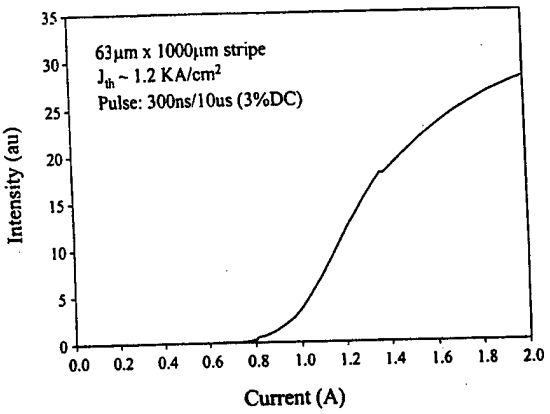


FIG. 5. Pulsed light output vs current characteristics of a GaInNAs TQW laser. The cavity length and stripe width are 1000 and 63 μm, respectively.

$Ga_{1-x}In_xN_yAs_{1-y}$ laser ($J_{th}\geqslant 3.4\,\mathrm{kA/cm}^2$) with an emitting wavelength longer than 1.15 μm. The characteristic temperature T_0, of the GaInNAs TQW laser diode was $\sim 127\,\mathrm{K}$, determined from the measurement of J_{th} from 0 to 50 °C. These data are very close to the Kondow *et al.* result.[1] More details on optical characteristics of these laser diodes will be reported elsewhere.[16]

In summary, the optical properties of OMVPE-grown $Ga_{0.7}In_{0.3}N_{0.003}As_{0.997}$ TQW laser diodes have been investigated. Significant amounts of Te ($0.3-2\times10^{20}\,\mathrm{cm}^{-3}$) were found in unintentionally doped GaInNAs/GaAs QWs, resulting in the poor optical properties of GaInNAs laser diodes. The longest lasing wavelength of GaInNAs laser achieved in this study is $\sim 1.2\,\mu$m. We have successfully improved the optical performance of GaInNAs laser diodes by using *in situ* HCl etching and OMVPE regrowth techniques to eliminate Te carryover in the QWs. Room-temperature pulsed operation of GaInNAs laser diodes with a J_{th} of $1.2\,\mathrm{kA/cm}^2$ and a T_0 of $\sim 127\,\mathrm{K}$ have been successfully demonstrated. These results are the best values reported for the 1.17–1.20 μm OMVPE-grown $Ga_{1-x}In_xN_yAs_{1-y}$ laser diodes with comparable device structures.

[1] M. Kondow, K. Uomi, A. Niwa, T. Kitatani, S. Watahiki, and Y. Yazawa, Jpn. J. Appl. Phys., Part 1 **35**, 1273 (1996).
[2] M. C. Larson, M. Kondow, T. Kitatani, K. Nakahara, K. Tamura, H. Inoue, and K. Uomi, IEEE Photonics Technol. Lett. **10**, 188 (1998).
[3] F. Höhnsdorf, J. Koch, C. Agert, and W. Stolz, J. Cryst. Growth **195**, 391 (1998).
[4] S. Sato and S. Satoh, Electron. Lett. **34**, 1495 (1998).
[5] S. Sato and S. Satoh, J. Cryst. Growth **192**, 381 (1998).
[6] M. Sato, J. Cryst. Growth **145**, 99 (1994).
[7] Y. Qiu, C. Jin, S. Francoeur, S. A. Nikishin, and H. Temkin, Appl. Phys. Lett. **72**, 1999 (1998).
[8] W. G. Bi and C. W. Tu, Appl. Phys. Lett. **70**, 1608 (1997).
[9] N. Y. Li, W. S. Wong, D. H. Tomich, K. L. Kavanagh, and C. W. Tu, J. Vac. Sci. Technol. B **14**, 2952 (1996).
[10] M. Kondow, K. Nakahara, T. Kitatani, M. Larson, and K. Uomi, presented at CLEO 1998, Paper No. CWL5.
[11] K. Nakahara, M. Kondow, T. Kitatani, M. C. Larson, and K. Uomi, IEEE Photonics Technol. Lett. **10**, 487 (1998).
[12] H. P. Xin and C. W. Tu, Appl. Phys. Lett. **72**, 2442 (1998).
[13] P. W. Li, N. Y. Li, and J. Cheng (unpublished).
[14] S. So, Surf. Sci. **56**, 97 (1976).
[15] N. Y. Li, C. P. Hains, K. Yang, P. W. Li, and J. C. Cheng (unpublished).
[16] J. C. Cheng, N. Y. Li, C. P. Hains, and K. Yang, IEEE Photonics Technol. Lett. (to be published).

Proceedings of the 1999 LEOS Annual Meeting, San Francisco, CA. *November 10, 1999.*

Near Room Temperature CW Lasing Operation of a Narrow-Stripe Oxide-Confined GaInNAs/GaAs Multi-Quantum Well Laser Grown by MOCVD

Kai Yang, C. P. Hains, N.Y. Li, and Julian Cheng

University of New Mexico

Center for High Technology Materials

1313 Goddard SE

Albuquerque, NM 87106

Phone: (505) 272-7934 kyang@chtm.unm.edu

ABSTRACT

The pulsed (J_{th} =1.0 kA/cm^2 at 23 °C) and cw (J_{th}=1.7 kA/cm^2 at 9 °C) lasing operation (λ=1.17 μm) of an 8 μm-wide oxide-confined stripe-geometry GaInNAs/GaAs MQW laser grown by MOCVD on a 6°-misoriented GaAs substrate are demonstrated.

Proceedings of the 1999 LEOS Annual Meeting, San Francisco, CA. *November 10, 1999.*

Near Room Temperature CW Lasing Operation of a Narrow-Stripe Oxide-Confined GaInNAs/GaAs Multi-Quantum Well Laser Grown by MOCVD

Kai Yang, C. P. Hains, N.Y. Li, and Julian Cheng
University of New Mexico, Center for High Technology Materials
1313 Goddard SE, Albuquerque, NM 87106

The GaInNAs/GaAs material system represents a promising single-epitaxial-growth approach for achieving long wavelength (1.3 μm) surface-emitting and edge-emitting lasers with a high characteristic temperature T_o on a conventional GaAs substrate. The performance of MOCVD-grown GaInNAs/GaAs quantum well (QW) lasers has lagged behind that of MBE-grown lasers until recently, when pulsed lasing operation was achieved at 1.28 μm by a single-QW laser with a threshold current density of J_{th} = 800 A/cm^2 [1], and at 1.17 μm by a 3QW laser with a current density of 667 A/cm^2 [2], while cw lasing was achieved at 1.24 μm by a two-QW laser with a J_{th} = 660 A/cm^2 [3] using broad-area lasers with a large stripe width (~100 μm). In order to reduce the width to smaller and more practical dimensions, while maintaining planarity and minimizing the effects of lateral current spreading, GaInNAs lasers have been fabricated using the lateral wet oxidation of two $Al_{0.98}Ga_{0.02}As$ layers adjacent to the active layer to confine the current to a smaller active area aperture (Fig. 1). This technique is readily scalable to active area dimensions as small as 2 μm. In order to improve upon the gain, the effect of (a) increasing the number of quantum wells (3QW), and (b) epitaxial growth on misoriented substrates (6°-off towards [111]A) have also been investigated. The pulsed and cw lasing operation of a 3QW $Ga_{0.7}In_{0.3}N_{0.003}As_{0.997}$/GaAs edge-emitting laser (λ=1.17 μm) have been achieved near room temperature for the first time using an oxide-confined laser design (Fig. 1), with the low threshold current densities of 1.0 kA/cm^2 and 1.7 kA/cm^2 (at 9 °C), respectively, for a narrow stripe width (8 μm). The active region consists of three 7 nm thick $Ga_{0.7}In_{0.3}N_{0.003}As_{0.997}$ quantum wells separated 10 nm thick GaAs barrier layers, and is bounded on either side by a 140 nm thick undoped GaAs waveguide layer. These are in-turn bounded by p-doped and n-doped $Al_{0.3}Ga_{0.7}As$ cladding layers, respectively, and a thin $Al_{0.98}Ga_{0.02}As$ selective oxidation layer was added at each GaAs/AlGaAs heterointerface. The epilayer structure was grown by MOCVD on n-type (100) GaAs substrates that are misoriented by 6° towards [111]A, which have demonstrated superior photoluminescence compared to structures grown on 0°-off substrates.

The pulsed lasing characteristics (for pulses of varying width, 3-5% duty cycle) of a GaInNAs laser (1 mm cavity length) at 300 K are shown in Fig. 2, which shows a threshold current of I_{th} = 82 mA and J_{th}=1.02 kA/cm^2 for the shortest (300 ns) pulses. The lasing spectrum is single mode to $I=1.2\times I_{th}$, with a side mode suppresion ratio (SMSR) of >20 dB. Figure 2 also shows the lasing characteristics for pulses of much longer duration (up to 1 ms), which incorporate the effects of thermal self-heating, with the longer pulses approximating quasi-cw lasing. For the 1 ms pulses, the threshold current is 105 mA, with J_{th} = 1.3 kA/cm^2.

True cw lasing characteristics have been obtained at temperatures as high as 10 °C, and are plotted in Figure 3 for several temperatures. The cw threshold current I_{th} is 98 mA (J_{th}=1.2 kA/cm^2) at 0 °C, and is 138 mA (J_{th}=1.7 kA/cm^2) at 9 °C. These are the lowest threshold current

densities achieved by a MOCVD-grown GaInNAs laser with a stripe width below 10 μm. The devices show good dc electrical characteristics, with a turn-on voltage of 1.35 and a very low series resistance (2-4 Ω). The threshold voltage V_{th} is 1.6V under short pulse operation, and is ~2V under cw operation at 6 °C.

[1]. F. Hohnsdorf, J. Koch, S. Leu, W. Stoltz, *et al.,*: Electron. Lett., vol. 35, pp. 571-572, 1999.
[2]. J, Cheng, N.Y. Li, C. P. Hains, K. Yang, Device Research Conference, June 1999.
[3]. S. Sato and S. Satoh, IEEE 16th Int. Semiconductor Laser Conf., PD-5, Nara, Japan, 1998.

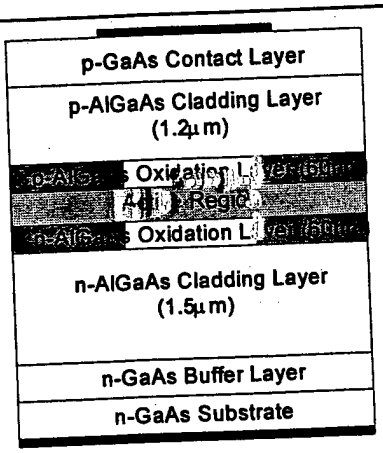


Figure 1. Schematic epilayer structure and device design of an oxide-confined GaInNAs laser.

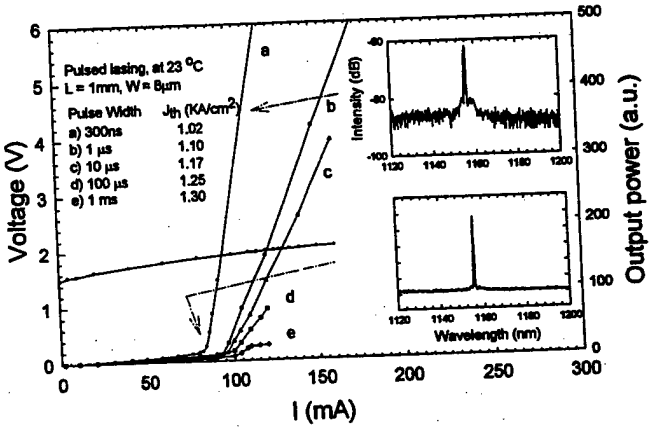


Fig. 2. The electrical and pulsed lasing characteristics at 300 K for pulses of different widths (300 ns to 1 ms) and a duty factor of 3%-5%. The insets show the lasing spectra for 300 ns pulses under different bias conditions.

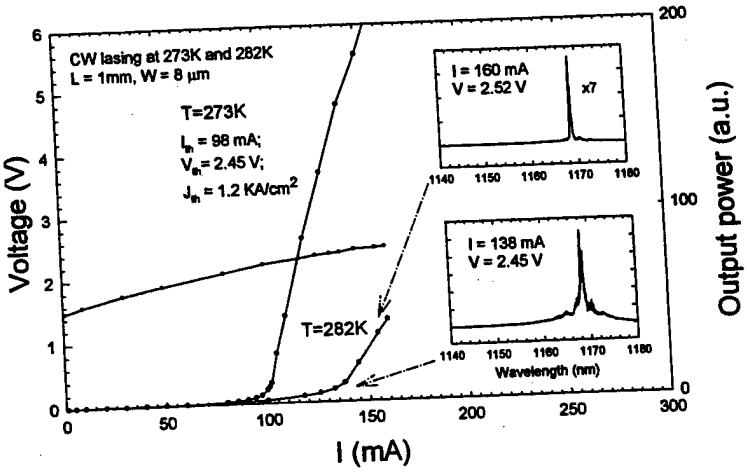


Fig.3 The dc electrical and cw lasing characteristics of The oxide-confined GaInNAs laser at temperatures from 0 °C to 9 °C. Insets show the cw lasing spectra at 9 °C under different bias conditions.

To be published in IEEE Photonics Technology Letters, Vol. 12, no. 2, 2000.

Efficient Continuous-Wave Lasing Operation of a Narrow-Stripe Oxide-Confined GaInNAs/GaAs Multi-Quantum Well Laser Grown by MOCVD

Kai Yang, C.P. Hains, and Julian Cheng

Abstract: **Efficient cw lasing operation has been achieved above room temperature by a triple-quantum well GaInNAs/GaAs laser diode grown on a 6°-misoriented GaAs substrate by MOCVD. Using a planar, oxide-confined, narrow-stripe (8 μm) laser geometry, continuous-wave lasing operation was achieved over a wide range of temperatures up to 57 °C. At room temperature, lasing occurs at a wavelength of 1.16 μm, with a high single-facet slope efficiency of 25% and a threshold current density of 1.3 kA/cm^2.**

The GaInNAs/GaAs material system represents a promising single-epitaxial-growth approach for achieving long wavelength (1.3 μm) vertical-cavity surface-emitting lasers (VCSEL's) on a conventional GaAs substrate [1], as well as edge-emitting lasers with a high characteristic temperature T_o. The growth of GaInNAs quantum wells on GaAs substrates can take advantage of the larger refractive index difference of AlGaAs/AlAs-based distributed Bragg reflector (DBR) mirrors to grow VCSELs with a more tractable total thickness, which is a distinct advantage over the use of InP-based DBR structures. Compared to the long wavelength laser diodes based on GaInAsP alloys, the GaInNAs/AlGaAs-based laser structures can provide better electron confinement, giving rise to a larger T_o and reduced temperature sensitivity for the laser [1-4]. The value of T_o has previously been determined to be ~125 K, which was obtained mostly under pulsed lasing operation. The lowest threshold current density for pulsed lasing operation was achieved at 1.28 μm by a single-quantum well (SQW) laser with a threshold current density of J_{th} = 800 A/cm^2 [5], and at 1.17 μm by a 3QW laser with a current density of 667 A/cm^2 [6]. Until recently, cw lasing for GaInNAs lasers has only been achieved at room temperature by a SQW, 1.3 μm laser grown by MBE [7], with J_{th}= 6.3 kA/cm^2, and by a two-QW, 1.3 μm ridge waveguide laser grown by MOCVD [8], the latter with J_{th}= 1.2 kA/cm^2. In order to achieve efficient cw lasing operation over a wide range of temperatures above room temperature, the operating current must be reduced by decreasing the width of the active region to much smaller dimensions. A simple means for achieving this while maintaining planarity and minimizing the effects of lateral current spreading is to confine the current to a small active area aperture by using the lateral wet oxidation of one or more $Al_{0.98}Ga_{0.02}As$ layers that are adjacent to the active layer [10,11]. This technique is readily scaleable to active area dimensions as small as 2 μm.

In this letter, the room-temperature cw lasing operation of a 3QW GaInNAs edge-emitting laser has been achieved for the first time using a lateral oxide-confinement design. The cw lasing operation was achieved over a wide range of temperatures (up to 57°C), with reasonably low threshold current density (0.98 kA/cm^2 at 0 °C, and 1.3 kA/cm^2 at 23 °C), high slope efficiency (28.5 % per facet at 0°C, 25 % at 23 °C) for devices with a narrow stripe width (8 μm). CW lasing occurs at room temperature with an emission wavelength of ~1.16 μm, a threshold current of 76 mA (J_{th} = 1.3 kA/cm^2), and a high single-facet slope efficiency of 25%.

The active region of the laser diode consists of three 7 nm thick $Ga_{0.7}In_{0.3}N_{0.003}As_{0.997}$ quantum wells separated by 10 nm thick GaAs barrier layers, and is bounded on either side by a 140 nm thick undoped GaAs waveguide layer. These are in-turn bounded by p-doped and n-doped $Al_{0.3}Ga_{0.7}As$ cladding layers with a thickness of 1.2 μm and 1.5 μm, respectively, and a thin $Al_{0.98}Ga_{0.02}As$ selective oxidation layer was added at each GaAs/AlGaAs heterointerface. The epilayer structure was grown by MOCVD on n-type (100) GaAs substrates that are misoriented by 6° towards [111]A, which have demonstrated superior photoluminescence (~30% higher radiative efficiency) compared to structures grown on 0°-off substrates [6]. The growth was performed by low pressure MOCVD using dimethylhydrazine (DMHy) as the nitrogen source, and the growth conditions have been described elsewhere [6].

The lasers were fabricated by first patterning and depositing the Ti/Pt/Au p-contact metal stripes (65 μm wide), then dry etching 91μm-wide mesas down to the substrate, and using selective lateral wet oxidation of the two $Al_{0.98}Ga_{0.02}As$ layers adjacent to the active region to define oxide layers that effectively confine the current to a small active area aperture

Manuscript received Sept. xx, 1999; revised Soct. Xx, 1999.
The authors are with the University of New Mexico, Center for High Technology Materials, 1313 Goddard SE, Albuquerque, NM 87106. This work was supported in part by the DARPAOptolectronics Materials Center at UNM, and by BMDO.

(8 μm wide). The substrate was then thinned to a thickness of ~120 μm, and AuGe/Ni/Au n-contact metal was deposited on the back substrate surface. The samples were cleaved into bars 720 μm in length and were bonded onto copper heat sinks prior to device characterization.

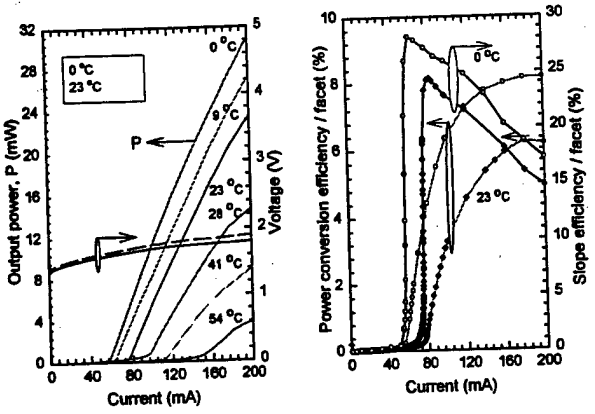


Figure 1. a) CW output power and voltage versus current for a narrow-stripe oxide-confined laser diode (L = 720 μm, W = 8 μm) at various temperatures. b) Single facet power conversion efficiency and slope efficiency for the same laser diode at 0 °C and 23 °C.

The electrical and cw lasing characteristics of a narrow-stripe oxide-confined GaInNAs laser (L = 720 μm long, W = 8 μm wide) at temperatures ranging from 0°C to 54 °C are shown in Fig. 1. The characteristics at room temperature show a threshold current of 76 mA (J_{th} = 1.3 kA/cm^2), a threshold voltage of 1.70 V, a single-facet slope efficiency of 25% and a single-facet power conversion efficiency of 6.3%, and an output power of 23 mW at a bias current of 200 mA. The corresponding parameters for 0 °C operation are 57 mA (J_{th} = 0.98 kA/cm^2), 1.66 V, 28.5%, 8.1%, and 31 mW, respectively. The threshold current increases with temperature, and cw lasing is observed over a wide temperature range up to 57 °C. The device also shows good dc electrical characteristics, with a turn-on voltage of 1.35 V and a very low series resistance of 2 Ω. The operating voltage of the laser diode remains less than 2 V for drive currents up to 200 mA throughout the entire temperature range from 0 °C to 54 °C. Figure 2 plots the inverse external slope efficiency (for both facets) as a function of the cavity length for a number of different GaInNAs lasers under cw lasing operation. From the slope and the y-axis intercept, the internal optical loss (α_I=4.2 cm^{-1}) and internal quantum efficiency (η_I=0.64) have been calculated. Excellent electrical and cw lasing performance has thus been achieved for the first time by a MOCVD-grown GaInNAs laser with an oxide-confined stripe width below 10 μm, with low threshold current density, low operating voltage, high differential slope efficiency and power conversion efficiency, and a wide temperature range for cw lasing operation.

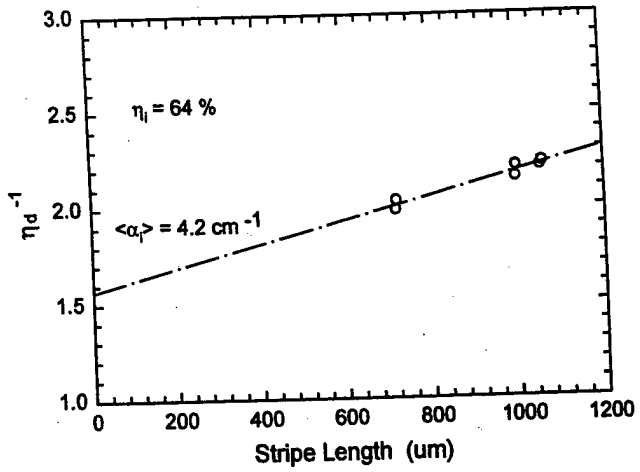


Figure 2. The inverse external slope efficiency of a GaInNAs laser (both facets) as a function of the cavity length at room temperature. From the slope and y-intercept, the optical loss (α_I=4.2 cm^{-1}) and internal quantum efficiency (η_I=0.64) have been calculated.

Figure 3 shows the room temperature cw lasing spectra of the GaInNAs MQW laser under different bias currents. The lasing spectrum is single mode at bias currents up to I=1.2×I_{th}, with a side mode suppression ratio (SMSR) of ~20 dB. The peak emission wavelength of the laser diode is 1.154 μm near threshold, and shifts to a longer wavelength with increasing drive current. At bias currents above 90 mA, two or more lasing modes occur. These represent different transverse modes with a wavelength spacing of ~2 nm, which is consistent with the transverse dimension of the cavity that is defined by the etched mesa (91 μm).

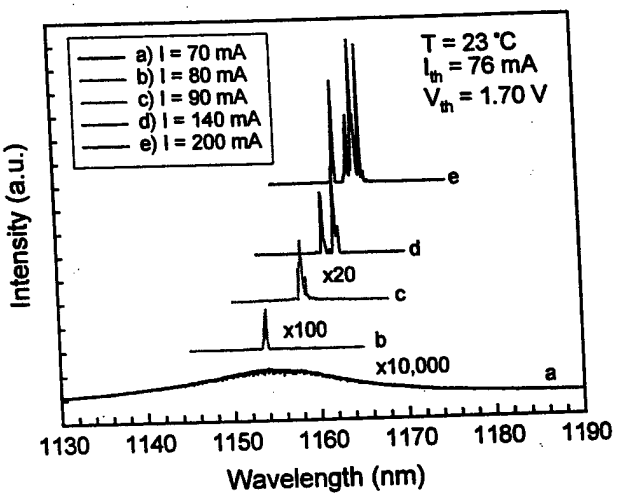


Figure 3. Emission spectra of the GaInNAs/GaAs MQW laser diode under cw operation at room temperature with different drive currents.

Finally, the temperature dependence of the lasing characteristics has been studied. Figure 3 plots the logarithm of the threshold current I_{th} for both pulsed and cw lasing as a function of the substrate temperature T_s, from which the characteristic temperature T_o is determined according to the relation: $I_{th} = I_o \exp(T_s/T_o)$. For pulsed lasing operation, the fit is linear and yields a T_o of 125 K. However for cw operation the fit is nonlinear, giving a value of T_o that varies from ~85 K at lower temperatures to ~56 K at higher temperatures. It can be shown that most of this non-linearity is due to thermal self-heating, which raises the junction temperature T_j substantially above the measured ambient temperature T_s. The rise in junction temperature ($\Delta T_j = T_j - T_s$) is governed by $\Delta T_j = R_{th} \times P_d$, where R_{th} is the thermal resistance and P_d is the measured power dissipation. The value of R_{th} (420 K/W) is obtained by measuring the shift in emission wavelength $\Delta\lambda$ with increasing power dissipation P_d (*i.e.*, by increasing the bias current), and relating ΔT_j to $\Delta\lambda$ using the known temperature dependence of the bandgap wavelength ($d\lambda/dT$~0.48 nm/K [1]), which is corroborated by the measured temperature dependence of the lasing wavelength for this device near threshold ($d\lambda/dT$~0.5 nm/K). After calculating the internal junction temperature T_j at threshold, log (I_{th}) is replotted as a function of T_j in Fig. 4, which shows a good linear fit over the entire range of temperature from 0°C to 54°C. From this fit, the characteristic temperature (T_o) is calculated to be 128 K, which is in close agreement with the value (125 K) derived from the pulsed lasing measurements. This shows that the reduction of T_o for cw lasing is primarily due to thermal self heating caused by a relatively high thermal resistance, which can be substantially reduced using better packaging to achieve a T_o that is closer to its intrinsic value f 125 K for an improved high temperature performance.

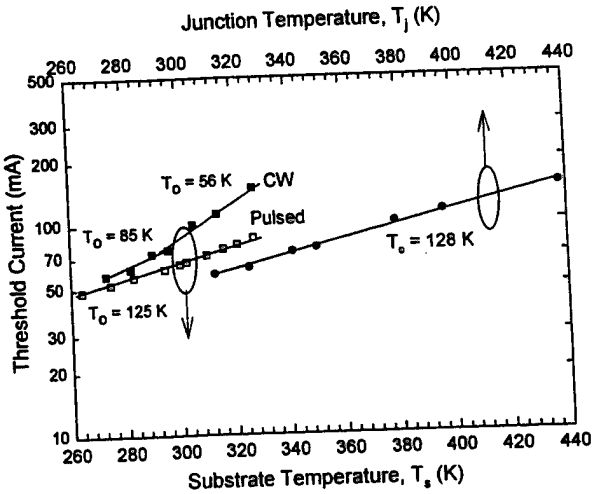


Figure 4. Temperature dependence of threshold current for the GaInNAs/GaAs MQW laser under cw and pulsed operations.

In conclusion, we have experimentally demonstrated, for the first time, the efficient cw lasing operation of a MOCVD-grown, narrow-stripe, oxide-confined MQW GaInNAs laser diode (L = 720 μm, W = 8 μm) at temperatures up to 57 °C (thermal cut-off). Excellent cw device performance was achieved, including a low threshold current density (1.3 kA/cm^2), low operating voltage (<1.7V), high differential slope efficiency (~50% for both facets at 23 °C) and power conversion efficiency (13% for both facets at 23 °C), and a wide temperature range for cw operation (up to 57 °C).

REFERENCES

[1] M. Kondow, T. Kitatani, S. Nakatsuka, M.C. Larson, K. Nakahara, Y. Yazawa, and M. Okai, "GaInNAs: a noval material for long-wavelength semiconductor lasers", IEEE J. Slect. Topics Quantum Electron., vol. 3, pp. 719-730, 1997.

[2] S. Sato, and S. Satoh, "Room temperature pulsed operation of strained GaInNAs/GaAs double quantum well laser diode grown by metal organic chemical vapour deposition", Electron. Lett., vol. 34, pp. 1495-1497, 1998.

[3] M. Kondow, S. Nakatsuka, T. Kitatani, Y. Yazawa, and M. Okai, "Room-temperature continuous wave operation of GaInNAs/GaAs laser diode", Electron. Lett., vol. 32, pp. 2244-2245, 1996.

[4] M. Kondow, S. Nakatsuka, T. Kitatani, Y. Yazawa, and M. Okai, "Room-temperature pulsed operation of GaInNAs laser diodes with excellent, high-temperature performance", Jpn. J. Appl. Phys., vol. 35, pp. 5711-5713, 1996.

[5] F. Hohnsdorf, J. Koch, S. Leu, W. Stoltz, B. Borchert, and M.Druminski, "(GaN)(InAs)/GaAs single quantum well lasers for emission wavelength in the range 1.28-1.38 μm", Electron. Lett., vol. 35, pp. 571-572, 1999.

[6] C.P. Hains, N.Y. Li, K. Yang, X.D. Huang, and J. Cheng, "Room-temperature pulsed operation of triple-quantum well GaInNAs/GaAs lasers with low threshold current density grown on misoriented GaAs substrates by MOCVD", IEEE Photonics Technol. Lett., Vol.11, No. 10, pp1208-1210, October, 1999.

[7] K. Nakahara, M. Kondow, T. Kitatani, M.C. Larson, and K. Uomi, "1.3 μm continuous-wave operation in GaInNAs quantum well lasers", IEEE Photonics Technol. Lett., Vol. 10, pp. 487-488, 1998.

[8] S. Sato, S. Satoh, "1.3 μm continuous-wave operation ofGaInNAs lasers grown by metal organic chemical vapour deposition", Electronics Letters, Vol.35, No.15, pp 1251-1252, July, 1999

[9] N.Y. Li, C.P. Hains, K. Yang, J. Lu, J. Cheng, and P.W. Li, "Organometallic vapor phase epitaxy growth and optical characteristics of almost 1.2 μm GaInNAs three-quantum-well laser diodes", Appl. Phys. Lett., Vol.75, No.8, pp1051-1053, August, 1999

[10] J.M. Dallesasse, N. Holonyak, Jr. , A. R. Sugg, T. A. Richard, and N. ElZein, "Hydrolyzation oxidation of $Al_xGa_{1-x}As$-AlAs-GaAs quantum well heterostructures and superlattices", Appl. Phys. Lett., Vol. 57, No. 26, pp2844-2846, 1990

[11] S.A. Maranowski, A. R. Sugg, E. I. Chen, and N. Holonyak, Jr. "Native oxide top-and bottom-confined narrow stripe p-n $Al_yGa_{1-y}As$-GaAs-$In_xGa_{1-x}As$ quantum well heterostructure laser" Appl. Phys. Lett., Vol.63, No.12, pp1660-1662, 1993

To be published in IEEE Photonics Technology Letters, Vol. 12, no. 2, Feb. 2000

Very Low Threshold Current Density Room Temperature Continuous-Wave Lasing from a Single-Layer InAs Quantum Dot Laser

Xiaodong Huang, A. Stintz, C. P. Hains, Julian Cheng, and K. J. Malloy.

Abstract– Continuous-wave (cw) lasing operation with a very low threshold current density (J_{th} = 32.5 A/cm^2) has been achieved at room temperature by a ridge waveguide quantum dot (QD) laser containing a single InAs QD layer embedded within a strained InGaAs quantum well (dot-in-well, or DWELL structure). Lasing proceeds via the QD ground state with an emission wavelength of 1.25 μm when the cavity length is longer than 4.2 mm. For a 5 mm long QD laser, cw lasing has been achieved at temperatures as high as 40 °C, with a characteristic temperature T_o of 41 K near room temperature. Lasers with a 20 μm stripe width have a differential slope efficiency of 32% and peak output power of >10 mW per facet (uncoated).

Index Terms–Quantum dots, semiconductor lasers, epitaxial growth, electroluminescence

Since it was first proposed [1], self-organized quantum dot (QD) layers [2] have been used successfully as the active gain medium for edge-emitting lasers operating in the 1.3μm wavelength range [3]-[8], and for vertical-cavity surface-emitting lasers (VCSEL's) emitting at shorter wavelengths [3], [9]-[10]. For many future optic communication and interconnect applications, it is desirable to achieve lasers that can operate at a much lower threshold current density while preserving lasing efficiency and high output power, and providing a higher characteristic temperature T_o. One of the advantages of QD lasers is their potential for achieving a long wavelength optical source on a GaAs substrate with an extremely low threshold current density, whose value has been theoretically predicted to be ~10A/cm^2 for QD layers with a 10% size dispersion [11]. Approaching this limit has posed a great challenge to both crystal growth and device design, especially for QD lasers operating near 1.3 μm, where the modal gain of the QD layer in the ground state readily saturates at values that are often less than 10 cm^{-1}. Efficient lasing, especially continuous-wave (cw) lasing above room temperature, thus requires lasers with a higher modal gain and very low optical losses, as well as reduced self-heating. In this letter, we describe the achievement of efficient cw lasing operation of edge-emitting QD lasers in the ground state (λ~1.25 μm) at temperatures up to 40 °C, using a ridge waveguide geometry with a narrow stripe width. These lasers are based on a single layer of InAs quantum dots embedded within an InGaAs quantum well (*i.e.*, a dot-in-well, or DWELL structure [8]), which provides a higher injection efficiency and larger optical gain. A very low cw lasing threshold current density of J_{th}=32.5A/cm^2 has been achieved at room temperature using a 9.2 mm long cavity with uncoated facets and a stripe width of W=20 μm, which is the lowest value ever reported. CW lasing occurred in the ground state of the QD lasers whose cavity length L is greater than 4.2 mm. For L=5 mm, cw lasing occurred in the ground state at temperatures as high as 40 °C, with a characteristic temperature of T_o= 41 K near room temperature. These lasers achieved a differential slope efficiency of 32% and a peak output power of >10 mW per (uncoated) facet, and the estimated internal losses are 4.4 cm^{-1}.

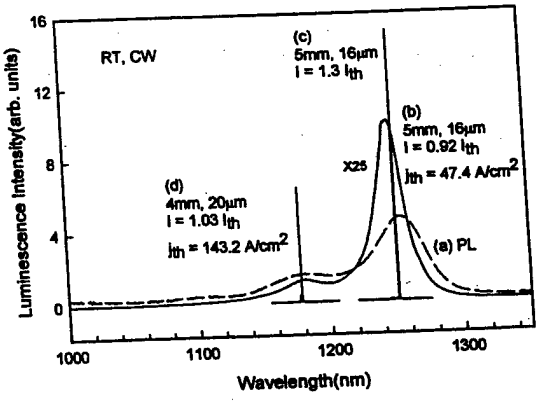


Fig. 1. (a) The photoluminescence spectrum of the as-grown wafer (dashed line) with a FWHM of 34 meV, (b) and (c) the eletroluminescence and ground state lasing spectra of a 5 mm QD laser below and above threshold, (d) the excited state lasing spectrum of a 4 mm long QD laser above threshold.

The QD laser structure follows the design reported in Ref. [7] and [8], and was grown by solid-source molecular beam epitaxy (MBE) on a (001) n$^+$-GaAs substrate. The epilayer structure consists of a 300 nm thick n-GaAs (10^{18} cm^{-3}) buffer, a 2 μm thick n-$Al_{0.7}Ga_{0.3}As$ (10^{17} cm^{-3}) lower cladding layer, a 219 nm thick GaAs waveguide layer in which the active "dot in a well" (DWELL) layer is embedded, a 50 nm thick p-$Al_{0.98}Ga_{0.02}As$ layer (10^{17} cm^{-3}), a 1.9 μm thick p-$Al_{0.7}Ga_{0.3}As$ (10^{17} cm^{-3}) upper cladding layer, and a 60

The authors are with the Center for High Technology Materials, University of New Mexico, 1313 Goddard Se, Albuquerque, NM 87106. This work was supported in part by the DARPA Optoelectronic Materials Center at UNM.

nm thick n^+-GaAs (3×10^{19} cm^{-3}) cap. The single DWELL layer, which is situated in the middle of the GaAs waveguide layer, contains InAs QD's with an equivalent coverage of 2.4 monolayers, which are embedded within a 9.6 nm $In_{0.15}Ga_{0.85}As$ quantum well (QW). The growth temperature is 510 °C for the QD's and the QW, but is 610 °C for the rest of the layers. Quantum dots formed under these condition usually have a density of $7\times10^{10}cm^{-2}$. The insertion of an $Al_{0.98}Ga_{0.02}As$ layer makes it possible to fabricate a narrow Al-oxide confined inner stripe laser with a planar structure by selective wet oxidation. In this work, standard ridge waveguide structures with a ridge width of 20 μm or 16 μm were fabricated.

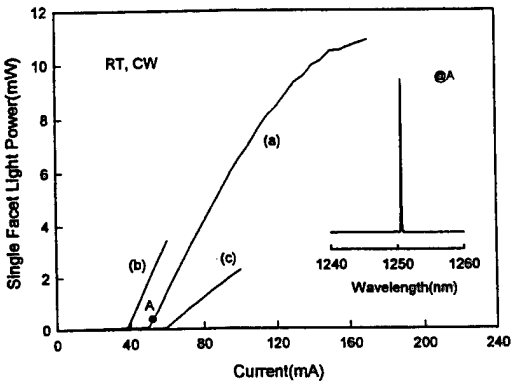


Fig. 2. The room temperature, single-facet, cw lasing characteristics of three QD lasers with different cavity lengths: (a) L=5 mm, W= 16 μm, (b) L=5.6 mm, W= 16 μm, (c) L=9.2 mm, W= 20 μm.

Device fabrication begins with formation of the ridges by wet chemical etching, followed by PECVD deposition of a thin Si_3N_4 film and plasma etching windows in the nitride above the ridges to define the stripe width and the contact area. After e-beam deposition of the Ti/Pt/Au p-contact, the sample substrate is lapped down to a thickness of ~125 μm, and AuGe/Ni/Au is e-beam deposited on the substrate to form the n-contact. The wafer is then cleaved into laser bars with a cavity length (L) ranging from 3.0 mm to 9.2 mm, whose facets are uncoated. For cw measurements, the lasers were soldered to a Cu heat sink in the n-side down configuration.

Room temperature photoluminescence (PL) measurement of the as-grown wafer is shown in Fig.1 (a). The ground state PL peak has a narrower spectral full-width at half-maximum (FWHM ≈34 meV) than the PL results reported in Ref. [8], indicating the improved homogeneity of the QD's. No luminescence from the InGaAs QW is observed. Fig.1 also shows the room temperature electroluminescence (EL) and lasing spectra of two lasers with different lengths under cw operation. Depending on cavity length, lasing proceeds via either the ground state (λ≈1.25 μm) or the first excited state (λ≈1.18 μm). For the laser with L= 5 mm and W=16 μm, lasing occurs in the ground state with a threshold current density of J_{th}= 47.4 A/cm^2. Fig. 1 (b) and (c) show the EL spectra of this laser below threshold (I = $0.92I_{th}$) and above threshold (I = $1.3I_{th}$), respectively, both of which are centered at 1.25 μm. Fig.1 (c) shows the excited state lasing spectrum (~1.18μm) of a shorter laser with L = 4 mm and W = 20 μm, with J_{th} = 143.2 A/cm^2.

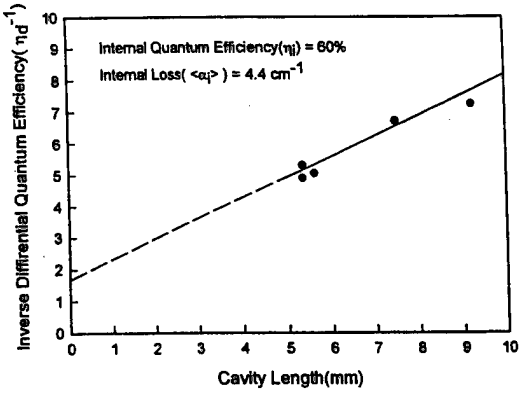


Fig. 3. The inverse differential slope efficiency $1/\eta_d$ (for both facets) plotted as a function of the cavity length L under bothcw lasing conditions. The y-intercept yields the internal quantum efficiency η_i, (60%) while the slope yields the internal optical loss α_{ll} (4.4 cm^{-1}).

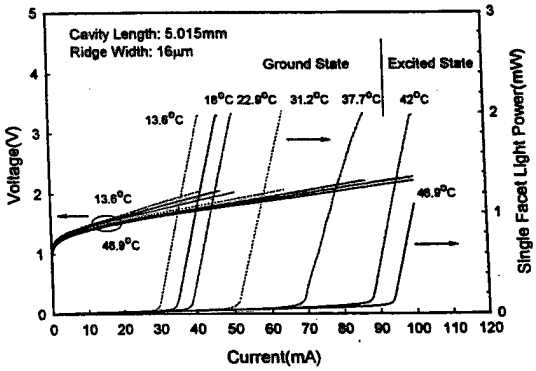


Fig. 4. The electrical characteristics and the single-facet, cw lasing characteristics of a DWELL laser at different temperatures.

CW lasing with a threshold current density below 50 A/cm^2 has been achieved in the ground state when L ≥ 5 mm. Fig. 2 shows the single-facet cw lasing characteristics of three lasers with different cavity lengths . For the laser with L = 5.6 mm and W = 20 μm (Fig. 2a), the threshold current density is J_{th} = 43.5A/cm^2 and the cw light output from a single facet exceeds 10 mW. Its lasing spectrum near threshold (I= $1.06I_{th}$) is shown in the inset of Fig. 2. Due to the smaller power dissipation of a narrow-stripe ridge waveguide structure, thermal rollover is reduced and cw lasing occurs even at a bias current of I=$3I_{th}$. For the device with L = 5 mm and W = 16 μm (Fig. 2b), the threshold current density is J_{th} = 47.4 A/cm^2, and the peak differential slope efficiency (η_d) for both facets is 32%. The lowest value of J_{th} obtained under cw lasing operation is 32.5 A/cm^2 (Fig. 2c), and 28.5 A/cm^2 for pulsed lasing operation, using a laser with L = 9.2 mm and W = 20 μm. The lowest threshold current densities reported previously

for QD lasers at room temperature were ~60 A/cm^2 for cw operation [3], [6] and 26 A/cm^2 for pulsed operation [8].

Figure 3 shows the linear dependence of the inverse differential slope efficiency η_d^{-1} (for both facets) on the cavity length L, from which the internal quantum efficiency (η_i= 60%) and the internal optical loss ($\langle\alpha_i\rangle$= 4.4 cm^{-1}) were derived. For shorter cavity lengths (L < 4.2 mm), cw lasing shifts to the first excited state (λ = 1.18 μm). The threshold gain of the shortest laser that is capable of lasing in the ground state is calculated to be 7 cm^{-1}, assuming a facet reflectivity of 0.32. Thus the modal gain of a single InAs QD layer in the ground state saturates at ~7 cm^{-1}, which is very low compared to that of a single QW.

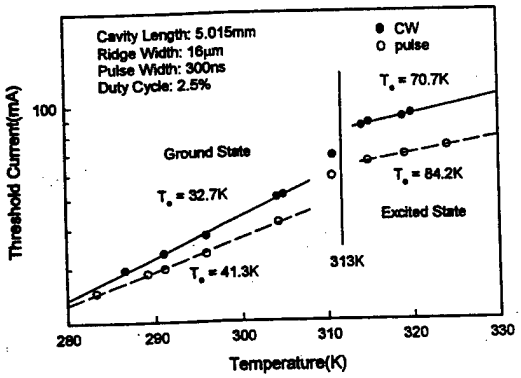


Fig. 5. Temperature dependence of the threshold current for both cw lasing (closed circles) and pulsed lasing (open circles). Lasing occurs in the ground state below 313 K, and in the excited state above 313 K.

The temperature dependence of the threshold current of a QD laser with L=5 mm and W=16μm has been measured under both cw and pulsed operation (300 ns pulses with a duty cycle of 2.5%). Figure 4 shows the single-facet cw lasing characteristics and electrical characteristics of this laser at temperatures ranging from 13.6 °C to 46.9 °C. The threshold voltage is < 2V throughout this temperature range. Lasing occurs in the ground state below 40 °C, but switches to the first excited state at higher temperatures. This is attributed to the reduction of the ground state gain of the QDs as a result thermally activated carrier loss at higher temperatures, and the increased band-filling in the first excited state as the ground state gain becomes saturated. The measured slope efficiency decreases with increasing temperature, but rises again after lasing has shifted to the excited state.

Fig. 5 plots the temperature dependence of the cw and pulsed threshold currents, from which the characteristic temperature, T_o, has been determined. At temperatures below 40 °C, T_o is 32.7 K for cw operation and is 41.3 K for pulsed operation. Above 40 °C, these values of T_o jump to 70.7 K and 84.2 K, respectively, as lasing switches into the excited state. The higher T_o of the excited state is a consequence of its higher degeneracy and larger density of state. In the ground state, T_o depends strongly on the cavity loss [7], which determines the proximity of the ground state modal gain to saturation. The higher the loss, the higher is the modal gain that is required to achieve lasing and the closer it is to saturation. Gain saturation causes increased band filling in the excited state, which competes with the ground state for carriers and thus increases J_{th} for ground state lasing. A lower T_o is thus expected for a laser whose modal gain in the ground state is near saturation. Since the cavity loss of the 5 mm laser is ~6.7 cm^{-1}, its modal gain is operating very close to gain saturation in the ground state (~7 cm^{-1}), giving rise to a relatively small T_o. The ratio of the modal gain to its saturation value is thus an important parameter that describes the degree of band filling. A higher gain saturation limit is thus desirable for improving the performance of QD lasers, especially for achieving a larger T_o. Multiple QD layers can also be useful in alleviating the gain saturation problem [12].

In summary, we have demonstrated the efficient cw lasing of InAs QD lasers at temperatures ranging from 13.6 °C to 40.0 °C, and have achieved a very low threshold current density (J_{th} = 32.5 A/cm^2) and a characteristic temperature of T_o=41 K. Lasing has been realized via either the ground state or the excited state depending on cavity length. Lasers with a slope efficiency of 32%, and an output power of 11 mW/facet have been achieved using a 5 mm long laser cavity.

REFERENCES

[1] Y. Arakawa, H. Sakaki, "Multidimensional quantum well alser and temperature dependence to of its threshold current," Appl. Phys. Lett., vol. 40, pp. 939-941, 1982

[2] N. N. Ledentsov, V. M. Ustinov, A. Yu. Egorov, A. E. Maximov, I. G. Tabatadze, and P. S. Kop'ev, "Optical properties of heterostructures with InGaAs-GaAs quantum clusters," Semicond., vol. 28, pp. 832-834, 1994

[3] D. Bimberg, N. N. Ledentsov, M. Grundmann, F. Heinrichsdorff, V. M. Ustinov, P. S. Kop'ev, M. V. Maximov, Zh. I. Alferov, J. A. Lott, "Application of self-organized quantum dots to edge emitting and vertical cavity lasers," Physica E, vol. 3, pp. 129-136, 1998

[4] D. L. Huffaker, G. Park, Z. Zou, O. B. Shchekin, and D. G. Deppe, "1.3μm room-temerature GaAs-based quantum-dot laser," Appl. Phys. Lett., vol. 73, pp. 2564-2566, 1998

[5] Z. Zou, O. B. Shchekin, G. Park, D.L. Huffaker, and D. G. Deppe, "Threshold temperature dependence of lateral-cavity quantum-dot lasers," IEEE Photon. Technol. Lett., vol. 10, pp. 1673-1675, 1998

[6] Yu. M. Shernyakov, D. A. Bedarev, E. Yu. Kondrat'eva, P. S. Kop'ev, A. R. Kovsh, N. A. Maleev, M. V. Maximov, S. S. Mikhrin, A. F. Tsatsul'nikov, V. M. Ustinov, B. V. Volovik, A. E. Zhukov, Zh. I. Alferov, N. N. Ledentsov, and D. Bimberg, "1.3μm GaAs-based laser using quantum dots obtained by activated spinodal decomposition," Electron. Lett., vol. 35, pp. 898-900, 1999

[7] L. F. Lester, A. Stintz, H. Li, T. C. Newell, E. A. Pease, B. A. Fuchs, and K. J. Malloy, "Optical characteristics of 1.24μm quantum dot lasers," IEEE Photon. Technol. Lett., vol. 11, pp. 931-933, 1999

[8] G. T. Liu, A. Stintz, H. Li, K. J. Malloy, and L. F. Lester, "Extremely low room-temperature threshold current density diode lasers usingInAs dots in an $In_{0.15}Ga_{0.85}As$ quantum well," Electron. Lett., vol. 35, pp. 1163-1165, 1999

[9] J. A. Lott, N. N. Ledentsov, V. M. Ustinov, A. Yu. Egorov, A. E. Zhukov, P. S. Kop'ev, Zh. I. Alferov, and D. Bimberg, "Vertical cavity lasers based on vertically coupled quantum dots," Electro.Lett., vol. 33, pp. 1150-1151, 1997

[10] D. L. Huffaker, H. Deng, and D. G. Deppe, "1.15μm wavelength oxide-confined quantum-dot vertical cavity surface-emitting laser," IEEE Photon. Technol. Lett., vol. 10, pp. 185-187, 1998

[11] M. Grundmann, D. Bimberg, "Theory of random-population for quantum dots,", Phys. Rev. B, vol. 55, pp. 9740-9745, 1997

[12] O. G. Schmidt, N. Kirstaedter, N. N. Ledentsov, M. –H. Mao, D. Bimberg, V. M. Ustinov, A. Y. Egorov, A. E. Zhukov, M. V. Maximov, P. S. Kop'ev, and Z. I. Alferov, "Prevention of Gain Saturation by multi-layer quantum dot lasers," Electron. Lett., vol. 32, pp. 1302-1304, 1998

**********End**********

FIGURE CAPTION

Fig. 1. (a) The photoluminescence spectrum of the as-grown wafer (dashed line) with a FWHM of 34 meV, (b) and (c) the eletroluminescence and ground state lasing spectra of a 5 mm QD laser below and above threshold, (d) the excited state lasing spectrum for a 4 mm QD laser above threshold.

Fig. 2. The room temperature, single-facet, cw lasing characteristics of three QD lasers with different cavity lengths: (a) L=5 mm, W= 16 μm, (b) L=5.6 mm, W= 16 μm, (c) L=9.2 mm, W= 20 μm.

Fig. 3. The inverse differential slope efficiency $1/\eta_d$ (for both facets) plotted as a function of the cavity length L under both pulsed (?) lasing conditions. The y-intercept yields the internal quantum efficiency η_i, while the slope uields the internal optical loss α_i.

Fig. 4. The electrical characteristics and the single-facet, cw lasing characteristics of a QD laser at different temperatures.

Fig. 5. Temperature dependence of the threshold current for both cw lasing (closed circles) and pulsed lasing (open circles). Lasing occurs in the ground state below 313 K, and in the excited state above 313 K.

To be published in IEEE Photonics Technology Letters Vol. 12, no. 1, January, 2000.

Efficient Double Intracavity-Contacted Vertical-Cavity Surface-Emitting Lasers with Very Low Threshold and Low Power Dissipation Designed for Cryogenic Applications

Kai Yang, C.P. Hains, and Julian Cheng, *Senior Member IEEE*

Abstract **- Efficient continuous wave operation of oxide-confined double intracavity-contacted InGaAs /GaAs vertical-cavity surface-emitting lasers (VCSEL) with low threshold voltage and low power dissipation has been achieved over a wide range of cryogenic temperatures (77K to 250K). Low operating voltages were obtained by routing current through two intra-cavity contacts to bypass both distributed Bragg reflector (DBR) mirrors, while lower optical losses were achieved by using undoped DBR mirrors with abrupt heterointerfaces. This resulted in low operating voltages (<1.6V), submilliampere threshold currents (I_{th} ~ 0.15 mA), low power dissipation (<0.9 mW at threshold) and a high power conversion efficiency (η_{eff} = 31 %).**

High-speed optical links based on VCSELs can provide power-efficient optical transfer of high-speed analog or digitized image data from infrared sensor arrays housed in a cryogenic environment to external electronic signal processors that may be situated locally or at some distance away. An optical link can provide both electrical and thermal isolation, as well as a larger bandwidth and a longer link span between the imaging array and the external processing electronics.

Vertical-cavity surface-emitting lasers (VCSEL's) can be designed for optimum performance at any desired temperature range by adjusting the relative positions of the lasing mode and the gain peak [1]. VCSELs operating at cryogenic temperatures offer superior lasing performance as a result of a higher differential gain coefficient, a higher quantum efficiency, lower losses, and lower noise, resulting in a higher modulation bandwidth [2], lower power dissipation, and a higher power conversion efficiency. Properly designed VCSELs can maintain their stable lasing characteristics over a very wide range of temperatures [3], thus providing an optical interconnect that is stable against thermal fluctuations.

Manuscript received Septemeber xx, 1999. This work was supported by the Army Federated Laboratories Advanced Sensors Program.
The authors are with the University of New Mexico, Center for High Technology Materials, 1313 Goddard SE, Albuquerque, NM 87106.

An efficient cryogenic optical link requires VCSELs with very low power dissipation at cryogenic temperatures. This in turn requires the VCSELs to have low operating currents and voltages that are compatible with on-board cryogenic CMOS drive circuits (≤ 2 mA and 3.3 V, respectively), as well as a large modulation bandwidth and temperature-insensitive operation. Low threshold current is readily achieved by reducing the transverse dimensions of the optical cavity, and as a result of the higher gain and lower losses at cryogenic temperatures. We have previously achieved cryogenic VCSELs that were optimized for efficient cw lasing operation at temperatures between 6 K and 150 K [1,3], and demonstrated the stable operation of gigabit-per-sec optical links over a wide range of temperatures [1]. While these VCSELs have excellent electrical and lasing characteristics, their threshold voltages remained relatively high (2-3V) at cryogenic temperatures, thus resulting in a higher power dissipation. At low temperatures (<100 K), the operating voltage of a VCSEL is limited by carrier transport across the energy barriers at the hetero-interfaces of the distributed Bragg reflector (DBR) mirrors, which is inefficient when the thermal energy kT of the carriers is small. Low operating voltages (<1.5 V) can be achieved by reducing the bandgap of the quantum wells using strained InGaAs quantum wells, and by using intra-cavity contacts to eliminate conduction through the hetero-interfacial barriers of the DBR mirrors. The latter should lead to low operating voltages that are insensitive to temperature, and also allows the use of undoped DBR mirrors with ungraded hetero-interfaces to reduce the optical losses and thus reduce the threshold optical gain for lasing. All of these features have been incorporated into the new cryogenic VCSEL design described below.

The MOCVD-grown VCSEL structure (fig. 1a) consists of a 1λ-thick graded index separate confinement heterostructure (GRINSCH) cavity containing four 7 nm thick $In_{0.2}Ga_{0.8}As/GaAs$ quantum wells (QW's) as the active layer. The cavity is bounded on each side by a graded interface to a 1/4λ-thick $Al_{0.98}Ga_{0.02}As$ oxidation layer ($1x10^{18}/cm^3$ doping), followed by a 3/4λ-thick GaAs contact layer, with the latter doped n-type and p-type, respectively. In the p-contact (n-contact), the doping is graded from $1x10^{18}/cm^3$ near the active region to

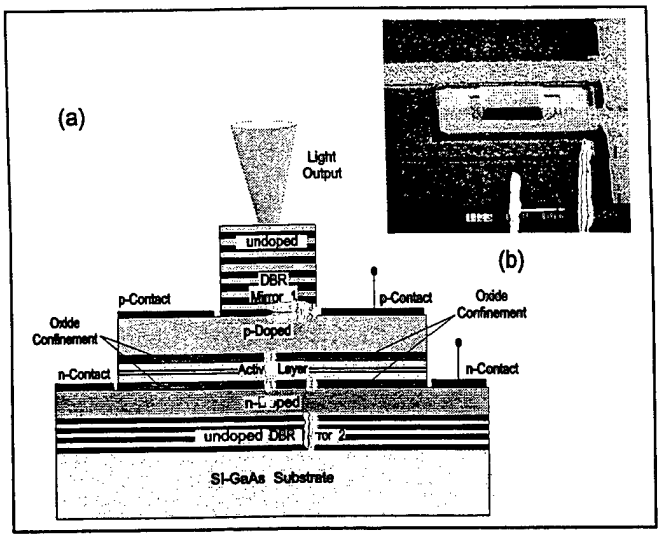


Figure 1 (a) Schematic design of a cryogenic VCSEL structure, and (b) the electron photomicrograph of a completed device.

$5x10^{18}/cm^3$ ($3x10^{18}/cm^3$) away from the active region. The entire structure is then sandwiched between top and bottom DBR mirrors consisting of 18 and 28.5 pairs of undoped $GaAs/Al_{0.92}Ga_{0.08}As$ quarter-wave layers, respectively. The DBR mirrors are undoped to minimize free carrier absorption, and the heterointerfaces are ungraded to reduce the mirror loss. In order to achieve optimum lasing operation at 100 K, the resonant cavity mode (~943 nm) of the VCSEL was intentionally detuned (*i.e.*, blue shifted) by 42 nm with respect to the gain peak (~985 nm) at room temperature. Since the cavity mode and the gain peak shift with temperature at rates of -0.059 nm/K and -0.28 nm/K, respectively, they would achieve optimum overlap at T~100 K.

The fabrication of the devices started with dry-etching of the top-mesa down to the p-contact layer using an inductively coupled plasma (ICP) etcher. The upper intracavity p-contact (Au/Zn/Au) was then patterned and deposited by electron-beam evaporation. Next, a second dry-etching step was carried out to define the bottom mesa, which contained the p-contact layer, the active layer, and the two oxidation layers, stopping at the lower and more heavily-doped portion of the n-contact layer. The active area current aperture was then formed by the selective oxidation of the $Al_{0.98}Ga_{0.02}As$ layers in a steam-saturated ambient at 425 °C, which yielded device apertures ranging from 5 μm to 15 μm. The n-contact (AuGe/Ni/Au) was then patterned and deposited on the lower n-contact layer. Finally interconnect metal and bonding pads were deposited using Ti/Au. Fig. 1(b) shows the SEM photograph of a completed device.

Intracavity-contacted VCSELs with oxide apertures ranging from 5 μm to 15 μm have been studied. All devices operated over the 77-375 K temperature range, but the minimum threshold current I_{th} was achieved at 115 K. Figure 2 shows the typical continuous wave (cw) light-vs-current characteristics of a 5 μm aperture VCSEL at different temperatures. The threshold current decreases from I_{th}=1.96 mA at room temperature to a minimum of I_{th}=150 μA at T=115 K, and then increases slightly as the temperature is further lowered to T=80 K. At T=115 K, this device achieved a threshold current of I_{th}=150 μA (J_{th} = 600 A/cm^2), a threshold voltage of V_{th}=1.40 V, a differential slope efficiency of 70 % and peak output power of 12.5 mW. The corresponding parameters for room temperature operation are 1.96 mA, 1.79 V, 30 %, and 2.8 mW, respectively. The lasing wavelength changes from 942 nm at 300 K to 929 nm at 100 K under low bias current (1.5 x I_{th}). The current-voltage characteristics of the device remain fairly stable over the temperature range measured, showing only a modest increase in voltage as the temperature is reduced (fig. 2).

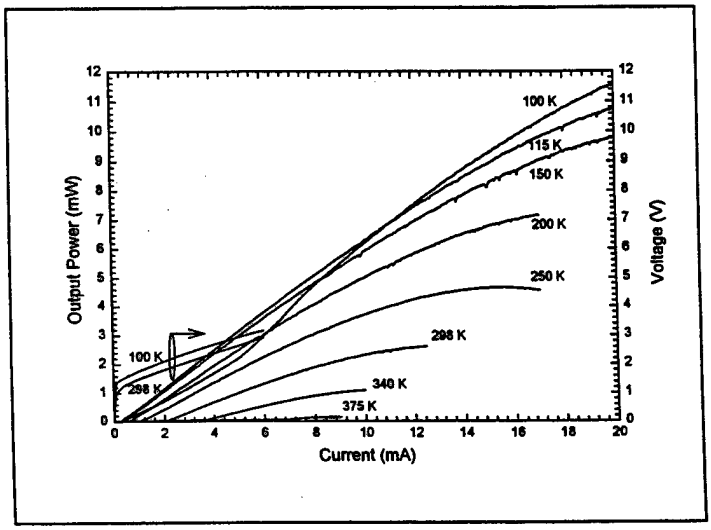


Figure 2 CW lasing characteristics and electrical characteristics of a cryogenic VCSEL with a 5 μm oxide aperture at various temperatures.

The lowest lasing threshold occurred at T=115 K, and not at T=100 K as designed. This is due in part to the inadequate wavelength de-tuning at 295 K, and in part to the onset of modal competition under low bias conditions at temperatures below T=115 K. The spectra of the devices measured at various current levels revealed stable lasing modes throughout the operating range down to T=115 K, whereas the lasing characteristics below T=100 K (figure 2) exhibited mode competition at low current levels, with one mode becoming dominant at higher bias levels. As the temperature is lowered from room temperature to T=115 K, the slope efficiency and peak output power both increase monotonically. At T=100 K, the slope efficiency decreases abruptly at low bias currents, and then increases at higher bias levels as one mode becomes dominant.

Figure 3 shows the important temperature dependence of the threshold voltage, threshold current and peak power conversion efficiency. The threshold voltage decreases monotonically with temperature, remaining below 1.6V from 80 K to 250 K. The power conversion

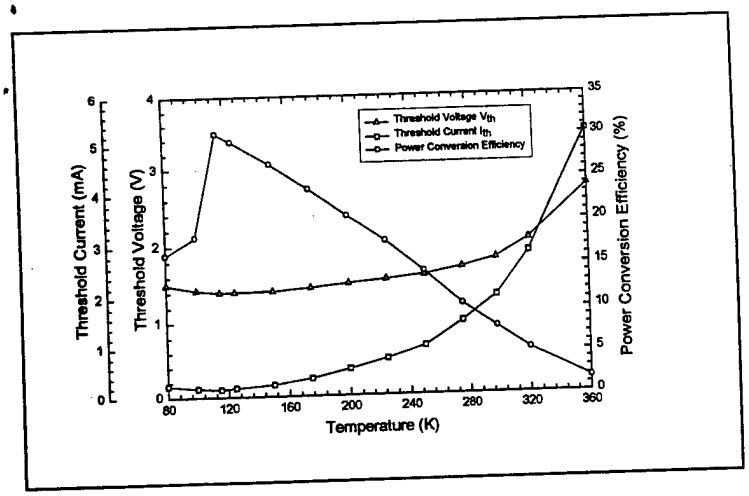


Figure 3 Temperature dependence of the threshold current, threshold voltage, and power conversion efficiency of a cryogenic VCSEL with a 5 μm oxide aperture.

efficiency increases linearly as the temperature is lowered, reaching a maximum value of ~31% at T=115 K. Figure 4 shows the power dissipation of the VCSEL as a function of temperature at several constant optical output power levels. At the optimum temperature (~115 K), the power dissipation is ~0.21 mW at threshold, 0.81 mW for P_{out} = 0.2 mW, 1.71 mW for P_{out} = 0.5 mW, and 3.36 mW for P_{out} =1.0 mW. The achievement of low power dissipation at low temperatures is a consequence of the low operating voltages and currents that have been achieved by the VCSEL design, as well as the high slope efficiency that resulted from a higher differential gain coefficient and a lower internal loss at low temperature.

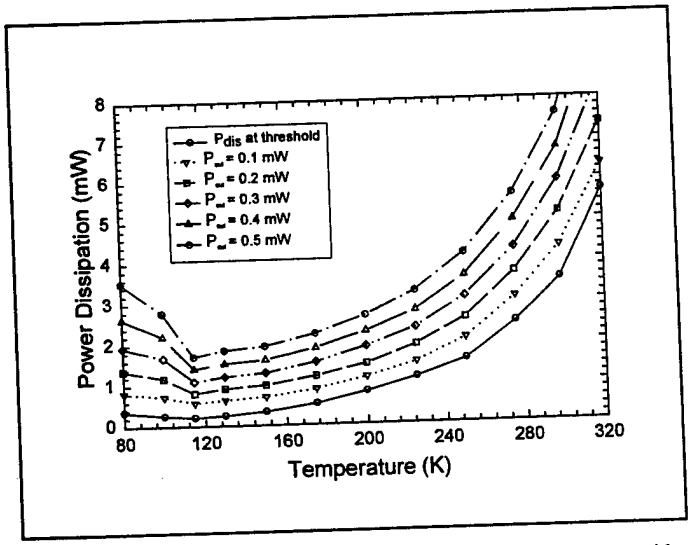


Figure 4 Power dissipation of a cryogenic VCSEL with 5 μm oxide aperture as a function of temperature, at threshold and at 0.1, 0.2, 0.3, 0.4, and 0.5 mW of cw optical output power.

In conclusion, VCSELs with low threshold voltage and low power dissipation have been achieved at cryogenic temperatures (77-375 K) using an oxide-confined design that employed double intracavity contacts and undoped DBRs, along with proper alignment of the cavity mode and the gain peak at low temperatures. Efficient cw lasing operation was observed over a wide temperature range (77 to 375 K), but the optimum lasing characteritsics occurred at 115K, including low threshold current (150 μA), low operating voltage (1.5 V), high peak output power (12.5 mW), high slope efficiency (70 %), high power conversion efficiency (up to 31%) and low power dissipation (0.2 mW at threshold) for VCSELs with a 5 μm aperture.

REFERENCES

[1] Y.A. Akulova, B.J. Thibeault, J. Ko, and L.A. Coldren, "Low-Temperature Optimized Vertical-Cavity Lasers with Submilliamp Threshold Currents over the 77-370 K Temperature Range", IEEE Photon. Technol. Lett., Vol. 9, pp. 277-279, March, 1997

[2] Bo Lu, Wen-Lin Luo, C. Hains, Julian Cheng, R.P. Schneider, R.P. Choquette, K.L. Lear, S.P. Kilcoyne, and J.C. Zolper, "High Efficiency and High-Power Vertical-Cavity Surface-Emitting Laser Designed for Cryogenic Applications", IEEE Photon. Technol. Lett., Vol. 7, pp. 447-448, May, 1995

[3] E. Goobar, M.G. Peters, G. Fish, and L.A. Coldren, "Highly Efficient Vertical-Cavity Surface-Emitting Lasers Optimized for Low-Temperature Operation", IEEE Photon. Technol. Lett., Vol. 7, pp. 851-853, August, 1995

[4] Edgard Goobar, Cathal Mahon, Frank H. Peters, and Larry A. Coldren, "Low-temperature Operation of Vertical Cavity Surface-Emitting Lasers", IEEE Photon. Technol. Lett., Vol. 7, pp. 7-9, January, 1995

[5] Bo Lu, Yin-Chen Lu, Julian Cheng, Richard P. Schneider, John C. Zolper, and Gary Goncher, "Gigabit-per-Second Cryogenic Optical Link Using Optimized Low-Temperature AlGaAs-GaAs Vertical-Cavity Surface-Emitting Lasers", IEEE J. Quantum Electron., Vol. 32, pp. 1347-1358, August, 1996

[6] G. Goncher, Bo Lu, Wen-Lin Luo, Julian Cheng, S. Hersee, S.Z. Sun, R.P. Schneider, J.C. Zolper, "Cryogenic Operation of AlGaAs-GaAs Vertical-Cavity Surface-Emitting Lasers at Temperatures from 200 K to 6 K", IEEE Photon. Technol. Lett., Vol. 8, pp. 316-318, March, 1996

[7] Bo Lu, P. Zhou, Julian Cheng, K.J. Malloy, and J.C. Zolper, "High temperature pulsed and continuous-wave operation and thermally stable threshold characteristics of vertical-cavity surface-emitting lasers grown by metalorganic chemical vapor deposition", Appl. Phys. Lett., Vol. 65, pp1337-1339, September, 1994

[8] B. Tell, K.F. Brown-Goebeler, R.E. Leibenguth, F.M. Baez, and Y.H. Lee, "Temperature dependence of GaAs-AlGaAs vertical-cavity surface-emitting lasers", Appl. Phys. Lett., Vol. 60, pp. 683-685, February, 1992

[9] J.J. Dudley, D.L. Crawford, and J.E. Bowers, "Temperature Dependence of the Properties of DBRs Used in Surface Normal Optoelectronic Devices", IEEE Photon. Technol. Lett., Vol. 4, pp. 311-314, April, 1992

Cryogenic VCSEL's with Chirped Multiple Quantum Wells for a Very Wide Temperature Range of CW Operation

G. G. Ortiz, *Member, IEEE*, C. P. Hains, Bo Lu, S. Z. Sun, Julian Cheng, *Senior Member, IEEE*, and J. C. Zolper

***Abstract*—Cryogenic optical data links require an efficient optical source with temperature-insensitive continuous-wave (CW) operation at low temperatures. Also, to simplify optical alignment, it is desirable to obtain CW operation over a broad temperature range that spans both the low and high temperatures. By the use of vertical-cavity surface-emitting lasers (VCSEL's) with chirped (nonuniform) multiple quantum wells (MQW's) to broaden the optical gain spectrum, CW operation has been achieved from 5–350 K, with improved characteristics in both the high- and low-temperature regimes. In particular, temperature-insensitive, submilliampere threshold current was achieved at temperatures from 5–50 K, with a threshold current density of 350 A/cm^2, and a threshold voltage that is below 3 V.**

VERTICAL-CAVITY surface-emitting laser (VCSEL)-based cryogenic optical links are potentially useful in applications requiring high-speed, parallel data transfer between processors in a cryogenic environment and room-temperature electronics, including high-speed super-computers and infra-red imaging systems such as focal plane arrays. These optical links require low-power dissipation, high bandwidth, low-to-moderate output power, and should be insensitive to fluctuations in the temperature of the cryo-chamber. We have previously demonstrated efficient continuous-wave (CW) lasing operation at cryogenic temperatures from 6–250 K [1]–[3], using a VCSEL design with uniform multiple quantum wells. The optical gain peak and lasing mode were intentionally de-tuned at 300 K so that they would come into alignment and achieve optimum CW operation at ~100 K. This device's threshold current had a minimum at this optimum temperature, but increased significantly at lower or higher temperatures. In order to extend optimum operation over a much broader temperature range to accommodate the different temperature requirements of diverse applications, we need to broaden the gain spectrum by introducing chirped (nonuniform) multiple quantum wells in the active region. This new VCSEL achieved efficient, thermally-stable CW operation over a wider range of cryogenic temperatures, with a stable sub-milliampere threshold current, a threshold voltage of less than 3 V, and a threshold power dissipation of <2 mW at temperatures from 5–50 K (<5 mW to 120 K). In addition to improving their tolerance to large temperature fluctuations in the cooling system, this design also extended the temperature range for CW operation from 5–350 K, thereby, making optical alignment possible without cooling.

Although the temperature range over which the VCSEL exhibits a low-threshold current can be extended by broadening the gain spectrum through the use of inhomogeneous multiple-quantum-wells, efficient lasing operation also requires that the gain of each quantum well be sufficiently high to compensate for the reduced gain contributions from other wells at the lasing wavelength. This is easily satisfied at lower temperatures, where the differential optical gain is significantly increased and the quantum efficiency is high (>80%) [1]–[3]. By using multiple quantum wells with different thickness (chirped MQW's), the threshold current of the VCSEL is reduced at both the low and high temperatures, and the overall temperature range of operation is extended. In this paper, we discuss the design and experimental demonstration of VCSEL's with a broadened gain spectrum, and the effect this has on its performance. A brief discussion of the first order gain calculations is included to qualitatively explain the experimental behavior of these devices as a function of temperature.

The gain spectrum can be broadened by using multiple quantum wells with different compositions [4] or different widths. In this work, the latter approach was chosen. For a comparative study, two VCSEL epi-layer structures were grown by low-pressure MOCVD, one containing an active region with four GaAs MQW's of a uniform thickness (80 Å), the other containing GaAs MQW's of different thickness (55, 70, 90, and 105 Å), with the wells separated by 100 Å thick $Al_{0.15}Ga_{0.85}As$ spacer layers. These structures are denoted as the "uniform MQW" and "chirped MQW" structures, respectively. Each structure contains a graded-index separate-confinement-heterostructure multiple-quantum-well (GRIN–SCH–MQW) active region sandwiched between a 24-pair, p-doped distributed-Bragg-reflector (DBR) on the top and a 43.5-pair, n-doped DBR on the bottom. All the heterointerfaces in each DBR have linearly-graded $Al_xGa_{1-x}As$

Manuscript received July 2, 1996; revised August 1, 1996. This work was supported by the Air Force Office of Scientific Research, the Federated Army Laboratories Sensors Program, and the Jet Propulsion Laboratory.

G. G. Ortiz is with the Center for High Technology Materials, EECE Building, Room 125, University of New Mexico, Albuquerque, NM 87131 USA on leave from the Jet Propulsion Laboratory, Pasadena, CA USA.

C. P. Hains, S. Z. Sun, and J. Cheng are with the Center for High Technology Materials, EECE Building, Room 125, University of New Mexico, Albuquerque, NM 87131 USA.

B. Lu was with the Center for High Technology Materials, EECE Building, Room 125, University of New Mexico, Albuquerque, NM 87131 USA. He is now with SDL Inc., San Jose, CA USA.

J. C. Zolper is with the Sandia National Laboratory, Albuquerque, NM 87185 USA.

Publisher Item Identifier S 1041-1135(96)08165-7.

1041–1135/96$05.00 © 1996 IEEE

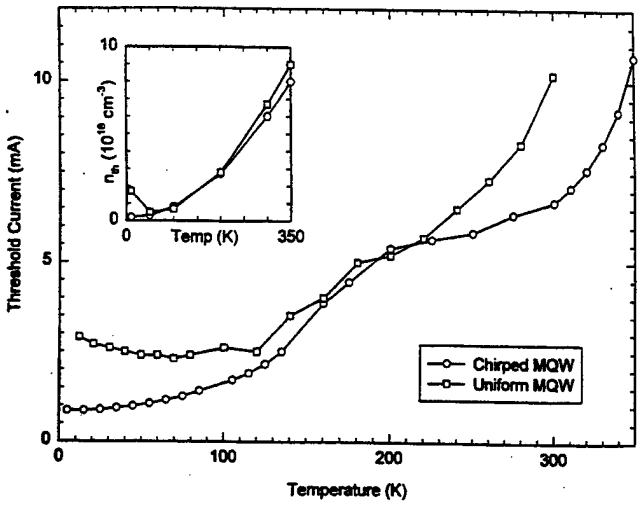


Fig. 1. Comparison of the measured threshold currents of a VCSEL with chirped multiple quantum wells and a VCSEL with uniform multiple quantum wells as a function of temperature. Inset shows the calculated threshold carrier density for both structures as a function of temperature.

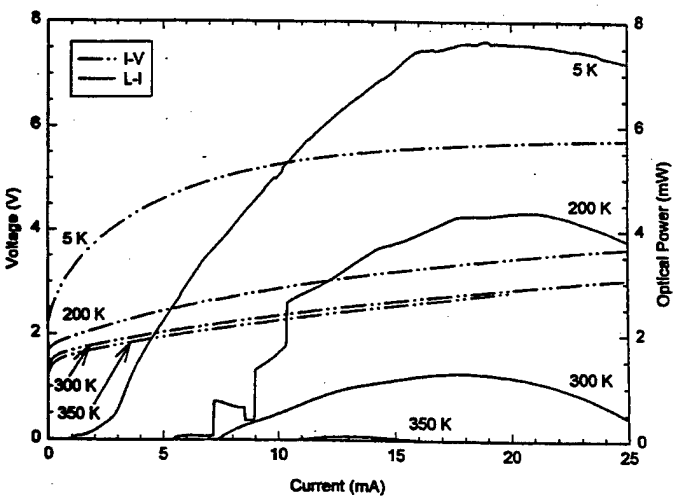


Fig. 2. Measured L–I and I–V characteristics of 16-μm diameter VCSEL with chirped multiple quantum wells at various temperatures.

compositions, and the doping concentration of the DBR layers is also graded from 5×10^{17} cm^{-3} near the active region to 2×10^{18} cm^{-3} away from the active region.

Fig. 1 shows the temperature dependence of the threshold currents for these two structures, each with a 16 μm diameter active region, demonstrating the improved performance of the chirped MQW structure at both the lower and higher temperature regimes. The temperature range for optimum, low-threshold current operation has been extended from ~120 K down to 5 K, with stable sub-milliampere threshold currents from 5–50 K, which reflects the expanded range of mode-gain alignment. The operating temperature range of the VCSEL, which was limited to 250 K for the uniform MQW structure [1], has been extended to 350 K using the chirped MQW's. The temperature dependence of both structures are very similar in the 130–200 K temperature range. Qualitatively similar behavior was also obtained for devices with 10-μm and 20-μm diameters from each wafer.

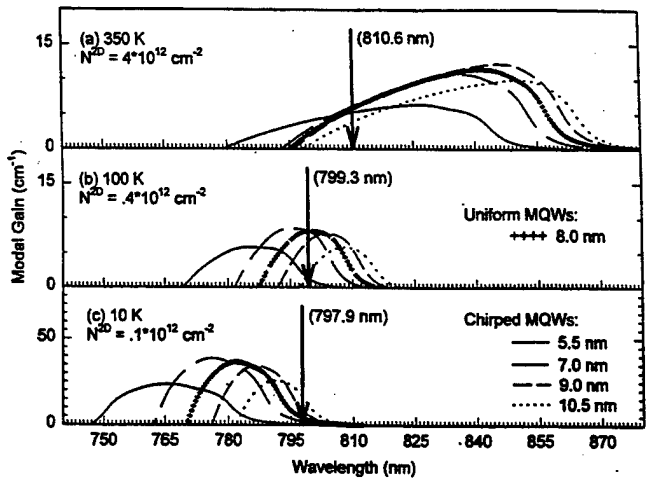


Fig. 3. Calculated modal gain spectrum for the uniform MQW VCSEL and the chirped MQW VCSEL at various temperatures. Arrow denotes the measured cavity mode.

Fig. 2 shows the typical light-current and current-voltage characteristics of a 16-μm diameter VCSEL with chirped MQW's at various temperatures. In the range of 150–250 K, the L–I characteristic shows a "kinked" behavior, indicative of strong modal competition. This figure also shows the L–I characteristics at lower and higher temperatures, with the kinked response significantly reduced in both regimes. Below 100 K, submilliampere threshold operation is obtained, with $I_{th} \sim 700$ μA ($J_{th} = 350$A/cm^2), $V_{th} < 3$ V, and a maximum output power of ~7.5 mW. The threshold voltage V_{th} remains below 3 V throughout the temperature range from 5–350 K.

To explain the improved performance, Fig. 3 compares the relative alignment between the lasing mode (determined experimentally) and the gain spectrum as a function of temperature, for both the uniform MQW structure and the chirped MQW structure. For the former, the cavity mode (~811 nm) is intentionally de-tuned from the gain peak (~850 nm) at room temperature [Fig. 3(a)] so that they come into alignment at the optimum design temperature of 100 K [Fig. 3(b)]. This effect is primarily due to the different temperature coefficients of the lasing mode (−0.05 nm/K above 150 K) and the gain peak (−0.25 nm/K above 150 K). As the temperature is decreased further, the gain spectrum continues to blue-shift relative to the lasing mode, placing the mode (~798 nm) at the tail end of the gain spectrum [Fig. 3(c)] and causing the threshold current to rise. Using a chirped MQW structure, the gain is spectrally broadened, and the modal gain remains high over a wider range of temperatures, as illustrated in Fig. 3. Above room temperature, the cavity mode is aligned near the gain peak of the 55-Å well [Fig. 3(a)]. As the temperature is decreased, the gain spectrum scans across the lasing mode, which becomes aligned to different gain peaks at different temperatures. In the 130–200 K temperature regime, the modal gain (at ~800 nm) is dominated by the contributions from the 70-Å and 90-Å quantum wells (compared with the 80 Å QW's of the uniform structure), and the lasing characteristics of both structures are very similar (Fig. 1). Decreasing the temperature further, the cavity mode (~798 nm) becomes aligned to the 105 Å

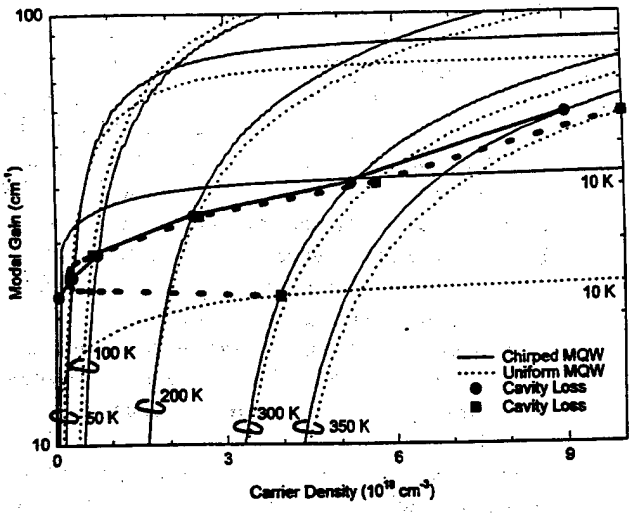


Fig. 4. Calculated modal gain as a function of carrier density for the uniform MQW VCSEL and the chirped MQW VCSEL for various temperatures. The estimated cavity losses at the different temperatures are indicated as bold symbols connected with bold curves.

QW with significant modal gain [Fig. 1(c)], and the threshold carrier density (and thus the threshold current) remains at a lower level down to 5 K. Therefore, by spectrally broadening the gain, the mode remains aligned with the gain peak over a larger range of temperatures.

As was shown in [2], the thermal stability of the cryogenic VCSEL's at low temperatures is not primarily caused by thermal self-heating, but by the reduced thermal de-tuning at very low temperatures. This has been further improved in the new chirped MQW structure by spreading out the gain spectrum to improve its stability against thermal detuning, by providing a high-modal gain over a broader range of temperatures (5–350 K), and by maintaining mode-gain alignment from 5–100 K.

Fig. 4 shows the calculated modal gain of both structures as a function of carrier density for various temperatures. To obtain an estimate of the threshold carrier density, the cavity loss has been estimated as a function of temperature. These losses consist primarily of the mirror loss, which is relatively insensitive to temperature [5] and the free carrier absorption loss, which is temperature-dependent [6]. By equating the total cavity loss with the modal gain at each temperature, the threshold carrier density has been obtained as a function of temperature (bold traces in Fig. 4), which is also plotted in the inset of Fig. 1. This clearly illustrates the higher modal gain and therefore lower threshold carrier density that are obtained at lower temperatures in the chirped MQW structure, which resulted in the very low threshold currents that were observed below 100 K. It also qualitatively explains the comparable threshold behavior in the 150–200-K regime, and the improved performance above 250 K. The calculations of Fig. 4 show that the lasing threshold for the two structures should be nearly the same at 100 K, while a comparison of the individual gain spectra shown in Fig. 3 for the corresponding carrier densities appears to suggest that the composite modal gain of the four uniform quantum wells is higher than that of the chirped quantum wells, and thus its threshold would be lower at 100 K. In fact, the actual difference is much smaller as a result of the differences in the optical field overlap factor for each well, which weigh more heavily the gain contributions from the two inner quantum wells in either structure. The composite gain for the uniform MQW's, while higher than that of the chirped quantum wells, is not four times the gain of a single well due to differences in the optical confinement. While the present model suffices to predict meaningful qualitative differences between the temperature behavior of the two structures, precise quantitative comparison with experiment is difficult due to variations in epitaxial growth conditions.

In these calculations, it was assumed that the carriers injected into the GRINSCH structure of the active region are distributed into the different quantum wells with equal probability, thereby yielding a uniform carrier density in the different quantum wells, whose carrier distributions are not in internal equilibrium (nonuniform quasi-Fermi levels). This assumption may be valid at lower temperatures, where inter-well carrier transport is impeded by poor thermal activation, but may not be so near room temperature [7]. To resolve the issue of carrier distribution amongst wells requires a detailed investigation of the carrier transport and recombination processes at different temperatures, which is beyond the scope of this work. A rigorous comparison of the threshold current and threshold carrier density must also take account of the recombination mechanisms, the quantum efficiency, and the role of the transverse modes.

In conclusion, we have achieved optimized VCSEL performance over a wider range of cryogenic temperatures by spectrally broadening the gain spectrum through the use of chirped quantum wells. Sub-milliamp threshold current was achieved in the temperature range from 5–50 K, which reflects the expanded range of mode-gain alignment, and efficient CW operation was achieved over a wide temperature range from 5–350 K. This approach can also be applied to improve the high-temperature operation of VCSEL's.

REFERENCES

[1] B. Lu, W.-L. Luo, C. Hains, J. Cheng, R. P. Schneider, K. D. Choquette, K. L. Lear, S. P. Kilcoyne, and J. C. Zolper, "High-efficiency, and high-power vertical-cavity surface-emitting lasers designed for cryogenic applications," *IEEE Photon. Technol. Lett.*, vol. 7, no. 5, pp. 447–448, 1995.

[2] G. Goncher, B. Lu, W.-L. Luo, J. Cheng, S. Hersee, S. Z. Sun, R. P. Schneider, and J. C. Zolper, "Cryogenic operation of AlGaAs–GaAs vertical-cavity surface-emitting lasers at temperatures from 200–6 K," *IEEE Photon. Technol. Lett.*, vol. 8, no. 3, pp. 316–318, 1996.

[3] B. Lu, Y.-C. Lu, J. Cheng, R. P. Schneider, J. C. Zolper, and G. Goncher, "Gb/s cryogenic optical link using optimized low-temperature AlGaAs–GaAs vertical-cavity surface-emitting lasers," *IEEE J. Quantum Electron.*, vol. 32, no. 8, Aug. 1996.

[4] M. Kajita, T. Kawakami, M. Nido, A. Kimura, T. Yoshikawa, K. Kurihara, Y. Sugimoto, and K. Kasahara, "Temperature characteristics of a vertical-cavity surface-emitting laser with a broad-gain bandwidth," *IEEE J. Select. Topics Quantum Electron.*, vol. 1, no. 2, pp. 654–660, June 1995.

[5] J. S. Blakemore, "Semiconducting and other major properties of gallium arsenide," *J. Appl. Phys.*, vol. 53, no. 10, pp. R123–R181, 1982.

[6] W. G. Spitzer and J. M. Whelan, "Infrared absorption and electron effective mass in n-type gallium arsenide," *Physical Rev.*, vol. 114, no. 1, pp. 59–63, 1959.

[7] P. A. Evans, P. Blood, and J. S. Roberts, "Carrier distribution in quantum well lasers," *Semiconduct. Sci. Technol.*, vol. 9, no. 9, pp. 1740–1743, 1994.

Gigabit-per-Second Cryogenic Optical Link Using Optimized Low-Temperature AlGaAs–GaAs Vertical-Cavity Surface-Emitting Lasers

Bo Lu, *Member, IEEE,* Yin-Chen Lu, Julian Cheng, *Senior Member, IEEE,* Richard P. Schneider, *Member, IEEE,* John C. Zolper, *Member, IEEE,* and Gary Goncher, *Member, IEEE*

***Abstract*— We describe the design of GaAs–AlGaAs vertical-cavity surface-emitting lasers (VCSEL's) that are optimized for operation at very low temperatures and the experimental demonstration of a free-space optical interconnect for cryogenic electronic systems using a VCSEL. We demonstrate high-speed modulation of the optical link at a data rate of up to 2 Gb/s at 77 K, with a very low bit-error rate of $<10^{-13}$, and thermally stable operation is achieved over a wide range of cryogenic temperatures without laser bias current compensation. Cryogenic VCSEL's with excellent lasing characteristics have been achieved over the entire temperature range from 150 K to 6 K, including high output power (22 mW), high power-conversion efficiency (32%), high slope efficiency (~100%), low threshold voltage (1.75 V) and current (1.7 mA), as well as a high-modulation bandwidth (12 GHz) for a 16 μm diameter device at 80 K.**

I. Introduction

MICROCAVITY semiconductor lasers operating at cryogenic temperatures offer superior lasing performance as a result of a higher differential-gain coefficient, a higher quantum efficiency, lower losses, lower noise [1], higher modulation bandwidth, lower power dissipation, and a higher power-conversion efficiency. Studies of the temperature dependence of vertical-cavity surface-emitting lasers (VCSEL's) [2]–[4] have shown that their slope and power efficiencies, optical output power, and power dissipation all improve dramatically as the temperature is reduced, which suggests that these microlasers are well suited as an optical source for cryogenic applications. In fact, the performance of VCSEL's at low temperatures can significantly exceed their room-temperature characteristics. Some of these characteristics, such as high efficiency and low power dissipation, make cryolasers particularly appealing for use as optical data links or free-space optical interconnects between low-temperature electronics in a hermetic cryogenic environment and external room-temperature electronics, taking advantage of the higher performance (higher speed and lower noise) of both the electronics and the diode laser at low temperatures. In space applications, extremely low temperatures are easily obtained, and in other applications, liquid nitrogen temperatures are becoming more practical due to the dramatic reduction in refrigeration cost. VCSEL's are particularly attractive for many of these applications since their surface-normal geometry and superior beam characteristics, such as small angular divergence and symmetrical beam shape, simplify optical coupling and packaging, making it easier to implement a free-space optical interconnect. It would also obviate the need for a fiber feedthrough, thus providing optical isolation without increasing thermal loss or package complexity.

As the operating temperature of a semiconductor laser is lowered, its performance typically improves due to an increase in the differential gain coefficient as well as an improved quantum efficiency. At low temperatures, the calculated gain of GaAs is much higher than that at room temperature at an equivalent current density, as a result of the narrower width of the gain spectrum [5]. For edge-emitting lasers, the threshold current decreases, while the slope efficiency increases monotonically with temperature down to as low as 5 K [6]. Their modulation frequency response at a constant output power typically increases with decreasing temperature, when not limited by parasitic elements in the laser structure or the contacts. These properties make it advantageous to operate lasers at low temperatures. VCSEL's, on the other hand, typically exhibit a somewhat parabolic dependence of threshold current on temperature, [7]–[10] which derives from the thermally-induced detuning of the lasing mode, the gain peak and the increased self-heating that results. The wavelengths of the gain peak and the Fabry–Perot resonance shift with temperature at different rates, since the temperature coefficient of the bandgap is significantly larger than that of the optical index or the cavity length. Some deleterious consequences of the misalignment are increases in the operating current and voltage, which increase the power dissipation. This can be alleviated by designing a VCSEL whose lasing mode and gain peak are intentionally detuned at

Manuscript received August 28, 1995; revised March 25, 1996. This work was supported in part by the Air Force Office for Scientific Research and the DARPA/ETO Optoelectronics Program, by DOE Contract DE-AC04-94AL85000, and by ARPA High Temperature Superconductor Program under Contract MDA972-92-C-0011.

B. Lu was with the Center for High Technology Materials, University of New Mexico, Albuquerque, NM 87131 USA. He is now with SDL, Inc., San Jose, CA USA.

Y.-C. Lu was with the Center for High Technology Materials, University of New Mexico, Albuquerque, NM 87131 USA. He is now with ArrayComm, San Jose, CA USA.

J. Cheng is with the Center for High Technology Materials, University of New Mexico, Albuquerque, NM 87131 USA.

R. P. Schneider was with the Sandia National Laboratories, Albuquerque, NM 87185 USA. He is now with Hewlett-Packard Laboratories, Palo Alto, CA USA.

J. C. Zolper is with the Sandia National Laboratories, Albuquerque, NM 87185 USA.

G. Goncher is with Tektronix, Inc., Beaverton, OR 97077 USA.

Publisher Item Identifier S 0018-9197(96)05590-X.

0018–9197/96$05.00 © 1996 IEEE

room temperature, but which become aligned at a designated lower temperature. This cryogenic VCSEL should then have lower threshold current and many of the same advantages that have been observed for cryogenic edge-emitting lasers. In practice, this is difficult to achieve, since efficient VCSEL operation at cryogenic temperatures requires a low operating voltage as well as a low threshold current, but the voltage and impedance of the VCSEL become unacceptably high at low temperatures [11], as the energy barriers at their hetero-interfaces become increasingly prohibitive to carrier transport when its height ΔE far exceeds the thermal energy kT. Their electrical characteristic at very low temperatures becomes increasingly nonlinear, often exhibiting a negative differential resistance. We will show that electrical transport can be greatly improved by tailoring the interfaces through continuous parabolic grading and/or selective doping, which produced lower voltages even at temperatures as low as 6 K.

In this paper, we discuss the design of VCSEL's that are optimized for operation at cryogenic temperatures ranging from 6 K to 150 K, by minimizing the threshold current and operating voltage to reduce the power dissipation and increase the power efficiency. We will demonstrate improved lasing characteristics at cryogenic temperatures, including a higher power efficiency, lower and more thermally stable threshold characteristics, and a larger modulation bandwidth. We will also describe the large-signal modulation characteristics of cryogenic VCSEL's at very low temperatures and show that a data rate of >2 Gb/s can be easily achieved at 77 K. We will also show that the modulation response is thermally stabilized across a temperature range of greater than 150 K under fixed operating conditions (constant drive current) without feedback current control.

Finally, we describe a cryogenic optical read-out link that uses a GaAs–AlGaAs cryogenic VCSEL and free-space to communicate high-speed optical data from the cryogenic medium to an external receiver. We will experimentally demonstrate the operation of an efficient cryogenic optical link that that can be driven by low-voltage CMOS circuits and which provides high-speed (up to 2 Gb/s), low-power dissipation (<10 mW), high-tolerance optical coupling, a very low bit-error rate (10–13), and stable operation over a wide temperature range.

II. Low-Temperature Characteristics of VCSEL's That are Optimized for High-Temperature Operation

The development of VCSEL's has made great strides in recent years, having achieved excellent room-temperature operating characteristics, including very low threshold current [12] and voltage [13], a low-series resistance [11], thermally stable electrical characteristics [11], and a high-power conversion efficiency [14]. The room temperature operation of proton-implant-isolated VCSEL's is generally limited by their relatively small slope efficiency and power-conversion efficiency, which are typically less than 50% and 20%, respectively. However, the external slope efficiency and the output power of proton-implant-isolated AlGaAs–GaAs VCSEL's improve dramatically as the temperature is decreased. Fig. 1(a) shows the light-current characteristics of a 16-μm-diameter VCSEL at temperatures ranging from 400 K to 90 K, showing a very high slope efficiency (>90%) and a maximum output power of 13 mW at 90 K [Fig. 1(b)]. These results suggest that VCSEL's can achieve superior performance at cryogenic temperatures. However, because this device was designed for optimum operation at room temperature, its threshold current and voltage increase monotonically with decreasing temperature as the lasing mode and gain peak become misaligned, thus resulting in a very large thermal dissipation and a low power-conversion efficiency at cryogenic temperatures, which must be corrected.

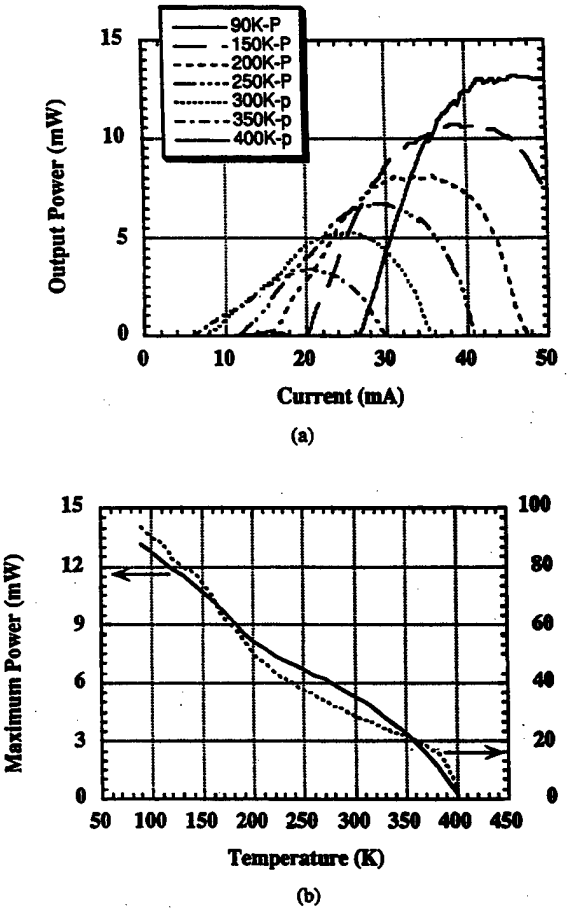


Fig. 1. (a) Light-current characteristics of a 16-μm-diameter VCSEL designed for optimum operation at room temperature, at temperatures ranging from 90 K to 400 K. (b) Its output power and differential slope efficiency as a function of temperature, showing an external slope efficiency of >90% at temperatures below 100 K.

III. Design of VCSEL's for Optimum Operation at Cryogenic Temperatures

A. Alignment of the Cavity Mode and Gain Peak at Cryogenic Temperatures

The lasing characteristics of diode lasers are strongly affected by the operating temperature. The threshold current of edge-emitting lasers typically exhibits an exponential dependence on temperature [15], which is given by

$$I_{\mathrm{th}}(T) = I_o \exp(T/T_o) \tag{1}$$

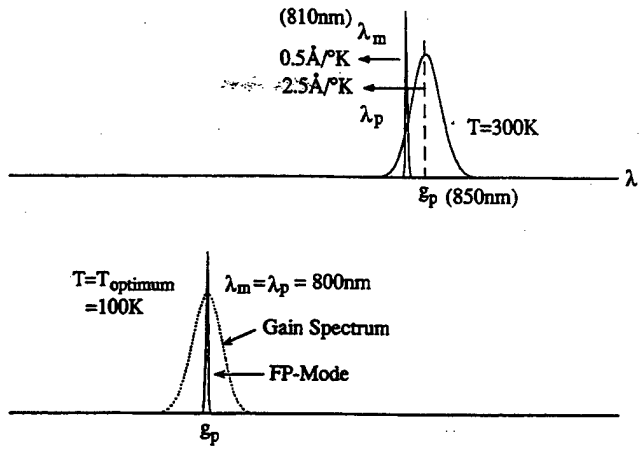


Fig. 2. A model of the temperature-dependent misalignment between the gain peak and the cavity mode, showing that optimum alignment is achieved at a temperature of ~100 K.

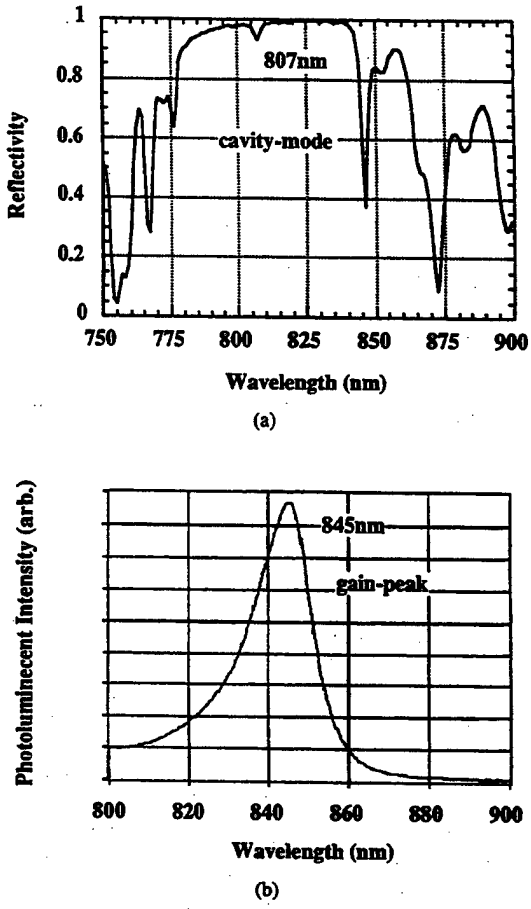


Fig. 3. Experimentally measured (a) photoreflectance and (b) PL spectra, indicating that the cavity mode is at 807 nm and the PL peak is near 845 nm.

where I_o is a constant and T_o is a characteristic temperature that depicts the temperature sensitivity of the lasing threshold. The increase in threshold current with temperature is due to a broadening of the gain spectrum and an increase in nonradiative recombination or carrier leakage [16], [17]. However, the temperature characteristics of VCSEL's are distinctly different from those of edge-emitting lasers, and the threshold cannot be represented simply by (1). For good lasing performance, VCSEL's also require close alignment between its Fabry–Perot cavity resonance and its gain peak, giving an added temperature dependence more pronounced than that governing conventional edge-emitting lasers. Since the gain spectrum has a quasi-parabolic profile, and the cavity mode and gain peak change with temperature at different rates, a parabolic dependence of threshold current on temperature is expected.

The temperature-induced detuning of the cavity mode and the gain peak is illustrated schematically in Fig. 2. The shift of the gain peak with temperature is largely due to the change in bandgap, while the shift of the cavity mode with temperature is related to the change in refractive index. The wavelength of the gain spectrum decreases with temperature at a faster rate (~2.5 Å/K) than the cavity mode (~0.5 Å/K), whose temperature coefficients are estimated from the temperature dependence of the bandgap and the refractive index of GaAs. If the cavity mode is intentionally shifted to the shorter wavelength side of the gain peak at room temperature, the VCSEL must be cooled in order to align the cavity mode and the gain peak, thereby achieving optimum lasing operation at lower temperatures.

In our cryogenic AlGaAs–GaAs VCSEL design, the cavity mode is intentionally blue-shifted with respect to the gain peak at room temperature, so that they become aligned at a lower temperature of ~80 K. The room-temperature photoreflectance spectrum of the VCSEL [Fig. 3(a)] shows that its Fabry–Perot cavity mode is located at 807 nm, while its room-temperature photoluminescence (PL) spectrum [Fig. 3(b)] indicates a peak at ~845 nm. While the lasing wavelength is a direct measure of the cavity mode, the PL spectrum does not provide a precise characterization of the gain spectrum, since it is typically measured at an excitation level that may not represent the conditions that are necessary to achieve lasing. The gain peak is typically red-shifted with respect to the peak of the PL spectrum as a result of the competition between thermal self-heating and carrier-induced band-filling effects, both of which increase with carrier injection. To determine the gain peak of the material at different temperatures more accurately, an edge-emitting laser needs to be fabricated. For InGaAs–GaAs quantum-well ridge-waveguide lasers, the difference between the PL peak and the lasing wavelength is ~5–10 nm [17]. For AlGaAs–GaAs lasers, the difference is expected to be in the same range. Within a few nanometers, the peaks in the PL and gain spectra will closely approximate each other. For our cryogenic VCSEL design with a PL peak at 845 nm at room temperature, the corresponding gain peak is estimated to be at ~850 nm, and the minimum threshold current is expected to be achieved at a temperature between 50 K and 100 K. Since a broad minimum has been observed in I_{th} spanning a wide temperature range [9], [10], the exact temperature at which the minimum threshold current occurs is not critical.

B. The Achievement of Low Operating Voltages and Thermally Stable Electrical Characteristics at Low Temperatures

In order to achieve low power dissipation and a high power-conversion efficiency at low temperatures, in addition

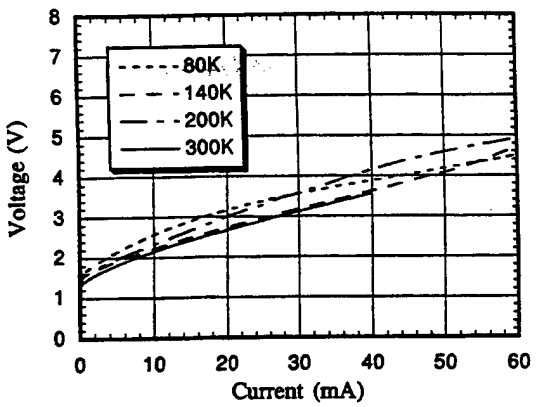
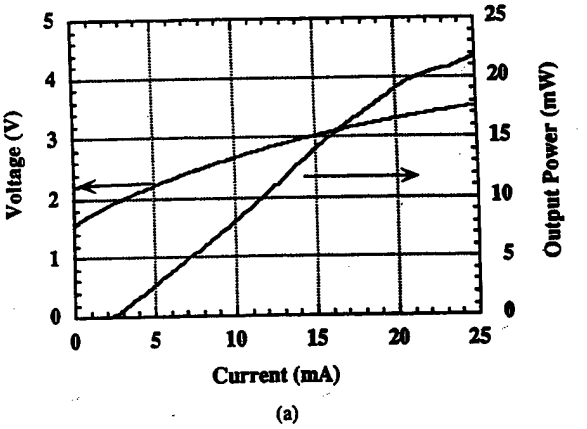


Fig. 4. The current-voltage characteristics of a 20-μm-diameter VCSEL with continuous parabolically-graded heterointerfaces, at temperatures ranging from 80 K to 300 K, showing thermally stable electrical characteristics.

to having a low threshold current and a high slope efficiency, the operating voltage must also be kept low. This is a more formidable obstacle, since the energy barriers at the VCSEL's distributed Bragg reflector (DBR) mirror heterointerfaces become more prohibitive to carrier emission and transport at low temperatures. The current passing through the barriers contains two components, including thermionic emission over the barriers and thermal-assisted tunneling through the barriers, both of which depend on the barrier height and thickness and are strongly temperature-dependent. The problem of the carrier transport across the heterojunctions has been theoretically modeled, and various techniques have been proposed to reduce the barrier height, including compositional grading of the heterointerfaces to reduce the barrier height (E_b) [18], [19] and heavy doping the interfaces to increase the barrier conductivity ($\sigma_\perp$). Most of these approaches depend on epitaxial-growth techniques, such as molecular-beam epitaxy (MBE) for step grading and delta-doping [21], and metalorganic chemical vapor deposition (MOCVD) for continuous compositional grading and selective doping [11]. Among the many approaches that have been studied, continuous grading of the heterointerfaces has thus far produced the lowest barrier height, the lowest series resistance, the lowest threshold voltage and the most thermally stable electrical characteristics [11], [13]. Continuous biparabolic grading of the heterointerfaces using MOCVD has produced a barrier height that approaches barrier-free bulk transport at room temperature [2], [22].

In our cryogenic VCSEL design, the upper and lower DBR mirrors contain 25 and 43.5 pairs of $Al_{0.96}Ga_{0.04}As$ and $Al_{0.25}Ga_{0.75}As$ quarter-wave layers, respectively, whose doping concentration is graded from $1 \times 10^{18}/cm^3$ near the contact surface to $5 \times 10^{17}/cm^3$ near the active region in order to minimize the free-carrier absorption and to reduce the bulk resistance in the DBR mirrors. All the heterointerfaces are graded continuously with a biparabolic profile, in which the Al composition is first varied parabolically from 96% to 65% (convex) and then from 65% to 25% (concave). This resulted in VCSEL's with very low operating voltages (even at 80 K) and thermally stable electrical characteristics. Fig. 4 shows the current-vs-voltage (*I–V*) characteristics of a 20-μm-diameter VCSEL at temperatures ranging from 80 K to 300 K. The



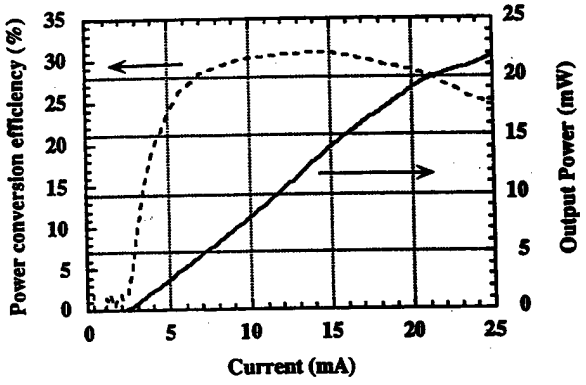


Fig. 5. (a) The light-current and current-voltage characteristics at 80 K, and (b) the power-conversion efficiency at 80 K, of a 20-μm-diameter VCSEL that is optimized for operation at ~100 K.

operating voltages are stable over a very wide temperature range, except for the small temperature dependence of the bandgap, and the carrier transport is ohmic over a large range of drive currents.

IV. The Performance of Cryogenic VCSELs at Low Temperatures (6 K to 150 K)

The performance of the optimized cryogenic VCSEL is improved dramatically at low temperatures, as illustrated by the light-current characteristics [Fig. 5(a)] and the electrical-to-optical power-conversion efficiency η_{eff} [Fig. 5(b)] of a 20-μm VCSEL operating at 80 K. At this temperature, the threshold current and voltage are 2.2 mA and 1.8 V, respectively, and the slope efficiency is 75%, while the maximum output power is 22 mW at a drive current of 25 mA. The light-current characteristic is linear up to a current level of almost $10 \times I_{th}$ (22 mA). The power conversion efficiency has a maximum value of 32%, and stays at a high level ($\eta_{eff} > 28\%$ over a broad range of currents (from 7 mA to 22 mA).

Fig. 6 shows the temperature dependence of V_{th} and I_{th}. The voltages are low (<2.4 V) and, except for the temperature dependence of the bandgap, are relatively stable (0.6 V change) over the entire temperature range from 80 K to 300 K, which is essential for low power dissipation. The minimum threshold current of 1.7 mA (J_{th} = 540 A/cm^2)

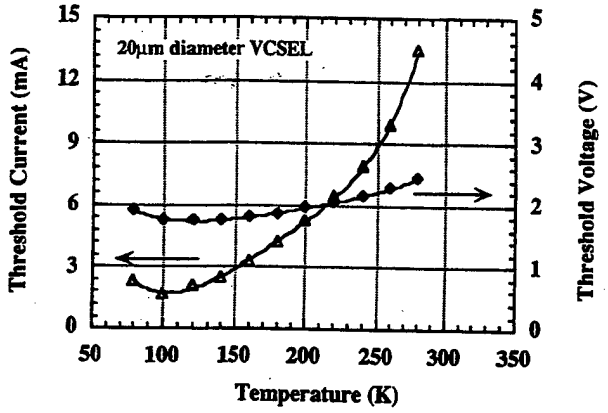


Fig. 6. The temperature dependence of the threshold current and threshold voltage of a VCSEL optimized for low-temperature operation, showing a minimum threshold at 100 K. The stable and low-threshold voltages result from the use of DBR mirrors with biparabolically graded heterointerfaces.

is achieved at 100 K in accordance with our design. The threshold voltage shows a similar temperature dependence with the threshold current. It contains two parts [9], including the voltage drop across the laser junction, and the voltage drop across the series resistance. The temperature variation of the former is dominated by the temperature dependence of the bandgap, while the latter is due to the temperature dependence of the threshold current and the series resistance. Fig. 4 shows that the series resistance remains nearly constant over the temperature range from 100 K to 300 K (40 Ω at 300 K and 50 Ω at 100 K), which results from the use of parabolic grading and selective doping to reduce the energy barrier at the heterointerfaces.

The temperature dependence of the threshold current is determined by several effects, including the mode-gain misalignment, nonradiative and leakage currents, and internal thermal self-heating, which will be discussed below. Submilliampere threshold current has been observed for some 16-μm devices, with I_{th} ~700 μA from 80 K to 5 K, and a corresponding threshold current density of 350 A/cm^2, which is amongst the lowest threshold current density ever achieved by an 850-nm, proton-implant-isolated, AlGaAs–GaAs VCSEL. Fig. 7(a) and (b) show its light-current and voltage-current characteristics at 77 K.

Low power dissipation is essential for cryogenic applications and has been achieved by VCSEL's with a low threshold current and a low operating voltage. Fig. 8 shows the power dissipation as a function of temperature at several constant levels of optical output power, which also represents the power-conversion efficiency, $\eta_{eff} = P_{out}/P_d$, as a function of temperature and bias current. At the optimum temperature (100 K), the power dissipation is 3 mW at threshold, 6 mW for P_{out} = 1 mW, 9 mW for P_{out} = 2.0 mW, and 32 mW for P_{out} = 10 mW. The low power dissipation at 80 K is a consequence of the lower operating voltage and current that have been achieved by design, as well as the high slope efficiency that results from a higher differential gain coefficient and a lower internal loss at low temperatures.

In some cryogenic applications of diode lasers, the operation temperature may be lower than 77 K. To see how the cryogenic

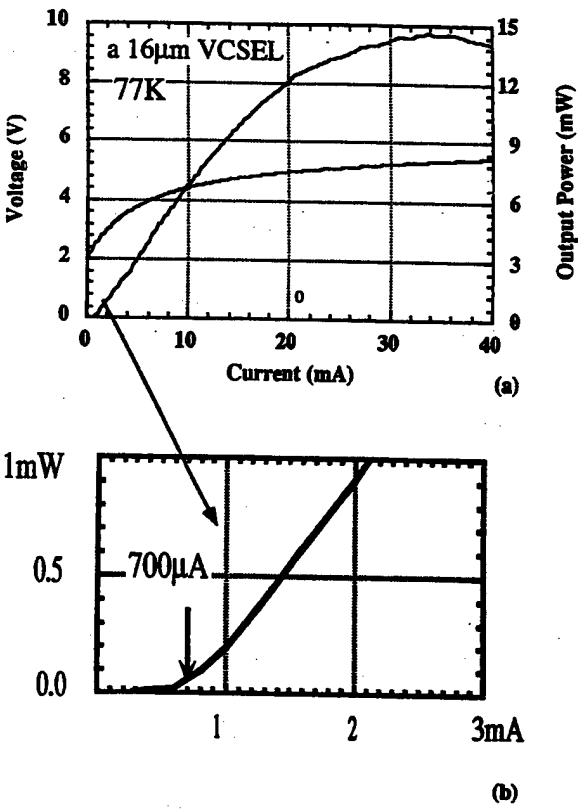


Fig. 7. (a) The dc electrical and lasing characteristics [magnified view in (b)] of a 16-μm-diameter cryogenic VCSEL at 80 K, which shows a threshold current of 700 μA, corresponding to a threshold current density of 350 A/cm^2. The threshold current remains close to 700 μA at temperatures down to 5 K, and the threshold voltage stays below 3 V.

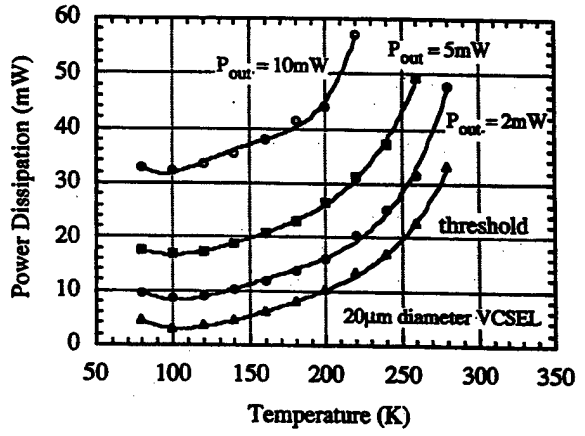


Fig. 8. The power dissipation of an optimized cryogenic VCSEL as a function of temperature, at several levels of constant optical output power.

VCSEL's that are designed for optimum operation at ~100 K perform at even lower temperatures, their characteristics have been measured over the temperature range from 6 K to 200 K. We found that the VCSEL's performance remains optimal, even improving somewhat, at temperatures as low as 6 K. The VCSEL's used in this study have linearly graded heterointerfaces that are selectively doped to a level of 1×10^{18}/cm^3. Their light-current characteristics at temperatures ranging from 6 K to 200 K are shown in Fig. 9. The optical output power

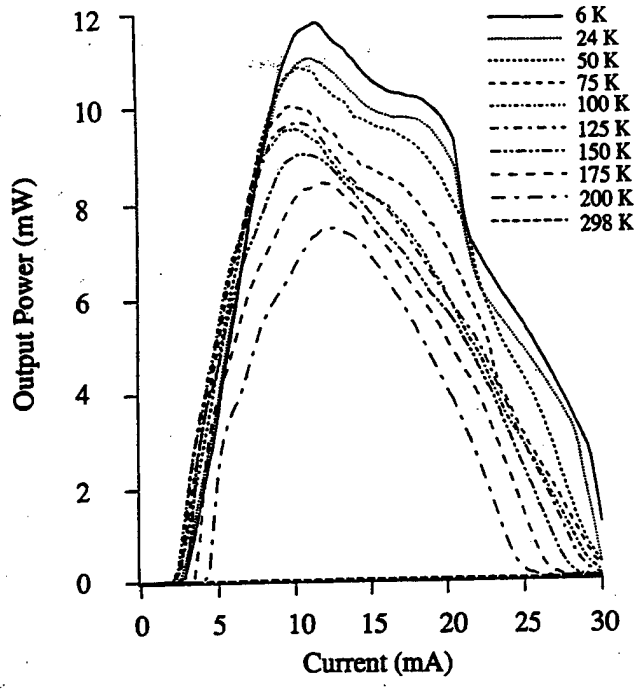


Fig. 9. The dc light-current characteristics of an optimized cryogenic VCSEL with a 16-μm active-area diameter and linearly graded DBR heterointerfaces at low temperatures, showing a relatively constant external slope efficiency of >70% at temperatures below 100 K.

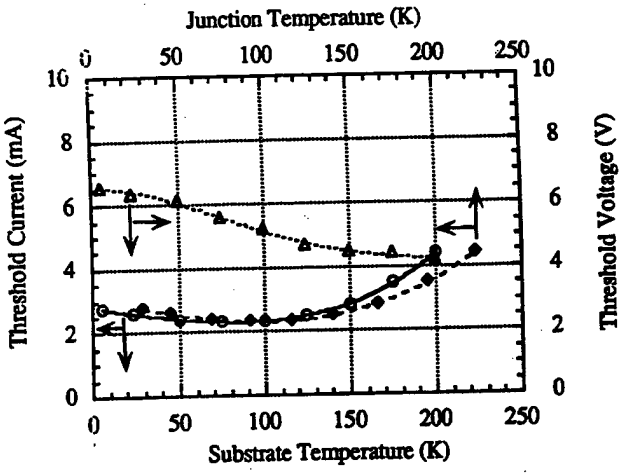


Fig. 10. The temperature dependence of the threshold current and voltage of a 16-μm-diameter VCSEL. Optimum performance is achieved from 6 K to 150 K. The threshold current is also shown as a function of the junction temperature to show the contribution of self-heating.

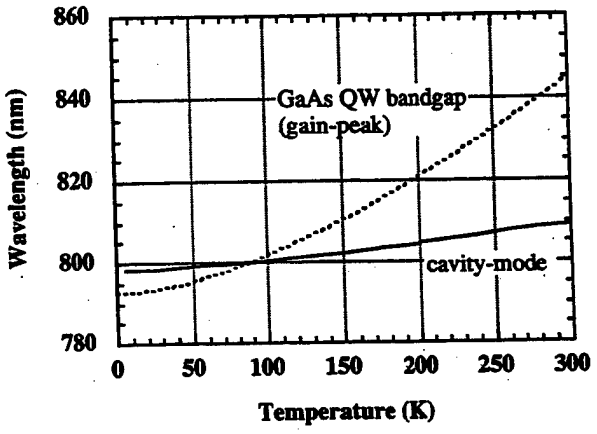


Fig. 11. The temperature dependence of the bandgap (approximating that of the gain peak) of a GaAs–AlGaAs quantum well and the cavity mode of the VCSEL. They show that the gain-mode misalignment is greatly reduced in the temperature range from 100 K to 6 K.

increases monotonically with decreasing temperature, attaining 12 mW at 6 K for a 16-μm device, while the external slope efficiency η_s also increases and approaches 100% at temperatures below 100 K. The increase in slope efficiency is due to an increase in both the internal quantum efficiency η_i and a decrease in the internal loss α_i (consisting mostly of free-carrier absorption), both of which tend to saturate below 100 K, resulting in a saturation of the external slope efficiency that can be seen in the *L–I* characteristics. Saturation of the external slope efficiency has been observed in edge-emitting lasers at temperatures below 100 K [6]. Although internal self-heating can in principle increase the apparent slope efficiency, this is not a dominant effect, as will be explained below.

The *L–I* characteristics show that the threshold current increases only marginally over the temperature range from 6 K to 100 K. The temperature dependence of the threshold current and voltage from 6 K to 200 K are shown in Fig. 10 for this 16-μm VCSEL. The increase in V_{th} is more pronounced as nonlinear transport across the heterointerfacial barriers imposes its effect on the VCSEL's electrical *(I–V)* characteristics at low temperatures. In contrast, the *L–I* characteristics show improved lasing performance despite the increasingly nonlinear *I–V* characteristics, showing that the slope efficiency remains high and the threshold current remains low.

The stable threshold current at temperatures below 100 K can be understood from the reduced thermal detuning of the cavity mode with respect to the gain peak at very low temperatures. The temperature dependence of the bandgap of III–V compound semiconductors is given by the expression [23]

$$E_g(T) = E_g(0) - \alpha T^2/(T+\beta) \qquad (2)$$

where $E_g(0)$ is the bandgap at $T = 0$ K and for GaAs, $\alpha = 5.402 \times 10^{-4}$, and $\beta = 204$ K. At low temperatures, where $T \ll 204$ K, the rate of increase of the bandgap with decreasing temperature is greatly reduced, and the slower shift in the gain peak now more closely tracks the change in the cavity mode as the temperature is lowered. The temperature coefficient of the lasing mode also decreases significantly at temperatures below 77 K, due to a smaller thermal expansion coefficient and smaller changes in the refractive index with temperature. The cavity mode and the gain peak track each other more closely and remain nearly aligned to each other at temperature below 77 K. This results in more stable threshold characteristics at temperatures between 77 K and 6 K. The temperature dependence of the bandgap and the lasing mode are both plotted in Fig. 11, for temperatures from 60 K to 300 K. The bandgap of the GaAs quantum well (80 Å well width

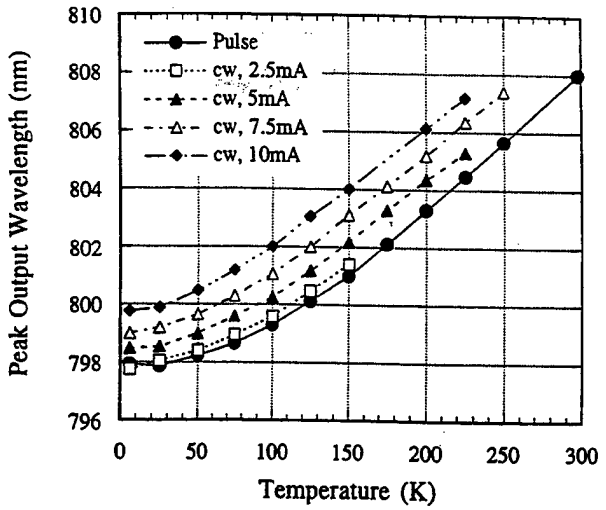
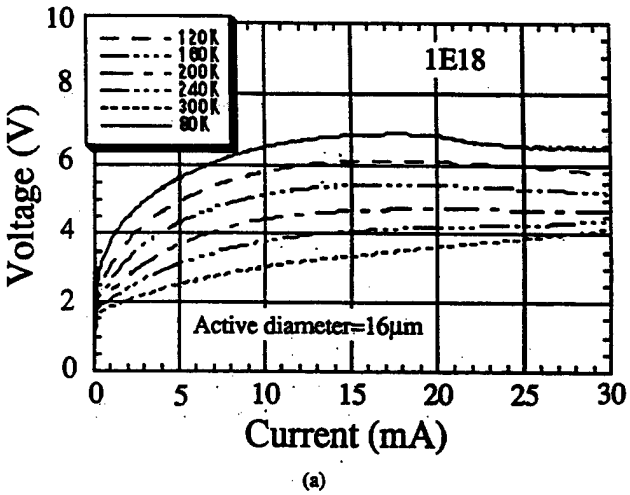


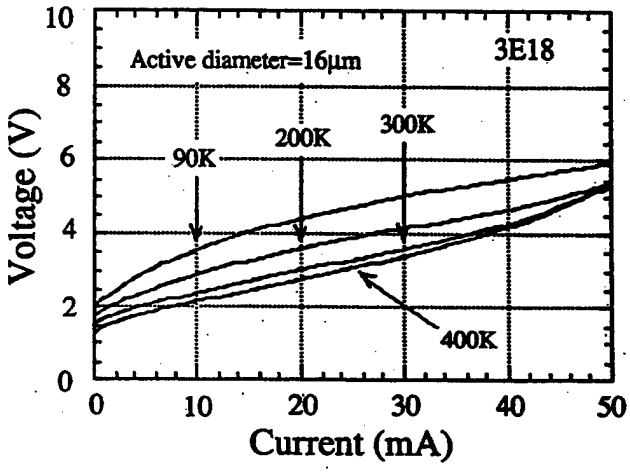
Fig. 12. The lasing wavelength of the VCSEL under pulsed and CW operation at constant bias current levels as a function of temperature.

with 100-Å-thick $Al_{0.15}Ga_{0.85}As$ barriers) is calculated, while the cavity-mode position is experimentally determined from the lasing wavelength of the VCSEL measured at different temperatures under pulsed conditions. Fig. 10 shows that the difference between the wavelengths of the cavity mode and the gain peak is zero at ~80 K (optimum alignment) and is smaller at the lower temperature side of 80 K than at the higher temperature side. Although the bandgap does not provide an accurate determination of the gain peak, its temperature dependence provides a qualitative indication of the temperature dependence of the latter. As discussed earlier, the difference is within a few nanometers.

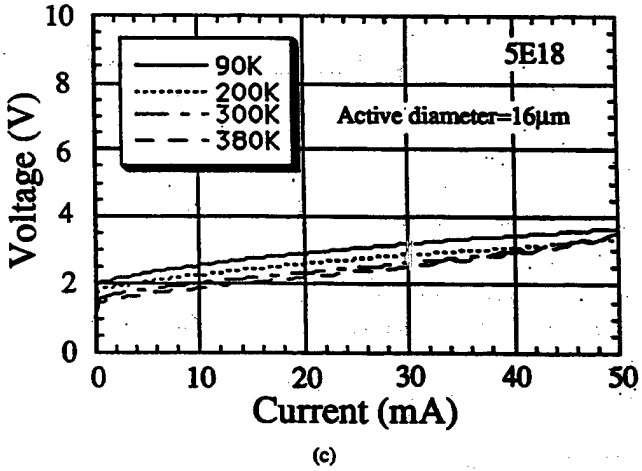
Another reason for the stable threshold current is due to thermal self-heating, which reduces the negative detuning of the lasing mode and the gain peak at the low-temperature side of the optimum alignment point (80 K), thus bringing the cavity mode and the gain peak into even closer alignment. Data for the temperature dependence of the wavelength at the band-edge of GaAs (2) is known to show a reduced temperature coefficient at low temperatures. Experimental measurements of the lasing wavelength of the VCSEL under pulsed (250-ns pulses at 4 kHz) and CW operation at different levels of constant current are compared in Fig. 12. The lasing wavelength varies with temperature in an approximately linear fashion from 125 K to 300 K, and is sublinear below 125 K. Comparison of the pulsed and CW data show that the sublinear temperature dependence of the lasing mode (and thus the refractive index) at low temperatures is intrinsic and is not purely the effect of self-heating. The lasing mode and the gain peak thus track each other more closely below the optimum operating temperature, resulting in a smaller negative thermal detuning (blue-shift) of the lasing mode with respect to the gain peak, which is reflected by a smaller variation of I_{th} with temperature. Their wavelength separation is further reduced by thermal self-heating within the VCSEL, which produces a red-shift of the gain peak that moves it closer to the cavity mode. This contribution of thermal self-heating to I_{th} can be determined by calculating the rise in junction



(a)



(b)



(c)

Fig. 13. The current-voltage characteristics at different temperatures for three VCSEL's with continuous linearly graded heterointerfaces but different doping concentrations of (a) $1 \times 10^{18}/cm^3$, (b) $3 \times 10^{18}/cm^3$, and (c) $5 \times 10^{18}/cm^3$.

temperature (~25 K), using the value of thermal resistance ($R_{th} \sim 1000$ K/W) that is obtained from Fig. 12 by comparing the corresponding temperatures at which the pulsed and CW

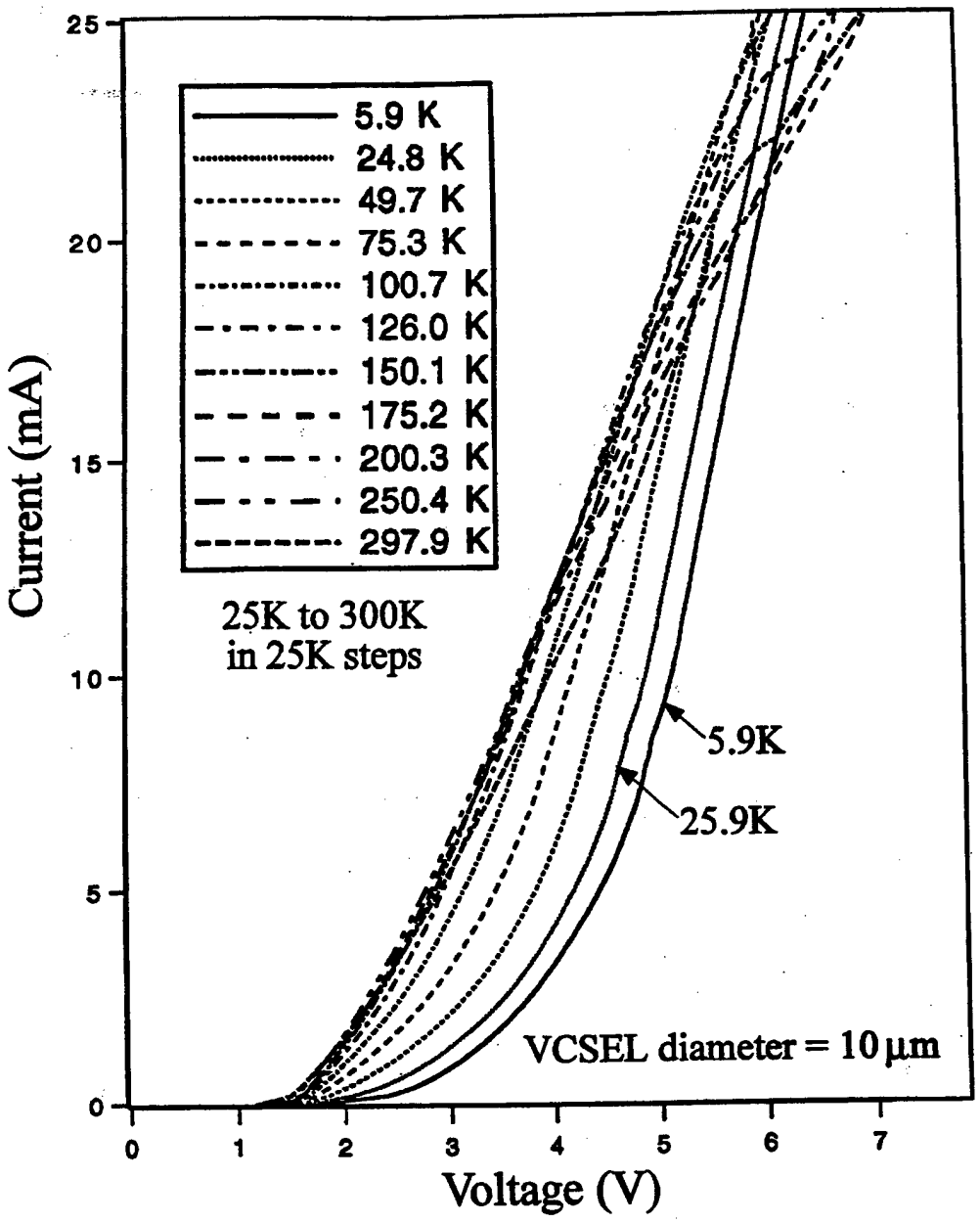


Fig. 14. The temperature dependence of the current-voltage characteristics of a 10-μm-diameter VCSEL with biparabolically graded mirror heterointerfaces.

operations produce the same emission wavelengths (see [9]). By plotting I_{th} as a function of both the substrate temperature (T_s) and the junction temperature (T_j), Fig. 10 shows that the change in I_{th} caused by self-heating is <10% below 150 K, and is <20% from 150 K to 200 K. Thus, the temperature dependence of I_{th} is for the most part intrinsic and is small as a result of the smaller rate of thermal detuning at low temperatures.

For this device, the operating voltage becomes high as the temperature is reduced below 77 K. From 150 K to 6 K, the electrical characteristics become increasingly nonlinear, with V_{th} increasing monotonically from 4.5 V to 6.5 V, which is due to the low doping concentration and higher barriers in the linearly graded heterointerfaces ($1 \times 10^{18}/cm^3$). For linearly graded heterointerfaces, the high doping plays a very important role in reducing the barrier height, which has been studied theoretically and was demonstrated experimentally using the temperature-dependence of the electrical characteristics [11]. Fig. 13 compares the voltage-versus-current characteristics of three VCSEL's with the same linearly graded heterointerfaces but different doping concentrations of $1 \times 10^{18}/cm^3$ [Fig. 13(a)], $3 \times 10^{18}/cm^3$ [Fig. 13(b)] and $5 \times 10^{18}/cm^3$ [Fig. 13(c)], respectively, at different temperatures ranging from 400 K to 80 K. The highest doped VCSEL has the most thermally stable electrical characteristics. Due to a relatively high operating voltage, the power efficiency of this VCSEL is relatively low (23% at 77 K, 20% at 6 K) compared to our previous result (32% at 77 K) for a 20-μm VCSEL with biparabolically graded heterointerfaces [2]. To further improve the low-temperature power efficiency, the operating voltage

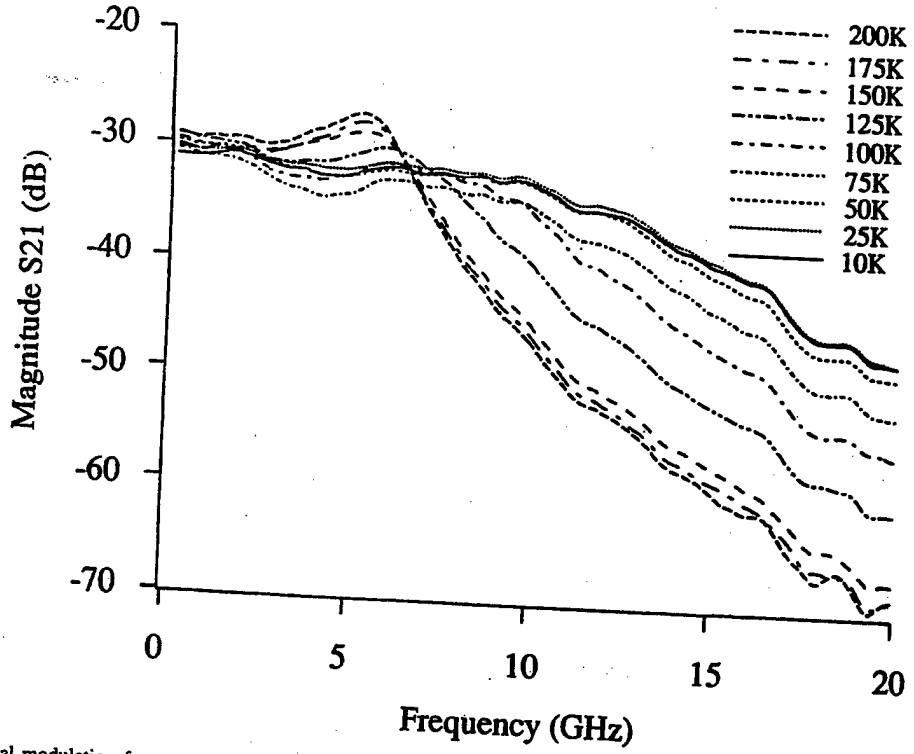


Fig. 15. The small-signal modulation frequency response of a 16-μm-diameter VCSEL at temperatures from 200 K to 10 K.

must be reduced, either by heavier doping of the interfaces, which would increase the internal loss and thus the threshold current, or by using parabolic grading. A parabolically graded heterointerface results in the lowest barrier height and thus gives rise to a smaller variation of the operating voltage with changing temperature, even when the doping concentration at the interfaces is low (e.g., $5 \times 10^{17}/\text{cm}^3$) [11], [23].

A 10-μm-diameter VCSEL with biparabolically graded DBR heterointerfaces that is specifically designed for low-temperature operation has been tested, showing improved I–V characteristics (Fig. 14) with no sign of negative differential resistance at temperatures as low as 6 K. At the minimum point of the I_{th} versus temperature curve, we have $V_{\text{th}} = 2.8$ V and $I_{\text{th}} = 3.5$ mA at 75 K, and $V_{\text{th}} = 4.2$ V and $I_{\text{th}} = 4.1$ mA at 6 K.

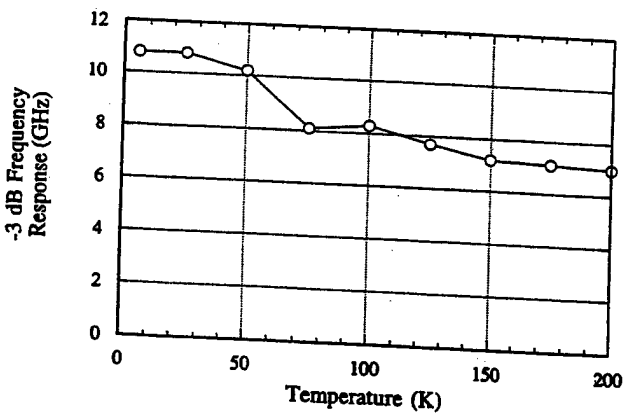


Fig. 16. The −3-dB modulation bandwidth of the 16-μm-diameter VCSEL as a function of temperature, showing a 70% improvement from 200 K to 10 K.

V. The Small-Signal Optical Modulation Response of VCSEL's at Cryogenic Temperatures

Another advantage of diode lasers operated at cryogenic temperatures is the higher modulation bandwidth that can be achieved, due to the combination of a higher differential gain coefficient, a lower threshold current, higher efficiency, and potential single-mode operation over a much wider current range (larger I/I_{th}). For VCSEL's, the situation is complicated by the gain-mode mismatch, one consequence of which is that the lasing performance does not necessarily improve as the temperature is reduced. But for VCSEL's whose lasing mode and gain peak are designed to be aligned at low temperatures, an improvement in bandwidth can be expected. Fig. 15 shows the small-signal modulation response of a 16-μm-diameter VCSEL with linearly graded interfaces at temperatures ranging from 10 K to 200 K. Fig. 16 shows its −3-dB modulation bandwidth as a function of temperature, which is 8.1 GHz at the temperature of minimum threshold (~100 K), and is 10.8 GHz at 10 K. The bandwidth increases with decreasing temperature, with an ~70% improvement from 200 K to 10 K. The relatively small bandwidth is limited by the parasitic capacitance and resistances that are inherent in a proton-implant-isolated VCSEL structure and by the multimode behavior of this relatively large-diameter device.

VI. The Application of VCSEL's in a Cryogenic Optical Data Link

In addition to their significantly improved performance at low temperatures, VCSEL's also have a small-beam divergence angle and circular-beam characteristics that facilitate

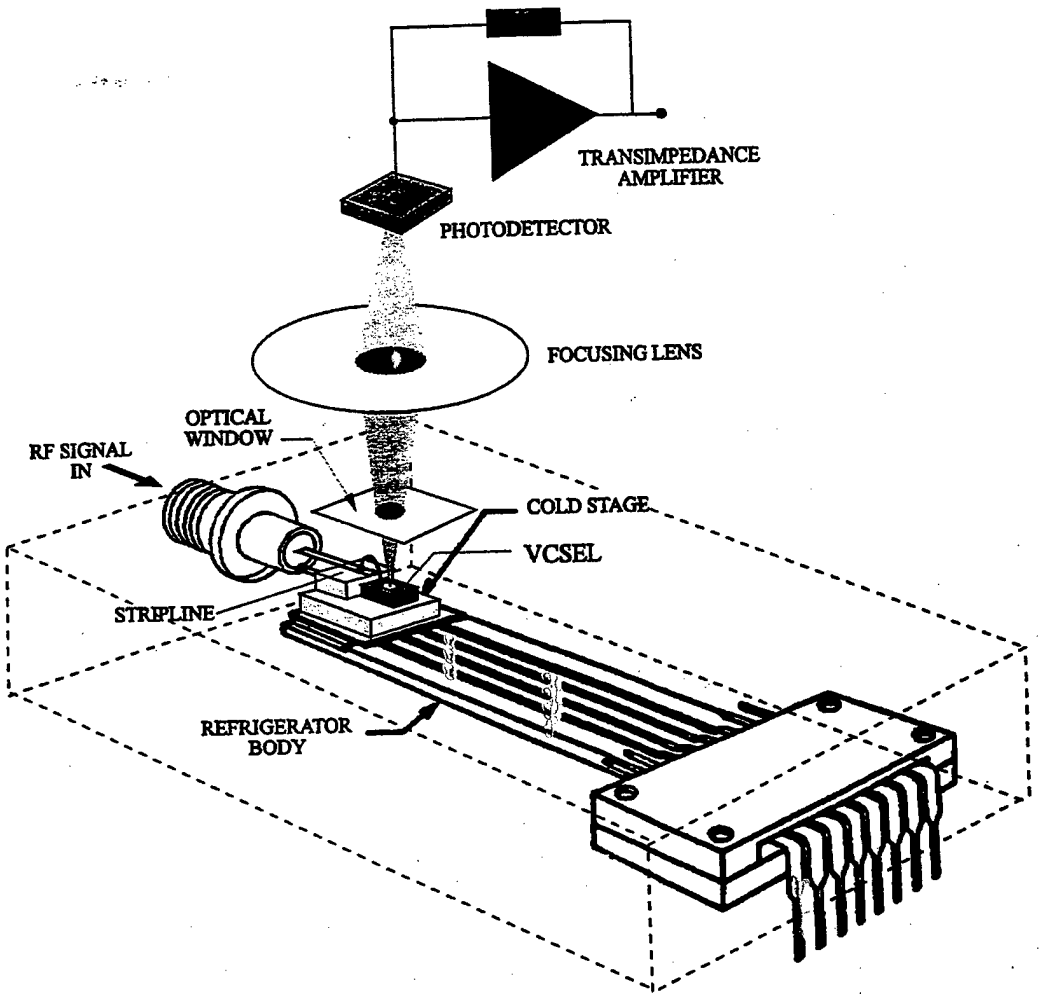


Fig. 17. Configuration of a high-speed cryogenic optical data link using an optimized VCSEL as the optical source and a free-space optical interconnect geometry.

optical coupling through an optical fiber or free space. Moreover, properly designed VCSEL's can maintain their stable lasing characteristics over a very wide range of temperatures, e.g., from 100 K to 200 K (Fig. 9), thereby providing an optical interconnect that is stable against thermal variations. For these reasons, VCSEL's are well suited as a high-speed optical source for cryogenic optical data link and optical interconnect applications. Unlike conventional optical communication applications that may require a data rate of 1 Gb/s or more, an optical link for focal-plane array readout currently requires only a relatively modest data rate in the range of 100–500 Mb/s, which is very easy to achieve using VCSEL's operating at cryogenic temperatures. However, since the heat-extraction efficiency of the cooling system is low at cryogenic temperatures, the power dissipation of the optoelectronic components must be minimized in a cryogenic optical data link.

A. Optical Readout for Cryogenic Focal-Plane Arrays

Infrared imaging systems have evolved from the early single focal-plane detector to a linear array with a line-scan mechanism and to larger two-dimensional (2-D) focal-plane arrays (FPA's). These have many military and industrial applications, ranging from atmospheric imaging and target search to noncontact surface examination, process monitoring and control in manufacturing. To minimize the thermal noise, these detector arrays are often housed in a hermetic cryogenic chamber and operate at temperatures below 100 K.

In a FPA, the sensor array is usually flip-chip bonded to the multiplexing readout circuit, from which electrical cables carry the signal to the external signal-processing electronics at room temperature. With increasing array size and more complicated image-processing requirements, the trend is to integrate more of the pre-processing functions, such as signal preamplification and A-to-D conversion, with the FPA within the cryo-chamber. As the required data throughput is increased, data transmission from the cryo-chamber to higher levels of external signal processing must occur at an increasingly higher data rate. The use of high-frequency electrical cables (especially for parallel links) increases thermal leakage as well as power dissipation within the chamber. A free-space optical link, on the other hand, provides a noninvasive optical connection between electronics in a hermetic cryogenic environment

and external electronic processors at room temperature. By eliminating the electrical wires, an optical link can provide a much larger bandwidth, lower thermal dissipation, and also a much longer link span.

B. Implementation of a VCSEL-Based Free-Space Optical Interconnect

To demonstrate the use of the VCSEL as a high-speed light source for a low-temperature free-space optical link, a 20-μm-diameter VCSEL with an optimum operating temperature of 77 K is mounted in a high-speed package that resides on a cold finger that is housed within a cryogenic chamber without any fiberoptic feed-through. Fig. 17 shows the configuration of the cryo-chamber and the experimental set-up for characterizing the high-frequency performance of a free-space optical interconnect using the VCSEL at low temperatures. The cooling system is a Joule–Thomson refrigerator, which is a vacuum chamber containing a thermal stage with a cold-finger whose temperature can be controlled from 80 K to 580 K, and which is thermally isolated from the external environment by the vacuum. The VCSEL sample is mounted on the thermal stage using a silicone heat-sink compound. For high-speed operation, the chamber is modified to provide electrical access to the VCSEL through a high-speed SMA launcher, which is located in close proximity to the thermal stage. To reduce the length and inductance of the wire bond, an intermediate ceramic strip containing a 50-Ω stripline is placed between the launcher and the sample. The light produced by the modulated VCSEL propagates through free space and is coupled out of the cryo-chamber through an optical window situated ~2 cm above the VCSEL's emitting surface. An external lens then focuses this low-divergence beam into the optical aperture (200 μm diameter) of a high-speed p-i-n photodetector, followed by a transimpedance preamplifier and a high-gain limiting ampifier that produces compatible logic output levels, and the eye diagrams are recorded by a communication-signal analyzer. The VCSEL is digitally modulated by a NRZ pseudorandom data sequence from a pattern generator, with a word length of $(2^{23} - 1)$ bits and a data rate of up to 2 Gb/s. The temperature of the cryo-chamber is varied in steps, while the bit-error-rate measurement is carried out at a constant temperature so that no error is accrued during the transitional periods.

The eye diagrams in Fig. 18 depict the modulation performance of the cryogenic optical link at 77 K under large-signal electrical modulation by NRZ pseudorandom data at a data rate of 2 Gb/s, 1 Gb/s, 500 Mb/s, and 200 Mb/s, respectively. The rise and fall times are limited by the speed of the photodetector, and modulation at a data rate >2 Gb/s is possible, as indicated by the small-signal modulation bandwidth of the VCSEL (Fig. 16). The eye-diagram at 1 Gb/s is wide open, and the transmission data accumulated over a long time period (2 h) shows that a bit-error rate of less than 10^{-13} can be achieved.

For cryogenic optical links, thermally stable operation would be desirable, since this would simplify the electric drive circuit by eliminating the need for feedback control to compensate for thermal changes. To establish the thermal

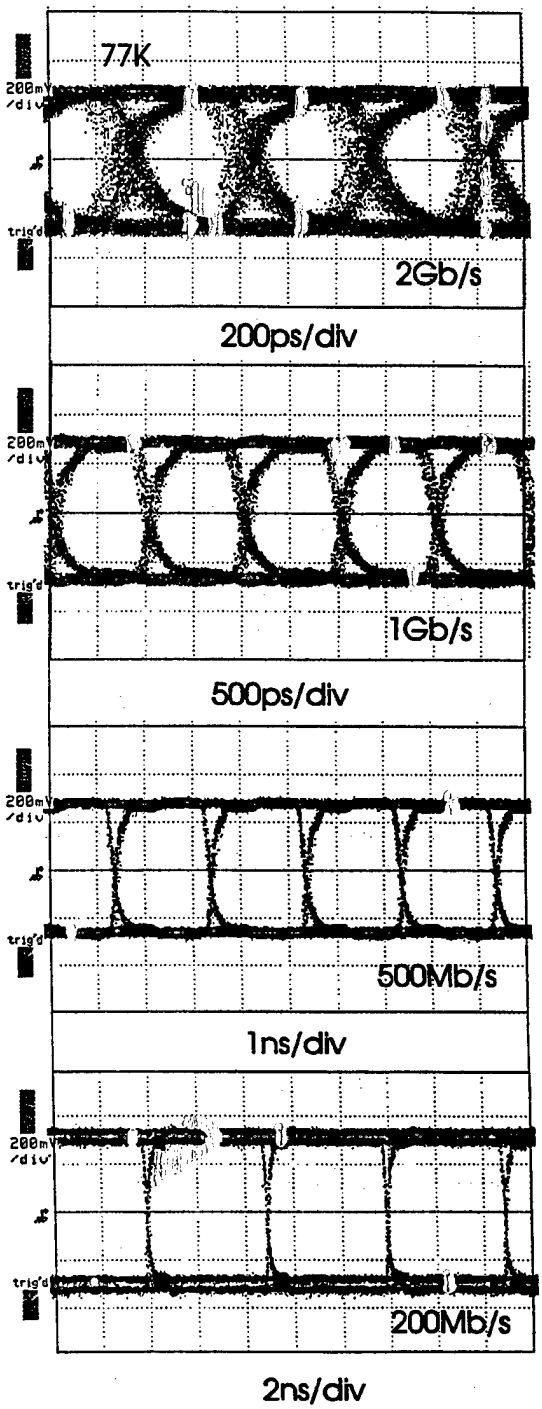


Fig. 18. Eye diagrams showing the large-signal response of the cryogenic optical link at 77 K to pseudorandom electrical modulation at a data rate of 2 Gb/s, 1 Gb/s, 500 Mb/s, and 200 Mb/s, respectively, with the VCSEL under similar bias conditions.

stability of this optical link, its large-signal modulation response has been measured at temperatures ranging from 77 K to 160 K. The eye-diagrams in Fig. 19 demonstrate the results of 1-Gb/s data modulation at temperatures varying from 77 K to 160 K in steps. The cryogenic VCSEL is biased at a fixed drive current (7.0 mA) and is modulated at a constant data rate (1 Gb/s). A comparison of the eye diagrams in

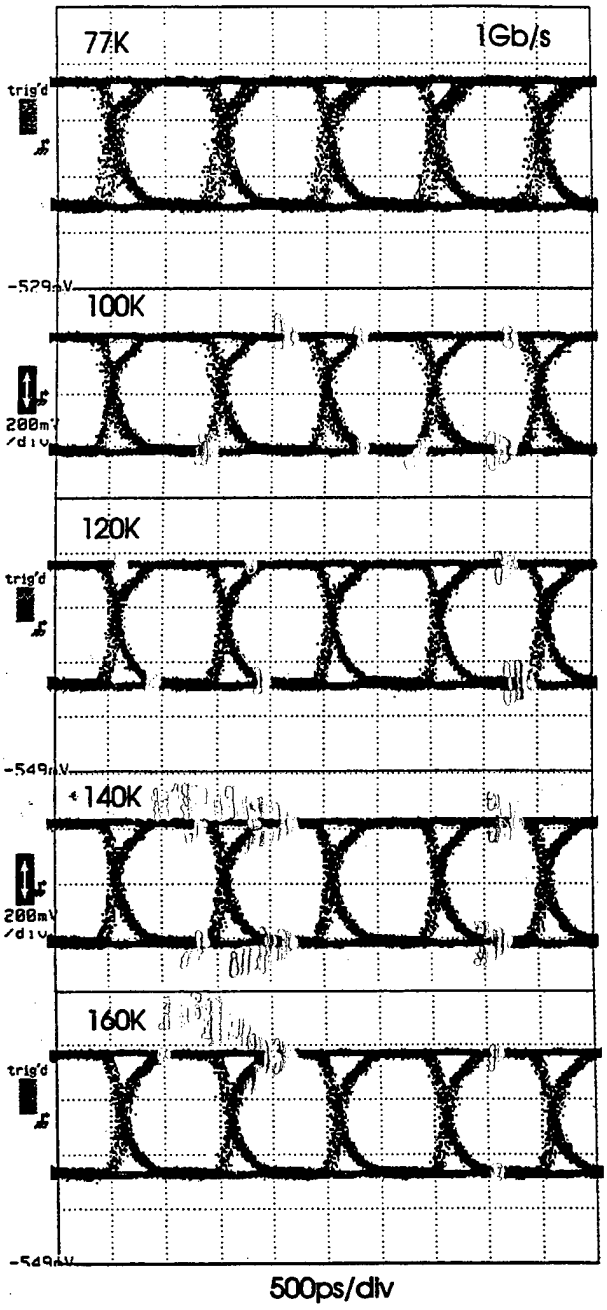


Fig. 19. Eye diagrams showing the nearly constant large-signal response of the cryogenic optical link to 1 Gb/s electrical data modulation, under a fixed current bias (7.0 mA) and at temperatures ranging from 77 K to 160 K.

Fig. 19 shows that a very stable modulation response (similar amplitudes and response times) is obtained over the entire temperature range from 77 K to 160 K. The threshold current of this device is 1.7 mA and threshold voltage is 1.8 V at ~100 K, which result in a low power dissipation. As we have discussed previously, the threshold current is very stable from 100 K to 10 K, once optimum gain-mode alignment is achieved at ~100 K and the slope efficiency saturates at close to 100%. We therefore expect the large signal response to remain stable even at the lower temperatures from 10 K to 77 K, thus providing stable lasing operation over a very wide temperature range from 10 K to 160 K (~150 K wide).

VII. Conclusion

We have designed and demonstrated AlGaAs–GaAs VCSEL's that are optimized for operation at cryogenic temperatures, achieving superior performance that includes lower threshold characteristics, high slope and power efficiencies, lower power dissipation, a wider modulation bandwidth, and thermally stable operation over a wide range of temperatures. Excellent VCSEL performance has been extended to even lower temperatures down to 5 K. The use of VCSEL's as a high-speed optical link for cryogenic applications has also been demonstrated. A free-space optical interconnect configuration has been designed, and high-frequency modulation at a data rate in excess of 2 Gb/s, as well as stable operation over a very wide temperature range of greater than 150 K, have been achieved. High-performance cryogenic VCSEL's thus represent a promising approach for low-temperature optical interconnect applications.

Acknowledgment

The authors gratefully acknowledge the technical assistance of J. Escobedo of Sandia National Laboratory.

References

[1] J. Katz, *Low Temperature Electronics*, R. K. Kirschman, Ed. Piscataway, NJ: IEEE Press, 1986, pp. 465–470.

[2] B. Lu, W.-L. Luo, C. Hains, J. Cheng, R. P. Schneider, K. D. Choquette, K. L. Lear, S. P. Kilcoyne, and J. C. Zolper, "High-efficiency and high-power vertical-cavity surface-emitting lasers designed for cryogenic applications," *IEEE Photon. Technol. Lett.*, vol. 7, May 1995.

[3] E. Goobar, C. Mahon, F. H. Peters, M. G. Peters, and L. A. Coldren, "Low-temperature operation of vertical-cavity surface-emitting laser'", *IEEE Photon. Technol. Lett.*, vol. 7, pp. 7–9, 1995.

[4] ——, "Highly efficient vertical-cavity surface-emitting lasers optimized for low-temperature operation," *IEEE Photon. Technol. Lett.*, vol. 7, pp. 851–853, 1995.

[5] N. K. Dutta and R. J. Nelson, "The case for Auger recombination in $In_{1-x}Ga_xAs_yP_{1-y}$," *J. Appl. Phys.*, vol. 53, p. 74, 1982.

[6] B. Zhao, T. R. Chen, L. E. Eng, Y. H. Zhuang, A. Shakouri, and A. Yariv, "Sub-100μA current operation of strained InGaAs quantum well lasers at low temperatures," *Appl. Phys. Lett.*, vol. 65, pp. 1805–1807, 1994.

[7] G. W. Taylor and P. A. Evaldsson, "Temperature dependent operation of vertical-cavity surface-emitting lasers," *IEEE J. Quantum Electron.*, vol. 30, pp. 2262, 1994.

[8] B. Tell, K. F. Brown-Goebeler, R. E. Leibenguth, F. M. Baez, and Y. H. Lee, "Temperature dependence of GaAs–AlGaAs vertical-cavity surface-emitting lasers," *Appl. Phys. Lett.*, vol. 8, pp. 683–685, 1992.

[9] B. Lu, P. Zhou, J. Cheng, K. J. Malloy, and J. C. Zolper, "High temperature pulsed and CW operation and thermally stable threshold characteristics of vertical-cavity surface-emitting lasers grown by metal-organic chemical vapor deposition," *Appl. Phys. Lett.*, vol. 65, pp. 1337–1339, 1994.

[10] R. A. Morgan, M. K. Hibbs-Brenner, T. M. Marta, R. A. Walterson, S. Bounnak, E. L. Kalweit, and J. A. Lehman, "200 °C, 96-nm wavelength range, continuously-wave lasing from unbonded GaAs MOVPE-grown vertical-cavity surface-emitting lasers," *IEEE Photon. Technol. Lett.*, vol. 7, pp. 441–443, 1995.

[11] P. Zhou, B. Lu, J. Cheng, K. J. Malloy, S. Z. Sun, S. D. Hersee, and J. C. Zolper, "Vertical-cavity surface-emiting lasers with thermally stable electrical characteristics," *J. Appl. Phys.*, vol. 77, pp. 2264–2267, 1995.

[12] M. M. MacDougal, P. D. Dapkus, V. Pudikov, H. Zhao, G. M. Yang, "Use of AlAs oxide/GaAs distributed Bragg reflectors to fabricate ultralow threshold-current vertical-cavity surface-emitting lasers," *Tech. Dig. CLEO'95*, vol. 15, pp. 56–57, 1995.

[13] R. A. Morgan, M. K. Hibbs-Brenner, T. M. Marta, R. A. Walterson, S. Bounnak, F. L. Kalweit, and J. A. Lehman, "200 °C, 96-nm wavelength range, continuous-wave lasing from unbonded GaAs MOVPE-grown vertical-cavity surface-emitting lasers," *IEEE Photon. Technol. Lett.*, vol. 7, pp. 441–443, 1995

[14] K. L. Lear, K. D. Choquette, R. P. Schneider, S. P. Kilcoyne, K. M. Geib, "Vertical-cavity surface-emitting lasers with 50% power conversion efficiency," *Tech. Dig. CLEO'95*, vol. 15, pp. 54–55, 1995.

[15] G. P. Agrawal and N. K. Dutta, *Long-Wavelength Semiconductor Lasers*. New York: Van Nostrand Reinhold, 1986, p. 129.

[16] N. K. Dutta, J. Lopata, D. L. Sivco, and A. Y. Cho, "Temperature dependence of threshold of strained quantum well lasers," *Appl. Phys. Lett.*, vol. 58, p 1175, 1991.

[17] S. Y. Shu, S. W. Corzine, Z. M. Chuang, K.-K. Law, D. B. Young, A. C. Gossard, L. A. Coldren, and J. L. Merz, "Temperature-dependent threshold and modulation characteristics in InGaAs/GaAs quantum-well ridge-waveguide lasers," *Appl. Phys. Lett.*, vol. 66, p. 2040, 1995.

[18] P. Zhou, J. Cheng, C. F. Schaus, S. Z. Sun, K. Zheng, E. Armore, C. Hains, W. Hsin, D. R. Myers, and G. A. Vawter, "Low series resistance high efficiency GaAs/AlGaAs vertical-cavity surface-emitting lasers with continuously-graded mirrors grown by MOCVD," *IEEE Photon. Technol. Lett.*, vol. 3, pp. 591–593, 1991.

[19] R. S. Geels, S. W. Corzine, J. W. Scott, D. B. Young, and L. A. Coldren, "Low threshold planarized vertical-cavity surface-emitting lasers," *IEEE Photon. Technol. Lett.*, vol. 2, pp. 234–236, 1990.

[20] D. Vakhsoori, J. W. Wynn, G. J. Zydzik, R. E. Leibenguth, M. T. Ason, K. Kojima, and R. A. Morgan, "Top surface emitting lasers with 1.9 V threshold voltage and the effect of spatial hole burning on their transverse mode operation and efficiencies," *Appl. Phys. Lett.*, vol. 62, pp. 1448–1450, 1993.

[21] K. Tai, L. Yang, Y. H. Wang, J. D. Wynn, and A. Y. Cho, "Drastic reduction of series resistance in doped semiconductor distributed Bragg reflectors for surface-emitting lasers," *Appl. Phys. Lett.*, vol. 56, pp. 2496–2498, 1990.

[22] E. F. Schubert, L. W. Tu, G. J. Zydik, R. F. Kopf, A. Benvenuti, and M. R. Pinto, "Elimination of heterojunction band discontinuities by modulation doping," *Appl. Phys. Lett.*, vol. 60, pp. 466–468, 1992.

[23] J. B. Blakemore, "Semiconducting and other major properties of gallium arsenide," *J. Appl. Phys.*, vol. 53, pp. R123–R181, 1982.

Bo Lu (M'96), photograph and biography not available at the time of publication.

Yin-Chen Lu, photograph and biography not available at the time of publication.

Julian Cheng (SM'81), photograph and biography not available at the time of publication.

Richard P. Schneider (M'96), photograph and biography not available at the time of publication.

John C. Zolper (M'90), photograph and biography not available at the time of publication.

Gary Goncher (M'92), photograph and biography not available at the time of publication.

Electrochemical Society Proceedings, Vol. 96-2, pp. 117-119, 1996
(Invited Paper)

RECONFIGURABLE, MULTI-POINT OPTICAL INTERCONNECTS USING VERTICAL-CAVITY SURFACE-EMITTING LASER-BASED OPTOELECTRONIC SWITCH ARRAYS

Julian Cheng
University of New Mexico, CHTM, Albuquerque, NM 87131

Vertical-cavity surface-emitting lasers (VCSELs) can be integrated with other other optoelectronic components to to form compact optoelectronic integrated circuits that perform complex optical functions, including optical switching/routing, multi-point optical interconnection, optoelectronic transceiver, and optical logic processing.

1. INTRODUCTION:

As high-speed computer processors are linked together to form interactive clusters and networks with a parallel processing capability, there is a need for real-time, parallel communication between processors at increasingly higher data rates. To distribute computing power amongst the processors and shared resources will require very large real-time data transfers that are well beyond the capacity of the traditional single access buses and simple point-to-point links. We describe a *dynamically reconfigurable optical interconnection architecture* and an optoelectronic switching technology for optically linking electronic processors together and routing data through parallel optical channels (fig.1), [1] using a network of optoelectronic switches that provide optical links between nodes and electrical access (an electrical ⇔ optical interface) to each processor.

2. VERTICAL-CAVITY SURFACE-EMITTING LASERS

An optical switching fabric based on vertical-cavity surface-emitting lasers (VCSELs) can provide parallel photonic pathways for clock distribution as well as input/output data communication between a large number of spatially distributed electronic processing elements. VCSELs are ideal for these applications because of their high power efficiency, low power dissipation, high modulation speed, low beam divergence, narrow spectral width, and integrability into arrays. VCSELs can also be integrated with other optoelectronic components to perform more complex optical interconnect and signal processing functions. Individual VCSELs have been used in point-to-point optical links operating at a multi-Gb/s data rate, and a VCSEL can be designed for optimum operation over any temperature regime, from cryogenic to high temperature.

3. VCSEL-BASED OPTOELECTRONIC INTEGRATED CIRCUITS (OEICs)

VCSEL arrays can be integrated with heterojunction bipolar transistors (HBTs) to form a compact optoelectronic interface for a parallel optical data link. Monolithic OEICs integrating VCSELs with GaAs/AlGaAs HBTs have achieved a very high electrical-to-optical conversion efficiency and a large bandwidth.[2] In addition to HBTs,

VCSELs have also been integrated with photodetectors and phototransistors to form compact OEICs that perform optical switching, routing, logic, and optoelectronic data conversion. Integrating VCSELs with heterojunction phototransistors (HPTs) and photothyristors has produced non-latching and latching optical switches, respectively. Latching switches are used in programmable optical logic gate arrays that can perform different logic functions. Non-latching switches can perform electrical and optical switching to convert data between different electrical and optical input/output formats.[2] We describe their design, switching performance, and use in transmission experiments through an optical fiber.

4. RECONFIGURABLE MULTI-POINT OPTICAL INTERCONNECTS

Reconfigurable routing between a large number of nodes can be achieved using a mutli-stage optical routing network in which each stage contains an array of binary optical routing switches (fig. 1) that provide multi-point interconnections between nodes. Each node can be routed optically to any other node by selecting a path through the switching fabric using a small number of intermediate hops. Arrays of binary optical routing switches have been made by integrating VCSELs with HBTs and photodetectors (PINs) in either a monolithic or hybrid format. Each switch node can transmit or receive optical data, or to re-route it optically to other nodes,[3] and contains an optoelectronic interface through which it communicates with an electronic processor. Each node (Fig. 2) contains a pair of PIN/HBT/VCSEL switches, whose closely spaced PINs form a single optical input port, while their VCSELs provide two spatially separated optical output ports. An optical signal incident upon the PIN pair switches on one or both VCSELs according to the routing control voltage applied to each switch. Reconfigurable optical switching and routing have been demonstrated at 500 Mb/s.[4] Multi-stage, optically cascaded switching and routing operations have also been demonstrated,[3] with a peak single-stage differential dc optical gain of 18.

5. ACKNOWLEDGMENTS

This work was supported in part by the ARPA optoelectronics program and by AFOSR.

REFERENCES:

[1] Julian Cheng, SPIE Proceedings Vol. 2400, Optoelectronic Interconnects III, pp. 160-169, 1995.

[2] Y. C. Lu, J. Cheng, J. C. Zolper, J. A. Klem, Electronics Lett., Vol. 31, No. 7, pp. 579-580, 1995.

[3] Bo Lu, Y.C. Lu, A. C. Alduino, G. G Ortiz, and Julian Cheng, J. Klem, R. P. Schneider, M. J. Hafich, and J. C. Zolper, IEEE Photonics Technol. Lett., Vol. 7, N0. 12, Dec. 1995.

[4] A. C. Alduino, G.G. Ortiz, C. Hains, Bo Lu, Y.C. Lu, Julian Cheng, R. P. Schneider, J. Klem, and J. C. Zolper, Electronics Lett., Vol. 31, No. 18, pp. 1570-1571, 1995.

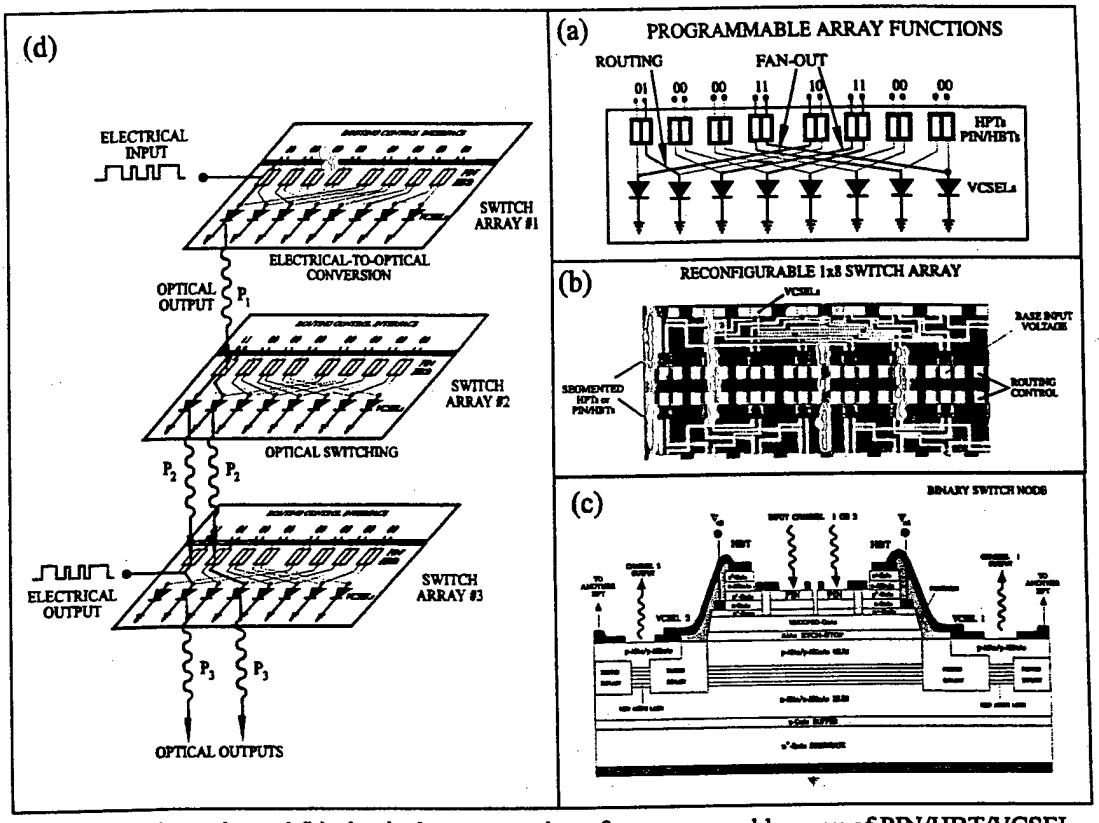


Fig. 1. (a) Schematic, and (b) physical representation of a programmable array of PIN/HBT/VCSEL switches that can be programmed to perform optical routing functions. The structure of a single binary optical switch is shown in (c). In (d) several switch arrays are optically cascaded to form a multi-stage routing network with electrical interfaces.

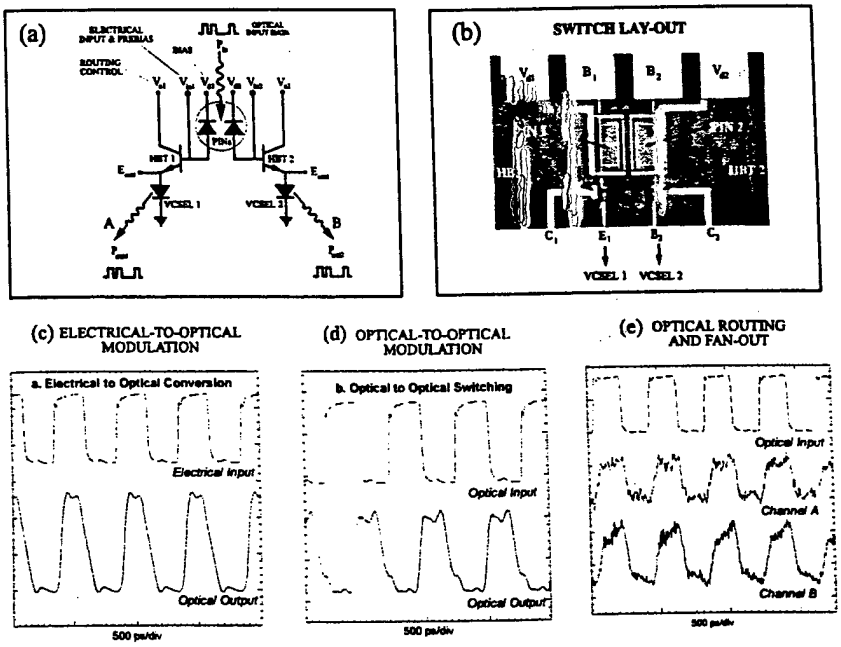


Fig. 2. Above: (a) the circuit design, and (b) the layout of a binary optical routing switch. Below: (c), (d), and (e) demonstrate its switching and routing operations.

High-speed optical transceiver and routing switch using VCSEL-based integrated optoelectronics

Julian Cheng, Y.-C. Lu, Bo Lu, G. G. Ortiz, A. C. Alduino, and C. P. Hains

University of New Mexico, Center for High Technology Materials
Albuquerque, NM 87131

H. Q. Hou, M. J. Hafich, G. A Vawter, and J. C. Zolper

Sandia National Laboratory, Albuquerque, NM 87156

ABSTRACT

Recent advances in the design of high-speed optical switches and transceivers for a reconfigurable, spatially-multiplexed optical interconnection network are described. Monolithic switches based on the integration of vertical-cavity surface-emitting lasers with heterojunction bipolar transistors and photodetectors have achieved switching operation at a data rate of close to 1 Gb/s. Optical transmission experiments through fibers have been carried out using these switches at a data rate between 650 Mb/s and 1 Gb/s. For future improvements in performance, the photonic and electronic elements should be separately integrated and independently optimized. To facilitate photonic integration, VCSELs and resonance-enhanced photodetectors have been integrated on the same substrate.

1. INTRODUCTION

Parallel optical interconnects based on vertical-cavity surface-emitting laser (VCSEL) arrays have begun to emerge from the laboratory and into the market place. The VCSEL possesses high optical power, high speed, and high efficiency, while producing much lower power dissipation and greater thermal stability. VCSEL-based optical interconnects may play a role at different levels of the interconnection hierarchy, including but not limited to multiprocessor networks and computer backplanes. But the VCSEL's potential lies beyond simple point-to-point optical links. Many future applications will require high-speed communication between parallel processors and shared memory resources on a continuous or more sustained basis. Demand for bandwidth on shared buses will become sufficiently high to make a switching solution necessary. A switched optical bus provides simultaneous data transfer between multiple nodes via non-conflicting paths, each of which can operate at the maximum bandwidth.

We have previously demonstrated a programmable optical interconnect architecture that can perform dynamic bus switching and data-path routing by optically interconnecting clusters of electronic processors across board-to-board or rack-to-rack distances.[1-3] As shown in fig. 1a, the processing elements and shared memory resources in each cluster are electrically connected in a bit-parallel fashion to a linear array of optical switches (fig. 1b), each of which respresents a single node of the network, and can either receive or transmit optical data to the nodes in other clusters. The inter-node optical paths can be reconfigured by simply programming the connections using a two-dimensional array of binary routing switches based on the integration of VCSELs with photodetectors (phototransistors, PIN photodiodes, and resonant photodetectors) and with GaAs HBT electronic technology. Each switch can also re-route the optical data, in addition to performing the optical transceiver functions. Any node can communicate optically with any other through a series of intermediate hops (fig. 1c), which can occur practically on-the-fly once the routing path is set up. Figures 2a and 2b show the design of a single routing switch node, while figures 2c, 2d, and 2e demonstrate its performance of optoelectronic conversion, optical switching, and optical routing, respectively, at ~400 Mb/s.[2] The switch design has been kept simple in order to focus on the basic optical and optoelectronic switching functions, deferring the more complex interface and logic functions to the processor electronics.

In this paper, we describe a newer version of this switch that can operate at a data rate of ~1 Gb/s. The higher speed performance is largely the result of improved HBT design. Using PIN/HBT/VCSEL switches as the optical transmitter and the optical receiver, respectively, high-speed fiber transmission experiments have also been carried out. In the future, we look for optical switches that can achieve a multi-GHz switching speed and an aggregate throughput of several hundred GHz.

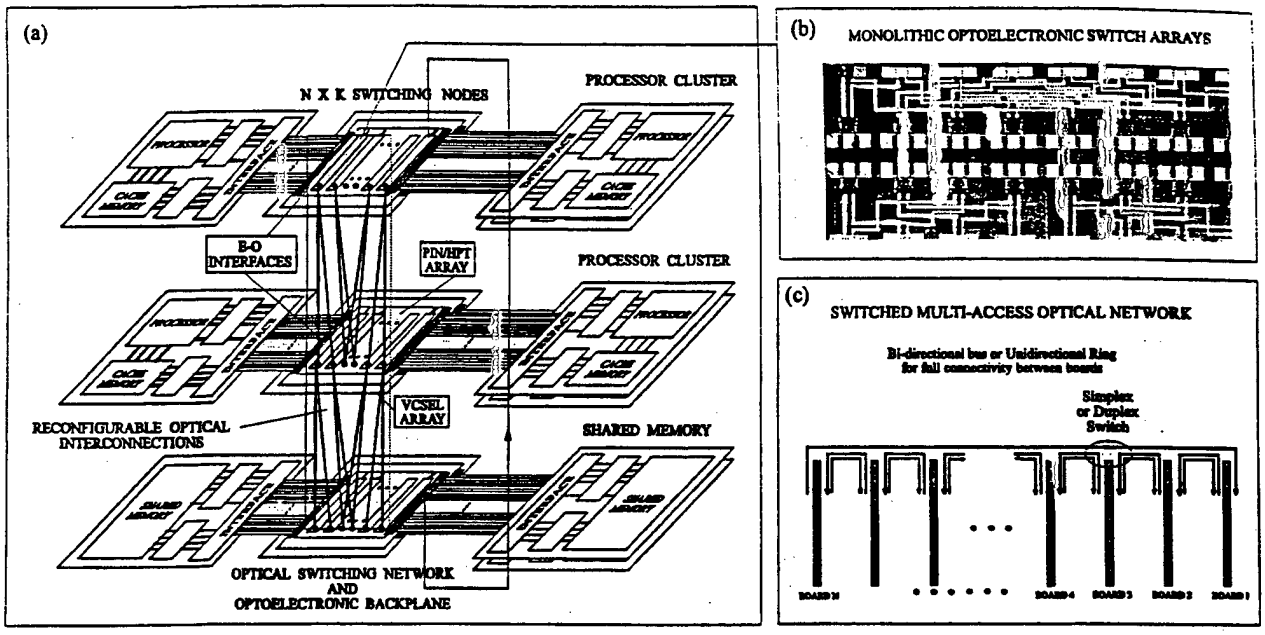


Fig. 1. (a) A dynamically reconfigurable, multi-access optical network with a uni-directional ring shuffle geometry, which uses monolithic optoelectronic switch arrays (b) to provide optoelectronic signal conversion and to reconfigure the optical routing paths through the network. (c) A switched optical network connecting processors on different boards, which can communicate with each other through parallel optical paths.

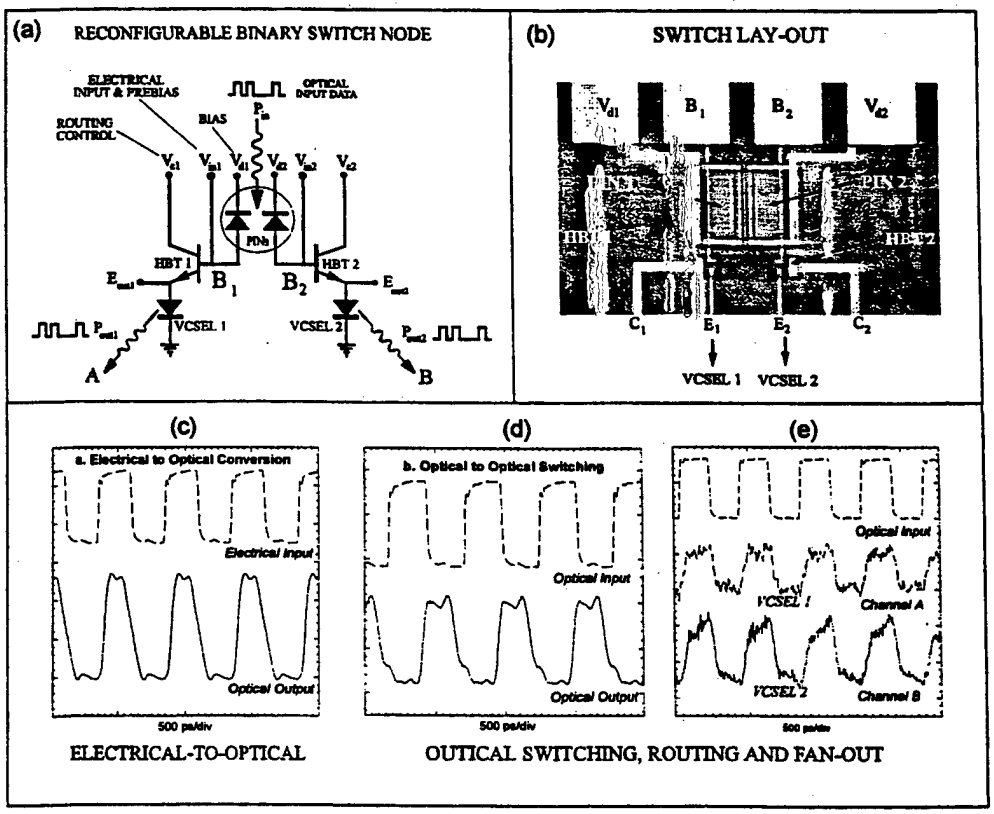


Fig. 2. (a) A 2x2 reconfigurable binary switch node containing two elementary PIN/HBT/VCSEL switches, which can perform optical routing as well as optoelectronic signal conversions, (b) shows the monolithic switch lay-out, and (c), (d), (e) the experimental demonstration of optoelectronic conversion, optical switching, and optical routing, respectively, at a data rate of > 400 Mb/s.

This will require not only faster HBTs, but also more efficient photodetectors and VCSELs with much lower power dissipation. We are looking at the separate integration of photonics and electronics to provide better optimization of each component. We will describe the monolithic integration of VCSELs and resonance-enhanced photodetectors (REPD) to achieve high-performance source and detector arrays. Switching performance can also be improved by using optoelectronic switch designs that require the VCSEL to be grown on a common p-GaAs substrate. The characteristics of p-side-down VCSELs are described.

2. DESIGN OF OPTICAL SWITCHES WITH IMPROVED SPEED PERFORMANCE

Switching performance can be extended to the Gb/s regime by improving the HBT design, and by separating the photodetector (PD) function from the HBT. To preserve the simple switch design, we begin with the HBT, whose speed performance is limited by the requirement of a high current gain and by the large capacitance of the PIN photodiode (base-collector junction) that is required for efficient optical coupling. By reducing the base resistance and minimizing the extrinsic base-collector junction area, an improved HBT/VCSEL switch was achieved whose characteristics are shown in fig. 3. Figure 3a shows the monolithic switch layout, while fig. 3b shows the current gain of different devices as a function of current density, with a peak gain of ~100 at a current density of ~10 kA/cm^2. The small-signal modulation response of the switch is shown in fig. 3c, wihich has a unity-gain bandwidth of 2.5 GHz. The base doping of this switch is very low ($2x10^{18}$/cm^3). To improve this bandwidth further will require the use of self-aligned HBT processes, as well as a thinner and much more heavily-doped base layer.

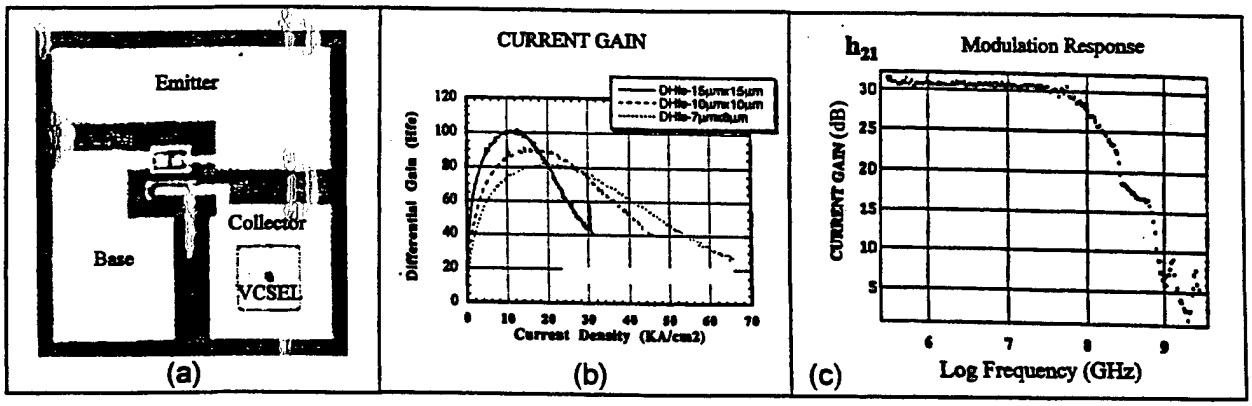


Fig. 3. (a) The lay-out of a monolithic HBT/VCSEL switch, (b) the current gain of HBTs with different emitter areas as a function of current density, (c) the modulation response of a 15 μm x 15 μm HBT.

A monolithic emitter-coupled VCSEL drive circuit (fig. 4b) was fabricated using this improved HBT technology.

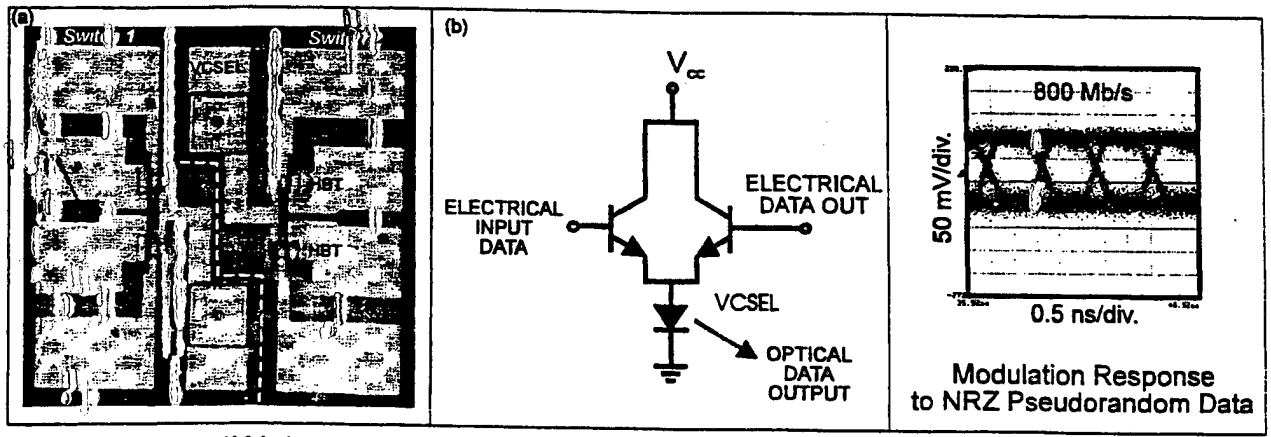


Fig. 4. (a) The monolithic lay-out, and (b) circuit design, of an emitter-coupled VCSEL drive circuit containing 2 HBTs and a VCSEL, and (c) its optical response to electrical modulation by 800 Mb/s NRZ pseudorandom data.

The lay-out in figure 4a shows two independent HBT/VCSEL switches, each containing two HBTs and a VCSEL. The switch has a 10%-to-90% rise-time of $\tau \sim 0.35$ ns (*c.f.*, 0.8 ns for previous switch designs[4]). Its response to pseudorandom data modulation (fig. 4c) shows a wide-open eye diagram at 800 Mb/s, with 1 Gb/s operation easily feasible. The displayed signal is in fact limited by the bandwidth of the receiver, which has a small-signal response of ~1 GHz.

3. PERFORMANCE OF MONOLITHIC OPTICAL SWITCHES AS OPTICAL TRANSCEIVERS

The use of the PIN/HBT/VCSEL switch as transmitter and optical routing switch has previously been demonstrated at a data rate of ~500 Mb/s [2]. The use of this same switch (not the faster HBT/VCSEL switch described in section 2) as an optical receiver has also been experimentally evaluated using optical transmission through different lengths of both single-mode (SM) and multi-mode (MM) fibers. Two different PIN/HBT/VCSEL switches are used as the transmitter and the receiver, respectively, as shown in fig. 5a. Optical transmission experiments were carried out across a short length (0.5 m) of both SM and MM fibers, at a data rate of 650 Mb/s and 1 Gb/s, respectively. The optical power (~0 dBm) from the VCSEL was coupled into a multi-mode fiber with >90% efficiency (< 0.5 dB coupling loss). The transmitted light was likelwise coupled to the PIN detector area of the receiver (PIN/HBT/VCSEL switch) with >90% efficiency. The uncoated PIN has an external quantum efficiency of ~59% (-2.3 dB, for a responsivity ~ 0.4 mA/mW), and the combined fiber transmission loss and dispersion is <3.5 dB/km at 650 Mb/s. Allowing a 3 dB margin for thermal variations and degradation, a power budget of ~10 dB would be required for a 1 km link operating at 650 Mb/s.

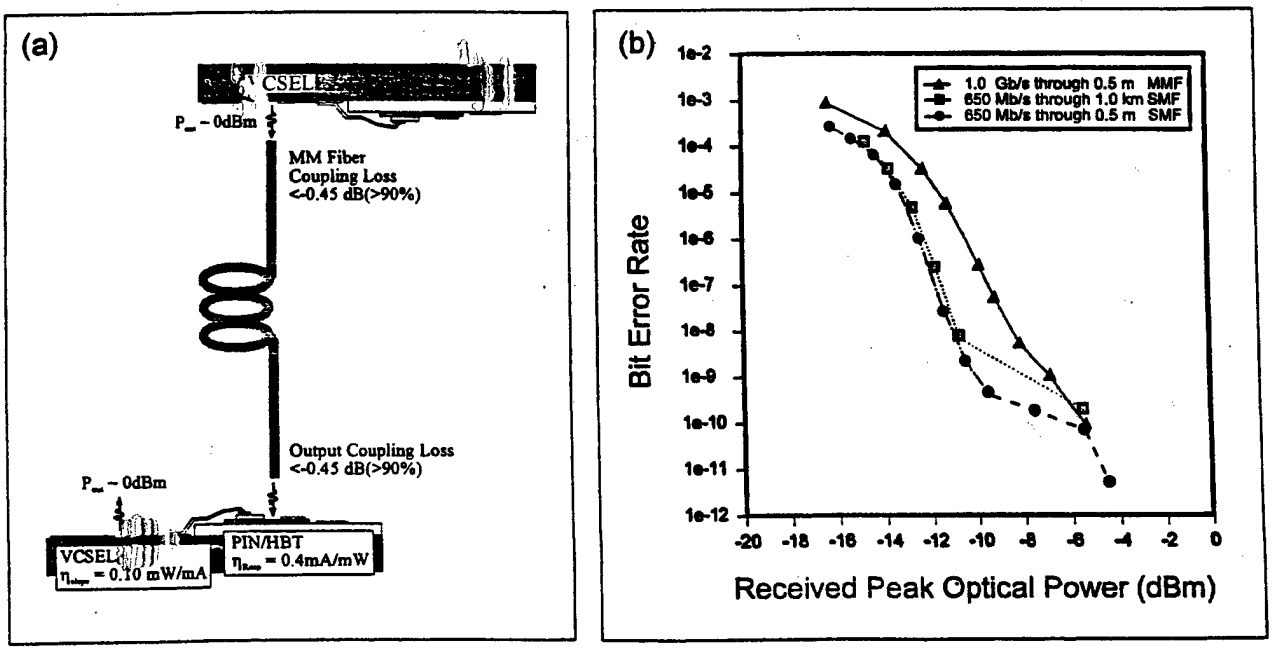


Fig. 5. (a) The experimental configuration for studying optical transmission through an optical fiber, using two PIN/HBT/VCSEL switches as the optical transmitter and optical receiver, respectively. (b) The bit error rate as a function of received optical power, for SM transmission at 650 Mb/s, and MM transmission at 1 Gb/s.

The experimental data (fig. 5b) shows that for 650 Mb/s transmission through a short (0.5 m) SM fiber, where dispersion and fiber loss are negligible, a bit-error-rate (BER) of 10^{-9} was achieved at an optical input signal level of ~10.5 dBm. This poor sensitivity shows that the input noise level of the PIN/HBT/VCSEL receiver is very high, which is not surprising for a low impedance front-end (input impedance < 500 Ω). There is also a flattening of the BER performance at larger signal levels, with a BER floor of ~10^{-10}, which is attributed to the modal noise produced by the interference between the different lasing modes as they propagate through a dispersive fiber, where various disturbances can produce mode-selective losses[5] that result in significant intensity fluctuations. The impact of these fluctuations are more pronounced in a SM fiber operating at wavelengths shorter than the cut-off of the second-order modes, where there are only a few propagation modes, than in the MM fiber, where there are many. For 650 Mb/s transmission across a 1 km length of SM

fiber. fig. 5b again shows a BER floor at ~10^{-10} at an optical power level of -5.5 dBm. Although a loss and dispersion-related shift of ~3 dB is expected, this was not observed, possibly due to variations in the coupling efficiency of light into a SM fiber. In the case of a short (0.5 m) multi-mode fiber, a BER of ~10^{-10} was achieved at a data rate of 1 Gb/s and at an optical power level of -5.5 dBm. This even lower sensitivity is due to the roll-off in the modulation response of the switches at both ends, and to the greater noise levels that exist at higher frequencies.

These results demonstrate that the PIN/HBT/VCSEL switch, in its present simple format, can provide a nearly sufficient power margin for transmission at ~ 650 Mb/s, but not at Gb/s data rates. A different receiver design is needed to achieve both better sensitivity and higher speed. However, a significant improvement in sensitivity can also be achieved by the use of a more efficient photodetector than is provided by the base-collector junction of the HBT.

4. FUTURE IMPROVEMENTS IN MONOLITHIC SWITCHING PERFORMANCE

4.a. Optical routing switches with inverted VCSELs grown on p-GaAs substrates

Figure 6a and 6c show several simple front-end configurations for a PIN/HBT/VCSEL switch, the former requiring VCSELs with a common n-substrate, the latter with a common p-substrate. Modeling studies show that greater speed performance can be achieved with the latter, which also simplifes the interconnect requirements in a switching array architecture (emitter-based vs collector-based routing control). Figure 6e shows the epilayer design and device structure of a binary routing switch based on an inverted VCSEL structure grown on a p-GaAs substrate.

VCSELs with nearly identical structures (except for the inverted doping) have been grown on both p-type and n-type GaAs substrates by MOCVD. Both structures contain a GRINSCH active region and linearly doped heterointerfaces, and has nearly identical doping profiles. Comparing 16 μm diameter devices, their current thresholds (5-6 mA) and electrical characteristics are comparable, although the p-substrate devices show a slightly lower series resistance (a smaller spreading resistance contribution). For these devices, the n-substrate VCSELs show a higher output power and greater slope efficiency than the p-substrate VCSELs. However, there is insufficient data at this time for a definitive comparison of these devices. Base on prima facie evidence, their performance may be assumed to be comparable.

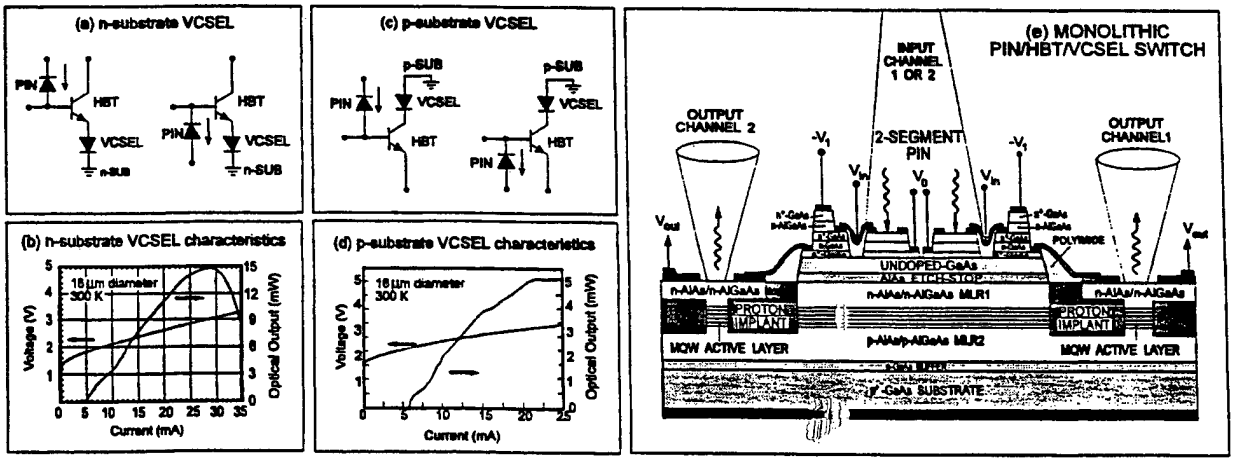


Fig. 6. Configurations for a simple PIN/HBT/VCSEL switch, with the VCSEL grown on (a) a n-type substrate, and (c) a p-type substrate, respectively. (b) and (d) compare the electrical and light-current characteristics of these devices, and (e) shows the epilayer structure and device lay-out of a monolithic binary routing switch based on a p-type substrate.

4.b. Monolithic photonic integration of VCSELs and resonance-enhanced photodetectors

Improved photoresponse (sensitivity and bandwidth) may be achieved by using resonance-enhanced photodetectors (REPDs), which can be monolithically integrated with the VCSEL on a common substrate (figure 7). This is an important development, since a large array of integrated VCSELs and REPDs can represent a fundamental building block for many

generic optical interconnect applications. In high density, parallel optical interconnect applications, it is often advantageous to monolithically integrate the photonic functions on a single substrate in order to achieve improved performance and to simplify packaging. As we have seen from the switching performance, it is desirable to have an epilayer design that does not require compromising the perfromance of any individual components - electronic or photonic. In particular, we would like to eliminate the gain-bandwidth trade-off that must be made when the HBT layers provide electronic gain as well as photodetection, which leads to a non-optimum design that compromises both the modulation bandwidth of the HBT and the responsivity of the PIN.

The optical source and photodetection functions can be integrated without compromising the performance of either, by monolithically integrating a VCSEL and a REPD using a single epilayer design.[6] The VCSEL and the REPD share a common multi-quantum-well active region that is enclosed within two different embedded resonance cavities. Each cavity is individually optimized to provide efficient operation for the VCSEL as well as the REPD. Since optimum VCSEL performance requires very high mirrror reflectivities, while optimum REPD performance requires a cavity with lower reflectivities, the use of a single design may compromise both. However, in the design shown in fig. 7a, the cavity of the REPD is embedded within the cavity of the VCSEL, so that the former cavity can be realized by chemically removing some of the DBR pairs from the upper mirror in the selected REPD regions of the wafer, while leaving the cavity intact in the VCSEL regions. The reduced Q of the REPD cavity provides a broader resonance-enhanced absorption window.

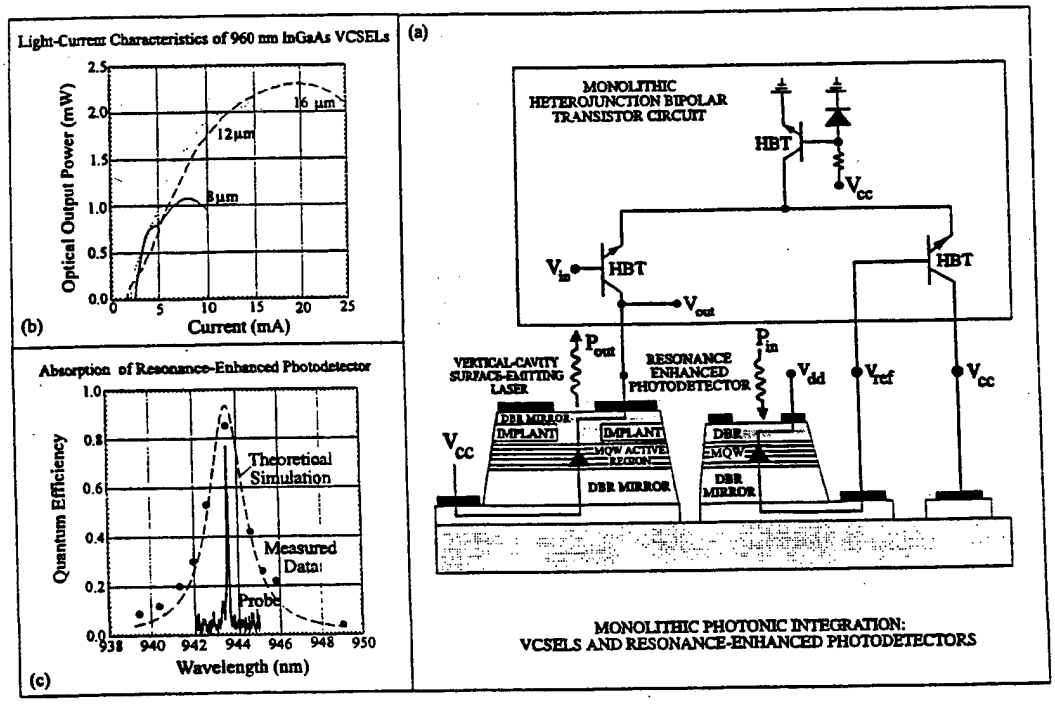


Fig. 7. (a) Epitaxial structure of the integrated VCSEL and REPD. The active region is composed of three 80 Å InGaAs quantum wells, and is placed between two distributed Bragg reflector (DBR) mirrors. The VCSEL uses all 24 mirror pairs of the upper DBR, while the REPD uses only 11. Also shown is a hybrid switching circuit separately integrating the photonic and electronic elements. (b) The light-current characteristics of VCSELs with an active area diameter of 8 μm, 12 μm, and 16 μm, respectively. (c) Measured (dots) and calculated (dashed line) values of the quantum efficiency of the REPD as a function of the wavelength of a tuned, narrow-band optical source (probe).

Experimentally, we have achieved REPDs with a quantum efficiencies of close to 90% (fig. 7c), and VCSELs (fig. 7b) with threshold current densities as low as 850 A/cm^2 and slope efficiencies as high as 50%. The measured external quantum efficiency of the detector is plotted as a function of wavelength in Fig. 7c, which compares favorably with the numerical simulation results. The photodetectors exhibited excellent performance across the sample, with peak responsivities as high as 0.65 A/W at λ=943.5 nm, corresponding to an external quantum efficiency of 85% at a reverse bias

of 3 V, and the width of the measured responsivity spectrum is ~20 Å. The VCSELs also demonstrated very good dc operating characteristics (fig. 7b). Devices with active area diameters varying from 8 μm to 16 μm exhibited threshold currents in the 1.5 - 2.5 mA range, differential quantum efficiencies of 20% to 50%, maximum output powers from 1.2 - 3.5 mW, and threshold current densities as low as 850 A/cm^2.

5. CONCLUSIONS

High-speed switching has been achieved by integrating VCSELs with PIN photodiodes and HBTs. Optical transmission studies using PIN/HBT/VCSEL switches as transmitter and receiver demonstrated that modulation at 650 Mb/s is possible across a 1 km distance, with a BER < 10^{-9}, and a sensitivity of -10 dBm at BER=$3x10^{-10}$. Monolithic optical transmitters consisting of HBTs and VCSELs have also been modulated at ~1 Gb/s. Switching performance can be further improved by the separate integration of photonics and electronics, and the photonic integration of high performance VCSELs and REPDs has been demonstrated. High performance p-substrate VCSELs have also been demonstrated, and will be used to improve switching performance in future monolithic switch designs.

6. REFERENCES

1. J. Cheng, Y. C. Lu, Bo Lu, A. Alduino, G. Ortiz, J. C. Zolper, J. Klem, G.A. Vawter, "High speed optical interconnect technology for a reconfigurable multi-processor network", *SPIE Proceedings Vol. 2400, Optoelectronic Interconnects III*, pp. 160-169, Feb. 1995.
2. Alduino A.C., Ortiz G.G., Hains C., Lu B., Lu Y.C.,Cheng J., Schneider R.P., Klem J., and Zolper J.C, "500 Mbit/s operation of a multi-functional binary optical switching fabric," *Elect. Lett.*, 1995, **31** (18), pp. 1570-1571.
3. Lu B., Lu Y.C., Alduino A.C., Ortiz G.G., and Cheng J., 'Optically-cascaded, multi-stage switching operation of a multifunctional binary optical/optoelectronic switch', IEEE *Photonics Technol. Lett.*, 1995, 7 (12), pp. 1427-1429.
4. Y. C. Lu, J. Cheng, P. Zhou, J. C. Zolper, J. A. Klem, "Integrated Optical/Optoelectronic Switch for Parallel Optical Interconnects", *Elect. Lett.*, Vol. 31, No. 7, pp. 579-580, May, 1995.
5. K. H. Hahn, M. R.Tan, Y. M. Houng, and S. Y. Wang, "Large area multi-transverse mode VCSELs for modal noisee reduction in multi-modee fiber systems," *Elec. Lett.*, vol. 29, pp.1482-1483, August 1993.
6. G. G. Ortiz, C. P. Hains, Julian Cheng, H. Q. Hou, and J. C. Zolper, "Monolithic integration of $In_{0.2}Ga_{0.8}As$ vertical-cavity surface-emitting lasers with resonance-enhanced quanum-welll photodetectors", *Elect. Lett.*, Vol. 32, No. 13, pp. 1205-1207, June 1996.

A RECONFIGURABLE, HIGH-SPEED OPTOELECTRONIC INTERCONNECT TECHNOLOGY FOR MULTI-PROCESSOR COMPUTERS

Julian Cheng
University of New Mexico, Center for High Technology Materials
EECE Building, Room 125, Albuquerque, NM 87131

ABSTRACT

We describe a compact optoelectronic switching technology for interconnecting multiple computer processors and shared memory modules together through dynamically reconfigurable optical paths to provide simultaneous, high speed communication amongst different nodes. Each switch provides an optical link to other nodes as well as electrical access to an individual processor, and it can perform optical and optoelectronic switching to convert digital data between various electrical and optical input/output formats. This multi-functional switching technology is based on the monolithic integration of arrays of vertical-cavity surface-emitting lasers with photodetectors and heterojunction bipolar transistors. The various digital switching and routing functions, as well as optically cascaded multi-stage operation, have been experimentally demonstrated.

1. INTRODUCTION:

As increasing numbers of high-speed digital processors are linked together to form interactive computer networks that provide a parallel processing capability, there is a growing need for a high speed bus that allows many processors to communicate simultaneously with each other and with shared memory facilities, through parallel transmission paths and at increasingly higher data rates. One example is high resolution image processing applications in which digitized image data from multiple remote sources must be individually decompressed, stored, and processed in real-time by a single multiprocessor computer. Another application requiring parallel, high-speed data transfer is multi-location video conferencing, which may require the real-time transfer, continuous processing and display of high resolution data from several remote locations, and the storage and acquisition of a vast amount of digital data in shared memory facilities. Both examples require parallel, multi-point data transfers that are beyond the capacity of the traditional (albeit high speed) single access buses and backplanes. Although the current computer memory hierarchy provides relatively slow data acquisition, which mitigates the need for a very high speed bus, it is expected that as new technologies improve the access to stored data, the serial, single-access bus will again become the bottleneck. To facilitate parallel computing operations, a multi-point, multi-access interconnection network will be needed to provide the simultaneous transfer and routing of data between multiple processors and their shared memory facilities. This paper describes a high-speed, *dynamically reconfigurable* optical interconnection technology that permits parallel data communication between a large number of electronic processors and shared memory facilities. Although parallel, point-to-point optical data links can be implemented using conventional transceivers without the switching function, switching provides a dynamically reconfigurable network with selectable access to the different network nodes.

2. THE OPTICAL INTERCONNECT ARCHITECTURE:

The multi-processor interconnect is based on the dynamic reconfiguration of a multi-stage, multi-path, spatial routing network with a closed ring geometry (Fig. 1).[1-3] Each stage contains a cluster of processors or shared memory modules that communicate with other clusters through a space-division-multiplexed, multi-stage network of optoelectronic switches, each of which provides an optical link to other nodes, as well as an electrical access to an associated electronic processor or shared memory module. The individual processors and shared memories in each cluster (stage) are compact multi-chip-modules (MCMs), several (N) of which reside on each board. Each stage (Fig. 2) also contains an (NxK) optoelectronic switching array that is electrically connected to each of the N processors in a bit-parallel fashion (K bits wide). By arranging the network in the form of a closed ring (Fig. 1), any node can be interconnected to any other by selecting a routing path through the switching fabric in a small number of hops. Space-division-multiplexed networks can provide a very large spatial bandwidth since large, compact switching matrices can be achieved by optoelectronic integration, and many parallel channels can be routed optically between nodes at the same time. Although this approach is limited to relatively short physical distances, it is well suited for the optical backplane of a multi-processor workstation or other dense processor clusters. As shown in Figures 2 and 3, each switch node must function as an optical transceiver by receiving or transmitting optical data, but it must also be able to perform switching operations to re-route data optically to the next stage (bypass mode), all in a bit-parallel fashion. The received optical data (P_{in}) is converted into electrical data (E_{out}), which is either *dropped* at that node, or is *regenerated* optically and routed to the next stage (P_{out}). The switch must also accept electrical input data (E_{in}) from a local

0-8194-1834-X/95/$6.00

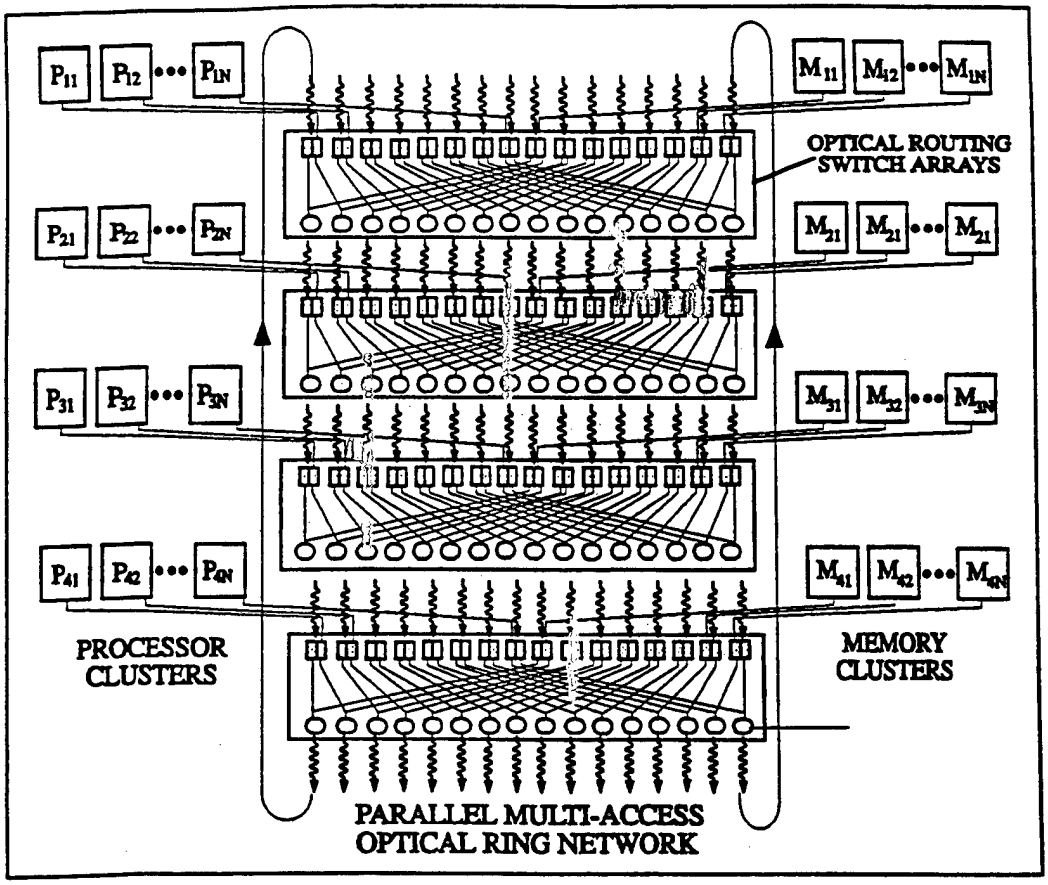


Figure 1. A reconfigurable, spatially-multiplexed, multi-stage optical interconnection network linking multiple processors and shared memory facilities together through a reconfigurable, multi-path, multi-access optical bus (backplane).

processor and convert it to an optical format (P_{out}) for transmission. Thus each switch must contain an optical source and a photodetector, as well as their drive circuitry and the switching functions, and it must be able to convert digital data between various electrical and optical input/output formats. As shown in the inset of Fig. 3, the input port of each node can be divided into two contiguous segments, each of which is connected to one or more output ports, thus forming a binary optical switch with reconfigurable routing capabilities.[1,4] By providing each binary switch with an optoelectronic interface to effect electrical⇔optical data conversion,[5,6] and electrically connecting a processor to each node (k bits wide), we have a high speed optical bus that allows the processors to communicate through parallel, reconfigurable optical interconnections. Each binary switch can now be modulated either by P_{in} from another node or by E_{in} from its associated processor, to produce a current modulation that is spatially routed to one or more nodes (fan-out) within the switch array, where it produces both a modulated electrical signal (E_{out}) that is sent to the corresponding processor and a regenerated optical output (P_{out}) that is optically transmitted to the next stage. The internal routing paths within each array can be reconfigured by choosing a set of control voltages. Parallel optical data channels propagate between stages (boards) through free space or through a weakly-guided medium, and are routed to other nodes in successive stages under electronic routing control. Either local or centralized routing control can be used, and both packet and circuit switching are possible. Since there is only a finite number of boards or routing stages, only a few monolithic optoelectronic switch arrays are needed to implement the entire network, representing a potentially low-cost solution to a reconfigurable optoelectronic backplane.

3. THE RECONFIGURABLE OPTOELECTRONIC SWITCHING TECHNOLOGY

This interconnect architecture can be implemented using a monolithic optoelectronic switching technology consisting of high-speed (155-622 Mb/s near term, >1Gb/s in the future) switches that can perform both optical and optoelectronic switching functions to convert data between various electrical and optical formats, and which are integrable into large arrays to route data in parallel through many dynamically reconfigurable optical channels. We will describe a technology based on

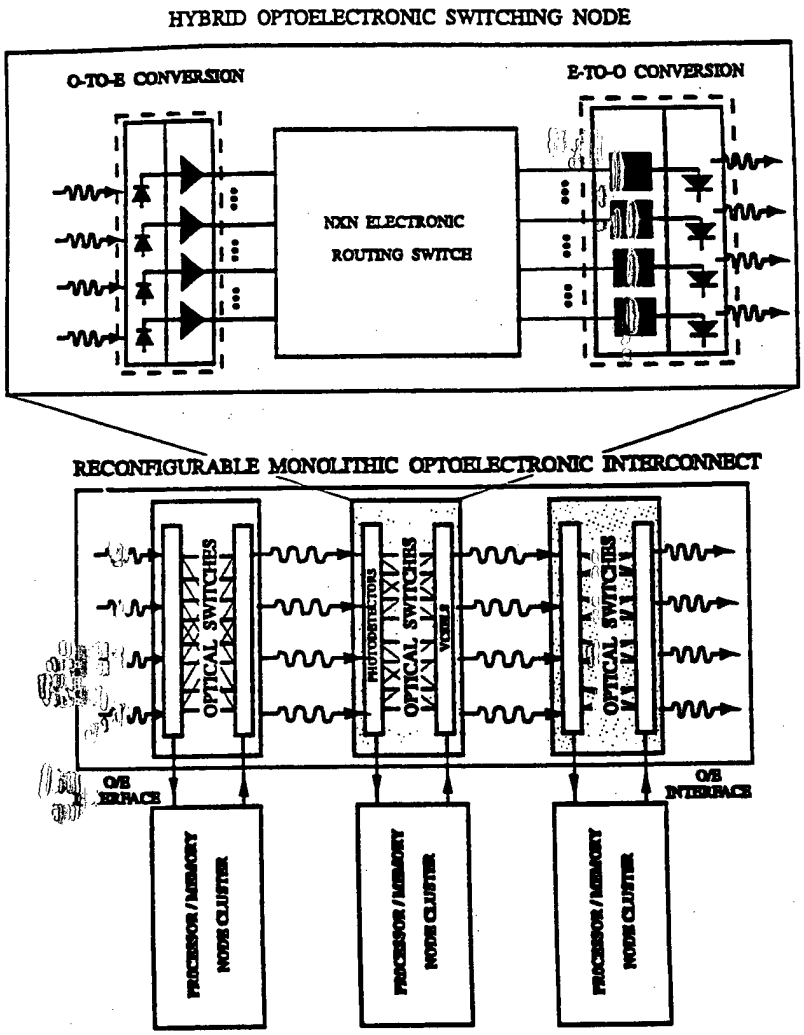


Figure 2. Schematic functional configuration of the optical backplane, in which each processor cluster is linked to an optical routing switch array through an optoelectronic interface, while data is routed optically between clusters. The switch array must perform some of the functions of a hybrid transceiver (as shown).

he integration of GaAlAs/GaAs vertical-cavity surface-emitting lasers (VCSELs), heterojunction bipolar transistors (HBTs), nd heterojunction phototransistors (HPTs) or PIN photodetectors. We use a switch design with minimum complexity to erform both the transceiver (optoelectronic conversion) and optical bypass functions. Binary configurations of these lementary HPT/VCSEL switches with segmented HPTs will then perform the more complex reconfigurable routing unctions.[3] We describe the switch design, and the experimental performance of the functions that are required by the nterconnect architecture.

A. VCSELS and VCSEL-based Optical Switches:

VCSELs are well suited for parallel optical interconnect applications since they are readily integrated into dense, wo-dimensional arrays to provide a compact, parallel, surface-normal architecture. The VCSEL also provides a coherent, high peed optical source with good optical beam quality, high output power, low power dissipation, good thermal stability, stable urrent-voltage characteristics, and a very wide operating temperature range.[4] The electrical and light-current characteristics f a typical 16 μm diameter VCSEL that is used in the switching experiments is shown in Figure 4. It produces a high output ower (up to 10 mW) and high power conversion efficiency (13.5%), and has thermally stable electrical characteristics, and ow operating voltages <3V over a wide range of temperatures. High performance optical and optoelectronic switches, with igh optical or optoelectronic gain and contrast, and moderately low optical switching energy, have been made by integrating he VCSEL alternatively with a HPT[1] or with a HBT.[5] These switches have also been combined into more complex

configurations to perform different spatial routing functions under simple voltage control.[2] These *multi-functional* switches can perform different combinations of electrical and optical switching functions at high data rates (>200Mb/s),[8,9] and exhibit electrical as well as optical gain.

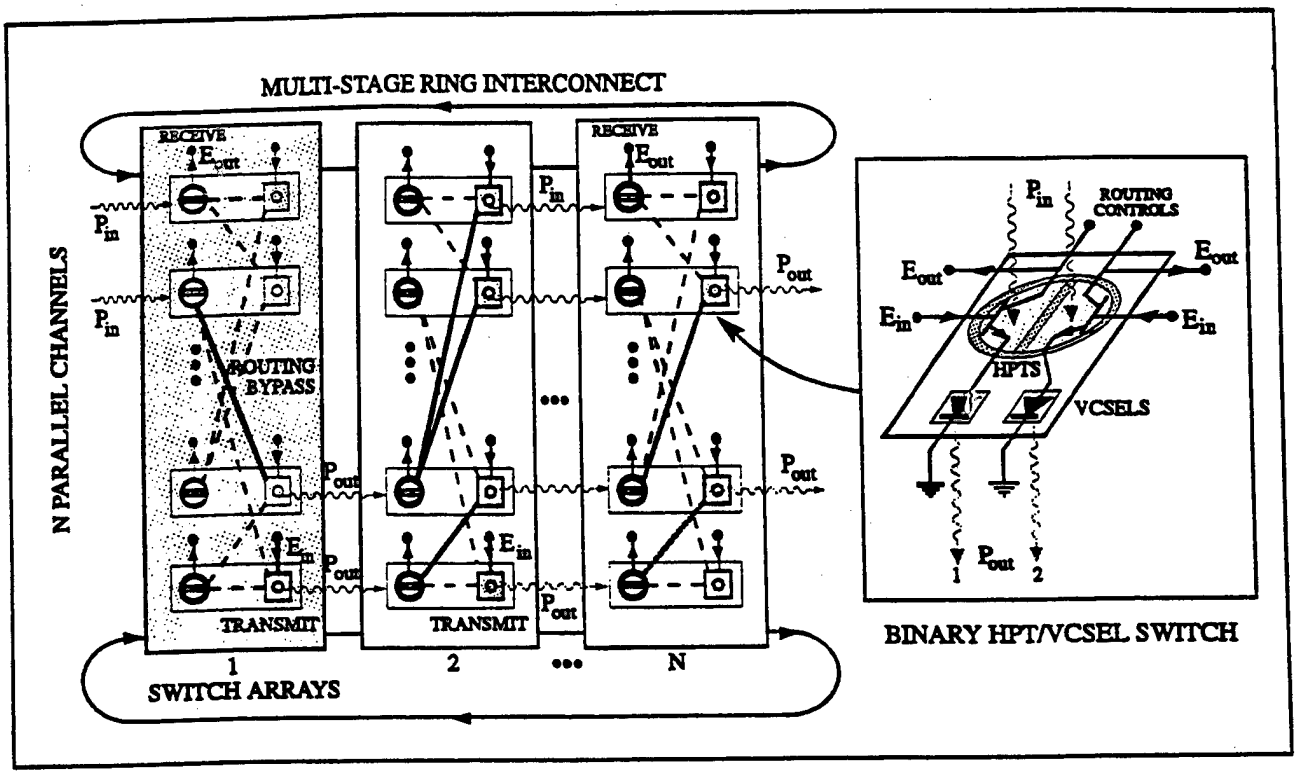


Figure 3. A reconfigurable, closed-ring, interconnect architecture linking clusters of nodes through parallel optical paths set by the optoelectronic switch arrays, with electrical input and output ports. Each switch (inset) contains a two-segment HPT interconnected individually to different VCSELs in the array, and can receive, transmit, or re-route optical signals as shown.

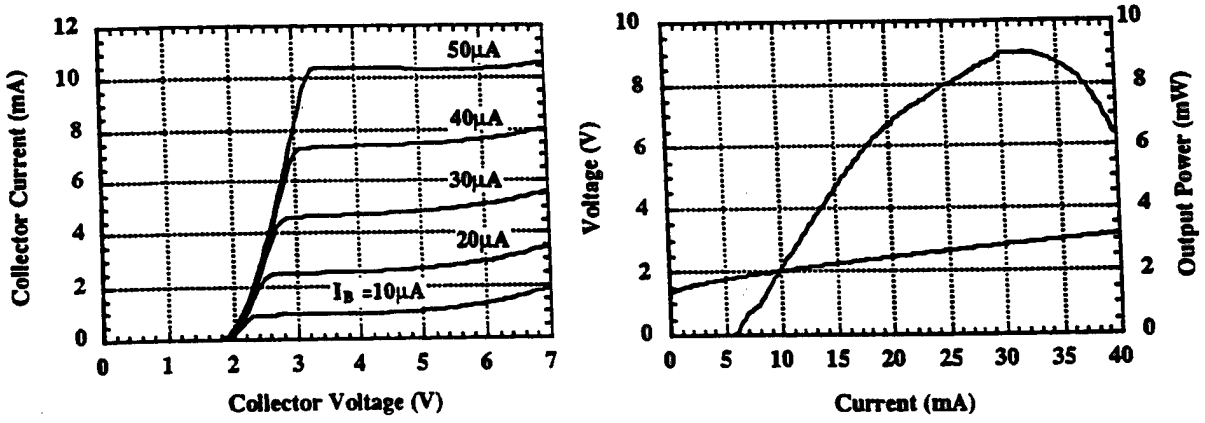


Figure 4. The dc characteristics of the components of a HBT/VCSEL switch: (a) the dc characteristics of a common-emitter HBT with a current gain of ~200, and (b) The current-voltage and light-current characteristics of a VCSEL with a 20μm active area.

3.B. Monolithic HBT/VCSEL Optoelectronic Switching Interface :

The integration of VCSELs with high speed electronics is driven by: 1) the desire to combine the optical source and its driver circuits into a single technology, and 2) to provide a simple optoelectronic interface for photonic switching

networks consisting of VCSEL-based optical switches. While the processors may communicate with each other through parallel optical channels, an optoelectronic interface is needed to allow each node to communicate with its electronic control and data processing functions. The interface performs high speed electrical ⇔ optical signal conversion to provide each node with a direct electrical link to the switching fabric. A *multi-functional* HBT/VCSEL optical and optoelectronic switch (Fig. 5) can perform different combinations of optical or optoelectronic switching functions to convert data between different electrical and optical input/output formats.[9] Input data packets in either an optical or electrical format can be combined to produce switched optical or electrical outputs. This flexibility allows us to construct the reconfigurable, three-dimensional, multi-stage switching fabric (bus) shown in Figures 1-3. This optical switching fabric contains a simple (K-bit wide) optoelectronic interface to each processor, which provides a convenient platform for combining electrical and optical input data packets into a common format. We will describe the design and performance of this monolithic optoelectronic switch, and the experimental demonstration of its digital switching and routing functions.

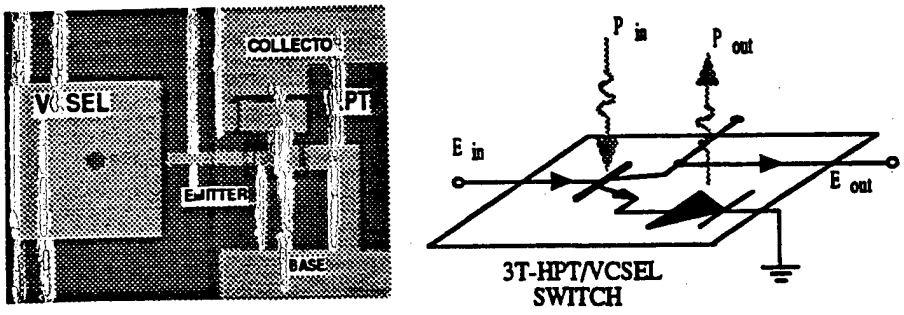


Figure 5. (a) Photomicrograph of the monolithic 3-terminal HPT/VCSEL switch, and (b) schematic diagram of its emitter-follow circuit, with optical input P_{in}, electrical input E_{in}, optical output P_{out}, and electrical output I_{out}.

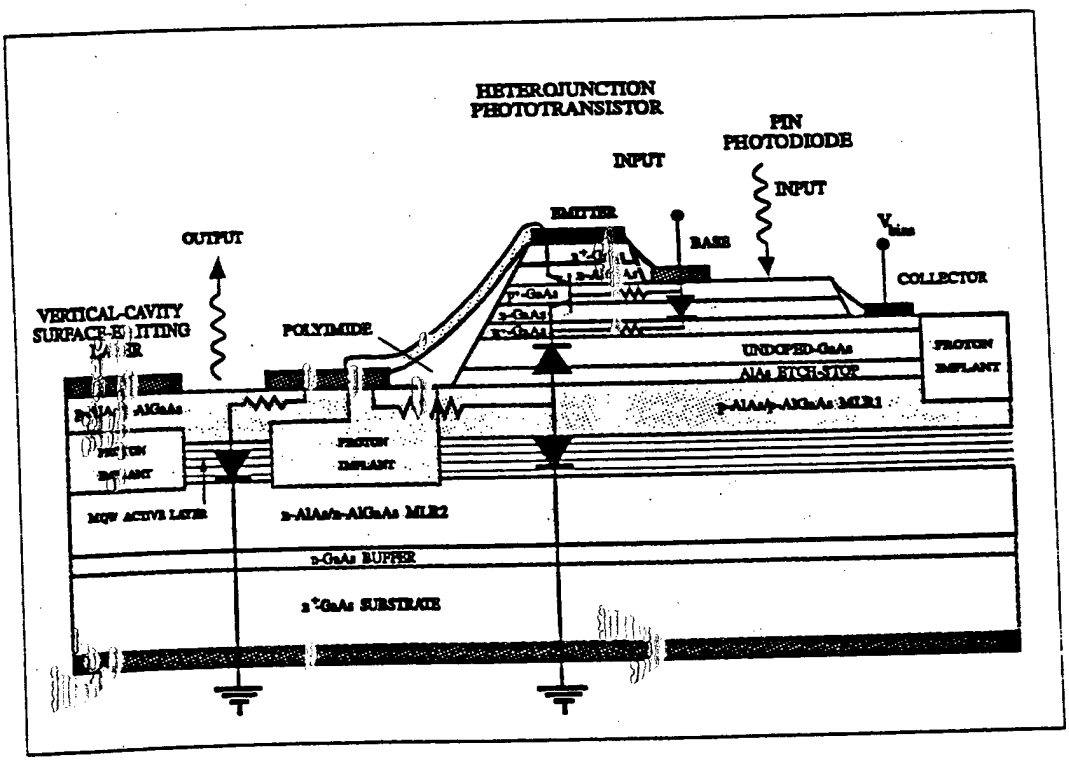


Figure 6. Epitaxial structure and device design of a monolithic, 3-terminal HPT/VCSEL switch with an emitter-follower geometry.

A very simple transceiver circuit is the HBT/VCSEL optoelectronic switch shown in Figure 5, which uses an emitter-follower configuration as mandated by the common n-substrate contact of the VCSELs. A common-emitter configuration would allow higher speed performance, but this requires that the VCSELs be grown on a p-type or a semi-insulating substrate. In the epitaxial design depicted in Figure 6, the HBT layers are grown above the VCSEL structure on an n-GaAs substrate, separated by an undoped GaAs isolation layer. The VCSEL active layer consists of a four-quantum-well, GaAs/AlGaAs graded-index separate-confinement heterostructure (GRINSCH), which is bounded by two distributed Bragg mirrors with continuously-graded hetero-interfaces.

Figure 7 shows[8] the small-signal, (a) electrical and (b) optical modulation response of an integrated HBT/VCSEL switch with a $10x10\mu m^2$ emitter area and a VCSEL active area diameter of $20\mu m$. The dc current gain of this device is $\beta=31$ at a collector current of $I_C=10mA$. At this bias level, the HBT saturates at 1.5V, while the VCSEL threshold voltage (current) is 2.1V (5.5mA), and switching can be effected with a collector bias of less than 5V. The relative small-signal response of the HBT collector current to a voltage modulation applied to the base is shown in Fig. 7a, which shows the forward transmission coefficient S_{21}, and the current gain h_{21}. The HBT has an unity gain bandwidth of 600MHz. Figure 7b shows the small-signal electrical-to-optical modulation response of the switch for different values of bias current, which has the typical resonant frequency response of a diode laser modulated above threshold, which is modified by the transconductance of the follower circuit. The modulation response saturates at a bandwidth of f_{max}~4GHz.

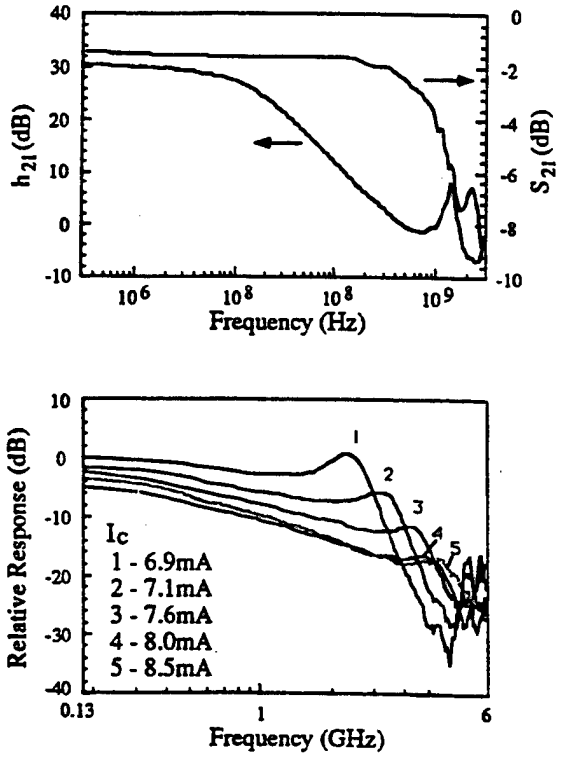


Figure 7: (a) The small-signal modulation response of the HBT/VCSEl switch, showing (a) the forward transmission coefficient S_{21} and the current gain h_{21}, and (b) the electrical-to-optical modulation response at different dc bias currents.

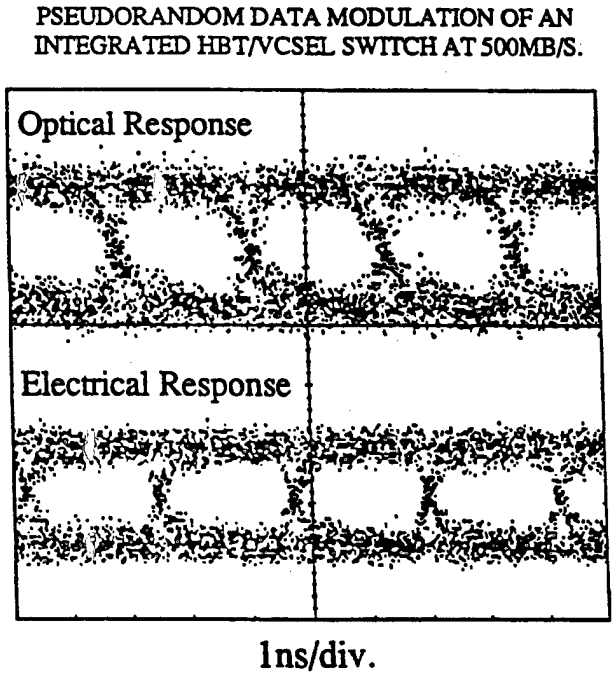


Figure 8. The eye diagram of an HBT/VCSEL switch under 500Mb/s pseudorandom data modulation, showing the modulated optical output of the VCSEL (upper trace) and the modulated collector current (bottom trace).

Figure 8 shows the eye diagrams of this HBT/VCSEL switch under large-signal pseudorandom data modulation at 500Mb/s. The upper trace represents the modulated light output of the VCSEL, while the lower trace shows the modulated collector current, with a 6.8mA current modulation superimposed on a 7.2mA dc bias. The modulated electrical pulses have 10%-90% transition time (~2.2τ) of 0.6ns, and shows no significant pulse narrowing due to a turn-on delay when the switch

is pre-biased above the lasing threshold. The same epitaxial structure can also be used as a platform for the integration of VCSELs with more complex HBT electronic logic circuits as well as phototransistors and to perform more extensive optoelectronic interface and switching functions.

The functional circuit diagram of a single three-terminal HPT/VCSEL switch (Fig. 5) shows that it can be switched by either an optical input P_{in} or by an electrical input E_{in} applied to the base of the HBT, producing both an optical output P_{out} and an electrical voltage modulation E_{out}. The switched output emerges as the optical output of the VCSEL or as the modulated collector current of the HPT, which can be coupled to an external circuit as a voltage modulation (Fig. 9). A dc bias can be applied at the base to pre-bias the VCSEL near threshold. The base also provides an input port for electronic data from a source processor. As shown in Fig. 9, the optical input produces an amplified collector current I_c and a voltage modulation E_{out}. The former modulates the VCSEL to produce a regenerated optical output (*O⇒O optical switching*), which is transmitted to the next node, while the latter represents the *optoelectronically-switched* electrical output (*O⇒E conversion*), which is received by the processor. An electrical input E_{in} (from a processor) applied to the base of the HPT also produces a modulated current I_c and a modulated voltage E_{out}. The former produces an *optoelectronically switched* optical output from the VCSEL (*E⇒O conversion*), which is transmitted to another node, while the latter represents the *electrically switched*(*E⇒E*) output data, which is received by another processor. Each processor can thus receive or transmit data through the optical switch.

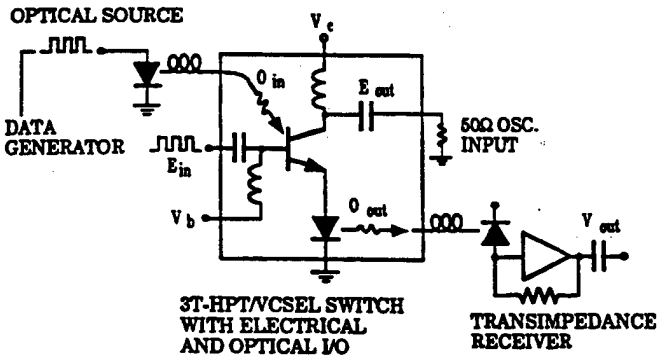


Figure 9. The experimental setup for measuring the switched electrical (I_{out}) and optical (P_{out}) outputs of the monolithic HPT/VCSEL switch in the presence of either electrical (E_{in}) or optical (P_{in}) inputs.

The various switching functions are experimentally demonstrated using different combinations of optical and electrical inout/output (Fig. 10). Two different data patterns modulate the optical and electrical inputs to the HPT during alternate, non-overlapping time intervals. The optical data is incident on the base-collector junction of the HPT, while the electrical data directly modulates the base of the HPT. The switch processes the electrical and optical input data packets, converting each into both a switched optical and electrical output, and combining them into a single packetized data stream. The first two traces in Figure 9 show the modulated collector current I_c in the presence of *only* the electrical (trace 1) or optical (trace 2) input data, demonstrating the achievement of (*E⇒E*) and (*O⇒E*) switching. Traces 3 and 4 show the modulated electrical output (I_c) and optical output (P_{out}) when optical and electrical input data are both present. Each trace contains replicas of both the optical and electrical inputs. Thus the switch has demonstrated the conversion of either electrical or optical data into both optical and electrical outputs at a data rate of ~200 Mb/s.

The optical and electrical output response of the integrated three-terminal HPT/VCSEL switch to either optical or electrical input modulation by large-signal, pseudorandom data at 200 Mb/s are summarized by the eye diagrams shown in Fig. 11, which are wide open. Figures 9-11 show that optical switching can be achieved at a data rate of >200 Mb/s, while electrical-to-optical data conversion can occur at a data rate well in excess of 500 Mb/s.

4. RECONFIGURABLE SPATIAL ROUTING WITH HPT/VCSEL SWITCHES:

An optical routing switch can be achieved using binary HPT/VCSEL switch configurations that spatially reconfigure and re-direct the surface-normal optical outputs of the VCSELs. Electrical routing within each stage is limited to very short distances within a compact two-dimensional array of switch nodes. Figure 12 shows the design and optical routing functions of a binary 1x2 switch, which can be used implements a shuffle network topology. Each node contains a segmented HPT optical input port, each of whose segments is serially connected to a different VCSEL representing a spatially-displaced output port, thus providing a fanout of 2. The data routing and optical fan-out functions are experimentally demonstrated in

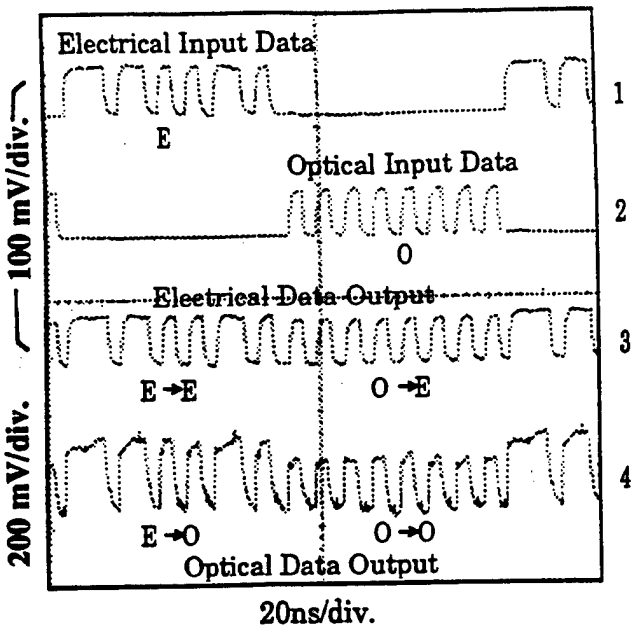


Figure 10. The experimental switching data, with traces 1 and 2 showing the electrical output E_{out}, represented by the amplified collector current I_c, in the presence of either the electrical input data E_{in} or the optical input data P_{in}, respectively. Traces 3 and 4 show the electrical output E_{out} and the optical output P_{out}, respectively, when both P_{in} and E_{in} are present. The optical and electrical input data packets are combined into a single data stream, which emerges in either an optical or electrical output data format.

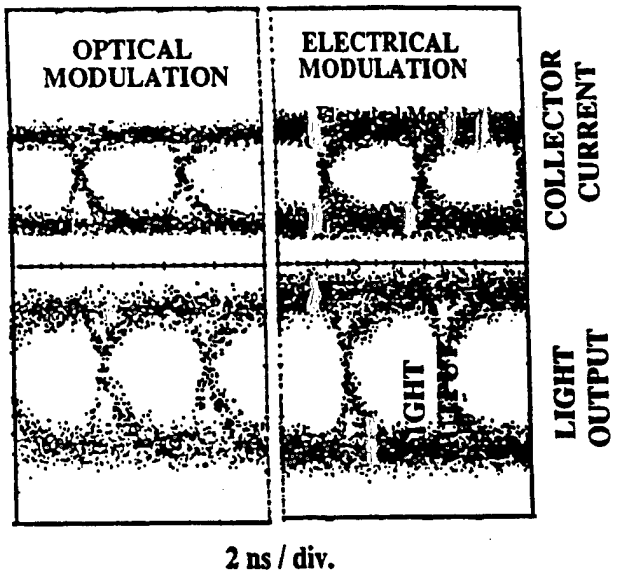
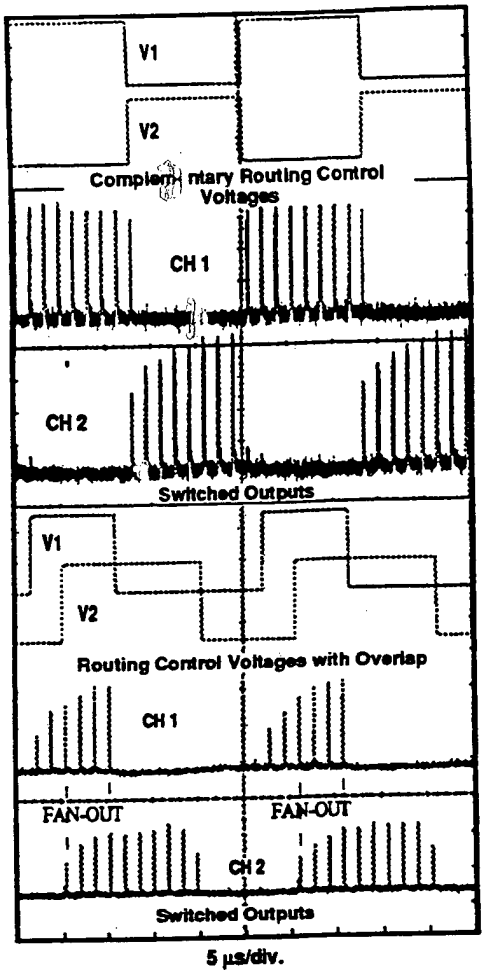


Figure 11: Eye-diagrams showing the optical (lower traces) and electrical (upper traces) response of a single HPT/VCSEL switch to large-signal, pseudorandom modulation by optical (left) and electrical (right) input data at 200 Mb/s.

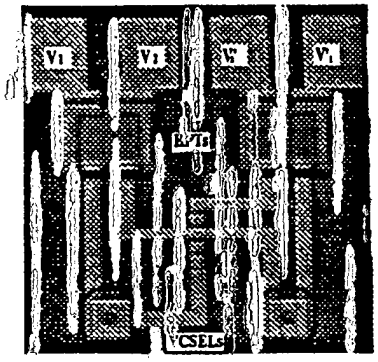
Figure 12a. Using simple voltage control of V_1 and V_2, packets of high speed optical data impinging on the HPT generate amplified photocurrents that modulate the VCSELs to produce optically regenerated outputs that emerge from either, neither or both of the output ports. Figure 13 shows a 2x2 optical bypass-exchange switch, which consists of two 1x2 switch nodes pairing the same two channels, and can be used to implement a Banyan network. Routing is controlled by two pairs of voltages, which select the bypass or exchange switching modes. The bypass-exchange operation of a monolithic 2x2 switch is experimentally demonstrated in Figure 13. As the control voltages are toggled, the optically regenerated pulses of the two input data channels emerge alternately from the same or opposite output ports (VCSELs).

5. OPTICALLY CASCADED SWITCHING OPERATION:

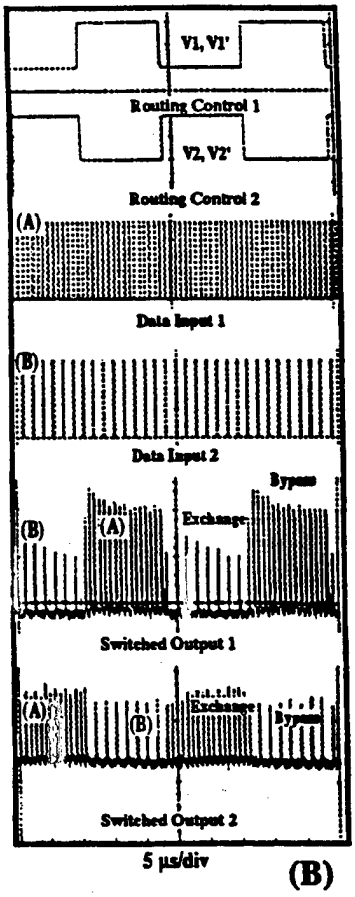
Monolithic 1x8 arrays of binary optical switches with electrical interfaces have been fabricated (Fig. 14) and used to demonstrate optically cascaded switching and routing operations. Each of the binary switches contains a photodetector element consisting of a small AlGaAs/GaAs HBT integrated with a GaAs PIN photodiode, which replaces the three-terminal HPT. Each element of the array has electrical input and output ports, and can perform both the optical switching and optoelectronic data conversion functions, as in the case of the 3-terminal HPT. As in the case of individual binary HPT/VCSEL optical switches, setting the control voltages of the entire array can produce many different routing configurations. Optically ascaded operation has been demonstrated by using three sequential 1x8 HBT/PIN/VCSEL switch arrays, which are optically coupled using fiber ribbon arrays. Their switching functions are schematically illustrated in Fig. 15. Using HBTs and VCSELs whose characteristics are shown in Fig. 4, optical switching with a dc optical gain of ~5 has been achieved. At present, optically cascaded switching operation has been demonstrated at a data rate of ~100 Mb/s, and electrical-to-optical data conversion at ~200 Mb/s. The achievement of a significant optical gain can compensate the optical partition losses and thus relaxes the optical coupling tolerances for cascaded optical switching operations, where an overall net optical gain of ~1 is needed between stages.

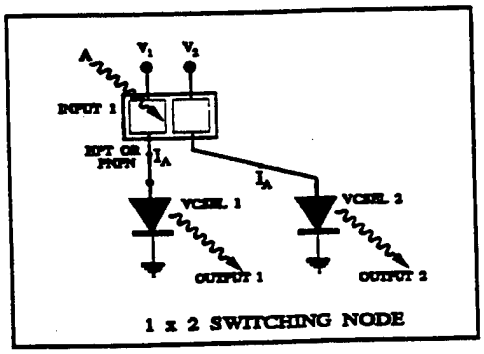


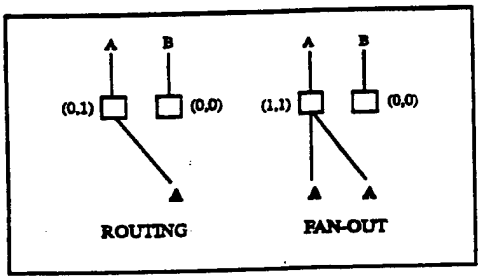
ROUTING CONTROL VOLTAGES



2X2 OPTICAL SWITCH

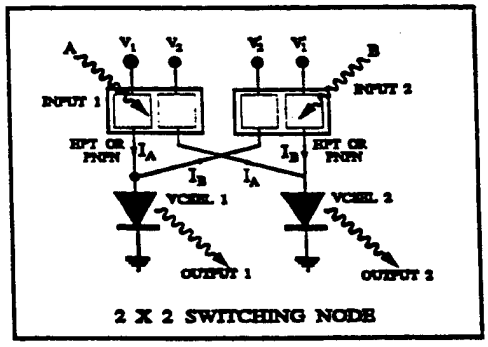


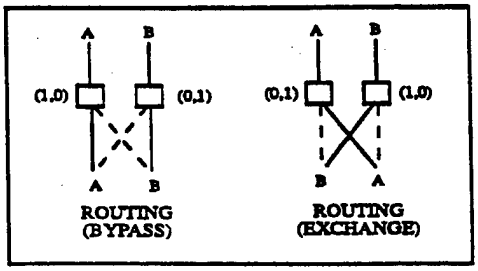




(b) SHUFFLE

Figure 12. Experimental demonstration of 1x2 optical switching, showing the routing control voltages and the optical output channels for the cases of (a) no fan-out, and (b) an optical fan-out of 2.





(a) BANYAN

Figure 13. Experimental demonstration of 2x2 optical switching, showing (a) the control voltages, (b) the input optical channels, and (c) the output optical channels, indicating bypass and exchange operations.

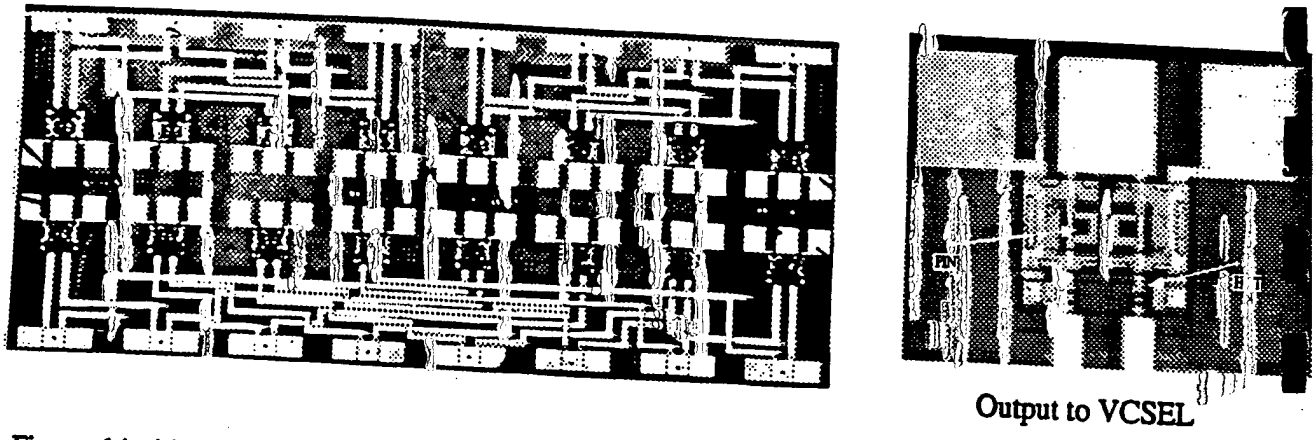


Figure 14. (a) A monolithic 1x8 array of segmented binary HPT/VCSEL switches with a shuffle routing topology and a common-emitter circuit geometry, and (b) shows that each binary switch contains a pair of HBTs and PIN photodiodes that are each interconnected to a different VCSEL.

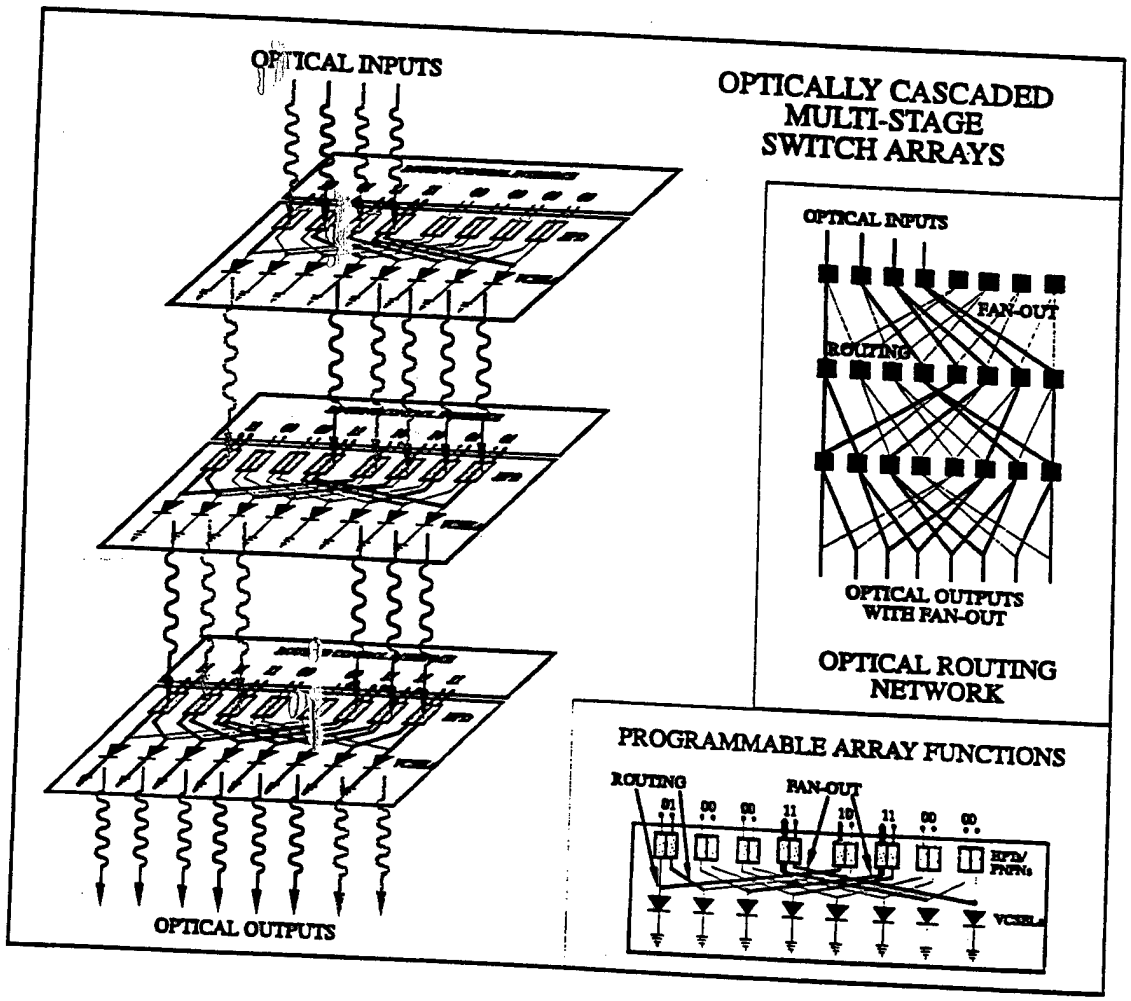


Figure 15. Schematic illustration of an optically cascaded multi-stage switching network, some of the programmable routing functions that are performed by each array (lower right inset), and the equivalent routing topology (upper right inset).

6. CONCLUSIONS:

We have described a new, multi-path optoelectronic backplane that provides parallel communication channels for a large number of processors via a reconfigurable, high-speed optical switching fabric. Using the three-terminal HPT/VCSEL or PIN/HBT/VCSEL switching technology, we have shown that high speed optical and optoelectronic switching can be achieved to convert data between various electrical and optical formats. By combining them into binary switch configurations, optical data can be spatially routed to different output ports in a simple, controllable manner. Using arrays of these binary switches, and connecting a processor to each node, we have a high speed optical bus that allow the processors to communicate through parallel, reconfigurable interconnections. We have also shown that sequential stages can be optically cascaded with a net optical gain. The next generation of switches will extend the current speed performance of both optical switching (200 Mb/s) and optoelectronic switching (>500 Mb/s) into the >1Gb/s regime.

7. ACKNOWLEDGMENTS:

Various parts of this work was made possible by the generous support of Rome Labs (Griffis Air Force Base), ARPA (MTO), and AFOSR (Bolling AFB). The contributions of Bo Lu, Yin-Chen Lu, D. Alduino, and S. Z. Sun of the University of New Mexico, and of J. C. Zolper, J. Klem, R. P. Schneider, G. A. Vawter, S. P. Kilcoyne, and J. Ascebedo of Sandia National Laboratories, are gratefully acknowledged.

8. REFERENCES:

[1] J. Cheng, P. Zhou, S. Z. Sun, and D. R. Myers, "Surface-emitting Laser-based Smart Pixels for Two-dimensional Optical Logic and Reconfigurable Optical Interconnections", IEEE J. of Quantum Electronics, Vol. 29, pp.741-756, 1993.

[2] J. Cheng, B. Lu, R. E. Leibenguth, A. C. Adams, J. A. Zopler, G. A. Vawter, S. A. Chalmers, "Monolithic photonic and optoelectronic technology for high-speed switching networks, reconfigurable optical interconnects, and optical data processing", SPIE Vol. 2155, Optoelectronic Signal Processing for Phased-Array Antennas IV, 1994.

[3] Y.-C. Lu, Julian Cheng, "A Reconfigurable Optoelectronic Interconnect Technology for Multi-Processor Networks ", Proc. of the 45th Electronics Components and Technology Conference, May 1995.

[4] Bo Lu, Ping Zhou, Y.C.Lu, J. Cheng, R.E. Leibenguth, A. C. Adams, J. L. Zilko, J. C. Zolper, K. L. Lear, S.A. Chalmers, G. A. Vawter, "Reconfigurable Binary Optical Routing Switches with Fan-out Based on the Integration of GaAs/AlGaAs Surface-Emitting Lasers and Heterojunction Phototransistors", IEEE Photonics Technology Letters, Vol. 6, No. 2, pp. 222-226, February 1994.

[5] P. Zhou, J. Cheng, J. C. Zolper, K. L. Lear, S. A. Chalmers, G.A.Vawter, R. E. Leibenguth, and A. C. Adams, "Monolithic Optotelectronic Switch Based on the Integration of a GaAs/AlGaAs Heterojunction Bipolar Transistor and a GaAs Vertical-Cavity Surface-Emitting Laser", *IEEE Photonics Technology Letters*, Vol. 5, pp. 1035-1038, 1993.

[6]. J. Cheng, P. Zhou, J. C. Zolper, K. L. Lear, G. A. Vawter, R. E. Leibenguth, A.C. Adams, "Reconfigurable Optical Switches with Monolithic Electrical-to-Optical Interfaces", SPIE Vol. 2153, Optoelectronic Interconnects II, pp. 315-322, 1994.

[7] Bo Lu, P. Zhou, J. Cheng, K. J. Malloy, "High Temperature Pulsed and CW Operation and Thermally Stable Threshold Characteristics of Vertical-Cavity Surface-Emitting Lasers Grown by MOCVD", Appl. Phys. Lett., Vol. 65, pp. 1337-1339,1994.

[8] Y. C. Lu, J. Cheng, P. Zhou, J. Klem, J. C. Zolper, "High Speed Electrical and Optical Modulation Response of Monolithic Switches Integrating a Heterojunction Phototransistor with a Surface-Emitting Laser", Electronics Lett., March 1995.

[9] Y. C. Lu, J. Cheng, J. Klem, J. C. Zolper, "Integrated Optical /Optoelectronic Switch for Parallel Optical Interconnects", to be published in Electronics Lett., April 1995.

[10]. Ping Zhou, Bo Lu, Julian Cheng, K.J.Malloy, S.Z.Sun, S.D.Hersee, and J.C.Zolpe.: 'Vertical-cavity surface-emitting lasers with thermally stable electrical characteristics', J. Applied Physics, March, 1995.

Indirect Measurement of the Magnitude of Ion Clustering at High Doping Densities in Er:ZBLAN Fibers

Balaji Srinivasan and Ravinder K. Jain
Center for High Tech Materials, Univ. of New Mexico, Albuquerque, NM 87106
Phone: (505) 272-7821, Fax: (505) 272-7801, email: balaji@chtm.unm.edu, jain@chtm.unm.edu

Gérard Monnom
Laboratoire de Physique de la Matiere Condensee, Univ. de Nice - Sophia Antipolis, France
email: Gerard.Monnom@unice.fr

Abstract

We report precise quantification of the percentage of ion clusters in Er:ZBLAN fibers via measurement of non-saturable optical absorption and fitting of this data to a simple theoretical model which includes the role of clustering. In particular, using this indirect measurement technique, we demonstrate the presence of 51% ions in clusters for such fibers with an average doping density of 10,000 ppm, whereas a similar fiber with an average doping density of 1,000 ppm shows negligible effects of clustering. Application of this technique to more precise design of Er:ZBLAN fiber lasers, characterization of the fiber drawing process, and more precise determination of cross-relaxation parameters in Er:ZBLAN fibers are discussed.

OCIS Codes: Erbium fiber, Fiber characterization, Fiber optic amplifiers and oscillators, Rare earth doped materials

The broadly tunable[1] 2.7 μm transition in Er:ZBLAN appears particularly attractive for the design of compact, high power CW fiber lasers[2] of excellent beam quality, as needed for applications ranging from endoscopic laser surgery[3] to countermeasures and spectroscopic monitoring[4]. As is well known, the longer lifetime of the lower laser level ($^4I_{13/2}$, 9.4 ms) compared to the upper laser level ($^4I_{11/2}$, 7.5 ms) of this transition poses a serious bottleneck[2,5], which in the past has been alleviated by complex mechanisms

such as: (1) selective depletion of the lower laser level via excited state absorption (ESA)[6,7], (2) excitation transfer of the energy from the $^4I_{13/2}$ lower laser level to an appropriate acceptor state (e.g. the $^3F_3$ level in Pr[8]), and (3) cascade lasing[9]. Recently, Poppe et al.[2] have demonstrated alleviation of this bottleneck and strongly enhanced efficiencies and output powers by a simpler alternative technique, viz. the use of fibers with high average concentrations (>10,000 ppm) of Er. It was hypothesized that such high concentrations not only reduce the problem of ground state bleaching[5], but also cause significantly enhanced cross-relaxation (denoted as #1 in Fig. 1), whose net effect is to relax the excitation from the lower laser level ($^4I_{13/2}$) to the ground state ($^4I_{15/2}$), while upconverting an adjacent ion to the $^4I_{9/2}$ state. With regards to the role of this cross-relaxation mechanism, a contrary piece of evidence has been reported for Er:ZBLAN bulk glasses by Bogdanov et al.[10], in which significant cross-relaxation was observed only at very high doping densities i.e., 150,000 ppm. One possible explanation for this contradiction is the presence of ions in clusters in highly doped Er:ZBLAN fibers.

This paper is targeted towards a more precise estimation of the magnitude of ion clustering in heavily doped Er:ZBLAN fibers. Such quantification of the amount of clustering is achieved by an indirect optical technique[11] based on the role of clusters for rapid repopulation of the ground state via cross-relaxation processes, evidenced by a sharp decrease in the "normal" saturation of absorption observed for various transitions from the ground state in Er:ZBLAN fibers. In particular, we demonstrate that over 50% of the Er ions are found in clusters in Er:ZBLAN fibers with nominal mean doping densities (N_m) of 10,000 ppm and higher; this is deduced from fits of our new theoretical model to careful measurements of the saturation of absorption at the $^4I_{15/2}$-$^4I_{11/2}$ transition (972 nm) in Er:ZBLAN fibers. Note that despite its indirect nature, this optical measurement technique is simpler and more useful for the precise quantification of the degree of clustering than the more direct alternative techniques, such as transmission electron microscopy[12] (TEM) and microprobe X-ray analysis[13].

The role of high densities of ions in clusters on the phenomenon of the saturation of absorption in Er can be explained as follows. At low Er doping densities, the long lifetimes of the excited states ($^4I_{11/2}$ and $^4I_{13/2}$) leads to the depletion of the ground state population, which in turn leads to saturation of

absorption at several transitions (from the ground state). However, at high Er doping densities, the cross-relaxation processes discussed above (see Fig. 1) cause depletion of the $^4I_{13/2}$ and the $^4I_{11/2}$ populations, thereby reducing this saturation of absorption. In particular, as elucidated by Maurice et al[11] for *Er:silica* fibers, the onset of cluster formation can cause an even greater increase in the non-saturable component of the absorption. This is because when a large number of ions (n) are in the $^4I_{13/2}$ or in the $^4I_{11/2}$ state and are adjacent to each other in a cluster, all (but one) are de-excited to the $^4I_{15/2}$ ground state by n/2 cross-relaxations; this enhanced de-excitation (and repopulation of the ground state) inhibits the saturation of absorption that is observed at low doping densities.

Although the modeling and precise quantification is significantly different for *Er:fluoride* fibers because of the longer lifetimes of several of the excited states (and the consequent increased importance of excited state absorption as well as of multiple cross-relaxation processes), the dominance of the cross-relaxation processes of Fig. 1 is still expected to be evidenced by a similar behavior in the saturation of absorption (and in the increase in the non-saturable absorption component at higher doping densities). Such a strong increase in the non-saturable absorption (NSA) in Er:ZBLAN fibers due to the onset of clustering is quantified precisely in this work with the use of a modified theoretical model described in further detail below. Some of the results obtained using our model are plotted in Fig. 2a along with our absorption data for fibers with mean Er doping densities of 1000 ppm (LeVerre Fluore, core diameter = 3 μm, NA= 0.21, length=67 cm) and 10,000 ppm (LeVerre Fluore, core diameter = 6 μm, NA=0.15, length=6.7 cm) respectively. The absorption measurements were done using a Ti:Sapphire laser tuned to 972 nm (peak wavelength of absorption). The absorption (α) is given simply by

$$\alpha = 10\log_{10}\left(\frac{P_{launch}}{P_{out}}\right)\ dB$$

where P_{launch} is the 972 nm power launched into these single mode fibers. Fig. 2b shows the absorption data for an Er:ZBLAN fiber fabricated by a different manufacturer (KDD/Thorlabs) with a mean concentration of 20,000 ppm (core diameter = 3.8 μm, NA=0.28, length=6.8 cm).

In comparison to the model of Maurice et al.[11], our model is modified by the incorporation of the long lifetimes of the excited states (τ_2=7.4 ms, τ_1=9.4 ms) leading to significant excited state absorption and the inclusion of the cross-relaxation process #2 from the $^4I_{11/2}$ level (because of the consequently higher population densities in this level for fluoride fibers). As elucidated by Maurice et al.[11], we have assumed that a certain fraction of ion population exists as homogeneously distributed ions in the fluoride host (denoted as n_i where i=0, 1, 2, 3 as shown in Fig. 1) and that the rest are distributed in clusters (denoted as n_i*). For the homogeneously distributed ions, the modified rate equations are written as:

$$\frac{\partial n_0}{\partial t} = -W_{02} n_0 + (\gamma_{10} + W_{11} n_1) n_1 + (\gamma_{20} + W_{20} + W_{22} n_2) n_2 + \gamma_{30} n_3 \quad \text{..... (1}a\text{)}$$

$$\frac{\partial n_1}{\partial t} = -(\gamma_{10} + 2W_{11} n_1) n_1 + \gamma_{21} n_2 + \gamma_{31} n_3 \quad \text{..... (1}b\text{)}$$

$$\frac{\partial n_2}{\partial t} = -(\gamma_2 + W_{20} + 2W_{22} n_2 + W_{23}) n_2 + \gamma_{32} n_3 + W_{02} n_0 + W_{11} n_1^2 \quad \text{..... (1}c\text{)}$$

$$\frac{\partial n_3}{\partial t} = -\gamma_3 n_3 + (W_{23} + W_{22} n_2) n_2 \quad \text{..... (1}d\text{)}$$

where W_{ij} is the absorption rate for the transition from level i to level j, W_{ji} is the stimulated emission rate, γ_{ij} is the sum of the radiative and non-radiative relaxation rate, and W_{ii} (i=1 or 2) are the cross-relaxation rates for the processes #1 and #2 shown in Fig. 1 such that $W_{ii}=\Omega_{ii}xN_m$, where Ω_{ij} is the cross-relaxation coefficient

Note that the fractions of ions that are present in clusters, n_0*, n_1*, and n_2*, are assumed to be 1, 0, and 0 respectively because of the rapid de-excitation of the populations of levels 1 and 2 due to cross-relaxation processes (as explained previously), whereas n_3* is assumed to be 0 since n_1* and n_2* are zero. The above rate equations were solved to obtain the fractional population density of the different energy levels which was then used to determine the evolution of the absorption along the length of the fiber as in Maurice et al[11].

Note that the model developed here uses measured values of lifetimes and branching ratios[13,14] as well as known cross-relaxation rates[15] and uses no free parameters for the fits other than an assumption of the fraction of total ions that are in clusters. Specifically, we used values of 1.2×10^{-25} cm^2 for the absorption cross-section (σ_p), 4×10^{-17} cm^3/sec for the cross-relaxation coefficient Ω_{11}, and 5×10^{-17} cm^3/sec for the cross-relaxation coefficient Ω_{22} in our model. As such, the excellent agreement between the model and the data gives a strong indication of the percentage of ions in clusters (51% in the N_m=10,000 ppm fiber and 70% in the N_m=20,000 ppm fiber, compared to none in the N_m=1000 ppm fiber). The presence of clusters also explains why fiber lasers based on fibers with average doping concentrations much lower than those specified by Bogdanov et al.[10] apparently show significant efficiency enhancements[2,16,17] due to cross-relaxation processes. Experiments are underway to correlate our estimates of the magnitude of clustering in such highly doped fibers through more direct and visually gratifying techniques such as TEM[12] or X-ray microprobes[13], despite the lack of precise quantification in these more direct techniques.

Work is in progress to further refine this model to calculate the populations of the upper and lower laser levels precisely, and thereby calculate the small signal and saturated gains for such Er:ZBLAN fibers at high mean doping densities (based on clustering levels predicted by fits similar to Fig. 2). Such a model should enable design and optimization of high power 2.7 μm fiber laser sources.

Precise quantification of clustering levels is also important for the improved design of flatband compact 1.55 μm Er-doped fluoride fiber amplifiers[18,19] (EDFFAs) and for the design of green upconversion-based Er:ZBLAN temperature sensors[20]. In EDFFAs, high ion densities will be advantageous for increased power extraction and compactness, but are inhibited by the rapid decrease in gain at the onset of clustering; on the other hand, in upconversion-based temperature sensors, clustering acts favorably to increase the intensity of the green fluorescence from the $^4S_{3/2}$ level due to enhancement of the cross-relaxation process #2 (Fig. 1).

Because clustering in rare earth doped fibers depends strongly on defect centers created, such measurement of clustering via measurement of saturable absorption also represents a powerful new diagnostic technique to evaluate the quality of the fiber drawing process. In related work (whose results

are shown in Figure 2b), we have observed cluster ion fractions of approximately 70% for fibers with N_m=20,000 ppm drawn by a different manufacturer (KDD/Thorlabs). Although correlation of the cluster fractions with the fiber drawing process (and drawing-induced defect generation) will be very useful for future applications, such analysis was not possible in our present work due to the unavailability of sufficient information about the drawing process from the two fiber manufacturers (apparently because of the proprietary nature of the process). Another study that would be of great interest for future applications is that of the dependence of the cluster fraction on the average doping concentration for each major fiber fabrication process. However, we would need a very large set of actual fibers (rather than relatively inexpensive bulk glasses) with different average doping concentrations, which was not possible, due to the prohibitive costs involved in fabricating each of the fluoride fibers.

Also, as expected for the experiments reported here, where the $^4I_{11/2}$ level (i.e. level 2 in the above model) is pumped directly, the fits of calculations based on the model to the data are found to be very sensitive to the exact value chosen for the cross-relaxation rate W_{22}. As such, this technique represents an extremely powerful method for estimating the cross-relaxation rate W_{22} with high precision compared to conventional methods that involve lifetime measurements as a function of concentration. Likewise, by measuring saturation of absorption while directly pumping level 1 (say, with 1480 nm radiation), one should be able to determine W_{11} with high precision. Additional studies are in progress to investigate the use of such NSA measurements, and corresponding fits to modeled estimates of absorption, to determine the cross-relaxation rates more precisely and reliably.

In summary, we report precise quantification of the percentage of ion clusters in Er:ZBLAN fibers via measurement of non-saturable optical absorption and fitting of this data to a simple theoretical model which includes the role of clustering. In particular, using this indirect measurement technique, we demonstrate the presence of 51% ions in clusters for such fibers with an average doping density of 10,000 ppm, whereas a similar fiber with an average doping density of 1,000 ppm shows negligible effects of clustering. Application of this technique to more precise design of Er:ZBLAN fiber lasers,

characterization of the fiber drawing process, and more precise determination of cross-relaxation parameters in Er:ZBLAN fibers have been proposed.

References:

1. F. Auzel, D. Meichenin, and H. Poignant, "Tunable Continuous-Wave, Room-Temperature Er^{3+}-Doped ZrF_4-Based Glass Laser Between 2.69 and 2.78 μm", Electron. Lett., **24**, 1463-1464 (1988)
2. E. Poppe, B. Srinivasan, and R.K. Jain, "980nm Diode-Pumped Continuous-Wave Mid-IR (2.7 μm) Fiber Laser", Electron. Lett., **34**, 2340 (1998)
3. K.F. Gibson and W.G. Kernohan, "Lasers in Medicine: A Review", J. Med. Engg. and Tech., **17**, 51-57 (1993); R. Kaufmann, A. Hartmann, R. Hibst, "Cutting and Skin-Ablative Properties of Pulsed Mid-Infrared Laser Surgery", J. Derm. Surg. And Onc., **20**, 112-118 (1994)
4. R.S. Eng, J.F. Butler, and K.J. Linden, "Tunable Diode-Laser Spectroscopy: An Invited Review", Opt. Engg., **19**, 945-960 (1980)
5. M. Pollnau, "The Route Toward a Diode-Pumped 1-W Erbium 3- μm Fiber Laser", IEEE J. Quantum Electron., **33**, 1982-1990 (1997)
6. M.C. Brierley, and P.W. France, "Continuous Wave Lasing at 2.7 μm in an Erbium-Doped Fluorozirconate Fibre", Electron. Lett., **24**, 935-937 (1988)
7. B. Srinivasan, E. Poppe, and R.K. Jain, "40 mW Single-Transverse-Mode Mid-IR (2.7 μm) CW Output from a Simple Mirror-Free 780-nm Diode-Pumpable Fiber Laser", OSA Technical Digest Series, **6**, 297 (1998)
8. J.Y. Allain, M. Monerie, and H. Poignant, "Energy Transfer in Er^{3+}/Pr^{3+}-Doped Fluoride Flass Fibres and Application to Lasing at 2.7 μm", Electron. Lett., **27**, 445-447 (1991)
9. M. Pollnau, Ch. Ghisler, C. Bunea, M. Bunea, W.Luthy, and H.P.Weber, "150 mW Unsaturated Output Power at 3 μm from a Single-Mode Fiber Erbium Cascade Laser", Appl Phys Lett, **66**, 3564-3566 (1995)
10. V.K. Bogdanov, W.E.K. Gibbs, D.J. Booth, J.S. Javorniczky, P.J. Newman, and D.R. MacFarlane, "Fluorescence from Highly-Doped Erbium Fluorozirconate Glasses Pumped at 800 nm", Opt. Commn., **132**, 73 (1996)

11. E. Maurice, G. Monnom, B. Dussardier, D.B. Ostrowsky, "Clustering-Induced Nonsaturable Absorption Phenomenon in Heavily Erbium-Doped Silica Fibers", Opt. Lett., **20**, 2487-2489 (1995)

12. B.J. Ainslie, S.P. Craig, R. Wyatt, and K. Moulding, "Optical and Structural-Analysis of Neodymium-Doped Silica-Based Optical Fiber", Mater. Lett., **8**, 204-208 (1989)

13. F. Auzel, D. Meichenin, and H. Poignant, "Laser Cross-Section and Quantum Yield of Er^{3+} at 2.7 μm in a ZrF_4-based Fluoride Glass", Elect. Lett., **24**, 909-910 (1988)

14. R.S. Quimby and W.J. Miniscalco, "Continuous-Wave Lasing on a Self-Terminating Transition", Appl. Opt., **28**, 14-16 (1989)

15. V.K. Bogdanov, W.E.K. Gibbs, D.J. Booth, J.S. Javorniczky, P.J. Newman, and D.R. MacFarlane, "Energy Exchange Processes in Er^{3+}-Doped Fluorozirconate Glasses", 11th Int. Symp. on Non-Oxide Glasses & New Optical Materials Proceedings, 417-422 (1998)

16. X. Zhao, B. Srinivasan, P. Pulaski, S. Gupta, and R.K. Jain, "Mirror-Free, High Power (~140mW) Diode-Pumped 2.7 μm CW Fiber Laser", Postdeadline paper, CLEO Europe '98 Tech. Digest (1998)

17. B. Srinivasan, E. Poppe, J. Tafoya, and R.K. Jain, "High-Power (400 mW) Diode-Pumped 2.7 μm Fiber Lasers Using Enhanced Er-Er Cross-Relaxation Processes", Electron. Lett., **35**, 1338-1340 (1999)

18. D. Bayart, B. Clesca, L. Hamon, and J.L. Beylat, "Experimental Investigation of the Gain Flatness Characteristics for 1.55 μm Erbium-Doped Fluoride Fiber Amplifiers", IEEE Photon. Tech. Lett., **6**, 613-615 (1994)

19. Y. Kimura, and M. Nakazawa, "Gain Characteristics of Erbium-Doped Fiber Amplifiers with High Erbium Concentration", Jpn. J. Appl. Phys., **32**, 1120-1125 (1993)

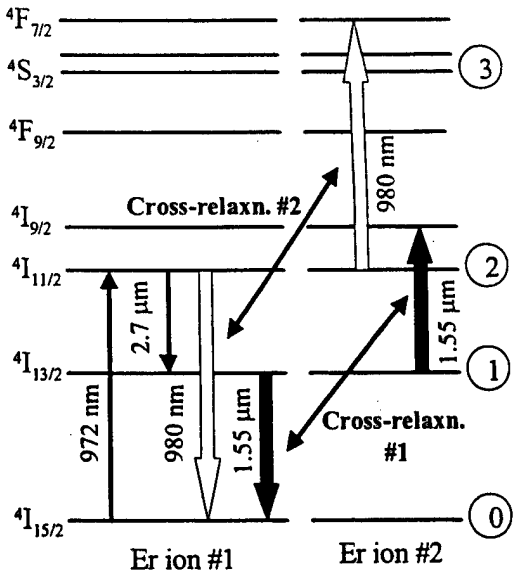
20. E. Maurice, G. Monnom, D.B. Ostrowsky, and G.W. Baxter, "High Dynamic Range Temperature Point Sensor Using Green Fluorescence Intensity Ratio in Erbium-Doped Silica Fiber", J Lightwave Tech., **13**, 1349-1353 (1995)

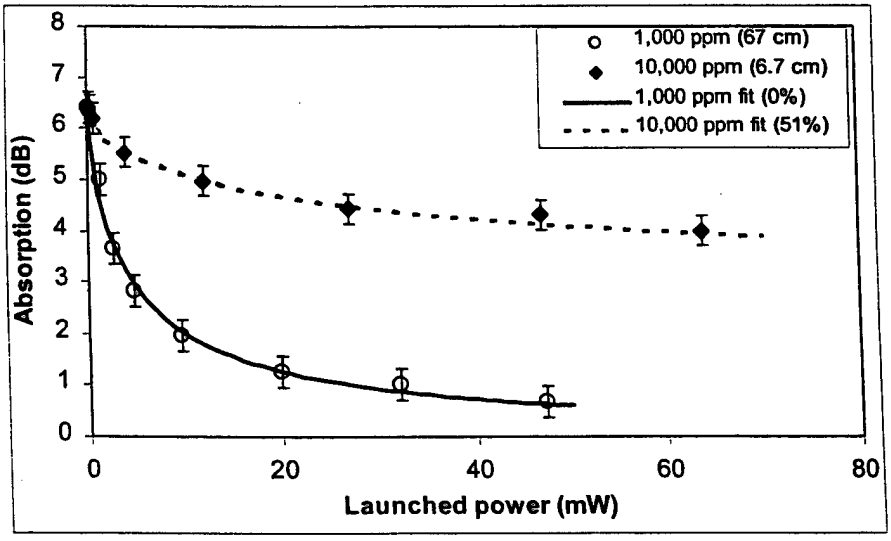
Figure Captions:

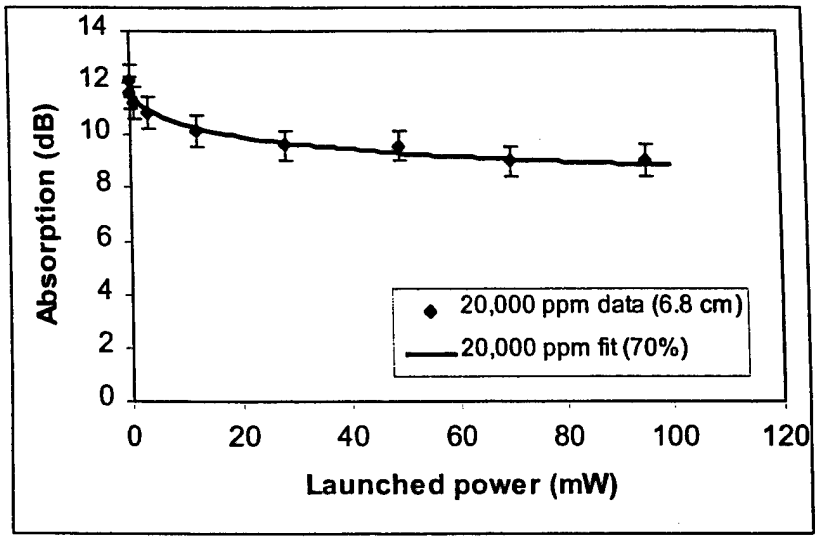
Figure 1. Energy level diagram of Er showing energy transfer due to cross-relaxation between two adjacent ions originally in the $^4I_{13/2}$ or the $^4I_{11/2}$ state

Figure 2a. A plot of the measured and calculated values of the absorption at 972 nm radiation as a function of launched power in two fibers corresponding to significantly different mean Er concentrations (N_m=1000 ppm and 10,000 ppm respectively)

Figure 2b. A plot of the measured and calculated values of the absorption at 972 nm radiation as a function of launched power for an Er:ZBLAN fiber with N_m=20,000 ppm


$^4F_{7/2}$
$^4S_{3/2}$
$^4F_{9/2}$
$^4I_{9/2}$
$^4I_{11/2}$
$^4I_{13/2}$
$^4I_{15/2}$
3
2
1
0
980 nm
Cross-relaxn. #2
2.7 µm
1.55 µm
972 nm
980 nm
1.55 µm
Cross-relaxn. #1
Er ion #1
Er ion #2


1,000 ppm (67 cm)
10,000 ppm (6.7 cm)
1,000 ppm fit (0%)
10,000 ppm fit (51%)
Absorption (dB)
Launched power (mW)
0
1
2
3
4
5
6
7
8
0
20
40
60
80


20,000 ppm data (6.8 cm)
20,000 ppm fit (70%)
Absorption (dB)
Launched power (mW)
0
2
4
6
8
10
12
14
0
20
40
60
80
100
120

980nm - Diode-Pumped Continuous Wave Mid-IR (2.7 μm) Fiber Laser

E. Poppe*, B. Srinivasan, and R.K. Jain

Center for High Technology Materials, Univ. of New Mexico, 1313 Goddard SE, 87106

Albuquerque NM, USA

* Dept. of Physical Electronics, Norwegian Univ. of Science of Technology, O.S.

Bragstadpl. 2, N-7034 Trondheim, Norway

We report a relatively efficient power-scalable mid-IR (2.7 μm) Er^{3+}:ZBLAN fiber laser pumped by readily available 980 nm laser diodes. The ~12 mW cw power levels reported here are significantly higher than those reported previously for any diode-pumped cw mid-IR fiber laser.

980nm - Diode-Pumped Continuous Wave Mid-IR (2.7 μm) Fiber Laser

E. Poppe*, B. Srinivasan, and R.K. Jain

Center for High Technology Materials, Univ. of New Mexico, 1313 Goddard SE, 87106

Albuquerque NM, USA

* Dept. of Physical Electronics, Norwegian Univ. of Science of Technology, O.S.

Bragstadpl. 2, N-7034 Trondheim, Norway

Compact and tunable, high-efficiency cw mid-IR lasers are needed for numerous applications, including *field-usable spectroscopic sensors* for environmental and industrial-process monitoring [1], [2], *master oscillators* in airborne or spaceborne high-power mid-IR MOPAs for countermeasures and for *surgery applications* [3]. Lead-salt diode lasers are limited by the need for cryogenic cooling, low power, and spatial, temporal, and spectral instabilities. Sb-based diode lasers and quantum cascade lasers are beginning to show significant improvements, but long-lived stable cw mid-IR outputs have not yet been achieved with these devices at room temperature [4]. On the other hand, diode-pumped fiber lasers represent an attractive alternative technology [5], [6], capable of delivering stable diffraction-limited cw room-temperature mid-IR emission, at least in limited wavelength ranges (such as in bands around 2.7 and 3.5 μm). Figure 1 shows a schematic diagram of a future compact and robust field-usable wavelength-tunable and directly modulatable mid-IR fiber laser suitable for ultra-sensitive detection of trace levels of species such as H_2S, HF, NO, and CO_2. A key initial step in this direction is the demonstration of relatively efficient and reliable diode-pumped mid-IR fiber lasers with output powers of the order of 10 mW.

In this Letter, we describe a relatively efficient power-scalable mid-IR (2.7 μm) Er^{3+}:ZBLAN fiber laser pumped by readily-available 980 nm laser diodes. The 12 mW cw output powers demonstrated here are significantly higher than those reported previously from any diode-pumped mid-IR fiber laser. The highest output powers reported previously from diode-pumped mid-IR fiber lasers are the 0.32 mW reported in a 2.7 μm Er:ZBLAN fiber laser by Allen et.al. [5] and the 2.1 mW demonstrated by Yanagita et.al. [6]. The latter used an Er:AZL fiber which is difficult to fabricate. Both these previous reports were based on diode pumps in the 790-800 nm wavelength range.

A key factor in the achievement of the relatively efficient performance reported in our work is the use of high Er concentrations (10,000 ppm) in a relatively long fiber (5.5 m) of double clad design, as elaborated below.

Our choice of a 980 nm pump wavelength for this work (instead of the more efficient 790-800 nm pumps traditionally used [5], [6]) was dictated by the ready commercial availability of multi-Watt power level 980 nm diode lasers (due to the relatively large market need for 1.55 μm EDFA pumps). A principal reason why 980 nm pumping is less efficient is the strong ESA cross section from the upper laser level ($^4I_{11/2}$) to $^4I_{7/2}$ and the lack of an appropriate 980 nm ESA process (as occurs with the 791 nm pump) to depopulate the lower laser level ($^4I_{13/2}$) [7], [8]. Some enhancement of the depopulation is needed because the lower laser level lifetime (9.4 ms) is longer than that of the upper laser level (7.5 ms). This problem is alleviated in part in our highly-doped Er:ZBLAN fiber by the onset of a cross-relaxation mechanism which relaxes the excitation from the lower laser level to the ground state ($^4I_{15/2}$) while upconverting an adjacent ion to the $^4I_{9/2}$ state via the Foster-interaction. We believe that this cross-relaxation mechanism is significantly enhanced by the presence of cluster formation in such fibers [9], [10]. In addition, the high concentrations and the double clad geometry used

here reduce the problem of ground state bleaching [11] that has apparently limited conversion efficiencies and output powers in earlier work [8], [12], using Ti:Sapphire laser pumps.

In our experiments, we used a nearly single transverse mode, 1 Watt 980 nm tapered amplifier diode laser [13] as the pump source, which was coupled by a free space lens into the Er:ZBLAN fiber. The double-clad fiber had a core diameter of 6 μm with an NA of 0.15, a length of 5.5 m, an Er^{3+} concentration of 10,000 ppm (in the core), and an inner cladding diameter of 125 μm. The pump radiation was coupled to the fiber through a 20x microscope objective, with a coupling efficiency to the core of approximately 50%. An additional 35% of pump light was coupled to the inner cladding although this latter portion experiences a significantly lower effective absorption coefficient during its transit through the 5.5 m long fiber. The net absorption coefficient is estimated as 60%. The choice of a double-clad fiber was dictated in part by improved utilization of the pump light with 980 nm diode pumping, and in part by our plans to demonstrate power scaling of the outputs of such fiber lasers with use of high power diode lasers. At the input end an HR mirror was butt-coupled to the fiber while the cleaved distal end was used as a 96% output coupler. Figure 2 shows the 2.7 μm output power as a function of absorbed pump power. The low lasing threshold of 30 mW for a 96% output coupler, and the fact that no saturation of the output power is observed even at the highest pump powers used, indicates that this laser can be further optimized to yield much higher output power.

Other lasing characteristics were also studied. When the pump laser was chopped at 100 Hz, we observed the onset of relaxation oscillations at frequencies varying from 5 kHz to 20 kHz, as shown in Figure 3. The increase in the oscillation frequency with increased pump power is characteristic of relaxation oscillations [14], which were not investigated in any further detail. Moreover, we observed a tendency of the output wavelength of the untuned fiber laser to increase with an increase in pump power (from be 2.71 μm near threshold to 2.76 μm at

120 mW pump powers), as reported by other researchers [6], [8], due to Stark splitting and state filling effects [8].

In summary, we have reported a power-scalable 2.7 μm Er:ZBLAN fiber laser pumped by readily available 980 nm laser diodes. 12 mW of output power was demonstrated. This was achieved by the use of a high Er concentration of 10,000 ppm in a double clad geometry. The contribution of various factors to this efficiency enhancement, including (1) circumvention of bleaching of ground state absorption and (2) improved population inversion due to cross-relaxation processes that are magnified by clustering effects, are currently being investigated in further detail. In addition, we are investigating the possibility of scaling the output powers of such lasers to >100 mW, which are needed for near-term endoscopic intra-ocular surgery and transmyocardial revascularization, with the use of higher power pump diodes, improved diode-to-fiber coupling efficiencies and longer double clad Er:ZBLAN fibers of designs similar to those reported here.

Acknowledgements:

E. Poppe would like to thank the mid-IR project at Norwegian Univ. of Science and Technology and the Norwegian Research Council for supporting his stay at Univ. of New Mexico. The authors also acknowledge the support from Air Force Office of Scientific Research.

List of figure captions:

Figure 1. Vision of a future compact and robust, wavelength-tunable and directly modulatable, diode-pumped Er:ZBLAN mid-IR fiber laser

Figure 2. cw mid-IR output power vs. absorbed pump power

Figure 3. Relaxation oscillation frequency vs. average absorbed power

References:

[1] Petrov, K.P., Tittel, F.K., Curl, R.F., Waltman, S., and Hollberg, L., 'Tunable infrared laser sources for spectroscopy and atmospheric trace gas detection', *Laser Spectroscopy. 12th Intern. Conf.*, 1995, pp. 356-359

[2] Eng, R.S., Butler, J. F., and Linden, K. J., 'Tunable diode laser spectroscopy: an invited review', *Opt. Eng.*, 1980, **19**, pp. 945-960

[3] Esterowitz, L. and Allen, R., 'Rare earth doped IR fiber lasers for medical applications', *Proc. of the SPIE Conf. on Infrared Fiber Optics*, 1989, **1084**, pp. 129-132.

[4] Hasenberg, T.C., Miles, R.H., Kost, A.R., and West, L., 'Recent advances in Sb-based midwave-infrared lasers', *IEEE J. Quantum Electron.*, 1997, **33**, (8), pp. 1403-1406

[5] Allen, R., Esterowitz, L., and Ginther, R.J., 'Diode-pumped single mode fluorozirconate fiber laser from the $^4I_{11/2} \rightarrow {}^4I_{13/2}$ transition in erbium', *Appl. Phys. Lett.*, 1990, **56**, (17), pp. 1635-1637

[6] Yanagita, H., Masuda, I., Yamashita, T., and Toratani, H.: 'Diode laser pumped Er^{3+} fibre laser operation between 2.7-2.8 μm', *Electron. Lett.*, 1990, **26**, (22), pp. 1836-1838.

[7] Pollnau, M., Spring, R., Wittwer, S., Lüthy, W., and Weber, H.P., 'Efficiency of erbium 3-μm crystal and fiber lasers', *IEEE J. Quantum Electron.*, 1996, **32**, (4), pp. 657-663

[8] Frerichs, Ch., 'Efficient Er^{3+}-doped cw fluorozirconate fiber laser operating at 2.7 μm pumped at 980 nm', *Intern. J. Infrared and Millimeter Waves*, 1994, **15**, (4), pp. 635-649.

[9] Dybdal, K., Bjerre, N., Pedersen, J.E., and Larsen, C.C., 'Spectroscopic properties of Er-doped silica fibers and preforms', *Proc. of the SPIE Conf. on Fiber Laser Sources and Amplifiers*, 1990, **1171**, pp. 209-218

[10] Maurice, E., Monnom, G., Dussardier, B., and Ostrowsky, D.B., 'Clustering-induced nonsaturable absorption phenomenon in heavily erbium-doped silica fibers', *Opt. Lett.*, 1995, **20**, (24) pp. 2487-2489

[11] Pollnau, M., 'The route towards a diode-pumped 1-W erbium 3-mm fiber laser', *IEEE J. Quantum Electron.*, 1997, **33**, (11), pp.1982-1989

[12] Bedö, S., Lüthy, W., and Weber, H.P., 'Limits in the output power in Er^{3+}:ZBLAN singlemode fibre lasers', *Electr. Lett.*, 1995, **31**, (3), pp.199-200

[13] Walpole, J.N., Kintzer, E.S. Chinn, S.R., Wang, C.A., and Missaggia, L.J., ' High-power strained-layer InGaAs/AlGaAs tapered traveling wave amplifier' *Appl. Phys. Lett.*, 1992, **61**, (7), pp. 740-742

[14] H. Haken, 'Laser theory', Springer-Verlag Berlin - Heidelberg - New York, 1983, section VI.9

rovide electron-hole conversion from the top *n*-mirror. This scheme has been demonstrated previously by other authors [1].

Following the growth, the reflectivity spectrum of the structure was measured. The cavity mode was found at 1.55μm, which was centred on a > 140nm stopband (reflectivity > 99%). The top DBR then was removed in order to examine the photoluminescence (PL) of the quantum wells. The PL peak was at ~1580nm, placing the cavity mode on the broad, short-wavelength shoulder of the PL spectrum. The mode and PL peak can be aligned by lowering the operation temperature.

Pillars with diameters ranging from 10 to 100μm were then fabricated by reactive ion etching using the top metal contact as an etch mask. Contacts were also deposited on the substrate backside.

The *L-I* and *I-V* results from a 25μm diameter pillar operated in pulsed-mode at room temperature are shown in Fig. 3. The threshold current is ~7mA, corresponding to a current density, J_{th}, of only 1.4kA/cm^2. The external differential quantum efficiency of this device was ~18% and the maximum power was ~2mW. Lasing was achieved up to 45°C with a threshold current of 15.5mA.

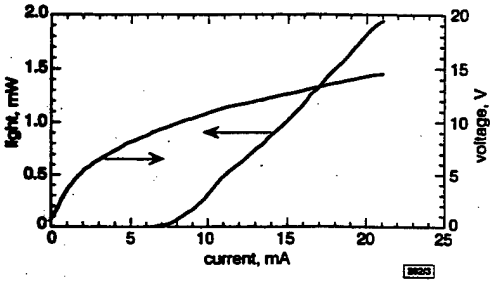


Fig. 3 *L-I and I-V plots of 25μm diameter device at room temperature in pulsed mode*
d = 25μm, *T* = 17°C

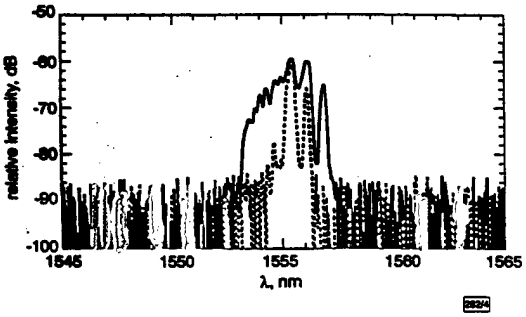


Fig. 4 *Lasing spectra of 25μm diameter device*
T = 17°C
- - - - *I* = 1.23I_{th}
——— *I* = 2.56I_{th}

As also seen in Fig. 3, the devices exhibit a high voltage that most likely is attributable to both a high contact resistance in this processing run and to the DBRs which have a relatively low doping level. By increasing the doping a few periods away from the cavity or by using intra-cavity contacts, we anticipate that this voltage drop can be reduced significantly without introducing additional optical losses.

The spectra of a 25μm diameter device biased at 1.23I_{th} and at 2.56*Ith* are shown in Fig. 4, revealing a lasing wavelength of 1.555μm and a strong multimode behaviour at the higher current.

In conclusion, electrically-pumped operation of AlGaAsSb-based VCSELs has been demonstrated. By combining high index-contrast DBRs made using this AlGaAsSb system and well-established AlInGaAs quantum well active regions, these lasers demonstrate that VCSELs operating at 1.55μm and employing a reasonable number of mirror periods can be grown in a single epitaxial step. CW operation is expected with a reduction in the series voltage and a better mode-gain alignment.

Acknowledgment: This work was supported by DARPA via the Heterogeneous Optoelectronics Technology Center.

© IEE 1999
20 May 1999
Electronics Letters Online No: 19990965
DOI: 10.1049/el:19990965

E. Hall (*Materials Department, University of California, Santa Barbara, CA 93106, USA*)

G. Almuneau, J.K. Kim, O. Sjölund, H. Kroemer and L.A. Coldren (*Electrical and Computer Engineering Department, University of California, Santa Barbara, CA 93106, USA*)

References

1 BOUCART, J., STARCK, C., PLAIS, A., DEROUIN, E., FORTIN, C., GABORIT, F., PINQUIER, A., GOLDSTEIN, L., CARPENTIER, D., and JACQUET, J.: 'RT pulsed operation of metamorphic VCSEL at 1.55 μm', *Electron. Lett.*, 1998, **34**, pp. 2133–2135

2 KAZMIERSKI, C., DEBRAY, J.P., MADANI, R., BOUADMA, M., ETRILLARD, J., SAGNES, I., ALEXANDRE, F., and QUILLEC, M.: 'First all-monolithic VCSELs on InP: +55C pulse lasing at 1.56μm with GaInAlAs/InP system'. IEEE-ISLC'98, Nara, Japan, 4-8 Oct. 1998, (Postdeadline Paper)

3 BLACK, K.A., ABRAHAM, P., MARGALIT, N.M., HEGBLOM, E.R., CHIU, Y.-J., PIPREK, J., BOWERS, J.E., and HU, E.L.: 'Double-fused 1.5 mu m vertical cavity lasers with record high To of 132 K at room temperature', *Electron. Lett.*, 1998, **34**, pp. 1947–1949

4 BLUM, O., KLEM, J.F., LEAR, K.L., VAWTER, G.A., and KURTZ, S.R.: 'Optically pumped, monolithic, all-epitaxial 1.56 μm vertical cavity surface emitting laser using Sb-based reflectors', *Electron. Lett.*, 1997, **33**, pp. 1878–1880

5 UNGARO, G., HARMAND, J.C., SAGNES, I., SERMAGE, B., DEBRAY, J.P., MERIADEC, C., RIVERA, T., OUDAR, J.L., and RAJ, R.: 'Room-temperature continuous-wave operation VCSEL at 1.48 μm with Sb-based Bragg reflector', *Electron. Lett.*, 1998, **34**, pp. 402–404

High-power (400mW) diode-pumped 2.7μm Er:ZBLAN fibre lasers using enhanced Er-Er cross-relaxation processes

B. Srinivasan, E. Poppe, J. Tafoya and R.K. Jain

The authors report the use of enhanced inter-ion cross-relaxation in Er:ZBLAN fibres of double clad geometries for the realisation of high-power (400mW) diode-pumped 2.7μm lasers. The enhanced Er-Er cross-relaxation was enabled by the formation of clusters, around drawing-induced defects, even at moderate mean doping densities in such fibres. Further extension of this work should enable multi-Watt CW power level lasers at 2.7μm in the foreseeable future.

There is a strong need for compact high-power (100mW to 1W) 2.7μm laser sources for several medical applications [1, 2] as well as for parts per billion (ppb) level spectroscopic monitoring [3] and infrared countermeasures. Fibre lasers based on the 2.7μm transition in Er:ZBLAN are particularly well-suited for several of the above applications. However, as has been frequently stated [4 – 8], the longer natural lifetime of the lower laser level ($^4I_{13/2}$, τ_{III} = 9.4ms) relative to that of the upper laser level ($^4I_{11/2}$, τ_{II} = 7.5ms) of the 2.7μm transition often results in a population bottleneck that inhibits efficient steady-state (CW) lasing in Er:ZBLAN fibre lasers. In previous work, this bottleneck has been alleviated by mechanisms such as: (i) selective depletion of the lower laser level via excited state absorption (ESA) [6], (ii) excitation transfer of the energy from the $^4I_{13/2}$ lower laser level to an appropriate acceptor state (e.g. the $^3F_3$ level in Pr [7]), and (iii) cascade lasing [9]. Despite the attainment of high CW output powers (150mW), cascade lasing is a cumbersome technique that requires the use of complicated multi-resonant mirror coatings and very high pump intensities; as such, this technique is not readily applicable for use with diode pumping.

We recently proposed and demonstrated a relatively simple and efficient technique, namely the use of enhanced cross-relaxation from the $^4I_{13/2}$ level (W_{11} process in Fig. 1) via clustering at high doping densities in Er:ZBLAN to alleviate the population bottleneck [8, 10 – 12]. In particular, we used a 980nm laser diode to pump a 10000ppm Er:ZBLAN 2.7μm fibre laser and achieved 10mW output power levels [8], which was an order of magnitude

improvement over CW power levels obtained previously from diode-pumped 2.7μm fibre lasers [5]. Subsequent ground state absorption measurements have exhibited dramatic reductions in the saturation of the ground state absorption at relatively low mean Er concentrations (10000ppm) in ZBLAN fibres, implying the presence of a significant percentage of ions in clusters [12]. Contrary to the report by Bogdanov *et al.* [13], where enhanced cross-relaxation was observed only for concentrations > 150000ppm, these studies indicated that significantly enhanced cross-relaxation can occur, due to the onset of Er ion clustering around drawing-induced defects, at doping densities that are low enough (20000ppm) to enable fabrication of high-quality low intrinsic loss fluoride fibres with current fibre fabrication techniques.

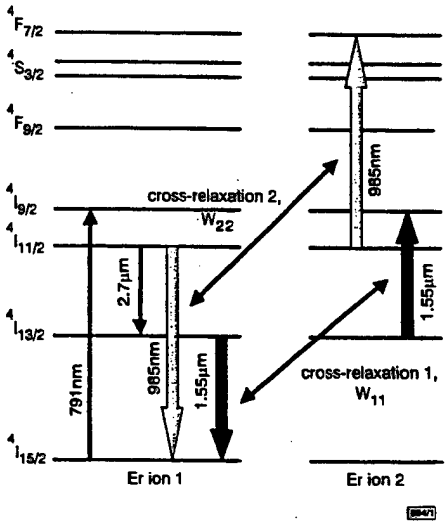


Fig. 1 *Energy level diagram of Er showing dominant cross-relaxation processes*

In this Letter, we describe high-power (400mW) CW diode-pumped operation of a 2.7μm fibre laser using mean Er concentrations of just 20000ppm in the singlemode core of a double-clad Er:ZBLAN fibre; a preliminary version of these results with all-Er fibres is described in [14]. Higher output powers have also been obtained recently with Er-Pr co-doped fibre lasers [15]. These power levels are more than an order of magnitude higher than any reported previously in a diode-pumped Er:ZBLAN fibre laser. As such, these results report nearly a three-orders-of-magnitude improvement in the output powers available from diode-pumped CW 2.7μm fibre lasers in a time span of < 2 years. Furthermore, the high slope efficiencies obtained (16%) and the lack of any evidence of saturation of the output power as well as the potential for the improvement of several factors (including better diode coupling and improved pump absorption) indicates scalability to Watt power levels in the very near future.

For the experiments reported here, we used a 10W 791nm OptoPower diode array as the pump source, which emits an 8mm square beam with a divergence of ~13mrad × 63 mrad. The pump wavelength was chosen to efficiently pump the $^4I_{15/2}$-$^4I_{9/2}$ transition, and to enhance the lower laser level-depleting excited state absorption (ESA) from the $^4I_{13/2}$ level to the $^2H_{11/2}$ level, while keeping the ESA from the $^4I_{11/2}$ upper laser level to the $^4F_{5/2}$ level as low as possible [16]. Based on the best available information [17] on the W_{11} and W_{22} cross-relaxation coefficients (Fig. 1) in highly-doped fluorides and the need to keep the intrinsic losses (particularly at 2.7μm) relatively low, we chose a mean Er concentration of 20000ppm (2%) for this work. Although such a concentration might not be optimal, the results reported here show a remarkable improvement in the performance of our 2.7μm fibre laser compared to previous reports on 2.7μm diode-pumped fibre lasers. For our experiments, we chose a concentric circular double-clad fibre [18] with a core diameter of 6.5μm, core-inner clad NA of 0.28, inner clad diameter of 125μm, and inner clad-outer clad NA of 0.55. The choice of a concentric circular double-clad fibre was based on the ease of fibre fabrication despite the fact that we expect higher diode-to-fibre coupling efficiencies and higher effective absorption with the use of other inner cladding shapes [19].

The pump was coupled into a multimode fibre with a core diameter of 365μm and an NA of 0.22 to homogenise the beam quality and match the resultant beamshape with the circular inner cladding of our double-clad fibre. The throughput efficiency of the multimode fibre was 85% and the coupling efficiency into the double-clad fibre was 55%. The background loss at 2.7μm in the fibre core and the effective absorption coefficient at the pump wavelength (791nm) were measured by the cutback method to be ~0.3 and 0.15dB/m, respectively. As a trade-off between high net absorption and intrinsic losses, we chose a fibre length of 20m.

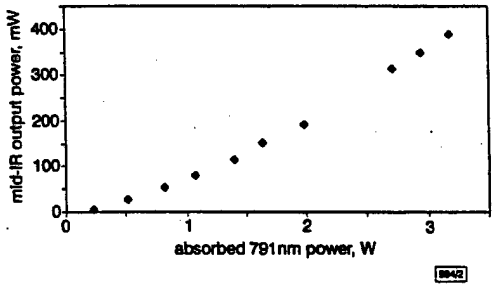


Fig. 2 *2.7μm output power against absorbed pump power for 20000ppm Er:ZBLAN fibre laser*

Fig. 2 shows the 2.7μm output power against absorbed pump power. Because of the high gain of the fibre achievable with the pump power densities used, CW lasing was easily achieved with just the 4% Fresnel reflections from the fibre ends. As seen from the plot, the threshold pump power was 400mW, implying a gain of 35.4dB at a threshold pump power density of 3.25kW/cm^2. An output power of 400mW was obtained at a pump power of 3.2W, corresponding to a slope efficiency of 16% with respect to absorbed power. For this plot, the output power was measured at the distal end of the fibre and we have assumed equal power from both ends of the fibre. The linearity of the plot clearly indicates scalability to Watt power levels in the near future using higher power diode arrays, multiple pump sources, and more efficient pump coupling techniques. We are currently pursuing such power scaling issues and expect to extend the 2.7μm laser output to multi-Watt power levels in the near future. Efforts are also under way to empirically determine the optimum dopant densities in Er-doped fibres by measuring the lifetimes of the $^4I_{11/2}$ and $^4I_{13/2}$ levels for different mean Er doping densities. Since drawing-induced defects enable cluster formation [20] (a phenomenon that is absent in conventional bulk glass fabrication), such lifetime studies will need to be performed in fibres rather than in bulk media.

© IEE 1999
18 June 1999
Electronics Letters Online No: 19990899
DOI: 10.1049/el:19990899

B. Srinivasan, J. Tafoya and R.K. Jain (*Center for High Technology Materials, University of New Mexico, Albuquerque, NM 87106, USA*)

E-mail: jain@chtm.unm.edu

E. Poppe (*Department of Physical Electronics, Norwegian University of Science and Technology, O.S. Bragstadpl. 2, N-7034 Trondheim, Norway*)

References

1 KAUFMANN, R., HARTMANN, A., and HIBST, R.: 'Cutting and skin-ablative properties of pulsed mid-infrared laser surgery', *J. Derm. Surg. and Oncol.*, 1994, **20**, pp. 112–118
2 GIBSON, K.F., and KERNOHAN, W.G.: 'Lasers in medicine: a review', *J. Med. Eng. Technol.*, 1993, **17**, pp. 51–57
3 ENG, R.S., BUTLER, J.F., and LINDEN, K.J.: 'Tunable diode laser spectroscopy: An invited review', *Opt. Eng.*, 1980, **19**, pp. 945–960
4 QUIMBY, R.S.: 'Continuous-wave lasing on a self-terminating transition', *Appl. Opt.*, 1989, **28**, pp. 14–16
5 ALLEN, R., ESTEROWITZ, L., and GINTHER, R.J.: 'Diode-pumped single-mode fluorozirconate fibre laser from the $^4I_{11/2}$ to $^4I_{13/2}$ transition in erbium', *Appl. Phys. Lett.*, 1990, **56**, (17), pp. 1635–1637

6 BRIERLEY, M.C., and FRANCE, P.W.: 'Continuous wave lasing at 2.7 μm in an erbium-doped fluorozirconate fibre', *Electron. Lett.*, 1988, **24**, (15), pp. 935–937
7 ALLAIN, J.Y., MONERIE, M., and POIGNANT, H.: 'Energy transfer in Er^{3+}/Pr^{3+}-doped fluoride glass fibres and application to lasing at 2.7 μm', *Electron. Lett.*, 1991, **27**, pp. 445–447
8 POPPE, E., SRINIVASAN, B., and JAIN, R.K.: '980nm-diode-pumped continuous wave mid-IR (2.7μm) fibre laser', *Electron. Lett.*, 1998, **34**, (24), pp. 2331–2333
9 POLLNAU, M., GHISLER, CH., BUNEA, G., LUTHY, W., and WEBER, H.P.: '150 mW unsaturated output power at 3μm from a single-mode-fiber erbium cascade laser', *Appl. Phys. Lett.*, 1995, **66**, (26), pp. 3564–3566
10 SRINIVASAN, B., POPPE, E., and JAIN, R.K.: '40mW single-transverse-mode mid-IR (2.7μm) CW output from a simple mirror-free 780-nm diode-pumpable fiber laser'. Tech. Dig. Conf. Lasers and Electro-Optics, San Francisco, CA, USA, 3–8 May 1998, Vol. 6, Paper CWM2, p. 297
11 POPPE, E., SRINIVASAN, B., and JAIN, R.K.: '980-nm diode-pumped power-scalable continuous wave mid-IR (2.7μm) fiber laser'. Tech. Dig. Conf. Lasers and Electro-Optics, San Francisco, CA, USA, 3–8 May 1998, Vol. 6, Paper CTuE7, pp. 80–81
12 SRINIVASAN, B., MONNOM, G., and JAIN, R.K.: 'Indirect measurement of the magnitude of ion clustering at high doping densities in Er:ZBLAN fibers', to be published in *Opt. Lett.*
13 BOGDANOV, V.K., GIBBS, W.E.K., BOOTH, D.J., JAVORNICZKY, J.S., NEWMAN, P.J., and MCFARLANE, D.R.: 'Fluorescence from high-doped erbium fluorozirconate glasses pumped at 800nm', *Opt. Commun.*, 1996, **132**, pp. 73–76
14 ZHAO, X., SRINIVASAN, B., PULASKI, P., GUPTA, S., and JAIN, R.K.: 'Mirror-free, high power (~140mW) diode-pumped 2.7μm CW fiber laser'. CLEO Europe '98, Glasgow, September 1998, Postdeadline Paper
15 SRINIVASAN, B., TAFOYA, J., and JAIN, R.K.: 'High-power 'Watt-level' CW operation of diode-pumped 2.7μm fiber lasers using efficient cross-relaxation and energy transfer mechanisms', *Opt. Express*, 1999, **4**, (12), pp. 490–495
16 POLLNAU, M., GHISLER, CH., LÜTHY, W., and WEBER, H.P.: 'Cross-sections of excited-state absorption at 800nm in erbium-doped ZBLAN fiber', *Appl. Phys. B, Lasers Opt.*, 1998, **67**, pp. 23–28
17 KNOWLES, D.S., and JENSSEN, H.P.: 'Upconversion versus Pr-deactivation for efficient 3μm laser operation in Er', *IEEE J. Quantum Electron.*, 1992, **QE-28**, (4), pp. 1197–1208
18 The fibre was obtained from Thorlabs, Inc., NJ, USA
19 LIU, A., and UEDA, K.: 'The absorption characteristics of circular, offset, and rectangular double-clad fibers', *Opt. Commun.*, 1996, **132**, pp. 511–518
20 AINSLIE, B.J., CRAIG, S.P., WYATT, R., and MOULDING, K.: 'Optical and structural analysis of neodymium-doped silica-based optical fibers', *Mater. Lett.*, 1989, **8**, pp. 204–208

Increased-area oxidised single-fundamental mode VCSEL with self-aligned shallow etched surface relief

H.J. Unold, M. Grabherr, F. Eberhard, F. Mederer, R. Jäger, M. Riedl and K.J. Ebeling

A self-aligning fabrication process is presented for enhancing the fundamental singlemode emission of selectively oxidised vertical cavity surface emitting lasers using a surface relief etching technique. The mechanism underlying the increase in threshold gain due to the use of a shallow surface relief is described and the results obtained for a 7μm device at 850nm are presented.

Introduction: Vertical cavity surface emitting lasers (VCSELs) have become the most frequently used light sources for many applications in the data-communications area [1] as well as many other fields where relatively low output powers of several milliwatts combined with good beam quality are required, such as laser printing [2] or optical storage [3]. Transverse singlemode VCSELs provide superior beam characteristics even for the most demanding applications. For good device performance, high efficiencies can be obtained using current confinement through selective oxidation. The drawback of this technique compared to ion implanted VCSELs is the stronger optical guiding which in turn requires smaller diameters (below 4μm) for singlemode emission [4]. However, this approach increases the series resistance significantly, limits the available output power and may shorten the device lifetime especially under high temperature operation. In the following we describe a technique for extending the active diameter range for singlemode emission up to 7μm.

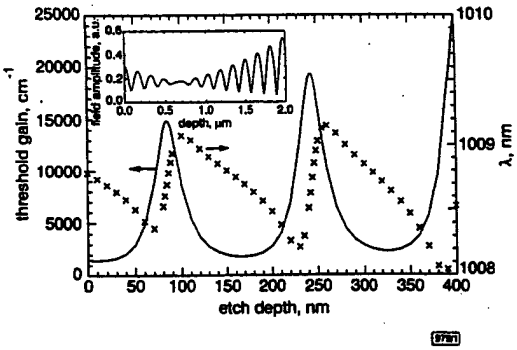


Fig. 1 *Calculated threshold gain and emission wavelength against etch depth in top Bragg mirror stack of standard InGaAs top-emitter structure*

Inset: portion of standing wave pattern close to output facet for etch depth of 80nm

Principle: When looking at the (low-order) set of modes that typically oscillate in multimode VCSELs, it is easily seen that the fundamental mode is the only one where the field intensity maximum is found to be at the centre of the structure. Therefore, a radially symmetric modification of the resonator is considered applicable to suppress those higher-order modes.

Fig. 1 shows the threshold gain and emission wavelength for a VCSEL structure with a 17.5-pair $GaAs/Al_{0.89}Ga_{0.11}As$ *p*-type Bragg reflector calculated using a linear matrix model threshold gain analysis. It can be seen that the threshold gain can easily be increased by a factor of 10 by etching into the top Bragg mirror stack. Since the waves reflected from the topmost (incomplete) Bragg pair do not match those from the remaining Bragg pairs, destructive interference occurs. Therefore, the threshold gain increases until the waves are at maximum mismatch. This situation is illustrated in the inset of Fig. 1, which shows the standing wave pattern for an etch depth of 80nm. After that, the threshold gain decreases again and the same sequence is repeated for the next Bragg pair but with an increase in magnitude. Therefore, for practical applications it is sufficient to etch to a depth of ~85nm, where the first local maximum of the threshold gain is observed. At the same time, it is necessary to precisely control the etch depth, since a small change in etch depth results in a large change in threshold gain.

When using conventional VCSEL structures, as in this example, care has to be taken not to etch into layers with large aluminium contents, since the subsequent selective oxidation step will then cause these layers to oxidise as well. This reduces the refractive index of the topmost layer of the Bragg stack, thus reducing the increase in threshold gain intended by the surface relief.

Device fabrication: Since the effect of the surface relief etching technique had already been shown in earlier work [5], a processing technique was sought which would allow both ease of fabrication and good reproducibility to be achieved. It is readily seen that for best results, it is crucial to achieve proper alignment of oxide aperture and surface relief. This is achieved by using a self-aligning three-layer photoresist technique. In a first two-layer resist step PMGI and AZ resists are patterned using a mask defining both the mesa location as well as the concentric surface relief. After removing the AZ resist, the surface relief is dry etched to the desired depth of several tens of nanometres by chemically assisted ion beam etching. The inner diameter of the etched surface reliefs is chosen to match the $1/e$-decay of the fundamental mode intensity profile. In a second lithography step, the surface relief structure is covered with AZ resist to protect it from the following wet chemical mesa etching step. The alignment tolerance of this step amounts to 7μm, which is sufficient for manual or even automatic alignment as seen from Fig. 2. After etching the mesa, selective oxidation of the AlAs layer is carried out, ensuring optimum

High-power "Watt-level" CW operation of diode-pumped 2.7 μm fiber lasers using efficient cross-relaxation and energy transfer mechanisms

B. Srinivasan, J. Tafoya and R. K. Jain

Center for High Technology Materials, University of New Mexico,

1313, Goddard SE, Albuquerque, NM 87106

balaji@chtm.unm.edu, chemist@unm.edu, jain@chtm.unm.edu

Abstract: We report the demonstration of high power (660 mW) CW operation of a diode-pumped mid-IR Er fiber laser. This was achieved by using efficient depopulation of the lower laser level via enhanced cross-relaxation between Er ions and energy transfer to Pr ions (at doping densities much higher than those used previously in Er:ZBLAN), along with optimal pumping of such lasers via custom-designed double-clad fluoride fibers.
©1999 Optical Society of America
OCIS codes: (140.3510) Fiber Lasers; (140.3480) Diode-Pumped Lasers; (060.2390) Infrared Fiber Optics; (140.3500) Erbium Lasers

References and links

1. L. Esterowitz, R. Allen, "Rare Earth Doped IR Fiber Lasers for Medical Applications," Proc. SPIE **1048**, 129-132 (1989).
2. K. F. Gibson and W. G. Kernohan, "Lasers in Medicine: A Review," J. Med. Engg. and Tech. **17**, 51-57 (1993).
3. O. Kermani, H. Lubatschowski, W. Ertmer and G. K. Krieglstein, "Internal Ablative Sinostomy Using a Fiber Delivered Q-Switched CTE:YAG Laser (2.69 μm)," Intl. Ophthalmology **17**, 211-215 (1993).
4. R. Kaufmann, A. Hartmann and R. Hibst, "Cutting and Skin-Ablative Properties of Pulsed Mid-Infrared Laser Surgery," J. Derm. Surg. & Oncol. **20**, 112-118 (1994).
5. R. Moosdorf, F. C. Schoebel and W. Hort, "Transmyocardial Laser Revascularization: Morphology, Pathophysiology and Historical Background of Indirect Myocardial Revascularization," Z. Kardiologie **86**, 149-164 (1997).
6. M. Pollnau, "The Route Toward a Diode-Pumped 1-W Erbium 3-μm Fiber Laser," IEEE J. Quantum Electron. **33**, 1982-1990 (1997).
7. E. Poppe, B. Srinivasan and R. K. Jain, "980nm-Diode-Pumped Continuous Wave Mid-IR (2.7 μm) Fiber Laser," Electron. Lett. **34**, 2331-2333 (1998).
8. R. S. Eng, J. F. Butler and K. J. Linden, "Tunable Diode Laser Spectroscopy: An Invited Review," Opt. Engg. **19**, 945-960 (1980).
9. T. Yamamoto, T. Komukai and Y. Miyajima, "Wide-Band Erbium-Doped Fluoride Fiber Optical Amplifier at 2.7 μm with Fluoride Fiber Wavelength-Division Multiplex Coupler," Jpn. J. Appl. Phys. **32**, L62-L64 (1993).
10. J. Y. Allain, M. Monerie and H. Poignant, "Energy Transfer in Er^{3+}/Pr^{3+}-Doped Fluoride Glass Fibres and Application to Lasing at 2.7 μm," Electron. Lett. **27**, 445-447 (1991).
11. M. Pollnau, Ch. Ghisler, G. Bunea M. Bunea, W. Lüthy and H. P. Weber, "150 mW Unsaturated Output Power at 3 μm from a Single-Mode-Fiber Erbium Cascade Laser," Appl. Phys. Lett. **66**, 3564-3566 (1995).
12. G. J. Kintz, R. Allen and L. Esterowitz, "CW and Pulsed 2.8 μm Laser Emission from Diode-Pumped Er^{3+}:$LiYF_4$ at Room Temperature," Appl. Phys. Lett. **50**, 1553-1555 (1987).
13. R. S. Quimby and W. J. Miniscalco, "Continuous-Wave Lasing on a Self-Terminating Transition," Electron. Lett. **28**, 14-16 (1989).
14. X. Zhao, B. Srinivasan, P. Pulaski, S. Gupta and R. K. Jain, "Mirror-Free, High Power (~140mW) Diode-Pumped 2.7 μm CW Fiber Laser," Postdeadline paper, CLEO Europe '98 Technical Digest (1998).
15. B. Srinivasan, G. Monnom and R. K. Jain, "Indirect Measurement of the Magnitude of Ion Clustering at High Doping Densities in Er:ZBLAN Fibers," to be published.
16. S. Bedö, W. Lüthy and H. P. Weber, "The Effective Absorption Coefficient in Double-Clad Fibers," Opt. Commn. **99**, 331-335 (1993).
17. A. Liu and K. Ueda, "The Absorption Characteristics of Circular, Offset, and Rectangular Double-Clad Fibers," Opt. Commn. **132**, 511-518 (1996).
18. D. S. Knowles and H. P. Jenssen, "Upconversion versus Pr-Deactivation for Efficient 3 μm Laser Operation in Er," IEEE J. Quantum. Electron. **28**, 1197-1208 (1992).
19. L. Wetenkamp, G. F. West and H. Többen, "Co-Doping Effects in $Erbium^{3+}$- and $Holmium^{3+}$-Doped ZBLAN Glasses," J. Non-Crystalline Solids **140**, 25-30 (1992).
20. These results were submitted for presentation at the Conference for Lasers and Electro-Optics (CLEO) '99 as a postdeadline paper on 4/26/99 (paper #CPD23, CLEO '99, Baltimore, May 23-28, 1999).
21. This fiber was obtained from Thorlabs, Inc., NJ, USA.

22. Note that the lifetime values quoted here were based on our own measurements in Er-doped ZBLAN fibers and as such show small deviations from other values reported in the literature for similar ZBLAN bulk samples and fibers and related fluoride hosts (see references 6,10,13,18).
23. V. K. Bogdanov, W. E. K. Gibbs, D. J. Booth, J. S. Javorniczky, P. J. Newman and D. R. MacFarlane, "Fluorescence from Highly-Doped Erbium Fluorozirconate Glasses Pumped at 800 nm," Opt. Commn. **132**, 73-76 (1996).
24. M. Pollnau, Ch. Ghisler, W. Lüthy and H. P. Weber, "Cross-Sections of Excited-State Absorption at 800 nm in Erbium-Doped ZBLAN Fiber," Appl. Phys. B **67**, 23-28 (1998).

Because of the strong water absorption near 3 μm in tissue and the consequent ultrashort penetration depths (of a few microns), compact high power (100 mW to 1 W) 2.7 μm laser sources with TEM_{00} beam quality have several important applications in ultrafine intra-ocular and endoscopic laser surgery including transmyocardial revascularization and other intra-arterial procedures [1-7]. Compact and efficient sources of mid-IR radiation are also needed for infrared countermeasures applications, and for ppb (parts per billion) level spectroscopic monitoring [8] of several important species such as carbon monoxide (CO), formaldehyde (H_2CO), nitric oxide (NO), nitrogen dioxide (NO_2), hydrogen sulphide (H_2S), arsine (AsH_3), and phosphine (PH_3).

The 2.7 μm transition in Er:ZBLAN is well-suited for several of the above applications. For instance, the broad tunability [9] of this transition (2.65-2.83 μm) should enable ppb spectral monitoring of H_2S (2.65 μm) and NO (2.7 μm). However, as has been frequently stated, the longer natural lifetime of the lower laser level ($^4I_{13/2}$, 9.4 ms) relative to that of the upper laser level ($^4I_{11/2}$, 7.5 ms) of the 2.7 μm transition often results in a population bottleneck that inhibits efficient steady-state (CW) lasing in Er:ZBLAN fiber lasers [6,7,10-12]; as such this transition has been frequently called "self-terminating" [10,13]. We have previously demonstrated alleviation of this bottleneck and strongly enhanced efficiencies and output powers [7,14] by a simple technique, namely the use of fibers with high concentrations (>10,000 ppm) of Er. It was hypothesized that such high concentrations not only reduce the problem of ground state bleaching, but also cause significantly enhanced cross-relaxation via the formation of Er ion clusters [15], whose net effect is to relax the excitation from the lower laser level ($^4I_{13/2}$) to the ground state ($^4I_{15/2}$), while upconverting an adjacent ion to the $^4I_{9/2}$ state. A fringe benefit of the use of high Er doping densities is the natural amenability of the consequent high core absorption to optimized designs of double-clad fibers [16,17] capable of being pumped by relatively inexpensive high power diode arrays.

In this Letter, we demonstrate further improvements in the power and efficiency of CW lasing at the 2.7 μm transition in Er^{3+}:ZBLAN fiber lasers by utilizing a complementary technique [6,10,18,19] for enhancing the rate of depletion of the $^4I_{13/2}$ level of Er by energy transfer to the $^3F_3$ and the $^3F_4$ levels of Pr (see Fig. 1). In particular, we demonstrate 660 mW

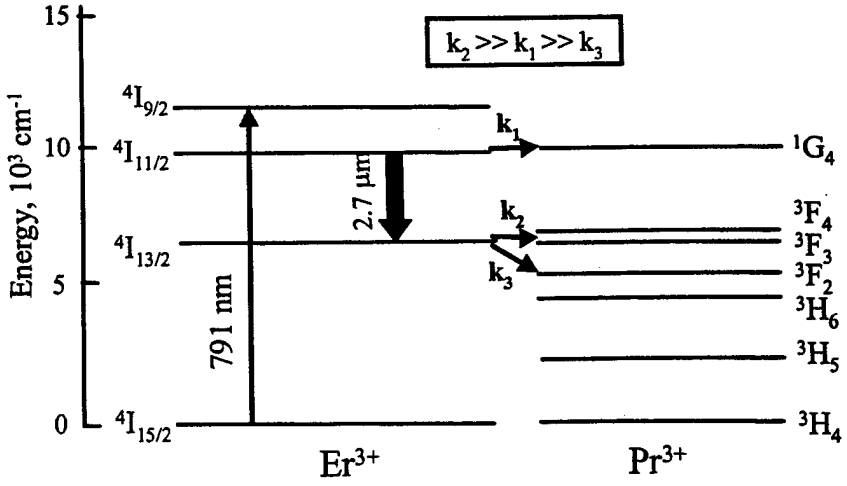


Figure 1. Dominant energy transfer pathways between laser levels in Er and resonantly-matched energy levels in Pr ($k_1 = 0.15 \times 10^3$ s^{-1} and $k_2 = 0.93 \times 10^3$ s^{-1} for our 20,000/5,000 ppm Er/Pr:ZBLAN fiber)

of CW output [20] from a 791 nm diode array-pumped Er/Pr:ZBLAN rectangular-clad fiber laser with a slope efficiency of 13% with respect to the absorbed pump power. The output power demonstrated here is nearly an order of magnitude higher than the highest powers previously reported [14] for a diode-pumped mid-IR fiber laser, and shows evidence of easy scalability to Watt power levels (by very simple improvements such as optimization of the Er-Pr concentrations, increase of the pump power and coupling efficiencies, and the use of optimized output coupling).

The fiber used in this work was a custom-designed rectangular-clad Er/Pr:ZBLAN fiber [21]. The rare-earth concentrations in the core (dia.=13 μm, NA=0.16) were chosen to be 20,000 ppm of Er and 5,000 ppm of Pr, based on the requirements of efficient absorption in Er and rapid depopulation of the lower laser level (via enhanced cross-relaxation in Er and efficient energy transfer to Pr). The lifetimes for the $^4I_{11/2}$ and the $^4I_{13/2}$ upper and lower laser levels were measured to be 2.5 ms and 0.7 ms respectively (corresponding to a lifetime ratio κ of 3.57) for this specific co-doped system versus lifetimes of 4 ms and 2 ms respectively (κ = 2.0) for a singly-doped 20,000 ppm Er:ZBLAN fiber, and 7.5 ms and 9.4 ms respectively (κ = 0.8) [22,23] for the traditional ≤1,000 ppm low concentration self-terminating 2.7 μm Er:ZBLAN laser. Further details on the criteria used for choosing such dopant concentrations

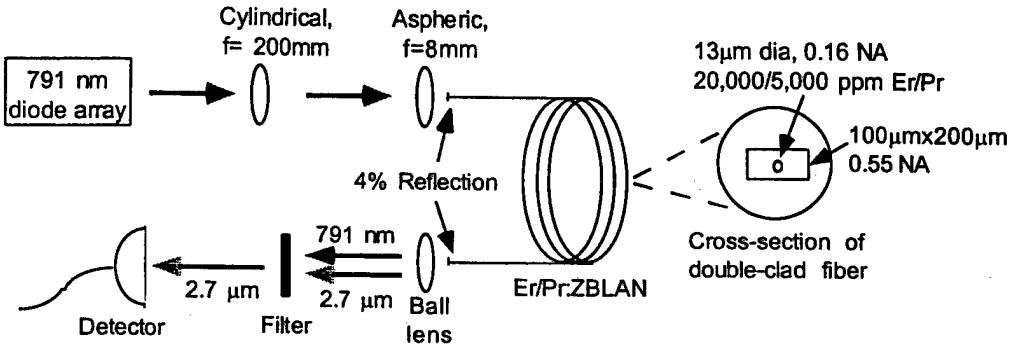


Figure 2. Schematic diagram of diode-pumped double-clad fiber laser

are given below. A schematic diagram of the diode-pumped fiber laser setup is illustrated in Fig. 2. In our work, we used an OptoPower 791 nm diode array capable of delivering 10 Watts as the pump source. The inner cladding dimensions and NA of the undoped cladding of the double-clad fiber were chosen to be (100μmx200μm) and 0.55 respectively to facilitate high coupling efficiencies for the diode beam (whose characteristics are 8 mm square size, 6.5 mrad divergence in the vertical plane and ~13 mrad divergence in the horizontal plane) to be used, as well as to obtain significantly high effective absorption coefficients [16,17]. In order to match the diode array beam shape to the rectangular-clad fiber, we used a cylindrical lens of 20 cm focal length and rotated its axis with respect to the plane of the diode array, to compensate simultaneously for beam-shaping and astigmatism effects and thereby optimize the coupling. The net coupling efficiency and the effective pump (791 nm) absorption coefficient were measured to be 65% and 0.6 dB/m respectively. Given the measured value of the effective pump absorption coefficient and the estimated value of the background losses (0.1 dB/m) at the lasing transition, we chose a fiber length of 14 m for the present experiments; the value of the measured pump absorption for the fiber was ~85%.

Fig. 3 shows a photograph of the experimental setup. Strong green (544 nm) fluorescence is observed when the diode radiation is coupled optimally to the fiber (and was used as a visual indicator to optimize coupling). As illustrated in Fig. 4, this fluorescence is caused by excited state absorption (ESA) [24] from the $^4I_{11/2}$ level to the $^4F_{5/2}$ level, followed by rapid non-radiative decay to the $^4S_{3/2}$ level and subsequent fluorescence from the $^4S_{3/2}$ level to the $^4I_{15/2}$ level. Despite its visual advantages (including facilitation of the optimization of coupling), this upconversion mechanism represents a detrimental pathway for depopulation of the upper laser level. As such, the choice of the 791 nm pump wavelength was made in part to reduce the detrimental effects of this ESA (the ESA cross-section at 791 nm is approximately

100 times weaker than that at the peak value at 808 nm). Even lower values of ESA from the $^4I_{11/2}$ level can be obtained by detuning the pump laser to shorter wavelengths, but at the

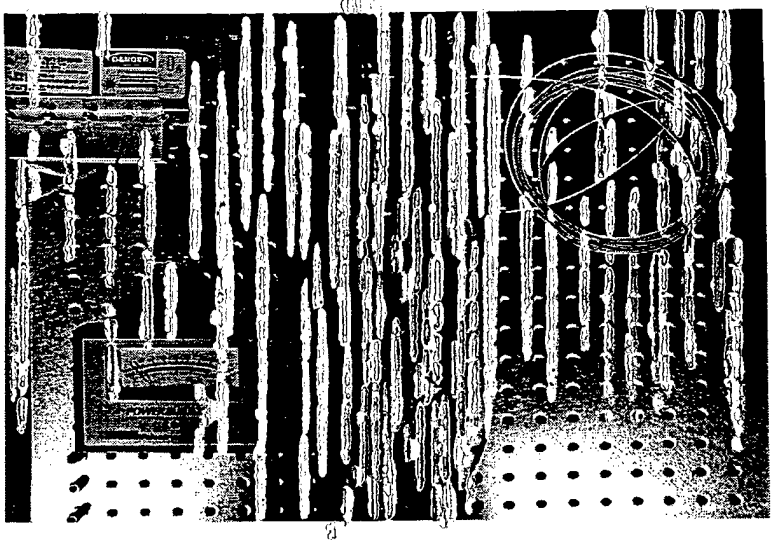


Figure 3. Photograph of the experimental setup shown schematically in Fig. 2

expense of reduced ground state absorption and a reduction in the "beneficial" lower laser level ($^4I_{13/2}$) depleting ESA. Wavelength detuning of the order of 2-3 nm may be optimum for this case, and is well within the tuning range of the pump diode array. For a given power level, precise optimization is best done by detuning the pump wavelength for highest output powers.

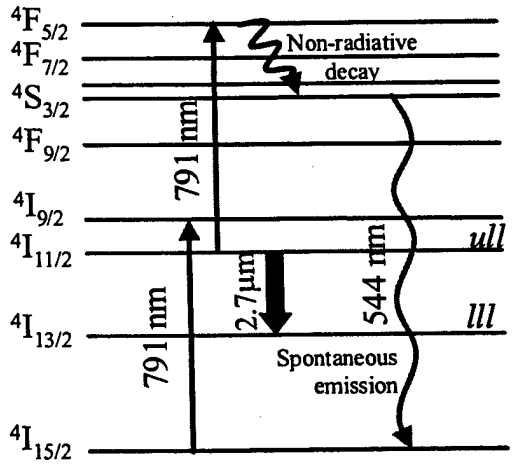


Figure 4. Role of the excited state absorption (of 791 nm) from the upper laser level ($^4I_{11/2}$) in generation of green (544 nm) upconversion fluorescence in the Er-doped fiber

Because of the availability of sufficiently high pump powers and gains, we were able to achieve lasing off the 4% Fresnel reflections from the two ends of the fiber. All the data reported here corresponds to this condition. Fig. 5 shows the 2.7 μm output power as a function of the absorbed 791 nm diode power. As seen from the above plot, the laser threshold is 330 mW and the slope efficiency is 13% with respect to the absorbed power. The linearity of the plot and the lack of any evidence of saturation at the high pump powers clearly

indicates scalability to over 1 Watt power levels simply by using higher pump powers or more efficient pump coupling and pump absorption techniques.

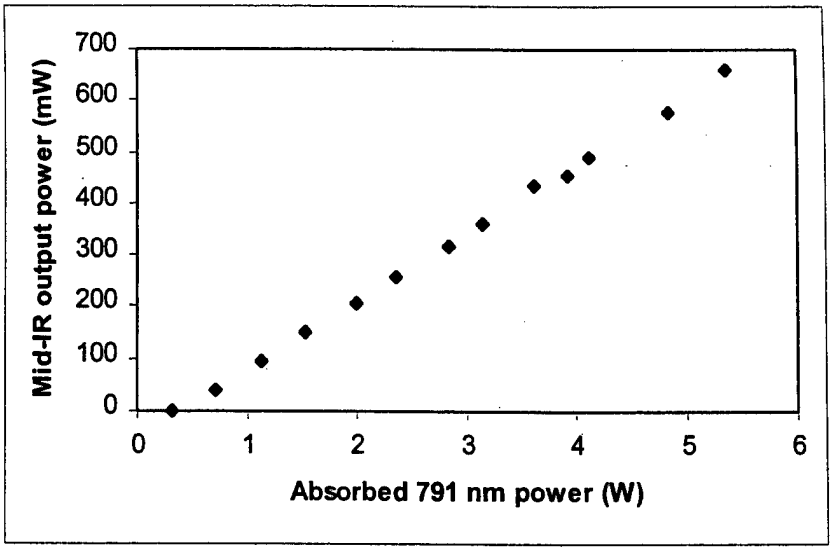


Figure 5. CW 2.7 μm output power vs. absorbed 791 nm pump power for our Er/Pr:ZBLAN fiber

Given the round-trip losses in the cavity, the round-trip gain is estimated to be as high as 29.4 dB at the threshold pump power density of 1.65 kW/cm^2. The significantly lower threshold pump densities used, compared to the ≥100 kW/cm^2 reported by earlier workers [10-12], are attributed to the choice of a double-clad fiber. The relatively high slope efficiency achieved in our work compared to other non-cascade lasing schemes [10,12] is attributed to relatively efficient depopulation of the lower laser level. Further improvements in the threshold pump densities and slope efficiencies can be made by further optimization of the dopant concentrations, optimization of the output coupling efficiency, and reduction of intra-cavity losses (background absorption in the fiber at the lasing wavelength and scattering losses at the fiber ends).

In order to further optimize the Er and Pr concentration, we are currently developing a detailed model for calculating the gain in such co-doped glasses, based in part on our own spectroscopic and lifetime measurements for the $^4I_{11/2}$ and the $^4I_{13/2}$ levels as a function of dopant concentrations, particularly for ZBLAN fibers (since these values tend to be different from those reported in bulk glasses [23]). Critical issues related to development of such a model are the rates of diffusion-assisted energy transfer and cross-relaxation in the presence of high fractions of Er ions in clusters [15] and the rates of depletion (k_2, k_1) of the $^4I_{13/2}$ and $^4I_{11/2}$ levels as a function of Pr concentration [18,19]; as such, we will measure these quantities empirically for a parametric set of Er: and Er/Pr:ZBLAN fibers for the development of a reliable model.

In future work, we will also investigate power scaling of such sources by coherent array and beam-combining techniques. Additional work is also in progress on the demonstration of wavelength-tunable and pulsed (Q-switched, mode-locked and master-oscillator-pulsed power amplifier) high peak power sources based on such 2.7 μm fiber lasers; the latter should also enable the generation of longer mid-IR wavelengths relatively easily via efficient nonlinear optical (Raman/Difference Frequency Generation) techniques.

In summary, we report the first demonstration of high power (660 mW) CW operation of a diode-pumped mid-IR Er fiber laser. This was achieved by using efficient depopulation of the lower laser level via enhanced cross-relaxation between Er ions and energy transfer to Pr ions (at doping densities much higher than those used previously in Er:ZBLAN), along with optimal pumping of such lasers via custom-designed double-clad fluoride fibers. With optimized coupling optics, higher pump powers, and improved fiber design, >1 Watt power levels at 2.7 μm are anticipated in the near future.

Acknowledgments

This work was supported by the Air Force Office of Scientific Research. The authors also thank S. Gupta of Optopower for discussion on beam coupling of the laser diode to double-clad fibers.

First Demonstration of Thermally-Poled Electro-Optically Tunable Fiber Bragg Gratings

B. Srinivasan and R.K. Jain, *Fellow, IEEE*

***Abstract*— We demonstrate electro-optic tuning of a fiber Bragg grating (FBG) fabricated in a thermally-poled fiber. 40 pm of tuning was demonstrated, corresponding to an electro-optic coefficient of 0.25 pm/V. Such electro-optic tunable FBGs have strong potential for numerous devices, including all-fiber amplitude modulators and high-speed tunable filters.**

***Index terms*—** Tunable Fiber Bragg Gratings, Fiber Devices, Thermally-Poled Glasses, Electro-Optic Glass Fibers

There is a growing need for all-fiber active devices for WDM and OTDM applications. For example, mode-locked all-fiber laser sources whose bandwidths are centered at specific WDM channel wavelengths in the 1.55 μm ITU grid are highly desirable for hybrid WDM/OTDM systems [1]. Passively mode-locked lasers are difficult to synchronize precisely to the clock frequencies used for signals in the OTDM channels. As such, actively mode-locked all-fiber lasers whose center wavelengths correspond to specific WDM channels are highly desirable.

In this Letter, we demonstrate a key component capable of actively mode-locking a fiber laser at pre-selected WDM wavelengths (using schemes similar to the one shown in Fig. 1), namely *a fiber Bragg grating (FBG) that is electro-optically tunable and modulatable at multi-GHz speeds*. Such e-o tunable FBGs can also be used for DWDM applications such as dynamic wavelength stabilization (suppression of relaxation oscillations) of grating-controlled narrow-linewidth semiconductor diode lasers [2] and fiber lasers [3], and for dynamic wavelength reconfigurability of add/drop switches [4].

Fiber Bragg gratings have been previously tuned by thermal [4,5] and strain-based [6-8] mechanisms. Unfortunately, these tuning methods are relatively slow, limiting their speed of operation (response times of the order of sub-milliseconds). On the other hand, electro-optically tuned FBGs not only have the promise of much larger bandwidths, but are also relatively insensitive to the excitation frequency, unlike piezo-electrically-tuned FBGs [9]. For instance, the mode-locked fiber laser concept based on an electro-optically modulatable FBG depicted

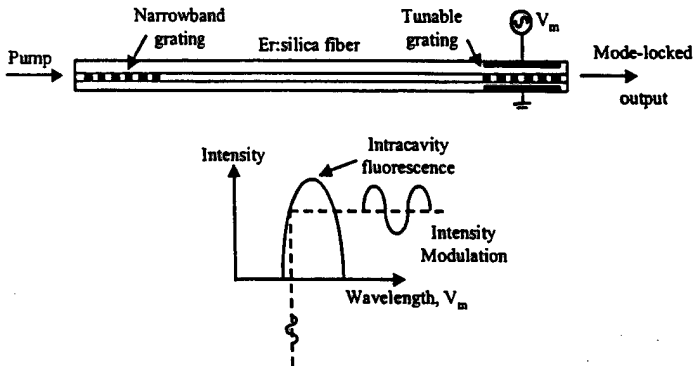


Figure 1. Conceptual diagram of an ultracompact actively mode-locked all-fiber laser based on an electro-optic tunable FBG modulator

schematically in Fig. 1 is difficult to achieve with any of the FBG tuning mechanisms used previously [4-9].

Electro-optically tunable FBGs, achieved by UV-poling process have been demonstrated previously by Fujiwara et al [10]; unfortunately, the UV-poling process has been difficult to reproduce and has been found to have limited stability [11]. The limited lifetime of the second-order nonlinearity (typically less than a few months at room temperature) induced by UV-poling is attributed to the relatively small activation energy (0.41 eV) of the GeE' defect centers [12], which is believed to be a key factor affecting the second-order nonlinearity induced by this process. In contrast, we have used the thermal-poling process, in which the second-order nonlinearity is assumed to be related to a large and relatively stable "frozen-in" space charge field [13,14]; as such, this nonlinearity has been shown to be more reliable and much more stable [15] than the nonlinearity induced by UV-poling.

In our experiments, we used hydrogen-loaded (100 atm., 50 °C, 2 days) D-shaped fibers (KVH Corp., 2x4 μm elliptical core with 15% GeO_2) for the Bragg grating fabrication. We exposed the fiber to 193 nm pulses from an ArF excimer laser (20 mJ/cm^2/pulse, 10 Hz rep rate, 20 mJ/pulse in a 1 cm^2 beam) for 20 mins through a phase mask having a period of 1072 nm. Two different FBGs were fabricated using this setup. One of them (FBG #1) had a 13 dB reflectivity and a 500 pm 3 dB bandwidth (estimated L=3 mm), whereas the other grating (FBG #2) had a 12 dB reflectivity and a 300 pm 3-dB bandwidth (estimated L=5

Both authors are with the Departments of Electrical Engineering and Computer Engineering and Center for High Technology Materials, University of New Mexico, Albuquerque, NM 87106; R.K. Jain is also with the Dept. of Physics and Astronomy; Email: jain@chtm.unm.edu

mm). A key issue in the fabrication of thermally poled FBGs is the decay of the grating at high poling temperatures (upto 260 °C) [16,17]. In our experiments, we pre-annealed the FBGs at 300 °C, consistent with established processes for their stabilization [16,17]. After annealing, the reflectivity of FBG #1 was 9 dB and that of FBG #2 was 7 dB. The flat side of the fiber was subsequently polished to ~5 μm from the core (70 μm total thickness) and processed for poling at 3.3 kV.

Fig. 2 shows the experimental setup used to measure the reflection and transmission spectra, as well as the tuning characteristics of the FBGs. An edge-emitting LED (ELED) was attached to a 70:30 coupler (70% in the through port, 30% in the cross-over port), which was mechanically spliced to the FBG. An optical spectrum analyzer (Ando AQ6315A, 0.05 nm resolution) was connected either at the transmission end of the FBG or at the reflection end of the 70:30 coupler to monitor both the transmission and reflection spectra.

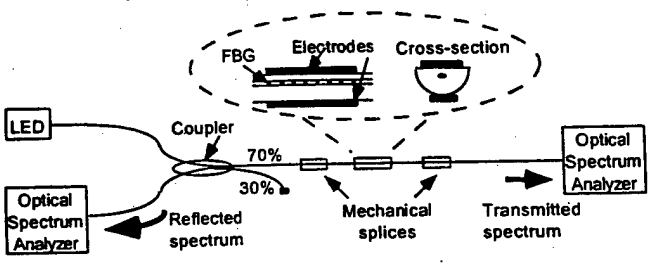


Fig. 2. Experimental setup for spectral characterization of FBGs

In preliminary experiments, a Cr/Au electrode (300/2000 Å thick) of 3 mm width and 20 mm length was deposited on the flat side of the D-shaped fiber. The reflection spectrum of the Bragg grating (FBG #1) is shown in Fig. 3. For an applied voltage of +5 kV (anode on the flat side of the D-shaped fiber), we observed a spectral shift of 10 pm, corresponding to an electro-optic coefficient of 0.06 pm/V.

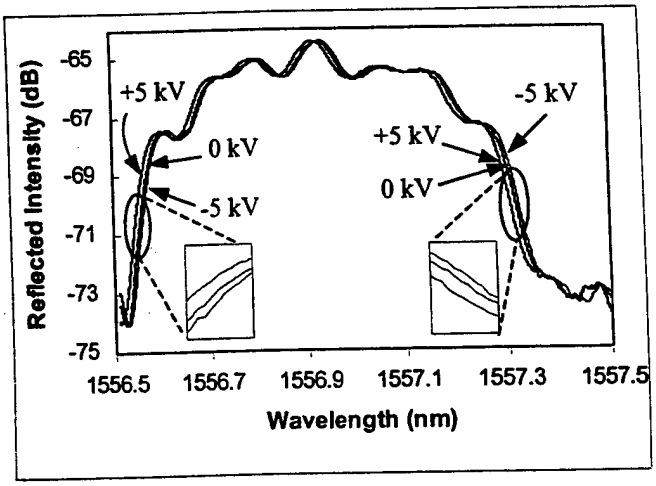


Figure 3. Reflection spectra of FBG #1 showing asymmetric shifts of 10 pm and 3 pm respectively for 5 kV applied voltage using positive and negative polarities

In order to verify that the spectral shift did not occur due to the piezoelectric effect or due to heating, we switched the polarity of the electrodes and observed a spectral shift in the opposite direction, confirming the electro-optic tuning mechanism. The spectral shift observed for –5 kV (cathode on the flat side of the fiber) was only ~3 pm. Such a result is presumably due to the polarity of the applied field matching that of the "frozen-in" electric field [13,14] for the positive polarity, and canceling the effect of the "frozen-in" electric field for the negative polarity.

In recent experiements, we lithographically deposited a 16 μm wide electrode on the flat side of the D-shaped fiber. Figure 4 illustrates the transmission spectrum of the Bragg grating (FBG #2) as a function of the applied voltage. For an applied DC voltage of 3 kV, we observe a shift of ~40 pm (5 GHz) in the Bragg grating spectrum. Unfortunately, the switching of the polarity of electrodes caused an inadvertant breakdown of the device, percluding the possibility of observing the transmission spectrum for the reversed polarity. Work is underway to fabricate more devices with better tuning characteristics than those described above.

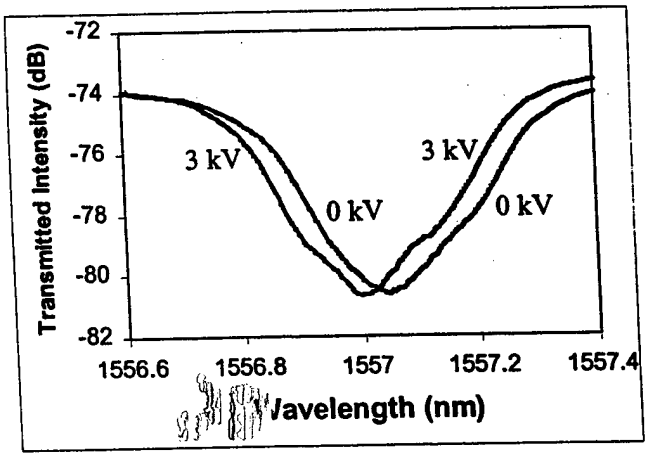


Figure 4. Transmission spectra of FBG #2 showing a 40 pm shift with an applied voltage of +3 kV

The spectral shift ($\Delta\lambda$) for a FBG whose reflectivity spectrum is centered at λ_B is given by

$$\Delta\lambda = \lambda_B \frac{\Delta n}{n}$$

where n is the mean refractive index of the fiber core and Δn is expressed as

$$\Delta n = \frac{1}{2} r n^3 \frac{V_t}{D}$$

where r is the electro-optic coefficient, D is the thickness of the D-shaped fiber, and V_t is the tuning voltage applied to the electrodes. The above observation of a wavelength shift of 40 pm for a tuning voltage of 3 kV corresponds to an electro-optic coefficient, $r = 0.25$ *pm/V*. Since previous

reports of thermal poling in bulk glasses [13] suggest that r = 1 pm/V is achievable using poling voltages of >5 kV, improved fiber designs are presently being studied to enable the use of such poling voltages and higher nonlinearites, which in turn will lead to much lower drive voltage requirements. Furthermore, we plan to use enhanced effective nonlinearities (by reduced fiber thicknesses) to reduce the tuning voltage to less than ten Volts, to enable devices that are more usable for telecom applications. Such improvements, along with traveling-wave electrode configurations, should facilitate the demonstration of 10 GHz amplitude modulators and high-speed dynamic reconfigurability of ADMs for 50 GHz DWDM systems.

For the FBG shown in Fig. 4, a depth of modulation of ~10% is achievable at center wavelengths of 1556.85 nm and 1557.2 nm respectively. This depth of modulation can be easily increased to a value of 20% by simply decreasing the bandwidth of the grating to 0.2 nm, for instance, by using longer FBGs. In addition, further increases in depth of modulation to 40% can be achieved by increasing the effective nonlinearity to 0.5 pm/V, say by reducing the thickness of the poled fiber segment to 30 μm. Such work is a key target of our current activity in this area.

In summary, we have demonstrated electro-optically tunable fiber Bragg gratings fabricated using thermally poled fibers. These devices appear very promising for numerous high-level devices such as the demonstration of ultra-compact mode-locked laser sources, and for several WDM applications such as dynamic wavelength stabilization of grating-controlled diode and/or fiber lasers, and for the development of dynamically reconfigurable add/drop switches.

Acknowledgments: This work was supported by DARPA and AFOSR. We thank Xiang-Cun Long for experimental assistance.

References:

1. A.E. Willner, "Mining the Optical Bandwidth for a Terabit Per Second", *IEEE Spectrum*, vol. 32, pp. 32-41, 1997.
2. D.M. Bird, J.R. Armitage, R. Kashyap, R.M.A. Fatah, and K.H. Cameron, "Narrow Line Semiconductor Laser Using Fiber Grating", *Electron. Lett.*, vol. 27, pp. 1115-1117, 1991.
3. V. Mizrahi, D.J. DiGiovanni, R.M. Atkins, S.G. Grubb, Y-K. Park, J-M.P. Delavaux, "Stable Single-Mode Erbium Fiber-Grating Laser For Digital Communication", *Jour. Lightwave Tech.*, vol. 11, pp. 2021-2025, 1993.
4. H. Okayama, Y. Ozeki and T. Kunii, "Dynamic Wavelength Selective Add/Drop Node Comprising Tunable Gratings", *Electron. Lett.*, vol. 33, pp. 881-882, 1997.
5. H.G. Limberger, N.H. Ky, D.M. Costantini, R.P. Salathe, C.A.P. Muller, and G.R. Fox, "Efficient Miniature Fiber-Optic Tunable Filter Based on Intracore Bragg Grating and Electrically Resistive Coating", *IEEE Photon. Tech. Lett.*, vol. 10, pp. 361-363, 1998.
6. A. Iocco, H.G. Limberger, and R.P. Salathe, "Bragg Grating Fast Tunable Filter", *Electron. Lett.*, vol. 33, pp. 2147-2148, 1997.
7. J.L. Cruz, A. Diez, M.V. Andres, A. Segura, B. Ortega and L. Dong, "Fibre Bragg Gratings Tuned and Chirped Using Magnetic Fields", *Electron Lett.*, vol. 33, pp. 235-236, 1997.
8. S. Jin, R.P. Espindola, H. Mavoori, T.A. Strasser and J.J. DeMarco, "Magnetically Programmable Fibre Bragg Gratings", *Electron. Lett.*, vol. 34, pp. 2158-2159, 1998.
9. H.G. Limberger, N.H. Ky, D.M. Costantini, R.P. Salathe, C.A.P. Muller, and G.R. Fox, "Efficient Active Bragg Grating Tunable Filters", paper BTuA5, *Proceedings of the Bragg Gratings and Photosensitivity Conference*, pp .265-267, 1998.
10. T. Fujiwara, D. Wong, Y. Zhao, S. Fleming, V. Grishina, S. Poole, "UV-Excited Poling and Electrically Tunable Bragg Gratings in a Germanosilicate Fiber", *OFC '95* post-deadline paper, PD6-1, 1995.
11. T. Fujiwara, M. Takahashi and A.J. Ikushima, "Decay Behavior of Second-Order Nonlinearity in GeO_2-SiO_2 Glasses Poled with UV-Radiation", *Electron. Lett.*, vol. 33, pp. 980-981, 1997.
12. T.E. Tsai, M.A. Saifi, E.J. Friebele, D.L. Griscom, and U. Österberg, "Correlation of Defect Centers with Second Harmonic Generation in Ge-Doped and Ge-P-Doped Silica-Core Single-Mode Fibers", *Opt. Lett.*, vol. 14, pp. 1023-1025, 1989.
13. R.A. Myers, N. Mukherjee, and S.R.J. Brueck, "Large Second-Order Nonlinearities in Poled Fused Silica", *Opt. Lett.*, vol . 16, pp. 1732-1734, 1991.
14. T.G. Alley and S.R.J. Brueck, "Visualization of the Nonlinear Optical Space-Charge Region of Bulk Thermally Poled Fused-Silica Glass", *Opt. Lett.*, vol. 23, pp. 1170-1172, 1998.
15. X-C. Long and S.R.J. Brueck, "Large-Signal Phase Retardation with a Poled Electro-Optic Fiber", *IEEE Photon. Tech. Lett.*, vol. 9, pp. 767-769, 1997.
16. T. Erdogan, V. Mizrahi, P.J. Lemaire, and D. Monroe, "Decay of Ultraviolet-Induced Fiber Bragg Gratings", *J. Appl. Phys.*, vol. 76, pp. 73-80, 1994.
17. B. Srinivasan and R.K. Jain, "As-Fabricated Thermally Stable Bragg Gratings in Hydrogen-Loaded Fibers", to be published

wer entire tuning range of 80 nm, and for obtaining much shorter pulse durations using appropriate passive mode-locking techniques.

General Physics Institute, Russian Academy of Sciences, Moscow, Russia

**Dipartamento di Fizica, University of Pisa, Italy*

1. J.E. Pinto *et al.*, Opt. Lett. **17**, 731 (1992).
2. F. Heine *et al.*, in *Advanced Solid-State Lasers*, Vol. 15 of OSA Proceedings Series (Optical Society of America, Washington, D.C., 1993), p. 403.
3. E. Sorokin *et al.*, J. Opt. Soc. Am B **10**, 1436 (1993).
4. D.J. Kuizenga and A.E. Siegman, IEEE J. Quantum Electron. **QE-6**, 694 (1970).

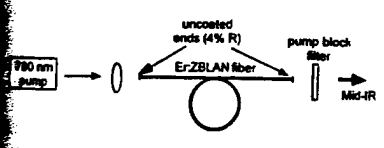
CWM2 **4:45 pm**

80 mW single-transverse-mode mid-IR (2.7 μm) cw output from a simple mirror-free 780-nm diode-pumpable fiber laser

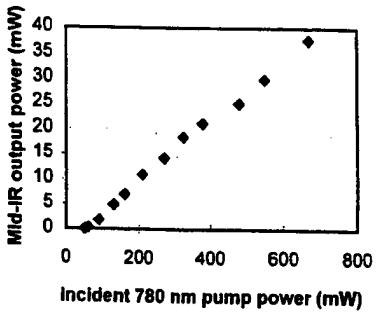
S. Srinivasan, E. Poppe,* R.K. Jain, *Center for High Technology Materials, University of New Mexico, Albuquerque, New Mexico 87106*

Compact and tunable, high-efficiency mid-IR laser sources are critically needed for a variety of applications including: (i) surgical cuts enabled by the strong water absorption at 2.7 μm in tissue,[1] (ii) mid-IR countermeasures, and (iii) environmental and industrial gases such as NO, H_2S, and water vapor. The first two applications typically require watts of mid-IR power and the latter requires a source that is tunable. The 2.7-μm transition in Er:ZBLAN fibers[2-5] is a promising candidate for the above applications due to its broad tunability (over 70 nm) and the demonstrated power scalability of fiber lasers, particularly with the use of double-clad designs. In this paper, we report over 40 mW of unsaturated single-transverse-mode output power from an Er:ZBLAN fiber laser of relatively simple construction, enabled in part by the use of high Er concentrations (10,000 ppm) and in part by the choice of 780 nm (vs. 791 nm) as the pump wavelength. The output powers from this laser should be readily scalable to the watt-power level with commercially available 780-nm diode pumps. As such, we believe this work represents the first report of the use of a double-clad fiber for a mid-IR fiber laser.

Figure 1 shows the experimental arrangement used in the present work. The choice of the fiber was based on our plans to replace the currently used 780-nm Ti:Al_2O_3 laser pump with high-power diode pumps of relatively low beam quality. As such, we used a 5.5-m-long double-clad Er:ZBLAN fiber, with 10,000 ppm Er in a 6-μm diameter, 0.15 NA single-mode amplifier core surrounded by a concentric



CWM2 Fig. 1. Schematic of the "mirror-free" Er:ZBLAN fiber laser.

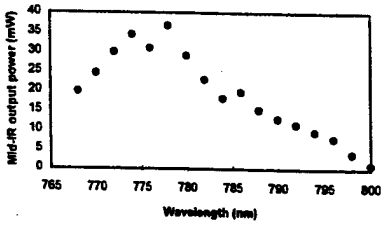


CWM2 Fig. 2. Output power as a function of incident pump power at 780 nm.

125-μm diameter diode pump-confining core ("inner clad") of 0.3 numerical aperture. In contrast to previously reported work[3,4] in which relatively expensive multiresonant mirrors (high R at 1.6 μm and 2.7 μm, and high T at the relatively short 780–800 nm pump wavelength), we chose a much simpler cavity design comprising simply of the 4% Fresnel reflections at the two uncoated fiber ends. Output power from the fiber laser was monitored by completely attenuating the 780-nm pump with a 2.7 μm (T = 90%) transmitting filter. A key feature of the work reported here is the use of high Er concentrations to facilitate depopulation of the long-lived lower laser level by crossrelaxation processes.[7] A companion key feature of the work reported here is the use of a pump wavelength of 780 nm (compared to the 791-nm pump wavelength used previously for excitation of the $^4I_{1\ 1/2}$ upper laser level via the $^4I_{9/2}$ pathway) to alleviate ground state bleaching problems[8]; this choice of pump wavelength is demonstrated to be approximately three times more efficient than the use of a 791-nm pump in our laser design, as elaborated below.

Figure 2 shows the P_{out} vs. P_{in} curve for this fiber laser when pumped by 780-nm single-transverse mode Ti:sapphire pump radiation that is directly coupled to the 6-μm amplifier core (coupling efficiency ~50%) corresponding to its current use as a simple "single clad" fiber. The vertical axis in Fig. 2 corresponds to mid-IR power output from both ends of the fiber laser, and lasing threshold corresponds to a gain of 5.85 dB/round trip at a pump power of ~25 mW corresponding to a pump power density of ~400 KW/cm^2. Note that even at the highest pump power levels, there is no evidence of saturation of the output power from this 2.7-μm fiber laser. As such, in a follow-on experiment currently in progress, comparable gains should be attainable with the use of ~20 W of diode pump power (Optopower Corp.) coupled partially into the core and partially into the diode-pump-confining 125-μm inner cladding; for this experiment, output power levels of the order of a watt are anticipated.

Figure 3 shows the "excitation spectrum" of such a fiber laser in the vicinity of 780 nm. Note that in contrast to a previous report[2] on the output power of such a mid-IR fiber laser as a function of the pump wavelength, in our work three times greater output power was obtained with the use of the 780-nm excitation wavelength when compared to the use of the more traditional 791-nm pump



CWM2 Fig. 3. Output power as a function of pump wavelength.

wavelength,[2-4] despite the higher ground state ($^4I_{15/2}$ to $^4I_{9/2}$) absorption at 791 nm. We are studying this effect in detail, and we currently ascribe the observed behavior to reduction in ground state bleaching effects,[8] as well as to the reduction of deleterious effects caused by significantly lower ESA[5,6] (from the upper laser level $^4I_{11/2}$ to $^4F_{5/2}$) for 780 nm (instead of 791 nm), and the wavelength dependence of the "beneficial" lower-level ($^4I_{13/2}$) depleting ESA to the ESA to the $^4H_{11/2}$ level.[5,6]

Results of diode pumping and power scalability issues will also be presented in detail in this talk, as well as the detailed role of the various excited-state absorption processes, and a comparison of the performance of this "mirror-free" laser with designs using traditional[3-5] multiresonant mirrors for "cascade lasing" of such Er:ZBLAN fiber lasers.

Department of Physical Electronics, Norwegian University of Science & Technology, Trondheim, Norway

1. L. Esterowitz, R. Allen, Proc. SPIE **1048**, 129 (1989).
2. R. Allen, L. Esterowitz, R.J. Ginther, Appl. Phys. Lett. **56**, 1635 (1990).
3. M. Pollnau, Ch. Ghisler, G. Bunea, W. Luthy, H.P. Weber, Appl. Phys. Lett. **66**, 26 (1995).
4. M. Pollnau, Ch. Ghisler, W. Luthy, H.P. Weber, J. Schneider, U.B. Unrau, Opt. Lett. **22**, 612 (1997).
5. M. Pollnau, R. Spring, Ch. Ghisler, S. Wittwer, W. Luthy, H.P. Weber, IEEE J. Quantum Electron. **32**, 657 (1996).
6. T.J. Whitley, C.A. Miller, R. Wyatt, M.C. Brierly, D. Szebesta, Electron. Lett. **27**, 1785 (1991).
7. G.J. Kintz, R. Allen, L. Esterowitz, Appl. Phys. Lett. **50**, 1553 (1987).
8. S. Bedo, M. Pollnau, W. Luthy, H.P. Weber, Opt. Commun. **116**, 81 (1995).

CWM3 **5:00 pm**

High-energy diode-pumped Ho:Tm:YLF laser for wind measurement from space

Upendra N. Singh, Jirong Yu,*
Mulugeta Petros,* Norman P. Barnes,
James C. Barnes, *NASA Langley Research Center, MS 474, Hampton, Virginia 23681-0001; E-mail: u.n.singh@larc.nasa.gov*

A narrow-linewidth all-solid-state laser system of low divergence with appreciable pulse-energy in the eyesafe region is required as an transmitter for the coherent wind lidar measurements from ground, air, and space-borne platform. Research efforts at NASA Langley Research Center (LaRC) were initiated to

Diode-Pumped High Power CW 2.7 μm Er Fiber Lasers

B. Srinivasan, J. Tafoya, and R.K. Jain
Center for High Technology Materials, Univ. of New Mexico, Albuquerque, NM 87106
Phone: (505) 272-7821, Fax: (505) 272-7801, Email: balaji@chtm.unm.edu

Because of the strong water absorption near 3 μm in tissue and the consequent ultrashort penetration depths (~few microns), compact high power (100 mW to 1 W) 2.7 μm laser sources with TEM_{00} beam quality [1-3] have several important applications in ultrafine intra-ocular and endoscopic laser surgery including transmyocardial revascularization and other intra-arterial procedures [1]. Compact and efficient sources of mid-IR radiation are also needed for infrared countermeasures applications, and for ppb (parts per billion) level spectroscopic monitoring [4] of various species such as NO and H_2S.

The 2.7 μm transition in Er:ZBLAN is well-suited for several of the above applications. However, as has been frequently stated, the longer natural lifetime of the lower laser level ($^4I_{13/2}$, 9.4 ms) relative to that of the upper laser level ($^4I_{11/2}$, 7.5 ms) of the 2.7 μm transition often results in a population bottleneck that inhibits efficient steady-state (CW) lasing in Er:ZBLAN fiber lasers [2,3]. We have successfully demonstrated – for the first time – "Watt-level" CW output powers (upto ~700 mW) in diode-pumped Er:ZBLAN fiber lasers. These results have been achieved by using efficient and novel depopulation mechanisms for the lower laser level, namely cross-relaxation between Er ions at high doping densities [5,6] and energy transfer to the $^3F_3$ and $^3F_4$ levels of Pr ions [7].

I. Efficient 2.7 μm Fiber Lasers Using Cross-Relaxation Processes:
The population bottleneck mentioned above can be alleviated through an enhanced cross-relaxation process [6] at high doping densities as has been observed by Bogdanov et al [5] at Er concentrations of >15% in ZBLAN bulk glasses. However, our recent measurements [6] have shown conclusively that the onset of Er ion clustering (presumably at sites corresponding to drawing-induced defects) can significantly enhance the cross-relaxation even at much lower doping densities (2%), corresponding to doping densities that are relatively easy to achieve with current fiber fabrication techniques. A fringe benefit of the use of high Er doping densities is the natural amenability of the consequent high core absorption to optimized designs of double-clad fibers capable of being pumped by relatively inexpensive high power diode arrays.

A 10 W OptoPower diode array operating at 795 nm was used to pump a custom-designed 20 m long Thorlabs 20,000 ppm double-clad (core dia.=3.8 μm, NA=0.28, inner clad dia.=125 μm, NA=0.5) 2.7 μm fiber laser, as depicted schematically in Fig. 1. The diode-to-double-clad fiber coupling efficiency and the pump absorption efficiency were 45% and 50% respectively. CW lasing was easily achieved with just the 4% Fresnel reflections from the fiber ends. In this initial setup, over 400 mW of CW 2.7 μm output has been obtained with a slope efficiency of 12% with respect to absorbed power. Work is in progress to scale the output power to >1 W by optimized coupling optics, and longer fiber lengths for higher absorption.

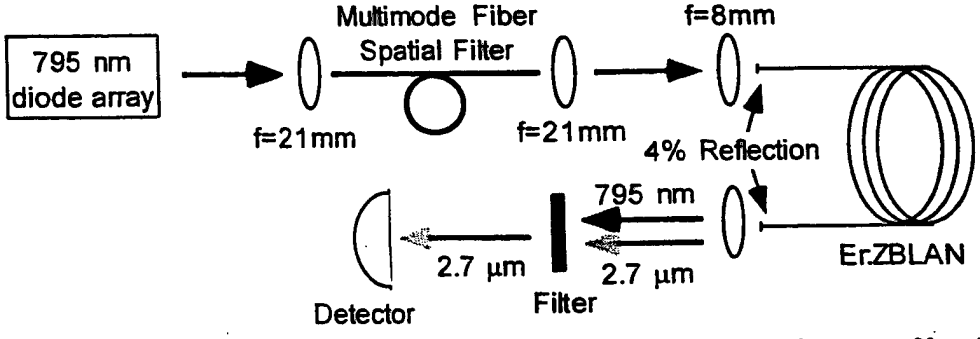


Figure 1. Schematic of multimode diode array-pumped high power CW 2.7 μm fiber laser

***II. Efficient 2.7 μm Fiber Lasers Using Energy Transfer to Pr Ions*:**

We have also demonstrated high power and efficient operation of the 2.7 μm transition in Er^{3+} by further enhancing the rate of depletion of the $^4I_{13/2}$ level of Er^{3+} by energy transfer to the $^3F_3$ and the $^3F_4$ levels of Pr^{3+} [7]. The rare-earth concentration was chosen to be 20,000 ppm of Er and 5,000 ppm of Pr based on the requirements of efficient absorption in Er^{3+} and rapid depopulation of the lower laser level (via enhanced cross-relaxation in Er and efficient energy transfer to Pr). The lifetime for the $^4I_{13/2}$ level was measured to be 0.7 ms for this specific co-doped system (vs. ~2 ms for a singly-doped 20,000 ppm Er:ZBLAN fiber). The inner cladding of the custom-made Thorlabs double-clad fiber was designed to be 100μmx200μm and 0.55 NA. In order to match the OptoPower 791 nm diode array beam shape to the rectangular-clad fiber, a cylindrical lens whose axis was rotated with respect to the plane of the diode array was used to optimize coupling; the net coupling efficiency and effective absorption coefficient were measured to be 65% and 0.6 dB/m respectively. The total absorption for the 14 m long fiber was ~85%.

Fig. 2 shows the 2.7 μm output power as a function of the absorbed 791 nm diode power. As seen from the above plot, the laser threshold is 330 mW and the slope efficiency is 13% with respect to the absorbed power; the threshold corresponds to a round-trip gain of 29.4 dB at a pump power density of 1.65 kW/cm^2. The linearity of the plot clearly indicates scalability to Watt power levels using higher pump powers or more efficient pump coupling and pump absorption techniques. In our presentation, we will elaborate on such power scaling issues, based on improved fiber designs (optimized doping densities, improved double-clad designs) and pump geometries, targeted on the development of highly efficient multi-Watt 2.7 μm CW lasers. We will also discuss future directions related to wavelength-tunable and pulsed (Q-switched and mode-locked) high peak power sources based on such lasers; the latter should also enable the generation of longer mid-IR wavelengths relatively easily via efficient nonlinear optical (Raman/DFG) techniques.

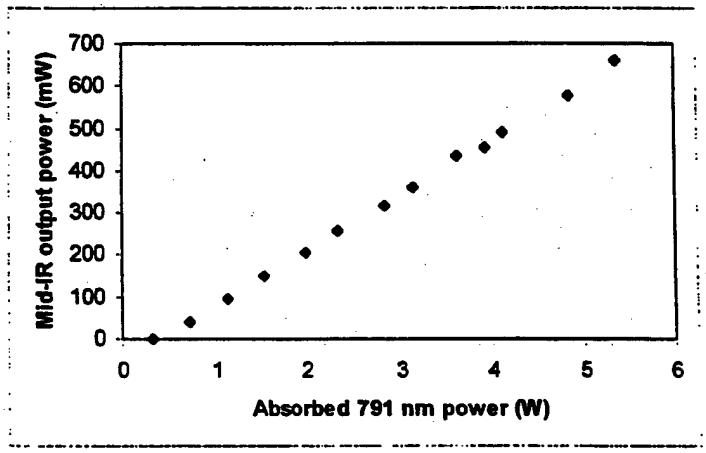


Figure 2. CW 2.7 μm power vs. absorbed diode power for 14 m long 20,000/5,000 ppm Er/Pr:ZBLAN fiber

References:

1. L. Esterowitz, R. Allen, *Rare Earth Doped IR Fiber Lasers for Medical Applications*, Proc. SPIE **1048**, 129-132 (1989)
2. M. Pollnau, *The Route Toward a Diode-Pumped 1-W Erbium 3-μm Fiber Laser*, IEEE J. Quantum Electron., **33**, 1982-1990 (1997)
3. E. Poppe, B. Srinivasan, and R.K. Jain, *980nm-Diode-Pumped Continuous Wave Mid-IR (2.7 μm) Fiber Laser*, Electron. Lett., **34**, 2331-2333 (1998)
4. R.S. Eng, J.F. Butler, and K.J. Linden, *Tunable Diode Laser Spectroscopy: An Invited Review*, Opt. Engg., **19**, 945-960 (1980)
5. V.K. Bogdanov, W.E.K. Gibbs, D.J. Booth, J.S. Javorniczky, P.J. Newman, D.R. McFarlane, *Fluorescence from High-Doped Erbium Fluorozirconate Glasses Pumped at 800 nm*, Optics Commn., **132**, 73 (1996)
6. B. Srinivasan, G. Monnom, and R.K. Jain, *Indirect Measurement of the Magnitude of Ion Clustering at High Doping Densities in Er:ZBLAN Fibers*, to be published
7. J.Y. Allain, M. Monerie, and H. Poignant, *Energy Transfer in Er^{3+}/Pr^{3+}-Doped Fluoride Glass Fibres and Application to Lasing at 2.7 μm*, Electron. Lett., **27**, 445-447 (1991)

A Compact Diode-Pumped Passively Q-switched Mid-IR Fiber Laser

N.J.C. Libatique, J.D. Tafoya, and R.K. Jain
Center for High Technology Materials, Univ. of New Mexico, 1313 Goddard SE, Albuquerque, NM 87106
Tel (505) 272-7821, Fax (505)272-7801, email: natl@chtm.unm.edu, jain@chtm.unm.edu

Abstract: This work describes the first observation of passive Q-switching (7 μs pulsewidth, 35 kHz rep rate) of a mid-IR fiber laser. This was achieved by using a liquid gallium mirror as a saturable absorber.
OCIS codes: (141.0140) Lasers & Laser Optics: (140.3510) Fiber Lasers, (140.3540) Q-switched Lasers

Watt-level diode-pumped *continuous wave* mid-infrared fiber lasers [1,2], based on double-clad high-concentration (>10,000 ppm) erbium-doped ZBLAN fiber materials, have been developed in recent years. Compact pulsed mid-IR laser sources based on similar fiber designs are a logical next step. Such pulsed fiber lasers with emission wavelengths in the vicinity of the 3 μm mid-infrared water absorption peak are needed for a number of medical applications [3-5]. In addition, in systems that require lightweight and efficient pulsed sources such as for airborne or spaceborne applications, passively Q-switched designs are preferred over actively Q-switched lasers because of their simplicity, compactness, and relative cost-effectiveness. This presentation describes the first demonstration on passive Q-switching of mid-IR rare-earth doped fiber lasers.

One of the more exciting methods for the passive Q-switching of fiber lasers is the use of the large optical nonlinearities in gallium which has been recently discovered [6, 7]. In particular, at 1.5 μm wavelengths, reflectivity changes as high as 30% have been stimulated for relatively low intensities of ~1kW/cm^2, and has been exploited [6, 7] in the Q-switching of fiber lasers emitting in the near-infrared (Yb:Silica/1060 nm, Er:Silica/1550 nm) spectral region. Because of significantly reduced absorption in the vicinity of 3 μm, it was not obvious that the Ga:glass mirror would work adequately for Q-switching the mid-IR Er:ZBLAN fiber laser. This work demonstrates that indeed the Ga:glass saturable absorber can be used to Q-switch lasers at the 3 μm range.

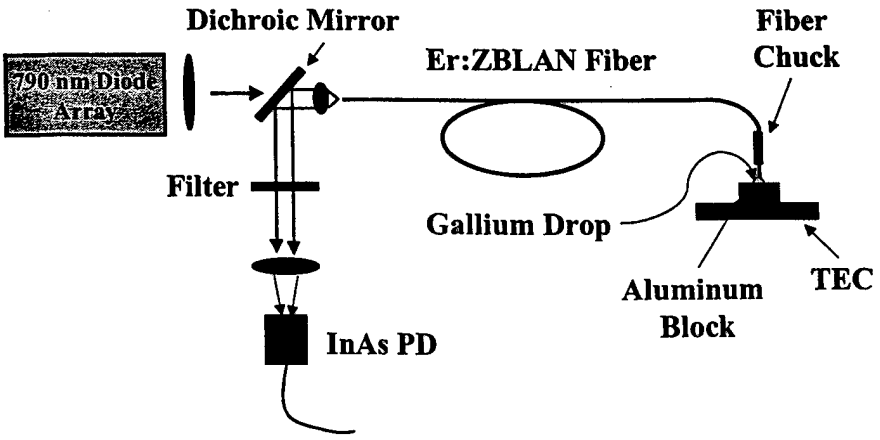
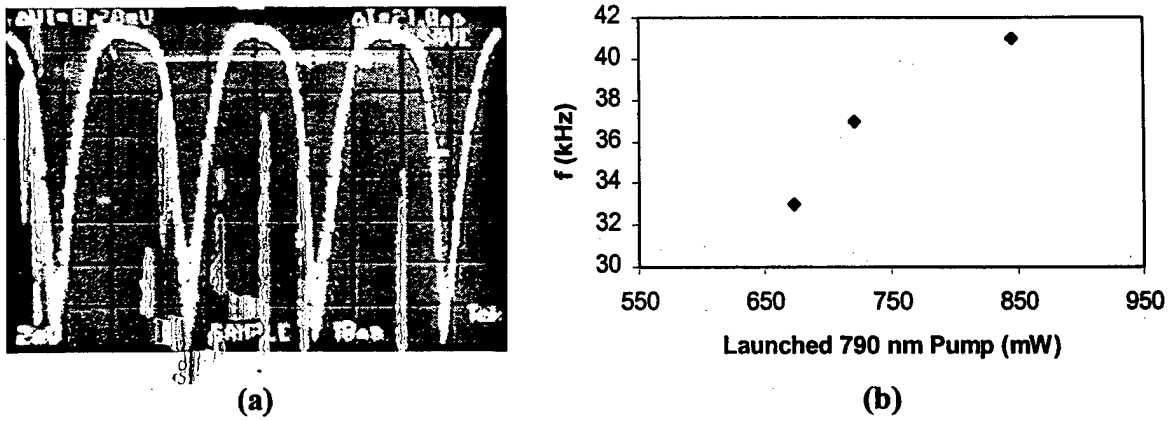


Fig. 1. Schematic of our pulsed mid-IR fiber laser using a butt-coupled liquid gallium mirror

A schematic of the experimental set-up is depicted in Figure 1. It consists of a simple Fabry-Perot cavity defined by the 4% Fresnel reflection off the pump end of the fiber, and a rear mirror defined by a gallium:fluoride glass interface. The gallium was held in a ~3 mm diameter dimple machined into an

aluminum block thermally contacted (using silicone paste) onto a thermoelectric cooler. The 20,000 ppm Er:ZBLAN (Thorlabs/KDD) double-clad fiber (L = 20m) was pumped with a high power 790 nm diode



(a) (b)

Fig. 2. Pulsed operation of a passively Q-switched Er:ZBLAN 2.8 μm fiber laser. (a) 7 μs pulsewidths (horizontal scale = 10 μs/div), (b) Repetition rate as function of launched pump powers.

array from Optopower. The pulsewidths and pulse shapes were measured with a fast (0.3 ns rise time) InAs photodetector.

When the Peltier cooler was set to temperatures from 10 to 25 °C, Q-switching was observed as depicted in Figure 2a. Unstable pulsing or CW lasing was observed outside the above-mentioned temperature range. For the data shown in Fig. 2a, the launched pump power was 720 mW and the Ga mirror was set to a temperature of 12.7 °C. At these settings, the observed pulse width was 7 μs at rep rates of 37 kHz. As is consistent with the behavior of passively Q-switched fiber lasers [8], the laser's repetition rate increased with pump power (Fig. 2b), while the pulse width had an inverse relation with the pump.

In conclusion, we have demonstrated a passively Q-switched Er:ZBLAN mid-infrared fiber laser based on a liquid gallium mirror saturable absorber. In particular we have shown that the gallium:fluoride (ZBLAN) glass system has a nonlinear response similar to the silicate glasses previously reported [7], at wavelengths as long as 2.8 μm. A detailed study of the optical nonlinearity of the Ga mirror through pump-probe experiments at the 2.8 μm band is in progress.

This work was supported by AFOSR.

References

1. Srinivasan B et.al., Electron. Lett., 35 #16, 1338-1340 (1999)
2. Srinivasan B et.al., Opt. Expr., 4(#12) , U10-U15, Jun 7, 1999
3. Ren Q. et.al., Lasers in Surgery and Medicine, 12, 274-281 (1992)
4. Wigdor HA et.al., Lasers in Surgery and Medicine, 16, 103-133 (1995)
5. Deckelbaum LI et.al., Lasers in Surgery and Medicine, 15, 315-341 (1994)
6. Bennet PJ, et. al., Appl. Phys. Lett. 73 #13, 17871789 (1998)
7. Petropoulos P et. al., Appl. Phys. Lett., 74 # 24, 3619-3621 (1999)
8. Barnes WL and Digonnet M, *Rare Earth Doped Fiber Lasers and Amplifiers,* (Marcel Dekker, Inc, 1993) Ch. 8.

A "Field-Usable" Diode-Pumped ~120 nm Wavelength-Tunable CW Mid-IR Fiber Laser

N.J.C. Libatique, J.D. Tafoya, N. Viswanathan, and R.K. Jain
Center for High Technology Materials, University of New Mexico, Albuquerque, NM 87106
Tel (505) 272-7821, Fax (505)272-7801, email: natl@chtm.unm.edu, jain@chtm.unm.edu

Abstract: We report tunable operation of a diode-pumped mid-IR Er-doped ZBLAN fiber laser. The output wavelengths were tunable from 2.71 μm - 2.83 μm with powers varying from 1 mW - 30 mW.
OCIS codes: (141.0140) Lasers & Laser Optics: (140.3510) Fiber Lasers, (140.3600) Tunable Lasers

The understanding of mid-IR laser sources in Er:ZBLAN materials has dramatically improved in the last two years [1,2], resulting in the demonstration [3] of high power (watt-level) diode-pumped 2.8 μm fiber lasers that exploit interionic cross-relaxation processes in novel materials with high erbium doping densities. Although tuning of Er:ZBLAN fiber lasers in the vicinity of 2.7 μm has been demonstrated earlier [4], this presentation describes the first demonstration of a *diode-pumped tunable* mid-IR fiber laser, as well as the first demonstration of tunable operation in the vicinity of 2.8 μm, as needed for high sensitivity spectroscopic detection of important trace gases (such as HF, NO, and water vapor). The compactness and portability of the present device lends promise for its field-usability in the foreseeable future.

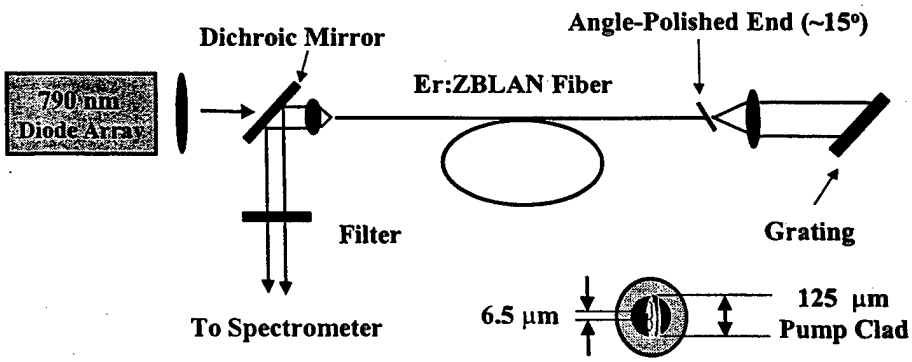


Fig 1. Schematic of tunable mid-IR fiber laser using a grating in the Littrow configuration. The inset at the lower right shows a cross-section of the double-clad fiber.

The experimental set-up is depicted in Fig. 1. A 20 meter long double clad Er:ZBLAN fiber (20,000 ppm erbium, from Thorlabs/KDD), pumped by a 790 nm Optopower diode array, was used as the gain medium. The laser cavity was formed by the 4% Fresnel reflection at the fiber end facing the pump and a bulk grating blazed at 2.6 μm (diffraction efficiency = 80%, θ_B = 15°4', 200 grooves/mm). Spectral data were taken with a CVI Digikrom 240 spectrometer.

Fig 2 shows output tuning curves (tuning range from 2.70 μm to 2.81 μm) when the laser was pumped at two different (195 mW, 285 mW) launched pump powers P_{pump}. As the pump power increases, the spectrum tends to shift to longer wavelengths. In particular, for P_{pump} = 1.13 W, the tunable output extended from 2.78 μm to 2.83 μm, and CW powers as high as 30 mW was obtained. This tendency to shift to longer wavelengths at high pump powers has been observed before in unintentionally-tuned erbium-doped bulk glass lasers [5], and is presumably due to re-absorption effects and the efficiency of the inter-ionic cross-relaxation process that depopulates the lower lasing level ($^4I_{13/2}$ manifold).

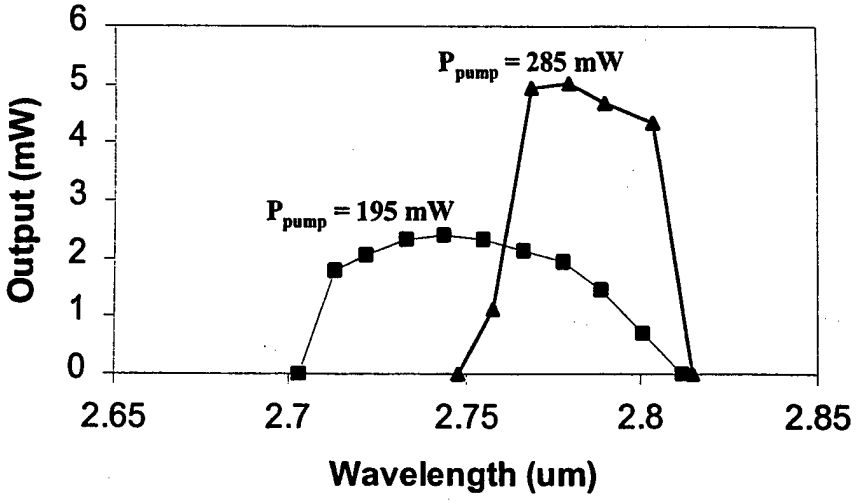


Fig.2. Tuning curves for diode-pumped Er:ZBLAN fiber laser at various launched 790 nm pump powers P_{pump}.

For these measurements, the observed linewidths were resolution-limited (~1 nm for the slit widths chosen). No attempts have yet been made to reduce the linewidths to the < 0.01 cm^{-1} values required for spectroscopic applications at this spectral region. Such linewidths can be achieved by the use of multiple dispersive elements (i.e. grating-prism combinations) or the employment of resonator designs[6] that interferometrically enhance mode selection (i.e. Fox-Smith resonators, multiple-arm cavities).

Efforts are underway to increase the output power of the tunable lasers by optimizing the fiber lengths and the output coupling, by improving the polishing of the fiber ends, and by reducing the losses caused by intra-cavity absorption due to water vapor with the use of enclosed cavities containing inert gases. Narrow linewidth laser sources are being constructed based on Littman-Metcalf resonator geometries and grating-prism combinations, with the option of using high-finesse Fabry-Perot filters as a next step to further improve the laser linewidth characteristics. The design of a relatively low-loss FBG-tuned near-monolithic cavity structure [1] is also in progress.

This work was supported by AFOSR.

References

1. Poppe E, Srinivasan B, and Jain RK, Electron. Lett., 34 (#24) pp. 2331-2333 (1998).
2. Srinivasan B, Poppe E, Tafoya J, and Jain RK, Electron. Lett., 35 (#16) pp. 1338-1340 (1999).
3. Srinivasan B et.al., Opt. Expr., 4(#12) , U10-U15, Jun 7, 1999.
4. Allain JY, Monerie M, and Poignant H, Electron. Lett., 27 (#5) pp. 445-447 (1991).
5. Auzel F, Meichenin, and Poignant H, Electron. Lett., 24 (#23) pp. 1463-1464 (1988).
6. Binks DJ, Ko DK, Gloster AW, and King TA, J. Opt. Soc. Am. B, 15 (#9), 2395-2403 (1998).

Strong Fiber Bragg Gratings With Significantly Enhanced Thermal Stability

B. Srinivasan and R.K. Jain
Center for High Technology Materials, Univ. of New Mexico,
1313 Goddard SE, Albuquerque, NM 87106
Phone: (505)272-7842, Fax: (505)272-7801, Email: jain@chtm.unm.edu

Abstract

We report the demonstration of thermally stable strong (10^{-3} index change) fiber Bragg gratings in germanosilicate fibers. Our one-step FBG writing/stabilization process uses a phase mask that transmits a significant fraction of the zeroth order.

Strong Fiber Bragg Gratings With Significantly Enhanced Thermal Stability

B. Srinivasan and R.K. Jain
Center for High Technology Materials, University of New Mexico,
1313 Goddard SE, Albuquerque, NM 87106
Phone: (505)272-7842, Fax: (505)272-7801, Email: jain@chtm.unm.edu

Strong, high reflectivity fiber Bragg gratings (FBGs) are critical in a wide variety of WDM devices including add-drop filters, demultiplexers, Raman amplifiers, and fiber laser sources [1]. The technique of hydrogen-loading [2] is well established for sensitizing germanosilicate fibers, leading to strong ($\Delta n > 10^{-3}$) index gratings in the fiber core. As such FBGs get integrated into critical telecommunication systems, their long-term stability has become an important issue [3]. In this paper, we report the demonstration of thermally stable strong (10^{-3} index change) fiber Bragg gratings in germanosilicate fibers using a phase mask that transmits a significant fraction of the zeroth order.

Although FBGs with index changes approaching 10^{-2} have been demonstrated in hydrogen-loaded fibers [4], the physical mechanism leading to enhanced photosensitivities and the thermal stability of the FBGs are not yet fully understood [5,6]. Patrick et al. [5] have reported a relatively comprehensive study on the stability of FBGs in H_2-loaded germanosilicate fibers. In particular, they noted that the annealing behavior of such FBGs was significantly different from that of FBGs fabricated in non-hydrogenated fibers. Subsequently, Egan et al. [6] reported data that contradicted the conclusions of Patrick et al. In particular, they found similar annealing behavior for FBGs irrespective of whether the boron-doped germanosilicate fibers were H_2-loaded or not. However, both studies (which used holographic interference of UV radiation for the FBG fabrication) reported poor thermal stability of the FBGs, i.e., the magnitude of the UV-induced index change (Δn) decreased to <25% of its original value for temperatures of 500 °C. This large decay for a relatively low thermal energy indicates that the majority of the index change originally created in these H_2-loaded fibers is due to defects with small activation energies ($kT < 0.62$ eV, shallow defects shown in Fig. 1). An important fundamental question that arises related to the stability of FBGs fabricated in H_2-loaded fibers is the issue of how the energy distribution of the defects can be controlled. We have performed studies on the annealing behavior of FBGs that can provide clues to the solution of the above problem, leading to the fabrication of thermally stable high reflectivity FBGs.

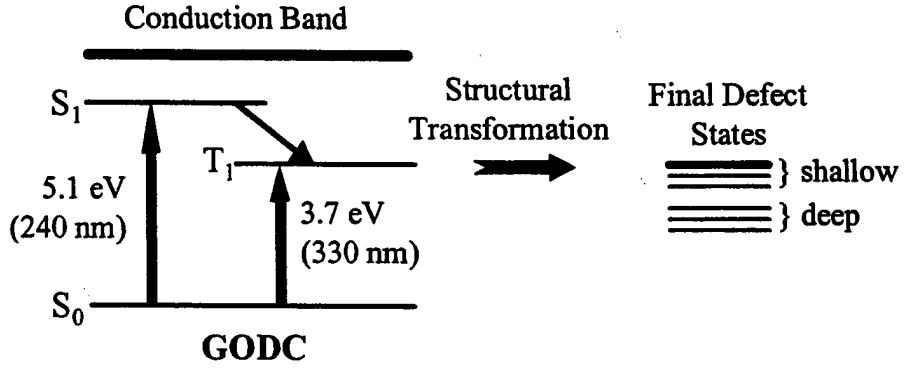


Figure 1. Conceptual diagram of the energy distribution of GODC defects after UV irradiation [7]

The above problem can also be approached from a different perspective – is it possible to tailor the defects such that they are more stable? Such an idea suggests a stabilization technique that requires an extra processing step in the fabrication of the FBGs. Indeed, Salik et al. [8] recently demonstrated stabilization of FBGs in non-H_2-loaded fibers by uniform UV illumination of fiber prior to or after the FBG fabrication, a process that eliminates the fraction of grating due to shallow defects by saturating them. But, such a procedure requires *a priori* knowledge of the fraction of index change due to shallow defects and also involves an extra processing step that is undesirable for mass manufacturing of such FBGs. To circumvent this problem, Salik et al. suggest an alternate stabilization technique in which they use a significant fraction of the zero order beam transmitted through a phase mask (which produces the interference pattern also) to uniformly illuminate the fiber, thereby saturating the shallow defects and stabilizing the FBG. They have reported preliminary results demonstrating successful implementation of this technique for relatively weak FBGs written in non-H_2 loaded fibers [8]. But, as Patrick et al. [5] had reported, the distribution of activation energies in H_2-loaded fibers is different from that in non-H_2-loaded fibers (which are well-described by the model of Erdogan et al. [3]). They also show that the species responsible for the index change in the H_2-loaded fiber dissociate at lower annealing temperatures than those in the unloaded fiber. Such studies clearly show that the stabilization techniques for non-H_2-loaded fibers may not necessarily be applicable for H_2-loaded fibers. Moreover, a simple, efficient stabilization technique has not yet been demonstrated for strong FBGs ($\Delta n > 10^{-3}$).

In this paper, we report recent studies on the stabilization of fiber Bragg gratings *while they are being fabricated*. Using this one-step writing/stabilization technique, we have demonstrated FBGs in H_2-loaded fibers that have superior thermal stability compared to those reported previously. A key advantage of this technique is that the large, stable index change leading to relatively strong ($\Delta n > 10^{-3}$) FBGs can be controlled *in-situ* and hence is commercially viable.

We used a 193 nm ArF laser with an energy density of 20 mJ/cm^2 at a repetition rate of 7 Hz in our experiments. We fabricated the FBGs ($\Delta n \sim 1.2 \times 10^{-3}$) by exposing SMF-28 fibers (~5% GeO_2), which have been H_2-loaded (1500 psi, 50 °C) for 72 hrs, through a custom phase mask (1072 nm period, 25% in zero order, 35% each in the first orders). The FBGs were subsequently annealed in a standard box oven capable of heating upto 1000 °C. One end of the FBG was mechanically spliced to a pigtailed LED and the other connected to an optical spectrum analyzer for in-situ monitoring of the FBG transmission. The temperature inside the oven was calibrated by an observed shift of the FBG spectrum [5]. The FBG transmission was monitored after 8 hours (to allow the Δn to stabilize at that particular temperature) at each annealing temperature. The corresponding index change was deduced and normalized with respect to the value at room temperature. Fig. 2 shows the response of index change to different annealing temperature for our FBGs compared to those of Patrick et al [5] and Egan et al. [6]. The plot clearly indicates the superior stability of FBGs fabricated using our custom phase mask as compared to holographic interference methods used in their work. The key factor leading to our results is the uniform illumination of the fiber by the zero order UV beam, which saturates the shallow defects and stabilizes the FBG. One disadvantage of this technique however, is the reduction in the fringe

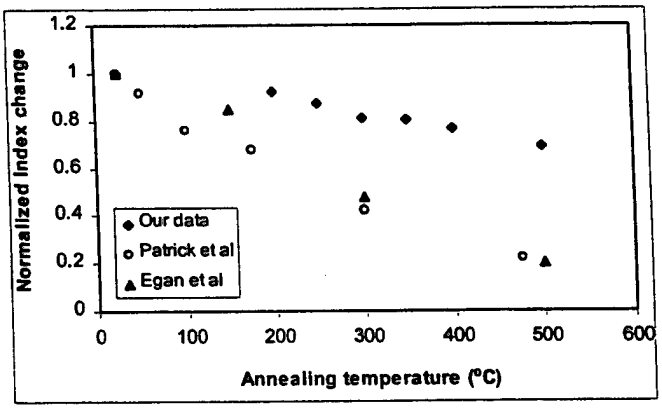


Figure 2. Plot illustrating the superior stability of FBGs in H_2-loaded fibers fabricated using our custom phase mask compared to those fabricated using holographic interference technique

contrast of the interference pattern. We are currently investigating the optimum percentage of the zero order scattered UV radiation (transmitted through the phase mask) such that stabilization of the FBG is achieved without seriously degrading the fringe contrast of the interference pattern.

In separate experiments, we observed that the thermal stability of a germanosilicate fiber with higher GeO_2 concentration was poor compared to SMF-28 fibers. In order to examine this in detail we fabricated FBGs of ~30 dB reflectivity in H_2-loaded fibers with three different GeO_2 concentrations viz. Corning SMF-28 fiber (~5% GeO_2), KVH e-core fiber (~18% GeO_2), and QPS "Photosensitive" fiber (30% GeO_2) using a phase mask that had 7% transmission in the zeroth order. Subsequently these FBGs were annealed at temperatures upto 750°C and the decay in the modulated index change was noted down. Fig. 3 shows the results of such annealing experiments. The annealing behavior for the three FBGs were found to be similar for temperatures upto 450°C (within error bars of 5%), indicating that the energy distribution of the shallow defects is similar. At higher temperatures the index change for the FBGs fabricated in fibers with higher GeO_2 concentrations decay faster than for the SMF-28 FBG. The annealing behavior at high temperatures indicates a higher density in the energy distribution of deep defects for GeO_2 concentrations of >18%. Furthermore, the above annealing behavior shows that thermally stable, strong gratings can be fabricated in hyrdogen-loaded fibers with very low (<5%) GeO_2 concentrations. Such an observation is critical for the design of FBGs with strong reflectivity as well as good thermal stability and is being currently investigated in detail.

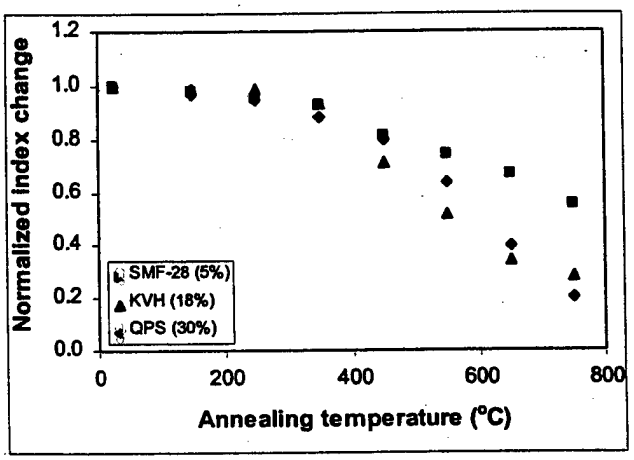


Figure 3. Plot illustrating different annealing behavior for FBGs fabricated in fibers with different GeO_2 concentrations

References:

1. C.R. Giles, "Lightwave Applications of Fiber Bragg Gratings", Jour. Lightwave Technol., vol. 15, pp. 1391-1404, 1997.
2. P.J. Lemaire, R.M. Atkins, V. Mizrahi, and W.A. Reed, 'High Pressure H_2 Loading as a Technique for Achieving Ultrahigh UV Photosensitivity and Thermal Sensitivity in GeO_2 Doped Optical Fibers', *Electron. Lett.*, vol. 29, pp. 1191-1193, 1993
3. T. Erdogan, V. Mizrahi, P.J. Lemaire, and D. Monroe, "Decay of Ultraviolet-Induced Fiber Bragg Gratings", *J. Appl. Phys.*, vol. 76, pp. 73-80, 1994
4. P.J. Lemaire, R.M. Atkins, V. Mizrahi, and W.A. Reed, "High Pressure H_2 Loading as a Technique for Achieving Ultrahigh UV Photosensitivity and Thermal Sensitivity in GeO2 Doped Optical Fibres", *Electron. Lett.*, vol. 29, pp. 1191-1193, 1993
5. H. Patrick, S.L. Gilbert, A. Ligard, and M.D. Gallagher, 'Annealing of Bragg Gratings in Hydrogen-Loaded Optical Fiber', *J. Appl. Phys.*, vol. 78, pp. 2940-2945, 1995
6. R.J. Egan, H.G. Inglis, P. Hill, P.A. Krug, and F. Ouellette, 'Effects of Hydrogen Loading and Grating Strength on the Thermal Stablily of Fiber Bragg Gratings', *OFC '96 Tech. Digest*, paper TuO3, pp. 83-84, 1996
7. D.S. Starodubov, V. Grubsky, J. Feinberg, B. Kobrin, and S. Juma, 'Bragg Grating Fabrication in Germanosilicate Fibers by use of Near-UV Light: a New Pathway for Refractive-Index Changes', *Opt. Lett.*, vol. **22**, pp. 1086-1088, 1997
8. E. Salik, D.S. Starodubov, V. Grubsky, & J. Feinberg, 'Thermally Stable Gratings in Optical Fibers without Temperature Annealing', *OFC'98 Tech. Digest*, paper ThD3, pp. 56-58, 1998

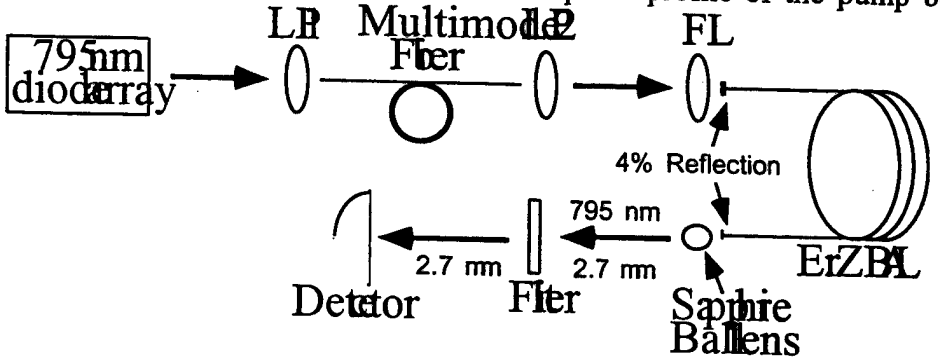
Mirror-Free, High Power (~140mW) Diode-Pumped 2.7 μm CW Fiber Laser

X. Zhao, B. Srinivasan, P. Pulaski, S. Gupta, and R.K. Jain*
Center for High Technology Materials, Univ. of New Mexico, Albuquerque, NM 87106
Phone: (505) 272-7821, Fax: (505) 272-7801
** Optopower Corp. Tucson, AZ*

Because of the strong water absorption near 3 μm in tissue and the consequent ultrashort penetration depths (of a few microns), compact high power (100 mW to 1 W) 2.7 μm laser sources with TEM_{00} beam quality have several important applications in ultrafine intra-ocular and endoscopic laser surgery including transmyocardial revascularization and other intra-arterial procedures[1]. In such applications, laser energy absorbed by the targeted tissue is capable of its coagulation or precise ablation with minimal damage to the remaining tissue. Other applications that could benefit from compact and efficient sources of mid-IR radiation include infrared countermeasures and spectroscopic sensing.

In this paper, we report stable high power (140 mW) CW output from a 2.7μm fiber laser. Note that these power levels represent over an order of magnitude increase in the power reported previously from diode-pumped Er:ZBLAN fiber lasers[2,3]. Moreover, in contrast with previous reports[4], in which 1000 ppm was identified as the optimal doping density, an unique enabling feature[3] leading to the results reported here *is the use of high Er doping densities (10,000 ppm),* which enables a rapid depletion of the lower laser level through cross-relaxation processes[5]. These high doping densities also enable the exploitation of double-clad fiber geometries, capable of being pumped by relatively inexpensive high power diode arrays, while keeping optimal fiber lengths relatively short, i.e. on the order of ten meters. Furthermore, we describe a simple mirrorless design which is directly pigtailable to the pump diode, representing a much more commercially viable alternative to previous high power 2.7 μm fiber laser designs, that invoke cascade lasing processes by using complex and expensive multi-resonant mirror coatings[6].

The experimental setup is shown in Fig. 1. The double-clad Er:ZBLAN fiber used was approximately 5 m long, with an Er doping density of 10,000 ppm in a single mode 6 μm, 0.15 NA core surrounded by a concentric 125 μm 0.3 NA cladding. The pump source was an Optopower diode array operating at a wavelength of 795 nm, and capable of yielding nearly 20 Watts of CW power in a 8 mm x 8 mm beam of 5 mrad divergence. A multimode silica fiber (250 μm core diameter) was used to condition the spatial profile of the pump beam so as to



LP: aspheric lens pair, f=12 mm; FL: aspheric focusing lens, f=6 mm

Figure 1. Schematic of multimode diode array-pumped mid-IR fiber laser

improve its coupling efficiency to the double-clad Er:ZBLAN fiber while inhibiting the possibility of damaging its ends. No dielectric mirrors were used for the laser cavity, and feedback was obtained simply by the ~4% Fresnel reflections at the two uncoated fiber ends.

The throughput (η_1) of the beam-shaping multimode fiber and the related lens pair (LP) was 55%. This near-collimated 9 mm diameter beam exiting the beam conditioning setup was then focused into the inner cladding of the double-clad Er:ZBLAN fiber by another aspheric lens (FL) of 7 mm diameter with a net coupling efficiency (η_2) of 40%, which includes a loss due to beam clipping. In this preliminary unoptimized setup, the effective launch efficiency ($\eta_3=\eta_1 x \eta_2$) of the diode array beam into the double-clad fiber was thus only 22%.

As observed through measurements of unabsorbed pump power at the end of the 5 m double-clad fiber, the effective absorption (α) of the pump light was only 19%, leading to utilization of only $\beta=\alpha \times \eta_3$ i.e., only 4% of the pump photons available at the output of the pump diode laser in this unoptimized experiment. Fig. 2 shows a plot of the output power as a function of the absorbed pump power. The mid-IR power in the figure corresponds to the total mid-IR power output from both ends of the fiber laser. There was no evidence of lasing at either 1.55 μm or 1.7 μm or the onset of the cascade lasing phenomenon[6] in our experiments, as verified carefully by detailed spectral observations. Note that even at the highest pump power level, there is no sign of saturation of the output power from this fiber laser, and the overall pump-to-mid-IR conversion efficiency is ~20% implying promise for a relatively efficient laser and high power outputs in future optimized designs.

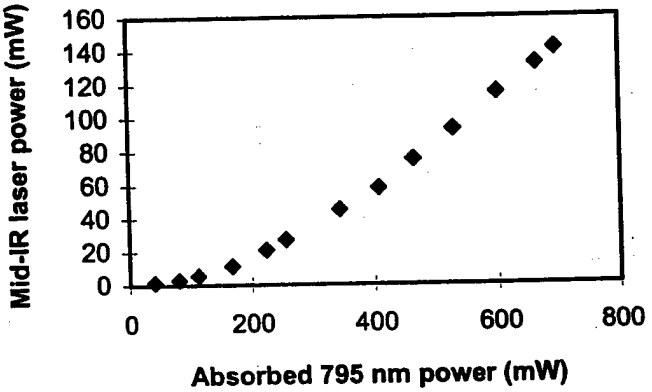


Figure 2. 2.7 μm laser output power vs. absorbed pump power for Er:ZBLAN double-clad fiber laser

One obvious improvement in the overall efficiency can be obtained with the use of longer fibers (tens of meters) to more completely absorb the pump radiation, thereby increasing α and β by approximately a factor of 5. Furthermore, we anticipate a factor of two improvement in η_2 through the use of a larger diameter aspheric lens, leading to an overall increase in the pump utilization parameter β by a factor of 10 (up to ~41%). Finally, the diode pump power can easily be increased to over 40 W by polarization multiplexing two 20 W arrays. As such, we anticipate output power scaling to well above 1 Watt level in the near future.

References:

1. L. Esterowitz, R. Allen, Proc. SPIE **1048**, 129 (1989)
2. H.Yanagita, et al., Electronic Letters, **26**, 1838 (1990)
3. E. Poppe, B. Srinivasan, and R.K. Jain, Postdeadline paper, LEOS Annual Meeting, San Francisco, 1997; B. Srinivasan, E. Poppe, and R.K. Jain, presented at CLEO '98
4. S. Bedo, W. Luthy, and H.P. Weber, Electronic Letters, **31**, 199 (1995)
5. G.J. Kintz, R. Allen, and L. Esterowitz, Appl. Phys. Lett., **50**, 1553 (1987)
6. Pollnau, Ch. Ghisler, G. Bunea, W. Luthy, H. P. Weber, App. Phys. Lett. **66**, 3564 (1995)

Enhancement of the Efficiency of 2.7 μm Er:ZBLAN Fiber Lasers Via Cluster Formation at High Doping Densities

B. Srinivasan, G. Monnom*, and R.K. Jain
Center for High Tech Materials, Univ. of New Mexico, Albuquerque, NM 87106
Phone: (505) 272-7821, Fax: (505) 272-7801, email: balaji@chtm.unm.edu
* Laboratoire de Physique de la Matiere Condensee, Univ. de Nice - Sophia Antipolis, France

Abstract

We have performed experiments and developed a model to determine the presence of clusters in Er:ZBLAN fibers at high doping densities, as well as studied their role on the enhancement of efficiency of 2.7 μm fiber lasers. Discussion of the design of 1 W double-clad 2.7 μm Er:ZBLAN fiber lasers will be presented.

Enhancement of the Efficiency of 2.7 μm Er:ZBLAN Fiber Lasers Via Cluster Formation at High Doping Densities

B. Srinivasan, G. Monnom*, and R.K. Jain
Center for High Tech Materials, Univ. of New Mexico, Albuquerque, NM 87106
Phone: (505) 272-7821, Fax: (505) 272-7801, email: balaji@chtm.unm.edu
* Laboratoire de Physique de la Matiere Condensee, Univ. de Nice - Sophia Antipolis, France

The broadly tunable[1] 2.7 μm transition in Er:ZBLAN appears particularly attractive for the design of compact, high power CW fiber lasers[2] of excellent beam quality, as needed for applications ranging from endoscopic laser surgery[3] to countermeasures and spectroscopic monitoring[4]. As is well known, the longer lifetime of the lower laser level ($^4I_{13/2}$, 9.4 ms) compared to the upper laser level ($^4I_{11/2}$, 7.5 ms) of this transition poses a serious bottleneck[2,5]. Recently, Poppe et al.[2] have demonstrated alleviation of this bottleneck and strongly enhanced efficiencies and output powers by a simple technique viz. the use of fibers with high concentrations (>10,000 ppm) of Er. It was hypothesized that such high concentrations not only reduce the problem of ground state bleaching[5], but also invoke several cross-relaxation mechanisms including the one shown in Fig. 1. On the contrary, Bogdanov et al.[6] have observed significant cross-relaxation only at very high doping densities i.e., 150,000 ppm in bulk Er:ZBLAN glasses.

This paper demonstrates conclusively that in contrast to bulk glasses, strong ion-ion interaction occurs in Er:ZBLAN fibers even at doping densities as low as 10,000 ppm. This is done by experimental and theoretical studies of saturation of absorption at 972 nm as a function of doping density, as well as by measurements of the lifetimes of the $^4I_{11/2}$ and the $^4I_{13/2}$ levels as a function of doping density. Future extension of these studies will help elucidate the optimum design for high power (~1 W) 2.7 μm Er:ZBLAN fiber lasers.

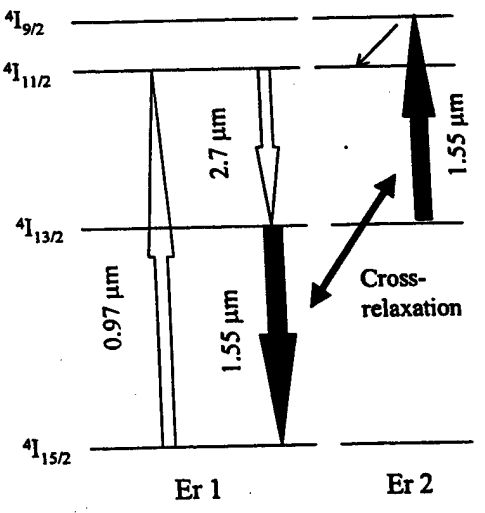


Figure 1. Energy level diagram of Er showing energy transfer due to cross-relaxation between two adjacent ions originally in the $^4I_{13/2}$ state level

As elucidated by Maurice et al.[7] for Er:silica fibers, the onset of cluster formation is evidenced by a rapid increase in the non-saturable component of the absorption (NSA). Such increase in NSA in fluoride fibers is corroborated by a modified theoretical model, some of the results of which are plotted in Fig.2 along with our absorption data for fibers with 1000 and 10,000 ppm Er doping densities. Note that the model

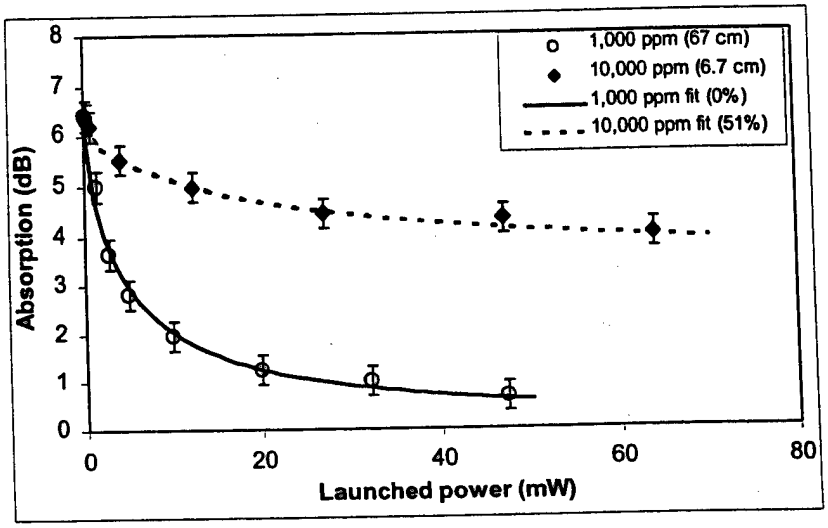


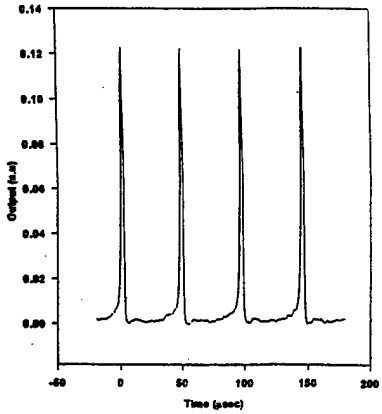
Figure 2. A plot of the measured and calculated values of the absorption at 972 nm radiation as a function of launched power in two fibers corresponding to significantly different Er concentrations (1000 ppm and 10,000 ppm)

developed here uses measured values of lifetimes and branching ratios[8,9] as well as known cross-relaxation rates[6] and uses no free parameters for the fits other than an assumption of the fraction of ions that are in clusters. As such, the excellent agreement between the model and the data gives a strong indication of the percentage of ions in clusters. The presence of such clusters satisfactorily explains why fiber lasers based on fibers with average doping concentrations much lower than those specified by Bogdanov et al.[6] apparently show high efficiency enhancements due to cross-relaxation processes. Our measurements of lifetimes of the $^4I_{11/2}$ and the $^4I_{13/2}$ levels as a function of the average doping densities in these fibers showed a significant decrease in the lifetime of these levels at concentrations approaching 10,000 ppm indicating a more rapid onset of cross-relaxation than that expected from the data of Bogdanov et al.[6], consistent with the above clustering model.

Work is still in progress to further refine this model to precisely calculate the populations of the upper and lower laser levels and the small signal and saturated gains for such Er:ZBLAN fibers with high doping densities (based on clustering levels predicted by fits similar to Fig. 2). Preliminary designs of double-clad fiber lasers targeted to producing 1 W CW mid-IR output powers with the use of high power (20 W) diode arrays are currently in place, and such demonstrations are awaiting the production of custom fibers.

References:

1. F. Auzel, D. Meichenin, and H. Poignant, Elect. Lett., **24**, 1463 (1988)
2. E. Poppe, B. Srinivasan, and R.K. Jain, Electron. Lett., **34**, 2340 (1998)
3. L. Esterowitz, R. Allen, Proc. SPIE **1048**, 129 (1989)
4. R.S. Eng, J.F. Butler, and K.J. Linden, Opt. Engg., **19**, 945 (1980)
5. M. Pollnau, IEEE J. Quantum Electron., **33**, 1982 (1997)
6. V.K. Bogdanov, W.E.K. Gibbs, D.J. Booth, J.S. Javorniczky et al., Opt. Commn., **132**, 73 (1996)
7. E. Maurice, G. Monnom, B. Dussardier, D.B. Ostrowsky, Opt. Lett., **20**, 2487 (1995)
8. R.S. Quimby and W.J. Miniscalco, Appl. Opt., **28**, 14 (1989)
9. F. Auzel, D. Meichenin, and H. Poignant, Elect. Lett., **24**, 909 (1988)



CTuE5 Fig. 3. A typical Q-switch pulse train as measured at an operating temperature of 17°C.

pump power over the stable operating regimes for two gallium temperatures; the pulse peak power is seen to increase as we move away from the gallium melting point thereby compensating for the decreasing nonlinearity of the mirror. Note, that Q-switching was not observed with a molten gallium mirror, or any other conventional reflector inserted within the cavity further confirming LGN as the Q-switching mechanism.

We believe these results represent a first demonstration of the application of LGN mirrors to laser systems illustrating their compatibility with waveguide devices. We anticipate that significant improvements in mirror design and laser performance will follow making use of the unique features of this manifestly nonlinear medium.

Department of Physics and Astronomy, University of Southampton, Southampton, United Kingdom

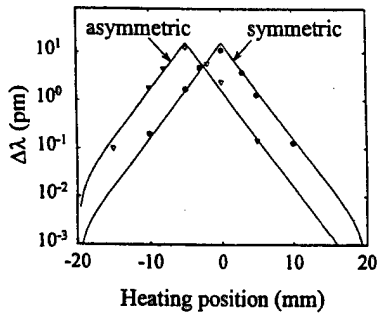
1. S. Dhanjal, S. Popov, I.R. Shatwell, Yu.P. Svirko, N.I. Zheludev, V. Gusev, Opt. Lett. 22, (December 15, 1997).
2. S. Dhanjal, I.R. Shatwell, Yu. P. Svirko, in *Quantum Electronics and Laser Science Conference*, Vol. 12 of 1997 OSA Technical Digest Series (Optical Society of America, Washington, D.C., 1997), p. 223.
3. P. Bennett, S. Dhanjal, P. Petropoulos, D.J. Richardson, N.I. Zheludev, submitted to IQEC'98.

CTuE6 9:30 am

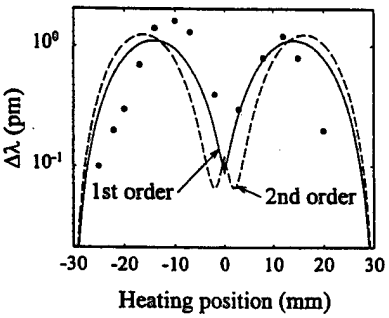
Characterization of intensity distribution in symmetric and asymmetric fiber DFB lasers

Erlend Rønnekleiv,* Morten Ibsen, Michael N. Zervas, Richard I. Laming, *Optoelectronic Research Centre, University of Southampton, Southampton, SO17 1BJ, United Kingdom*

Distributed feedback (DFB) lasers are complex structures and the understanding of how they operate depends much on simulations. Measurements of intensity distributions in laser cavities can provide information about grating strength, grating uniformity as well as the order of the operating longitudinal mode. Theoretical models can also be confirmed. Intensity measurements by scanning the side-emission from a 980-pumped DFB Er-fiber laser have been demonstrated previously.[1] In this paper we demonstrate an alternative simple method that can be used also with 1480-pumping. The technique is applied to characterize symmetric and asymmetric DFB lasers for the first time to our knowledge.



CTuE6 Fig. 1. Dots and triangles: Heat-induced wavelength shifts measured for two 40-mm DFBs with the Bragg phase shift at the center and at −5 mm, respectively. Lines: Theoretical fits to measurements.



CTuE6 Fig. 2. Dots: Heat-induced wavelength shifts measured for a 60-mm DFB. Lines: Theoretical phase-shift sensitivities for the first- and second-higher order longitudinal modes of a uniform DFB structure.

Simulations made of various nonuniform DFB structures show that a phase perturbation added to the laser structure will result in laser wavelength shift $\Delta\lambda$ that is proportional to the geometrical mean $\sqrt{(I_r I_l)}$ of the right $[I_r]$ and left $[I_l]$ traveling intensities at the perturbation point. Laser intensity distributions can therefore be determined by scanning a phase perturbation along the cavity and measuring the resulting wavelength shift.

In our experiment the radiation from a halogen lamp was focused onto a small spot on a DFB fiber laser, causing a heat-induced phase shift. The resulting wavelength shift was read out using a scanning Fabry–Perot interferometer. Er/Yb fiber[2] was used for the lasers, which were operating in the 1550-band and pumped with 100 mW at 1480 nm from one end.

Figure 1 shows results for one symmetric and one asymmetric 40-mm DFB laser, both lasing in their fundamental longitudinal modes. In the asymmetric device the Bragg phase shift was offset by −5 mm from the center. The total output powers from the symmetric and asymmetric devices were 470 μW and 30 μW, respectively, with left to right output power ratios of 1:1 and 600:1 (±10%). The low output from the asymmetric device can be attributed to a nonoptimimum total grating strength[3] and should be straightforward to improve.

It is known that the fundamental mode intensity in a DFB laser will have a maximum at the phase-shift position. Further, it can be shown that the slopes of the measured sensitivity curves $[\delta\log(\Delta\lambda)/\delta z]$ are proportional to the grating strength κ. Therefore, both phase-shift positions and grating strength can be determined from the measurements in Fig. 1.

The solid lines in Fig. 1 show theoretical values for the wavelength shift $[\Delta\lambda = \delta\lambda/\delta\phi \cdot \Delta\phi]$ caused by a locally-induced phase shift of $\Delta\phi = 0.53$ rad in the symmetric and asymmetric geometries, assuming uniform DFBs with $\kappa = 230\ \mathrm{m}^{-1}$. The deviations between the measured and calculated sensitivities at the phase-shift positions can be attributed to the 2-mm-size of the heating spot used.

Figure 2 shows the measured heating response for a $L = 60$ mm DFB. The dip at the center indicates that the laser is not operating in its fundamental mode. This may be due to phase errors in the grating period, combined with a relatively high κL value of about 14. For comparison, simulated sensitivities for the first two higher-order modes of a uniform DFB structure, assuming $\kappa = 230\ \mathrm{m}^{-1}$ and $\Delta\phi = 0.28$ rad, are also shown. The first- and second-order modes can be qualitatively distinguished by the absence and presence, respectively, of a local intensity maximum at the phase-shift position. The characterized laser is therefore shown to operate in its first-order longitudinal mode.

In conclusion we have presented a simple technique for measurement of power distributions along phase-shifted DFB lasers. This is used to locate the position of the built-in phase shift and to determine the grating strength (Fig. 1), as well as to determine the order of the operating longitudinal mode (Figs. 1 and 2). We have also demonstrated, for the first time to our knowledge, directional fiber laser output by use of a true asymmetric phase-shifted DFB structure.[4]

E. Rønnekleiv is a Ph.D. student on leave from the NTNU university in Norway. He is employed and sponsored by Optoplan AS, Norway.

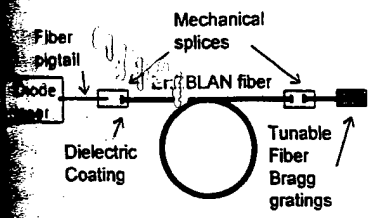
1. W.H. Loh, B.N. Samson, J.P. de Sandro, Appl. Phys. Lett. 69, 3773–5 (1996).
2. L. Dong, W.H. Loh, J.E. Caplen, J.D. Minelly, L. Reekie, Opt. Lett. 22, 694–6 (1997).
3. V.C. Lauridsen, T. Søndergaard, P. Varming, J.H. Povlsen, in *ECOC 97 Proceedings*, Vol. 3, 1997, pp. 39–42.
4. W.H. Loh, L. Dong, J.E. Caplen, Appl. Phys. Lett. 69, 2151–3 (1996).

CTuE7 9:45 am

980-nm diode-pumped power-scalable continuous wave mid-IR (2.7 μm) fiber laser

Erik Poppe, Balaji Srinivasan,* Ravi Jain,* *Department of Physical Electronics, Norwegian University of Science of Technology, Trondheim, Norway*

Compact and tunable, high-efficiency mid-infrared lasers are needed for numerous appli-

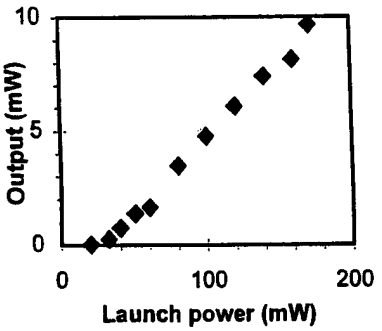


CTuE7 Fig. 1. Schematic of a tunable, diode-pumped Er:ZBLAN mid-IR fiber laser.

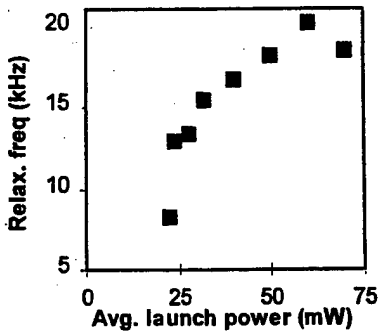
ons, including (1) field-usable spectro-ic sensors for environmental and strial-process monitoring and (2) master illators in airborne or spaceborne high-er mid-IR MOPAs for various counter-sure applications. Lead-salt diode lasers limited by the need for cryogenic cooling, power, and spatial, temporal, and spectral abilities. Sb-based and quantum cascade e lasers seem to be more promising, but -lived stable cw mid-IR outputs have not been achieved with these devices at room perature. On the other hand, diode-mped fiber lasers are an attractive alterna-technology, delivering stable diffraction-ited cw room-temperature mid-IR ission, at least in limited wavelength ges[1-3] (such as in bands around 2.7 μm and μm). Figure 1 shows a vision for future mpact field-usable tunable mid-IR fiber la-suitable for the above-stated applications. In this talk, we describe a relatively efficient wer-scalable mid-IR (2.7 μm) Er^{3+}:ZBLAN er laser pumped by readily available 980-nm er diodes. The ~10 mW cw power levels monstrated here are significantly higher an those reported previously from any Er^{3+}: BLAN diode-pumped mid-IR fiber laser, sumably because the high erbium concen-tions (10,000 ppm) used enable rapid deple-n of the lower laser level through cross-axation processes.

In our experiments, we used a nearly-le-transverse-mode, 1-W 980-nm tapered lifier diode laser[5] as the pump source, ch was coupled by a free-space lens into the BLAN fiber. The fiber was double-clad, a core diameter of 6 μm, a length of 5.5 m, Er^{3+} concentration of 10,000 ppm (in the ore), and an inner cladding diameter of 125 m. The choice of a double-clad fiber was tated by our plans for power scaling of the tputs of such a fiber laser with use of high-wer diode lasers. At the input end an HR irror was butt-coupled to the fiber while the eaved distal end was used as a 96% output upler. Figure 2 shows the 2.7-μm output wer as a function of launched pump power. he low lasing threshold of 30 mW for a 96% utput coupler, and the fact that no saturation f the output power is observed even at the ighest pump powers used indicates that this aser can be further optimized to yield much igher output powers.

Our choice of a 980-nm pump wavelength or this work (instead of the more efficient 791-nm pumps traditionally used[1,3]) was dic-ated by the ready availability of multiwatt power level 980-nm diode lasers (due to the elatively large market need for 1.55-μm EDFA pumps). A principal reason why



CTuE7 Fig. 2. P_{out} versus P_{in} for cw pump.



CTuE7 Fig. 3. Relaxation oscillation frequency versus launched pump power.

980-nm pumps are less efficient for pumping of the 2.7-μm transition in erbium is the lack of an appropriate 980-nm ESA process (as occurs with the 791-nm pump) to depopulate the lower laser level ($^4I_{13/2}$), whose lifetime (9.4 ms) is longer than that (7.5 ms) of the upper laser level ($^4I_{11/2}$). As such, the 2.7-μm Er:ZBLAN laser transition is expected (at first glance) to be self-terminating with the use of a 980-nm pump. The data presented here clearly demonstrates the possibility of relatively efficient cw operation, partly consistent with the theory of Quimby *et al.*,[5] and partly because of the onset of a cross-relaxation mechanism that depletes the lower laser level ($^4I_{13/2}$) in one ion while upconverting the other ion to the $^4I_{11/2}$ state[6]; this high cross-relaxation rate is possible due to the high erbium concentrations (10,000 ppm) used, and is being investigated in further detail. Nevertheless, the lack of saturation at the highest pump power levels used is particularly interesting, and bodes good promise for future power scaling experiments.

Work is currently in progress to demonstrate tuning of the output of such a laser with the use of a PZT-tuned fiber Bragg grating reflector similar to that shown in Fig 1. In our talk, we will also describe several other observations, including a natural tendency of the untuned laser to shift to longer wavelengths with increased pump power, and the onset of relaxation oscillations at frequencies varying from 5 kHz to 20 kHz (see Fig. 3), when pumped with a chopped pump (at 100 Hz). Issues related to power scaling of such double-clad fiber lasers with the use of high-power multimode diode pumps will also be discussed.

*Center for High Technology Materials, University of New Mexico, Albuquerque, New Mexico

1. R. Allen, L. Esterowitz, R.J. Ginther, Appl. Phys. Lett. **56**, 1635 (1990).
2. Ch. Frerichs, Int. J. Infrared Millim Waves **15**, 635 (1994).
3. M. Pollnau, Ch. Ghisler, W. Luthy, H.P. Weber, J. Schneider, U.B. Unrau, Opt. Lett. **22**, 612 (1997).
4. J.N. Walpole, E.S. Kintzer, S.R. Chinn, C.A. Wang, L.J. Missaggia, Appl. Phys. Lett. **61**, 740 (1992).
5. R.S. Quimby and W.J. Miniscalco, Appl. Opt. **28**, 14 (1989).
6. G.J. Kintz, R. Allen, L. Esterowitz, Appl. Phys. Lett. **50**, 1553 (1987).

JTuA

8:00 am–10:00 am
Room 200–212

Joint Session on Ultrashort X-ray Pulses: Generation and Applications

Brent Dane, *Lawrence Livermore National Laboratory, Presider*

JTuA1 (Invited) 8:00 am

Generation of coherent XUV radiation in the water window

Ch. Spielmann, M. Schnürer, N.H. Burnett,* C. Kan,* Z. Cheng, T. Brabec, F. Krausz, *Abteilung Quantenelektronik und Lasertechnik, Technische Universität Wien, Gusshausstr. 27, A-1040 Wien, Austria; E-mail: spielmann@ps1.iaee.towien.ac.at*

Free atoms exposed to an intense laser field (10^{14}–10^{15} W/cm^2) were shown to emit high harmonics of the incident radiation several years ago. The origin of this coherent XUV radiation is an electron that is first freed by means of tunneling ionization, subsequently accelerated by the strong laser field, and eventually brought back by the same field to its parent ion some half a cycle later. Recombination of the energetic electron with the ion results in the emission of short-wavelength radiation. The process is repeated over many cycles, giving rise to a discrete harmonic spectrum. Depletion of the ground state during irradiation by a femtosecond pulse comprising many optical cycles sets a limit to the highest harmonic photon energies achievable at a given pulse duration.

Recently 0.1-TW, 5-fs pulses at a repetition rate of 1 kHz became available in the near infrared. Owing to the extremely short pulse duration, ionization is virtually confined to merely one optical cycle. As a result, harmonics at significantly shorter wavelengths can be expected. Recent experimental and theoretical research suggest that the high-power 5-fs pulses reported above should allow the generation of (spatially) coherent soft x-rays in the water window (2.3–4.4 nm), i.e., between the oxygen and carbon K edges, in a spectral range, which is extremely important for the study of microscopic biological structures.[1,2] Our experiments have verified these expectations. Short wavelength radiation is emitted (in a

High Power Continuous Wave Mid-Infrared Fiber Lasers

B. Srinivasan and R.K. Jain
Center for High Technology Materials,
Univ. of New Mexico, Albuquerque, New Mexico

Because of the strong water absorption near 3 μm in tissue and the consequent ultrashort penetration depths (of a few microns), compact high power (100 mW to 1 W) 2.7 μm laser sources with TEM_{00} beam quality[1] have several important applications in ultrafine intra-ocular and endoscopic laser surgery including transmyocardial revascularization and other intra-arterial procedures[2]. In such applications, laser energy absorbed by the target tissue is capable of its coagulation or precise ablation with minimal damage to the remaining tissue. Other applications that could benefit from compact and efficient sources of mid-IR radiation include infrared countermeasures and spectroscopic monitoring[3].

The 2.7 μm transition in Er:ZBLAN is well-suited for many of the above applications. However, as is well known, the longer lifetime of the lower laser level ($^4I_{13/2}$, 9.4 ms) compared to the upper laser level ($^4I_{11/2}$, 7.5 ms) of the 2.7 μm transition poses a serious bottleneck[1,4], which in the past has been alleviated by complex mechanisms such as: (1) selective depletion of the lower laser level via excited state absorption (ESA)[5,6], (2) excitation transfer of the energy from the $^4I_{13/2}$ lower laser level to an appropriate acceptor state (e.g. the $^3F_3$ level in Pr[7]), and (3) cascade lasing[8]. Recently, we have demonstrated alleviation of this bottleneck and strongly enhanced efficiencies and output powers by a simpler alternative technique, namely the use of fibers with high concentrations (>10,000 ppm) of Er[1]. It was hypothesized that such high concentrations not only reduce the problem of ground state bleaching[4], but also invoke a cross-relaxation mechanism (Fig. 1), namely the "W_{11}" process[4], which relaxes the excitation from the lower laser level ($^4I_{13/2}$) to the ground state ($^4I_{15/2}$) while upconverting an adjacent ion to the $^4I_{9/2}$ state.

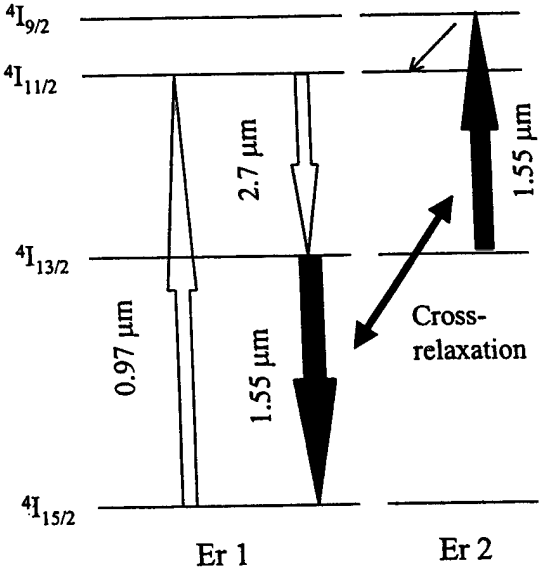


Figure 1. Energy level diagram of Er showing energy transfer due to cross-relaxation between two adjacent ions that are both initially in $^4I_{13/2}$ state

With regards to the role of the above-mentioned cross-relaxation mechanism, a contrary piece of evidence has been reported for Er:ZBLAN bulk glasses by Bogdanov et al.[9], in which significant cross-relaxation was observed only at very high doping densities i.e., 150,000 ppm. Since the optical properties of highly doped fibers can be different from those of apparently similar glasses, due to defects induced during the fiber drawing process[10], in part due to the onset of a "clustering" phenomenon, as has been observed frequently in silica fibers[11,12], it is important to investigate the presence of clusters in highly-doped Er:ZBLAN fibers as a function of doping concentration. In this paper, we describe our results on such studies, notably our measurements on the saturation of the ground state absorption at 972 nm and on fluorescence lifetimes of the $^4I_{11/2}$ and the $^4I_{13/2}$ energy

levels as a function of concentration. These studies demonstrate that unlike the case for low doping densities (1000 ppm), at high doping densities (10,000 ppm) the ground state ($^4I_{15/2}$) is replenished rapidly, presumably by a cross-relaxation process whose rate is high enough to be explainable only by the presence of clusters in these highly doped Er:ZBLAN fibers. We also describe our recent 2.7 μm fiber laser results, including those from 980 nm and 790 nm diode-pumped 2.7 μm fiber lasers which use Er:ZBLAN fibers with high (10,000 ppm) doping densities. We have been able to demonstrate improved efficiencies and output powers from such lasers, presumably due to the presence of clusters in such fibers invoking the cross-relaxation process shown in Fig. 1. Future extension of these studies will help elucidate the optimum design for high power (~1 W) diode pumped CW mid-IR (2.7 μm) Er:ZBLAN fiber lasers.

As stated briefly above, at low Er doping densities, the presence of the population bottleneck at $^4I_{13/2}$ is evident by the depletion of the ground state population, which leads to saturation of absorption at several transitions (from the ground state). However, at high Er doping densities, the cross-relaxation process discussed above (see Fig. 1) can cause depletion of the $^4I_{13/2}$ population, thereby reducing this saturation of absorption. In particular, as elucidated by Maurice et al[11] for Er:silica fibers, the onset of cluster formation can cause an even greater increase in the non-saturable component of the absorption. This is because when a large number of ions (n) are in the $^4I_{13/2}$ state and are adjacent to each other in a cluster, all (but one) are de-excited to the $^4I_{15/2}$ ground state by n/2 cross-relaxations; this enhanced de-excitation inhibits the saturation of absorption that is observed at low doping densities. Although the situation is a little different in Er:ZBLAN fluoride fibers because of the longer lifetimes of several of the excited states and the consequent increased importance of excited state absorption as well as of multiple cross-relaxation processes, the dominance of the cross-relaxation process of Fig. 1 is still expected to be evidenced by a strong increase in the non-saturable absorption (NSA).

We have performed a detailed experimental and theoretical study on the dependence of the saturation of the absorption at the $^4I_{15/2}$-$^4I_{11/2}$ transition of Erbium in single mode fluoride fibers with varying concentrations of Er. In our experiments, the saturation of absorption was measured with a Ti:Sapphire laser tuned to 972 nm (peak wavelength of absorption for the $^4I_{15/2}$-$^4I_{11/2}$ transition). One of the Er:ZBLAN fibers used had a nominal doping density of 1,000 ppm doping concentration, while the other doping density was 10,000 ppm. The lengths of the two fibers were chosen to be 67 cms and 6.7 cms respectively. The unabsorbed power (P_{out}) coming out of the fiber was measured with a Si detector. The launch efficiency for the two fibers was determined to be 46% and 53% respectively by detuning the T:Sapphire laser to an off-resonance wavelength. The absorption (α) of the Er:ZBLAN fiber is given by

$$\alpha = 10\log_{10}\left(\frac{P_{launch}}{P_{out}}\right) dB$$

where P_{launch} is the 972 nm power launched into these single mode fibers

Figure 2 below shows the absorption curves for the 1,000 ppm and 10,000 ppm Er-doped fibers as a function of the launched 972 nm power. It should be noted that the absorption curves are relatively flat for launched powers >20 mW and that the data points shown represent an error bar of approximately 0.4 dB. The extremely low levels of saturable absorption (larger NSA) observed for the 10,000 ppm fiber implies that a significantly large proportion of ions are present

in clusters at high doping concentrations. We will also present results of a theoretical model for NSA based on fast cross-relaxation in clusters. Fitting the data to NSA predictions from this

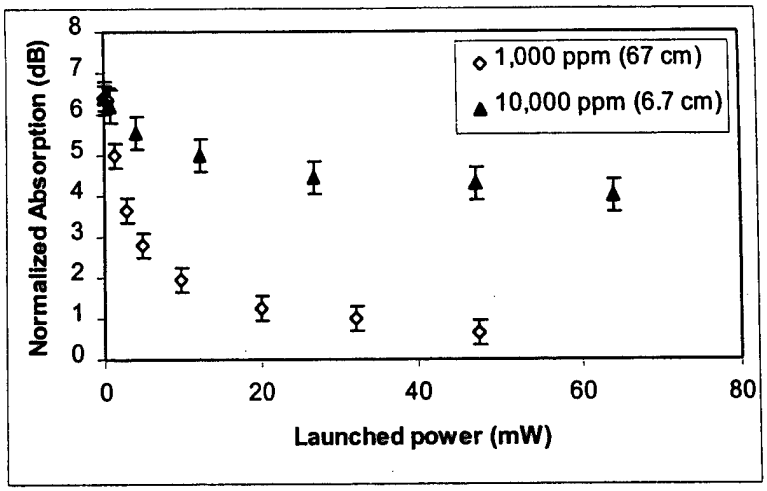


Figure 2. A plot of the measured values of the absorption at 972 nm radiation as a function of the launched power in two fibers corresponding to significantly different Er concentrations (1000 ppm and 10,000 ppm)

model were used to estimate the percentage of ions present in the form of clusters. It was found that approximately 50% of the ions in the 10,000 ppm fiber are in clusters (in which they "behave" like they are in a "local" environment with doping densities that exceed 400,000 ppm!).

Since the high levels of NSA observed here in highly-doped fibers (Fig. 2) are indicative of a strong increase in the W_{11} cross-relaxation process shown in Fig. 1, a corroborative evidence for such increase in the cross-relaxation rate can be obtained via studying fluorescence lifetime quenching of the $^4I_{13/2}$ energy level due to this cross-relaxation process. Simultaneous quenching also occurs for the $^4I_{11/2}$ energy level due to another cross-relaxation process[4], namely W_{22}, that upconverts one of the Er ions to the $^4F_{7/2}$ energy level. In order to verify the role of these cross-relaxation processes more directly, we measured the fluorescence lifetime for the $^4I_{13/2}$ and the $^4I_{11/2}$ energy levels as a function of the Er doping concentration. The Ti:Sapphire laser was tuned to 980 nm or 800 nm to measure the 1.55 μm fluorescence (from $^4I_{13/2}$) or the 0.98 μm fluorescence (from $^4I_{11/2}$) respectively. Although the fluorescence decay curves were observed to be multi-exponential, they were approximated as single exponential decays for simplicity.

Figure 3 shows the results of the fluorescence lifetime measurements for the $^4I_{13/2}$ and the $^4I_{11/2}$ energy levels as a function of the Er concentration. The lifetimes for the two levels did not change significantly for the 1,000 ppm and 5,000 ppm doping (9.6 ms and 7.4 ms respectively), but they decreased to 8 ms and 6.8 ms respectively at 10,000 ppm Er concentration. This behavior clearly illustrates

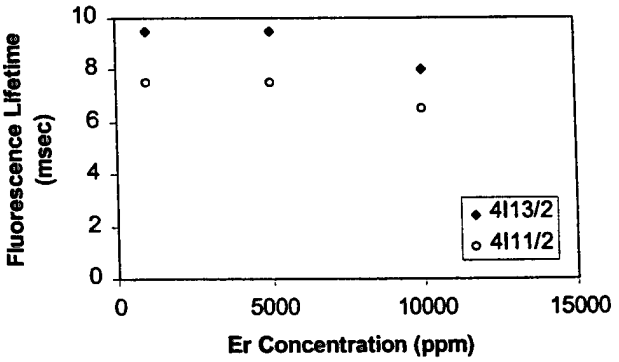


Figure 3. Fluorescence lifetime measurements showing quenching at high Er-doping densities

lifetime quenching beyond the 5,000 ppm Er concentration due to the onset of cross-relaxation processes. A key factor in favor of the laser performance is that the lifetime quenching of the lower laser level ($^4I_{13/2}$) is higher than that of the upper laser level ($^4I_{11/2}$), which permits alleviation of the population bottleneck problem mentioned above.

The observations of NSA and lifetime quenching imply the usefulness of high Er concentrations for 2.7 μm Er:ZBLAN fiber lasers not only because of the alleviation of the population bottleneck in the $^4I_{13/2}$ level, but also because of *the availability of a higher number of Er ions*. These high doping densities also enable exploitation of double-clad fiber geometries, capable of being pumped by relatively inexpensive high power diode arrays, while keeping optimal fiber lengths relatively short, i.e. on the order of ten meters.

In initial experiments, we used a nearly single transverse mode, 1 Watt 980 nm tapered amplifier diode laser[13] as the pump source, which was coupled by a free space lens into a double-clad Er:ZBLAN fiber. Our choice of a 980 nm pump wavelength for this work (instead of the more efficient 790-800 nm pumps traditionally used[4,8]) was dictated by the ready commercial availability of multi-Watt power level 980 nm diode lasers (due to the relatively large market need for 1.55 μm EDFA pumps). The double-clad fiber had a core diameter of 6 μm with an NA of 0.15, a length of 5.5 m, an Er^{3+} concentration of 10,000 ppm (in the core), and an inner cladding diameter of 125 μm. The pump radiation was coupled to the fiber through a 20x microscope objective, with a coupling efficiency to the core of approximately 50%. An additional 35% of pump light was coupled to the inner cladding although this latter portion experiences a significantly lower effective absorption coefficient during its transit through the 5.5 m long fiber. The net absorption coefficient is estimated as 60%. The choice of a double-clad fiber was dictated in part by improved utilization of the pump light with 980 nm diode pumping, and in part by our plans to demonstrate power scaling of the outputs of such fiber lasers with use of high power diode lasers (as elaborated below). At the input end an HR mirror was butt-coupled to the fiber while the cleaved distal end was used as a 96% output coupler. Figure 4 shows the 2.7 μm output power as a function of launched pump power. The low lasing threshold of 30 mW for a 96% output coupler, and the fact that no saturation of the output power is observed even at the highest pump powers used, indicates that this laser can be further optimized to yield much higher output power.

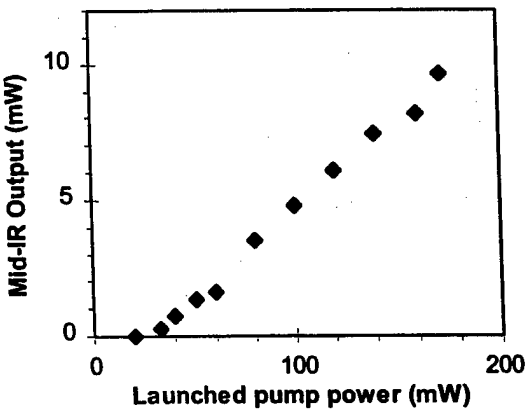
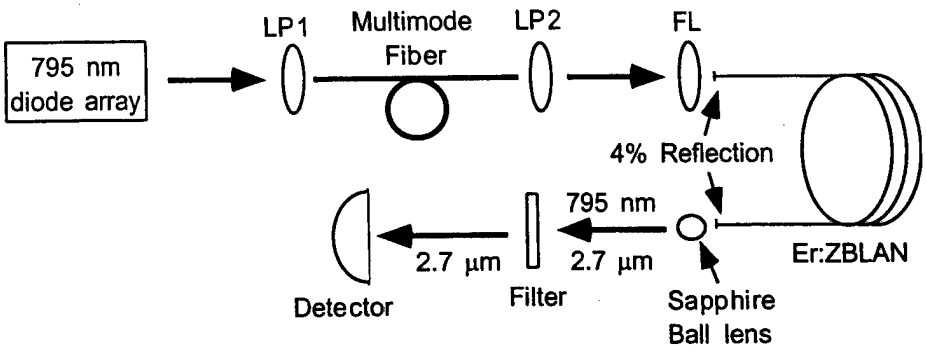


Figure 4. Mid-IR laser power vs. launched 980 nm pump power for Er:ZBLAN fiber

In more recent work, we have used a high power diode array (OptoPower) operating at 795 nm with the same double-clad Er fiber, as depicted schematically in Fig. 5. The diode array output was conditioned with beam-shaping lenses to yield an 8 mm x 8 mm beam of 5 mrad divergence. A multimode silica fiber (250 μm core diameter) was used to further condition the spatial profile of the pump beam so as to improve its coupling efficiency to the double-clad Er:ZBLAN fiber while inhibiting the possibility of damaging its ends.



LP: aspheric lens pair, f=12 mm; FL: aspheric focusing lens, f=6 mm

Figure 5. Schematic of multimode diode array-pumped mid-IR fiber laser

In preliminary experiments using the above setup, we have been able to obtain lasing with just the 4% Fresnel reflections from the fiber ends at threshold absorbed pump power levels of 100 mW (which implies at least a 28 dB round-trip gain in this fiber at the 100 mW pump-power levels). In this preliminary non-optimized setup, over 100 mW of CW 2.7 μm output has already been observed. Efforts are currently underway to demonstrate 1 Watt power levels from our double-clad fiber laser.

In summary, we have demonstrated the usefulness of high concentration Er fluoride fibers for high efficiency, high power 2.7 μm lasers. This is assisted by the onset of rapid cross-relaxation processes which remove the traditional "population bottleneck" in the lower laser level, evidence for which is presented here by data and models on the saturation of absorption and studies of lifetime quenching as a function of Er concentration. Design of high power fiber lasers based on double-clad fibers and diode array pumps will be presented, along with our preliminary results from such sources, targeted to a goal of producing >1 Watt CW 2.7 μm single mode fiber lasers in the very near future.

Acknowledgements: *The authors would like to acknowledge E. Poppe, X. Zhao, P. Pulaski, and J. Tafoya for assistance with the experimental data presented here, and G. Monnom and Y.K. Behl for assistance with the model and useful discussions.*

References:

1. E. Poppe, B. Srinivasan, and R.K. Jain, Electron. Lett., **34**, 2340 (1998)
2. L. Esterowitz, R. Allen, Proc. SPIE **1048**, 129 (1989)
3. R.S. Eng, J.F. Butler, and K.J. Linden, Opt. Engg., **19**, 945 (1980)
4. M. Pollnau, IEEE J. Quantum Electron., **33**, 1982 (1997)
5. M.C. Brierley, and P.W. France, Electron. Lett., **24**, 936 (1988)
6. B. Srinivasan, E. Poppe, and R.K. Jain, OSA Technical Digest Series, **6**, 297 (1998)
7. J.Y. Allain, M. Monerie, and H. Poignant, Electron. Lett., **27**, 445 (1991)
8. M. Pollnau, Ch. Ghisler, G. Bunea, W. Luthy, H. P. Weber, App. Phys. Lett. **66**, 3564 (1995)

9. V.K. Bogdanov, W.E.K. Gibbs, D.J. Booth, J.S. Javorniczky, P.J. Newman, D.R. McFarlane, Optics Commn., **132**, 73 (1996)
10. K. Dybdal, N. Bjerre, J.E. Pedersen, and C.C. Larsen, SPIE Proc. on Fiber Laser Sources & Amplifiers, **1171**, 209 (1989)
11. E. Maurice, G. Monnom, B. Dussardier, D.B. Ostrowsky, Opt. Lett., **20**, 2487 (1995)
12. J.L. Wagener, P.F. Wysocki, M.J.F. Digonnet, H.J. Shaw, and D.J. DiGiovanni, Opt. Lett., **18**, 2014 (1993)
13. J.N. Walpole, E.S. Kintzer, S.R. Chinn, C.A. Wang, and L.J. Missaggia, Appl. Phys. Lett., **61**, 740 (1992)

Presented at CLEO/Europe'98 Postdeadline Session

Mirror-Free, High Power (~140mW) Diode-Pumped 2.7 μm CW Fiber Laser

X. Zhao, B. Srinivasan, P. Pulaski, S. Gupta, and R.K. Jain*

Center for High Technology Materials, Univ. of New Mexico, Albuquerque, NM 87106

Phone: (505) 272-7821, Fax: (505) 272-7801

** Optopower Corp., Tucson, AZ*

Abstract

We report high power (~140 mW) CW 2.7 μm operation from a simple, mirror-free double-clad Er:ZBLAN fiber laser which uses a commercial 795 nm diode array as the pump source. With improvements in diode-to-fiber coupling efficiencies, and with the use of longer fibers, we anticipate power scaling to levels of over 1 Watt.

Cr:LiSAF system[6] requiring 8 diodes at 670 nm. The oscillator provided pulses as short as 25 fs with an average power output as high as 58 mW. The tunability was similar to that of the Cr:LiSAF system of Ref. 6. The amplifier delivered up to 1 μJ pulses at a repetition rate of 5 kHz with compressed pulse durations ranging from 200 fs to 45 ps, uncompressed.

The Argon ion pumped system and the diode-pumped Cr:LiSGAF system were both used to demonstrate the sub-μJ threshold energy required for ablation in glass and to investigate the relative performance of picosecond and femtosecond pulses (Fig. 2). A study of the difference in ablation features in metals with respect to pulse duration is underway. The system has also been investigated as a tool for the restoration of antique paintings and we are currently investigating its application to the ablation of biological tissue.

1. A. A. Oraevsky, L. B. Da Silva, A. M. Rubenchik, M. D. Freit, M. E. Glinsky, M. D. Perry, B. M. Mammini, W. Small, IV, and B. C. Stuart: "Plasma mediated ablation of biological tissues with nanosecond-to-femtosecond laser pulses: relative role of linear and nonlinear absorption," IEEE Journal of Selected Topics in Quantum Electronics, 2,4 801–809 (1996).
2. C. Momma, S. Nolte, B. N. Chichkov, F. V. Alvensleben and A. Tunnermann, "Precise laser ablation with ultrashort pulses," Applied Surface Science 109, 15–19 (1997).
3. B. C. Stuart, M. D. Feit, A. M. Rubenchik, B. W. Shore and M. D. Perry, "Laser-Induced damage in dielectrics with Nanosecond to Subpicosecond Pulses," Physical Review Letters, 74, pp. 2248–2251 (1995).
4. P. P. Pronko, S. K. Dutta, J. Squier, J. V. Rudd, D. Du and G. Mourou, "Machining of sub-micron holes using a femtosecond laser at 800 nm," Optics Comm. 114, 106–110 (1995).
5. S. C. W. Hyde, N. P. Barry, R. Mellish, R. Jones, P. M. W. French, J. R. Taylor, C. J. van der Poel and A. Valster, "Argon-ion-pumped and diode-pumped all-solid-state femtosecond Cr:LiSAF regenerative amplifiers," Optics Letters 20, 160–162 (1995).
6. R. Mellish, N. P. Barry, S. C. W. Hyde, R. Jones, P. M. W. French, J. R. Taylor, C. J. van der Poel and A. Valster, "Diode-pumped Cr:LiSAF all-solid-state femtosecond oscillator and regenerative amplifiers," Optics Letters 20, 2312–2314 (1995).

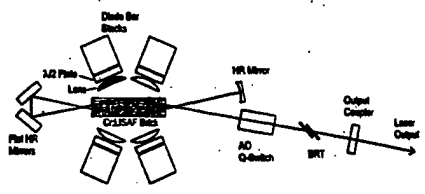
CThT5 **5:30 pm**

A high energy diode-pumped Cr:LISAF laser for water vapor differential absorption lidar

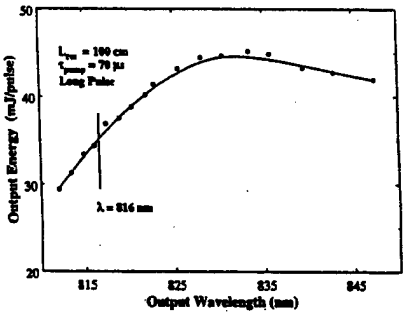
Viktor Fromzel, Coorg R. Prasad, Christyl Johnson,* Norman P. Barnes,* Gerald H. Kim,** Roy D. Mead,** *Science and Engineering Services, Inc., Burtonsville, Maryland 20866 USA; E-mail: sesi@sesi-md.com*

The near-IR absorption bands in the 810–830 nm and 930–950 nm range are well suited for remote measurements of water vapor with differential absorption lidar. Diode-pumped Cr:LiSAF laser which can be tuned over these bands has a great potential as a compact and efficient, narrow linewidth source for atmospheric water vapor DIAL. Here we present the gain, wavelength tuning and output characteristics of a high energy Cr:LiSAF laser that is being developed for use in an airborne water vapor DIAL system. The laser gain module consists of a 5.5% doped 6 × 6 × 25 mm Cr^{3+}:LiSAF slab pumped from two sides by eight 690 nm diode stacks. For obtaining high extraction efficiency and good laser beam quality a total internal reflection approach is used. Figure 1 shows the 120 cm long standing wave laser resonator consisting of a high reflective (HR) 2 m RoC concave mirror, two 45° HR flat mirrors and a flat output coupler (R = 60 to 75%). A three-plate birefringent tuner (BRT) and an acousto-optic Q-switch were inserted in the cavity for tuning and line narrowing, and providing Q-switched operation.

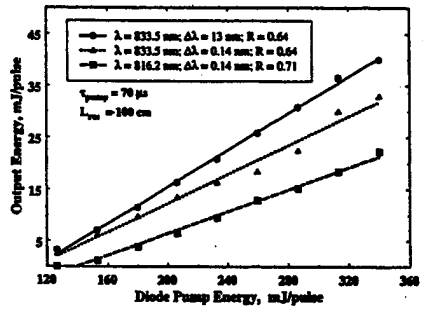
The small signal gains of the laser G_p and G_s for *p*- and *s*-polarization were measured as a function of the probe wavelength. The maximum value of G_p is about 0.79 at 825 nm for 340 mJ pump energy, and about 0.74 at λ = 834 nm, and 0.71 at λ = 816 nm. Figure 2 shows the tuning curve for the laser in long pulse operation. It is seen that the reduction in performance at the shorter wavelength is more rapid than expected from small signal gain (Fig. 1). The most likely reason of such quick reduction in the laser performance is the increased loss due to self absorption in Cr:LiSAF at shorter wavelengths. Figure 3 shows the Q-switched performance of the laser. When the line width of the laser is reduced from Δλ = 13 nm to 0.14 nm by the BRT, the output energy reduces from about 41 mJ to 34 mJ/pulse (nearly 20% reduction) for the same pump energy (340 mJ). This can be assigned to inhomogeneous emission line broadening that prevents the full extraction of the output in a narrow laser line. The slope efficiency is about 18% for the broad band output. It is seen from Fig. 3 the laser output at 816 nm is significantly lower (≈23 mJ at 340 mJ pump energy) than that at 835 nm. Although the reduction in the gain at 816 nm is only about 12%, the reduction in laser output is much higher (35%). As stated above, we can associate it with increasing of self absorption losses at 816 nm wavelength in Cr:LiSAF crystal.



CThT5 Fig. 1. Schematic of the standing wave resonator layout for the diode-pumped Cr:LiSAF Q-switched laser with total internal reflection configuration. The BRT (birefringent tuner) is for wavelength tuning.



CThT5 Fig. 2. Tuning curve for the diode-pumped Cr:LiSAF laser. Pump energy = 280 mJ. Output coupler mirror R = 70%.



CThT5 Fig. 3. Q-switched performance of the diode-pumped Cr:LiSAF laser. The top line is for the case where the laser spectrum is broad (Δλ = 13 nm) and λ = 835 nm, the second line is for the same wavelength but the linewidth is narrow, Δλ = 0.14 nm. The third line is for λ = 816 nm and narrow linewidth Δλ = 0.14 nm.

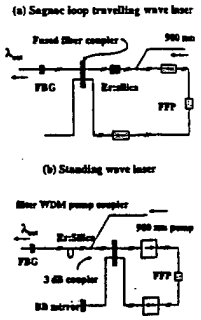
**NASA Langley Research Center, Hampton, Virginia 23681 USA*
***Aculight Corporation, Bothell, Washington 98011 USA*

CThT6 **5:45 pm**

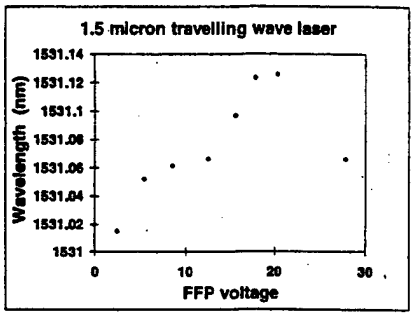
Novel wavelength-modulatable and continously tunable narrow-linewidth fiber lasers for trace gas spectroscopy

Nathaniel C. Libatique, Kevin Hsu, Ravinder K. Jain, *Center for High Technology Materials, 1313 Goddard SE, Albuquerque, New Mexico 87106 USA; E-mail: natl@chtm.unm.edu*

For trace gas monitoring, compact tunable (20–30 GHz), wavelength modulatable sources with output powers in the order of ~100 μW and linewidths better than 100 MHz are in great demand for wavelength modulation spectroscopy.[1–6] Tunable fiber laser sources;[7–12] with their intrinsic long cavities



CThT6 Fig. 1. Novel standing wave and travelling wave tunable laser designs.



CThT6 Fig. 2. Tuning curve for travelling wave laser.

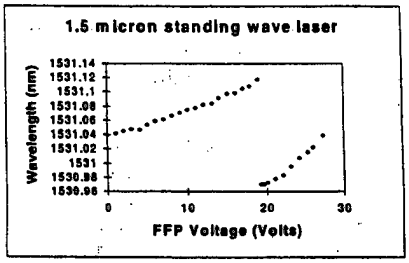
and narrow linewidth outputs, are attractive alternatives.

In this paper we report on the design and implementation of novel continuously tunable 1.5 μm fiber lasers based on the combination of fiber Bragg gratings and the transmissive filtering properties of high finesse fiber Fabry-Perot (FFP) filters. Built from off-the-shelf components, the concept is simple and easily adaptable to many wavelength ranges depending on the choice of fiber Bragg grating and/or doped glass medium.

In our initial experiment, we used a ring laser cavity. In place of the bulk grating used in more traditional designs,[12] we employed a 0.08 nm LW FBG, with a reflectivity of 25%, centered at 1531.08 in a Sagnac loop geometry. The FFP provides intracavity wavelength tunability to the source. The filter has a 20 GHz free spectral range (FSR) and a 20 MHz linewidth (LW). The isolators prevent unwanted reflective feedback from the high reflectivity FFP mirror surfaces.

An instrument-limited linewidth of 0.05 nm and 15 GHz of maximum tuning centered in the vicinity of the FBG peak were demonstrated. The observed output powers (2 mW max), however, showed 10% fluctuations, and spectral instability (estimated to be ~1 GHz) was a problem with this particular design. The roundtrip path of the travelling wave reflected off the FBG includes two 3 dB losses from the fused coupler for every traversal of the gain medium. This weakens the FBG feedback mechanism.

This consideration led us to the linear cavity design. This second laser is composed of the principal cavity formed by the FBG, the gain section, and the FFP loop. Other subcavities, such as the FFP loop itself and that formed between the FBG and the HR mirror, will cause



CThT6 Fig. 3. Tuning curve for standing wave laser.

the laser to oscillate at the points where the modes coincide. The effective linear cavity FSR will be larger than the ring laser's due to this vernier effect.[12]

The standing wave laser exhibited 19 GHz of maximum tuning. Within the limits of the optical spectrum analyzer resolution, no spectral peak instabilities were discernible. In addition, output power fluctuations improved to ~1%, suggesting greater stability due to reduced longitudinal mode competition within the FFPs 20 MHz transmission LW due to the larger effective FSR.

Instrument-limited, narrow linewidth (<0.05 nm) modes were observed. Because of the mode selective properties of long cavity fiber lasers, we expect linewidths better than 50 kHz from scanning Fabry-Perot interferometry and delayed self-heterodyne interferometry experiments that are currently in progress. It should also be possible to extract the modulation depth through a modified homodyne setup.

Experiments on acethylene and ammonia, which have significant absorption lines at the near infrared, will be conducted. We are also in the process of developing similar designs at other wavelengths, such as 2.7 μm using ErZBLAN.

With linewidths expected to be better than 50 kHz, fast electronic tunability, output powers in the mW range, capability for switching between fixed wavelengths, and flexible wavelength range selection through the choice of readily available FBGs, the source appears promising for wavelength modulation spectroscopy, differential absorption spectroscopy and frequency multiplexed spectroscopy applications.

Micron Optics, Atlanta, Georgia 30329 USA; E-mail: formosa@mindspring.com

1. A. N. Dharamsi *et. al.*, Appl. Phys. Lett. 65, 2257 (1994).
2. D. B. Oh, *et. al.*, Appl. Opt. 37, 2499 (1998).
3. J. Reid and D. Labrie, Appl. Phys. B26, 203 (1981).
4. D. S. Bomse, A. C. Stanton and J. A. Silver, Appl. Opt. 31, 718 (1992).
5. Q-V. Nguyen *et. al.*, Opt. Lett. 19, 2134 (1994).
6. D. B. Oh and D. C. Hovde, Appl. Opt. 32, 7002 (1995).
7. K. J. Vahala, N. Park, J. W. Dawson, and S. Sanders, US Patent No. 5,504,771, April 2, 1996.
8. J. L. Zyskind *et. al.*, Electron. Lett. 27, 2148 (1991).
9. Y. Zhao, C. Shu, CFE6 CLEO 1998, 517.
10. A. J. Gloag, N. Langford, I. Bennion, L. Zhang, Optics Comunications, 123, 553 (1996).
11. C. R. Cochlain and R. J. Mears, Electron. Lett. 28,2 124 (1992).
12. C.-C. Lee *et al.*, CthO47 CLEO 1998, 417.

CThT7 **6:00 pm**

Novel intra-cavity diffractive mode selecting element designs for high-power laser applications

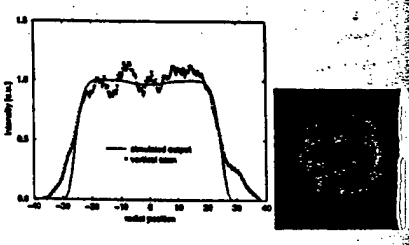
Karsten Ballüder, Mohammad R. Taghizadeh, *Department of Physics, Heriot-Watt University, Edinburgh EH14 4AS, United Kingdom; E-mail: karsten@phy.hw.ac.uk*

We apply diffractive optical elements for intra-cavity mode selection. The systems studied include CW and pulsed setups and both linear and ring-cavities. Results from numerical simulations and experimental results are presented.

We use diffractive optical elements (DOE) for intra-cavity mode selection to shape the fundamental mode of laser resonators. Using a phase-conjugating mode selecting element (MSE) in the master oscillator of a high-power laser system, we are able to produce a near-perfect super-Gaussian mode with a flat intensity profile which is able to extract much higher energy from the amplifier than a Gaussian TEM_{00} mode and avoid gain medium self-focusing effects.

We present different designs for operation in a 1 m cavity length Nd:YAG master oscillator, both for a diffractive mirror and for a transmissive design to be used together with the existing cavity mirror. Both designs are surface relief phase elements fabricated in fused silica using photolithography with reactive-ion etching to produce 16 level elements for use in transmission or reflection. Results from numerical simulations and experimental measurements (Fig. 1) are presented. Deviations from the desired flat top are no more than approx. 15%.

In addition to customised master oscillators, we use MSEs in re-generative cavities to re-shape the beam profile of an existing, unmodified master oscillator. We report what we believe is the first application of diffractive phase elements for transverse mode selection in laser ring cavities. A design for a regenerative ring cavity producing an eighth order super-Gaussian intensity profile beam is presented. Our results show that it is possible to



CThT7 Fig. 1. Experimental result showing the flat-top intensity beam profile of a customised master oscillator.

Nanoheteroepitaxy: The Application of nanostructuring and substrate compliance to the heteroepitaxy of mismatched semiconductor materials

D. Zubia[a] and S. D. Hersee[b]
Center for High Technology Materials, University of New Mexico, 1313 Goddard, SE, Albuquerque, New Mexico 87106

(Received 2 October 1998; accepted for publication 26 January 1999)

This article describes an approach to the heteroepitaxy of lattice mismatched semiconductors, that we call nanoheteroepitaxy. The theory developed here shows that the 3D stress relief mechanisms that are active when an epilayer is nucleated as an array of nanoscale islands on a compliant patterned substrate, will significantly reduce the strain energy in the epilayer and extend the critical thickness dramatically. Calculations show that with the scale of patterning that is achievable with advanced lithography (10–100 nm) we can eliminate mismatch dislocations from heterojunctions that are mismatched by as much as 4.2%. © *1999 American Institute of Physics.* [S0021-8979(99)03109-6]

I. INTRODUCTION

Traditional semiconductor epitaxial growth using planar, monolithic substrates has progressed from homoepitaxy to lattice-matched heteroepitaxy and recently to pseudomorphic, lattice-mismatched systems where small amounts of strain are accommodated in very thin films. In cases where a large lattice mismatch is unavoidable (e.g., GaN), then selective nucleation followed by lateral epitaxial overgrowth has also been shown to be successful in limiting the effects of mismatch defects by localizing them to inactive regions of the wafer.[1]

This article describes an approach to defect reduction in mismatched heterogeneous epilayer–substrate systems that we call nanoheteroepitaxy. Nanoheteroepitaxy exploits state-of-the-art lithography to pattern a substrate surface with nanoscale features (10–100 nm) prior to growth. Selective epitaxial growth is then performed and the epilayer nucleates as an array of nanoscale islands. The additional stress relief mechanisms available to nanoscale islands as compared to a conventional planar epilayer are illustrated in Fig. 1. In a conventional planar structure the epilayer can only deform vertically (a) to relieve mismatch stress. In contrast, a nanoheteroepitaxy "island," consisting of a patterned substrate (lower part) and a selectively grown epilayer (upper part), can deform vertically (a) and laterally (b). Thus the mismatch strain is distributed in three dimensions. In addition, the partitioning of strain between the epilayer and the substrate that occurs in nanoheteroepitaxy, will further reduce the amount of strain in the epilayer. Finally, if mismatch dislocations are formed in the island they can glide or climb to an island edge (c), assuming the glide plane is suitably oriented. In conventional planar heteroepitaxy dislocations are unlikely to reach the sample edge and they will remain in the epilayer (d).

The additional stress relief mechanisms, that are available to the nanoheteroepitaxy sample, will allow the epilayer to remain coherent (undefected) well beyond the critical thickness calculated for the case of planar (one-dimensional) epitaxy. Experimental evidence for these effects exists in the literature describing the formation of Stranski–Krastanov (SK) islands in highly mismatched heteroepitaxy. For example, Eaglesham and Cerullo[2] found that SK islands of pure Ge could be grown defect free on Si, for island thicknesses up to 500 Å, which is 50× higher than the critical thickness for the conventional planar growth of Ge on Si.

This article develops the theory of nanoheteroepitaxy, extending the previous theory of growth on patterned substrates by Luryi and Suhir[3] to include the effects of compliance in the substrate. It is shown that strain energy in the epitaxial layer can be significantly reduced by combining the effects of nanostructuring and substrate compliance. The theory is then applied to two technologically important semiconductor epi/substrate systems; Si–Ge/Si, and $InP/Ga_{0.51}In_{0.49}P/GaAs$. With the scale of patterning that is now reachable using advanced lithography[4–6] the theory of nanoheteroepitaxy predicts that mismatch defects can be eliminated when the lattice mismatch is 4.2% or less. In more highly mismatched systems, where the complete elimination of defects is not possible, the nanoheteroepitaxy approach is expected to yield significant reductions in defect density.

II. THEORY OF NANOHETEROEPITAXY

"Island" or "mesa" patterning followed by selective growth has already been shown to be an effective method for reducing the threading dislocation density in an epilayer compared to that in an underlying substrate. It was shown[7] that island diameters in the range 10–400 μm allowed a 100×–10× reduction, respectively, in the threading dislocation density, when $In_xGa_{1-x}As$ ($x=0.5$) was grown on GaAs. In this case the dislocation reduction resulted from the threading dislocations having sufficient mobility to reach the mesa edges during the high temperature growth cycle. Furthermore, Hull *et al.*,[8] have shown that a continuous coalesced film can be obtained by exploiting lateral growth be-

[a]Electronic mail: dauzubia@chtm.unm.edu
[b]Electronic mail: shersee@chtm.unm.edu

 © 1999 American Institute of Physics

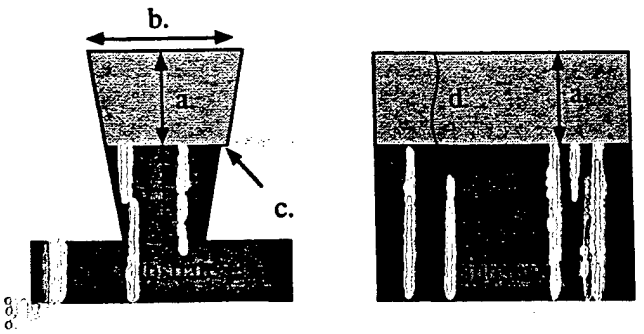


FIG. 1. Mismatch stress relief mechanisms available to nanoheteroepitaxy islands (left-hand side) and to a conventional planar heteroepitaxy sample (right-hand side).

tween such mesas. While mesas of this size (10 μm and above) can be effective in reducing the density of threading dislocations, at this scale the patterning has little effect on the density of interfacial mismatch dislocations.

It was predicted in 1986 by Luryi and Suhir[3] that a reduction in the density of interfacial mismatch dislocations could be achieved if the size of the mesas or islands could be reduced to the 10–100 nm scale. When an epilayer nucleates as an array of noninteracting, discrete islands, and later coalesces as shown in Fig. 2, the mismatch stress was shown[3] to acquire a dependence on y and z.

The stress in the epitaxial layer was shown to be of the form

$$\sigma_{\text{epi}}(y,z)=\epsilon_T\frac{Y_{\text{epi}}}{1-\nu_{\text{epi}}}\chi(y,z)e^{-\pi z/2l}, \tag{1}$$

where $\epsilon_T=2(|a_{\text{epi}}-a_{\text{sub}}|)/(a_{\text{epi}}+a_{\text{sub}})$ is the total lattice mismatch strain, ν_{epi} is Poisson's ratio for the epilayer material, Y_{epi} is Young's modulus for the epilayer material. $2l$ is the island diameter and $\chi(y,z)$ characterizes the lateral stress distribution[9] as

$$\chi(y,z)=\begin{cases}1-\dfrac{\cosh ky}{\cosh kl}, & z\leqslant h^{\text{eff}}\\ 1, & z\geqslant h^{\text{eff}}\end{cases}. \tag{2}$$

The stress decays exponentially in the z direction with a characteristic length, $2l/\pi$. k is the interfacial compliance

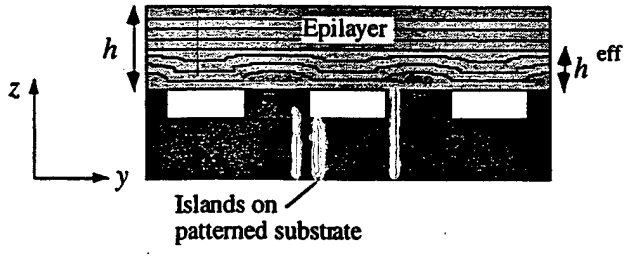


FIG. 2. Epitaxial growth nucleates selectively on the patterned substrate islands of diameter $2l$. Lateral epitaxy allows the film to coalesce after a sufficient epilayer thickness has been grown. The effects of mismatch strain decrease exponentially in the vertical (z) direction and are negligible beyond an effective thickness h^{eff}.

parameter[3,9] that is related to the characteristic length of exponential decay of the *strain energy*, h^{eff}, by the equation

$$k=\left(\frac{3}{2}\frac{1-\nu}{1+\nu}\right)^{1/2}\frac{1}{h^{\text{eff}}}. \tag{3}$$

Equation (1) assumes the substrate is completely rigid and makes no allowance for substrate compliance. In practice we expect the substrate part of a nanoscale island to also undergo elastic deformation as shown in Fig. 1. We therefore propose that the stress within the substrate part of the island will also acquire a dependence on y and z similar to that of Eq. (1). To introduce substrate compliancy into the theory of nanoheteroepitaxy, we first review the partitioning of strain between the epilayer and substrate for the case of a planar (unpatterned) compliant substrate.

III. STRAIN PARTITIONING IN COMPLIANT SUBSTRATES WITH NO PATTERNING

At the heart of substrate compliancy is strain partitioning which moves a portion of the mismatch strain into the substrate thus reducing the strain in the epitaxial layer. Hirth and Evans[10] and Lo[11] showed that for a planar structure, substrate compliancy is leveraged when the substrate is thinned, allowing a significant part of the mismatch strain to be shifted to the substrate. In a coherent interface, the total lattice mismatch strain, ϵ_T must equal the sum of the strains in the epitaxial layer and substrate:[10]

$$\epsilon_T=\epsilon_{\text{epi}}+\epsilon_{\text{sub}}, \tag{4}$$

where ϵ_{epi} and ϵ_{sub} are the partitioned strains in the epitaxial layer and substrate, respectively.

For coherent {100} interfaces in cubic materials possessing isotropic elastic constants there will be equal biaxial stresses ($\sigma_{11}=\sigma_{22}=\sigma$) and strains ($\epsilon_{11}=\epsilon_{22}=\epsilon$) with zero shear stresses and strains. Using this result and the boundary condition $\sigma_{33}=0$, yields the well known in-plane stress–strain relationship[12]

$$\sigma=Y\epsilon/(1-\nu). \tag{5}$$

As pointed out by Hirth and Evans,[10] static equilibrium in the bimaterial structure dictates that the net force on the system must be zero, thus

$$\sigma_{\text{epi}}h_{\text{epi}}+\sigma_{\text{sub}}h_{\text{sub}}=0, \tag{6}$$

where h_{epi} and h_{sub} are the thicknesses of the epitaxial layer and substrate, respectively. Combining Eqs. (4), (5), and (6) we obtain expressions for the partitioned strains that highlight the functional dependence of the strains on the thickness ratio $h_{\text{epi}}/h_{\text{sub}}$

$$\epsilon_{\text{epi}}=\frac{\epsilon_T}{1+\left(K\dfrac{h_{\text{epi}}}{h_{\text{sub}}}\right)}, \tag{7}$$

$$\epsilon_{\text{sub}}=\frac{\epsilon_T}{1+\left(\dfrac{1}{K}\dfrac{h_{\text{sub}}}{h_{\text{epi}}}\right)}, \tag{8}$$

where K is given by

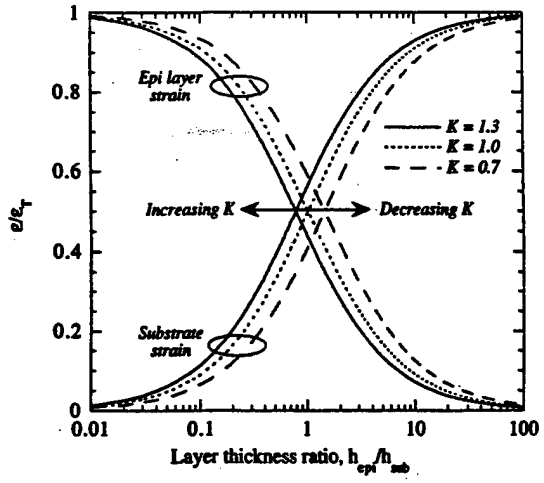


FIG. 3. Strain partitioning for a planar (unpatterned) sample.

$$K=\frac{Y_{epi}}{(1-\nu_{epi})}\frac{(1-\nu_{sub})}{Y_{sub}}. \tag{9}$$

Figure 3 plots the normalized partitioned strains, $\epsilon_{sub}/\epsilon_T$ and $\epsilon_{epi}/\epsilon_T$, as a function of the thickness ratio, h_{epi}/h_{sub}, for three values of K. Notice that partitioning becomes significant when $Kh_{epi}/h_{sub}>0.01$ at which point compliancy is leveraged. During heteroepitaxial growth the ratio Kh_{epi}/h_{sub}, increases causing the strain partitioning to vary as the growth progresses. At the beginning of growth all of the strain is accommodated in the epilayer. As the epilayer thickness increases, more and more of the strain is accommodated in the substrate. Heteroepitaxial growth must therefore initially pass through a regime of noncompliance even on compliant substrates.

IV. THEORY OF NANOHETEROPITAXY INCLUDING SUBSTRATE COMPLIANCE

Returning to nanoheteroepitaxy and following an approach similar to that of Luryi and Suhir,[3] we can now account for substrate compliancy by expressing the stresses in the epitaxial layer and substrate as

$$\sigma_{epi}(y,z)=\epsilon_{epi_0}\frac{Y_{epi}}{1-\nu_{epi}}\chi(y,z)e^{-\pi z/2l}, \tag{10}$$

$$\sigma_{sub}(y,z)=\epsilon_{sub_0}\frac{Y_{sub}}{1-\nu_{sub}}\chi(y,z)e^{\pi z/2l}, \tag{11}$$

where ϵ_{epi_0} and ϵ_{sub_0} are the partitioned epitaxial and substrate strains at the interface, respectively. This is equivalent to partitioning the stress distribution calculated earlier[3] between the substrate and epilayer parts of the nanoheteroepitaxy island. The partitioning will of course be thickness dependent.

The lateral stress distribution is highly uniform up until close to the edge of the island where the stress quickly drops to zero. For simplicity we will therefore assume that χ is uniform and equal to unity, this allows static equilibrium condition to be given by

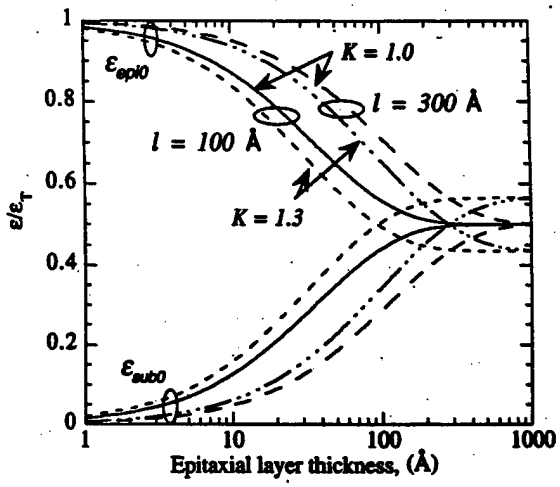


FIG. 4. Strain partitioning during nanoheteroepitaxy. The nanoisland diameter is $2l$ and the substrate thickness was arbitrarily set to 500 Å.

$$\int_0^{h_{epi}}\sigma_{epi}(z)dz+\int_{-h_{sub}}^{0}\sigma_{sub}(z)dz=0. \tag{12}$$

Combining Eqs. (1), (4), and (12) and integrating yields the interfacial partitioned strains for the nanostructured sample

$$\epsilon_{epi_0}=\frac{\epsilon_T}{1+\left(K\dfrac{(1-\exp(-\pi h_{epi}/2l))}{(1-\exp(-\pi h_{sub}/2l))}\right)}, \tag{13}$$

$$\epsilon_{sub_0}=\frac{\epsilon_T}{1+\left(\dfrac{1}{K}\dfrac{(1-\exp(-\pi h_{sub}/2l))}{(1-\exp(-\pi h_{epi}/2l))}\right)}. \tag{14}$$

Figure 4 plots the interfacial strain partitioning as a function of epitaxial layer thickness for nanostructured islands with radii (l) of 100 and 300 Å and for K values of $K=1$ and $K=1.3$. In Fig. 4, ϵ_{epi_0} is the strain in the epilayer and ϵ_{sub_0} is the strain in the substrate and both strains are plotted normalized, i.e., as ϵ/ϵ_T. The degree of strain partitioning in the nanostructured case has an asymptotic limit that depends on K and not on Kh_{epi}/h_{sub}. This arises from the concept introduced by Luryi and Suhir that the stress decays exponentially with characteristic length $2l/\pi$, that is, the strain partitioning functions [Eqs. (13) and (14)] decouple from the material thickness for thicknesses $h>2l/\pi$. As we have also allowed the substrate to deform, there will be an effective range in the substrate as well as in the epilayer. Once the epilayer thickness (and substrate thickness) have exceeded these values there will be no further change in the partitioning of mismatch strain. Thus the elastic constants for epilayer and substrate combinations will determine the asymptote in Fig. 4. It should be noted, however, that partitioning occurs more rapidly in the nanostructured case than for the planar (unpatterned) case. This is important when considering that the strain appears as a squared factor in the strain energy expression. Thus a factor of two reduction in the strain corresponds to a fourfold reduction in the strain energy.

Neglecting bending, the strain energy density per unit volume is of the form[3]

$$\omega(y,z)=\frac{1-\nu}{Y}\sigma(y,z)^2. \tag{15}$$

The areal strain energy density in the system is the sum of the strain energies in the epitaxial layer and substrate, and is given by

$$E(y)=\int_0^{h_{\rm epi}}\omega_{\rm epi}(y,z)dz+\int_{-h_{\rm sub}}^{0}\omega_{\rm sub}(y,z)dz. \tag{16}$$

The distribution function, χ, gives E a y dependence, however, from the form of χ it is clear that E has a maximum at $y=0$. Setting $y=0$ and integrating the two terms in Eq. (16) yields solutions for the maximum areal strain energy density in the epitaxial and substrate layers, respectively:

$$E_{\rm epi}=\frac{Y_{\rm epi}}{1-\nu_{\rm epi}}\epsilon_{\rm epi_0}^2[1-\mathrm{sech}(k_{\rm epi}l)]^2 \times\frac{l}{\pi}[1-\exp(-\pi h_{\rm epi}/l)], \tag{17}$$

$$E_{\rm sub}=\frac{Y_{\rm sub}}{1-\nu_{\rm sub}}\epsilon_{\rm sub_0}^2[1-\mathrm{sech}(k_{\rm sub}l)]^2 \times\frac{l}{\pi}[1-\exp(-\pi h_{\rm sub}/l)]. \tag{18}$$

Using the approach of Luryi and Suhir[3] and comparing the form of these equations with the strain energy for the planar case

$$E=\frac{Y}{1-\nu}\epsilon^2 h \tag{19}$$

we can define an effective layer thickness as

$$h_{\rm epi}^{\rm eff}=[1-\mathrm{sech}(k_{\rm epi}l)]^2\frac{1}{\pi}[1-\exp(-\pi h_{\rm epi}/l)], \tag{20}$$

similarly for the substrate. Since k depends on $h^{\rm eff}$, Eq. (20) can be solved by searching for the root. Equations (17) and (18) can now be written in the form

$$E_{\rm epi}=\frac{Y_{\rm epi}}{1-\nu_{\rm epi}}\epsilon_{\rm epi_0}^2 h_{\rm epi}^{\rm eff}, \tag{21}$$

$$E_{\rm sub}=\frac{Y_{\rm sub}}{1-\nu_{\rm sub}}\epsilon_{\rm sub_0}^2 h_{\rm sub}^{\rm eff}. \tag{22}$$

V. APPLICATION OF NANOHETEROEPITAXY TO SEMICONDUCTOR MATERIALS

We now apply the theory of nanoheteroepitaxy to some well-known mismatched materials systems. To do this we compare the strain energy in the system with the areal energy required to form a dislocation in the epilayer. In most semiconductor systems it will take less energy to form a screw dislocation than an edge dislocation and the screw dislocation energy is typically given by[13]

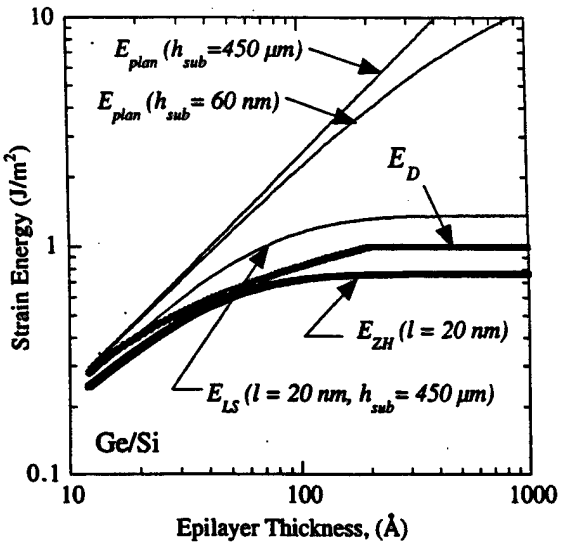


FIG. 5. Plots of strain energy vs epilayer thickness for Ge on Si using the different models discussed in this article. (l=20 nm for the LS and ZH models.)

$$E_D\approx\frac{Yb^2}{4\pi(1-\nu)w_D}\ln\left(\frac{R}{b}\right), \tag{23}$$

where b is the magnitude of the Burger's vector and w_D is the effective interfacial width of an isolated linear dislocation. R is the distance between the dislocation and the nearest free surface.[3,14] It should be noted that Eq. (23) is inaccurate when R is very small (i.e., when R approaches the atomic scale of the Burger's vector). Thus a crossing of the E and E_D curves for epilayer thicknesses less than ~10 Å will yield an inaccurate value of the critical layer thickness. In conventional heteroepitaxy, R is simply equal to the epilayer thickness. For compliant nanostructured substrates, R is modified to

$$R=\min(h_{\rm epi},h_{\rm sub},l), \tag{24}$$

to account for the case where the epitaxial layer surface may not always be the closest surface to the heterointerface in the nanoheteroepitaxy sample.

In the following plots it is assumed that if the strain energy within the epilayer is less than the energy required to form a screw dislocation then the epilayer will remain coherent.

A. Example 1: Pure Ge on Si [total mismatch (ϵ_T) =4.2%]

Figure 5 plots the strain energy in the system as a function of epilayer thickness for different types of substrate/epilayer structures discussed in this article and for E_D, calculated from Eq. (23). The maximum strain energy in the epilayer occurs for a thick planar substrate with no nanostructuring or compliancy effects. This is represented by the curve $E_{\rm plan}$, $h_{\rm sub}$=450 μm. When substrate compliancy is introduced ($E_{\rm plan}$, $h_{\rm sub}$=60 nm) the effects of strain partitioning become significant when the epilayer thickness reaches ~6 nm. The effect of nanostructuring alone (no compliancy) is shown by curve $E_{\rm LS}$ which is calculated using the original Luryi and Suhir model.[3] The minimum strain energy in the

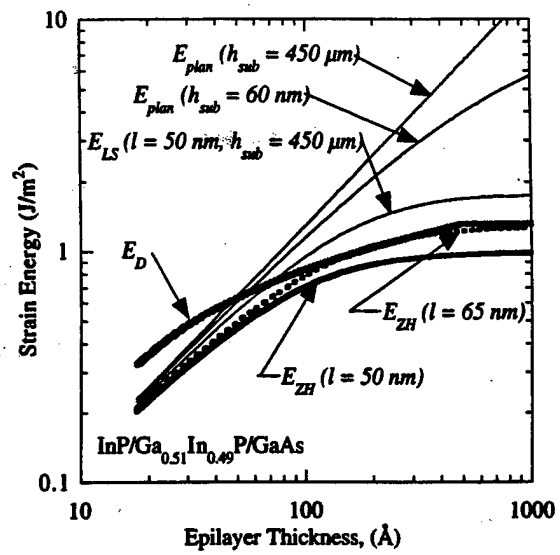


FIG. 6. Plots of strain energy vs epilayer thickness for InP/GaInP lattice matched to GaAs. Island radius is $l=50$ nm for the LS model and $l=50$ nm and $l=65$ nm for the ZH model.

system is represented by the nanoheteroepitaxy approach, curve E_{ZH}, where the combined effects of nanostructuring and substrate compliance are included. From Fig. 5, it appears that nanoheteroepitaxy will extend the critical thickness to infinity in this system, when the island radius is 20 nm or less.

B. Example 2: InP on $Ga_{0.51}In_{0.49}P$ on GaAs [total mismatch (ϵ_T)=3.7%]

In this system the $Ga_{0.51}In_{0.49}P$ and GaAs are lattice matched and the mismatch of 3.7% therefore occurs at the InP/$Ga_{0.51}In_{0.49}P$ heterojunction. Figure 6 plots the strain energy in the system as a function of epilayer thickness for the different approaches shown in the previous example and for two island radii ($l=50$ nm and $l=65$ nm) for the nanoheteroepitaxy approach. Nanoheteroepitaxy theory (curves E_{ZH}) predicts that the maximum island radius that can be tolerated before dislocation formation is approximately $l=65$ nm. At this radius the strain energy in the nanoheteroepitaxy curve and the dislocation formation energy curve intercept. This is in good agreement with recent observations by Porsche *et al.*,[15] who found that InP islands could be grown apparently dislocation-free on $Ga_{0.51}In_{0.49}P$ and with base diameters up to approximately 100–120 nm, (i.e., with island radii of $l=50$–60 nm).

VI. CONCLUSIONS

According to the theory of nanoheteroepitaxy described here, with nano-island radii in the 10 nm to 100 nm range it is possible to eliminate mismatch defects for heteroepitaxial layers that are mismatched by as much as 4.2%. In more highly mismatched systems (e.g. GaN on sapphire) a significant reduction in defect density is also expected. This theory is currently being tested at CHTM using metalorganic chemical vapor deposition selective growth on substrates patterned by advanced interferometric lithography and using self-assembled island growth. The results of this study will be reported elsewhere.

ACKNOWLEDGMENTS

The authors wish to cite Dr. S.R.J. Brueck and Dr. S. Zaidi of CHTM for useful discussions and wish to acknowledge the support of AFOSR and DARPA for this work.

[1] S. Nakamura, M. Senoh, S. Nagahama, N. Iwase, T. Yamada, T. Matsushita, H. Kiyoku, Y. Sugimoto, T. Kozaki, H. Umemoto, M. Sano, and K. Chocho, Appl. Phys. Lett. **72**, 211 (1998).
[2] D. J. Eaglesham and M. Cerullo, Phys. Rev. Lett. **64**, 1943 (1990).
[3] S. Luryi and E. Suhir, Appl. Phys. Lett. **49**, 140 (1986).
[4] S. H. Zaidi, A. S. Chu, and S. R. J. Brueck, J. Appl. Phys. **80**, 6997 (1996).
[5] S. H. Zaidi and S. R. J. Brueck, Opt. Commun. **135**, 264 (1997).
[6] S. H. Zaidi, S. R. J. Brueck, F. M. Schellenberg, R. Scott Mackay, K. Uekert, and J. J. Persoff, Proc. SPIE **3048**, 248 (1997).
[7] E. A. Fitzgerald, G. P. Watson, R. E. Proano, D. G. Ast, P. D. Kirchner, G. D. Petit, and J. M. Woodall, J. Appl. Phys. **65**, 2688 (1989).
[8] R. Hull, J. C. Bean, L. C. Peticolas, G. S. Higashi, M. L. Green, D. Bahnck, and D. Brasen, Appl. Phys. Lett. **60**, 1468 (1992).
[9] E. Suhir, J. Appl. Mech. **53**, 657 (1986).
[10] J. P. Hirth and A. G. Evans, J. Appl. Phys. **60**, 2372 (1986).
[11] Y. H. Lo, Appl. Phys. Lett. **59**, 2311 (1991).
[12] See, for example, P. L. Gould, *Introduction to Linear Elasticity*, 2nd ed. (Springer, New York, 1994), p. 108.
[13] R. People and J. C. Bean, Appl. Phys. Lett. **47**, 322 (1985).
[14] F. R. N. Nabarro, *Theory of Crystal Dislocations* (Clarendon, Oxford, 1967), p. 73.
[15] J. Porsche, A. Ruf, M. Geiger, and F. Scholz, J. Cryst. Growth **195**, 591 (1998).

Nanoheteroepitaxial growth of GaN on Si by organometallic vapor phase epitaxy

D. Zubia, S. H. Zaidi, S. R. J. Brueck*, S. D. Hersee
Center for High Technology Materials and Electrical and Computer Engineering Dept., University of New Mexico
*Also Department of Physics and Astronomy, University of New Mexico

(submitted to Appl. Phys. Lett. 7/99)

Nanoheteroepitaxy has recently been proposed as a technique for significantly extending the thickness of pseudomorphic growth in mismatched heterostructures. This article reports the first experimental application of nanoheteroepitaxy for the growth of GaN on patterned <111> oriented silicon-on-insulator substrates by organometallic vapor phase epitaxy. Transmission electron microscopy reveals that the defect concentration decays rapidly away from the heterointerface as predicted by nanoheteroepitaxy theory. The melting point of the nanoscale islands is found to be significantly reduced, enhancing substrate compliance and further reducing the strain energy in the GaN epitaxial layer.

Nanoheteroepitaxy[1] (NHE) exploits 3-dimensional stress relief mechanisms that are available to nanoscale islands to reduce the strain energy in lattice-mismatched material systems. The NHE approach consists of patterning a substrate into a 2-dimensional array of 10 to 300 nm sized nucleation islands and then selectively growing epitaxial material vertically on the islands (FIG 1, point a). This is followed by lateral overgrowth to achieve coalescence (FIG 1, point b). In contrast to current epitaxial lateral overgrowth[2], and pendeo[3] approaches, where the patterning is on the scale of 1-10 μm, the nanoscale patterning in NHE allows enhanced substrate compliance mechanisms to operate. For example, in addition to strain partitioning similar to that found in planar compliant structures[4], stress in the NHE sample decays exponentially away from the heterointerface with a characteristic decay length proportional to the diameter of the island. Strain partitioning and stress decay interact synergistically to significantly lower the strain energy in nanostructural lattice mismatched material systems. NHE theory predicts that mismatch dislocation formation can be eliminated from materials systems with a lattice mismatch in the range of 0-4%. In material systems with larger lattice mismatch such as GaN on Si (20% lattice mismatch) defects are probably unavoidable, however as we show below, NHE results in a significant reduction in the local defect density in nanostructural GaN/Si islands.

Nanoheteroepitaxy was investigated using organometallic vapor phase epitaxy (OMVPE) growth of GaN on the patterned surface silicon layer of commercial <111> silicon-on-insulator (SOI) wafers manufactured by the separation by implantation of oxygen (SIMOX) process. The SOI wafers were patterned using interferometric lithography and reactive ion etching[5, 6] to form a square 2-dimensional array of silicon islands on top of a field of SiO_2 as illustrated in FIG 1. The height of the islands was 40 nm while the diameter varied between 90 to 300 nm. Island periodicity was 360 and 900 nm. GaN was then selectively grown on the silicon islands using a three step sequence consisting of an in-situ cleaning at a temperature of 878°C for 5 minutes under a hydrogen atmosphere, a low temperature (543°C) nucleating layer deposition and finally main epilayer growth at high temperature (1031°C). This yielded a GaN island thickness of 100 to 200 nm. The exposed SiO_2 layer in the SOI served as a convenient mask for the selective growth of GaN on silicon. The SOI structure allowed efficient implementation of the patterning and selective growth requirements of the NHE approach.

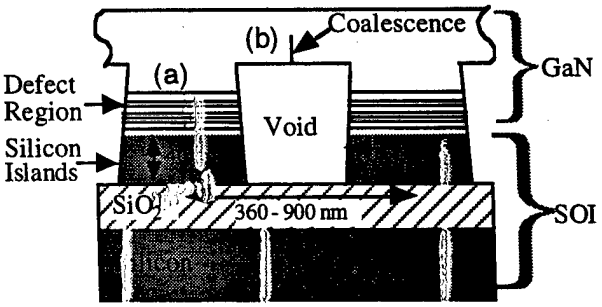


FIG 1. Shows the patterned SOI substrate with islands created in the upper Si layer. The selective growth of GaN is also illustrated. A defected region is located at the heterointerface.

In addition to exploiting 3-dimensional stress relief mechanisms due to geometrical effects, nanostructuring can also enable other stress relief effects due to the large surface-to-volume ratio of nanoscale structures. For example, in material systems in which the epitaxial material has a larger melting point than the substrate, compliance can be actively enhanced due to softening of the nanoscale substrate islands at growth temperatures well below the substrate bulk melting point. Evidence of substrate softening is shown in FIG 2 which compares the size and shape of silicon nanometer sized islands (a) without and (b) with heat treatment at 1110°C for 10 minutes. FIG 2 shows that mass transport has occurred due to melting in the heat-treated sample. This indicates that the melting point for these silicon islands has been reduced from its bulk value of 1412°C to less than 1110°C. The in-situ cleaning temperature previously used for GaN growth on sapphire[7] is 1100°C, however, because of this observed melting we have now reduced the in-situ clean temperature to 878°C. A reduction of melting point

is anticipated from recent results on nanophase materials which has shown that the materials properties (including the melting point) of nanometer scale particles are significantly modified.[8] In the case of NHE this reduced melting point can be utilized during growth to soften the silicon islands (i.e., reduce their elastic modulus) and enhance substrate compliance. We call this effect active compliance.

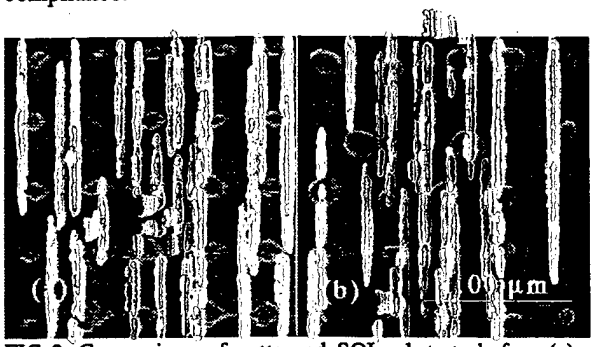


FIG 2. Comparison of patterned SOI substrate before (a) and after (b) heating to 1110°C. The change of shape indicates that the silicon islands have melted.

While not explicitly discussed in the original NHE model[1], active compliance can be incorporated in the strain partitioning equations by adjusting the *elastic compliance ratio*, K, given by

$$K = Y_{epi}(1-\nu_{sub})/[Y_{sub}(1-\nu_{epi})] \quad (1)$$

where Y is Young's modulus and ν the Poisson's ratio in the epitaxial material and the substrate materials. At low temperatures, well below the actual melting point of the epitaxial and substrate materials, the Young's moduli of these materials are equal to their respective bulk values. For a higher growth temperature, near the reduced melting point of the substrate island, Y_{sub} will be reduced causing K to be increased above its bulk value, K_o. The impact of active compliance on strain partitioning is illustrated in FIG 3, which shows the effect that increasing K has on the normalized strain, $\varepsilon/\varepsilon_T$, in the epitaxial and substrate layers, where ε_T is the total mismatch strain. It is not known at this time by how much the value of K can be increased beyond K_o, however, to illustrate the active compliance effect, an increased value of $3K_o$ was arbitrarily chosen for comparison in FIG 3. The graph shows that active compliance enhances strain partitioning by increasing the partitioning at a given thickness and increasing the ultimate degree of strain partitioning. In addition, active compliance works to directly lower the total strain energy in the system when Y_{sub} is reduced because strain energy is proportional to the Young's modulus.[1]

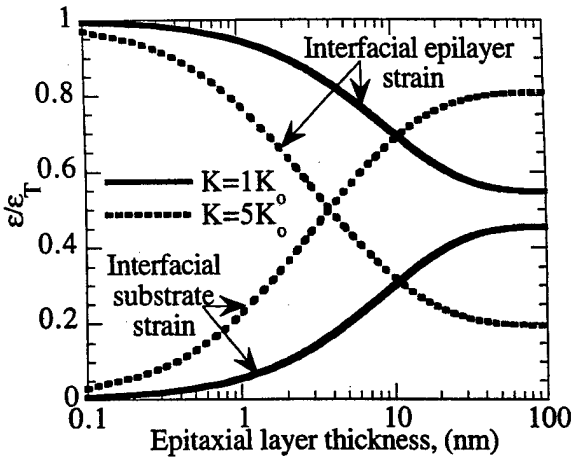


FIG 3. Plots the normalized interfacial strain in the epilayer and substrate versus epilayer thickness. Without active compliance (solid lines) the final amount of strain in the epilayer and substrate are similar. With active compliance (dashed lines) much more of the total strain is transferred to the substrate.

Island size is a critical parameter in NHE as it controls both the elastic modulus through the actual melting point of the substrate island and the characteristic decay length of the strain energy. During selective epitaxy, the island size and spacing will also control the effective growth rate at the island.

Cross-section transmission electron microscopy (XTEM) micrographs of GaN growth on two silicon islands, one 80 nm in diameter and the other 280 nm in

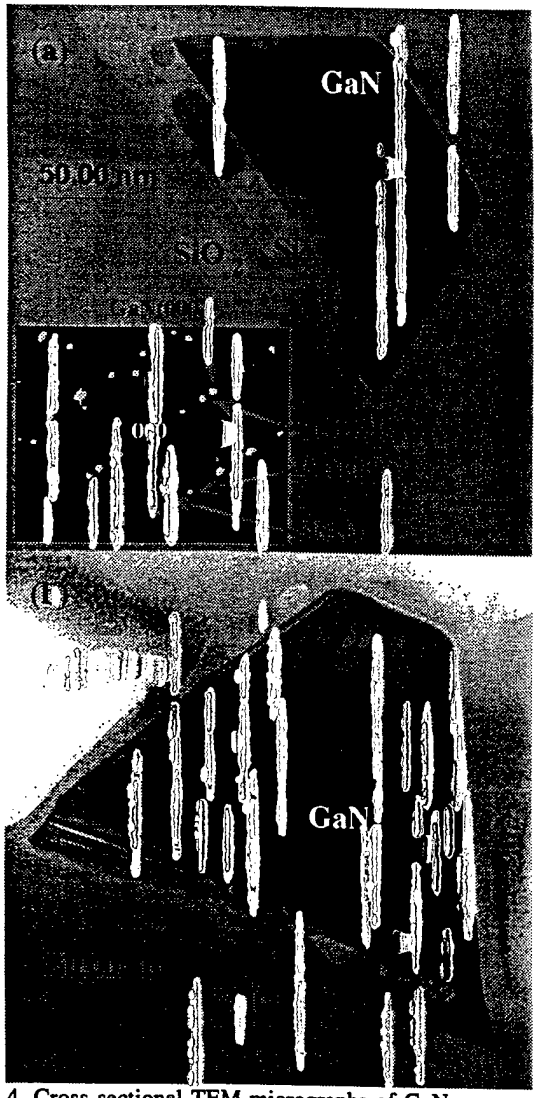


FIG 4. Cross-sectional TEM micrographs of GaN grown on Si islands on the patterned SOI substrate. Both figures show defects at the heterointerface but high quality GaN away from the interface. The electron diffraction pattern reveals the epitaxial relationship between GaN and Si. XTEM images were acquired with a JEOL 2010 high-resolution analytical electron microscope at the University of New Mexico.

diameter, are shown in FIG 4. In both cases the defects are concentrated near the GaN/Si heterointerface and the defect density decays rapidly to vanish at approximately 20-50 nm from the interface. In FIG 4a, strain field contours can be observed in the defect-free region. The general shape of the strain contours indicates that the strain originates at the GaN/Si heterointerface. The contour lines broaden and separate, away from the heterointerface, indicating a decaying strain field in agreement with the predictions of NHE theory. Lateral growth of GaN, extending beyond the edges of the silicon island, is also observed. The electron diffraction pattern from the sample in FIG 4a (inset) reveals the relative crystallographic orientation of GaN and Si as GaN[0001] // Si[111]. Thus the silicon island is acting as an epitaxial template. FIG 4b shows a threading dislocation in the GaN, indicating that the mechanism that creates threading dislocations was not suppressed sufficiently to prevent the formation of the threading dislocation in this particular island. FIG 4a and 4b also show that GaN grows preferentially on the (111) surface of the silicon island, suggesting that selective growth via crystallographic orientation (i.e. use surface patterning instead of using an oxide mask) may be achievable for this material system.

High-resolution XTEM (FIG 5) reveals stacking faults in the GaN near the interface (FIG 5a) and a highly defected silicon layer at the interface. Segmented silicon lattice planes lying within the 2.0 nm thick defected layer, in some areas penetrating as much as three lattice planes (0.95 nm) into the layer, indicate that the layer is composed of silicon, implying that much of the mismatch strain is being taken up by the silicon. FIG 5b shows that GaN is locally of highly quality away from the interface.

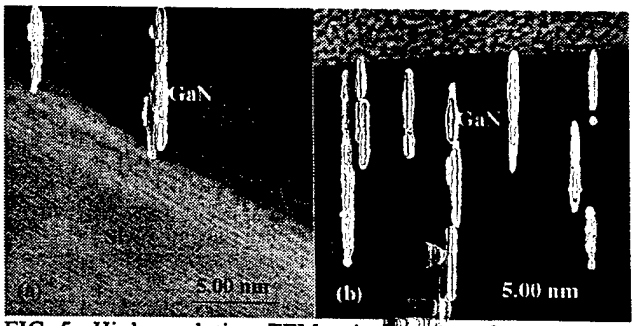


FIG 5. High-resolution TEM micrographs of (a) GaN/Si heterointerface and (b) GaN away from the interface.

In this first experimental demonstration of nanoheteroepitaxy, results are presented on the selective-area OMVPE growth of GaN on a novel, patterned SOI substrate. A reduced melting point is observed for nanoscale silicon islands enabling active compliance effects that work to further enhance strain partitioning and reduce strain energy. Electron microscopy reveals that the defect concentration decays rapidly away from the GaN/Si heterointerface, in agreement with NHE theory. Beyond this defected region, the GaN appears to be of high quality. Current work is focussing on evaluating the quality of the material grown by the NHE approach including the coalescence region and other effects such as differential thermal expansion and will be discussed elsewhere. Partial support for this work was provided by the Air Force Office of Scientific Research.

[1]D. Zubia and S. D. Hersee, J. Appl. Phys. **85**, 6492 (1999).
[2]S. Nakamura, J. Cryst. Growth **195**, 242 (1998).
[3]T. S. Zheleva, S. A. Smith, D B. Thomson, T. Gehrke, K. J. Linthicum, P. Rajagopal, E. Carlson, W. M. Ashmawi,

and R. F. Davis, MRS Internet J. Nitride Semicond. Res. 4S1, G3.38 (1999).
[4]J. P. Hirth and A. G. Evans, J. Appl. Phys. **60**, 1468 (1992) and Y. H. Lo, Appl. Phys. Lett. **59**, 2311 (1991).
[5]S. H. Zaidi, A. S. Chu, S. R. J. Brueck, Mat. Res. Soc. Symp. Proc. **358**, 957 (1995).
[6]S. H. Zaidi, A. S. Chu, S. R. J. Brueck, J. Appl. Phys. **80**, 6997 (1996).
[7]S.D. Hersee, J. Ramer, K. Zheng, C.F. Kranenberg, K. Malloy, M. Banas, and M. Goorsky, J. Electron. Mat. **24**, 1519 (1995).
[8]A. Goldstein, Handbook of nanophase materials, Marcel Dekker, New York, pp. 3-4 (1997)

The Microstructure of Metalorganic-Chemical-Vapor-Deposition GaN on Sapphire

S.D. Hersee, J.C. Ramer, and K.J. Malloy

MRS BULLETIN
REPRINT

Reprinted from Materials Research Society
MRS Bulletin, Volume22, Number 7,
July 1997

The Microstructure of Metalorganic-Chemical-Vapor-Deposition GaN on Sapphire

S.D. Hersee, J.C. Ramer, and K.J. Malloy

Introduction

The group-III-N materials (GaN and its related alloys, InGaN and AlGaN) are a rapidly emerging family of compound semiconductors that have great potential for a wide range of optoelectronics and electronics applications.

GaN-based blue light-emitting diodes (LEDs) are commercially available[1] and can already be found in full-color, billboard-size displays in major cities in Japan. Achievement of continuous-wave (cw) laser operation at blue wavelengths[2] will lead to the commercialization of these coherent sources probably within the next few years. Like other semiconductor lasers, these devices can be manufactured relatively cheaply (eventually for a few dollars), and they are expected to replace current ($1,000 and up) ultraviolet and blue-laser sources in medical spectroscopy, high-density information storage, and in projection displays.

This article reviews the key role of the crystal structure of GaN grown on sapphire, which is currently the most widely used substrate. We trace the origin of this crystal structure from nucleation and show how it evolves as growth proceeds. We show that the final GaN film is an ordered polycrystal (rather than a single crystal), in which the individual grains are of high crystalline quality but are "tilted" and "twisted" with respect to one another. We conclude by speculating on how this microstructure may explain the unusual optical and electrical properties of GaN.

The High Dislocation Density of GaN on Sapphire

Throughout the history of semiconductors, much effort has been devoted to improving the perfection of the basic semiconductor crystal and in particular to reducing the concentration of dislocations. In silicon-based metal-oxide-semiconductor devices, dislocations reduce the gate oxide breakdown voltage and increase gate leakage currents.[3] In GaAs- and InP-based LEDs and lasers, dislocations degrade optoelectronic as well as electronic performance.[4] When injected carriers recombine in the vicinity of dislocations, the recombination energy tends to heat the crystal rather than produce light. This nonradiative recombination appears as dark spots and dark lines in the otherwise bright emitting regions of these devices, reducing their intensity and their reliability. In today's high-quality semiconductors such as silicon and GaAs, dislocation densities of $<0.1\ cm^{-2}$ and $\sim 50\ cm^{-2}$, respectively, are routinely achieved.

Cross-sectional transmission-electron microscopy (TEM) examinations by many groups,[5-9] of "state-of-the-art" GaN grown on sapphire have revealed that the GaN layer contains a relatively high dislocation density (see Figure 1) in the range 10^8–$10^{10}\ cm^{-2}$. Yet efficient blue LEDs[1] and cw lasers[2] have been fabricated from material similar to that shown in Figure 1. Has nature been very

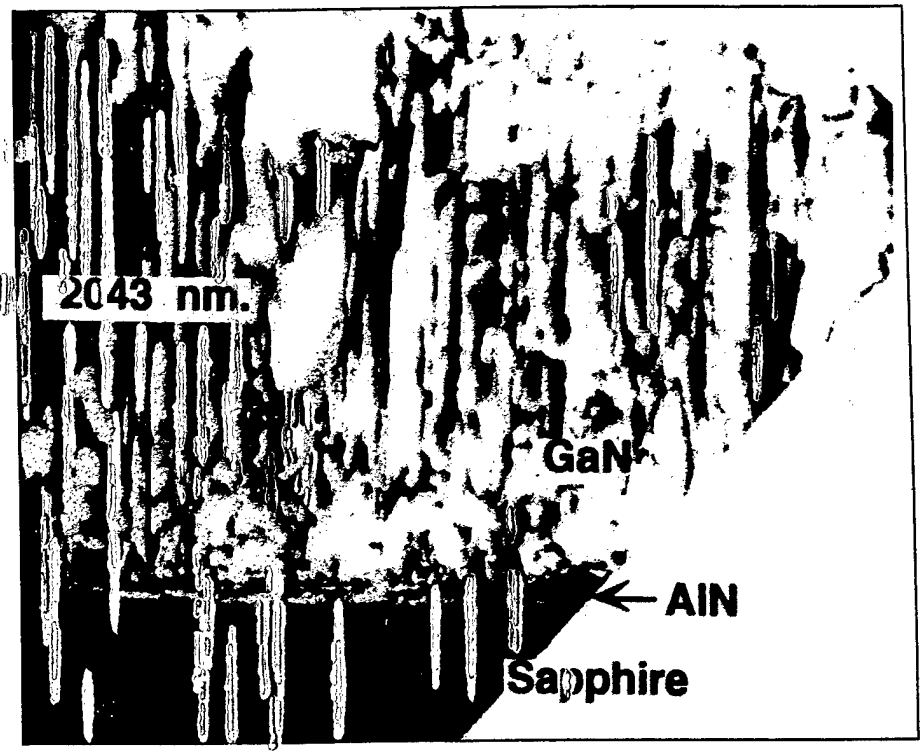


Figure 1. A cross-sectional transmission-electron-microscopy micrograph (taken at the University of New Mexico) of a GaN/AlN/sapphire structure. The dislocations show an approximately ⟨0001⟩ line direction.

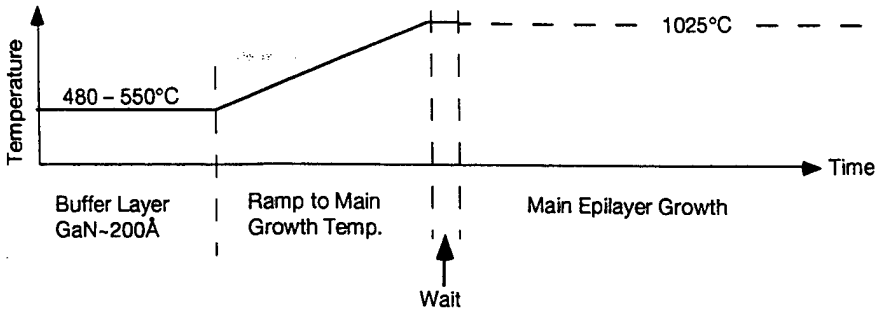


Figure 2. Growth schedule for metalorganic-chemical-vapor-deposition GaN. After growth of a low-temperature buffer layer, the temperature is raised to 1025°C for growth of the main GaN layers.

kind and made dislocations in GaN benign? Can we completely ignore the presence of this dislocation density in the III-N materials and devices, whereas such a density would be prohibitive in other III-V devices? To answer these questions it is necessary to understand how and where dislocations form in GaN. This requires understanding of the crystal microstructure for GaN.

MOCVD Growth of GaN on Sapphire

The pioneering work of Hiramatsu et al.[5] and Nakamura et al.[10] showed that optimum electrical and optical-quality GaN films were obtained on [0001] sapphire when a thin, low-temperature AlN or GaN buffer layer was used to initiate the growth process. To understand the special microstructure of GaN on sapphire, we need to trace its evolution from this initial nucleation at low temperature through the subsequent stages of the metalorganic-chemical-vapor-deposition (MOCVD) growth process.

The growth sequence used in our work was based on the previous work of Hiramatsu[5] and Nakamura,[10] and begins by the growth of a GaN buffer at a low temperature in the range of 480–600°C (Figure 2). The growth is then stopped while the substrate temperature is raised to the main growth temperature of 1025°C under an ammonia flow and is allowed to stabilize at this temperature. The duration of this temperature-ramping and stabilization cycle is typically 10 min. However as shown in the following discussion, this ramp duration is an important parameter for obtaining optimum GaN quality. The growth is then restarted, and the main GaN epilayers are grown at 1025°C and at a chamber pressure of 100 Torr.

GaN Nucleation on Sapphire

Atomic-force-microscopy (AFM) images of nominally 200-Å-thick, low-temperature GaN buffer layers in their as-deposited state are displayed in Figure 3 for two deposition temperatures. Figure 3a is a buffer grown at 550°C and shows the columnar or "island" growth habit previously observed by Hiramatsu et al.[5] for AlN buffers. The islands are less well-developed when the buffer is grown at a lower temperature of 480°C (Figure 3b), indicating that surface kinetics play an important role in the buffer morphology.

Island (Volmer-Weber) growth is frequently observed when a thin film of a heterogeneous material with a different lattice parameter and/or a different crystal structure is deposited[11] onto a crystalline substrate. When there is a large difference in crystal structure or lattice parameter, a two-dimensional, thin film will contain a high concentration of unsatisfied bonds per unit area and a high surface energy. The overall free energy of the system can therefore be lowered (and the number of unsatisfied bonds reduced) if the thin film can reorder itself into coherent three-dimensional (3D) islands. Both GaN and sapphire are nominally hexagonal-close-packed (hcp) structures (sapphire has a slightly distorted hcp structure), but they have very different lattice parameters (a_{GaN} = 3.189 Å, $a_{Al_2O_3}$ = 4.758 Å, c_{GaN} = 5.185 Å, $c_{Al_2O_3}$ = 12.991 Å). Furthermore several groups including ours[5–7] have shown that while the sapphire and epitaxial GaN [0001] crystal orientations are parallel, the unit cell of the GaN is rotated by 30° about the *c*-axis with respect to the sapphire unit cell (i.e., the $[1\bar{1}00]$ GaN direction is parallel to the $[1\bar{2}10]$ sapphire direction). Given these significant differences, it is not surprising that an "island" type of reordering (Volmer-Weber growth) is observed in this material system.

Figure 4 shows AFM measurements on these buffer layers after the temperature was ramped to the main growth temperature of 1025°C. Clearly there is further rearrangement of the buffer material during this ramping period. Compared to the 480°C buffer, the 550°C buffer (Figure 4a) shows larger well-developed islands that are approximately 200–300-Å high. The 480°C buffer (Figure 4b) is also modified by the anneal but retains a much smoother morphology after ramping with a typical peak-to-valley roughness of ~100 Å. The morphology of the buffer layer after ramping continues to reflect its as-deposited state. This suggests that the kinetic barriers to surface diffusion and the rearrangement of the thin film into islands are significant at the low temperatures used for growth of the buffer layer.

Using modern x-ray-diffraction (XRD) equipment, it is possible to measure the crystallinity of these thin buffer layers. Such measurements for the GaN (0002) reflection reveal broad x-ray rocking-curve peaks (Figure 5a) that are a convolution of two components. At lower intensity, there is a broad peak with a full width half maximum (FWHM) of approximately 1–2 degrees. Extensive broadening of the XRD peak is anticipated due to the small thickness of the buffer layer. However the width of this broad low-intensity component is consistent with high-resolution cross-sectional TEM observations of Qian et al.,[8] who found that the buffer-layer nuclei or "islands" were misoriented by up to 3 degrees. At the center of this broad peak (Figure 5a) is a narrow, higher intensity peak, indicating a preferred orientation among the polycrystalline islands.

Figure 5b shows the integrated intensity under the full (0002) XRD peak as a function of the buffer-layer deposition rate. At a low deposition rate, more of the buffer material is crystalline and therefore contributes to the XRD peak intensity. For higher growth rates, the area under the full XRD peak decreases, indicating that more of the buffer material is deposited in an amorphous state or in polycrystalline grains that are grossly misoriented.

The AFM images of Figure 6 reveal that larger nuclei or "islands" are formed at the lower buffer growth rate. This is consistent with a kinetically limited island or Volmer-Weber growth where a lower growth rate and a higher tempera-

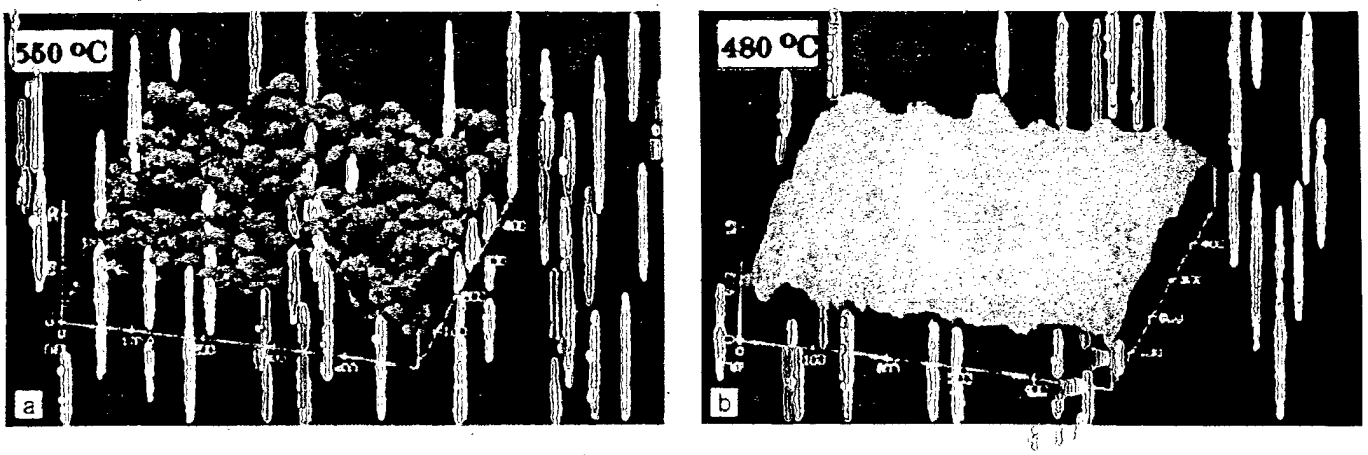


Figure 3. Atomic-force-microscopy (AFM) measurements on buffer layers grown at (a) 550°C and (b) 480°C. Each image represents a 0.5 μm × 0.5 μm area of the sample.

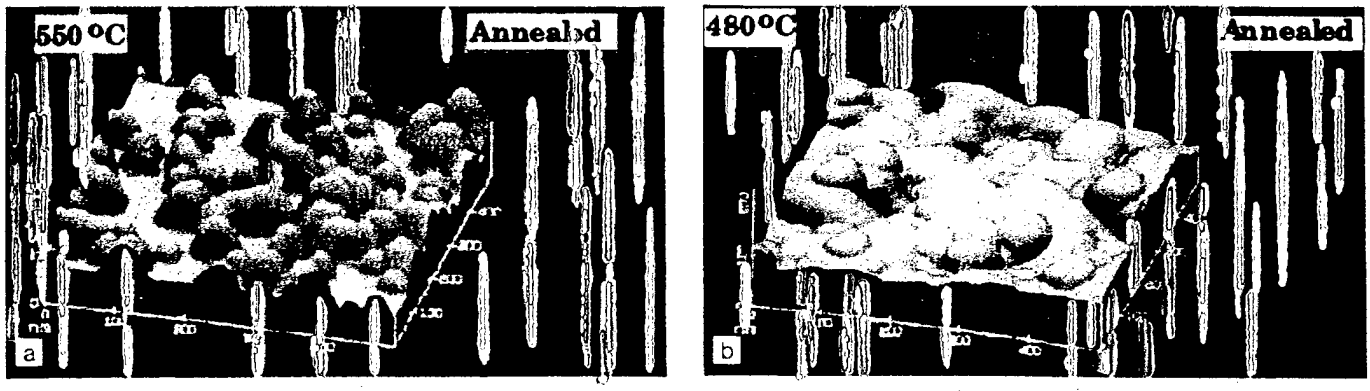


Figure 4. Atomic-force-microscopy measurements on buffer layers annealed for 20 min during ramp to main growth temperature. (a) Buffer initially grown at 550°C. (b) Buffer initially grown at 480°C. (Images are at the same scale as those in Figure 3.)

ture will both increase the size of the 3D islands.[12]

Ramping to Higher Growth Temperature

After deposition of the buffer layer, the sample is ramped to the higher growth temperature where the main device structure is grown. Annealing occurs during this ramping, and this further modifies the crystallinity of the buffer as reported by Wickenden.[13] A series of GaN buffer-layer samples were subjected to different ramp anneal durations between 0 and 20 min. These samples were then removed from the reactor for XRD and AFM characterization. (Wickenden[12] showed that anneal times greater than 20 min led to degradation of the morphology and crystalline quality of the GaN buffer layers.) Figure 7 combines AFM and XRD data for as-grown (zero ramp duration) and ramp-annealed GaN buffers on *c*-plane sapphire substrates.

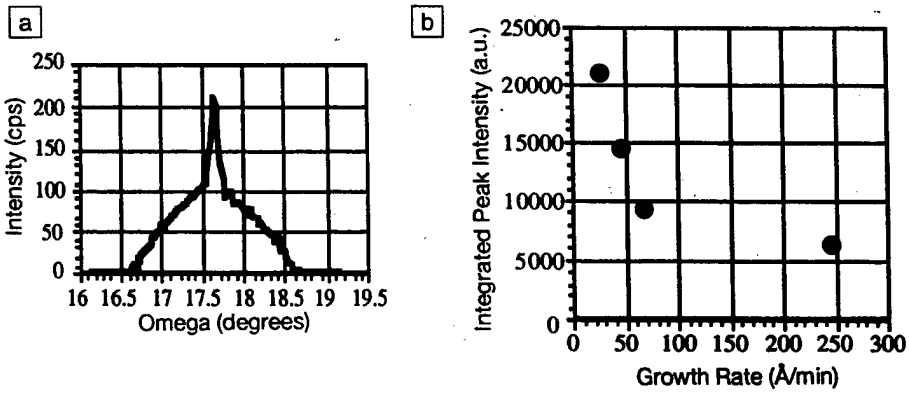


Figure 5. (a) "Double" x-ray-diffraction (XRD) peak showing a broad low-intensity peak that is topped by a narrow high-intensity peak indicating a preferred orientation among the buffer "islands." (b) Integrated peak intensity versus growth rate showing that a higher fraction of the buffer material is crystalline (rather than amorphous) when the buffer is grown more slowly.

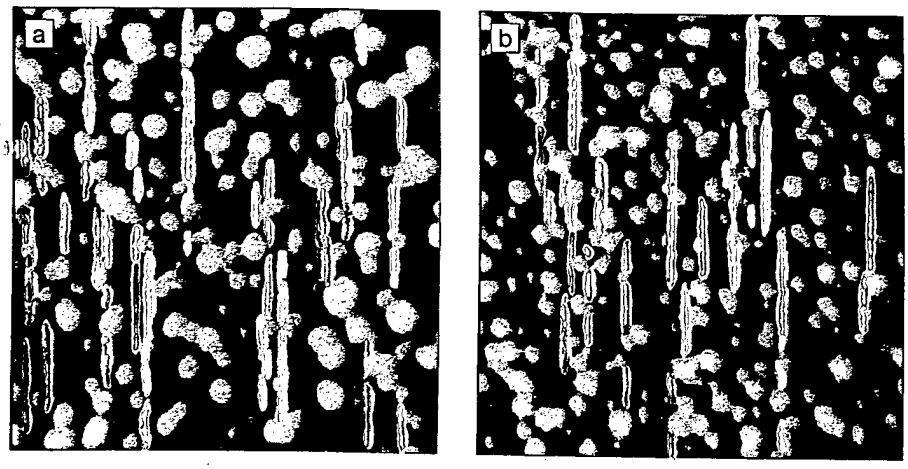


Figure 6. Atomic-force-microscopy images of GaN buffer layers on c-sapphire. Surface area scanned is 0.4 μm × 0.4 μm in each case. Lighter regions correspond to raised surface features. (a) Growth rate at 30 Å/min. (b) Growth rate at 70 Å/min.

The AFM images show that the island size increases with the ramp duration. Furthermore the XRD measurements show the narrow high-intensity peak component growing at the expense of the lower intensity, broader part of the peak. This indicates that as annealing proceeds, larger islands that are more closely oriented, are forming.

These measurements show that the GaN buffer layers consist initially of a dense array of growth islands (similar to the AlN buffer layers reported by Hiramatsu et al.[5]) whose size and crystallinity are limited by surface kinetics and are controlled by deposition parameters including temperature, flux, and ramp duration. Other growth parameters that affect surface diffusion (e.g., substrate polarity) are also anticipated to influence the structure of the buffer layer and are under investigation.

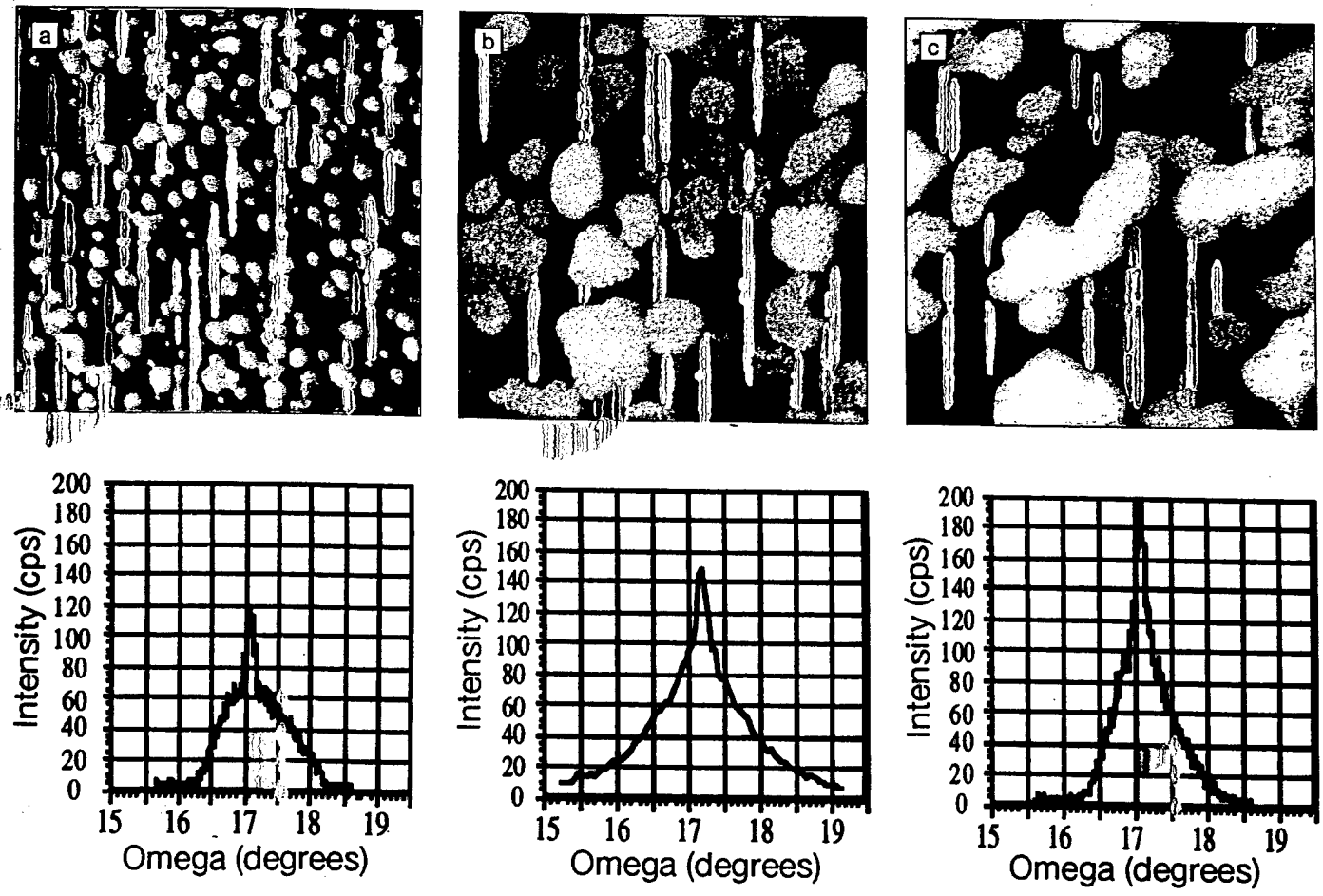


Figure 7. Atomic-force-microscopy and XRD (0002) peaks for GaN buffer layers on c-plane sapphire for different ramp anneal times. The AFM image area is 0.4 μm × 0.4 μm in each case, with lighter regions corresponding to higher surface features. (a) No ramp (as-deposited). (b) 10-min ramp. (c) 20-min ramp.

Correlation of Buffer and Thick Layers

The influence of the buffer layer is readily observed in the surface morphology of the main GaN epilayer. When the buffer layer is absent or is grown far from optimum conditions, the subsequently grown GaN epilayer is generally milky-white in appearance, is opaque, and has a rough surface.[10,14] Such material can be highly polycrystalline, as indicated by a very broad (0002) peak in an x-ray rocking-curve measurement. In contrast, specular, thick GaN films can be obtained after optimizing the buffer deposition conditions (thickness, growth temperature, growth rate, and ramp duration), and the conditions (temperature, V/III ratio) for growth at the higher temperature.[13]

The critical importance of the buffer layer is further illustrated in Table I, which lists the FWHM of the (0002) XRD peak for 5-μm-thick GaN epilayers grown on buffer layers deposited at different rates. These data show a direct correlation between the crystallinity of the buffer layer and the crystallinity of 5-μm GaN films grown on top of these buffer layers.

To understand the full implications of the data of Table I, it is important that we clarify the origin of FWHM broadening for XRD peaks. High-resolution XRD can discriminate between broadening of an x-ray peak due to strain (a range of crystal plane spacing) and broadening due to mosaicity (a range of misorientation for a particular set of crystal planes). In the context of GaN, this distinction is vital as it reveals important information about the microstructure. Figures 8a and 8b plot the separate contributions to broadening made by mosaicity and strain for the GaN (0002) XRD peak, and for epilayers of different thicknesses. Mosaicity broadening is dominant throughout the complete range of layer thickness. Also the mosaicity broadening decreases with increasing layer thickness. Thus the trend observed during buffer-layer annealing (Figure 7), where the relative tilt of the [0001] crystal directions of the different islands decreases as the growth proceeds, continues to operate even after several microns of GaN growth have occurred. Strain broadening (Figure 8b) for these layers remains small at between 18 and 33 arc seconds, indicating a high crystal quality within each island or crystal grain. Thus the GaN epilayer appears to be well-relaxed, in agreement with the observations by Ponce et al.[15] Furthermore the constant value of strain broadening demonstrated by Figure 8b is also expected from the work of Qian et al.[8] They proposed that the lack of an inclined slip plane in GaN grown on [0001] sapphire will preclude the elimination of dislocations, and the dislocation density will therefore remain unchanged as the layer thickness increases.

Table I: Full Width Half Maximum (FWHM) of the GaN Epilyer (0002) X-Ray-Diffraction (XRD) Peak for Several Values of Buffer-Layer Deposition Rate.

Buffer Growth Rate (Å/min)	FWHM of 5-μm GaN Epilayer (0002) XRD Peak (arc sec)
30	180
70	250
90	320

Similar results are found for the asymmetric (11$\bar{2}$2) reflections shown in Figures 9 and 10. Figure 9 plots strain broadening (vertical axis) versus mosaicity broadening (horizontal axis) for a 6-μm GaN epilayer in a "reciprocal space map." Again mosaicity is the dominant cause of broadening, having a FWHM value (width at the "max/2" contour) of 0.14 degrees compared to the strain-broadening value of 0.03 degrees for this (11$\bar{2}$2) reflection. This means that the polycrystalline grains are twisted with respect to one another as well as tilted.

The strain-broadening contribution shown in Figure 9 is higher (~100 arcseconds) than the value of 18 arcseconds observed for the (0002) planes. This difference is expected as the strain broadening associated with the inclined (11$\bar{2}$2) planes will be influenced by all of the dislocations within the epilayer. Strain broadening associated with the (0001) planes will not be influenced by the [0001] oriented edge dislocations (which are by far the most numerous) as their Burgers

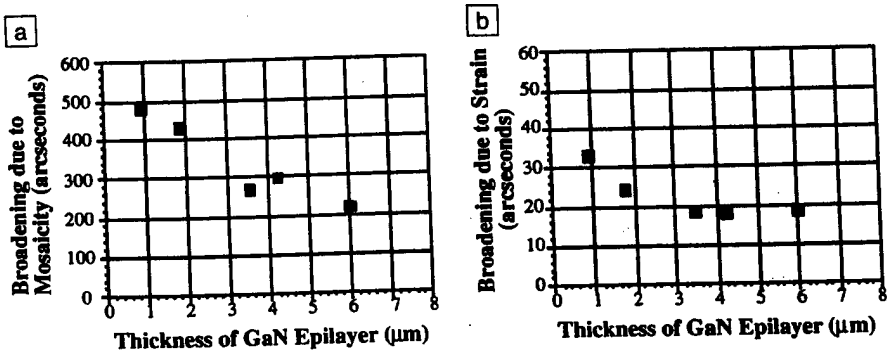


Figure 8. Contributions to broadening of the (0002) XRD peak made by (a) mosaicity and (b) strain.

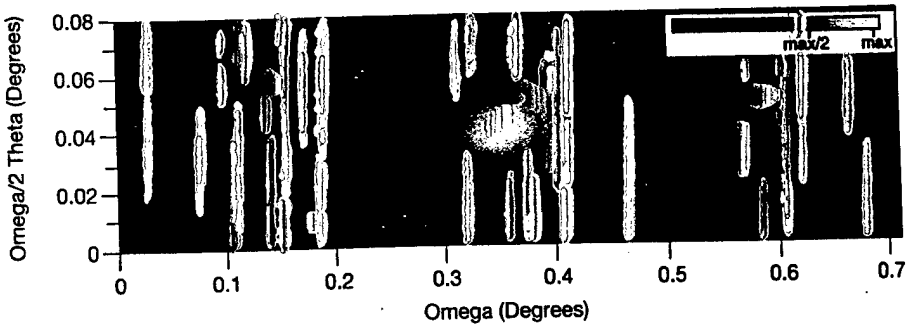


Figure 9. Reciprocal space map (strain versus mosaicity) for (11$\bar{2}$2) asymmetric reflection.

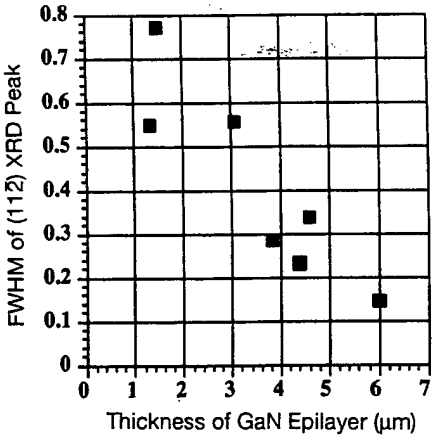


Figure 10. Variation of full width half maximum with layer thickness for asymmetric (11$\bar{2}$2) reflection.

vector lies in the basal (0001) plane.[16]

Figure 10 plots the FWHM value of the peak intensity (mosaicity) for the (11$\bar{2}$2) asymmetric reflection as a function of layer thickness. Again we observe a decreasing mosaicity with increasing layer thickness. Taken in conjunction with Figure 8a, this means that as the layer thickness increases the range of "tilt" and "twist" in the polycrystals decreases—that is, the crystal grains become more closely aligned as the film thickness increases.

Microstructure Model

From these measurements we conclude that the initial stage of GaN growth on sapphire is described by the original model credited to Hiramatsu et al.,[5] where the buffer layer nucleates as discrete "islands" or columns. This behavior is essentially Volmer-Weber growth (as expected because of the large lattice mismatch between GaN and sapphire), but in a temperature regime where surface kinetics also play an important role. X-ray-diffraction measurements show that as growth proceeds, these polycrystalline islands or grains grow and a preferred orientation emerges among them. For thick GaN layers, large values of mosaicity are measured for the symmetric [0001] and asymmetric (11$\bar{2}$2) reflections, indicating that even though the polycrystals have coalesced and a continuous specular film has been obtained, the film remains an **ordered** polycrystal and does not become a single crystal (Figure 11). The relative "tilt" and "twist" between these polycrystals decreases as the layer thickness increases, showing that the film continues to evolve toward a more ordered structure as growth proceeds. The grain boundaries remain the primary defected regions of the epilayer. When the dislocation density has stabilized (after several thousands of angstroms of growth[5]), the remaining dislocations are mainly clustered at the grain boundaries between polycrystals.[8] The small value of strain broadening observed for the (0002) and (11$\bar{2}$2) reflections indicates that within each GaN polycrystal grain, the crystal quality is high.

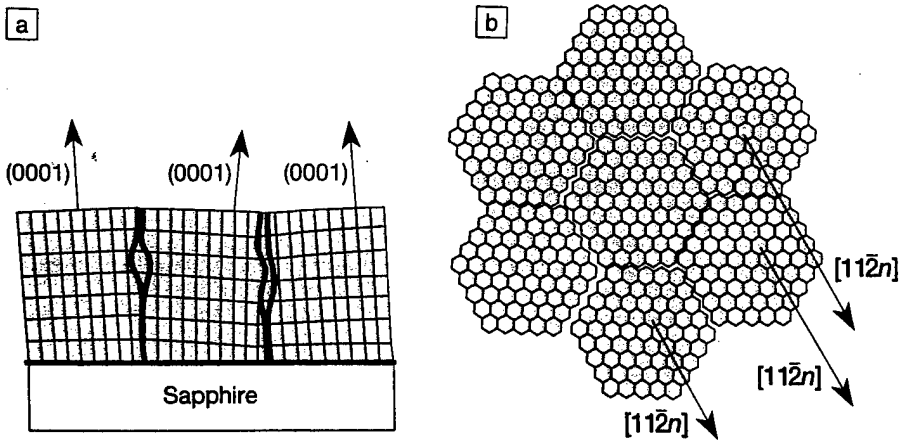


Figure 11. Ordered polycrystalline microstructure of GaN on sapphire. (a) Side view showing relative "tilt" of (0001) directions between crystal grains. (b) Plan view showing relative "twist" of polycrystal (11$\bar{2}$n) directions. Dislocations mainly originate at the grain boundaries.

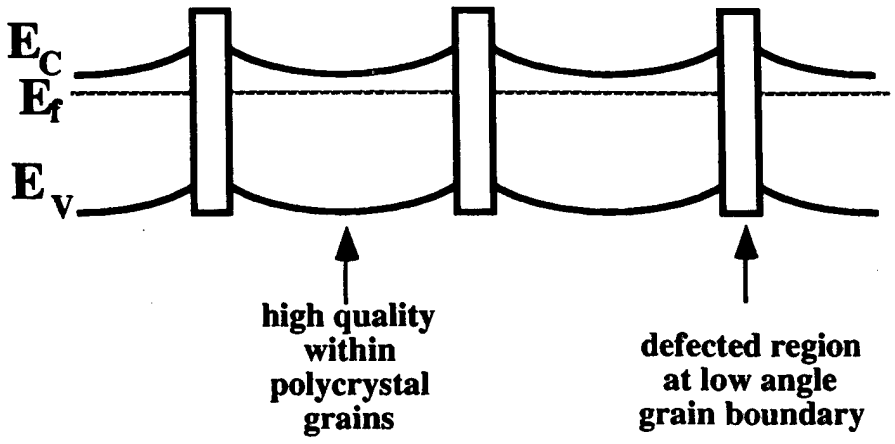


Figure 12. The band structure of n-type polysilicon.

The Influence of GaN Microstructure on Optical and Electrical Properties

We have determined that GaN on sapphire is an ordered polycrystal composed of high-quality polycrystalline grains that are misoriented (tilted and twisted) with respect to each other. The grain boundaries are the primary locations for dislocations and other defects. Armed with this knowledge, we can address our initial question: "Are dislocations benign in GaN?" While the following ideas are speculative and require further verification, we offer them to the community as a basis for discussion.

To understand the unusual optical and electrical properties of GaN on sapphire, we believe it is instructive to examine a more well-known polycrystal, polysilicon. In poly-Si, the grain boundary can be modeled[17] as a thin region of lower conductivity that contains localized energy states and deforms the band structure as shown in Figure 12. Such band-bending will tend to localize electrons within the crystallites and away from the grain boundaries. If the polycrystalline structure of GaN were to ex-

hibit a similar band structure, then the localization of free electrons (coupled with the short diffusion length for holes) would tend to localize recombination events within the polycrystal grains—that is, in the high-quality region of the crystal. Spatially resolved cathodoluminescence measurements by Ponce et al.[18] suggest that part of the yellow (2.2 eV) emission is associated with the grain-boundary regions of the GaN polycrystal. Furthermore they show a significantly reduced intensity of the yellow emission in a sample that has larger polycrystal grains, indicating that there is some localization of carriers within the polycrystal grains. The localization of carriers within the grains and away from the main clusters of dislocations, which are at the grain boundaries, might explain the insensitivity of recombination events to dislocations in GaN.

Continuing this speculation, we would anticipate a significant difference between vertical carrier transport, where an uninterrupted vertical conduction path exists within single high-quality grains, and lateral carrier transport, where carriers must traverse grain boundaries either by "hopping" between localized states or by tunneling (Figure 13).

At higher doping levels, the width of the depletion regions associated with band-bending will be reduced and lateral transport across the grain boundary will be easier. In poly-Si this effect appears as a mobility "edge," where the carrier mobility rapidly increases at some critical value of doping[16] at which the effect of the grain-boundary depletion regions becomes minimal. Figures 14a and 14b plot the resistivity and mobility of GaN, respectively, each as a function of doping concentration. Gallium nitride also exhibits a strong mobility "edge," with the mobility decreasing rapidly below a doping concentration of 10^{17} cm^{-3}, lending support to the suggestion that the band structure of polycrystalline GaN is similar to that of poly-Si.

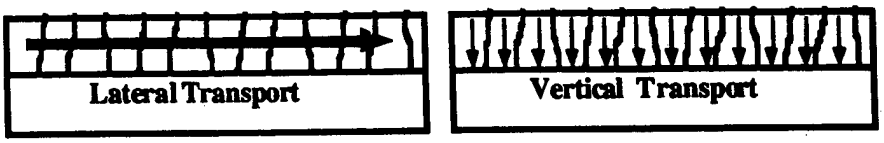


Figure 13. Vertical and lateral carrier transport within polycrystalline GaN.

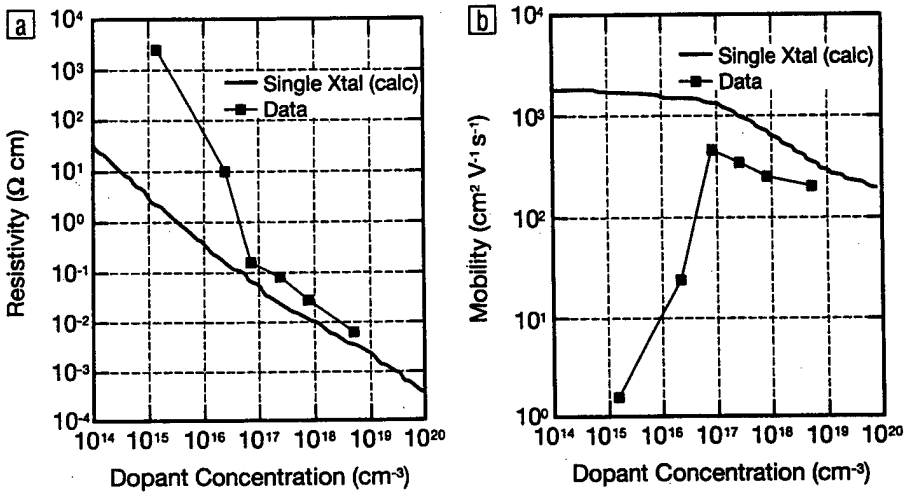


Figure 14. Plots of n-type GaN (a) resistivity and (b) mobility plots as a function of doping concentration.

Conclusions

We have shown that GaN on sapphire adopts a Volmer-Weber or "island" growth habit from the outset due to the large mismatch strain between these materials. This reorganization of the deposited material is generically similar to other ordering processes, in that it results from the system reorganizing to minimize the total free energy. As growth proceeds, these polycrystalline islands grow in size and become more closely aligned. However the final (thick) epilayer remains an ordered poycrystalline material composed of high-quality polycrystalline grains that are misoriented (tilted and twisted) with respect to each other. We suggest that the band structure of polycrystalline GaN may be similar to that of polysilicon. This could explain the high efficiency of GaN LEDs despite the presence of a significant dislocation density, because band-bending would localize carrier recombination away from grain-boundary defected regions. The observation of a mobility "edge" in GaN lends further support to this suggestion. Understanding the detailed role of microstructure in controlling the optical and electrical properties of GaN remains a critical issue to the advance of GaN as a new semiconductor for optoelectronic and electronic applications.

References

1. S. Nakamura, M. Senoh, N. Iwasa, S. Nagahama, T. Yamada, and T. Mukai, *Jpn. J. Appl. Phys.* **34** (1995) p. L1332.
2. S. Nakamura, M. Senoh, S. Nagahama, N. Iwasa, T. Yamada, T. Matsushita, and Y. Sugimoto, presented at Symposium N, Materials Research Society, Boston, December 2–6, 1996.
3. H. Huff and F. Shimura, *Solid State Technol.*, (1983) p. 103.
4. P. Petroff and R.L. Hartman, *Appl. Phys. Lett.* **25** (1973) p. 226.
5. K. Hiramatsu, S. Itoh, H. Amano, I. Akasaki, N. Kuwano, T. Shiraishi, and K. Oki, *J. Cryst. Growth* **115** (1991) p. 628.
6. R.C. Powell, N.E. Lee, Y.W. Kim, and K.E. Greene, *J. Appl. Phys.* **73** (1993) p. 189.
7. S. Chadda, M. Pelcynski, K. Malloy, and S.D. Hersee, in *Growth, Processing, and Characterization of Semiconductor Heterostructures*, edited by G. Gumbs, S. Luryi, B. Weiss, and G.W. Wicks (Mater. Res. Soc. Symp. Proc. **326**, Pittsburgh, 1994) p. 353.
8. W. Qian, M. Skowronski, M. De Graef, K. Doverspike, L.B. Rowland, and D.K. Gaskill, *Appl. Phys. Lett.* **66** (1995) p. 1252.
9. F.A. Ponce, B.S. Krusor, J.S. Major, Jr., W.E. Plano, and D.F. Welch, *ibid.* **67** (1995) p. 410.
10. S. Nakamura, *Jpn. J. Appl. Phys.* **30** (1991) p. L1705.
11. R.W. Vook, *SPIE* **346** (1982).
12. For example, see M. Ohring, *The Materials Science of Thin Films* (Academic Press, Inc., San Diego, 1992).
13. A.E. Wickenden, D.K. Wickenden, and T.J. Kistenmacher, *J. Appl. Phys.* **75** (1994) p. 5367.
14. S.D. Hersee, J. Ramer, K. Zheng, C.F. Kranenberg, K. Malloy, M. Banas, and M. Goorsky, *J. Electron. Mater.* **24** (1995) p. 1519.
15. F. Ponce, Workshop on Wide-Gap Nitrides (St. Louis, October, 1994).
16. B. Heying, X.H. Wu, S. Keller, Y. Li, D. Kapolnek, B.P. Keller, S.P. DenBaars, and J.S. Speck, *Appl. Phys. Lett.* **68** (1996) p. 643.
17. D.M. Kim, A.N. Khondker, S.S. Ahmed, and R.R. Shah, *IEEE Trans. Electron Devices* **ED-31** (1984) p. 480.
18. F.A. Ponce, D.P. Bour, W. Gotz, and P.J. Wright, *Appl. Phys. Lett.* **68** (1996) p. 57. □

Journal of Electronic Materials, Vol. 26, No. 10, 1997

Stability and Interface Abruptness of $In_xGa_{1-x}N/In_yGa_{1-y}N$ Multiple Quantum Well Structures Grown by OMVPE

J.C. RAMER, D. ZUBIA, G. LIU, and S.D. HERSEE

Center for High Technology Materials, University of New Mexico, Albuquerque, NM 87106

The abruptness of hetero-interfaces in InGaN multiple quantum well structures is shown to degrade when a high temperature growth follows growth of the multiple quantum well (MQW) region, as is generally required for the growth of full device structures. We have analyzed MQW samples both with and without high temperature GaN "cap" layers, using x-ray diffraction (XRD), grazing incidence x-ray reflection (GIXR), and photoluminescence. While all of these techniques indicate a degradation of the MQW structure when it is followed by growth at high temperature, GIXR is shown to be especially sensitive to changes of heterointerface abruptness. GIXR measurements indicate that the heterojunctions are less abrupt in samples that have high temperature cap layers, as compared to samples with no cap layer. Furthermore, the degree of roughening is found to increase with the duration of growth of the high temperature cap layer. The degradation of the heterointerfaces is also accompanied by a reduction in the intensity of satellite peaks in the x-ray diffraction spectrum.

Key words: Grazing incidence x-ray reflectivity (GIXR), InGaN quantum wells, metalorganic chemical vapor deposition (MOCVD), x-ray diffraction (XRD)

INTRODUCTION

During the last year, Nakamura et al. have announced the continuous wave (CW) operation of electrically injected, III-nitride based lasers.[1] The active region of these CW devices and of earlier pulsed laser diodes[2-4] consists of an $In_{0.20}Ga_{0.80}N/In_{0.05}Ga_{0.95}N$ multiple quantum well (MQW) structure containing between three and ten quantum wells. For these lasers and for MQW devices in general, it is necessary to grow AlGaN and GaN at high temperature subsequent to the growth of the MQW region. The stability of the MQW InGaN layers during this high temperature growth is therefore expected to be an important factor in the performance and reproducibility of these devices. Thompson et al.[5] have reported an apparent instability when very thin (~25Å) InGaN single wells were exposed to the metalorganic chemical vapor deposition (MOCVD) reaction chamber ambient during ramping to the higher growth temperature. This work examines the stability of InGaN MQW structures and in particular interface abruptness when high temperature cap layers of varying duration are grown after the MQW region.

(Received March 26, 1997; accepted May 1, 1997)

EXPERIMENTAL PROCEDURES

Samples used in this study were grown at low pressure (100 Torr), in a horizontal metalorganic vapor phase epitaxy (MOVPE) reactor. Purified H_2 and N_2 were used as carrier gases along with trimethylgallium [$(CH_3)_3Ga$], trimethylindium [$(CH_3)_3In$], trimethylaluminum [$(CH_3)_3Al$], and ammonia [NH_3] source gases. Nominally [0001] oriented two inch sapphire wafers (Union Carbide) were used and these were cleaned ex-situ by a 5 min wash in a warm solution of $HCl:H_2O_2:H_2O$ 1:1:4. After loading, the samples were further cleaned by a 10 min bake under hydrogen at 1100°C. Growth was initiated at 480°C by deposition of a 250Å thick GaN buffer layer. The reactor temperature was then raised to 1040°C where a 3 μm thick undoped GaN layer was grown. This served as the starting point for all of the

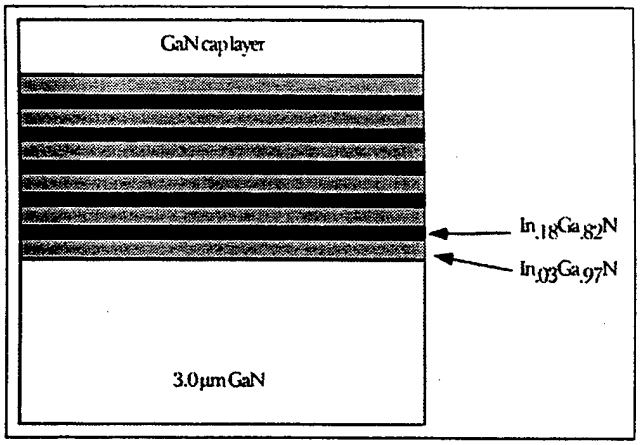


Fig. 1. Example layer structure for capped InGaN MQW samples. Uncapped samples are terminated with a $In_{0.03}Ga_{0.97}N$ layer.

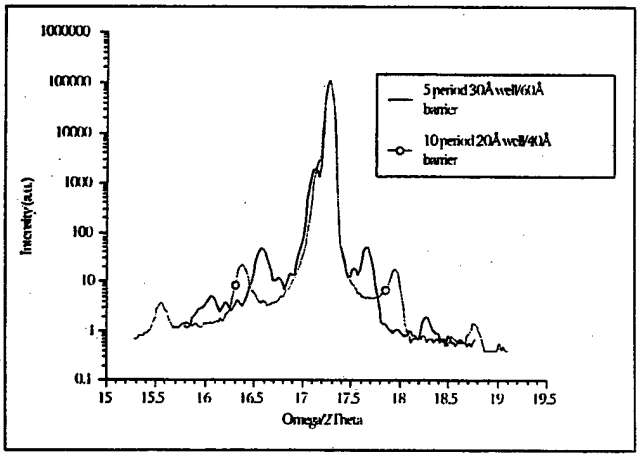


Fig. 2. (002) ω/2θ x-ray diffraction spectra for uncapped InGaN MQW samples.

MQWstructures grown in this study. The InGaN layers comprising the MQW region were grown at lower reactor temperatures, between 750 to 840°C. In these growths, the InN mole fraction was controlled by the growth temperature and the flow rates of TMIn and TMGa. The MQW region consisted of $In_{0.03}Ga_{0.97}N$ barrier layers and $In_{0.18}Ga_{0.32}N$ well layers that were grown at a rate of 25 and 10Å/min, respectively. (Growth rates were extrapolated from calibrations on thicker InGaN layers, and were consistent with the actual thickness of the layers in the MQW samples, as later determined by grazing incidence x-ray reflectivity (GIXR) measurements.)

A series of MQW samples were grown, some with and some without high temperature growth of GaN after the MQW region (Fig. 1). The samples with no high temperature cap layer were simply terminated with a $In_{0.03}Ga_{0.97}N$ barrier layer and cooled under NH_3 and N_2. The samples with cap layers, were rapidly ramped up in temperature to 1040°C, and held at this temperature for several minutes while growing a thin GaN cap layer. The thickness of the GaN cap layer was kept below 1000Å so that the GIXR measurement would be sensitive to the underlying interfaces in the InGaN MQW.

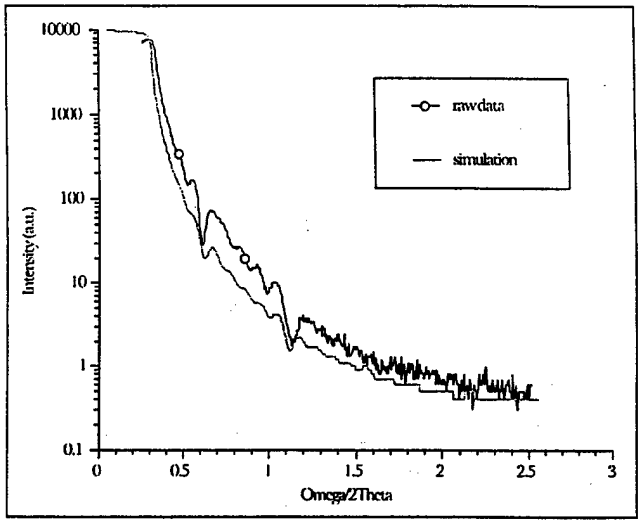


Fig. 3. Grazing incidence x-ray reflectivity spectra for an uncapped five-period 30Å well/60Å barrier InGaN MQW structure. The simulation shown assumes ideally abrupt interfaces and well/barrier dimensions of 28 and 62Å, respectively.

X-ray diffraction (XRD) and GIXR data were collected on a Philips MRD diffractometer with the Bartels monochromator in the 4 bounce (220) geometry. A 100 μm detector slit was used for the GIXR scans in order to minimize the effect of the diffuse scatter and sample curvature on the collected data.

Analytical simulations of the GIXR data were performed with the commercial software package "PC-GIXA" (Philips Analytical X-ray Division). This simulation is based on Maxwell's equations as applied to reflection and transmission from planar interfaces. The simulation is valid for any material, regardless of its crystal structure or microstructural quality, and relies only on the index of refraction and thickness of the various materials within the structure. The simulation does not account for curvature of the sample, which for GaN on sapphire samples is a significant issue. For example, the radius of curvature of a 3.0 μm thick undoped GaN on sapphire sample is 15–18 m (as measured by XRD). The effects of sample curvature can be minimized by reducing the surface area examined during the GIXR measurement, however, the residual sample curvature was found to have a noticeable smoothing effect on the low angle features (just beyond the critical angle) of the GIXR data.

RESULTS

InGaN MQW Structures with No Cap Layer

ω/2θ x-ray diffraction scans were performed on two samples with the following InGaN MQW structures: Sample 1: five-period 30Å well/60Å barrier, and Sample 2: ten period 20Å well/40Å barrier. Both samples were grown on 3.0 μm thick GaN layers as described above. The XRD scans are shown in Fig. 2. The angular separation of adjacent satellite peaks is related to the period (D) of the superlattice structure by

$$D = (L_i - L_j)\lambda/[2\,(\mathrm{Sin}\,(\theta_i) - \mathrm{Sin}\,(\theta_j)] \qquad (1)$$

where, L_i and L_j are satellite diffraction order indices, and θ_i and θ_j correspond to the Bragg angles of satellite L_i and L_j. As shown in Fig. 2, a smaller superlattice period leads to a larger angular separation between satellite peaks. The superlattice periods calculated using Eq. (1), are 92Å for sample 1 (design value 90Å) and 58Å for sample 2 (design value 60Å), showing good agreement between designed and measured values. Close examination of Fig. 2 also reveals that on the five-period sample there are fringes between the satellite peaks. The periodicity of these finer fringes corresponds to the total thickness of the InGaN MQW region. Such fringes were not visible in the ten-period structure because the total thickness of the MQW region was too large (and therefore the fringe spacing was too small) to be able to be resolved with the detector resolution used in these scans.

GIXR was also used to characterize these samples. This technique, as the name implies, uses a grazing incidence x-ray beam to study the specular reflectivity of the structure as a function of incident angle, for angles above the critical angle for total external reflection. GIXR is analogous to optical reflectivity and interference between reflected beams modulates the reflected signal and can easily be related to layer thicknesses within the structure.[7] The strength of these spectral features is proportional to the difference in the index of refraction (at x-ray wavelength) at the heterointerfaces, which for the $In_{0.18}Ga_{0.82}N$ quantum wells and $In_{0.03}Ga_{0.97}N$ barrier layers is quite small. However, these features are distinguishable in our GIXR plots. Because of its grazing incidence and short wavelength, GIXR is also extremely sensitive to surface and heterointerface roughness.

The GIXR spectrum for sample 1 (five-period 30Å well/60Å barrier, no cap layer) is shown in Fig. 3. A simulated spectrum, assuming perfectly abrupt heterointerfaces (0.0Å root mean square [RMS] roughness) is also shown. The agreement between the measured and simulated spectra is excellent indicating that the heterointerfaces are highly abrupt in this sample. Furthermore, from the periodicity and location of the mimina occurring at 0.55 and 1.1 degrees in this spectrum we confirm that the quantum well and barrier layer thicknesses are correct to within one monolayer.

The room temperature photoluminescence (PL) is shown in Fig. 4 for samples 1 and 2. The full width at half maximum (FWHM) of the band edge peak for sample #1 and #2 are 15 and 14 nm, respectively. The shorter bandedge PL wavelength for the ten-period 20Å well/40Å barrier sample (#2) is assumed to be due to size-quantization effects in the very thin wells used for this sample.

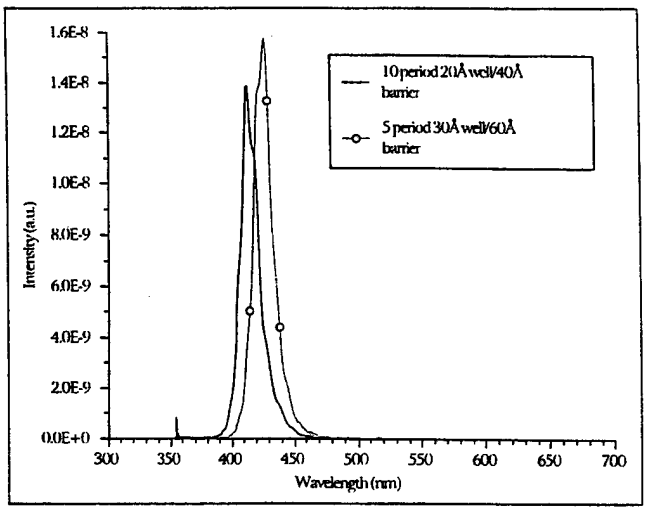


Fig. 4. Room temperature PL from two uncapped InGaN MQW samples. Peak positions and FWHM values for the samples are 412, 14, 426, and 15 nm, respectively.

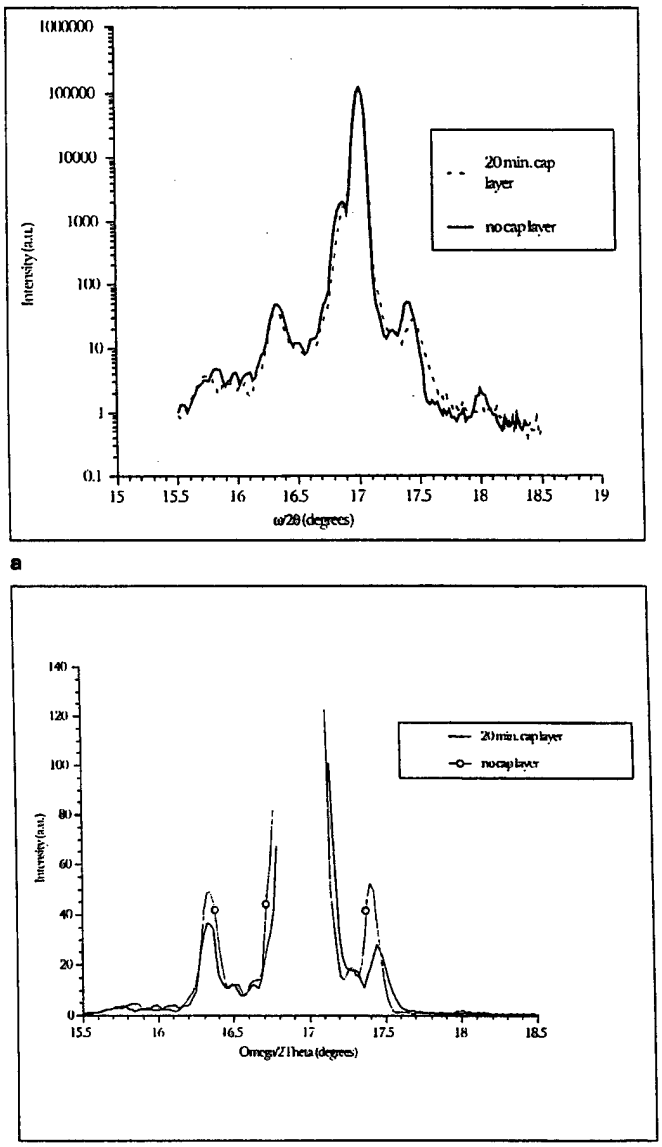
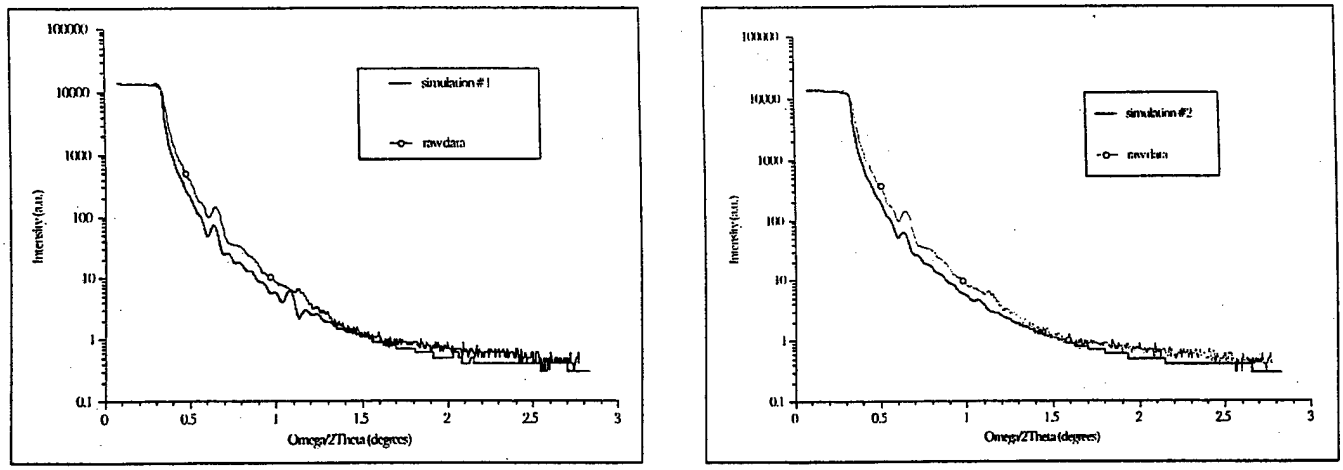


Fig. 5. (a) (002) ω/2θ x-ray diffraction spectra from nominally identical InGaN MQW structures with different cap layers, and (b) (002) ω/2θ x-ray diffraction spectra for the 20 min cap sample and the uncapped sample shown on a linear scale.



a b

Fig. 6. (a) GIXR spectrum from a five-period 30Å well/60Å barrier InGaN MQW sample with 4 min GaN cap layer grown at 1040°C. Simulation #1 is computed assuming perfect interfaces, and (b) GIXR spectrum from sample described in Fig. 6a with a simulation calculated assuming 12Å RMS roughness at each interface in the InGaN MQW region. Such a simulation is in much closer agreement with the actual data than the "ideal" simulation of Fig. 6a.

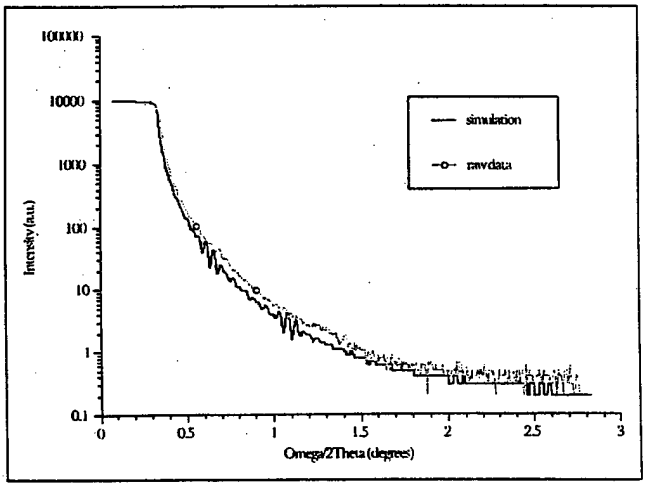


Fig. 7. GIXR spectrum for a five-period 30Å well/60Å barrier InGaN MQW sample with 20 min GaN cap growth at 1040°C. Along with the measured data, a simulation is included that assumes all ideal interfaces.

InGaN MQW Structures with High Temperature GaN Cap Layers

Samples containing the five-period 30Å well/60Å barrier MQW region were also capped with a GaN layer grown at 1040°C. The thickness of the GaN cap layer was kept below 1000Å in order to maximize the sensitivity of the GIXR analysis to the underlying periodic InGaN structure. After the growth of the last InGaN layer in the structure, the growth was stopped for 70 s while the reactor temperature was raised to the GaN growth temperature. For sample #4, the GaN growth duration was 20 min, giving 800Å of GaN. The $\omega/2\theta$ XRD scan from this capped sample is compared to the uncapped sample (#1) in Figs. 5a and 5b. A decrease in the satellite peak intensities relative to the uncapped sample is evident especially on the higher angle side of the XRD spectrum.

Measured and simulated GIXR spectra are shown for the samples capped for 4 min and 20 min in Figs. 6a, 6b, and 7. In Fig. 6b, simulation (II) assumes a 12Å RMS roughness at each of the MQW interfaces, and correctly washes out the higher angle fringes while still agreeing for the lower angle portion of the scan range. Simulation (I) (Fig. 6a) assumes zero roughness at each interface in the sample. For sample #4 as shown in Fig. 7, there was too much roughening to allow accurate simulation of the GIXR spectrum. A simulation based on perfect (0Å RMS roughness) is shown in Fig. 7 as a reference.

Note also that the top surface of each sample, the GaN cap layer, must be simulated using a roughness of 3–4Å RMS in order to maintain agreement with the high angle fall off of the reflectivity. The slope of the high angle portion of the reflectivity scan also has a significant dependence on the size of the detector aperture used during the data acquisition, indicating that there is significant diffuse scatter from the surface of the sample for these capped MQW structures.

DISCUSSION OF RESULTS

The results presented above show that uncapped InGaN MQW structures can be grown with good control of layer thickness and composition and that they have abrupt heterointerfaces. When these samples are ramped to higher temperature and capped with a GaN layer, the GIXR data indicates that the heterointerfaces become rougher. Furthermore, XRD measurements indicate that the compositional profile of the MQW region has changed, i.e., that the MQW region is unstable at high temperature.

Recent analyses using high resolution x-ray diffraction (HRXRD) on InGaN/GaN MQW structures,[6] having no cap layer and containing InN mole fractions of 6–9%, has shown these structures to be coherently strained. No evidence of strain induced relaxation was evident as shown by reciprocal space maps of asymmetric reflections. We are attempting to repeat these measurements for the samples grown here with

GaN cap layers. As yet, we can find no evidence that strain induced creation of mismatch dislocations is causing the roughening observed in these MQW structures.

Recent work by Piner[8] et al. shows that the presence of hydrogen during the MOVPE growth of InGaN, strongly reduces the mole fraction of InN that can be incorporated into an InGaN film. While the physical nature of this effect is as yet undetermined, we believe that the surface roughening and instability of the InGaN MQW region described here may be caused by the same phenomenon as observed by Piner et al. A simple calculation adds weight to this hypothesis. From the activation of p-type doping in GaN (where approximately three microns of p-type GaN can be activated in a 20 min anneal at ~700°C), we can calculate a hydrogen diffusion coefficient of 7.5 E–11 cm^2/s. (This assumes the activation anneal is driving hydrogen out of the p-type layer.)

Using this diffusion coefficient, it would take less than 1 s (at 700°C) for hydrogen to diffuse completely through our MQW region (total thickness ~400Å). So whether the hydrogen is present during growth (as discussed by Piner et al.) or after the growth of the MQW region (as described here), it is reasonable to assume that the phenomenon observed by Piner et al. is occurring in both cases. Piner et al. showed that the InN mole fraction decreases with increasing hydrogen and with increasing temperature. As we ramp our MQW samples to higher temperature (under an NH_3/N_2 ambient), we therefore expect that the equilibrium value of In in the MQW region will fall and that we will lose indium from the sample surface. Segregation of indium to the sample surface and then into the vapor would typically result in the presence of liquid In on the surface. Equilibrium driven intermixing between indium and the MQW region could therefore account for the heterojunction roughening that we observe in the capped structures (indium would attempt to dissolve the MQW as the sample temperature was lowered. Close examination of the GIXR spectra reveals that an improved "fit" between the measured and simulated spectra is obtained when a higher roughness value is used for the surface GaN layer than would be expected for normal GaN on sapphire. This supports the above hypothesis that indium is segregating to the sample surface. Capping the MQW region with AlGaN before raising the reactor temperature, as in Refs. 1–4, would also be expected to reduce In segregation as the AlGaN chemical bonding is stronger than for GaN. We are currently analyzing MQW samples capped with AlGaN and preliminary XRD and GIXR results show an improved stability.

CONCLUSION

Using GIXR and XRD, we have observed significant interface degradation in InGaN MQW structures that have been capped by a higher temperature GaN growth. Using analytical GIXR simulation software, the acquired data is shown to be consistent with MQW interface and surface roughening of the sample. The degree of the interface degradation is shown to increase with time at high temperature. It is suggested that these results are consistent with indium segregation and that the phenomenon observed by Piner et al. may be also be in action here. Preliminary data using an AlGaN cap after the MQW region indicates a reduced roughening and needs to be investigated further.

REFERENCES

1. S. Nakamura, M. Senoh, S. Nagahama, N. Iwasa, T. Yamada, T. Matsushita, Y. Sugimoto and H. Kiyoku, *Appl. Phys. Lett.* 69 (20), 3034 (1996).
2. S. Nakamura, M. Senoh, S. Nagahama, N. Iwasa, T. Yamada, T. Matsushita, Y. Sugimoto and H. Kiyoku, *Appl. Phys. Lett.* 69 (10), 1477 (1996).
3. S. Nakamura, M. Senoh, S. Nagahama, N. Iwasa, T. Yamada, T. Matsushita, H. Kiyoku and Y. Sugimoto, *Appl. Phys. Lett.* 68 (23), 3269 (1996).
4. S. Nakamura, M. Senoh, S. Nagahama, N. Iwasa, T. Yamada, T. Matsushita, H. Kiyoku and Y. Sugimoto, *Appl. Phys. Lett.* 69 (15), 2105 (1996).
5. A.G.Thompson, M. Schurman, Z.C. Feng, R.F. Karlicek, T. Salagaj, C.A. Tran and R.A. Stall, *J. Nitride Semiconductor Research* (1), Article 24 (1996).
6. W. Li, P. Bergmen, I. Ivanov, W. Ni, H. Amano and I. Akasa, *Appl. Phys. Lett.* 69 (22) 3390 (1996).
7. D.K. Bowen and B.K. Tanner, *Nanotechnology* 4, 175 (1993).
8. E.L. Piner, M.K. Behbehani, N.A. El-Masry, F.G. McIntosh, J.C. Roberts, K.S. Boutros and S.M. Bedair, *Appl. Phys. Lett.* 70 (4) 461 (1997).